Dik Farhall

AFFDL–TR–78–151

RECOVERY SYSTEMS DESIGN GUIDE

IRVIN INDUSTRIES INC.
CALIFORNIA DIVISION
15001 SOUTH FIGUEROA STREET
GARDENA, CALIFORNIA 90248

DECEMBER 1978

TECHNICAL REPORT AFFDL–TR–78–151
FINAL REPORT FOR PERIOD JUNE 1975 TO JUNE 1978

Approved for public release; distribution unlimited

AIR FORCE FLIGHT DYNAMICS LABORATORY
AIR FORCE WRIGHT AERONAUTICAL LABORATORIES
AIR FORCE SYSTEMS COMMAND
WRIGHT–PATTERSON AIR FORCE BASE, OHIO 45433

NOTICE

When Government drawings, specifications, or other data are used for any purpose other than in connection with a definitely related Government procurement operation, the United States Government thereby incurs no responsibility nor any obligation whatsoever; and the fact that the Government may have formulated, furnished, or in any way supplied the said drawings, specifications, or other data, is not to be regarded by implication or otherwise as in any manner licensing the holder or any other person or corporation, or conveying any rights or permission to manufacture, use, or sell any patented invention that may in any way be related thereto.

This report has been reviewed by the Information Office (IO) and is releasable to the National Technical Information Service (NTIS). At NTIS, it will be available to the general public, including foreign nations.

This technical report has been reviewed and is approved for publication.

JAMES H. DEWEESE
Project Engineer
Recovery & Crew Station Branch
Vehicle Equipment Division

EDWIN R. SCHULTZ, Chief
Recovery & Crew Station Branch
Vehicle Equipment Division

FOR THE COMMANDER

AMBROSE B. NUTT
Director
Vehicle Equipment Division

Copies of this report should not be returned unless return is required by security considerations, contractual obligations, or notice on a specific document.

UNCLASSIFIED

SECURITY CLASSIFICATION OF THIS PAGE *(When Data Entered)*

REPORT DOCUMENTATION PAGE		READ INSTRUCTIONS BEFORE COMPLETING FORM
1. REPORT NUMBER AFFDL-TR-78-151	2. GOVT ACCESSION NO.	3. RECIPIENT'S CATALOG NUMBER
4. TITLE *(and Subtitle)* RECOVERY SYSTEM DESIGN GUIDE		5. TYPE OF REPORT & PERIOD COVERED Final Technical Report 1 June 1975 – 30 June 1978
		6. PERFORMING ORG. REPORT NUMBER
7. AUTHOR*(s)* E. G. Ewing H. W. Bixby T. W. Knacke		8. CONTRACT OR GRANT NUMBER*(s)* F33616-75-C-3081
9. PERFORMING ORGANIZATION NAME AND ADDRESS Irvin Industries Inc. California Division 15001 South Figueroa Street Gardena, California 90248		10. PROGRAM ELEMENT, PROJECT, TASK AREA & WORK UNIT NUMBERS Program Element 62201F Project 2402, Task 240203 Work Unit 24020310
11. CONTROLLING OFFICE NAME AND ADDRESS Air Force Flight Dynamics Laboratory AF Wright Aeronautical Laboratories, AFSC Wright-Patterson Air Force Base, Ohio 45433		12. REPORT DATE December 1978
		13. NUMBER OF PAGES 458
14. MONITORING AGENCY NAME & ADDRESS*(if different from Controlling Office)*		15. SECURITY CLASS. *(of this report)* Unclassified
		15a. DECLASSIFICATION/DOWNGRADING SCHEDULE

16. DISTRIBUTION STATEMENT *(of this Report)*

Approved for public release; distribution unlimited.

17. DISTRIBUTION STATEMENT *(of the abstract entered in Block 20, if different from Report)*

18. SUPPLEMENTARY NOTES

19. KEY WORDS *(Continue on reverse side if necessary and identify by block number)*

Parachutes
Recovery
Air Drop
Deployable Aerodynamic Decelerators
Impact Attenuation
Handbook

20. ABSTRACT *(Continue on reverse side if necessary and identify by block number)*

This document serves as the third revision to the USAF Parachute Handbook which was first published in 1951. The data and information represent the current state of the art relative to recovery system design and development. The initial chapters describe representative recovery applications, components, subsystems, material, manufacture and testing. The final chapters provide empirical data and analytical methods useful for predicting performance and presenting a definitive design of selected components into a reliable recovery system.

DD FORM 1 JAN 73 1473 EDITION OF 1 NOV 65 IS OBSOLETE

UNCLASSIFIED

SECURITY CLASSIFICATION OF THIS PAGE *(When Data Entered)*

FOREWORD

This handbook was first published in March 1951 as the United States Air Force Parachute Handbook intended to supply the practicing engineer and others with a reference work which was authoritative in character and which covered the field of design and construction of parachutes, test equipment and test methods associated with parachute development. By December 1956, sufficient new data had been accumulated to revise the original handbook to an expanded second edition. In June 1963, a second revision[382] was published which further broadened the content and technical scope, as reflected by its title: Performance and Design Criteria for Deployable Aerodynamic Decelerators.

This third revision is titled Recovery Systems Design Guide, based on the recognition that other systems beside decelerators are increasingly involved which affect the overall process of recovery system design and component selection, and for which technical data have been gathered pertaining to their application, design, construction, and testing.

The effort required for this revision was performed during the period 1 June 1975 to 30 June 1978. The report was submitted by Irvin Industries Inc., California Division, for publication in September 1978.

This revision was accomplished under Contract No. F33615-75-C-3081, Project 2402, Task 240203, for the Air Force Flight Dynamics Laboratory, Wright-Patterson Air Force Base, Ohio. The Air Force Contract Managers for the project were Mr. R. H. Walker and Mr. J. H. DeWeese, (AFFDL/FER).

Principal authors contracted by Irvin Industries Inc. for this revision were Mr. E. G. Ewing, Mr. H. W. Bixby, and Mr. T. W. Knacke. Important contributions were also made by numerous individuals from various U.S. Air Force, Navy and Army agencies as well as NASA and private industry in reviewing the revised material.

TABLE OF CONTENTS

CHAPTER		PAGE
	INTRODUCTION	xxxiii
1	APPLICATIONS	2
	VEHICLE RECOVERY	2
	Recovery of Target Drones and Remotely Piloted Vehicles	2
	Missile Recovery	5
	Sounding Rockets and Reentry Vehicles	5
	Spacecraft Recovery	6
	Booster Recovery	18
	EMERGENCY RECOVERY	21
	Requirements	22
	Personnel Emergency Parachute Types	23
	Bailout	27
	Ejection Seats	27
	Tractor Rocket Escape System	29
	Encapsulated Seats and Aircraft Crew Modules	30
	AIRDROP OF MATERIAL AND PERSONNEL	35
	Airdrop Aircraft	35
	Airdrop of Material	37
	Airdrop of Personnel	46
	AIRCRAFT DECELERATION AND SPIN RECOVERY	49
	Landing Deceleration (Drag) Parachutes	49
	Landing Approach Parachutes	53
	Spin Recovery Parachutes	53
	ORDNANCE	56
	Bomb Deceleration	56
	Torpedo and Mine Deceleration	58
	Parachutes for Radar Targets, Flares and ECM Jammers	58
	Sonar Buoy Deceleration	59
	AERIAL PICKUP	60
	Air-to-Air Retrieval Systems	60
	Surface-to-Air Pickup	66
	SPECIAL USES	66
	Deceleration of Surface Vehicles	66
	Sport Parachutes	67
	Smoke Jumping	68
	Miscellaneous Systems	69

TABLE OF CONTENTS (Continued)

CHAPTER		PAGE
2	DEPLOYABLE AERODYNAMIC DECELERATORS	73
	DECELERATOR CHARACTERISTICS	73
	PARACHUTES	78
	Canopy Geometry	78
	Solid Cloth Parachutes	82
	Slotted Canopy Parachutes	95
	Rotating Parachutes	101
	Low Glide Parachutes	103
	Medium Glide Parachutes	103
	High Glide Parachutes	104
	DECELERATORS OTHER THAN PARACHUTES	109
	Balloon Types	109
	Rotor Blade Types	110
3	COMPONENTS AND SUBSYSTEMS	111
	CONTROL/ACTUATION SUBSYSTEMS	111
	Control/Actuation Subsystems	111
	Control Components	113
	Actuating Components	117
	DECELERATOR SUBSYSTEM	128
	Stowage and Deployment Components	128
	Suspension Networks Components	133
	Hardware	135
	TERMINATION PHASE SUBSYSTEM	138
	Impact Attenuation Subsystems	138
	Location Devices	139
	Flotation Devices	140
4	MATERIALS AND MANUFACTURE	143
	MATERIALS	143
	Textile Fibers and Yarns	143
	Recovery System Textiles	153
	Coated Fabrics and Films	178
	Crushables	179
	FABRICATION METHODS	181
	Layout, Marking, Cutting	181
	Machine Stitching	181

TABLE OF CONTENTS (Continued)

CHAPTER		PAGE
4 (Cont)	CONSTRUCTION DETAILS	185
	Cloth Structural Elements	185
	Line Connections	186
	QUALITY ASSURANCE	190
	Receiving Inspection	191
	In-Process Inspection	191
	Final Inspection	191
	FACTORY EQUIPMENT	191
	Hand Tools and Special Fixtures	191
	Sewing Machines	193
5	TESTING AND OPERATIONS	197
	TEST METHODS AND CAPABILITIES	198
	Free Flight Testing	198
	Captive or Tow Testing	204
	Support Testing	207
	TEST FACILITIES AND EQUIPMENT	213
	Instrumented Ranges	213
	High Speed Sled Tracks	217
	Wind Tunnels	218
	TEST VEHICLES	224
	Flight Test Vehicles	224
	Track Test Vehicles	227
	TEST INSTRUMENTATION	227
	Test Item Instrumentation	227
	Test Vehicle Instrumentation	231
	Range Instrumentation	232
6	PERFORMANCE	235
	DEPLOYMENT	235
	Deployment Sequences	235
	Deployment Forces (Snatch)	236
	Estimation of Maximum Differential Velocity	240
	Canopy Distributed Mass During Deployment	242
	Reduction of Snatch Forces	242
	High Onset Impact Shock	243

TABLE OF CONTENTS (Continued)

CHAPTER		PAGE
6 (Cont)	INFLATION	243
	The Inflation Process	243
	Canopy Area Growth During Inflation	247
	Inflation of Clustered Canopies	247
	Canopy Inflation Aids	248
	Critical Opening Speed "Squidding"	249
	Canopy Filling Time	250
	Opening Forces	253
	Clustered Parachute Opening Forces	261
	STEADY AERODYNAMIC FORCES	262
	Drag Coefficient	262
	Axial Force Coefficient	264
	Parachute Cluster Drag Coefficient	264
	Descent Characteristics	268
	Towing Body Wake Effects	277
	Effect of Design Parameters on Decelerator Drag	286
	DRAG AREA CONTROL	295
	Canopy Skirt Reefing	295
	Reefed High Glide Parachutes	296
	Multi-Stage Suspension Line Reefing	299
	Canopy Apex Retraction	299
	STABILITY	299
	Static Stability - Circular Canopy	299
	High Glide Canopy	301
	Tandem Parachute	303
	Dynamic Stability	307
	INTERNAL LOAD DISTRIBUTION	308
	Suspension Members	308
	Canopy	309
	Measurement of Canopy Pressure Distribution	309
	Measurement of Canopy Stress Distribution	311
	AERODYNAMIC HEATING	313
	Heat Resistant Drogue Structures	313
	TERMINAL PHASE	319
	Aerial Engagement	319
	Landing Dynamics	319
	Impact Attenuation	321

TABLE OF CONTENTS (Continued)

CHAPTER		PAGE
6 (Cont)	RELIABILITY	326
	Typical Malfunctions	326
	Causes of Unreliability	327
	System Reliability	330
7	ANALYTICAL METHODS	331
	FUNDAMENTAL RELATIONSHIPS	331
	Scaling Laws	331
	Similarity Criteria	332
	Scaling Laws for Other Planets	333
	PREDICTION OF SYSTEM MOTION	333
	System Motion During Decelerator Deployment	333
	System Motion During Deceleration Inflation	334
	Dynamic Interaction of Body and Decelerator	335
	PREDICTION OF DEPLOYMENT IMPACT LOADS	336
	Effective Spring Constant	338
	Calculation of Δv_{max}	339
	Effect of Distributed Decelerator Mass	339
	PREDICTION OF OPENING LOADS	340
	Load Factor Method	341
	Mass-Time Method	341
	Apparent Air Mass	342
	The Added Air Mass of a Parachute	344
	Apparent Moment of Inertia	345
	Six-Degrees of Freedom - Kinematic Model	345
	Canopy Mass-Momentum Method	346
	Spring Mass-Momentum Model	349
	Finite-Element Elastic Model	350
	Theoretical Approach	350
	Probable Accuracy of Opening Load Prediction Methods	351
	STRESS ANALYSIS	351
	Margin of Safety	351
	Prediction of Internal Loads	351
	Canopy of General Shape	352
	Circular Parachutes	352
	Solid Cloth Canopies	353
	The Inflation Energy Transfer Method	353
	The Pressure Strain Equilibrium Method	356
	Reefing Line Loads	365

TABLE OF CONTENTS (Continued)

CHAPTER		PAGE
7 (Cont)	High-Glide Parachute Structures	365
	AERODYNAMIC HEATING TEMPERATURES	367
	Total Energy Balance	367
	The Disk-Gap-Band Canopy in Low Density Environment	370
	The Ballute in the Wake of an Axi-Symmetric Body	370
	WAKE FLOW CHARACTERISTIC	373
	Subsonic Wake	373
	Supersonic Wake	375
	STABILITY	378
	Drogue-Body Systems	378
	Systems in Steady Descent	380
	Elastic Systems with Unsteady Conditions	382
	High-Glide Systems	383
	PREDICTION OF LANDING DYNAMICS	386
	Mathematical Models	386
	Impact Attenuation	387
	Pre-Contact Retardation	390
	Decelerator System Weight Optimization	391
	RELIABILITY ASSESSMENT	392
	Definition of Reliability	392
	Reliability Distributions	393
	Single-Use Versus Multiple Use	393
	Overall System Reliability	394
	Component Reliability Analysis	396
	Evaluation of Operational Terms	398
	Computation of Reliability	399
	Interpretation	400
8	DESIGN	401
	DESIGN CRITERIA	402
	Towing Body and Mission Constraints	402
	Decelerator Subsystem Characteristics	402
REFERENCES		437
INDEX		455

LIST OF ILLUSTRATIONS

FIGURE		PAGE
1.1	Recovery Configurations for MQM-74C and KD 2R-5	3
1.2	USD-5 Recovery System	3
1.3	Typical High Altitude Probe Trajectory	6
1.4	Descent Profile for a Mars Landing	8
1.5	Deployment Sequence of the Venus Probe Decelerator	10
1.6	Mercury Recovery System Installation	11
1.7	Gemini Parachute System	13
1.8	Gemini Ejection Seat with Deployed Ballute	14
1.9	Gemini Paraglider Deployment	14
1.10	Apollo Recovery System Deployment for Normal Landing	16
1.11	Apollo Drogue and Main Parachute Assemblies	18
1.12	Solid Rocket Booster Recovery Sequence	19
1.13	Solid Rocket Booster Recovery System	20
1.14	Aces II Operation Mode Zones	28
1.15	Aces II, Mode 1 Operation	28
1.16	Aces II, Mode 2 Operation	29
1.17	Tractor Rocket Escape System Operation	29
1.17	Tractor Rocket Escape System Operation (Continued)	30
1.18	Encapsulated Seat Pre-Ejection Sequence	30
1.19	F-111 Crew Module Configuration	33
1.20	F-111 Crew Module Low Speed Ejection Sequence	34
1.21	Aircraft Crew Module	34
1.22	Standard Airdrop Method	38
1.23	"LAPES" Airdrop System	39
1.24	High Altitude Airdrop Resupply System (HAARS), First Stage Configuration	40
1.25	Parachute Extraction Force and Extraction Speed vs Time for a 35 Ft Parachute Extracting a 50,000 Lb. Load	45
1.26	T-10, Personnel Troup Parachute Assembly	46
1.27	T-10 Paratrooper Parachute, Basic Configuration	46
1.28	MC-1-1B Parachute (T-10 Parachute with Anti-Inversion Net and TU Slots)	48
1.29	B-52 with Landing Drag Parachute Deployed	50
1.30	Typical Landing Drag Chute Assembly	51
1.31	Spin Recovery Parachute and Deployment Sequence	54
1.32	F-15 Spin Recovery Parachute, Deployment Sequence	55
1.33	Mark 82 AID	58
1.34	Trapeze/Helicopter (HH-53) Midair Retrieval System	62
1.35	JC-130 Midair Retrieval System	62
1.36	Extended Skirt Parachute with Conical Extension	64
1.37	BQM - 34 F (Supersonic Target) Midair Retrieval in Progress	64
1.38	100 Ft. Tandem Engagement Parachute (GR-14) for AQM-34V	65
1.39	64 Ft. Diameter Annular Tandem Parachute with 2000 Test Vehicle	65
1.40	Smoke Jumper Fully Equipped with FS-10 Parachute	68
1.41	Schematic Of Parachute Balloon Train Of Air-Launch Communications Relay Balloon	71
2.1	Parts of a Parachute	78
2.2	Flat Patterns of a Gore	79

LIST OF ILLUSTRATIONS (Continued)

FIGURE		PAGE
2.3	Planform and Construction Schematic for a Flat Circular Parachute	79
2.4	Construction Schematic of Conical Canopy	80
2.5	Shape of an Inflated Gore	80
2.6	MC-1-1B Parachute	103
2.7	The LeMoigne Parachute	104
2.8	Sailwing	108
2.9	Volplane	108
2.10	Balloon Decelerator	109
2.11	Ballute Geometry	109
2.12	Attached Inflatable Decelerators	110
2.13	Ram-Air Inflated Decelerator	110
2.14	Paravulcoon System	110
2.15	Rotor	110
3.1	Single Mode Recovery Sequence	112
3.2	Control Subsystem Diagram for Emergency Recovery of Space Capsule	114
3.3	Typical Cartridge Configuration	116
3.4	Deployment Gun	117
3.5	Typical Mortar Design and Performance Data	118
3.6	Ejector Bags	119
3.7	F-1B Automatice Release Installed in Parachute	120
3.8	FXC Model 11000 Automatic Opener Installed in Parachute	120
3.9	Irvin Hitefinder Automatic Parachute Release	120
3.10	Canopy Spreader Gun	121
3.11	Reefing Line Cutter	121
3.12	Reefing Line Cutter and Mounting Bracket	122
3.13	Parachute Canopy Release Assembly, Spring Actuated Hook Type	122
3.14	MARS Release	123
3.15	Mineature MARS Release	123
3.16	Extraction Force Transfer Coupling System (High Capacity)	123
3.17	Latch Assembly	124
3.18	Cargo Parachute Release, 5000 Pound Capacity	125
3.19	Multiple Release Assembly with Adapter, Slings, and Cutter Installed	125
3.20	Cargo Parachute Release, 35,000 Pound Capacity	126
3.21	A/P 28S-2 Personnel Harness Release	127
3.22	Personnel Canopy Release	127
3.23	Cartridge Actuated In Line Strap Cutter	127
3.24	Parachute Canopy Release Assembly, Latch Type	128
3.25	Single Initiator Parachute Release	128
3.26	Components of Typical Decelerator Subsystems	129
3.27	Typical Storage Compartment	129
3.28	Typical Pack Army/Air Force	130
3.29	Pack Showing Flaps	130
3.30	Vane Type Pilot Chute	130
3.31	Several Different Deployment Bags	131
3.32	Line-Bight Locks Inside a Deployment Bag	131

FIGURE		PAGE
3.33	Quarter Deployment Bag	132
3.34	Skirt Hesitator/Uses Reefing Line Cutters	132
3.35	Deployment Sleeve	133
3.36	Typical Riser with Branches	134
3.37	Typical Extraction and Force Transfer Sequence	134
3.38	Representative Cargo Harness Assembly	135
3.39	Harness Configuration for Vehicle Stabilization	135
3.40	Two Position Harness	135
3.41	Hardware	136
3.42	Cut Knives	137
3.43	Typical Riser Assembly Using Clevis Links	137
3.44	Cargo Parachute Load Couplers	137
3.45	Typical Installation with Load Coupler and Large Clevises	138
4.1	Stress vs Strain of a Polymeric Fiber	146
4.2	Tenacity vs Elongation of Textile Fibers	146
4.2	Tenacity vs Elongation of Textile Fibers (Continued)	147
4.3	Tenacity – Elongation: Effect of Loading Rate	149
4.4	Rupture Tenacity as a Function of Tensile Test Temperature (stress values based upon denier measured at 70° F)	151
4.5	Initial Modulus of Yarns as a Function of Tensile Test Temperature (based upon at-temperature yarn dimensions)	152
4.6	Load vs Elongation of Cords	159
4.7	Effect of Anisotropic Honeycomb Structure on Crushing Stress with Angular Impact	180
4.8	Stress-Strain of Crushable Structures	180
4.9	Stitch Type 301	183
4.10	Stitch Type 308	183
4.11	Stitch Type 304	183
4.12	Stitch Type 101	183
4.13	Stitch Type 401	183
4.14	Dependence of Seam Efficiency on Stitches per Inch	184
4.15	Fabric Orientation	184
4.16	Typical Flat Fabric Seams and Hems	185
4.17	Cross-section of a Typical Ribbon Canopy Gore	186
4.18	Example of Stitch Patterns	186
4.19	Cord Line Attachment with Butterfly	187
4.20	Webbing Type Line Attachment	187
4.21	Suspension Line Connection to Skirt Loop Attachment	187
4.22	Tapered Radial/Suspension Line Joint	188
4.23	Continuous Radial/Suspension Line	188
4.24	Suspension Line Loop, Style A	188
4.25	Branched Riser With Metal Links	189
4.26	Branched Riser With Stitched Line Joints	189
4.27	Integral Line Riser	189
4.28	Typical Web Connect Method	190
4.29	Typical Webbing Riser Joint Configuration	190

LIST OF ILLUSTRATIONS (Continued)

FIGURE		PAGE
4.30	Suspension Line Tensioning and Marking Apparatus	192
4.31	Four Needle Sewing Machine Set-Up for Ribbon Parachute	193
4.32	Parachute Packing Tools	194
4.33	Hydraulic Packing Press	195
4.34	Schematic of General Utility Decelerator Packing Press Facility	196
5.1	Altitude vs Mach Number, Decelerator Performance Regimes	199
5.2	Aircraft with Drop Test Vehicle Mounted on Wing Pylon	200
5.3	Helium Filled Balloon Used as Launch Platform	203
5.4	Generalized Carrier Balloon Performance Chart	203
5.5	Test Vehicle Launch From Ground	203
5.6	Parachute Whirl-Tower Test Facility	203
5.7	F-5 Aircraft Testing of 15- Foot Ringslot Deceleration Parachute	206
5.8	Truck Tow Test Rig for Experimental Gliding Parachute	206
5.9	Representative Textile Testing Machine for Comparatively Heavier Textile Forms	208
5.10	Representative Testile Testing Machine for Fabrics and Light Cordage	209
5.11	Schematic Diagram of Textile Impact-Testing Apparatus	209
5.12	Pilot Chute Bridle Dynamic Test Apparatus	210
5.13	Suspension Line Impact Loading Apparatus for Strain Rates of 50% to 200%/Sec	210
5.14	Schematic of Pressure Time History at an Arbitrary Location Along Shock Tube	211
5.15	The Frazier Air Permeability Instrument	211
5.16	Air Permeability Apparatus	211
5.17	Inclined-Plane Apparatus for Measuring Coefficient of Sliding Friction	212
5.18	The Hanging Loop Method of Measuring the Relative Stiffness of Thin Flexible Materials	212
5.19	White Sands Test Complex	214
5.20	Eglin Gulf Test Range, Florida	214
5.21	National Parachute Test Range, California	215
5.22	Seat Ejection Test on High Speed Test Track	217
5.23	High Speed Decelerator-Tow Sled	217
5.24	Weight-Bomb Test Vehicle	224
5.25	Schematic of an Airdrop Test Platform Assembly	226
5.26	Cylindrical Test Vehicle	226
5.27	The Arrowhead Sled	228
5.28	The Tomahawk Sled	228
5.29	The Bushwhacker Sled	229
5.30	Details and Calibration of Elastomeric Strain Gauge	229
5.31	Differential Pressure Transducer with Compensation for Linear Acceleration	230
5.32	Omega Stress Transducer	230
5.33	Typical Electric Strain-Gauge Force Transducer	231
6.1	Schematic of Different Deployment Sequences	236
6.2	Snatch and Opening Forces of a 28 Ft. D_o Solid Flat Circular Parachute	236
6.3	System Geometry During Deployment to End of Line-Stretch	237
6.4A	Relative Load-Elongation of Nylon Webbing from Twice Repeated Static Tests	238
6.4B	Tension-Strain Pattern Generated by Successive Impact Loads of Decreasing Magnitude	238
6.4C	Ratio of Impact Peak Load to Static Load Versus Inverse Elongation ($1/\epsilon$)	239

LIST OF ILLUSTRATIONS (Continued)

FIGURE		PAGE
6.4D	Typical Impact Loading Cycles of 400-Lb Nylon Cord	239
6.5	Approximate Body-Canopy Separation Velocity at Line-Stretch	240
6.6	Comparison of Measured and Computed Snatch Forces of Heavy Ribbon Parachutes for Different Mass Distributions	241
6.7	Effect of Deployment Bag on Relative Magnitude of Snatch Force During Deployment of a 28 Ft. D_o Solid Flat Circular Parachute	242
6.8	Force Record for Pilot Chute Bridle Test	243
6.9A	States in Parachute Inflation	244
6.9B	Intermediate Stages of Inflation Process Added by Skirt Reefing	244
6.10A	Normalized Canopy Area Growth During Inflation of 28 Ft. (D_o) Solid Flat Circular Parachute	245
6.10B	Normalized Canopy Area Growth During Inflation of 35 Ft. (D_o) 10% Flat Extended Skirt Parachute	246
6.11	Measured Area Growth During Inflation of 85.6 Ft. (D_o) Modified Ringsail Parachute With Two Reefed States (S'_p = Projected Area at End of Stage)	246
6.12	Schematic - Blanketing of Canopy Air Inlet by Inward Folding of Skirt Fabric Between Suspension Lines With and Without Pocket Bands	247
6.13	Effect of Skirt Spreading Gun and Canopy Apex Retraction on the Opening Time of Personnel Parachutes	247
6.14	Parachute Critical Opening Speed Vs, Total Effective Porosity	248
6.15	Measured Filling Time Vs Snatch Velocity of Solid Cloth Circular Parachute (Non-Reefed)	249
6.16	Effect of Compressibility on Filling Distance of Non-Reefed Parachutes	251
6.17	Apparent Variation of Filling Time With Velocity for Slotted Canopies (Infinite Mass Condition)	252
6.18	Upper Limit Effect of Compressibility on Parachute Filling Distance	253
6.19	Solid Cloth Circular Parachute Opening Force Characteristics Non-Reefed	254
6.20	Opening Force Characteristics, Type C-9 Parachute	256
6.21	Measured Force vs Normalized Time During Inflation of T-10H (High Strength) 35 Ft. (D_o) 10% Extended Skirt Parachute Deployed Lines - First Horizontally From Cylindrical Vehicle	256
6.22	Airdrop and Recovery Parachutes - Typical Opening Force vs Time	257
6.23	Typical Opening Forces of Aircraft Deceleration Parachutes	257
6.24	Comparison Between Inflating Canopy Shape and Generated Force	258
6.25	Parachute Opening Load Factor Vs Mass Ratio	259
6.26	Opening Forces of 48 Ft. (D_o) Ribbon Parachute in Clusters of Three with Canopies Tied Together at Skirt Tangency Points	260
6.27	Opening Force-Time History for Cluster of Two 12.8 Ft. D_o Ringsails Reefed 13% D_o for 8 Seconds Deployed at 299 FPS (TAS) at 10,246 Feet Altitude	262
6.28	Axial Force Coefficient Versus Angle of Attack, M = 0.1	265
6.29	Axial Force Coefficient Vs Angle of Attack, M = 0.5, 0.8	266
6.30	Effect of Clustering on Drag Coefficient	267
6.31	Cluster of Four 100 Ft. (D_o) G-11A Parachutes	268
6.32	Performance Characteristics of Three Flat Circular Ribbon Drogues in Cluster Configuration	269
6.33	Generalized Decelerator System in Stable Equilibrium Descent Through Homogeneous Air Mass	270

FIGURE		PAGE
6.34	Averaging Drag Coefficient and Rate of Descent Data	271
6.35	Parachute Drag Coefficient vs Equilibrium Rate of Descent at Sea Level (Circular Canopies)	273
6.36A	Variation of L/D and Aerodynamic Coefficients With Angle of Attack	274
6.36B	Effect of Wing Loading (W/S_W) on Components of Glide Over Controllable Range of L/D Modulation	274
6.37	Twin-Keel Parawing Performance	275
6.38	Parafoil Measured Turning Characteristics	276
6.39	Decelerator Systems Subject to Strong Wake Effects	276
6.40	Subsonic Wake Flow Characteristics	278
6.41	Velocity Distribution in Wake of Bodies of Revolution	279
6.42	Velocity Distribution in Accordance With Analytical and Experimental Studies	280
6.43	Wake Drag Coefficient for Small Circular Models (Disk and Hemispherical Cup)	280
6.44	Wake Width & Center-Line Velocity Increment vs Distance From Body of Revolution	281
6.45	Impact Pressure Ratio on Wake Centerline Ogive-Cylinder & Hemispherical Cup	281
6.46	Drag Coefficient of Experimental Tandem Canopy Systems	281
6.47	Schlieren Photograph of the Flow Fields About a Hyperflo Type Parachute at M 4.0	283
6.48	Schematic of Unmodified Supersonic Wake Details and Nomenclature for Body of Revolution	283
6.49	Sketch of Flow Patterns Around Primary Bodies Alone at Supersonic Speeds	284
6.50	Types of Leading Body-Trailing Body Flow Field Interactions	284
6.51	Drag Coefficient of Small Rigid Models in Wake of Simulated Ogive-Cylinder	285
6.52	Wake Conditions Behind a Cone-Cylinder with a Trailing Hyperflo Type Parachute for Various Free-Stream Reynolds Numbers at M = 3.0	286
6.53	Scale Model Viking Entry Forebodies and a Faried Body	287
6.54	Effect of Forebody Shape on C_{D_o}	287
6.55	Variation of Disk-Gap-Band Parachute Coefficient with Free Stream Mach No.	287
6.56	Typical Variation of Mechanical and Effective Porosities of Nylon Parachute Cloth With Differential Pressure	288
6.57	Effective Porosity versus Pressure Ratio for Various Nylon Cloth Materials	289
6.57	Effective Porosity versus Pressure Ratio for Various Nylon Cloth Materials (Continued)	290
6.58	Effect of Canopy Porosity on Parachute Drag Coefficient	291
6.59	Variation of Canopy Projected Diameter With Effective Length of Suspension Lines in Small Models	291
6.60	Effective Rigging Length With Multiple Riser Attachments	292
6.61	Effect of Suspension Line Effective Length on Parachute Drag Coefficient	292
6.62	Effect of Canopy Fineness Ratio on Drag Coefficient	294
6.63	Variation of Parachute Drag Coefficient With Scale	295
6.64	Drag Area Ratio vs. Reefing Ratio for Solid Circular, Extended Skirt, Ringslot, Ringsail and Ribbon Parachutes	296
6.65	Variation of C_{D_p} With Reefing Ratio	297
6.66	Measured Peak g's vs Opening Stage of 4000 Ft^2 (S_W) Twin Keel Parawing	297
6.67	Parawing Descending in Reefed Mode	298
6.68	Clustered Canopies with Apexes Retracted	298
6.69	Retraction of Canopy Apex with Axial Line	300
6.70	Typical Static and Dynamic Stability Characteristics of Parachute-Body System	300

LIST OF ILLUSTRATIONS (Continued)

FIGURE		PAGE
6.71	The System of Axes Used for Static Stability Considerations	301
6.72	Measured Moment Coefficients vs Angle of Attack for Small Cloth Canopies in Wind Tunnel	302
6.73	Effect of Air Permeability on C_{M_o} vs α of Small Solid Flat Circular Canopies in Wind Tunnel	302
6.74	Schematic of Bomb Wake Downwash Due to Body-Lift (With Stabilization Para.)	303
6.75	Static Stability of Booster Model with Ballute	304
6.76	Longitudinal Aerodynamic Characteristics of Parafoil Designs II and III	305
6.77	Effects of an Increase in Dynamic Pressure on Longitudinal Aerodynamic Characteristics of a Twin-Keel All Flexible Parawing	305
6.78	System of Axis and the Positive Direction of the Forces, Moments and Angles Used in the Presentation of the Data	306
6.79	Effect of Gliding on Position Stability of MARS-H Engagement Canopy	307
6.80	Schematic of Mid-Air Retrieval System and Coordinates	308
6.81	Effect of Sphere Drogue on Amplitude Decay of Entry-Body Angle of Attack	309
6.82	Distribution of Suspension Line Loads for Each Opening Stage of Reefed 4000 Ft^2 (S_W) Twin Keel Parawing	310
6.83	Distribution of Suspension Line-Riser Loads in Each Parachute Cluster at ΣF (Max.)	310
6.84	Cargo Suspension Sling with Four Legs	311
6.85	Differential Pressure Coefficient $C_p = \Delta p/q_s$ and Corresponding Projected Area Ratio S_p/S_o, Opening Shock Faxtor $F/C_D S_o q_s$ and Dynamic Pressure Coefficient q/q_s versus Time Ratio	311
6.86	Calculated and Measured Drag Area	312
6.87	Measured Circumferential and Radial Stresses	312
6.88A	Canopy Stress and Total Force Measured on a 28 Gore Solid Flat Circular Model Parachute	312
6.88B	Canopy Stress and Total Force Measured on a 32 Gore Ringslot Model Parachute	312
6.89	Measured Opening Forces and Canopy Stress of Model Ringslot Canopy	313
6.89	Measured Opening Forces and Canopy Stress of Model Ringslot Canopy (Continued)	314
6.89	Measured Opening Forces and Canopy Stress of Model Ringslot Canopy (Continued)	315
6.90	Typical Body - Drogue Supersonic Flow Field	316
6.91	Aerodynamic Heating of Parasonic Drogue, SP-5, Deployed at Mach 5.5, 120,000 Ft. Altitude	318
6.92	Aerodynamic Heating of a Nomex Ballute Flight Test TB-4	319
6.93	An Example of a Mid-Air Retrieval Sequence	320
6.94	Variation of Compressive Resistance With Deformation of Energy Absorber	321
6.95	Experimental Impact Bag Performance	323
6.96	Air Bag System Vertical Drop Test	323
6.97	Maximum Inflated Dimensions Impact Bag	324
6.98	Low Level Air Drop with Pre-Contact Deceleration by Retrorockets	326
6.99	Thrust vs Time for TE-M-421-1 and TE-M-421-3 Rockets at 60° F	326
7.1	Drag Area Growth History of Inflating Decelerators	334
7.2	Schematic Geometry of Vehicle and Parachute	335
7.3	Vehicle Orientation at Drogue Parachute Line Stretch	336
7.4	Results of Dynamic Interaction Analysis	336
7.5	System Geometry During Deployment	337

LIST OF ILLUSTRATIONS (Continued)

FIGURE		PAGE
7.6	Average Static Load - Strain Characteristic of 1" Nylon Webbing	337
7.7	Measured Vs Simulated Dynamic Stress - Strain Characteristics of 400 lb Nylon Suspension Line Cord	338
		339
7.8	System Configuration During Deployment	342
7.9	Mass Time Method; Calculated vs Measured Opening Loads	344
7.10	Resistance Coefficient vs Dimensionless Acceleration Parameter AD/V^2	346
7.11	Measured Apparent Moment of Inertia of Rigid Canopy Models vs (λ_g)	347
7.12	Canopy Geometry and Trajectory Coordinates	348
7.13	Measured and Predicted Characteristics of Disk-Gap-Band Parachute	349
7.13	Measured and Predicted Characteristics of Disk-Gap-Band Parachute (Continued)	349
7.14	Details of Spring Mass-Momentum Model of Inflating Polysymmetric Parachute	354
7.15	Stress-Strain Relationships in Circular Canopy of General Profile and Bias Construction	355
7.16	Variation of Canopy Shape and Stress During Inflation	357
7.17	Structural Model of Slotted Parachute	358
7.17	Structural Model of Slotted Parachute (Continued)	359
7.18	Pressure Distribution in Inflating Parachutes	361
7.19A	Flow Diagram for Program CANO	362
7.19B	Flow Diagram Detail Showing Skirt Equilibrium for an Unreefed Parachute	363
7.19C	Flow Diagram Detail Showing Skirt Equilibrium for a Reefed Parachute	364
7.20	Flow Diagram for Program CANO 1	365
7.21	Relative Reefing Line Load	366
7.22A	Circular Approximation of Spanwise Profile of the Twin Keel Parawing	366
7.22B	Comparison of Predicted and Measured Line Loads for Twin Keel Parawing	368
7.23	Flow Field of Supersonic Drogue for Dynamic Heating Analysis	368
7.24	Sonic Reynolds No. and P_3/P_4 Vs Mach No.	371
7.25	Experimental Heat Transfer Results (Upstream) for Parachute Ribbon Grids	371
7.26	Comparison of Upstream and Downstream Experimental Heat Transfer Results	372
7.27	Distribution of Heat Transfer Coefficients on Upstream Side of Ribbon Grid	372
7.28	Stagnation Point Heat Transfer to Ribbon Grid (Upstream)	372
7.29	Calculated Temperatures in Crown of 40 Ft. D_o Disk-Gap-Band Parachute	373
7.30	Unified Wake Transition Criterion for Ballute Flight Test TB-4	374
7.31	Vehicle - Ballute Flow Field Schematic	374
7.32	Pressure Distribution Over Ballute	374
7.33	Ballute Cold Wall Heat Flux Rate	376
7.34	Wake Coefficients vs (x/d_b)	376
7.35	Diameter of Wake	376
7.36	Average Dynamic Pressure on Decelerator in Body Wake	377
7.37	Geometry of Bodies Used for Experiments	379
7.38	Dynamic Stability of Descending Parachute	379
7.39	Typical Parachute Dynamic Stability Predictions (Shuttle Booster Recovery System)	380
7.40	Parachute System Geometry and Coordinate System	381
7.41	Typical Variation of Parachute Force Coefficient with α	382
7.42	Effect of Froude Number and Slenderness Ratio on Stability C_{A_o} = 0.7 - Zero Porosity	382
7.43	Drogue Effect Initial Conditions	383
7.44	Predicted Drogue Effects on SRB Motion	383
7.45	Shuttle Booster (SRB) Main Parachute Stability	

LIST OF ILLUSTRATIONS (Continued)

FIGURE		PAGE
7.45	Shuttle Booster (SRB) Main Parachute Stability (Continued)	384
7.46	Summary of Aerodynamics of Sonic Rigid Model Single Keel Parawing	384
7.47	Typical Dynamic Pitching Characteristics of Tethered Semi-Rigid Parafoil Model	385
7.48	Comparison of Predicted and Measured Aerodynamic Characteristics of Rigid and Flexible Parawing Models	385
7.48	Comparison of Predicted and Measured Aerodynamic Characteristics of Rigid and Flexible Parawing Models (Continued)	386
7.49	General Characteristics of Impact Attenuation System Vs Vehicle Vertical V_e and Load Factor	388
7.50	Characteristic Impact Bag Input Data for Analysis of Landing Dynamics	389
7.51	Variation of Optimum Design Rate of Descent with Effective Specific Impulse of Landing Retrorocket	392
7.52	Reliability From a Series of Trials	395
7.53	Reliability Levels for a Series of Tests With and Without Failures	395
7.54	The Normal Distribution	398
7.55	Exaggerated Stress-Strength Distribution	398
8.1	Density and Gravity Ratios as a Function of Altitude	403
8.2	Pocket Band Dimensions for Circular Canopies	406
8.3	Typical Crown Slot Control Tape on Circular Canopies	406
8.4	The Development of Gore Coordinates for Circular Canopy of General Profile	408
8.5	Total Porosity vs. Canopy Diameter for Flat Circular Ribbon Canopies	409
8.6	Recommended Total Porosity of Ringslot Canopy Design	409
8.7	Twin - Keel Parawing Inflation with Suspension Line Reefing in Four Steps	420
8.8	Continuous Suspension Line Reefing by Sliding Rings with Drag-Panel	420
8.9	Temperature Strength Loss of High Tenacity Synthetic Textile Fibers	426
8.10	Schematic Arrangement of Two Different Deployment Bag Designs	428
8.11	Ejection Mortar Weight Data	431
8.12	Rocket Specific Impulse Ratio Vs Burn Time	432
8.13	Parachute Weight Vs D_o Typical for Classes L and I	433
8.14	Parachute Weight Vs D_o and Construction Class	433
8.15	Recovery System Weight Breakdown	435
8.16	Approximate Body - Canopy Separation Velocity at Line-Strength	436

LIST OF TABLES

TABLE		PAGE
A	Units of Measure	xxxvi
B	Weights and Measures	xxxvii
C	Properties of Earth's Atmosphere as a Function of Altitude	xxxviii
D	Typical Ground Wind Velocities in Continental United States	xl
E	Physical Relationships of Planets	xli
1.1	Technical Data of the Mercury Parachute System	12
1.2	Apollo Parachute System Data	17
1.3	Solid Rocket Booster Recovery Parachute Data	20
1.4	Air Force Personnel Emergency Parachutes	25
1.5	U. S. Navy Personnel Emergency Parachutes	26
1.6	Comparison of Several Encapsulated Seats, Crew Modules and a Typical Ejection Seat	31
1.7	B-1 Crew Module, Main Parachute Deployment Sequence	35
1.8	Aircraft Used for Airdrop	36
1.9	Container Summary for Helicopter Airdrop	37
1.10	List of Standard Airdrop Main Recovery Parachutes	43
1.11	Extraction Parachute Types	44
1.12	List of Personnel Parachute Assemblies	47
1.13	T-10 Parachute and T-10 Reserve Parachute Dimensions	48
1.14	Aircraft Deceleration Parachutes	51
1.15	Parachute Systems for Spin and Stall Recovery	54
1.16	Comparison of Nylon and Kevlar B-61 Bomb Retardation Parachutes	57
1.17	Comparison of Mid-Air Retrieval Parachute Systems	63
2.1	Solid Textile Parachutes	75
2.2	Slotted Textile Parachutes	76
2.3	Rotating Parachutes	76
2.4	Gliding Parachutes	77
2.5	Decelerators Other Than Parachutes	77
3.1	Radio Beacon Characteristics	140
3.2	SOFAR Bomb Characteristics	140
4.1	Mechanical Properties of Fibers and Filament Yarns	149
4.1	Mechanical Properties of Fibers and Filament Yarns (Continued)	150
4.2	Cotton Sewing Threads	155
4.3	Nylon Sewing Threads	156
4.4	Polyester Sewing Threads	157
4.5	Thread, Nylon, Non Melting	158
4.6	Thread, Para-Aramid, Intermediate Modulus	158
4.7	Nylon Cords with Core	159
4.8	Coreless Braided Nylon Cords	160
4.9	Cord, Aromatic Polyamide, Non Melting	161
4.10	Cord, Coreless, Para-Aramid, Intermediate Modulus	161
4.11	Cotton Webbing	162
4.12	Nylon Webbing	163
4.13	Nylon Webbing	164

LIST OF TABLES (Continued)

TABLE		PAGE
4.14	Nylon Webbing, Tubular	164
4.15	Nylon Webbing	164
4.16	Nylon Webbing	165
4.17	Polyester Webbing	165
4.18	Polyester Webbing	165
4.19	Polyester Webbing, Impregnated	166
4.20	Low Modulus Aramid Webbing	166
4.21	Low Modulus Aramid Tubular Webbing	167
4.22	Low Modulus Aramid Webbing, Tubular with Nylon Core	167
4.23	Tape and Webbing, Textile, Para-Aramid, Intermediate Modulus	167
4.23	Tape and Webbing, Textile, Para-Aramid, Intermediate Modulus (Continued)	168
4.24	Webbing, Textile, Tubular, Para-Aramid, Intermediate Modulus	169
4.25	Cotton Tape and Webbing	169
4.26	Rayon Tape and Webbing	170
4.27	Nylon Tape and Webbing	170
4.28	Nylon Tape and Webbing	171
4.29	Nylon Tape	171
4.30	Nylon Tape	171
4.31	Nylon Tape	172
4.32	Nylon Tape	173
4.33	Cotton Cloth	174
4.34	Nylon or Rayon Cloth	174
4.35	Light Weight Nylon Cloth	175
4.36	Medium Weight Nylon Cloth	175
4.37	Heavy Weight Nylon Cloth	175
4.38	Nylon Duck	176
4.39	Light Nylon Cloth	176
4.40	Low Modulus Aramid Cloth	176
4.41	Honeycomb Characteristics	180
5.1	Aircraft Achievable Launch Conditions	201
5.2	Textile Materials Testing	208
5.3	Decelerator Testing, Principal Facilities and Capabilities	216
5.4	Subsonic Wind Tunnels	219
5.5	Transonic, Supersonic and Hypersonic Wind Tunnels	223
5.6	Airdrop Test Vehicles	225
6.1	Parachute Average Relative Filling Distances (Measured)	255
6.2	Measured Opening Forces of Clustered Parachutes	263
6.3	Effective Rigging Length for Clustered Parachutes	264
6.4	Effective Rigging Length for Clustered G-11A and G-12D Parachutes	264
6.5	Parameters of Symmetrical Parachute Clusters	267
6.6	Summary, Rate of Descent Measurements	272
6.7	Parafoil $(L/D)_{max}$ vs Aspect Ratio	272
6.8	Parafoil $(L/D)_{max}$ in Free Flight	272
6.9	Mid-Air Retrieval System Drag Efficiencies and Specific Drag Areas	282

LIST OF TABLES (Continued)

TABLE		PAGE
6.10	Parafoil Opening Force Coefficient	299
6.11	Dimensional Characteristics	303
6.12	Summary of Impact Bag Dynamic Performance Data	325
6.13	8-Year Malfunction Statistics Personnel Drop Record	329
6.14	8-Year Supply/Equipment Drop Record	330
7.1	Added Air Mass Coefficient of Hollow Shells	344
8.1	Sample Calculations for Sizing Main Parachute	404
8.2	Effect of Shortened Vent Lines ($D_v/D_o = 0.10$)	407
8.3	System A Opening Forces (Non-Reefed)	410
8.4	Permanent Reefing Shape as a Function of No. of Gores	411
8.5	Lead Canopy Worst Case Opening Loads	413
8.6	Recommended Parachute Design Factors	415
8.7	Steerable Parachute Comparison for System D	418
8.8A	Ribbon Parachute Material Strength Requirements	425
8.8B	Material Strength Requirements for Other Than Ribbon Parachutes	425
8.9	Pilot Parachute Relative Drag Area	429
8.10	Pilot Parachute Performance	429
8.11	Constants *a* and *b* for Various Canopy Titles and Canopy Materials	434
8.12	Decelerator Pack Densities	435

– LIST OF SYMBOLS –

A	Area (cross section or frontal)
A'	Dimensionless apparent moment of inertia
A_p	Allowable Strength Factor
AR	Aspect Ratio
a	Acceleration
B	Number of blades (autorotor); Volumetric rate of discharge; Added mass coefficient
b	Span or spanwise dimension; Adiabatic recovery factor
C	Coefficient, constant or factor (general)
C_A	Aerodynamic Force Coefficient = $C_L^2 + C_D^2$
C_D	Drag Coefficient
C_{D_C}	Cluster Drag Coefficient
C_{D_o}	Drag Coefficient (canopy area S_o)
C_{D_p}	Drag Coefficient (projected area S_p)
C_d	Discharge Coefficient
C_f	Coefficient of Friction
C_L	Lift Coefficient
C_M	Aerodynamic Moment Coefficient
C_N	Normal or Side Force Coefficient
C_p	Pressure Coefficient
C_R	Radial Force Coefficient
C_T	Axial Force Coefficient
C_X	Opening Load Factor
c	Chord or chord-wise dimension; Effective porosity, factor related to suspension line convergence
c^*	Characteristic Velocity
c_p	Specific Heat
c_s	Velocity of Sound
C_DA	Drag Area of Forebody or Vehicle
C_DS	Effective Drag Area
D	Diameter; Drag
D_F	Design Factor
D_o	Nominal Diameter of Canopy = $(4S_o/\pi)^{1/2}$
D_p	Projected Inflated Diameter of Canopy = $(4S_p/\pi)^{1/2}$
D_r	Diameter of reefing line circle
D_v	Vent Diameter
d_t	Nozzle Throat Diameter
E	Young's Modulus of Elasticity (f/ϵ)
E_K	Kinetic Energy
Eu	Euler Number ($p/\rho v^2$)
e	Strength loss factor (abrasion); Gore width dimension; Material stiffness
e_s	Width of Gore at Skirt
e_v	Width of Gore at Vent
e'	Length of Gore Chord in Inflated Canopy
F	Force; Structural Load
F_c	Constant Force; Steady-Stage Drag
F	Limit Load

F_N	Normal Force
F_o	Opening Force
F_X	Maximum or Peak Opening Force
Fr	Froude Number $(v/(gl)^{1/2})$
F_s	Impact (Snatch) Force
F_T	Tension Force
F_{ult}	Ultimate Load
f	Unit Stress, Frequency; Dimensionless Force; "a function of"
f'	Unit Tensile Load
G	Load Factor
g	Acceleration due to gravity
g_o	Acceleration of gravitation at planet's mean surface
H	Convective Heat Transfer Coefficient
h	Height or Altitude; Height of a point on the canopy or gore layout relative to apex
h_e	Height of Energy Absorbing Mechanism
h_f	Height of Fullness Transition on Gore Layout relative to apex
h_g	Height of Gore from vent to skirt
h_p	Height or Length of Inflated Canopy including any super-structure
h_s	Height of Gore Layout from vertex to skirt
h'	Height of any point on constructed profile of canopy projected on axis
Δh	Working Stroke of Energy Absorber
I	Mass Moment of Inertia; Impulse
I'	Apparent Moment of Inertia
i	Specific Impulse; Strength Loss Factor (vacuum)
j	Safety Factor
K	Constant of Proportionality or Factor (general)
K_a	Added Air Mass Coefficient
K_f	Dimensionless Filling Time Parameter
Kn	Knudsen Number
Kp	Kaplun Number
K_s	Dimensionless filling distance parameter
k	Strength Loss Factor (fatigue); Thermal Conductivity Coefficient
k_m	Mass Ratio
L	Lift
L/D	Glide Ratio $(\equiv v_H/v_V)$
l	Length
l_c	Cluster Rigging Length
l_e	Effective Suspension Line Length
l_R	Length of Risers
l_r	Length of Reefing Line
l_s	Length of Suspension Line
l_T	Canopy Trailing Distance
Δl	Elongation of Tensile Member
M	Mach Number (v/c_s); Moment; Total Mass of System
M_S	Margin of Safety
m	Mass
m_a	Added Air Mass $(m' + m_i)$
m'	Apparent Mass

m_b	Mass of Body
m_i	Included Mass
N	Any Integral Number
Nu	Nusselt Number (hl/k)
n	Any Number; Filling Time Exponent
n_C	Number of Parachutes in Cluster
o	Strength Loss Factor (water absorption)
P	Strength (material); Pressure (absolute)
P_A	Allowable Unit Strength of Material
P_R	Rated or Minimum Unit Strength of Material
Pr	Prandtl Number ($C_p\mu/k$)
ΔP	Pressure (differential or gage)
Q	Quantity of Heat; Enthalpy or Heat Content
q	Aerodynamic Pressure ($\rho v^2/2$)
$\dot{q}$	Heat Flux Rate
R	Universal Gas Constant; Characteristic Radius of Axisymmetric Canopy
Re	Reynolds Number ($lv\rho/\mu$)
R_m	Mass Ratio ($\rho(C_D S)^{3/2}/M$)
R_W	Weight Ratio
r	Radius
r_p	Inflated Radius of Circular Canopy
r'	Radius of Surface of Revolution of any point on constructed profile
S	Area (decelerator)
S_F	Safety Factor
S_f	Footprint Area
S_g	Area of Gore
S_j	Area of Exhaust Jet Cross Section
S_o	Nominal Surface Area of Canopy
S_p	Projected Frontal Area of Inflated Canopy
S_λ	Total Open Area of Slotted Canopy
S_σ	Total Imporous Area of Canopy
s	Distance Along Trajectory or Flight Path; Factor for Asymmetrical Loads
s_f	Filling Distance
T	Temperature (absolute); Thrust, Dimensionless Filling Time (t/t_f)
T_{cr}	Critical Unit Tensile Load
t	Time
t_f	Filling Time
u	Seam or Joint Efficiency
V	Volume
v	Velocity
v_e	Equilibrium Velocity
v_H	Horizontal Velocity
v_s	Velocity at Line-Stretch (Snatch)
v_V	Vertical Velocity, Sinking Speed, or Rate of Descent
v_λ	Average Through-Flow Velocity
W	Weight; Total Weight of System
w	Unit Weight

m_b	Mass of Body
m_i	Included Mass
N	Any Integral Number
Nu	Nusselt Number (hl/k)
n	Any Number; Filling Time Exponent
n_C	Number of Parachutes in Cluster
o	Strength Loss Factor (water absorption)
P	Strength (material); Pressure (absolute)
P_A	Allowable Unit Strength of Material
P_R	Rated or Minimum Unit Strength of Material
Pr	Prandtl Number ($C_p\mu/k$)
ΔP	Pressure (differential or gage)
Q	Quantity of Heat; Enthalpy or Heat Content
q	Aerodynamic Pressure ($\rho v^2/2$)
$\dot{q}$	Heat Flux Rate
R	Universal Gas Constant; Characteristic Radius of Axisymmetric Canopy
Re	Reynolds Number ($lv\rho/\mu$)
R_m	Mass Ratio ($\rho(C_D S)^{3/2}/M$)
R_w	Weight Ratio
r	Radius
r_p	Inflated Radius of Circular Canopy
r'	Radius of Surface of Revolution of any point on constructed profile
S	Area (decelerator)
S_F	Safety Factor
S_f	Footprint Area
S_g	Area of Gore
S_j	Area of Exhaust Jet Cross Section
S_o	Nominal Surface Area of Canopy
S_p	Projected Frontal Area of Inflated Canopy
S_λ	Total Open Area of Slotted Canopy
S_σ	Total Imporous Area of Canopy
s	Distance Along Trajectory or Flight Path; Factor for Asymmetrical Loads
s_f	Filling Distance
T	Temperature (absolute); Thrust, Dimensionless Filling Time (t/t_f)
T_{cr}	Critical Unit Tensile Load
t	Time
t_f	Filling Time
u	Seam or Joint Efficiency
V	Volume
v	Velocity
v_e	Equilibrium Velocity
v_H	Horizontal Velocity
v_s	Velocity at Line-Stretch (Snatch)
v_V	Vertical Velocity, Sinking Speed, or Rate of Descent
v_λ	Average Through-Flow Velocity
W	Weight; Total Weight of System
w	Unit Weight

– SYMBOLS (Continued) –

Z	Number of Suspension Lines; Number of Identical Cords, Webs, or Tape Plies in a Structural member
Z_w	Wake Width Ratio

– GREEK SYMBOLS –

α	Angle of Attack; Gore section half-angle of bulge between radials
β	Angle of Yaw; Gore Vertex Angle; Factors in landing impulse (β_1,β_2)
Γ	Angle of Elevation
γ	Ratio of Specific Heats; Angle = 90 - α
Δ	Small Increment or Difference (differential)
δ	Weight Density, Boundary layer thickness
δ_l	Lineal Weight Density
ϵ	Unit Strain or Relative Elongation ($\Delta l/l$); Emissivity
ζ	Reefed Drag Area Ratio $(C_D S)_r/(C_D S)_o$
η	Efficiency
θ	Angle of Flight Path from Horizontal; Gore width half-angle in inflated canopy; Thickness of Material
κ	Spring Constant (F/el)
Λ	Relative Porosity; Wing L.E. angle of sweep
λ	Porosity of air-permeability; Wave Length; Molecular mean free path
λ_g	Geometric Porosity of Canopy
λ_{gc}	Geometric Porosity of Canopy Crown
λ_m	Mechanical Porosity of Fabric
λ_T	Total Porosity of Canopy
μ	Absolute Viscosity; Constructed angle between canopy sidewall and plane of skirt
ν	Kinematic Viscosity
ξ	Damping Factor
ξ_g	Ratio of Gravitational Accelerations (g/g_o)
π_o	Polygon Shape Factor
ρ	Mass Density of Air or Fluid
ρ_l	Lineal Mass Density
ρ_o	Air Density at Mean Sea Level
Σ	Summation; Combined
σ	Air Density Ratio (ρ/ρ_o); Standard deviation
τ	Strength Loss Factor (temperature)
Φ	Body Wake Flow Parameter
ϕ	Angle of Suspension Lines from Longitudinal Axis; Flow Deflection Angle
ϕ_c	Average Angle of Parachute Riser from Cluster Axis
ψ	Angle of Canopy Skirt from Longitudinal Axis
Ω	Angular Velocity; Relative flexibility
ω	Angular Acceleration
$\sim$	Approximately
$\approx$	Approximately Equal To
$\equiv$	Identical To

– SUBSCRIPTS –

A	aerodynamic; adiabatic; allowable
a	air; absolute
B	air bag
b	bridle; body; burn
C	crown; cluster; cone
c	canopy; constant
cr	critical
cp	center panel
D	drag; decelerator
d	deployment
dr	disreef
E	Engagement Canopy; Drogue
e	equilibrium; Exit; entering; engagement; energy absorbing material
F	footprint; factor
f	filling; friction
g	Gore
g	Geometric
H	Horizontal
i	Initial; inlet; impact; inflated portion
j	jet
K	kinetic
k	Keel
L	Lift; Leading
l	Line; Lagging; Laboratory
M	aerodynamic moment; main canopy
m	mass; maximum or peak; Mechanical
N	Normal or Side
o	nominal; full open; at mean sea level; reference condition
P	parachute; pressure; strength
p	projected; pilot chute
r	reefed; radial; relative
R	risers; rated; rocket; radial; ratio
S	skirt; safety
s	suspension lines; snatch; distance (filling)
T	total; transverse; axial; Trailing; Tangential
t	tension
ult	ultimate
V	vertical; vehicle
v	vent
W	wing; wall
w	wall; wind; wake; weight
X	opening peak load
x	X - direction
y	Y - direction
z	Z - direction

– SUBSCRIPTS (Continued) –

ι	Inertial
κ	Elasticity
λ	Canopy ventilation
σ	Imporous
∞	Free Stream; far away

– SUPERSCRIPTS –

*	Reference value
–	Average or mean value
′	Similar or reference values
•	Rate of change of variable with time
••	Second derivative of variable with respect to time

– ABBREVIATIONS –

Btu	British Thermal Unit
DR	Disreef
DOF	Degrees of Freedom
EAS	Equivalent Air Speed
fps	Feet per second
IAS	Indicated air speed
min	Minimum
MSL	Mean sea level
psf	Pounds per square foot
psia	Pounds per square inch, absolute
psig	Pounds per square inch, gage
RPV	Remotely piloted vehicle
ST	Stagnation point
TAS	True air speed
vs	Versus

INTRODUCTION

Recovery is a term popularly used to identify the process of arresting a state of motion and bringing to rest a valuable object (payload) by means of a deployable aerodynamic decelerator. Both minimal damage and retrieval are implied in the recovery purpose and concept, hence, recovery often incorporates provisions to soften the impact of landing and to disconnect the decelerator after landing. The payload may be an airborne crewman, a data capsule, a supply package or an entire air vehicle. Its state of motion relates to the performance limits of the payload carrier defined by an envelope of achievable speed and altitude conditions for stable, normal flight, or in an emergency for unstable, erratic flight. Recovery usually employs a parachute as its principal component, but other types of deployable aerodynamic decelerators are also used. The definition of recovery extends to arresting the motion of aircraft or payloads on or near the ground by means of a parachute. Thus, recovery is a sequence of events which may include deceleration, stabilization, steady descent in atmosphere, landing, locating, retrieval and sometimes refurbishment if the purpose of recovery is to enable use of the recovered object, over and over. In some recovery cycles, the descending parachute is intercepted in mid-air, thus modifying the nature of the landing event and expediting retrieval. A recovery system is the combination of special components incorporated in and integrated with a flight vehicle system to effect recovery of the vehicle or its payload under predictable conditions considered during its design.

The role of recovery varies according to application and is closely allied to the development progress of the parachute. Initially developed as a rescue device for airmen in trouble, when aircraft were relatively slow and escape was easy, the parachute has kept pace with expanding requirements imposed over the years by aircraft capable of higher speeds and altitudes, demanding materials resistant to increased temperature and loads without a penalty in weight. Today, recovery provides not only "emergency rescue", but also "expediency" as exemplified by delivery from air of personnel and equipment in military actions or firefighting, and "economy" in the operational reuse or development of air vehicles. Recovery also provides numerous minor roles in special applications, e.g., retardation or slow descent of an object or instrument "on station" such as an illumination flare or wind-drift target.

The purpose of this handbook is to serve as an authoritative reference for all aspects from application to design definition and development of recovery systems and components. The initial chapters present the state-of-the-art by describing representative recovery applications, components, subsystems, materials, manufacture and testing. The final chapters provide technical data and analytical methods useful for predicting performance and presenting a definitive design of selected components into an installable and operable recovery system.

Background

The history of parachutes dates back to medieval days. Earliest evidence from Chinese archives indicates that parachute-like devices were used as early as the 12th Century. Pictorial evidence of the drag device principle appeared in the sketchbook of Leonardo da Vinci in 1514, but historic records show actual implementation occurred late in the 18th Century, in experiments and by exhibitionists jumping from balloons. The years of experimentation with parachutes until the start of the 20th Century produced little more than crude, unreliable devices. Early parachutes were held open by a rigid framework. These were gradually replaced by versions which introduced the central vent for improved stability and all flexible types which could be folded and packed in a bag.

When World War I began in 1914, airmen did not carry parachutes. Post war-time improvements in life-saving parachutes were rapid and many features were introduced which are in common use today including static line and pilot chute deployment, harness attachment, and bag containment. Experiments continued in the U.S. which resulted in acceptance in 1919, of the "free" parachute system, released from the pack by the operator after he jumped. Testing of this parachute type, and further experimentation with other types continued in this country and abroad. The first parachute which was standardized by the U.S. Air Service after extensive development effort, was of the seat type, for use by pilots and crew members. The first service type parachute became standard in 1924 and consisted of a pack containing a flat circu-

lar solid cloth canopy of bias cut silk, 24 feet in diameter, incorporating a three-point harness release. A later version was increased to 28 feet in diameter.

As early as 1928 it was apparent that parachutes for such specific applications as premeditated jumps (paratroops) and airdrop of supplies had to be developed. Experiments and development of parachutes for these applications were limited in the United States until 1940 when an official paratroop training program was established at Fort Benning, Georgia. Also, concerted attempts were made to airdrop military equipment of significant weight, which led to the use of larger parachutes, and to arrangements of canopies in clusters.

For many years silk was the favored material for parachutes. Unavailability of silk led to experiments with man-made textiles. Rayon was used for cargo parachutes, and by the end of 1942, most other materials were being replaced by nylon.

Prior to 1940, steps taken to design and produce parachutes were primarily unscientific and arbitrary. The cut-and-try approach prevailed and the only prerequisite for parachute design and construction appeared to be a knowledge of the sewing trade. Not until the beginning of World War II was emphasis placed upon the scientific approach to parachute design and performance prediction. The Germans and British deserve credit for initial adherence to scientific investigations to establish more fundamental aspects of design and operation. Most major developments in parachutes to satisfy diverse applications have occurred during and since World War II.

The British varied canopy shape and cloth porosity to optimize opening reliability and limit stress in personnel parachutes. Their investigations produced extensive data on the phenomena of squidding and filling rates. Their workmanship and construction techniques were well developed.

Two unique parachute types, the ribbon parachute and the guide-surface parachute, originated during the war in Germany. Both types were developed to a high degree of excellence after theoretical study and experimental effort. Because of its excellent stability characteristic, the guide-surface parachute was employed operationally for trajectory control of bombs, mines, torpedoes and missile components. The ribbon parachute was first used effectively for in-flight and landing deceleration of manned gliders. With further use, reefing was introduced and developed to reduce parachute opening loads and to add a means to control glider ground approach angle and speed. The ribbon parachute also provided good stability and was soon applied to deceleration control of conventional aircraft, and later to jet aircraft. First attempts to recover guided missiles or missile components (V-1 and V-2) were successfully accomplished in 1944 using ribbon parachutes, as was stabilization and deceleration of the first ejection seat in early 1945. Concurrently, extensive theoretical efforts were pursued by the Germans to analyze the operation of parachutes and to obtain fundamental knowledge about their aerodynamic behavior.

Since World War II, the scope and extent of research and development, particularly in the United States, has experienced a sizeable increase, in order to keep pace with advancements in aircraft, ballistic missiles, and spacecraft of various kinds. The primary center for research and development in the area of parachutes and recovery technology has been and still is at Wright Field. Other government agencies also have pursued research pertaining to their area of specialization in the recovery field.

During the 1950's the US Air Force (Parachute Branch, Equipment Laboratory, Air Materiel Command) conducted or sponsored a number of projects designed to develop operational parachute systems for a variety of applications. These ranged from emergency escape of aircraft crew members to the delivery of military personnel, equipment and weapons by airdrop, and including the in-flight and ground retardation of jet aircraft as well as recovery of target drones and missile components. The clustering of parachutes of all sizes and nearly all types, became standard operational procedure for final stage airdrop applications of heavy equipment or vehicles. However, major emphasis was placed upon efforts to extend the operational capabilities of textile parachute canopies into the supersonic and high dynamic pressure flight regimes with applied research programs to increase fundamental knowledge in the field of aerodynamic deceleration.

As the speed and altitude ceiling of aircraft increased, concepts for emergency escape of crew members became more complex. Recovery of high speed missiles and research vehicles presented a new challenge to the performance capability of parachutes. In order to satisfy temperature resistance and shock flow transition stability requirements which develop with supersonic to hypersonic air flow, special canopy shapes and structures were investigated. Some of the more successful high speed drag devices were balloon shaped and could not be classified as parachutes. Other non-parachute decelerator concepts included rotating blades and trailing rigid cones. Thus, the initially singular parachute field was broadened into what is now recognized as deployable aerodynamic decelerator technology. With the advent of higher speeds and altitudes, recovery was accomplished with stages of deceleration in order to control and limit peak loads. A drogue parachute was deployed to provide stabilization and initial retardation prior to main parachute deployment. Additional

deceleration stages were possible by deploying the parachutes in a temporarily reefed state.

The 1960's and 1970's saw the successful utilization of aerodynamic decelerators to meet the continued challenges of higher velocities, higher altitudes, and more complex operational parameters. This was the result of the broadening of knowledge in engineering and scientific approaches to analyze and predict the performance of parachutes and other aerodynamic decelerators. The use of this knowledge manifested itself in the success of sophisticated recovery programs such as the Apollo spacecraft, when the world watched the return of men from the Moon. Significant advances in high-glide, guidable decelerators were made by the introduction of ram-air, airfoil types of "parachutes". Pilots and aircrew members enjoyed the increased safety of reliable, though more complicated emergency escape systems. The introduction of Kevlar threads, fabrics, and webbings as an alternate for Nylon has opened up new possibilities in the production of stronger and lighter aerodynamic decelerators for use where exceedingly stringent volume constraints exist.

Parachute Data Bank

The sources of information used in this Handbook may be found in the List of References. Most References are available to the public through normal channels from originating agencies or on request from the Defense Documentation Center (DDC). There were numerous reports reviewed in the process of composing the Handbook, which including the references, constitute a ***Bibliography*** of literature considered useful on the subject of parachute and recovery. The bibliography is maintained in an up-to-date listing as the basic source of information employed in a computerized data storage and retrieval system known as the ***Parachute Data Bank***. The Data Bank currently stores only design details and performance information extracted from the various bibliographic sources. A FORTRAN extended program provides highly flexible and very selective retrieval of stored data. Procedures for utilization of the Data Bank are outlined in Reference 192. The Data Bank will be found most useful on those problems which have confronted the recovery system designer/investigator who needs performance data. The involvement in laborious, haphazard data searches may be greatly reduced. Coordination between the Data Bank and various organizations throughout the technical field should focus attention on more precise terminology as well as more meaningful data reporting and eventual accession, whether of a narrative, numerical, logical or tabular nature.

Units of Measure

Throughout the Handbook, the English units of measure (feet, pounds, seconds) predominate. However, the most commonly used units from both the English system and from the metric system (centimeters, grams, seconds) are listed in Table A with their abbreviations as used throughout the Handbook, and the conversion factors for translating values into units of either system are given in Table B.

Earth and Planetary Environments

Aerodynamic deceleration devices may be employed over a wide range of altitudes and Mach numbers. For greatest effectiveness, they should operate in a region where the density of the atmosphere is sufficient to produce a positive and continuous resistance force. In Earth's atmosphere, the density even above 600,000 feet altitude will decelerate a relatively large aerodynamic drag device and alter the trajectory of its payload. The atmospheres of Venus and Mars, although different from Earth's atmosphere, have been penetrated with instrumented vehicles using parachutes, and the gravitational forces and the atmospheric properties of these and other planets are of interest for recovery purposes.

In space flight applications, the effect of exposure to long duration ambient vacuum and temperature gradients on a stowed recovery system may be partial strength loss due to out-gas or aging of some polymeric materials and finishes.

Properties of Earth's Atmosphere. The atmosphere as a fluid blanket surrounding Earth varies in density, temperature, viscosity and to a small degree, in composition according to distance above the surface. The best current estimates of the variation of atmospheric properties with altitude are given by the 1976 US Standard Atmosphere[568]. Table C summarizes mean pressure, density, temperature and the speed of sound as a function of geometric altitude, Z. Geometric altitude is the physical distance along the line of force due to gravity which is a straight radius line at the poles and at the equator, but bends polewards as latitude is increased, influenced by the combined effects of gravity and centrifugal force on the atmosphere. Geopotential altitude, H, differs in numerical value taking into account the variation of acceleration due to gravity.

Atmospheric density is expressed in slugs per cubic foot, when a ***slug*** is a gravitational unit of mass in the fps system, and a pound force can impart an acceleration of one foot per second per second. At sea level, ρ, the symbol for density equals 0.00237689 lbs sec^2 ft^4, or slugs 1 ft^3. Values in Table C represent an average of the overall relevant data without spatial or temporal variations. Measurements were obtained[568]

by a variety of techniques and the accuracy of the data summarized in Table C is estimated to be ±10 percent. Although inaccruacy increases with altitude, mean densities have been generally confirmed by observations. Temporal variations of the atmospheric density and density variations with latitude deserve considerations.

The variation of ambient temperature with altitude is a significant factor, as is true of all atmospheric parameters, the temperature at any specific location and time may be somewhat different from that given in the table, due, for example, to seasonal and latitudinal variations. The dominating influence upon the temperature is the sun: the intensity and angle of incidence of the sun's rays on the surface, and the duration of exposure.

Typical ground wind velocities for various cities in the United States are given in Table D as these are important factors influencing the terminal portion of a decelerator operation.

Physical Relationships of Planets. Gaseous atmospheres surround the major outer planets, and some of their large satellites. Except for Venus and Mars, densities of planetary atmospheres are unknown, although some knowlege exists of gaseous composition through occulation. Table E gives physical relationships of Venus, Mars and Jupiter in terms of Earth data. Applications of recovery incorporation for the purpose of aiding atmospheric penetration and descent should consider environments in transit as well as the properties of the gaseous media of performance. Interplanetary vacuum varies from 10^{-13} Tor at lunar distance to 10^{-23} Tor absolute pressure.

TABLE A UNITS OF MEASURE

Liquid Measure

US gallons (gal)
liters (l)

Mass (Weight, Avoirdupois)

ounces (oz)
pounds (lb) or (lbm)
grains (gr)
tons (t)
grams (gm)
kilograms (kg)

Force

pounds (lb) or (lbf)
Newtons (N)

Velocity

feet per second (ft/sec) or (fps)
miles per hour (mi/hr) or (mph)
knots (kt)
meters per second (m/sec)
kilometers per hour (km/hr)

Length Measure

mil
inches (in)
feet (ft)
yards (yd)
miles (mi)
nautical miles (nm)
micron
centimeters (cm)
millimeters (mm)
meters (m)
kilometers (km)

Density

pounds per cubic inch (lb/in^3)
pounds per cubic foot (lb/ft^3)
grams per cubic centimeter (gm/cm^3)

Cubic Measure

cubic inches (cu in) or (in^3)
cubic feet (cu ft) or (ft^3)
cubic centimeters (cu cm) or (cm^3)
cubic meters (cu m) or (m^3)

Temperature

degrees Fahrenheit (°F)
degrees Kelvin (°K)
degrees Centigrade (°C)

Pressure

pounds per square inch (lb/in^2) or (psi)
pounds per square foot (lb/ft^2) or (psf)

Acceleration

feet per second per second (ft/sec^2)
meters per second per second (m/sec^2)

Square Measure

square inches (sq in) or (in^2)
square feet (sq ft) or (ft^2)
square yards (sq yd) or (yd^2)
square miles (sq mi) or (mi^2)
square centimeters (sq cm) or (cm^2)
square meters (sq m) or (m^2)
square kilometers (sq km) or (km^2)

TABLE B WEIGHTS AND MEASURES

Length Measure

1 mil = .001 inch

1 foot = 12 inches = 30.480 centimeters = .3048 meter

1 yard = 36 inches = 91.440 centimeters = .9144 meter

1 mile = 1760 yards = 5280 feet = 1609.344 meters = 1.609 kilometer

1 nautical mile = 6076.10 feet = 1.5078 statute mile = 1.8519952 kilometer

1 meter = 100 centimeters = 3.28084 feet = 39.37008 inches

1 micron = 0.000001 meter = 0.00003937 inch

Square Measure

1 square foot = 144 square inches = .092903 square meter

1 square yard = 9 square feet = . 836127 square meter

1 square mile = 640 acres = 2.590 square kilometer

1 square meter = 1.9599 square yard = 10.763911 square feet

Cubic Measure

1 cubic foot = 1728 cubic inches = 28,316.846 cubic centimeters

1 cubic meter = 35.314674 cubic feet = 61,023.749 cubic inches

Liquid Measure

1 US gallon = 231 cubic inches = 3.7854118 liters

1 cubic foot = 7.48 US gallons = 28.31488 liters

1 liter = 1000 cubic centimeters = 61.023755 cubic inches

1 liter = .0353198 cubic foot = .2641721 US gallon

Mass (Weight, Avoirdupois)

1 ounce = 437.5 grains = 28.349 grams

1 pound = 16 ounces = 453.5924 grams = .4536 kilogram

1 ton = 2000 pounds = 907.20 kilograms = .9072 metric ton

1 kilogram = 1000 grams = 2.204622 pounds = 35.273958 ounces

Velocity

1 foot per second = .6818181 mile per hour = .3048 meter per second

1 mile per hour = .8689784 knot = 1.609 kilometer per hour

1 knot (nautical mile per hour) = 1.15078 statute mile per hour

1 meter per second = 3.28084 feet per second = 2.2369363 miles per hour

1 kilometer per hour = .5399581 knots = .6213712 miles per hour

Acceleration

1 foot per second per second = .3048 meter per second per second

32.174 feet per second per second = 9.80665 meters per second per second

1 meter per second per second = 3.2808398 feet per second per second

TABLE B WEIGHTS AND MEASURES (Cont'd)

Force

1 pound = 4.44822165 Newtons
1 Newton = .22408089 pounds

Pressure

1 pound per square inch = 144 pounds per square foot
1 pound per square inch = .68947571 Newtons per square centimeter
1 pound per square foot = 47.880258 Newtons per square meter
1 Newton per square meter = .0208854 pound per square foot

Density

1 ounce per cubic inch = 1.7299621 grams per cubic centimeter
1 pound per cubic foot = 16.018467 kilogram per cubic meter
1 gram per cubic centimeter = 62.427955 pounds per cubic foot

Temperature

0 degrees Fahrenheit = 255 degrees Kelvin = -18 degrees Centigrade
32 degrees Fahrenheit = 273 degrees Kelvin = 0 degrees Centigrade
0 degrees Kelvin = -459.67 degrees Fahrenheit = -273 degrees Centigrade
(degrees Fahrenheit = 9/5 degrees Kelvin -459.67)
(degrees Kelvin = 5/9 degrees Fahrenheit +459.67)

TABLE C PROPERTIES OF EARTH'S ATMOSPHERE AS A FUNCTION OF ALTITUDE

Altitude		Pressure	Density		Temp.	Speed of Sound
Z, ft	H, ft	P, lbs/ft^2	ρ, slugs/ft^3	$\left(\frac{\rho}{\rho_o}\right)^{-\frac{1}{2}}$	T, °F	c_s, ft/sec
0	0	2116.22 +0	.237689 -2	1.0000 +0	59.000	1116.45
1000	1000	2040.86	.230812	1.0148	55.434	1112.61
2000	2000	1967.69	.224088	1.0299	51.868	1108.75
3000	3000	1896.67	.217516	1.0453	48.303	1104.88
4000	3999	1827.75	.211093	1.0611	44.738	1100.99
5000	4999	1760.87	.204817	1.0773	41.173	1097.10
6000	5998	1696.00	.198685	1.0938	37.609	1093.19
7000	6998	1633.08	.192695	1.1106	34.045	1089.26
8000	7997	1572.07	.186845	1.1279	30.482	1085.32
9000	8996	1512.93	.181133	1.1455	26.918	1081.37
10000	9995	1455.60 +0	.175555 -2	1.1636 +0	23.355	1077.40
11000	10994	1400.09	.170110	1.1821	19.793	1073.42
12000	11993	1346.24	.164796	1.2010	16.231	1069.43
13000	12992	1294.12	.159610	1.2203	12.669	1065.42
14000	13991	1243.65	.154551	1.2401	9.107	1061.40
15000	14989	1194.79	.149616	1.2604	5.546	1057.36

TABLE C PROPERTIES OF EARTH'S ATMOSPHERE AS A FUNCTION OF ALTITUDE (Cont'd)

Altitude		Pressure	Density	$\left(\frac{\rho}{\rho_o}\right)^{-1/2}$	Temp.	Speed of Sound
Z, ft	H, ft	P, lbs/ft^2	ρ, slugs/ft^3		T, °F	c_s, ft/sec
16000	15988	1147.50	.144802	1.2812	1.985	1053.30
17000	16986	1101.74	.140109	1.3025	-1.575	1049.23
18000	17984	1057.48	.135533	1.3243	-5.135	1045.15
19000	18983	1014.67	.131072	1.3466	-8.695	1041.05
20000	19981	9732.75 -1	.126726 -2	1.3695 +0	-12.255	1036.93
21000	20979	9332.66	.122491	1.3930	-15.814	1032.80
22000	21977	8946.02	.118365	1.4171	-19.373	1028.65
23000	22975	8572.49	.114347	1.4418	-22.931	1024.48
24000	23972	8211.72	.110435	1.4671	-26.489	1020.30
25000	24970	7863.38	.106626	1.4930	-30.047	1016.10
26000	25968	7527.14	.102919	1.5197	-33.605	1011.89
27000	26965	7202.66	.993112 -3	1.5471	-37.162	1007.65
28000	27962	6889.64	.958016	1.5751	-40.719	1003.40
29000	28960	6587.75	.923680	1.6040	-44.275	999.14
30000	29957	6296.69 -1	.890686 -3	1.6336 +0	-47.831	994.85
31000	30954	6016.15	.858416	1.6640	-51.387	990.55
32000	31951	5745.85	.827050	1.6953	-54.942	986.22
33000	32948	5485.50	.796572	1.7274	-58.497	981.88
34000	33945	5234.80	.766963	1.7604	-62.052	977.52
35000	34941	4993.49	.738206	1.7944	-65.606	973.14
36000	35938	4761.28	.710284	1.8293	-69.160	968.75
37000	36934	4536.63	.678007	1.8723	-69.700	968.08
38000	37931	4326.40	.646302	1.9177	-69.700	968.08
39000	38927	4124.10	.616082	1.9642	-69.700	968.08
40000	39923	3931.29 -1	.587278 -3	2.0118 +0	-69.700	968.08
41000	40921	3747.50	.559823	2.0605	-69.700	968.08
42000	41916	3572.33	.533655	2.1105	-69.700	968.08
43000	42912	3405.36	.508711	2.1616	-69.700	968.08
44000	43907	3246.20	.484936	2.2139	-69.700	968.08
45000	44903	3094.50	.462274	2.2675	-69.700	968.08
46000	45899	2949.90	.440673	2.3224	-69.700	968.08
47000	46894	2812.08 -1	.420084 -3	2.3787 +0	-69.700	968.08
48000	47890	2680.70	.400458	2.4363	-69.700	968.08
49000	48885	2555.47	.381751	2.4953	-69.700	968.08
50000	49880	2436.11 -1	.363919 -3	2.5556 +0	-69.700	968.08
51000	50876	2322.33	.346922	2.6175	-69.700	968.08
52000	51871	2213.67	.330721	2.6809	-69.700	968.08
53000	52866	2110.49	.315277	2.7457	-69.700	968.08
54000	53861	2011.95	.300556	2.8121	-69.700	968.08
55000	54855	1918.01	.286524	2.8802	-69.700	968.08
56000	55850	1828.47	.273148	2.9499	-69.700	968.08
57000	56845	1743.12	.260397	3.0212	-69.700	968.08
58000	57839	1661.76	.248243	3.0943	-69.700	968.08
59000	58834	1584.21	.236658	3.1692	-69.700	968.08
60000	59828	1510.28 -1	.225614 -3	3.2458 +0	-69.700	968.08
61000	60822	1439.81	.215086	3.3242	-69.700	968.08
62000	61816	1372.63	.205051	3.4046	-69.700	968.08

TABLE C PROPERTIES OF EARTH'S ATMOSPHERE AS A FUNCTION OF ALTITUDE (Cont'd)

63000	62810	1308.59	.195485	3.4870	-69.700	968.08
64000	63804	1247.55	.186365	3.5713	-69.700	968.08
65000	64798	1189.35	.177673	3.6576	-69.700	968.08
66000	65792	1133.88	.169344	3.7464	-69.604	968.20
67000	66785	1081.05	.161299	3.8395	-69.059	968.87
68000	67779	1030.76	.153513	3.9348	-68.514	969.55
69000	68772	9828.71 -2	.146178	4.0324	-67.969	970.22
70000	69766	9372.76 -2	.139203 -3	4.1322 +0	-67.424	970.90
72000	71752	8938.59	.132571	4.3388	-66.334	972.24
74000	73738	8525.13	.126263	4.5550	-66.244	973.59
76000	75724	7058.82	.103970	4.7813	-64.155	974.93
78000	77709	6425.82	.943868	5.0183	-63.066	976.28
80000	79694	5851.20	.857110	5.2659	-61.977	977.62
82000	81679	5329.42	.778546	5.5255	-60.888	978.95
84000	82671	4855.49	.707382	5.7968	-59.799	980.29
86000	85647	4424.91	.642902	6.0805	-58.711	981.62
88000	87630	4033.60	.584461	6.3771	-57.623	982.95
90000	89613	3677.88 -2	.531480 -4	6.6876 +0	-56.535	984.28
92000	91596	3354.42	.483433	7.0121	-55.447	985.61
94000	93578	3060.22	.439851	7.3513	-54.359	986.93
96000	95560	2792.56	.400305	7.7059	-53.272	988.26
98000	97542	2548.98	.364413	8.0762	-52.185	989.58
100000	99523	2327.25	.331829	8.4631	-51.098	990.90
102000	101504	2125.36	.302238	8.8684	-50.011	992.21
104000	103484	1941.48	.275360	9.2911	-48.925	993.53
106000	105464	1773.99	.250654	9.7380	-47.368	995.41
108000	107444	1621.85	.227480	1.0222 +1	-44.326	999.07
110000	109423	1483.75 -2	.206598 -4	1.0726 +1	-41.286	1002.72
112000	111402	1358.31	.187767	1.1251	-38.246	1006.36
114000	113380	1244.29	.170773	1.1798	-35.207	1009.98
116000	115358	1140.57	.155426	1.2337	-32.168	1013.59

TABLE D TYPICAL GROUND WIND VELOCITIES IN CONTINENTAL U.S.

Station	Wind Velocity – mph	
	Mean	Extreme
Albuquerque	8.9	90
Cleveland	10.8	74
Denver	9.0	56
Detroit	10.2	46
Galveston	11.0	100+
Helena	7.9	73

TABLE D TYPICAL GROUND WIND VELOCITIES IN CONTINENTAL U.S. (Cont'd)

Key West	11.3	122
Little Rock	8.2	65
Miami	9.0	74
Minneapolis	10.6	92
Nashville	7.9	73
New Orleans	8.4	98
New York	9.5	70
Omaha	10.9	109
Philadelphia	9.6	73
Portland (Oregon)	7.7	88
St. Louis	9.5	91
San Diego	6.7	51
Spokane	8.6	59
Washington, D.C.	9.3	78
Mt. Washington (N.H.)	35.2	231

TABLE E PHYSICAL RELATIONSHIPS OF PLANETS

	Earth	Venus	Mars	Jupiter
Mean distance from Sun (compared to Earth) =	91.416 x 10^6 mi	.7228	1.5233	5.2025
Orbital eccentricity	.016	.0068	.0934	.0484
Orbital inclination to Earth orbit		3.40°	1.6°	
Mean orbital velocity	18.50 mps	21.76 mps	14.99 mps	8.11 mps
Mass (compared to Earth) =	13.184 x 10^{24} lb	.8167	.1073	317.93
Diameter (compared to Earth) =	7918.2 mi	.95	.531	10.95
Density (H_20 = 1)	5.519	5.256	3.907	1.337
Density (compared to Earth) =	344.5 lb/ft^3	.9524	.7188	.2422
Gravity, surface, Earth =	32.117 fps^2	.9049	.3627	.2305
Escape velocity		6.3 mps	3.2 mps	
Side-real period	365.26 days	224.7 days	1.881 years	11.861 years
Axial inclination	23.45°	179°	25° 12'	3.117°
Rotational period	23.934 hours	243 days	24.62 hours	9.842 hours

CHAPTER 1

APPLICATIONS

Recovery systems cover a wide range of applications, including landing deceleration of aircraft, the Earth landing of the Apollo crew module, and airdrop of personnel and equipment as representative examples. All recovery systems have one component in common, a deployable aerodynamic decelerator. The decelerator may be single or multiple ballistic parachutes, a gliding parachute, a self inflating or pressure inflated drag balloon, mechanical dive brakes, rotors or umbrella type devices that can be stowed and unfurled for operation.

The type of recovery system used depends upon a number of factors, including the type of body or vehicle to be recovered, the recovery operational envelope, the experience and available knowledge from similar recovery systems in the applicable technical field and, often more important, the time and funds available for development. The latter may dictate use of a more proven conventional system in preference to a higher performance (lower weight, volume, load) but less proven system. Each recovery system selection and development should take into account and evaluate such requirements as:

System reliability

Performance envelope (supersonic operation, high altitude performance, stability, glide capability, no impact damage, etc.)

Low parachute opening and ground impact loads

Landing accuracy

Low recovery system weight and volume

Simplicity of design

Location, flotation, survival gear

Multiple reuse

Simplicity of maintenance, operation and refurbishment

Prime system interface

Automatic checkout

Resistance to environmental and battle damage

Long time storage capability

Suitability for military operation

Low development, acquisition and life cycle cost

Different recovery system applications have a different priority rating for the afore-listed requirements. For example, a system that provides the primary means of landing personnel, such as the parachute system for a manned spacecraft, will have reliability as the highest priority. An airdrop system, where the payload may cost less than the recovery system will by necessity, stress acquisition cost and reuse in multiple operations for low life cycle cost. The difference in maintenance cost is well demonstrated in the comparison between the 1½ hour packing time for a 100-ft diameter airdrop parachute and the 30 hours required for densely packing an 83.5 diameter Apollo main parachute.

This chapter contains descriptions and discussion of a number of recovery systems, many of which are or have been operational. Recovery system applications are grouped in technical areas of vehicle recovery, emergency escape from aircraft, airdrop of personnel and equipment, aircraft deceleration and control, mid-air retrieval and special applications. Each section contains a discussion of typical requirements for the application, special design approaches and a description of specific recovery systems within the particular application group. Specific recovery systems were selected based on operational experience, uniqueness of concept, performance requirements and also on the availability of data to the authors and the technical community in general.

VEHICLE RECOVERY

Vehicles that have employed recovery as a necessary sequential function include target drones, remotely piloted vehicles, missiles, sounding rocket payloads, manned or unmanned flight mission controlled by a pilot, or an autonomous on-board guidance unit, prior to using the recovery system.

Recovery of Target Drones and Remotely Piloted Vehicles.

Target drones generally are small, reusable, ground controlled air vehicles in the 200 to 2000 lb class that simulate the optical, electromagnetic and electro-optical signatures of operational aircraft. Their flight performance frequently duplicates that of existing aircraft in order to provide realistic target practice for air-to-air and ground-to-air weapons. Target drones are flown in friendly territory, on controlled test ranges and recovered in designated areas; they frequently receive aerial damage due to target practice.

Remotely piloted vehicles (RPV's) are ground or air-launched, use ground control or autonomous navigation, weigh up to 7,000 lbs and perform reconnaissance, electronic countermeasure, strike or other mission functions in support of operational aircraft. They are more sophisticated than aerial drones, carry more sensitive electronic equipment and fly over hostile territory in combat areas. RPV velocities range from 50 knots to high subsonic speeds.

Economy of operation is achieved by maximum reuse of both vehicle types, usually facilitated by recovery with minimal damage, using a simple retrieval method and requiring minimum refurbishment cost and time. The following requirements are typical to meet this goal:

Recovery capability from any point in the total flight performance envelope (for target drones that may be partially damaged in target practice).

Minimal damage to vehicle or on-board equipment.

Simple, low cost recovery system design of minimum weight and volume which can be easily installed.

Capability of long time storage and operation under extreme environmental conditions.

Cost effective retrieval and refurbishment cycle.

Landing accuracy.

Insensitivity to combat or target practice damage.

Low life cycle cost.

Representative Systems. Several typical target drone and RPV recovery systems are described in the following paragraphs.

KD2R-5 and MQM-74C Target Drones. The first target drone of the US Armed Forces, becoming operational in 1943, was the Radioplane QQ-2. By 1950, this original drone had developed into the Army and Air Force QQ-19 and later the Navy KD2R-5 aerial targets weighing approximately 350 lb at recovery with a maximum velocity of slightly above 200 knots.

The MQM-74C target drone, developed during the 1960's, has a recovery weight of 360 lbs, a maximum velocity of 500 knots and carries more sensitive electronic equipment than the KD2R-5. An efficient 30-ft diameter, fully extended skirt parachute lands the MQM-74C at a sea level rate of descent of 22 fps. The target drone impacts at an angle of 65 degrees to the horizontal and uses a crushable fiberglass nose cone as an impact shock attenuator. The pressure packed parachute is stowed in a removable fiberglass container located on the upper side of the fuselage in front of the vertical stabilizer. Command from the ground controller, or an emergency command, de-energizes a solenoid that releases the spring loaded clamshell doors of the MQM-74C parachute compartment. The spring loaded pilot chute ejects, opens behind the vertical stabilizer and extracts the reefed main parachute. The parachute system, including pilot chute, bridle, riser and ground disconnect, weighs 17 pounds.

The MQM-74C recovery system is also used in the KD2R-5. Figure 1.1 shows the arrangement and the main dimensions for both the MQM-74C and the KD2R-5 recovery systems, the difference being that the MQM-74C parachute employs reefing and the KD2R-5 parachute without reefing, uses a skirt hesitator and a different vehicle attitude at landing. Deployment of the main parachute past the vertical stabilizer is controlled by pilot chute drag force which keeps tension on all elements of the deploying main parachute. A smooth stabilizer with no protruding parts and a slanting leading edge prevents snagging of the parachute. An automatic ground disconnect disengages the parachute at landing to prevent ground dragging in high surface winds. The ground disconnect device works on the load relaxation principle and has a built-in time delay to prevent disengagement during parachute opening. Water flotation is accomplished on the KD2R-5 by water-proof compartments. The MQM-74C floats in a horizontal attitude by means of a water-tight nose section housing all electronic equipment and a (stored) gas inflated flotation bag attached to the tail of the vehicle. The land and water recovery system of both target drones has proven to be reliable, simple in operation, and easy to maintain and refurbish. A simple recovery system of this type is usually suitable

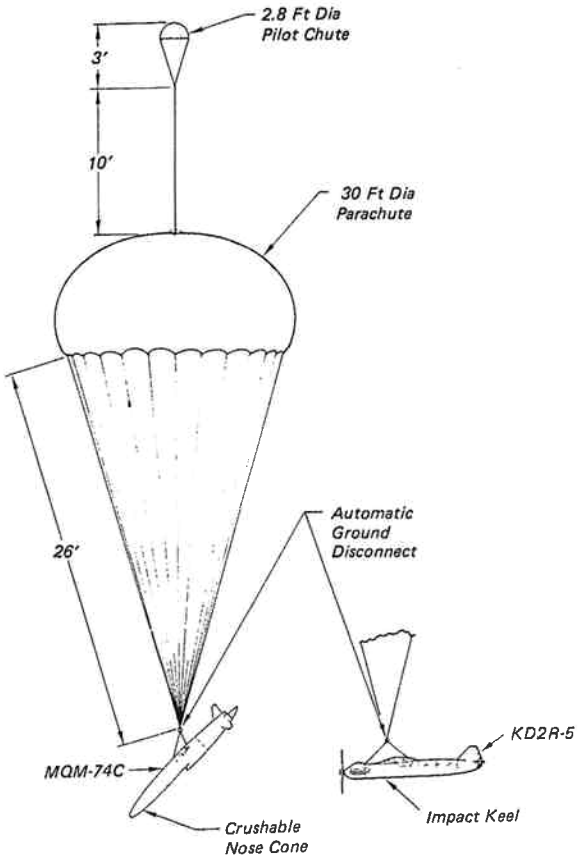


Figure 1.1 Recovery Configurations for MQM-74C and KDR-5

for lightweight vehicles where emergency high speed parachute deployment is not required and where relatively large parachute opening and impact loads of approximately 10 to 20 g's can be accepted.

U.S. Army/Fairchild USD-5 Reconnaissance RPV. The Aircraft Division of the Fairchild Corporation in the early 1960's developed for the US Army, a reconnaissance drone with a maximum speed of 500 knots, a launch weight of 7800 lbs and a side-looking aerial radar, as the prime sensor. The recovery system concept was determined by the following requirements:

The radar sensor necessitated limiting the parachute forces to 3 g's and the landing deceleration to 8 g's.

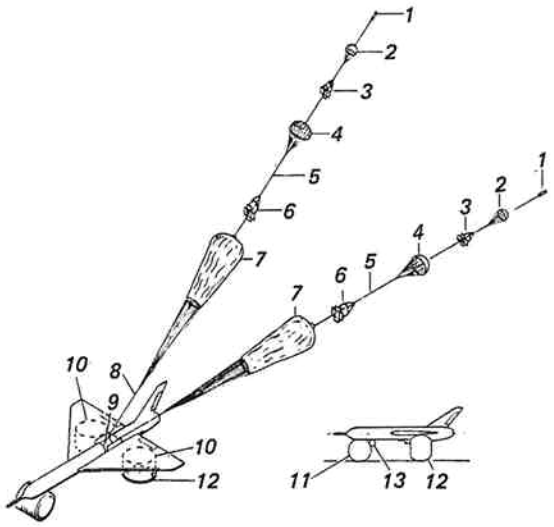
Direct ground contact of the drone had to be avoided to prevent structural damage when landing in rough terrain.

The recovery system must be deployed from a compartment in front of a large vertical stabilizer.

A high speed recovery system, covering the total flight envelope, was required for the development flight test phase.

The recovery system was fully qualified in a series of recovery system tests [1] and drone flights.

A cluster of two 78-ft diameter conical full-extended-skirt parachutes lowered the vehicle with a landing weight of 4800 lbs at a rate of descent of 22 fps. Airbags were used for ground impact attenuation. Figure 1.2 shows the parachute and airbag system.



1. *Drogue Gun Slug*
2. *Pilot Chute (2.3 Ft D_o Ringslot)*
3. *Deployment Bag for Extractor Parachute*
4. *Extractor Parachute (7 Ft D_o Ringslot)*
5. *Bridle for Extractor Parachute*
6. *Deployment Bag for Main Parachute*
7. *Main Parachute (78 Ft D_o Conical Full Extended Skirt)*
8. *Riser*
9. *Parachute Compartment in Fuselage*
10. *Airbag Compartment in Wing*
11. *Forward Airbag (1)*
12. *Aft Airbag (2)*
13. *Non-deflating Nose Bag*

Figure 1.2 USD-5 Recovery System

Recovery was initiated with pneumatic opening of the clamshell doors, using the landing bag air supply as a power source. Two drogue slugs were then fired 45 degrees aft and up, to pull two 2.3 ft diameter pilot chutes past the stabilizer. These pilot chutes deployed two 7-ft diameter ringslot extraction parachutes, which in turn extracted the 78-ft diameter main parachutes. The two main parachutes were deployed independently left and right of the vertical stabilizer. The main parachutes were reefed in one step for four seconds. All pilot chute and extraction parachute risers were long enough to permit parachute inflation behind the vertical stabilizer. Deployment bags were designed with off-center handles to augment lift-out from the parachute compartment and outward deflection away from the stabilizer. The main parachute system was qualified for a 250 knot opening speed without surpassing the 3 g's load limit. The airbag system consisted of two dual compartment cylindrical wing bags and a sausage shaped nose bag with a small 15-inch diameter non-deflatable auxiliary airbag attached to the main bag. The two wing bags located well behind the center of gravity of the vehicle, deflated the lower compartments upon ground contact. The nose bag deflated fully and the drone came to rest on the non-deflating auxiliary nose bag and the two upper compartments of the wing bags. This system proved quite effective and landed the USD-5 undamaged in numerous flights during the service test phase.

CL-89 Battlefield Reconnaissance RPV. Canadair in Montreal, Canada has developed a small battlefield reconnaissance RPV that is in use with several NATO countries. The 400 knot, 250 pound RPV uses a drogue parachute, main parachute, airbag recovery system and a unique homing beacon for a fully automatic landing. A 500 ft landing circle accuracy is claimed for this day or night all-weather reconnaissance RPV[2].

AQM/BGM-34 Remotely Piloted Vehicle Series. Teledyne Ryan Aeronautical has developed, for the USAF, a series of RPV's which includes the AQM-34M/L reconnaissance RPV, the AQM-34H and -34V ECM RPV's and the multi-mission BGM-34C RPV. These vehicles use helicopter mid-air retrieval for recovery. This retrieval system is discussed in detail on page 60.

High Altitude Supersonic Target. A high altitude supersonic target (HAST) has been developed by the Beech Aircraft Company [3,177]. It covers a performance range from Mach 1.2 at 35,000 to Mach 4 at 100,000 ft powered by a hybrid rocket engine. Launch of the 1200-lb drone is by aircraft, and recovery is by helicopter mid-air retrieval. The operational recovery system starts with decreasing the drone velocity to slightly below Mach 1, and the altitude to below 50,000 feet. It then deploys a 6.9 ft diameter conical ribbon parachute for initial deceleration and descent to 15,000 feet.

At this altitude, the drogue parachute disconnects and deploys a 45.5 ft diameter reefed Ringsail parachute for mid-air retrieval. This concept depends on the drone having completed its mission without suffering damage that could prevent it from reaching the recovery altitude and speed. Efforts are under way to allow recovery from most of the flight performance envelope. This may result in use of a 5.8 ft diameter Hemisflo ribbon parachute capable of being operated at speeds in excess of Mach 2 for decelerating the drone to the operating envelope of the second drogue parachute. A flotation system will be included to facilitate water recovery in case parachute deployment occurs beyond the reach of the retrieval helicopter or at drone weights and rates of descent too high for mid-air retrieval. Unique features of this recovery system are the short coupling of the drogue parachute to the vehicle, made possible by the slender streamlined vehicle body, and the large Ringsail main parachute which combines a high drag with the slotted design necessary for the helicopter retrieval hook to engage. The main parachute size, which is near maximum for direct mid-air engagement, avoids the problems of the tandem parachute mid-air retrieval system discussed on page 64 . Use of Kevlar material for the fabrication of the first and second stage drogue parachutes combined with high density packing procedures will help in reducing the stowed volume of this advanced recovery system.

Special Design Considerations. Positive parachute deployment from the stowage compartment into good airflow behind the vehicle is one of the prime requisites for reliable parachute operation. Small drones successfully use spring loaded pilot chutes and ejected doors for pilot chute deployment. Large vehicles need forced deployment of the initial parachute such as the drogue gun deployed pilot chutes of the USD-5, or the mortar and catapult ejected drogue parachutes of the Apollo and F-111 crew capsules. A favorable parachute installation is used in the Teledyne Ryan Firebee target drones and the related -34 RPV series. The drogue parachute and main parachute are stowed one behind the other in the tail of the vehicle. Ejection of the tail cone deploys the drogue parachute which stays attached to the main parachute housing. At main parachute deployment

command below 15,000 feet, this housing disconnects and is pulled away by the drogue parachute thereby deploying the main parachute.

Recovery of an out-of-control vehicle requires forced deployment of the drogue parachute away from the effective range of the spinning or tumbling vehicle. This is best accomplished by mortar deployment of the drogue parachute.

Experience has shown that for reliability reasons, two independent sequencing systems are advisable. This includes dual sensors for deployment and terminal recovery commands, dual initiators, possible dual actuators and similar functions. Normal recovery is initiated by ground command or ground beacon. Recovery may be started also by engine or electrical power failure, loss of the ground command channel or by command of the range safety officer.

A no-impact-damage landing can be achieved for small, unsophisticated drones with a low rate of descent and a sturdy vehicle design. All larger vehicles, and those with sensitive electronics gear, will require either mid-air retrieval or such impact attenuation systems as crushables, frangibles, airbags or retrorockets. Which system to choose is a function of the mission concept, the allowable impact deceleration and the vehicle design[4,5].

Missile Recovery

In the 1950's and early 1960's, recovery was selectively applied to missiles during research and development testing, primarily for the purpose of after-flight vehicle and component inspection and failure analysis. The development of recovery systems for fast flying, possible out-of-control missiles proved to be difficult. Weight and space in missiles is at a premium and the recovery system should have a high probability of success for the first flight, where it may be needed most. Few missile recovery projects materialized. As the art of electronic measurements and real-time flight data monitoring and transmission progressed, recovery of the actual missile became less important.

One interesting project was the recovery of the Terrier ship-to-air missile for inspection and possible training reuse. A successful multi-use recovery system was developed for the training version of the Matador/Mace missile, but it was never used operationally. A similar approach is presently being investigated for the airlaunched cruise missile (ALCM). Requirements for recovery of training missiles are similar to those for the reuse of target drones and RPV's. The following paragraphs provide data on specific missile recovery projects.

Terrier Missile Recovery System. In the early 1950's, the Radioplane Company developed a recovery system for the 850-lb Terrier ship-to-air missile[6]. Recovery was initiated at Mach 1.0 to 1.2 using a 3.0 ft diameter ribbed guide surface drogue parachute, 23 ft diameter solid conical main parachute and a water flotation recovery system. The intent was to reuse missiles for training flights. Six flights were performed with limited recovery success. The concept did not prove practical, considering the cost of the extended water recovery operation and the refurbishment of the sea water soaked missile.

Matador/Mace Recovery. In the late 1950's, the Air Force investigated the recovery of Matador/Mace training missiles for reuse. The 10,000 lb missile was recovered by reducing the speed to 200 knots and using a mortar ejected pilot/drogue parachute for deploying three each, 100 ft diameter tri-conical main descent parachutes. Two sausage shaped dual compartment airbags around the front and the rear of the fuselage, cushioned the landing impact and kept the missile off the ground. Successful recovery tests were conducted [7,8].

Air Launched Cruise Missile Mid-Air Retrieval. A recovery system for ALCM vehicles flown in training flights, is under development. The vehicle weighing in excess of 1500 lbs will conduct a pull-up maneuver prior to parachute deployment. Helicopter mid-air retrieval is planned for final recovery. Several mid-air retrieval parachute concepts are being investigated.

Sounding Rockets and Reentry Vehicles

Sounding rockets and reentry vehicles vary widely in mission purpose, flight trajectories, apogee altitude, reentry angles and reentry velocities. Nevertheless, there are basic similarities in the concept and design of recovery systems for returning the payloads. Apogee altitudes vary from approximately 200,000 feet for the HASP (High Altitude Sounding Probe) to the 1,200 mile apogee of the NERV (Nuclear Emulsion Reentry Vehicle). The corresponding reentry velocities vary from approximately 2,000 fps to 20,000 fps.

Recovery System Approach and Design. Reentry and descent velocities of probes and nose cones ejected from rockets, flying harpin or steep trajectories will vary from about 2,000 to 20,000 fps. Capsules from Earth orbiting vehicles are ejected at about 25,000 fps. The Apollo spacecraft reentered the Earth's atmosphere in a shallow trajectory at 36,000 fps. Aerodynamic deceleration starts as soon as the

vehicle enters the continuum flow atmosphere at 200,000 to 300,000 feet altitude. Aerobee[9], HASP and other sounding rockets take measurements on the ascending trajectory, separate the instrumented nose cone near apogee and by proper location of the center of gravity, the nose cone descends in a flat spin. Spinning nose sections (probes) of up to several hundred pounds weight, obtain ballistic coefficients of 50 to 100 psf which decelerates the probe to between 200 and 400 fps at 5,000 to 10,000 feet altitude, sufficient for main parachute deployment[10,11]. Lightweight parachutes can be deployed at altitudes up to 250,000 feet if a slow, stable descent through the upper atmosphere is required[12]. For higher altitudes and higher ballistic coefficient, vehicles with large flared skirts or dive brakes[13] may be used for initial deceleration followed by parachutes in the Mach 3 range or ram-air inflated balloons for speeds of Mach 4 or greater[10,14]. Decelerator design selection considerations are aerodynamic heating, inflation stability, low or high dynamic pressures and altitude and time available for deceleration. Hemisflo ribbon parachutes and the Ballute[15] have been used successfully for these high Mach applications. Figure 1.3 shows a a typical high altitude probe trajectory profile.

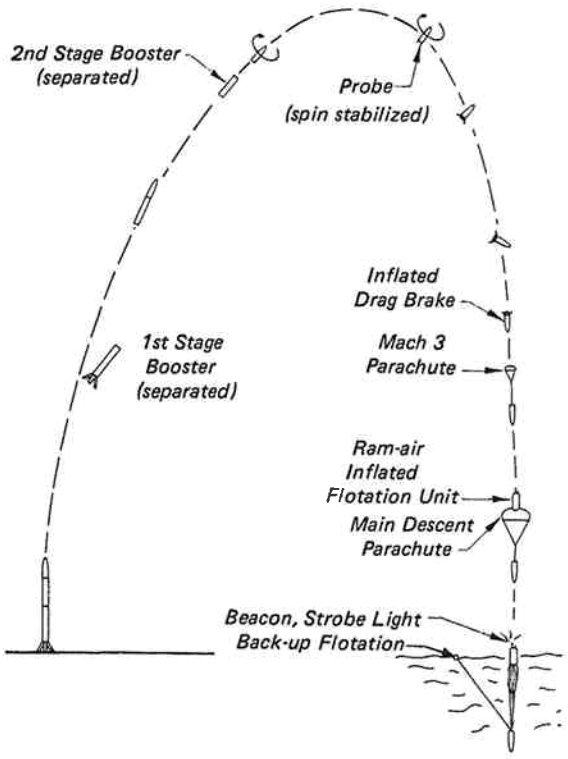


Figure 1.3 Typical High Altitude Probe Trajectory

Nose cones of the Jupiter C, the NERV and the NASA "Big Shot", (the latter took pictures of the inflating Earth orbiting Echo II balloon in 1961) reentered at speeds up to 20,000 fps. Aerodynamic deceleration for the stable or rotating, lightweight, large diameter nose cones was provided by ballistic coefficients in the 50 to 150 psf range. This resulted in aerodynamic deceleration to velocities in the Mach 0.7 to 1.5 range at 5,000 to 10,000 feet altitude. Single parachutes,deployed at these speeds provided water entry velocities from 80 to 100 fps. Recognized problems were ejection of the parachute through the vehicle wake into good airflow for proper inflation, a swivel to prevent parachute wrap-up by a rotating nose cone and heat protection of the recovery system.

Today's nose cones are usually heavier, have smaller nose radii and more slender cone angles with resultant W/C_DS values in excess of 1,000 psf and terminal sea level velocities of up to 5,000 fps. Efforts to recover these vehicles involves ejection of all non-essential mass for reduction of W/C_DS, development of high temperature resistant dive brakes, development of Kevlar and other high temperature materials[16].

The terminal phase of the recovery sequence, mid-air retrieval, ground landing or water landing, determines the parachute type and size necessary. Mid-air retrieval parachutes need a descent rate of 20 to 25 fps at 10,000 feet altitude for both rotary wing and fixed wing aircraft recovery. These parachutes are opened at altitudes of 15,000 to 40,000 feet to provide sufficient time for the retrieval aircraft to acquire and approach the descending parachute vehicle system. Mid-air retrieval starts at 10,000 to 15,000 feet altitude and requires special parachutes of reinforced slotted design or tandem parachute systems discussed in detail on page 64 .

Ground landing requires descent velocities of about 20 fps and possibly impact attenuation equipment in order to prevent damage. The resultant large parachutes have considerable weight and volume which is frequently not acceptable. Water entry permits entry velocities of 50 to 100 fps with correspondingly smaller and lighter parachutes but adds inflation, location and retrieval equipment.

Spacecraft Recovery

The subject of spacecraft recovery covers a wide variety of vehicle systems and applications. Spacecraft recovery systems can be grouped as follows:

1. Earth orbiting research vehicle recovery systems
2. Planetary spacecraft descent systems
3. Manned spacecraft terrestial landing systems

The first group involves such Earth orbiting research vehicles as Discoverer and Biosatellite. The second group consists of the two Viking Mars landers and the Pioneer-Venus spacecraft which will descend to the surface of the planet Venus in late 1978. Both of these programs use parachutes for controlling part of the descent trajectory, but not for landing. The third group includes the crew modules of the Mercury, Gemini and Apollo spacecraft as well as the Russian Vostok and Soyuz space vehicles.

Requirements for Spacecraft Recovery. Reliability, minimum weight and volume, suitability for space environment and protection against reentry heating are primary requirements common to all spacecraft recovery systems.

Reliability. It is obvious that parachutes that form part of a manned mission require the highest reliability possible. A second reason for high reliability is cost of spacecraft systems. When the Apollo II command module landed after the first completed moon mission, it had cost the U.S. taxpayer approximately $400,000 per pound of Apollo command module returned to Earth. The cost figures for other recoverable spacecraft are probably similar. Apollo, Gemini and Mercury in addition, had to cope with the fact that the nation and the world were watching the U.S. space effort.

Low Weight and Volume. The cost of getting one pound of spacecraft on its way to the planets is lower than the cost of landing a spacecraft but is still many thousands of dollars per pound. Every pound saved on the recovery system saves considerable funds, or frees weight and volume for instrumentation that serves the primary mission purpose of exploring space. To obtain minimum weight and volume, and still have a reliable system, requires an unusual amount of analysis, a high performance, low loads design and a test program that provides the maximum assurance that the system will work as designed.

Space Environment. Extreme low pressures and temperatures are encountered in interplanetary space. These conditions will cause outgassing of all volatile components such as moisture, oils, coating and finishes contained in such decelerator materials as nylon, Dacron and Kevlar. This can conceivably change the property characteristics of these materials. In addition, a chemically hostile atmospheric environment may be encountered on some of the planets.

Aerodynamic Heating. The Apollo command module reenters the Earth's atmosphere at a velocity of 36,000 fps resulting in heat shield temperatures in excess of 5000°F. The temperature environment required protection for the recovery system as well as selection of suitable parachute materials.

Recovery of Earth Orbiting Research Vehicles. Recoverable spacecraft in this category are the Biosatellite[17] and the Discoverer type spacecraft. Both vehicles gather information while cruising in Earth orbits. The Biosatellite served as home for a primate (monkey). The orbiting vehicle consisted of the recoverable reentry capsule containing the primate, a secondary life support system, all gathered data and the reentry and recovery subsystems. The primary life support system and most of the instrumentation was housed in a non-recoverable adapter. This adapter was separated from the recovery capsule shortly before reentry. The blunt nose cone and large diameter body resulted in a low ballistic coefficient and caused reentry deceleration of the vehicle to high subsonic speeds at sufficient altitude to eject the rear heat shield which deployed a 7-ft diameter unreefed ribbon drogue parachute. The drogue parachute then deploys a reefed 36-ft diameter Ringslot main recovery parachute suitable for mid-air retrieval by C-130 aircraft. The weight of the total parachute assembly was 37.5 lbs. Flotation, location and water pick-up equipment permitted water retrieval in case mid-air retrieval could not be accompolished. All recovery sequencing and propellant actuated functions were redundant for reliability reasons.

The Discoverer reentry capsule is very similar to the Biosatellite capsule. It has a total capsule weight of 180 lbs. The drogue parachute is a 5.4 ft diameter conical ribbon parachute. A 29.8 ft diameter reefed Ringslot parachute is used as a descent and mid-air retrieval parachute. The drogue parachute is deployed at altitudes up to 70,000 feet and the main parachute up to 50,000 feet. This provides sufficient time for the C-130 mid-air retrieval aircraft to acquire and approach the capsule. The total parachute assembly weighs 23.8 lbs. Location, flotation and water retrieval gear (in case of mid-air retrieval failure) is similar to the Biosatellite recovery system.

Planetary Entry Trajectory Control by Parachute. In July and August of 1976, two Viking instrument packages, called landers, soft-landed on the surface of the planet Mars. In September, 1977, two Pioneer probes started on their way to the planet Venus.

They are scheduled to arrive in December 1978 and eject four pods that will descend through the Venus atmosphere. Both Mars landers have used parachutes and one of the Pioneer-Venus pods will use a parachute for partial trajectory control. Both parachute systems are designed to operate in atmospheric densities quite different from that of Earth. The Mars atmosphere is cold and has approximately 1/100 of the Earth's atmosphere. The atmosphere on the planet Venus is about 100 times as dense as the Earth's atmosphere, and surface temperatures are close to 900°F. Also, the chemical compositions of the Mars and Venus atmospheres are quite different from that of the Earth. Atmospheric conditions on Venus are reasonably well established, whereas knowledge of the atmospheric conditions on Mars' surface were limited, requiring the parachute system to be operative over a wide Mach number and dynamic pressure range. The purpose of the Mars mission, in addition, required the planetary landing system to be biologically clean, necessitating extensive sterilization of the lander and all its subsystems. NASA, the responsible agency for both programs, established a systematic development, test and qualification program for both decelerator systems.

The Venus mission does not require a biologically clean system, therefore, was easier to define, develop and test.

Viking Lander Parachute System. The planned sequence of events for the Viking-Mars lander is shown in Figure 1.4. After separation from the Mars orbiter the lander entered the Mars atmosphere at about 800,000 feet altitude. Up to this time the lander was contained in the bioshield, sealed, pressurized and protected from biological contamination prior to entering the Mars atmosphere. The bioshield was ejected after deorbit. The lander, heat protected and decelerated by its large diameter aeroshell, was controlled in pitch and yaw by an on-board attitude control system. A radar altimeter sensed and communicated altitude information. Upon reaching an altitude of 21,000 feet above the Mars surface and a nominal velocity of 1200 fps, a 53-ft diameter disk-gap-band parachute (non-reefed) was mortar ejected and opened in about three seconds in the wake of the large aeroshell. Seven seconds later the aeroshell ejected and three landing foot-pads extended. At 4000 feet altitude and a nominal velocity of about 200 fps, the parachute was disconnected and the descent engines were fired.

At the start of the Viking program large uncertainties existed concerning the Martian atmosphere. This required possible parachute operation from Mach 2.1 to low subsonic speeds and at a dynamic pressure range from 0.5 to 10 psf. Viking mission constraints dictated minimum weight and volume for recovery components, a parachute that functioned in the wake of the large aeroshell lander forebody within a defined drag area and opening load range, a parachute that operated after being pressure packed for thirty-six months, and a recovery system that did not contaminate the atmosphere and surface of the planet Mars[18].

NASA established three programs for selection, development and qualification of the parachute decelerator system. The Planetary Entry Parachute Program (PEPP) used rockets and balloon launched experiments to test disk-gap-band, ringsail and cross parachutes, and some Ballutes at altitudes above 100,000 feet and Mach numbers from 1.0 to 2.6. Based on the PEPP tests, NASA selected the disk-gap-band parachute for the Viking mission[19]. In two subsequent programs, Low Altitude Drop Tests (LADT) and Balloon Launched Decelerator Tests (BLDT), NASA developed and qualified the 53-ft diameter disk-gap-band parachute as the Viking decelerator. The LADT series used a B-57 aircraft flying at 50,000 feet as a test platform and investigated parachute opening loads and stresses at values up to 1.5 times the predicted design loads. Parachutes were modified based on test results[20]. The final parachute design and decelerator system were qualified in the BLDT program using a boilerplate lander and all end item components including the final mortar[21].

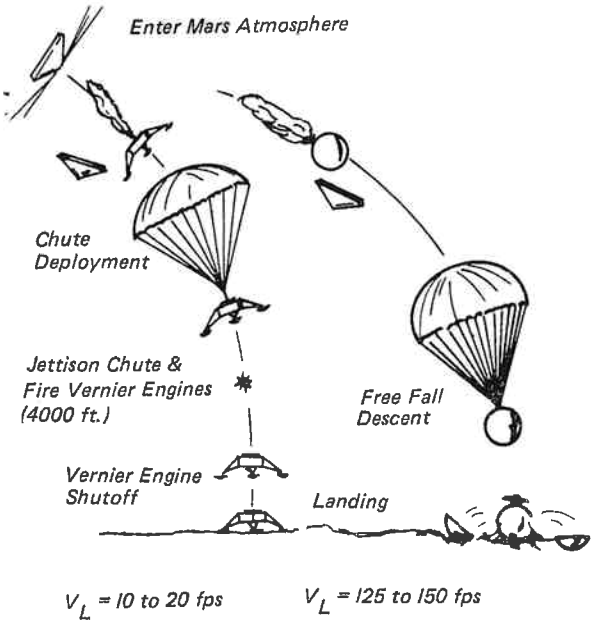


Figure 1.4 Descent Profile for A Mars Landing

In order to meet the biologically clean lander requirements for the Mars mission, the following steps were taken:

Polyester (Dacron 52) material was used for all textile parts to minimize shrinkage and cloth outgassing

All parts were retained

The decelerator system and total lander were subjected to several sterilization cycles at 275°F and then sealed for installation into the lander

Pioneer-Venus Probe Parachute System. Of the four probes that will descend through the Venus atmosphere in December 1978, the so-called "large probe" will use a parachute during its travel through the Venus cloud cover. The purpose of the large probe is to conduct a sounding of the extremes of the Venus atmosphere, to make in situ measurements of the atmospheric structure, its composition and to investigate the cloud cover distribution, composition and interaction with light and thermal radiation. The probe is ejected from a mother vehicle which enters the Venus atmosphere at about 320,000 feet at a velocity of 38,100 fps. The instrument container is a spherical titanium pressure vessel surrounded and protected by an aeroshell heatshield and rear cover quite similar to the Mars Lander arrangement. The 56-inch diameter aeroshell decelerates the 670 lb probe to a velocity of Mach 0.8 at 220,000 feet. At this altitude a 2.5 ft diameter guide surface pilot chute is mortar ejected, removes the rear cover and extracts the 16.2 ft diameter ribbon main descent parachute. The opening force of the main parachute disconnects and ejects the aeroshell heatshield. The 29-inch diameter instrument container descends on the parachute for nineteen minutes to 155,000 feet. At this point, the velocity is so low that the parachute is jettisoned. Thirty-seven minutes later, the probe impacts on the surface of Venus and ends its mission.

Parachute design is based on its primary function, to decelerate and stabilize the instrument container during its descent through the Venus cloud cover. Surface pressure, temperature and altitude gradients are reasonably well known. The parachute deployment conditions therefore, are better defined than they were for the design of the Mars lander decelerator. Also, no requirements exist for a biologically clean vehicle, thus eliminating the need for sterilization. Polyester was selected as parachute material since it has better resistance than nylon to sulphuric acid, one of the ingredients of the Venus atmosphere. Further, the effects of interplanetary space environment on material characteristics are well established from the Viking program.

The Pioneer-Venus parachute must provide stable descent with less than three degrees of oscillation, parachute opening at Mach 0.8 and a dynamic pressure of 69 psf, a drag area of 108 ± 5 ft^2, an opening load = 9100 lbs for a maximum vehicle weight of 670 lbs, and the parachute vehicle system must descend at a trim angle of two-degrees. A 16.2 ft diameter, 20 degree conical ribbon parachute was selected. It has twenty gores, a total porosity of 24.1 percent, a suspension line length ratio, l_e/D_o, of 1.22 and is fabricated from heat-set polyester material. A skirt control line is used to limit over-inflation and thereby restrict opening loads and canopy breathing in the wake of the forebody. This control method was developed for, and is discussed in, the subsequent Apollo spacecraft description.

Design verification tests were conducted at the National Parachute Test Range at El Centro. A bomb type test vehicle was used, dropped from an F-4 aircraft flying at 40,000 feet altitude. All design requirements were verified in the test, including a 1.25 dynamic pressure overload.

The final qualification test was conducted with a simulated Venus probe vehicle weighing 670 lbs and carried to altitude on a balloon at the White Sands Missile Range. The probe vehicle was released at 90,000 feet altitude and the entire parachute system was deployed and tested. The test arrangement, simulating the Venus probe, is shown in Figure 1.5 Reference 22 describes the Venus probe, the parachute system used, and the two test programs for verification and qualification of the parachute system.

Manned Spacecraft Parachute Landing Systems. United States manned spacecraft, Mercury, Gemini, and Apollo as well as Russian manned spacecraft, Vostok and Soyuz, have employed parachute systems for the landing phase of the space mission and for mission abort emergencies.

The following ground rules were established for meeting the Mercury landing system performance and reliability requirements and have been used for projects Gemini and Apollo in a form adopted to their particular mission:

The final landing on all abort cases are considered operational landings.

No single component or subsystem failure can cause loss of the crew or total system failure (redundant system requirement).

The design of the recovery system will be based on existing technology.

Weight and volume of the system will be kept to an absolute minimum.

Parachute and landing forces are to be kept to a

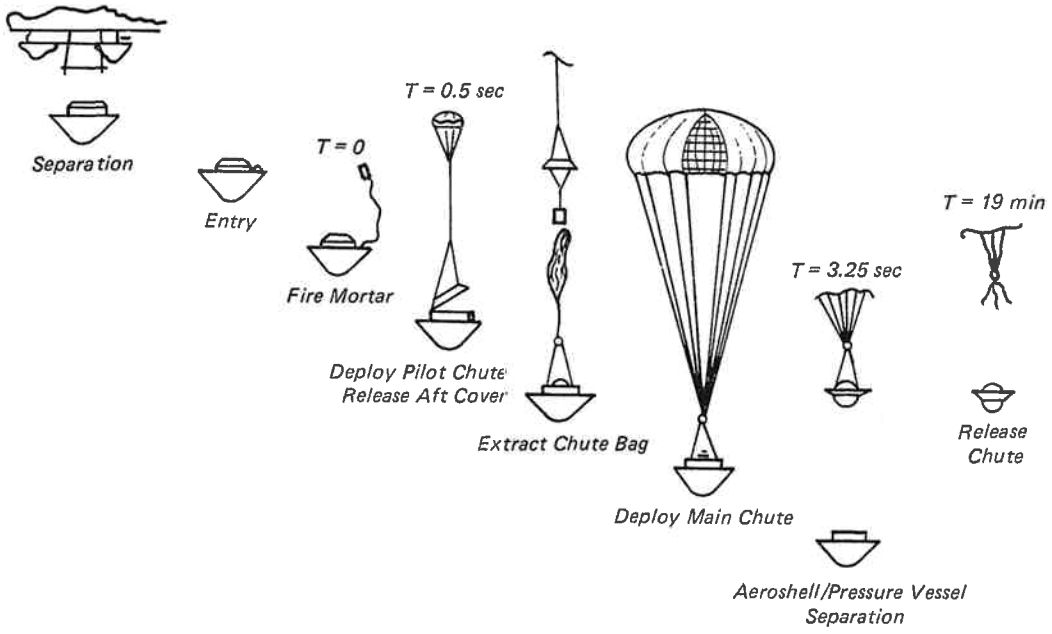


Figure 1.5 Deployment Sequence Of The Venus Probe Decelerator

level that permits the astronauts to perform immediate post-flight functions.

All functions related to parachute deployment and landing must be performed by a dual automatic system, backed up by astronaut override capability.

All components, subsystems and the total system will be design load tested, over-load tested and fully qualified prior to the first space flight.

Prudent implementation of these requirements resulted in fifty-six consecutive, successful parachute spacecraft landings including thirty-one manned landings (six Mercury, ten Gemini, eleven Apollo, three Spacelab and one Apollo-Soyuz flight). Twice in the Mercury program the parachute landing system was used in aborts of unmanned flights. On the Apollo 15 flight, one of the main parachutes was damaged after opening and deflated, the only anomaly in fifty-six spacecraft landings.

Unforseen problems were caused by spacecraft weight growth of thirty percent on Mercury and sixty percent on Apollo. Spacecraft weight growth caused a predictable associated increase in deployment, velocity, parachute forces, parachute weights and pressure packing demands. In addition, unexpected subsonic instability of the spacecraft made parachute deployment more complex and increased parachute loads. Other problems included chemical effects of attitude control motor fuels on textile parachute components and the wake effect of the large spacecraft forebodies on the drag area decrease and load increase of the drogue parachutes. Exposure to the extra-terrestrial space environment of the Apollo mission between Earth and moon did not cause a suspected textile material degradation, a fact later confirmed in the parachute systems for the Mars Viking unmanned lander.

All maximum parachute loads, minimum deployment altitude and critical deployment time conditions resulted from abort or single failure mode test conditions.

Mercury Parachute Landing System. The design requirements[23] for the Mercury landing system specified a capability to land:

on land or water after normal reentry, with landing being an emergency

from mission aborts covering the time from just prior to lift-off to orbit insertion

The Mercury spacecraft after deorbit was stabilized by an on-board reaction control system (RCS) and decelerated by its own drag to subsonic velocity at around 30,000 feet. A 6-ft diameter ribbon drogue parachute was mortar deployed at altitudes from 20,000 to 40,000 feet, primarily for stabilizing the spacecraft during subsonic descent. The drogue parachute was attached to the antenna section at the upper part of the spacecraft, by a 24-ft long polyester riser and a three-leg steel cable harness. At 10,000 feet altitude the antenna section was disconnected and a reefed 63-ft diameter Ringsail parachute deployed. After main parachute opening the forward heat shield lowered to deploy an impact attenuation bag. The spacecraft landed at a rate of descent of 28 fps. The drogue parachute was designed and tested for speeds up to Mach 1.5 at 70,000 feet altitude for emergency deployment in case of spacecraft stability problems. The main parachute and the impact bags were designed for possible land landings at up to 5000 feet altitude, and the impact bag was to reduce ground impact deceleration from 45 to 15 g's. The automatic sequencing system deployed the drogue parachute and main parachute at 21,000 and 10,000 feet altitude, respectively. Manual override by the astronauts permitted drogue parachute deployment at higher altitudes and speeds. There was no reserve drogue parachute since even an instable spacecraft would have decelerated by its own drag to the allowable deployment velocity of the main parachute at 10,000 feet. The astronauts had green and red lights to indicate proper parachute deployment or a malfunction. In the latter case, the astronaut could manually check all prior deployment functions and if necessary, deploy the reserve main parachute by manual control. Table 1.1 gives technical details of the Mercury parachute system and Figure 1.6 shows the installation of the primary and the reserve main parachute. Parallel sequencing systems were used for controlling all automatic deployment functions.

In actual use the parachute system functioned as designed in twenty flights including six manned flights and two unmanned abort emergencies. On two occasions the astronaut deployed the drogue parachute above 21,000 feet by manual override command. The reserve main parachute was never used.

Gemini Parachute Landing System. The Gemini Earth orbiting spacecraft was a two-man vehicle based on the Mercury design. Its purpose was to investigate fourteen day orbital flights, develop rendezvous and docking techniques, and to test advanced subsystems suitable for the Apollo moon mission. NASA specified land landing by Paraglider and an ejection seat back-up system as the means for landing the astronauts. In addition, a parachute water landing system similar to the Mercury system, was developed as a back-up in case the Paraglider system should not be ready for early Gemini flights. The intention was to eliminate the heavy escape tower used on Mercury and to provide land landing capability in a preselected area. When the Paraglider program encountered problems, the NASA Manned Spaceflight Center in Houston started an in-house program for the development of a land landing capabiltiy using a steerable

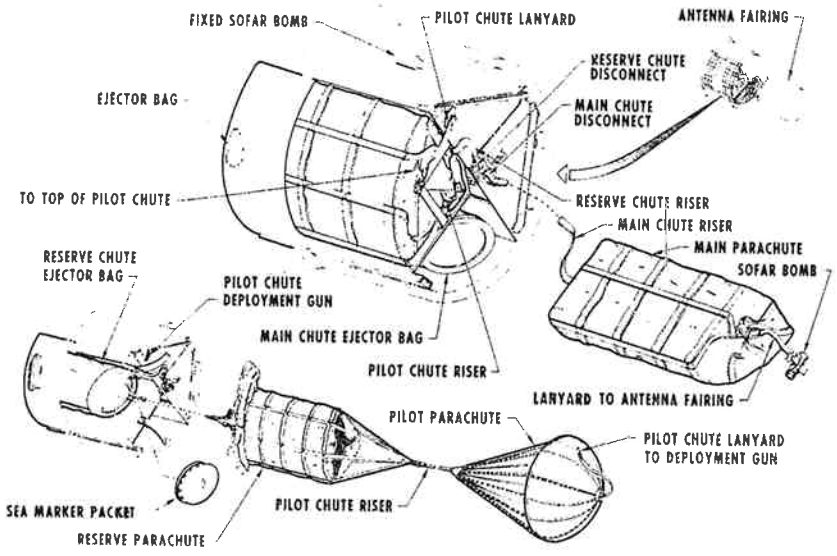


Figure 1.6 Mercury Recovery System Installation

TABLE 1.1 TECHNICAL DATA OF THE MERCURY PARACHUTE SYSTEM

Item	Units	Drogue Parachute	Main Parachute
Number		1	2 (1 Reserve)
Diameter, D_o	(ft)	6.0/6.87	63.1
Type		30° Conical Ribbon	Ringsail
Reefed, D_R/D_o	(%)	No	12%, 4 sec
No. of Suspension Lines		8	48
Strength of Suspension Lines	(lbs)	1000	550
Weight	(lbs)	2.9	56
Line Length Ratio	(l_e/D_o)	1.0	.92
Riser Material	—	Polyester	Nylon
Riser Length	(ft)	19.7	4
Riser Strength	(lbs)	7000	9000
Riser Weight	(lbs)	2.67	—
Harness		3 Steel Cables	—
Assembly Weight	(lbs)	6.43	60.2
Design Load	(lbs)	3800	10,000
Design Altitude	(ft)	42,000	10,000
Design Speed		M = 1.5	164 KEAS
Test Load (max)	(lbs)	5500	14,000
Test Altitude (max)	(ft)	70,000	10,000
Test Speed (max)		M = 1.5	190 KEAS
Suspended Weight	(lbs)	2900	2900
Rate of Descent	(fps)	—	28

The reserve main parachute was identical to the primary main parachute, but it was deployed upon pilot command by a drogue slug deployed, 6-ft diameter pilot chute.

Parasail parachute for glide approach, and landing rockets for vertical impact attenuation.

The requirements for the Mercury and Gemini water landing systems were closely related since both vehicles enter the Earth atmosphere from Earth orbital flight. The weight of the Gemini capsule was 4400 lbs compared to 2900 lbs for the Mercury capsule. The Gemini spacecraft did not enter ballistically as the Mercury capsule, but maintained an angle of attack giving a glide ratio of about 0.4 for a limited crossrange capability which somewhat affected the initial parachute deployment conditions. The Paraglider land landing program was cancelled half way through the Gemini development program and the back-up parachute system developed as the primary system, for landing in water. The ejection seat was maintained for back-up escape.

The parachute system is shown in Figure I.7 It consisted of a mortar deployed 8.3 ft diameter, 20-degree conical, ribbon drogue parachute reefed to 43 percent (D_R/D_o) for sixteen seconds. The parachute was designed for a dynamic pressure of 142 psf, with twelve 750 lb suspension lines. An 18.2 ft diameter reefed Ringsail parachute was used in tandem with the drogue parachute to remove the rendezvous and recovery (R & R) section which housed the main parachute. The pilot chute has sixteen 500 lb suspension lines and was reefed to 11.5 percent (D_R/D_o) for six seconds. The pilot chute could be mortar deployed upon astronaut command in case of drogue parachute failure. The main parachute, an 84.2 ft diameter Ringsail with seventy-two suspension lines of 550 lbs strength each, was reefed to 10.5 percent (D_R/D_o) for ten seconds, and was designed for a dynamic pressure of 120 psf. It lowered the Gemini capsule with a rate of descent of 29 fps at water landing. The capsule was supported under the parachute in a harness with a hang angle of 35 degrees from horizontal. This favorable water entry attitude eliminated the need for a landing impact attenuation bag

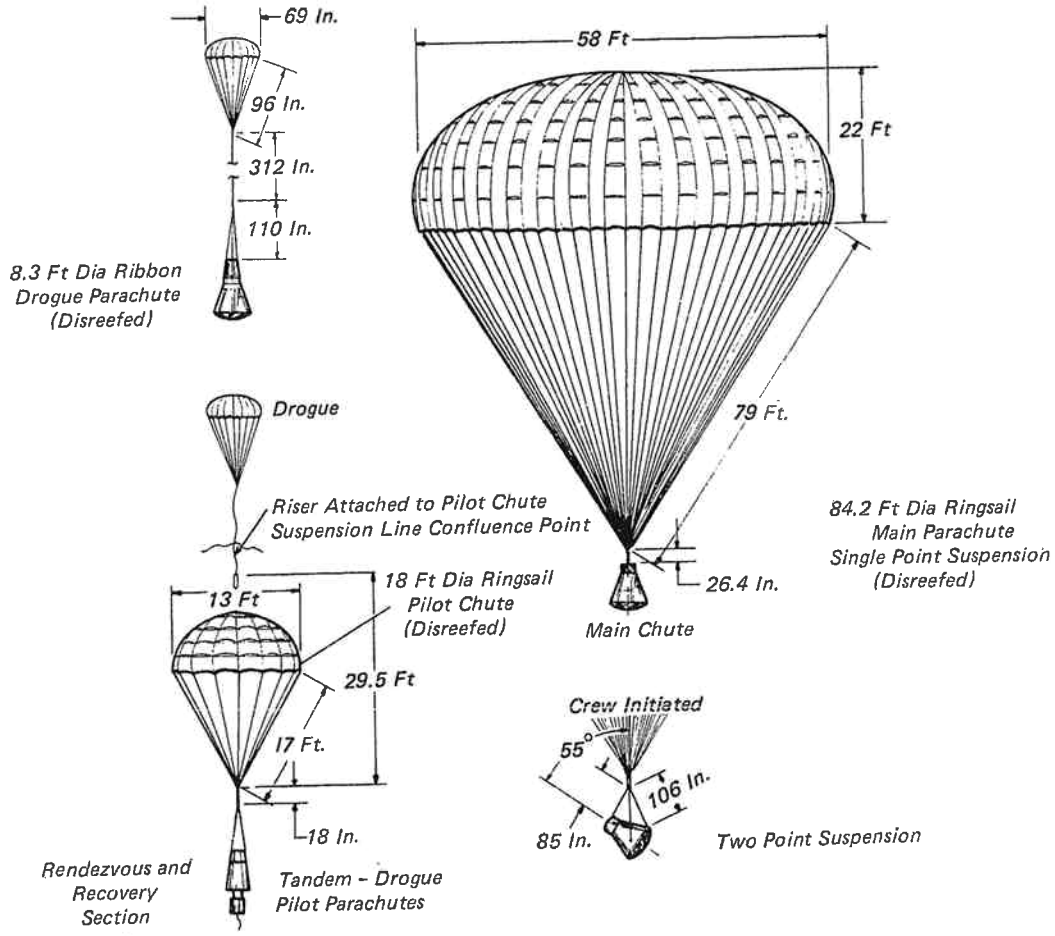


Figure 1.7 Gemini Parachute System

as used on the Mercury capsule. All parachute deployment functions were initiated manually by the astronauts with no automatic back-up system.

The drogue parachute, which had the primary purpose of stabilizing the capsule, was deployed by astronaut command while passing through the 50,000 ft altitude level with a barostatically controlled warning light actuated at 40,000 feet altitude. At 10,600 feet, another barostatically controlled warning light signaled the astronaut to deploy the main parachute, which started by disconnecting the drogue parachute to extract the pilot chute attached to the R & R section. After 2.5 seconds, the R & R section which housed the main parachute, was disconnected, pulled away from the capsule and extracted the main parachute. The reason for the large pilot chute was to lower the R & R section at a low rate of descent to avoid recontact with the capsule. After full main parachute inflation the astronaut actuated a disconnect that transferred the main parachute from the single riser to the V-harness for water landing. The main parachute was jettisoned by astronaut command after water impact similar to the Mercury procedure. The Gemini main parachute system was designed to limit the maximum parachute force to 16,000 lbs and the water impact deceleration to less than 15 g's[492,557]

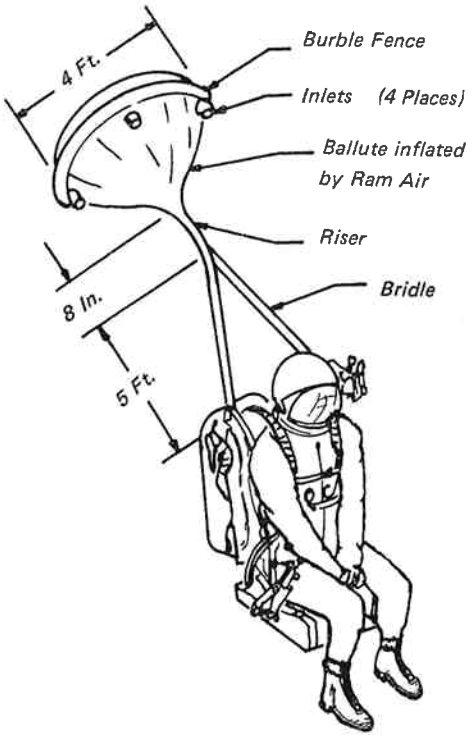


Figure 1.8 Gemini Ejection Seat with Deployed Ballute

Ejection seats were the means for back-up escape. The operating envelope extended from pad-abort (zero-zero case) to an altitude of 70,000 feet at a speed of Mach 2.86 and a maximum dynamic pressure of 820 psf. The seat system consisted of the ejection seat, seat rocket catapult, crew module hatch actuating system, personnel parachute and the survival equipment. The escape system was successfully tested for the required performance envelope; however, NASA restricted its operational use to 15,000 feet altitude to avoid inteference with the booster and crew module, and to minimize time-related water survival hazzards. A Ballute provided astronaut stabilization in case of high altitude bailout as shown in Figure 1.8. It was determined in tests, that a 48-inch diameter unit was required to provide sufficient stability and to limit rotation to an acceptable level. Other subsystems, procedures and survival equipment are quite similar to aircraft escape systems.

The Paraglider land landing concept[23, 24] is shown in Figure 1.9 The 8.3 ft diameter drogue parachute used for spacecraft stabilization was deployed at 60,000 feet altitude. At 50,000 feet the R & R section was disconnected and removed by the drogue parachute. The Paraglider was then deployed and inflated. The Paraglider design which was the predecessor of the single keel NASA Parawing had a wing area of 714 ft^2 and (stored) gas inflated leading edges and keel. NASA Ames wind tunnel tests predicted a glide ratio of better than three, and a flare-out capability. In half and full scale tests, problems were encountered with deployment and inflation of the Paraglider. Tests conducted in February 1964, appeared to have solved most of these problems.

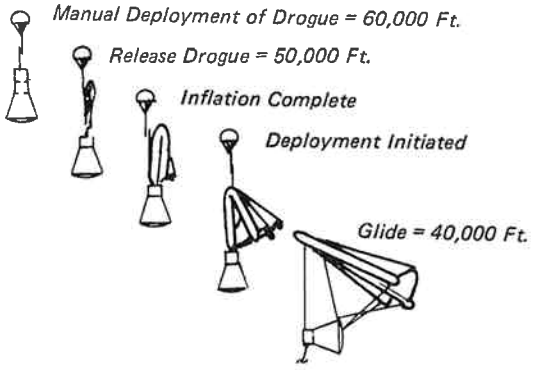


Figure 1.9 Gemini Paraglider Deployment

However, the remaining time, prior to Gemini flights, was too short to assume timely solutions to controlled flight, flare-out landing, and stowage problems. The program was cancelled in February 1964.

A program was started in September 1962 as an in-house effort of the NASA Manned Spaceflight Center in Houston, Texas to develop a land landing system suitable for the Gemini capsule[25, 26] The system consists of a 70 ft diameter Parasail parachute with a glide ratio of about 1.1. Retrorockets were incorporated for decreasing the vertical velocity to less than 5 fps prior to impact and for limiting the landing deceleration to less than 5 g's. The need to compensate for winds up to 50 fps with this low *L/D* parachute, resulted in a high vertical velocity that could not be overcome with a flareout maneuver. The solution was a rocket with a two step thrust level and a ground feeler for rocket initiation. The first thrust level decelerated the vehicle to near zero vertical velocity above ground. The second thrust level, with a thrust slightly below vehicle weight lowered the capsule gently to the ground. This approach permitted large variations in weight and landing altitude. The landing system, including a flight control mechanism, a visual and electronic on-board landing reference system, rockets and the total installation, was developed to a status where the system could have been used for the Gemini spacecraft, if required.

Apollo Crew Module Earth Landing System. The operational requirements for the Apollo Earth landing system were defined by the mission concept and environment, that of landing on the moon surface and returning safely to Earth. NASA defined a probability figure for a successful mission which in turn established reliability requirements for all subsystems and components. This approach was reflected in the following ground rules and design criteria:

Water landing was the primary landing mode, and emergency land landing should not cause major injury to the astronauts.

All mission aborts were operational modes and required back-up systems.

The primary landing system consisted of one drogue parachute and two main parachutes, backed up by one drogue parachute and one main parachute.

No single component or subsystem failure should cause loss of crew or mission.

Single failure such as loss of one drogue or one main parachute should be considered. The probability of double failures is below the reliability threshold level.

The parachute landing system reliability had to be equal to or better than 0.99996.

Components that control active functions such as barostats had to be designed for prevention of non-functioning as well as prevention of premature functioning.

A minimum factor of safety of 1.35 had to be proven in ultimate load tests for all parachute stages.

All parachutes should be independently deployed and should use active deployment means.

Some of these rules did not apply at the start of the program, but evolved as the landing system progressed through three crew module development stages. These were Block I with a weight of 8200 and 9500 pounds, Block II with a weight of 11,000 pounds, and Block II H (improved capability), a final version after the crew module fire with 13,000 pounds. Despite the increase in crew module weight, there was no increase in the total parachute load that could be applied to the command module structure, and no increase in storage volume for the parachute system.

The Apollo parachute system, as described in References 27 and 28 , is likely the most thoroughly engineered and tested parachute system ever used.

The sequence of deployment for normal reentry landing is shown in Figure 1.10. The forward heatshield of the crew module which surrounds the airlock and protects the parachute installation, was ejected at an altitude of 25,000 feet by barostat signal. The heatshield was lowered by parachute at a slow rate of descent to prevent recontact with the command module. At 1.6 seconds after heatshield ejection, two reefed 16.5 ft diameter drogue parachutes were mortar deployed and disreefed after six seconds. One drogue parachute constituted the primary system, the second drogue was a back-up parachute but was simultaneously deployed to simplify drogue parachute failure sensing the main parachute deployment. At 10,000 feet altitude, both drogue parachutes were disconnected by barostat signal and three 7.2 ft diameter ringslot pilot chutes were mortar ejected normal to the command module main axis. The pilot chutes extracted the three reefed 83.5 ft diameter Ringsail main parachutes which were disreefed in two steps after six and ten seconds. Only two parachutes formed the primary system, but the third (back-up) parachute (deployed simultaneously for simplicity reasons), also provided a lower water entry velocity. Parallel fully automatic sequencing systems were used for all deployment functions with an astronaut manual override as back-up. The astronauts could deploy the drogue parachutes above 25,000 feet altitude in case of command module

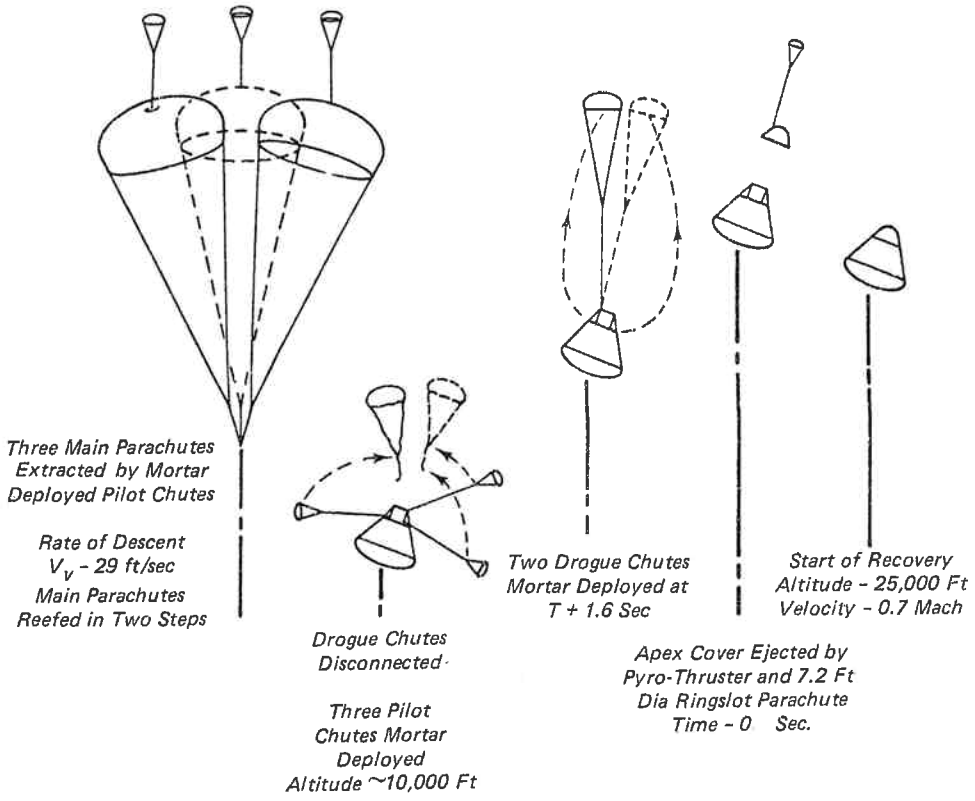


Figure 1.10 Apollo Recovery System Deployment For Normal Landing

stability problems. Parachute disengagement after landing was strictly upon astronaut command.

The command module was lifted off the booster by the launch escape rockets. A time controlled deployment sequence was used for pad-abort, and a time and barostat controlled sequence for high altitude abort

The design and installation of the final Block II H parachute system was critically affected by the sixty percent growth in command module weight, the command module instability, the wake effect of the large forebody, the required protection against reentry heating and the extreme pressure packing requirements. The final parachute system is shown in Figure 1.11 and detailed in Table 1.2. The total recovery system weight including mortars, risers and deployment bags for the two drogue and three main parachute systems was 573 lbs. The following recovery system characteristics are of special technical interest.

Riser Heat Protection and Attachment. Starting with Block II, it was concluded that the docking tunnel of the unstable command module could contact the drogue, pilot and main parachute risers. Steel cables were substituted for the lower portion of all three risers. Stowing the steel cables in the mortars and avoiding cable kinking was solved by use of flexible four-ply steel cables for drogue and pilot parachutes, pre-twisting them and casting them for stowage in lightweight foam which shattered at deployment. All drogue and main parachute risers were individually attached to the command module in the so-called flower pot. Cutting of individual cable wires on the seams of the titanium flower pot was avoided by wrapping all cables with lead tape.

Parallel and series redundancy was used in the sequencing system, the reefing system and certain propellant activated functions. The two sequencing systems that controlled automatic parachute deployment contained two barostat units each for drogue

TABLE 1.2 APOLLO PARACHUTE SYSTEM DATA

Item	Units	Drogue Parachute	Main Parachute
Number		2	3
Diameter (D_o)	(ft)	16.5	83.5
Type		25° Conical ribbon	Ringsail
No. of gores/lines		20	68
Line length ratio	(l_e/D_o)	2.0	1.48
Strength of lines	(lbs)	2500	650
Porosity	(%)	22.4	12.5
Reefing		1 step	2 steps
Reefing (D_R/D_o)		42.8%	8.4% (mid-gore) 24.8% (mid-gore)
Drag area, full open	(ft^2)	114	4200
Parachute assy. weight	(lbs)	49.86*	135.5**
Design dynamic pressure	max (psf)	204	90
Dynamic pressure	min (psf)	10	30
Deployment altitude	(ft)	3000-40,000	2500-18,000
Limit load	(lbs)	17,200 (Reefed open)	22,900 (Stage 2 reefed open)

* includes mortar and riser
** includes riser

parachute and main parachute deployment. For each step, four barostats were used, two in series and two in parallel; this protected against premature operation and ensured functioning at the right altitude. Dual independent reefing lines with two cutters each were used for the drogue parachute and the first reefing stage of the main parachute. This assured cutting of the lines at the proper time and protected against catastrophic parachute failure caused by premature severance of only one reefing line. No dual lines were required for the second reefing stage of the main parachute since premature severance would not have caused a catastrophic parachute failure. All propellant units used double initiators actuated by both sequencing systems.

The main parachutes were installed in three of the four quadrants surrounding the center airlock. Heat protection required that a one-inch gap be maintained between the parachute packs and the forward heat-shield. This space penalty coupled with the increased parachute weight and volume due to the command module weight increase, caused major packing problems. The final solution included stainless steel reefing rings and cutters to avoid bending, protective layering to prevent damage to the parachute cloth, stepwise packing of canopies, lines and risers with associated vacuum suction to remove entrapped air, Teflon powder lubricants, a one-week packing time and X-ray inspection of each pack. The packed parachute was then stowed under vacuum in a wooden form duplicating the parachute stowage compartment and wrapped with two layers of plastic film. These measures solved the packing problem but greatly increased packing time and cost.

Extensive textile material tests were conducted at a 10^{-6} torr vacuum combined with duplicating reentry pressure rise and temperature conditioning. The strength degradation due to vacuum was below

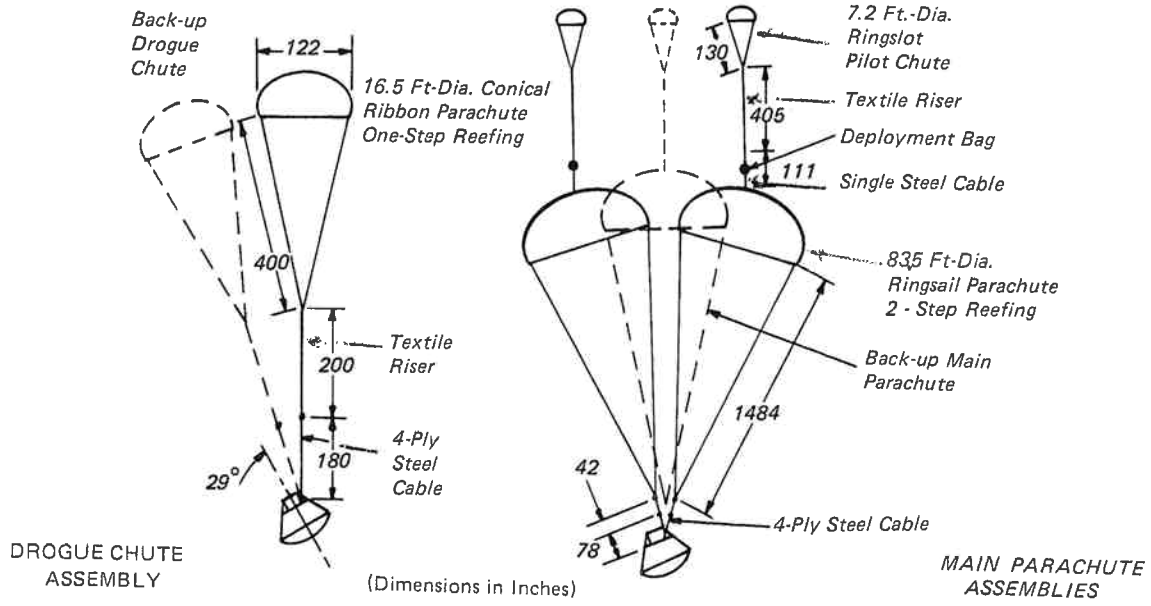


Figure 1.11 Apollo Drogue And Main Parachute Assemblies

five percent. This was less than the degradation caused by the 165°F temperature due to reentry heating and the unexpected heating of the outside of the main parachute deployment bags due to airflow from the hot rear heatshield.

The Apollo parachute landing system effort was the largest of all U.S. parachute recovery system development programs. It resulted in fifteen consecutive, successful manned landings, eleven for Apollo, three for Spacelab and one for the joint U.S.-USSR Apollo-Soyuz flight.

Booster Recovery

Recovery of boosters has been extensively studied since the days of WAC Corporal and the Redstone rocket and some attempts were started but never completed. More than 100 reports have been published on booster recovery studies of vehicles up to NERVA size with recovery by ballistic parachutes, gliding parachutes, hot air balloons, retrorockets, wings and about every other conceivable means. More serious studies included recovery of the first stage Minuteman booster and the Saturn SI-C boosters[29].

Space Shuttle Requirements. The first decision to recover a booster for reuse was made when the National Aeronautics and Space Administration established the Space Shuttle program and included a requirement for recovery of the solid rocket boosters[30]. In initial feasibility studies, liquid propellant boosters in the 500,000 lb class were considered, but in 1972 NASA decided on two solid propellant rockets for first stage boosters.

The Space Shuttle System consists of three major components: the Orbiter, the External Tank containing liquid oxygen and liquid hydrogen for the orbiter engines and two Solid Rocket Boosters (SRB) strapped to the outside of the External Tank. The Space Shuttle is launched at the Kennedy Space Center (KSC) in Florida from a vertical position and fires simultaneously, the main Orbiter engines and the SRB's, whose thrust is programmed by internal design. Burn-out of the SRB occurs after 122 seconds at an altitude of 140,000 feet at a speed of approximately 4400 fps at a trajectory angle of 28 degrees to the horizontal. Booster separation is accomplished with separation rockets. The empty booster shells, weighing approximately 175,000 lbs each, reach an apogee altitude of 200,000 feet and reenter broadside, decelerating to subsonic speeds. Parachute recovery is initiated at approximately 16,000 feet. The recovery system is designed for a water entry velocity of 85 fps. The boosters and the main recovery components are recovered by ship, transported

back to the launch area and refurbished for reuse. NASA is aiming at twenty launches per booster and ten to twenty flights per recovery system.

Recovery System Operation and Design. Figure 1.12 shows the Solid Rocket Booster recovery sequence[31]. A command from the Orbiter prior to booster separation, arms the recovery system and two altitude switches. The booster descends into the lower atmosphere in a nearly horizontal attitude. At 16,000 feet altitude and a dynamic pressure of 190 psf, the first altitude switch initiates thruster ejection of the small nose cap of the booster. Separation of the nose cap deploys an 11.2 ft diameter conical ribbon pilot chute stored below the nose cap. Force from the fully inflated pilot chute opens the drogue parachute retention straps and rotates the drogue parachute deployment bag from its mounting on the deck of the nose frustum. The pilot chute then deploys the 54-ft diameter conical ribbon drogue parachute in its first reefed stage. The reefed drogue parachute starts the rotation of the booster into an axial alignment with the relative airstream. After seven seconds, the drogue parachute opens to its second stage, and disreefs fully after twelve seconds.

At a nominal altitude of 6600 feet, a second altitude switch initiates separation of the nose frustum from the booster body by means of a linear shaped charge. The drogue parachute pulls the frustum away from the booster and deploys three, 115-ft diameter conical ribbon main parachutes. These parachutes disreef in two stages after ten and seventeen seconds each. The configuration and dimensions of all three parachute assemblies are shown in Figure 1.13 and are listed in Table 1.3. Each deploying main parachute pulls a foam plastic float and a self-floating location aid unit from the deployment bag. These devices are attached to the parachute apex with energy absorbing lanyards.

At water impact, six attachment fittings that connect the three main parachutes to the booster body, two per parachute, are disconnected and the parachutes descend to the water. The parachute suspension lines are pulled down by the metal disconnect fitting until each parachute is suspended vertically from its float. A reefing cutter separates the location unit, containing an RF beacon and a strobe light from the parachute float; however, the location unit remains tethered to the float. During the first actual booster recoveries, NASA will investigate a method where the main parachutes remain tethered to the boosters. The drogue parachute hanging on its own float, remains tethered to the self-floating nose frustum which has its own RF beacon and strobe light attached to the top of the frustum. The booster which floats seventy-five percent emerged in a vertical position, also is equipped with location gear.

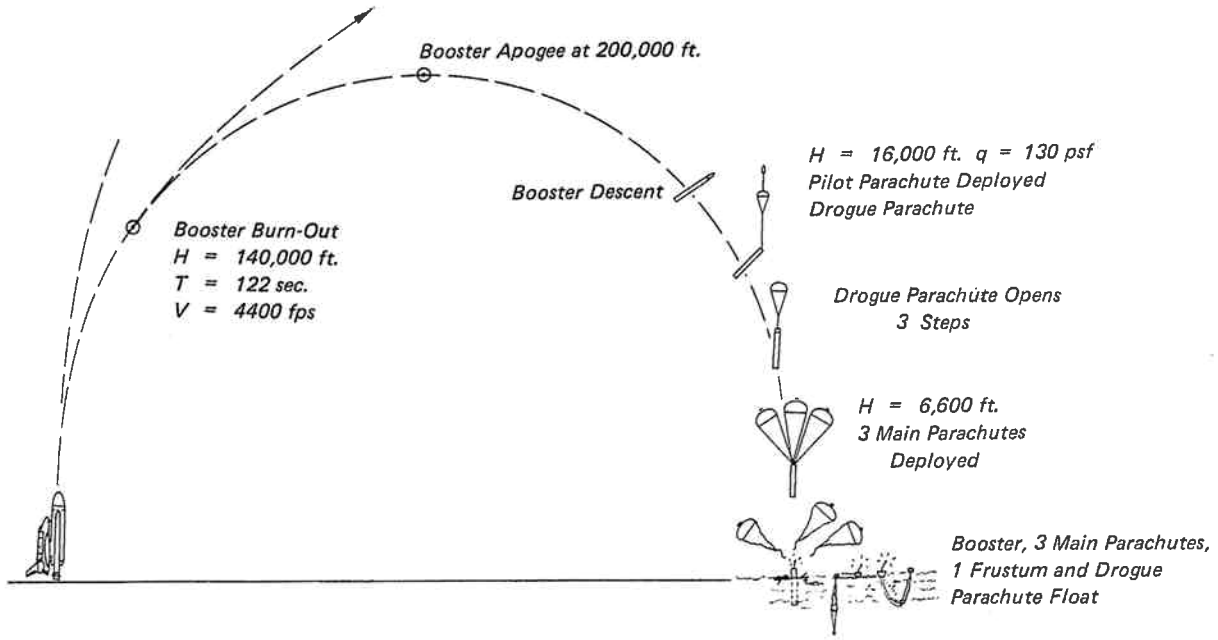


Figure 1.12 Solid Rocket Booster Recovery Sequence

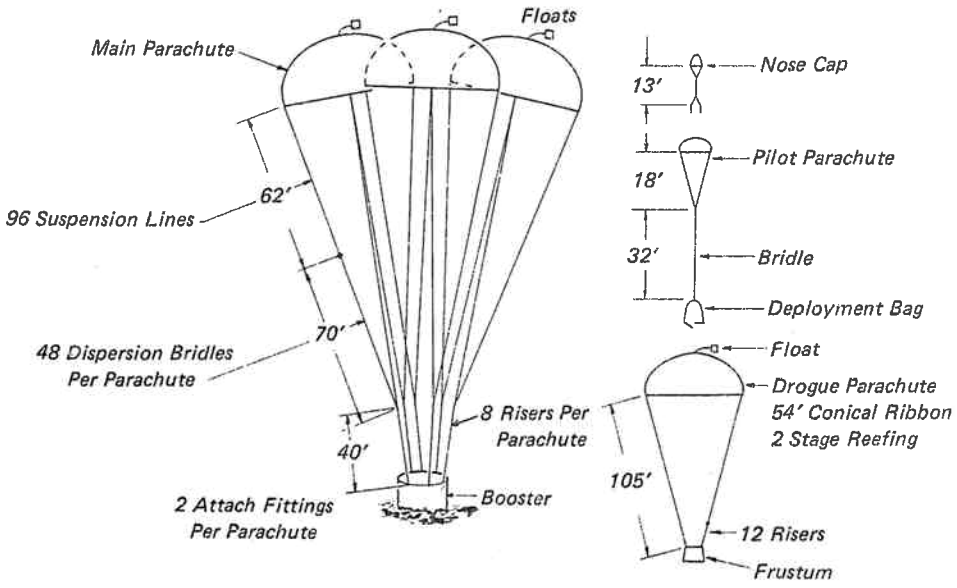


Figure 1.13 Solid Rocket Booster Recovery System

TABLE 1.3 SOLID ROCKET BOOSTER RECOVERY PARACHUTE DATA

Parameter	Pilot Chute	ue Chute	Main Parachute
Number of parachutes	SRB Figure 1 2 of 2	1	3
Type	Section 3.1.4	al ribbon	Conical ribbon
Diameter D_o, feet	page 7	54	115
Number of lines		60	96
Length of lines, ι_e, feet		00.5	132
Number of risers		12	8
Length of riser, ι_r, feet		1.5	40
Trailing distance ratio, X/i		.05	9.91
Weight of parachute, lbs		112	1502 each
Weight of parachute assem		224	1656 each

(1) D_b = Maximum foreb dge and forebody trailing edge.

(2) Includes flotation foa

Retrieval, Refurbishment and Reuse Considerations. The booster with main parachutes and the frustum with the attached drogue parachute enter the water approximately 120 to 140 miles off the Florida coast within a dispersion ellipse of approximately nine by six miles. The recovery crew, waiting outside the dispersion ellipse, locates the booster floating upright in the water and closes the rocket nozzle with a plug. The water inside the booster is replaced with compressed air, which causes the booster to change to a horizontally floating position. The floating booster is then towed to the Kennedy Space Center and lifted from the water by crane. The seven sections of the booster, the nose section, the four rocket propellant sections and the nozzle section with the thrust vector control mechanism, are disassembled and prepared for refurbishment.

The main parachutes, floating vertically in the water, are wound on drums. The drums with the main parachutes, and the nose frustum with the attached drogue parachute, are taken aboard ship and returned to the KSC. The parachutes are brought to the "defouling area", attached to an overhead monorail, straightened out and pulled into wash tubs. Washing is accomplished by recirculating regular tap water and moving the parachutes until the water salt content is below 0.5 percent. The parachutes are then removed and placed in forced air dryers where air, at 160°F, is circulated through the parachutes for several hours. Thereafter, parachutes are inspected, repaired as necessary, and released for repacking. No precise procedures for inspection, rejection or acceptance have been established at this time.

Special design considerations for ten to twenty use cycles have included analysis of aircraft landing deceleration parachute procedures. These parachutes are used as many as twenty-five to fifty times. A total design factor of 3.0 was established for all parachute components, which include the factor of safety and all degrading factors such as seam connections, fatigue, humidity, etc.

EMERGENCY RECOVERY

Recovery systems which enable emergency escape of crewmembers from disabled aircraft encompass a wider operational envelope of initial conditions than any other recovery system, with the possible exception of manned spacecraft. Primary trainers, aircraft capable of vertical take-off and landing (VTOL) and helicopters operate in the low speed and low altitude region of the emergency escape envelope. The medium velocity range is covered by cargo, patrol and aerial tanker aircraft. In the high subsonic and supersonic range, advanced trainers, bombers, fighters and special aircraft extend the escape envelope requirement to dynamic pressures in excess of 1200 psf, speeds beyond Mach 3.0 and altitudes above 80,000 feet. Escape systems consist of multiple subsystems which eject the crewmember from the aircraft, provide for stabilization and deceleration, effect man-seat separation (when applicable) and obtain final descent by a single or multiple parachute.

Five different modes of emergency escape are defined:

(1) Bailout, where the crewmember leaves the aircraft under his own power by means of a door, escape hatch or over the side, and uses a manually or automatically opened personnel parachute for landing.

(2) Tractor rocket extraction, where the crewmember is pulled from the seat and out of the aircraft by a tractor rocket (Yankee System); the personnel emergency parachute opening is initiated either manually or by automatic control.

(3) Ejection seat where the crewmember is catapulted from the aircraft and propelled upward in the rocket boosted seat. One or several parachutes are used sequentially to stabilize the seat. After man-seat separation, an automatically deployed personnel parachute lowers the crewmember to the ground.

(4) Encapsulated seat, where the crewmember is catapulted and rocket ejected from the aircraft in an encapsulated seat, stabilized by a drogue parachute and aerodynamic means, and lands in the encapsulated seat using a large final descent parachute and ground impact attenuator.

(5) Crew module, where the entire aircraft crew escapes in a module which forms part of the aircraft. The module is separated from the aircraft by solid propellant or mechanical means, rocket ejected, stabilized by parachutes and other drag devices, and lands with the crew inside the module using a large single or cluster of parachutes and a ground impact attenuation system.

Reference 32 suggests certain applications (speed/altitude) ranges for the various escape systems described above.

Parachutes are major components of escape systems, but have to be integrated with other subsystems to form the total recovery system which in turn has to be integrated into the air vehicle. In this section, requirements for design and application of emergency personnel parachutes, and parachutes for escape sytems are discussed, followed by descriptions of representative systems.

Requirements

Emergency escape systems are designed to meet the following criteria: the aircraft crewmember must survive emergency escape in a condition suitable for him to aid in his own survival. References 33, 34 and 35 provide general requirements for emergency escape systems.

These escape criteria establish the following parachute requirements:

- reliability of parachute operation,
- fast parachute opening,
- low parachute opening forces and ground impact stresses within the physiological limitations,
- low parachute oscillation,
- personnel harness with comfortable fit and good load distribution,
- parachute quick disconnect for landing, donning the harness and for aircraft ingress and egress,
- low weight and volume of the parachute assembly and ease of maintenance and service.

Desirable requirements include:

- low cost,
- canopy collapse after water landing, and
- suitability for long time storage, long repacking interval and compatible with a wide spectrum of operational environments.

With the exception of reliability, the above requirements are not necessarily in the order of importance.

Reliability. The fact that operational reliability of a crew escape system parachute is the number one priority is self-explanatory. For aircrew escape, parachute operation in the wake of a large, unstable, forebody must be reliable after deployment has been initiated within a wide speed and altitude range.

Fast Opening. An emergency escape parachute should open rapidly at low speed to maximize crewmember survival. Numerous design approaches have been investigated including pull-down-vent lines, parachute canopy ballistic spreaders, stepwise disreefing and other methods in order to achieve these performance characteristics in a single design. Each of these techniques has brought improvements in certain areas but introduced problems in others.

Low Opening Force. The total canopy opening process should provide low snatch force as well as low canopy opening force. Parachute force application to the human body is a complex process and involves magnitude of force, force duration, force onset rates, direction of force and the combined effect of deceleration in three orthogonal planes. In addition, a free falling human body has a different response to applied forces than a body restrained in a seat or a crew module. References 39 and 40 contain comprehensive coverage of the biological and physiological aspect of flying and escape.

Low Rate of Descent. A sea level rate of descent of 20 fps for a 200 lb man or a 24 fps vertical velocity for a 98th percentile man and equipment (295 lb weight) are the accepted standards. However, a lower rate of descent is always welcome if it can be obtained within the permissible weight, volume and parachute force and opening time limitations.

Parachute Oscillation. A 20 degree oscillation is currently considered as an acceptable maximum amplitude. Present trends are to tighten this requirement for personnel parachutes. Escape systems that use ground impact attenuation systems require that osciallations be less than 10 degrees from vertical.

Malfunction Prevention. Such malfunctions as canopy inversions can adversely effect rate of descent and cause canopy damage.

Comfortable Harness Fit and Load Distribution. Parachute harnesses are worn for many hours and should be as comfortable as feasible without compromising integrity. This is sometimes detrimental to a good parachute load distribution in the harness which encourages dissemination of the load over a wide body area.

Parachute Quick Disconnect. After landing, a means of rapidly disconnecting the parachute from the crewmember is required to prevent dragging in high surface winds across ground or water. Quick-disconnects are also used for connecting the crewmember to a personnel parachute that is part of an ejection seat and for quick egress from the seat in case of ground emergencies. A single point quick-disconnect that serves all these applications can have significant advantages.

Low Weight and Volume. Weight and volume affect pilot comfort and mobility, escape system volume and aircraft design.

Ease of Maintenance and Service. The repacking cycle for personnel parachutes and the complex maintenance of explosive components sequencing and separation systems can affect the in-service-time of aircraft. Long time storage, long repacking intervals, the need for elaborate inspection and packing equipment and insensitiveness to the aircraft and operational environment are some of the requirements that affect the maintenance of personnel parachute and escape systems.

Canopy Collapse after Water Landing. Crewmembers that land in water during high surface winds may not be able to move their arms forward against water resistance to actuate the canopy disconnects. This can result in drowning. A fully automatic water actuated canopy disconnect or other automated means of canopy collapse is desired.

Personnel Emergency Parachute Types

The Parachute Board of the U.S. Air Service in 1924 introduced a 28 ft diameter flat parachute canopy with 28 gores and suspension lines as the integral part of personnel emergency parachutes for air crews. This parachute in modified form still is in use today by military services as a personnel emergency parachute.[41] Generally known as the C-9 canopy, it has withstood all attempts to replace it with a "better" parachute as a general application item. The outstanding characteristic of this parachute is its reliability of opening under adverse deployment conditions.

Numerous modifications of the C-9 parachute have been tested or introduced into service to obtain specific improvements.

Quarter Bag. A small deployment bag, called a quarter bag, encloses the skirt of the canopy and incorporates stowage of the suspension lines on the outside of this flat bag in stow loops. At parachute deployment the pilot chute ejects and pulls the canopy, with its skirt enclosed in the quarter bag, away from the parachute pack and removes the suspension lines from the stow loops on the outside of the quarter bag. This keeps the mouth of the canopy closed until line stretch occurs. Use of the quarter bag results in beter control of canopy opening, lower opening forces and a slightly higher operational speed. A different parachute pack is used with the quarter bag than when a quarter bag is not used.

Canopy Spreader. The U.S. Navy has developed and put in service the "Ballistic Spreader Gun." This is a propellant actuated device held at the skirt level inside the parachute canopy. At line stretch, small weights attached to each suspension line are fired radially outward to about 1/3 of the inflated canopy diameter. This creates an instantaneous mouth opening of the canopy and resultant faster canopy inflation. Canopy inflation time at low speeds is decreased by about 25 percent, with little change in inflation time at high speed. Use of the canopy spreader produces higher parachute opening loads at low speeds. The canopy spreader is installed in most Navy ejection seat parachutes with the exception of the seats installed on T-33 and OV-10 aircraft.

Pull Down Vent Line. To obtain faster low speed C-9 canopy inflation the U.S. Air Force and Navy have tested and put in service a pull down vent line.[42, 43, 44, 45] This line attaches to the two rear risers and to the inside of the canopy vent. This line pulls the vent of the inflated parachute down to slightly above the level of the skirt. The intent is to achieve a resultant shorter inflation time and distance. A vent line weak link normally breaks before full canopy opening depending on the air speed magnitude.

Four Line Release System. The USAF has adopted the "Four Line Release System."[46] After the crewmember has a fully inflated parachute, he disconnects four suspension lines. This causes a vent at the skirt of the parachute through which entrapped air escapes radially thereby creating a reaction force and glide in the opposite direction. Gliding stabilizes the para-

chute and slightly decreases the vertical velocity. The latest design uses a daisy chain arrangement which disconnects four lines, numbers 1, 2, 27 and 28. Daisy chain disconnect lanyards are attached to lines 3 and 26 which can be used for steering the parachute. Decreased oscillation and increased maneuverability are the primary benefits. Control of the parachute glide provides a means of avoiding ground obstacles and turning into the wind prior to landing.

Water Deflation Pockets. The U.S. Navy has developed "Water Deflation Pockets" for collapsing parachutes that are dragged through the water by high surface winds.[47,48] These pockets are attached on the outside of alternate gores at the skirt, with the opening opposite to the direction of flight. In case of water dragging, the pockets on the water surface will with water and collapse the parachute.

Other Personnel Emergency Parachutes. In the last 25 years the services have made several attempts to develop an improved personnel emergency parachute. Several designs have been introduced but have not survived. Their superiority in certain areas was always overshadowed by shortcomings in other areas limiting their general usefulness.

Conical 26 Ft Personnel Parachute. The U.S. Navy in the late 1950s developed a 26 foot diameter solid conical parachute.[49] The parachute had less weight and volume and was slightly more stable than the C-9 parachute. However, it had a higher rate of descent and higher opening loads. It is still in service in the Navy NB-6 parachute assembly used with the C-1A aircraft.

Skysail. A personnel version of the Ringsail parachute, 29.5 feet in diameter, was tested and used in service by the U.S. Navy.[50] Its pro's and con's were quite similar to the Guide Surface personnel parachute.

The U.S. Army T-10 parachute is used in one USAF ejection seat application, and British design parachutes are used in several Martin-Baker ejection seat models. Numerous other parachute designs were tested for personnel parachute applications but were never put in service including the Disk-Gap-Band parachute[51], the Star parachute[52], the Cross parachute[53] and a parachute of stretch fabric[54]. None of these parachutes satisfactorily met the stringent requirements of personnel emergency escape.

A list of C-9 parachute modifications and the parachutes temporarily used as replacement and later removed from service indicate one fact. The Services are still searching for a personnel emergency parachute with less weight and volume, a low rate of descent, faster opening at low speed and acceptable opening loads. The parachute must be as reliable for deployment from adverse conditions, and as easy to maintain and repair as the "old reliable" C-9 parachute.

Most emergency personnel parachutes used by the Armed Services use the canopy-first deployment method. The parachute pack is opened by manual or automatic ripcord pull. This frees a spring loaded 36 inch diameter pilot chute which ejects itself into the airflow and deploys the parachute in a canopy, suspension lines and riser sequence. In order to provide deployment control, the U.S. Air Force has used skirt hesitators, and is now using the quarter-bag deployment method for high speed and most ejection seat applications.

A typical personnel parachute pack consists of a back panel with four flaps that enclose the canopy and pilot chute. The flaps are frequently closed with three or four cones and pull pins. Pull of the ripcord extracts the pins. The spring loaded flaps open and the pilot chute ejects. One USAF high speed personnel parachute uses a two pin smooth pack (BA-18) in connection with the quarter deployment bag.

All personnel parachutes used for emergency escape use an automatic parachute pack opener. This device incorporates an altitude limiter that prevents automatic parachute opening at altitudes above 14,000 to 15,000 feet and a time delay to prevent opening at speeds in excess of 200 knots. The well known F-1B spring actuated automatic parachute ripcord release is being replaced in all military personnel parachute assemblies with a cartridge actuated automatic opener known as FXC models 7000 and 11000.

Table 1.4 lists U.S. Air Force personnel emergency parachutes and Table 1.5 lists U.S. Navy personnel emergency parachutes. A more detailed listing of parachutes and what type is used in what aircraft can be found for the Air Force in Reference 55, and for the Navy in Reference 56. In U.S. Army helicopters, liaison and reconnaissance aircraft, Air Force style parachutes are used.

TABLE 1.4 AIR FORCE PERSONNEL EMERGENCY PARACHUTES

PARACHUTE ASSEMBLY	PART NO.	PARACHUTE TYPE	DEPLOY-MENT AID	OPENING AID	MANUAL RIPCORD	AUTO-MATIC OPENER	CANOPY RELEASE	HARNESS TYPE (PACK)	PARACHUTE CONTAINER	AIRCRAFT APPLICATION
BA-18	50C7024-18	C-9	None	None	Yes	F-1B	Capewell	Class H	Soft	B-52, C-130 C-141
BA-21	50C7024-21	C-9	None	None	Yes	F-1B	Capewell	Class H	Soft	B-52
BA-22	50C7024-22	C-9	None	None	Yes	F-1B	Capewell	Class H	Soft	T-33, F-101, T-37, C-5A
BA-25	50C7024-25	C-9	None	PDVL	Yes	Model 11,000	Capewell	Class H	Soft	T-38, F-100
BA-27	50C7024-27	C-9	None	PDVL	Yes	Model 11,000	Capewell	Class H	Soft	B-52
B-29	50C7024-29	C-9	None	None	Yes	None	Capewell	Class H	Soft	UH-1, CH-3, H-53, C-130, C-141
CA-12	50C7023-12	C-9	None	None	Yes	F-1B	Capewell	Class H	Chest, Soft	CH-3, H-53, C-130, C-141
SA-20	50C7025-20	C-9	None	None	Yes	F-1B	Capewell	Class H	Seat, Soft	
– –	A/P28S-20	C-9	None	None	Yes	Model 7000	Koch	PCU/15 PCU/16	Semi-Rigid	A-7
– –	A/P28S-21	C-9	None	None	Yes	Model 7000	Koch	PCU/15 PCU/16	Semi-Rigid	F-15
– –	A/P28S-22	C-9	External Pilot Chute	Spreading Gun	Yes	Model 7000	Koch	PCU/15 PCU/16	Semi-Rigid	F-16
– –	A/P28S-23	C-9	External Pilot Chute	Spreading Gun	Yes	Model 7000	Koch	PCU/15 PCU/16	Semi-Rigid	A-10
– –	32-821552-302	C-9	External Pilot Chute	Antisquid Line	Yes	Martin Baker	Koch	PCU/15	Rigid	F-4
– –	32-821552-13	C-9	External Pilot Chute	Antisquid Line	Yes	Martin Baker	Koch	PCU/15	Rigid	F-4
– –	68E28997	C-9	External Pilot Chute	Spreading Gun	Yes	F-1B	Capewell	Class H	Soft	F-102, F-101
– –	811058-401	C-9	Drogue Gun	None	Yes	Weber	Capewell	Class H	Soft	F-105
– –	65C1501	C-9	Drogue Gun	None	Yes	Weber	Capewell	Class H	Soft	F-106
– –	300-535040-101	C-9	Drogue Gun	None	Yes	Static Line	Koch	PCU/15	Soft	OV-10
– –	300-535040-201	C-9	Drogue Gun	None	Yes	Static Line	Koch	PCU/15	Soft	OV-10
ACES	J114509-507	C-9	Catapult	None	No	Seat Sequencer	Frost	PCU/15	Rigid	F-16, A-10, TF-15
ACES	J114309-509	C-9	Catapult	None	No	Seat Sequencer	Frost	PCU/15	Rigid	F-15

TABLE 1.5 U.S. NAVY PERSONNEL EMERGENCY PARACHUTES

PARACHUTE ASSEMBLY	PARACHUTE TYPE	DEPLOYMENT AID	OPENING AID	MANUAL RIPCORD	AUTO-MATIC OPENER	PARA-CHUTE DISCONNECT	HARNESS TYPE	PARACHUTE CONTAINER (PACK)	AIRCRAFT APPLICATION
NB-6[1]	28' SF[2]	Spring Pilot Chute	None	Yes	Model 7000	None	NB-6	Semi-Rigid Back Pack	P-2, S-2, T-28, T-34
NB-7/7D[4]	28' SF	Spring Pilot Chute	None	Yes	Model 700	Koch	MA-2	Semi-Rigid Back Pack	C-2, E-2, TA-3B, A-3
NB-8	28' SF	Spring Pilot Chute	None	Yes	Model 700	Koch	NB-8	Semi-Rigid Back Pack	A-3, C-121, C-130, CH-96 CH-53, P-3, UN-1, U-1, T-39
NC-3[1]	28' SF	Spring Pilot Chute	None	Yes	None	Quick Con-nect Snap	NC-3R NC-30	Semi-Rigid Chest Pack	C-47, C-117, C-121, C-130, C-131, P-2, T-28, U-1, U-6, U-11, HU-16
NS-3[1]	28' SF	Spring Pilot Chute	None	Yes	Model 7000	None	NS-3	Semi-Rigid Seat Pack	T-33 Ejection Seat
NES-8B[1]	28' SF	Drogue Gun	PDVL[3]	Yes	None	Koch	MA-2	Seat Mounted Shell w/Flaps	Martin-Baker Ejec.Seat in F-4, F-8
NES-12	28' SF	Spring Pilot Chute	Spread Gun	Yes	Model 7000	Koch	MA-2	Shell with Cloth Flaps	MDAC ESCAPAC, A-4F/M/N EA-4F, TA-4 A-7, S-3
NES-14A	28' SF	Drogue Gun	PDVL	Yes	None	Koch	MA-2	Shell with Cloth Flaps	Martin-Baker Eject.Seat A-6 AE-6, F-14
NES-15A	28' SF	Drogue Gun	Spread Gun	Yes	Model 7000	Koch	MA-2	Semi-Rigid Back Pack	North American Rockwell HS-1 Ejec.Seat in RA-SA
NES-16B/C	28' SF	Spring Pilot Chute	Spread Gun	Yes	Model 7000	Koch	MA-2	Semi-Rigid Back Pack	MDAC ESCAPAC A-4B/C/E/L
NES-19A	28' SF	Drogue Gun and Rocket	Spread Gun	No	None	Koch	MA-2	Rigid, Seat Mounted	Stencel SEV-3/A Eject.Seat AV-8A
NES-21A	s8' SF	Internal Pilot Chute	None	Yes	Model 7000	None	MA-2	Semi-Rigid Seat Pack	Lockheed Seat T-33
NES-25A	28' SF	Drogue Gun	Spread Gun	Yes	Model 7000	Koch	MA-2	Semi-Rigid Seat Pack	North American Rockwell LS-1 Eject.Seat OV-10

(1) NB = Back Style; NC = Chest Style; NS = Seat Style; NES = Eject.Seat Style
(2) SF = Solid Flat Circular;
(3) PDVL = Pull Down Vent Line
(4) NB-7 and NB-7D differ in arrangement of survival equipment

Bailout

All personnel flying military aircraft without mechanical escape means (ejection seats, rocket extraction systems, crew modules) use personnel parachutes for escape in case of emergencies. Aircraft so classified include the C-47, C-117, C-121, C-130, C-141, cargo type aircraft, KC-135 tankers, T-29, T-28, T-34, T-39 trainers, all helicopters and liaison type aircraft. The exceptions are military multi-engine air transport flights; passengers on these flights are not required to wear personnel parachutes. Depending on the type of aircraft, the mission flown and the work to be performed during the mission, personnel will use back or chest type parachute assemblies. A parachute assembly includes the parachute, the pack and harness, and may include a survival kit, life raft and other equipment. All parachute assemblies used by Army, Navy and Air Force for bailout incorporate a 28 ft diameter solid flat circular parachute (C-9) or the 26 ft conical parachute.

Ejection Seats

The idea of ejecting crews from disabled aircraft was advanced in the late 1920s. Ejecting aircraft crews solves several escape problems. It permits crews to leave aircraft that fly at high speeds or are in high deceleration spinning or tumbling motions. It protects the crewmembers during exit from contact with the aircraft and provides for safe escape from low speed ground level emergencies. The first operational ejection seat was introduced near the end of World War II in the German night fighter, He 219. It immediately exposed some general ejection seat problems. Adequate seat trajectory height was required to clear the tail of the aircraft. Stabilization of the seat in pitch and yaw was necessary immediately after ejection, as well as proper man-seat separation; fast main parachute opening at low speeds and low altitudes was essential. A small drogue parachute was used for seat stabilization and mechanical means were employed for man-seat separation and fast deployment of the main parachute.

When aircraft speeds increased in the early 1950s, protection of the seat occupant against certain consequences of wind blast became a problem which was one of the reasons for development of encapsulated seat and crew modules.

Seat Stabilization. Unmodified ejection seats are aerodynamically unstable in pitch, yaw and roll. Attempts at inherent aerodynamic seat stabilization have only been partially successful necessitating augmentation with drogue parachutes. The drogue parachute should be of sufficient size and its bridle of proper design to provide stability in pitch and yaw. Properly designed drogue parachutes can dampen but can not eliminate roll. Operational ejection seats have drogue parachutes ranging in drag area from 7 to 24 sq-ft with 9 to 18 sq-ft being the average drag area. Drogue parachutes are effective for seat stabilization at speeds above 200 to 250 knots, but are not always sufficient at lower speeds. They are sometimes augmented in the low speed range by such stabilization systems as STAPAC and DART. Stabilization of the occupied seat during descent from high altitude requires a minimum effective drag area of approximately 10 sq-ft for stability in pitch and yaw. A swivel may be required to prevent parachute induced rotation of the seat or wrap-up of suspension lines. The opening forces should not exceed human tolerances and the drogue should open as rapidly as possible in order to be effective as soon as the seat clears the aircraft. Most drogue parachutes are either drogue gun or mortar deployed to facilitate fast and positive deployment. A small extraction parachute for drogue parachute deployment is sometimes used. One system uses a small rocket to directionally deploy the drogue.

Main Parachutes. All U.S. manufactured seats, with one exception, use the 28 ft diameter C-9 personnel parachute assembly. The Martin-Baker, Mark 10, seat proposed for the Navy F-18 aircraft uses a British Aeroconical parachute.[57] Parachutes used with ejection seats should provide fast inflation at low speed, limit the opening force at high speeds to avoid parachute damage and injury to the occupant, support high speed transfer from drogue to main parachute and provide low rate of descent and stability at landing. Pull down vent lines and spreader guns described in the previous section are used by Air Force and Navy to obtain fast parachute inflation in low speed ejections. Main parachute opening speeds are limited to 225 to 250 knots for the altitude range of zero to 15,000 ft. An "Advanced Concept Ejection Seat", ACES II, uses a reefed main parachute which increases the transfer speed by approximately 50 knots; this shortens the time on drogue parachute. Descent and landing is handled in detail in the previous discussion of the C-9 parachute.

Deployment of the ejection seat personnel parachute occurs by either drogue parachute extraction,

pilot chute extraction, independent mortar deployment or by a lanyard-to-seat system. Deploying the personnel parachute with the drogue parachute still attached to the seat and jettisoning the drogue parachute as soon as the personnel parachute becomes force bearing (line stretch) is a preferred method since it maintains seat stability during the drogue parachute to personnel parachute load transfer. Latest seat designs use only the force provided by the opening personnel parachute to extract the man from the seat.

ACES II Parachute System. The "ACES II" is a typical modern ejection seat and will be used in such advanced USAF aircraft as the F-15, F-16 fighters, the A-10 support aircraft and will be the escape system for the B-1 aircraft, starting at aircraft Serial No. 4.

The parachute system for the ACES II seat consists of a drogue parachute assembly and a reefed 28 ft C-9 parachute assembly. [58, 59] In the high speed mode, as soon as the upper part of the ejection seat leaves the rails, a 2.0 ft diameter Hemisflo ribbon extraction parachute, drogue gun deployed with a 1.0 lb slug is launched to, in tur, extract a 5.0 ft diameter Hemisflo drogue parachute. At 1.17 seconds after ejection initiation, the reefed 28 ft C-9 parachute is catapult deployed from the seat. Approximately fifteen-hundredths of a second later, when the 28 ft parachute becomes force bearing (line stretch), the drogue parachute is jettisoned. The occupant is disconnected from the seat at 0.1 seconds after drogue disconnect and pulled away from the seat by the inflating main parachute. The 1.15 seconds reefing delay is actuated at main parachute ejection (not at parachute line stretch). As a consequence, at low speed deployment, full reefed inflation is obtained at approximately the time of disreefing, thus causing no delay in main parachute inflation. Deploying the parachute at its maximum speed of 250 ± 25 knots causes a 0.6 second reefed opening delay of the fast inflating parachute and a resultant decrease in maximum parachute force. In case of catapult malfunction, the main parachute is deployed by the pilot chute released at seat-man separation with the reefing cutters initiated in the conventional way, with lanyards attached to the suspension lines.

Operation of the ACES II seat is controlled by a three-mode sensing and control system, (see Figure 1.14 . In Mode 1, the low speed operation, covering the range below 250 knots and altitudes below

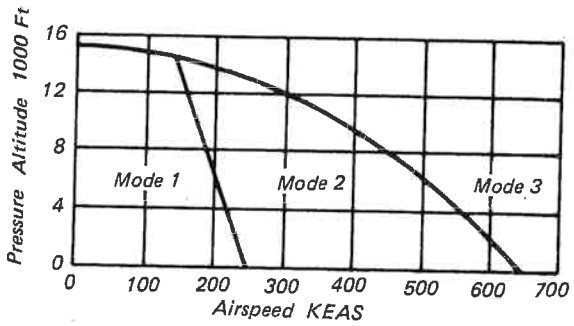


Figure 1.14 Aces II Operation Mode Zones

15,000 feet, the drogue parachute is by-passed and the main parachute is deployed 0.2 seconds after seat ejection (see Figure 1.15). Man-seat separation occurs at 0.25 second thereafter with full main parachute inflation occuring in approximately 1.8 seconds.

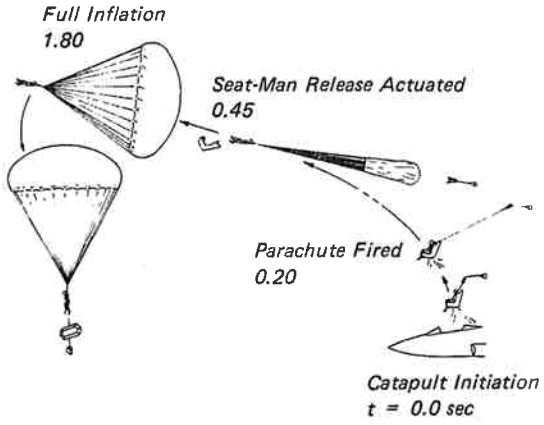


Figure 1.15 Aces II, Mode 1 Operation

A rocket, gimballing in one axis and slaved to a gyro, is used to control the seat in pitch, and is kno[illegible] the STAPAC system. At speeds above 250 knots, [illegible] below 15,000 feet, Mode 2 is operative (see Figure 1.16). Mode 2 uses the drogue parachute/personn[illegible] parachute deployment sequence previously descrit[illegible]. At ejection, above 15,000 feet Mode 3 is used. [illegible]his deploys the drogue parachute immediately as in Mode 2, but keeps the crewmember in the seat and delays man-seat separation and main parachute deployment until the seat passes through the 15,000 feet level. The concept of keeping the man in the seat stabilized

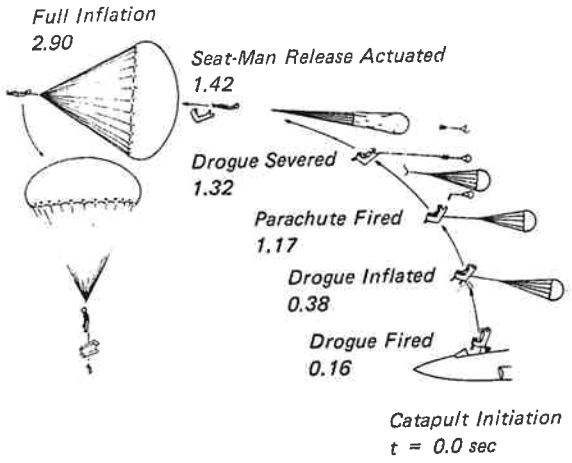


Figure 1.16 Aces II , Mode 2 Operation

by the drogue parachute for bailouts above 15,000 feet is used in many modern ejection seat systems, and was used on the Gemini spacecraft backup ejection seat.

The ACES II three-mode operation is controlled by two pressure sensors attached to the seat and coupled to an electronic sequencer. The ACES II seat also uses electrical signals for sequence control instead of the conventional mechanical-explosive component signal transmission. This has a distinct advantage with regard to redundancy, check-out, weight and volume, and performance variations due to temperature variations; however, it needs its own power supply.

Other modern ejection seats besides the ACES II seat include the Stencel SIII-series seats,[60] the Lockheed seat used in the SR-71 aircraft[61] and the British Martin-Baker Mark 19 seat.

Tractor Rocket Escape System

The tractor Rocket Escape System (Yankee System)[62] uses an upward fired rocket to pull the pilot or crewmember out of the seat and away from the aircraft. Figure 1.17 shows this concept. The primary components of the system are the seat, the parachute backpack assembly, the tractor rocket system and the control and monitoring system. The aircraft seat upon ejection command moves upward in the aircraft to a point where it assures proper exit of the seat occupant from the aircraft. The drogue chute and main parachute, a head rest, the inertia reel, pilot restraint system and the survival kit form a unit attached by means of a back board to the pilot. The tractor rocket is attached to the pilot with a connecting towline. Upon ejection command, the pilot is restrained in the backpack by the inertial reel harness, the aircraft canopy is removed, the tractor rocket and the seat catapult are fired. The extraction force gradually increases to the equivalent of 12 g's and pulls the man from the aircraft and out of the upward moving seat which remains in the aircraft. At low speed, a pilot chute immediately deploys the main parachute. At higher speed, a time and barostatic control unit delays the pilot chute deployment of the main parachute until the speed has decayed to

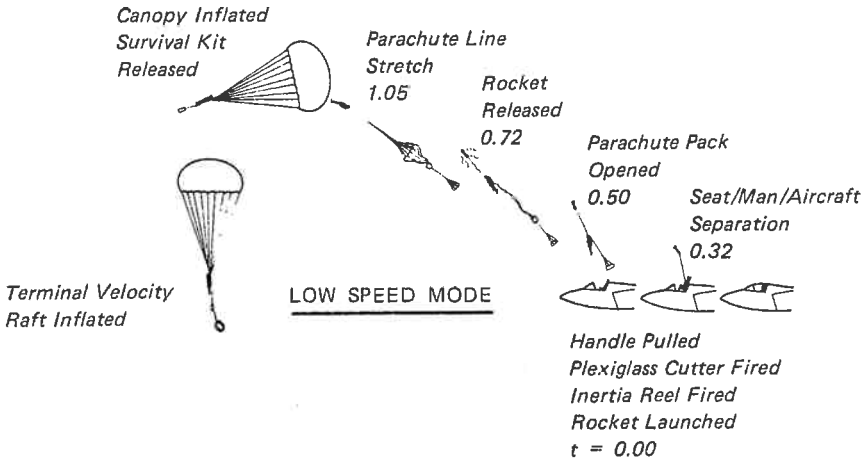


Figure 1.17 Tractor Rocket Escape System Operation

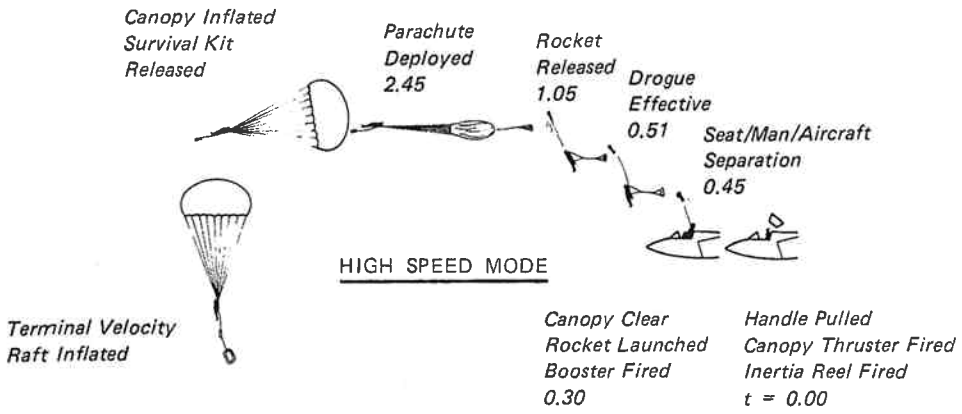


Figure 1.17 Tractor Rocket Escape System Operation (Continued)

approximately 250 KEAS. This system was used successfully in the U.S. Navy A-1 aircraft series[63] and is still used in the T-28 trainer and liaison aircraft with the extraction speed limited to about 300 knots.

Encapsulated Seats and Aircraft Crew Modules

Studies of encapsulated seats and crew modules began in the early 1950's and were implemented in the three encapsulated seats of the B-58 and the four encapsulated seats of the B-70 aircraft in the early 1960's. A three man crew module for the F-111 aircraft became operational in the mid-sixties and the 4/6 man crew module for the B-1 aircraft was qualified in the mid-seventies. Encapsulated seats and crew modules have been developed for bomber aircraft only and offer the following advantages:

- Flying in a shirt sleeve environment without pressure suits, personnel parachute and survival gear attached to the occupant.
- Ejection at high dynamic pressures without fear of blast injuries.

The disadvantages of encapsulated seats and crew modules are:

- Weight of the unit per crew member
- Complexity of the installation
- Extensive maintenance and overhaul requirements especially for crew modules.

The parachute recovery systems used on proven encapsulated seats and crew modules are a mixture of aircraft ejection seat systems and spacecraft recovery systems.

Table 1.6 gives a summary of the four qualified encapsulated seats and crew modules and compares them with a typical high performance ejection seat. Reference 64 provides a summary of the B-58, B-70 and F-111 escape systems.

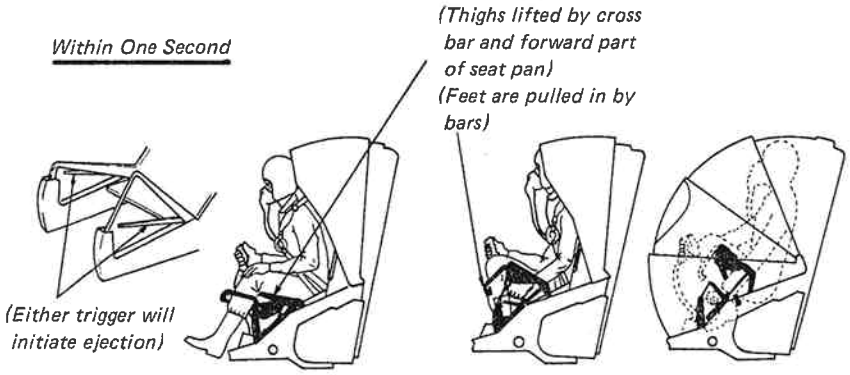


Figure 1.18 Encapsulated Seat Pre-Ejection Sequence

TABLE 1.6 COMPARISON OF SEVERAL ENCAPSULATED SEATS, CREW MODULES AND A TYPICAL EJECTION SEAT

AIRCRAFT		B-58	B-70	F-111	B-1	HIGH PERFORMANCE EJECTION SEAT
Type of Escape		Encapsulated Seat	Encapsulated Seat	Crew Module	Crew Module	—
No. of Crew Members		3	2 (4)	2	4 Operational 6 Training	1 to 6
Escape Unit Weight[1]	Lb	506	510	2900	6000/9000	150
Weight/Crew Member	Lb/Cm	506	510	1450	1500	150
Stabilization Means		Ext. Fins, Drogue Chute	Telescope 9 Ft Booms Equipped w/Drogue Chutes	Crew Module Extension Drogue Chute Glove, Pitch Flaps	Crew Module Fins Spoilers, Drogue Chute	Drogue Chute
Drogue Chute Type/Size		3.45 Ft. D_o Hemisflo Ribbon	25 Ft. D_o Hemisflo (2 ea)	6.0 Ft. D_o Hemisflo	14.2 Ft. Varied Porosity Ribbon	4 Ft to 6 Ft D_o Hemisflo Ribbon
Main Parachute Type/Size		41 Ft. D_o Ringsail	34.5 Ft. D_o 10% Ext. Skirt	70 Ft. D_o Ringsail	69.5 Ft. D_o Ringsail (3 ea)	28 Ft. D_o Solid Flat
Trajectory Altitude For Zero-Zero Ejection	Feet	200 (50)[3]		450 (80)[3]	450	200 (50)[3]
Parachute System Wt	Lb	45 (MP); 52 (DP)[2]	31.25 (MP)[2] 0.75 (DP)	108 (MP); 33 (DP)[2]	342 (MP); 43 (DP)[2]	
Impact System Type/Weight	Lb	Crushable Unit 511 Lb	Impact Bag	Impact Bag	Impact Bag	Not Used
Maint./Refurb. Level		Medium	Medium	High	Very High	Low
Flotation		4 Ea Flotation Bags	4 Ea Flotation Bags	1 Front, 2 Aft 2 Uprighting Bags	2 Front, 2 Aft 2 Uprighting Bags	Life Raft
Location Aids, Survival		Chaff, Beacon, UHF 3 Days Arctic, 15 Days Food	Chaff, Beason	Chaff, Beacon, UHF	Chaff, Beacon, UHF	
Crew Module Tested At		Zero to 650 KEAS Zero to 45,000 Ft	70 to 650 KEAS Zero to 37,000 Ft	Zero to 800 KEAS Zero to 35,000 Ft		600 to 650 Knots

(1) Without Crew Member
(2) MP = Main Parachute; DP = Drogue Parachute
(3) Max. Flight Trajectory, ( ) = Parachute Fully Inflated

B-58 Encapsulated Seat. The B-58 aircraft was originally equipped with three ejection seats (pilot and two crew members). Encapsulated ejection seats were investigated as a possible solution for improving pilot comfort during long duration flights. When the encapsulated seat development proved successful, all operational B-58 aircraft were re-equipped with them during 1962/64. Figure 1.18 shows the seat in various stages of encapsulation. The B-58 capsule functions similar to an open ejection seat during normal flight, except that a pressure suit, parachute and survival gear is not worn by the occupant. If pressurization is lost, the crewmember pulls a handle on either side of the seat initiating encapsulation and pressurization. Escape is initiated by a trigger under either side handle. The following sequence of events then occur: (1) the seat occupant's legs, hips and shoulders are retracted; (2) the three clam shell doors are closed and pressurization activated; (3) the aircraft canopy is jettisoned followed in 0.3 seconds by rocket catapult ejection of the seat/man; (4) as the encapsulated seat leaves the aircraft, a 3.45 ft diameter Hemisflo ribbon stabilization parachute is deployed followed by propellant actuated extension of the stabilization frome with attached fins, initiation of the oxygen system and ejection of chaff; (5) after any required delay (due to speed/altitude conditions at time of ejection), a reefed 41 ft diameter Ringsail main parachute is deployed; (6) five seconds later the main parachute interim attachment point is disconnected and the capsule repositions to the landing attitude and the stabilization frame is retracted and two cylindrical impact shock absorbers deployed; (7) shortly thereafter, the flotation booms extend and all remaining live pyrotechnics are fired; (8) upon land impact, the flower pot deformation of the extended cylindrical shock absorbers and shearing action of the fins cutting into seat flanges limit the impact shock to human tolerance levels; the extended flotation booms serving as anti-roll devices; (9) after landing, the main parachute is manually released; if water impact, release of the main parachute also activates inflation of four flotation bags.

B-70 Encapsulated Seat. The B-70 aircraft had four crewmembers equipped with four ejectable encapsulated seats. The sequence of ejection is very similar to the B-58 encapsulated seat. Two (2) nine ft long stabilization booms extend immediately after seat ejection and separation from the aircraft. Two each 2.13 ft diameter Hemisflo ribbon stabilization parachutes are stored in the tip of the booms and deployed 0.5 seconds after boom extension; they assist the booms in providing stability while descending from high altitude and during low speed ejections. The main descent parachute is a 34.5 ft diameter ten-percent extended skirt parachute. At altitudes below 15,000 feet, deployment of the main descent parachute is initiated two seconds after crewmember ejection or as soon as the encapsulated seat speed decreases to 400 KEAS. At this point, the cover of the parachute compartment is ejected and a pilot chute deployed from a bag attached to the cover. The pilot chute extracts and deploys the main parachute which is reefed for two (2) seconds to a reefing ratio of 4.8 percent. Two seconds after main parachute deployment, an air bag is pressure inflated with stored nitrogen and serves as ground impact attenuator.

The B-70 seat capsules were part of the original concept and therefore more comfortable and more organically integrated into the aircraft as compared to the B-58 encapsulated seat which replaced existing ejection seats. Multiple seat-capsules similar to multipul ejection seats create the problem of: (1) who initiates ejection of individual or of all encapsulated seats; (2) what time-staggered sequencing and what ejection direction is employed to avoid capsule collision; (3) how is separation maintained when ejecting from out-of-control flight conditions? These and other questions led to the development of aircraft crew escape modules which eject the entire crew in one capsule.

F-111 Crew Module. The F-111 is the first operational aircraft to use a module for crew escape. The crew module, as shown in Figure 1.19 forms an integral part of the forward aircraft fuselage and encompasses the pressurized cabin and part of the wing-fuselage portion called the "glove". The two-men crew module is fully self-contained and independent of aircraft electrical, hydraulic and pneumatic systems.

In case of emergency, the crew module is pressurized, its emergency oxygen system is activated and it is severed (cut) from the aircraft by Flexible Linear Shaped Charges (FLSC) placed in a groove under the aircraft skin around the crew module. The FLSC are fired by Shielded Mild Detonating Cord (SMDC). The same method is used for cutting control, tubing and wire connections to the aircraft and for the severance of covers for the parachute, airbag and flotation bag compartments. It is obvious from Figure 1.19 that a

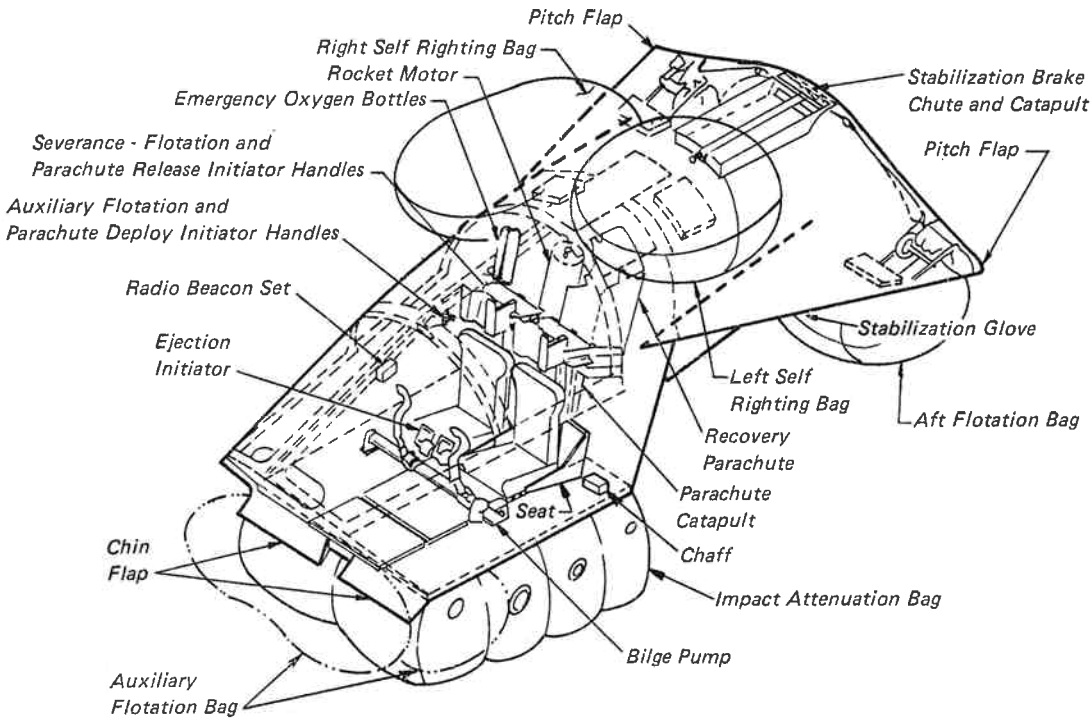


Figure 1.19 F111 Crew Module Configuration

crew module provides more space than an encapsulated seat for crew comfort and for the storage of flight gear, impact attenuation, flotation, location and land and water survival equipment. References 65 and 66 give a good description of the total crew escape module and its subsystems.

Figure 1.20 shows the escape sequence. At time zero, the crew is restrained in their seats, the module is pressurized and emergency oxygen is provided. This status can be maintained and reversed without ejection if required. At 0 + 0.5 seconds, the crew module is cut free from the aircraft and a dual-mode solid propellant rocket motor is ignited. At speeds below 300 KEAS, a high thrust level is used. Above 300 knots, a second nozzle is opened on the upper part of the rocket motor; this reduces thrust, keeps deceleration forces down and in connection with module lift, provides sufficient altitude for proper main parachute inflation. At 0 + 0.67 seconds the stabilization parachute is catapult ejected. A reefed 70 ft diameter Ringsail main parachute is subsequently deployed in a three-mode sequence, controlled by dynamic pressure (q) and deceleration (g) sensors. At speeds below 300 KEAS and altitudes below 15,000 feet, the main parachute is catapult ejected at 0 + 1.75 seconds from the upper part of the module glove. Between 300 and 450 KEAS, the main parachute is deployed at 0 + 2.75 seconds and above 450 knots, parachute deployment is delayed by a q-sensor for 0 + 5 seconds or by a g-sensor until the module deceleration has decayed below 2.2 g's. Ground impact attentuation bags inflate 3.5 seconds after main parachute deployment and 4.9 seconds thereafter, the module repositions into the landing attitude. Water flotation and uprighting bags are manually deployed.

B-1 Crew Escape Module. The B-1 aircraft in its original version used a crew module for emergency escape.[67] The B-1 crew module is quite similar in its escape envelope, aircraft installation and severance system to the F-111 installation. The crew module has a separation weight of approximately 9000 pounds and uses a short stablization glove, extendable fins and spoilers for pitch and yaw stabilization; this is augmented by a swivelling Vernier rocket motor slaved to a horizontal/vertical reference system and a stabilization parachute. Figure 1.21 shows the crew module with fins, spoilers, rockets and parachute recovery system installation in the rear glove compartment.

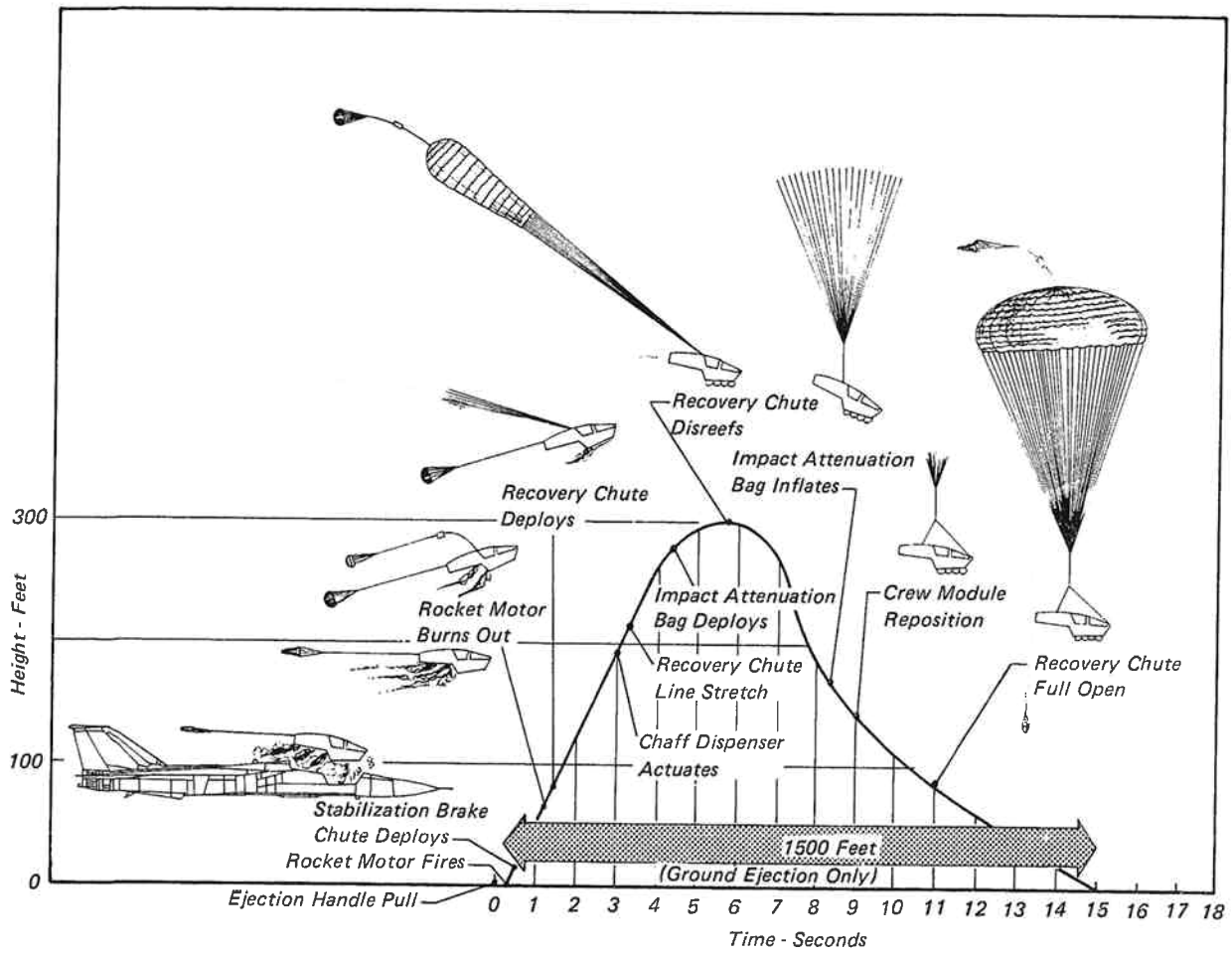


Figure 1.20 F-111 Crew Module Low Speed Ejection Sequence

In case of emergency, the crew module is pressurized, emergency oxygen is supplied and is severed from the aircraft and rocket ejected. At crew module separation, the fixed ejection rocket and the Vernier rocket are ignited and fins and spoilers are extended. At 0 + 0.15 seconds after separation, the reefed 14.2 ft diameter ribbon stabilization parachute is mortar deployed from the rear of the glove compartment, inflates and disreefs 1.75 seconds after line stretch. Three each reefed 69.8 ft diameter Ringsail parachutes are used for final recovery.[68] A four (4) mode concept as shown in Table 1.7 is used for controlling the deployment of the main parachute cluster. The parachute deployment signal disconnects the stabilization parachute and 0.3 seconds later simultaneously ejects two (2) pilot parachutes which in turn extract the three Ringsail main parachutes which disreef 2.5 seconds after line stretch. Five and a half seconds later, the crew module repositions into the landing attitude and the gas inflated ground impact attenuation airbags deploy.

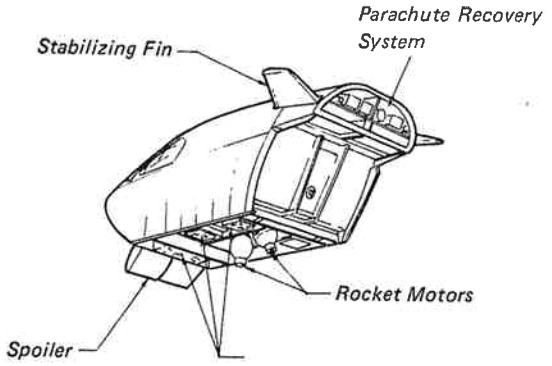


Figure 1.21 Aircraft Crew Module

TABLE 1.7 B-1 CREW MODULE, MAIN PARACHUTE DEPLOYMENT SEQUENCE

ALTITUDE, FT	AIRSPEED, KEAS	PILOT MORTAR INITIATION*
> 15,500 ± 500	All	Inhibited by aneroid
< 15,500 ± 500	> 300 ± 15	3.0 ± 0.32 sec after initiation of ejection
< 15,500 ± 500	> 195 ± 15 to 300 ± 15	2.25 ± 0.25 sec after initiation of ejection
< 15,500 ± 500	< 195 ± 15	0.40 sec after initiation of ejection

* Will not occur unless longitudinal G is less than 3.0 ± 0.1.

AIRDROP OF MATERIAL AND PERSONNEL

This section discusses parachute systems used for load extraction from the aircraft, for load deceleration and descent prior to ground contact or for stabilization in high altitude drops. In each case, the parachute system forms an integral part of the airdrop system. This section includes also a short discussion of aircraft used for airdrop operations, and of the various airdrop methods. It defines consideration and requirements for the design of airdrop parachute systems and describes the parachute systems and related equipment presently in use.

Airdrop of personnel, primarily paratroopers, requires highly reliable equipment for transporting the paratrooper/jumper from the aircraft to the ground; the personnel parachute systems used are discussed at the end of this section.

Airdrop Aircraft

Table 1.8 lists performance data of winged and rotary wing aircraft used for airdrop operations. The C-119 aircraft has been removed from the U.S. Armed Services inventory but is still in service with foreign nations. The monorail automatic container delivery system is not used anymore in modern cargo aircraft. The airdrop system in the table refers to the various types of airdrop methods discussed subsequently in this chapter. The C-130 cargo aircraft, "the airdrop work horse", is presently rated for loads of 35,000 lb airdrop weight. The C-130 is being used for all airdrop systems from LAPES to high altitude container drops [69-72]. The C-141 handles all airdrops with the exception of LAPES [73,74]. The C-5 has been qualified for airdrop of military equipment but is presently not approved for this type of operation [75,76]. The DeHavilland CV-7A, in service with the Air Force Reserve, is being used for airdrop of personnel and material.

The Air Force has tested the standard, personnel, CDS and LAPES airdrop capability of both the YC-14 and YC-15 STOL aircraft. Helicopters are used by the Army and the Marine Corps for airdrop of personnel and containers. Table 1.9 gives weight ranges, parachutes used, aircraft speeds and minimum drop altitudes for CH-46 and CH-53 container aircrops [558].

Each material airdrop mission involves loading and restraining the load and parachute system in the aircraft. Vehicles and large equipment are placed and secured on platforms which are loaded in the aircraft using the automatic dual rail restraint system. The platforms are extracted by means of the parachute extraction system from the aircraft cargo compartment.

The skate wheel conveyors and side buffer boards used in the C-119 in connection with extraction parachute actuated shear webs have been replaced in the C-130 and C-141 with a semi-automatic dual rail system [71,72]. This dual rail system is used with the Type

TABLE 1.8 AIRCRAFT USED FOR AIRDROP

AIRCRAFT	MAXIMUM COMPARTMENT SIZE, IN. L/W/H	AIRDROP CAPACITY LB	UNIT AIRDROP CAPACITY LB	AIRDROP SPEED KEAS	AIRCRAFT INSTALLATION	AIRDROP SYSTEM	PARATROOPERS
C-119, Fairchild	371/105/86	24,000	14,000	110-130	Monorail Conveyor/Board	Containers Platform, Standard	48
C-130, Lockheed	492/120/109	35,000	35,000	130	Dual Rail, Auto. Restraint	LAPES, CDS, Standard, HI-ALT, Spec.	64
C-141, Lockheed	840/123/109	70,000	35,000	150	Dual Rail, Auto. Restraint	CDS, Standard, HI-ALT, Spec.	120
C-5, Lockheed	1450/228/162	220,000	40,000	150±10	Not Approved for Material Airdrop		75
CV-7A, DeHavilland	373/92/78	12,000	12,000	100-120	Dual Rail	Standard Airdrop	25
CH-53, Sikorski	360/96/77	20,000	20,000	50-120	Container Handling	Gravity	
CH-47, Boeing	366/90/78	16,000	12,000	50-120	Container	Gravity	

TABLE 1.9 CONTAINER SUMMARY FOR HELICOPTER AIRDROP

CONTAINER WEIGHT LB	CARGO TYPE	PARACHUTE TYPE	PILOT CHUTE SIZE	DROP SPEED KNOTS	DROP ALTITUDE FEET
300 - 500	A-7A Cargo Sling	G-13 or G-14		80 - 120	500
800 - 1000	A-22 Cargo Bag	2 X G-13 2 X G-14		80 - 120	500
1000 - 2000	A-22 Cargo Bag	G-12D	68"	80 - 120	600

II Standard Army modular platform and the Air Force Type A/E 23H-1 extended aluminum LAPES platform (w/o skids for C-141 use). In the C-130 the left hand restraining rail contains detent notches which engage corresponding indents in the platforms for fore and aft restraint in accordance with MIL-A-8421 tiedown requirements of 3 g's forward, 3 g's aft, 2 g's up and 1.5 g's lateral. This refers to the restaint between platform and aircraft as well as platform, loads and parachute systems. For LAPES drops the restraint of the load to the platform is increased to 12 g's forward and 6 g's in the other directions.

In adverse weather the aircraft pilot reaches the computed air release point (CARP) for airdropping the load by use of the Advanced Weather Aerial Delivery System (AWADS). This is a combined aircraft navigation radar and computer system installed on some C-130E aircraft and used as "pathfinders". It senses aircraft heading and course, determines the magnitude and direction of winds effecting the aircraft course and provides automatic updating and correction for CARP. It also handles interformation positioning and station keeping tasks[77] .

Upon reaching the CARP, the pilot commands airdrop by initiating the pendulum extraction system [78] . The extraction parachute, stored in a deployment bag attached to the pendulum release, falls free and by means of the pendulum line, swings in an arc to the rear of aircraft for good parachute deployment in the wake of the aircraft. A 60 foot (C-130) or 120 foot (C-141) long extraction line connects the extraction parachute to the platform. Prior to deployment of the extraction parachute, the manual detents of the left hand dual rail have been removed and the platform is restrained in the aircraft only by the spring loaded detents of the opposite rail. As soon as the force of the extraction parachute reaches the preset force level of the detents, the platform is released and extracted. After the platform leaves the aircraft, the extraction parachute is disconnected from the platform by either extraction force transfer coupling or static line/cutter systems and deploys the main parachute for standard airdrop. A similar LAPES extraction process is described in the next section. The parachute extraction force which varies with platform weight, ranges from 0.7 to 3.0 g's. The higher values are used for LAPES extraction. In sequential platform drops the extraction parachute for the follow-on platform is stored on the preceding platform and deployed upon separation of the platform from the aircraft.

Considerable details on the aircraft used for airdrop, installations and equipment used can be found in Reference 79.

Airdrop of Material

In WW II men and material were airdropped from altitudes of 1000 to 2000 feet at aircraft velocities of 80 to 100 knots. This method had to be drastically modified in the post-war years for the following reasons: (a) enemy counter action, as experienced in South East Asia, made it desirable for aircraft to approach below radar detection altitude or above AAA (Anti-Aircraft Artillery) effective range, (b) minimum speed of today's aircraft, used for airdrop, has increased to 120 to 150 knots and (c) the weight of individual items to be dropped has grown to 36,000 lbs and is approaching 50,000 lbs.

These requirements have resulted in supplementing the standard airdrop method (airdrops from altitudes of 500 to 1500 feet) with the LAPES (low Altitude Parachute Extraction System and with high altitude airdrop systems now under development. Stronger and more effective parachute systems and load platforms were developed that can handle the higher drop speeds and heavier weights.

Medium and Low Altitude Airdrop. The important methods for airdropping military equipment are:

(1) Standard Airdrop Method

(2) LAPES (Low Altitude Parachute Extraction System)

(3) CDS (Container Delivery System)

Standard Airdrop Method. Figure 1.22 shows the drop sequence. The material to be dropped is loaded on airdrop platforms and restrained in the cargo compartment of the drop aircraft using the dual rail aircraft cargo handling system. Upon the pilots command the extraction parachute is pendulum ejected, inflates, and pulls the platform from the aircraft. After platform extraction the parachute disconnects (extraction force transfer) and removes the main parachute bag(s) from the load, the main parachute(s) inflate and lower the platform to the ground with a rate of descent of 20 to 30 ft/sec commensurate with the allowable impact deceleration of the cargo. Generally 6 to 12 inches of paper honeycomb is used between load and platform for impact attenuation. Several platforms may be extracted sequentially from the C-130 and the C-141 aircraft depending on the weight and size of the material to be airdropped. Platform loads in the 3000 to 36,000 pound range, use single or clusters of up to three each 64 ft diameter (G-12) or eight each 100 ft diameter (G-11) parachutes. Drop altitudes between 800 and 1500 feet are required depending on platform weight, size and number of parachutes used. This drop altitude is sometimes undesirable due to possible AAA (Anti-Aircraft Artillery) fire and airdrop accuracy. However, standard airdrop method is well developed and is being used for single loads up to 35,000 pounds [80-82].

Container Delivery System (CDS). Methods for delivery of multiple A-22 containers have been developed for both the C-130 and C-141 aircraft [83,84]. The goal is to drop as many containers in as short a delivery distance as possible. The C-130 can airdrop up to

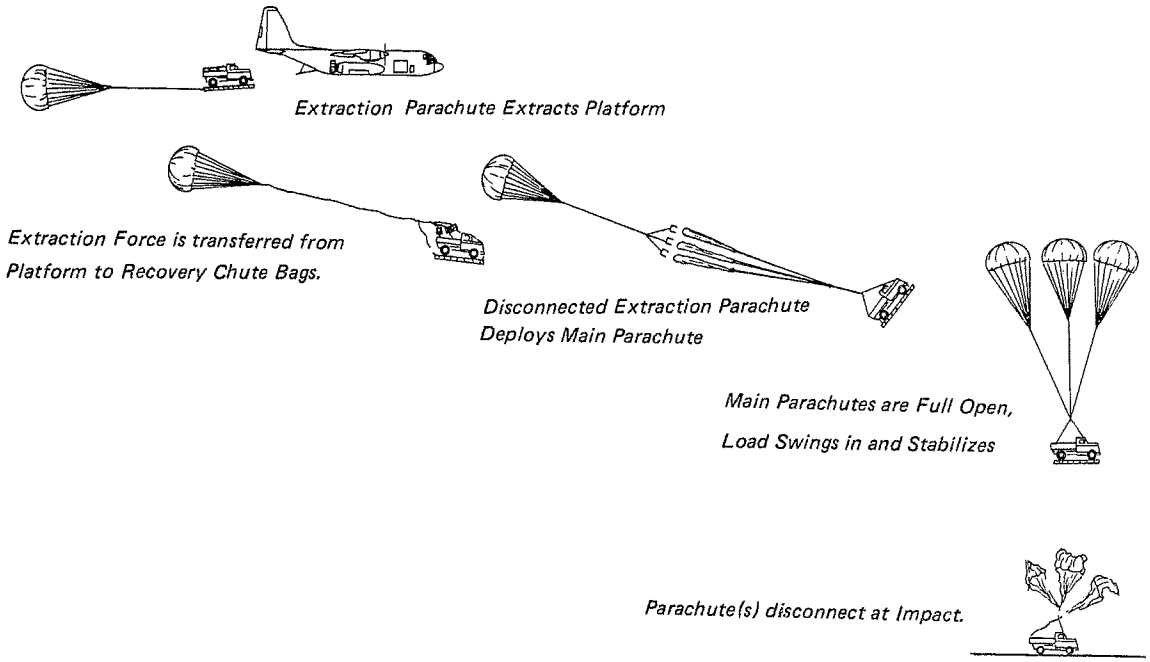


Figure 1.22 Standard Airdrop Method

16 each, 2200 lb A-22 containers in two rows from the rear of the aircraft and the C-141 can drop up to 28 each, 2200 lb A-22 containers in two rows. The containers are restrained in the aircraft with tiedown chains. Shortly before the drop the aircraft is placed in a slight nose-up attitude ($\approx 3° - 4°$) by the pilot, the main part of the tiedown system is then removed leaving only nylon straps as a rear barrier. At the drop point, the pilot actuates a switch which cuts the restraint webbings by shear knife action. This allows the two most rearward containers to leave the aircraft by gravity drop with the static line deployed pilot parachute for each container. This sequence of gravity drop, static line deployed pilot chute and pilot chute deployed parachute continues until all containers have left the aircraft.

Low Altitude Parachute Extraction Method (LAPES). Figure 1.23 shows the LAPES airdrop method. The C-130, the only aircraft currently used for LAPES, approaches below radar detection altitude. On approach to the drop zone, the pilot deploys a 15 ft diameter ringslot drogue parachute using the pendulum deployment system. The drogue chute is attached to the aircraft by means of a tow fitting using a standard 60 ft extraction line. Upon reaching the drop zone the pilot drops to approximately 5 feet above ground and releases the drogue parachute which in turn deploys a large parachute or parachute cluster that extracts the platform from the aft end of the aircraft cargo compartment. The platform drops to the ground, stabilized and decelerated by the large extraction parachute and ground friction. Up to three (3) platforms connected by flexible couplings can be extracted by this method. The force of the extraction parachute should be close to 3 g's related to the platform weight(s) at the beginning of the extraction cycle. The parachute(s) force is guided through the approximate center of gravity of the platform/load assembly by a combination of couplings and clevises. Depending on the type of load to be extracted, the extraction force line is attached to the platform or the load. USAF Technical Order T.O. 1C-130-9 defines the LAPES C-130 aircraft restraint and extraction system. Extraction parachute sizes used for LAPES are discussed later in this section.

The Air Force Type A/E 29H-1 (METRIC) platform was developed for accommodating the higher vertical impact loads frequently encountered in LAPES drops and to meet the requirement for attaching the extraction line to the platform. The total load dropped from the C-130 with three coupled platforms has been as high as 46,000 pounds.

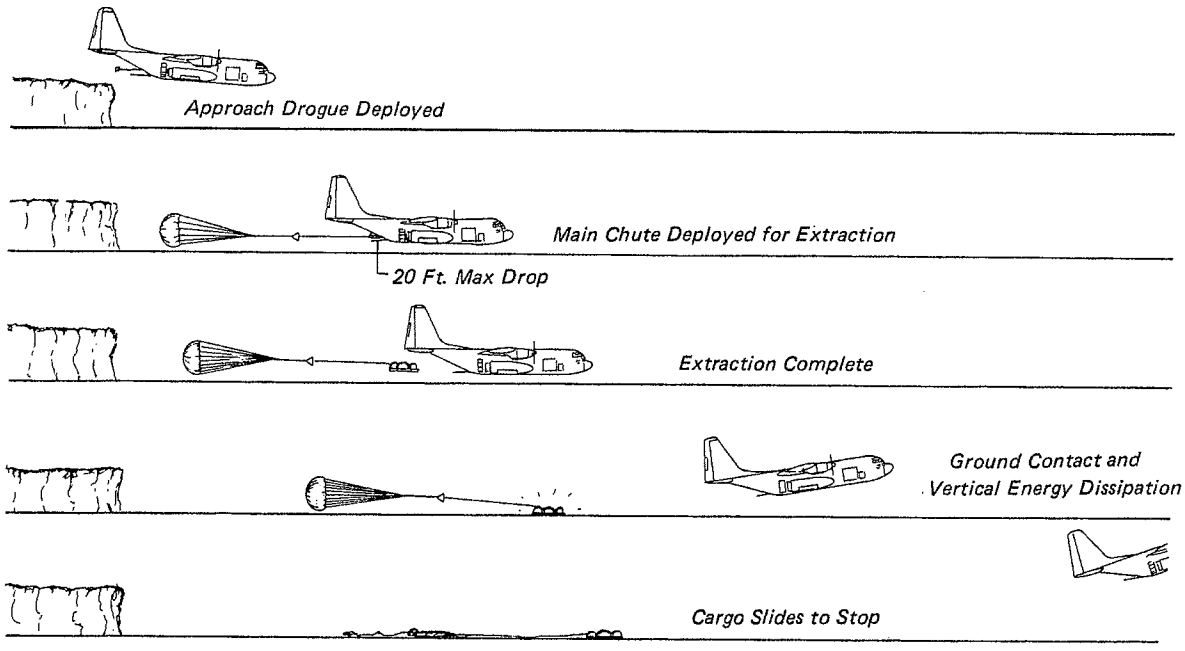


Figure 1.23 "LAPES" Airdrop System

The advantages of the LAPES airdrop method are obvious: the aircraft approaches below radar detection altitude, the exposure to AAA fire is greatly reduced, the delivery is very accurate and sighting of the airdrop event by hostile forces is diminished. Disadvantages are the need for reasonably level terrain for final aircraft approach and drop platform deceleration of several hundred feet after drop, the pilot must fly low enough (about 5 feet) to avoid excessive vertical impact loads and the restraint of the loads on the platform must be rugged enough to withstand the high vertical and horizontal deceleration forces. References 85 through 88 describe the development, testing and qualification of LAPES.

High Speed, Low Altitude Fighter Container Drop: A finned aluminum cargo container (CTV2A, formerly M4A) has been developed for under-wing carriage by fighter aircraft at speeds up to 550 knots [89]. The container can be dropped at speeds up to 400 knots from altitudes of 300 to 500 feet. A 34-ft diameter reefed ringslot parachute decelerates the container prior to impact. A crushable nose section is sued for impact attenuation. The container can accommodate loads up to 500 pounds.

High Speed, Low Altitude C-130 Container Drop: This method, also referred to as High Speed, Low Level Airdrop System (HSLLADS) delivers A-21 containers at a minimum altitude of 250 feet and maximum speeds of 250 knots with the C-130 Combat Talon aircraft [90,91]. The containers are stored at the rear of the C-130 cargo compartment and ejected from the ramp of a Combat Talon aircraft by the sling ejection delivery system (SEDS). A static line attached to the aircraft deploys a 22 or 28 foot diameter cargo extraction parachute which is used as the main recovery parachute. The sling shot ejection delivery system can deploy four 500 lb modified A-21 containers. Additional impact shock absorbing material is required for most of these drops.

Information on other delivery methods and British activities in this area can be found in Reference 576, 577, 580 and 581.

High Altitude Airdrop Methods. High altitude airdrop methods have been developed to escape the AAA and Anti-Aircraft missile firings [92-98]. This requires drops from 10,000 feet or more above ground level. The U.S. Army is investigating two high altitude airdrop systems: the High Altitude Airdrop Resupply System (HAARS), formerly designated the High Level Container Airdrop System(HLCADS) and the Ultra High Level Container Airdrop System (UHLCADS).

High Altitude Airdrop Resupply System (HAARS). The U.S. Army is in the process of developing this airdrop system which airdrops A-22 containers from altitudes of 10,000 feet and above. The containers are equipped with a two-parachute system. A standard 68 inch pilot chute is static line deployed after container gravity drop from the rear of the C-130 aircraft. The pilot chute is attached to the container with a V-sling and stabilizes a 2200 lb, A-22 container at a rate of descent of 250 ft/sec. At an altitude of 800 to 1000 feet above ground, the stabilization parachute is disconnected by a pyrotechnic disconnect actuated by a barostatic device. The disconnected stabilization parachute deploys a 64 ft diameter G-12 main parachute attached to the A-22 container by an inner V-sling. The G-12 parachute uses a pull-down vent line (PDVL) for faster opening. This concept as shown in Figure 1.24 is currently used for the A-22 container.

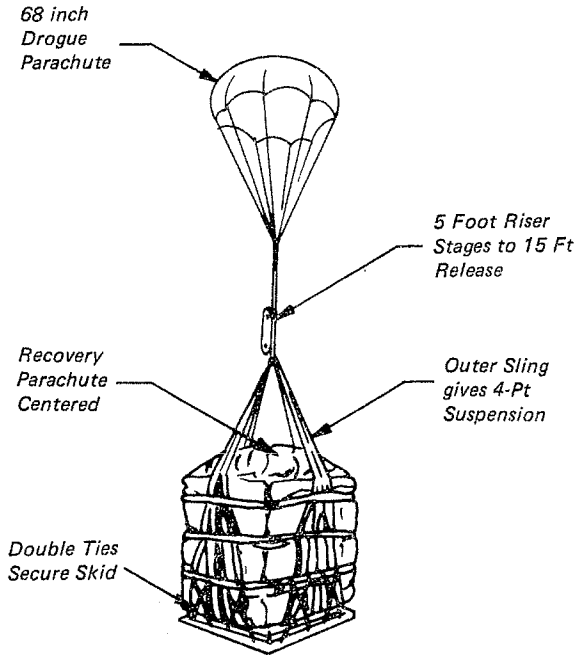


Figure 1.24 High Altitude Airdrop Resupply System (HAARS), First Stage Configuration

Under a 1975 NARADCOM program, high altitude drop tests were conducted with platforms stabilized and decelerated by a two-stage parachute system. The same parachute was used for extraction and stabilization. The tests covered platforms 8 to 12 feet long, weighing 2,700 to 15,100 lbs which resulted in the first stage stabilization parachutes or rates of descent from 162 to 306 ft/sec. The platforms were hanging vertically on the stabilization parachutes which were separated by timed disconnect devices and deployed standard main parachutes. The feasibility of the sequencing concept was demonstrated; however, platform pitch stability problems were encountered whenever the C.G. of the platform was not forward of the platform 50 percent line.

Ultra-High Level Container Airdrop System (UHLCADS). The U.S. Army, Natick R & D Command, is investigating a cargo container that can free-fall from high altitude in stable descent and be recovered by parachute shortly before ground contact [98]. The container, similar in size to the proven A-22 cargo container uses the forward compartment for cargo and the rear of the 100 inch long container for stabilization. The latest version has longitudinal cut-outs in the rear of the container which serve somewhat as stabilizing fins. The containers are designed for loads from 1200 to 2200 pounds.

Barometric altimeters for signalling the main parachute deployment are scheduled for use. Tests on this system are still in progress.

Airdrop Parachute Systems. Parachute systems are involved in the following phases of airdrop operations:

(1) rigging and installation of extraction and descent parachute assemblies in the aircraft and on the drop load,

(2) extraction parachute deployment, disconnect of the airdrop load (platform) from the aircraft restraint system and extraction of the load from the aircraft cargo compartment,

(3) deceleration, stabilization and descent of the load by parachute,

(4) landing, impact attenuation and disconnect of the parachute assemblies from the load, and

(5) retrieval and refurbishment of the parachute assemblies for reuse.

This extensive use of parachutes in airdrop operations establishes the following considerations and requirements for their application:

(1) reliability of parachute operation and system integration,

(2) safety of the aircraft during rigging, flight, parachute deployment and load extraction phases,

(3) parachute rate of descent and stability compatable with system requirements and no damage or acceptable damage at landing,

(4) uniformity and repeatability of parachute deployment and opening, and suitability for cluster operation,

(5) ease and simplicity of packing, rigging and maintenance of the parachute assembly, and load and aircraft installation, and

(6) multiple use and low cost.

Specialized requirements may include:

(1) fast and uniform extraction parachute deployment, inflation and load extraction,

(2) safety means to comply with load hang-up and parachute failure during load extraction and incorporation of these emergency procedures into aircraft T.O.'s,

(3) minimum aircraft C.G. shift during extraction,

(4) good parachute force transfer into the load,

(5) parachute opening and oscillation damping during descent,

(6) quick parachute disconnect and derigging from load after landing, and

(7) parachute landing with the equipment dropped ready for operational use.

Main Recovery Parachutes. Operational experience has defined certain parachute system design restraints. The size and weight of the present 100 ft D_o G-11 parachute assembly, weighing about 250 lb, may be the upper practical limit for handling, packing and loading prior to drop and retrieval after drop. Materials used must be of sufficient strength to withstand rough handling in maintenance, landing and ground retrieval.

Airdrop parachutes in use today are tailored to the specific types of containers and platforms used:

Container, Platform	Weight Range	Parachute(s) Used
A-7A, A-21	200 to 500 lb	Single G-13, G-14
A-22	500 to 2200 lb	Single G-12
	500 to 1000 (2 Chutes)	Clustered, G-14
	1000 to 1500 (3 Chutes)	Clustered, G-13
Platform	2500 to 35,000 lbs	Single & Clustered G-11

The 32 ft D_o, G-13, the 64 ft D_o, G-12 and the 100 ft D_o, G-11 parachutes were developed in the late 1940's and early 1950's. All attempts to replace these "old" parachutes with "better" parachutes have failed so far with the exception of the 34 ft D_o, G-14 parachute which was developed in the mid-1960's as a replacement for the G-13. Looking at performance and cost effectiveness, a "new" parachute must be either lower in cost for the same performance or better in performance for the same cost. Cost has proven to be the over-riding factor for airdrop parachutes. Parachute material accounts for 60 to 80 percent of acquisition cost. Extensive investigations to develop lower cost materials than those presently used have not been successful, nor have attempts to develop one-time-use expendable parachutes.

Rates of descent in the 20 to 30 ft/sec range are used for most airdrop equipment. All sensitive container and platform loads use paper honeycomb for impact attenuation.

Single parachutes used for airdrop should oscillate not more than approximately 10 to 15 degrees. Parachute clusters, used for airdrop cargo weighing in excess of 3000 lb, have less than 10 degrees of oscillation.

Table 1.10 lists commonly used airdrop parachutes. The G-13 has been used extensively in unreefed condition for recovery of A-1, A-7A containers and cargo bundles up to 500 lb in weight [99,100].

The G-14 parachute developed by the U.S. Army Natick R & D Command is of biconical design with a single slot.

The G-12 parachute is used single and in clusters and due to its heavy material is well suited for handling and multiple use[101,102]. Tests have been conducted[97] to use the parachute with a pull-down vent line (PDVL) of 51 ft length for decreasing the canopy filling time and thereby, the drop altitude, however, no PDVL version has been standardized so far.

The 100 ft nominal diameter G-11 parachute was developed in the mid-1940's primarily for platform airdrops.

Reefing was added to the G-11 parachute in an early development stage to permit use of the parachute in cluster application. Use of a 20 foot long reefing line and a 2-second reefing cutter stopped parachute growth in an early stage of inflation and permitted all parachutes to reach full reefed inflation which supported a reasonable uniform full inflation. The uniformity or non-uniformity of inflation that may be expected is discussed in Chapter 6. Longer reefing times generally improve the uniformity of cluster inflation but also increase the resultant opening time and the required drop altitude. References primarily concerned with the G-11 parachute are [74], [76], [81] and [103].

Several G-11 parachute modifications have been investigated to improve performance or obtain special characteristics such as a shorter parachute opening time. One modification investigated was the use of a 95 ft long center line which connects the canopy vent to the parachute suspension confluence. Pulling the vent down slightly above the level of the parachute skirt creates a toroidal annular shape of the parachute canopy which results in a shorter filling time and higher drag area. This results in an increase of about 25 percent in opening force. the USAF tested numerous center line versions and arrangements however, no published USAF report on G-11 with center lines is available. The U.S. Army Natick R & D Command, in Reference [104] and [105] investigated and tested the adapted version of this modification, the G-11B parachute. This parachute uses a 60 ft long reefing line and four, 2-second cutters. Reference [105] quotes the primary gain as a 250 to 300 feet lower drop altitude and the possibility of a 500 ft drop altitude for a single or cluster of two G-11B parachutes until reaching the desired rate of descent of 25 ft/sec on the "system second vertical" position.

The U.S. Army investigated the addition of an internal parachute for decreasing the filling time of the parachute canopy[106]. The added complexity did not compensate for a marginal improvement.

The U.S. Army Natick R & D Command developed, tested and qualified a 135 ft, nominal diameter, solid flat cargo parachute[107]. This parachute is roughly equivalent in performance to two 100 ft diameter G-11A parachutes. The parachute was extensively tested; [75,76] however, one of its operational drawbacks is the weight of 450 lbs for a full parachute assembly, a weight difficult to handle in packing and mainten-

TABLE 1.10 LIST OF STANDARD AIRDROP MAIN RECOVERY PARACHUTES

PARACHUTE TYPE	NOMINAL DIAMETER D_o FEET	NO. OF GORES SUSP. LINES	EFFECTIVE L_S/D_o	MATERIAL CANOPY TYPE	MATERIAL CANOPY STR. LB/IN	MATERIAL SUSP. LINES TYPE	MATERIAL SUSP. LINES STR. LB	WEIGHT LBS[1]	MAX VELOCITY KNOTS	PERFORMANCE WT LB	PERFORMANCE V_e FT/SEC
G-13 Hemispherical	32.4	20	0.93	Cotton		Rayon	400	40	150	500[2]	29[3]
G-14[4] Single-Slot Biconical	34	32	0.8	Cotton	48	Cotton	400	37.5	150	500	27
G-12D Solid Flat	64	64	0.8	Nylon	90	Nylon	1000	130	200[5]	2200	28
G-11A Solid Flat	100	120	0.8	Nylon	50	Nylon	550	250	150	3500[6]	22
G-11B[8] Solid Flat	100	120	0.9 to 1.1	Nylon	50	Nylon	550	275	150	5000[7]	25
135 Ft[10] Solid Flat	135	160	1.25	Nylon	50	Nylon	550	460	150	9000[9]	22

(1) Assembly weight includes deployment bag, bridle, static line
(2) Max Payload Weight
(3) For quoted max payload
(4) Replacement for G-13
(5) Higher for single reefed parachutes
(6) In clusters up to 50,000 lbs
(7) In clusters up to 15,000 lbs
(8) Pull-Down Vent Line
(9) In clusters up to 50,000 lbs
(10) Not in Service

ance. Also, retrieval of such a heavy parachute after drop requires special care and preferably special equipment. The parachute has not been standardized for use by the Armed Services but is available if the need for such a large parachute should arise[108,109].

The U.S. Air Force in the early 1950's investigated 150 ft and 200 ft diameter cargo parachutes for the airdrop of heavy cargo platforms. Tests showed the parachutes to be technically feasible but impractical in the field due to size and weight. It made packing, rigging and field retrieval after drop difficult, requiring large facilities for packing and excessive personnel for retrieval. Also, the long parachute opening times in excess of 20 seconds for the 200 ft diameter parachute were undesirable[110,111].

Field experience in WW II and Korea showed that parachutes in combat were never recovered due to the battlefield environment. It was therefore, logical to investigate the development of one-time use, or as they were called, "expendable" parachutes. Both the Air Force and the Army conducted studies and tests on materials, substantially lower in cost than standard parachute materials. Investigated were paper, plastic films and laminates, spun nylon and other materials. Difficulties were encountered in bonding of gores, attachment of suspension lines and stiffness of the material in packing and handling. The low porosity material developed high opening loads in airdrops and the parachutes were quite unstable. Designing porosity into the canopies in the form of slots and holes

defeated the low cost aspect. Efforts in this area were discontinued after several unsuccessful development programs[112,113,114]

The feasibility of airdropping loads in excess of 50,000 lbs is discussed in references 115 and 116. Airdrop of loads up to 90,000 lbs appears possible with the C-5 aircraft. Recovery of the 165,000 lb SRB booster from the C-5 aircraft are discussed later in this chapter. Both systems show the possibility of extracting and recovering loads in excess of 50,000 lbs.

Extraction Parachutes[117-123]. Parachutes for extracting loads, and especially platforms from aircraft were introduced in the late 1940's. In the early 1950's, the USAF introduced the pendulum swing-arm deployment method for ejecting extraction parachutes from the aircraft cargo compartment starting with the C-82 aircraft. An extraction force of 0.7 to 1.5 times the load of the platform to be extracted (0.7 to 1.5 g's) was found to be a practical approach for the standard airdrop method. The introduction of LAPES necessitated extraction and platform deceleration forces of up to 3 g's. This decreased the extraction time and the required stability and control response of the aircraft. It also decreased the ground slide of the platform after extraction.

Extraction parachutes must have a high reliability of operation to comply with aircraft safety during the extraction process. A high degree of uniformity and repeatability of the extraction force is required to assure predictable aircraft stability and control responses. The extraction parachute(s) must be sufficiently stable, so as not to interfere with aircraft control or platform extraction.

All previously mentioned main parachute requirements regarding cost, ease of packing, maintenance and ground retrieval apply equally well to extraction parachutes.

Table 1.11 lists standardized extraction parachutes presently in the inventory or qualified. All extraction parachutes presently in service are of Ringslot design. The heavy duty 28 ft diameter extraction parachute

TABLE 1.11 EXTRACTION PARACHUTE TYPES

NOMINAL DIAMETER FT	TYPE	NO. OF GORES	L_s/D_o RATIO	CANOPY MATERIAL	SUSP.LINE BREAKING STRENGTH LB	PARACHUTE WEIGHT LB	USED FOR	DRAWING NUMBER
15	Ringslot	16	1.0	2.25 oz Nylon	1000	8.0	Std/ LAPES	57J6032
22	Ringslot	28	1.0	3.5 oz Nylon	1500	27.5	Std/ LAPES	52K6329
28	Ringslot	30	1.0	2.25 oz Nylon	2000	36.5	Std/ LAPES	58K6326
28 (1)	Ringslot	36	1.0	3.5 oz Nylon	2300	68.5	Std/ LAPES	67K1901
35	Single-Slot	32	1.0	3.5 oz Nylon	4000	96.0	Special	68K373
35 (2)	Ringslot	32	1.0	3.5 oz Nylon	4000	90.0	Special	68K372

(1) Heavy duty extraction parachute
(2) Experimental extraction parachute

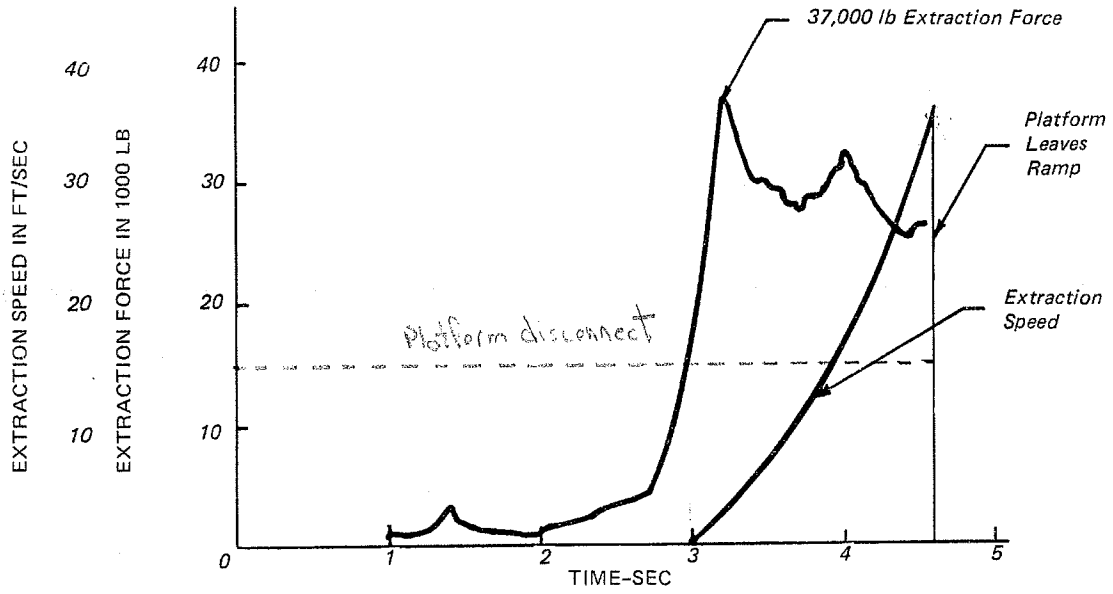


Figure 1.25 Parachute Extraction Force and Extraction Speed vs Time For a 35 Ft Parachute Extracting a 50,000 Lb Load

was required for standard airdrop extractions at speeds up to 150 knots. The lighter 28 ft diameter parachute will become obsolete to assure a minimum of system components. The 35 ft diameter parachute was developed for possible use with loads in excess of 35,000 lb [119]. It is a flat circular type of either Ring-slot or single-slot design. This parachute is fully qualified but is not in the operational inventory since clusters of 28 ft parachutes are being used to extract these heavy loads. Recommended combinations of extraction parachute size and platform loads for standard airdrop and LAPES are found in Reference 124

Figure 1.25 shows the parachute extraction force and platform extraction velocity vs time for a 35 ft diameter parachute extracting a 50,000 lb load platform. The rail release fittings did not disconnect the platform until a parachute load of 15,000 lb was reached. This provided for a fast extraction, a high extraction velocity and avoided excessive aircraft pitch-up due to the load moving aft in the aircraft.

Special Airdrop Systems. Airdrop of supplies and equipment has frequently encountered such special requirements as airdrop of sensitive equipment, precision airdrop without enemy detection of the airdrop, airdrop into inaccessible jungle or mountainous areas and related tasks.

Retrorockets for terminal impact attenuation permit a higher rate of descent, a lighter parachute system and a close-to-zero-impact velocity. A ground sensor is required for firing the rockets at the right altitude above ground. The rocket installation either in the platform or in the riser between platform and parachute is complex and obviously expensive. The U.S. Army in the 1960's conducted an extensive development test program of a parachute-rocket airdrop system for use with load platforms. The feasibility was proven; however, the program was terminated due to the development of the LAPES concept, a more cost-effective and operationally preferable approach [125-129]. The Russians have developed an operational parachute/retrorocket system for the airdrop of heavy loads.

Numerous, unsatisfactory attempts have been made to develop a precision airdrop landing system using gliding, maneuverable parachutes, so successfully used by sport jumpers and military personnel. The approach appears technically feasible. However, it requires a fully automatic vehicle three-axis and flight path control system somewhat similar to a fully automatic aircraft landing system, a task not operationally solved at this time. Gliding, maneuverable parachutes are discussed in detail in Chapters 6 and 7. Efforts to develop precision airdrop systems using

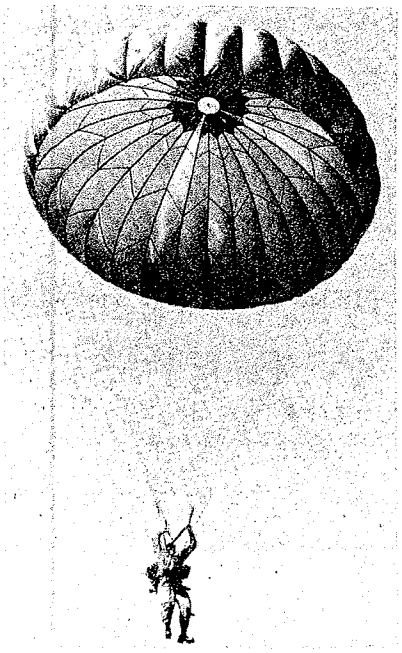


Figure 1.26 T-10 , Personnel Troop Parachute Assembly



Figure 1.27 T-10 Paratrooper Parachute, Basic Configuration

maneuverable parachutes are found in References 130 through 136.

Attempts have been made to airdrop parachute/load systems at very low altitude and have the parachute ascend to obtain the required altitude for full parachute opening and proper load landing attitude [137,138]. This method is discussed in detail under the delivery of ordnance; however, it is considered impractical for airdrop of equipment and personnel.

Airdrop of Personnel

U.S. Army paratroopers, paramedics and special forces establish the primary requirements for a premeditated jump parachute system. The T-7 troop parachute assembly used in WW II was a modified 28 ft diameter aircraft escape parachute equipped with a 24 ft diameter reserve parachute and a quick-divestable harness. Both parachutes were of solid flat design. In the early 1950's, a 35 ft diameter, 10 percent extended skirt parachute (T-10), was standardized as troop personnel parachute and modifications were made to the T-7 reserve parachute and harness to conform to the larger main parachute. This T-10 parachute in modified form is in use today (see Figures 1.26 and 1.27). All paratrooper parachutes use static line deployment with the static line attached to the aircraft. This assures uniform opening of all parachutes at the same distance after leaving the aircraft and minimizes mid-air collision and interference. The C-130 and the C-141 exit the paratroopers in two rows on both sides of the aircraft at time intervals of approximately 0.5 to 1.0 seconds. The result (at jump speeds of ~130 knots) is a considerable spread of the paratroopers on the ground; a problem that has not been solved. Most paratroopers, paramedics and special forces personnel, carry considerable equipment which effects the harness design and positioning of main and reserve parachutes. The jump altitude should be as low as safety permits for better landing accuracy. However, the use of a reserve parachute necessitates a minimum jump altitude above ground of 1200 to 1500 feet in order for the jumper to be able to recognize a parachute malfunction and to activate the reserve parachute. Gliding maneuverable parachutes will greatly increase the landing accuracy while jumping from altitudes of 1500 feet and above. High performance gliding parachutes require an extensive amount of training, appropriate for sport jumpers but not acceptable for most military personnel that use the parachute only as a means of transportation to arrive at a particular location in order to perform a mission. Currently, military application maneuverable parachutes have been limited to those with glide ratios of up to 1.1. Reserve parachutes are used for all train-

ing missions as well as for paramedics and special forces jumps. In actual combat jumps, no reserve parachutes have been used.

For special missions, free-fall parachute systems have been used by all services using a variation of the T-10 troop parachute as main parachute (MC-3) and manual operation and/or automatic parachute opening by barostatic actuators.

Personnel Parachute Systems. Personnel parachutes have two over-riding design considerations:

(1) the system must have the highest degree of reliability possible, and

(2) the user must land uninjured and ready to perform the assigned mission.

Table 1.12 lists parachutes presently used in the Armed Services as premeditated jump parachutes. The table uses the U.S. Army definitions as the Army has responsibility for these parachutes. All systems, with the exception of the MC-3 (Paracommander) use the original 35 ft diameter 10% flat extended skirt para-

TABLE 1.12 LIST OF PERSONNEL PARACHUTE ASSEMBLIES

TYPE	T-10	T-10A	T-10B	MC-1	MC-1-1	MC-1-1B	MC-1-2	MC-2	MC-3
Main Parachute	35 Ft Ext.Skirt	35 Ft	35 Ft	35 Ft	35 Ft	35 Ft	35 Ft	35 Ft	Para-Com-mander
Reserve Parachute	24 Ft Solid Flat Canopy	24 Ft	24 Ft	24 Ft	24 Ft	24 Ft	24 Ft	24 Ft	24 Ft
Anti-Inversion Net		X	X			X			
TU Maneuver Slots					X	X	X		
Elliptical Opening (Tojo)				X				X (1)	
Pilot Chute							36"	36"	40"
Static Line Deployment	X	X	X	X	X	X			
Manual Deploy.						X	X	X	X
Barostat Deployment							X	X	X
Harness	Central Release	Central Release	Parachute Disconnect (2)	Central Release	Central Release	Parachute Disconnect (2)	Parachute Disconnect (2)		
Comments			Present Troop Parachute		Similar To Navy NSP-1	Present Troop Parachute	Similar To Navy NSP-2		

(1) Elliptical opening plus 2 slots
(2) Two each shoulder located parachute disconnects

TABLE 1.13 T-10 PARACHUTE AND T-10 RESERVE PARACHUTE DIMENSIONS

TYPE	T-10	T-10 RESERVE
Design	10% Extended Skirt	Solid Flat
Diameter, D_o	35.0 Ft	24.0 Ft
No. of Gores	30 Ea	24 Ea
Length of Suspension Lines	25.5 Ft	20 Ft
Strength of Suspension Lines	375 Lb	550 Lb
Effective L_s/D_o	0.84	0.9
Canopy Material	1.1 oz/yd^2 Nylon	1.1 oz/yd^2 Nylon
Parachute Weight	13.85 Lb	10.4 Lb
Maximum Jump Speed	150 Kn	150 Kn
Pocket Bands	50 %	—

chute. A 24 ft diameter solid flat parachute is used as reserve parachute. Design details for both are given in Table 1.13 . The assembly includes a harness with means for quick release of either the total harness or the parachute. Numerous changes have been investigated for either improving the performance or overcoming deficiencies. This includes the anti-inversion net, provisions for gliding and maneuvering, and means for obtaining a more comfortable and quicker divestible harness.

In the mid-1960's it was suggested to equip the skirt of the parachute with a net extension which, during static line deployment, would prevent the leading edge of the skirt to slip through two adjacent lines of the trailing edge of the canopy skirt. A nylon mesh net with 1.75 inch square openings was tested first. It retarded opening times. The final version is a net made from knotless braided nylon with square openings 3.75 inches wide. This net is attached to the canopy skirt and the suspension lines and extends 18 inches down from the skirt. In addition, two apex centering loops are used that assure proper centering of the static line during suspension line and canopy deployment (see Figure 1.28). The Anti-Inversion net, in its present form has made opening more uniform and greatly increased its reliability and the jumpers confidence in his equipment [139,140].

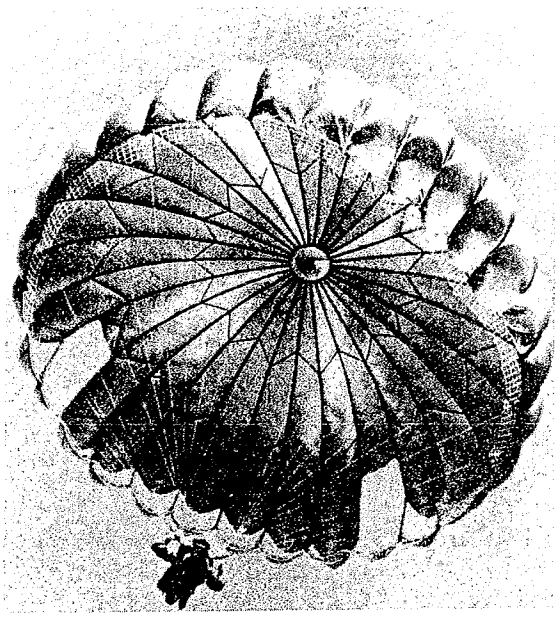


Figure 1.28 MC-1-1B Parachute (T-10 Parachute with Anti-Inversion Net and TU Slots)

The U.S. Air Force in 1956 conducted a comparison test program of T-10 parachutes equipped with modifications for gliding and maneuvering; this resulted in the T-10 parachute with elliptical openings and slip risers called the Tojo parachute [141]. It has a glide ratio of approximately 0.6 to 0.7 and a turn rate of 9 seconds for a 180 degree turn.

Figure 1.28 shows the TU Slot version of the T-10 parachute. It consists of seven center slots and two long and two short turn slots equipped with control lines. This parachute has a glide ratio of about 0.8 and can be turned 180 degrees in 4.5 seconds [142-144]. Tests proved that the effect of the TU slot on parachute opening time is negligible and that it does not effect the opening reliability. The basic T-10 with the TU slots is called the T-10A/B and the T-10 with slots and anti-inversion net is called the MC-1-1B. The T-10B and the MC-1-1B are presently in service with the U.S. Army.

The MC-3 parachute, see Table 1.12, is a military version of the commercially available Paracommander parachute. It has a glide ratio of 1.1 to 1.0 and a faster turn rate than the MC-1-1B [145].

The T-10 reserve parachute listed in Table 1.13, is a solid flat parachute of 24 ft diameter. Whenever a reserve parachute is deployed, there exists the danger of entanglement with the streaming or partially inflated main parachute. Many methods have been investigated and tested to overcome this problem [146 - 150]. The U.S. Army recommends disconnecting the malfunctioning MC-3 main parachute before deploying the reserve parachute. This requires a quick acting main parachute disconnect.

Special Concepts of Personnel Airdrop Systems. The idea of airdropping a small military unit and all its equipment in a container was first investigated at the end of WW II and has been discussed intermittently ever since. Presently, paratroopers after airdrop, are spread out over a considerable distance. The idea of airdropping a small self-contained fighting unit landing in one place, ready for action is intriguing to the military planner. References [151] and [152] discuss this approach and make suggestions for a solution.

AIRCRAFT DECELERATION AND SPIN RECOVERY

Parachutes have proven to be very effective for decelerating aircraft during landing approach, landing roll and for recovery from spins and stalls. The first known test using a parachute as a landing brake, was conducted in 1923 at McCook Field, near the present Wright-Patterson AFB, in Ohio. A conventional man-carrying parachute was used to reduce the landing roll of a DeHavilland biplane. In 1933, the Germans investigated the feasibility of developing parachutes suitable for the in-flight and landing deceleration of aircraft. As a result of these investigations, the ribbon parachute was developed and successfully tested in 1937 as a landing brake for a Junkers W-34 aircraft. The ribbon parachute proved to be adequately stable, opened reliably, had a low opening shock and did not interfere with the controllability of the aircraft. Ribbon parachutes were used during WWII by the Germans as landing deceleration parachutes and as retractable aircraft dive brakes.

The development of jet aircraft resulted in high landing speeds and associated long landing rolls. The B-47 bomber was the first U.S. aircraft to be equipped with a landing deceleration (drag) parachute and soon was followed by the F-94 fighter and the B-52 bomber. The drag parachute of the B-47 decreased the landing roll by 25 to 40 percent depending on touchdown speed and runway conditions. Drag parachutes are most effective on wet or icy runways and for high speed emergency landings. The aircraft drag parachute, originally intended as an emergency device, soon proved to be effective for saving tires and brakes. This resulted in general use of the parachute for all landings.

The B-47, in addition to the landing drag parachute, used an approach angle, and improved the landing accuracy.

Parachutes are used today on most military and some civilian aircraft for spin and deep stall recovery. Many aircraft during the flight test phase, must demonstrate spin and deep stall recovery characteristics. Parachutes installed in the tail of the aircraft have been used successfully for termination of the spin and for stall recovery.

Landing Deceleration (Drag) Parachutes

Application and Operation. Landing drag parachutes produce their maximum decelerating force immediately after opening following aircraft touchdown, or at a time when wheel brakes are not very effective. This is important for unfavorable landing conditions such as wet or icy runways and for emergencies such as aborted take-offs, malfunctioning brakes and over-speed landings without flaps.

In operation, the aircraft pilot makes a normal approach and landing and deploys the drag parachute at, or right after, touchdown. (Figure 1.29 shows the B-52 with landing drag parachute deployed). Reliable parachute deployment and opening involves the total process from pilot command to main parachute full opening. Figure 1.30 shows a typical drag parachute assembly consisting of pilot chute, pilot chute bridle, drag parachute deployment bag, drag parachute, and riser and aircraft attachment/disconnect fitting. Upon pilot action, the aircraft drag parachute compartment door is opened and the pilot chute is ejected. The pilot chute by means of the bridle extracts the drag parachute deployment bag from its compartment. The bag opens and deploys riser, suspension lines and parachute canopy. Brakes are applied at a speed of approximately 80 knots. At the end of the landing roll, the pilot keeps the drag parachute inflated and off the runway by rolling at low speed to a designated parachute drop-off area, generally located near the end of the runway, where the pilot jettisons the drag parachute. The pilot should not try to reinflate the parachute after collapse or drag it to the hangar area. This will result in parachute damage due to ground friction and soiling by the exhaust of the jet engine. Pilots can control inflation by applying enough engine power to keep the parachute inflated even at very low speeds. The parachute, independent of the location of the aircraft attachment point, will ride above ground due to the airflow around the canopy. Ground personnel will retrieve the jettisoned parachute and return it to the packing loft for inspection, repair, repacking and storage for reuse. Single drag parachutes have been used more than 150 times. The normal life span is 25 to 50 cycles. Qualified maintenance personnel inspect and approve or reject the parachute for further use, normally governed by Tech. Orders and by Specification Mil-D-9056.

Parachute Requirements and Design. Aircraft deceleration parachutes must meet the following requirements:

Minimal oscillation, to avoid interference with control of the aircraft.

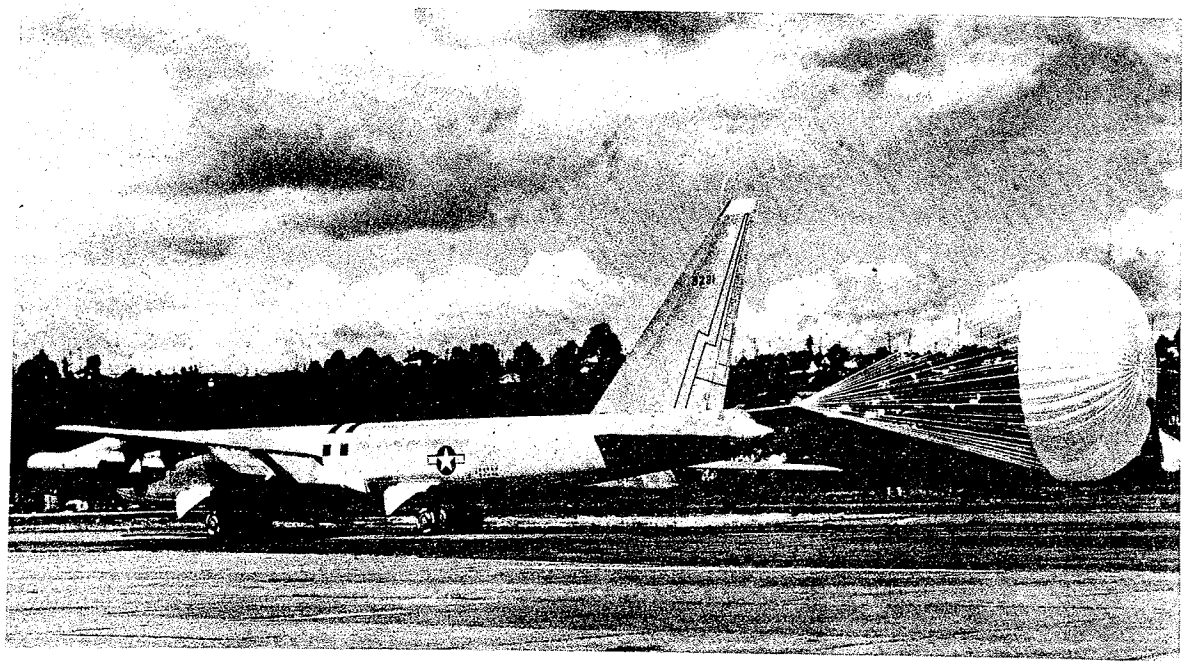


Figure 1.29 B-52 With Landing Drag Parachute Deployed

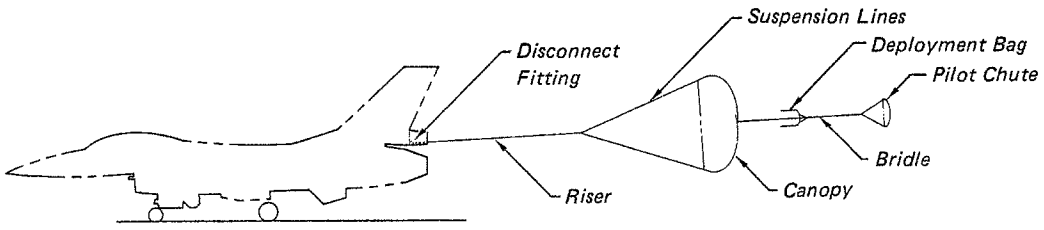


Figure 1.30 Typical Landing Drag Chute Assembly

Reliable opening in the wake of the aircraft.

High drag but low opening peak load.

Low weight and volume.

Suitability for repeated use.

Ease of maintenance and installation.

Low cost.

The ribbon parachute, as previously mentioned, was specifically developed as a stable parachute that would not interfere with aircraft control. An added benefit is its low opening load factor and its insensitiveness to local damage.

The ringslot parachute was developed in 1951 at Wright Field as a low cost replacement of the ribbon parachute and is used today on many U.S. and foreign fighters. Several foreign countries are using the Cross parachute which is employed in this country as a drag brake for automobile dragsters. A varied porosity version of the conical ribbon parachute type using continuous ribbons has been introduced recently as an aircraft drag parachute. Characteristics of these and other parachute types are listed in Tables on pages 75 through 77. Table 1.14 lists aircraft deceleration parachutes currently in use.

It is of the utmost importance that the pilot chute be ejected into good airflow, open quickly and extract the drag parachute bag. If the pilot chute is too small, the bag may fall to the runway and be damaged. If the pilot chute is too large, it may delay or prevent opening of the drag parachute. The deploy-

TABLE 1.14 AIRCRAFT DECELERATION PARACHUTES

Type	Aircraft	Diameter ft	Type	No. of Gores	Deployment Velocity knots
MB-5	F-100	16	Ringslot	20	190
MB-6	F-101	15.5	Ringslot	20	200
MB-7	F-104	16	Ringslot	20	200
MB-8	F-105	20	Ribbon*	24	225
A-28A-1	F-106	14.5	Ringslot	20	220
–	F-5	15	Ringslot	20	180
MB-1	B-47 (approach)	16	Ringslot	20	195
D-1	B-47	32	Ribbon	36	160
D-2	B-52	44	Ribbon	48	170
–	B-58	24	Ringslot	28	190
–	F-16**	23	Ribbon*	24	200
–	TA-7E	15	Ringslot	20	180

* Varied porosity continuous ribbon

** Norwegian version

ment bag should closely contain the drag parachute and riser and its packed shape should conform to the aircraft compartment outline. The bag should.be large enough to prevent movements in the aircraft compartment and loose enough to ensure easy bag extraction. Normally a two-compartment bag is used separating the parachute canopy from the suspension lines and riser. Stow loops and tie cords are used to hold components in place and subsequently deploy them in an orderly fashion, e.g., the riser, suspension lines and canopy, in that sequence. This concept is known as riser-first deployment. Good stowage provisions and sequential deployment of components is especially important for large bombers employing parachutes with diameters of more than 20 to 30 feet.

A low location of the aircraft riser attachment point coupled with a large diameter drag parachute may cause the parachute force line to go below the center of gravity of the aircraft resulting in high loads on the forward landing gear. This can be somewhat alleviated by a longer riser or use of a cluster with a low resultant force line. A longer riser will reduce the drag loss but increase riser weight and deployment time. A riser length of 1.0 to 1.5 times the nominal parachute diameter was recommended in Reference 153 a value now considered too conservative. The riser length is determined more by the riser force line to aircraft center of gravity relationship, by avoiding drag losses in the wake of the aircraft, and by protecting the drag parachute from the heat plume of the jet engine. Fighter drag parachutes, as a rule have long risers, whereas the B-52 drag parachute with no center engine and a high location of the riser attach point has a very short riser.

The parachute must be designed with multiple use in mind. All parts of the assembly should be designed for and protected against abrasion and rough handling. Major components should be easily detachable from each other to facilitate replacement. Risers are formed either from multiple layers of textile webbings or from bundled continuous suspension lines. The latter approach is used on the B-52 drag parachute riser since it proved to be impossible to design a webbing riser with sufficient strength and flexibility. Risers frequently need protection from the heat of jet exhaust. Nomex sleeves, coated braided metal sleeves and similar techniques are used. The riser connection to the aircraft is either a metal fitting or a loop formed by the textile riser that engages a release mechanism in the aircraft.

The aircraft manufacturer determines the required parachute drag for a given maximum landing velocity. This in turn determines the drag area (C_DS) of the parachute. Parachute size, opening load factor, applied factor of safety and design factors for abrasion, multiple use, connection efficiencies between canopy and suspension lines and suspension lines and riser determine the required material strength, and thereby, the weight of the parachute assembly.

Suitability for aircraft operational environment, ease of maintenance and operation and low cost are self-explanatory or have been mentioned previously. This involves minimum support equipment, ease of repair, packing storage and installation. Total cost includes acquisition cost, refurbishment cost and the number of possible reuses.

Pressure packing a parachute, a technique extensively used in airborne vehicle recovery, is avoided for aircraft drag parachutes to minimize the need for support equipment and decrease packing time and complexity.

Aircraft Installation. The parachute installation has to conform to the aircraft and not the other way around. However, a reliable aircraft drag parachute system should comply with the following recommendations:

Suitable drag parachute compartment location

Suitable drag parachute compartment configuration

Safe drag parachute, "lock, deploy and jettison" mechanism

The parachute compartment should be located on the upper side and to the rear of the fuselage, smooth on the inside with rounded corners and a sloped rear wall to facilitate extraction of the drag parachute bag by the pilot parachute. The deployment path of the bag should be clear of protrusions and obstacles that can cause hang-ups of pilot chute or bag. The pilot chute installation should assure immediate ejection after the compartment door is opened. A good pilot chute location is on the inside of the compartment door or on top of the drag parachute deployment bag, with the pilot chute held in place with flaps actuated by the opening of the compartment door. If the compartment is on the side of the fuselage, the bag must be positioned and held in place by flaps that are opened by the deploying pilot chute. An underfuselage installation, as used on the B-47, should be avoided. Such parachutes are difficult to install in overhead locations and require the undesirable canopy-first-deployment concept, (see Chapter 6). The location of the drag parachute compartment should permit easy access and simple installation of the parachute assembly by maintenance personnel. Safety precautions are required to prevent ground personnel injuries from inadvertent opening of compartment doors and pilot chutes being ejected. The sometimes primitive conditions of front line operation should be considered.

To prevent problems caused by inadvertent in-flight deployment of the drag parachute, two approaches are used:

The hook of the release mechanism that connects the parachute to the aircraft, is not engaged until the pilot is ready to deploy the drag parachute.

A fail-safe break link in the riser fitting separates if the parachute is deployed above a safe velocity.

The first approach is generally preferred.

A single handle in the cockpit, accessible to pilot and co-pilot, provides all three functions required for parachute operation. The first three to four inches of handle pull engages the hook that connects the parachute riser to the aircraft. Pulling beyond the first stop opens the compartment door, ejects the pilot chute and starts deployment of the drag parachute. To jettison the drag parachute, the handle is turned 90 degrees and the pull is completed. Some aircrafts use an up and down movement of the handle. In every case, three distinctly different movements are required. Compartment door opening at pilot command should automatically eject the spring loaded pilot chute. The compartment must be shielded against engine heat and moisture and the compartment door must open when covered with ice. Maximum allowable compartment temperature is 250°F for nylon parachutes. It is preferable to have the temperature limited to 200°F. Future use of Kevlar material (see Chapter 4) will result in smaller compartments and higher allowable compartment temperatures.

Landing Approach Parachute

The B-47 bomber used a 16-ft dia. Ringslot parachute for descent from high altitude and for landing approach. The aerodynamically clean B-47 surpassed the allowable speed limits during a steep descent, and in "ground controlled" approach had difficulties making a touchdown at the beginning of the runway. This was overcome by using the approach parachute which increased the aircraft drag and steepened the glide angle. The parachute could be deployed at an altitude of 40,000 feet, and was often used for descent, approach and during touchdown and roll-out, in place of the landing drag parachute. Subsequent aircraft used more effective flaps and spoilers; the use of the approach parachute, therefore, is more of historic interest. Details of the approach parachute design, installation and use can be found in Reference 382 and in reports published on the B-47 approach parachute[26,153].

Spin Recovery Parachutes

Most military and some civilian aircraft must be subjected to spin tests as part of the flight test program. During these spin demonstrations, the aircraft is generally equipped with a tail-mounted spin recovery parachute system an emergency recovery device in case the aircraft control surfaces are unsuccessful in achieving recovery from the spin. The fully developed spin is normally considered the most critical design condition for the spin recovery parachute system. An aircraft in fully developed spin descends vertically with the wing fully stalled at an angle of attack ranging from 40 to 90 degrees while rotating around a vertical axis at a high rate of turn.

The fully developed spin is primarily a yawing motion and therefore, the most effective means of recovery from it, is to apply an opposing yawing moment. Consideration must also be given to the gyroscopic moments which result from application of other than yaw moments or forces. Film records have shown an aircraft making six turns in seven seconds and changing to inverted spin and back, before the spin recovery parachute was deployed, ending this wild gyration. These violent aircraft motions require positive parachute deployment away from the effective range of the spinning aircraft and into good airflow.

System Considerations. Aircraft spin recovery parachute system design involves determination of size and type of parachute, length of connecting riser, deployment method for getting the parachute into good airflow, and the pilot controlled mechanism for deploying and jettisoning the parachute. Reference 154 presents a compilation of information relative to these design parameters.

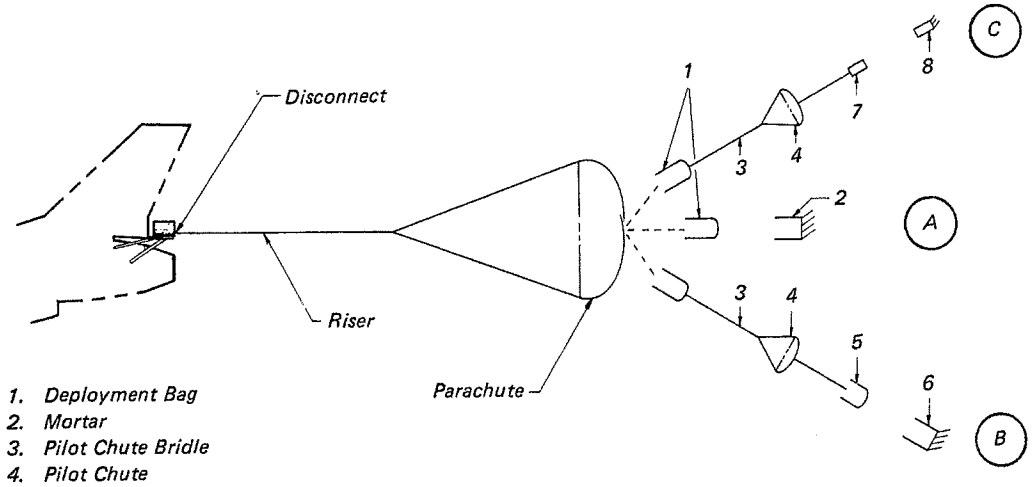
The size of the spin recovery parachute and the riser length is best determined in model spin tests. As an alternative, Table 1.15 lists pertinent data for several spin recovery parachute systems. Using the relationship of parachute drag area to wing area gives a ratio of 0.5 to 0.7 for aircraft in the 70,000 lb weight class and a ratio of 0.8 to 1.0 for aircraft of about 20,000 lb weight. The parachute used should be stable, have high drag, and a low opening load factor in order to obtain the maximum drag force with a minimum required weight and stowage volume. The distance from the leading edge of the parachute canopy to the rear of the aircraft fuselage is important to ensure parachute inflation in the wake of the spinning aircraft. For the parachutes listed, the ratio of this distance divided by the nominal parachute diameter varies between 2.8 and 3.8 with the higher ratio used for the more recent aircraft.

Three different spin parachute deployment methods which have been used successfully, are illustrated in Figure 1.31.

Method A Mortar deployment of main parachute

TABLE 1.15 PARACHUTE SYSTEMS FOR SPIN AND STALL RECOVERY

Aircraft	Gross Weight lbs	Deployment Velocity kts	Parachute Size D_O ft	Line Length l_e ft	Riser Length l_R ft	Trailing Distance D_O	Parachute Type	Deployment Method *(Fig. 1.31)*	Function
DC-9	108,000	210	24	24	136	6.3	Ribbon	A	Stall Rec.
T-38	11,000	185	24.8	35	45	3.2	Ribbon	C	Spin Rec.
F-105	50,000	200	21	21	45	3.7	Ringslot	C	Spin Rec.
F-14	53,000	185	26	26	74	3.8	Ribbon	A	Spin Rec.
S-3A	42,500	140	28	28	47	2.7	Ribbon	A	Spin Rec.
F-16	20,000	188	28	28	50	2.8	Ribbon	A	Spin Rec.
F-5E	15,000	185	24.8	25	45	3.2	Ribbon	B	Spin Rec.
F-17	22,000	188	26	26	76	3.9	Ribbon	A	Spin Rec.



1. *Deployment Bag*
2. *Mortar*
3. *Pilot Chute Bridle*
4. *Pilot Chute*
5. *Pilot Chute Bag*
6. *Pilot Chute Mortar*
7. *Pilot Chute Slug*
8. *Drogue Gun*

A. *Deployment Concept*
B. *Deployment Concept*
C. *Deployment Concept*

Figure 1.31 Spin Recovery Parachute and Deployment Sequence

Method B Mortar deployment of a pilot chute which in turn extracts main parachute

Method C Drogue slug deployment of pilot chute

Method A must be judged to be the most positive since it uses the smallest number of components and ejects the main parachute directly. However, this assumes that the mortar ejection is powerful enough to effect strip-off of the deployment bag plus lines to canopy stretch of the parachute. Mortar deployment of the pilot chute, Method B, is the next best approach. The pilot chute must be ejected into good airflow with a connecting bridle that has roughly the same length as the combined main parachute riser and suspension lines. This approach requires more time for total parachute deployment. Deploying the pilot chute with a drogue gun, Method C, has been used with good results for several installations; however, it requires more components in the system and increases the possibility of interference. In the spin parachute system for the T-38 aircraft, the pilot chute was not spring-ejected but deployed with a drogue slug. This was changed on the F-5 aircraft to a mortar ejected pilot chute and on the F-17, to a mortar deployed main parachute. Figure 1.32 shows steps in the progressive deployment of the F-15 spin recovery parachute.

Component Design. Ribbon and ringslot parachutes have been used exclusively as spin recovery parachutes.

Risers are formed from multiple layers of webbing and stowed together with the parachute in the main deployment bag. The riser during deployment, must be protected against contact with parts of the aircraft or the jet engine. This can be done by locating the riser attachment point at the very rear of the fuselage and by shielding the riser.

The discussion of deployment bags for landing drag parachutes applies also to spin parachutes. The riser-first deployment method should be used.

Vane type pilot chutes are required to ensure orientation of the pilot chute in the direction of the airflow. The drag area of the pilot chute should be about three-percent of the drag area of the main parachute, similar to landing drag parachutes. Deployment components including drogue guns, mortars and deployment sleeves, are described in Chapter 3.

Aircraft Installation. The discussion for landing drag parachute installation applies equally well for spin recovery parachutes, but it is even more important to assure a free path for the ejected and extracted pilot chute or main parachute deployment bag. The riser attach fitting must be located so that the riser can move in a 360 degree circle through a 75 degree arc around the tail of the aircraft. The aircraft must be stressed for accepting the parachute loads in the same directions. The riser attachment mechanism should comply with the requirements discussed for landing drag parachutes. It should be disengaged in flight, engaged prior to parachute deployment and be positive in jettisoning after use.

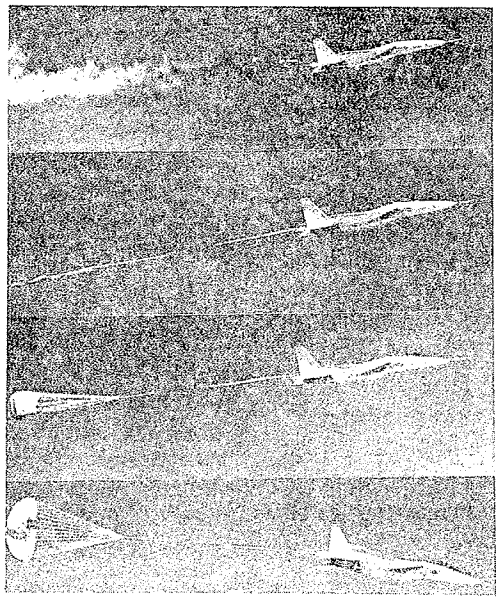


Figure 1.32 F-15 Spin Recovery Parachute, Deployment Sequence

ORDNANCE

The application of aerodynamic decelerators for stabilization, deceleration and recovery of military ordnance devices covers a wide range of equipment. One of the earliest examples was an attempt in World War II to replace the rigid fins of conventional bombs with stabilization parachutes which shortened the length of the bombs and permitted placement of more ordnance in aircraft bomb bays. The Guide Surface parachute was specifically developed for this application. A second example tried in World War II, was the equipping of conventional bombs with large parachutes to permit bomb drops from aircraft flying at altitudes below 300 feet. The resulting bomb deceleration allowed the aircraft to escape the effective splinter range of the bomb and produced bomb impact angles of more than 60 degrees for more effective bomb fragmentation patterns. Airdropped torpedos and mines were equipped with parachutes which allowed drops at high aircraft speeds without destroying the ordnance at water impact or having it ricochet at the water surface, due to too shallow an entry angle.

The use of decelerators for the stabilization and deceleration of ordnance devices has been greatly refined since World War II. The introduction of nuclear bombs made their deceleration mandatory in order to allow the drop aircraft to gain sufficient time and distance to escape the effective range of the bomb blast. Fast opening, high drag decelerators of great structural strength are in use for this application. Lifting decelerators are being investigated to obtain more time and distance for very low altitude drops.

Parachutes have been used since World War I to decelerate illuminating flares fired from guns or dropped from aircraft, in order to gain maximum illumination time for the burning candle. Airdropped electronic countermeasure (ECM) jammers use aerodynamic decelerators to obtain maximum operating time while slowly descending on the deceleration device. Deceleration and stabilization of airdropped sonar buoys is necessary for placing them in the desired location and preventing damage at water impact.

Bomb Deceleration

Aerodynamic decelerator devices for bombs must meet the following operational requirements:

1. Maximum reliability of operation and sufficient effectiveness to assure safe separation between drop aircraft and bomb blast.
2. The allowable opening speed must be commensurate with the operation speed of the drop aircraft.
3. The bomb impact angle must be sufficiently steep and the impact velocity sufficiently low to: a) prevent ricochet of the bomb at impact especially on hard surfaces (concrete), b) prevent fracturing of the bomb at impact, and c) provide a desired fragmentation pattern.
4. Provide high decelerating forces but have a low peak opening load.
5. Stabilize the ordnance so as to obtain a predictable, repeatable trajectory, suitable for automatic weapons control system.
6. Long time storage coupled with environmental protection as well as interchangability of the assembly.
7. Low weight and volume, simplicity of operation, low maintenance and ease of handling are standard requirements.

The USAF Aeronautical Systems Division at Wright Patterson AFB, and the Sandia Laboratories at Albuquerque, New Mexico have done most of the development of decelerators for nuclear bombs with the Sandia Laboratories presently being the responsible government agency.

The Air Force Armament Development Test Center (ADTC) at Eglin AFB, Florida is monitoring the development of decelerators for the stabilization and retardation of conventional bombs.

The deceleration of bombs covers approximately the following performance range:

weights from 100 lb to 45,000 lb

launch altitudes from 100 ft to 45,000 ft, and

launch velocities from low subsonic to speeds in excess of Mach 2

Aerodynamic decelerators used or tested single or in clusters have ranged in diameter from as low as 4 feet to 120 feet. Recent development emphasis has been on low altitude, high speed deceleration and on the conversion from nylon material to higher strength Kevlar.

A Bomb Retardation System of Kevlar. The B-61 nuclear ordnance device, which has a total weight of 765 pounds, is presently equipped with a 17 ft diameter conical ribbon parachute constructed of nylon material, which decelerates the bomb to an impact velocity of approximately 75 feet per second. The Sandia Laboratories has conducted tests with a 24 ft diameter conical ribbon parachute which uses Kevlar 29 material for all suspension lines, radials, skirt and vent tapes, and for most of the horizontal and vertical ribbons. Both parachutes fit into the same parachute

TABLE 1.16 COMPARISON OF NYLON AND KEVLAR B-61 BOMB RETARDATION PARACHUTES

Characteristics	Nylon Parachute	Kevlar Parachute
Parachute diameter, D_o (ft)	17.0	24.0
Parachute type	Conical ribbon	Conical ribbon
No. of suspension lines	24	24
Suspension line strength (lbs)	10,000	13,500
Horizontal ribbon strength (lbs)	3000/2000/1000	3000/2000/1000
Porosity (geometric) (%)	21.5	20
Impact velocity (ft/sec)	75	50
Parachute weight (lbs)	84	85
Parachute volume (ft^3)	2.12	2.12

compartment and have about the same weight. The 24 ft Kevlar parachute produces a much higher decelerating force which is a distinct advantage for low altitude drops. Table 1.16 lists a comparison of both parachutes.

Launched at Mach 1.4, the 24 ft diameter Kevlar parachute produces a retarding force of 90,000 lbs and decelerates the bomb in two seconds from 700 knots to 60 ft/sec.

The parachute deployment system has some interesting features. The parachute is packed in a two-leaf cylindrical bag, split in the middle and pressure packed with mechanical tools and corset type lacing. The deployment bag has a cylindrical opening along its center for placing it around the telescoping ejector tube. It is inserted from the rear and attached to a pressure plate at the end of the ejector tube by means of two heavy webbing straps extending forward around the deployment bag. Upon ejection, the tube ruptures six sheer pins that hold the short tail cap in place and ejects the deployment bag by means of the pressure plate and the two webbing straps. At full bag stretch, sheer knives cut the lacing. An ejection speed of 150 to 170 ft/sec produces full line and canopy stretch. The pressure plate and the two webbing straps stay attached to the vent of the parachute.

All parachutes used for bomb retardation are manufactured to finished dimensions (see Chapter 4). This guarantees that the parachute will have the highest possible degree of aerodynamic uniformity in resulting trajectories, an absolute necessity for dropping bombs with a fully automated weapons management system.

A Bomb Lifting Decelerator. An interesting concept has been developed by Sandia Laboratories for the B-77 nuclear bomb. The parachute is modified so as to produce a lifting trajectory, thereby increasing the time and distance of aircraft bomb blast separation. The parachute used is a conical ribbon parachute equipped in one section with slanted horizontal ribbons. These slanted ribbons create an airfoil type effect which lifts the bomb up to 100 feet above the aircraft bomb release altitude. Since parachutes cannot provide roll stability, a roll control system was developed consisting of a reference unit, a gas generator and eight exhaust nozzles that control the bomb attitude during the lifting flight[155,156].

Bomb Deceleration by Attached Inflatable Decelerator (AID). The Air Force and US Army have investigated and tested balloon type decelerators (Ballute) for the stabilization and deceleration of conventional bombs and bomblets dropped from high and low altitude. Similar to deceleration by parachute, the purpose of a balloon type, attached inflatable decelerator (AID) is to obtain safe separation, stable fall, deceleration and low speed ground impact[157-163,164]. Typical payloads are the 500 lb Mark 82 and the 2000 lb Mark 84 conventional general purpose bombs. AID subsystems for these bombs have been tested at speeds up to 700 knots and at altitudes as low as 100 feet. Figure 1.33 shows the general AID bomb arrangement. Deployment of the AID is initiated by a short lanyard after aircraft bomb separation. Upon lanyard stretch, a spring loaded rear cover is ejected and the AID deployed.

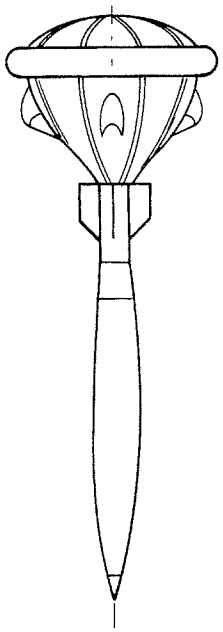


Figure 1.33 Mark 82 AID

Inflation of the AID by ram-air takes from 0.1 to 0.2 seconds.

Bomblet Deceleration. Small AID subsystems are being tested for the stabilization and deceleration of bomblets dropped in dispenser containers. After drop from the aircraft the container spins up and ejects the bomblets. A typical bomblet is 2½ inches in diameter, 6 inches long, weighs 3½ pounds and uses a 7.75 inch diameter AID. Ejection of the bomblet from the dispenser moves a sleeve which frees the AID for ram-air inflation. The AID provides a low impact fuze action and fragmentation pattern.

Torpedo and Mine Deceleration

Deceleration of airdropped mines and torpedos prior to water entry is mandatory to assure proper operation of the ordnance after water emersion. The ordnance after separation from the drop aircraft must be stabilized in the retarded trajectory and enter the water at an angle and at a velocity that will not damage the ordnance or cause broaching at water entry or resubmergence after water emersion. The deceleration device must disconnect either at water entry or at a preselected water depth.

Operational needs may dictate drop altitudes as low as 100 feet to avoid detection and hostile counteraction. Most requirements defined for bomb deceleration apply equally well for mine and torpedo deceleration. The final water entry and subsequent underwater operation impose the following additional requirements:

1. The water entry velocity must be limited to 150 to 300 ft/sec depending upon the ordnance device.
2. The water entry angle must be tailored to the requirement of the specific ordnance device.
3. A mechanism must be provided for automatic disconnect of the decelerator at water entry or at a preselected water depth.
4. The decelerator assembly must be designed to meet specific storage and handling requirements for on-board ship use.

Guide Surface parachutes were used almost exclusively for the stabilization of torpedos up to the late sixties. Their excellent stability provided for stable flight and good water entry. The search for lower cost and lower volume decelerators led to extensive development work on the Cross parachute. The primary emphasis at this time is on the use of the Cross parachute for most U.S. Navy ordnance. The primary development agency for Naval ordnance is the Naval Surface Weapons Center (NSWC) Silver Springs, MD.

A typical decelerator subsystem for a 2400 pound ordnance device has the following design and performance data:

The decelerator is a Cross parachute with surface area of 29.4 square feet, a drag area of 18 square feet, and 16 suspension lines 11 feet long of 4000 pounds strength each.

The parachute canopy is manufactured from 4.0 oz/yd^2 nylon material and the parachute weights 15 pounds.

The maximum opening velocity is 550 knots and the water entry velocity if 150 to 200 ft/sec.

Parachutes for Radar Targets, Flares and ECM Jammers

Target parachute, battlefield illumination flares and airdropped electronic counter-measure (ECM) jammers use or have used aerodynamic decelerators to provide a low rate of descent.

Target Parachutes. Target parachutes furnish an aerial radar target for ground and aerial gunnery and missile firing practice. They are designed to have a specific mono or bi-static radar cross-section based on a radar return signal similar to enemy aircraft or missiles. The radar reflecting surface is reated by manufacturing the parachute canopy from aluminum or sliver coated material and by arranging the material in a canopy pattern that best duplicates the desired radar return signal. Attempts have been made to obtain the typical glint and scintillation patterns of radar returns by having the parachute rotate or oscillate in a predetermined mode number. Target para-

chutes are currently not in use by the Services due to their lack of forward velocity, their inability to perform evasive flight maneuvers and the difficulty to really duplicate the complex radar return signal of air vehicles over a wide range of azimuth and elevation angles. Target parachutes still are in use by several foreign countries.

Battlefield Illumination Flares. Two types of battlefield illumination flares are cannon fired flare shells and airdropped large illuminating flares[165,166]. Cannon fired flares permit visual night observation of the battlefield by ground forces. Airdropped flares are used for illuminating the ground for aerial photography. Both types have been used in large numbers in World War II and the southeast Asia conflict.

Flare shells are fired from 60mm, 105mm, 155mm and even larger caliber guns. The flare shell consists of the shell, the candle, which after ignition, provides the illumination, the parachute assembly that decelerates the candle and provides a low rate of descent during the burning period, and the ejection mechanism which ejects the candle and parachute after a specific preset time. The flare shell is subjected to accelerations of 8000 to 20,000 g's during the initial firing, an acceleration that the decelerator assembly must be able to withstand. The candle with the parachute assembly is ejected at shell velocity of 1200 to 2400 feet per second and a shell rotation of 125 to 240 revolutions per second. The weight of the candle/decelerator assembly ranges from approximately 2.4 lbs for the 60mm round to 10 lbs for the 155mm round. Parachute diameters vary for the same units from approximately 24 inches to 100 inches in diameter. Balloon material used for the parachute canopy during World War II has been replaced with nylon fabric.

This application of decelerators makes long-time storage and compliance with MIL-SPEC environmental conditions an essential requirement. Parachutes used are primarily solid flat type parachutes. Both stable and oscillating parachutes are used. A swinging candle under an oscillating parachute is claimed to provide better differentiation of certain target details. The primary development agency for flare shells and their retarder assemblies is the US Army/RADCOM, formerly the Piccatiny Arsenal, in Dover, N.J. 07801.

ECM Jammer Deceleration. Aerodynamic deceleration devices have been investigated and extensively tested for small ECM jammers dropped from aircraft in dispenser containers and ejected from the containers by small pyro-units or by centrifugal forces[167]. The individual jammers were in the 'below 10 pounds' weight class. Small parachutes of ballistic, gliding and rotating design were tested to obtain low descent and desirable dispersion rates. The decelerators met the operational requirements for the purpose intended.

Sonar Buoy Deceleration

Sonar buoys are under-water listening devices that may be dropped from rotary or winged aircraft. Deceleration and stabilization of the buoys is required to achieve allowable water entry velocity and for obtaining a predictable trajectory. Airdropped sonar devices range in weight from 20 to 100 pounds. Drop speeds range from 50 to 60 knots for helicopters, to 400 knots for modern anti-submarine warfare (ASW) aircraft such as the P 3-V. Drop altitudes range from close to the surface for helicopters up to 40,000 feet. The sensing equipment in the buoys requires a low water entry velocity to avoid impact damage.

A typical sonar buoy assembly is a tubular container 5-inches in diameter and 36-inches long. A two stage parachute system is housed in the rear of the tubular structure. After drop from the aircraft, a static line frees a spring loaded wind flap attached to the rear cover and held in position along the outside of the container. The wind flap spreads away from the container and the resultant air drag moves cover and attached wind flap to the rear. A line attached to the rear cover extracts and deploys an 11.5-inch diameter ribbon drogue parachute of 0.45 ft^2 drag area. This drogue parachute stabilizes the buoy and decelerates it to a velocity of about 190 ft/sec. A combined altitude sensor/time delay mechanism disconnects the drogue parachute and extracts the main parachute when passing through the 3000 foot altitude level. For drops below 3000 feet, the altitude sensor is blocked and the drogue is disconnected after a 2.5 second time delay. The main descent parachute with a drag area of 4.2 ft^2, decelerates the buoy to a water entry velocity of 60 ft/sec. The volume required for the parachute recovery system is about 25 cubic inches. At water entry the main parachute may be disconnected to avoid wind dragging. A stable predictable descent trajectory is mandatory in order to place the sonar buoy in a preselected location[168-170].

The US Navy organization, primarily responsible for the development of sonar buoy recovery systems, is the Naval Air Development Center, Air Vehicle Technology Department, Warminster, PA.

AERIAL PICKUP

Aerial pickup is one of three methods associated with the retrieval phase of a total recovery cycle; the others of course, are land and water retrieval. Aerial pickup is a means of payload transfer, either air-to-air called "Mid-air Retrieval", or surface-to-air which includes pickup from land and water. Items that have been retrieved by aerial pickup include personnel, supplies, atmospheric probes, target drones, remotely piloted vehicles (RPV's) and aircraft.

Air-to-Air Retrieval Systems

Air-to-air retrieval involves a fixed wing or rotary wing aircraft equipped with retrieval equipment as the airborne pickup vehicle. Two primary aircraft pickup systems have evolved, the All American "Trapeze" method and the "Fulton System".

The Trapeze method trails hooks attached to extensible poles and cables behind the aircraft. The payload to be retrieved, descends on a parachute. The target for the aircraft retrieval gear to engage, is either the main parachute, a tube-like extension of the main parachute, a special small parachute above the main parachute (referred to as the tandem parachute system), or a balloon. The pilot of the retrieval aircraft spots the parachute system, synchronizes his descent speed with that of the payload and intercepts the engagement target which slides between two poles attached to the rear of the aircraft and is caught by the hooks attached to the winch cables. The force in the cables disconnects the loop from the poles and trails the parachute and payload behind the aircraft. The winch, controlled by a load-sensing mechanism, reels the payload up to the aircraft for boarding or for tow, to the loading area.

The Fulton system uses a yoke attached to the nose of the aircraft[171] The pilot flies the yoke into a cable connecting the payload and the parachute or balloon, engages the cable and transfers the cable or tow line to the aircraft winch for boarding or tow to the landing area. The same yoke concept can be used for air-to-air and surface-to-air retrieval.

Both fixed-wing aircraft and helicopters are used operationally for mid-air retrieval with fixed-wing aircraft having the advantage of a longer range and higher altitude operation, also payloads such as nose cones and containers, can be boarded and returned over long distances. Fixed-wing aircraft cannot recover vehicles with wing spans wider than the aircraft cargo door, i.e., aerial targets and RPV's. Towing the vehicles is impractical for stability-in-tow and landing reasons.

With helicopter mid-air retrieval, it is possible to recover large winged air vehicles, tow them to a suitable landing area and deposit them undamaged in a landing cradle. However, helicopters cannot tow large collapsed parachutes due to the air drag involved. The different mid-air retrieval methods (helicopters and fixed wing aircraft, Trapeze and Fulton systems) primarily use parachutes as payload descent systems.

Requirements. Experience gained with the various aircraft and descent systems has established requirements that apply to all systems; most important are the following:

The main parachute rate of descent must be compatible with the operational intercept velocity for the particular aircraft type used.

The intercept target (main parachute, parachute extension, engagement parachute, balloon or others) must be fully inflated and stable in pitch and yaw.

Rotation of the main parachute must be limited to 1½ degrees per second.

Gliding or irregular side motions of the engagement target should be avoided.

Minimum weight and volume is essential for all engagement and load transmitting components.

The main parachute should collapse easily and symmetrically to facilitate helicopter tow, and fixed wing aircraft reel-in.

Main Parachute Rate of Descent. The JC-130 aircraft is the most frequently used fixed wing retrieval aircraft. A maximum sink rate of 20 fps at 10,000 feet altitude is necessary to maintain good aircraft speed and control for the intercept process. Similarly, the HH-53 and HH-3 helicopters can accommodate a maximum rate of descent of 25 fps at 10,000 feet altitude. The altitude requirement is based on intercept operations starting at an altitude of 10,000 feet or slightly above; this provides sufficient time for multiple engagement passes.

Stability of Engagement Target. The retrieval aircraft operates best if it can maintain a steady rate of descent and a straight flight path. The parachute system therefore, should not develop irregular movements. This is very important for the engagement parachute of tandem parachute systems. These engagement parachutes operate in the large wake of the main descent parachute and have a tendency to move toward the periphery of the large wake and wander around in irregular motions. The use of gliding systems that may stabilize main and engagement parachutes also has drawbacks as disscussed later.

Main Parachute Rotation. Rotation of single parachute systems is acceptable as long as it does not interfere with proper operation and disconnect of the main parachute due to the orientation of the engagement parachute load line which require that the aircraft approach from a discrete direction[172,173]

Gliding Parachute. In an attempt to stabilize the tandem parachute system, tests have been made with gliding main parachute systems. This forced the engagement parachute to the rear of the glide path and provided a stable system that could be approached from the rear (the so-called six o' clock position) for engagement. The problem with this approach is that gliding parachutes have a tendency to turn, and it is difficult to limit the turn rate to less than 1½ degrees per second, the acceptable level for helicopter intercept. Approach from the rear of the gliding parachute system proved to be difficult. The load line between the engagement parachute and main parachute became slack due to the geometry of the descending parachute system with resultant contact between load line and the helicopter. If the aircraft approached from the front, and the parachute system turned, the aircraft was not able to follow the flight path of a strongly turning parachute system in the developing curved pursuit, or engagement from the side, a difficult maneuver.

Minimum Weight and Volume. The weight of retrieval parachutes is increased considerably due to the engagement webbing system that is caught by the hook(s) of the aircraft and the riser network that guides the engagement and tow forces into the payload. This is especially true with the tandem system that requires a long load line between engagement parachute and main parachute.

Parachute Collapse in Helicopter Tow. The large aerodynamic drag and the flapping motions of collapsed or partially collapsed parachutes in helicopter tow make it impractical to tow parachutes of about more than 45 feet in diameter with the available HH-53 and HH-3 helicopters. Certain parachute types used as main parachutes have a tendency to partially reinflate in tow, depending upon how and where the parachute was engaged by the aircraft hook. These problems indicate the desirability of a system where the main descent parachute is either completely collapsed or disconnected after aircraft hook engagement.

Mid-air Retrieval Aircraft Systems. The Trapeze mid-air retrieval system, Figure 1.34, consists of a load limiting powered-winch and associated load sensing and control equipment, the pickup poles with mounting arrangement, the pickup cables with engagement hooks and fairings and guides for leading the winch cables. Retrieval gear also includes fixtures to assist in boarding nose cones, instrumented containers and similar equipment.

The model 80-H winch used in the HH-53[174] and HH-3[175] helicopters has a rated capacity of 4000 lbs with a 50 percent overload capability. The best helicopter engagement speed is approximately 50 to 60 knots. The load control system limits pickup loads to between 1½ and 2 g's by paying out the pickup cable immediately after engagement and reeling the cable in as soon as a steady pull condition is obtained.

The JC-130 aircraft arrangement, Figure 1.35, is similar, but it uses the model 90 winch with a capacity of 3000 lbs. Engagement loads are limited to between 3 and 6 g's depending upon payload weight and load setting of the winch control system. The poles extend 28 feet outside the aircraft, are spread 20 feet at the end and extend downward 43 degrees and outward 11 degrees. The cables are nylon ropes with six hooks attached, four at the poles and two in the span between the poles. Pay-out of the cables after engagement may extend to 250 feet depending upon payload weight, engagement speed and winch load setting.

The Fulton mid-air retrieval system uses a yoke attached to the nose of the retrieval aircraft. Arms of the yoke are approximately 10 feet long and spread 60 to 90 degrees apart. The pilot flies the yoke into the cable between parachute or balloon and payload. A clamping device at the connection between yoke and the nose of the aircraft snatches the cable. The cable trails back, is hooked by the crew of the aircraft and transferred to the aircraft winch for boarding or tow. This system has been used successfully for weights up to approximately 400 pounds. The balloon or parachute is destroyed upon contact. This system is in operation today for the retrieval of personnel and equipment with fixed-wing aircraft but it is not suitable for helicopter retrieval.

Single Parachute System. This early system was developed in the late fifties and used in August 1960 to recover the Discoverer satellite capsule[176] in the first successful mid-air retrieval. The single descent and engagement parachute is of a standard, stable ringslot parachute design. The canopy is reinforced with lateral and radial webbings and load lines. Load lines replace some of the suspension lines and extend to the connection with the payload. The retrieval aircraft engages the canopy with its hook-cable system

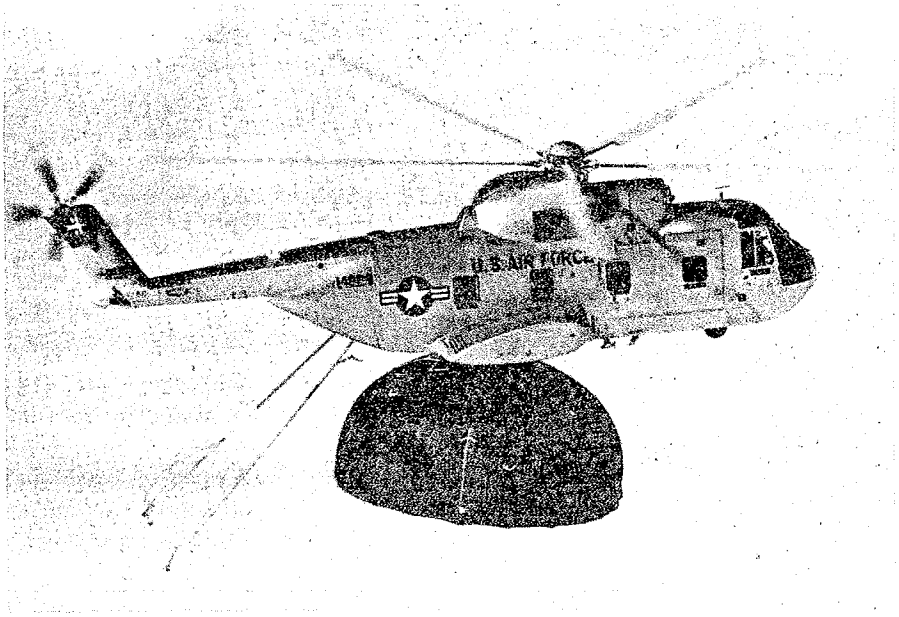


Figure 1.34 Trapeze/Helicopter (HH-53) Midair Retrieval System

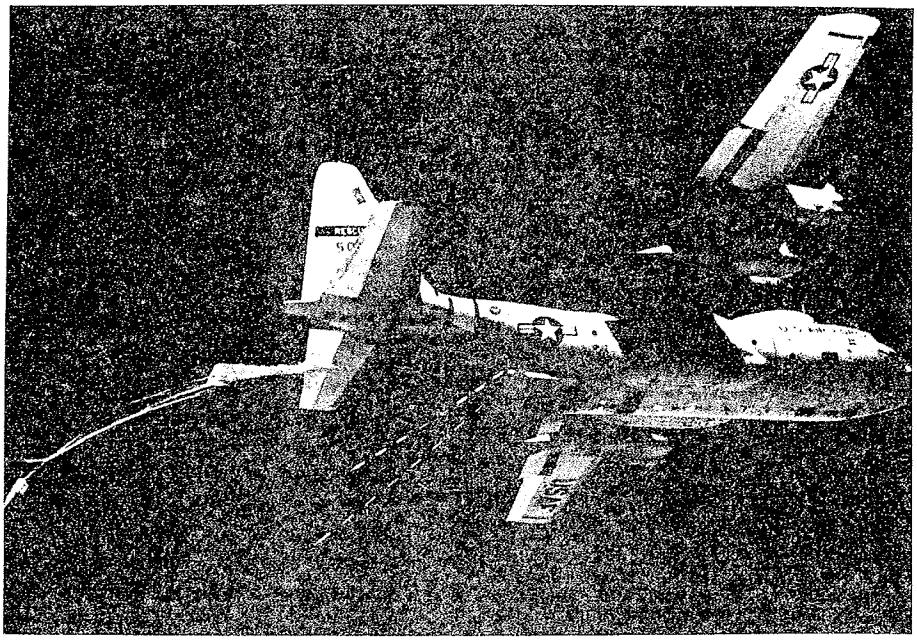


Figure 1.35 JC-130 Midair Retrieval System

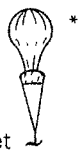
catching some of the lateral and radial load lines. Engagement collapses the canopy and starts towing the payload. Reel-out and reel-in of the cable with the attached payload is controlled by the load limiting winch. Payloads that can be recovered with this parachute system are limited in the size of the parachute canopy that the pole-hook system can engage without sliding off, and in the size of the collapsed parachute that a helicopter can tow.

The largest single parachute in use, and probably the present limit, is the 45.5 ft diameter ringslot parachute used for helicopter mid-air retrieval of the HAST (High Altitude Supersonic Target) [3, 177]. The 455 ft diameter parachute is of conical ringslot design with 36 gores and suspension lines of 400 lbs strength. Two laterals around the canopy and two radial tape-suspension line loops of 2000 lbs strength form the engagement network. The total weight of main parachute is 29 lbs.

With highly trained pilots, the single parachute system has produced a better than 95 percent recovery rate. The different payload weights for the same parachute size in Table 1.17 are due to the difference in required rate of descent for fixed wing aircraft and helicopter mid-air retrieval.

Parachute with Conical Extension. This parachute concept as shown in Figure 1.36 is still a single parachute but uses a conical extension on top of the canopy as the engagement target for the aircraft retrieval hooks. The extension overcomes the canopy diameter limitation for engagement by fixed wing aircraft, but the parachute size is still limited for helicopter tow. Parachutes of this type have been successfully tested and retrieved with the JC-130 aircraft with parachutes ranging from approximately 40 to 70 feet in diameter and payload weights approaching 2000 lbs [178]. All parachutes have the same size conical

TABLE 1.17 COMPARISON OF MID-AIR RETRIEVAL PARACHUTE SYSTEMS

Parachute System	Configuration	Payload Capability		Operational Systems	Comments
		Helicopter	Fixed Wing		
Single Parachute		~650 lbs	~500 lbs	Discoverer Biosatellite HAST	Parachute diameter limited by permissible target size. Stable, very reliable.
Extended Skirt Parachute with Conical Extension		~650 lbs	>2000 lbs	Atmospheric Probes	Parachute diameter for helicopter pickup limited to ~45 feet. Cone requires careful attention.
Tandem Parachute System		>4000 lbs	>4000 lbs	BQM 34F AQM 34V BGM 34C	Stability (wandering) of engagement parachute and rotation of main parachute can cause problems.
Annular Parachute System		>4000 lbs	>4000 lbs	Tested	In development
Balloon Parachute System		~300 lbs	~300 lbs	Tested	Developed but not in service.

* = Engagement target

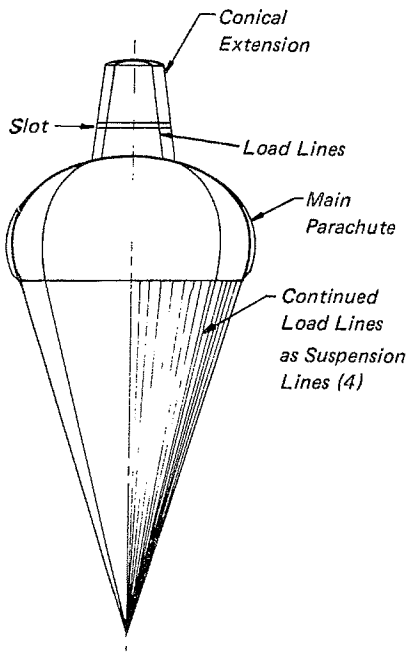


Figure 1.36 Extended Skirt Parachute With Conical Extension

extension; 15 feet high with a base diameter of 12 feet and a top diameter of 10 feet. Slots are provided in the cone for proper inflation. During mid-air retrieval the engagement gear of the aircraft hooks into a lateral and radial webbing network in the conical extension which guides the loads over a central vent point into several reinforced suspension lines and resultant uniform collapse of the main parachute canopy. A typical parachute is the 53 ft diameter model used for the mid-air retrieval of an atmospheric probe[179]. The parachute is a fully extended skirt parachute with the standard conical extension, and fifty-six suspension lines. Fifty-two lines are of 400 lbs strength and four lines are of 6000 lbs strength; the latter serve as load lines for transmitting the engagement loads into the payload. The weight of the parachute is 42 lbs. The parachute is reefed for 4 seconds and opened at an altitude of 45,000 feet. Opening the parachute at this altitude gives the JC-130 retrieval aircraft sufficient time to locate and approach the parachute and to start its midair retrieval passes at 10,000 to 15,000 feet.

The Tandem Parachute System. The inability of helicopters to tow large deflated parachutes for payloads above 500 to 700 lbs led to the development of the tandem parachute system. A main parachute provides the required rate of descent, and a small parachute attached with a load line above the main parachute serves as an engagement parachute. The load line connects to the vent of the main parachute, runs along the outside of the parachute canopy and down the suspension lines to the connection point with the payload. When the retrieval aircraft engages the target parachute and puts force in the load line, the main parachute disconnects from the load line at the vent and at the payload and falls free. The engagement parachute and load line are reeled aboard the aircraft and the payload or vehicle is towed behind the helicopter to the landing area. This system is used for the helicopter mid-air retrieval of target drones and RPV's as shown in Figure 1.37. The recovery weight is limited currently by the capability of the available model 80 winch which is rated at 4000 pounds.

The tandem system has stability problems with the engagement parachute. The large wake behind the main parachute requires the distance between the leading edge of the engagement parachute and the main parachute crown to be three to four times that of the inflated diameter of the main parachute with a



Figure 1.37 BQM - 34 F (Supersonic Target) Midair Retrieval in Progress

resultant long and heavy load line. Even at this distance, the engagement parachute will stay at the outside edge of the wake and may rotate around the wake or penetrate it in irregular motions which frequently interfere with proper engagement by the retrieval aircraft. The location of the load line along one radial of the main canopy requires that the aircraft approach from exactly the opposite direction to assure disconnect of the load line without damage to the reusable main parachute. This is referred to as the load line being located at the 12 o'clock position, the approach being made from the six o'clock position. If the main parachute rotates, the helicopter must follow to assure approach from the six o'clock direction for proper load line disconnect. The long load line also is subject to ship-like motions which start at the vent of the main parachute, and are then augmented in the load line and transferred to the engagement parachute causing inflation instability. Several programs were undertaken by USAF/ASD to investigate and improve the performance of the two primary systems now in use, the 79.6 ft diameter tandem parachute system used for the BQM-34F supersonic target drone and the 100 ft diameter parachute system used for both the AQM-34 and BQM-34 RPV's.[180-182] Figure 1.38 shows the arrangement and dimensions of the 100 ft diameter GR-14 tandem parachute system used for the AQM-34V RPV.

The annular tandem parachute system, as shown in Figure 1.39 was developed in the mid-sixties. It consists of an annular main parachute and a ringsail engagement parachute closely coupled to the crown of the main parachute. The large vent of the main parachute results in good airflow behind the center of the parachute and good inflation and stable flight of the engagement parachute. Two other advantages, when compared to the extended skirt with conical extension and the tandem parachute, are the high drag coefficient of the annular parachute and the short load lines of the engagement parachute. Both characteristics contribute to a low system weight. This parachute system has been tested with weights up to 2000 lbs using a 64 ft diameter parachute retrieved by a JC-130 aircraft.[183, 184]

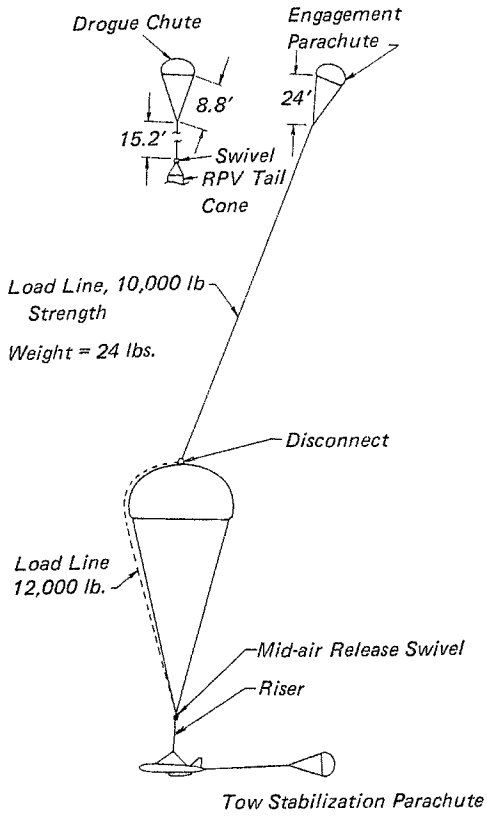


Figure 1.38 100 Ft. Tandem Engagement Parachute (GR-14) for AQM-34V

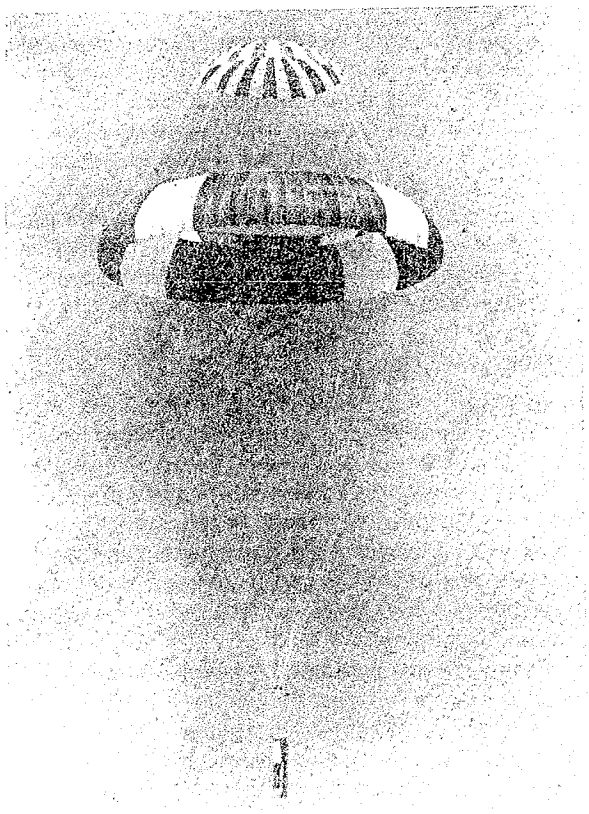


Figure 1.39 64 Ft. Diameter Annular Tandem Parachute with 2000 Test Vehicle

Other Mid-air Retrieval Concepts. Both the US Air Force and Navy have investigated concepts for mid-air retrieval of aircrews that escaped from disabled aircraft. The idea was to keep the crew member on his parachute in the air until a retrieval aircraft arrived, or use one aircraft of a flight of fighters as a rescue aircraft.

The Air Force PARD system (Pilot Airborne Recovery Device) concept utilizes a hot air balloon which inflates after the personnel parachute is opened and keeps the pilot in the air for sixty minutes until a rescue aircraft arrived. The pilot is reeled into the aircraft or towed to friendly territory, released and allowed to descent on his own.

The Navy investigated the so-called "Buddy System" where each fighter group would contain one fighter aircraft equipped to rescue bailed-out airmen. Two concepts were investigated. The "PORT-I" concept equipped the rescue fighter with a canard paravane towed on a steel cable offset and behind the aircraft. The personnel parachute of the bailed pilot would trail a small parachute behind the main parachute similar to the mid-air retrieval tandem parachute system. The paravane would intercept the cable between pilot chute and main parachute, tow the pilot to friendly territory, release the cable and the pilot would descend on his reinflated personnel parachute. The second concept, "PORT-II" (also called "The Wind Fending Line Engagement System") used the Fulton concept with the nose yoke, but in addition, ran cables from the nose of the aircraft to both wing tips and had an engagement unit on each wing tip for catching and engaging the line between pilot chute and personnel parachute. Both systems were investigated and tested[171,185,186].

Surface-to-Air Pickup

Land-to-air and water-to-air retrieval are not recovery systems that use aerodynamic decelerators as the primary means of retrieval, the principal subject of this handbook. However, surface-to-air retrieval systems are normally handled by the same companies and government organizations that handle recovery systems. It appears therefore appropriate to provide notes and references for those interested in this type of retrieval.

Systems for the retrieval of reentry nose cones, probes, samples from aboard ship and from the water, have been developed for quick return to the laboratory. One typical system developed for water-to-air retrieval of the Bio-satellite capsule, in the event mid-air retrieval should not be successful, incorporated a balloon attached by cable to the floating capsule and an aircraft equipped with the Trapeze cable-hook system for retrieval[187]. A complete unmanned water-to-air retrieval system was developed in the early sixties[188].

A "Long-Line" retrieval system concept was extensively investigated by the USAF. It consists of a fixed-wing aircraft trailing a long cable. The aircraft starts circling, and by proper circling techniques, speed and cable length, a condition is reached where the end of the cable will hover stationary over a location on the ground. The technique was a means to deliver cargo to waiting persons on the ground and to pickup cargo in return[189-191]. This method is being used successfully to supply and to keep contact with jungle outposts using small commercial aircraft.

SPECIAL USES

This section covers those uses of aerodynamic decelerators that cannot be identified easily as representative of the previous described applications. Special uses include the deceleration of surface vehicles (racing cars and speed boats), parachute sport jumping, airdrop of forest fire fighters, aerial drop of oil spill containment equipment, the well publicized airdrop and retardation of a Minuteman ballistic missile, balloon related recovery systems and the employment of aerodynamic decelerators as underwater braking devices. There are, most likely, other special examples; however, unless the recovery concept has a potential for general application of aerodynamic decelerators, it has not been included.

Deceleration of Surface Vehicles

The use of parachutes for stopping high acceleration racing automobiles (dragsters) after the end of a high speed run is a familiar sight on television. This application of a decelerator is similar to the landing deceleration of aircraft. When the need for stopping dragsters was first apparent, it was a natural course to use aircraft deceleration type ribbon and ringslot parachutes, either new or military surplus. When the supply of surplus parachutes ran out, dragster owners looked for a lower cost replacement of equal drag and stability. This was found in the Cross parachute which is used today in several variations for dragster and speedboat deceleration. Parachutes utilized for dragster deceleration are designed to meet the following requirements:

Dragster weight (lbs)	1500 to 3500
Deployment velocity (mph)	150 to 300
Required deceleration distance	$\leq$ 1/4 mile
Max. allowable deceleration (g's)	5 to 10

The parachutes are generally stowed in a bag similar to chest packs for personnel parachutes and closed with a cone and pin. A pull of a ripcord cable attached to a lever in the dragster cockpit deploys the parachute. A coil spring pilot chute stowed at the top of the pack is ejected into the airstream to deploy the main parachute. Frequently, two main parachutes are used for safety reasons. Cross parachutes with nominal diameters of 8 to 10 feet are used. The parachute weighs 3 to 5 pounds and the total assembly weight is approximately 5 to 8 pounds.

Land and water speed record vehicles have used parachutes to decelerate the vehicle at the end of the speed run, or for emergencies if the vehicle became unstable. 'In several record trials at the Bonneville Salt Flats, high speed racers, out of control, were stabilized and disaster avoided by timely deployment of the recovery/stabilization parachute. With the vehicle in a sideways or semi-sideways position, the vehicles were found to oscillate in a horizontal plane when the parachute was first deployed, a motion that dampened out quickly. However, the deployed parachute prevented sideways roll or end-over-end motion of the vehicle. These parachutes used at speeds up to 600 miles per hour, are generally ribbon parachutes, drogue gun or mortar deployed.

Emergency recovery parachutes are also in use for racing boats, either to stabilize the total boat, similar to racing cars, or to recover the speedboat pilot only. In case of an emergency, the pilot deploys his personnel parachute and is pulled free and away from the out-of-control racer.

Sport Parachutes

Competitive parachuting, as introduced in the United States in 1926 by professional parachutist Joe Crane, was confined solely to "spot-landing" contests. The winner was the parachutist who landed closest to the center of circle marked on the airfield. Thus was born the desire for a parachute whose motion in the air and drift over the ground could be controlled. The only means of directional control for the jumper during those days was by riser manipulation. The parachutist, by riser pull, deformed the canopy in such a way that deflected airflow would impart some horizontal "glide" to the parachute. By pulling the risers still further, the parachutist could increase his rate of descent significantly.

Initial Attempts at Steerability. Patent files contain many early ideas for making parachutes steerable, but the first reliable and widely used steerable parachute design was the Hoffman Triangle Parachute introduced in 1929. Horizontal motion was achieved by air flowing out one corner of the triangular shaped canopy which was cut straight across without any suspension lines.

New impetus for the design of steerable parachutes came from an initial investigation in 1939 by the US Forest Service in parachuting firefighters into wooded areas. In this project, the steerable Eagle parachute was used. The parachute assembly supplied by the Eagle Parachute Company consisted of a 30 ft diameter main parachute carried on the back, and a chest pack reserve parachute, which was 27 feet in diameter, both manually ripcord operated. Both parachutes had design features which made them maneuverable.

The canopy was a flat circular design. However, two cloth extensions were incorporated into the skirt, each projected at 45° angles rearward. The suspension line system for the canopy was provided with short, secondary lines. Attached at some distance above the skirt, and of such length that when the canopy was inflated, the upper portion assumed a spherical shape, and the lower portion assumed a semi-lobed configuration. The two rearward facing extension lobes directed the airflow which imparted a forward glide to the parachute. Control lines leading from the extensions to the rear risers allowed the smoke-jumper to "close" the lobed extensions, thus causing the parachute to turn. The parachute had a forward glide of 5 to 8 miles per hour.

A blank gore parachute developed in England in the late 1950's, received wide acceptance throughout Europe for its reliability and steerability. In 1956, this parachute design was introduced by Jacques Istel to the new, fast-growing sport of parachuting in the United States. This was followed by a period of numerous modifications to the standard, readily available C-9 parachute with variations of holes and "cuts" extending across from three to seven gores.

Demand for higher performing sport parachutes was met in 1964 when the Para-Commander assembly was put on the market. This parachute, based on a parachute concept of Pierre LeMoigne of France, soon proved to outclass other sport parachute designs.

High Performance Sport Parachutes. The introduction of the Parawing as a sport jumping parachute in 1968 may be considered the beginning of high performance gliding parachute usage. This parachute, based on original concepts of Francis Rogallo, permitted sport parachutists to make a "dead-center" landing at parachuting meets. Since that time however, the overwhelming popularity of the so-called "squares" has placed them in the leading position for sport parachuting because of their high glide ratio,

rapid turn rates, and minimal weight and volume. Square parachutes are based on pioneering work of Domina C. Jalbert, who recognized the advantages of a ram-air, winged airfoil configuration. This led to a design popularly known as the "Parafoil". Variations of the Parafoil [399], presently in wide use, are the Strato-Cloud, Para-Plane [476] and the Viking. A related design is the Volplane [402]. Regulations controlling sport jumping and techniques and equipment are found in Reference [196].

Smoke-Jumping

Interest by the US Forest Service for utilizing aviation to combat forest fires dates back to 1919 [197]. This early recognition that aviation could help in managing and protecting forest lands, led to the organization of a forest fire patrol along California's Sierra Madre Mountain Range.

In 1939, it was demonstrated that the parachute could serve as an adjunct to the airplane to transport and deliver firefighters to burning timber zones.

Firefighting Parachute Types. Making premeditated parachute jumps into rocky and wooded terrain indicated the need for parachutes that had a low rate of descent and were maneuverable to a suitable degree.

The initial maneuverable parachute design utilized by the US Forest Service was the Eagle described in the preceding section. The parachute currently being utilized, is designated the Model FS-10.

The FS-10 parachute uses a 7-gore "TU" modification described and illustrated in Fig. 2.6. Other standard T-10 parachute components used in the FS-10 parachute assembly are the pack assembly, deployment bag, pack waistband extension, and the standard 24 ft diameter chest reserve pack assembly. In order to meet the specific demands of smoke-jumping, the FS-10 uses the Forest Service designed riser assembly, harness assembly (Model H-4), ancillary protective back pad, and modified extensions to the waistband. The standard T-10 pack assembly is modified by the addition of riser tack tabs to its tray. A two-color scheme is used on the canopy. The parachute can achieve a 180° turn in 4.5 seconds and a forward speed of 14 fps. Figure 1.40 shows a smoke-jumper's full equipment, including a FS-10 parachute.

Present Smoke-Jumping Parachute Criteria. Increasing jumper equipment weight indicates the need for a larger canopy than the present 35 ft diameter basic T-10 (MC-1-1B) parachute. The present FS-10 parachute weight of 34 pounds combined with approximately 41 pounds jump gear weight (suit, helmet, let-down line, etc.) and personal gear, results in an equipment-for-jump weight of 75 pounds, most of which will be "pack-out" weight at the end of an operation.

The following Forest Service criteria for a parachute beyond the FS-10 to be used in smoke-jumping operations are based on a 230 pound load at sea level under standard atmosphere conditions:



Figure 1.40 Smoke Jumper Fully Equipped with FS-10 Parachute

1. Maximum rate of descent during "hands off" control to be 14 to 16 feet per second.
2. Maximum forward speed of 20 feet per second with braking. Braking not to increase the rate of descent to more than 17 feet per second. Minimum forward speed of 14 feet per second.
3. Maximum oscillation during "hands off" flight of 4°. Canopy stability during maneuvering, "damping" equal to FS-10.
4. Maximum opening shock, equal to FS-10, ±25%.
5. Turn rate shall be 9 seconds or less for a 360° revolution.
6. Maximum deployment speed of 150 miles per hour.
7. Minimum jumper exit altitude of 1000 feet above ground level (AGL).
8. Conventional single-stage static line and D-bag deployment. Even skirt, circular canopy such as T-10, although not restricted to extended skirt gore shape. Maximum opening time, from exit to parachute fully open, not to exceed FS-10; compatible with manual reserve deployment.
9. Performance and deployment reliability should approach that of FS-10.
10. Two-color canopy scheme to give good visibility against timbered background, and to show canopy front and rear direction.
11. Complete system "pack-out" weight not to exceed FS-10; light as possible desirable.
12. Maximum parachute assembly cost, $1000.

Miscellaneous Systems

Many interesting and technically advanced parachute systems have been developed which evolve from typical base applications, but extend the fundamental techniques into new useful areas to satisfy a special need. Several such systems have started with the equipment and background experience obtained in aerial delivery of supplies and equipment.

Airdrop of Oil Spill Containment Barrier. The US Coast Guard is charged with the responsibility for containment and removal of oil spills in coastal and high sea waters. One of the systems developed consists of a line of four feet high, elastomer coated, nylon curtains supported by vertical struts and flotation devices. This curtain is strung in the water to encircle the oil spill and prevent further spreading. At the request of the Coast Guard, the USAF 6511th Test Squadron at the National Parachute Test Range, El Centro, California, in cooperation with a parachute company and a platform development company, developed a system for dropping these oil containment barriers[198,199]. The curtains are packed in dropable containers that are tailored to the dimensions of a C-130 aircraft cargo compartment. Each container holds 612 running feet of the containment curtain. Several unique devices and special procedures had to be developed to meet aerial drop, flight safety and flotation requirements of the barrier drop. The basic concept follows the standard aerial delivery procedures used by the US Army and Air Force for airdrop of supplies. Special features include a redesign load transfer system for switching the extraction parachute to its function as pilot chute for deploying the 100 ft diameter G-11A main descent parachutes. Also, platform to aircraft tiedowns and disconnect fittings had to be redesigned to accommodate the large dimension barrier curtain box. A special disconnect was designed to ensure non-interference of the parachute with the oil containment curtains after water impact. This project is a good example of how an existing system can be modified to meet a specific requirement.

Airdrop of Flotable Rubber Oil Tanks. The Coast Guard oil spill containment effort includes the use of large, bladder type, flexible, flotable oil tanks that store up to 140,000 gallons of fluid. These oil tanks are placed next to the stricken tankers or at the periphery of oil spills. Oil in the tanker or spilled oil can then be pumped into these rubber tanks and removed. The development of a system for aerial delivery and airdrop of these large tanks at the scene of a disaster is described in Reference 578.

Airdrop/Airlaunch of a Ballistic Missile. The Air Force, in 1974, demonstrated the feasibility of extracting and parachute stabilizing, a Minuteman I intercontinental ballistic missile from a C-5A aircraft followed by subsequent air launch. The Air Force had previously demonstrated the airdrop of a single 40,000 lb platform from the C-5A cargo aircraft and the C-5A's capability to airdrop 160,000 lbs in a sequential multiple load [75]. Feasibility of airdropping single platform loads of 70,000 lbs was established by computer simulation. Several methods for air launching a Minuteman missile from a C-5A cargo aircraft were studied including vertical launch tubes, forward and aft gravity launch bays and several other approaches. The method selected for demonstration operates in sequences as follows:

a. Platform extraction through the aircraft aft

door of a cradle mounted platform restrained missile.

b. Removal of missile restraint following clearance from the aircraft which allowed the constant extraction force application to the platform to separate the cradle/platform assembly from the missile and deploy three each, 32 ft diameter ribbon stabilization parachutes.

c. Stabilized descent of missile prior to launch.

It was determined that this method, previously developed by the 6511th Test Squadron for air launch of bomb type vehicles from cargo aircraft, required the minimum aircraft modification and used a large amount of existing equipment and proven aircraft drop procedures. It was also the safest and most cost effective approach.

The development and test program demonstrated the feasibility of extracting an 86,000 lb missile/cradle system separating the cradle/platform from the missile and stabilizing the missile prior to launch. Basic aspects of the program that required careful analysis and tests were the aircraft installation and the aircraft control response to the extensive shift in center of gravity during missile extraction. Installation considerations included the procedures for aircraft loading and vehicle tiedown, crew training, extraction of the modified missile/cradle platform with proven parachute extraction procedures and the various connect/disconnect functions required for restraining the cradle in the aircraft. Deployment considerations included retention of the extraction system to the platform, the separation of the cradle/platform from the missile and the deployment of the missile stabilization parachute system. The following missile/cradle extraction and stabilization parachute deployment sequence was used.

Upon drop command, two 32-ft diameter ribbon extraction parachutes were deployed by the standard extraction parachute ejection system. These parachutes were attached with a 170-ft extraction riser to the cradle/platform.

When the parachute load reached a predetermined level, the platform/cradle was disconnected from the aircraft restraint rails and extracted through the aft cargo doors. The extraction force for the 86,000 lb missile/cradle system was approximately 60,000 pounds.

Four seconds after the missile/cradle left the aircraft, circumferential straps that connected the missile to the cradle were pyro-disconnected. The extraction parachutes retarded the cradle, the missile fell free.

Separation of the missile from the cradle deployed three 32-ft ribbon stabilization parachutes stowed on the cradle and attached to the missile. These parachutes after opening, stabilized the missile in the vertical position.

On the last of three missile drops, the first stage Minuteman motor was fired for ten seconds immediately following the disconnect of the stabilization parachutes.

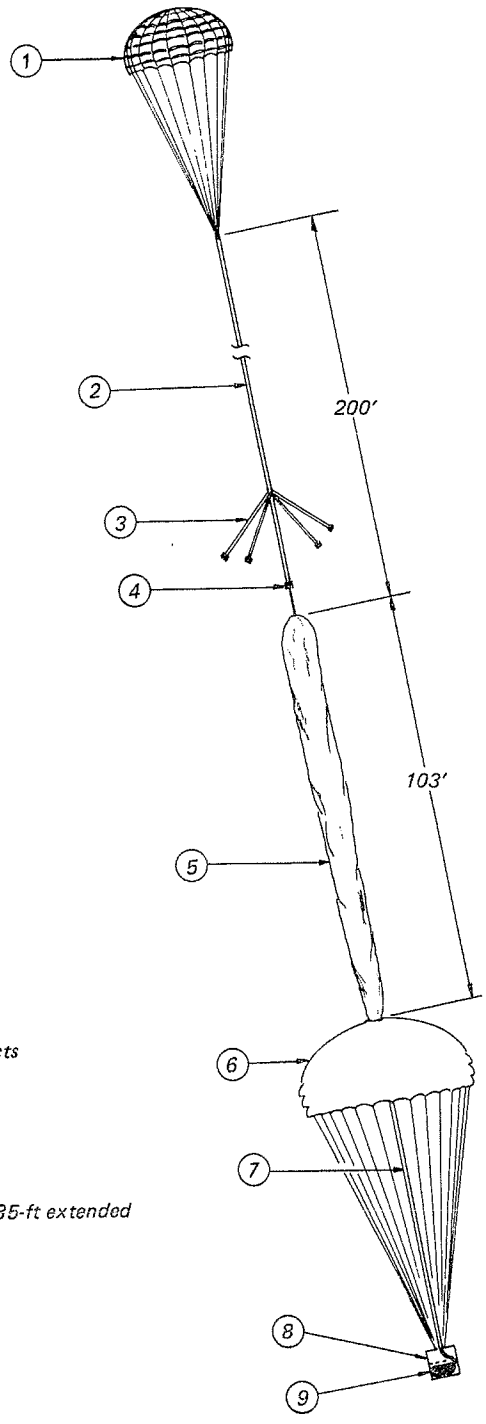
The Air Force conducted a careful test program approaching the final system drop in a logical weight, speed, load build-up and crew training approach. Testing included five extraction parachute tests, six crew training tests and seven weight build-up tests. Weight build-up tests used a simulated load platform weighing up to 86,000 pounds, extracted and stabilized with the stabilization parachute system. Platforms were then recovered using clusters of up to ten 100-ft each G-11A cargo parachutes for final descent. Airdrop launch speeds ranged from 159 to 178 knots with the final three missile drops made at an indicated airspeed of 160 knots and 20,000 ft pressure altitude. Reference 200 gives an account of the systematic conscientious flight safety approach to this test of the heaviest single weight ever airdropped.

Air-Launched Balloon-Supported Relay Station. A system being developed places a communications relay station at a given location and to float at a desired altitude by means of a balloon.

The entire system, consisting of the relay station, the balloon, liquid helium for balloon inflation, the parachute extraction and balloon deployment system and related gear, weighs 1500 lbs and is stored in a cubical container. The system is air-launched from the cargo compartment of a C-130 aircraft at 25,000 feet altitude by means of a standard extraction system. A 28-ft diameter ringslot parachute is deployed by the pendulum release method on a 200-ft extraction line which connects with a four-legged harness to the four corners of the container. Ten seconds after extraction, the four-legged harness is disconnected from the 1200 lb descending container and in turn deploys a 42-ft diameter ringsail main parachute. A 150,000 cubic ft balloon is stowed in a bag above and around the vent of the main parachute. The parachute inflates around a center line that keeps the 28-ft extraction parachute attached to the container. An appropriate time after main parachute inflation, the balloon bag is opened and the inflation of the balloon starts from the liquid helium cryogenic unit on the bottom of the container. The extraction parachute remains attached to the top of the balloon through initial inflation to support and control stretch. After the balloon is half inflated, the extraction parachute is disconnected in order to lower the system weight and avoid destabilizing forces on the balloon. After

full balloon inflation, the 1000 lb cryogenic unit is disconnected from the container and recovered with three 35-ft diameter T-10 extended skirt parachutes.

Numerous tests have been conducted at the National Parachute Test Range with this complex system. These tests have defined good components and identified areas that need improvement as development of this system progresses[201-203]. Figure 1.41 shows a schematic of the parachute balloon train.



1. *28-ft ringslot extraction parachute*
2. *200-ft extraction line*
3. *Four harness legs with pyro-disconnects*
4. *Extraction line disconnect*
5. *150,000 cu.ft. balloon*
6. *42-ft ringsail main parachute*
7. *Center line*
8. *Container*
9. *Droppable cryogenic unit with three 35-ft extended skirt parachutes*

Figure 1.41 Schematic Of Parachute Balloon Train Of Air-Launch Communications Relay Balloon.

CHAPTER 2

DEPLOYABLE AERODYNAMIC DECELERATORS

A recovery system is made up of components which, functioning together, provide for the controlled deceleration and stabilization of a body in flight or moving on the ground. Most applications involve an airborne body for which the system also provides controlled descent and flight termination functions. The most important component of a recovery system is the deployable aerodynamic decelerator. Other components of the system may provide the means for deployment of the decelerator, control of forces, support for the suspended body, landing impact attenuation, and in some cases, automatic detachment of the decelerator when its function ends.

The primary operational features of a deceleration device are its drag and stability characteristics. Lift may be incorporated in a decelerator to provide divergence from a ballistic path such as gliding to a target landing spot. Drag, stability and lift characteristics determine the performance effectiveness of a deployable aerodynamic decelerator. These characteristics vary with the design configuration of the decelerator. This chapter describes configurations of various decelerator types, supported by limited performance and weight data to permit comparison of one decelerator type with another.

Decelerators are normally required to be efficient in terms of weight or packed volume per unit area. Hence, an important decelerator feature is a flexible structure that can be folded or compressed into a relatively dense package. Also important is the decelerator's capability of being deployed from the stowed position and rapidly inflated to create a required aerodynamic force-producing configuration. Deployment and opening force characteristics of a decelerator are significant factors affecting not only weight and packed volume of the decelerator, but also the integrity of structure and contents of the object being recovered.

The construction geometry of a decelerator determines its operational shape and the nature of aerodynamic forces generated. The designs discussed in the following sections represent those which have been sufficiently investigated to obtain performance data, and are used in operational recovery systems, or have shown potential for future applications. Although parachutes predominate as the decelerator class most frequently accommodated in a recovery system, decelerators other than parachutes are described which possess features of special advantage, particularly in the high temperature, high velocity performance regimes.

DECELERATOR CHARACTERISTICS

Shape factors for decelerators are summarized in tabulated form, along with general performance characteristics. Numerical values in the tables represent either an approximate mean value, normally suitable for preliminary performance assessment, or a range of values influenced by geometric factors, canopy porosity, operating altitude and velocity. Where a range depicts a wide spread of the term average, it is necessary to excercise careful judgement in applying a unit value, even for a preliminary performance assessment. A proper judgement could be based on an understanding of influencing parameters and their effects on performance characteristics as discussed in Chapter 6.

A summary of decelerator comparable features are contained in Tables 2.1 through 2.5. Plan and profile views define the constructed shape of each decelerator type, followed by a factor which relates a basic construction dimension D_C, to the decelerator's nominal diameter, D_O, based on reference area, S_O. Inflated shape is similarly defined by the ratio, D_p/D_O, where projected diameter, D_p, is a variable dimension. These terms and their relationships are defined starting on page 79.

Drag efficiency is reflected in the term, C_{D_O}, a coefficient of aerodynamic drag force related to the total decelerator surface area, S_O. The drag coefficient varies within a characteristic range, influenced by such factors as canopy size, number of gores, canopy porosity, suspension line length, air density, and rate of descent. In Table 2.1, the solid cloth parachutes used for descent which show large oscillation angles also show a wide spread in C_{D_O}. Values are from data (see Chapter 6) obtained at rates of descent between 17 and 30 fps, the higher values of drag coefficient occurring at the low velocities. The lower values are representative of normal operational conditions within the subsonic regime. Drag coefficients at supersonic speeds are given in Chapter 6.

The opening load factor, C_X, in the table is the ratio of the characteristic peak opening force to the steady state drag force during inflation at a constant

flow velocity, the "infinite mass" condition. A value of this factor near unity is desired in non-reefed parachutes such as man-carrying, aircraft landing deceleration, ordnance retardation and first stage drogue parachutes. The control of canopy area growth by reefing has lessened the importance of the opening load factor characteristic in applications where reefing is feasible.

The average angle of oscillation in the tables is a range of observed pendular motions for decelerators from very small scale models in a wind tunnel, to parachutes in excess of 100 ft diameter in free desent. Large oscillations indicated for the solid textile parachutes are associated with parachute sizes less than 30 ft diameter. Parachutes with this degree of instability also have a tendency to glide instead of oscillating depending on the surface loading W/S_o. Stability of parachutes is discussed in detail in Chapter 6.

General applications of decelerators are listed by functional purpose, i.e., a drogue is an initial stage decelerator, sometimes operating effectively at supersonic speeds. Other decelerators provide ground deceleration, cargo extraction, body stabilization, or final descent functions.

TABLE 2.1 SOLID TEXTILE PARACHUTES

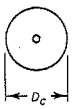
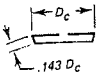
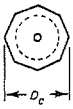
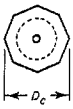
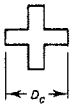
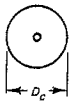
Type	Constructed Shape		$\frac{D_c}{D_o}$	Inflated Shape $\frac{D_p}{D_o}$	Drag Coef. C_{D_o} Range	Opening Load Factor C_X (Inf. Mass)	Average Angle of Oscillation	General Application
	Plan	Profile						
Flat Circular			1.00	.67 to .70	.75 to .80	~1.8	±10° to ±40°	Descent
Conical			.93 to .95	.70	.75 to .90	~1.8	±10° to ±30°	Descent
Bi-Conical			.90 to .95	.70	.75 to .92	~1.8	±10° to ±30°	Descent
Tri-Conical			.90 to .95	.70	.80 to .96	~1.8	±10° to ±20°	Descent
Extended Skirt 10 % Flat			.86	.66 to .70	.78 to .87	~1.4	±10° to ±15°	Descent
Extended Skirt 14.3 % Full			.81	.66 to .70	.75 to .90	~1.4	±10° to ±15°	Descent
Hemispherical			.71	.66	.62 to .77	~1.6	±10° to ±15°	Descent
Guide Surface (Ribbed)			.63	.62	.28 .to .42	~1.1	0° to ±2°	Stabilization Drogue
Guide Surface (Ribless)			.66	.63	.30 to .34	~1.4	0° to ±3°	Pilot, Drogue
Annular			1.04	.94	.95 to 1.00	~1.4	<±6°	Descent
Cross			1.15 to 1.19	.66 to .72	.60 to .78	~1.2	0° to ±3°	Descent, Deceleration

TABLE 2.2 SLOTTED TEXTILE PARACHUTES

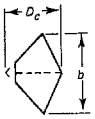
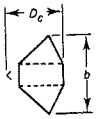
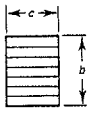
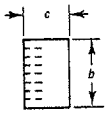
Type	Constructed Shape			Inflated Shape	Drag Coef.	Opening Load Factor	Average Angle of Oscillation	General Application
	Plan	Profile	$\frac{D_c}{D_o}$	$\frac{D_p}{D_o}$	C_{D_o} Range	C_X (Inf. Mass)		
Flat Ribbon			1.00	.67	.45 to .50	~1.05	0° to ±3°	Drogue, Descent, Deceleration
Conical Ribbon			.95 to .97	.70	.50 to .55	~1.05	0° to ±3°	Descent, Deceleration
Conical Ribbon (Varied Porosity)			.97	.70	.55 to .65	1.05 to 1.30	0° to ±3°	Drogue, Descent, Deceleration
Ribbon (Hemisflo)			.62	.62	.30* to .46	1.00 to 1.30	±2°	Supersonic Drogue
Ringslot			1.00	.67 to .70	.56 to .65	~1.05	0° to ±5°	Extraction, Deceleration
Ringsail			1.16	.69	.75 to .90	~1.10	±5° to ±10°	Descent
Disc-Gap-Band			.73	.65	.52 to .58	~1.30	±10° to ±15°	Descent

*Supersonic

TABLE 2.3 ROTATING PARACHUTES

Type	Constructed Shape			Inflated Shape	Drag Coef.	Opening Load Factor	Average Angle of Oscillation	General Application
	Plan	Profile	$\frac{D_c}{D_o}$	$\frac{D_p}{D_o}$	C_{D_o} Range	C_X (Inf. Mass)		
Rotafoil		——	1.05	.90	.85 to .99	1.05	0° to ±2°	Drogue
Vortex Ring		— —	1.90	N/A	1.5 to 1.8	1.1 to 1.2	0° to ±2°	Descent

TABLE 2.4 GLIDING PARACHUTES

Type	Constructed Shape: Plan	Constructed Shape: Profile	Area Ratio $\frac{S_W}{S_O}$	Aerodynamic Force Coef. C_R Range	Glide Ratio $\left(\frac{L}{D}\right)_{max}$	General Application
Tojo, TU Slots, etc.			1.0	.85 to .90	0.5 to 0.7	Descent
LeMoigne			1.0	.90 to 1.00	1.1	Descent
Parawing (Single Keel)			1.0	.90 to 1.10	2.0 to 2.5	Descent
Parawing (Twin Keel)			1.0	1.00 to 1.10	2.8* to 3.2	Descent
Parafoil			.27	.75 to .85	2.3* to 3.5	Descent
Sailwing			.80 to .90	N/A	2.5* to 3.5	Descent
Volplane			.60	N/A	2.0* to 3.0	Descent

*Glide ratio is affected by aspect ratio AR, and canopy loading, W/S_O.

TABLE 2.5 DECELERATORS OTHER THAN PARACHUTES

Type	Constructed Shape: Plan	Constructed Shape: Profile	$\frac{D_C}{D_O}$	Inflated Shape $\frac{D_P}{D_O}$	Drag Coef. C_{D_O} Range	Opening Load C_X (Inf. Mass)	Average Angle of Oscillation	General Application
Balloon (Ballute)			.51	.51	.51* to 1.20	~1.0	<±1°	Stabilization Drogue

*Supersonic

PARACHUTES

Parachutes constitute the major class of deployable aerodynamic decelerators. The type designations relate generally to the profile of the canopy, its planform, or other characteristic feature. The different parachute designs fall into two broad categories; solid textile and slotted. Within both categories, most parachute types have evolved from the geometry of the basic flat circular canopy. Others, through unique features of construction have achieved excellent stability, lower cost or gliding performance.

The shape of a parachute when inflated and the number and arrangement of suspension lines may vary greatly from one type to another, but all possess symmetry about a central axis, or, at least about a plane through the system axis. Inflated shape can be varied by a modification of construction. A principal reason for the existence of numerous types of parachutes is optimization of one or more performance characteristics, but it is the construction geometry that separates one parachute type from another.

In the following paragraphs, the different parts of a parachute are defined, and geometric data are provided for a number of established types. For reference, specific parachute and applications data, including size, number of gores, material used, length of lines, parachute weight, suspended load, rate of descent, and maximum deployment velocity, are listed for developed and operational parachutes representative of each type.

The principal components of a parachute are the canopy and the suspension lines. The *canopy* is the cloth surface that inflates to a developed shape, producing an aerodynamic force. Its purpose is to apply a retarding or stabilizing force as it is drawn through the air by a falling or moving body. *Suspension lines* transmit the retarding force from canopy to body, usually through a riser at the towing end. A riser forms a single load carrying member below the convergence of suspension lines, and may extend above the convergence point as branches which attach to groups of suspension lines. The vectorial point of convergence of all suspension lines of a parachute is commonly referred to as the *confluence point.* The distance from canopy skirt to the confluence point is the effective suspension line length, l_e. A riser is treated as a separate sub-assembly unless formed by continuation of the suspension lines, or if for other reasons it cannot be separated from the parachute assembly.

The parts of a typical parachute are identified in Figure 2.1. The *crown* of a canopy is the region of cloth area above the major diameter of the inflated shape, whereas the portion below to the leading edge

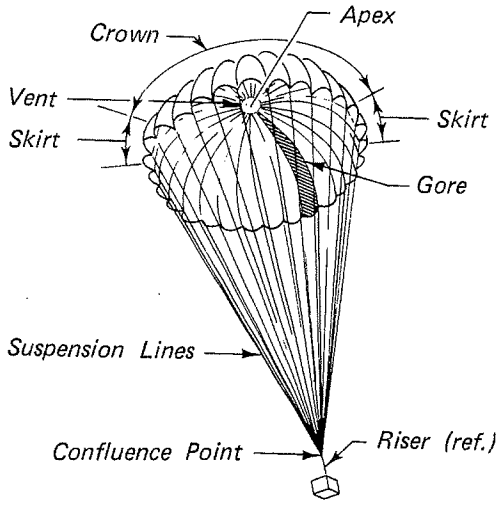


Figure 2.1 Parts of a Parachute

of the canopy is known as the *skirt.* The circular opening at the center of the crown is called the *vent.* The vent is normally less than one percent of the canopy area. It serves to simplify fabrication and provides relief for the initial surge of air that impacts the top of the canopy at the start of inflation. *Vent lines* are line segments or portions of continuous lines fixed to opposed points on the vent hem. They provide structural continuity across the canopy to each suspension line. The *apex* is the topmost point of an inflated canopy, and normally refers to the point where vent lines cross. A *gore* is a tapered or triangular fabric segment of a canopy.

Canopy Geometry

A conventional parachute canopy is formed from an even number of identical gores joined one to another by means of a *main seam,* or, for a canopy of circular planform, a *radial seam.* A gore extends from the top edge of the *vent hem* to the bottom edge of the *skirt hem,* e.g., gore height, h_g, is the centerline distance from apex to skirt edge, h_s, less vent height, h_v, shown in Figure 2.2. A triangular gore has a vertex angle, β, and gore width varies from e_v at the vent hem, to e_s at the skirt hem. The flat pattern of gore, if other than a straight sided geometric shape, may be defined more explicity by ordinates of e, as h varies from h_v to h_s. Fig. 2.2 shows two patterns for a flat gore layout. A gore of solid cloth will consist of sections sewn together either in bias or block pattern. The number of sections in a gore is usually determined by the cloth width seam allowance. With *bias* construction, section seams and yarns lie in

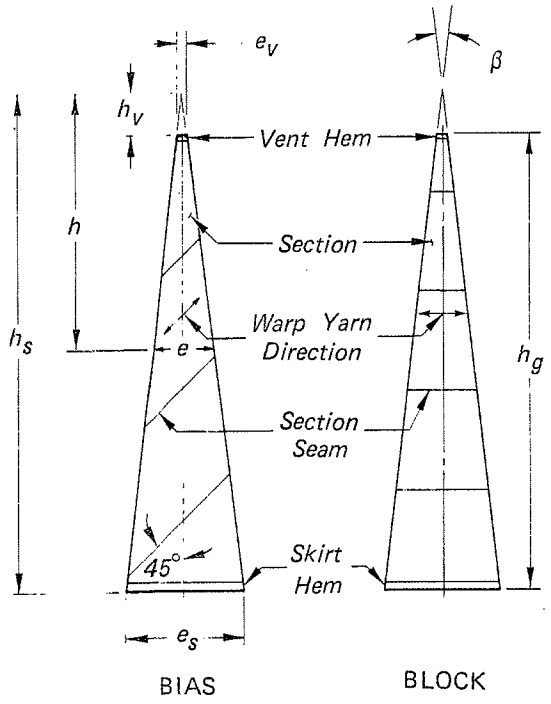


Figure 2.2 Flat Patterns of a Gore

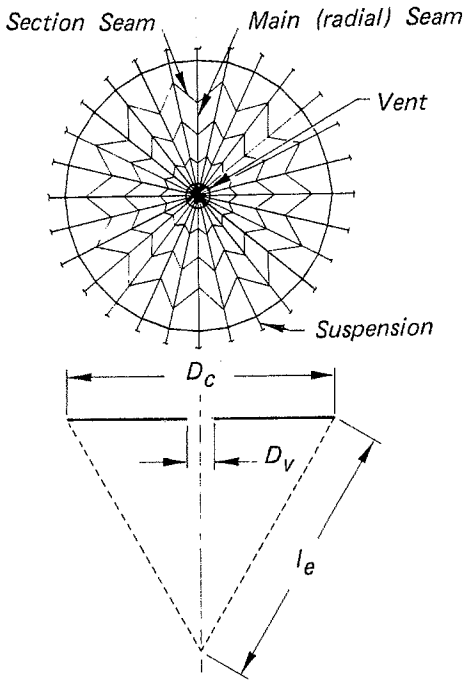


Figure 2.3 Planform and Construction Schematic for a Flat Circular Parachute

a direction 45 degrees to the center line of the gore, and adjacent gores are alternated so that diagonal seams meet at the radial seams as illustrated in Figure 2.3. With *block* construction, the cloth direction, or more specifically, the direction of warp yarns, is either parallel or perpendicular to the gore centerline.

Constructed Shape. For purposes of uniform comparison and reference, a parachute's size is based upon canopy constructed surface area, normally referred to as ***nominal area,*** S_O. For most canopy designs, nominal area is computed as the sum of the gore areas inclusive of vent area, slots and other openings within the gore outline. Areas of surfaces, such as ribs, flares, panels or additions for fullness to the cloth are also included. ***Nominal diameter,*** D_O, is defined as the computed diameter of a circle of area S_O. The nominal diameter, D_O, usually differs from the principal ***construction dimension,*** D_C, of a canopy. As a reference dimension, D_C, is the constructed diameter of a circular parachute canopy, defined as the distance between points where maximum width of opposing gores intersects the radial seam. Thus, constructed diameter is measured along the radial seam, and not along the gore centerline. The constructed diameter, D_C, of a flat canopy and the vent diameter, D_V, are shown in a construction schematic diagram of Fig. 2.3. The dotted line is a scale representation of suspension effective length, $l_e = D_O$.

The desired constructed shape of a parachute is determined by gore geometry and the number of gores in the canopy. For a flat circular canopy, the sum of the gore angles, $\Sigma\beta$, around the apex will total 360 degrees, e.g., for a given number of gores, N, each gore will have a vertex angle of $\beta = 360/N$ degrees.

If a canopy is constructed of triangular gores whose $\Sigma\beta$ is less than 360 degrees, a ***conical*** canopy is the result. Figure 2.4 shows a construction schematic of a conical canopy. The cone angle, μ, is the angle between the gore radial seam centerline and its corresponding flat projection.

A disadvantage of the conical canopy shape is extra tautness in the mid-crown region, leading to higher hoop stress in the fabric. Adding width to the gore fabric to create fullness in the transverse direction relieves high stress by reducing local radius of curvature. ***Fullness*** is a term applied to the amount that a flat fabric dimension exceeds the basic gore width. Providing fullness near the vent for stress relief is a common design practice. Other parachute types use variations of the basic triangular gore to gain improved performance.

Shaping the gore to a bi-conical profile relieves the concentrated stress at mid-crown of the conical constructed shape. The first cone has a smaller base

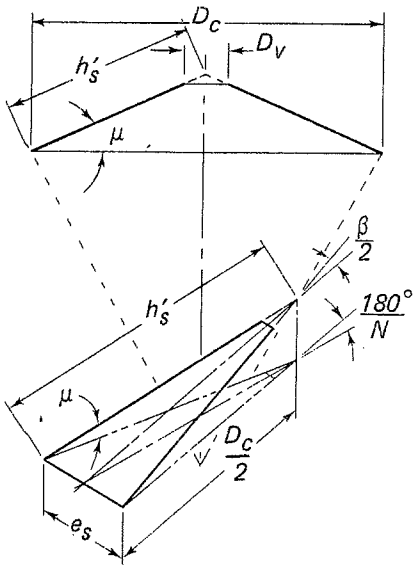


Figure 2.4 Construction Schematic of Conical Canopy

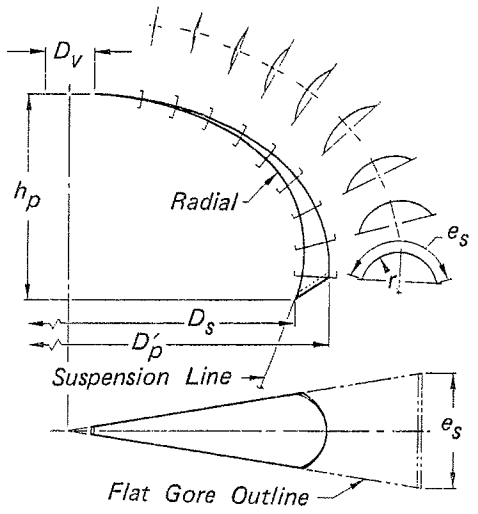


Figure 2.5 Shape of an Inflated Gore

angle, μ, than the second cone. The tri-conical design goes a step further toward specialization of constructed shape with three conical surfaces. Bi- and Tri-conical designs exist in many forms, varying both in constructed dimensions and cone angles. A polyconical parachute of ten equal slope lengths has been manufactured and successfully tested. The trend toward a rounded construction profile appears more effective than the flat circular or the plain conical parachute types.

Better stability and a lower opening load factor is achieved by extending the ***skirt.*** There are several methods for shaping the gore to extend the skirt. A ***flat extended skirt*** is obtained by tapering the gore beyond the point of maximum width at the same angle as the vertex angle β. A ***full extended skirt*** is obtained by tapering the extension of the gore at an angle, ϕ_l, formed by two adjacent suspension lines which come together at the confluence point of a construction schematic. The amount of extension is given as a percent that one gore extension exceeds the constructed diameter. The taper angle of a full extension is determined by the suspension line effective length, l_e, and the skirt extension dimension.

Inflated Shape. Under aerodynamic loading, a typical canopy assumes a concave scalloped contour when it fills to its inflated shape, with fabric and lines taut due to tension forces. A measurement of projected area, S_p, can be converted to ***projected diameter,*** D_p, defined as the diameter of a circle of area, S_p. Frequently the maximum width dimension, D'_p, is used, the distance across the canopy at the gore centerline. The projected height of the canopy, h_p, is the measurement from the apex to the plane at points of juncture of skirt hem and suspension lines. Skirt diameter, D_s, is the diameter of a circle through these points. Figure 2.5 shows the outward curvature of the gore between radial seams to vary from a small displacement near the vent, to a large displacement at the skirt.

The importance of geometry is better understood when it is realized that the aerodynamic forces generated by a parachute relate to its inflated shape. Therefore, the area ratio, S_p/S_o and the diameter ratio D_p/D_o, are important drag related parameters of any ballistic type decelerator.

The effective length of suspension lines, l_e, usually influences the shape and projected area of an inflated canopy, making the ratio, l_e/D_o, a major design parameter for most parachute types. Exceptions are guide surface, hemispherical and extended skirt types with relatively inflexible skirt diameters.

Typical features of parachutes are more clearly defined in subsequent pages. For most types, canopy shapes are shown as both a constructed cross-section and as a profile outline when fully inflated. Numerical expressions are given which either relate basic gore dimensions to canopy surface geometry, indicate shape factors or note preferred line length ratios. Illustrations, for purposes of scale, show suspension line effective length, l_e, equal to the nominal diameter, D_o.

Specific reference data are listed in tabular form representing operating examples of parachute types described. Designations are noted for standard military designs. Parachute size is given as a diameter, D_o, in feet. The number of gores, length of lines, material used, and parachute weight further define the parachute. Canopy and line materials are identified by fiber and textile weight or strength values. More complete information may be found in the materials' tables of Chapter 4. Parachute weight values may be assumed to include only suspension lines extending to the confluence point. The recoverable payload is identified and values are listed for payload weight, maximum deployment velocity, rate of descent and any special conditions which apply to use of the parachute. Rate of descent is given at sea level equivalent, and maximum deployment velocity in knots, indicated air speed (KIAS).

In comparing one parachute type with another, relative features are based on canopies of equal nominal area, S_o.

Solid Cloth Parachutes

Flat Circular. The canopy is a regular polygon of N sides, constructed as a flat surface with a central vent. It's design is the basis for most circular parachutes, other types being variations in gore pattern and general geometry. Flat circular parachutes are simple and economical to construct, handle and inspect, and are often used in clusters. They are in wide use for personnel and airdrop applications. This parachute is very reliable. Data for several specific flat circular parachute and load configurations are listed below for drag coefficient increase and improved inflation characteristics.

$$h_s = \left[\frac{S_o}{N \tan (180°/N)}\right]^{1/2}$$

$$e_s = 2h_s \tan (180°/N)$$

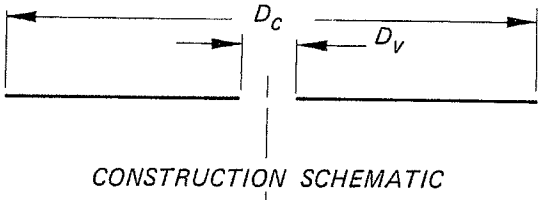
Generally :

$$S_v < 0.01\ S_o$$

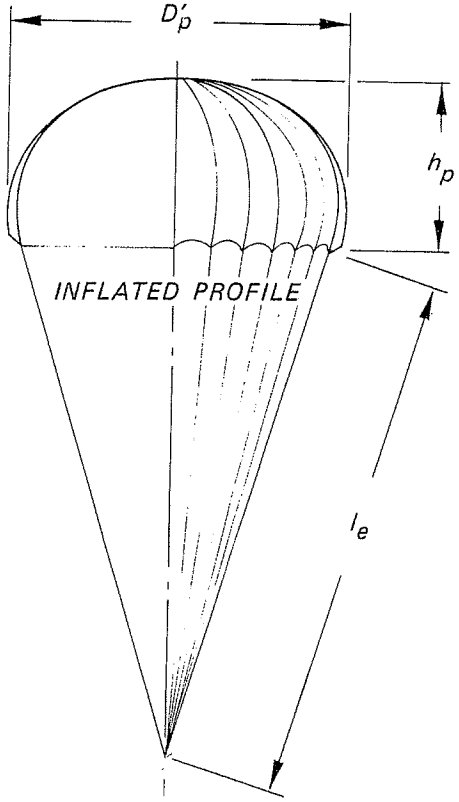
$$\frac{l_e}{D_o} \approx 0.80 \text{ to } 1.25$$

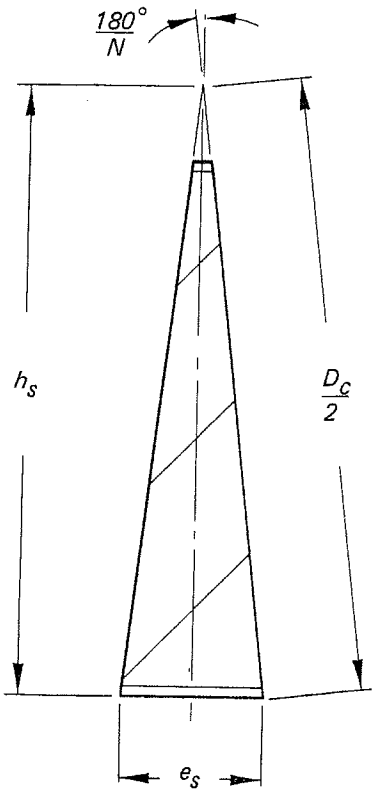
$$\frac{D'_p}{D_o} \approx 0.67$$

$$\frac{h_p}{D'_p} \approx 0.41$$



CONSTRUCTION SCHEMATIC

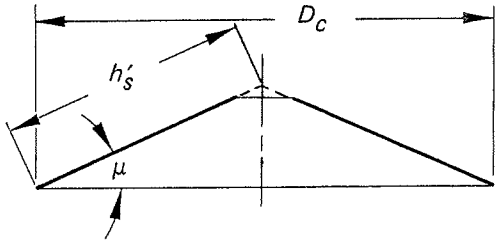




GORE LAYOUT

Designation and Size D_o, ft	Canopy (nylon) oz/yd²	No. of Gores N	Line Str. (nylon) lbs	Line Length l_e/D_o	Parachute Weight lbs	Payload	Payload Weight lbs	Max. Deploy. Velocity	Rate of Descent fps	Special Conditions	Ref.
C-9 28	1.1	28	550	.82	11.3	Personnel	200	275 kts	20.0		
G-12 64	2.25	64	1000	.80	130	Cargo	2,200	200 kts	28.0		204
G-11A 100	1.6	120	550	.80	215	Cargo	3,500	150 kts	25.0	Reefed	204
135	1.6	160	550	1.25	460	Cargo	50,000	150 kts	22.0	Cluster of 6	194

Conical. The canopy is constructed as the surface of a regular pyramid of N sides and base angle, μ, by joining gores having a vertex angle, β, less than $360^\circ/N$. It s design is a minor variation of the flat circular canopy. The conical parachute is as simple and economical to construct, handle and inspect as the flat circular and serves similar applications. As a result of drop tests with models conducted in 1949, conical parachutes with up to 30° cone angles showed approximately ten percent higher drag than solid flat parachutes of the same surface area. Subsequent full scale tests using 28 ft and 32 ft diameter parachutes confirmed these results. Data for specific conical parachute and load configurations are listed below.



CONSTRUCTION SCHEMATIC

$$\beta = 2 \sin^{-1}\left[\left(\sin \frac{180^\circ}{N}\right) \cos \mu\right]$$

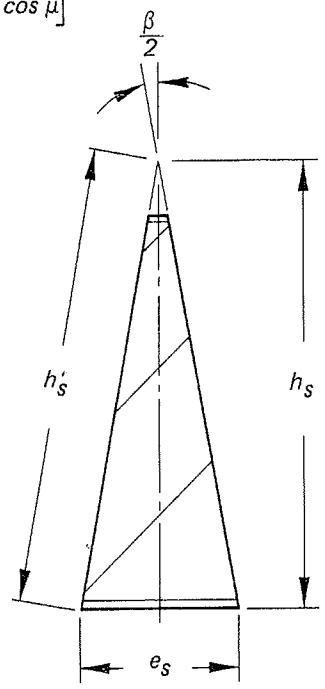
$$h_s = \left[\frac{S_o}{N \tan \beta/2}\right]^{1/2}$$

$$e_s = 2 h_s \tan \beta/2$$

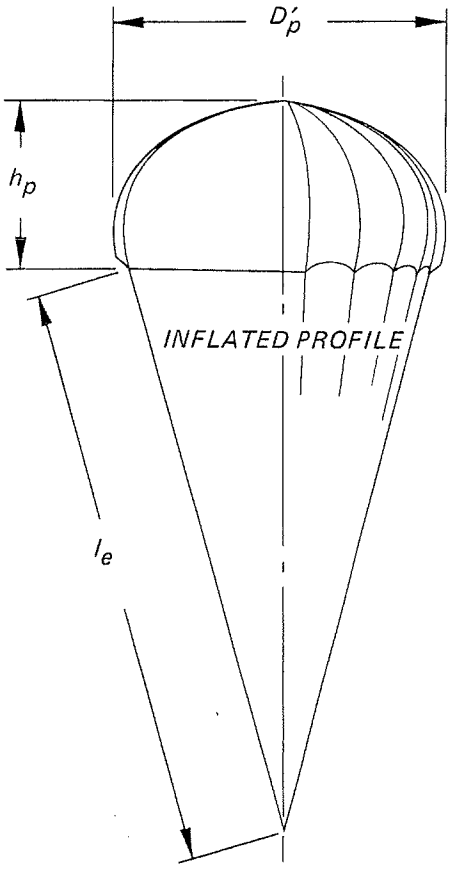
Generally :

$$S_v < 0.01\ S_o$$

$$\frac{l_e}{D_o} = 0.80 \text{ to } 1.2$$

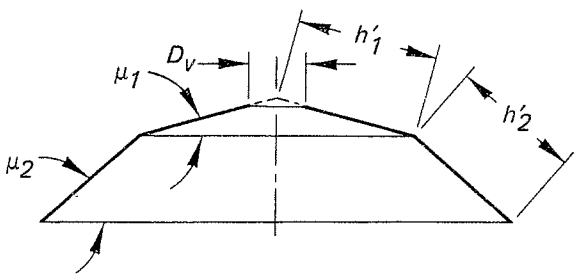


GORE LAYOUT

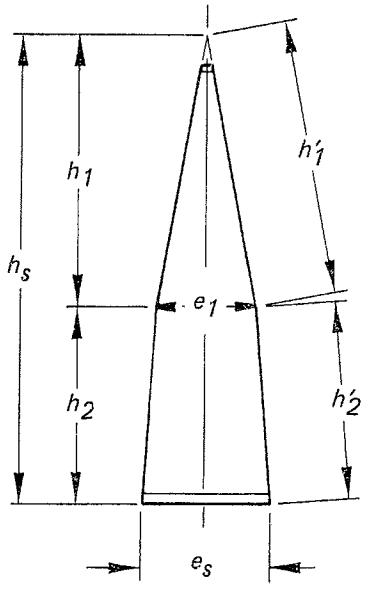


Size D_o, ft	Cone Angle μ	Canopy (nylon) oz/yd^2	No. of Gores N	Line Str. (nylon) lbs	Line Length l_e/D_o	Parachute Weight lbs	Payload	Payload Weight lbs	Max. Deploy. Velocity	Rate of Descent fps	Special Conditions	Ref.
26	25°	1.1	24	550	.8	8.1	Personnel	200	275 kts	19.5		49
67	25°	1.1 2.25	60	750	1.2	86	Missile	1800	200 kts	20.0	Reefed	205
95	25°	1.6 2.25	108	550	1.0	163	Missile	3500	275 kts	22.0	Reefed	206

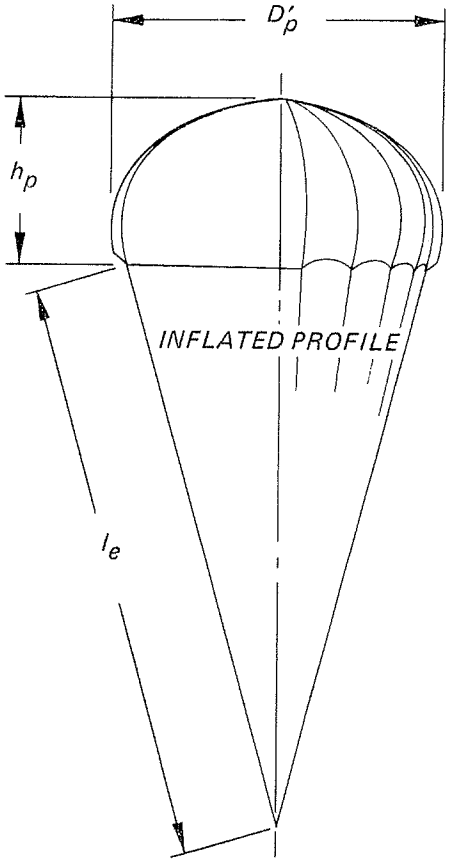
Bi-Conical. The canopy is constructed as the surface of a regular pyramid and a pyramid frustum of *N* sides by joining gores of a shape illustrated. It's design is a variation of the conical canopy. The bi-conical parachute is reasonably simple and economical to construct. It serves applications which are typical for flat circular parachutes with better stability and drag performance. Data for specific bi-conical parachute and load configurations are listed below. Both examples were constructed with the skirt at 90°, approaching an extended skirt profile.



CONSTRUCTION SCHEMATIC

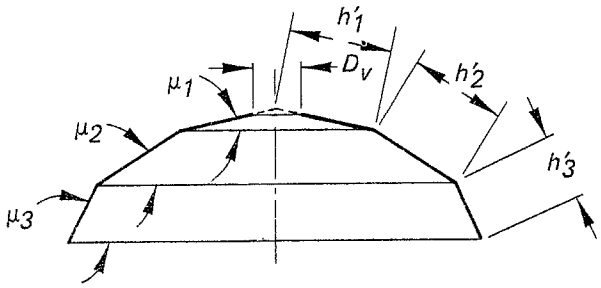


GORE LAYOUT

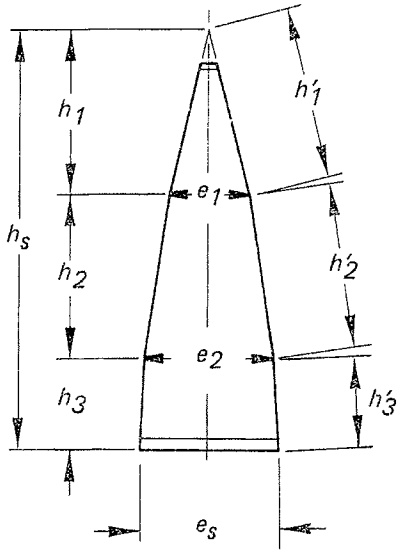


Size	Cone Angles		Canopy (nylon)	No. of Gores	Line Str. (nylon)	Line Length	Parachute Weight	Payload	Payload Weight	Max. Deploy. Velocity	Rate of Descent	User
D_o,ft	μ_1	μ_2	oz/yd^2	*N*	lbs	l_e/D_o	lbs		lbs		fps	
28	25°	90°	1.1 2.25	24	400	.95	9.9	Nose Cone	275	300 kts	20.0	(Nike)
36.4	25°	90°	1.1	30	375	.95	15.9	Personnel	300	200 kts	16.2	US Army

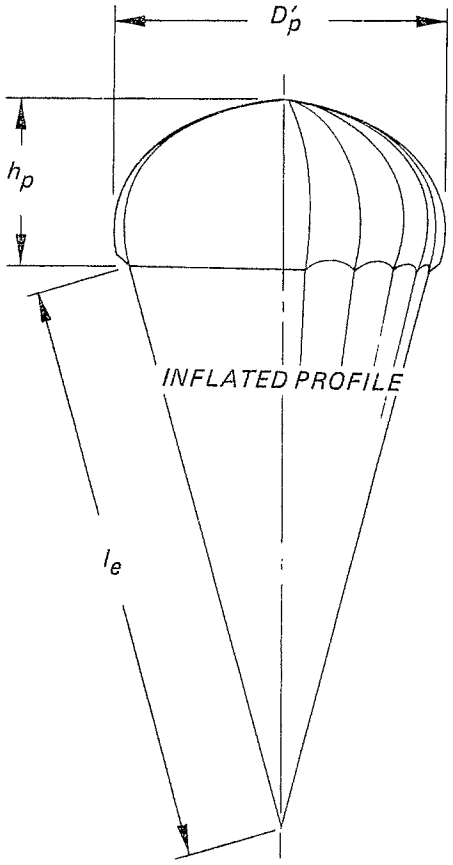
Tri-Conical. The canopy is constructed as a regular pyramid and two frustums of N sides by joining gores of a shape illustrated. The tri-conical parachute is reasonably simple and economical to construct. It serves applications which are typical for flat circular parachutes with better stability and drag performance. Data for specific tri-conical parachute and load configurations are listed below. These were developed as main descent parachutes for mid-air retrieval systems used in conjunction with a trailing engagement parachute.



CONSTRUCTION SCHEMATIC

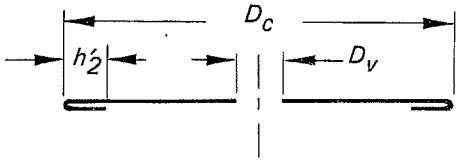


GORE LAYOUT

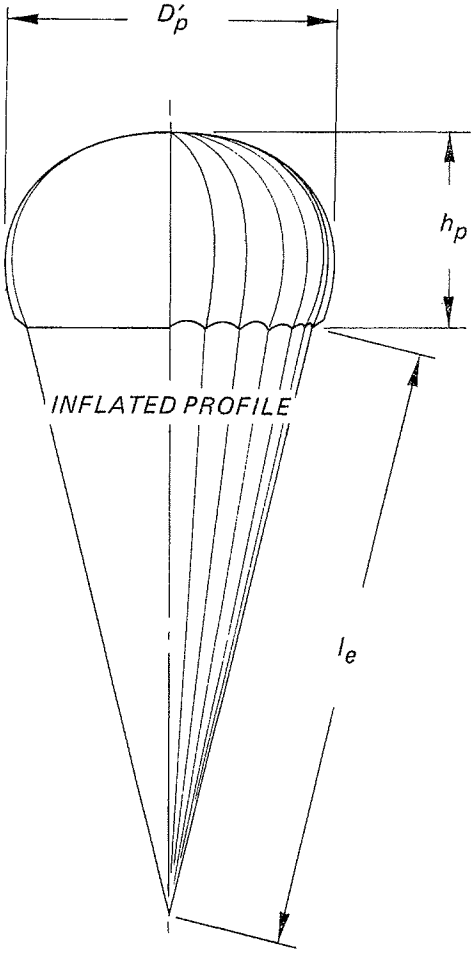


Size D_o,ft	Cone Angles μ	Canopy (nylon) oz/yd^2	No. of Gores N	Line Str. (nylon) lbs	Line Length l_e/D_o	Parachute Weight lbs	Payload	Payload Weight lbs	Max. Deploy. Velocity	Rate of Descent fps	Special Conditions	Ref.
79.6	N/A	1.1 2.25	64	350	.83	71.3	RPVs	1800	125 kts	21	Reefed	
100	N/A	1.1 2.25	88	400	.95	117	RPVs	2500	190 kts	21	Reefed	

Flat Extended Skirt. The canopy is characterized by a flat polygonal surface to which is added an extension in the form of an annular flat ring of a width designated as a percent of the flat surface diameter as illustrated by the construction schematic. The flat extension is achieved by shaping the gore as indicated. A 10 percent extension has proven a common choice, although 12.5 and 14 percent extensions have been tried. Flat extended skirt canopies are more complex to design, but with proper patterns they are no more complicated to form and assemble than the flat circular. Extended skirt parachutes have slightly higher drag, longer filling times and lower opening forces than flat circular parachutes of identical S_o. Data for specific flat extended skirt parachute and load configurations are listed below.



CONSTRUCTION SCHEMATIC



For 10% Extension:

$h'_2 = 0.1\ D_c$ *(by definition)*

$$h_1 = .858 \left[\frac{S_o}{\tan (180^\circ/N)}\right]^{1/2}$$

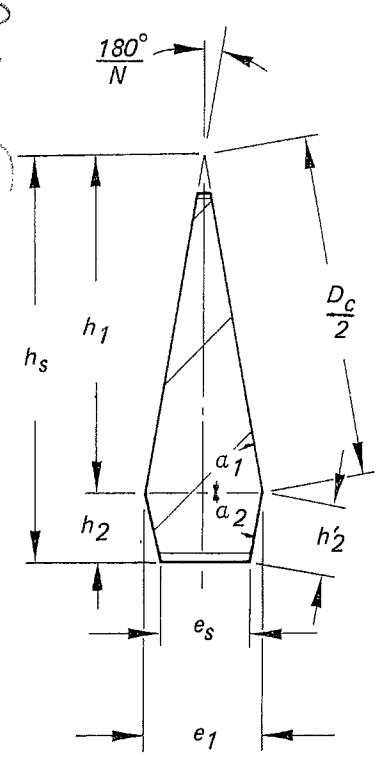
$h_2 = 0.2\ h_1$

$a_1 = a_2 = 90^\circ - (180^\circ/N)$

$e_1 = 2\ h_1 \tan (180^\circ/N)$

$e_s = 0.8\ e_1$

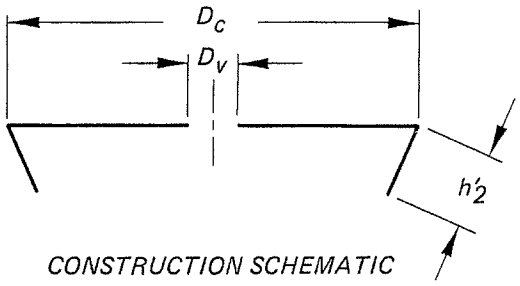
$l_e/D_o = 0.84$ *to* 1.0



GORE LAYOUT

Designation and Size D_o, ft	Canopy (nylon) oz/yd²	No. of Gores N	Line Str. (nylon) lbs	Line Length l_e/D_o	Parachute Weight lbs	Payload	Payload Weight lbs	Max. Deploy. Velocity	Rate of Descent fps	Remarks	Ref.
T-10 35	1.1	30	375	.84	13.85	Paratroops	200	300 kts	16		
34.5	1.1 2.25	36	750	.85	20.50	Capsule Seat	700	490 kts	28	Reefed (B-70)	1

Full Extended Skirt. The canopy is characterized by a flat polygonal surface to which an added extension takes the constructed form of an inverted pyramid frustum having the same convergence angle as the suspension lines. The full extension is achieved by shaping the gore as shown. An extended length which is 14.3 percent of the flat surface diameter has proven an effective and common choice. These canopies are sufficiently reliable for airdrop and drone recovery applications. Data for specific full extended skirt parachute and load configurations are given below.



CONSTRUCTION SCHEMATIC

For 14.3% Extension :

$h'_2 = 0.143\ D_c$ *(by definition)*

$h_1 = 0.5\ D_c \cos\ (180°/N)$

$e_1 = D_c \sin\ (180°/N)$

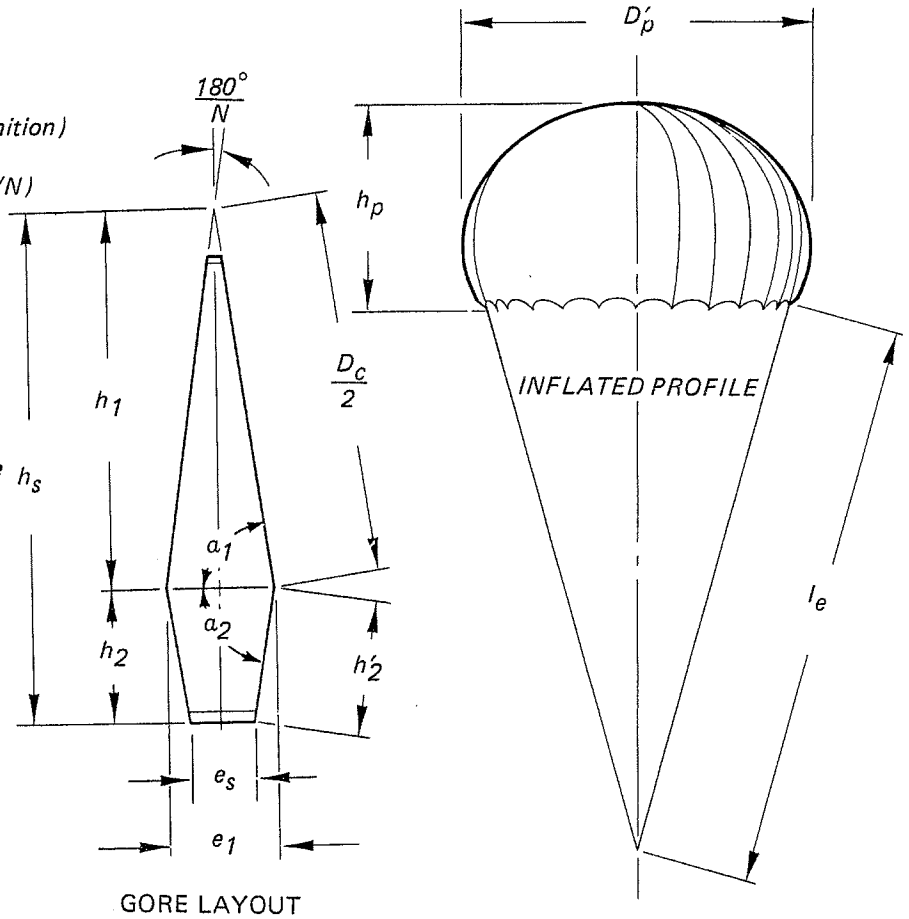
$e_s = e_1 l_e/(l_e + 0.143\ D_c)$

$a_1 = 90 - 180°/N$

$a_2 = 90 - \phi_l/2$

ϕ_l = *line convergence angle*

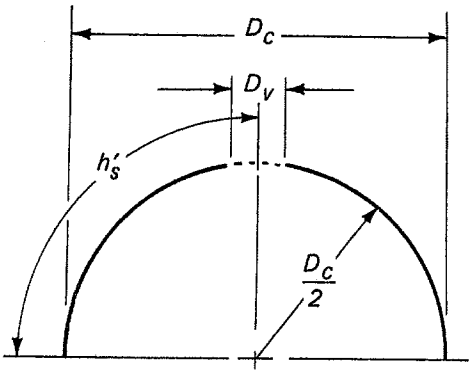
$\frac{l_e}{D_o}$ = *0.85 to 1.0*



GORE LAYOUT

Size D_o, ft	Canopy (nylon) oz/yd^2	No. of Gores N	Line Str. (nylon) lbs	Line Length l_e/D_o	Parachute Weight lbs	Payload	Payload Weight lbs	Max. Deploy. Velocity	Rate of Descent fps	Special Conditions	Ref.
30	1.1 2.25	24	650	.95	12.46	Drone	400	300 kts	23.0	MQM-74C	N/A
67.3	1.1 2.25	52	550	.92	62.0	Drone	1800	275 kts	22.0	Reefed	208
78	1.1 2.25	64	400	.95	64.5	Drone	4800	225 kts	23.5	Reefed	1

Hemispherical. The constructed shape of this canopy is a hemispherical surface. The gore is designed so that the flat width dimension is the horizontal arc distance between radial seamlines. The inflated shape approaches the constructed profile under load. The hemispherical parachute is more stable than the flat circular type and is used primarily for airdrop of supplies. Data for a specific hemispherical parachute and load configuration are given below. The G-13 has been produced in quantity using cotton and rayon fabrics, with rayon suspension lines.



CONSTRUCTION SCHEMATIC

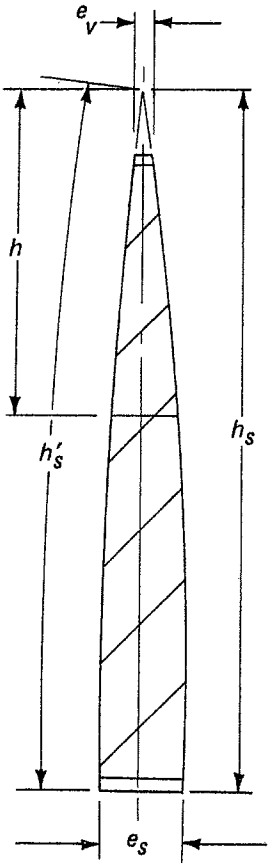
$D_c = (2 S_o / \pi)^{1/2}$

$h'_s = \pi D_c / 4$

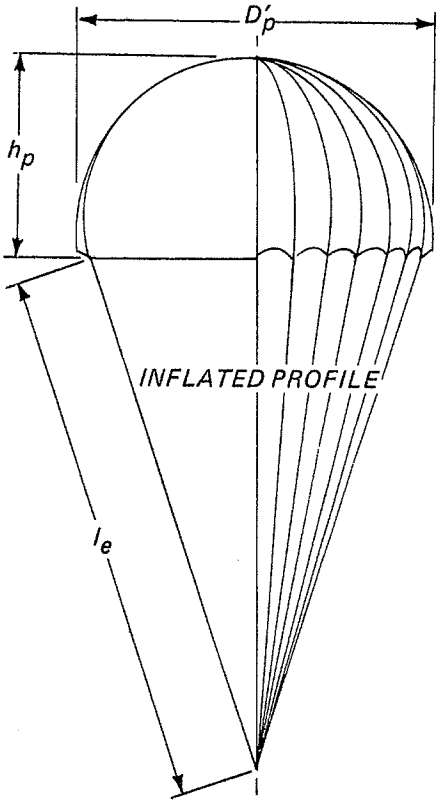
$e_s = \pi D_c / N$

$h_s \approx h'_s$

$\frac{l_e}{D_o} = 1.0$



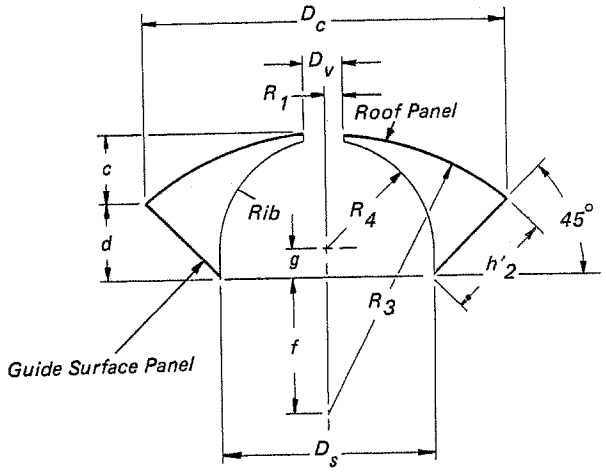
GORE LAYOUT



INFLATED PROFILE

Designation and Size D_o, ft	Canopy (rayon) oz/yd²	No. of Gores N	Line Str. (rayon) lbs	Line Length l_e/D_o	Parachute Weight lbs	Payload	Payload Weight lbs	Max. Deploy. Velocity	Rate of Descent fps	Remarks	Ref.
G-13 32.4	4.25	20	400	.93	40	Cargo	500	150 kts	29		99

Guide Surface, Ribbed. The canopy is constructed with a slightly rounded crown or roof, and an inverted conical front or "guide surface" extending from roof edge to skirt hem. Ribs, placed between gores in a plane with the suspension lines, help to maintain the constructed profile during operation. The guide surface parachute was specifically developed as a stabilization device for bombs, mines, torpedoes and similar bodies. Its good stability comes from the abrupt flow separation edge of its largest diameter and the guide surface slope of the skirt. Low porosity cloth is used in the roof and guide surfaces to promote fast inflation and to help maintain its characteristic shape. The ribbed guide surface parachute is reliable and very stable. However, it has a low drag coefficient and is difficult to manufacture. Data are given below for 12-gore and 16-gore ribbed guide surface parachutes 6.5 ft in diameter, behind a rocket propelled sled test vehicle.



CONSTRUCTION SCHEMATIC

$D_p \approx 0.95\ D_c$

$D_v = 0.10\ D_c$

$D_s = 0.60\ D_c$

$h'_1 = 0.55\ D_c$

$h'_2 = 0.28\ D_c$

$e_1 = 1.2\pi D_c/N$

$e_s = 0.6\pi D_c/N$

$l_e \approx 1.33\ D_c$

$R_1 = 0.05\ D_c$

$R_2 = 2.5\ D_c/N$

$R_3 = 0.75\ D_c$

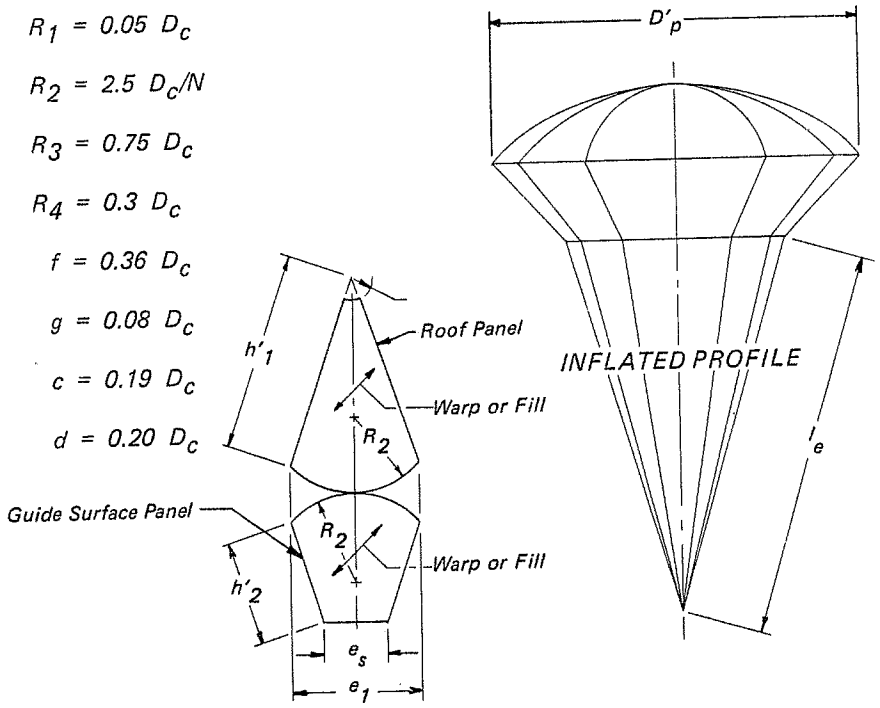
$R_4 = 0.3\ D_c$

$f = 0.36\ D_c$

$g = 0.08\ D_c$

$c = 0.19\ D_c$

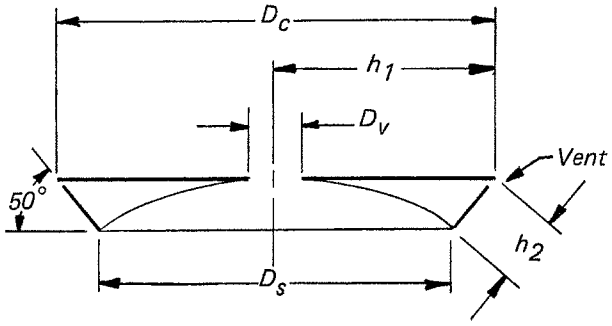
$d = 0.20\ D_c$



GORE LAYOUT

Size D_c, ft	Canopy (nylon) oz/yd^2	No. of Gores N	Line Str. (nylon) lbs	Line Length ft	Suspended Load lbs	Max. Deploy. Velocity	Remarks	Ref.
6.5	7	12	2250	8.65	Inf. Mass	405 kts	Sled Test	209
6.5	14	16	9000	8.65	Inf. Mass	600 kts	Sled Test	209

Guide Surface, Ribless. In the ribless guide surface canopy, the desired shape is obtained by modifying the gore outline. The roof panel is widened to extend around the edge of the guide surface panel to the skirt edge, eliminating the rib. The resulting flow-separation edge is less abrupt, accounting for a slightly higher oscillation angle than the ribbed version. A slit vent at the outer edge of each guide surface panel also helps to promote flow separation. Construction is simplified by avoiding the rib. Dimensions for roof and guide surface panels depend upon diameter and the number of gores in the canopy. A key to pattern outlines is given on the opposite page. Data for specific ribless guide surface parachute and load configurations are listed below.



CONSTRUCTION SCHEMATIC

$D_p' \approx .95\ D_c$

$D_s = .7\ D_c$

$h_1 = .5\ D_c$

$h_1 = .6\ D_c$ *(6 panel design only)*

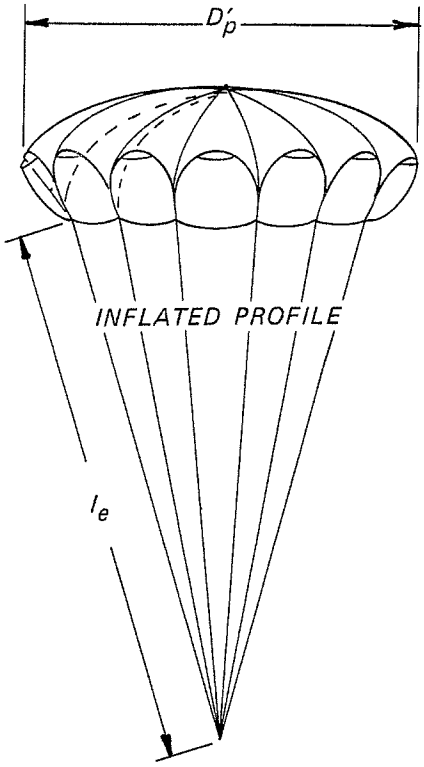
$h_2 = .23\ D_c$

$h_2 = .27\ D_c$ *(6 panel design only)*

$e_1 = .10\ D_c$

$l_e \approx 1.33\ D_c$

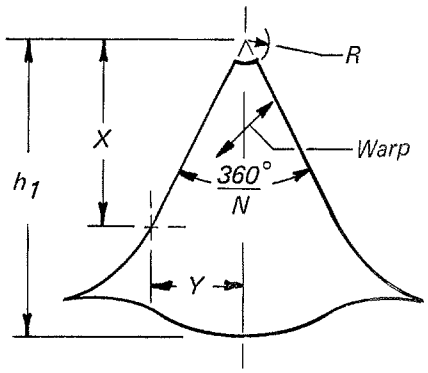
$D_v = .10\ D_c$ *to* $.15\ D_c$ *(varies with number of panels)*



Size D_c, ft	Canopy (nylon) oz/yd^2	No. of Gores N	Line Str. (nylon) lbs	Line Length ft	Parachute Weight lbs	Payload	Payload Weight lbs	Max. Deploy. Velocity	Remarks	Ref.
4.81	2.25	12	750	9.3	4.5	Ordnance	132	500 kts	Ordnance	210
6.5	14.00	16	4000	8.65	N/A		Inf. Mass	720 kts	Sled Test	209

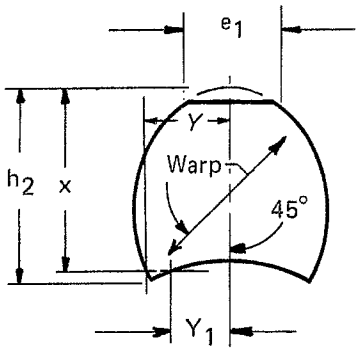
ROOF PATTERN

Panels	6	8	10	12	14	16	20
X/h_1	Y/X	Y/X	Y/X	Y/X	Y/X	Y/X	Y/X
.10	.605	.532	.465	.394	.346	.303	.260
.15	.605	.520	.464	.394	.344	.3045	.257
.20	.605	.516	.461	.394	.348	.305	.258
.30	.605	.514	.462	.407	.352	.307	.259
.40	.605	.511	.459	.410	.354	.311	.263
.50	.605	.511	.463	.416	.362	.317	.275
.60	.605	.509	.469	.428	.378	.336	.294
.70	.613	.525	.481	.441	.403	.366	.328
.80	.676	.588	.545	.495	.464	.434	.402
.832	.725						
.866		.713					
.875			.696	.676			
.882					.652		
.888						.622	
.896							.590
.90	.428	.496	.512	.527	.538	.554	.569
.95	.280	.261	.261	.261	.261	.261	.261
.975	.193	.1625	.1625	.1625	.1625	.1625	.1625
1.0	0	0	0	0	0	0	0

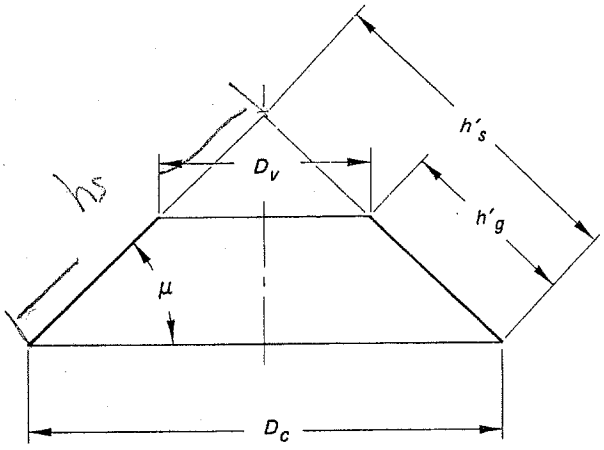


GUIDE SURFACE PATTERN

Panels	6	8	10	12	14	16	20
X/h_2	Y/X	Y/X	Y/X	Y/X	Y/X	Y/X	Y/X
.05	5.56	5.52	4.83	4.33	4.12	3.85	3.535
.10	3.85	3.81	3.52	3.21	3.01	2.77	2.42
.15	3.08	2.96	2.76	2.58	2.37	2.18	1.90
.20	2.54	2.43	2.285	2.13	1.975	1.82	1.605
.30	1.93	1.80	1.69	1.58	1.48	1.37	1.215
.40	1.56	1.42	1.335	1.25	1.18	1.075	.953
.50	1.314	1.17	1.10	1.03	.965	.882	.772
.60	1.138	.977	.919	.86	.80	.729	.636
.70	1.01	.823	.769	.722	.672	.615	.528
.80	.89	.705	.655	.61	.568	.517	.440
.885	.808 .000						
.90	.796 .278	.603	.558	.515	.472	.43	.3665
.919		.586 .000					
.922			.540 .000				
.93				.491 .000			
.937					.442 .000		
.944						.397 .000	
.95	.757 .613	.559 .305	.515 .261	.472 .226	.432 .161	.394 .0896	.334
.954							.328 .000
1.0	.72	.517	.474	.430	.393	.358	.3025



Annular. The canopy is constructed as the surface of a regular pyramid frustum of N sides and base angle, μ, in the same manner defined for a conical canopy. Although designed as a conical surface, the Annular canopy is otherwise similar to the Airfoil designed circa 1947 as a portion of a sphere. These parachutes differ from other parachutes by the nature of their large central opening and the addition of interior suspension lines. The annular parachute has a higher drag coefficient than most solid material types, but the maximum deployment speed at which little or no damage occurs is lower. Two sets of suspension lines complicate construction and rigging. Data from tests of specific parachute and load configurations are listed below. These parachutes were tested in combination with a ringsail engagement parachute for general mid-air retrieval applications.



CONSTRUCTION SCHEMATIC

$$h_s = \frac{D_c}{2\cos\mu}$$

$$h_g = \frac{2\,S_o}{N\,(e_s + e_v)}$$

$$\beta = 2\sin^{-1}\left[\left(\sin\frac{180^\circ}{N}\right)\cos\mu\right]$$

$$h_s = \left[\frac{S_o}{N\tan\beta/2}\right]^{1/2}$$

$$e_s = 2\,h_s\tan\beta/2$$

$$\frac{D_v}{D_c} = 0.5 \text{ to } 0.8$$

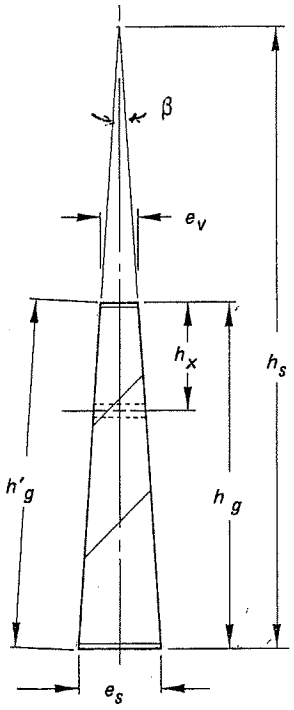
$$(l_a - l_b)/h'_g = 0.40$$

$$l_b/h'_g = 0.66 \text{ to } 0.75$$

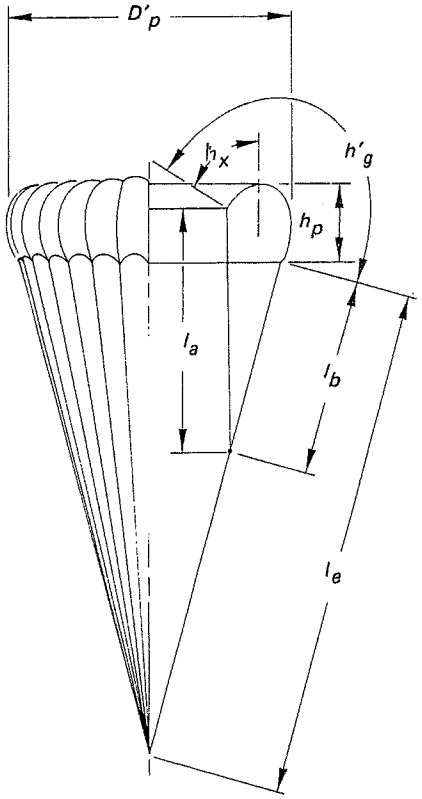
$$h_x = 0.5\,(l_a + l_b + h_g) - l_a$$

(h_x locates pressure relief vent when needed)

The large central opening is not included in the determination of S_o.



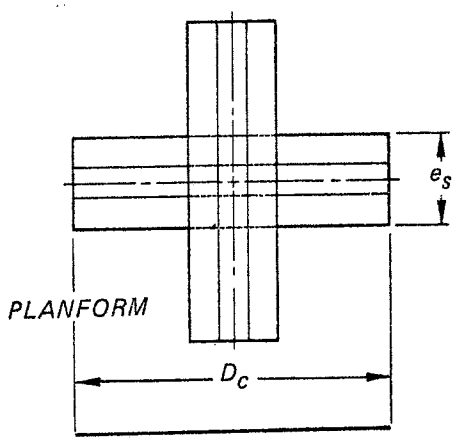
GORE LAYOUT



INFLATED PROFILE

Size D_o, ft	Canopy (nylon) oz/yd^2	Cone Angle μ	No. of Gores N	Line Str. (nylon) lbs	Line Length l_e/D_o	Parachute Weight lbs	Payload Weight lbs	Max. Deploy. Velocity	Rate of Descent fps	Application	Ref.
42	1.1	45°	44	400	1.25	39	870	124 kts	23.9	Systems for mid-air retrieval	184
64	1.1	45°	60	400	1.25	81.3	2000	171 kts	22.4		184

Cross. The cross parachute, a French development, is finding increased use for deceleration in applications that require good stability and low cost. The design is simple. The canopy consists of two identical cloth rectangles, crossed and joined to each other at the square intersection to form a flat surface having four equal arms. Suspension lines are attached to the outer edges of four arms. Some versions employ tie cords between corners of adjacent arms. The Cross parachute is similar in stability performance and drag efficiency to the ringslot parachute, but it has a tendency to rotate. It is popular as a deceleration parachute for ground vehicles (dragsters). Recent applications include stabilization and deceleration of air dropped naval weapons [53,211] and low rate of descent high altitude probe experiments.



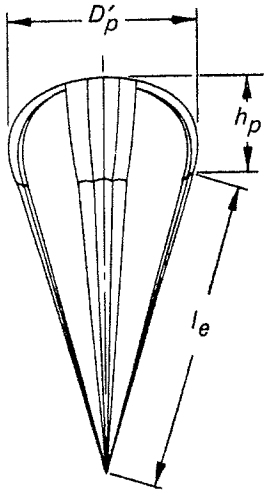
CONSTRUCTION SCHEMATIC

$$S_o = 2 D_c e_s - e_s^2$$

Generally:

$$\frac{l_e}{D_o} = 1 \text{ to } 2$$

$$\frac{e_s}{D_c} = 0.263 \text{ to } 0.333$$



INFLATED PROFILE

Size D_o, ft	Canopy (nylon) oz/yd²	Dimension D_c ft	e_s ft	Line Str. (nylon) lbs	No. of Lines Z	Line Length l_e/D_o	Parachute Weight lbs	Payload	Vehicle Weight lbs	Max Deploy. Velocity	Rate of Descent fps	Application	Ref.
54.3	0.3 silk	63	16	100	28	1.16	17.5	Inst. Package	120	564 kts	8.0	Hi Alt Probe	210
9.8	7.0 nylon	14	3	4000	16	1.78	7.0	(Dragster)	3000	300 mph	N/A	Ground Deceleration	

Supersonic-X. The canopy is constructed as a continuous surface of revolution with a minimum of drag producing discontinuities. When operating at design conditions, it simulates a divergent-convergent inlet in subcritical operation within a predictable freestream supersonic flow field. Models of this parachute have been tested[212] in the Mach number range from 1.75 to 8.0. Performance in a drogue application may be characterized by good inflation, excellent oscillatory stability, average drag, fair inflation stability and poor shock wave stability. Performance is discussed in Chapter 6. The exit area is not included in S_o.

$D_{ex} = .3\ D_c$

$D_{in} = .8\ D_c$

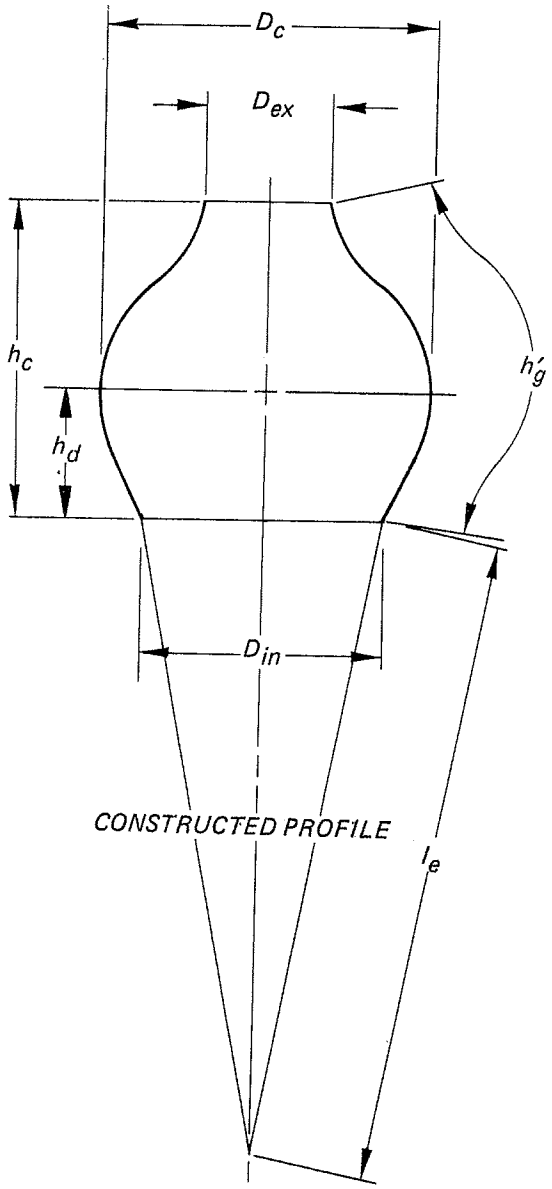
$l_e = 2\ D_c$

$h_g = .9538\ D_c$

$e_{max} = \pi\ D_c/N$

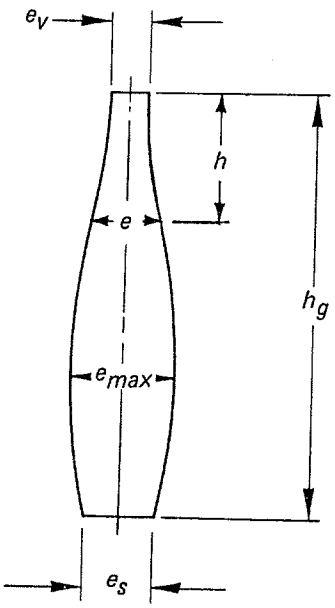
$h_c = .775\ D_c$

$h_d = .3375\ D_c$



Gore Coordinates:

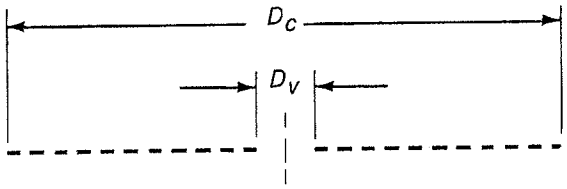
$\frac{h}{h_g}$	$\frac{e}{e_{max}}$
0	.230
.056	.317
.109	.367
.214	.527
.319	.703
.423	.856
.528	.955
.633	.997
.685	.997
.790	.947
.895	.875
1.00	.798



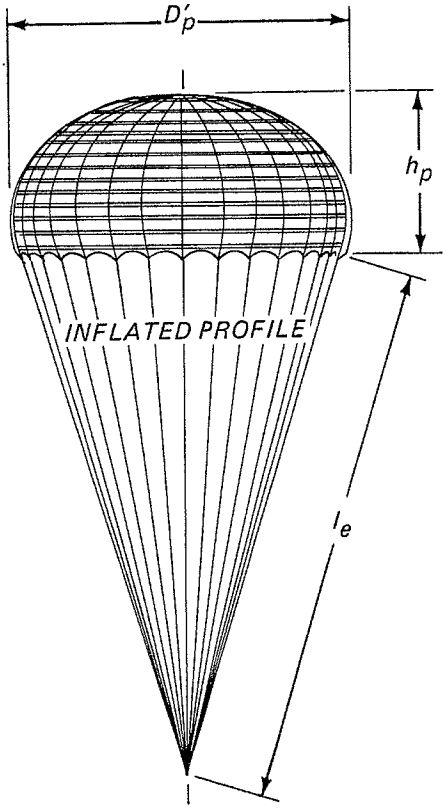
GORE LAYOUT

Slotted Canopy Parachutes

Flat Circular Ribbon. The canopy is a flat circular design and consists of concentric ribbons, usually two inches in width, supported by smaller horizontally spaced tapes and radial ribbons at gore edges. Ribbons and tapes are accurately spaced to provide the desired ratio of open space to solid fabric over the entire canopy. Gores are triangular and dimensions are determined in the same manner as for the solid cloth flat circular parachute. The flat circular ribbon parachute has a lower drag efficiency than the solid cloth parachutes. However, its stability is excellent and the maximum opening force is low in comparison. The canopy is relatively slow in opening and its performance reliability depends on specific design parameters. Compared to solid cloth parachute canopies, the flat circular ribbon canopy is more difficult to manufacture. Data for specific flat circular ribbon parachute and load configurations are given below.



CONSTRUCTION SCHEMATIC



(A regular polygon of N sides)

$$h_s = \left[\frac{S_o}{N \tan (180^\circ/N)}\right]^{1/2}$$

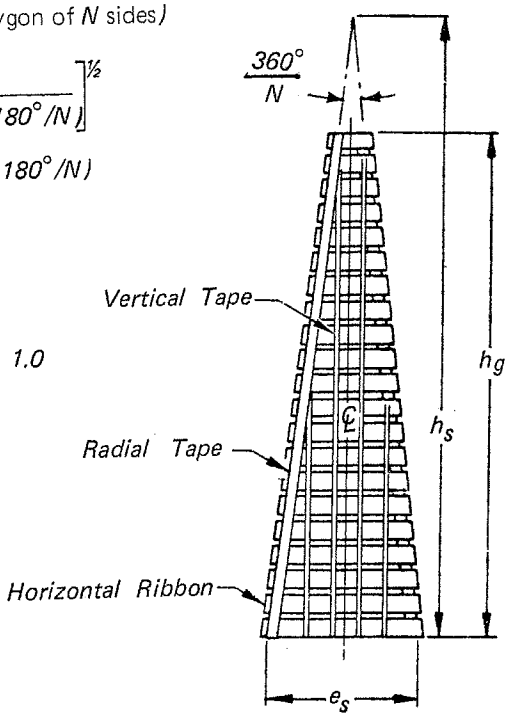
$$e_s = 2h_s \tan (180^\circ/N)$$

Generally:

$S_v < 0.01\ S_o$

$\frac{l_e}{D_o} \approx 0.85$ to 1.0

$\frac{D'_p}{D_o} \approx 0.67$

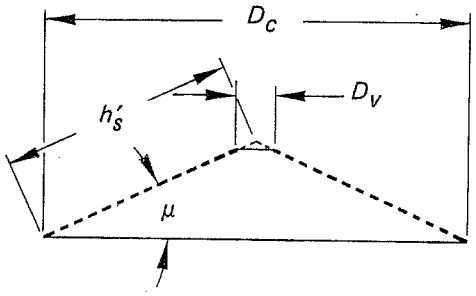


GORE LAYOUT

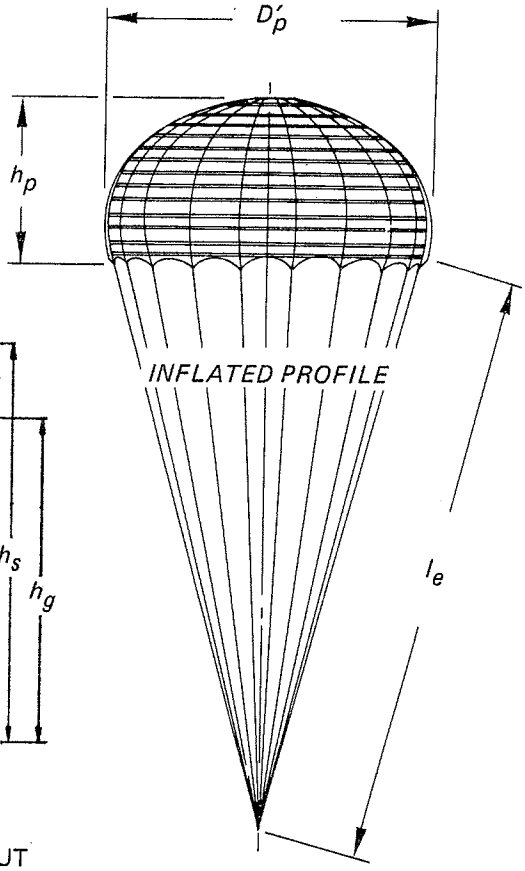
Size D_o, ft	*Ribbon (nylon)* lbs	No. of Gores *N*	Line Str. (nylon) lbs	Line Length l_e/D_o	Parachute Weight lbs	Vehicle Weight lbs	Max. Deploy. Velocity	Application	Remarks	Ref.
32	300	36	2250	1.0	60	160,000	160 kts	B-47 Brake	(obsolete)	
44	300	48	4000	1.0	108	320,000	180 kts	B-52 Brake	Reused	

Conical Ribbon. The constructed shape of this canopy is obtained in the same manner as that described for solid cloth conical parachutes. Gores, like the flat circular ribbon design, are composed of a grid of horizontal ribbons spaced and retained at close intervals by narrow vertical tapes. Radial tapes which extend from the vent to the skirt are sewn together in the joining of adjacent gores.

The conical ribbon parachute shows higher drag than the flat circular ribbon just as the solid cloth conical parachute does over the solid flat parachute of equal area. Data for several specific conical ribbon parachute and load configurations are listed below.



CONSTRUCTION SCHEMATIC



Varied Porosity. Unlike other parachutes of the conical ribbon classification, the gore of the 14.2 ft diameter drogue parachute in the table below is constructed with geometric porosity varied in three levels, increasing from vent to skirt, e.g., the upper one-third of the gore uses closer spacing and the lower one-third, a wider ribbon spacing than the center section. With this parachute, a drag coefficient, $C_{D_o} = 0.64$, was obtained in wind tunnel tests without loss of stability. However, the opening load factor increased (see Table 2.2).

$$h_s = \left[\frac{S_o}{N \tan \beta/2}\right]^{1/2}$$

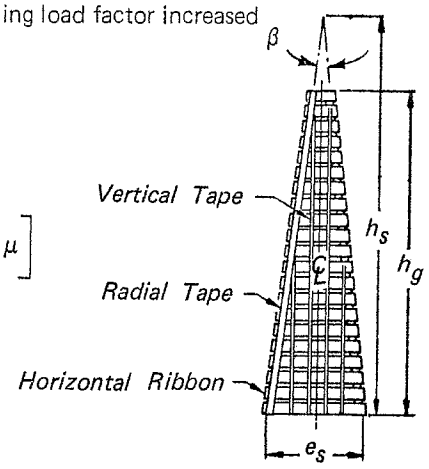
$$e_s = 2 h_s \tan \beta/2$$

$$\beta = 2 \sin^{-1} \left[\left(\sin \frac{180^\circ}{N}\right) \cos \mu\right]$$

Generally:

$$S_v < 0.01\ S_o$$

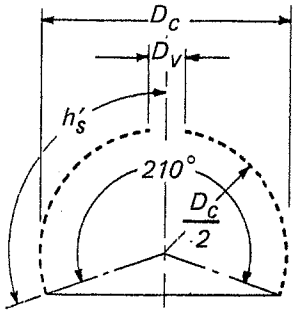
$$\frac{l_e}{D_o} = 1.00 \text{ to } 2.0$$



GORE LAYOUT

Size D_o, ft	Cone Angle μ	Ribbon (nylon) lbs	No. of Gores N	Geom. Porosity λ_g, %	Line Str. (nylon) lbs	Line Length l_e/D_o	Parachute Weight lbs	Payload	Payload Weight lbs	Max. Deploy. Cond.	Rate of Descent fps	Special Cond.	Ref.
16.5	25°	300	20	26.5	2000	2.0	25.2	Apollo	13,000	204 psf	310	Drogue	27
115	20°	1000 400	96	16	6000	1.7	1400	Booster	164,000	200 psf	85	Cluster of 3	
17.0	20°	3000 2000	24	25	10000	1.0	76	Ordnance	715	800 kts	71		
14.2	20°	2000 1500 1000	32	10/14/17	6000	2.0	75	B-1 Capsule	8700	1.6 M 1600 psf		Drogue	213

Hemisflo. The constructed shape of this canopy is a spherical surface which continues 15 degrees past a hemisphere at the skirt as shown. The canopy design retains effective drag and stability performance over the range from Mach 1.5 to 2.5, although conical ribbon parachutes are as good or better at speeds below Mach 1.5. Hemisflo parachutes are used almost exclusively for drogue applications which require stabilization and retardation at supersonic speeds. Data for specific configurations are given below. The 6.0 ft diameter drogue parachute in the table, is used with the F-111 crew capsule.



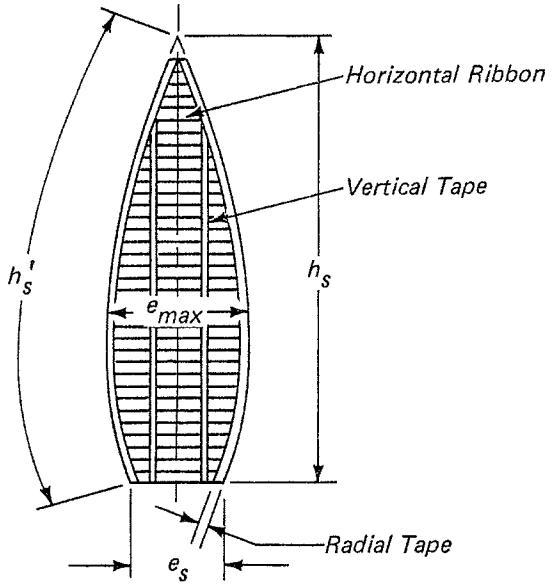
CONSTRUCTION SCHEMATIC

$$D_c = \left[\frac{360\, S_o}{210\, \pi}\right]^{1/2}$$

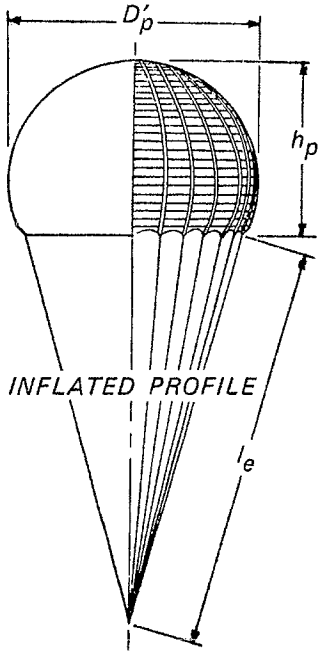
$$e_{max} = \pi D_c / N$$

$$h'_s = 0.9163\ D_c$$

$$\frac{l_e}{D_o} = 2.0$$



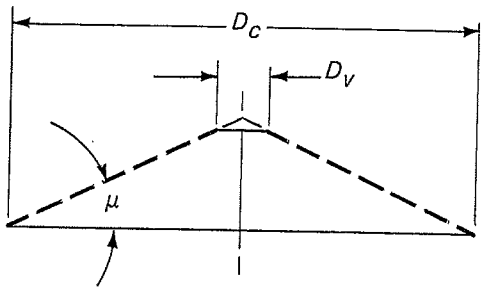
GORE LAYOUT



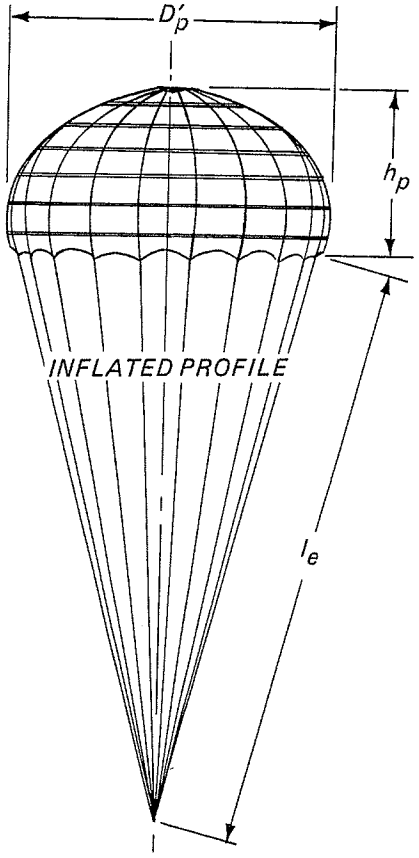
Size D_o, ft	Ribbon Str. (nylon) lbs	Geom. Porosity λ_g	No. of Gores N	Line Str. (nylon) lbs	Line Length l_e/D_o	Parachute Weight lbs	Application	Suspended Load lbs	Max. Deploy. Conditions	Special Conditions	Ref.
5.00	650	18%	16	1500	2.0	4.5	Eject. Seat	370	600 kts	(Mach 2.4)	60
6.0	500	15%	16	2400	2.0	3.4	Capsule	3400	500 kts	(Mach 2.2)	214
16	3000	14%	32	10000	2.0	130	Research	150,000	2900 psf	Reefed	215

Ringslot. This parachute exists in flat and conical designs. The canopy is constructed of wide concentric cloth strips with intervening slots in a manner similar to the assembly of ribbon designs. Fewer operations are required, simplifying manufacture and reducing cost compared with ribbon parachutes. For overall basic dimensions, see flat circular and conical parachute data.

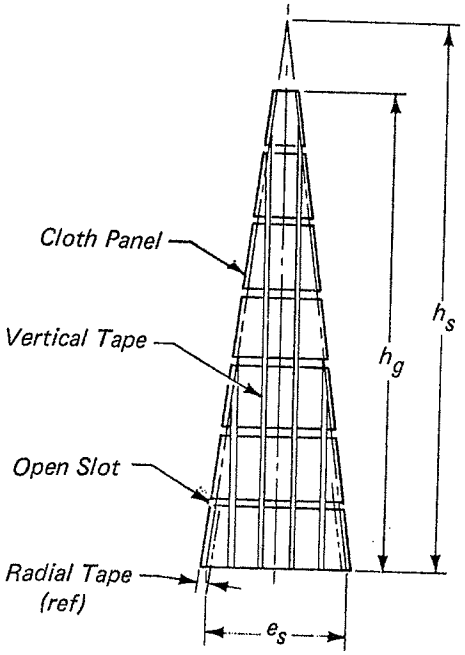
Performance characteristics are between those of the ribbon and solid cloth types. Ringslot parachutes are being used for aircraft landing deceleration, extraction of air drop equipment and final recovery parachutes. Opening reliability is comparable to ribbon parachutes. Data for specific ringslot parachutes are listed below.



CONSTRUCTED SCHEMATIC



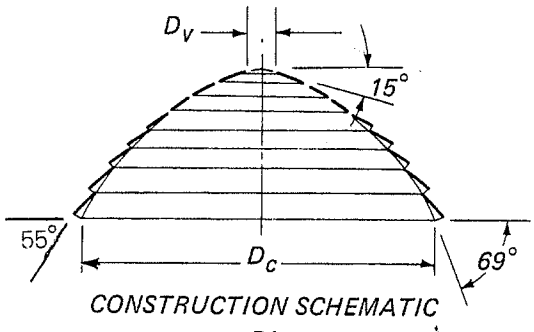
INFLATED PROFILE



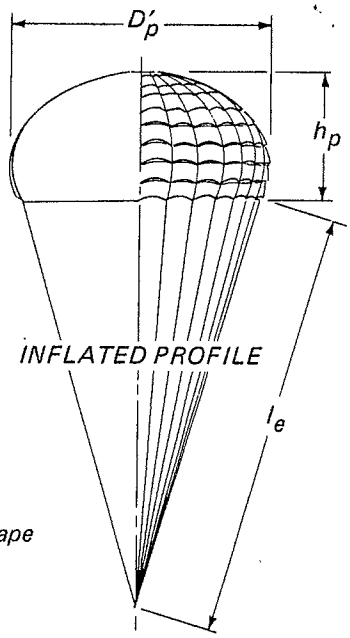
GORE LAYOUT

Size D_o, ft	Cone μ	Canopy (nylon) oz/yd^2	Geom. Porosity	No. of Gores N	Line Str. (nylon) lbs	Line Length l_e/D_o	Parachute Weight lbs	Application	Suspended Load lbs	Max. Deploy. Velocity	Remarks	Ref.
16	0°	2.25		20	1500	1.0	13.75	Landing Brake	Aircraft	200 kts	Reused	
28	20°	3.5		24	1500	1.0	47.0	Load Extraction	20,000	150 kts	Reused	121
24	20°	2.25		24	400	1.0	22.4	Tandem Engagement	2500	200 kts	Mid-air retrieval	216

Ringsail. This parachute design is complex and develops a unique shape from the combination of a curved basic profile and fullness at the leading edge of annular cloth rings. The constructed profile is a circular arc, tangent to a 15° cone at the apex and tangent to a 55° cone at the skirt edge. Earlier designs, including a personnel type known as Skysail and the Mercury main parachute, were based on a quarter-spherical profile. The ringsail canopy is constructed of wide concentric cloth strips, spaced apart in the upper crown with slots like the ringslot, but adjacent over the remainder of the canopy, obtaining geometric porosity through crescent-shaped slots resulting from the cloth dimension between radials being longer for the leading edge of each sail than the trailing edge of the sail below it. Geometric features including sail fullness, (f_1 = trailing edge and f_2 = leading edge fullness), are illustrated on this page. The determination of geometric porosity of crescent shaped slots is a complex process (see Reference 217) Data for several specific parachute and load configurations are listed below. The Apollo main parachute is a modification of the standard ringsail design, having 75 percent of the fifth (of 12) ring removed.



CONSTRUCTION SCHEMATIC



INFLATED PROFILE

$N = 0.76\ D_c$ to $0.88\ D_o$

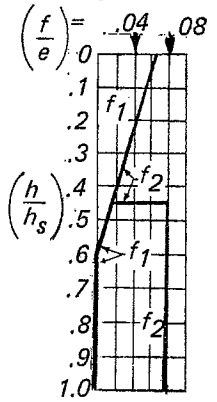
$e_s = 6.44\ (h_s/N)\ \sin 54°$

$h_s = 0.519\ D_o$

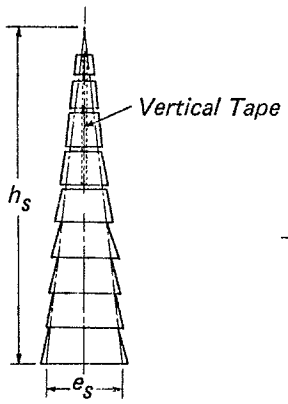
$\frac{l_e}{D_o} = 0.97$ to 1.45

$\frac{h_p}{D'_p} \approx 0.41$

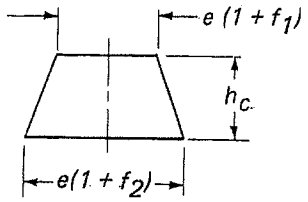
h_c = width of cloth = 24 to 36 inches



FULLNESS (f) DISTRIBUTION



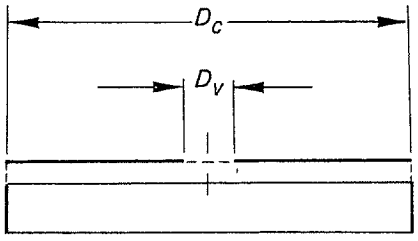
GORE LAYOUT



SAIL DETAIL

Size D_o, ft	Canopy (nylon) oz/yd^2	Geom. Porosity λ_g	No. of Gores N	Line Str. (nylon) lbs	Line Length l_e/D_o	Parachute Weight lbs	Application	Suspended Load lbs	Max. Deploy. Velocity	Rate of Descent fps	Comment	Ref.
29.6	1.1 2.25	14	24	550	.98	11.0	Personnel	250	275 kts	18.0	Skysail	217
63.1	1.1 2.25	7.1	48	550	.97	70.0	Mercury	2340	150 kts	32	Reefed	
85.6	1.1 2.25	12.0	68	650	1.45	145	Apollo	13,000	163 kts	31.4	Cluster of 3, Reefed	
189.5	1.1 2.25 3.5		156	650	1.18	557	Research	20,560	153 kts	26.0	Reefed	217

Disk-Gap-Band. The canopy is constructed as a flat circular disk and a cylindrical band separated vertically by an open space. A gore consists of a triangular top and rectangular bottom as illustrated. The disk, gap and band areas are 53 percent, 12 percent and 35 percent respectively of the total (nominal) area S_o. Data for a specific disk-gap-band parachute and load configuration are given below. Polyester materials were used for the Viking 53 ft diameter parachute to withstand the effects of heat sterilization and densely packed storage until deployed in the Martian atmosphere.



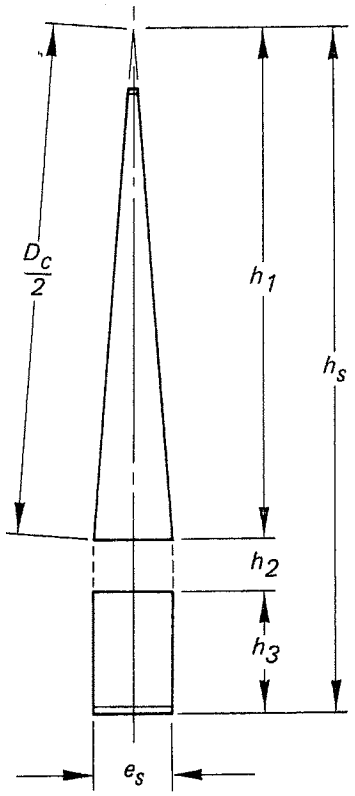
CONSTRUCTED PROFILE

$$h_1 = \left[\frac{S_o}{1.887\ N \tan(180°/N)}\right]^{1/2}$$

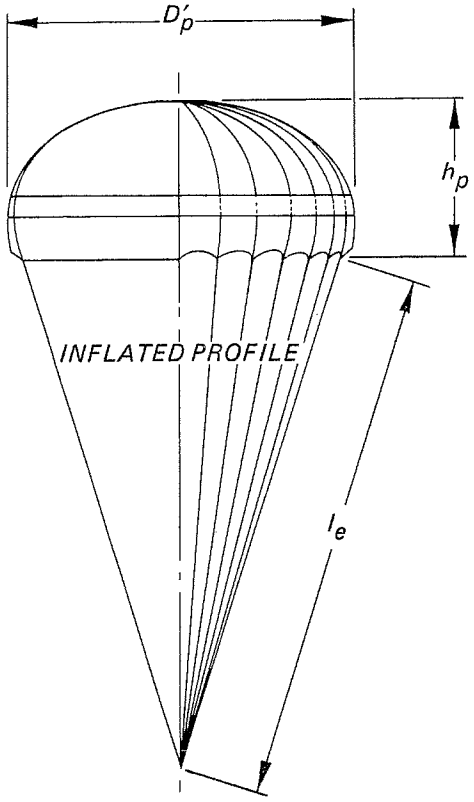
$$h_2 = 0.113\, h_1$$

$$h_3 = 0.33\, h_1$$

$$e_s = 2h_1 \tan(180°/N)$$



GORE LAYOUT



Size D_o, ft	Geom. Porosity λ_g	Canopy (polyester) oz/yd²	No. of Gores N	Line Str. (polyester) lbs	Line Length l_e/D_o	Parachute Weight lbs	Payload	Payload Weight lbs	Max. Deploy. Speed	Rate of Descent fps	Remarks	Ref.
53	12%	1.5 2.25	48	880	1.69	95.5	Mars Lander	1650	M = 1.6 1400 fps	100	Viking	21

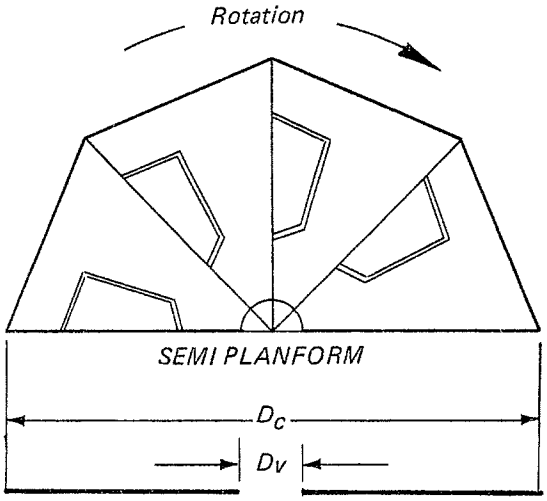
Rotating Parachutes

Rotation of parachutes has been achieved by providing unsymmetrical openings in gores to create a cascade of rotationally identical pitched sails, or by assembly of a number of identical fabric sails rigged to provide the desired pitch and twist. Improved parachute performance and weight efficiency is obtained in return for the added complication of the rotational function and the need for a swivel in the rigging. Both the Rotafoil and Vortex Ring parachutes have a low opening load factor, good stability and high drag. These parachutes work well if limited to 10 ft diameter or smaller. Problems in inflation and rotation have occurred with larger parachutes.

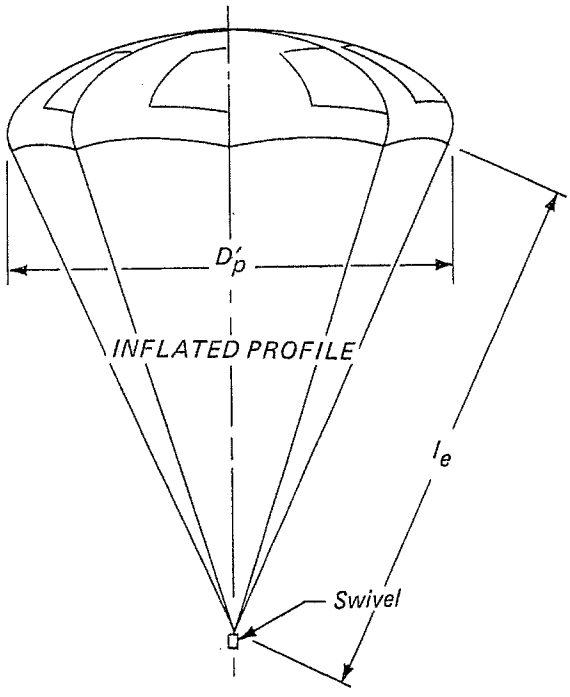
Rotafoil. The canopy is constructed as a flat polygon of gores having an open slot on one side as shown. The parachute is relatively low in bulk and weight, not counting the necessary swivel. Slot areas should equal 20% S_O at 10 ft D_O, and increase to 32% for very small rotafoils. Data are given below for a specific rotafoil parachute used as a drogue stage decelerator.

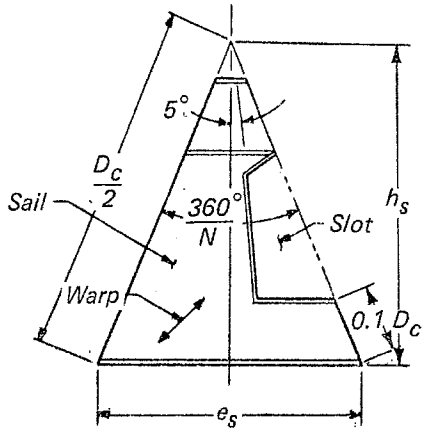
$$h_s = \left[\frac{S_O}{N \tan (180^\circ/N)}\right]^{1/2}$$

$$e_s = 2 h_s \tan (180^\circ/N)$$



CONSTRUCTION SCHEMATIC





GORE LAYOUT

Size D_O, ft	Canopy (nylon) oz/yd^2	No. of Gores N	Line Str. (nylon) lbs	Line Length l_e/D_O	Parachute Weight lbs	Payload	Payload Weight lbs	Max. Deploy. Velocity	Remarks	Ref.
3.80	3.5	6	1500	1.0	1.78	Drone	390	345 kts	Swivel included	218

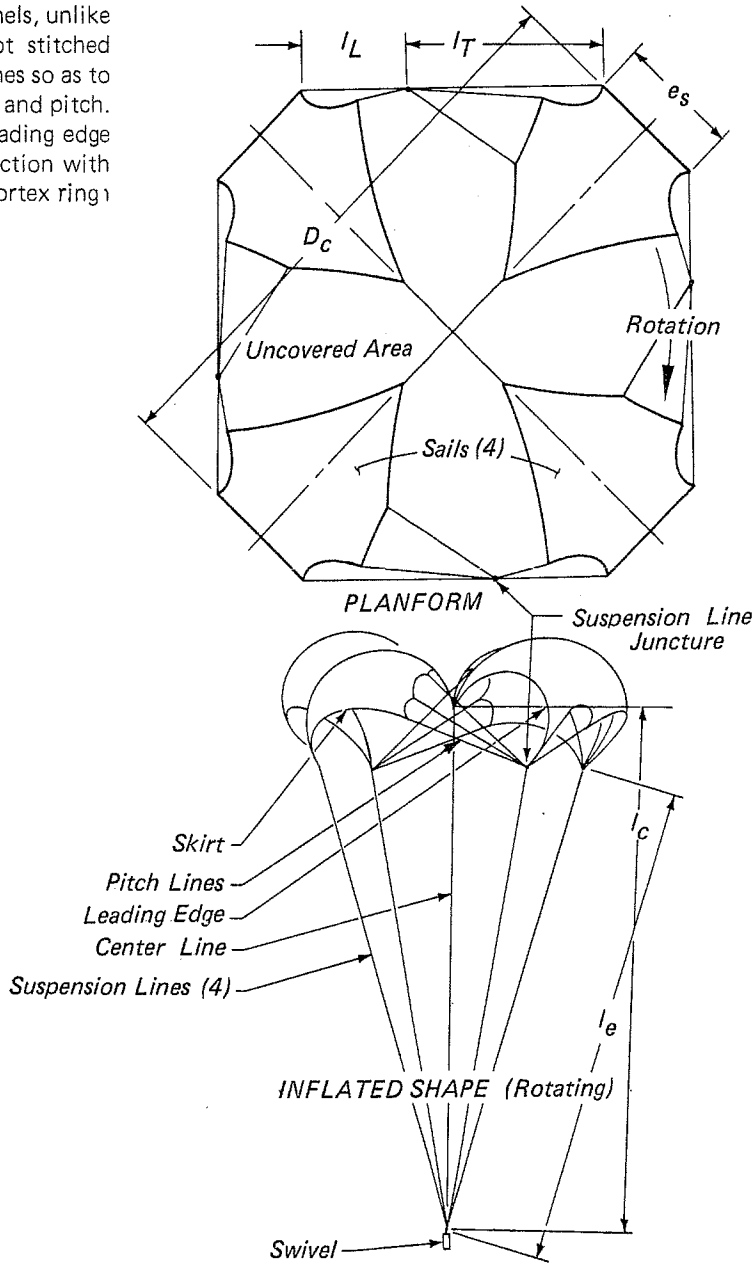
Vortex Ring. The canopy consists of four sail-like panels that rotate about its apex in the manner of helicopter blades in autorotation. The panels, unlike gores of conventional parachutes, are not stitched together but are tailored and rigged with lines so as to produce a desired distribution of convexity and pitch. Pitch is obtained by employing shorter leading edge lines than trailing edge lines from the junction with each suspension line. Data for specific vortex ring parachutes are given below.

$D_c = (4.59\, S_o)^{1/2}$

$\frac{l_e}{D_c} = 1.0$ (optimum)

$\frac{l_c}{D_c} = 0.94$ to 1.05

$(l_T - l_L)/D_c = 0.125$ (optimum)



Size D_o, ft	Canopy (nylon) oz/yd^2	No. of Panels	Line Str. (nylon) lbs	Line Length l_e/D_o	Parachute Weight lbs	Payload	Payload Weight lbs	Rate of Descent fps	Max. Deploy. Velocity	Remarks	Ref.
9.5	1.1	4	275	.85	5	Flare	25	25	400 kts	Reefed	
105.0	1.1	4	2250	.65	29	Missile	1600	21	130 kts	Reefed	

Low Glide Parachutes

A gliding parachute differs from the ballistic parachute by being symmetrical about a plane through its axis, introducing a right and left side as well as a forward and rearward direction in the plane of symmetry. Steerable versions require directional control manipulation, usually through movement of suspension or separate control lines.

Gliding parachutes vary widely in canopy planform and constructed profile from slightly modified typical circular forms to shapes simulating aircraft wings. Early steerable parachutes were developed by modifying the solid flat circular and extended skirt canopies of man-carrying parachutes. Ringsail and ribbon types have also been altered to provide glide and steerability. The modification generally added exhaust slots, openings or flaps which forced part of the air in the canopy to escape in a singular direction normal to the vertical parachute axis. The reaction force caused the parachute to move in the opposite direction, with the added benefit of creating a lift force due to the flow of air over the leading curved surface of the canopy. Most low-glide parachutes are made steerable by opening or closing slots and flaps asymmetrically, to create a torque or turning force. Opening and closing of the flaps is accomplished by control lines actuated by the jumper or by a guidance and control system attached to the descending vehicle. The term ***low glide*** refers to a class of gliding parachutes capable of a maximum glide ratio, $(L/D)_{max}$, less than 1.0, and includes the modified circular types described below.

Derry Slot. The Type E-1 parachute has a 28 ft diameter flat circular type canopy made steerable[207] by two strategically located "Derry" slots positioned symmetrically aft of the canopy lateral axis, one on each side of the directional axis. The slot design causes outflowing air to deflect rearward. Control lines attach to the lower edge of the slots, and when either line is pulled down, the slot deforms, reducing the exhaust from the deformed slot.

The Type A/P28S-3 and A/P28S-10 parachutes[207] use a basic MC-1 flat extended skirt canopy modified with a large elliptical orifice over five gores of the canopy. The main seam radial tapes cross over the opening to preserve shape and integrity of the structure. Directional control is obtained through a set of "slip" risers, operated to warp the inflated shape of the canopy.

T & U Slot. Numerous circular flat and extended skirt parachute types have been modified with L, T, and double T slots, resulting in glide ratios, $(L/D)_{max}$ between 0.5 and 0.7. One of the more recent gliding parachutes is a seven gore TU slot design used by paratroops, illustrated in Figure 2.6.

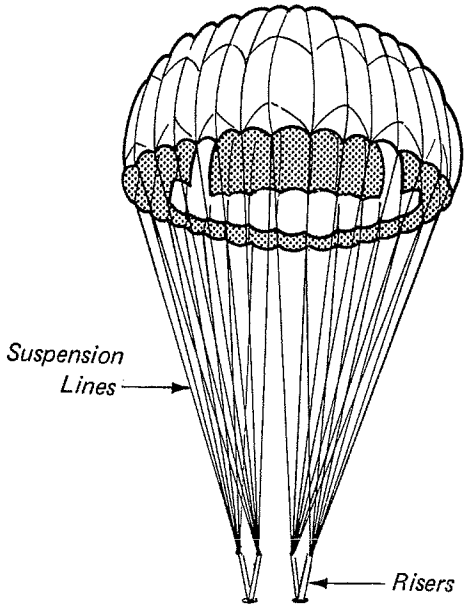


Figure 2.6 MC-1-1B Parachute

Medium Glide Parachutes

Gliding parachutes capable of glide ratios between 1.0 and 2.0 are classified as ***medium glide*** designs.

LeMoigne. A developed sports parachute invented by LeMoigne of France, has a retracted apex and employs a succession of rearward directed slots to attain effective glide and steerability. An American version of the LeMoigne sport parachute is the "Para Commander" shown in Figure 2.7. This parachute develops a maximum glide ratio of approximately 1.2. The "Parasail" parachute is a larger version of the LeMoigne type developed during the Gemini Program.

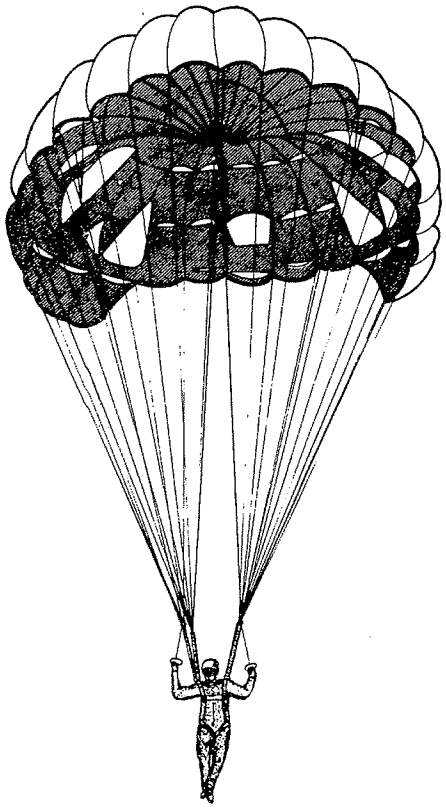


Figure 2.7 The LeMoigne Parachute

High-Glide Parachutes

The term ***high-glide*** refers to parachutes with glide ratios greater than 2.0. These parachutes are characterized by airfoil type canopy cross-sections and wing type planforms. A wing-like shape with low porosity material creates a rather flat single or double membrane canopy. Typical high-glide parachutes are the Parawing, originated by Rogallo , the Parafoil, invented by Jalbert and further developed by Nikolaides[219], the Sailwing developed by Barish and the Volplane developed by the Pioneer Parachute Company.

The Parawing and Sailwing are single membrane canopies. The Parafoil has a ram-air inflated, double membrane airfoil cross-section. Approximately one-third of the chord length of the Volplane is a double membrane, ram-air inflated, airfoil leading edge. All high-glide parachutes are equipped for steering by means of wing tip or trailing edge lines. Pulling the lines creates either aileron or spoiler effects, or wing-tip angle of attack changes. A certain amount of glide control for steepening or flattening the glide path and for flare-out is practiced by sport jumpers. To obtain such modulation with remote steering or with a fully automatic navigation and landing system has proven difficult. The control forces and control line movements are high compared to aircraft type controls and are in the range of 4 to 6 percent of the total resultant aerodynamic force acting on the canopy. Such forces can be handled easily by jumpers but require considerable electrical power, control line movements and a weight penalty for large high-glide parachutes used with vehicles of several thousand pounds weight. Reference 220 which describes the development of a ground controlled high-glide parachute system for the landing of a 6000 lb spacecraft points out some of the difficulties involved.

Another characteristic of high-glide parachutes is the high peak opening force caused by the low porosity material used for the canopies. Wind tunnel tests show opening loads are nearly 50 percent higher than those experienced with solid circular flat parachutes. Controlling peak forces usually requires multiple reefing for large systems in order to stay within allowable limits of vehicle load and parachute weight. Many sport jumpers use reefing for decreasing the opening force even at relatively low jump speeds.

Aircraft wing terminology has been adopted for high performance gliding parachutes. It is convenient to relate the aerodynamic forces to the flat planform area of the lifting surface, S_W. Since S_O includes the area of all fabric surfaces in the canopy, the ratio S_W/S_O is indicative of the effectiveness with which the fabric is used to create the lifting surface. The weight of the canopy tends to be proportional to the inverse ratio S_O/S_W.

Aspect ratio is a significant parameter affecting the aerodynamic performance of gliding parachutes. ***Aspect ratio*** is a measure of slenderness of the wing planform, determined by the equation

$$AR = \frac{b^2}{S_W}$$

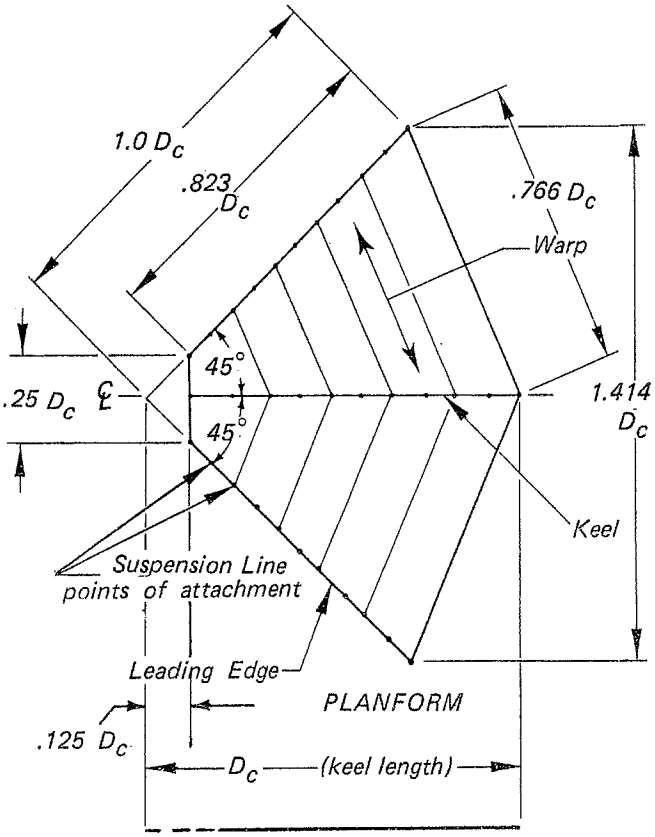
where b = wing span. An increase in aspect ratio of the canopy increases the glide ratio of a gliding parachute. Increasing the aspect ratio also introduces deployment and canopy opening complexities, especially on large parachutes.

Parawing, Single Keel. The canopy is fabricated from two flat isosceles triangles joined with vertex forward and short side trailing as shown. The joined sides form a keel along the center line of symmetry. The reference construction dimension, D_c, is the keel length [220]. However, the point of the canopy is tucked under, thus forming an airfoil type leading edge. Suspension lines are attached along the keel and the two leading edges. The length of the suspension lines varies chordwise in order to position the canopy at an angle of attack to the flight path. The strength of suspension lines also varies with location and share of canopy loading. This variation in line length and in line strength complicates fabrication, packing and deployment. Changing the glide ratio in flight by changing the angle of attack is difficult. Steering control is obtained by pulling either wing tip to turn in that direction. Parawings are used as steerable high-glide sport parachutes and have been tested successfully with large loads to a size of 4000 ft^2 and wing span of 107 feet. Jumpers obtain a limited glide modulation by manipulating both wingtips and keel lines. This is difficult to obtain on larger systems due to the weight and complexity of the required control system.

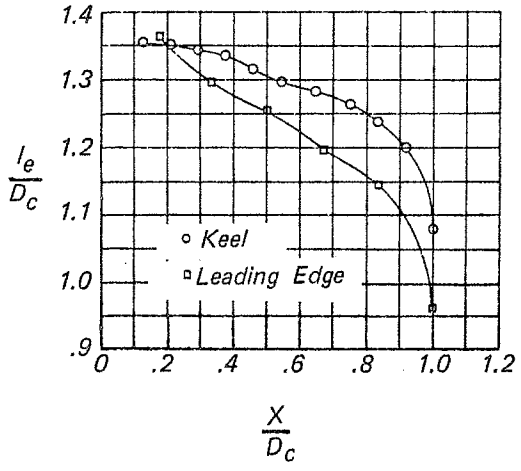
$$D_c = (S_W/0.692)^{1/2}$$

$$\frac{l_e}{D_c} = 1.0$$

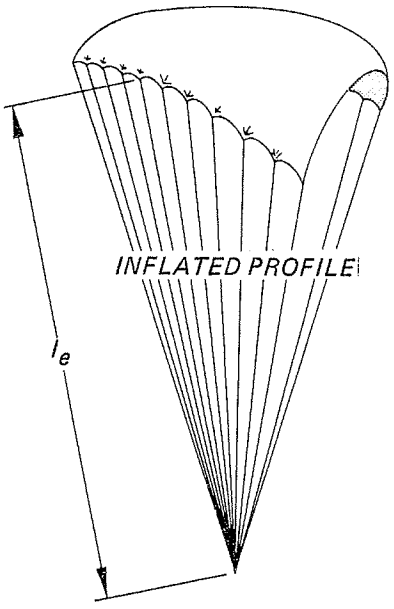
$$AR = \frac{(1.414\,D_c)^2}{S_W} = 2.89$$



CONSTRUCTION SCHEMATIC



Line Location and Length Distribution



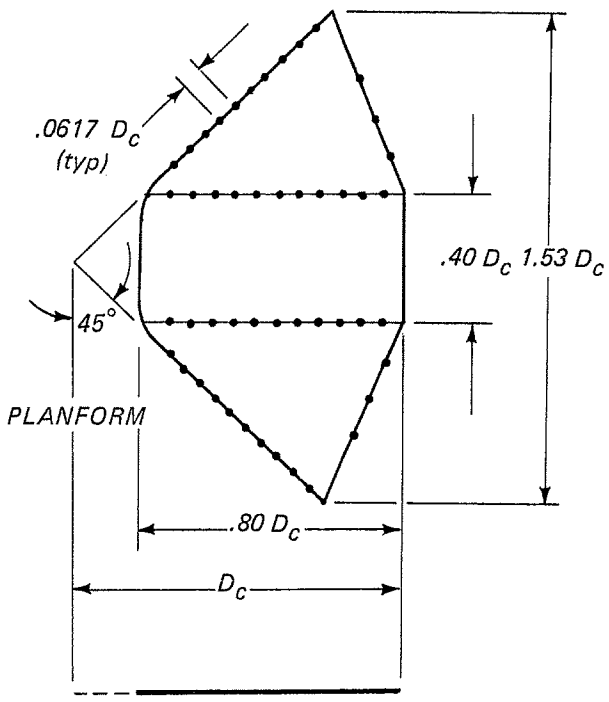
Parawing, Twin Keel. The canopy is fabricated from two flat isosceles triangles with a rectangular panel between, as shown. Identical keels are formed where the sides of the rectangle join the triangles. The reference construction dimension, D_c, is length of the canopy centerline from the trailing edge of the rectangle to the point of intersection with the projected leading edge lines. The front of the rectangle is rounded to form an airfoil-like leading edge.

The twin keel Parawing performs with slightly better glide ratio than the single keel version, largely due to its higher aspect ratio.[220] Other versions of twin keel Parawings have been tried which varied the rectangle width and shape (to trapezoid) registering improved performance in some.

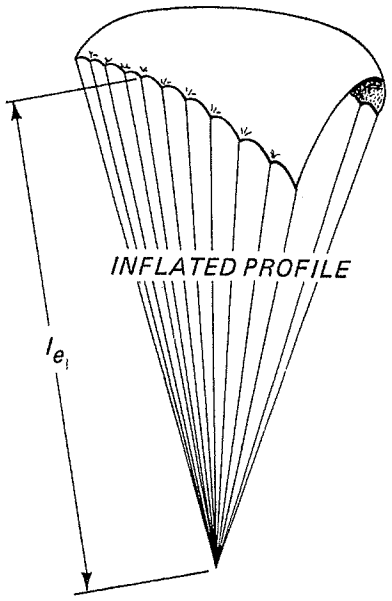
$$D_c = (S_w/.773)^{1/2}$$

$$\frac{l_e}{D_c} = 1.0$$

$$AR = \frac{(1.53\,D_c)^2}{S_w} = 3.02$$



CONSTRUCTION SCHEMATIC



Parafoil. The canopy is constructed in the form of a rectangular wing with an upper and lower surface held in place by spaced internal ribs that form box-type airfoil shaped cells. During operation, these cells are ram-air inflated through openings in the leading edge. The suspension lines attach with a system of triangular flares to the underside, thus providing a form keeping system for load distribution into the vertical ribs. This design results in a good aerodynamic shape but is penalized by material not contributing directly as lifting surface. It is easy to increase aspect ratio on this design and thereby improve glide performance if within limits which preserve reliable, uniform inflation. Turn control is obtained by lines attached to the trailing edges creating an aileron type of effect. Parafoil designs are in use for sport jumping. Large Parafoils up to 3200 ft^2 and aspect ratios of 2.0 have been tested by the Air Force. All comments concerning high opening loads and complexity of ground and automatic flight control of Parawings apply equally well to Parafoils.

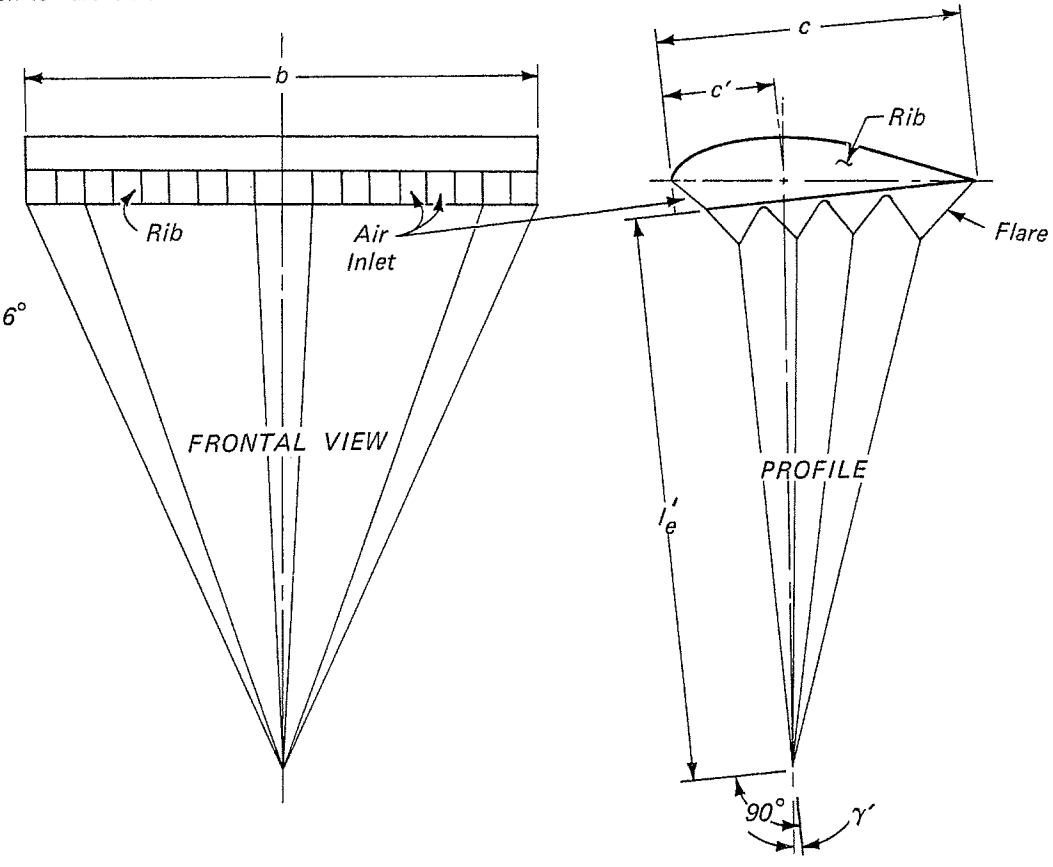
$S_W = bc$

$AR = b^2/S_W$

$l'_e = 1.5\,b$

$c' = 0.35\,c$

$\gamma' = 7^\circ$ to 13.6°



Sailwing. The Sailwing is a single membrane wing-like parachute fabricated from low porosity textile material. The canopy surface is rectangular with an aspect ratio of 3 or better. The forward edge of the wing is pulled under by means of tabs and short lines to give an airfoil type leading edge. Large triangular flares are attached to the wing tips and along several chord lines extending approximately one-third the distance to the suspension line confluence point. These flares give the canopy a scallop-like appearance illustrated in Figure 2.8. They provide directional stability and support inflation. Steering control is manipulated by wing tip lines. Characteristics typical of high-glide, high aspect ratio, low porosity textile parachutes apply to Sailwing, which has been successfully tested up to man-carrying sizes.

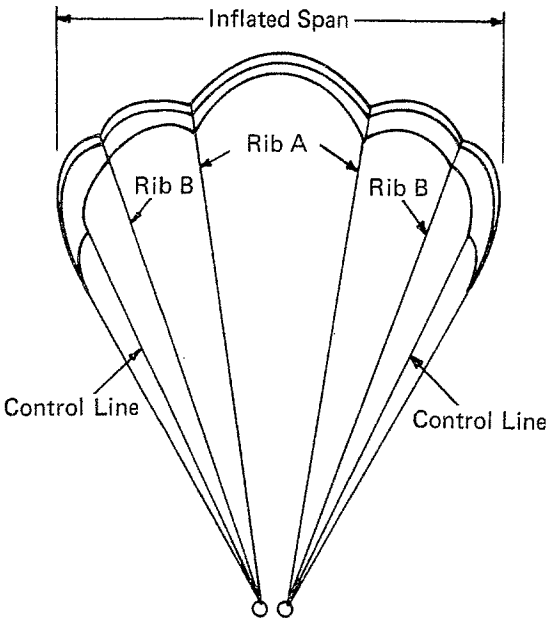


Figure 2.8 Sailwing

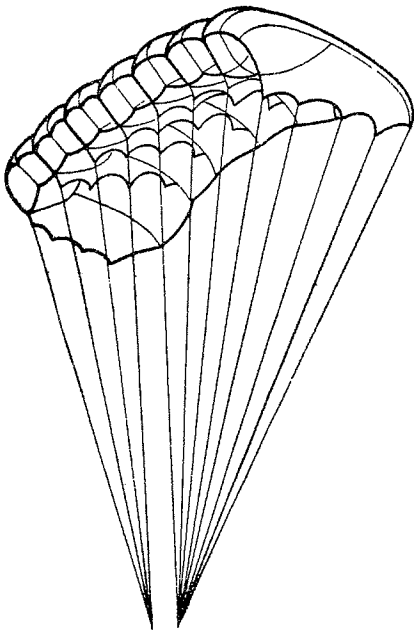


Figure 2.9 Volplane

Volplane. The Volplane has an airfoil canopy with a ram-air inflated front. The lower surface of the airfoil ends at 30 to 40 percent of the chord length. Openings at the leading edge and multiple cell construction provide an inflated front part of the wing-like parachute. The suspension lines are attached by means of flares along the chord lines. General design and turn control is similar to the Parafoil. Control lines attached to multiple points at outside trailing edges deform the canopy and induce a turn toward the side where the lines are pulled. Low porosity material is used throughout.

DECELERATORS OTHER THAN PARACHUTES

Although parachutes are an efficient form of deployable aerodynamic decelerator for the majority of recovery requirements, applications exist in which balloon type and rotor type devices have special advantages. These advantages usually appear at the fringe of conditions compatible with reliable operation of parachutes. Inflation may be uncertain at very low air densities, or high frequency flutter may occur at hypersonic speeds in combination with high temperatures generated by aerodynamic heating.

In the following paragraphs, the geometric and performance features of established inflatable envelopes and blade type rotating decelerators are described.

Balloon Types

Inflatable closed-envelope decelerators evolved from early experiments with towed spherical balloons. The sphere provided a high drag blunt body, and was fabricated from material with very low porosity in order to stay inflated from a stored gas source.

The investigations of various configurations[222] were first conducted to test deployment up to Mach 4 at 200,000 feet, and later up to Mach 10 between 120,000 and 200,000 feet altitude. A "burble fence" was incorporated to provide flow separation for subsonic stability. The fence was a tubular ring affixed to the balloon just aft of the sphere's maximum diameter as shown in Figure 2.10. Suspension lines extended over the top of the sphere and around the radials, leaving the balloon surface from the point of tangency to the line confluence point.

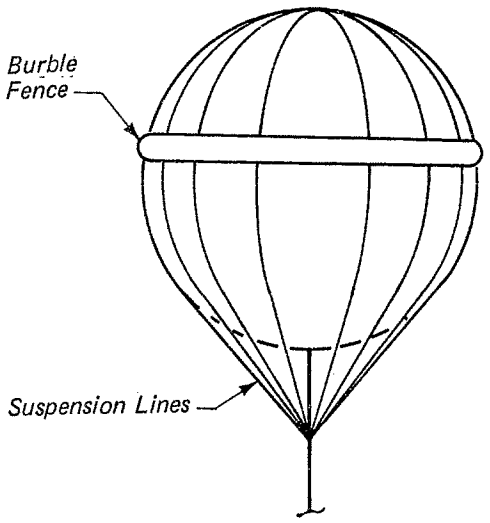


Figure 2.10 Balloon Decelerator

Ballute. The trailing spherical balloon as a decelerator became known as a "Ballute" and has evolved to a more uniformly stressed shape, shown in Figure 2.11, which incorporates the cone of suspension lines into radial members of the balloon forward surface. The compressed gas supply was replaced by ram-air inflation to minimize installed weight. Air scoops forward of the Ballute's maximum diameter provide air inlets for inflation and ram pressure to fill and maintain its final shape.

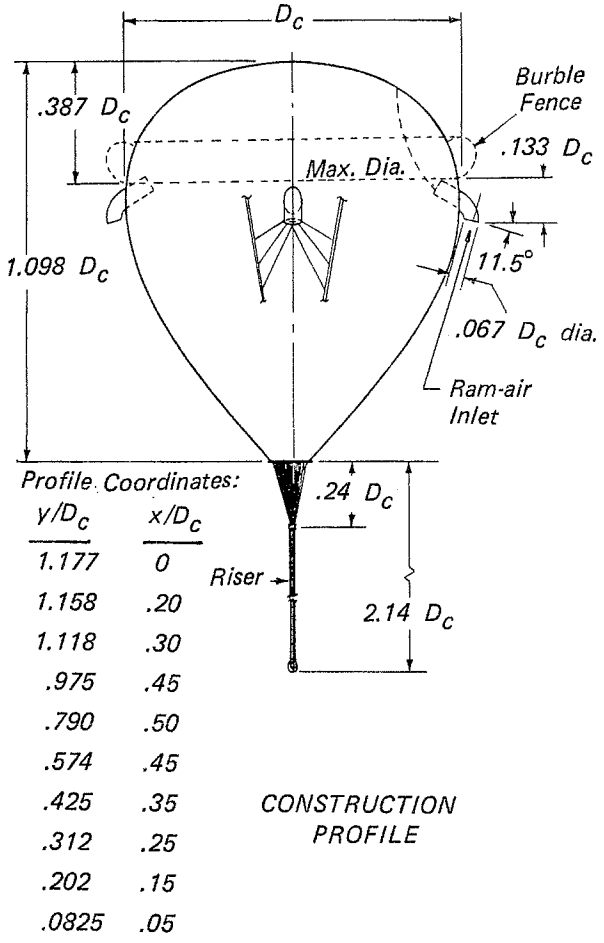


Figure 2.11 Ballute Geometry

Attached Inflatables. These decelerators are balloon types connected directly to the base of the vehicle without an intermediary riser or tethered suspension. Provisions for deployment may involve an inflation source or projection of ram-air inlets into the airstream. Attached inflatable decelerators applied to bluff bodies[223] are illustrated in Figure 2.12. Another attached balloon type drag augmentor is shown in Figure 2.13 which deploys from a low drag vehicle and inflates with ram-air[224].

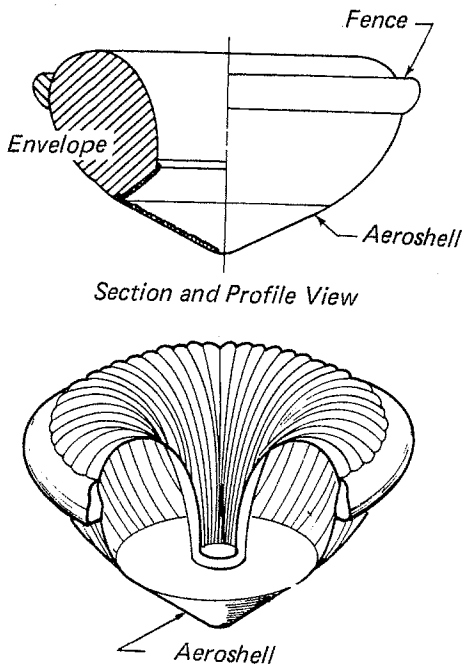


Figure 2.12 Attached Inflatable Decelerators

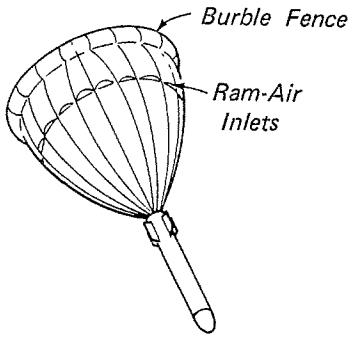


Figure 2.13 Ram-Air Inflated Decelerator

Paravulcoon. A unique concept employs this balloon decelerator in a final stage. After the vehicle has been retarded to a velocity at which the balloon envelope is deployed, the Paravulcoon inflates and the air within its envelope is heated to transform it from a decelerator into a true aerostat, Figure 2.14.

Rotor Blade Types

In its simplest form the rotor decelerator consists of a pair of rigid autogiro-type blades mounted on a rotor hub with provisions for folding the blades aft

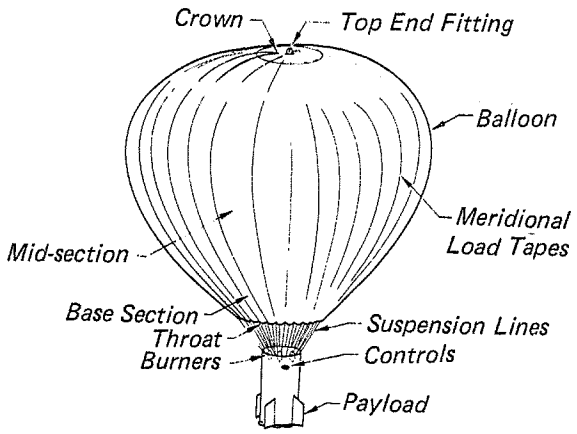


Figure 2.14 Paravulcoon System

into the trailing position for stowage and deployment. Also on the hub is a mechanism to ensure synchronous unfolding of the blades from the stowed position into the normal operating position. Since autorotational spin-up occurs during the deployment sequence, synchronization of blade extension is essential to the maintenance of dynamic balance, i.e., to prevent eccentric gyrations of destructive amplitude. Figure 2.15 shows the stowed and deployed arrangement of a rotor having two rigid blades. Details of a Rotochute test vehicle which incorporates all the features of a rotor recovery system, and detailed theoretical and experimental investigation of a four-bladed stored energy rotor recovery system are reported in Reference 225.

Other concepts, some tested experimentally, embody telescoping rigid blades, or stowable flexible blades. The flexible designs include thin sheet metal blades capable of being rolled into coils against the hub, single-surface fabric blades with ballasted tips, and tubular inflatable fabric blades. Synchronization of the extension of such blades during spin-up has proven difficult in practice.

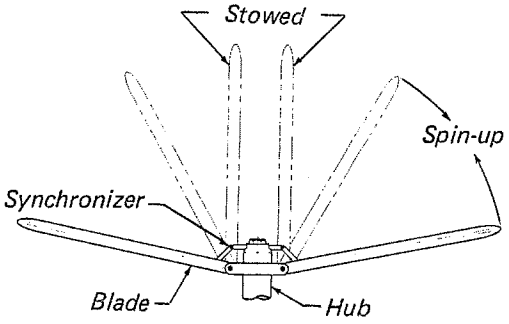


Figure 2.15 Rotor

CHAPTER 3

COMPONENTS AND SUBSYSTEMS

Components other than decelerators are described which form the subsystems of a total recovery system. Major categories are the decelerator subsystem, control/actuation subsystem and termination phase subsystem. Within each of these general headings there are various subsystem types. For instance, the decelerator subsystem could feature a parachute, a rotor or a gas pressure inflated balloon design, or the termination phase subsystem might incorporate a retrorocket or an airbag landing energy absorber. Each individual subsystem would consist of its unique major components and related supporting elements.

Operational features of recovery system components are developed with consideration for high reliability, safety, and efficiency in terms of low weight and minimum volume. Many of these components have evolved over long periods of operational use, changing when necessary to meet new requirements. In the following sections, components associated with specific subsystem types are described. However, there are many qualified components available from various suppliers which are not included. Only a representative listing is given of typical items currently used in recovery applications.

CONTROL/ACTUATION SUBSYSTEMS

The components which control and activate recovery sequences make up the control/actuation subsystem. A single item often provides the only control function needed, that of initiating deployment which results in an automatic sequence of recovery events, e.g., a ripcord on a personnel parachute pack or a static line on an airdrop load. For some applications the control/actuation subsystem could consist of a variety of electrical, hydraulic, pneumatic, pyrotechnic and mechanical items with associated wiring, tubing or interconnecting hardware. A typical group would include a set of sensors, timers, initiators and actuators, disposed in an arrangement that is effective for its functional requirements and efficient in terms of limiting the weight, volume and cost added to the vehicle. The use of pyrotechnic items introduces a special concern for safety of the system and caution in the procedures which control handling and installation of cartridges and other explosive devices.

When a hydraulic or pneumatic system exists in a flight vehicle, it is sometimes expedient to add components to perform recovery functions using available fluid or gas pressure and accumulator capacity from the vehicle primary subsystem. Similarly, vehicle electrical power is often used to energize recovery control functions; however, an independent electrical source may be required in the event of vehicle power failure. The components described in this section include common items, some of which are used in complex recovery systems, such as manned spacecraft subject to various abort modes. To properly orient the different categories of control components, two examples of representative functional sequences are presented in the first part of the section. Components are described in the paragraphs which follow, under the general categories of control components and actuating components.

Control/Actuation Subsystem

Consideration of a representative recovery sequence such as that diagrammed in Figure 3.1 helps to clarify the types of control/actuation subsystem functions required in a single-mode recovery system. This set of components executes one sequence of events at whatever speed and altitude conditions prevail upon receipt of the recovery initiation signal. In the diagram, the first column identifies the required control functions. The second column lists the actions required to perform the functions listed in column one. The third column lists typical control/actuation hardware used to perform the required functions. The system could apply to a high-speed target drone that is normally recovered by radio signal command given at the end of a planned flight at known speed and altitude conditions. The system is also designed to recover the vehicle when a fail-safe sensor initiates automatic recovery if engine power is lost or if any one of several other flight termination conditions occur. Other fail-safe initiation conditions might include loss of command radio carrier, loss of electrical power, or loss of flight stability. The one-second delay relay prevents false signals from causing inadvertent recovery. A recovery signal ejects the

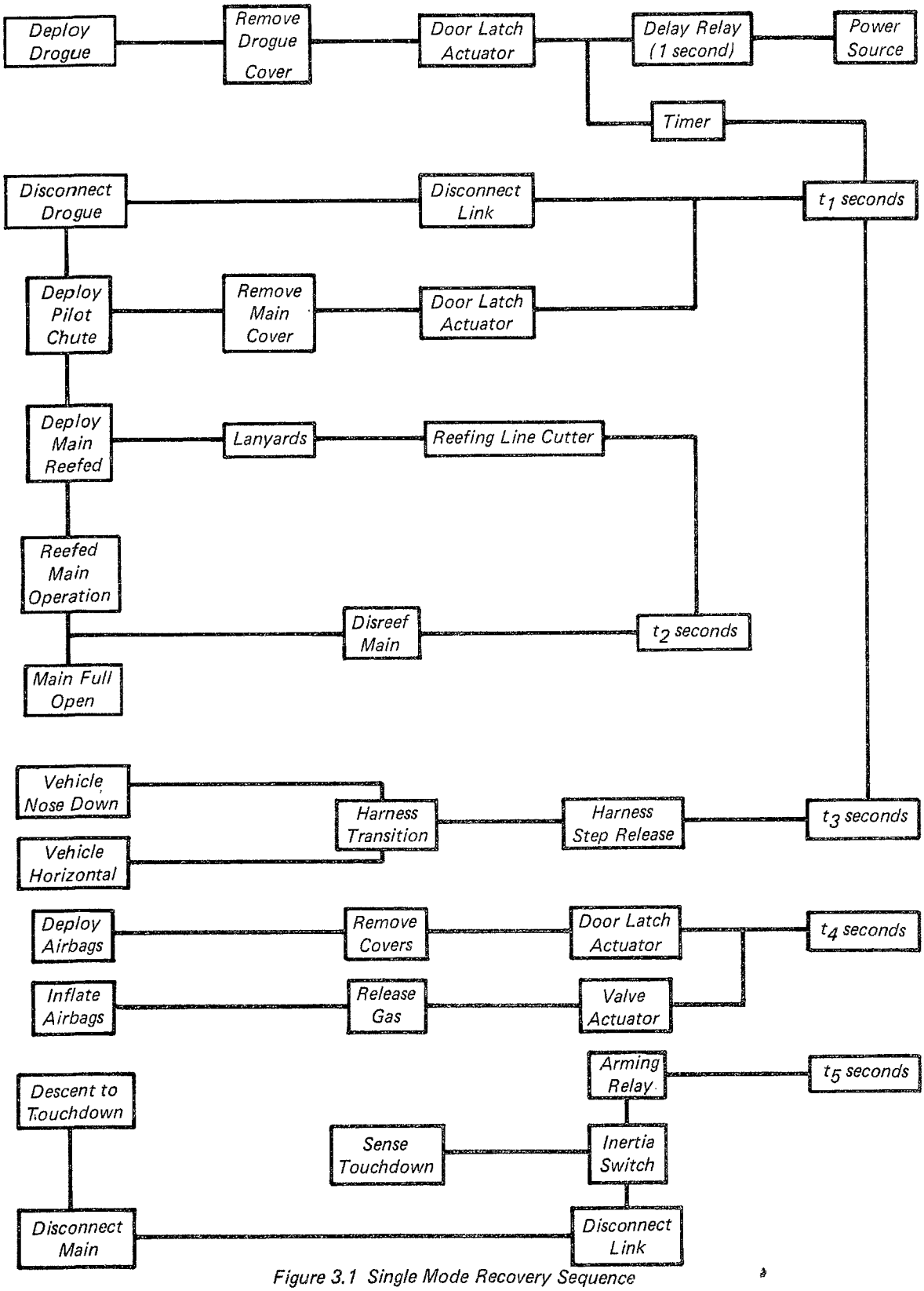


Figure 3.1 Single Mode Recovery Sequence

drogue and starts the timer which operates on an independent battery or the vehicle power source. The control functions follow in a preset sequence.

A variation of this sequence could be obtained by using two timers and placing a baroswitch in series with the drogue interval timers. Then above a preset maximum altitude desired for main parachute deployment, disconnect of the drogue will be delayed until the system has descended to that altitude. The second timer would then be started by the main deployment signal (and drogue disconnect) to sequence the desired functions after the main parachute is fully inflated.

A more complex control/actuation subsystem, a multi-mode concept to provide for several in-flight abort possibilities, is shown by the diagram of Figure 3.2. The example applies to a lifting body shaped one-man escape capsule from a design study[226]. The total spacecraft was intended for launch to a 200-mile orbit and return with normal landing on airstrips without deployment of the emergency system. Conditions considered in the design of the escape and recovery system were the following abort modes:

A. off-pad and early boost
B. during boost above 50,000 ft
C. during late launch phase
D. escape from orbit
E. after deorbit retrofire
F. during reentry, and
G/H. at low altitude during glide and landing

Control Components

Components required to provide control functions may include power sources; event times, and acceleration and pressure switches. Switching relays, diodes and fuses are also incorporated in many electrically operated recovery control subsystems.

Power Sources. Electrical power availability in military aircraft, drones, missiles and spacecraft varies in type and power factors. Twenty-eight volt ac or dc systems are usually available. Items requiring heating or energizing may require an independent source of power, particularly if the payload being recovered separates from the primary power source or as a back-up source in the event of primary power failures. Batteries of various types and sizes have been used, depending upon the current requirements and the duration of demand. Other considerations including the operating temperature range and the length of time from installation of the charged battery to use without recharging may influence the choice of a battery type.

Storage Batteries. High efficiency storage batteries using alkaline electrolytes have been used as independent power sources for many recovery systems. Two basic types are available: nickel-cadmium batteries and silver-zinc batteries. Both types have the characteristics of high current discharge capability, operation at temperatures down to -60°F, leak-proof sealed cases, and long life. The individual cell voltage is nominally 1.2 volts for the nickel-cadmium type and 1.5 for the silver-zinc type.

Reserve Cells. For certain uses, shelf-life of many years without maintenance, followed by a short-term usage cycle dictates use of a power source known as a reserve cell or thermal battery. In this type of battery, the plates are pre-charged and the electrolyte is stored separately in an internal breakable capsule. Upon actuation (generally by lanyard pull), a pyrotechnic cartridge within the cell fires, breaking the electrolyte capsule, dispensing the electrolyte throughout the cell and heating the cell to a high temperature (above 200°F).

Because of the high temperature, a small battery of this type generates a high voltage and current capacity until it cools down. The relative high cost of the reserve cell when compared to the larger rechargeable alkaline storage batteries has inhibited widespread use of the reserve cell.

Salt Water Batteries. Payloads which touch down at sea often require power to operate post-landing recovery/location/retrieval devices. Salt water switches and salt water batteries are used to close electrical circuits, power parachute disconnects, initiate inflation of flotation gear and power radio or flashing light beacons. Salt water batteries consist of two or more metal plates, slightly separated in a case with ports to provide free flow of sea water.

After several hours of operation, salt water batteries may decrease their output because of an accumulation of gas bubbles or a layer of chemical deposit on the plates. Special provisions must be made to prevent such an accumulation if more than a few hours of operation are needed.

Timing Devices. A "timer" is any device which controls the elapsed time between a start signal and an action such as a switch closure or mechanical displacement to initiate an event. A common type of timer is electro-mechanical, a switch bank driven by clock spring or electric motor. Thermal delay switches are another type of timer which, when electric current is applied, operate on the bimetal spring principle to close after an elapsed interval. Still

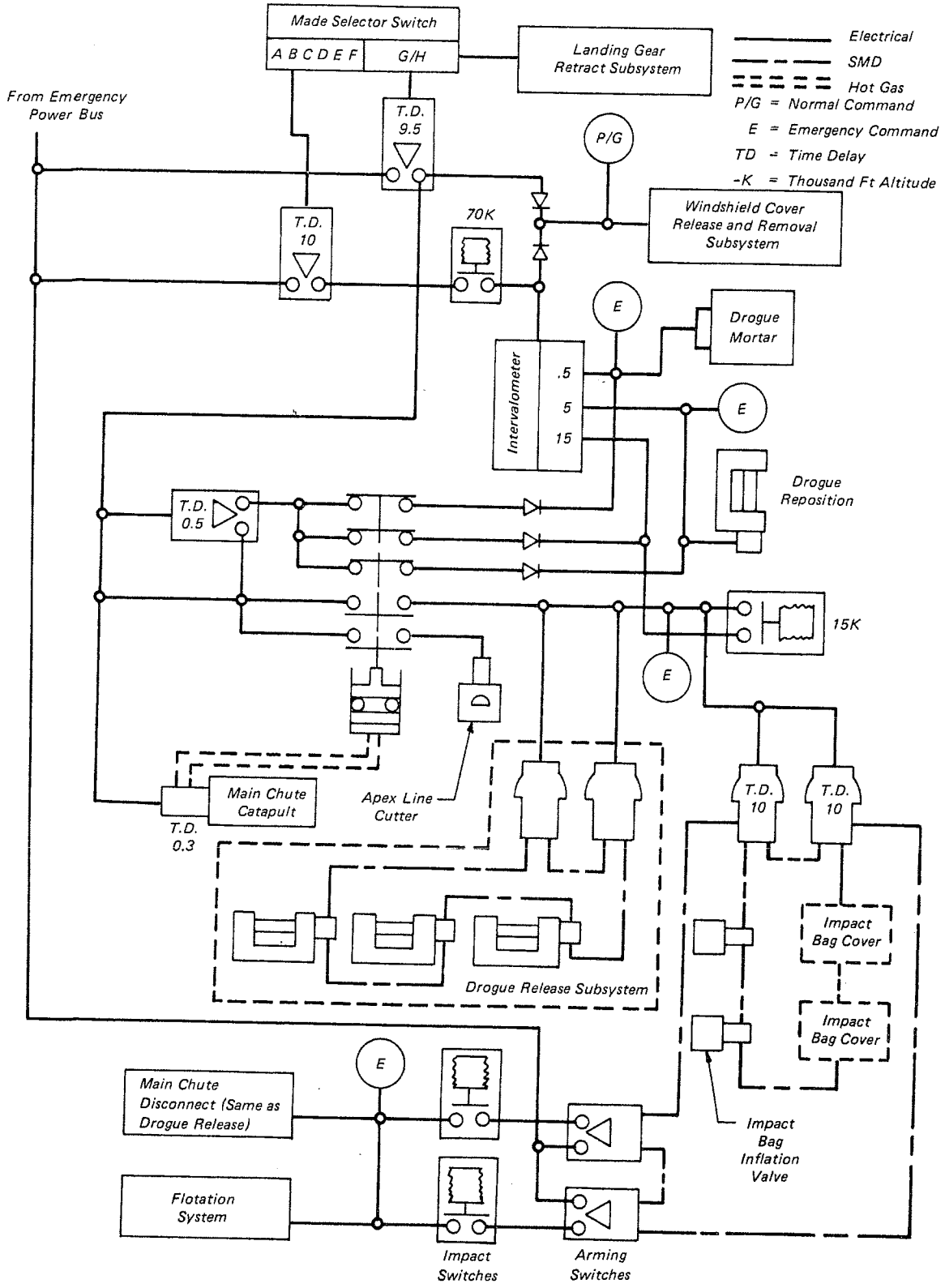


Figure 3.2 Control Subsystem Diagram for Emergency Recovery of Space Capsule

another is the pyrotechnic delay train as used in reefing line cutters and pyrotechnic time delay switches. A simple mechanical delay latching device may use a dash-pot principle for delaying release or engagement of a latch. This principle is used for a screw-driver-adjustable, lanyard-initiated time delay switch. Electronic delay timers employing resistance/capacitance circuits are commonly used to produce reliable and accurate timing for an event controller.

Switching Devices. Operation of various recovery system stages at discrete operational conditions calls for use of appropriate switching devices. Among the transient conditions under which recovery system staging may be desired are acceleration, altitude, and dynamic pressure and distance above ground. A list of such recovery system operating conditions and related sensor switches is given below:

Condition Sensed	Switching Device
Pressure Altitude	Barometric pressure switch
Dynamic pressure	Differential pressure switch
Fluid pressure (engine oil)	Fluid pressure switch
Loss of electrical power	Magnetic-hold relay
Pre-touchdown height	Contact probe
Absolute terrain clearance	Radar altimeter switch
Landing impact	Inertia (acceleration) switch
Sea water immersion	Salt water switch
Relaxation of load	Spring release

Pressure Switches. Many control/actuating subsystem components operate on a change in pressure whether working in a gaseous or liquid medium. Pressure switches employ a diaphragm (or bellows) to convert a change in pressure into diaphragm movement. This motion is then used to operate the contacts of an electrical switch or a mechanical pawl at a selected threshold level.

Altitude Switches. Altitude sensors generally depend on a diaphragm or bellows-type aneroid (a sealed cell) which expands during ascent and contracts during descent according to ambient pressure. After the aneroid has moved a predetermined distance, which occurs at a specific pressure altitude, a switch closes in a circuit connecting an electrical power source with an initiator of the controlled device.

Altitude switches (barometric switches) are frequently used to initiate deployment of first or final stage decelerators in a descending mode. They may also be used to arm a circuit in the ascending mode. A variety of baroswitches are commercially available with adjustable or fixed settings. As a pressure sensor operating over a limited absolute range, their sensitivity and accuracy are influenced by the size and flexing characteristics of the diaphragm or bellows used.

Dynamic Pressure Switches. Change in dynamic pressure is used in some recovery systems to signal either the deployment of a first stage decelerator or separation of a decelerator and deployment of a subsequent stage parachute. Since dynamic pressure is the difference between impact pressure and static (ambient) pressure, a dynamic pressure switch senses the difference between impact pressure on one side of the diaphragm and static pressure on the other side. If the payload is not perfectly stable aerodynamically, care must be taken in locating the static orifices to prevent them from sensing impact pressure. Where vehicle attitude cannot be predicted, several static orifices at different locations are connected to an averaging plenum chamber. Static pressure for the pressure switch is then picked up from the plenum chamber.

Acceleration Switches. Acceleration switches characteristically operate on the principle of a suspended mass moving against the reaction of a spring. At a predetermined movement of the mass, an electrical contact is closed or a mechanical pawl is tripped. A continuous measurement of acceleration or deceleration can also be obtained by employing a strain-gage wire as the spring. Acceleration of the mass in this sensor is converted to a tensile force on the strain gage which in turn changes resistance as its length is changed. Used as an active arm of a Wheatstone bridge circuit, the resistance of the strain-gage wire is calibrated to read in units of *G* (acceleration of gravity).

Initiating Devices. An *initiator* is a subsystem component which starts an irreversible, but sometimes arrestable, recovery function or event. In a direct sense, the term "initiator" is usually used to identify an element containing a pyrotechnic charge, such as an electrically or mechanically triggered cartridge, a primer or detonator. Electrical cartridges, primers and detonators are commercially available, either as a metal jacketed charge with insulated wire leads projecting from the base, or in the form of a threaded metal cartridge with a standard electrical connector fitting.

The term "initiators" may be applied to non-pyrotechnic items including a ripcord assembly of a personnel parachute pack, a lock-pin with an extraction

lanyard which frees a pilot chute, an electromagnetic latch which frees a recovery compartment cover, or a solenoid flood valve which frees compressed gas in a storage vessel to inflate airbags or flotation devices.

Cartridges. A cartridge is a small, electrically fired pyrotechnic device used to ignite a larger propellant charge such as a rocket igniter. A cartridge also produces a gas pressure when ignited, which may be used to initiate a mechanical function. A typical cartridge is shown in Figure 3.3, consisting of a cylindrical metal body with a two or four pin electrical connector at one end and a thin metal closure disc at the other end. The electrical pins protrude through the back of an insulating disc that forms the base of the connector and extends into the interior of the cartridge. A small-diameter-high resistance wire known as a "bridgewire" is welded or soldered across two pins. Dual bridgewires are connected to the pins of a four pin connector. The bridgewire is coated with an ignition-sensitive explosive mix called "match-head compound" formed in a bead and surrounded by a pressed pyrotechnic charge. An ignition mix of powder surrounds the bridgewires. A booster or primer charge is usually located adjacent to the ignition mix and this is followed by an output charge. A *primer* or *a detonator* is constructed in the same way, but the explosive composition is designed to create a shock output that will set off detonation in a high explosive.

Safing and Arming. Control/actuation subsystems which employ pyrotechnic or electrical components are usually designed with one or more safing or arming provisions. In most cases, a pre-takeoff arming function is included, and in addition, a launch arming function can be used.

Electrically operated control/actuation subsystems may be disarmed during ground operations by means of a manually actuated open/close battery power switch. A versatile safing/arming arrangement is the use of a multiple-pin electrical connector. By routing power cables and pyro firing wires to the connector, the actuator circuits can be grounded, opened or closed when a suitably wired mating connector is installed.

For safing, the mating connector opens the power circuits and shorts the pyro circuits to ground. For arming, the mating connector closes the power circuits and lifts the pyro circuits from ground.

Secondary safing/arming functions after take-off may be accomplished in several ways. In vehicles

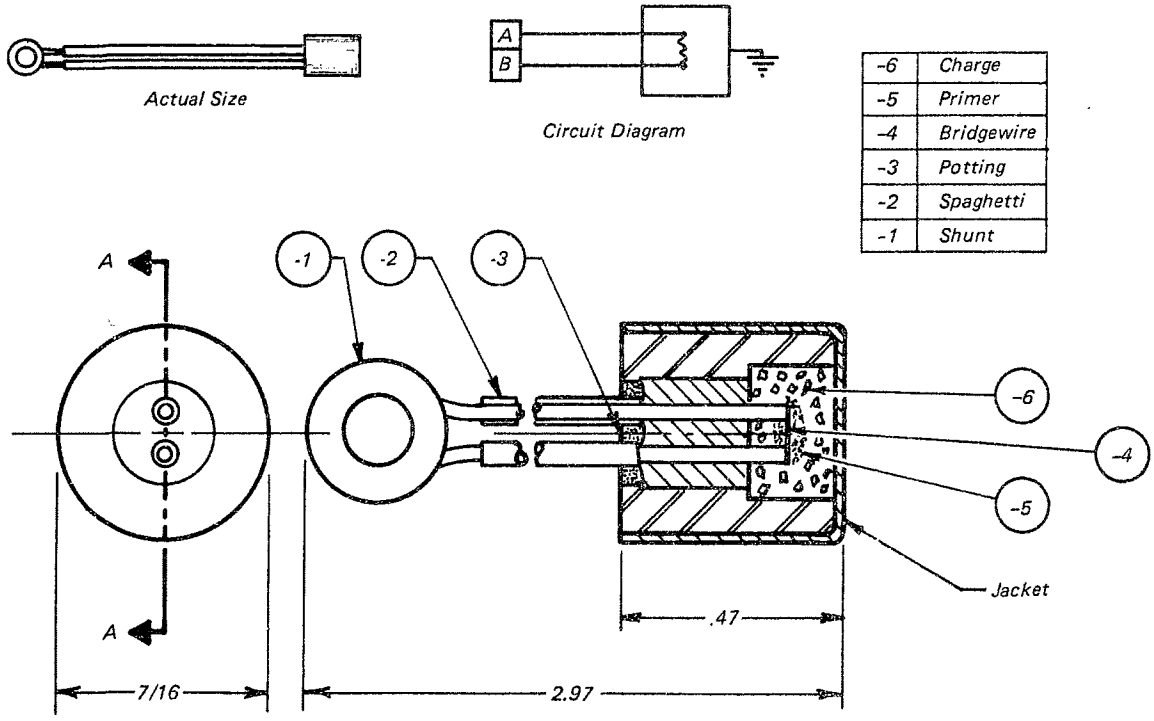


Figure 3.3 Typical Cartridge Configuration

that are air-launched from a carrier aircraft, an electrical signal from the aircraft can close a latching relay in the recovery controller or can start an arming timer. An alternative method that is often used incorporates a normally closed lanyard operated switch. When the vehicle separates from the carrier aircraft, a lanyard is withdrawn from an arming switch in the controller circuits. For ground launched vehicles, a position switch and mechanical or electrical timer may be used to arm the controller after lift off.

Actuating Components

An ***actuator*** is a device, activated by a controller or initiator, to cause a major recovery function such as forced parachute deployment, parachute pack opening, staged inflation (reefing) or parachute disconnect.

Deployment Actuating Devices. Deployment actuating devices constitute a special class of recovery system actuators designed specifically to mechanically initiate the operation of an aerodynamic decelerator, including pilot chutes, extraction parachutes, drogues or main parachutes.

Among the commonly used deployment actuators are:

A coiled metal spring integrated with pilot-chute structure

Gravity pendulum hold extraction-chute pack at rear of cargo aircraft rigged for airdrop

Spring or elastomer-powered catapult

Deployment gun or drogue gun (sometimes called slug-gun)

Ejector Bag (sometimes called blast-bag)

Thruster powered by propellant cartridge or compressed gas supply

Telescoping catapult guns

Tractor rockets

Drogue Deployment Gun. Many recovery systems deploy a first stage drogue decelerator or pilot chute by means of a "drogue gun". A piston weighing from 1/4 pound to one pound (depending on the weight of parachute to be deployed) is propelled from the payload at a muzzle velocity of 100 to 300 fps (depending on dynamic pressure and attitude at deployment). A lanyard or bridle from the "slug" (piston) tows the parachute along behind. Usually the parachute is enclosed in a deployment bag which continues with the slug to separate from the inflated parachute. Figure 3.4 shows a representative drogue deployment gun design.

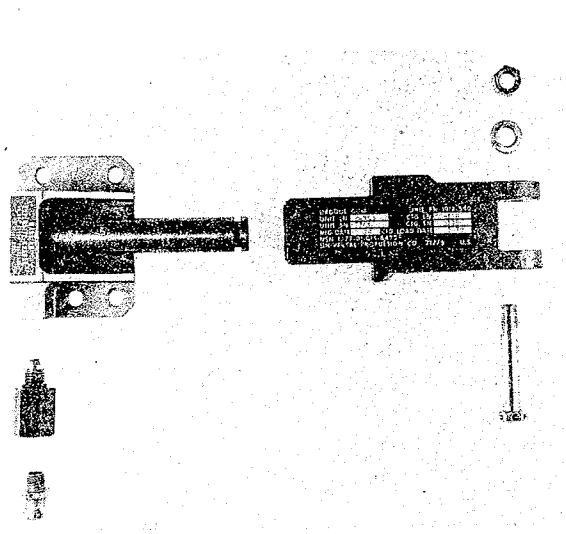


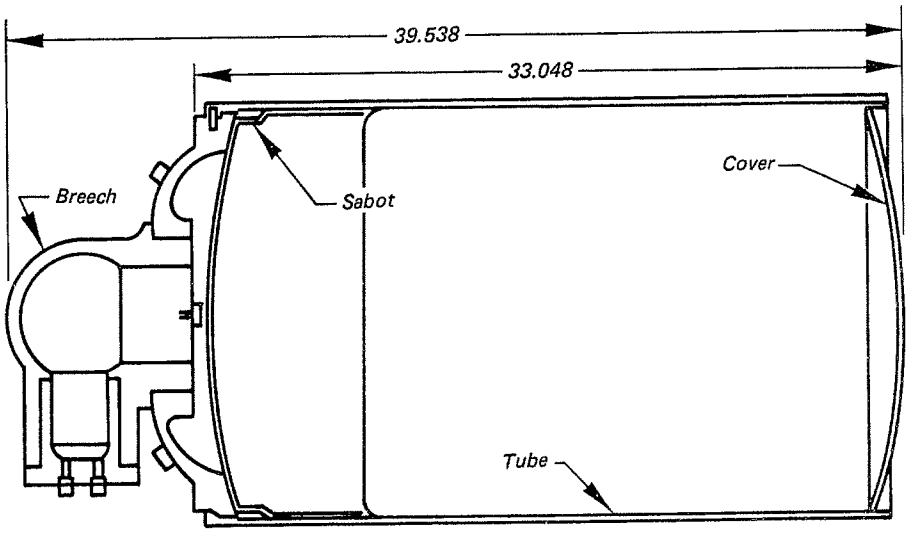
Figure 3.4 Deployment Gun

Deployment Mortar. Where parachute compartment location or payload instability present the possibility of decelerator deployment in a cross-wind or into the wind direction, a deployment mortar is usually used to achieve orderly, reliable deployment. Parachutes weighing from less than 1 pound to over 100 pounds have been successfully mortar deployed at velocities from low subsonic to over Mach 2.0.

Mortars consist of a tube, generally cylindrical, a tight fitting cover held in place with shear pins, shear screws or break links, and a piston known as a ***sabot.*** This is placed inside the base of the mortar tube and serves several purposes:

1. It protects the parachute from the hot gases
2. It provides an O-ring or cup seal to prevent blow-by of the propellant gas, and
3. in some designs the sabot is attached to the mortar base until a threshold gas pressure behind the sabot fractures a calibrated break-bolt or shear pins. Typical mortar design and performance is shown in Figure 3.5.

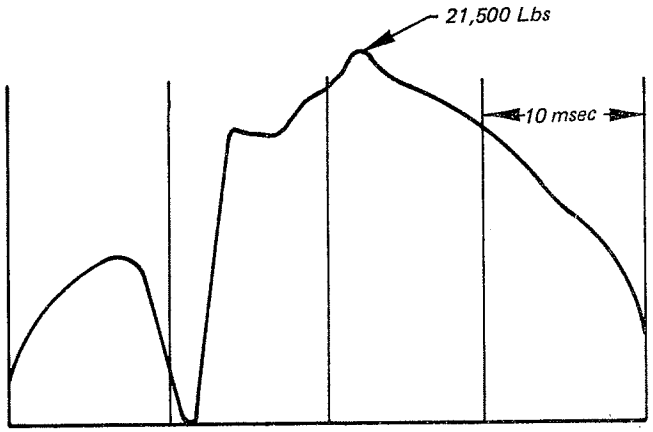
Tractor Rocket. A solid rocket has been successfully used both as a means of deploying an aircraft spin-stabilization parachute and to extract crew members from aircraft not equipped with ejection seats. Reaction of the rocket exhaust through multiple canted nozzles located at the top of the motor casing provides spin stabilization. The payload is connected to the base of the rocket casing through a steel cable and swivel. The weight of a tractor rocket is comparable to that of a mortar to provide equivalent performance.



a) Mortar Assembly (Uses eroding orifice)

	Weights		
Tube	54.5 lbs.	Mortar Vol.	3 cu. ft.
Breech	16.2 lbs.	Parachute Wt.	120 lbs.
Cartridge	2.9 lbs.	Breech Press. Max.	14,700 psi
Sabot	5.5 lbs.	Tube Press. Max.	124 psi
Cover	2.2 lbs.	Reaction Max.	21,500 psi
Total	81.3 lbs.	Muzzle Vel.	134 fps

b) Weight and Design Data



c) Reaction Time-Load History

Figure 3.5 Typical Mortar Design And Performance Data

Catapult/Telescoping Thruster. Telescoping catapults or thrusters are used to deploy the parachute from the aft end of air dropped streamlined stores. The parachute is stowed around the catapult barrel which is located on the longitudinal centerline of the parachute compartment. The breech, cartridge and inner fixed tube member are attached to the forward bulkhead of the parachute compartment. The outer tube attaches to a rigid aft closure or tailcone, and the parachute pack is attached in turn to the rigid aft closure.

When the cartridge is fired, the aft closure, outer barrel and parachute are ejected. In the three-tube catapult design, the intermediate telescopic tube remains with the payload.

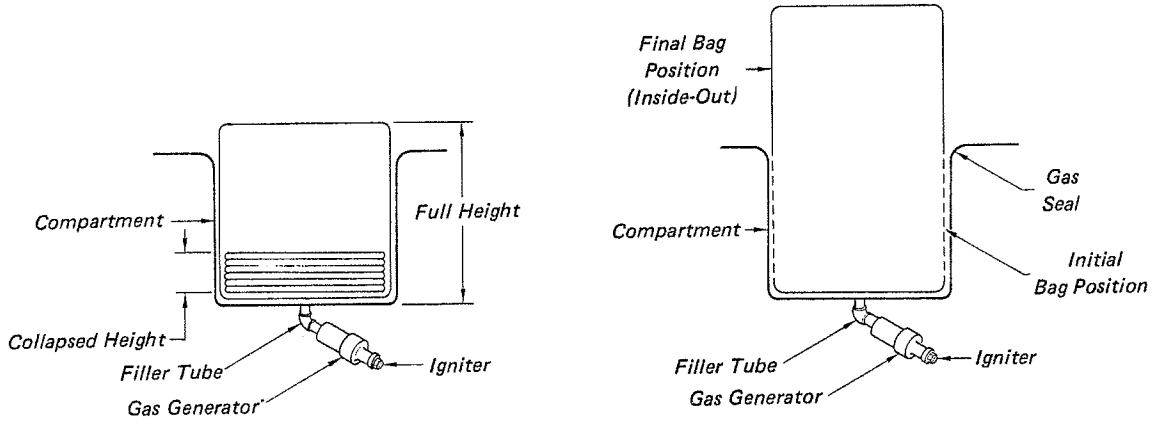
Blast Bag (or Ejector Bag). It is sometimes advantageous to eject a parachute from its compartment with a pneumatic device known as either a "blast bag" or "ejector bag". A blast bag may be used as the primary deployment actuator in a manner similar to a mortar, or it may be used as a secondary device to assist a primary deployment device such as an ejector gun.

The bags are constructed of fabric such as nylon, Nomex, etc., with a flexible coating such as rubber or neoprene to provide zero porosity. They are rapidly filled by a pyrotechnic gas generator. "Cold-gas" generators with gas temperatures of 400° 600°F are often used. Another alternative is the use of a normal temperature gas generator (1000° 2000°F) with a heat exchanger ahead of the inlet to the bag.

Two types of ejector bags are used. The single stroke type is illustrated in Figure 3.6(a). The double stroke type is shown in Figure 3.6(b).

Pack Opening Actuators. Self-contained pack opening actuators are used with military escape parachutes to permit safe escape under hazardous high velocity and/or high altitude flight conditions. Common to all pack opening actuators are a delay timer, aneroid, arming pin, arming cable, hand pull knob and means for connecting the arming cable or knob to the aircraft or ejection seat structure.

In the automatic mode, a typical sequence starts with the arming cable being pulled by separation of the crewman from his ejection seat. If the escape altitude is greater than the aneroid setting, the jumper falls to the preset altitude at which time the ripcord actuator is enabled to operate. In some models, the timer is then started and the ripcord is pulled at the end of the time delay interval. In other models, the timer runs concurrently during the free fall to the preset altitude.



a) Single Stroke

b) Double Stroke

Figure 3.6 Ejector Bags

Automatic Ripcord Releases. Automatic openers are used in personnel parachute pack assemblies. The principle elements in each are an altitude sensor, a timing device and a ripcord puller. The altitude sensor is an aneroid mechanism which blocks the timer escapement and prevenst operation of the coil spring ripcord release at all altitudes more than 1500 feet above its dial setting. The F-1B automatic parachute ripcord release is shown in Figure 3.7.

An aneroid/timer automatic ripcord release, known as the FXC Model 11,000 is in widespread use in military personnel parachute assemblies. The aneroid bellows blocks a trigger, which when released at the preset altitude hits a percussion-initiated pyrotechnic delay cartridge. At the end of the pyrotechnic time delay, the cartridge propellant charge fires into a cylinder, moving a piston. The piston pulls the parachute ripcord. The FXC Model 11,000 automatic opener is illustrated in Figure 3.8.

The Irvin Hitefinder includes both a time delay and altitude setting function. The parachute opening altitude may be preset at any altitude up to 14,000 feet. A choice of fixed time delays between 0.3 and 6.0 seconds is available. It weights 0.40 pounds. The Hitefinder is shown in Figure 3.9.

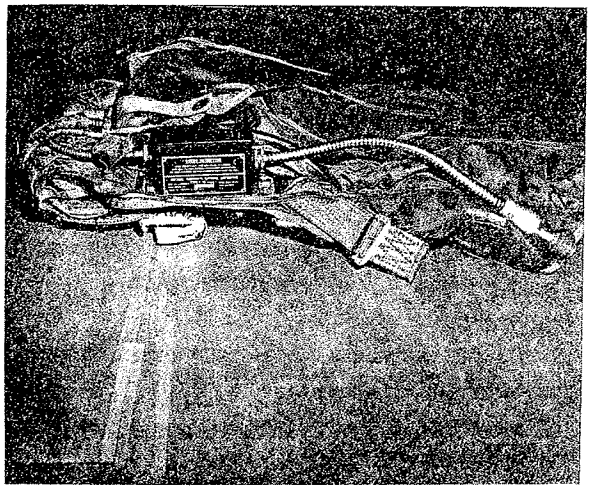


Figure 3.7 F-1B Automatic Release Installed in Parachute

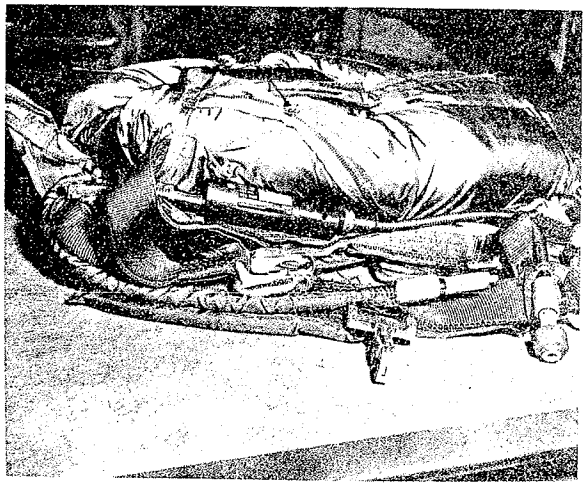


Figure 3.8 FXC Model 11000 Automatic Opener Installed In Parachute

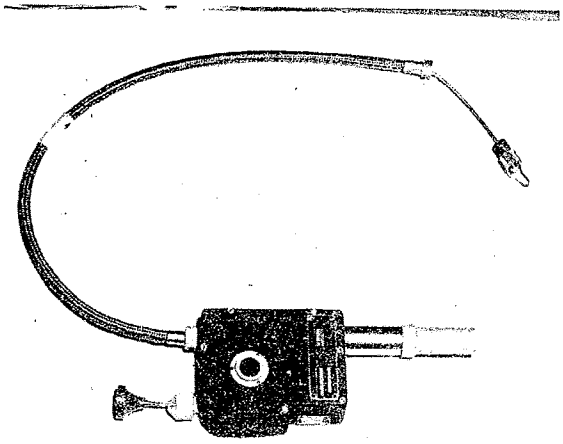


Figure 3.9 Irvin Hitefinder Automatic Parachute Release

Inflation Phase Actuators. Pyro/mechanical devices are used to control the forces developed during parachute inflation and to modulate the rate of inflation.

Canopy Spreader Gun. The need for a recovery parachute that opens quickly at very low speeds and altitudes (zero-zero conditions) has been met in a C-9 personnel version with a pyrotechnic device[227], a multi-radial barreled gun. The gun is positioned at the mouth of the canopy by a retaining cord extending from the canopy apex to the skirt. Figure 3.10 shows the spreading gun assembly with retaining cord at the top and arming lanyard arrangement below. Each of its fourteen projectiles propels adjacent pairs of suspension lines radially outward when the gun is fired.

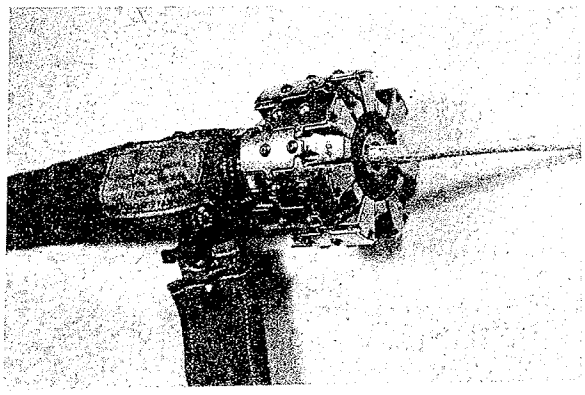


Figure 3.10 Canopy Spreader Gun

Reefing Cutters. Reefing line cutters are available in a variety of sizes and delay times. A cutaway view of a typical cutter assembly is shown in Figure 3.11. The small cylindrical device has a transverse hole at one end through which the reefing line passes. At the opposite end is a lanyard operated sear and firing pin. When the firing pin impacts the primer, the delay powder train is initiated by the flash, and the delay mix burns lengthwise until it reaches the propellant charge behind the knife. The explosive pressure developed then drives the knife and reefing line into the anvil, completely cutting the line. Figure 3.12 shows details of a common small cutter (750-lb nylon cord capacity) and its mounting bracket which may be hand-stitched to the canopy. The cutter then mounts with a small locking ring when the groove of the cutter and the slot of the mounting bracket are aligned. The safety pin must be removed during the parachute packing process. Line cutters are usually available in anodized aluminum, but may be obtained in stainless steel with the pyrotechnic elements hermetically sealed. Steel bodies are recommended if dense pressure packing of the parachute is anticipated. Larger sizes are available (2500-lb nylon cord capacity) similar to the small unit, and others (9000-lb nylon cord capacity) with 2-inches more length and 3/4-inch body diameter are representative. Time delays to 30 seconds and a tolerance of ±10 percent at standard temperature are reasonable, but over a wide temperature range, the accuracy may vary as much as ±25 percent.

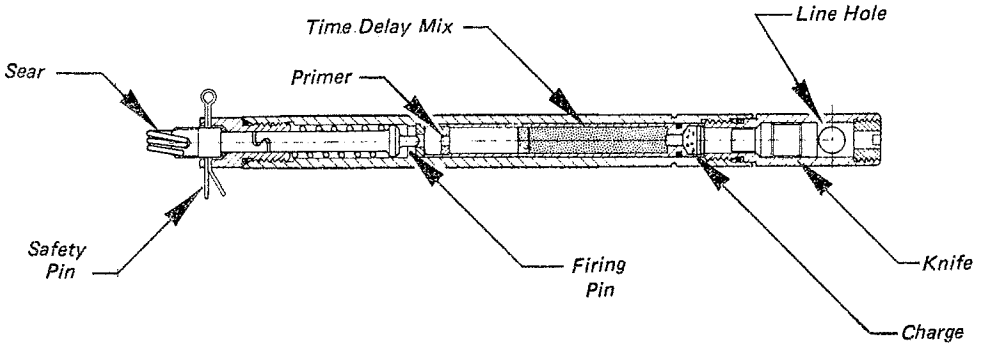


Figure 3.11 Reefing Line Cutter

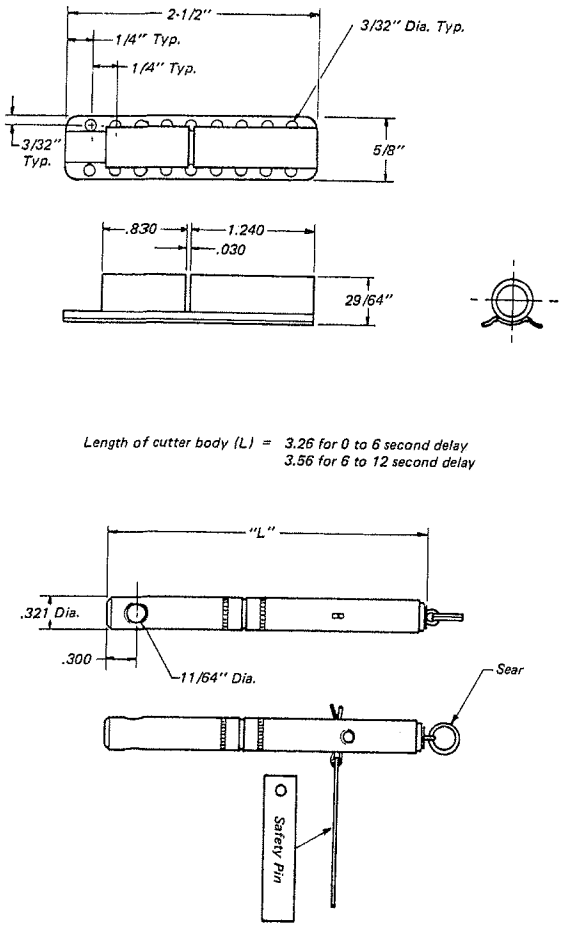


Figure 3.12 Reefing Line Cutter and Mounting Bracket

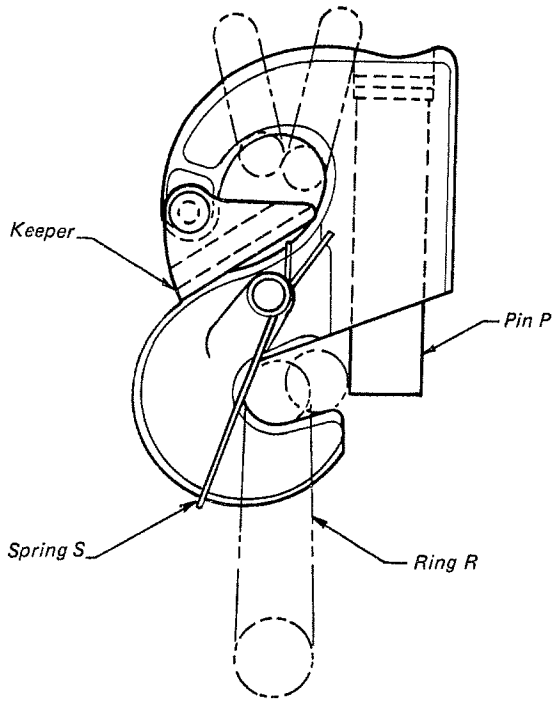


Figure 3.13 Parachute Canopy Release Assembly, Spring Actuated Hook Type

Staging Releases and Disconnects. Mechanical, electrical, pyrotechnic and combinations of mechanical, electrical and pyrotechnic methods are used to separate parachutes from payloads. Disconnects that operate in flight and others that operate at landing have been used.

Mechanically Actuated Release. A spring-actuated hook release that has been used in drone recovery, is shown in Figure 3.13. While the drone is in flight, the spring *S* pushes ring *R* against pin *P*, holding the pin in place. As the parachute is deployed, a load is placed on the ring, and the ring and spring move to the position shown in Figure 3.13, at the same time relieving the friction between the ring and pin. The pin is designed to fall free of the cylinder, when in a vertical position, approximately 10 seconds after release of the friction of the ring. When the vehicle touches the ground and the load is partially relaxed, the spring forces the ring off the then unobstructed hook, disconnecting the parachute canopy. Disadvantages of this design are that foreign matter in the cylinder may cause improper operation of the pin, and that the reduction of imposed stress caused by air currents may result in mid-air separation of the load and parachute canopy.

MARS Release. In aerial recovery systems known as "MARS" (Mid-Air Recovery System), the main parachute is separated from the payload when the recovery helicopter engages the target parachute. This disconnect function is performed by a mechanical actuator known as a "MARS Release". (See Figure 3.14).

The force transmitted from the helicopter at the time of pick-up through the load line to the MARS Release, causes the main-chute-retention shear pin to be fractured. Rotation of the release as the payload swings up behind the helicopter then causes the main parachute attachment fitting to drop off the MARS Release.

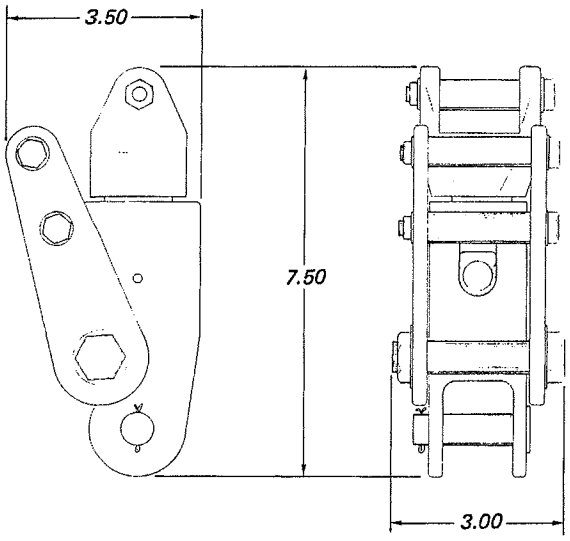


Figure 3.14 MARS Release

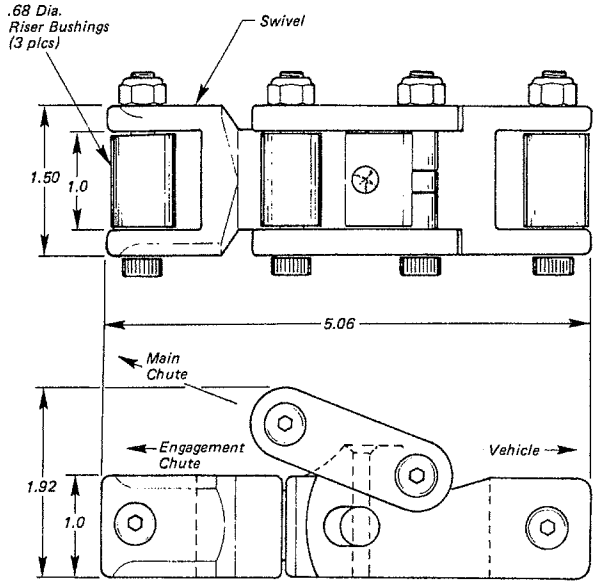


Figure 3.15 Miniature MARS Release

A miniaturized version, designed for use with the Air Launched Cruise Missile is shown in Figure 3.15.

Airdrop Extraction Release. A heavy load capacity transfer coupling arrangement is shown in Figure 3.16. The extraction parachute connects to the load and to the recovery parachutes in deployment bags through a modified three-spool link type load coupling with a latch fitting. The extraction load path goes directly to the cargo through a pintle, latch and connector link assembly until exit of the platform from the aircraft causes mechanical release of the latch. The extraction parachute force then transfers to the deployment bridles to effect deployment of the main parachutes. A cross-section view of the dis-

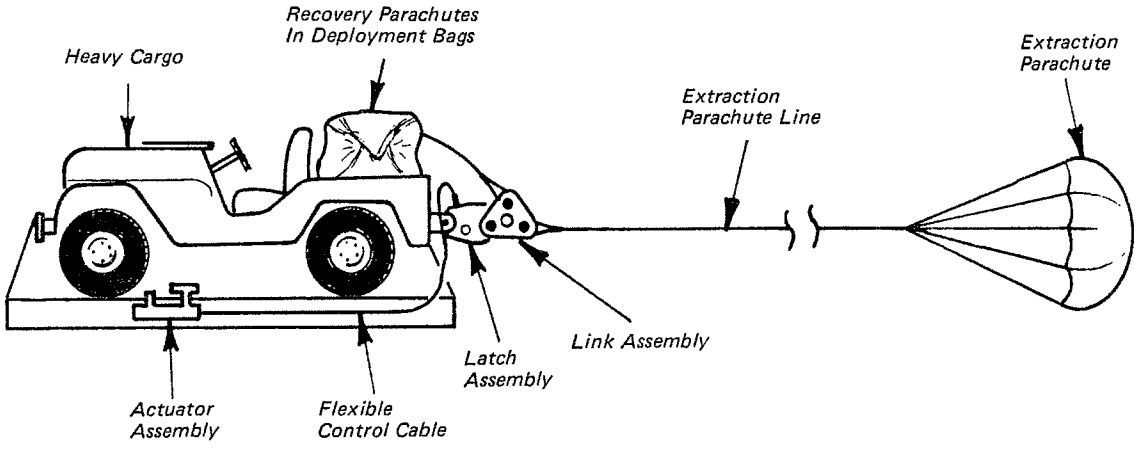


Figure 3.16 Extraction Force Transfer Coupling System (High Capacity)

connect latch assembly (see Figure 3.17) shows the arrangement of the retainer hook as it engages the cam member of the link assembly. Movement of the actuator releases the catch from the lock link, allowing the retainer hook linkage enough offset to free the cam. An open link safety device is added in the deployment line between the recovery parachute deployment bags and the extraction force transfer link. It is rigged to the platform with a 1000 lb restraint tie. The device consists of a locking link, an insertion link and a shear pin. The insertion link is held only by a 200-pound resistance force of the shear pin until a locking cam is triggered by lanyard force of a proper platform travel distance. In an emergency, e.g., in the event the aircraft siderail locks failed to release when the extraction parachute force was applied, the attachment at the platform would be cut away, the extraction line force would shear the pin and the insertion link would leave the aircraft leaving the recovery parachutes undisturbed.

Airdrop Ground Release. Most types of airdrop parachutes remain inflated under moderate wind velocities (10 knots or more) and tend to drag or overturn the load after ground impact. A *disconnect* is a mechanical device used primarily to separate the parachute from the load after ground contact, reducing the chances of damage to the load. Most disconnects operate on the principle of load-stress reduction and incorporate a time-delay element to prevent premature mid-air release during parachute deployment and descent. Disconnects are usually installed between the harness legs of the load and the parachute riser or riser branches, and are available for load capacities ranging from 200 to 35,000 pounds.

Cargo Release, 5000 Pound. The disconnect device shown in Figure 3.18 is used with one G-11A cargo parachute, one to three G-12D cargo parachutes or one G-12C cargo parachute. The eight pound mechanism uses a 20-second delay cartridge. Typical

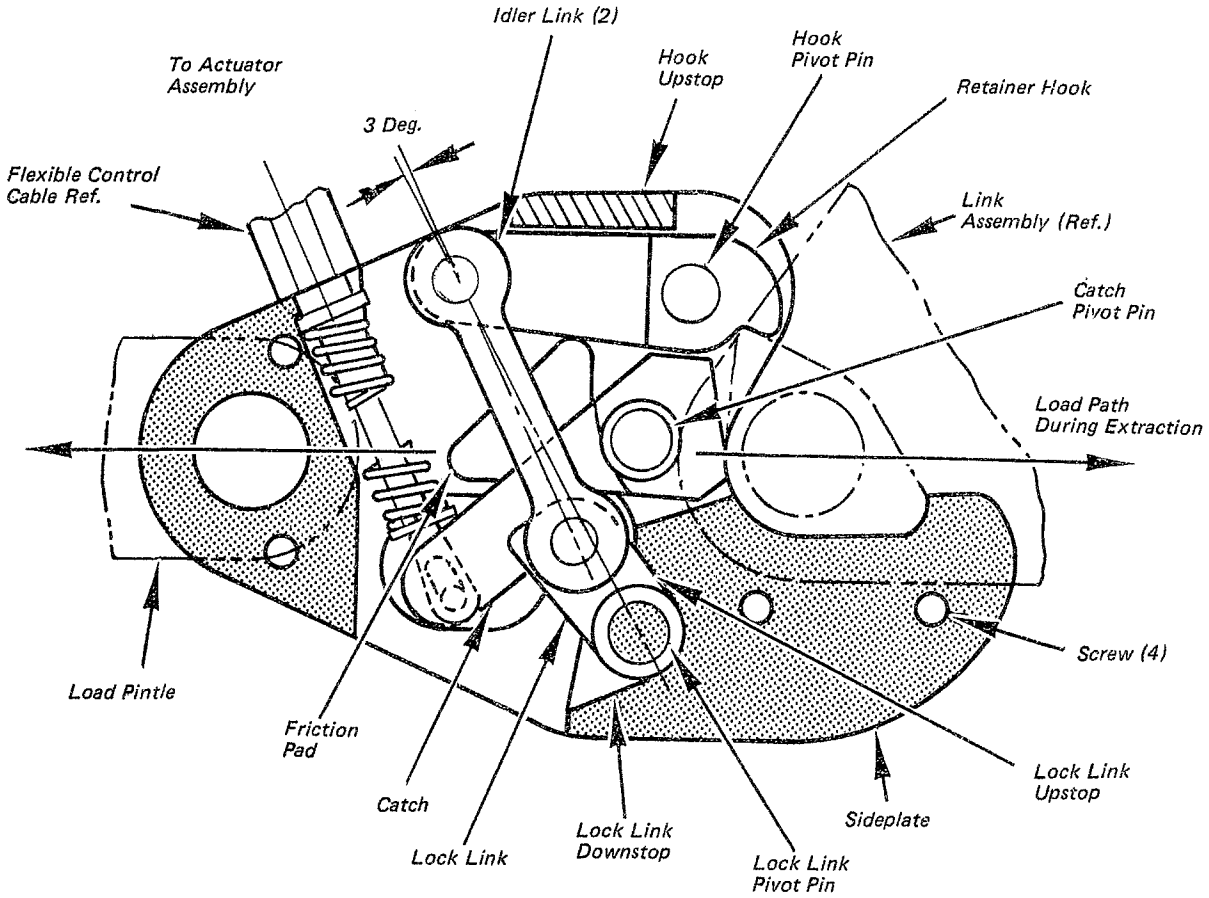


Figure 3.17 Latch Assembly

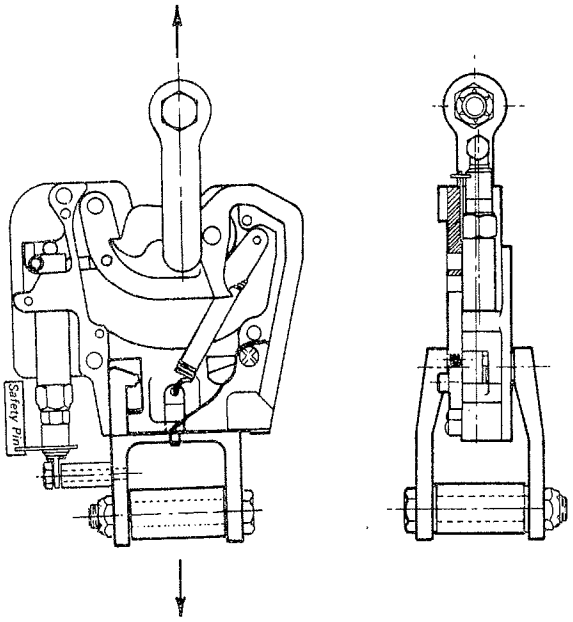


Figure 3.18 Cargo Parachute Release, 5000 Pound Capacity

rigging arrangements which include the 5000-pound disconnect are illustrated in Figures 3.43 and 3.45. Because this device operates on reduction of load tension at ground contact and because in strong winds the parachute remains partially inflated, preventing reduction of tension in the risers, it does not function reliably in winds of over 25 knots[228].

Multiple Release, 20,000 Pound. The multiple release device, Figure 3.19 may be used with loads requiring use and disconnect of three to six G-11A cargo parachutes. A 10-second delay reefing line cutter is required. A release adapter is added for attachment of two clevises. The basic disconnect weighs 31 pounds.

M-2 Cargo Release, 35,000 Pounds. The disconnect device shown in Figure 3.20 is used with six to eight G-11A cargo parachutes. The mechanism was designed to tilt 18 degrees to either side of its vertical plans, and uses a mechanical timer delay device to prevent release of cargo in mid-air. The basic disconnect weighs 17 pounds and measures 9.25 x 8.5 x 17 inches overall.

Personnel-Parachute Releases. Personnel parachute releases are used to jettison the canopy after touchdown to prevent injury to the jumper from dragging. They are of two types, usually manually activated: harness releases and canopy releases. The A/P 28S-2 harness release (Figure 3.21) is used to collect and attach the restraining straps of the parachute harness to a central point on the body of the wearer. Manual actuation of the device simultaneously releases several straps, freeing the harness and canopy from the body. The canopy release (Figure 3.22) is used to separate the canopy from the harness, which remains on the wearer. Two such releases are required for a canopy, one connecting each canopy riser to the appropriate point on the harness. Release activation is manual; each must be opened separately to free the jumper of the canopy.

Ordnance Actuated Releases. Release of decelerators from the payload is commonly achieved through use of explosive powered guillotine disconnects, cartridge actuated pin pullers, explosive nuts, explosive bolts, swing arm disconnects and linear shaped charges.

Pyrotechnic Guillotine Cutters. A typical guillotine disconnect is similar to a reefing cutter in principle of operation (see Figure 3.11). An electrical or mechanical impulse fires a primer, either starting a time delay train burning or igniting the propellant charge in a zero delay unit. At the end of the delay train interval, a propellant charge drives a piston with guillotine knife attached. The knife blade cuts through webbing, cords or cables and inbeds in a metal anvil.

An example of a cartridge actuated in-line strap cutter designed to cut six plies of 10,000 pound (or five plies of 12,000 pound) nylon webbing is shown in Figure 3.23.

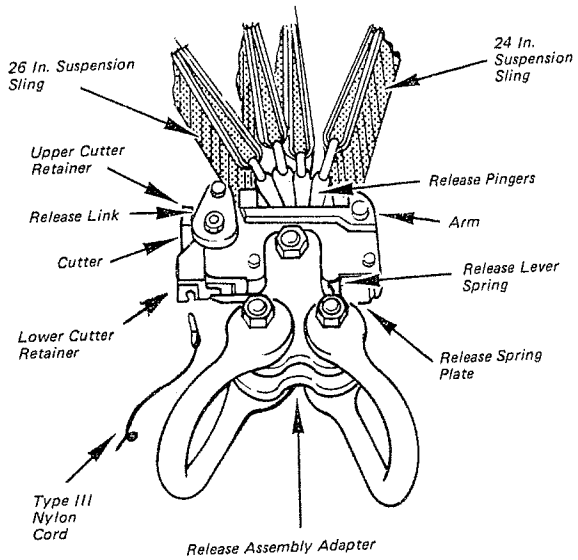
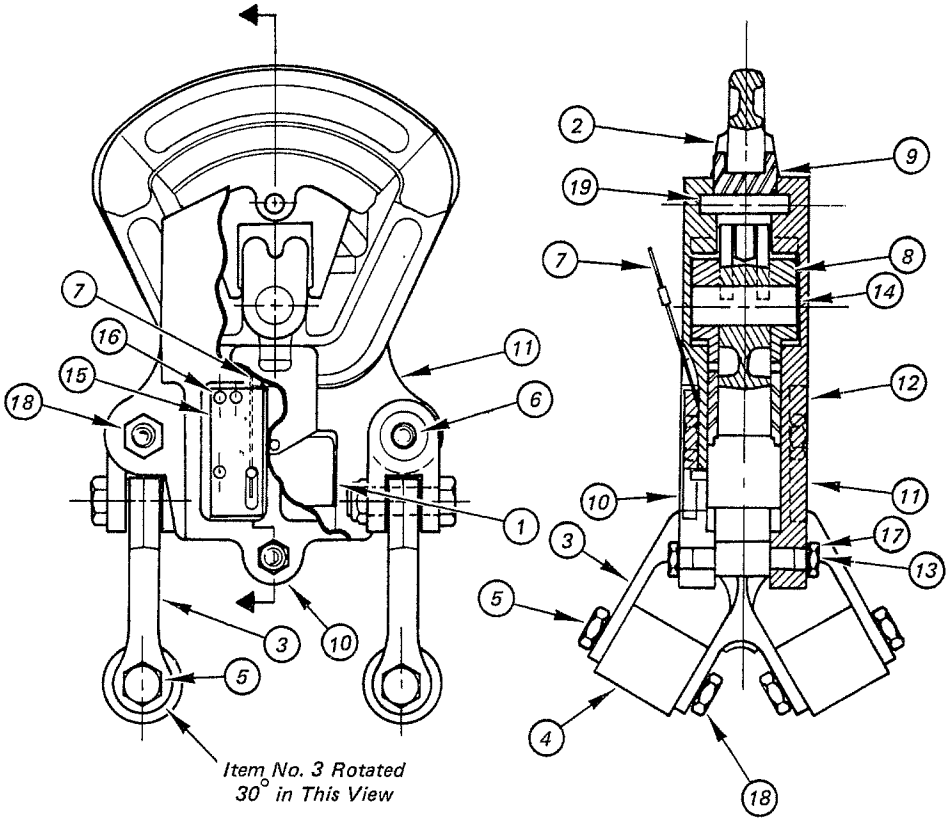


Figure 3.19 Multiple Release Assembly with Adapter, Slings, and Cutter Installed



Item No.	Part No.	Title	Qty.
1	11-1-894	Time Delay - Assembly of	1
2	11-1-477	Link, Suspension - Upper	1
3	11-1-479	Link, Lower Suspension Assy of	2
4	11-1-480	Sleeve, Lower Suspension Link	4
5	11-1-481	Bolt, Sleeve	4
6	11-1-482	Stud	2
7	11-1-493	Wire, Rleease-Sub-assembly of	1
8	11-1-511	Toggle	2
9	11-1-512	Clamp, Retaining	1
10	11-1-513-P1	Plate, Side	1
11	11-1-513-P2	Plate, Side	1
12	11-1-514	Slide, Lock Toggle	2
13	11-1-562	Stud	1
14	11-1-563	Shaft, Toggle	1
15	11-1-899	Guide, Release Wire	1
16	MS-35691	SCR, Cap Hex Soc Hd 10-32 UNF 2A x ¼ lg	3
17	MS-35691-829	Jam Nut ½-20 UNF-2B	2
18	MS-35691-1029	Jam Nut 5/8-18 UNF-2B	8
19	11-1-594	Pin, Retaining Clamp	1

Figure 3.20 Cargo Parachute Release, 35,000 Pound Capacity

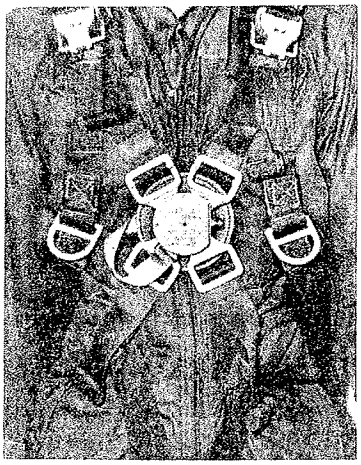


Figure 3.21 A/P 28S-2 Personnel Harness Release

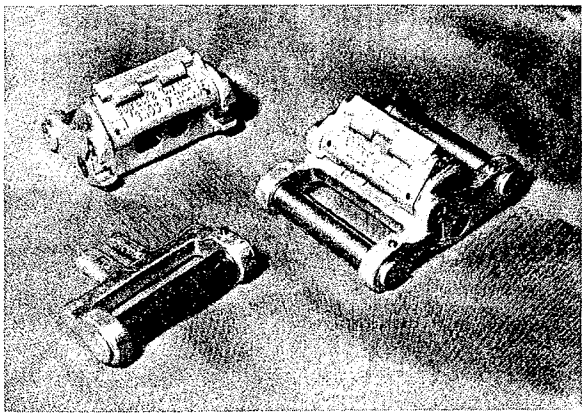


Figure 3.22 Personnel Canopy Release

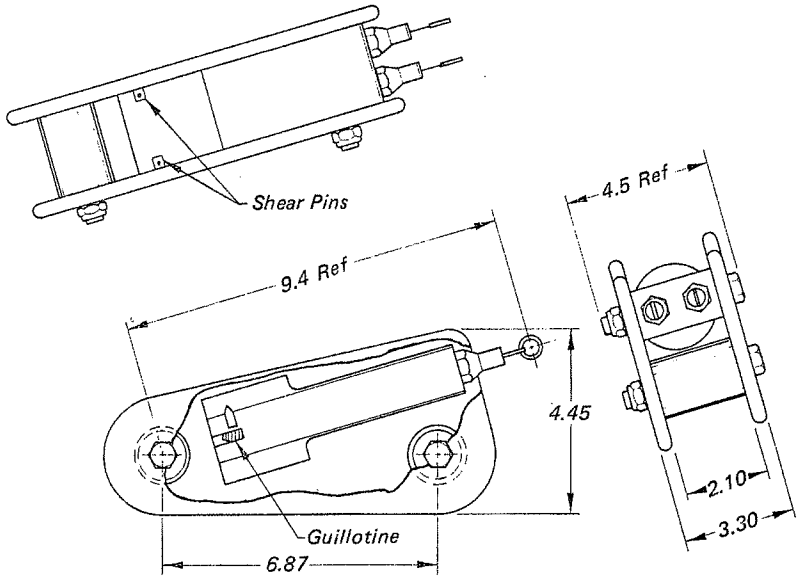


Figure 3.23 Cartridge Actuated In Line Strap Cutter

Pin Puller Disconnects. Releases have been used where pyrotechnically generated gas pressure is used to remove a clevis pin, thus disconnecting the decelerator riser end loop.

Swing Arm Disconnects. Several versions of cartridge or squib actuated swing-arm disconnects have been used in missile drone and spacecraft recovery systems. In this scheme, a hollow hinge pin is held in place by a piston inside the hollow pin. Gas pressure from the cartridge pushes the piston, freeing the hinge pin to rotate through an arc of approximately 180 degrees. The riser end loop slips off the hinge pin as it rotates, permitting the decelerator to sepa-

rate from the payload. Figure 3.24 shows the early model, known as a "Radioplane" release which uses electric squibs (with lead wires). Figure 3.25 illustrates an improved (Gould) model which uses a threaded case electrical cartridge.

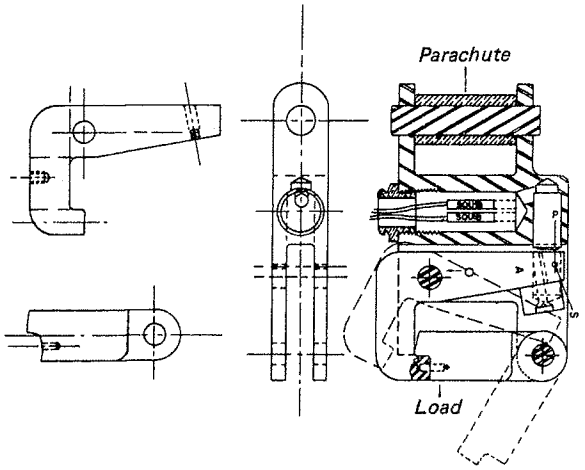


Figure 3.24 Parachute Canopy Release Assembly, Latch Type

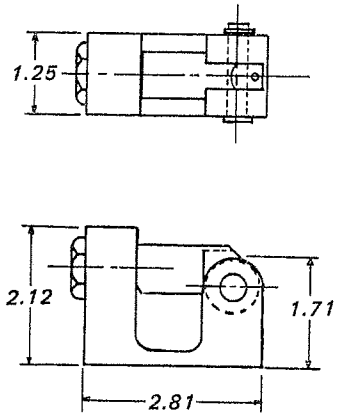


Figure 3.25 Single Initiator Parachute Release

Explosive Bolts, Explosive Nuts. Explosive bolts or explosive nuts have been used to cause separation of a decelerator riser or a section of the payload structure (with decelerator attached). A typical release operated by an explosive bolt is the "hand clasp" fitting used in conjunction with the Mid-Air Recovery System (MARS) release.

Shaped Charge. Two types of explosive shaped charge have been used to perform the decelerator disconnect function. In one type, the riser webbing is severed by the blast of hot gas from a shaped charge in a housing that surrounds the webbing. In the other type, metal support structure for the decelerator is cut by a ring of linear shaped charge or mild detonating fuse.

DECELERATOR SUBSYSTEM

Parachutes, rotors and inflatable balloon type decelerators are described in Chapter 2 and a few construction details related to parachutes are shown in Chapter 4. These items are the major components of their respective type decelerator subsystems. Components of the subsystem other than decelerators are described and discussed in this section. They are either suspension members or items which contribute to the stowage or deployment of the decelerator, plus interconnecting metal parts. With the decelerator included, this group of components constitutes a decelerator subsystem. Representative decelerator subsystem components are identified in Figure 3.26.

Stowage and Deployment Components

Stowage Components. Decelerator subsystem details are generally similar within the several recovery system application categories except in the method of containment. Personnel and airdrop systems are of necessity unsophisticated, and deployable components are usually contained and mounted in a pack assembly external to the load. On the other hand, flight vehicle recovery systems usually require that deployable components be stowed within the vehicle contour in order that flight characteristics of the vehicle be preserved until recovery is initiated.

Compartments. Provisions in a flight vehicle for containment and interfacing with the decelerator subsystem may take the form of a simple tailcone shell or a special shaped cavity with a thin metal cover as shown in Figure 3.27. The Mercury system installation is an example of a more complex stowage arrangement (see Fig. 1.6). Compartment shape

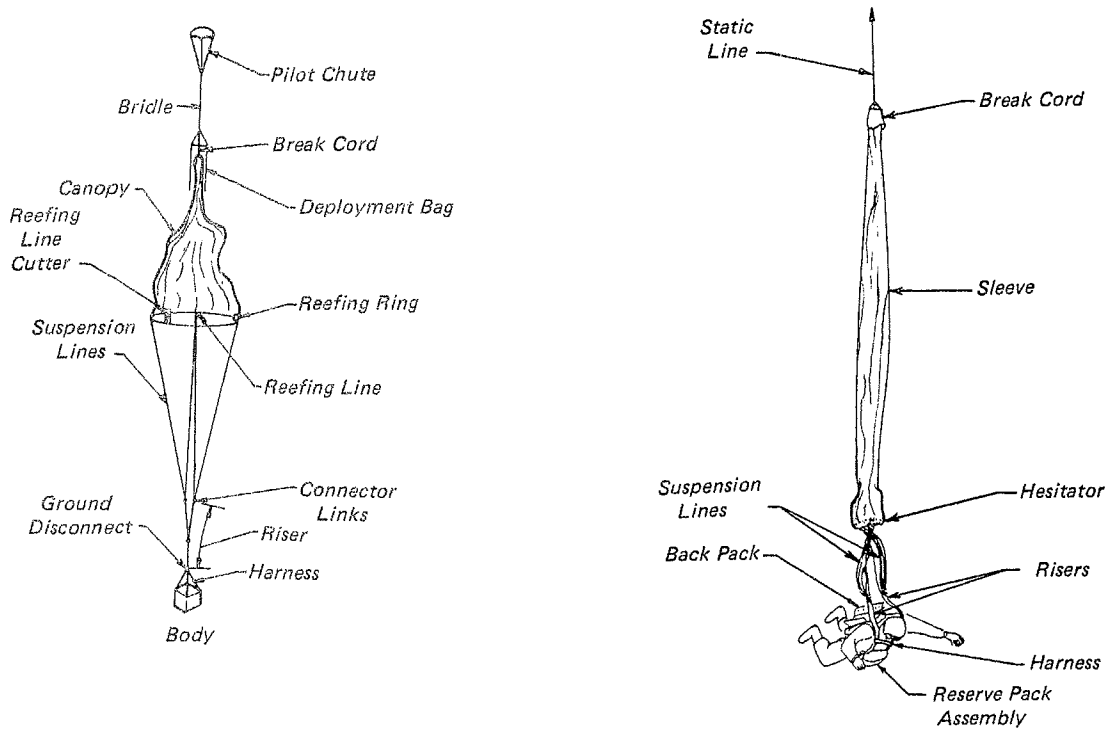


Figure 3.26 Components of Typical Decelerator Subsystems

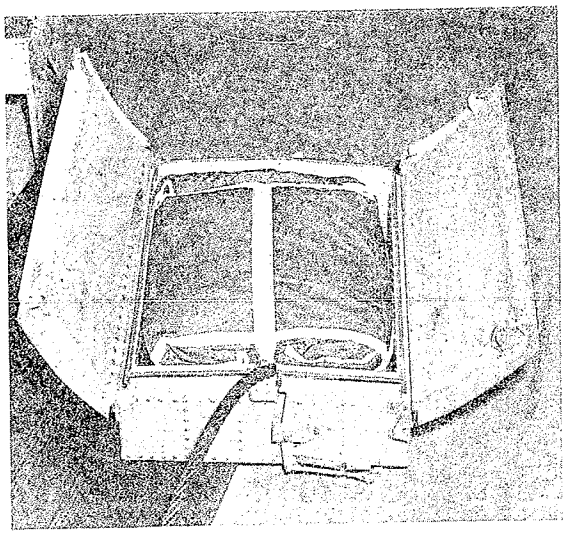


Figure 3.27 Typical Storage Compartment

and decelerator attachment details are dependent upon the particular vehicle design for available space and structure. Separable compartment liners constructed of sheet metal or fiberglass laminate provide a smooth surfaced container for parachute stowage in a vehicle. Fabric flaps attached to the compartment walls are sometimes incorporated to provide temporary restraint of the main parachute pack during a drogue stage or during pilot chute deployment from the same compartment. A cylindrical mortar could serve as the stowage compartment to house a single stage decelerator system while it also provides the actuation means for deployment. Although components, such as compartment liners, attachment hardware and access covers are normally considered part of the vehicle, some recovery systems have been packaged with these parts in an integral assembly that requires nothing more than to be inserted into the vehicle cavity and bolted in place to complete the recovery system installation.

Packs. Decelerator packs are designed for insertion into a rigid compartment, or to be strapped on the outside of a payload and remain in place during extraction and deployment of the decelerator. The personnel parachute pack is of the latter type. Packs are constructed of nylon fabric forming a center panel usually with stiffeners, plus side and end flaps

which fold over and contain the arranged layers of the parachute canopy and suspension lines. Standard personnel packs are in use for different types of parachutes and for attachment to the back, chest, or seat of the wearer. An example of a typical pack is shown in Figure 3.28 . Standard US Army and Air Force packs and US Navy containers (synonomous with packs) are listed in References 229 and 230 respectively.

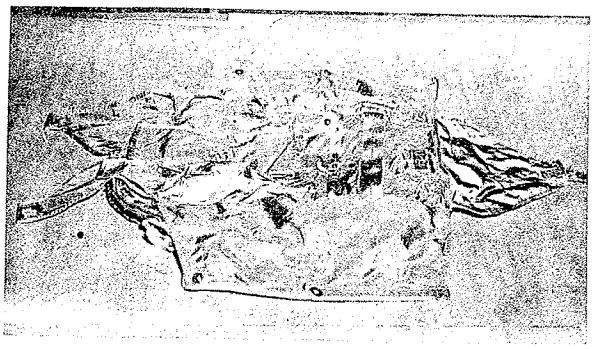


Figure 3.28 Typical Pack Army/Air Force

Personnel packs are anchored to the body harness. They are designed to unlock at the pull of a ripcord or a static line. Because the pack remains with the body, deployment from a pack is normally "canopy-first" with suspension lines and risers stowed to progressively unfold and deploy from cloth loops or channels stitched to the pack backing or flaps as depicted in Figure 3.29. Some pack assembly arrangements incorporate a modified bag or sleeve to restrain opening of the deployed canopy. The bag or sleeve restrains the canopy skirt until stretch of the final loop of suspension lines deploys from the bag.

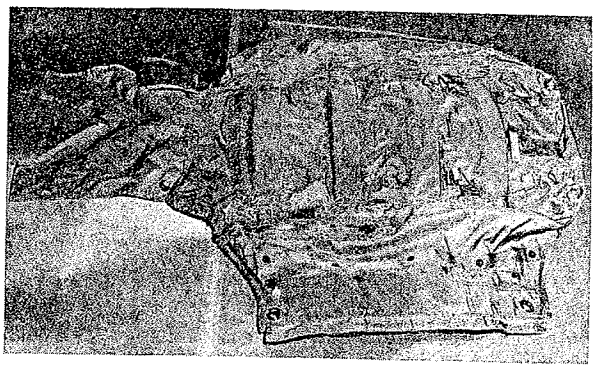


Figure 3.29 Pack Showing Flaps

Sequence Flaps. In some instances, the use of sequencing flaps is useful in achieving retention and subsequent release of a parachute system. This is advantageous for recovery systems which have stowage and related deployment problems. Several means of securing and releasing sequence flaps (cutters, pins, etc.) are used.

Deployment Components. Items which provide either a continuing deployment force (pilot chute, static line), or in some way restrict the mouth of a parachute from opening while suspension lines and canopy are incrementally extended, are classed as deployment components. These items move away from the body with the deploying decelerator, as distinguished from a stowage component class.

Pilot Parachutes. A *pilot chute* is a small parachute used to aid and accelerate main parachute deployment. Pilot chutes may be of the conventional ringslot, ribbon and ribless guide-surface types, or of specialized design having shaped solid cloth canopies with ribs or vanes and internal springs (Figure 3.30). The internal spring ejects the parachute and aids opening. The vanes align the parachute with the airstream and ensure good opening reliability. Used in sizes to 6 ft there are numerous designs of the canopy including hemispherical, biconical, square, etc.

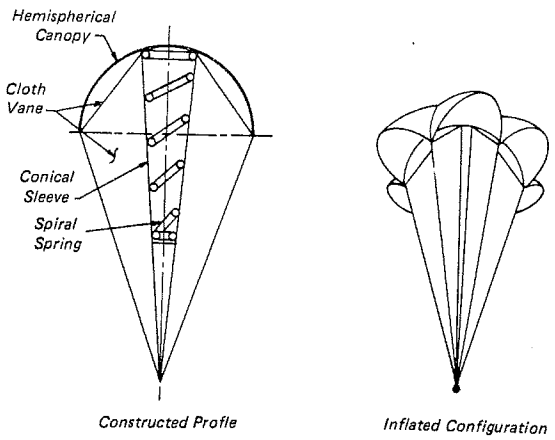


Figure 3.30 Vane Type Pilot Chute

Bridles. A *bridle* is a connecting line, usually used to attach a pilot chute to the apex of a large parachute, or to a deployment bag as shown in Figure 3.26. Bridles are constructed of line material, usually of nylon webbing or cord, with a loop provided at each end to facilitate attachment to parachute apex lines and a pilot chute. Bridle length and strength depend upon conditions of their specific use and therefore, are not found as standard supply items except in personnel or aerial delivery kits.

Static Lines. A *static-line* is a fixed bridle between the launch aircraft and the parachute apex, or between the launch aircraft and a deployment bag or sleeve. Static lines are similar to bridles in material and design. Their length is usually determined by the minimum safe clearance distance from the launch aircraft.

Break Cords. A *break cord* is a thread, light cord or tape used as a tie link or restraint that is intended to break under load during deployment. For example a "break cord" is used to attach a static line to a parachute apex.

Bags. A *deployment bag* is a parachute container used to provide controlled and incremental, orderly deployment of riser, suspension lines and canopy, in that order, as the bag moves away from the body in the process.

Full Bags. Deployment bags are used in all types of recovery systems and are made in a variety of configurations, some highly specialized. Essential features include separate compartments for canopy and suspension lines, plus closure flaps locked with line bights or other means of ensuring unlocking at line-stretch. Provisions are made for retaining the suspension lines in short bights, and deployment bags designed for bridle extraction (rather than forcible ejection) have strong longitudinal reinforcement members integrated with a bridle harness on the down-stream end. Pictures of several different deployment bags are presented in Figure 3.31.

Closure flaps of deployment bags are often secured closed with textile tape or webbing loops which must be strong enough to stay locked during handling, installation, and deployment, yet unlock or open readily at the proper point near the end of the deployment sequence. Figure 3.32 illustrates a simple method of keeping a packed parachute in its deployment bag until the lines are fully deployed. The underneath flap has two "locking" loops which extend through matching slot holes in the over-flap. Where inner flaps separate the line and canopy compartments, the last two bights of the suspension line

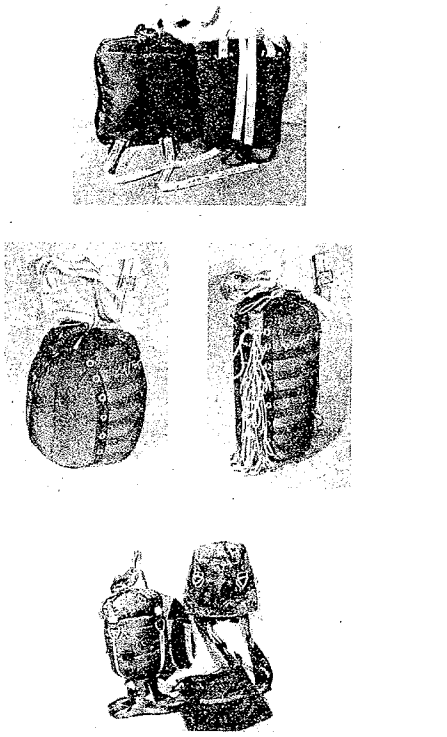


Figure 3.31 Several Different Deployment Bags

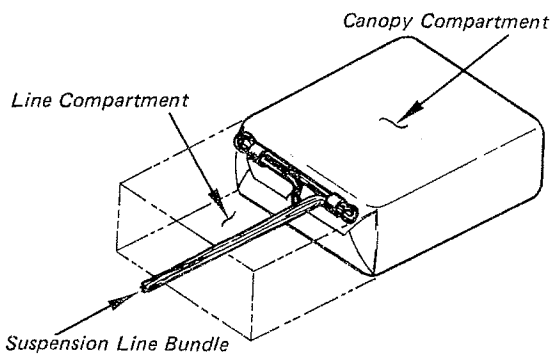


Figure 3.32 Line-Bight Locks Inside a Deployment Bag

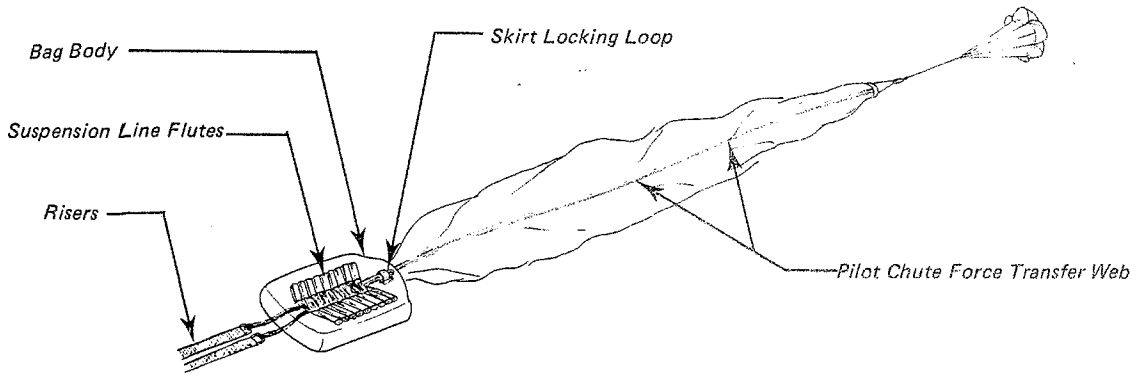


Figure 3.33 Quarter Deployment Bag

bundle are inserted through the loops to lock the canopy compartment. Line stows filling the remainder of the line compartment of the deployment bag are similarly held in place by line stows passing through locking loops in the closure flaps at the end of the deployment bag.

Quarter Bags. A quarter bag (Figure 3. 33) takes the form of a modified deployment bag tightly embracing and containing only the lower quarter of the canopy. Suspension lines are stowed on the outside in a series of bights secured snugly in a series of cloth tunnels or flutes. A skirt binder locking loop at one end of the array completes an arrangement which has the advantage of preventing the premature opening of the canopy mouth during "canopy-first" deployment until the lines are fully stretched.

Skirt Hesitators. A ***hesitator*** is a restrictive tie, usually a combination of encircling webbing or tape loops secured with a break cord, which wraps around the folded skirt of a canopy. A bight of the suspension line bundle is usually included to break and free the hesitator at line stretch. Hesitators take several forms depending on requirements. An example of a parachute skirt hesitator which uses reefing line cutters to free it is shown in Figure 3.34.

Sleeves. A ***sleeve*** is a tapered fabric tube used to contain and restrain the stretched out canopy during the deployment process.

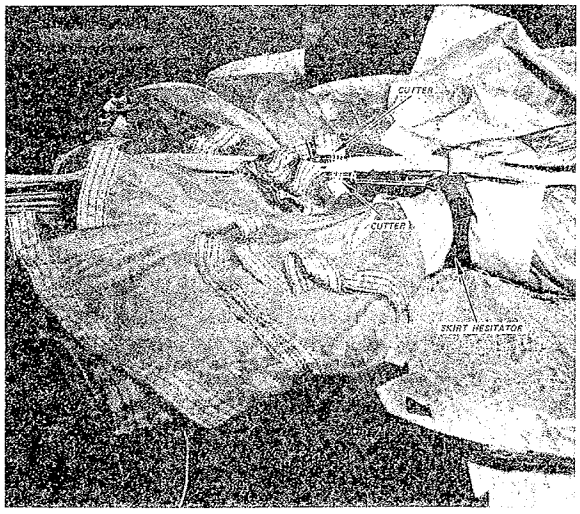


Figure 3.34 Skirt Hesitator/Uses Reefing Line Cutters

Full Sleeves. The full canopy sleeve (Figure 3.35) is designed to perform the same functions as the quarter bag with the added security and protection provided for the canopy during "canopy-first" deployment. This feature makes the sleeve well adapted to ensure orderly deployment of more complex canopies, e.g., gliding parachutes, when the use of a conventional deployment bag is not satisfactory.

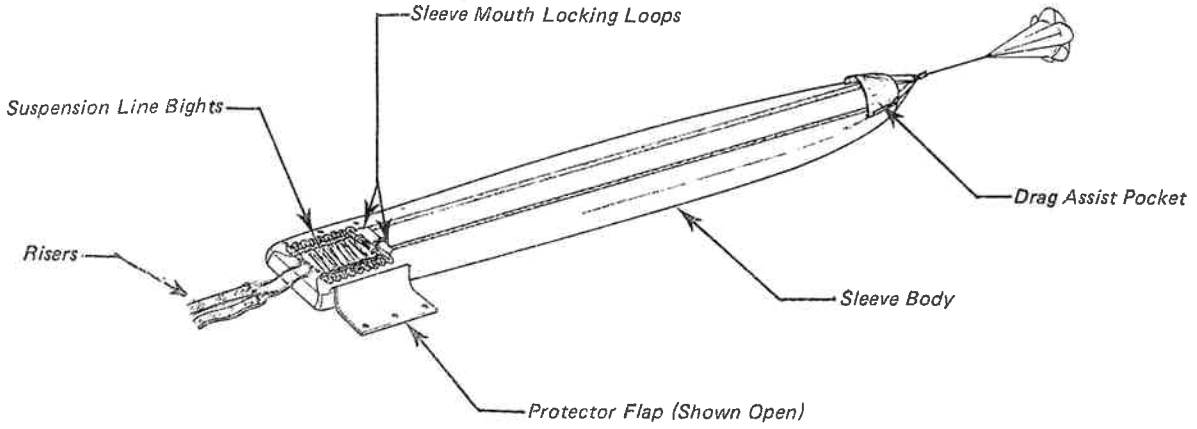


Figure 3.35 Deployment Sleeve

Aprons. Deployment aprons resemble deployment sleeves, with the exception that they are not tubular in configuration. Although it performs the same beneficial deployment functions of both a quarter bag or a sleeve, its wrap-around configuration allows it to expose the deployed canopy at full line stretch with the added advantage of its being permanently attached to the canopy. Aprons may be designed to fully enclose the whole canopy, like a sleeve or just the skirt portion, like a quarter bag. In both cases, it remains attached after the parachute is fully opened.

Suspension Network Components

As a general rule, decelerator suspension lines are not attached directly to the recoverable body or payload unless unusual requirements prevail. A weight saving may be gained by omitting the riser, the harness, and that portion of suspension lines length not needed to preserve a proper confluence angle. However, the saving may be offset by the inconvenience or complexity of multiple attachment points and, in some installations, the problems of packing and deployment interference. Because of the numerous suspension configurations possible, each case must be judged on its own suitability to meet requirements.

Ordinarily the harness serves to translate decelerator forces from the riser to two or more points on the body. A desired body attitude also may be established by selecting harness leg lengths to attachment points at a proper distance on each side of the vehicle center of gravity.

Risers. A riser is a flexible load bearing member, the elements of which are usually all-textile, but may be steel cable or part textile and part cable. The decelerator end of the riser often has two or more branches to which the decelerator suspension lines are attached. The number of branches depends upon the number of suspension lines to be accommodated and size of the lines. A keeper is usually incorporated at the confluence point where the single riser divides into branches. A ***keeper*** is a length of webbing formed as a snug collar around suspension lines or riser branches to resist parting forces at the confluence point or at the neck of end loops. Figure 3. 36 shows a typical riser assembly constructed using layers of textile webbing arranged with a large loop at the load end, and smaller loops on each riser branch at the opposite end. The loop method shown is only one of several ways to attach suspension lines to risers. Other means of line attachment are discussed starting on page 189. The length of a riser varies according to its use. A short riser may suffice for a single main parachute, whereas longer lengths are usually used for drogue decelerators or parachutes in a cluster arrangement.

An extra large parachute may employ long riser branches above the confluence point. The 100 ft diameter G-11A parachute, for example, employs twelve 50 ft branches and 30 ft long suspension lines. The length of riser below the confluence point is 20 ft in length, and the procedure for extending the riser for cluster use is to add riser extensions in 20 ft increment slings[79]. A ***cargo sling*** is a continuous loop of nylon webbing made in standard strengths and lengths, used for cargo rigging.

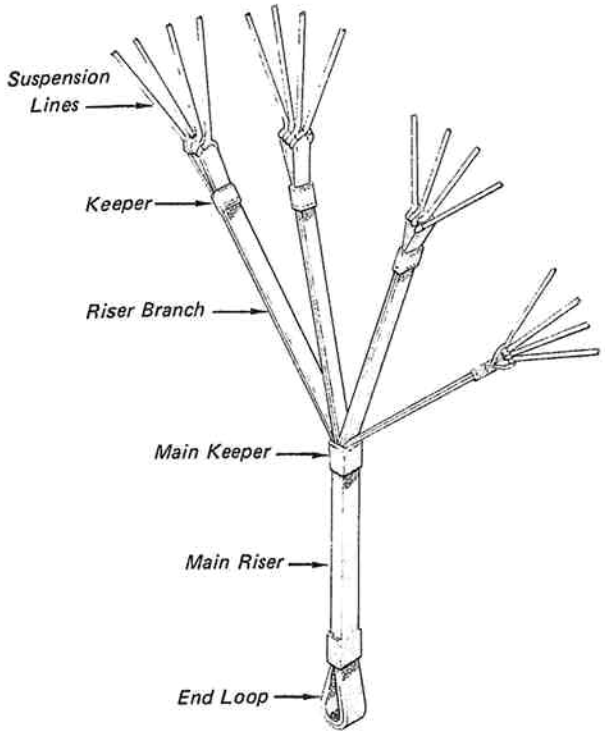


Figure 3.36 Typical Riser with Branches

Extraction Lines. Cargo loads, too large or too heavy to be packed into airdrop containers are placed on and secured to a platform. Platform airdrops, employ an extraction parachute to provide the steady force required to pull the load rearward and out of the aircraft. An ***extraction line*** is a long "riser" connecting the extraction parachute to the load. The line length must be sufficient to minimize aircraft-wake effects. A representative extraction line could be made up of three 20 ft slings. Figure 3.37 shows a typical extraction and transfer sequence to main parachute deployment.

Harnesses. A typical suspension arrangement for cargo is represented in Figure 3.38, where the harness consists of standard sling elements to four hardpoints on the load. Similar systems are used for military vehicles but with a load bearing platform and paper honeycomb rigged beneath the load for absorbing the energy of impact [231]

Harness design is governed mainly by the body configurations or the nature of the payload. The harness members are usually made of textile webbing, but may be of stranded steel cable if conditions warrant. Harness attachment points must straddle the decelerator force vector through the vehicle center of gravity in order to achieve stability. Representative harness configurations to effect vehicle stabilization are shown in Figure 3.39.

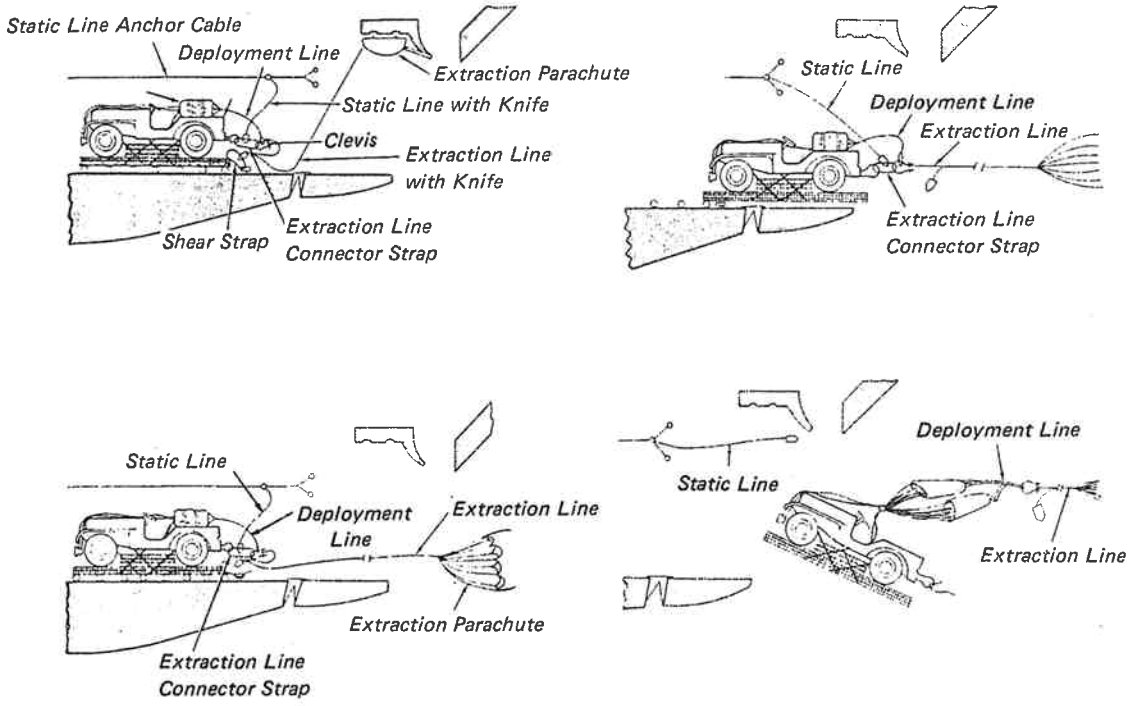


Figure 3.37 Typical Extraction and Force Transfer Sequence

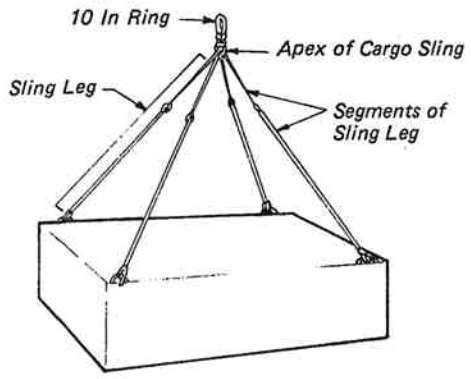


Figure 3.38 Representative Cargo Harness Assembly

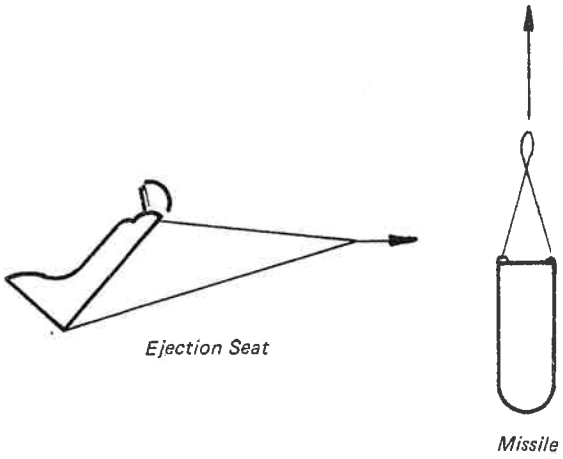


Figure 3.39 Harness Configuration for Vehicle Stabilization

Some recoverable vehicles have more than one functional attitude during the recovery sequence. This changing geometrical requirement has been accommodated by an unconstrained harness on vehicles able to withstand the shock and rotational acceleration induced when the opening force of the decelerator loads only the forward leg of the harness (see Figure 3.40). The vehicle quickly stabilizes and presents a horizontal landing attitude when descending vertically. The second example shows a stable harness arrangement in two positions, the second position resulting from disconnect of a point on one leg of the first position harness. This two-stage harness arrangement accommodates parachute opening forces in one direction on the vehicle, and after reaching

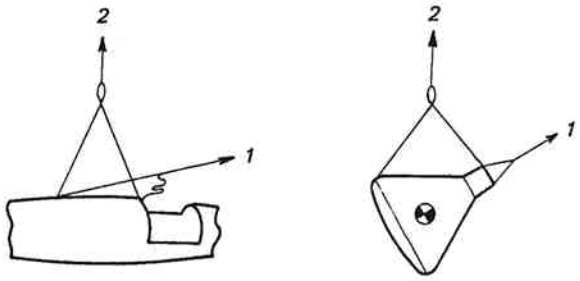


Figure 3.40 Two Position Harness

equilibrium descent conditions, changes to a more acceptable vehicle attitude for water entry of a man-carrying spacecraft.

The personnel body harness is primarily a webbing seat "swing" which transmits opening forces to the wearer's torso in the most desirable manner. Risers may be releasable or an integral part of the body harness. Chest strap, back straps, and leg straps contain the torso within the seat "swing" portion of the harness assembly during parachute opening. The use of adjustable type hardware increases the adaptability, comfort, and safety of personnel harnesses.

Hardware

The functional and service requirements of decelerator subsystems are supplied by a variety of metal connector links, adapters, harness snaps, rings, buckles, release links, and various miscellaneous pieces of hardware. Most of the load bearing links are forged to a smooth and rounded shape from alloy steel, heat treated for high strength and finished with cadmium plate or phosphate coating. Commonly used personnel parachute hardware items, most of which are depicted in Figure 3.41 are commercially available from a number of respectable suppliers. Typical of most linkage items is a 1-3/4 inch wide by at least 1/4 inch opening to accommodate standard harness straps and webbing.

Connector Links. Connector links are used to attach suspension lines directly to risers or to attach one part of a harness to another. There are three basic types.

Solid. A solid link is a rectangular ring used mostly for fixed harness joints, and occasionally for line connectors.

Separable. Links are made in two parts which can be separated to engage a webbing loop, reassembled and locked with two screws. Separable links are a principal means for joining groups of suspension lines to a riser branch (see Fig. 4.25).

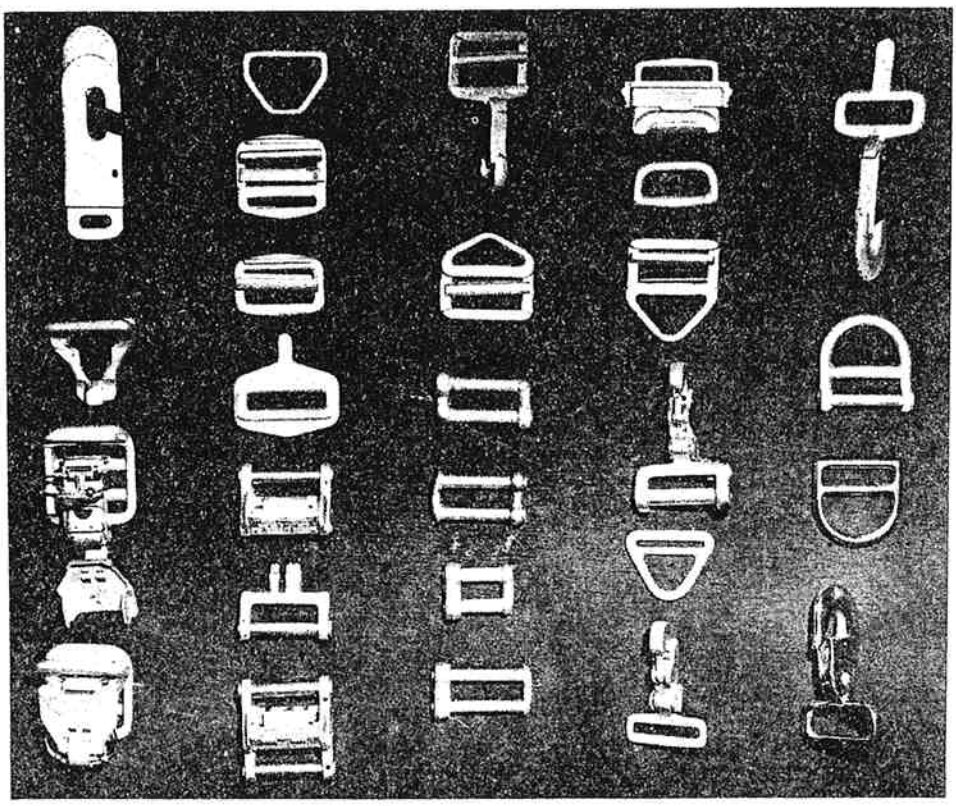


Figure 3.41 Hardware

Speed. A speed link has a removable end bar which snaps into place and is locked with a single screw. They are easy to loosen with a screw driver and quick to disassemble and assemble.

Adapters. An adapter has a rectangular frame and a sliding "friction" or fixed center bar. They are used for adjustment rather than connection of straps.

Rings. D-rings mate with snaps and are usually mounted to webbing ends by a stitched (fixed) loop since they are non-adjustable. Most D-rings are 5000 pounds rated strength. V-rings are similar to D-rings except in ring shape, and may be adjustable or non-adjustable. A rated load capacity of 2500 pounds is typical.

Snaps. Snaps or "snaphooks" usually mount to webbing ends in order to connect easily and reliably to rings mounted elsewhere on a harness or webbing. The hook includes a spring loaded guard to prevent inadvertent disconnect, once engaged. Snaps which are adjustable include a sliding bar for binding the position of the webbing loop against slippage under load.

Cut Knifes. With only the decelerator riser end protruding, deployment bag closure flaps are usually locked closed with a strong lacing that must be cut as soon as the bag moves out of its compartment far enough to stretch the risers. A cut knife of the type shown in Figure 3.42 is used for this purpose, usually actuated by a short lanyard attached to an external riser bight. Packs may be secured and opened with a cut knife attached to a static line for canopy-first deployment. The cut knife must be secured to the pack or harness with three thread "tacks" to prevent any cutting action prior to its actuation.

Swivels. Swivels are integrated into a riser/suspension line system of rotating or spinning payloads being recovered in order to prevent suspension line winding or twisting, and possible resultant parachute opening failure. Swivels are available in various sizes and configurations.

Reefing Rings. Parachute reefing rings are available in 1/2-inch and 5/8-inch diameter hole size, made of carbon steel, smoothly finished with rounded edges and cadmium or chromium plate. Larger

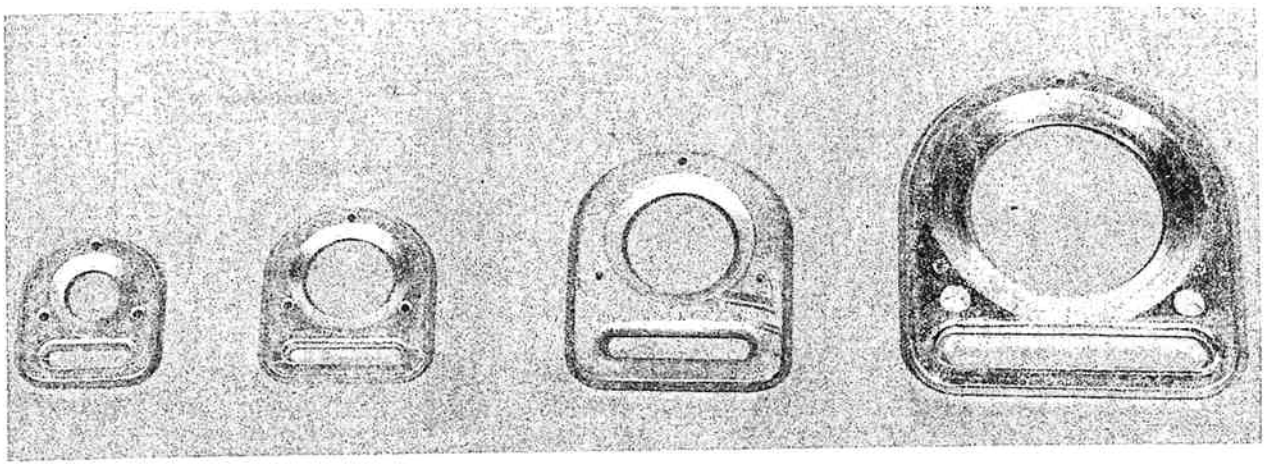


Figure 3. 42 Cut Knives

and stronger rings and double rings have been fabricated to satisfy special reefing requirements.

Clevises. A "clevis" is a U-shaped metal fitting with a hole at the ends, aligned to receive a thru-bolt or a pin. They are available commercially over a wide range of sizes and load capacities. Figure 3.43 shows a typical cargo suspension main riser assembly using clevis links.

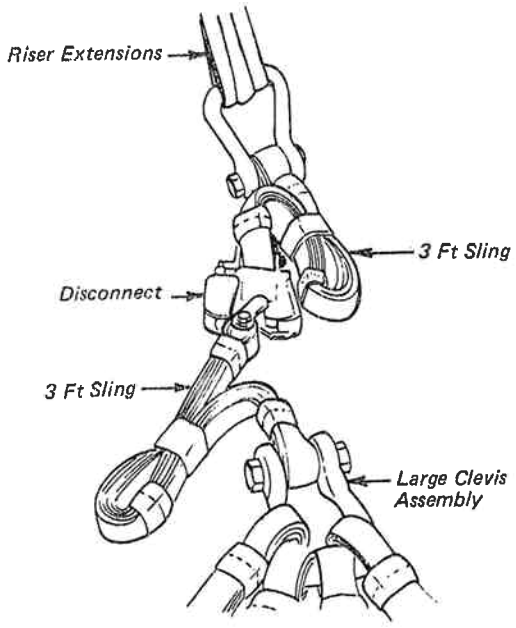


Figure 3.43 Typical Riser Assembly Using Clevis Links

Load Couplers. Load couplers are metal connector links consisting of a desired number of properly spaced spools between side plates, held together with thru-bolts or pins (see Figure 3.44). Various rigging arrangements are possible between heavy cargo loads and multiple parachutes using large clevises, load couplers and disconnects. Two arrangements are shown in Figure 3.45.

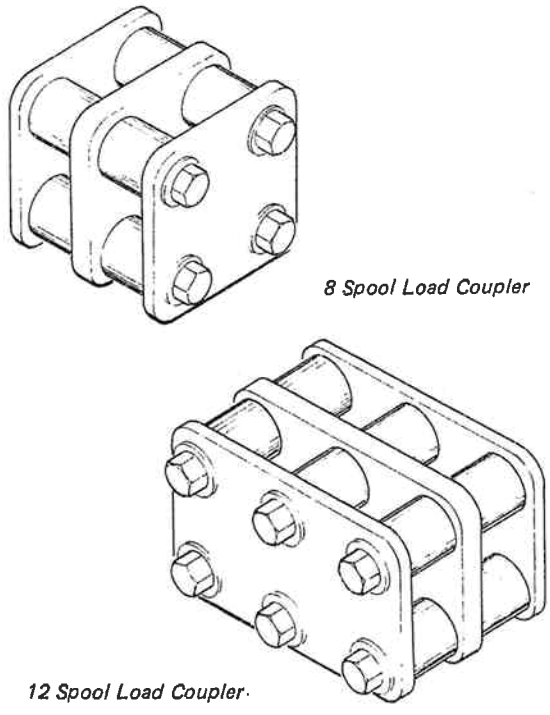


Figure 3.44 Cargo Parachute Load Couplers

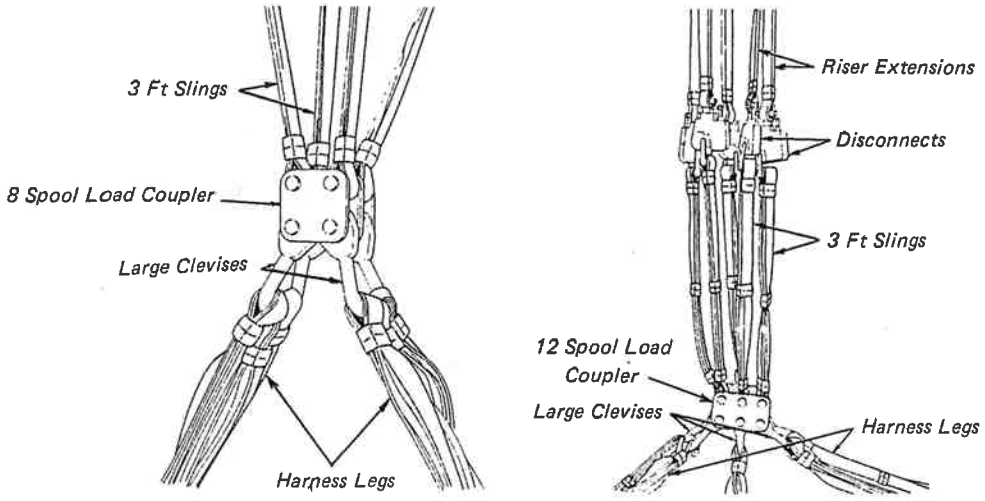


Figure 3.45 Typical Installation with Load Coupler and Large Clevises

Service Disconnects. Essentially a service disconnect is a small load coupler usually comprising side plates with only one bolt or spool arrangement at each end. This is required for simple installations requiring the use of a simple riser assembly.

TERMINATION PHASE SUBSYSTEM

Termination phase subsystems may include impact attenuation provisions, location devices and flotation devices. Special cases such as automatic, remote weather stations also include a payload stand-up or anti-toppling subsystem and an antenna erection subsystem.

Impact Attenuation Subsystems

Impact attenuation subsystems vary greatly in complexity from simple passive members such as penetrating ground spikes to highly sophisticated dynamic or self powered retarders. The landing subsystem may include both a pre-contact retarding device such as a retrorocket and some form of energy absorbing media such as crushable structure or honeycomb.

Retrograde Rockets. A high weight-efficiency recovery system results from selection of a high descent velocity (40-100 ft/sec) in combination with a retrograde landing rocket (or rockets). A cross plot of descent system and retrorocket weights vs descent velocity will identify the maximum efficiency point (minimum weight).

Penetrating Impact Attenuators. Surface penetration and displacement of mass is effective in reduction of landing impact. This method of impact attenuation has been used both for land and water landing.

Ground Penetration Nose Spikes. These have been used to absorb landing energy and decrease the velocity of the main body of the landing module at landing. Penetration spikes have several advantages:

a) they are passive, requiring no mechanism for operation.
b) they are inexpensive, and
c) they have good reliability

They have the following disadvantages:

a) their length may preclude carrying in bomb bays
b) excessive weight
c) limited to low ground wind operating conditions
d) not effective in rocky landing zones
e) side loads at the base of the spike in a wind drift landing require structural reinforcement of vehicle nose/spike attachment.

Knife Edge Water Entry. Excessive water landing shocks may be reduced on some shape vehicles by ensuring other than a flat-plate landing attitude. By using differential front and aft harness leg lengths, the vehicle can be suspended at such an attitude that a

sharp edged corner knifes into the water, rather than hitting flat. (Gemini and Apollo spacecraft used this principle.)

Pneumatic Landing Bags. Air inflated landing bags have been used to cushion landing shock of missiles, drones and spacecraft. Air bags have the advantages of providing light, low volume attenuators with large reaction footprint areas resulting in low-G deceleration (3-4 G's). Disadvantages are the tendency to topple or for the payload to roll off the top of the bag, inflation/ pressurization complexity, sensitivity to altitude of landing terrain, parachute oscillation and ground wind.

Two classes of pneumatic landing bags have been used extensively - low pressure bags and high pressure bags. The low pressure bags operate at an initial inflation pressure of 0.5 to 1.0 psig and peak pressure during the deceleration stroke of 5 to 10 psig. High pressure bags operate at an initial inflation pressure of 5-10 psig and peak pressure of 15-20 psig. Low pressure types use multiple burst diaphragms while the high pressure type use one or two metal blow-out diaphragms. The low pressure type is lighter than the high pressure type but is limited to use with light to medium weight vehicles (0-4000 lb), having large expanses of underside skin area (for force reaction). High pressure type impact bags are particularly effective for vehicles of high weight (over 2000 lb) and low underside reaction area. Particular care must be taken in designing high pressure airbags to exhaust the air rapidly enough to prevent the payload from bouncing.

Foam Filled Landing Bags. Foam filled impact bags have been developed for use with a remotely piloted vehicle (RPV) weighing over 3000 pounds. The foam is formed by mixing two liquids together in the form of sprays. When using urethane foam, the time required to fill the bag and for the foam to set-up is as low as 60 seconds. A new foam under development by the U. S. Army set-up in 5-10 seconds. The density of the 60 second foam is approximately one pound per cubic foot and uses a total of approximately 1.2 pounds of chemicals to produce one cubic foot of foam.

Foam filled impact bags have the following advantages over pneumatic impact bags:

a) insensitive to being punctured by sharp ground objects
b) improved stability in gliding or side drift landings
c) higher energy absorption than with air-filled bags

Crushable Structure. Crushable structure, either integral or auxiliary can be an efficient way of attenuating impact at landing. Crushable energy absorbers include:

Foamed plastics (urethane, styrofoam, etc.)
Balsa wood
Aluminum honeycomb
Paper honeycomb - radial
Paper honeycomb - block
Fiberglass - plastic honeycomb

The underside of the vehicle structure may be filled with foamed plastic, balsa wood, or honeycomb to increase the energy absorption capacity of the basic structure.

If sufficient stowage volume is available, crushable material may be incorporated for deployment beneath the vehicle.

Combination Attenuators. In many vehicles a combination of two or more methods of attenuating landing shock is used. An example is the Apollo 3-man command module, where the following attenuators were used:

a) the heat shield structure deformed
b) the astronaut couches were suspended by shock absorbing struts
c) crushable foam was incorporated in the astronaut couches

Location Devices

Location of a vehicle or payload after it has been lowered safely to the Earth's surface is aided by including one or more location devices in the recovery system. Typical locating aids include visual, radio frequency, and acoustical devices.

Radio Frequency Devices. Radio Transmitters with direction finding antennae are useful over relatively long ranges. Modern versions of the World War II "SARAH" (Search And Rescue And Homing) beacon are effective for distances of several hundred miles. Location of vehicles or parachutes in rough terrain can be greatly simplified through use of a short range (1-5 miles) radio transmitter and direction finding antenna. Table 3.1 lists the characteristics of the short and long distance radio beacons.

Chaff. Short pieces of aluminum foil or aluminized glass fibers (1"-2" long) will show a radar return and by being ejected from a vehicle at high altitude, may be used to locate it while still in the air.

TABLE 3.1 RADIO BEACON CHARACTERISTICS

Beacon Type	Range Miles	Frequency M Hz	Power Watts	Size Inches	Weight Lb*	Minimum Duration Hours
SARAH		235 or 243	***			
AFX-1	.5 to 5**	150-163	0.1	.75" Dia. x 5.0"	.12	6
AFP-6	1 to 10**	150-163	0.1	1.25" x 2.25" x 3.5"	.75	250

* Includes battery
** .5 to 1 mile ground to ground, 5 - 10 miles ground to air
*** 10 to 100 watts available

Radar Transponders (RAdio Direction And Range). Radar beacons may be included in flight vehicles to transmit a return signal in response to radar interrogation.

Visual Devices. The most effective visual location aid is the high intensity flashing light beacon. Typical beacons emit from .5 to 2 million candle power at rates of 1/2 to 2 strobe flashes per second. Depending on ambient light conditions and search aircraft altitude, the flashing light beacon can be seen up to 10-20 miles. Durations of 24 hours or longer are readily achievable.

Other visual location devices are smoke generators, fluoresceine dye, reflective paint on vehicle surfaces and bright colored parachutes. Smoke generators are limited in usefullness by their short duration of operation. Fluoresceine dye spreads a yellow-green slick on the water surface that persists for up to 24 hours, depending on size of the packet, the surface wind velocity and sea state.

Acoustical Devices. For deep water landing sites, two acoustical locating devices have been used, "SOFAR" bombs and "SONAR" devices.

SOFAR Bombs (SOund Firing And Ranging). The SOFAR bomb is a miniature depth charge, designed to detonate at a preselected water depth. Its location is determined through triangulation by several listening stations from as far away as 10,000 miles. The preset water firing depth is usually at least 1,000 feet below the surface. The effective range depends primarily on weight of explosive charge, although temperature inversion layers may affect the useable range. Sizes, weights and typical range distances for various sizes of SOFAR bombs are shown in Table 3.2.

TABLE 3.2 SOFAR BOMB CHARACTERISTICS

Length, Inches	Total Weight, Lb	Explosive Weight, Lb	Firing Depth, Feet
10.06	9.8	4.0	3.000 - 4000
7.742	3.0	1.0	3000 - 4000
4.752	2.0	0.5	3000 - 4000

SONAR Pinger (SOund Navigating And Ranging). Small sonar pingers which emit an acoustical pulse are useful as an aid in localizing an object in the water. Their range is limited by the depth and power of the transmitter and the power of the receiver/direction finder.

Flotation Devices

For water landing, flotation of the vehicle to ensure its retrieval by recovery craft (boat, helicopter, etc.) may be effected by augmenting its inherent buoyancy in several ways:

a) Low density plastic foam installed in the interstices or unused space of unsealed compartments
b) Sealed compartments and empty fuel tanks
c) Inflatable bladders placed to fill open bays in the body, e.g., main decelerator compartment
d) Deployable gas envelopes stowed in internal

compartments or in external fairings, pods or blisters, usually inflated during descent

e) One or more ram-air inflated envelopes mounted on the parachute harness or on the apex of the canopy

Item (c) may first function as an ejector bag to displace the main decelerator from its compartment when direct unassisted extraction by pilot chute, or similar means, is difficult and subject to random delays.

Deployable gas envelopes also may be employed with inherently buoyant vehicles for purposes of stabilization, or, as in the case of the Apollo command module, for righting the craft from the inverted stable floating attitude. These are usually inflated after splashdown.

Flotation Bags. Flotation bag designs have been developed in two basic forms:

a) A sealed gas envelope assembled from segments of coated fabric with stitched, cemented, or vulcanized seams

b) A porous structural cloth outer envelope assembled by stitching and sealed with a vulcanized gas envelope (inner tube) of thin neoprene or silicone rubber.

Approach (a) has seen wider use, being simpler to fabricate, but is structurally inefficient and has a low tolerance for water impact when inflated. Approach (b) has seen limited use under severe operational conditions, lightweight units withstanding water impact at greater than 90 fps in the inflated condition.

Flotation bags other than the ram-air inflated designs may be inflated by the same methods used in airbag landing systems. Compressed air, nitrogen and carbon dioxide are common inflation gases. Because the released gas is discharged at high velocity and experiences a large temperature drop due to free expansion, it is usually necessary to feed the flotation bag through a diffuser or other means of slowing and heating the gas to avoid damaging the envelope sealant. An ambient-air aspirator also may be used for this function, reducing the compressed gas supply required for full inflation at the same time.

Flotation bags inflated prior to splashdown are subject to increasing external atmospheric pressure while the contained gas supply usually is absorbing heat and increasing in temperature. These effects work counter to each other and both should be taken into account when determining the required internal differential pressure at sea level. Since the envelope feed-line is sealed with a check-valve, only a reduction in pressure can be transmitted back through the system to a pressure regulator, if such is required. Thus, the increase in gas pressure due to heating during the descent must be allowed for in the structural design along with the compression impulse due to water impact.

Engagement Aids. The flotation gear usually includes provisions for supporting a structural member in an accessible position for grappling and engagement of the vehicle retrieval mechanism, e.g., boathook, helicopter towline, etc. Consideration should be given to the problems of retrieval by boat in rough seas and of helicopter crew safety at low altitudes.

CHAPTER 4

MATERIALS AND MANUFACTURE

Recovery systems or their component subsystems are constructed and prepared by skilled and semi-skilled personnel, adhering to time tested fabrication practices in which principles of safety and reliability are emphasized. Primary components are textile structures (parachutes, air bags and suspension members) which are subject to dynamic loading during a recovery sequence. Their designs range from relatively simple forms to complex flexible structures. This chapter presents technology pertaining principally to the materials and manufacture of those subsystems incorporating textile components, and includes pertinent data on textiles as well as details of construction, assembly, steps of fabrication and inspection.

Progress in the technology of fibrous materials continues to provide better, more economical, and more efficient solutions to the problems of specific systems, and in particular to the problem of degradation when subjected to severe environments. Relatively new polymeric fibers, known as aramids, are proving effective in textile applications requiring strength at temperatures higher than those which limit the capabilities of conventional nylon and polyester fibers. A high modulus aramid, now in quantity production, also has a potential for achieving lighter weight, reduced volume textile components.

Manufacture of recovery system components and their assembly into a deliverable system, often in a packed ready-to-operate form, involves established procedures of control and accountability. Such procedures affect identity of materials, fabrication to dimension of component parts, final assembly including functioning lanyards, actuators and disconnect devices. Systematic inspection parallels the manufacturing process. These procedures are described, including the equipment used in manufacturing and inspection functions.

MATERIALS

Most materials used for deployable portions of recovery systems, when reduced to their simplest element – fiber or film – respond to stress with nearly proportional strain within greatly abbreviated limits. Since varying conditions (temperature, heat treatment, and stress-strain rate) change markedly the relationship of any given substance, results of experiments must continuously be utilized to determine limits in the variation of behavior of these visco-elastic materials from the behavior of other structural materials.

In general, current nylon and polyester fabrics are suitable for typical parachute applications. The major problems arise where high temperatures are encountered, e.g., aerodynamic heating with deployment at high speed, friction-generated heat during deployment, and storage entailing elevated temperatures. Also, limitations of system stowage bulk and weight frequently govern design.

Fundamental characteristics of textile fibers and yarns are described in this section, followed by basic information of textile forms used to fabricate recovery system components. Most applicable fibers are derived synthetically, including many from polymeric chemical compounds. Of special interest are fibers with a capacity to absorb energy of loading, or those which retain useful strength margins at elevated temperatures. Polymers are also useful as films, coatings, adhesives, rigid and semi-rigid foams or special structural forms. Characteristics of crushable structural materials used for impact attenuation are also included.

Textile Fibers and Yarns

Before the advent of man-made fibers, parachutes and other textile goods had to be made from natural fibers such as cotton, silk, wool, and flax. The first man-made fiber, rayon, was commercially produced in the United States in 1910. Rayon is made from cellulose, the fibrous substance of all forms of plant life, which is then regenerated into fiber form. Acetate fibers, introduced in 1924, are made from acetylated cellulose. Nylon, the first fiber synthesized from chemicals, has been commercially produced in the United States since 1939. Extensive research since World War II has produced and developed numerous organic fibers, many of which are in high volume demand for today's textiles.

The ingredients of most man-made fibers come from plentiful, low-cost raw materials. Organic fibers, other than cellulosic rayons and acetates, are made by chemically combining four basic elements; carbon from petroleum or natural gas, nitrogen and oxygen

from the air, and hydrogen from water, to form long chain polymers from which fibers are synthesized. In synthetic fibers, the long, chain-like molecules are oriented by mechanical means to produce a material whose highly anisotropic mechanical properties are superior to molded or cast specimens of the same m material. Most man-mande fibers are formed by forcing the polymer, in a syrupy (solubilized or at melt) state at about the consistence of molasses, through tiny holes. The filaments emerging from the holes are then hardened or solidified. The device through which the material is forced is called a spinneret. The process of extrusion and hardening is called *filament* because of its singular continuous length. During or after hardening, the filaments of a structural fiber may be stretched, reducing the fiber cross-section and causing the molecules to arrange themselves in a more oriented pattern. A high degree of orientation will result in a higher breaking stress, lower corresponding elongation, high chemical stability and low dye affinity. Optimum strength and energy absorbing properties may be contained in fibers through proper control of heat and stretch during the manufacturing process. Thus, manufactured fibers may be "engineered" to exhibit special qualities and characteristics for specific end purposes.

Yarns consisting of two or more filaments assembled or held together by twist or otherwise are called *filament yarns.* When a single filament is woven or otherwise used as a yarn, thread or line, it is referred to as a *monofilament.* Yarns from *staple* (short fibers) are more irregular, and therefore are less efficient than filament yarns of equivalent material. Staple yarns may be distinguished from filament yarns by the short ends of fibers projecting from the yarn surface which produce a fuzzy effect. Added physical properties are achieved in yarns through the use of machinery to impart to the filaments a number of twists or turns which may be locked in by heat setting. A yarn made up of filaments which are essentially parallel or running together with the same twist is known as a "singles yarn". A small amount of twist in a singles yarn helps to keep untensioned filaments together and to equalize minor differences in length. Most singles yarns, whether continuous or from staple, usually contain more than 15 filaments.

The size of yarn is identified by a *yarn number* which is a measure of its linear density. Staple yarns use the "cotton count" method which gives the length per unit weight in number of hanks (each 840 yards) which equal one pound to denote the yarn number; i.e., in one pound of No. 10 cotton yarn there are ten hanks or 8400 yards. It should be noted that cotton count varies indirectly with yarn size.

With filament yarns, the "denier*" method is used which gives a direct yarn number, weight per unit length. Size of a filament also can be expressed in grams per denier units of linear density. The lower the denier, the finer the filament or yarn.

The number of twists noted in turns per inch (tpi), given a yarn at the spinning frame depends on its use — weaving, knitting, braiding, cordage, etc. An empirical constant, called a *twist multiplier* is used, which, when multiplied by the square root of the yarn number, gives the number of turns per inch to be inserted in staple yarns.

$$\text{Twist (tpi)} = \text{twist multiplier} \times \sqrt{\text{yarn number}}$$

A different constant or twist multiplier is used for each type of yarn. It represents a quantative index of the relative steepness of the helix angle. The twist to be inserted in filament yarns, or yarns identified by direct yarn number, is determined as follows.

$$\text{Twist (tpi)} = \frac{73 \times \text{twist multiplier}}{\sqrt{\text{denier}}}$$

The direction of twist in the yarn is referred to as "Z" or "S". Z twist is also called regular or warp twist. The yarn helix has an oblique line (when held vertically) which runs from left to upper right as the center line in the letter Z. S twist, also called reverse twist, has a helical line from left to lower right as the center of the letter S.

Fiber Properties. Cross-sectional shapes and sizes of fibers can vary widely. However, a typical or representative manufactured filament is round, or nearly round in cross-section, and about a three denier size. A 3.1 denier nylon filament, for example, has a diameter of approximately ¾ mil (.00077 inch) and is extremely supple. Fibers which have a high modulus require a smaller cross-section or *denier* to provide equal textile flexibility.

Natural Fibers. Although used extensively in the past, natural fibers are no longer in general use in parachute canopy fabrics. Cotton cloths, webbings and tapes, however, do find application in fabric accessories; and silk sometimes qualifies better than nylon for limited special purpose lightweight canopy applications.

* Denier. Grams (mass) of 9000 meters of yarn. A yarn number, presently being adopted world-wide, the *tex* method intended for all yarns, is the grams (mass) of 1000 meters of yarn.

Cotton . . . fibers are ribbon-like, tubular with tubes often collapsed and very irregular in size as well as shape. Cotton fiber contains 88 to 96 percent cellulose. Typical yarns are spun from staple lengths ranging from ½ inch to 1½ inches. Cotton fiber is highly moisture absorbent, strong, burns without melting and resists most organic solvents, but is disintegrated by concentrated sulfuric acid. Unless treated, cotton may be attacked by fungus, bacteria and some insects.

Silk . . . fibers are smooth, triangular in cross-section, and glossy in appearance. Silk is a protein fiber and resembles wool in chemical structure, but contains no sulfur as does wool. It consists largely of the amino acid *alanine.* Silk fabrics burn without a sooty residue, the temperature of decomposition being about 629°F. The fiber dissolves acids and strong alkalies. Silk may be attacked by fungus, bacteria and insects.

Manufactured Fibers. The U. S. Federal Trade Commission[232] has established generic names to identify most manufactured fibers. Below are listed the physical properties of textile fibers within each name group; most are long-chain synthetic polymers, briefly defined by a key to the molecular structure of their fiber forming substances. Only properties of fibers applicable to recovery system textiles are considered, omitting those produced for special commercial yarn applications. Experimentally produced fibers, not generically classified, are fluorocarbon, graphite and special polymers developed for strength at elevated temperatures. Fiber characteristics may vary within a generic group depending on the manufacturer's methods. Many fibers are produced by more than one manufacturer, but certain fibers and yarns are obtainable only from a single source. Trade names of applicable popular fibers are given with the manufacturer referenced in the following list describing representative physical properties of man-made fibers.

Polyester . . . at least 85% an ester of a substituted aromatic carboxylic acid, including terephthalate units and hydroxy-benzoate units (Dacron). Fibers are strong, durable, quick drying, resistant, resilient and resistant to most chemicals, although they dissolve and decompose in concentrated sulphuric acid. In dry heat the fiber resists degradation and discoloration up to 300 F. In flame, the fiber burns with melting, but when withdrawn is usually self-extinguishing.

Rayon . . . regenerated cellulose. Fibers are highly absorbent, durable and economical. Rayon does not melt but loses strength above 300°F and decomposes at 350° to 464°F. Rayon burns readily. The effect of age is slight to none. Sunlight causes loss of strength after prolonged exposure.

Nylon . . . a polyamide in which less than 85% of the amide linkages are attached directly to two aromatic rings (nylon 6, nylon 6,6).) The fiber is strong, durable, elastic, abrasion resistant and only slightly absorbent. Oxadizing agents and mineral acids cause degradation of nylon depending upon time of exposure, temperature and concentration. The fiber is essentially inert to alkalies and is generally not affected by organic solvents except some phenolii compounds and formic acid. In dry heat, nylon 6,6 resists degradation and discoloration up to 250°F. It sticks at 445°F and melts at 415°F). In flame, the fiber burns slowly with melting and is usually self-extinguishing when removed from flame. Originally "nylon" was not a generic term but was DuPont's name for their hexamethylene diamene—adipic acid condensation polymer. Because both the amine and the acid contain 6 carbon atoms. this most popular nylon is called type 6,6. The so-called nylon 6 is derived from amino acid monomer and caprolactam to polymerize amino-caproic acid (6 carbon atoms).

Aramid . . . a polyamide in which at least 85% of the amide linkages are attached directly to two aromatic rings (Nomex, Kevlar). The fiber is strong, durable, dimensionally stable, resists heat and is only slightly absorbent. Aramid fibers do not melt and are self-extinguishing when removed from flame. Nomex has elastic and energy absorption properties similar to nylon, but maintains its strength when exposed to elevated temperatures for long periods. It degrades rapidly above 550°F. Kevlar is a high modulus (low stretch) fiber which exhibits very good strength and stability, even at temperatures in excess of 500°F.

Fluorocarbon . . . polymerized from tetrafluoroethylene monomer (Teflon). The fiber is non-absorbent, resists high temperature and most chemicals. The fiber does not degrade below 400°F. It sublimes above 550°F and vapors are toxic. It presents a very low oeifficient of friction in contact with other materials.

Polybenzimidazole (PBI) . . . spun from polyphenylene and bibenzimidazole. The fiber is stronger than other polymeric fibers at temperatures above 500°F. PBI is durable, elastic and stable like nylon except non-melting, and its absorbency is similar to cotton and rayon.

Tensile Strength. The absolute value of a fiber's strength must be related to its cross-sectional area or to its linear density. Tensile strength is normally given in pounds per square inch (psi), however, the textile trade uses the term "tenacity" to describe strength on a grams (force) per denier (gpd) basis. It is easier to determine a fiber's or yarn's relative fineness by weighing a known length of a specimen,

rather than measuring its cross-sectional area. Also, yarn weight is an important textile physical and economic factor. Since denier is based upon weight per unit length, it follows that tenacity is influenced by specific gravity of the fiber material, while strength per unit area (stress) is not. Specific gravity is defined as the ratio of the unit volume weight of a substance to that of water at 4°C. To convert tenacity to stress, the following relationship applies:

Stress (psi) = 12,800 x specific gravity x tenacity (gpd)

The tensile properties of a structural fiber are best illustrated by its stress vs strain characteristics, or in textile terms, its tenacity vs elongation pattern. Polymeric fibers are "non-Hookean" i.e., they do not obey Hooke's law which states that the strain (elongation) is linearly proportional to the applied stress. Figure 4.1 exemplifies the stress-strain pattern of a common polymeric fiber. It shows an original region OA which is approximately linear. Point A is

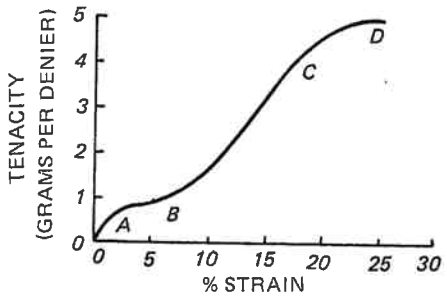


Figure 4.1 Stress vs Strain of a Polymeric Fiber

called the "proportional limit". Beyond this point, region AB develops where additional incremental loading produces proportionately larger increases in elongation due to the propensity of the fiber to "creep" or slowly elongate under steady load. A slope change occurs at point B, followed by a stiffening region BC where additional loads beyond B cause smaller changes in elongation. Finally there is a second flow region, CD, which often terminates at a point of rupture, D. Stress-strain patterns of other fibers vary in slope and length of flow regions. These and other high polymers such as rubbers, elastomers, and plastics are said to be "viscoelastic". The molecular and structural nature of these materials is such that during selected periods of progressive loading they may function elastically or with viscous flow or both in varying amounts at the same time under tension in one time loading to rupture.

Figure 4.2 shows fiber tenacity versus percent elongation diagrams for a variety of fibers at standard conditions. These curves portray general rather than exact values of strength and elasticity of fibers. Specific fiber information may be obtained from yarn manufacturers. The selection of a fiber for a particular purpose, of course, is dependent upon many property requirements. The shape of the stress-strain curve is important in terms of the fiber's influence on such end textile properties as breaking or tear strength energy absorption, dimensional stability and abrasion resistance. Variations occur in stress-strain properties of a textile if the fibers are cyclically loaded and relaxed below rupture during use.

In the curves of Fig. 4.2, a vertical nib shows rupture at breaking tenacity and maximum strain. Each produced fiber, due to chemical composition, processing, finishing and other factors controlled by the manufacturer, has its own characteristic curve and minimum rupture point. For example, a high tenacity polyester fiber (Dacron 52), produced by DuPont, will show a different stress-strain curve than a high tenacity polyester fiber produced by Fibre Industries or Beaunit. Also, a manufacturer may produce more than one high tenacity polyester fiber. Hence, critical textile components may require traceability of fiber source and definition in the process of quality assurance of the end product. The curves of Fig. 4.2 are from data in manufacturer's technical information bullentins unless otherwise noted.

In evaluating fibers and filament yarns, breaking tenacity, breaking elongation, stiffness, toughness, and elastic recovery are some of the properties which influence selection of a textile material. Table 4.1 lists those mechanical properties of the more widely used fibers and yarns having recovery system applica-

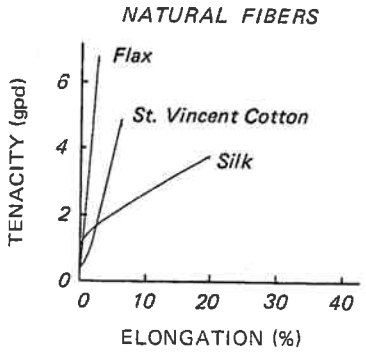
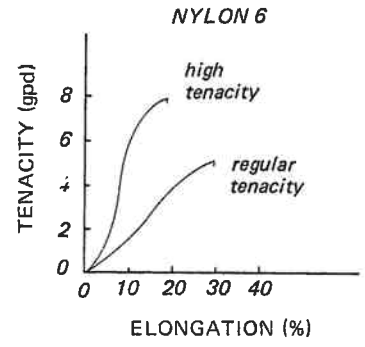
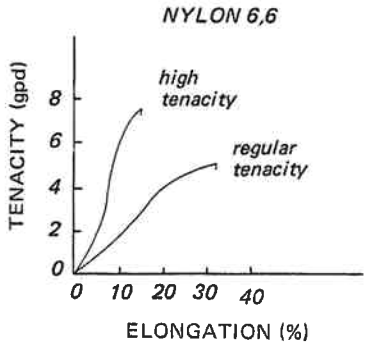
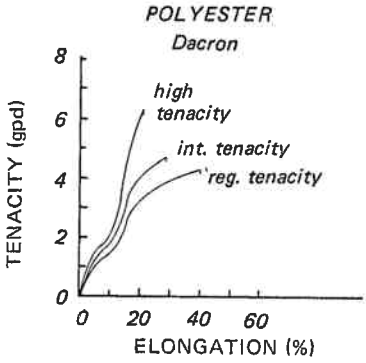
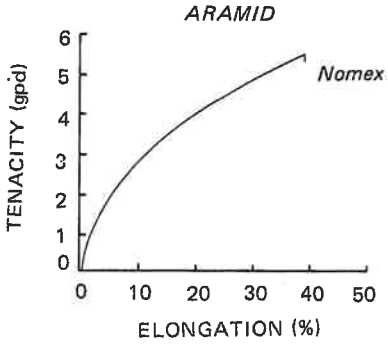


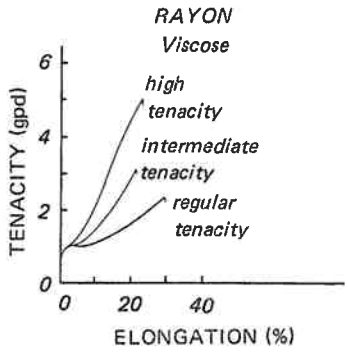
Figure 4.2 Tenacity vs Elongation Of Textile Fibers











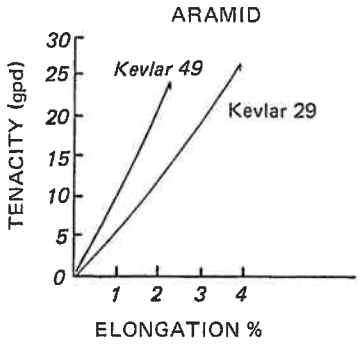


Figure 4.2 (Cont'd) Tenacity vs Elongation of Textile Fibers

tion potential. The first column gives the *specific gravity* of the material in grams per cubic centimeter.

Breaking tenacity in the second column, denotes strength in grams per denier at the point of rupture. A fiber with high breaking tenacity is proper to use where weight efficiency is needed in fabrics, cordage or threads. Column three gives *breaking elongation,* a percent measure of the amount of stretch at the point of rupture. As a general rule, high strength fibers have low elongation.

The ratio of change in stress to change in strain defines the "modulus" of a material represented as the slope of the stress-strain curve. High modulus materials are stiff and show small elongation under load. Low modulus materials are extensible and show high elongation under load. Column four of Table 4.1 gives the *initial modulus* (portion OA in Fig. 4.1) to denote relative resistance to stretch of the material. Terms are grams per denier. A high stretch resistance may be desirable in textiles intended for repeated use, since a material retains its original dimensions if not extended to the permanent set point.

The area under the load-elongation curve is a measure of work done or energy absorbed by the filament or yarn. This property is called "toughness". When given at the point of rupture, *work-to-break* is an index indicating energy absorption capacity referred to a unit of mass of the material and expressed in gram-centimeters per denier centimeter, which simplifies to grams per denier.

Table 4.1 continues with the textile property *strain recovery,* the ratio of recovered distance to extended length. If most of the elongation is non-recoverable secondary creep, the energy absorption capacity on a subsequent use may be significantly reduced to the point where failure will result. Listed values show the percent recovery of fibers and filament yarns which have been strained by various amounts. Strain recovery consists of two types of return; immediate elastic recovery and delayed recovery. The difference between final unloaded length and original length of a fiber or yarn occurs as permanent set. After being strained 4%, type 300 nylon (DuPont) will return to its original unstrained dimension; recovering approximately half the strain immediately and half after a delay of several seconds from a momentary applied load. Even after strain to 50% of rupture elongation, this type of nylon recovers 94%, and has a permanent set of only 6%. Nylon's recovery capability, coupled with its high energy absorption, permits it repeatedly to undergo loading up to its recovery limit. The more quickly and completely a fiber recovers from an imposed strain, the more nearly elastic it is. A highly elastic fiber with high strength and energy absorption capability is considered optimum in textiles for many recovery system applications.

The moisture content of a textile material will influence its weight, its general dimensions, and many of its physical properties. *Moisture regain* is a percentage weight of water absorbed by a fiber over its bone dry weight after reaching equilibrium at 65% relative humidity and 70°F.

In the next two columns of Table 4.1 are noted the fifty percent and zero strength temperatures of principal structured fibers. For more specific in-between values, manufacturers data should be consulted.

For each material, there is a *critical velocity,* defined as that velocity at which the yarn ruptures immediately on longitudinal impact, and at the point of impact. At ballistic speeds, viscoelasticity has no opportunity to function, limiting the energy absorption capacity of the material to immediate elastic deflection applied at or less than the speed of sound in the material, the velocity of the stress wave in the fiber being the critical velocity. The final column of Table 4.1 gives the critical velocity for several of the higher strength fibers and yarns.

Textile materials are often called upon to withstand "high speed" or "impact" loading. Decelerator fabrics, suspension lines, risers and harnesses are typical examples of textile products which must have high impact strength. In textile processing, fibers or yarns may be impacted at low loads but at high frequencies. During fabrication a sewing machine causes thread to be impacted at velocities up to 180 ft/sec with short loading pulses of less than one millisecond duration. In cases where textiles are subjected to impact forces it is required that they have the capacity to absorb large amounts of energy in an exceedingly small period of time.

In the laboratory the load-elongation diagram of a fabric or cord is normally measured on a tensile testing machine capable of loading a specimen at rates no greater than 400 percent per minute,. . . . a relatively slow rate of deformation when compared with service conditions. At loading rates below the critical velocity, breaking strengths of most viscoelastic materials are greater, and rupture elongations are less, when tested under "impact" conditions as compared with "static" or low extension rate conditions. A simple explanation of this phenomenon is that at slow speeds the viscoelastic fibers have time to deform, and so, plastic flow rather than immediate failure takes place, with accompanying greater elongation to rupture. Under impact conditions the viscous components of the fiber require more stress to cause deformations at high speed. Figure 4.3 shows tenacity-elongation curves for a few high tenacity fibers at differing strain rates.

TABLE 4.1 MECHANICAL PROPERTIES OF FIBERS AND FILAMENT YARNS

(Determined at 65% Relative Humidity and 70°F)

	Specific Gravity (gm/cm^3)	Breaking Tenacity (gpd)	Breaking Elongation (%)	Initial Modulus (gpd)	Work-To Break (gpd)
Cotton	1.54	3.0 – 4.9	3 – 7	60 – 70	.15
Flax	1.50	1.50	2.7 – 3.3	175	.08
Silk	1.34	1.34	10 – 25	60 – 116	.40 – .80
Acrylic	1.14 & 1.19	2.0 – 3.5	20 – 40	4 – 13	.26 – .58
Modacrylic	1.30 & 1.37	2.5 – 3.0	35 – 39	7 – 8	.44 – .58
Polyester,					
Dacron (regular)	1.38	2.8 – 5.6	24 – 42	10 – 30	.40 – 1.10
Dacron (hi-ten.)	1.39	6.3 – 9.5	12 – 25	30 – 120	.50 – .70
others	1.22 & 1.38	2.5 – 6.3	24 – 45	8 – 18	.37 – 1.10
Rayon					
viscose (regular)	1.52	1.5 – 2.4	15 – 30	5 – 16	.18 – .22
viscose (int. ten.)	1.52	2.0 – 3.2	10 – 20	12 – 32	.16 – .24
viscose (hi - ten.)	1.52	3.0 – 5.0	9 – 22	14 – 56	.22 – .33
Nylon					
nylon 6 (regular)	1.14	4.5 – 5.8	26 – 32	14 – 22	.72 – .75
nylon 6 (hi - ten.)	1.14	6.8 – 8.6	16 – 28	24 – 54	.69 – .95
nylon 6, 6 (regular)	1.14	4.6 – 5.9	24 – 40	12 – 25	.71 – .92
nylon 6, 6 (hi - ten.)	1.14	5.9 – 9.8	16 – 28	21 – 58	.74 – .83
Polybenzimidazole (PBI)	1.32	5.0	23	115	

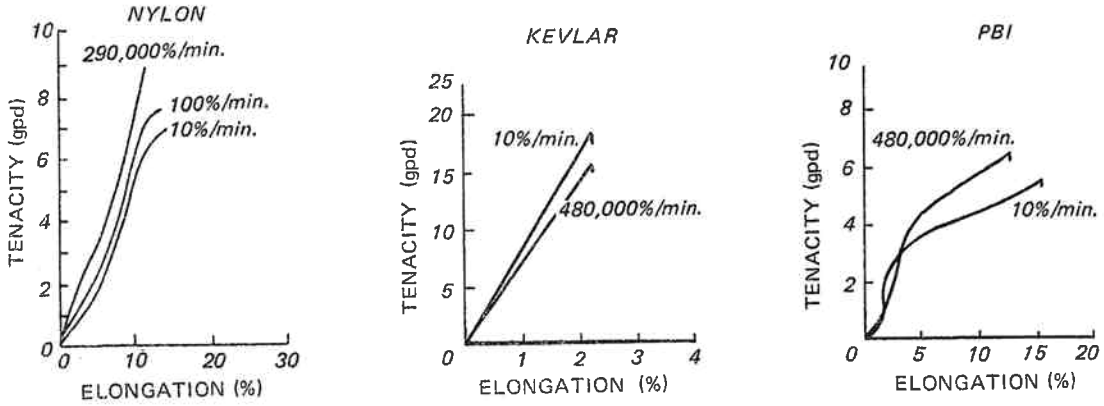


Figure 4.3 Tenacity – Elongation: Effect of Loading Rate

TABLE 4.1 (cont'd) MECHANICAL PROPERTIES OF FIBERS AND FILAMENT YARNS

(Determined at 65% RH and 70°F, except strength at temperature)

	Strain Recovery (% @ % ϵ)	Moisture Regain (%)	50% Str. Temp. (°F)	Zero Str. Temp. (°F)	Critical Velocity (ft/sec)
Cotton	45 @ 5	8.5 – 10.3			
Flax	65 @ 2	12			
Silk	51 @ 10	11			
Polyester					
Dacron (regular)	76 @ 3	.4			
Dacron (hi-ten.)	88 @ 3	.4	400	473	1550
others	95 @ 5	.6			
Rayon					
viscose (regular)	30 @ 20	11 – 13			
viscose (int. - ten.)	97 @ 2	11 – 13			
viscose (hi - ten.)	100 @ 2	11 – 13			
Nylon					
Nylon 6 (regular)	90 @ 10	3 – 5			
Nylon 6 (hi - ten.)	100 @ 4	3 – 5		412	
Nylon 6,6 (regular)	88 @ 3	4.0 – 4.5			
Nylon (hi - ten.)	89 @ 3	4.0 – 4.5	350	475	2020
Aramid					
Nomex·		6.5	540	700	1450
Kevlar	100 @ 3	7.0	750	930	1870
Polybenzamidazole (PBI)		11 – 13	640	850	

Two aspects must be clearly separated in evaluating the effect of heat upon fiber properties: (1) tensile properties of fibers tested at elevated temperatures; (2) tensile properties of fibers tested at room temperature after exposure to elevated temperatures for selected time periods. The former indicates the capability of the material to perform at the required elevated temperature. The latter is often used as a criterion of heat degradation resistance. Fabric degradation by heat normally is a function of temperature, time, relative humidity, and air circulation. Since many heat degradation processes involve oxidation, the greater the air circulation the greater will be the amount of oxygen which comes in contact with the fiber, with more rapid degradation. In an application where an item will be subjected to tension at an elevated temperature, selection of a fiber which could become soft and extensible at that temperature must be avoided. The effect of temperature on the rupture tenacity and initial modulus of representative parachute materials is depicted in Figures 4.4 and 4.5.

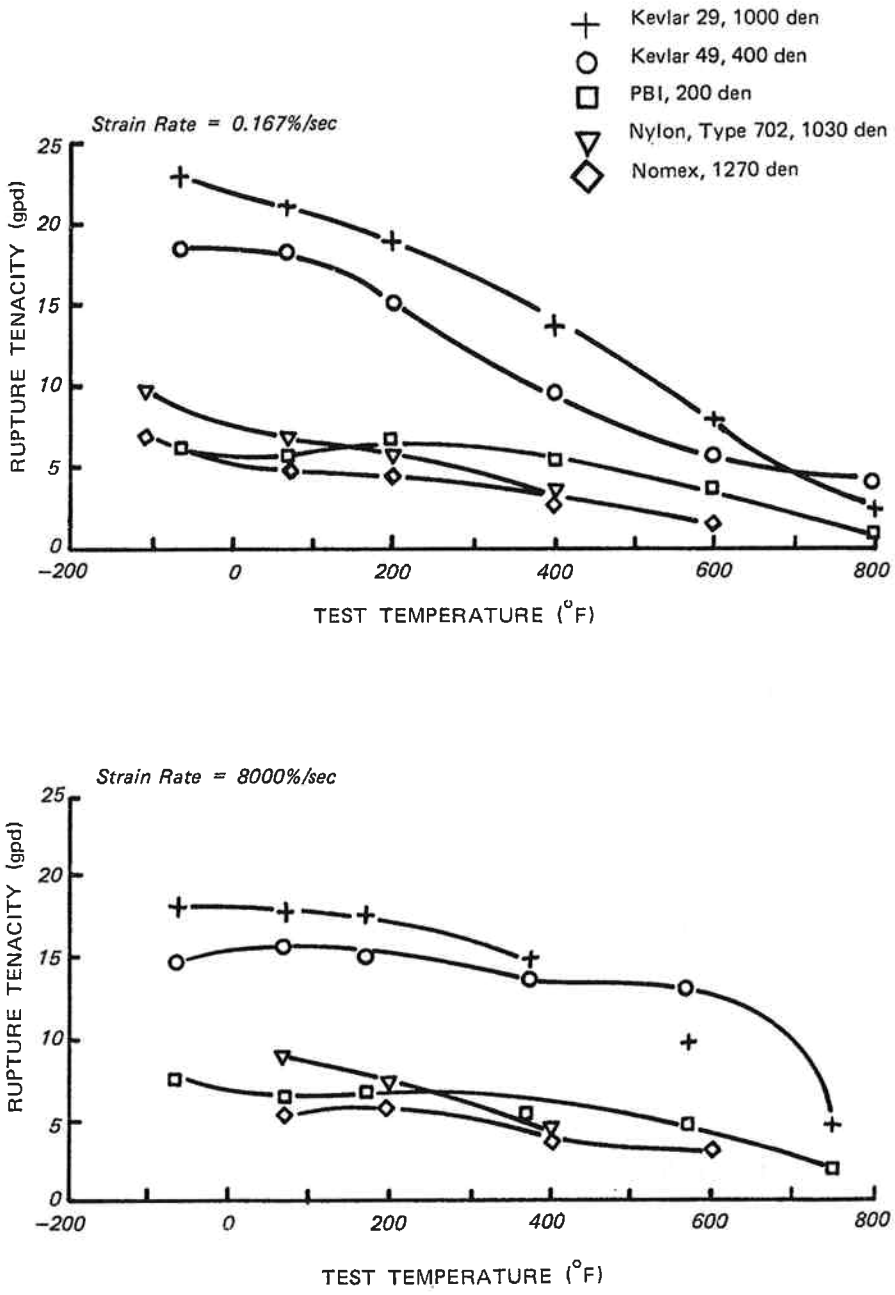


Figure 4.4 Rupture Tenacity as à Function of Tensile Test Temperature (stress values based upon denier measured at 70°F) (Ref. 579)

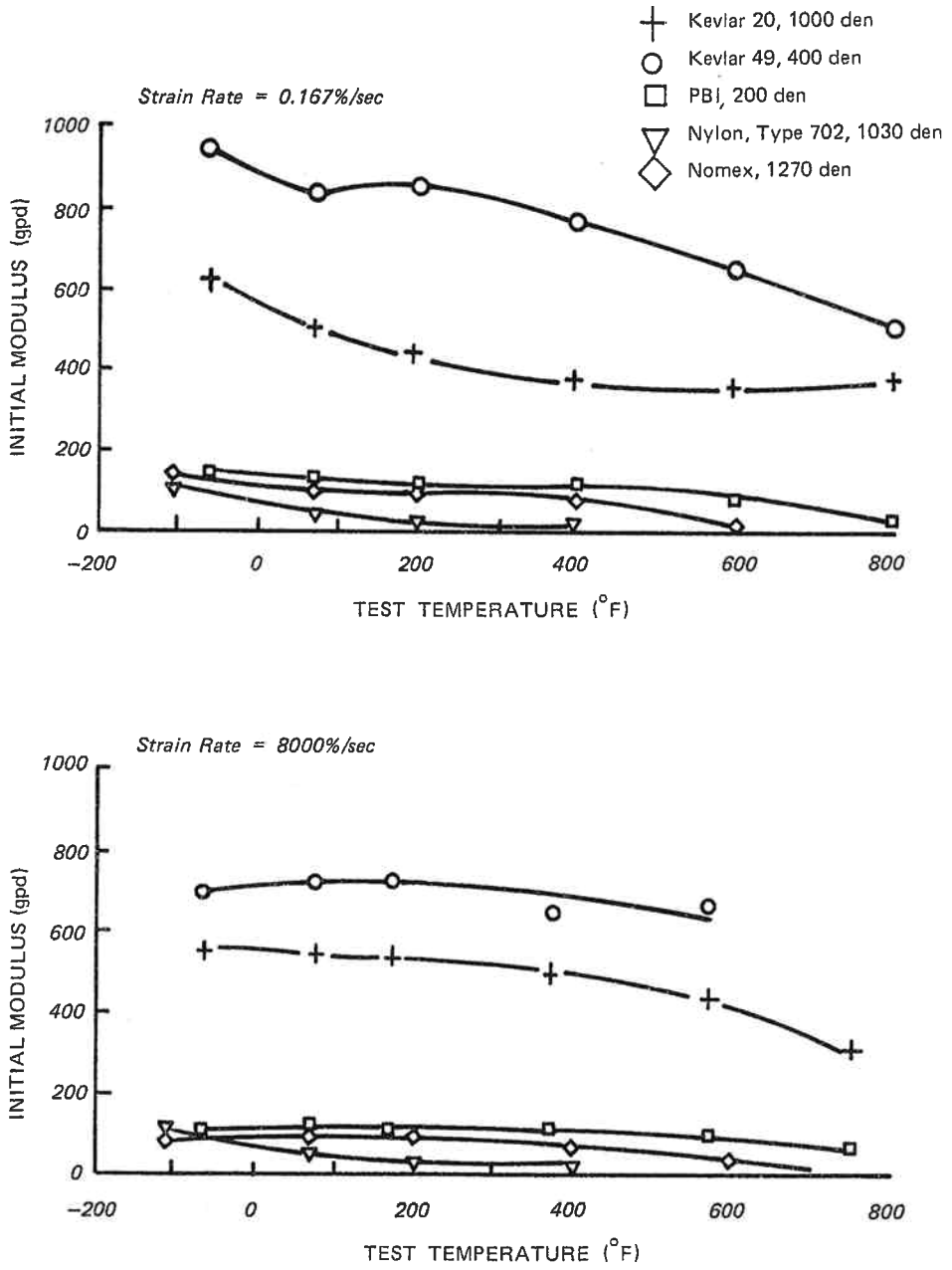


Figure 4.5 Initial Modulus of Yarns as a Function of Tensile Test Temperature (based upon at-temperature yarn dimensions) (Ref. 579)

Recovery System Textiles

Textiles are used in recovery system applications in the form of sewing threads, cords, webbing, tapes, ribbons, felts and broad woven fabrics. Their principal uses are the construction of deployable systems for deceleration, descent control, landing energy absorption, or flotation. Textiles are also used in the construction of auxiliary devices such as parachute packs, deployment bags, and harnesses. The use of textiles in such applications requires knowledge not only of strength, elongation, flexibility, and response to environments, but also of air permeability, sewability and other factors not usually vital to the use of more conventional structural materials. The physical appearance and engineering properties of a textile component are dependent upon many variables, beginning with the nature of the fiber and the properties of the yarn. Proper utilization of the several interdependent variables permits the engineering design of textile forms with desired weave, texture, finish, fabric cover factor, fabric density, and thickness. These factors in turn influence such properties as breaking and tear strength, flexibility, abrasion resistance, air permeability and overall weight efficiency.

Textile Properties. There is no single source of data on properties for all pertinent textiles. The mechanical structure, strength, weight, volume, and dimensions (and for some textile forms, elongation and air permeability) of standard nylon, polyester, aramid, cotton and rayon materials are described in appropriate government specifications. Tables summarizing much of these data are to be found on pages 155 through 176.

Strength-to-Weight Ratio. Where minimum weight is a design objective, an efficiency index which may be applied to candidate textile forms is its ***strength-to-weight ratio***. In selecting cords, tapes or webbings for suspension lines, risers, bridles or other single direction load members, this index may be determined as

$$\frac{\text{breaking strength (pounds)}}{\text{weight (pounds per foot)}} = \text{index (feet)}$$

The strength-to-weight ratio thus derived is a measure in length of unloaded cord which will cause rupture by its weight alone. Values between 80,000 ft and 20,000 ft are encompassed by nylon cords, with the higher figure being the most efficient. The strength-to-weight ratio of cloth is similar, having the same units

$$\frac{\text{breaking strength (lbs/ft)}}{\text{weight (lbs/ft}^2\text{)}} = \text{index (feet)}$$

Air Permeability. The amount of air which can flow through a fabric at a given pressure differential across the fabric is a function of the fabric weave, the number of yarns per inch, yarn crimp, and yarn cross-sectional shape, the latter influenced by yarn denier and yarn twist. All of these variables control the shape and open area interstices within and between yarns through which air-flow takes place. The number of warp and filling yarns per inch is known as the ***thread count***. For a given yarn number, the larger the thread count, the more dense and opaque is the fabric. The ratio of fabric area occupied by yarn to the total fabric area is called the ***cover factor.***

In textile terminology, ***air permeability*** is the volumetric flow rate of air per unit of cloth area under a certain differential pressure. Textile porosity is defined as the percentage of open space within the volume of a fabric, as the air holes in a sponge. In parachute terminology, ***porosity*** refers to the ratio of open area to total area of the canopy and is denoted as geometric porosity, λg, expressed in percent.

Air flow through a textile fabric obeys the general rules for fluid flow through an orifice. However, fabric orifices which exist because of the interlacing of warp and filling yarns are small in size, odd in shape and large in number. These seriously complicate air flow calculations. The classical expression for the flow of an incompressible fluid through an orifice states that the volume flow is directly proportional to the product of the orifice area and the square root of the pressure differential across the orifice. The proportionality constant includes coefficients of contraction and velocity, the approach area, the fluid density, the gravitational constant. For any fabric, air flow at a selected pressure differential is directly proportional to the product of the amount of open area within the fabric through which the air can flow, and the square root of the pressure drop across the fabric:

$$Q = K\,(FA)\,\Delta p^{1/2}$$

where Q = volume flow rate per unit fabric area

FA = Free Area (fractional area of the total fabric area not occupied by yarns.

K = proportionality constant dependent on fabric geometry and other fluid flow factors

Δp = pressure differential across the fabric

For a hypothetical fabric composed fo perfectly circular yarns which do not elongate under applied pressure differential, the air flow can be calculated from the above formula, provided K is known. However, most textile fibers are viscoelastic, and deform under tensions which develope as a result of the pressure applied. The determination of air permeability becomes further complicated because, as the pressure increases, the yarn elongations produce changes in the shape of the interstices and the total free area increases, thus producing a concomitant increase in air flow.

In the laboratory, air permeability is measured in cubic feet of air per square foot of fabric per minute at a pressure differential across the fabric equivalent to one-half inch of water (U.S. Standard. Much higher differentials may develop in actual use of fabrics in parachutes. Any construction factor or finishing technique which changes the area, shape or length of the air flow path can appreciably change air permeability. The effect of yarn twist is to increase air permeability with increase in pressure differential, since more turns per inch under tension reduce yarn diameter. Yarn crimp permits the yarn to extend easily, thus opening up the fabric and increasing the free area. Hot calendering is often used to reduce fabric air permeability by flattening the yarns so that their cross-sectional shapes are elliptical rather than circular, thus reducing free area.

Tear Resistance. A broad woven fabric under load will tend to rip progressively once failure starts and develops a high local concentraction of tension at the cross yarns immediately ahead of the rip. Resistance to tearing usually results when the unbroken yarns are able to slide together forming a bundle strong enough to take the increased load as a group. So-called "rip-stop" fabrics are woven with two yarns together at regular intervals in an otherwise plain woven cloth for the purpose of promoting bundle strength. Weave patterns other than plain weave are characteristically more tear resistant, but cannot provide as efficient cover and low air permeability in a lightweight fabric for parachutes in low canopy loading applications.

Abrasion Resistance. Textiles are flexible and, depending upon the end use, repreated flexing as well as pure abrasion can contribute to product failure. The evaluation of abrasion resistance of a textile requires consideration of service performance and environments of the intended application. If two fabrics can be subjected to repeated rubbing or flexing cycles in the laboratory, they can be evaluated for relative appearance, strength loss, thickness loss, or the like. However, the correlation of actural conditions is crucial.

During parachute deployment, textiles move relative to each other or over metal or plastic parts, and frictional forces are generated. Nylon is particularly susceptible to melting from the heat generated when a parachute canopy moves in contact with lines which become taut at line stretch, or when a sleeve is withdrawn over an uninflated, stretched-out canopy. Fabric strength, elongation, smoothness, dimensional stability, abrasion resistance, seam slippage, and the tendency to generate a static electric charge are all dependent upon the friction property of a textile.

Abrasion resistance of textile forms, principally tapes and webbings, have been improved by increased yarn twist. Some webbing designs have three or more plies woven together with binder yarns to minimize the number of exposed yarns at the surface.

Sewability. Parachute textiles are normally assembled using conventional sewing techniques, including use of thread of the same material as the woven fabric. Good sewability results from a proper combination of thread compatibility with machine action and proper fabric density and flexibility of materials being joined. In heavy strap assemblies excessive material build-up should be avoided which could degrade the thread or fabric through contact with a sewing machine needle that is hot due to frictional heating.

Textile Forms. The various textile forms used in construction of recovery system components are normally procured to specification. In the following pages, federal and military specification data are summarized and presented in tables as a reference source, useful in the evaluation and selection of textile materials for parachutes and related items. Frequently the singles yarn denier, filament count, twist, number of plied yarns, twist direction and turns per inch are specified. As a precaution, final design should be based upon information from the latest issue of the referenced specification. Further, there are details of weave pattern plus methods of test and inspection in the printed specification which are not repeated herein.

Sewing Threads. Threads and cords for machine and hand sewing are available in many constructions and sizes in cotton, nylon, polyester, Nomex and Kevlar aramid. Characteristics of sewing threads defined by government specifications are given in Tables 4.2 through 4.6. Listed properties of minimum breaking strength, maximum weight in terms of minimum length per pound, ply and minimum final twist where noted are specified limit values. A class of thread usually identifies more than one limit of breaking

* Note: The following statements apply in general to the tables of textile characteristics throughout this chapter.

Although safe practice dictates use of the specification minimum strength as the design point, the result will generally result in an over-designed component with more weight and bulk than is necessary to meet minimum requirements.

Specification for manufacture of nylon cloth, ribbons, tape, webbing, cords and thread call for yarn that is a bright, high tenacity, light and heat resistant, polyamide prepared from hexamethylene diamine and adipic acid (nylon 6.6) or its derivatives, and the yarn shall not be bleached in any manner or process.

Air permeability of cloth is determined at a pressure differential equivalent to one-half inch of water unless otherwise noted.

Weight is given in terms of length per pound for threads or cords. The maximum limit in weight is intended, and so must be represented by a minimum limit for length in accordance with the simplified practice of measuring, used by the textile trade.

TABLE 4.2 COTTON SEWING THREADS

Data from V-T-276, Reference 233

Type	Size (ticket) (number)	Min. Break Str. (lbs)	Min. Length per Lb. (yds)	Ply	Type	Size (ticket) (number)	Min. Break Str. (lbs)	Min. Length per Lb. (yds)	Ply
I A&B	140*	1.1	23,000	2	I C	0	2.6	10,281	3
	90	0.9	17,946	2		A	2.8	9,216	3
	70	1.2	14,065	2		B	3.2	7,761	3
						C	4.0	6,010	3
	40	2.3	9,500	or 2 3	II A	30	2.5	7,531	3
	70	1.5	13,441	3					
	70**	1.6	15,120	3	III A&B	10	6.5	2,501	3
	50	1.9	10,081	3		8	7.0	2,001	3
	40	2.1	8,401	3		9	10.0	1,831	4
	30	3.0	6,441	3		8	11.0	1,501	4
	20	3.8	5,040	3		10	9.5	1,901	4
	50	2.0	11,836	4		10	12.5	1,501	5
	40	2.5	9,406	4		10	15.5	1,275	6
	36	2.7	8,536	4					
	30	3.2	7,276	4	IV A&B	8	15	1,601	4
	24	4.1	5,721	4		8	20	1,221	5
	20	4.7	5,041	4		8	24	1,001	6
	16	5.5	3,881	4		8	28	871	7
	12	7.5	2,811	4		8	32	761	8
						8	36	676	9
I C	36	1.3	14,401	2		8	40	611	10
	30	1.6	11,001	2		8	44	551	1
						8	48	501	12
	000	1.7	15,521	3					
	00	2.1	12,221	3					

* Made from high grade cotton

** Long staple cotton yarn, S twist

Type I: Machine Thread: A-soft finish; B-glazed; C-mercerized
II: Basting Thread: A-glazed
III: Heavy Thread: A-soft; B-glazed
IV: Shoe Thread: A-soft; B-glazed
Color: May be specified
Use: Sewing cotton materials

TABLE 4.3 NYLON SEWING THREADS

Data from V-T-295, Reference 234

Type	Size	Min. Break Str. (lbs)	Min. Length per Lb (yds)	Ply	Min. Final Twist (tpi)
I	0000	.85	45,200	2	17
	000	1.30	29,500	3	13
	00	1.85	25,800	2	12
	A	2.75	16,900	3	10
	AA	3.90	12,600	2 or 3	9
	B	5.50	8,200	2 or 3	7
	E	8.50	5,600	3	6
	F	11	3,750	4	5
	FF	16	2,725	3	4
	FFF	17	2,900	3	4
	3	24	1,800	3	5
	4	32	1,300	3	4
	5	40	1,000	3	3½
	6	50	850	3	3
	7	60	725	3	3
	8	68	625	3	2½
	9	80	550	3	2½
	10	90	450	3	2
II	0000	.85	40,000	2	16
	000	1.30	26,000	3	12
	00	1.85	23,000	2	12
	A	2.75	15,000	3	9
	AA	3.90	11,800	2 or 3	8
	B	5.50	7,375	2 or 3	6
	E	8.50	5,000	3	5
	F	11	3,350	4	4
	FF	16	2,450	3	3½
	3	24	1,690	3	4½
	4	32	1,200	3	4
	5	40	950	3	3½
	6	50	775	3	3
	7	70	650	3	3
	8	68	575	3	2½
	9	80	500	3	2½
	10	90	450	3	2
III	0000	0.85	49,000	1	
	000	1.30	34,400	1	
	00	1.85	23,900	1	
	A	2.75	16,350	1	
	AA	3.40	13,300	1	
	B	5.50	8,000	1	
	E	8.50	5,200	1	
	F	11	3,850		
	FF	16	2,500	1	
	3	24	1,700	1	
	4	32	1,300	1	
	5	40	1,000	1	
	6	50	850	1	
	7	60	725	1	
	8	68	625	1	
	9	80	600	1	
	10	90	510	1	
IV	A	3.50	13,000	2	
	C	5.75	8,900	2	
	E	11	4,300	2	
V	6	20	2,320	3	
	8	16	2,920	3	
	10	14	3,310	3	
	12	11.20	4,180	3	

Break Elongation: Class I, 22% maximum; Class II, 33% maximum (except FFF and numbered thread sizes shall be 40% maximum), Types I and II only; 40% maximum, Types III, IV and V.

Type: I, twisted soft multiple cord; II, twisted bonded multiple cord; III, bonded monocord; IV, hand sewing twist (waxed); V, buttonhole twist (hand sewing, waxed).

Use: Only Types I and II, Class I thread are normally authorized for use in construction of parachutes and other flight safety equipment.

elongation. When specified, the lower elongation is usually satisfied by high tenacity yarn. Types of thread differentiate between finished treatments such as softness, bonding, twist, waxing, etc.

Kevlar aramid is a relatively new fiber with good potential for use in parachute textiles. According to Reference 237 sewing threads of Kevlar 29 aramid have been produced in standard constructions and tested for sewability on commercial high speed sewing machines. No major problems were encountered. In designing the Kevlar 29 threads, diameter was felt to be the most important criterion. Consequently, each size of Kevlar thread was made to the same diameter as its nylon counterpart so that in all cases the threads are significantly stronger than nylon. Even though knot and loop strength efficiencies are lower than those of nylon (50-60% for Kevlar), absolute values are nevertheless approximately twice those of a similar sized nylon product. Table 4.6 presents properties of Kevlar 29 aramid thread in a few nylon thread sizes.

TABLE 4.4 POLYESTER SEWING THREADS

Data from V-T-285, Reference 235

Type	Size	Min. Break Str. (lbs)	Break Elong. (%)	Min. Length per Lb. (yds)	Ply	Min. Final Twist (tpi)
Type I, Class I	00	1.4	25*	26,500	2	12
	A	2.0	25*	17,600	3	10
	AA	3.0	25*	13,200	2	9
	B	4.3	25*	8,500	2 or 3	7
	E	8.0	20*	5,700	3	6
	F	10.6	20*	4,200	4	5
	FF	16.0	20*	2.600	3	4
	3	24	15*	1,800	3	5
	4	32	15*	1,370	3	4
	5	40	15*	1,120	3	4
	6	48	15*	900	3	3
	7	54	15*	780	3	3
	8	60	15*	680	3 or 5	3
	9	65	15*	660	3	3
	10	70	15*	590	3 or 6	2.5
Type I, Class 3	00	1.25	15-35	21,200	2	11
	A	1.90	15-35	13,650	3	9
	B	3.80	15-35	7,000	2 or 3	6
	E	6.80	15-35	4,550	3	5
	F	7.60	15-35	3,500	4	4
	3	20.40	15-35	1,450	3	3
	4	27.25	15-35	910	3	3
	5	34.00	15-35	700	3	3
	6	41.00	15-35	600	3	2.5
	7	47.70	15-35	515	3	2

* Maximum elongation for Class I low elongation thread.

Type I, twisted soft multiple cord; Type II, twisted bonded multiple cord; and Type III, bonded monocord.[235]
Class 1, low elongation thread.
Class 3, heat stable - low shrinkage thread.
Use: The Type I, Class 3 thread is specifically intended for use in parachutes that are subject to exposure at elevated temperatures.

TABLE 4.5 THREAD, NYLON, NON MELTING

Data from MIL-T-43636, Reference 236

Type	Size	Min. Break Str. (lbs)	Max. Break Elong. (%)	Min. Length per Lb. (yds)	Ply	Min. Final Twist (tpi)
I	B	3.4	38	8900	2	7
	E	5.2	38	6000	3	6
	F	6.9	38	4500	4	5
	FF	10.2	38	3000	3	4
	3	15.4	42	2000	3	4½
	4	20.5	42	1500	3	4
	5	25.6	42	1200	3	3½
	6	30.7	42	1000	3	3
	7	35.8	42	850	3	3
II	B	3.4	38	8400	2	7
	E	5.2	38	5700	3	6
	F	6.9	38	4200	4	5
	FF	10.2	38	2800	3	4
	3	15.4	42	1900	3	4½
	4	20.5	42	1400	3	4
	5	25.6	42	1150	3	3½
	6	30.7	42	950	3	3
	7	35.8	42	800	3	3

Material: Nomex, manufactured by E. I. DuPont de Nemours and Co., Inc.
Type I: Twisted, soft multiple cord. Type II: Twisted, bonded multiple cord.
For Type III, bonded monocord, see Ref.236.
Use: Sewing protective clothing, other flight safety equipment and parachute use at 200° to 400°F.

TABLE 4.6 THREAD, PARA-ARAMID, INTERMEDIATE MODULUS

Data from MIL-T-87128, Reference 271

Size	Min. Break Str. (lbs)	Min. Length per Lb. (yds)	Yarns		Twist (tpi)	
			denier	ply	singles	ply
A	8	20,000	100	2	20S	10 Z
B	16	10,000	200	2	12S	6 Z
E	25	6,700	200	3	12S	6 Z
F	35	5,000	200	4	10S	5 Z
FF	60	3,350	400	3	8S	4 Z
3	80	2,100	400	5	10S	5 Z
5	150	1,050	1000	4	7S	3½Z
6	175	900	1500	3	6S	3 Z
8	225	550	1500	5	5S	2½Z

Material: Kevlar 29, manufactured by E. I. DuPont de Nemours and Co., Inc.
Type: Twisted, soft multiple cord.
Finish: Waxed or with a resin finish. Add suffix "R" to thread size if desired with polyvinyl butyral resin treatment. Allow ½ to 1% dry add-on weight (½ to 1% fewer yds/lb).

Braided Cords. Cords for suspension lines, risers, tow cables and numerous equipage applications are available in standard constructions and strengths, in cotton, nylon, polyester and Nomex aramid. Cords of braid construction are available in a broad range of sizes and strengths. A braid is a tubular-type fabric formed by the diagonal intersection of yarns, each yarn assuming the shape of a helix. There are no warp and filling yarns in the sense of a woven fabric. Instead, only the warps may be considered to intersect as a plain weave (one over one), or a basket weave (two over two). A braiding machine uses two sets of spools containing the braiding yarns. One set runs clockwise, the other counter-clockwise, both in a horizontal plane. The clockwise and counter-clockwise passes cause the two sets of yarns to intersect, thus producing a tubular braid. Depending upon the number of spools (carriers), the nature of the yarn, and the path of the spools, various types of braids can be produced. The tube can be braided about a central core of yarns, thus producing a firm cord composed of a ***core*** and braided ***sleeve.*** A core and sleeve cord must be designed to have equal ultimate rupture elongation in both core and sleeve for efficiency.

Properties of minimum breaking strength, minimum breaking elongation, maximum weight in terms of minimum length per pound, and yarn data are listed for nylon and aramid cords in Tables 4.7 through 4.10 as specified limits and values.

Load-Elongation of Cords. Characteristic curves of Figure 4.6 are representative of the load performance of cords in tension. These curves are composites formulated from static test data on typical nylon braided cords listed in Table 4.8, and Dacron cords similarly woven to these specifications. The curves represent a mean from data that varied with normal distribution in strength within one type by as much as 6% and elongation by 17%. Performance mean curves of all types tested (usually identified by rated strength) showed the same degree of variation. The load-elongation pattern of Figure 4.6 may be useful for preliminary design purposes, but should be supported with adequate test sampling of the specific cord procurement lot for critical design.

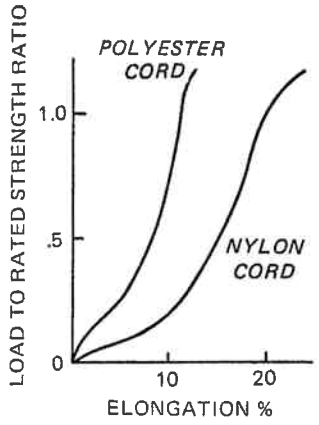


Figure 4.6 Load vs Elongation of Cords

TABLE 4.7 NYLON CORDS WITH CORE

Data from MIL-C-5040, Reference 238

Type	Min. Break Str. (lbs)	Min. Break Elong. (%)	Min. Length per Lb. (ft)	Sleeve	Yarn	Picks per inch	Core Yarn		
				denier	ply		ends	denier	ply
I	100	30	1050	70	3	26-28	4-7	210	3
IA	100	30	1050	210	3	26-28			
II	400	30	315	210	3	26-28	4-7	210	5-3
IIA	225	30	495	210	3	26-28			
III	550	30	225	210	3	26-28	7-9	210	5-3
IV	750	30	165	210	3	26-28	11	210	10-6 16-8

Type IA and IIA are coreless; Type II has one black yarn in sleeve.
Color: Natural, olive drab or sage green.
Use: Personnel parachute suspension lines and equipage.

TABLE 4.8 CORELESS BRAIDED NYLON CORDS

Data from MIL-C-7515, Reference 239

Type	Min. Break Str. (lbs)	Min. Break Elong. (%)	Min. Length per Lb. (ft)	Braid Yarn			Picks per inch
				denier	ply	ends	
I	400	20	330	210	3	48	11-13
Ia	400	20	330	840	1	32	13-13½
II	550	20	255	840	1	48	10-12
IIa	530*	20	300	840	1	40	14-16
III	750	20	150	210	3	96	8½-10
IIIa	800	20	175	840	1	72	10-12
IV	1000	20	120	840	1	96	7-9
V	1500	20	90	840	1	144	6½-8
VI	2000	20	60	840	1	192	4½-6½
VII	2500	20	45	840	1	224	4½-6
VIII	3000	20	36	840	1	288	5½-7½
IX	4000	20	27	840	4	96	5½-7
X	5000	20	22	840	4	120	4½-6
XI	300	20	480	210	1	112	14-15½
XII	0000	20	12	210	7	576	4-5
XIIa	0000	20	12	210	7	576	4-5
XIII	50	20	2700	70	1	64	22½-26
XIIIa	50	20	3000	210	1	16	17-19
XIV	100	20	1200	210	1	48	21-24
XV	200	20	675	210	3	24	13-16
XVI	1250	20	105	840	1	112	6½-8
XVII	1750	20	75	840	1	160	5½-7
XVIII	2250	20	51	840	1	208	5-6
XIX	3500	20	30	840	1	336	5½-7
XX	4500	20	24	840	4	108	5½-6½
XXI	5500	20	18	840	4	132	4½-5½
XXII	6000	20	15	840	4	144	4½-5½

* Maximum limit is 570 lbs.

Color: Natural, olive drab, sage green.

Use: Cargo type parachutes (Ia and IIIa for low cost parachutes; IIa for weak link in a personnel parachute line; XI for tow cables).

TABLE 4.9 CORD, AROMATIC POLYMIDE, NON MELTING

Data from MIL-C-83242, Reference 240

Type	Min. Break Str. (lbs)	Min. Break Elong. (%)	Min. Length per Lb. (ft)	Core Yarns		Sleeve Yarns		Strength Translation Efficiency (%)	Diameter (inch)
				denier	ply	denier	ply		
I	100	20	780	coreless		200	4		
II	375	20	230	200	7&3	200	4		
III	550	20	165	200	7&3	200	4		

Material: Nomex; manufactured by E. I. DuPont de Nemours and Co., Inc.
Color: Natural
Use: Personnel parachute suspension lines; equipage

TABLE 4.10 CORD, CORELESS, PARA-ARAMID, INTERMEDIATE MODULUS

Data from MIL-C-87129, Reference 272

TYPE	BREAKING STRENGTH (lb/min)	NO. OF CARRIERS	ENDS/ CARRIER	TOTAL ENDS	BASIC YARN DENIER	SINGLE YARNS FINAL PLIED YARN	YARN TWIST (turns/ inch)*	PICKS/ INCH	LENGTH LB (ft min)
I	35	4	1	4	200	1	5.0	9.0	15,000
II	70	8	1	8	200	1	5.0	18.0	7,200
III	140	8	1	8	400	1	5.0	12.0	3,600
IV	400	16	1	16	200	3	2.5	15.0	1,200
V	600	16	1	16	1,000	1	4.0	12.5	800
VI	750	16	1	16	1,500	1	3.0	10.5	475
VII	1000	16	1	16	1,000	2	2.1	10.0	375
VIII	1500	16	1	16	1,500	2	1.8	8.0	225
IX	2000	16	1	16	1,500	3	1.0	6.5	150
X	3500	16	1	16	1,500	6	1.0	5.5	75
XI	5000	24	1	24	1,500	5	1.0	5.5	65
XII	6500	24	1	24	1,500	6	1.0	4.0	55

* Half of the carriers S twist, half of the carriers Z twist

Narrow Woven Fabrics. The strength of a structure depends upon the total denier of the yarns being broken, the tenacity of those yarns, and the strength translation efficiency, i.e., the effectiveness with which yarn tenacity is translated into tenacity of the structure. In any material, two basic (but not independent) choices can be made, namely the denier and number of warp yarns to be used. The basis for this selection must be strength and width of the narrow fabric being made, for in such materials, the filling yarns serve only to hold the structure together, and have little influence on the strength, except to the extent that they may affect the strength translation efficiency of the warp yarns.

Aramid yarns are currently limited to a minimum 200 denier in the producer's production size, although, nylon, polyester and a few other yarns are produced in 20 to 30 denier size. Yarn strengths vary from effects of twist. Hence, the optimum strength of narrow woven fabrics may depend on twist as well as yarn denier. Yarn denier is selected to provide bulk of the weave in a structure of specified width, i.e., neither too tight nor too loose. A tight fabric is difficult to weave. Excessive looseness results in a sleazy fabric which is unsuitable for most applications, though its strength translation efficiency may be high. A thinner low porosity fabric may be woven from the finer yarns. A higher cost of low denier yarns is sometimes a compromising factor in choosing aramid yarns.

Webbings and tapes for parachute canopy structural and reinforcement members, risers, suspension lines, harnesses and numerous equipage applications are available in cotton, rayon, nylon, polyester, Nomex and Kevlar aramid. Certain of these narrow woven fabrics are classed as ribbons and ring bands for the construction of ribbon and ringslot parachute canopies. Characteristics of the available range of webbings and tapes defined by current military specifications are given in Tables 4.11 through 4.32.

TABLE 4.11 COTTON WEBBING

Data from MIL-W-5665, Reference 241

Type	Min. Break Str. (lbs)	Width (inch)	Max. Weight (oz/yd)	Thickness (inch)	Warp Ends	
					ply	number
I	350	9/16±1/16	.40	.040–.050	4	68
II	575	1±1/16	.75	.040–.050	4	122
III	750	1-1/4±1/16	.90	.040–.050	4	158
IV	1900	3±1/8	2.50	.050–.100	3	220
V	3100	5±1/8	4.30	.050–.100	3	350
VI	1800	1-3/4±1/16	3.00	.070–.090	5	116
VII	2600	1-3/4±1/16	3.00	.140–.170	7	122
VIII	2900	1-3/4±1/16	3.00	.075–.095	7	132
IX	4500	3±1/8	4.65	.090–.115	6	175
X	5000	1-3/4±1/16	3.60	.130–.160	6	160
XII	1000	1-3/4±1/16	1.25	.040–.060	4	220
XIII	3400	1-3/4±1/16	3.40	.095–.130	6	126
XV	4500	1-3/4±1/16	3.50	.130–.150	6	150
XVI	2700	1-3/4±1/16	2.60	.090–.115	7	124
XVII	1000	1±1/16	1.25	.075–.095	5	70
XVIII	1250	2-1/2±1/16	1.40	;050–.060	4	270
XIX	2500	2±1/16	3.68	.120–.150		139
XX	200	5/8±1/16	.45	.075–.095	3	40

* Filling yarns on these webbings are nylon.

Color: Natural, olive drab or other.
Filling: Types VII, X, XV, and XVI nylon filament yarn.
Use: Cargo parachute harness, packs, drop kits, tie down lines, hoists, slings, etc.
Class: IA (undyed; not fungus proofed); IB (undyed; fungus proofed); 2A (dyed; not fungus proofed) 2B (dyed; fungus proofed); 3 (resin dyed; fungus proofed during dyeing).

TABLE 4.12 NYLON WEBBING

Data from MIL-W-4088[242] and MIL-W-27265[243] (impregnated)

Type	Min. Break Str. (lbs)	Width (inch)	Max. Weight (oz/yd)	Thickness (inch)	Yarn denier & filament	Ply W	Ply B	Ply F	Min. Warp ends	Picks per inch
I	500	9/16±1/32	0.28	.025–.040	420/68*	1		1	92	34
Ia	600	3/4±1/32	0.32	.025–.035	420/68*	1		1	108	34
II	600	1±1/32	0.42	.025–.040	420/68*	1		1	134	34
III	800	1 1/4±1/32	0.52	.025–.040	420/68*	1		1	168	34
IV	1,800	3±1/8	1.20	.025–.040	420/68*	1		1	400	34
VI	2.500	1 23/32±1/16	1.15	.030–.050	840/140	2		2	114	21
VII	5,500	1 23/32±1/16	2.35	.060–.100	840/140	2	1	2	256	26
VIII	3,600	1 23/32±1/16	1.60	.040–.070	840/140	2		2	166	18
VIIIa	6,300	3±3/32	2.80	.040–.070	840/140	2		2	280	18
VIIIb	4,500	2±1/16	1.80	.040–.070	840/140	2		2	192	18
VIIIc	5,300	2 1/4±1/16	2.10	.040–.070	840/140	2		2	222	18
IX	9,000	3±3/32	4.00	.065–.100	840/140	3	2	2	288	28
X	8,700	1 23/32±3/32	3.70	.105–.140	840/140	3	1	2	288	22
XII	1,200	1 23/32±1/16	.85	.025–.040	420/68*	1		1	266	34
XIII	6,500	1 23/32±1/16	2.90	.080–.120	840/140	2	1	2	315	24
XIV	1,200	1/2±1/32	.80	.070–.100	210/34	7		7	91	36
XV	1,500	2±1/16	1.25	.035–.050	840/140	2		2	88	15
XVI	4,500	1 23/32±1/16	2.00	.045–.080	840/140	2		2	198	17
XVII	2,500	1±1/16	1.15	.045–.070	840/140	2		2	114	15
XVIII	6,000	1±1/16	2.05	.100–.160	840/140	2		2	260	18
XIX	10,000	1 3/4±3/32	4.10	.100–.130	840/140	2		2	280	18
XX	9,000	1±3/32	3.25	.170–.210	840/140	5	1	3	188	19
XXI	3,600	1 1/4±1/16	1.70	.065–.085	210/34	5		10	260	25
XXII	9,500	1 23/32±3/32	3.50	.090–.120	840/68	3		2	259	18
XXIII	12,000	1 1/8±3/32	3.70	.200–.300	840/140	3	2	3	315	15
XXIV	5,500	1 15/16±3/32	2.25	.055–.075	840/140	2		3	244	17
XXV	4,500	1±1/16	1.50	.080–.125	840/140	2	1	2	189	22
XXVI	15,000	1 3/4±1/16	4.90	.150–.180	840/140	5		3	236	16
XXVII	6,500	1 23/32±1/16	2.90	.085–.110	840/68	3		2	215	24
XXVIII	8,700	2 1/4±3/32	3.80	.080–.110	840/140	3	1	2	288	22

* Values for warp yarns only. Filling yarns for these webbings are 840/140.

Material: Class 1 - critical use (shuttle loom nylon 6,6): Class 2 - non-critical use (shuttleless loom and nylon 6 optional) applies to Types VIII, VIIIa, VIIIb, VIIIc, when used solely for equipage or non-life support items.

Color: Natural, olive drab, sage green, yellow

Weave: For details of weave and type identification, see Reference 242.

Use: Parachutes and accessories

Note: This webbing is also available, resin impregnated (MIL-W-27265, Class R), or latex impregnated (MIL-W-27265, Class L). Impregnated webbing tolerances + 10% in weight and 12% in thickness.

TABLE 4.13 NYLON WEBBING

Data from MIL-W-83279, Reference 244

Type	Min. Break Str. (lbs)	Width (inch)	Max. Weight (oz/yd)	Thickness (inch)	Warp Ends ply	Warp Ends no.	Binder ply	Binder ends	Filling min. picks per inch ply	Filling min. picks per inch no.
I	6,000	.80	1.8	.20	3	150	1	24	3	16
II	9,000	.90	2.5	.22	5	138	1	22	3	16
III	12,000	1.00	3;3	;26	7	132	1	21	5	13

Yarn: 840 denier, 140 filaments, ½ Z turns per inch
Color: Natural
Ident : Type I, black thread in selvage; Type II, red thread in selvage; Type III, yellow thread in selvage
Use: Aerial retrieval parachutes and accessories

TABLE 4.14 NYLON WEBBING, TUBULAR

Data from MIL-W-5625, Reference 245

Min. Break Str. (lbs)	Width (inch)	Max. Weight (oz/yd)	Thickness (inch)	Warp Ends ply	Warp Ends no.	Filling min. picks per inch ply	Filling min. picks per inch no.
950	3/8	.40	.090				
1000	1/2	.50	.090	1	111	26	1
1500	9/16	.60	.090	1	137	26	1
1850	5/8	.70	.100	2	89	26	2
2300	3/4	.95	.120	2	109	26	2
3100	7/8	1.00	.120				
4000	1	1.70	.120	2	159	26	2

Color: Natural
Ident : 1/2, 3/4 and 1 inch, black yarn center one face; 9/16 inch, black yarn center, both faces; 5/8 inch, 2 black separated by 3 white yarns
Use: Parachute construction

TABLE 4.15 NYLON WEBBING

Data from MIL-W-27657, Reference 246

Type	Min. Break Str. (lbs)	Width (inches)	Max. Weight (oz/yd)	Thickness (inch)	Warp Ends ply	Warp Ends no.	Binder Ends ply	Binder Ends no.	Filling min. picks per inch ply	Filling min. picks per inch no.
I	3,000	3/4±1/16	.90	.080--.095	2	105	1	7	2	22
II	4,000	1±1/16	1.25	.090—.110	2	145	1	9	2	22
III	6,000	1±1/16	1.65	.100--.120	2	224			2	16
IV	8,700	1-23/32±1/16	2.40	.080--.100	2	324			2	18
V	9,000	1±1/16	2.40	.175—.195	3	224			2	17
VI	10,000	1-3/4±1/16	2.70	.115--.135	2	250			2	18

Yarn: 840/140 ultraviolet resistant
Color: Natural
Use: Aerial retrieval equipment

TABLE 4.16 NYLON WEBBING

Data from MIL-W-9049, Reference 247

Min. Break Str. (lbs)	Width (inches)	Max. Weight (oz/yd)	Min. Break Elong. (%)	Length of Loop (inch)	Min. Loop Str. (lbs)	Warp min. ends per inch ply	no.	tpi	Filling min. picks per inch ply	no.	tpi
400	1/4±1/16	.22	20	1/4±1/16	185	1	180	42	2	60	2½S

Cut Lengths: Class I, 2-5/8 to 2-7/8; class 2, 3-5/8 to 3-7/8; class 3, 5-7/8 to 6-1/8.
Color: Natural
Use: Locking and reinforcing parachute packs

TABLE 4.17 POLYESTER WEBBING

Data from MIL-W-25339, Reference 248

Type	Min. Break Str. (lbs)	Width (inch)	Max. Weight (oz/yd)	Thickness (inch)	Warp min. ends per inch ply	no.	Filling min. picks per inch ply	no.
I	1800	1-23/32±1/16	1.30	.040–.050	7	108	9	18
II	3000	1±1/32	1.80	.110–.140	10	120	10	20
III	8700	1-23/32±1/16	3.75	.125–.145	10	210	9	20
IV	9700	2±1/16	4.35	.110–.130	10	346	10	18

Yarn: 220 denier, high tenacity, continuous filament, 2½ – 3½ tpi.
Color: Natural
Ident: Type I, two red threads at center of warp; Type III, two green threads at center
Use: Parachutes exposed to high temperature conditions

TABLE 4.18 POLYESTER WEBBING

Data from MIL-W-25361, Reference 249

Type	Min. Break Str. (lbs)	Width (inch)	Max. Weight (oz/yd)	Thickness (inch)	Max. % Elongation at 2500 lb	3000 lb	90% of break
I	3600	1-23/32±1/16	1.65	.040–.065	18		
II	6000	1-23/32±1/16	2.10	.060–.080		13	17.5
III	7000	1-23/32±1/16	2.50	.075–.090		12	17.5
IV	8700	3±1/8	3.50	.065–.085		12	18.5

Color: Natural
Use: Safety belts, harnesses

TABLE 4.19 POLYESTER WEBBING, IMPREGNATED

Data from MIL-W-19078, Reference 250

Condition	Min. Break Str. (lbs)	Width (inch)	Max. Weight (oz/yd)	Thickness (inch)	Warp Ends ply	Warp Ends no.	Filling picks per inch
Untreated		1-23/32±1/16	3.00		2	256	26
Treated	6000		3.30*	.075–.115			

Weight*: Untreated plus .30 oz/yd max.
Latex: Natural or polyisoprene with curatives
Use: Safety belt shoulder harnesses

TABLE 4.20 LOW MODULUS ARAMID WEBBING

Data from MIL-W-38283, Reference 251

Type	Min. Break Str. (lbs)	Width (inch)	Max. Weight (oz/yd)	Thickness (inch)	Warp min. ends ply	Warp min. ends no.	Yarn denier W&F	Filling min. picks per inch ply	Filling min. picks per inch no.
I	500	9/16±1/32	.28	.025–.040	4	70	200	2	34
II	600	1±1/32	.40	.015–.030	4	80	200	2	34
III	5,500	1-23/32±1/16	2.75	.080–.110	2	250	1200	2	20
IV	3,600	1-23/32±1/16	1.75	.055–.075	2	154	1200	1	16
V	9,000	3-1/32±1/8	4.50	.075–.110	2	403	1200	2	22
VI	8,700	1-23/32±1/16	4.35	.145–.175	3	259	1200	2	18
VII	1,200	1-23/32±1/16	.70	.015–.030	4	146	200	2	34
VIII	6,500	1-23/32±1/16	3.00	.090–.120	2	272	1200	2	17
IX	6,000	1±1/16	2.70	.140–.175	2	252	1200	2	17
X	10,000	1-3/4±1/16	4.30	.140–.175	3	282	1200	2	17
XI	9,000	1±1/16	4.10	.220–.260	4	199	1200	2	18
XII	7,300	1-23/32±1/16	3.40	.090–.120	2	305	1200	2	17
XIII	800	1-1/4±1/32	.50	.015–.030	4	106	200	2	34
XIV	2,500	1±1/32	1.20	.060–.080	2	192	1200	1	14
XV	1,700	1-1/2±1/16	1.35	.045–.065	1	177	1200	1	47

Yarn: Twist of plied yarns shall be 2-½ turns per inch min.
Material: Nomex; manufactured by E. I. DuPont de Nemours & Co., Inc.
Binder: Types III, V, VI, XI and XV include a single binder, 1200 denier in warp.
Color: Olive green
Use: Parachute construction and accessories, safety belts, bomb hoists and slings, etc.

TABLE 4.21 LOW MODULUS ARAMID TUBULAR WEBBING

Data from MIL-W-38282, Reference 252

Type	Min. Break Str. (lb)	Width (inch)	Max. Weight (oz/yd)	Min. Break Elong. (%)	Max. Thickness (inch)	Warp Ends ply	Warp Ends no.	Filling picks per inch
I	1400	9/16±1/16	.60	12	.080	4	149	24
II	2300	3/4±1/16	.95	15	.095	8	125	24
III	4000	1±1/16	1.60	20	.120	8	211	24

Yarn: 200±15 denier; 100 filaments, twist 2½ turns per inch
Material: Nomex; manufactured by E. I. DuPont de Nemours & Co., Inc.
Color: Sage green
Use: Parachute construction

TABLE 4.22 LOW MODULUS ARAMID WEBBING, TUBULAR WITH NYLON CORE

Data from MIL-W-81528, Reference 253

Min. Break Str. (lbs)	Min. Elong. (%)	Width (inch)	Max. Weight (oz/yd)	Thickness (inch)	Warp min. ends webbing	Warp min. ends core	Filling min. picks per inch
2400	18±2*	1/2±1/16	1.00	.120–.160	288	80	60

* Applies to test elongation at 2000 lb tension

Yarn: Tubular warp 200 denier , Core warp 210 denier, 10 ply or 1100 denier, 2 ply.
Material: Nomex for tubular webbing; nylon 66 for core yarn.
Color: Not specified
Use: Drogue withdrawal line for ejection seat system.

TABLE 4.23 TAPE AND WEBBING, TEXTILE, PARA-ARAMID INTERMEDIATE MODULUS

Data from MIL-T-87130, Reference 273

TYPE	CLASS	WIDTH (inches)	MAX. WEIGHT (oz/yd)	MIN. BREAKING STRENGTH (lb)	WARP DENIER	WARP PLY	WARP TOTAL ENDS	FILL DENIER	FILL PLY	FILL PICKS (per in)	WEAVE
I	1	½	.05	250	200	1	42	200	1	35	Plain
	2	½	.09	550	400	1	39	400	1	22	Plain
	3	½	.12	800	200	1	122	200	1	35	1/3 Twill – Center Reversal
	4	½	.56	3,500	1500	1	79	1000	1	24	Plain
II	1	9/16	.13	800	400	1	58	400	1	32	Plain
IV	1	¾	.10	500	200	1	90	200	1	38	Plain
	4	¾	.50	3,000	1500	2	31	1500	1	12	Plain
	5	¾	.60	4,100	1500	2	41	1500	1	11	Plain

TABLE 4.23 (Continued)

Data from MIL-T-87130, Reference 273

TYPE	CLASS	WIDTH (Inches)	MAX. WEIGHT (oz/yd)	MIN. BREAKING STRENGTH (lb)	WARP DENIER	WARP PLY	WARP TOTAL ENDS	FILL DENIER	FILL PLY	FILL PICKS (per in)	WEAVE
VI	2	1	.12	525	200	1	90	200	1	50	Plain
	3	1	.11	750	200	1	108	200	1	35	Plain
	4	1	.23	1,400	400	1	102	400	1	31	Plain
	5	1	.22	1,500	400	1	108	400	1	26	Plain
	6	1	.36	2,400	1500	2	24	1500	1	14	Plain
	7	1	.44	3,200	1000	2	48	1000	1	15	Plain
	8	1	.55	3,000	1500	2	30	1000	1	12	Plain
	9	1	1.00	6,000	1500	3	44	1500	1	10	Plain
	10	1	1.50	9,500	1500	3	76	1500	1	8	2/2 HBT - Center Reversal
	11	1	1.65	12,500	1500	3	89	1500	1	9	Plain
VII	1	1-⅛	.23	1,100	400	1	96	400	1	34	
	2	1-⅛	.45	2,750	1000	2	45	1000	2	12	Plain
	6	1-⅛	2.00	13,500	1500	2	140	1500	2	14	5/1 HBT - Center Reversal
VIII	1	1-¼	.23	800	400	1	60	1000	1	26	Plain
IX	1	1-½	.12	500	200	1	82	200	1	48	Plain
	2	1-½		1,100	200	1	172	200	1	36	Plain
	5	1-½		3,000	1000	1	96	1000	1	18	Plain
X	1	1-¾	.17	1,000	200	1	156	200	1	34	Plain
	2	1-¾	.35	1,200	400	1	103	1000	1	23	Plain
	3	1-¾	.45	2,500	1000	1	84	1000	1	16	Plain
	5	1-¾	.60	4,000	1000	2	55	1000	1	15	Plain
	6	1-¾	.80	4,500	1500	2	50	1500	1	17	Plain
	7	1-¾	1.00	6,500	1500	1	140	1500	1	11	Plain
	8	1-¾	1.20	8,000	1500	2	88	1000	1	10	Plain
	9	1-¾	1.75	10,000	1500	2	127	1500	1	12	2/2 HBT - Center Reversal
	11	1-¾	2.40	15,000	1500	3	121	1500	1	13	Double Plain
	13	1-¾	2.50	20,000	1500	3	137	1500	1	9	Double Plain
XI	3	2	.121	400	200	1	60	200	1	50	Plain(1)
	5	2	.15	600	200	1	96	200	1	50	Plain
	7	2	.16	800	200	1	124	200	1	42	Plain
	9a	2	.23	1,000	200	1	164	200	1	46	Plain(2)
	9b	2	.18	1,000	200	1	150	200	1	45	Plain
	11	2	.26	1,500	400	1	108	400	1	31	Plain
	13	2	.32	2,000	400	1	142	400	1	30	Plain
	14	2	.37	2,500	1000	1	77	400	1	26	Plain
	15	2	.44	3,000	1000	1	96	400	1	24	Plain
	16	2	.60	4,000	1000	2	58	1000	1	20	Plain
	17	2	.80	5,000	1500	1	110	1500	1	13	Plain
	19	2	1.05	8,000	1500	1	160	1500	1	12	Plain

(1) Coating is needed for seamability
(2) 6 turns per inch in warp yarn

TABLE 4.24 WEBBING, TUBULAR, PARA-ARAMID, INTERMEDIATE MODULUS

Data from MIL-W-87127, Reference 274

TYPE	WIDTH (in) (1)	WEIGHT LIN. YD (max) (oz/yd)	BREAKING STRENGTH (lb min) (3)	ENDS IN WARP	PICKS PER INCH (2)	SINGLE YARN/ FINAL PLIED YARN		YARN DENIER	
						WARP	FILL	WARP	FILL
I	1/2	0.25	1250	39	40	1	1	1000	1000
II	9/16	0.30	1500	45	34	1	1	1000	1000
III	9/16	0.35	2000	41	27	1	1	1500	1000
IV	3/4	0.50	2800	59	27	1	1	1500	1500
V	1	0.70	3500	81	27	1	1	1500	1500

(1) Width tolerance ± 1/16 inch
(2) Half on each side of flattened tube
(3) Requirement based on any single specimen

TABLE 4.25 COTTON TAPE AND WEBBING

Data from MIL-T-5661, Reference 254

Type	Min. Break Str. (lbs)	Width (inch)	Max. Weight (oz/yd)	Weave	Warp Ends		Filling	
					no.	ply	picks per in.	ply
I	80	1/4±1/32	.11	plain	7	4	20	2
	120	3/8±1/32	.15		10	4	20	2
	150	1/2±1/32	.22		14	4	20	2
	170	5/8±1/32	.28		18	4	20	2
	200	3/4±1/32	.33		22	4	20	2
	250	1±1/32	.47		30	4	20	2
II	110	1/2±1/32	.15	double	142	2	48	2
	165	3/4±1/32	.22	herringbone	212	2	48	2
	220	1±1/32	.29		284	2	48	2
	275	1-1/4±1/32	.36		356	2	48	2
	330	1-1/2±1/32	.43		426	2	48	2
	375	1-3/4±1/32	.50		496	2	48	2
	425	2±1/32	.57		568	2	48	2
III	45	1/2±1/32	.10	twill	64	2	60	1
	55	5/8±1/32	.12		85	2	60	1
	75	3/4±1/32	.14		96	2	60	1
V	350	1±1/32	.65	plain	48	4	16	4
	650	2±1/32	1.30	tranverse	96	4	16	4
VI	80	5/8±1/32	.23	non-elastic	154	2	46	2
	375	1±1/32	.98		173	2	52	2

Color: Natural (bleached)
Use: Type I, Reinforcing tape on fabric; others, binding and reinforcing parachute packs.

TABLE 4.26 RAYON TAPE AND WEBBING

Data from MIL-T-5237, Reference 255

Type	Min. Break Str. (lbs)	Width (inch)	Min. Length per lb (ft)	Min. Warp Ends	Min. Picks per in.	Weave
I	50	9/16±1/32	600	48	36	plain
I	100	1-1/8±1/32	300	94	36	plain
I	140	1-1/4±1/32	240	116	30	herringbone twill
Ia	160	3/8±1/32	300	30	36	herringbone twill
Ia	500	9/16±1/32	120	280	21	plain
Ia	500	1±1/32	96	90	36	plain
Ia	750	1-5/8±1/32	45	136	36	herringbone twill
II	125	1/8±1/32	375	23	24	tubular plain
II	100	3/16±1/32	300	30	30	tubular plain
II	40	1/2±1/32	120	81	30	tubular plain
II	40	9/16±1/32	120	81	20	tubular plain
II	23	5/8±1/32	69	130	52	tubular plain

Yarn: Filling shall be 275 denier min.
Material: Bright multifilament viscose rayon
Color: Natural
Use: Parachute canopies in bomb applications.

TABLE 4.27 NYLON TAPE AND WEBBING

Data from MIL-T-5038, Reference 256

Type	Min. Break Str. (lbs)	Min. Break Elong. (%)	Width (inch)	Max. Weight (oz/yd)	Thickness (inch)
II, Tape	900	18	2±1/32	.40	.025–.035
	1300	18	1-1/2±1/32	.60	.025–.035
	1700	18	2±1/32	.80	.025–.035
III, Tape	200	28	3/8±1/32	.12	.015–.025
	250	18	1/2±1/32	.15	.015–.025
	400	18	3/4±1/32	.20	.015–.025
	525	18	1±1/32	.40	.015–.025
	900	18	1-1/2±1/32	.40	.015–.025
IV, Webbing	550	18	1/2±1/32	.35	.030–.040
	625	18	5/8±1/32	.40	.030–.040
	1000	18	1±1/32	.50	.030–.040
	1100	18	1-1/8±1/32	.60	.030–.040
	1500	18	1-1/2±1/32	.75	.030–.040
V, Tape	500	18	9/16±1/32	.20	.020–.030
VI, Tape	425	18	3/4±1/32	.20	.020–.030

Color: Natural
Use: Binding and reinforcing parachute packs

TABLE 4.28 NYLON TAPE AND WEBBING

Data from MIL-T-8363, Reference 257

Type	Min. Break Str. (lbs)	Width (inch)	Max. Weight (oz/yd)	Thickness (inch)	Warp Ends ply	Warp Ends no.	Filling picks ply	Filling picks per in.	Filling picks denier
I	350	5/16 1/32	.08 min	.030–.040	1	121	1	60	210/34
II	290	7/16 1/32	.09 min	.020–.030	1	98	1	72	210/34
III	400	3/4 1/16	.50 max	.050–.060	2	88	3/3	48	210/34
IV	2600	3/4 1/16	1.05 max	.070–.085	2/1	135	1	24	840/140
V	1000	25/32 1/16	.70 max	.050–.060	4	87	10	32	260/17

Color: Sage green
Use: Intended for flight clothing and accessories

TABLE 4.29 NYLON TAPE

Data from MIL-T-5666, Reference 258

Min. Break Str. (lbs)	Min. Break Elong. (%)	Width (inch)	Max. Weight (oz/yd)	Thickness (inch)	Warp Ends	Picks per in.
500	20	1-3/4±1/16	.40	.020–.025	199	84

Yarn: Warp denier 210 ± 5%; filling denier 420 ± 5%; twist 2-½ turns per inch min.
Color: Sage green; olive drab
Use: Parachute packs

TABLE 4.30 NYLON TAPE

Data from MIL-T-6134, Reference 259

Type	Min. Break Str. (lbs)	Min. Break Elong. (%)	Width (inch)	Max. Weight (oz/yd)	Thickness (inch)	Warp Ends ply	Warp Ends no.	Filling picks ply	Filling picks per in.
I	525	16	1±1/16	.400	.025–.045	1	206	4	44
II	300	14	1±1/16	.145	.010–.030	1	104	2	58

Yarn: Warp denier 210; twist 2-½ turns per inch min. (Filling yarn twist, Type II = 15 tpi)
Color: Natural
Use: Parachutes; Type I for skirt bands; Type II for reinforcing bands

TABLE 4.31 NYLON TAPE

Data from MIL-T-5608, Reference 260

Class	Type	Max. Break Str. (lbs)	Min. Break Elong. (%)	Width (inch)	Min. Length per lb (ft)	Warp Ends denier	Warp Ends min. no.	Filling denier	Filling picks per inch
A	I	13	18	1/4±1/64	3900	20	72	40	140
	II	18	18	3/8±1/64	2625	20	104	40	140
	III	43	18	5/8±1/32	1320	20	237	40	140
	IV	65	18	1-1/4±1/16	780	20	352	40	140
	V	96	18	2±1/16	495	20	537	40	140
B	I	22	18	1/4±1/64	2910	30	86	40	118
	II	33	18	3/8±1/64	1950	30	126	40	118
	III	70	18	5/8±1/32	1080	30	237	40	118
	IV	120	18	1-1/4±1/16	630	30	392	40	118
	V	200	18	2±1/16	360	30	657	40	–
	VI	500	18	5±3/16	150	30	1616	40	–
C	I	39	22	1/4±1/64	2310	40	100	40	82
	II	58	22	3/8±1/32	1565	40	148	40	82
	III	90	22	5/8±1/32	1005	40	227	40	82
	IV	158	22	1-1/4±1/16	480	40	457	40	82
	V	300	22	2±1/16	300	40	757	40	80
D	I	280	18	1-1/4±1/16	240	210	94	210/2	52
	II	460	18	2±1/16	135	210	154	210/2	52
E	I	650	18	1-1/4±1/16	150	210	240	210/2	36
	II	1000	18	2±1/16	90	210	378	210/2	36
	III	1500	–	2±1/16	66	420	280/1	420	36
	IV	2000	–	2±1/16	51	420	378/1	420	36
	V	3000	–	2±1/16	39	840/1	260	840/1	26
	VI	4000	–	2±1/16	33	840/1	350	420/1	24

Yarn: Class A tapes are semi-dull, normal tenacity, light-resistant nylon; others are bright, high tenacity, heat and light-resistant nylon.

Color: Natural except Class B, Type VI (international orange) and Class C, Type V (yellow).

Air Permeability: 150 cfm/ft^2 for Class A, B and C, two inches or wider ribbons.

Use: Construction of ribbon parachutes.

TABLE 4.32 NYLON TAPE

Data from MIL-T-27746, Reference 261

Min. Break Str. (lbs/in) Warp body	Fill selv.	Total Width (inch)	Each Selvage (inch)	Max. Weight (oz/yd)	Air Permeability (cfm/ft^2)	Min. Yarn Count (yarns/in) Warp body	Warp selv.	Fill
625	900 450	11±1/4	1-1/8±1/16	3.5	70±20	48	41	36

Yarn: Selvage – 2 ends of 840/140 denier woven as 1: twist 2-3/4 "Z" turns per inch.
Color: Natural
Use: For construction of ringslot parachutes.

Broad Woven Fabrics. Textile fabrics are woven on a loom with warp yarns running the bolt length direction and filling yarns at right angles fed from shuttles which return alternately from side to side. The edge of the woven fabric is usually reinforced with strong warp threads in a "selvage" having good tear resistance. Fabrics are available for parachute construction in nylon, polyester, Nomex aramid, rayon, and cotton. Material weights vary from 1 to 14 oz/yd^2. Broad woven fabrics are available from the loom in standard 36-inch or other width rolls, with warp and fill yarns usually the same in strength and number per inch. In very lightweight fabrics, tear resistance is critical requiring a special ripstop weave, and low air permeability is hard to maintain. Selvages provide strong edges for seaming, but cut cloth edges require special care in fabrication. Because of the limitation in Kevlar aramid yarn deniers available today, the lightest broad woven fabric of acceptable porosity which can be made from 200 denier Kevlar yarn is about 2½ oz/yd^2. This has strength equivalent to nylon fabric weighing about 7 oz/yd^2. As a result, weight savings can be realized only on the heavier nylon fabrics, many of which are duck weaves used in parachute packs.

Characteristics of textile fabrics currently available and defined by military specifications are given in Tables 4.33 through 4.40.

TABLE 4.33 COTTON CLOTH

Data from MIL-C-4279, Reference 262

Type	Min. Weight (oz/yd^2)	Min. Break Str. (lbs) Warp	Fill	Min. Tear Str. (lbs) Warp	Fill	Air Permeability (cfm/ft^2)	Min. Yarns per inch Warp	Fill
II	3.5	48	42	3.0	2.5	170–230	54	56
III	3.6	48	45	3.0	2.5	130–190	56	58

Weave: Plain
Finish: Type III (softener and mildew inhibitor treated)
Use: Cargo parachute canopies

TABLE 4.34 NYLON OR RAYON CLOTH

Data from MIL-C-19262, Reference 263

Type	Class	Max. Weight (oz/yd^2)	Total Ribbon Width (inch)	Included Selvage Width (inch)	Min. Break Str. (lbs/in) Warp	Fill	Min. Elong. both directions (%)	Min. Tear Str. Warp	Fill	Min. Selvage Str. (lbs)	Air Permeability (cfm/ft^2)
I	A	5	13±1/4	1-1/4±1/8	350	130	25	45	20	475	45–75
I	B	8	13±1/4	1-1/4±1/8	560	210	30	70	30	775	45–75
I	C	10	11±1/4	1-1/8±1/8	625	425	30	75	60	625	60–100
II	A	5	13±1/4	1-1/4±1/8	250	160	10	35	25	385	45–75
II	B	8	13±1/4	1-1/4±1/8	400	260	10	55	44	620	45–75
II	C	10	11±1/4	1-1/8±1/8	500	330	10	70	55	775	60–100

Material: Type I, nylon; Type II, saponified acetate (rayon)
Width: Overall cloth - 40 to 48 inches forming three or more ribbons with dupe selvage edges constrained with leno locked ends. Separation filling yarns 1/2±1/8 inch between ribbons.
Use: Ringslot parachute canopies used with underwater ordnance.

TABLE 4.35 LIGHT WEIGHT NYLON CLOTH

Data from MIL-C-7020, Reference 264

Type	Max. Weight (oz/yd^2)	Max. Thickness (inch)		Min. Break Str. (lbs/in)		Min. Elong. (%)	Min. Tear Str. (lbs)		Air Permeability (cfm/ft^2)	Min. Yarns per inch		Min. Selvage Break (lbs)
		Body	Selv.	Warp	Fill	W&F	Warp	Fill		Warp	Fill	
I	1.1	.003		42	42	20	5	5	80–120	120	120	
Ia	1.1	.003	.005	42	42	20	5	5	80–120	120	120	56
II	1.6	.004		50	50	20	5	5	100–160	120	76	
IIa	1.6	.004	.006	50	50	20	5	5	100–160	120	76	66
III	1.6	.004		50	50	20	4	4	100–160	120	76	
IIIa	1.6	.004	.006	50	50	20	4	4	100–160	120	76	66

Weave: Ripstop - Types I, Ia, III, IIIa; Twill - Types II and IIa.
Yarn: Warp, five turns per inch minimum twist.
Color: Natural (orange when specified)
Width: 36.5±.5 inches including 1/2±1/16 inch selvage (types Ia, IIa, and IIIa).
Use: Parachute canopies.

TABLE 4.36 MEDIUM WEIGHT NYLON CLOTH

Data from MIL-C-7350, Reference 265

Type	Max. Weight (oz/yd^2)	Max. Thickness (inch)	Min. Break Str. (lbs/in)		Min. Elong. (%)	Min. Tear Str. (lbs)		Air Permeability (cfm/ft^2)	Min. Yarns per inch		Min. Twist (tpi)	
			Warp	Fill	W&F	Warp	Fill		Warp	Fill	Warp	Fill
I	2.25	.0068	90	90	25	10	10	100–150	70	70	5	5
II	3.50	.0140	135	125	25	30	30	150–200	52	52	6	6

Finish: Heat set and calendered
Color: Natural; yellow for aircraft deceleration parachutes
Width: 36.5±.5 inches
Use: Cargo and aircraft deceleration parachute canopies

TABLE 4.37 HEAVY WEIGHT NYLON CLOTH

Data from MIL-C-8021, Reference 266

Type	Max. Weight (oz/yd^2)	Min. Thick. (inch)	Min. Break Str. (lbs/in)		Min. Elong. (%)		Min. Tear Str. (lbs)		Min. Yarns per inch		Yarn ply	Air Permeability (cfm/ft^2) water pressure	
			Warp	Fill	Warp	Fill	Warp	Fill	Warp	Fill	W&F	½ inch	20 inches
I	4.75	.020	200	200	25	25	15	15	70	70	single	50–90	450–650
II	7.00	.024	300	300	25	25	20	20	20	53	2	50–90	450–650
IIa	10.50	.025	500	500	25	25	75	75	40	38	4	50–90	650–750
III	14.00	.035	600	600	25	25	75	75	38	38	single	15–55	250–450

Color: Natural
Width: 36.5±.5 inches
Use: Cargo and deceleration parachutes

TABLE 4.38 NYLON DUCK

Data from MIL-C-7219, Reference 267

Type	Max. Weight (oz/yd^2)	Min. Break Str. (lbs/in) Warp	Fill	Min. Tear Str. (lbs) Warp	Fill	Air Permeability* (cfm/ft^2)	Min. Yarns per inch Warp	Fill	Yarn Ply Warp	Fill	Min. Water* Resist. (cm/H_2O)	Max. Shrinkage (%) Warp	Fill
I	9.50	400	300	35	45	5	80	38	2	3	25	2.5	2.0
II	8.75	400	150	35	20	5	78	38	2	2	30	2.5	2.0
III	7.25	325	275	20	20	8	60	45	2	2	25	2.0	2.0

*Applicable only to Class 3 (subjected to boiling water for 15 minutes).

Finish: Class I, untreated; Class 2, non-durable water repellent treated; Class 3, durable water repellent treated.
Use: Parachute packs and equipage.

TABLE 4.39 LIGHT NYLON CLOTH

Data from MIL-C-498, Reference 268

Type	Max. Weight (oz/yd^2)	Min. Break Str. (lbs/in) Warp	Fill	Min. Elong. (%) Warp	Fill	Min. Tear Str. (lbs) Warp	Fill	Min. Yarns per inch Warp	Fill	Air Permeability (cfm/ft^2)
D	.88	40	40	20	20	2.5	2.5	90	90	300–500
H	2.20	65	65			5.0	4.0	104	91	60–100

Yarn: Type D, 30 denier; Type H, 70 denier multifilament nylon.
Weave: Plain
Finish: May be heat treated and calendered to achieve air permeability.
Use: For ammunition and flare parachutes.

TABLE 4.40 LOW MODULUS ARAMID CLOTH

Data from MIL-C-38351, Reference 269

Type	Class	Max. Weight (oz/yd^2)	Max. Thick. (inch)	Min. Break Str. (lbs/in) Warp	Fill	Min. Break Elong. (%) Warp	Fill	Min. Tear Str. (lbs) Warp	Fill	Air Permeability (cfm/ft^2)	Min. Yarns per inch Warp	Fill	Min. Yarn ply Warp	Fill
I	1	4.7	.011	165	165	30	30	14	14	40–70	74	74	1	1
I	2	6.7	.020	265	200	25	25	20	20	50–80	63	48	2	2
I	3	12.0	.032	425	425	15	15	75	75	40–80	38	38	5	5
II	1	7.0	.015	250	190	35	25	15	15	8 max	60	45	2	2
II	2	18.0	.036	950	950						59	60	5	5

Yarn: 200±15 denier Nomex; manufactured by E. I. DuPont de Nemours & Co., Inc.
Aging: Minimum breaking strength after aging shall be 85 percent of unaged breaking strength.
Finish: Type II, Class 2 resin treated. Minimum stiffness - warp .45 to .65 inch-lbs; fill .65 to .85 inch-lbs.
Color: Natural, sage green
Use: Parachute canopies, packs and pack stiffners.

Experimental Materials. Research and development of textiles for recovery systems applications has been directed toward properties of increased environmental resistance (especially high temperature), improved mechanical strength with minimum bulk, increased energy absorption, low porosity lightweight cloth and low-cost textiles. Experimental fabric constructions have been prepared and tested for parachute applications including knit, triaxial woven and stretch fabrics, each of which appears to have potential advantages, but requires more development.

High Temperature Resistant Materials. Approaches to the development of textiles capable of performing at temperatures above 300°F include research on high melting-point organic polymers [275], the use of protective coatings for heat resistance and cooling by mass transfer, parachute designs in which fractional destruction of the canopy by heat can be tolerated after initial deployment, and fabrics [276] woven of fine metallic wires, high melting glasses, coated refractory fibers, metal and metal oxide whiskers and ceramic fibers.

The most developed of the temperature-resistant textiles are those woven of Nomex aramid, a synthetic organic fiber which does not melt, but loses all tensile strength at 700°F. More recently available on the market, and therefore less developed in recovery system textile applications are those woven of Kevlar aramid, which loses all strength at 930°F. Aramids do not melt, drip or fuse together as nylon does when exposed to flame, and they have good resistance to commonly used solvents and chemicals, Bisbenzimidazobenzophenanthroline (BBB), Polyimide, and Polybenzimidazole (PBI) polymers have been produced as fibers experimentally with demonstrated heat resistance properties in yarn and textiles. PBI is now in early stages of industrial production. Its room temperature strength is retained to 475°F with long exposure, and retains usable strength to 1000°F with short exposure. (BBB fiber samples have shown tensile properties exceeding four grams per denier tenacity and 15% elongation at room temperature, and thermal stability (strength and durability) in various environments up to 1100°F [277] BBB fiber also shows good retention of tensile properties in loop, knot and yarn configurations, low moisture sensitivity, good light stability, good abrasion resistance and dimensional stability. Small (5 and 8 inch) Supersonic-X model parachutes constructed of BBB and Kevlar 29 textiles have been tested in low density wind tunnel wake flow tests at free stream temperatures to 760°F [278]

Experimental work [276] with fabrics woven from single-drawn and bundle-drawn stainless steel and superalloy wire indicates that such fabrics should be suitable as decelerator construction material for high temperature use in such devices as space vehicle drag producing surfaces. These materials can be made strong enough to carry the aerodynamic pressure loading, are foldable into a compartment of a vehicle, will be unaffected by the high vacuum environment during space travel and will resist high Mach number thermal environments to 1500°F during atmospheric entry. Through the process of bundle drawing, 0.5 mil fibers have been produced in the superalloy Chromel R and woven in 100 filament yarns into plain, basket and twill weave fabrics having greatly improved properties over the monofilament mesh fabric. A major penalty of wire fabrics is their weight (13 to 24 required ounces per square yard) and high cost.

A severe thermal environment requires a structure which is non-porous, so that the relatively cool boundary layer is not bled off with consequent increase in heat transfer to the material. In addition, the emmissivity of the metal woven fabric must be high, so that the effect of aerodynamic heating can be reduced by radiation as efficiently as possible. In order to achieve a suitable nonporous fabric, silicone rubber and other high temperature flexible coatings are utilized on the metal woven fabric.

Lightweight Materials. Problems of excess bulk and weight in stowed recovery systems are frequently the result of insufficient planning to define space requirements or to allow for growth in vehicle weight or performance criteria without corresponding increases in allocated compartment volume. The alternatives to more space and weight allowance are usually an increase in pack density or a redesign using higher strength-to-weight ratio textiles. Parachute textile specifications are so written that materials produced in accordance with their provisions usually have actual breaking strengths with ample excess over the minimum specified. To take advantage of the actual strength margin of textiles requires testing of as-received materials, or purchase from the supplier of only the product which betters specification strength or weight by a fixed amount. When requirements are tight, some advantage may be gained by selecting weaves having higher translation efficiency without compromise of air permeability, energy absorption, abrasion resistance, or other important properties. Very lightweight fabrics are woven of low denier

yarns. In order to achieve low air permeability, the fabric is flattened between heated rollers, a process called *"calendering"*.

Low Cost Materials. Materials have been investigated for application to low-cost expendable parachutes. They include both plain and scrim-reinforced nylon paper, polyester paper, polypropylene film, reinforced polyethylene film, and cotton fabrics for canopies. Suspension line materials include braided polyethylene, braided nylon, and braided fine and coarse filament polypropylene cord. Plastic films and braided cords form better seam joints and line attachments by heat sealing and cementing than by sewing.

Air drops of experimental solid flat circular and ringslot canopies fabricated of the above materials have been achieved successfully with suspended loads from 300 to 1500 pounds [275].

Coated Fabrics and Films

Gliding parachutes with wing-like canopies and balloon type decelerators require their principal fabric to be of low, or near zero, air permeability material. Conventional woven cloth usually proves to be unsuitable because the required low level of air permeability cannot be achieved, particularly when the fabric is subjected to biaxial stress. Although the application of a coating will produce low permeability, some conventional coating materials present an undesirable adhesion problem between the coated surfaces under pressure packing conditions. Other penalizing factors are the added weight of the coating, a reduced tear strength, and accompanying stiffness. The tearing strength of woven fabrics is higher than the tearing strength of corresponding weight films or papers, for example, because of the deformability of the weave which more effectively dissipates the stress away from the point of the tear. Application of a coating to a woven fabric, however, tends to reduce this deformability by sticking the yarns together at the intersections and filling the interstices of the fabric with a plug of coating material. The degree to which the fabric becomes immobilized by coating depends upon the elastic properties of the coating material. Ripstop fabrics lose their effective resistance to tear propagation when a coating is added to the material, reducing tear strength to the equivalent of an uncoated plain weave fabric.

Coating Materials. Some polymers useful for making fibers, discussed on page 144, are equally useful in modified form, as fabric coating or impregnating materials. Instead of being extruded as fibers, they are prepared more simply as either plastic or elastomeric (rubber-like) materials for direct application. Cellulosics, polyamides, polyesters, acrylics, vinyl chlorides and alcohols, vinylidene chlorides, polyolefins, polyurethanes, and natural and synthetic elastomers or rubbers are used as films or coatings. Natural rubber is obtained from the latex of a cultivated tree. Synthetics derive from polymerized acrylics, butadienes or isobutylenes. Some of the more popular synthetic rubbers are identified:

Butyl Rubber . . . Isobutylene copolymerized with isoprene. Butyl rubber has good heat and weather aging resistance. Trade names are "Enjay Butyl" (Enjay) and "Hycar" 2202 (Goodrich).

Polysulfide Rubber . . .Prepared from ehtylene dichloride and sodium polysulfide has excellent resistance to oils, fuels and solvents. Trade name "Thiokol" (Thiokol Chemical).

Chloroprene Rubber . . A polymer of two chlorobutadiene -1, 3. It was developed by DuPont and marketed under the trade name "Neoprene" (now a generic term). Multifilament nylon and polyester fabrics are neoprene coated for outdoor applications where resistance to weathering, abrasion and flexing over extended periods of time are important factors. Neoprene also possesses good resistance to oils, greases, gasoline, acids and alkalies.

Chlorinated Chlorosulfonated Polyethylene . . . . . Another synthetic rubber developed by DuPont is called "Hypalon". Hypalon coated fabrics have outstanding abrasion and outdoor weathering resistance properties.

Silicone Rubber . . . . . A silicone polymer's basic structure consists of silicon-oxygen linkages rather than carbon-carbon linkages. Dimethyl dichlorosilane is the monomer from which most silicone rubbers are prepared. Outstanding properties include high and low temperature stability as well as heat resistance. Trade names are "Silastic" and "RTV" (General Electric).

Fluorinated Rubbers . . . .Fluorine base polymers have been developed such as "Teflon" and "Viton" by DuPont and "Kel F" by 3M Company. "Viton A" is useful for coatings capable of withstanding temperatures as high as 600°F, and it has outstanding chemcal, solvent, fuel and lubricant resistance at elevated temperatures.

Di-Iso-Cyanates. . .A toluene di-iso-cyanate monomer reacts extremely rapidly with polyesters or polyethers to form polyurethanes. In the presence of water or a "blowing agent" a foam is formed, the polyesters usually producing flexible foams, and the polyethers producing rigid foams. Foamed polyurethanes are useful as thermal insulators, bonded by heat fusion or by adhesives to fabrics.

Schulman [279] reports that a coating procedure consisting of two base coats of a soft polyurethane cover-

ed with a coat of nylon when applied to one side of appropriately designed basket-weave nylon fabrics have been produced which represent an improvement over presently available fabrics, particularly with respect to tearing strength and ability to be pressure packed without adhesion. Six experimental coated fabrics ranging in weight from 1.8 oz/yd^2 to 6.0 oz/yd^2 were tested and found to retain most of the strength characteristics of the original woven fabric.

Inflatable landing or flotation bags usually require a relatively air-tight membrane material capable of withstanding a relatively high differential pressure during inflation and landing. Lightweight balanced fabric constructions with approximately equal strength in warp and filling are used for this purpose. These fabrics are woven and finished to meet rigid specifications including a high degree of heat stabilization in the finishing process to minimize distortion of the final product.

Films. Certain basic polymers useful for making fibers possess sufficient strength and tear resistance to be useful in film form. Most popular are the sealable polyolefins and polyvinyls. For special purpose parachutes, polyester has proved the most satisfactory film from a strength and efficiency standpoint. Films which have found use in other commercial applications are nylon, polyvinyl-fluoride, and polyimide (Kapton by DuPont). These films have properties of potential use in the recovery systems.

Polyester . . . . . .films are produced in thicknesses down to 1/4 mil (Mylar, DuPont). The film retains good physical properties over a wide temperature range (-94° to +300°F). It is available with an ultimate tensile strength of 25,000 psi and ultimate elongation of 120 percent (or 45,000 psi and 40 percent at higher tensile modulus). Other properties are generally similar to polyester fibers in Table 4.1, showing good characteristics of tensile impact energy, shear strength and dimensional stability. Polyester film is often coated with a vacuum deposited silver or aluminized surface to provide a parachute or balloon with light or radar reflection capability. Polyester films are not heat sealable.

Crushables

One form of energy absorbing media employed for impact attenuation exists as homogeneous cellular blocks or pads, placed under a platform or load to provide a nearly constant deceleration force to overcome the vertical velocity of the system after initial contact with the ground. The energy absorbing item may be constructed of balsa, or fabricated as a honeycomb structure with cell walls of aluminum, paper or high strength plastic laminates such as fiberglass-polyester, nylon-phenolic or equivalent with cells oriented in the vertical direction, or formed as a rigid plastic foam of polyurethane, epoxy, glass, phenolic or similar structural resins. Where the delivered load is of simple shape and the volume of cushion material can be externally accommodated, the block form joins the payload configuration as an add-on. In other applications it is often necessary to incorporate the crushable structure within the vehicle flight profile, i.e., a nose cone, tail appendage, keel structure or deployable struts.

Honeycomb Structures. Paper honeycomb is fabricated by joining alternate layers of kraft paper with parallel bond lines spaced between lineal bonds of adjacent layers. When the bonded paper sheets are expanded laterally, hexigon shaped cells become a core when rigidized by bonding on top and bottom face sheets to form a honeycomb panel. Three-inch thick panels in four sizes per MIL-H-9884 [280] are used to make up dissipaters for the landing shock of air-dropped material. The honeycomb panel is cut into sections and made into stacks which an average crushing stress of 6300 ± 900 psf to 70 percent strain.

The density of the expanded structure is determined by the weight of the paper plus adhesive, divided by the volume after expansion. This simple structure forming technique is used in fabricating honeycombs of aluminum foil and plastic materials also. The width of the cell, the weight and strength of sheet material and cell height of the block are parameters that influence the crushing stress and energy absorbing characteristics of the honeycomb structure. Mechanical properties of representative paper honeycomb [281] and honeycomb structures [282] of aluminum, nylon reinforced phenolic and heat resistant phenolic are listed for a few specific examples in Table 4.41.

Honeycomb clearly is anisotropic; however, the lateral direction weakness in paper honeycomb is not significant unless impact occurs at an angle to cell alignment exceeding 10 degrees. Figure 4.7 shows the effect on crushing stress of impacting a sloped surface with aluminum and paper honeycomb (materials listed in Table 4.41). From experiments with paper honeycomb [281], crushing strength . . . . .

- is essentially independent of impact velocity in the range from 20 to 90 fps,
- is not sensitive to uniformity of cell size, paper weight, or type of glue,
- is directly related to density of the material and to the bearing area of the honeycomb panel, and
- decreases with decreasing area at a ratio of the area of the outside row of cells to the total area.

Entrapped air in the cells contributes greater energy absorption capacity than do vented cell structures.

	Aluminum Ref: 282	Paper Ref: 281
Impact Velocity: fps	14	16-19
Section Area: in^2	20	304
Crushing Stress, psi	124	43.8

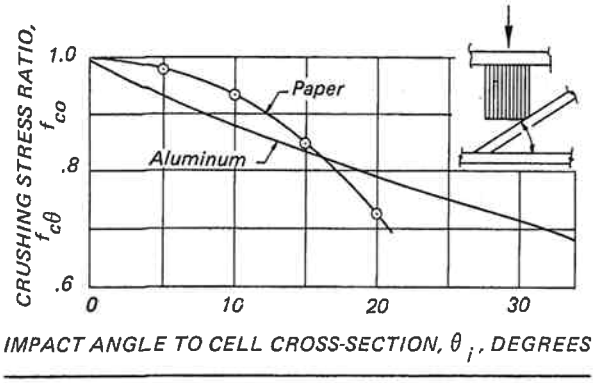


Figure 4.7 Effect of Anisotropic Honeycomb Structure on Crushing Stress with Angular Impact

TABLE 4.41 HONEYCOMB CHARACTERISTICS

Material	Density (lbs/ft³)	Cell Size (inch)	Average Crushing Stress (psi)	Specific Energy (ft-lb/lb)
80 lb Kraft Paper:				
open cell	1.55	1/2	27.0	1750
closed cell	1.55	1/2	31.5	2050
Aluminum .001" 5052	2.1	1/4	124	6800
Nylon Phenolic	2.5	3/16	55	2530
	4.2	1/4	290	8400
	6.5	3/8	600	10100
Heat Resistant Phenolic	2.4	3/16	50	2220
	4.2	1/4	280	7680
	6.1	3/8	625	11800

Figure 4.8 shows the typical stress-strain characteristic of honeycomb structures when compressed in the cell direction. The stress rises rapidly to a peak at the start of crushing and levels immediately to a nearly constant stress throughout the energy absorbing stroke. Bottoming starts at about eighty percent strain and would rise to a very high value if all impact energy were not dissipated.

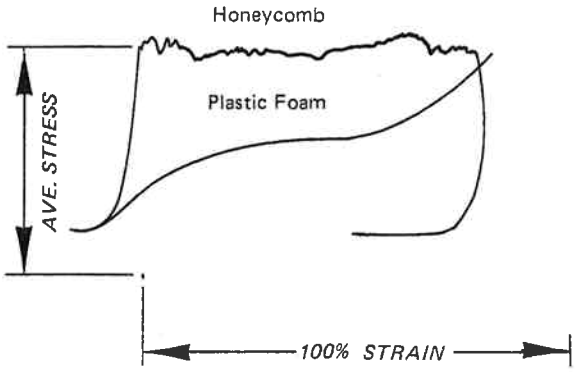


Figure 4.8 Stress-Strain of Crushable Structures

Foams and Low-Density Compounds. Many types of foams and low-density materials are available commercially or can be formulated for energy absorbing cushions under landing loads. Perhaps the most widely used is a rigid urethane foam which is a reaction product of a disocyanate with a polyester resin mixed with small amounts of water, an emulsifier and a catalyst. Homogeneous foams are easily obtained which provide a compressive strength (at yield point) of 20 psi for a foam density of 2 lb/ft³ and may range to 100 psi for 6 lb/ft³ as a representative example. The shape of the stress-strain curve shows a progressively rising stress after yield that lacks the plateau feature of honeycomb.

Because the foaming reaction is rapid, the potential of producing a semi-rigid landing cushion during the descent phase of a recovery sequence by mixing the ingredients through injecting nozzles into a deployed fabric bag has been investigated [283].

FABRICATION METHODS

The methods by which a parachute, Ballute, landing bag, flotation bag, or associated recovery system accessory may be assembled from its component parts are limited in number and variety by two factors. One is the equipment that is available, principally sewing machines; the other is the restriction imposed by the mechanical properties of applicable textile materials. While these restrictions are of major importance in the economics of recovery systems manufacturing, fabrication methods also have considerable influence on the resultant strength, elasticity, and flexibility of the structure. These constitute design criteria relating mainly to fabrication details of seams, joints, hems, the attendant types of which depend on their location and function.

Procedures used in the manufacture of textile parachutes are typical and generally applicable to other decelerator types. Basic steps are:

layout, marking and cutting of cloth, line,

pre-assembly of parts by heat tacking or basting

sub-assembly of gores with single or multiple rows of machine stitching

joining of gores, generally with multiple rows of machine stitching

attaching of radial or concentric reinforcing tapes, generally with multiple rows of machine stitching, and,

connecting of suspension lines, generally with zig zag machine stitching

Canopies and inflatable envelopes constructed of film and coated fabrics are usually joined using adhesives, sometimes with, but often without stitching. Bonding strength efficiency is usually the criteria which determines the suitability of the joining method used. In this section the processes of manufacture are described which apply in particular to the construction of parachutes designed for economy of fabrication coupled with safety, by achieving optimum joint efficiency and serviceability through simplicity of construction. The number of parts and operations must be the fewest possible consistent with functional requirements, and preference is given to operations which can be performed to advantage on the various high performance machines available to the sewing trade.

Layout, Marking, Cutting

The large number of pieces of material which must be handled and assembled to form a parachute mandates that layout markings and indexing points be held to a minimum wherever possible. Paper patterns which include seam allowance are used to outline solid cloth gore sections for cutting. Since section edges can be cut accurately enough to serve as mating points during gore fabrication, layout marks are not usually required on the fabric sections in the construction of canopies; this is also applicable to main seam and hem bases. Some dimensional variations will result from the lack of uniformity in the lay-up of successive layers of the fabric during the cutting operation. The inherent flexibility of weave patterns makes this a difficult factor to control.

Webbings, tapes and cords are measured and marked under tension to assure uniformity. The tension force specified should be sufficient so as to remove the "mechanical" elongation (a function of any weave pattern) of the particular item being measured and marked. Manufacturing experience has indicated that this tension should be about five percent of the rated tensile strength ot the textile item being utilized, except in the case of high strength materials, where this rule-of-thumb requirement would necessitate the application of unusually high tensions. In construction where suspension lines are continuous from link to link and are routed through the main radial seams, or otherwise cross the canopy, the skirt and vent intersection points are marked on the lines. If the lines are stitched directly to the cloth surface only at the skirt and vent, the intervening fullness of fabric usually presents no problem, especially in the case of canopies thirty-five feet or less in diameter. In all types of construction requiring the continuous attachment of tapes, webbings and circumferential bands to the exterior surface of the cloth, uniform distribution of cloth fullness along the seam is difficult to achieve. This is especially true in the case of bias constructed gores. It is therefore frequently necessary to provide numerous intermediate indexing marks on both tape and cloth surfaces to guide the sewing. Also, tacking or basting is frequently useful in addition to marking. The main seams provide indexing points for circumferential bands so that only the tape need be marked for each intersection. Radial dimension marks, however, are frequently needed on the canopy assembly to place reinforcing bands at intermediate locations between skirt and vent. Cross seams joining points will often satisfy this requirement. A problem of distributing fullness along a seam arises, especially with bias-cut fabric. Even though the measured lengths of cloth and tape are the same, the cloth seam stretches easily compared to the tape. This difference diminishes with increasing weight of fabric. The tools used in the process of marking and cutting are described on page 192 .

Machine Stitching

Stitching with thread by any of a variety of sewing machines and sometimes by hand, is the traditional

method of joining textiles. Strong, efficient junctures result when the optimum number, spacing, and pattern of stitches are employed. There are a number of types of stitches, seams and stitching formations for the fabrication of sewn items.

The most widely used type of stitch is the two-thread, lock stitch formed by the majority of sewing machines. Zig-zag stitching, both single and double throw, is valuable in parachute manufacturing, primarily because seams so joined are capable of full elongation without creating excessive tensile in the stitching thread. Depending upon strength and width required in a continuous seam, efficient stitching is derived by the use of two, three and four needle machines. Several difficulties of varying importance arise in the stitching together of parachute components. These difficulties must be considered carefully. In machine sewing, differential feed can occur between the upper and lower pieces of material being joined, thus causing end mating-points to pull out of register as the seam is sewn. Yarn filaments can be broken by needle penetration, thereby weakening the basic fabric. The thread itself may be weakened or broken in thick joints and at seam intersections as a result of increased friction of penetration attending the superimposition of successive rows of stitches. High-speed sewing may weaken nylon materials by frictional overheating. These problems are minimized by the use of sewing machines which have "compound feeds" and "pullers", which move and guide evenly the layers of material being sewed. Also, sewing machines may be set to operate at optimized maximum speeds in order to prevent frictional needle-material overheating, or the machine may be equipped with a needle "cooler" (directed jet of air) to prevent excessive needle temperatures.

When differential feed or "creep" of materials cannot be overcome to the extent required by the dimensional tolerances of the structure, basting may become necessary. ***Basting*** is the temporary holding of two or more pieces of fabric together until they are permanently assembled, and is usually accomplished by light or temporary sewing. Adhesives also have been utilized, but only in certain instances, such as in small scale canopy construction. Adhesives are considered undesirable because of possible deleterious effects on fabric, particularly at elevated temperatures. Where the use of an adhesive is permissible for basting, the quantity applied to one point must be carefully metered so that the area of fabric affected has a minimal diameter (generally, approximately 0.1 in). All of the thicknesses of material at the seam joint should be joined by one application on the centerline or midpoint. The adhesive should set quickly and remain flexible with age. Successive tack spots on the same seam must be as widely spaced as practicable. Similarly, if heat-tacking of synthetics is used for basting, the same rules apply to the "spot weld" joints produced by localized melting of the material.

Strength of Joints and Seams. A ***seam*** is defined as two or more plies of cloth joined by a series of stitches. A complete seam designation contains the type of stitch, the seam class, the type within the class, and the number of rows of stitching as specified by Federal Standard No. 751, Reference 284. For example, 301-LSc-2 means type 301 stitch, LS class, c type of that class, with two rows of stitching. When joining textile elements into one complete structure, it is important to make junctions in such a manner that the strength of the joint is not below the strength of the textile elements. This ideal is not always realized. A ***joint efficiency*** is determined from the following relationship,

$$\text{Joint Efficiency Factor}(\%) = \frac{(\text{str. of joint}) \times 100}{(\text{str. of material joined})}$$

Seam strength varies with orientation of fabric to the seam line and with choice of stitch. Failure can occur in either or both of two ways. The first is by failure of the stitching thread, and the second, by failure of the materials being joined. Thread failures should normally occur in the efficiency factor range below one hundred percent. When the joint-efficiency factor approaches the upper limit, failure is generally a fabric failure. At the joining line of a seam, the fabric may fail with a lower strength value than if the failure were in the unsewed fabric. The probable cause for this is either the weakening of the material by cutting or damaging of the yarns as the needle passes through the fabric, or a local reduction of elongation caused by the tightness of the stitching.

The generally recognized characteristics of a properly constructed seam are strength, elasticity, durability, security and appearance. These characteristics must be balanced with the properties of the material in forming an optimum seam. A prime consideration is the structural integrity of any stitching/seam combination which is to be used. The elements affecting the strength of a finished seam are discussed in the following paragraphs.

Type of Stitch. There are many different types of stitches available[284] which are practicable. The most frequently used stitch is type 301 shown in Figure 4.9. This type of stitch is formed with two threads: one needle thread, and one bobbin thread. A loop of the needle thread passes through the material and interlaces with the bobbin thread. The needle thread is then pulled back so that the interlacing will be midway between surfaces of the materials being sewn.

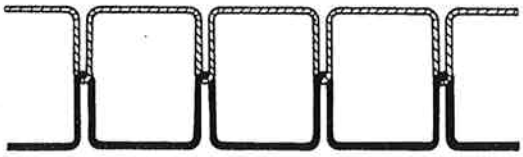


Figure 4.9 Stitch Type 301

Zigzag stitching is used in parachute manufacturing where lines or tapes must be secured in one place by an area of evenly spaced stitches. It is also useful on joints or seams where flexibility of the material should be maintained without creating excessive tensile stress in the thread itself. The most widely used zigzag stitch is the Stitch Type 308 commonly called the "double" throw zigzag stitch. This stitch, shown in Figure 4.10, is exactly the same as stitch type 301, except that successive pairs of stitches form a summetrical zigzag pattern.

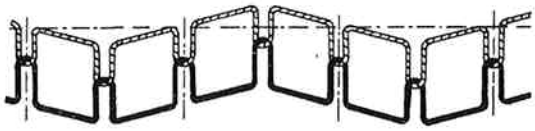


Figure 4.10 Stitch Type 308

The "single" throw zig zag stitch shown in Figure 4.11 is classified as Stitch Type 304, and is exactly the same as stitch type 301 except that successive single stitches form a symmetrical zigzag pattern.

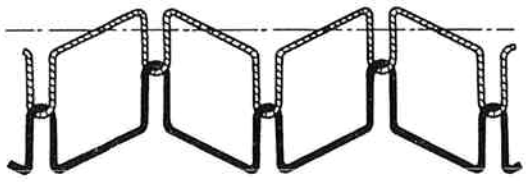


Figure 4.11 Stitch Type 304

When necessary to perform temporary sewing operations, a "basting" sewing machine is used which forms the Stitch Type 101. This stitch, shown in Figure 4.12, is formed with one needle thread which passes through the material and interloops with itself on the undersurface of the material. Depending on the strength and width required in a continuous seam, efficient stitching is derived by the use of two, three or four needle machines. For the specific operation of joining radial tapes into radial seams on ribbon

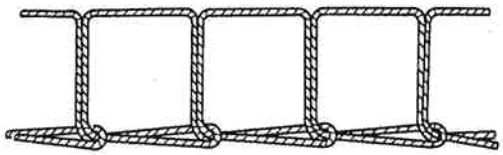


Figure 4.12 Stitch Type 101

machine. This machine forms a compound-chain stitch, (Stitch Type 401), shown in Figure 4.13. This type of stitch is formed with two threads: one needle of stitch is formed with two threads: one needle thread, and one looper thread. Loops of the needle thread pass through the material and interlace and interloop with loops of looper thread. The interloopings are drawn against the underside of the bottom ply of material.

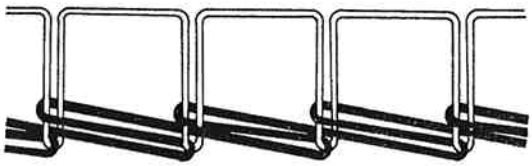


Figure 4.13 Stitch Type 401

Type of Thread. Thread strength depends on the thread material and thread size. It is good practice to use a thread of the same material as the fabric being sewn. Nylon and cotton threads are used extensively. Size and strength of these and other sewing threads are listed in Tables 4.2 through 4.6. When thread breakage causes seam failure, the use of heavier thread in the majority of cases improves the strength of a seam, even though such usage requires a larger needle and may cause greater yarn damage during sewing[285].

Stitches per Inch. The number of stitches per inch used depends on the seam strength required and the thread material, but they are restricted by the working range of a given sewing machine. Both the number of stitches per inch and the pattern (number of rows) are varied to achieve the desired strength. Investigations[285] show that where seams fail due to stitching, an increase in stitches per inch and number of rows would increase the strength up to some point where the closeness of sewing penetrations might be the cause of failure.

As the breaking strength of the fabric is surely not increased as the number of rows or stitches per inch is increased, it can be assumed that the thread failure, not cloth strength, is the initial contributing factor.

However, if the strength of the cloth is reached, the addition of more stitches cannot make the seam any stronger. The dependence of seam efficiency on stitches per inch for various canopy cloth materials and rows of stitches is graphically illustrated in Figure 4.14. Lowest efficiencies were obtained in the tests with the heavier fabrics where thread failures occurred. If these tests were repeated using larger threads, their respective efficiencies could be expected to increase.

Thread Tension. Highest strength in the two-thread, lock stitch is obtained when the tension means on the sewing machine, for both the upper and lower thread forming the stitch, are so adjusted that the stitch "lock" is positioned midway between the surfaces of the completed seam. Also, over-tightness of either one or both upper and lower thread tensions has two effects which are undesirable in seams.

(a) Finished length of the seam, especially in the case of a bias seam, is shorter than the cut length of the material because of gathering between each needle stitching point.

(b) Binding together of the material creates friction which reduces the desirable flexibility and elongation characteristics of the textile juncture.

Seam or Stitching Type. A change in seam type or stitching type will often produce better seam efficiencies. For instance, a change from Stitch Type 401 (compound chain) to Stitch Type 301 (lock) can increase efficiencies significantly [285]. Also seams constructed with material edges turned under will be much stronger than a plain-lap seam. Seam strength also varies with the orientation of the fabric weave pattern to the seam. Results from the strength tests of orthogonal and 45-degree bias seams (see Figure 4.15 demonstrate that the latter seam-orientation produces greater seam efficiency.

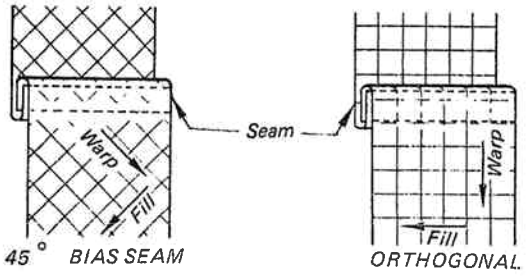


Figure 4.15 Fabric Orientation

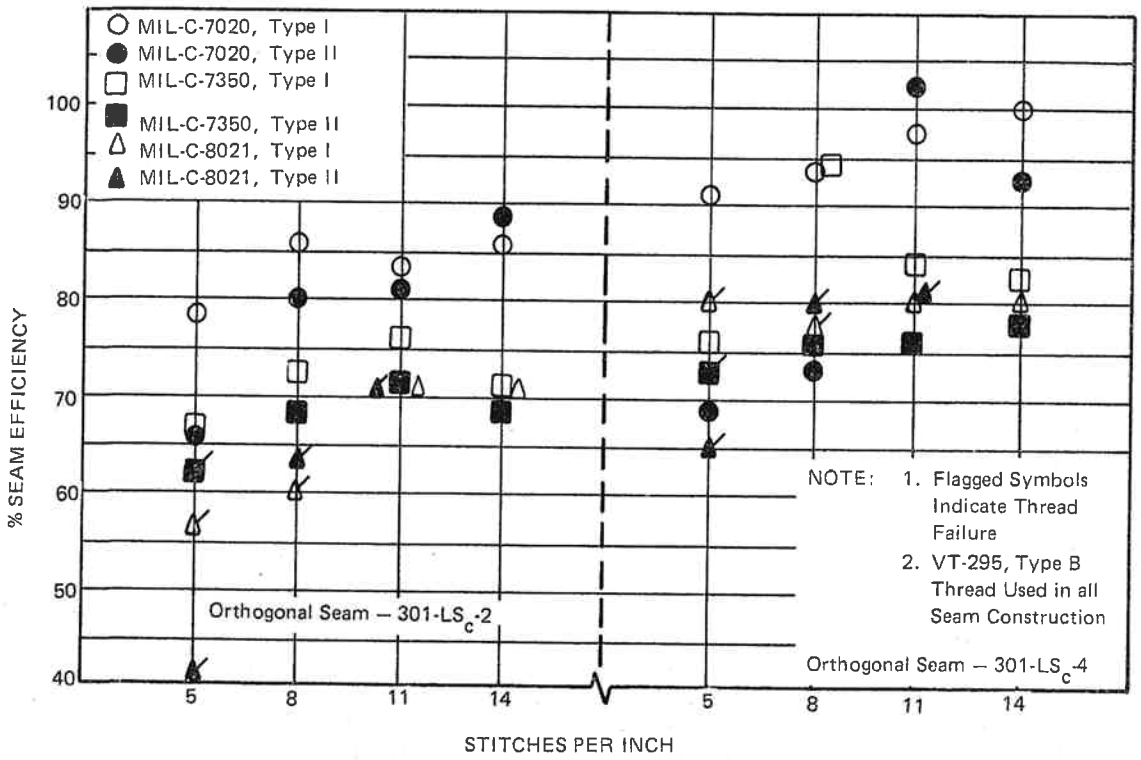


Figure 4.14 Dependence of Seam Efficiency on Stitches per Inch

CONSTRUCTION DETAILS

Details of stitching and finish fabrication of a parachute or other textile component of a recovery system differ with purpose. Normally such details are dictated by function – direction and magnitude of load, or flexibility for folding. Where functional reliability is not adversely affected, the stitching or fabrication detail may be dictated by economy, i.e., a repeated operation suitably achieved using a sewing machine and mechanical guides.

This section presents typical details of construction that would be found on a drawing or specification prepared for manufacture. Canopy seams, hems and structural joints are illustrated which are in common use. A variety of stitch patterns are illustrated which are used in attaching tapes or to produce joints in circumferential bands, harness webbing or risers. Methods of attaching suspension lines to canopies and details of splicing and making loop ends in both flat webbing and braided cord are shown.

Cloth Structural Elements

In parachute construction, development of solid cloth gores requires section seams (see Fig. 2.2) which join woven edges, *selvages*, of bolt width cloth, leaving cut edges at the sides of the gore. Gores are then joined, one to another, by bringing the cut edges together in main seams along radial lines. To complete the solid cloth canopy, the skirt hem and the vent hem are formed, also at a cut edge of the fabric, if of bias construction. Seams of guide surface canopies and canopies of other shaped parachute types are more complex where ribs, flares and angular edges must be joined along curved lines.

A slotted canopy gore is usually an assembly of many more parts, with rings or ribbons placed horizontally such that selvages are free and the ends of the material extend to the sides of the gore. Before slotted gores are joined, a radial tape or webbing serves as a continuous member at the gore edge to hold rings or ribbons in place until the seam is completed.

Seams and Hems. Figure 4.16 presents several typical flat fabric hems and seams. The width of an integral reinforcing tape, and the number of rows and spacing of stitching, is determined by strength and other functional requirements. The width of hem or seam allowance is governed by its type. A plain hem or seam is used where a selvage is of sufficient strength or fraying of an exposed cut edge is not objectionable. Otherwise, an additional turn of fabric is required to place the cut edge inside. The rolled hem and the French-fell seam (type LSc)[284] are commonly employed for this reason, as well as for their slightly greater strength. A bound hem is used occasionally such as on the skirt and vent bands of a canopy, but more often a reinforced rolled hem is used. There a reinforcing tape or continuous webbing is bound into the hem.

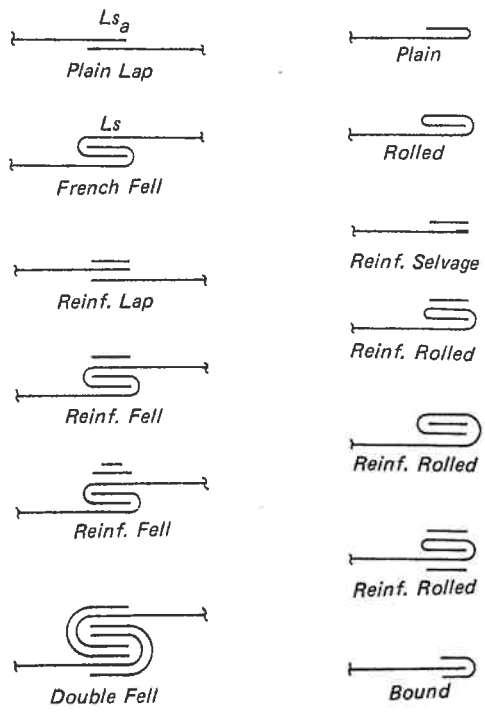


Figure 4.16 Typical Flat Fabric Seams and Hems

Canopies with geometric porosity have many free edges which must be hemmed, except where selvages are strong enough alone, as in the ribbon type canopy. Cloth is also woven in various widths on special order strength or triple strength selvage by adding warp yarns in the edge weave. Cloth with special width and strong selvages are often used on ringslot and ringsail canopies if the extra cost for these features is warranted. Otherwise standard cloth widths are used, or lesser widths are cut with hem allowance.

The major load-carrying members of a slotted canopy are the horizontal ribbons or rings and the radial members which transfer the load to the suspension lines. A typical ribbon gore layout will be found on page 95 , and a cross-section showing lap seams at the radials using eight rows of stitching are shown in Figure 4.17. All canopies require different structural fabrication details depending on the magnitude of loads imposed on them and the mechanical efficiencies that are possible. For example, the eight rows of

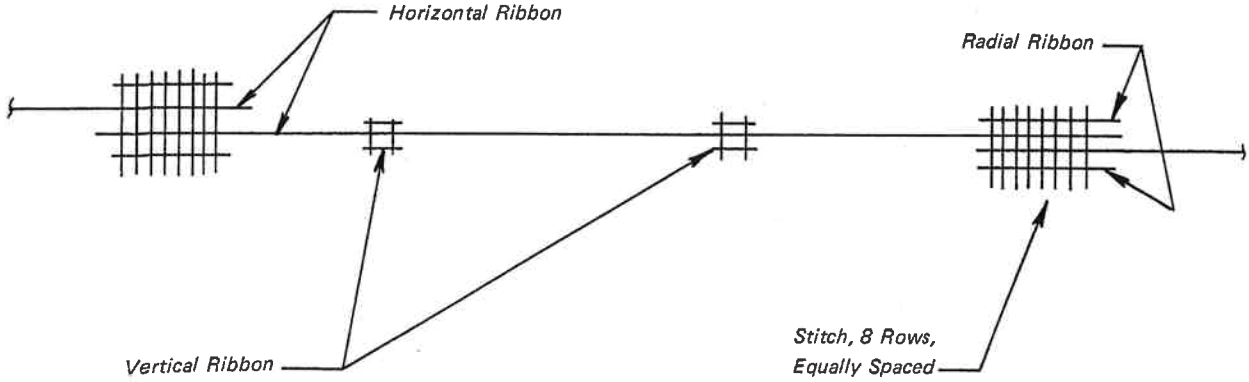


Figure 4.17 Cross-section of a Typical Ribbon Canopy Gore

radial stitching are required to splice the lapped horizontal ribbons. The spliced joint will hold ribbons up to 2000 lbs. When heavier ribbons are used, a four-point cross stitch pattern, as shown in Figure 4.18 is required in addition to the eight rows of stitching.

In order to improve the horizontal ribbon joint efficiency and to reduce canopy bulk and the number of stitching patterns, a continuous ribbon construction may be used. Fabrication techniques for the continuous ribbon canopy are similar in gore layout and tacking, but handling is more complex. Each horizontal ribbon, although a single layer requires a slight "dart" at the radial seam to adjust to the angle of the gore edge. Ends of ribbons must be lap-joined at one or two radial seams, preferably each ribbon at different radials.

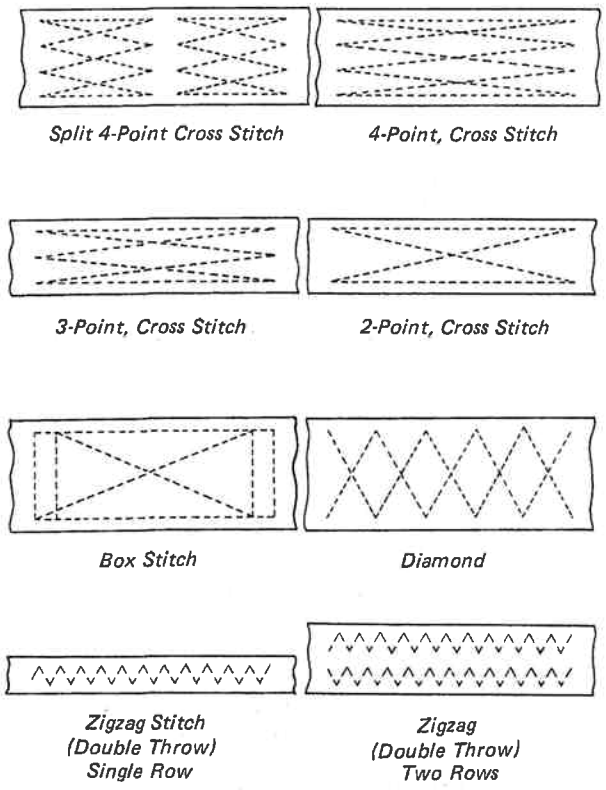


Figure 4.18 Example of Stitch Patterns

Stitch Patterns. Examples of widely used stitch patterns in the construction of parachute canopies and accessories are shown in Fig. 4.18. At one time the box-stitch and the single row zigzag stitch were the typical patterns. However, tests have demonstrated the higher efficiencies of the multiple point cross-stitch patterns. Their principal advantage comes from the fewer stitch points at the ends, a feature which tends to preserve the material base strength into the joint, where the box-stitch presents a line of weakened fabric at the start of the joint. A principal benefit of the cross-stitch joint is its twist flexibility and its distribution of prying loads to all threads in tension.

Zigzag stitching continues to be widely used in securing cords, such as suspension lines, to their attachment points. This type of stitching, even if necessary in two or more rows, lends itself to high production requirements, and also where it is difficult to handle an object being sewed, such as attaching vent lines to heavy parachute canopies.

Line Connections

There are three different types of joints in the suspension line system: the line-to-skirt type, the line-to riser type, and the line-to-line type.

Skirt Attachments. In the suspension line-to-skirt joints, the suspension line joins the skirt periphery at a point where the main radial seams joins the skirt

hem. The suspension line can be either a continuation of all or part of the members that make up the radial seam or it can be a separate member that is attached to the skirt. The former is always sewed to the canopy in the skirt band area, with reinforcement if required. The latter can be of two general types, a loop connection or an entirely sewed connection. In general, a looped joint is more efficient that the completely sewed joint, displaying a joint efficiency factor of approximately 90 percent, compared to 80 percent for the entirely sewed type. A "butterfly" reinforcement is often used to prevent suspension line tear-out should there be any irregular sharp angular displacement of the line during the opening of the parachute (see Figure 4.19). The method of construction of the joint is partly suggested by the size of the members being joined. Other than this, a type is selected which has proved satisfactory in the past. Exceptions to this selection method are canopies constructed to their respective specifications, such as the circular ribbon[286], ringslot[287], and guide surface types.

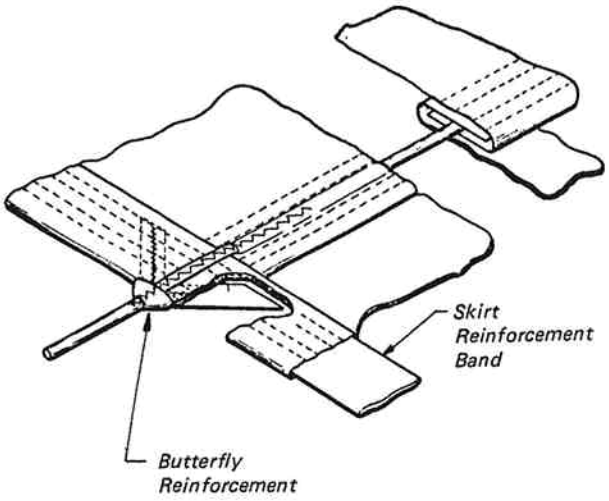


Figure 4.19 Cord Line Attachment with Butterfly

In addition to the common practice of sewing suspension lines to the drag-producing surface at the skirt and vent with double-throw zig zag stitching, there are additional practices in common use mainly on slotted parachutes with radial and vertical tapes.

Lines may be lapped over and stitched to the ends of each main radial ribbon or reinforcement tape at the skirt as shown in Figure 4.20.

Lines may be sewed to loops formed at the end of each main radial-ribbon as shown in Figure 4.21.

Tapered radial tape-line joints are used largely on ringsail canopies. Figure 4.22 illustrates the two steps used in fabricating this juncture.

Lines may be formed as continuous extensions of main radial-ribbons, made of narrow webbing.

Suspension lines may be continuous (link to link) over the canopy, sewn from the skirt to the vent with four rows of stitching.

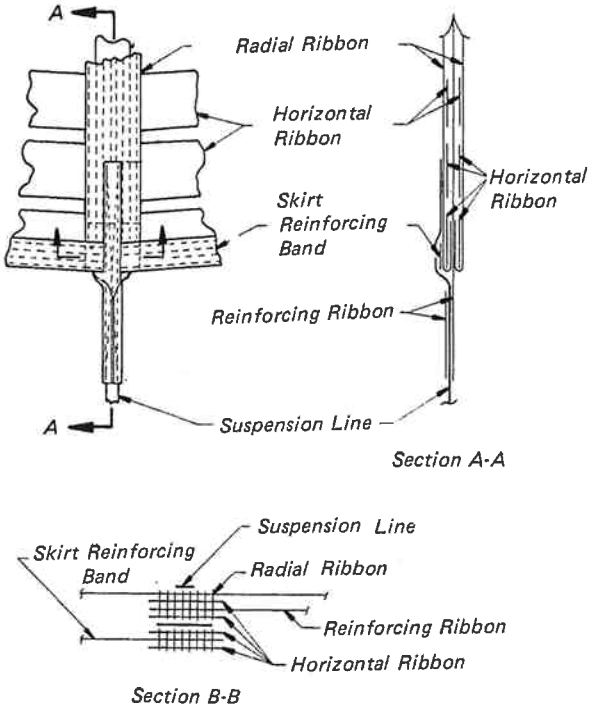


Figure 4.20 Webbing Type Line Attachment

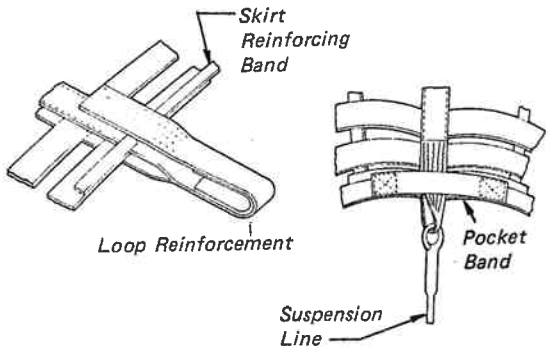


Figure 4.21 Suspension Line Connection to Skirt Loop Attachment

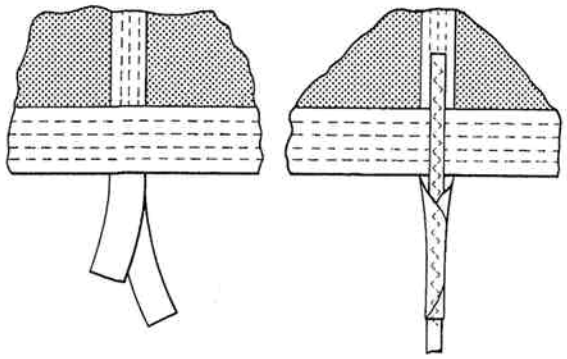


Figure 4.22 Tapered Radial/Suspension Line Joint

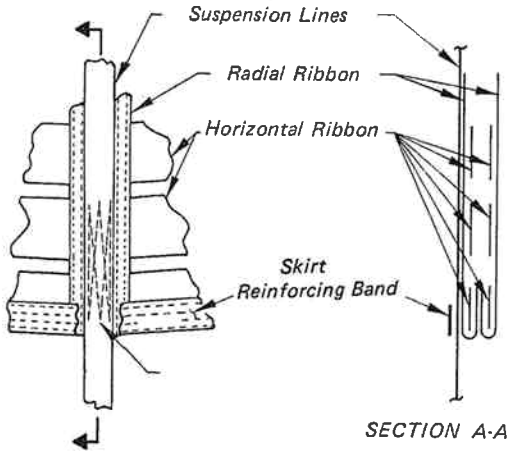


Figure 4.23 Continuous Radial/Suspension Line

Joint reinforcements at the skirt, made of short lengths of tape or webbing, include:

a single-lapped doubler,

two piece doublers, inside and out, and combinations of doublers, butterflies, and looped rib-extensions, and

a single piece of webbing which provides for suspension-line reinforcement and attachment of the reefing ring to the skirt, as shown in Figure 4.23.

Line Splicing. The suspension line-to-line joint, in its most common form, is a stitched lap joint where the use of a flat textile member is involved. When the use of coreless braided cord is involved, strong line-to-line (and loops joints) are possible (Table 4.8) by inserting one end through the braided wall of the cord and securing with some type of minimal sewing. The high efficiency of this type of joint technique results from the so-called "Chinese-finger-trap" principle. The end remaining within the braided cord should be finished with a long taper in order to further increase the high joint efficiency factor.

Splicable braided cord is available in nylon, polyester and Kevlar aramid materials. Several examples of coreless braided cord splices and applicable parameters are shown in Figure 4.24.

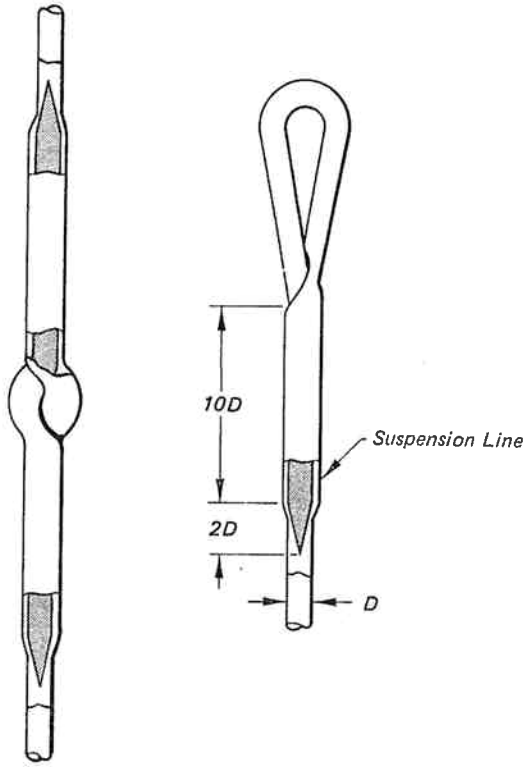


Figure 4.24 Suspension Line Loop, Style A

Riser Attachments. In the suspension line-to-riser attachment joint, two basic configuration are used. One is an entirely joined by sewing type and the other a combination loop-and-sewed joint which can include a metal link fitting. The use of separable type of metal link in the latter is by far the more common method. Any system of textile members which connects the canopy's suspension lines to the load being carried comprises the riser system. Different requirements for riser design give rise to the need of various configurations. In the following paragraphs, three typical riser configurations are described.

Figure 4.25 shows the simplest arrangement, typically used on cargo type parachutes. Heavy webbing forms the legs of the riser, which may be comparatively long. A single keeper helps to form a loop to which the load is connected. Attachment of the suspension lines to their respective riser legs is ordinarily made using a metal fitting, usually a separable link.

The riser detail of Figure 4.26 is used for applications where the parachute canopy trails a substantial distance behind the load, and where repeated usage is indicated, such as on an aircraft landing deceleration parachute system. Movable keepers, as illustrated, are employed to retain the webs at the other end. Suspension lines attach to their respective riser legs through a metal fitting (separable link) or by sewing the line directly to the webbing.

The riser in Figure 4.27 is suitable for applications where the parachute canopy trails a substantial distance behind the load, minimal weight and volume are of utmost importance, and one-time usage is indicated, such as a drogue parachute on a space vehicle. In this arrangement, the "riser" portion of this textile combination is formed from a continuation of the suspension lines.

Buffers or other protective elements should be employed extensively to prevent nylon-to-nylon friction burns and attendant damage. Keepers used to form confluence points should be designed to minimize relative movement of all textile members. Long risers should have their members joined together so as to prevent their disarrangement and any subsequent

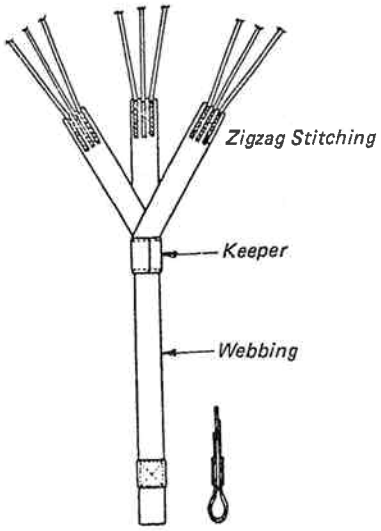


Figure 4.26 Branched Riser With Stitched Line Joints

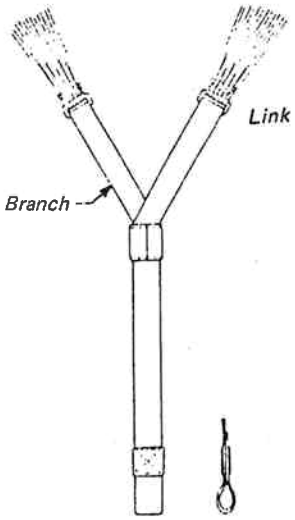


Figure 4.25 Branched Riser With Metal Links

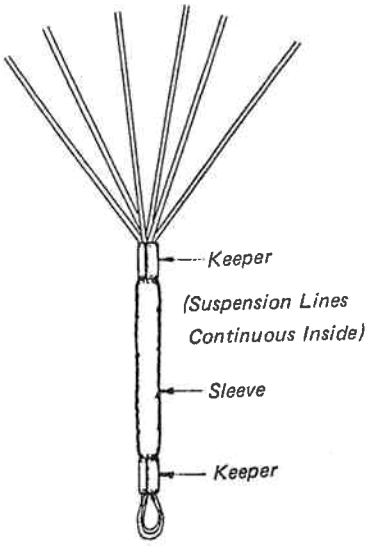


Figure 4.27 Integral Line Riser

flapping or slapping one another. Figure 4.28 illustrates how this may be accomplished by any of three methods; namely, small "joiner" webs, rows of machine sewing, hand sewing (intermittent tacking), or by enclosing the entire riser in a protective sleeve. Optimum results are often obtained by using some combination of all three methods.

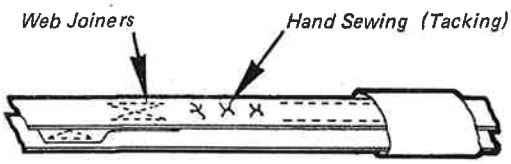
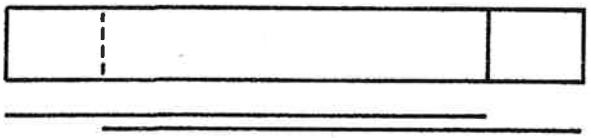
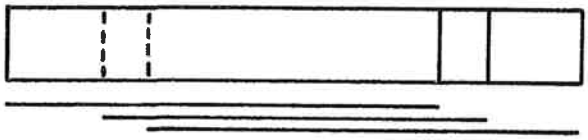


Figure 4.28 Typical Web Connect Method

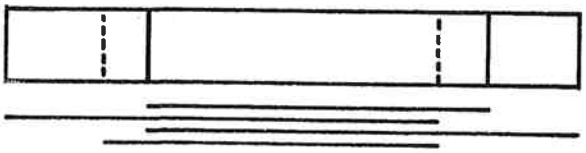
Loop and sewed junctures are the weakest points in a riser system. The sewing stitch patterns previously discussed and shown in Fig. 4.20 are used in riser fabrication. Figure 4.29 shows typical webbing joint configurations used in riser fabrication. Riser attachments normally are joints made by looping one or more webs over a metal fitting bar. It has been found that the diameter of such a bar or link has a strong influence on the efficiency of the juncture, especially when multiple plies of webbing are used. In general, joint efficiency decreases as the bolt diameter decreases. For example, two ply of 3000 lb webbing around an 0.5 inch bolt develops only 75 percent of rated strength. Pull tests should be performed on any newly designed loop-to-bolt juncture to assure that the desired strength is developed.



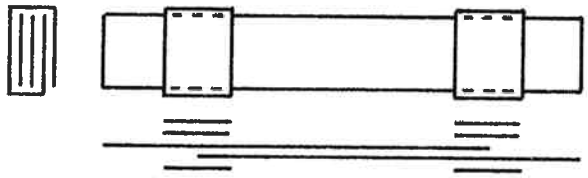
Simple Lap Joint



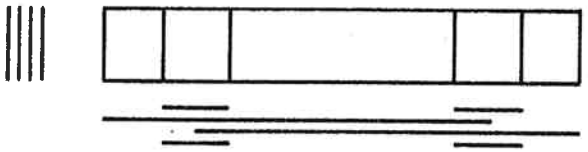
Lap Joint, w/Reinforced Piece



Lap Joint, w/Reinforced Laps



Lap Joint, w/Wrap Reinforce



Lap Joint, w/End Lap Reinforce

Figure 4.29 Typical Webbing Riser Joint Configuration

QUALITY ASSURANCE

A quality assurance program, by applying the aspects of quality control and inspection to the manufacturing process, helps to ensure an end-product ready for final system assembly which complies with technical and contractual requirements. Such requirements are established by drawings, specifications or specific conditions of a purchase order, and often require compliance checks by government inspectors or those who have final system responsibility. Quality assurance practices are measures for achieving full reliability of performance of a product with a high level of confidence. The steps of folding and packing a personnel parachute are so important, for example, that only qualified riggers are permitted to perform pack preparations.

Typical inspection procedures which parallel the steps of parachute fabrication and packing are described in this section. Such practices apply also to most textile components and hardware that make up a recovery system. Initial checks are made of conformity to purchase order (specification or drawing) of materials and hardware received by the manufacturer. A check list, called a "traveler", is assigned a product serial number which accompanies allotted material from stock through fabrication and packing steps, obtaining verification checks for each inspection operation listed until the completed serial numbered product is accepted for delivery to its user. Although parachute folding and packing is often accomplished in the field (outside the factory), procedures and equipment required are the same.

Receiving Inspection

Materials which are to be used in the fabrication of parachute systems are required to have a vendor supplied "certification statement of conformance", and whatever other specifically related data which will establish the suitability for their use in fabrication. This data will delineate test results and related information in order to demonstrate material compliance with their respective specifications. Materials received by the manufacturer are rechecked when received to further establish the acceptability of any goods which are to be used.

Tests conducted by the manufacturer are an important part of materials certification. Tests are performed on fabrics to establish their tensile strength as well as their tear resistance. In the case of cloth used in canopies, tests to ascertain their air permeability characteristics are also conducted. In some cases, bolts of fabrics will be scrutinized over a light machine in order to detect weave defects before they are incorporated into the parachute canopy structure. Samples of webbings and tapes will also be tested for tensile strength. Other physical properties, such as weight, width, or thickness, may also be determined for specification compliance.

In-Process Inspection

In-process inspection procedures are accomplished during the fabrication of subassemblies, assemblies and associated build-up fabrication operations leading to the end-item. These inspections are orderly, coordinated with appropriate fabrication procedures at vital points. Thus, in-process inspection results in a timely detection of fabrication defects before their incorporation into the final end-item, where subsequent renovations are often exceedingly difficult and costly to accomplish.

In the manufacture of solid canopies, important in-process inspection points are at the termination of sewing the section seams (usually a two-needle fell seam), to form a gore and at the subsequent operation of sewing gore main seams, (usually a four-needle fell seam), to form the completed canopy. Both of these inspection processes are accomplished by passing the seams over a "light" table whose source of illumination serves to cast shadows and indicate correct or incorrect configuration folds. Visual inspection of gore and canopy seams of slotted canopy parachutes are usually made without the use of a light table. Subsequent in-process inspection points will vary with the complexity of the type parachute being manufactured. Likewise, components such as risers, harnesses, containers, bridles and deployment bags, may or may not be subjected to intermediate inspection operations depending upon the complexity of their design and the attendant sewing operations involved.

Final Inspection

End-item inspection ensures that the completed article or assembly meets dimensional and relevant structural parameters denoted in specifications and drawings. Final inspections are usually conducted on the same type of table used for packing parachute assemblies into their containers or deployment bags. For a simple parachute system, such as a low speed cargo parachute assembly, the inspection would involve only a recheck of the basic components (parachute, risers, deployment bag, static-line) and any associated simple assemblage geometry. On the other hand, more complex systems require examination of ancillary lanyards, housings, complicated matings of risers or bridle combinations, and similar fabrication or structural consolidations.

FACTORY EQUIPMENT

Prior to World War II, the manufacture of parachutes involved only simple equipment and methods. Parachutes in use were almost exclusively personnel type, solid flat-circular with comparatively simple harnesses and containers. Production lots were small, and the need for economy was secondary. During World War II, both economic and quantity production of parachutes became urgent. A number of sewing-trade companies, largely garment producers, entered the parachute industry and introduced many new manufacturing sewing methods which remain to this day as standard parachute fabrication procedures. Additional stimuli for motivating significant advances in fabrication of parachute systems were provided by the introduction of new designs such as high speed drogue parachutes, Ballutes and extra-large or strong canopy structures. The necessity for containing decelerator systems in limited stowage space, especially the newer concepts, led to the design and use of special apparatus for pressure packing.

Hand Tools and Special Fixtures

Initial fabrication operations require tools that lend themselves to the concept of mass production in order to satisfy the need for economy, while adhering to the requirement for consistent accuracy regardless of the number of units being produced.

Patterns. The aforementioned goals are initially obtained through the use of patterns. Patterns for solid cloth parachute canopies are gore and cloth

width section dimensions based on the surface geometry delineated for parachute types in Chapter 2. To these basic dimensions must be added seam allowances in order that the finished gore attain its correct shape. Gore section patterns for ribbon, ringslot and ringsail canopies are made in a similar manner. The actual production of a gore pattern for ribbon type parachutes is more involved since accurate spacing is required for horizontal and vertical ribbons. Creating patterns for deployment bags often requires a "tailoring" knowledge, since the patterns should produce a container slightly under the dimensions of the parachute system's compartment. This is especially true for irregularly shaped compartments. Patterns for the various portions of a deployment bag (flaps, sides, etc.) are often provided with marking holes or slots through which locating points for sewing on webbings or tapes may be marked. The actual layout of fabrics used in canopies and other components is accomplished through the use of a fabric "lay" machine traveling back and forth over a long, smooth table. This wheeled conveyor machine, traveling on guide rails, carries the bolt of fabric with a free end threaded through a series of rollers. In this manner it is possible to accurately lay multiple plies of cloth upon the table. The number of plies and resultant height is dependent on the weight (thickness) of fabric, the available length of the table, and the desired production goal. By this method, it is possible to achieve accurate lays of fabric as high as four to six inches, consisting of 200 to 300 plies. Guide cutting lines can now be transferred from patterns to a paper sheet on the top of the lay. By arranging the pattern marks to minimize waste, especially when cutting various pieces for a complicated deployment bag, a significant savings in material can be effected.

Cutting Knives. Cutting the layered fabric in an accurate manner is performed by the the use of high speed fabric cutting machines. These hand-guided machines are equipped with a rapidly whirling circular cutting blade or a rapidly oscillating vertical cutting blade. When cutting deployment bag portions, the accuracy and utility of the cutting operation may be enhanced by the use of cloth "drills". It is possible, by using the fine, long drill bit of this machine, to make any duplicate series of marking or location holes in each individual layer of fabric in the fabric lay.

Line Marking Fixture. A specially equipped table rack, used widely in the parachute industry, provides equal tensioning and accurate marking for cutting of all suspension lines that go into a single parachute canopy. This device and table are shown in Figure 4.30. The table traversed by two sets of "pulleys", of which one is stationary and the other movable. The movable set is provided with a means of measuring the load force placed upon it when lines are under tension. The machine is initially loaded by running cordage alternately back and forth between both pulley systems to produce a parallel set of lines. This step is shown in Figure 4.30. The pulley systems are then separated to a correct length, and a predetermined force is applied to the whole system. The lines are strummed in order to equalize tension. Immediately following this, the lines are marked using a jigged system to indicate sewing points, i.e., both the vent attachment and skirt attachment points. The final step is to release the tension load on the pulley system, cut and remove the suspension lines from the table as a group.

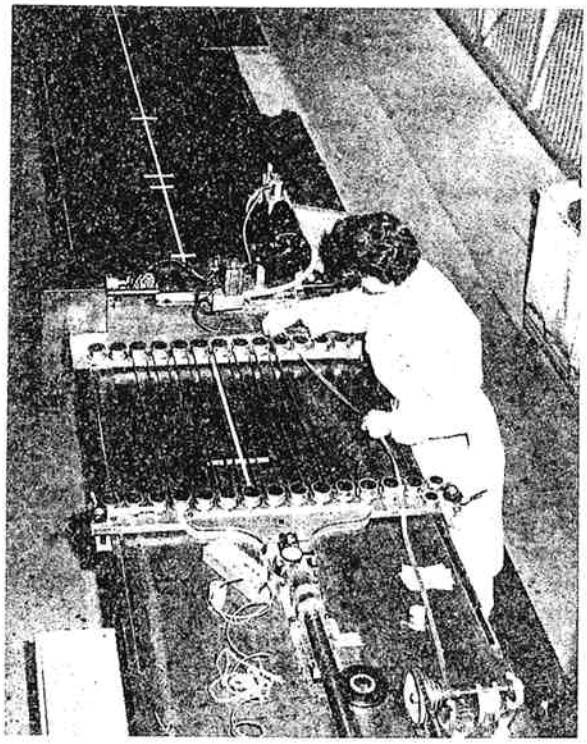


Figure 4.30 Suspension Line Tensioning and Marketing Apparatus

Other marking and cutting operations for the multiplicity of webbing or tapes that are used in the fabrication of parachute systems are performed using a variety of combination devices. Where the mass output of many pieces of identical length webbings is required, there is a machine available which will simultaneously reel off and cut these pieces from a full roll in a rapid and accurate fashion.

Cut ends of cotton webbing and tape are usually dipped into a 50/50 mixture of paraffin and beeswax

in order to reduce any tendency for unraveling. Nylon cordage, webbing, and tape are simultaneously cut and fused against unraveling by using either an electrically heated knife or hot wire which has high enough temperature to smoothly sever and weld the nylon ends by its melting action.

Sewing Machines

Sewing machines suitable for the production of parachutes are governed by the requirements in Federal Specification 00-S-256, Reference 288. In some cases, standard industrial sewing machines may be modified to better perform a specific sewing operation peculiar to a specific parachute sewing requirement. The use of multiple (2, 3, or 4) needle sewing machines is common practice for such operations as main seams, radial and vertical tapes, as well as skirt and vent bands. For certain large ribbon parachutes, an eight-needle sewing machine, with a type 401 chain stitch, has been used successfully for sewing thick radial seams.

Ancillary devices attached to the sewing machine further aid in fulfilling specific requirements. Folders preform layers of cloth into the proper seam configuration as they are sewed, and guides are used to form hems. "Pullers" on many machines maintain a steady even tension on the seam being sewed without any added attention of the sewing machine operator. Figure 4.31 shows a four-needle set-up for sewing ribbon parachutes, the "puller" can be seen behind the needle bar. For certain heavy-duty sewing operations, the addition of a needle-cooler and thread lubricator is often desirable. Certain design features of many industrial sewing machines may accelerate and facilitate various fabrication operations, with resultant economy, and increased product quality. Specifically, such features as compound feeds (combination moving pressure feet and needle feeds) allow the rapid sewing of heavy multi-layer seams, even those of great length, without displacement (creep) of the adjoining layers. Of special interest is the use of a family of automatic sewing machines developed from the basic automatic bar-tack sewing machine. This machine is fitted with a pattern-wheel which controls the lateral and longitudinal movements of the material placed under the sewing foot. This is accomplished by a grooved circumferential channel with a series of cam-like faces upon which the end of a control rod "rides" thus resulting in a prescribed stitch pattern or block of sewing. When using such a sewing machine, the operator's main responsibility is to see that the portion being sewed is correctly positioned under the pressure foot, and then depresses the starting pedal. The machine proceeds to sew the desired stitch pattern and stops automatically when the stitching is completed. Specific uses for this family of sewing machines are for attaching pocket-bands and "V" reinforcement tapes to the canopy's skirt, as well as other similar operations where numerous identical stitch patterns must be accomplished.

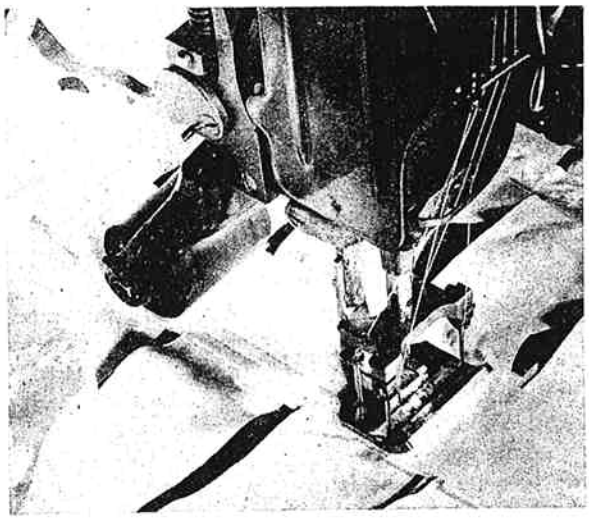


Figure 4.31 Four Needle Sewing Machine Set-Up For Ribbon Parachute

Inspection and Packing Equipment

Inspection Tables. Tables equipped with a light source are a principal tool for inspection. "Light" tables vary in size and configuration, but all are extremely smooth surfaced tables with a smooth plate-glass (usually frosted) set flush with the table top. All portions of the table which might come in contact with the fabric must be free of anything which could snag or pull the fabric's weave. The light source should extend full length beneath the center of the glass section. The glass viewing surface may be flat or it may be canted at an angle to the viewing inspector. Other physical characteristics of this table will depend on the particular inspection procedure point it is being used for. A typical inspection light table used to examine seams of solid cloth canopies is triangular, approximately 15 to 18 feet long, 3 feet high, and tapering in width from 2 to 3 feet.

Packing Tables. Packing tables, used to extend and "flake" or fold parachutes in preparation for final packing into containers or deployment bags, must be adequately wide, long and smooth. The working surface is finished smoothly, e.g., polished hard board, and free of any defects which could cause snagging or pulling the threads of fine fabrics. Physical characteristics of the table will vary with usage requirements. Typical packing tables stand about 30 to 36 inches high. Table minimum width

and length depend on the type parachute being packed, the length being at least equal to the stretched length of the pleated canopy portion, suspension lines, and risers. A typical packing table for rigging personnel parachutes is three feet wide and 40 to 45 feet long. A table as wide as six feet and well over one hundred feet long is used for packing large cargo or or aerospace vehicle recovery parachutes.

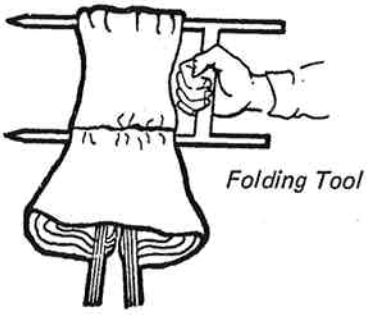
Tensioning Devices. Packing tables are equipped with suitable tensioning devices designed to place the stretched-out parachute under a uniform tension to facilitate the flaking and folding process of the canopy's gores. On small tables this device could be a simple webbing, quick-adjustable hardware snap arrangement, or on large packing tables, a more powerful winch arrangement.

Bins. Bins should be located convenient to the packing and inspection tables. They must be able to accommodate unpacked parachutes. The bin surfaces must be smooth and free of cracks, nails, or other objects which might snag or pull the material. Most suitable are canvas bins supported by a metal frame on casters, which allows the bin to be moved conveniently from sewing tables to packing, inspection and storage areas.

Packing Tools. The following tools are generally considered necessary for packing (see Figure 4.32).



Line Separator



Folding Tool

Items identified with an asterisk should have a warning flag attached to them.

Line Separator: A small, slotted stand used to hold the suspension lines in their respective group for packing.

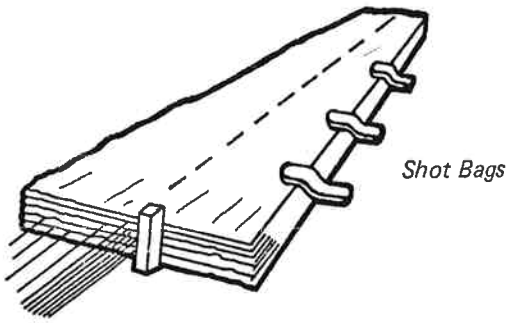
Shot Bags:* Cloth sacks, generally about 18 inches by 4 inches, filled with about 4 lbs of lead shot, used to hold material or lines in temporary placement. They are particularly useful for holding the folded half of a canopy while the other half is being folded.

Folding Tool: A device used to fold the canopy to the correct width or length so that it will fit the container properly.

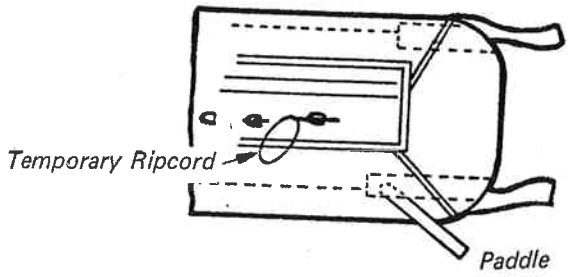
Temporary Ripcord:* A short ripcord with pins, inserted into the locking cones or loops of the pack to hold the side flaps in place, so that the end flaps may be placed in position to insert the permanent ripcord.

Seal Press: A hand-operated device used to secure the seal applied by the packer or inspector to seal the packed parachute against tampering.

Assortment of Small Tools: Long-nosed pliers, knife, 6-inch shears, 10-inch shears, needles (sharp, blunt, and curved) hammer, packing paddle, 6-inch steel tape, hook, palm. Tools must be kept free of dirt, grease, burrs and rough edges.



Shot Bags



Temporary Ripcord

Paddle

Figure 4.32 Parachute Packing Tools

Packing Presses. Increased demands for space conservation in aircraft and aerospace systems using textile aerodynamic decelerators have led to the development of pressure-packing techniques. The hydraulic press is the most common means of achieving minimum volume of a folded and contained parachute. Figure 4.33 shows one type of small hydraulic press having a long stroke pivoted cylinder with extendable arm that can be positioned over the opening of the parachute container or packing box. The press may be driven by either compressed air or a hydraulic fluid pump. Compressed air at 150-200 psi provides moderate pack densities and has the advantage of rapid extension or extraction of the arm. Fluid pressures in the order of 1500 psi are needed to achieve maximum pack densities (~45 lb/ft^3). Larger presses to a capacity of 100 tons with up to 100 inches between vertical supports and 80 inches clear vertical height are used for pressure-packing large parachutes.

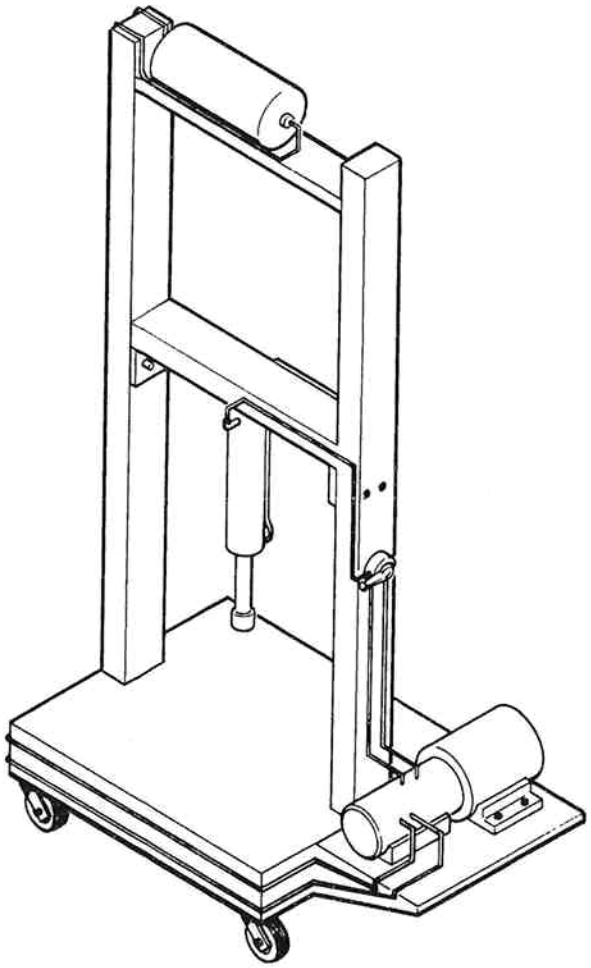


Figure 4.33 Hydraulic Packing Press

As illustrated in Figure 4.34, the press is positioned at the end of the parachute packing table where the stretched-out parachute can be fed progressively into the container in a series of "S" folds between successive applications of the press arm. A pressure foot on the end of the extendable arm of suitable shape and size provides the pressing surface against the material being compressed. For rigidity, these are constructed of thick hardwood, pressed wood or metal with a smooth surface and edges as required.

Vacuum packing is another method of condensing the uncompressed folded parachute. The tools for vacuum packing include a plastic bag to contain the folded parachute, a vacuum pump and the interconnecting hoses and air-tight seals. Evacuation of the air from the plastic bag with an efficient pump causes ambient air pressure to be uniformly exerted upon the parachute pack in all directions. Vacuum packing provides only moderate pack densities (~33 lb/ft^3), but is a useful technique suitable for remote locations or in conjunction with pressure packing methods. Vacuum packs in sealed plastic bags are good items for long time shelf storage.

An alternate technique used for preserving the compressed shape of a pack to expand with removal of pressure has been overcome by storing under pressure for thirty days. Similar results have been achieved by placing the vacuum pack (or a pack under pressure) in a 175°F (for nylon) oven until heated then allowed to cool. The time required varies with thickness of the pack, and the heating and cooling cycle takes less than 24-hours. Required equipment is an autoclave of adequate dimensions and controlled heat source. Similar equipment is used for the sterilization cycling that was part of the Viking Lander parachute system.

Another means to achieve minimum pack size is a hand lacing process of the parachute container, which can be accomplished with simple tools. This method is best applied to a cylindrical shape, where circumferential cross-lacing between rows of grommets at the pack cover edges can be drawn together to close the container compressing the contents. This method is suitable for moderate pack densities, but is slow and not adequate for complex shapes.

Post-Packing Inspection. High density packing techniques impose large forces on the packed system (as high as 40 tons force on the illustrated system). The packing forces and the movement and shifting of the parachute as the pack volume decreases combine to cause damage to the parachute's components. It

has become common practice to x-ray high density packed parachute systems to determine if any damage has occurred to components such as reefing rings and pyrotechnic cutters, which can be visualized by x-ray examination. This has been only a partial quality control step in post packing inspection. since the nylon components have remained invisible under x-ray inspection techniques. It is desirable to examine selected critical nylon components, such as reefing lines and arming lanyards, after packing for structural integrity. An example situation would be two reefing rings shifting during packing in such a manner as to pinch or completely sever a reefing line. Under conventional x-ray technique this impending failure would be undetectable. This void led to the evaluation of various x-ray absorbing coatings suitable for use on nylon parachute cord. (Ref. 289)

Both lead acetate and cadmium chloride satisfied the x-ray opaqueness requirement for use on critical nylon components in the high density parachute pack. The lead acetate "2 hour soak" in a solution concentrated of 36 g/100 ml distilled water seemed to provide the best overall results in terms of x-ray absorption, strength retention, flexibility, and cost. A 13% decrease in the tensile strength of the cord could be expected after treatment.

It was noted that the lead acetate presented a potential toxicity hazard to personnel involved with the application of the coating and the handling of the treated material. The coated cord should be dyed in order to allow easy identification in a work environment. Special safety procedures should also be followed to prevent personnel from being exposed to dangerous levels of the toxic materials.

FACTORY EQUIPMENT

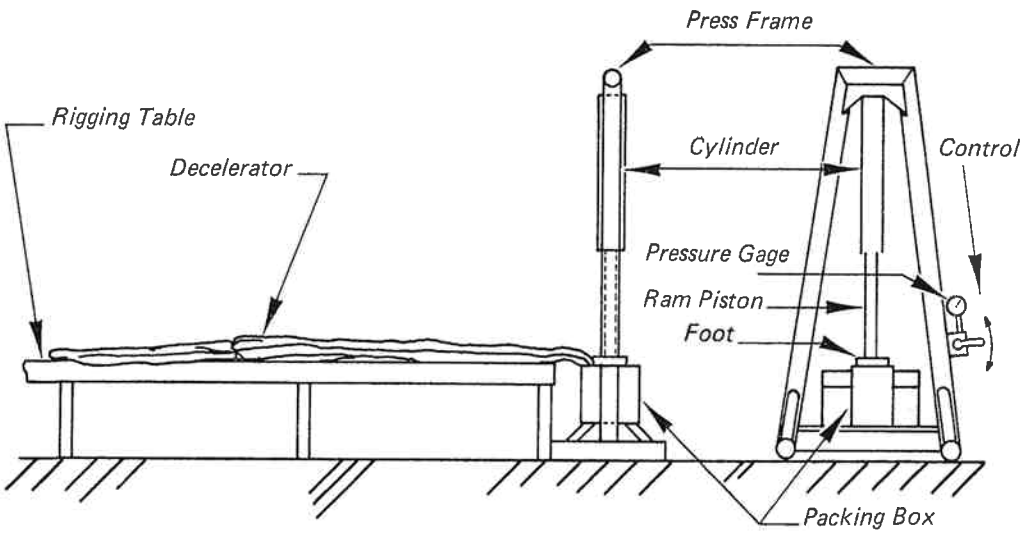


Figure 4.34 Schematic of General Utility Decelerator Packing Press Facility

CHAPTER 5

TESTING AND OPERATIONS

When tests are to be performed, the type and number of tests required depend upon the purpose to be served. Test objectives may range from basic research, aimed at advancing the state-of-the-art, to obtaining specific application-oriented data for evaluation of a component or qualification of a system. Types of tests are identified as either functional or performance tests. Functional tests are those conducted to demonstrate whether a component (or system) functions as predicted when subjected to a known set of conditions. Performance tests are those conducted to obtain and evaluate specific performance characteristics of an item, or various comparative items, over a wide range of operating conditions. Functional tests provide a "yes" or "no" answer, and are frequently conducted without instrumentation in the flight article. Measures which simplify a normally complex test operation will improve chances for successful testing and reduce overall program costs. Cost and scheduling factors of a test program are often a paramount consideration.

A recovery system of new design must be tested under closely simulated operational and environmental conditions to verify its performance characteristics, and to obtain a degree of confidence in its functional reliability. The requirement for testing applies in particular to types of aerodynamic decelerators which differ from standard design or which must operate at high speed, extremely low or high dynamic pressures, or under environmental conditions not normally encountered by parachutes and related recovery system components.

Testing requirements develop from a need for basic research or from the need to verify predicted aims of a recovery system design. Decelerator design and performance prediction remain a strongly empirical science from which arises a steady demand for experimentally derived coefficients, factors, exponents, and base values. It should be an extra objective of test programs to acquire and fully document test data (test items, equipment, test conditions, procedures, results) in a form that will add to the total data bank of recovery system knowledge. Reliable and accurate test data are being applied successfully to mathematical models that show reasonable agreement with experiment.

The development and use of complex computer programs for the prediction of parachute opening forces and internal loads has had a bonus effect on testing requirements by virtue of the computer's ability to iterate long calculations in a short period of time. The result is a speeded-up trial and error process through which empirical coefficients for the evaluation of air mass, canopy pressure distributions, stability derivatives, and the like can be deduced from limited measurements obtained in tests that were instrumented for acquisition of other data. The technique will be found in Chapter 7 in connection with several different computerized analytical methods.

Availability of reliable and accurate testing methods and testing equipment is essential to successful and meaningful exploratory and experimental research and development. But economic aspects associated with achieving close simulation of extreme environmental and operational conditions are often a major barrier. For that reason, decelerator design parameters checked in wind tunnel tests, or performance characteristics verified by other relatively inexpensive testing methods are useful in support of design for specific applications. Such tests may reduce the number of total systems tests required to demonstrate airworthiness or to qualify system performance. Systems tests should be performed with an actual or closely simulated prototype vehicle in free flight, since the dynamic and wake characteristics of the flight vehicle tend to change the effective performance of a decelerator from its characteristics in undisturbed flow.

A recovery system may be one of several subsystems comprising an operational missile system, spacecraft system or military aircraft, to cite the more complex application examples. Recovery system components and functions must be tested separately, then system-integrated with other subsystems of the flight vehicle before they are considered qualified and "operational". This chapter presents a comprehensive picture of available and proven testing methods, facilities and equipment for development of recovery systems and components (principally aerodynamic decelerators).

TEST METHODS AND CAPABILITIES

Selection of testing methods to be employed in a given development program is guided by test requirements, and tempered by cost and scheduling considerations. Outdoor test schedules, of course, are subject to vagaries of weather. Decelerator testing costs tend to rise in proportion to the weight, speed and altitude limits of the system performance envelope, and in proportion to the reliability requirements or operational complexity of the system. Reliability requirements are most stringent for man-rated recovery systems or decelerator systems for planetary probes. Final decelerator testing costs can be a large fraction of total development program costs. Therefore, in planning a test program, the number of costly full-scale flight tests may be held to a minimum, if supported by trustworthy data from small model tests conducted under closely controlled conditions. The cost effectiveness of small model testing depends upon the quality of the models and how rigorously the scaling laws have been observed in the design of the tests. Insufficient attention to critical details will yield misleading, if not erroneous results. Interpretation of small scale model test data in terms of full scale free-flight conditions is a difficult and demanding task. The worst aspect of this problem has been encountered in many parachute programs, e.g., the small scale parachute will inflate readily or fly stabily while the full scale model will not. The problem of scale correlation emphasizes the importance of analyzing testing requirements when selecting testing methods and designing tests. Testing requirements are born of performance prediction analysis and design criteria, discussed in Chapter 8.

In this section are described the various testing methods used for the development of recovery systems. Testing methods applicable to aerodynamic decelerators are either non-restraint methods or captive methods. Non-restraint methods are valuable for their capability to simulate operational free-flight conditions, whereas test results from captive methods usually are affected in varying degrees by the influence of the restraint. Free-flight testing methods are dependent upon the means to achieve operational envelope conditions of a system, and range from ground launch (using booster rockets to reach high altitude, high speed flight) to simple airdrop techniques or vertical wind tunnels. Captive methods may also provide operational envelope conditions, but only at one point of performance at a time, as in a wind tunnel. Comparative and specific performance data on various types of decelerators are obtainable with accuracy in wind tunnels under controlled conditions at reasonable cost.

Ability to perform tests under controlled conditions, availability and accuracy of test data, economics of testing, and achievement of specific operational and environmental conditions are among the factors governing the selection and choice of a particular test method. In some instances, the only worthwhile testing will be by means of full-scale free-flight tests. In other instances, utilization of other types of test methods will produce substantial savings in cost, more rapid testing, more precise control of desired test-conditions and more accurate and complete acquisition of performance data.

Free Flight Testing

The conventional textile parachute once served primarily as a means of aiding escape from airborne vehicles under premeditated or emergency conditions. While the parachute is still used for this purpose, the field of use for parachutes, and deployable aerodynamic decelerators in general, has continuously expanded in the direction of variety in the function of devices and increased severity of the environment in which some decelerators are required to perform. Free-flight operational conditions in terms of altitude, speed, dynamic pressure and stagnation temperature within the Earth's atmosphere are shown in Figure 5.1 as zones attainable by various launch methods. Excepting those tests near the ground in zone F, free-flight testing of full scale decelerators is accomplished by either "gravity drop" methods, zones A and B, or by "boosted vehicle" methods, zones C and D. The potential for extreme temperature due to aerodynamic heating is indicated by the rise in stagnation temperature, T_s, with increasing Mach number. Gravity drop tests are those in which an unpowered test vehicle with its packed and attached test-item is launched from a stationary or moving aerial platform to free-fall under the influence of gravity. When the desired test speed or altitude is reached, the test item is deployed for performance evaluation. Boosted vehicle tests are those in which the test vehicle with its packed and attached test item is launched from the ground or from an aerial platform and boosted by suitable rocket engines to desired speeds and altitudes prior to deployment.

A principle advantage of the free-flight test method is the absence of physical restraint on the motion of the decelerator-load system. Free-flight provides a finite mass test capability and allows for the dynamic simulation of vehicle effects on the decelerator after deployment, and vice-versa. The full range of test conditions can be duplicated by this method and the actual performance of complete system functions may be demonstrated. Observation and measurements of system stability, flight trajectory, rate of

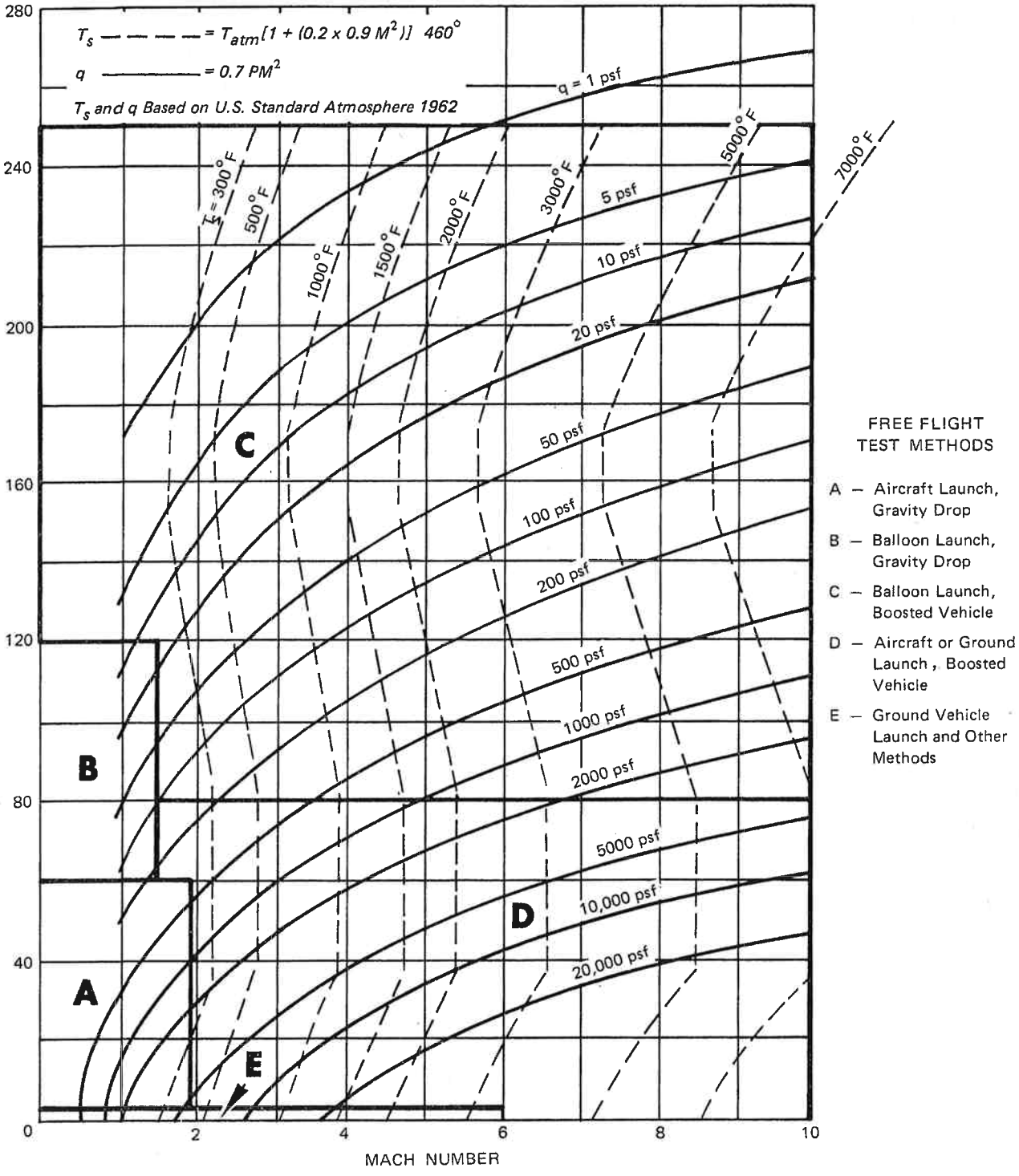


Figure 5.1 Altitude vs Mach Number, Decelerator Performance Regimes

descent, drift tendencies, and other phenomena are also attainable during tests. A disadvantage of free-flight testing methods, when compared to captive methods, is the difficulty to control and measure test conditions and to observe precise motion of test items. Of course the extreme complexity of test equipment and high costs, especially for high-speed and high-altitude test programs, is sometimes unavoidable.

Gravity drop-testing, although generally satisfying only the subsonic speed regime, may be extended into the transonic and low supersonic speed range by launching streamlined, aerodynamically clean test vehicles having high ballistic coefficients, from fighter type aircraft or from high altitude balloon-borne platforms.

A boosted vehicle launch configuration usually takes the form of a drop-type test vehicle with a rocket motor added. At the end of powered flight, the spent booster may be separated, so that the test configuration simulates an operational vehicle in flight at the test-point. Size of the added rocket motor is a function of the impulse required to reach test-point conditions; which means for some configurations the booster may be much larger than the test body. Then the suspension point and stabilizer requirements are dictated largely by the booster dynamics. Vehicle weight and attachment loads will determine the limits of launch configuration size in relation to airborne platforms and their lift and flight capacities. Numerous factors, including cost, must be considered in the analysis which chooses between air-launch and ground-launch for a boosted vehicle.

Drop-Testing from Aircraft. The most commonly used method for free-flight testing of deployable aerodynamic decelerators utilizes cargo, bomber, fighter aircraft or helicopter as the launch platform for a gravity drop-test vehicle. With fighter-type aircraft, the test vehicle is usually suspended from a pylon mount and bomb release mechanism under the wing as shown in Figure 5.2, or centered under the fuselage. "Drop" is initiated by the pilot's remote activation of the bomb release at desired drop point conditions of aircraft speed, altitude and direction over the test range. Similar wing mounting provisions are available on bomber type aircraft and have been adapted to helicopters and other aircraft as well, for test operations. Bombers can usually accommodate an even larger single drop load in their bomb bay.

With cargo aircraft, the test load can be large or small, but the method of launch requires the test load to be moved out the rear door, unlike a straight drop or downward ejection from a wing pylon. For gravity drops, small loads have been pushed out the rear of

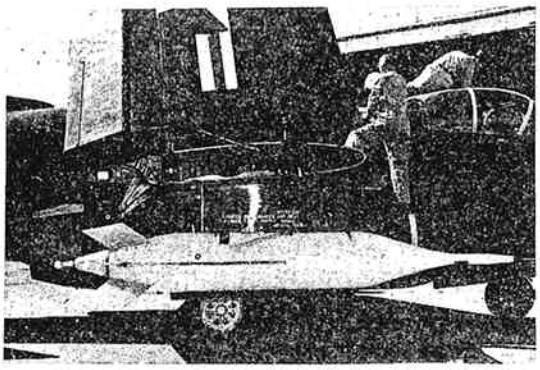


Figure 5.2 Aircraft with Drop Test Vehicle Mounted on Wing Pylon

the aircraft, but with large loads, an extraction parachute, as used in aerial delivery procedures, provides the force to remove the test load. If it is intended that the test vehicle accelerate to test point conditions by gravity, the extraction parachute will be disconnected after extraction. Tests of a parachute or decelerator system dropped in this manner may be for any recovery application, and are not to be confused with tests on the operational performance of cargo delivery systems.

Achievable test launch conditions are listed in Table 5.1 for several currently used aircraft. Launching of unusual loads and velocities have been obtained with special preparation. The F-4E has been used to reach a test velocity of Mach 1.7 with a test vehicle weighing 8700 pounds mounted on the fuselage centerline, and 2500 pounds on a wing pylon.

The B-52 has carried single vehicles of acceptable shape weighing 50,000 pounds (X-15). The C-5A has accommodated a total droppable load of 87,320 pounds extracted rearward, but it is not a designated aircraft for regular recovery system development test launchings. The current upper limit for conventional airdrops is approximately 50,000 pounds for a vehicle test point of Mach 0.6 and 15,000 feet altitude when launched from an aircraft such as the C-130 [290].

Drop testing of recovery systems and decelerators from aircraft is accomplished with a "short delay" drop, if the carrier aircraft is flown at a speed, altitude and path angle close to the test-point flight conditions. In a "long delay" drop, the carrier aircraft is flown well above the desired test-point altitude at drop actuation, to allow the vehicle time to achieve the desired test initiation point conditions [20]. Air dropping by rearward extraction from a cargo bay also can be executed with either short or long deployment delays.

Gravity drop testing from aircraft is the principal method in use at the National Parachute Test Range, El Centro. However, this type of activity is regularly

TABLE 5.1 AIRCRAFT ACHIEVABLE LAUNCH CONDITIONS

Aircraft Type	Maximum Single Load Drop Weight (lbs)	Maximum Drop Altitude (ft)	Maximum Speed at Maximum Drop Altitude (kts)	Maximum Level Flight Drop Speed at 5,000 ft (kts)	Maximum Level Flight Drop Speed at 20,000 ft (kts)	Minimum Drop Speed (kts)	Remarks
YF-4J	4300	50,000	Mach 2.1	750	750	180	Special aircraft has in-flight ejection seat test capability
F-4	4300	45,000	Mach 1.5	600	600	180	Special max. single load of 8700 lbs has been launched
A-3B	2000	40,000	240	450	370	150	
TA-4	3575	35,000	300	475	375	130	
A-6	3500	40,000	450	500	422	150	
NU-1B	300	12,500	100	115		55	Aircraft normally used for live jumps and dummy drop
C-117	300	12,500	140	140		90	Aircraft normally used for live jumps and dummy drop
C-130	50,000	30,000	150	150	150	110	Max. speed at drops is with ramp and doors open
C-141	35,000	20,000	191	200	191	120	Max. speed at drop is with ramp and doors open
C-5A	40,000	20,000	175	155	175	126	Special max. single load of 87,320 lbs has been extracted
B-52	30,000	47,000	245	280	280	163	Special max. single load of 50,000 lbs has been launched

supported at other bases including Edwards AFB, Tonopah Test Range and US Army Yuma Proving Ground.

Boosted Vehicle Launch from Aircraft. Test vehicles have been powered by single, clustered or staged solid propellant rocket motors. In most cases, a boosted test vehicle was launched from aircraft with the same techniques used for gravity drop testing, but with booster initiation at a safe free-fall distance from the aircraft. Launch aircraft, bomb-rack release and launch procedures are similar to gravity drop except where special safety precautions dictate differences. Boosted test vehicles have not been used extensively for decelerator testing, largely because it presents a potential hazard of rocket proximity to aircraft in an untested flight configuration.

Test Vehicle Launch from High-Altitude Carrier Balloons. For the purpose of testing and determining performance characteristics of decelerators at subsonic or supersonic speeds and at altitudes above the ceiling altitude of conventional test aircraft, helium-filled high-altitude polyethylene balloons are sometimes used. They provide a launch platform from which an unpowered test vehicle is released for a programmed descent[291], or a boosted test vehicle is launched on a planned trajectory [291 – 294]. A separate vehicle recovery parachute in the extended state as shown in Figure 5.3 is usually incorporated in the balloon-load train to avoid loss of the test vehicle should the balloon system fail during ascent. Balloon launched rocket powered vehicles have attained test-point velocities approaching Mach 2.5 at altitudes up to 150,000 feet with high-drag test vehicles weighing approximately 1900 pounds[294]. As the required weight goes up, attainable altitudes (and speeds) go down for this free-flight test method as shown in the generalized performace chart for carrier balloons in Figure 5.4.

At equilibrium altitude, boosted test vehicles have been launched through the apex of the balloon or at an upward angle to miss its envelope. In the latter case, a capability for azimuth control of the launch direction was achieved by "sun seekers" coupled with pulse jets to rotate the balloon and platform.

Testing with large balloons is expensive compared to other testing methods and is used when the test conditions cannot be achieved by less expensive methods. Launching of large balloons for test drop purposes is limited to periods when ground wind velocity is zero or nearly so, and cross wind patterns aloft must be reasonably steady for placing the balloon over the test range by the time maximum altitude is reached.

Balloon launches for the testing of decelerators and recovery systems are performed by the Air Force Geophysical Laboratory Group at the Missile Development Center, Holloman AFB.

Test Vehicle Launch from Ground. A common method of launching boosted vehicles for aerodynamic decelerator tests is from a ground-based launcher (Figure 5.5)[293,295]. Short rails guide the test vehicle during its initial period of acceleration.

Selection of the rocket propulsion units and staging for launching of test vehicles must be predicated on an analysis of several considerations, among which are performance, range safety, aerodynamics, reliability, structure and thermal effects. The primary consideration in determining rocket-motor staging is reliability in attaining the desired velocity-altitude conditions in the test. Selection of the booster units for the various stages should include consideration of relative rocket size to achieve near-optimum mass-ratio for the stages, efficiency, cost, reliability, and previous record of performance. Selection of the initial stage rocket is also influenced by thermal and inertial loading considerations. To minimize aerodynamic heating and the g-load effects during boost, the initial stage should have a relatively long burning time. Generalized performance capabilities of decelerator test vehicles (W = 250, 500 and 800 lbs) for various solid fuel rocket-booster combinations are found in Ref. [224]. The trajectories shown are not necessarily optimum from the standpoint of aerodynamic heating and range consideration. This is especially true for the higher velocities. For such cases, the range and aerodynamic heating considerations can have a strong influence on the design of the vehicle system, the initial launch altitude of the vehicle, and staging operations.

Testing from Whirl Tower. The problems of conducting and observing controlled experiments with full-scale parachutes under normal or near-normal operating conditions led to the development of the Parachute Whirl Tower Test Facility (Figure 5.6) located at the National Parachute Test Range, El Centro. In addition to precise speed controls and a predictable flight-path, the whirl tower provides free-fall test data and evaluation of personnel sized parachutes by releasing the parachute-load system from all restraints during the test. This is made possible by mounting the test vehicle with a parachute pack on a release device inside a streamlined nacelle suspended from the whirling arm of the tower. Parachute deployment is effected immediately after release from the whirling nacelle by means of a short static-line. Since the action of centripetal force ceases at the in-

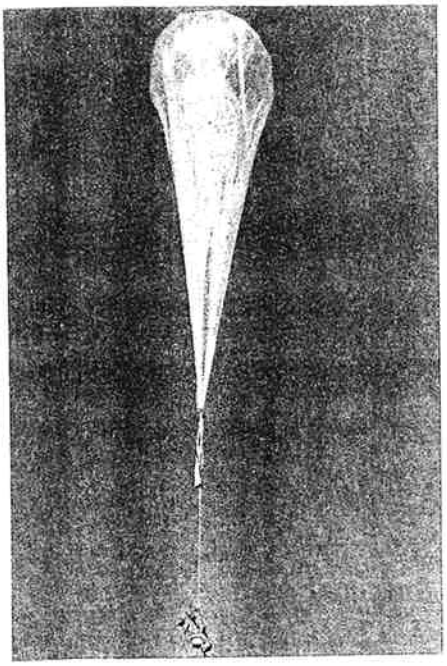


Figure 5.3 Helium Filled Balloon Used As Launch Platform

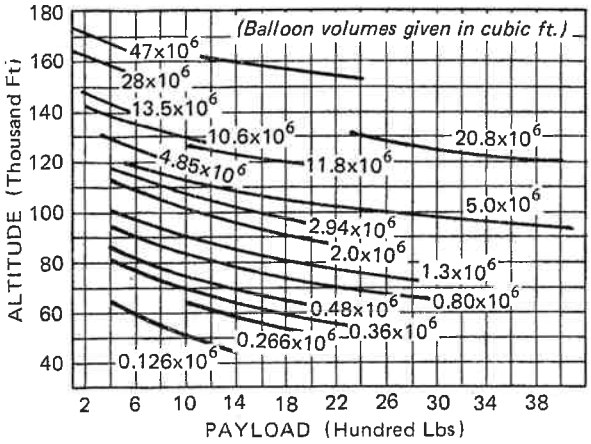


Figure 5.4 Generalized Carrier Balloon Performance Chart

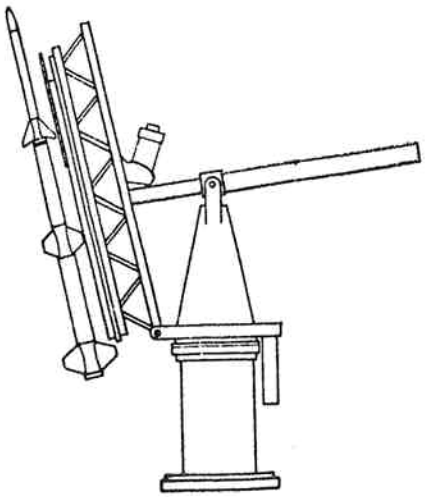


Figure 5.5 Test Vehicle Launch From Ground

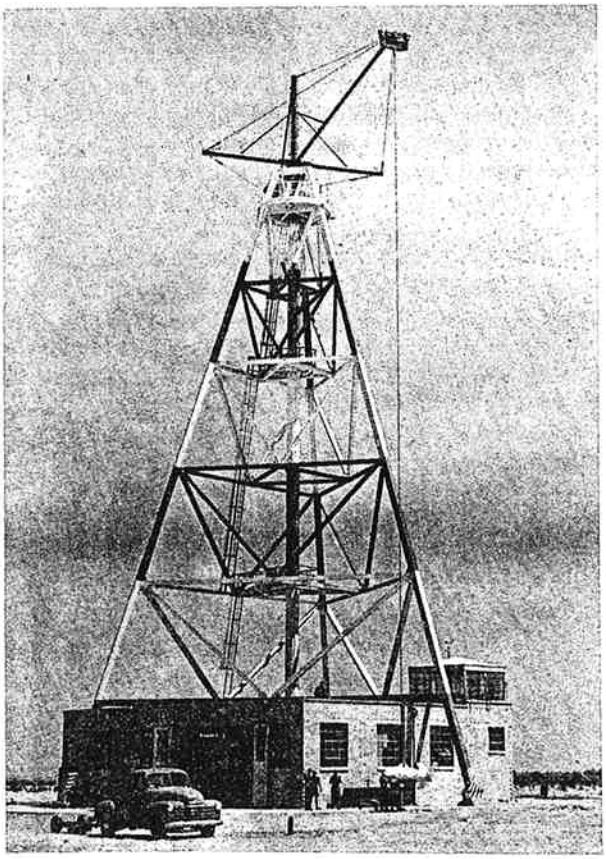


Figure 5.6 Parachute Whirl-Tower Test Facility

stant of release, the free-flying parachute-load system follows a predetermined course similar to the trajectory encountered in normal drops from aircraft. The height of the release point generally is sufficient to enable the canopy to reach the stabilized, fully inflated condition of normal operation for a brief interval prior to touchdown of the suspended load. Because the flight trajectory is short and its direction reproducible within narrow limits, very complete fixed instrumentation coverage is possible.

Structurally, the parachute whirl tower consists of a truncated steel tripod erected to support a vertical central drive-shaft. At a point 120 feet above the ground, a counter-balanced boom is secured to the central drive-shaft. From the arm of the boom, a 115 ft flexible steel cable is suspended 56 feet outboard of the central drive-shaft. The cable supports a streamlined nacelle which incorporates equipment to carry and release test loads with parachutes to be tested. The whirl tower has a maximum working radius of 172 feet and is powered by a 2800 hp electric motor. Two test vehicles are presently available for whirl-tower testing: (1) a nacelle with provisions for mounting a torso dummy, and (2) a general-purpose test vehicle at loads from 250 to 550 lbs. In the nacelle tests, the dummy can be released at speeds up to 350 knots. The nacelle in this case provides a streamlined shape to support a stable, high-speed test run. In the use of the general-purpose test vehicle, test speeds up to 400 knots have been attained. A compartment of 13 inches diameter and 30 inches length is available for stowage of the test item. Normal instrumentation at the site consists of telemetering systems and photographic instrumentation placed at strategic locations around the test facility.

Gun-Launched Ballistic Vehicles. The compressed air gun,[271,296,297] or mortar-launched ballistic projectile method of decelerator free-flight testing has been employed as an economical substitute for aircraft drop tests or ground-launched rockets. In an experimental decelerator development program, for example, the method enables the performance of a large number of functional tests, starting with high-velocity deployment shortly after launch of the upward leg of the trajectory, followed by low-velocity descent from apogee. Limited performance data may be obtained with relatively simple range instrumentation.

Ejected Vehicle Sled Launch. High speed rocket sleds are used as moving platforms for the upward launching of decelerator test vehicles with which a short free-flight trajectory is sufficient for evaluation of system deceleration and stability. The method is particularly well adapted for aircrew escape systems—ejection seats, nose capsules and crew modules—employing attitude stabilization drogues. The complete recovery sequence of aircrew escape systems designed to operate at high speeds and essentially zero altitude may be observed close-up with a comprehensive instrumental set-up along the track.

Other Free-Flight Testing. Limited testing of small decelerators has been conducted within high bay enclosed shelters and in wind tunnels. Free descent of parachutes can be closely simulated in vertical wind tunnels, or the inflation transient at high speeds can be approximated by allowing the model to fly down a horizontal tunnel between launching point and arresting gear [298 – 303].

The kiting characteristics of gliding parachutes permits short free descent tests to be performed after the gliding parachute has gained enough altitude with the aid of a tow-line and a suitable towing vehicle[132].

Captive or Tow Testing

In the area of captive or tow testing of deployable aerodynamic decelerators, the following test methods have been used:

aircraft tow tests, in which the decelerator is deployed behind the test aircraft either in flight or on the runway,

rocket-sled tests, in which the test vehicle is propelled by suitable rocket-propulsion units along a railed track with the decelerator deployed after a desired velocity has been reached,

truck tow tests of ballistic or gliding parachutes

water-tow tests, in which two-dimensional or three-dimensional test models are towed in water, and

wind-tunnel testing

Advantages of captive or tow testing are the control of initial test conditions, accurate and precise measurement of performance parameters, the use of recoverable and reusable test-vehicles, and the frequency of tests obtainable. In some cases, the cost of testing is significantly lower than that obtainable with other test methods. There are however, disadvantages to captive or tow testing. In all cases the test item is restrained, allowing only limited freedom of motion during test. All testing is conducted near infinite-mass operating conditions, meaning that the velocity decay during test-item inflation is small or non-existent.

Aircraft Tow. Towing parachutes behind aircraft has proven a satisfactory method of testing. If the parachute is intended for aircraft landing deceleration or cargo extraction, the parachute system designed

for a particular aircraft should be tested behind that aircraft in order that the performance characteristics of the parachute system are accurately determined under true operating limits. Aircraft such as C-130, C-141 and C-5A[304,305] have been equipped with onboard oscillographs or telemetric equipment attached to strain gage links in extraction lines to measure forces and deployment times of test parachutes. Forces up to 68,000 lb have been recorded prior to release of towed parachutes in these tests. As a means of development of parachutes for use other than aircraft deceleration or cargo extraction, this method has only limited application because of aircraft wake effects, personnel safety, and requirements for aircraft modification to accommodate the test system.

Taxi-test aircraft have been utilized to obtain performance data on various parachute designs and systems for aircraft landing deceleration (Figure 5.7). Parachute deployment, drag, and to some extent, stability characteristics have been determined at speeds up to 130 knots on a 12,000 ft runway. Parachutes of diameter up to 35 feet were tested. Instrumentation to measure and record parachute forces, ground speed, and various other data on a common time-base was installed in the test aircraft.

To determine specific parachute performance characteristics at high deployment speeds and higher altitudes, and to evaluate the performance of parachute systems for inflight applications, various jet aircraft have been used successfully as tow-test aircraft. Parachutes with diameters up to 16 feet have been deployed at speeds up to 195 knots without impairing the safety of flight. The aircraft were equipped with instrumentation to measure and record parachute forces, aircraft speed, and other operational data versus time.

An F-104B airplane was modified to investigate the drag and stability characteristics of a ballute decelerator in the wake of an asymmetrical airplane[306]. Decelerator deployments were initiated at a Mach number of 1.3 and an altitude of 15,240 meters (50,000 feet) and terminated when the airplane had decelerated to a Mach number of 0.5.

Rocket-Sled Tow. Rocket powered track-bound vehicles have been used successfully for determining deployment and aerodynamic characteristics as well as general performance of parachutes and other decelerators at subsonic, transonic and supersonic speeds. Facilities consist of straight, precisely aligned, single or dual-rails along which the test-sled can move. The decelerator or system to be tested is stowed on the sled vehicle and remains attached after deployment. Track tests have a few advantages over other test methods. Large-size decelerator models or even full-scale parachutes may be used, thus avoiding the effect of dimensional scale-factors. High dynamic pressures permit testing that can establish structural safety factors. Disadvantages of this test method include the fact that testing is limited to one atmosphere density, and usable test periods are of short duration since the test period is limited by the track length and by the length of time the sled can be maintained at required test velocities. Also, propulsion costs may be high, especially for testing at the high velocities.

Track facilities currently used for testing deployable aerodynamic decelerators are located at the Air Force Armament Development Test Center, Holloman Air Force Base, Air Force Special Weapons Center; Kirtland Air Force Base, and Naval Weapons Center, China Lake.

Truck Tow. The use of a truck to tow small parachutes permits close up study of parachute operation and avoids costly delays typical of testing from aircraft. The parachute is attached to a framework of sufficient height to provide parachute-road clearance. Figure 5.8 illustrates a typical truck-tow test arrangement for a gliding parachute model attached to an outrigger boom.

Water Tow. An inexpensive means of testing aerodynamic deceleration devices is available in the water-tow test method, or in flow of a liquid with a free surface in a gravity field. This method, particularly in "shallow water" tests[307,308] is well suited for the study of precise internal and external aerodynamic characteristics during supersonic operation of flexible deceleration devices and primary-secondary body combinations. Also in "deep water" tests[309], this method provides strength-testing of deceleration devices under high dynamic pressures. Naturally, there are limitations to water tow testing with respect to the velocity that can be simulated. For two-dimensional model testing, this limit is given by boundaries in validity of the water surface-wave analogy, whereas for deep-water tow the limit is reached at an equivalent Mach number of 0.8, when cavitation around the test item usually develops. The analogy of the flow of a liquid with a free surface in a gravity field to the two-dimensional flow of a compressible gas has been known for some time. References 310, 311, 312, 313 and 314 provide further data relating hydraulic analogy with supersonic flow.

Based upon deep-water test results, the following comparison may be made between parachute performance characteristics in water and in air under equivalent velocity and dynamic pressure conditions:

The opening shock factor associated with a particular decelerator type is larger in air than it is

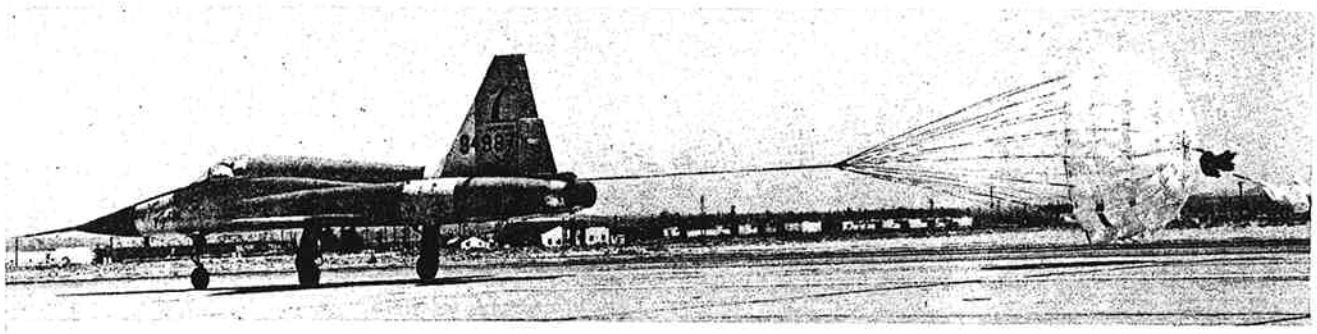


Figure 5.7 F-5 Aircraft Testing of 15-Foot Ringslot Deceleration Parachute

for the same type in water. This is because of the difference in the rate of loading by the air and water masses.

The drag area of a solid cloth parachute towed in water is higher than that of the same parachute in air, because of effective porosity differences.

Although the subsonic drag of a decelerator increases in air as its distance behind a primary body is lengthened, this trend is reversed in water. It is believed that in water there exists a "super-velocity" region in that portion of the wake to which the aerodynamic decelerator is exposed, diminishing with distance behind a primary body in water is highest "close-in" and decreases as the canopy is moved downstream. A deep water tow facility that has been used for parachute testing is the David Taylor Model Basin, Bureau of Naval Weapons, Carderock, MD.

Wind Tunnel Testing. The use of wind tunnels for the measurement of aerodynamic characteristics and the acquisition of performance data for the design of aerodynamic decelerators is the most productive of captive test methods. Results from wind-tunnel tests have contributed significantly to the advancement of aerodynamic decelerator technology. Although wind-tunnel testing is not well suited for the study and determination of all of the aerodynamic and performance characteristics of decelerators, this test method nevertheless presents advantages that balance shortcomings of some of the data. Advantages of using the wind tunnel, compared with other test methods are:

Steady state test conditions are subject to close control.

Measurement of maximum precision may be made.

Test conditions may be changed quickly.

Air flow around decelerators may be made visible[315 – 322].

Within certain limits, comparative performance relationships and trends usually correlate with full-scale free-flight behavior[323]

Disadvantages of the method arise mainly from the limitation of size or physical scale of models which can be investigated, the restraints placed on their freedom of motion, the maximum dynamic pressure limits of unstable models, and the uncertainty of correlation with full-scale free stream conditions. A number of test problems are encountered during wind tunnel tests, of which the most difficult are:

wind tunnel blocking and wall effects,

testing below critical Reynolds numbers,

direct measurement of canopy side loads,

and mounting models to minimize flow separation effects.

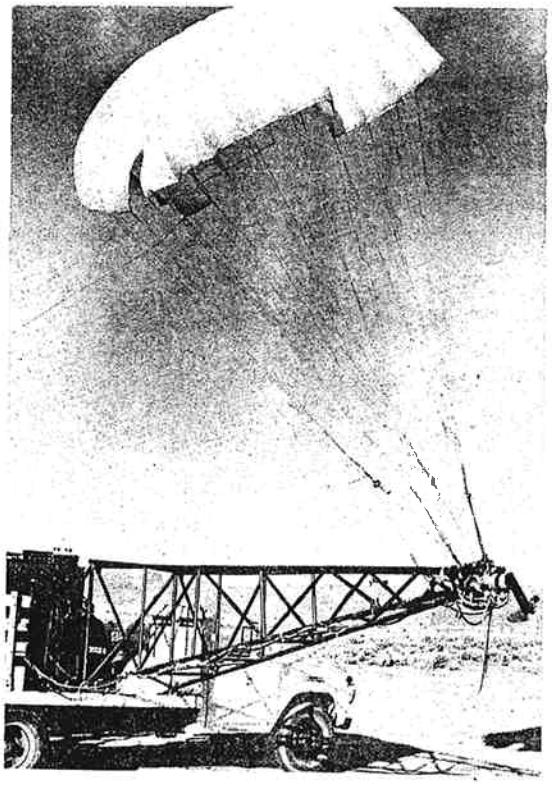


Figure 5.8 Truck Tow Test Rig for Experimental Gliding Parachute

Blocking effects arise when the ratio of the model projected area to the test-section area is large. For subsonic testing, the maximum ratio of model area to test section area should not be larger than approximately fifteen-percent if blocking effects are to be minimized. This area ratio applies primarily to opening-shock measurements of canopies. For the determination of aerodynamic coefficients, smaller models should be utilized. For best results, the projected area of the inflated aerodynamic decelerator model should not exceed 10 to 15 percent of the test section area.

Wind tunnel tests are generally conducted above critical Reynolds number in order to avoid scale effects. As in aircraft work, an attempt is made to achieve Reynolds number equivalent to actual full-scale test or operational conditions; however, this has seldom been feasible because of the large canopy diameters.

The requirements for wind tunnel testing at supersonic speeds are more stringent. The positioning of the decelerator model in the test section is critical and mounts must be rigid. Trailing models are limited to a range of downstream positions that will not be intersected by mount and body shock waves reflected from the tunnel walls.

Decelerator models in a supersonic wind tunnel must be structurally strong enough to withstand sustained operation far beyond the demands of an operational item. Instability pulsation and fluttering will tend to limit the maximum dynamic pressure of the tests, or the use of over-strength models will introduce unfavorable scale factors with respect to stiffness and elasticity. Wind tunnel facilities currently used for testing supersonic decelerator types are located at the Arnold Air Force Station, Tennessee.

Support Testing

Support tests are those conducted on recovery system components and materials to obtain, at low cost, functional verification or specific data in support of (and usually prior to) expensive major development operations such as flight testing. Ground tests or bench tests are often used to demonstrate functional integrity of a decelerator or a component of the system. Other tests are made to learn exact characteristics of materials, for example, in the investigation of failures to determine cause. Tests of this nature employ laboratory methods and equipment. Simple laboratory tests, such as the results of chemical analysis, determining weathering qualities, establishing abrasion resistance, or determining the friction coefficient of a material, are made with reference to their effect on the primary characteristics. Since required characteristics for textiles in other fields are somewhat similar, the testing equipment for recovery system textiles has been borrowed or adapted from these other fields. However, characteristics such as air permeability and elongation under stress are more thoroughly investigated. The methods described in the following paragraphs are primarily for textile testing. Some testing is done on aerodynamic decelerator hardware, but this follows the same pattern as any metal testing . . . such as bending and hardness testing and radiographic analysis. A number of instruments are commercially available for all of these tests.

Both static and dynamic laboratory test equipment are needed to adequately evaluate mechanical properties, functional characteristics and performance of every part of a recovery system. Measurement of the mechanical properties of textiles and energy absorbing materials are a normal function of the manufacturers of decelerator and landing systems. Complex testing, such as the discrete vibration spectrum or extreme vacuum, sometimes required in flight environment simulation, may be delegated to an independent test laboratory or an available government facility.

Simulated Deployment. Several different kinds of deployment tests are performed with varying degrees of sophistication depending on the purpose.

The static extraction force required to strip a deployment bag from a packed decelerator is usually measured as a function of displacement on a long smooth table.

The motion of a deploying decelerator may be evaluated to a degree under static conditions by impulsive extraction or ejection of the pack from its compartment in the vehicle or in a partial dummy vehicle. A stretched elastic "shock-cord" has been used for this purpose to simulate the drag of the pilot chute or prior-stage drogue.

Static mortar firings and ejection tests may be performed with either dummy or actual decelerator packs to evaluate muzzle velocities and the behavior of the decelerator and deployment bag during the stretchout sequence.

Recovery system deployment sequencing may be evaluated with actual or dummy vehicles at rest on the ground for detailed instrumental and photographic coverage of the complete series of events in real time. Reference 324 describes a dynamic simulation technique which utilized a moving truck to achieve stretchout of a packed parachute. The packed parachute is mounted on the truck bed and the main riser anchored to the ground. As the truck accelerates, the parachute deploys.

Deployment impact loads and bridle failure modes are duplicated with several different kinds of dynamic loading equipment, some highly specialized.

The release and inflation of airbags for impact attenuation or flotation, and the deployment of other landing devices may be checked for function and operating time prior to or in conjunction with appropriate drop impact tests.

Function and Performance Checks. Recovery system sequencers, actuators and control sensors are tested in a laboratory by a variety of methods to evaluate functional adequacy, reliability, and performance. Measurements usually involve force or pressure transients as a function of time obtained by recording transducer outputs on tape or film.

Materials Testing. Laboratory testing of materials consists mainly of measuring the mechanical properties of textiles. A variety of both standardized special apparatus and instruments are available for this purpose. Other materials such as energy absorbing honeycombs or structural foams also have been subjected to comprehensive laboratory testing, primarily impact loading, to determine their suitability for various shock attenuation needs usually associated with recovery system landing dynamics.

Laboratory equipment for the measurement of the mechanical properties of textiles of importance to the function of aerodynamic decelerators includes that for tensile strength and strain both static and dynamic, air permeability at low and high pressures under various loading conditions, tearing strength, resistance to fatigue and abrasion, surface smoothness, stiffness and toughness. Decelerator materials tests are made to confirm that the materials when received, meet the requirements of procurement specifications prior to manufacture. Other tests determine seam and joint strength values for use in structural evaluation, or provide data for failure analysis of the system or components. Similar tests are conducted to determine properties of new materials which may be applicable to decelerator usage. Textile test methods are specified in Federal Standard 191[325]. Methods used to achieve the above objectives are listed in Table 5.2. Tests of joints, seams and splices for the evaluation of system strength characteristics employ the same test methods.

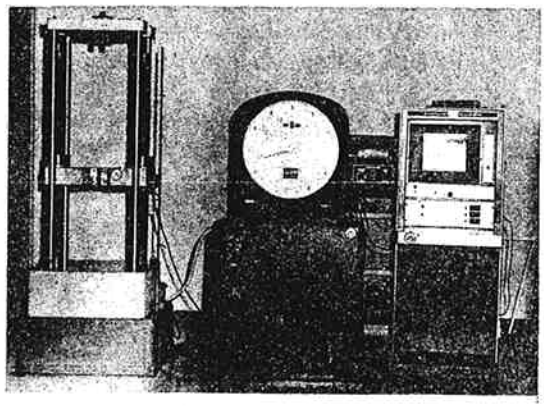


Figure 5.9 Representative Textile Testing Machine for Comparatively Heavier Textile Forms

TABLE 5.2 TEXTILE MATERIALS TESTING

Type of Material	Test Data Required	Test Method (FED STD 191)
Cloth	Breaking strength and elongation	5134
	Tearing strength	5104
	Air permeability	5450.1
Cord	Breaking strength and elongation	4102
Tape & Webbing	Breaking strength and elongation	5100
Thread	Breaking strength elongation, tenacity	4100.1

Tensile Strength and Elongation. Standard tensile testing machines such as those illustrated in Figure 5.9 are used to measure the strength of different textile forms, e.g., cord, tape, webbing, ribbon and prepared strips of cloth. The material ends are gripped in self-clamping jaws, such as split cylinders, around which the textile form is wrapped in a way that minimizes end-effects. The proper grip of clamp is as important as the tensile testing instrument. If the specimen is not held correctly, errors will result. A break occurring at the jaws is not an acceptable failure mode for ultimate strength evaluation. The elongation of the specimen at rupture is usually measured at the same time to yield corresponding values of the ultimate strength and elongation of the material.

Strength factors are measured under many different conditions depending upon the purpose of the tests. Normally, they are determined in terms of standard dry-specimen conditions at 70°F (±2°) and 65 percent (±1%) relative humidity. Continuous load-elongation (stress-strain) measurements are obtained in graphical form by attaching a suitable recording instrument to a predetermined gage-length of the specimen between the jaws. Test set-ups must be carefully prepared when carried to rupture because the strain metering arrangement will experience high velocity displacement following failure of the specimen.

Narrow woven forms (ribbon, tape, webbing) provide a convenient self-base for unit strength measurements because of the inherent difficulties in evaluating the tensile stress over a unit cross-sectional area of the test specimen. Textile forms of substantial width, principally cloth, are converted into test speci-

mens that will yield a measure of the strength per unit width. In the "ravel-strip" method (5104)[325], a test specimen of the desired unit width (one inch) is prepared by cutting a strip of cloth parallel to the warp (or fill) yarns and then reducing it to the final test dimension by removal of excess warp (or fill) yarns on both sides of the unit width. This is typical for one direction tensile test methods. Synchronous bi-axial strength measurements require more complex apparatus. To simulate biaxial loading experienced by cloth in a parachute canopy under air pressure is extremely difficult.

Tensile strength may be tested at elevated temperatures by either surrounding the test specimen with a heating unit between the jaws of the machine or by placing the entire apparatus in an autoclave. The heating unit is replaced with a refrigeration unit for strength measurements at low temperatures. Special laboratory equipment may be required for the measurement of textile strengths at transient low and high temperatures.

Tearing Strength. The tearing strength of a textile fabric is defined as the force required to start or continue a tear. A tear failure entails the successive breakage of warp or fill yarns along a continuous line, each yarn failing in tension. A representative testing machine used for measuring tearing strength is shown in Figure 5.10.

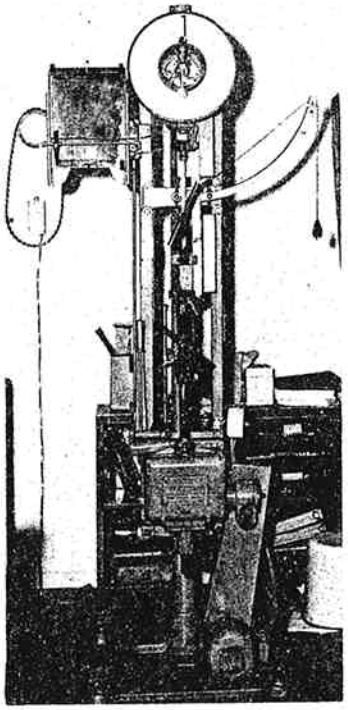


Figure 5.10 Representative Textile Testing Machine for Fabrics and Light Cordage

The resistance of textiles to tearing stresses is important to the structural integrity of decelerators in the free edges of fabric members subject to non-uniform tensile running loads or to stress concentrations where the fabric is reinforced by superimposed tapes. Tear resistance also helps limit the propagation of fabric breaks caused by the initial pressure pulse of the inflating canopy. Two methods of measuring tearing strength are the "tongue" method (5134)[325] and the "trapezoid" method (5136)[325]. The tongue method is used to measure the tearing strengths of fabric having approximately equal tensile strengths in the warp and fill directions. The trapezoid method is used when the warp and fill strengths are unequal.

Impact Strength. Because of its importance to decelerator performance, the impact strength of textiles has received increasing attention in the industry, and a variety of laboratory testing methods have been developed. The typical static tensile test has a specimen loading rate in the order of two percent of the ultimate strength per second. On the other hand, a relatively moderate parachute loading rate during inflation is closer to 100 percent per second, while high-onset impacts up to about 2500 percent per second have been experienced during deployment and have been reproduced with special laboratory equipment. Another relative measure of loading rate is the impact velocity applied to an unstretched specimen of a given length; representative maxima during deployment fall in the range from 250 to 300 fps. At these velocities the mass-inertia of the material inhibits its elastic response such that a short segment at one end may be loaded to the breaking point before the balance of the specimen is stressed, e.i., the critical velocity of the material may be exceeded.

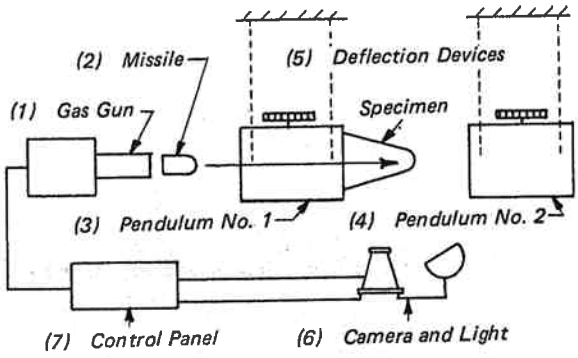


Figure 5.11 Schematic Diagram of Textile Impact-Testing Apparatus (Ref 326)

Laboratory apparatus has been assembled for measurement of the impact strength of texitile materials over a broad range of loading rates. Test specimens may be loaded by impact of gas propelled projectile[326], Figure 5.11, engaging the rim of a rotating flywheel[327], Figure 5.12, a fluid driven piston in a hydraulic ram, Figure 5.13, and air pressure waves generated in a shock tube[328], Figure 5.14. The apparatus illustrated schematically in Fig. 5.11 consists of a gas gun and missile, two ballistic pendulums and suitable instrumentation. A round-nosed missile weighing

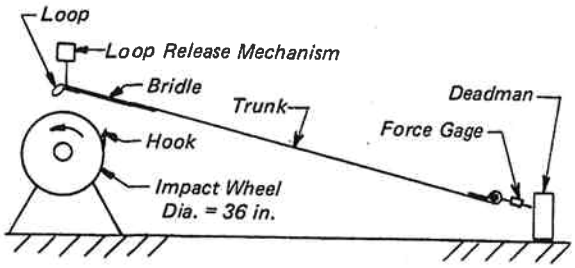


Figure 5.12 Pilot-Chute Bridle Dynamic Test Apparatus

between one-half and ten pounds is projected from the gas gun at the desired velocity. The projectile strikes the test specimen mounted on pendulum No. 1 with sufficient energy to rupture the material at the apex of the "V". The projectile then continues to pendulum No. 2 which absorbs its residuals energy. Given the masses of the missile and of the two pendulums, the recorded displacement of the pendulum is proportional to the energy absorbed. The energy absorbed by the test specimen is indicated by the vertical displacement of pendulum No. 1. The residual motion of the projectile and pendulums, and the behavior of the test specimen during impact are recorded by a camera with illumination provided by a mulit-flash light source of known frequency.

Also, a simple drop-weight technique has been successfully employed by several investigators[329,330] to provide material load-elongation data under dynamic loading. The experiments in Reference 329 consisted of suspending the weight in some raised position (webbing collapsed or bowed) and letting it drop. The transient oscillations in webbing force were detected by a load cell built into the static webbing connection. Displacements of the weight were detected by a slidearm arrangement driving a LVDT, Linear Variable Differential Transformer, and a back-up potentiometer.

Air Permeability. Several different methods of measuring the air permeability of fabric are in use. The one embodied in standard permeometers designed to measure the volumetric through-flow rate at a specified differential pressure, consists of an electric air blower and duct with an orifice over which the specimen is clamped (Figure 5.15). The U.S. Standard method measures flow in terms of cubic feet per minute per square foot of area with ½-inch of water pressure-drop across the fabric specimen. These devices accommodate cloth specimens larger than the orifice size, and most accept complete parachute canopies for spot-evaluation of the permeability or nominal "mechanical porosity" at selected points across the fabric surface.

Other more flexible permeometer equipment is used to obtain air through-flow measurements over a wide range of differential pressures (Figure 5.16) and in some cases, with the cloth subjected to both mono- and bi-axial loading. Methods of measuring the effective porosity of ribbon grids also have been developed[332].

Coefficient of Friction. Frictional heating of textiles during decelerator deployment, cause local weakening of the decelerator structure. While such damage may be slight, it sometimes provides the focus for premature failure of the inflating canopy at a sub-design load.

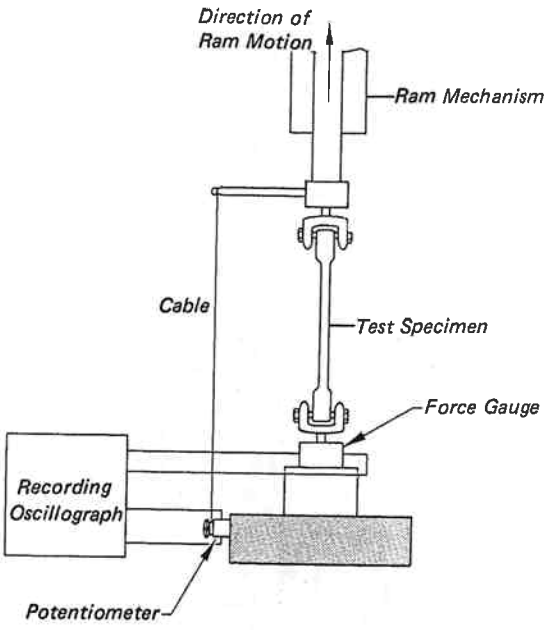


Figure 5.13 Suspension Line Impact Loading Apparatus for Strain Rates of 50% to 200%/Sec. (Ref. 331)

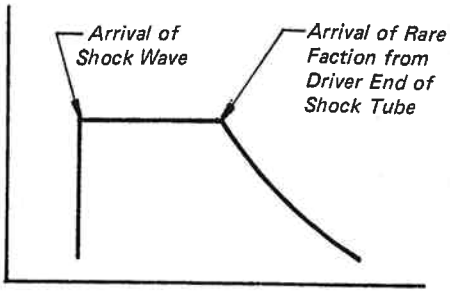


Figure 5.14 Schematic of Pressure Time History at an Arbitrary Location Along Shock Tube

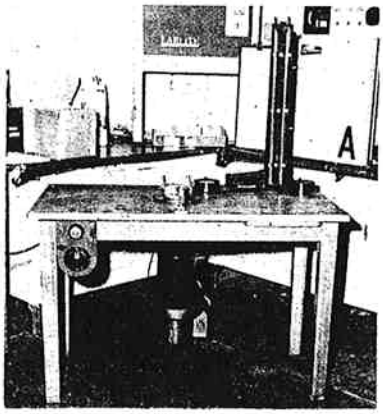
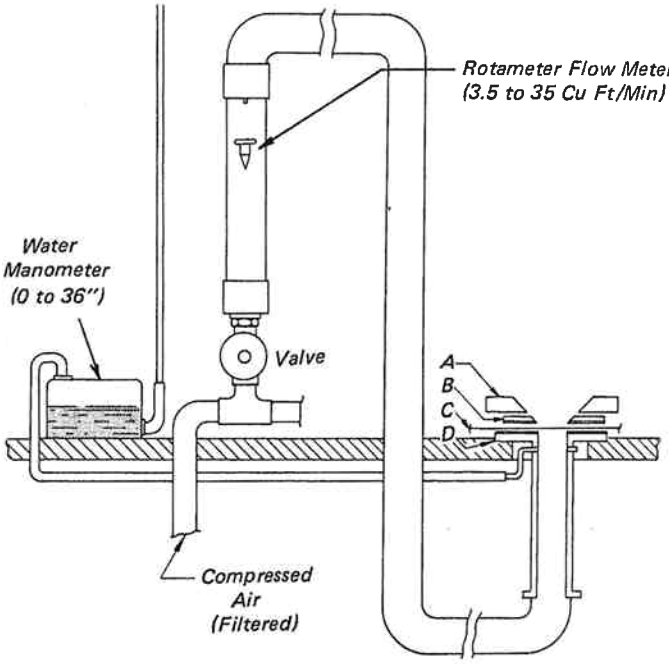


Figure 5.15 The Frazier Air Permeability Instrument



A Lead Sealing Weight
B Steel Flange, Rubber Faced on Underside
C Fabric Test Piece
D Upper Flange of Test Cell, Rubber Faced

Figure 5.16 Air Permeability Apparatus

The coefficient of sliding friction between two fabrics or between fabric and other materials may be easily measured by the inclined-plane apparatus illustrated in Figure 5.17. One specimen is taped to the plane surface and the other to a weighted block. The angle of the inclined plane is increased until the block begins to slide. The coefficient of sliding friction, $C_f = \tan \phi$.

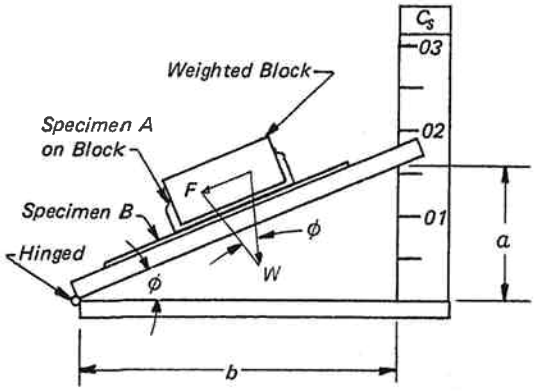


Figure 5.17 Inclined-Plane Apparatus for Measuring Coefficient of Sliding Friction

Stiffness. The relative stiffness of cloth and other textile forms contributes to the overall stiffness of decelerator assemblies resulting from the internal friction of plied materials stitched together in the seams. Since structural stiffness or resistance to bending

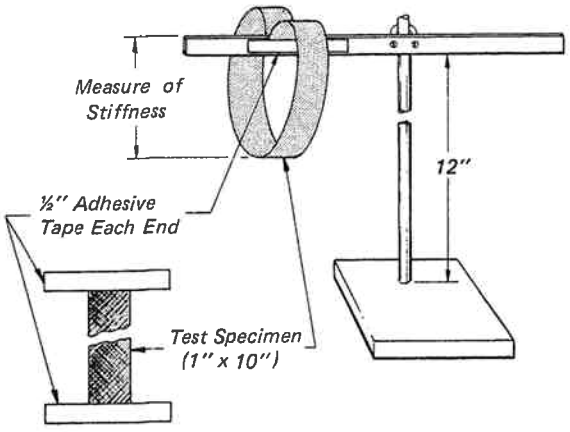


Figure 5.18 The Hanging Loop Method of Measuring the Relative Stiffness of Thin Flexible Materials.

modifies the shape of the inflated canopy it can influence performance of decelerators of heavyweight construction and of small scale wind tunnel models.

A standard method (5200)[325] of measuring the relative stiffness of textile materials is illustrated in Figure 5.18. Each test specimen is sheared to form a one-inch wide strip ten inches long. When the strip is taped to the horizontal arm as shown, the gage length, l', of the material droops to the loop length, l', which is measured. Since l' is inversely proportional to the stiffness of the strip, the relative stiffness of the material may be evaluated as $\Omega_o = 1-(2l'/l)$.

Strength of Joints and Seams. Decelerator subassemblies and joint and seam samples may be subjected to strength tests in the laboratory. When standard equipment will not accept the test specimens for any reason, special test jigs and fixtures may be assembled for the purpose. Joint efficiencies are determined relative to the strength of the materials being joined, and, in tape and webbing loops, as a function of the diameter of the retaining bolt or bar. Test methods for impact loading plain textile materials are also used to evaluate seams and joints. High stress is encountered at seams and reinforcements where changes in density occur. Each component of the textile assembly has a critical impact loading velocity above which it will fail without transmitting any load.

Environmental Simulation. All components making up a total flight system are subject to various environments throughout their operational employment life, including logistical phases of transport, storage, preparation handling before use, and retrieval or refurbishment handling after use. During flight, the deployable components of a recovery system remain in packed status until initiated. Depending upon the recovery system application, exposure to operational environments may range from moderate conditions to unusual extremes in temperature, humidity, altitude, shock, vibration, other components of a recovery system, i.e., devices made of metal, glass and rigid parts may be vulnerable to such environments when induced by functioning rocket motors, aircraft engines and explosive actuators. Environmental test methods are accomplished with laboratory facilities in accordance with MIL-STD-810[333]. The apparatus used for conducting tests is available at most independent test laboratories and major industries involved with aerospace requirements. Descriptions and characteristics of environment simulating equipment are readily available, so are not included herein[334].

Landing Condition Simulation. Simulation of ground landing conditions that occur during the impact phase of parachute-retarded equipment, supplies and various types of vehicles, require a facil-

ity which can hoist the load above the ground to a release height sufficient to provide at impact a desired vertical velocity, and usually means to impart a horizontal (maximum wind drift or glide) velocity[334,335] A mobile or fixed crane of proper height and lift capacity will satisfy vertical velocity requirements. Horizontal velocity has been provided by more sophisticated test structures employing an inclined rail or pendulum principle.

TEST FACILITIES AND EQUIPMENT

Several test ranges exist within the continental United States which are fully instrumented and have been used extensively for free flight test operations of missiles, drones, aircraft and other vehicles, many of which employ recovery systems. These ranges have provided complete vehicle systems testing, and in some cases, subsystem or component testing of decelerators and other related subsystems. They are capable of supporting flight tests with high performance aircraft or other launch means. Most ranges have the equipment to obtain accurate trajectory data and excellent photographic coverage of a test vehicle in flight, recording such events as deployment and behavior of a trailing decelerator with real-time correlation. Some have laboratory test equipment and other support testing capabilities.

Wind tunnels, normally used on a continuous basis to support aircraft and missile aerodynamic research and development, are usually available for decelerator testing. Those with large cross-sections or with high-speed low-density air-flow, have been particularly useful for parachute testing.

In this section, range facilities, testing equipment and ground based instrumentation are briefly described which have been used in recovery system development.

Instrumented Ranges

Test range facilities and capabilities are identified and summarized in Table 5.3. Only one test range is devoted exclusively to recovery system research, development, test and evaluation. Data contained in the table are general in nature, suitable only for preliminary planning purposes. A prospective user should contact the test range for specific data regarding requirements and schedules when anticipating use of facilities. Table 5.3 lists types of recovery system tests of test methods, and various test support services available. Ground instrumentation employed at the various ranges and other support services are described starting on page 232.

Air Force Flight Test Center. Edwards Air Force Base, California is located 100 miles north of Los Angeles. The test range is approximately 5 miles wide by 14 miles long. The principal use of the range is the flight testing of aircraft. Development of parachutes and related components through the use of air launch and gravity drop testing techniques can be performed on this range. Human escape methods, aerial speed retardation and landing of personnel, material equipment, and all aspects of recovery, rescue and survival are included in the total scope.

Facilities for test preparation of parachutes and test vehicles for aircraft launch are available. Various types of ground handling equipment and airborne test vehicles are in inventory. Support services provided by the base include test vehicle preparation, checkout, parachute handling and test hardware retrieval. Chase and search airplanes and helicopters are available. Optical and photographic data are acquired by real-time coordinated cinetheodolites and tracking motion picture cameras. Other data are obtained with telemetry. Photo processing and data reduction can be provided.

White Sands Missile Range. The White Sands test complex is a combination of test ranges and facilities located in south central New Mexico. The principal test area is the US Army White Sands Missile Range with headquarters located 60 miles north of El Paso, Texas. The range is approximately 40 miles wide by 100 miles in length, with range area extensions (shown in Figure 5.19) which can be placed under ground and airspace control. Its principal use is for missile and gunnery development by the US Army, but its various drop range areas are also used by the other armed services and NASA for operations from their own launch and test bases. The NASA White Sands Test Facility, Fort Bliss and Holloman Air Force Base facilities greatly enhance the overall capability of the White Sands test complex.

Radar, optics, weather data and telemetry are coupled to a real-time data system with total range communications for data reduction purposes, or they can be used independently with the smaller area plotting facilities. Holloman Air Force Base is located 40 miles northeast of White Sands on the eastern border of the range, and 15 miles west of Alamogordo, New Mexico. Facilities useful for recovery system and decelerator development are rocket launch areas, a high speed test track and a high altitude balloon launch facility. Excellent work areas are on hand with ground handling equipment available for most sizes of test vehicles. Ample ground vehicles, cranes, weapons carriers, trucks, airplanes and helicopters are available for search and retrieval.

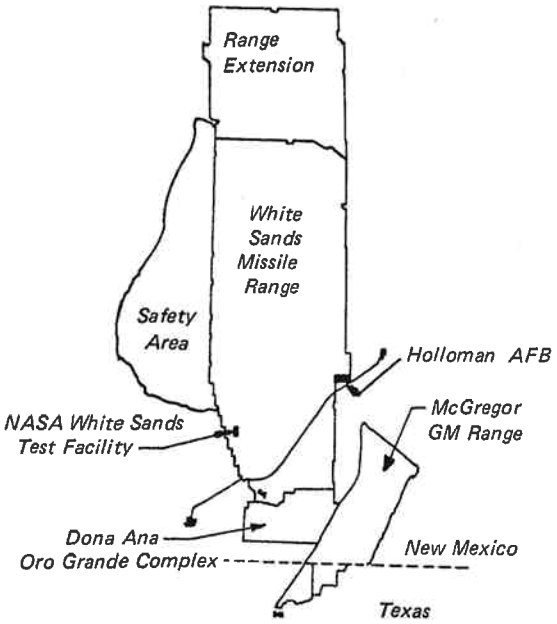


Figure 5.19 White Sands Test Complex

Services provided by the base include well established explosives handling capability. Optical and photographic data are obtained on 35, 70 and 170mm intermotion ribbon frame, and 35mm rotating prism cameras, cinetheodolites, tracking telescopes and ballistic cameras. Other data acquisition equipment are radar, velocimeter and telemetry.

The balloon launch facility is managed by the Air Force Geophysics Laboratory, Bedford, Massachusetts. The Holloman Detachment is a self-contained development and support group which has a remote operations capability for performing flights wherever the need may exist. In addition to its own engineering and support staff, the Holloman facility has a laboratory and two large assembly areas, meteorological support as well as operating a command and control center. Balloons are normally launched at Holloman or at several sites located on the White Sands Missile Range.

Eglin Gulf Test Range. Eglin Air Force Base is situated on the northern gulf coast of Florida 60 miles east of Pensacola. The range extends south and eastward over the Gulf of Mexico between azimuth 130° and 180° as shown by Figure 5.20. The principal use of the range is to develop tactical airborne equipment for the US Air Force. Facilities include three usable rocket launchers plus an integrated blockhouse.

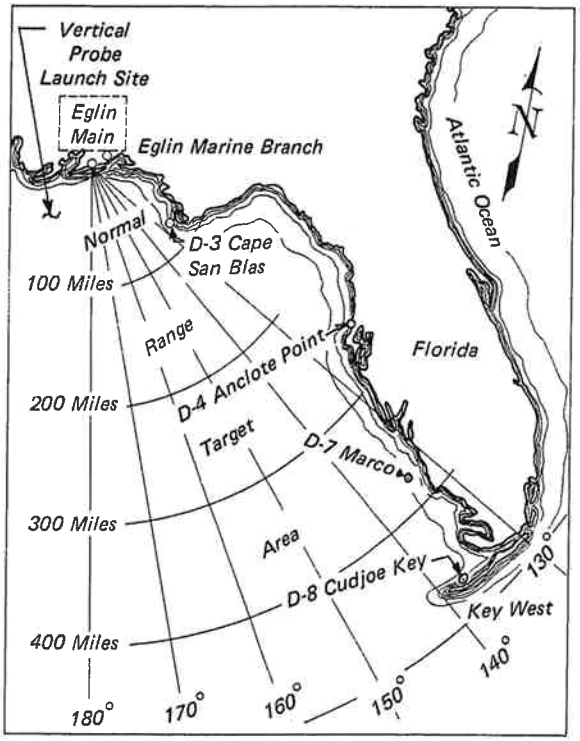


Figure 5.20 Eglin Gulf Test Range, Florida

Launchers are limited to elevation angles not in excess of 88 or 89°. Ground handling equipment is available for boosters and test vehicles. Boats provided with special hoisting gear and retrieval equipment are available. Airplanes and helicopters are also maintained for search operations.

Services provided by the base include trained explosive handling personnel, trained boat crews, skin divers and Navy deep sea divers when necessary. Optical and photographic data are acquired by real time coordinated cinetheodolites, tracking telescopic motion picture cameras and ballistic cameras. Other time based data are obtained with radars, and telemetry. Boats and aircraft are equipped with radio search receivers.

Range safety requirements permit omission of a destruct system if safe impacts can be predicted to a minimum of 3-sigma dispersion. Average yearly test cancellations are approximately 10 percent at the Eglin range due to weather.

National Parachute Test Range. This range is located directly west and northwest of El Centro, California. The range area includes two desert drop zones and one water drop zone at the Salton Sea as shown by Figure 5.21. The principal function of this range is the development of parachutes, other aerodynamic deceleration devices and related recovery components

through the use of air launch and gravity drop testing techniques. Total scope includes human escape methods, aerial speed retardation, landing of personnel, materiel and equipment, i.e., all aspects of recovery, rescue and survival for all branches of the military services and NASA.

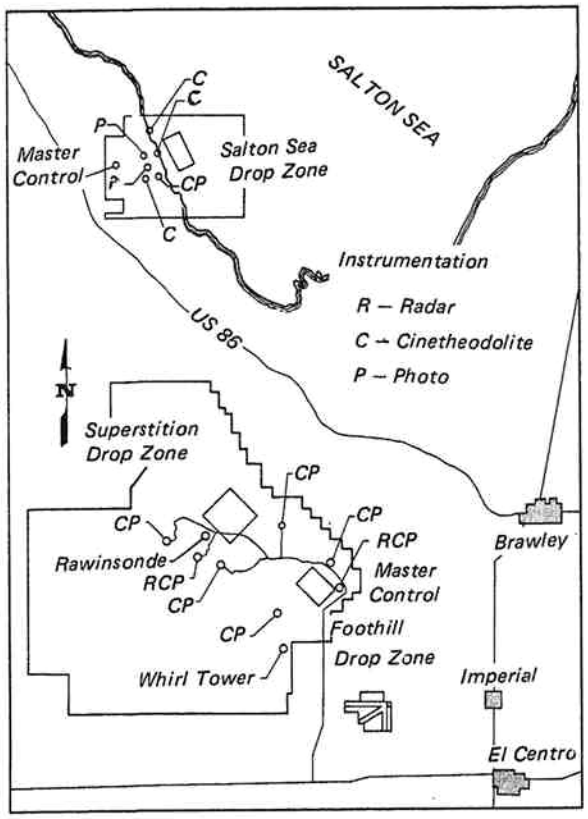


Figure 5.21 National Parachute Test Range, California

Facilities are provided for preparation and aircraft launch of test decelerators over desert or sea drop zones. Rocket-launch and explosive handling facilities are not available at this base. Ground handling equipment, search airplanes and helicopters are available. The whirl tower test facility described on page 202 and a textile materials testing laboratory are located on this base.

Services provided by the base include parachute handling, retrieval, cleaning, drying, repair, modification and packing. Optical and photographic data are acquired by time coordinated cinetheodolites, and tracking telescopic motion picture cameras. Other data are obtained with tracking radar telemetry. Photo processing and limited data reduction can be provided.

The materials laboratory is equipped with a full line of textile testing machines including 5,000-lbs, 20,000-lbs and 125,000-lbs capacity machines. The 125,000-lbs machine is designed for testing webbing and has the travel capacity for high elongation materials. Other equipment includes an Instron tensile tester, Elmendorf tear tester, Shiefer abrasion tester, air permeability testers, weatherometer and altitude-temperature-humidity chambers.

Tonopah Test Range. This range is 624 miles in area located approximately 170 miles northwest of Las Vegas, Nevada. It is operated for the U.S. Defense Nuclear Authority (DNA) by Sandia Laboratories. The range provides non-nuclear test and data acquisition for weapons development and other DNA activities. Facilities are available for preparation and launch of single and multi-stage rockets as well as free-fall and related drops from subsonic and supersonic aircraft. [336]

Optical and photographic coverage are provided by means of cinetheodolites and tracking telescopes. Further support in data acquisition is obtained with radar tracking and telemetry systems. Facilities and services are available to other government agencies and contractors on the basis of non-interference with DNA programs.

U. S. Army Yuma Proving Ground. The facilities and main base are located 14 miles northeast of Yuma, Arizona. The principal use of the range is to support development testing of air delivery and air movable equipment, including aerial retardation and airdrop. There are three instrumented land drop zones and a water zone available. A controlled impact test facility is located adjacent to the Laguna Army Air Field as are facilities for parachute fabrication, maintenance, packing and rigging. Range instrumentation includes telemetry, radar, cinetheodolites, photography, television and laser tracking equipment which are deployed as required for each test series.

Dugway Proving Ground. Aircraft stationed at Hill Air Force Base, Utah operate over the proving ground range area in development of midair retrieval recovery systems. Crews trained in midair retrieval techniques maintain their capability by practicing intercepts on parachuted descent loads on a periodic basis. Retrieval gear equipped C-130 aircraft and HH-3 and HH-34 helicopters and crews.

TABLE 5.3 DECELERATOR TESTING, PRINCIPAL FACILITIES AND CAPABILITIES

Range	Types of Tests	Test Support Services
Air Force Flight Test Center (Edwards Air Force Base) Lancaster, California Control Agency: USAF Range Size: 5 mi x 14 mi	A/C Drops A/C Tow A/C Flight	Telemetry, Cinetheodolites, Telescopic tracking cameras, Ground-to-air movie cameras, Video recording and playback, Rawinsonde, Data reduction, Photo processing laboratory. Space positioning on test range, IRIG timing system
White Sands Missile Range (integrated) White Sands Missile Range, N.M. Control Agency: US Army Range Size: 40 mi x 100 mi Holloman Air Force Base Alamogordo, New Mexico	A/C Drops A/C Tow Balloon Launch Sled Tow Sled Launch Ground Launch	Telemetry, Cinetheodolites, Telescopic tracking cameras, Ground-to-air movie cameras, Video recording and playback, Rawinsonde, Radar tracking, Documentary movie (16mm), IRIG timing system
Eglin Gulf Test Range Eglin Air Force Base, Florida Control Agency: USAF Range Size: 200 mi x 500 mi over water.	A/C Drops A/C Tow Ground Launch	Telemetry, Cinetheodolites, Telescopic tracking Rawinsonde, Data reduction, Ground-to-air movie cameras, Photo processing laboratory, IRIG timing system
National Parachute Test Range (integrated) El Centro, California Control Agency: DoD . Range Size: 6 mi x 14 mi (land); 5 mi x 10 mi (water)	A/C Drops A/C Tow Personnel Whirl Tower	Telemetry, Cinetheodolites, Telescopic tracking cameras, Ground-to-air movie cameras, Video recording and playback, Rawinsonde, Radar tracking, Laser (Range Mode), Parachute drying tower, Packing and fabrication laboratory, Data reduction, Photo laboratory, Space positioning on test range, IRIG timing system
Naval Weapons Center China Lake, California Control Agency: USN Range Size: 30 mi x 40 mi	Sled Tow Sled Launch A/C Launch Ballistics	Telemetry, Cinetheodolites, Telescopic tracking cameras, Ground-to-air movie cameras, Video recording and playback, Radar tracking, Data reduction, Photo laboratory, Space positioning on track range, IRIG timing system
Tonopah Test Range Tonopah, Nevada Control Agency: DNA Range Size: 10 mi x 25 mi	A/C Drops A/C Tow Ground Launch	Telemetry, Cinetheodolite, Telescopic tracking cameras (35mm), Video recording and playback, Rawinsonde, Radar tracking, Documentary photography (16mm)
Yuma Proving Ground Yuma, Arizona Control Agency. US Army	A/C Drops Personnel	Telemetry, Cinetheodolites, Telescopic tracking cameras, Video recording and playback, Laser tracking

Ballistic Ranges. Ballistic test facilities are used primarily for aerophysics research including the measurement of shock patterns, wake variations and aerodynamic stability characteristics of very small-scale bodies. Their use for decelerator research is quite limited but suitable for special detail information of decelerators at hyper-velocity conditions. Detail information on the capabilities and addresses of a number of ballistic ranges in the United States and foreign countries can be found in Reference 337.

High Speed Sled Tracks

Track facilities[334] are used to simulate flight trajectories under accurately programmed, closely controlled, and rigorously monitored conditions. In effect, the track can be used as a giant outdoor wind tunnel making possible many experiments not possible in conventional facilities.

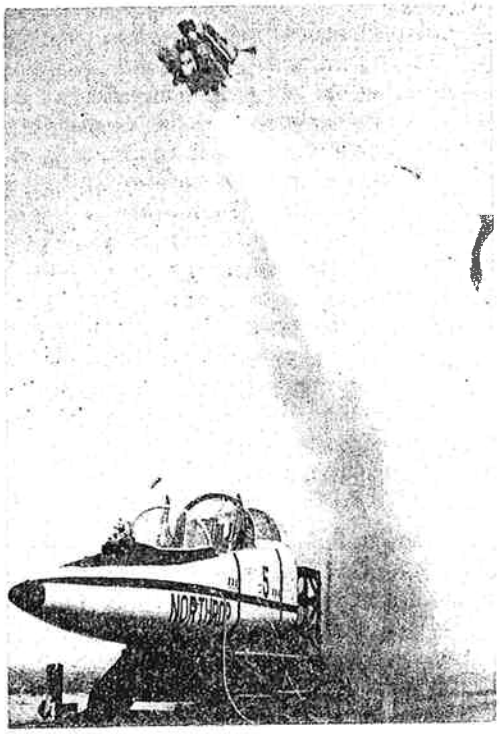


Figure 5.22 Seat Ejection Test on High Speed Test Track

Holloman High Speed Test Track. The track facility is operated by the 6585th Test Group at Holloman AFB, New Mexico. The 50,788 feet long track is the longest dual rail precisely aligned and instrumented facility of its kind. The test item and instrumentation are moved along a straight line path by rocket sleds. Sled speeds up to 7000 fps (Mach 6) are attained on a routine basis. Depending upon mission requirements payloads range from 100 pounds to 30,000 pounds. A majority of recovery oriented



Figure 5.23 High Speed Decelerator-Tow Sled

track tests have been for ejection system development, Figure 5.22, but sled vehicles suitable for towing decelerators are also available at Holloman. Figure 5.23 shows a test sled capable of Mach 3 speed and 100,000 lbs test load with the decelerator attachment point 7 feet above the rails. Other sleds good for Mach 1.5 are available with decelerator attachments 10 feet and 15 feet above the rails.

Sleds travel on a set of heavy duty crane rails spaced seven feet apart on a foundation designed to resist vertical (down) loads of 70,000 pounds per slipper on any two slippers. Water is used to decelerate and stop the test sled at the conclusion of a run. A water trough 60-inches by 14-inches is located between the rails. For every 130-inch interval over the entire length of the track, there is a holding fixture into which a frangible dam can be inserted. Water in the trough between dams is picked up by a scoop mounted on the sled to decelerate the test vehicle.

NWC Supersonic Research Tracks. Three separate test tracks are used at the Naval Weapons Center, China Lake, California[559]. They differ essentially in their length, weight capability, precision of alignment, degree of instrumentation and method of sled braking.

The major portion of test work is carried out on the Supersonic Naval Ordnance Research Track (SNORT), but the B-4 transonic and G-4 terminal and

ballistics test tracks and special purpose areas, provide a high degree of diversification.

Sandia Track. The test track is located at Kirtland Air Force Base, Albuquerque, New Mexico. The 5000 feet long, dual rail 22-inch gauge track is operated by Sandia Laboratories for the Air Force Special Weapons Center and is available for use on other government programs on a non-interference basis. Maximum test velocity, where the sled is stopped at the track end by water brake, is approximately 4000 feet per second. An upward 2-degree ramp in the last 300 feet of track permits a velocity up to 6000 feet per second to be attained with the sled leaving the end of the track. Laser controlled tracking gives well centered high speed motion picture coverage of the test item and provides accurate space position, velocity and acceleration data within a few minutes after the test. High speed strip cameras, placed along the track give excellent sequence coverage of test article motion and behavior. In addition to tow testing, vehicles weighing up to 2200 lbs may be ejected upward from the sled to obtain free flight data.

SMART Track, Hurricane Mesa, Utah. A dual track of 12,000 feet long is located atop Hurricane Mesa, Utah. The track which is operated for the USAF by Stanley Aviation Company can be used to eject vehicles such as ejection seats and escape capsules over a 3000 foot cliff. A water brake is available. However, to achieve maximum test velocities, the sled also goes over the cliff and is recovered by parachute.

Wind Tunnels

An inventory[560] of aeronautical ground research facilities includes a long list of wind tunnels suitable for aerodynamic decelerator testing. Table 5.4 lists subsonic tunnels and Table 5.5 lists transonic and supersonic tunnels that are representative and have been useful in parachute and decelerator development. The first two tunnels in Table 5.4 are of the vertical flow type. All others are horizontal, closed circuit, continuous flow tunnels. Although the tables list only government owned tunnel facilities, there are a number of industrial and institutional wind tunnels available [560] that can provide conditions for decelerator research and development testing.

Low Speed Air Flow Test Facilities. Parachute characteristics of drag, stability, inflated shape and lift to drag ratio under steady state conditions (and infinite mass load) can be studied with accurate results in subsonic wind tunnels. The deployment process, in which drag and shape grow rapidly, has also been studied, but with limited useful data obtained. Best utility of subsonic wind tunnels appears to be for investigation of characteristics related to specific needs, to be followed eventually by free-flight tests for verification. Large scale models provide data which agree more closely with final performance. Therefore large area tunnels are especially desirable for parachute testing. Subsonic tunnel facilities are described in the following paragraphs.

AFFDL Vertical Wind Tunnel. This facility, located at Wright-Patterson AFB, Ohio, is a vertical, atmospheric, annular return, continuous flow type wind tunnel with a 12-foot free jet. The air is drawn up through the 12-foot long test section by a four bladed fan, 16-feet in diameter. The tunnel is powered by a variable rpm 1000 hp main drive.

The wind tunnel is used to determine the drag and stability characteristics of parachutes, rotary type decelerators and primary vehicles with and without augmenting drag devices, and to investigate the spin and recovery characteristics of flight vehicles. The tunnel is equipped with a gauss ring to magnetically actuate spin-recovery control surface deflections on the model. A sting balance, capable of six-component measurements, is available which may be affixed to a support structure downstream of the nozzle. The support structure can provide remote control of the sting in pitch, roll and yaw. Motion picture and still photographic coverage of tests are available. A twelve channel analog to digital data acquisition system is used to record model force and moment data, model positioning and airspeed in the test section. Data reduction is accomplished off site.

NASA Langley Spin Tunnel. This facility, located at Hampton, Virginia, is a free-spin tunnel with a closed throat and an annular return passage. The vertical test section has 12 sides and is 20 feet across the flats by 25 feet high. The test medium is air. The turbulence factor is 2. Tunnel speed is variable from 0 to 90 fps with accelerations to 15 ft/sec^2. This facility is powered by a 1300 hp main drive.

The tunnel is used to investigate spin characteristics of dynamically scaled models. A gauss ring surrounding the test section is used to actuate spin-recovery control settings. Force and moment testing is performed using a gooseneck rotary arm model support which permits angles of attack and sideslip from 0 to 360° to be set. Data recording consists of motion pictures.

NASA Ames 40-Foot by 80-Foot Subsonic Wind Tunnel. This facilitiy, located at Moffett Field, California, is a large, subsonic, closed circuit, single return,

TABLE 5.4 SUBSONIC WIND TUNNELS

Facility Name Organization Location	Type of Facility Type of Throat	Test Section Size (ft)	Mach Range	Reynolds Number (10^6/ft)	Total Temp (°R)	Dynamic Pressure (psf)
AFFDL Vertical Wind Tunnel Wright-Patterson AFB, Ohio	Annular return, continuous flow, open throat	12 dia. x 12	0 to .14	0 to .91	Ambient	0 to 26
NASA Langley Spin Tunnel Hampton, Virginia	Annular return, continuous flow, closed throat	25 x 20	0 to .08	0 to .62	Ambient	0 to 10
NASA Ames 40-foot by 80-foot Subsonic Wind Tunnel Moffett Field, Calif.	Closed circuit, single return, continuous flow, closed throat	40 x 80	0 to .3	0 to .21	Ambient to 600	0 to 138
NASA Langley Full Scale Tunnel Hampton, Virginia	Closed circuit, double return, continuous flow, open throat	30 x 60 x 56	0 to .14	0 to 1.0	Ambient	0 to 30
NASA Langley V/STOL Transition Research Wind Tunnel Hampton, Virginia	Closed circuit, single return, continuous flow, closed throat	14.5 x 21.75 x 50	0 to .32	0 to .55	Ambient	0 to 135
NASA Ames 7-foot by 10-foot Subsonic Wind Tunnel Moffett Field, Calif.	Closed circuit, single return, continuous flow, closed throat	7 x 10 x 15	0 to .33	.0 to .23	Ambient	0 to 210
NASA Langley High Speed 7-foot by 10-foot Tunnel Hampton, Virginia	Closed circuit single return, continuous flow, closed throat	6.6 x 9.6 x 10	.2 to .9	.1 to 3.2	490 to 620	200 to 750
NASA Ames 12-foot Pressure Tunnel Moffett Field, Calif.	Closed circuit, single return, variable density, closed throat	11.3 dia. x 18	0 to .98	0 to 9.0	500 to 625	50 to 600

atmospheric wind tunnel. The test section is 40 by 80 feet. The tunnel has a contraction ratio of 8 to 1. The air is driven by six 40-foot-diameter fans, each powered by a 6000-horsepower electric motor. The speed of the airflow through the test section is continuously variable from zero to the maximum.

The tunnel is used primarily for testing the low speed characteristics of high-performance aircraft and spacecraft, and for testing V/STOL aircraft and rotorcraft. This facility has been found to be particularly useful for research and development testing of large scale gliding parachutes. A conventional support-strut system and a set of variable-height struts are available for studying the effects of ground proximity. Data are recorded on: Tunnel scale system (digital) 10 channels, Auxiliary data (digital) 480 channels, Analog tape 14 channels and reduced site with cards read into computer.

NASA Langley Full-Scale Tunnel. This facility, located at Hampton, Virginia, is a continuous flow, double return, open throat type tunnel. The test section is 30 feet by 60 feet by 56 feet. Airspeed range is from 25 to 110 mph in 24 steps. A separate speed control is available permitting a continuous airspeed variation from 0 to approximately 40 mph. This facility is powered by an 8000 hp main drive.

The tunnel is equipped for free-flight dynamic model studies, and shielded struts are available for model support. A reflection plane floor 42 feet wide and 32 feet long can be installed for full scale semispan wing investigations. Data are recorded with 60 channels on a data acquisition system and reduced off site. This facility can accomodate models up to 40 foot wing span and weighing 15,000 pounds.

NASA Langley V/STOL Transition Research Wind Tunnel. This is a closed circuit, single return, continuous flow atmospheric type V/STOL tunnel. The test section is 14.5 feet high by 21.75 feet wide by 50 feet long, which can be operated as a closed tunnel with slotted walls or as one or more open configurations by removing the side walls and ceiling. The speed is variable from 0 to 200 knots. This tunnel has a contraction ratio of 9 to 1. The facility is powered by an 8000 hp main drive.

This tunnel is capable of force, moment and pressure studies of full span and semispan powered and unpowered V/STOL, parawing and ground transport models. A moving belt ground board with boundary layer suction and variable speed capabilities for operation at test section flow velocities can be installed for ground effects tests. A universal model support system utilizes a three joint rotary sting with ±45° of pitch, ±45° of yaw and a point of vertical traverse. This system is mounted on horizontal turntable with ±165° of rotation. Data are recorded with 60 channels and reduced off site.

NASA Ames 7-Foot by 10-Foot Subsonic Wind Tunnel. This tunnel is a closed circuit, single return, atmospheric facility powered by a variable speed, 1800 hp motor which drives a fixed pitch fan. The tunnel has a rectangular test section 7 feet high, 10 feet wide and 15 feet long and a contraction ratio of 14.14 to 1.

The tunnel is capable of most aerodynamic type tests, 2-D airfoils, jet flap models and V/STOL models with scaled propulsion units. This tunnel can accommodate two-dimensional models spanning the tunnel height with supports at both floor and ceiling and three-dimensional models which can be supported by one vertical strut. Continuous angle of attack variation from 0° to ± 180° is available. Data are recorded on tapes, mechanically printed (6 channels), and the cards are then read into a computer at the computing center.

NASA Langley High Speed 7-Foot by 10-Foot Tunnel. This is a closed circuit, single return, continuous flow, atmospheric type tunnel. The test section is 6.6 feet wide by 9.6 feet high by 10 feet long. The tunnel is cooled by an air exchange system which introduces filtered atmospheric air into the diffuser a short distance downstream from the test section. A series of four turbulence damping screens of 16-mesh wire is installed in the settling chamber. This facility is powered by a 14,000 hp main drive.

The facility is used for static and dynamic studies of the aerodynamic characteristics of aircraft and spacecraft. Model mounting consists of sting support system, forced oscillation apparatus, and sidewall turntable. Only a limited amount of dynamic data instrumentation is available. Closed circuit television is available for monitoring tests.

NASA Ames 12-Foot Pressure Tunnel. This is a closed circuit, continuous flow, single return, variable density, low turbulence tunnel that operates at subsonic speeds up to slightly less than Mach 1.0. The wind tunnel is powered by a two-state, axial-flow fan driven by electric motors totaling 12,000 horsepower. Airspeed in the test section is controlled by variation of the rotational speed of the fan. The test section is 11.3 feet in diameter and is 18-feet long. Eight fine-mesh screens in the settling chamber, together with the large contraction ratio of 25 to 1, provide an airstream of exceptionally low turbulence.

The facility is used for testing force and moment, pressure, and dynamic stability. This tunnel is well suited for research on missile ground-wind loads. An external balance and internal strain-gage balances are

available. Ground plane and semispan mounting are available with turntable movement of ±20°. A special mounting drive system is available for high angle of attack. There are no facilities for schlieren or shadowgraph flow visualization, but motion pictures of the test may be taken. Data are recorded on a Beckman 210 medium speed recorder and processed through a centrally located Honeywell H-800 computer system.

High Speed Air Flow Test Facilities. Decelerators which deploy and operate at supersonic speeds are usually drogue units followed by larger staged parachutes which operate subsonically, or those that deploy and operate supersonically in low density atmosphere. Tunnel facilities are available with variable density and controlled temperature air. Transonic, supersonic and hypersonic tunnels are available as Air Force facilities at the Arnold Engineering Development Center, Tennessee. Reference **561** provides more extensive information relative to the capability and use of AEDC facilities.

AEDC PWT 16 Foot Transonic and Supersonic Tunnels. The PWT 16-ft Transonic Tunnel (Propulsion Wind Tunnel, Transonic (16T)) is a continuous-flow closed-circuit tunnel capable of operation within a Mach number range of 0.20 to 1.60. The tunnel can be operated within a stagnation pressure range of 120 to 4000 psfa depending upon the Mach number. The stagnation temperature can be varied from an average minimum of about 80 to a maximum of 160°F as a function of cooling water temperature. Using a special cooling system of mineral spirits, liquid nitrogen, and liquid air, the stagnation temperature range can be varied from +30 to -30°F.

The PWT 16-ft supersonic tunnel (Propulsion Wind Tunnel, Supersonic (16S)) is a continuous flow closed circuit tunnel designed to operate within a Mach number range of 1.5 to 6.0. The 16S has been operated at Mach numbers from 1.50 to 4.75. Mach numbers above 3.4 require operation of the main drive and PES compressors in series. The plant configuration changes required for this series operation must be made with the tunnel operating and use a significant amount of test time to accomplish. Test programs that require Mach numbers greater than 3.4 should anticipate the change in productivity that accompanies such operation.

The testing of large-scale aerodynamic models and full-scale air-breathing or rocket propulsion systems is possible in Tunnel 16T at Mach numbers from 0.20 to 1.60 and at altitudes from sea level to about 90,000 ft and in Tunnel 16S at Mach numbers from 1.50 to 4.75 at altitudes from about 50,000 to approximately 150,000 ft. (Tunnel 16S is temporarily limited to maximum of $M = 2.4$ and about 110,000 ft.)

The ability to control Mach number, altitude and temperature independently makes it possible to conduct aerodynamic and propulsion investigations under conditions closely approximating those of free flight.

Because of their large size, the PWT 16-ft tunnels are quite adaptable to the testing of many full-scale decelerator devices. Parachutes or decelerators up to about five feet in diameter can be deployed without any appreciable change in tunnel conditions. Larger parachutes can be tested; however, the available ranges of tunnel parameters may be compromised.

AEDC, Von Karman Facility Supersonic Wind Tunnel A. Tunnel A is a 40 by 40-in., continuous closed-circuit, variable density, supersonic wind tunnel with a Mach number range of 1.5 to 6.

The tunnel is served by the main compressor system which provides a wide range of mass flows and stagnation pressures up to a maximum of 200 psia. Incorporation of the high-pressure reservoir and vacuum sphere provides rapid changes of pressure level required for different test points, thus permitting maximum tunnel utilization.

The primary model support is housed in a tank directly underneath the test section. The model support is injected into the test section and translated upstream to the test area. Upon concluding the test, the model support is retracted in a similar manner. The tank is sealed from the test section and vented to atmosphere while the tunnel is running to allow access to the model and model support. After the desired model change or modification, the tank is vented to the test section, the doors separating the tank and test section are opened, and the model is injected into the airstream and translated forward to the test position. The minimum time required for injecting the model is 8 sec. and translating forward 8 sec. for a total time of 16 sec. Time required for retracting is approximately the same.

Models are generally supported from the rear by stings which attach to the roll sting hub, or adapter hub, mounted on top of the single-ended support strut. The support system will accommodate a vertical load of 3500 lb or a horizontal load of 1500 lb applied at the nominal model center of rotation and a maximum resultant force of 3800 lb.

Models may be tested in free flight to obtain drag, damping, pitching-moment rate, and base pressure data that are free of interference sometimes present because of the model support system. To achieve free flight, models are launched upstream in the test section with a pneumatic launcher. The launcher may be retracted into the test section tank for reload-

ing and launching models while the tunnel is running continuously. The test model size is somewhat unrestricted; however, typical models are on the order of 6 to 10 inch in length. Models weighing up to 2.5 lb may be launched at velocities up to 100 ft/sec.

NASA Langley 16-Foot Transonic Tunnel. This is a closed circuit, single return, continuous flow, atmospheric tunnel. Speeds up to Mach 1.05 are obtained with a combination of main drive and test-section plenum suction. The slotted octagonal test section nominally measures 15.5 feet across the flats. The test section length is 22 feet for speeds up to Mach 1.0 and 8 feet for speeds above Mach 1.0. The tunnel is equipped with an air exchanger with adjustable intake and exit vanes to provide some temperature control. This facility has a main drive of 60,000 hp. A 36,000 hp compressor provides test section plenum suction.

The tunnel is used for force, moment, pressure, and propulsion-air-frame integration studies. Model mounting consists of sting, sting-strut, and fixed strut arrangements. Propulsion simulation studies can be made for hot jet exhaust utilizing decomposition of hydrogen peroxide or using dry, cold, high pressure air. The high pressure (15 lb/sec at 1000 psi) air system and model mounting apparatus is compatible with identical systems in the Langley 4 by 4-foot supersonic pressure tunnel and ground test stand. A shadowgraph system is available for flow visualization. Data are recorded with 99 channels on a Beckman 210 and reduced off-site with a CDC 6600 computer system.

NASA Ames 14-Foot Transonic Wind Tunnel. This tunnel was created by extensive modification of the former 16-foot diameter high speed tunnel. It is a closed circuit, single return, continuous flow, atmospheric type tunnel. The test section is slotted and is 13.5 feet by 13.9 feet by 33.75 feet. The nozzle has adjustable, flexible walls. Air temperature in the tunnel is controlled by an air exchanger. The tunnel air is driven by a three-stage, axial-flow compressor powered by three electric motors mounted in tandem outside the wind tunnel. The drive system is rated 110,000 horsepower continuously or 132,000 horsepower for one hour. The speed of the motors is continuously variable over the operating range.

For conventional, steady-state tests, models are generally supported on a sting. Internal strain gage balances are used for measuring forces and moments. Facilities for measuring multiple steady or rapidly fluctuating pressure are available. For tests involving aerostructural dynamics, model shakers with hydraulic power supply and appropriate readout facilities are available. A schlieren system for flow visualization is available, but vibration generally precludes fine definition. Data are recorded on a Beckman 210 medium speed recorder and processed through a centrally located Honeywell H-800 computer system.

NASA Ames 11-Foot Transonic Tunnel (unitary). This tunnel is the transonic leg of the Ames Unitary facility. It is a closed circuit, single return, continuous flow, variable-density tunnel. The 11 by 11 by 22 foot test section is slotted to permit transonic testing. The nozzle has adjustable sidewalls. The tunnel air is driven by a three-stage axial flow compressor powered by four wound-motor induction motors. The speed of the motors is varied as necessary to provide the desired Mach number. The motors have a combined output of 180,000 horsepower for continuous operation or 216,000 horsepower for one hour. Tunnel temperature is controlled by after-coolers and a cooling tower. Four 300,000 cubic foot storage tanks provide dry air for tunnel pressurization.

The tunnel is used for force and moment, pressure, internal air-flow-inlet, and dynamic stability tests. A traversing strut which supports the sting body is mounted vertically downstream from the test section. Internal, strain-gage balances are used for measuring forces and moments. Facilities for measuring multiple steady or fluctuating pressure are available. A schlieren system is available for the study of flow patterns by direct viewing or photographing. Also, a system for obtaining 20 by 40-inch photographic shadowgraph negatives is available. Data are recorded on a Beckman 210 medium speed recorder and processed through a centrally located Honeywell H-800 computer system.

TABLE 5.5 TRANSONIC, SUPERSONIC AND HYPERSONIC WIND TUNNELS

Facility Name Organization Location	Type of Facility Type of Throat	Test Section Size (ft)	Mach Range	Reynolds Number (10^6/ft)	Total Temp (°R)	Dynamic Pressure (psf)
AEDC 16-foot Transonic Propulsion Wind Tunnel Arnold AFS, Tennessee	Closed circuit, single return, variable density, continuous flow	16 x 16 x 40	.2 to 1.6	.1 to 7.5	410 to 620	3.3 to 1300
NASA Langley 16-foot Transonic Tunnel Hampton, Virginia	Closed circuit, single return, atmospheric, continuous flow	15.5 octag. x 22	.2 to 1.3	1.2 to 3.7	510 to 640	57 to 905
NASA Ames 14-foot Transonic Wind Tunnel Moffett Field, Calif.	Closed circuit, single return, atmospheric, continuous flow	13.5 x 13.9 x 33.75	.6 to 1.2	2.8 to 5.2	500 to 640	425 to 885
NASA Ames 11-foot Transonic Wind Tunnel (Unitary) Moffett Field, Calif.	Closed circuit, single return, variable density, continuous flow	11 x 11 x 22	.5 to 1.4	1.7 to 9.4	540 to 610	150 to 2000
AEDC 16-foot Supersonic Propulsion Wind Tunnel Arnold AFS, Tennessee	Closed circuit, single return, variable density, continuous flow	16 x 16 x 40	1.5 to 4.75	.1 to 2.6	560 to 1110	30 to 570
NASA Ames 8-foot by 7-foot Tunnel Supersonic (Unitary) Moffett Field, Calif.	Closed circuit, single return, variable density, continuous flow	8 x 7 x 16	2.4 to 3.5	.5 to 5.0	580 to	200 to 1000
AEDC, VKF Supersonic Wind Tunnel (A) Arnold AFS, Tennessee	Closed circuit, variable density, continuous flow	3.33 x 3.33 x 7	1.5 to 6.0	.3 to 9.2	530 to 750	49 to 1800
AEDC, VKF Hypersonic Wind Tunnel (B) Arnold AFS, Tennessee	Closed circuit, recycling, variable density, continuous flow	4.33 dia.	6 and 8	.3 to 4.7	850 to 1350	43 to 590

TEST VEHICLES

In a free flight test of a recovery system, the test vehicle represents the mass on which ejection, air drag and decelerator forces act to retard and control its descent to a landing. The test vehicle also serves as a carrier for instruments to acquire data of decelerator performance and vehicle-decelerator-environment interaction. This section describes various types of test vehicles. Successful recovery of the test vehicles may be a requirement of the test cycle, where a portion of the data are acquired by on-board photographic cameras or other self contained measuring instruments.

Flight Test Vehicles

Several standardized vehicles are used for decelerator testing, primarily those required for development of personnel and airdrop parachutes. In addition, there are various platform types, weight-bombs and cylindrical test vehicles suitable for functional airdrops of the primary decelerators of many systems. Beyond this inventory of relatively simple airdrop vehicles, the testing requirements of more complex decelerator systems and components usually can be satisfied only with vehicles designed for the purpose. In general, powered vehicles developed for individual applied research programs are seldom usable on other programs without requiring major modification.

Gravity Drop. Torso dummies and anthropomorphic dummies belong to the gravity drop class of test vehicles. Other vehicles in this class are platform types and bomb-like or similar ogive-cylinder configurations. Characteristics of standardized gravity drop test vehicles are summarized in Table 5.6. Those listed are test vehicles currently available at the National Parachute Test Range, El Centro. In the table, the value in the "maximum speed" column represents the free-fall terminal velocity (in knots equivalent air speed) of a stable test vehicle. Higher test speeds may be possible for bomb-rack launched test vehicles depending upon the speed capability of the carrying aircraft and the interval from launch to deployment.

Dummies and Weight-Bombs. In all tests where the dimensions, mass and mechanical properties of the human form are relevant, such as ejection seats or other escape systems, an instrumented articulated anthropomorphic dummy is a test substitute for a live subject. The torso type dummy is adequate as a vehicle of proper mass adapted for personnel parachute testing along with attached container and body harness.

Various weight bombs are commonly used with minimal instrumentation to perform functional drop tests of large parachutes. Weight-bomb test vehicles are made from standard bomb casings ranging in size form the 500-lb general purpose bomb to the 4000-lb light case bomb. Casings have been modified by welding a flat steel plate to the bottom surface to distribute the floor bearing loads and facilitate handling of the test vehicle. A parachute adapter plate, attached to the end of the bomb casing is designed to take maximum allowable forces indicated in Table 5.6. This class of test vehicle provides a weight range from 200 to 10,000 pounds. There are no parachute compartments in the test vehicle. The parachute pack is mounted on the bomb as shown in Figure 5.24. The usual carrying aircraft is a cargo type with a rear door, the C-130 being utilized most extensively.

Test Platforms. The weighted steel "tub" is a platform type test vehicle used primarily for development of aerial delivery parachutes and systems. Five sizes of steel tubs are available. Platform weight can be ballasted to the required load by adding steel bars which fit inside the tub transversely and are anchored in place. Suspension lugs at corners and at platform midlength provide six attachment points for suspension harness members. A schematic of a typical air-drop test platform and rigging are shown in Figure 5.25. The platform assembly includes paper honeycomb between the weighted steel tub and the load-bearing platform at the bottom. Adequate tie-down rings are provided along both sides, and all corners are rounded to prevent damage to textile members. A unique feature of the cargo extraction recovery system is the "open-link" safety device in the deployment line between the extraction system and the recovery system. The device prevents transfer of the extraction load to the parachute system unless the open link is closed, indicating the platform has left the aircraft.

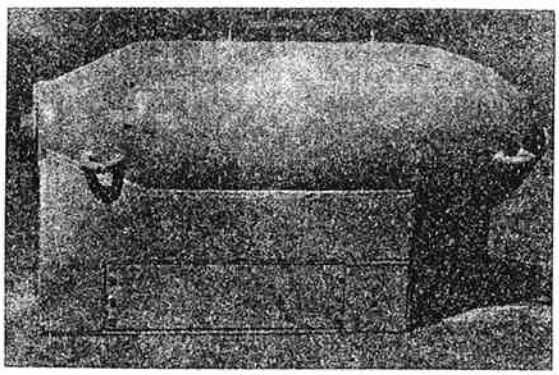
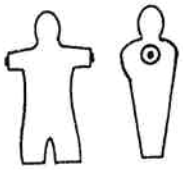
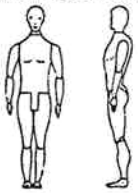
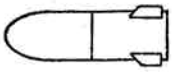
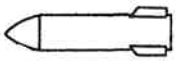
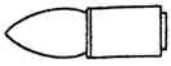
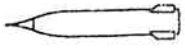
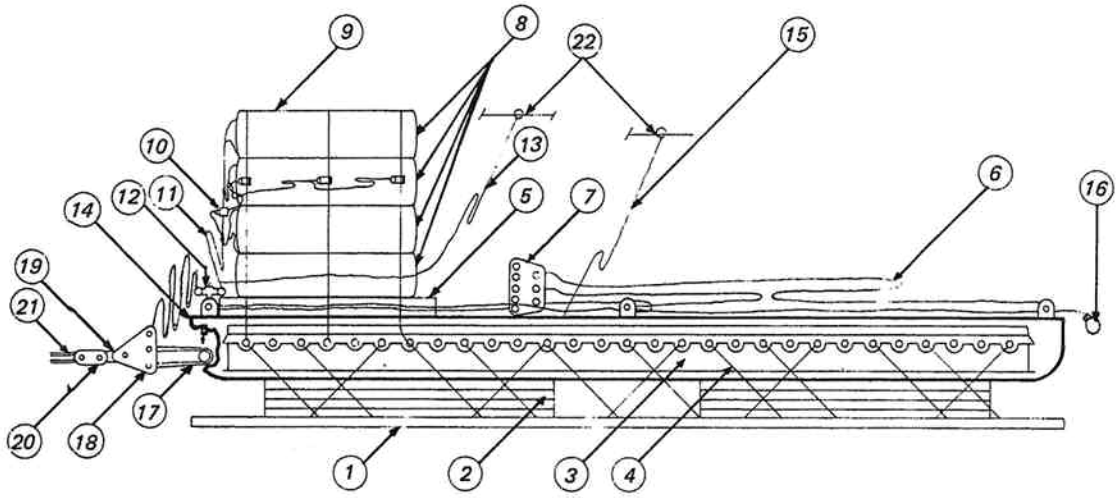


Figure 5.24 Weight-Bomb Test Vehicle

TABLE 5.6 AIRDROP TEST VEHICLES

Type Test Vehicle	Basic Structure	Dimensions (inches)	Min. Wt. (lbs)	Max. Wt. (lbs)	Max. Load (g's)	Max. Speed (knots)	Parachute Compartment (cu. ft.)
Torso Dummy 	Rubber steel reinf.	36 x 18 x 16	132	206	100	220	None
Anthropomorphic 	Rubber steel reinf.	68 x 18 x 16	132	206	80	210	None
Weight-Bomb 	GP 500	52 x 14 dia.	200	1,000	15	340	None
	GP 1000	67 x 18½ dia.	500	3,000	10	380	None
	LC 4000	100 x 35 dia.	4,000	10,000	5	480	None
Platform (welded steel) 	6-Ft Tub	72 x 48 x 12	1,500	3,000	10	290	None
	8-Ft Tub	96 x 90 x 24	3,500	10,000	10	410	None
	12-Ft Tub	144 x 90 x 24	3,800	18,000	10	520	None
(plus honeycomb)	18½-Ft Tub	222 x 90 x 24	9,000	30,000	10	525	None
	24-Ft Tub	288 x 90 x 24	14,000	50,000	10	530	None
Cylindrical 	GP 500	120 x 14 dia.	400	1,000	20	465	3.83
	GP 1000	120 x 18½ dia.	1,000	2,400	20	545	9.32
	GP 2000	152 x 23 dia.	1,500	3,000	15	530	17.75
	LC 4000	156 x 35 dia.	3,000	9,000	10	630	60.00
	T-10	160 x 37½ dia.	12,000	25,000	7	760	60.00
Transonic 	Trans. III	175 x 24½ dia.	2,000	6,000	10	820	9.50



1 *Load-Bearing Platform*
2 *Paper Honeycomb*
3 *Weight-Test Platform*
4 *Tiedown Webbing or Chains*
5 *Parachute Tray*
6 *Suspension Risers*
7 *Suspension Block*
8 *G-11A or G-12D Cargo Recovery Parachutes*
9 *Parachute Restraint, 6000-lb Nylon Webbing with Cutter Knives*
10 *G-11A Clevis*
11 *Deployment Line*
12 *Open Link Safety Clevis*
13 *Activation Lanyard, Safety Clevis*
14 *Spring-Powered Knife Assembly*
15 *Activation Lanyard, Spring-Powered Knife Assembly*
16 *Manual Activation Lanyard Spring Powered Knife Assembly*
17 *Spring-Powered Knife Assembly Cutter Web*
18 *Four-Point Clevis*
19 *Strain Gage Link*
20 *Two or Four-Point Strain Gage Adapter Clevis*
21 *Rope Extraction Line*
22 *Aircraft Anchor Cable*

Figure 5.25 Schematic of an Airdrop Test Platform Assembly

Cylindrical Test Vehicles. Another class of test vehicle, the so-called "cylindrical" type, in the weight range from 400 to 25,000 pounds, is utilized for parachute testing in the medium-subsonic speed range. Like the weight-bomb, the cylindrical test vehicle is made by modifying bomb casings, but the vehicle length is extended with a cylindrical shell, supporting stabilizing fins and camera pods as shown in Figure 5.26. The cylindrical cavity provides space to contain the parachute pack and other desirable test components. The instrumentation which can be used in the cylindrical test-vehicle includes a choice of camera equipment, tensiometers, and telemetry equipment to sense and record opening-forces, equivalent air-speed, dynamic pressure, altitude and the time sequence of the recovery functions.

Transonic test vehicles are aerodynamically clean, high fineness ratio versions of the cylindrical type, capable of attaining speeds of Mach 1.0 or better during free-fall from aerial drop. The Transonic III was designed as a double stage parachute test vehicle capable of recovery after failure of the first stage test parachute.

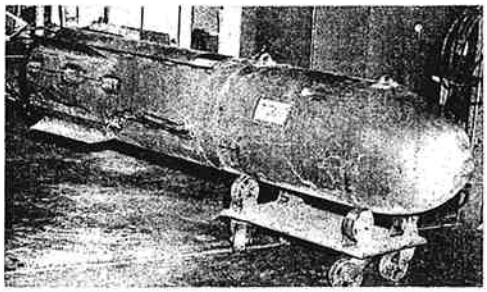


Figure 5.26 Cylindrical Test Vehicle

Boosted Test Vehicles. Free-flight testing of decelerators at speeds greater than transonic has necessitated a departure from the gravity-drop test method. Test missiles have been developed that were powered by means of solid propellant rocket motors. Test velocities over Mach 4.0 and altitudes above 200,000 feet have been reached with rocket powered test vehicles.

Track Test Vehicles

Track test vehicles are commonly referred to as "sleds" because their interface with the rails consists of steel shoes (Slippers) which are in sliding contact with the rails. Typical sled test vehicles used for parachute testing are those located at the Holloman Track; the Arrowhead, Tomahawk and Bushwhacker.

The Arrowhead Sled. The Arrowhead sled is a solid fuel rocket motor powered test vehicle specifically designed for parachute testing at high dynamic pressures. The Arrowhead sled is designated as IDS 6328 by the Holloman Track and operates either as a single stage vehicle or, with a noncaptive pusher sled, as a two-stage test vehicle. Carrying up to five Nike rocket motors on its captive PDS 6328-1 pusher sled, the Arrowhead sled is capable of developing a total of approximately 245,000 lb of thrust. In this configuration, the initial weight of 11,700 lb can be accelerated to a speed of Mach 1.89 at rocket motor burnout. Burnout weight is approximately 7,900 lb and the empty weight of the Arrowhead sled is approximately 4,100 lb. With the addition of the PDS 6328-2 first-stage noncaptive pusher sled containing five Nike rocket motors, the Arrowhead sled can be accelerated to Mach 2.55 at motor burnout. A three-view sketch giving basic overall dimensions of the Arrowhead sled is shown in Figure 5.27.

The Tomahawk Sled. The Tomahawk sled is also a solid fuel rocket powered parachute test vehicle which operates either as a single-stage or as a two-stage vehicle. It is designated as IDS 6301 by the Holloman Track. For this program, eight 2.2 KS 11,000 rocket motors, which develop approximately 90,000 lb of thrust for 2.2 seconds, were carried on the Tomahawk sled and four 2.2 KS 11,000 rocket motors were carried on the noncaptive IDS 5802-1 pusher sled. In this configuration, the initial weight of 7,800 lb can be accelerated to approximately Mach 1.3 at rocket motor burnout. The burnout weight is about 6,200 lb and the empty weight of the Tomahawk sled is about 5,300 lb. Figure 5.28 shows a three-view sketch giving basic overall dimensions of the Tomahawk sled.

The Bushwhacker Sled. The Bushwhacker sled was designed and manufactured by the 6585th Test Group, Test Track and Aeronautical Test Divisions. It replaces the Tomahawk sled and offers significant improvement in load capacity and test item size. Design and performance characteristics are as follows:

Height:	15 Feet
Length:	40 Feet
Loaded Weight:	16,000 Pounds
Empty Weight:	11,000 Pounds
Maximum Velocity:	Mach = 1.5
On Board Propulsion:	4 Nike Rocket Motors
Total On Board Thrust:	188,000 Pounds
Maximum Parachute Size:	22 Foot Diameter
Maximum Load Capacity:	200,000 Pounds
Material:	Steel and Aluminum

Figure 5.29 shows a three-view sketch giving basic overall dimensions of the Bushwhacker sled.

TEST INSTRUMENTATION

It is feasible to obtain parametric performance data during the use of test vehicles through the availability of various instrumentation methods. This section delineates these methods and associated techniques, and illustrates how the data obtained enhances the utility of test vehicles so equipped. The availability of these measurements has augmented the knowledge required to make increasingly accurate our analytic methods and resultant predictions of decelerator performance.

Test Item Instrumentation

Comparatively recent instrumentation techniques are now available for determining the magnitudes of the various physical phenomena associated with decelerators as they are operated. For instance, in the case of parachutes, it is possible to obtain measurements of important operational characteristics as the parachute deploys, the canopy fills and opens, and terminal velocity is reached and continues.

Measurement of Strain. In order to obtain information on the stress distribution in a parachute canopy, a means of measuring strain of lightweight textiles is desirable. The direct measurement of structural strain in a decelerator during inflation and steady

operation has been obtained continuously[338] with an array of miniature elastomeric strain-gages of the type illustrated in Figure 5.30. Strain can be measured with any force transducers calibrated to read strain and able to move with the stretch of a fabric or measured material.

Measurement of Pressure Distribution. Strain gage type measure transducers have been developed[339] to measure the distribution of the local pressure (internal, external and differential) over a parachute canopy during its inflation phase, during model wind tunnel tests[340] and full scale free flight tests[341].

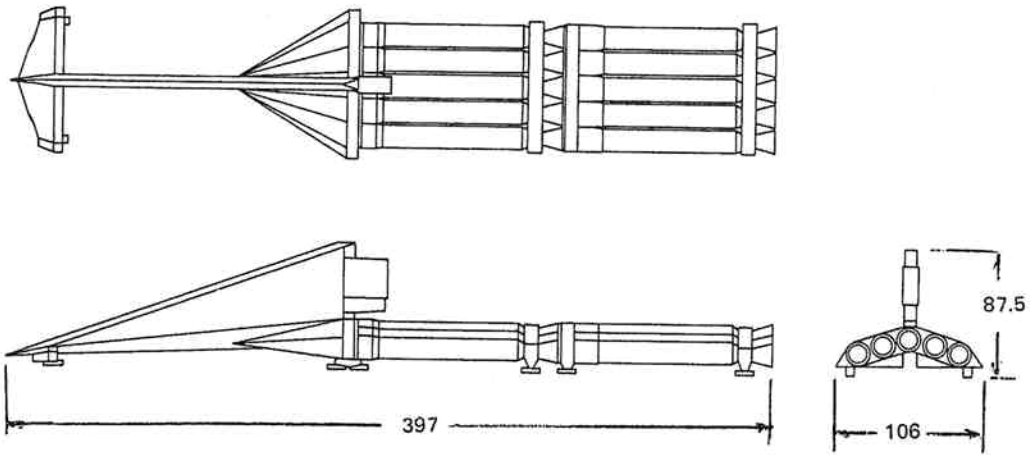


Figure 5.27 The Arrowhead Sled

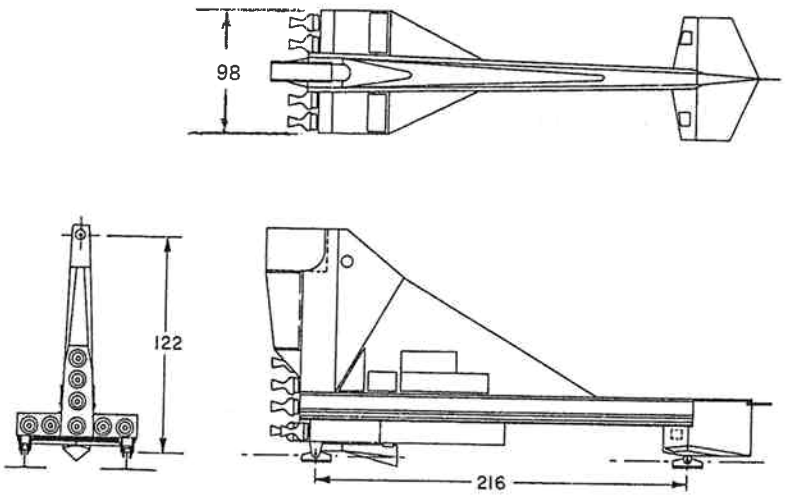


Figure 5.28 The Tomahawk Sled

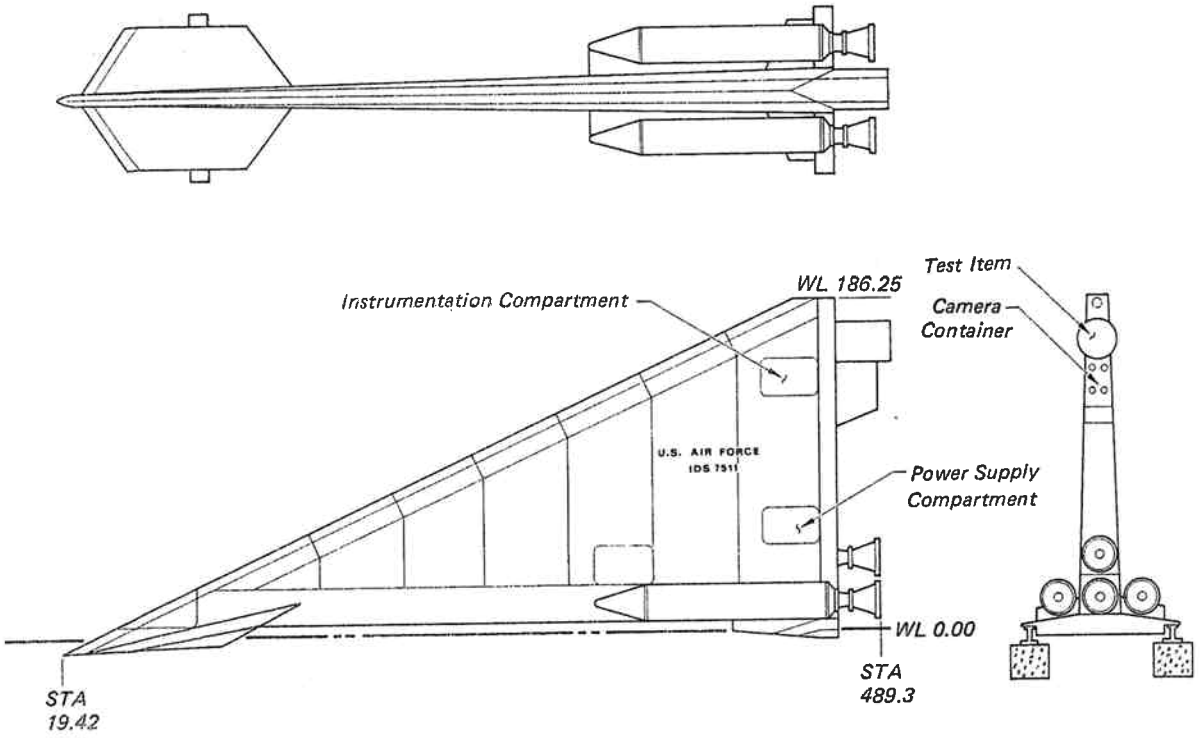


Figure 5.29 The Bushwhacker Sled

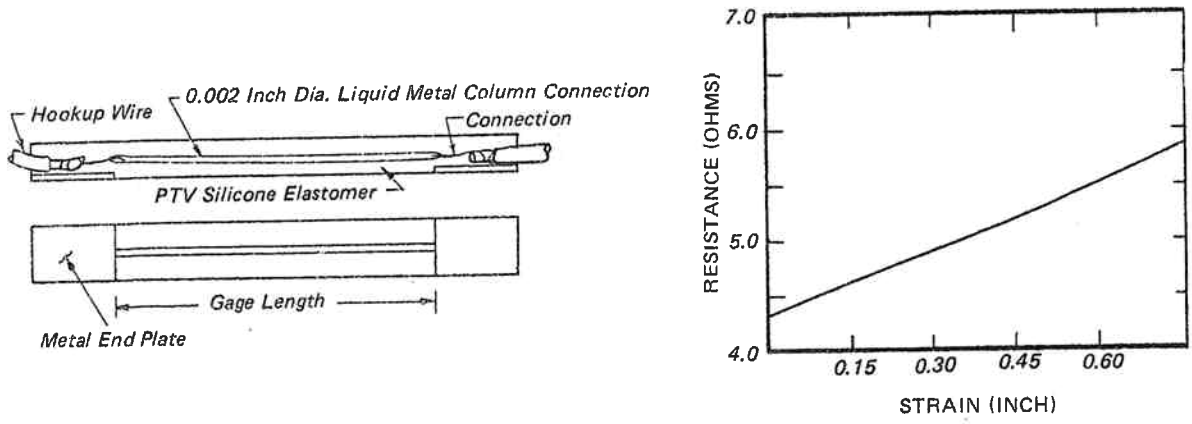
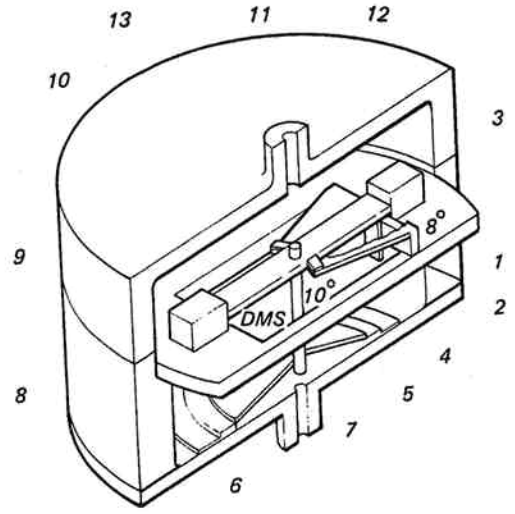


Figure 5.30 Details and Calibration of Elastomeric Strain Gauge



1, *Central part of housing*
2. *Upper part of housing*
3. *Housing cover*
4. *Artificial material*
5, 6, 7. *Assembled aluminum membrane*
8. *Frame*
9. *Bonding element struts*
10. *Bonding element*
11. *Struts against horizontal movement*
12. *Compensation weights*
13. *Connection between membrane and bonding element*

Figure 5.31. Differential Pressure Transducer with Compensation for Linear Acceleration

Figure 5.31 is a perspective view of the entire transducer. A beam (bending element) on two bearings is centrally connected by a thin steel wire to an aluminum-membrane. This membrane is softly stretched by means of a foil of artificial material (a Hostaphan-foil has proven to be convenient) in a frame. The strain gages are bonded to the bending element as near as possible to the point of the highest bending moment, which is the center of the bending element. By optimization of the size of the membrane and the dimensions of the bending element the high sensitivity required together with a high natural frequency was achieved. To have no influences on the output signal resulting merely from the pressure acting on the membrane, the mass acceleration forces of the membrane and of the bending element itself were to be compensated for. This was achieved by projecting the bending element beyond the two bearings and by attaching small weights to the projecting ends. In this manner an acceleration acting on the transducer is compensated for because the moments due to the mass acceleration forces on the membrane and on the bending element are balanced by the moments developed due to the forces acting on the additional masses (weights) mounted on the ends of the bending element. Exact adjustment can be obtained by means of a centrifuge. At a linear acceleration of 200 g the additional weights will be changed until there is no measured bending of the bending element [1]. The characteristics of the transducer are listed below:

Differential pressure range:	±20 mbar
Excitation (bridge supply voltage):	5 V (current: 40 mA)
Internal resistance:	120 Ω
Natural frequency:	300 Hz
Weight.	9 g
Diameter:	30 mm
Height:	8 mm

Measurement of Temperature. Temperature measurements are obtained with instruments employing either electric thermocouples or thermistors as the sensing elements. A bi-metal thermocouple emits an easily calibrated voltage, proportional to the temperature differential between the "hot" and "cold" junctions. A typical calibration for an iron/constantan thermocouple is 30°F per millivolt in the range from 0 to 800°F. Chromel/constantan thermocouples are available and used over a range from -100 to 1500°F. Chromel/alumel thermocouples are available over a range from 0 to 2000°F.

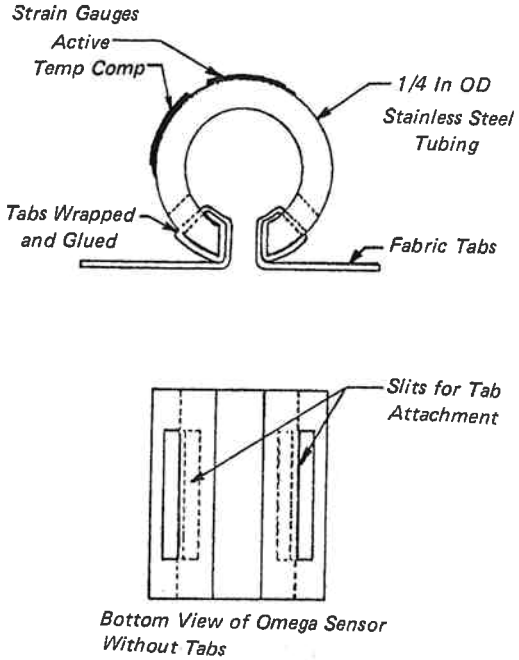


Figure 5.32 Omega Stress Transducer

Measurement of Stress. A miniature "Omega" stress transducer[342,343] designed for measuring parachute canopy internal loads is illustrated in Figure 5.32. Its design is based on the fact that a curved beam experiences very high stresses and deformation when exposed to bending. Such a curved beam can be obtained by cutting a slit in a short section of a tube made out of an elastic material. A strain gage suitably bonded to this beam can be used to register deformation of the beam.

In order to prevent the gore curvature from influencing the beam deformation, the curved beam has to be fastened to the canopy cloth by means of hinged links or flexible tabs.

Test Vehicle Instrumentation

Instruments mounted on or within the recovery test vehicle, are used to measure loads, acceleration, angular motion, rotational rates and signals for the deployment process. In addition it is frequently necessary to correlate these measured data with photographic evidence of such events as door openings, parachute deployment and inflation, relative motion of decelerator and vehicle, and a number of other features depending upon the type of recovery system undergoing test. Instruments on the test vehicle have also been used for backup of range instrumentation data.

Prospective users should contact the selected test range to coordinate instrumentation requirements, equipment, procedures and data processing. The experience and equipment available at these ranges should lead to good instrumentation coverage with fast response and the most economical method suitable for obtaining test results.

Telemetry. The remote terminal of a telemetry system consists of a signal coder, multiplexing unit, amplifier, power supply, antenna system and various sensing and measuring end instruments known as transducers. In FM telemetry systems, the physical quantity to be measured is converted by a transducer to an equivalent electrical signal. The signal is used to frequency-modulate a subcarrier oscillator in one of the standard subcarrier bands. The outputs of the subcarrier oscillators are mixed and used to frequency-modulate the transmitter.

Subcarrier Oscillators. Four general classifications of subcarrier oscillators are voltage-controlled, resistance bridge, inductance-controlled and saturable reactive. Each type is used for a specific purpose and, in general, the four are not interchangeable.

Voltage-controlled oscillators are widely used to measure a-c or d-c voltages. These voltages may be

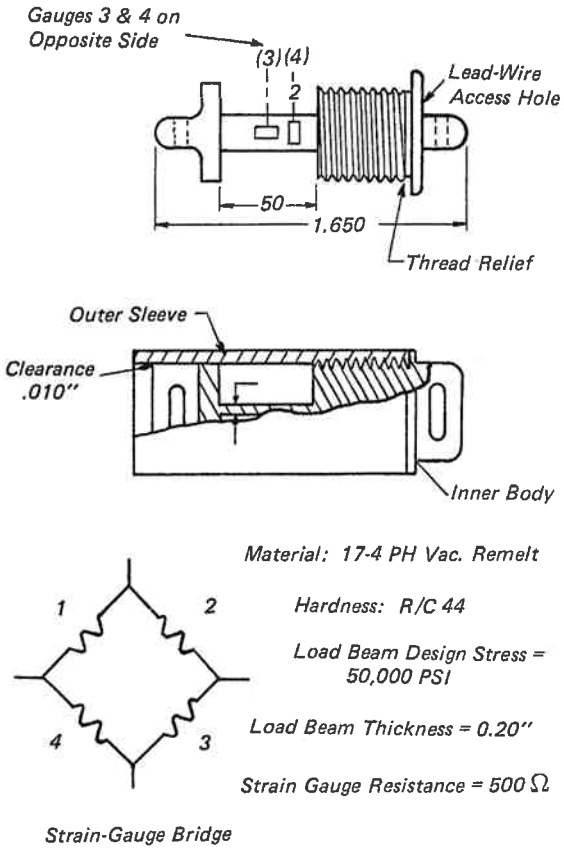


Figure 5.33 Typical Electric Strain-Gauge Force Transducer

the output of appropriate transducers or may be voltages of the quantity being measured. Most of the voltage-controlled oscillators are available as plug-in units and are pretuned at the factory. Prepackaged plug-in filters for harmonic suppression are also available.

The resistance-bridge oscillator consists of a phase-shift oscillator employing a resistance bridge as a part of the phase-shift network. A change in the resistance of any one of the four bridge elements will produce a proportional change in the oscillator-bridge combination. This type of oscillator is designed for transducers employing strain-gage elements and is recommended for use in one or more arms of a four-arm resistance bridge.

Inductance-controlled oscillators are used primarily with variable-inductance transducers. The oscillator circuit is basically a Hartley LC with the transducer constituting the inductive portion of the tank circuit. As the transducer inductance is changed by the action of the quantity to be measured, the frequency of the oscillator is varied, thus producing a frequency-modulated subcarrier signal proportional

to the applied stimulus. In general, the inductance oscillators are rugged, stable, physically small, and light in weight.

Reactance oscillators employ saturable reactors which are current-controlled pickups. Coils of the reactor are used as inductance elements to modulate the oscillator. This type of oscillator is used for measuring current, small voltages, or temperature.

Measurement of Force. A calibrated load cell is the common instrument for measuring dynamic force at a parachute riser attachment. Figure 5.33 shows details of a miniature load cell employing a strain-gage link with a resistance bridge as the transducer element bonded to the load beam surfaces. The working range is a function of the strength and elastic limit of the load-bearing member. Strain-gage load cells should be installed so as to avoid bending moments in the stressed beam or secondary acceleration effects. This is best accomplished with a universal joint free motion, preferably at the vehicle.

Measurement of Pressure. A strain-gage force transducer driven by a sealed piston is a common means for measuring pressure, the calibration being in terms of force per unit area. Other pressure sensing transducers may employ displacement of a diaphragm, Bourdon tube or sylphon bellows. Potentiometric type pressure transducers also are used. Measurement of altitude-pressure requires barometric type instruments similar to the above, calibrated for the atmospheric static pressure profile over the desired altitude range. The location of pressure ports to ensure true static readings sometimes entails special plumbing to the transducer.

Measurement of Dynamic Pressure. Instruments for the measurement of differential pressure and relative airflow velocity are closely related. The free-stream dynamic pressure is measured with Pitot-static tube as the difference between the total pressure and the static pressure, and translated mechanically and therefore electrically into equivalent air speed units based on sealevel density of air. When the density is known, the true air speed can be calculated.

Measurement of Acceleration. Gravitational forces or forces expressed in "g's" (multiples of the mass of the tested body) are measured along one or more of three orthogonal axes. Accelerations along these axes that can be tolerated by the human body, form criteria for the dynamic response index limits. Thus, acceleration instruments are used in live and dummy tests during seat ejection or bail-out to measure linear and rotational motions, the acceleration effects on the human body of air blast, of parachute opening, and in crew modules, the accelerations due to landing impact. Accelerometers are normally placed in the center of gravity of a test vehicle, but they also may be used to measure high acceleration occuring during the parachute deployment and opening process on such devices as reefing line cutters attached to the canopy skirt.

The accelerometer transducer uses strain-gage bridge, force sensing semiconductors or piezo-electric element principles which involve deformation under the inertia force of a moving mass. Instruments of high accuracy are commercially available.

Photographic Analysis. The value of test vehicles for decelerator testing is greatly enhanced by the utilization of a variety of on-board photographic equipment. This provides a permanent visual record of decelerator operational events which may be reviewed accurately and repeatedly with possible correlation to other measurements. Cameras are usually mounted on the outside of the test vehicle in protective coverings, and aimed to best cover the deploying and opening decelerator. Internal mounting of photographic equipment is also employed.

Initially, the 16mm GSAP camera, modified for use in test vehicles, was almost exclusively used because of its availability and low cost. As requirements for increased tolerance to high "g" loads, a need for wider choice of lens, and wider range of frame rates became apparent, more sophisticated types of cameras were developed and became available. This has resulted in the improved visual study of parachute operational behavior, which is especially important when malfunctions or other operational anomalies occur. A typical, widely used camera of the more sophisticated type mentioned is the Photo-Sonics 16mm-1F. Its ability to operate successfully under loadings as high as 100 "g"s is but one of its assets. Frame rates range from 200 to 1000 frames per second. Water tight seals provide protection from water submersion for a period of several hours. The choice of a variety of lens increases the utility of this camera. Electric power required is optional 6 to 28 volts DC, or 10 to 48 volts DC. Of prime importance is its timing light, which makes event sequencing analysis possible.

Range Instrumentation

Data acquisition methods at each range employ similar equipment. Exact descriptions and peformance specifications will be found in the Range User's Handbook furnished by the range operation agency. In the following paragraphs are general descriptions of range instrumentation. Included are cinetheodolites, telescopic cameras, telemetry, closed circuit

television, tracking radar and laser equipment. Meteorological data are obtained by making surface observations at several range locations. Wind direction and velocity are determined by Rawing, a system using a balloon-borne radio transmitter modulated by pressure, temperature and humidity and tracked by a radio receiver, the antenna of which is slaved to the signal being received.

Time Coordination. On most test ranges, all data acquisition and handling is controlled by Inter-Range Instrumentation Group (IRIG) systems. The heart of such control is the IRIG timing system. The timing system generates pulse rates, cinetheodolite control pulses and accurately synchronized time codes which are transmitted and simultaneously captured on ground station motion picture, telemetry, radar, television or other records. Airborne cameras require an independent timing reference which can be correlated with the ground based IRIG timing system. Such correlation is important for proper definition of such recovery events as line stretch, time of snatch force, multiple opening forces and transfer from drogue to main parachute. These data are most important in case of anomalies or failure. Electrically initiated events such as test vehicle separation from the aircraft, parachute compartment cover ejection, drogue parachute disconnect, main parachute deployment initiation, ground impact attenuator deployment initiation and main parachute disconnect may be telemetered and recorded. In order that test analysis be meaningful, data from all measurement gathering sources should be properly time coordinated.

Space Positioning. Optical tracking cinetheodolites, designed to provide angular measurement of the line-of-site from the instrument to the flight test vehicle, are stationed along the flight range. The vehicle image, angle data and timing are recorded on film simultaneously. A minimum of two instruments are required to determine vehicle spacial position. Cinetheodolites are a prime source of vehicle trajectory information, e.g., position, velocity and acceleration. Data are obtained at speeds up to thirty frames per second with Contraves cinetheodolites. Each film frame registers transmitted signals for correlation with other types of instrumentation being used. Most ranges are equipped with semi-automatic film reading systems which provide for rapid conversion of the data for computer input purposes.

Telescopic Cameras. Ground based telescopic motion picture cameras on tracking mounts are used to obtain decelerator deployment and inflation performance data during a recovery sequence. These instruments may vary in telescopic power, frame rates and film sizes (16, 35 and 70mm). Some tracking mounts are also equipped with a distance measuring or tracking laser. Recording rates are usually twenty-four frames per second. Rates as high as five hundred frames per second have been used making possible very detailed step by step sequencing of deployment and inflation events.

Television. Closed circuit television systems provide real time viewing of tests with high resolution coverage originating at selected range camera sites. Video signals are transmitted by microwave to the master control station where video tape recording may be utilized for replay on demand.

Tracking Radars. Air vehicles can be skin-tracked or beacon-tracked by radar to provide accurate trajectory data and instant range space position. Radar may also be used to locate and follow a Rawin instrument or provide range safety surveillance. In an aircraft launch test operation, radar can be used to vector the aircraft to a predetermined release point so that the test item will impact on the range in an optimum position for photographic coverage. The test controller examines predicted trajectories for the vehicle with both functioning and non-functioning recovery systems, considers wind direction and the stipulated test conditions (air speed and drop altitude) and plots the release point. After release, the radar signal is transferred to the test vehicle to obtain a plot of altitude versus time and the ground projection of the test item's flight path. From radar triangulation or range and angle data, the impact spot can be located on the range to aid search and deployment of retrieval crews.

Laser Tracking. Contraves (Cinetheodolites-35mm 10 or 30 frames per second) sites at Edwards A.F.B., CA, El Centro (National Parachute Test Range), CA, and Sandia Laboratories, Albuquerque, NM are now utilizing laser tracking as an aid in obtaining space positioning data. The laser is mounted parallel to the 35mm camera on a common tracker mount.

In conjunction with the laser is a laser reflector, which is mounted on the drop test vehicle. This laser reflector is a flexible piece of scotchlite No.7610 (3M) which was a "look" angle of 30° on a flat surface. Look angles of 60° can be achieved on a curved surface. The type of laser being used is a Neodymium - Gallium Arsenide laser. Safety goggles must be used when working near this laser.

The laser tracking method of range data acquisition gives more rapid results. Data on trajectories is available for examination in less time.

Telemetry. The most flexible data-gathering

method available is provided by telemetry systems. Radio signals are transmitted to ground receiving units that provide for recording the measurements made at the test vehicle during the sequence of controlled events, whether aircrew escape, airborne cargo delivery or deceleration and landing provided by a vehicle recovery system.

A telemetry system consists of one or more remote sensing devices which collect measurements and convert them into a form suitable for simultaneous transmission on a single carrier (radio) frequency to a ground receiving station. Here the signals are decoded and the various measurements are separated and fed into equipment for processing, quick display, recording for storage and later analysis.

The use of telemetry is controlled by IRIG which adopted "frequency modulation" (FM) as the method for signal transmission. Three frequency bands, P-Band (216-260 MHz), L-Band (1435-1540 MHz), and S-Band (2200-2300 MHz), are currently assigned. The higher transmission frequencies are the more desirable because they afford shorter wave length and wider band width. Short wave lengths permit shorter length antennas on the flight vehicle at high transmission efficiencies. Wide band width favors greater transmission capacity and accuracy of data. However, the higher frequency transmitters and receivers are heavier and more expensive.

Modulating techniques vary with requirements. Until recently FM/FM telemetry was used exclusively, e.g., remote measurements were converted into subcarrier frequency modulated messages and transmitted on a common FM carrier frequency. The required band width per subcarrier (channel), limits the number of continuous measurements transmissible to between 8 and 12 due to practical considerations. Commutation is a means of expanding data transmission capacity by having one or more channels carry discrete short intervals of several on-going measurements in a repeating cycle. Certain data are adequately monitored by multiplexing signals, but others which exhibit sudden and frequent variation usually require a continuous channel. FM/FM through extensive use has reached a high state of development and reliability, but with only 8 to 10 channels, FM/FM may provide insufficient capacity for complex multi-measurement test requirements. The Apollo boilerplate test vehicle used twelve channels of information over two carrier frequencies, and for reliability these signals were recorded with a back-up single on-board magnetic tape recorder.

For complex testing "pulse code modulation" (PCM), "pulse amplitude modulation" (PAM), or "pulse duration modulation" (PDM), systems are available for use at several ranges. The PAM/FM and PDM/FM systems provide greater flexibility and capacity for measurement data than the FM/FM system. PAM/FM telemetry was found to be accurate within 2 to 2½ percent . PCM/FM provides the same flexibility as PAM/FM, with accuracy determined to be one-half percent in transmission, or even better in analog to digital conversion. The higher accuracy exacts a penalty in complexity and equipment cost. The Air Force used PCM/FM telemetry for transmission of 200 measurements of data in simultaneous testing of four ejection seats launched from a rocket propelled sled simulating the nose section of the B-1 bomber.

Data Processing. The data that are received as signals at telemetry ground stations must be conditioned, demultiplexed and digitized. Such processing is accomplished at a central data control station where various units convert raw data to usable form for display or storage, introducing timing definition and correlated data from other instrument systems. Data recording and processing services appropriate to each set of range instrumentation are available at all bases. Data obtained from cinetheodolite film, telemetry, radar, video or atmospheric sounding records may be processed to bring results into a meaningful data package suitable for engineering analysis. For special tests or special analysis requirements, the software systems are sometimes modified. Data can be presented in either digital, tabular or graphic forms, appropriate to the type of test analysis desired.

CHAPTER 6

PERFORMANCE

Knowledge of the aerodynamic and operational characteristics of decelerators and related devices is prerequisite to the design of dependable recovery systems and the prediction of their performance in the operational environment. Representative performance data, primarily empirical in character, is summarized in this chapter as an aid to understanding decelerator theory, applicable analytical methods and design criteria.

Information is presented in the light of contemporary theoretical formulations relating measured behavior to decelerator system parameters and known physical laws. But the emphasis here, is on "how it works" rather than on the elaboration of approximate mathematical models, reserving more complete analytical treatment for Chapter 7. Some comparisons of measured and predicted performance are made to indicate the accuracy level attainable with various analytical methods and to illustrate the types of empirical coefficients and other data needed for their successful application. The complexity of the subject is clarified somewhat by disecting and examining separate elements of the varied physical processes involved in decelerator operation.

During the operation of a typical recovery system the major component subsystems go through a sequence of functional phases each of which must be properly executed before the next can begin and carry the total operation to a successful conclusion. In general terms these functional phases are:

Deployment
Inflation
Deceleration
Descent
Termination

For convenience the subject matter is presented in this sequence, although it is recognized that the functional phases are not sharply separated in real system operation and some systems do not have a descent phase. For example, some canopy inflation may occur during deployment, and usually during inflation the system decelerates as the canopy drag area increases. But each functional phase is represented by a different set of design criteria and design parameters.

While much of the aerodynamic and other data presented is useful for preliminary design and performance estimates, it serves mainly as an aid to understanding the complex physical processes involved in the operation of parachutes and related devices. The results of small model tests are essentially of qualitative value which itself is a function of the accuracy of the models. The strong influence of decelerator flexibility, elasticity and effective porosity on performance and the fact that these properties vary both with scale and operational conditions lends emphasis to the importance of full scale flight testing in this field. Efforts to reduce dependence on such testing are reflected by new analytical approaches presented in Chapter 7. The empirical data given here are representative of the current state of the art as established by the results of numerous model and full scale test programs sponsored by both government agencies and private industry.

DEPLOYMENT

Deployment is one of the major functional phases in the operation of a recovery system. Most of the available data relate specifically to deployment of parachutes, but the principles discussed are generally applicable to all types of decelerators. In the following paragraphs, different methods of deployment are described in conjunction with resulting forces and means of limiting peak impact loads.

Deployment Sequences

Applied to parachutes and similar aerodynamic decelerators the term ***deployment*** denotes the sequence of preliminary actions starting with separation of the decelerator from the recoverable body and ending when its rigging is fully stretched. Deployment may be initiated and powered by one or a combination of the devices described in Chapter 3, e.g., static line, pilot chute, or mortar. The process, being short and impulsive, is attended by an impact load, or loads.

The different deployment methods fall into two broad categories characterized by the order in which the decelerator members are allowed to payout after initiation. ***Canopy-first*** deployment of a parachute is effected with an attached bridle or, in many cases, a static line which applies a tensile force to progressively unfold the canopy from its container. After the canopy skirt emerges from the container the order of events is determined by whether the suspension lines are stowed in a container which is attached to the body, or the outside of a container temporarily attached to the canopy, e.g., sleeve or quarter bag as described in Chapter 3.

Lines-first deployment is effected by means of a deployment bag, or separable container, which may be extracted by an attached bridle and pilot chute or forcibly ejected from the vehicle. In either case, the entire decelerator moves away from the vehicle in the deployment bag with risers and lines progressively unfolding followed by the canopy as the bag is stripped away. Each deployment method provides a different order in which the decelerator mass may be progressively separated from the body, either

canopy, suspension lines and risers (canopy-first deployment with lines and risers stowed in a container attached to the body). (Figure 6.1a)

riser, suspension lines, and canopy (lines-first deployment with decelerator stowed in a deployment bag or similar separable container). (Figure 6.1b)

canopy, risers, and suspension lines (canopy-first deployment with lines and risers stowed on sleeve or quarter bag), a combination of the above methods (Figure 6.1c)

These different mass distributions (coupled with effective drag forces, material elasticity, and the deployment method) determine, first, the rate at which the principal mass components are decelerated to separate from the body and, second, the number and magnitude of the impulses involved in re-accelerating the mass components to the velocity of the body.

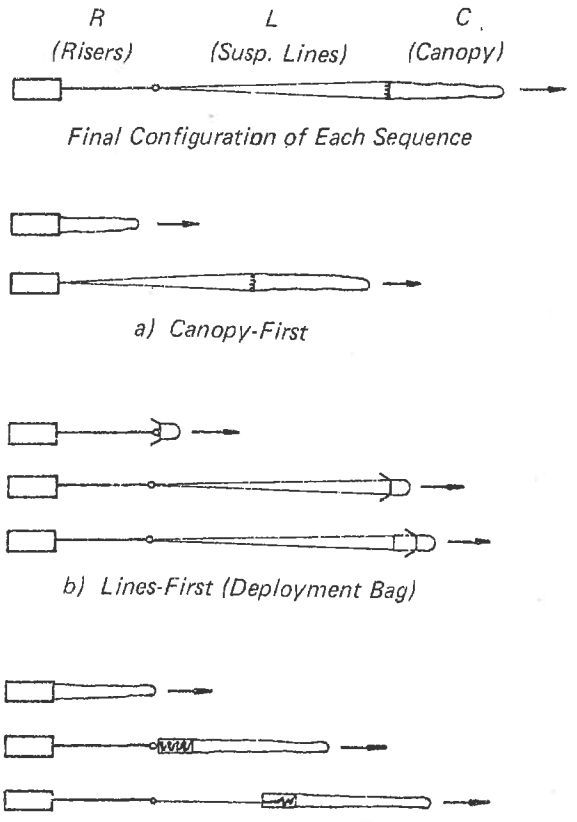


Figure 6.1 Schematic of Different Deployment Sequences

Deployment Forces (Snatch)

The impact load generated by the impulsive re-acceleration of all or part of the decelerator mass is responsible for the sharp-edged force transient traditionally called the ***snatch force*** (Figure 6.2). In the great majority of recovery system operations the snatch force has not been a critical load because peak opening forces are greater in magnitude and duration. The occurrence of extreme snatch forces often is the result of faulty design and may be corrected by minor system changes.

The high-onset shock generated by the snatch force can cause critical inertial forces in attached

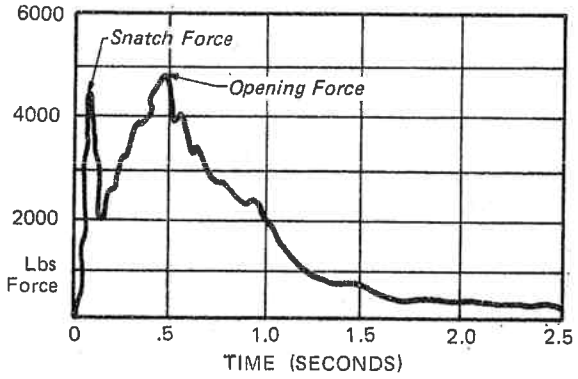


Figure 6.2 Snatch and Opening Forces of a 28 Ft D_o Solid Flat Circular Parachute

devices such as reefing line cutters and has been known to break the pyrotechnic fuse train or prevent the firing pin from actuating the percussion initiator in a cutter improperly mounted on the skirt. It is clear that the inertial force acts toward the apex of the canopy, creating compression in a fuse train with initiator pointing forward and tension in a fuse train with initiator pointing aft. Snatch-generated inertial loads also are capable of tearing reefing line cutters loose from their moorings on the canopy.

Other severe high-onset shock effects have been experienced in systems in which the main parachute is deployed by a permanently attached pilot chute. In such systems line stretch occurs with pilot chute fully inflated. The result is an impact load augmented by pilot chute drag, and included air mass momentum.

The potential for generating high-onset shocks also exists in the common practice of deploying a decelerator by a prior stage drogue, with its riser connected through a jumper bridle to the deployment bag. Excess slack length is the usual cause. If the bridle itself is not broken, the contents of the deployment bag may be disorganized or dumped by failure of retaining members.

A typical lines-first deployment sequence is illustrated schematically in Figure 6.3. The canopy mass, constrained to a minimum drag configuration, is caused to decelerate faster than the towing body, until it reaches position (2). It arrives at position (2) with a maximum differential velocity, Δv_{max}, relative to the body, at which point the suspension lines and riser come taut and begin to stretch. As the suspension lines stretch, the canopy mass (or a major fraction of it) is re-accelerated such that at position (3), $\Delta v = 0$ and the total elongation of the line bundle is Δl.

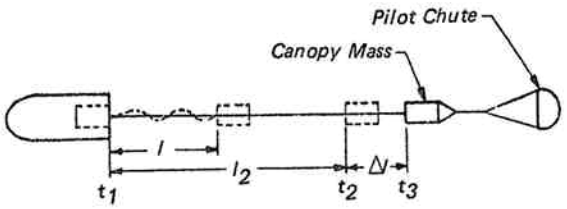


Figure 6.3 System Geometry During Deployment to End of Line-Stretch

As shown in Figure 6.2, after viscoelastic elongation of the stretched line bundle has absorbed all the kinetic energy of the deployed decelerator, the axial tensile load will have passed through a transient peak, i.e., the snatch force. The snatch force is actually the sum of three components:

$$F_s = F_i + D - W_p \sin\theta \qquad 6\text{-}1$$

The inertial component, F_i, is large while the drag and weight components may be negligibly small. Drag is not negligible when the pilot chute is retained. The relationship of the inertial components to pertinent parameters of the system is indicated by this approximate formula.

$$F_i = \Delta v_{max}(m\kappa)^{1/2} \qquad 6\text{-}2$$

Where $m = m_c + (m_l + m_R)/2$

m_c = mass of canopy

m_l = mass of suspension lines

m_R = mass of risers

and κ is the effective "spring constant" of the line-riser bundle. The mass of an attached pilot chute with its included air mass is added to m_c when applicable.

The effective spring constant, κ, represents the force required to stretch the line-riser bundle a unit distance. The static stress-strain curves presented in Figure 6.4A are broadly characteristic of nylon textile cords and webbing. For typical impact velocities the force rises more steeply with elongation, and ultimate strengths are higher than static maxima (see Figure 6.4C). Groom[330] demonstrated the basic response of nylon textiles to repeated impact loads by the method illustrated in Figure 6.4B along with typical results. The test specimens were made of 1500 lb 5/8 inch nylon webbing.

McCarty[329] investigated the load-elongation characteristics of nylon suspension line cord under both static and impact load conditions. Figure 6.4C shows how the ratio of the impact to static load increases as the elongation decreases for loading rates from 120–690 per unit per second. Typical single and double impact loading cycles are shown in Figure 6.4D, both measured and computed. All test specimens were 400 lb nylon cord (MIL-C-5040E, Type II).

In terms of the properties of the materials in the line-riser bundle, when the riser is an integral extension of Z suspension lines.

$$\kappa = Z F_T / l_2 (\epsilon - \epsilon_o) \qquad 6\text{-}3$$

where F_T is the tensile load required to produce a relative elongation ϵ in one cord, l_2 is the unstretched length, and ϵ_o is the initial strain, which may be related to the creep not present at high loading rates. When the initial strain is not set equal to zero, ϵ_o may be selected so that κ will be close to the average of the non-linear variation over the working load range of interest. This would logically bracket the design limit load, $(F_T/P_R = 0.4$ to $0.6)$ where P_R is the ultimate rated strength of the material, rather than extend to the ultimate, because generally κ at ultimate

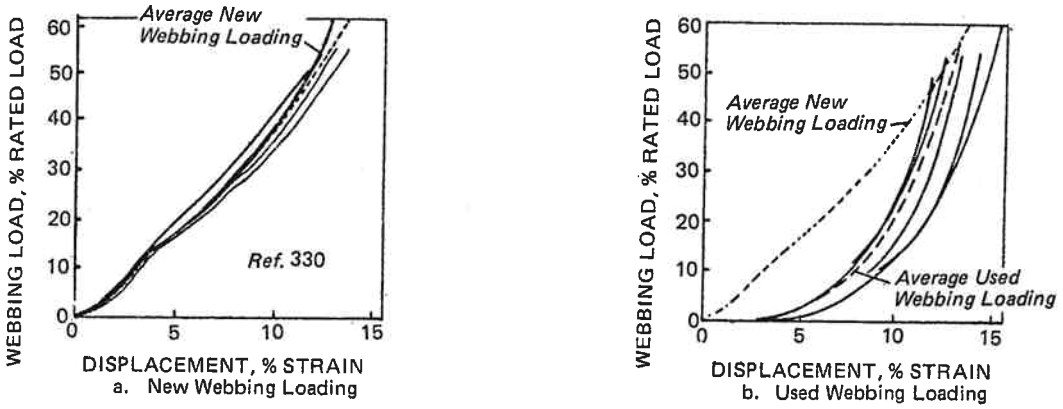


Figure 6.4A Relative Load-Elongation of Nylon Webbing from Twice Repeated Static Tests

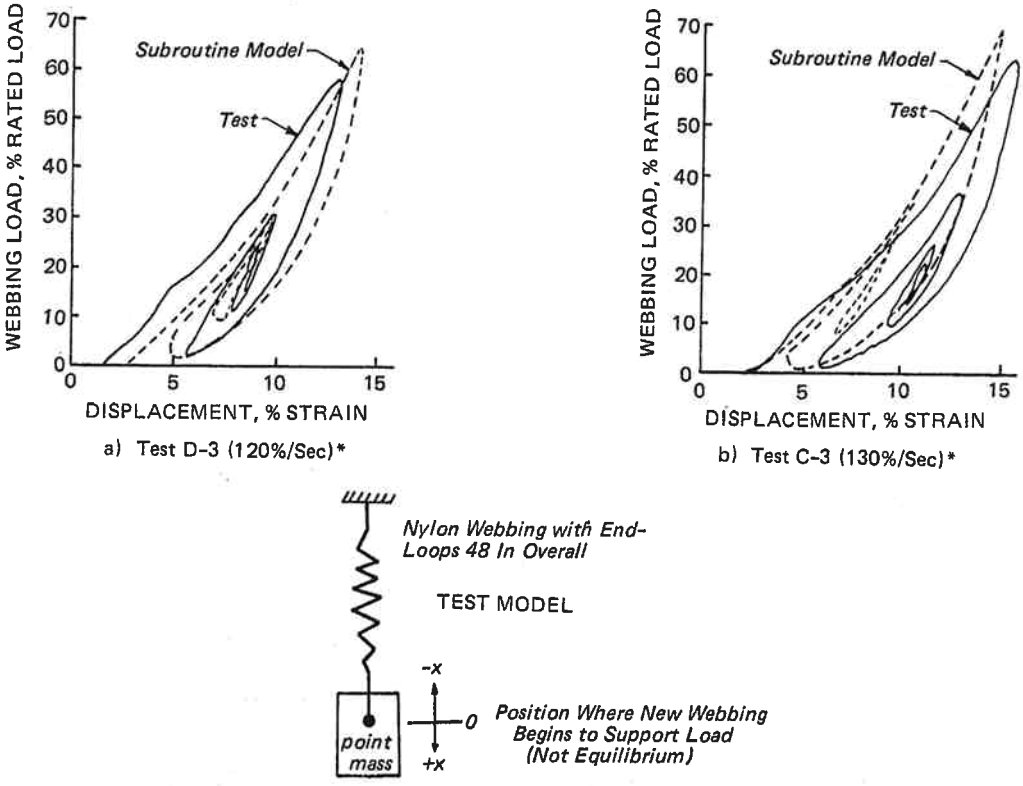


Figure 6.4B Tension-Strain Pattern Generated by Successive Impact Loads of Decreasing Magnitude (Ref. 330)

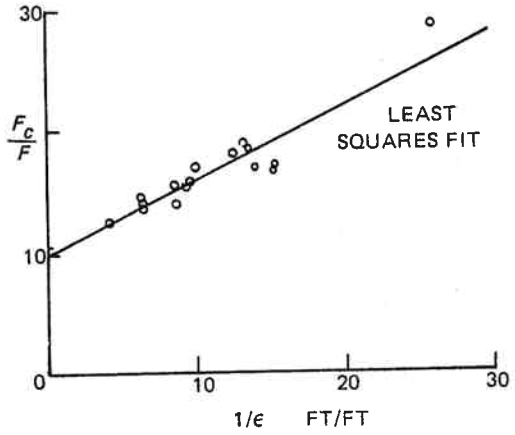
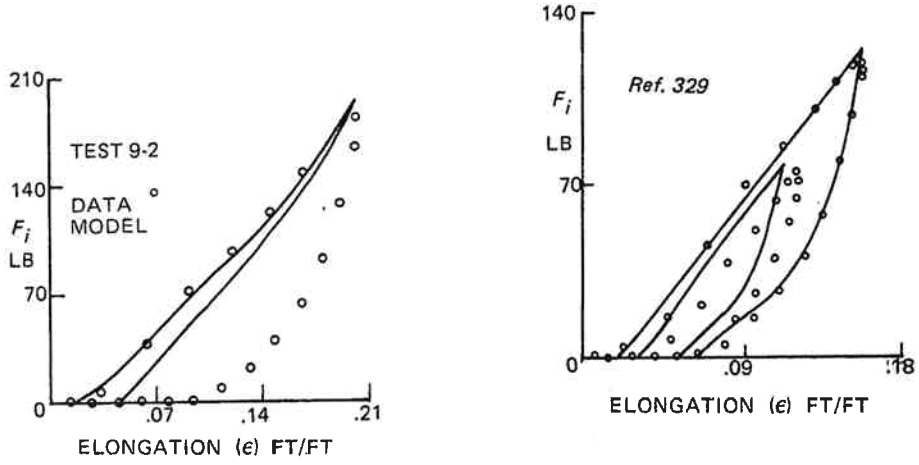


Figure 6.4C Ratio of Impact Peak Load to Static Load. Versus Inverse Elongation (1/ϵ)



a) Load Vs Elongation for Single Impact Cycle (with preliminary computer run)

b) Measured Vs Computed Load-Elongation for Two Impact Loading Cycles

Figure 6.4D Typical Impact Loading Cycles of 400-Lb Nylon Cord

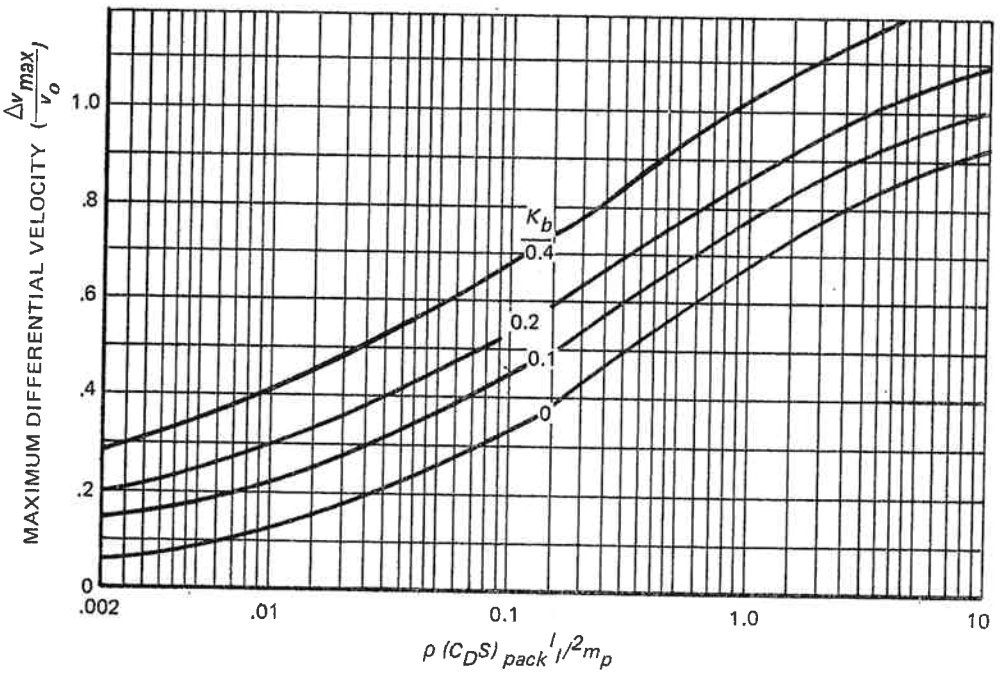


Figure 6.5 Approximate Body-Canopy Separation Velocity at Line-Stretch

is less than κ at limit, and use of the latter would yield more conservative results for design purposes. However, a failure analysis would be made with κ at ultimate.

Treating composite members (lines with webbing risers, etc.) as a compound spring

$$l/\kappa = l/\kappa_1 + l/\kappa_2 + \ldots\ldots l/\kappa_n \qquad 6\text{-}4$$

Owing to their viscoelastic properties, textile members function like "soft" springs only during the first application of a limit load. As shown in Figure 6.4B, hysteresis is large and the rebound slight because the elastic recovery is relatively small. For subsequent applications of repeated loads, the effective spring constant will be higher than initially. This alone would tend to make the opening force more critical than a preceding snatch force of acceptable magnitude, because the energy absorbing capacity of the suspension lines becomes significantly smaller after the first major load transient. Therefore, the spring constant evaluated as described above would tend to be valid only for the first major impact load, or for the increments of subsequent loads that exceed the preceding load over a short interval of time.

The maximum differential velocity, Δv_{max}, is difficult to determine but may be measured in suitably instrumented tests, or may be estimated with the following short method.

Estimation of Maximum Differential Velocity

Wolf developed the following short method of estimating the body-canopy separation velocity at line-stretch. It has proven to be quite useful because for many practical systems the approximation to measured values is close. The functional relationship

$$\Delta v_{max}/v_o = f\,[\rho\,(C_DS)_p\,l_l/2m_p] \qquad 6\text{-}5$$

is plotted in Figure 6.5 for differential values of the body acceleration parameter

$$K_b = l_l g \sin\theta/v_o^2 - (\rho\,C_DA\,l_l/2m_b)\,(v_b/v_o)^2 \qquad 6\text{-}6$$

where

v_o = initial velocity of body and decelerator

$(C_DS)_p$ = drag area of deploying decelerator (w/pilot chute when applicable)

l_l = unstretched length of lines and risers

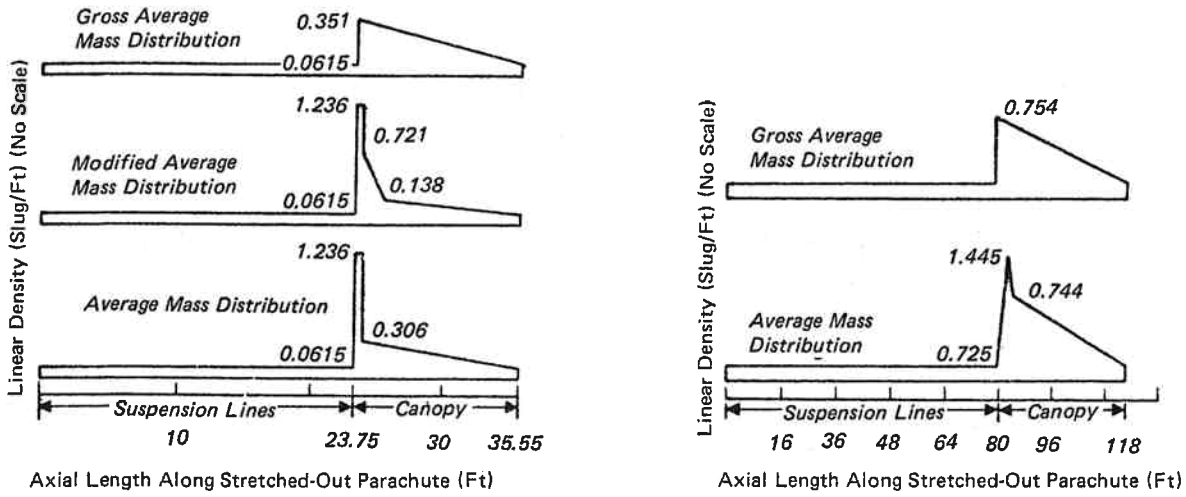
m_p = mass of decelerator = $m_c + m_l/2$

m_b = mass of body

C_DA = drag area of body

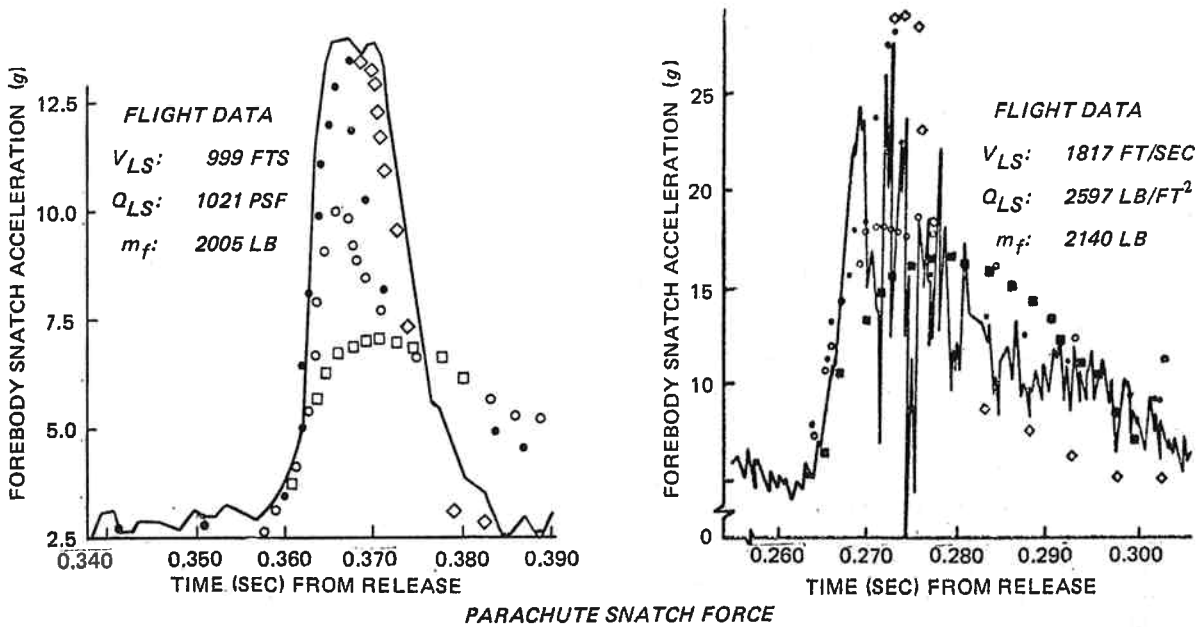
v_b = velocity of body at line stretch

The curve for $K_b = 0$ corresponds to decelerator deployment from a body approaching terminal conditions. For other cases when acceleration of the body is significant $K_b > 0$ and should be taken into account.



Parachute Mass Distribution

COMPUTED CURVES		COMPUTED CURVES	
MASS DISTRIBUTION	Δt_m (MILLISECONDS)	MASS DISTRIBUTION	Δt_m (MILLISECONDS)
○ Averaged	0.0	○ Averaged	0.0
● Averaged	5.0	● Averaged	6.0
◇ Modified	5.0	◇ Modified	6.0
□ Gross Averaged	0.0	□ Gross Averaged	0.0



PARACHUTE SNATCH FORCE

Figure 6.6 *Comparison of Measured and Computed Snatch Forces of Heavy Ribbon Parachutes for Different Mass Distributions (Ref. 348)*

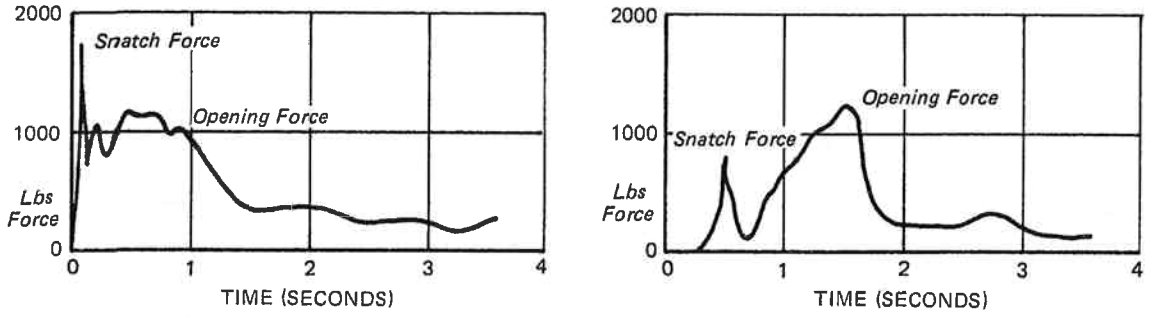


Figure 6.7 Effect of Deployment Bag on Relative Magnitude of Snatch Force During Deployment of a 28 Ft D_o Solid Flat Circular Parachute

The differential velocity between the deploying canopy and the towing body may be augmented by forcible ejection of the decelerator, which tends to shorten the time to line-stretch[346,347]. The effect is too variable to generalize when the decelerator is ejected at some angle to the flight path rather than directly downstream. Very often the transversely ejected decelerator will reach line-stretch before the deployment members have been swept back to the trailing position. The snatch force is seldom critical in such cases.

Canopy Distributed Mass During Deployment

Referring back to Figure 6.3, the line bundle has a distributed mass, each increment of which attains a different Δv between zero and Δv_{max} before being re-accelerated to the system velocity. Also, the canopy bundle has a distributed mass that may be concentrated in a deployment bag during the interval t_1 to t_2, but which during the interval t_2 to t_3 can be partially re-distributed, the bag containing the crown continuing to decelerate while the skirt mass is being re-accelerated. The entire deployment process is resisted somewhat by the variable force required to extract lines and canopy from the deployment bag. In those cases when the straight-aft deployment interval is short and the trajectory of the pack deviates very little from that of the towing body the parachute deployment process can be viewed as one-dimensional (tangent to the body trajectory), and the effects of the variable mass distribution may be more readily visualized. This approach to the study of snatch force was adopted by McVey and Wolf[348], where it was found that detail allotment of average mass distribution in the system is critical. A comparison of measured and computed snatch force histories for two different parachutes in test operations is presented in Figure 6.6. The effect of different assumptions as to details of canopy mass distributions are indicated. The time required for the canopy mass to respond to unlocking of the retaining flaps inside the deployment bag is denoted by Δt_m. (See also Chapter 7.)

Reduction of Snatch Forces

Clearly, the energy absorbing capacity of decelerator materials such as woven nylon and similar textiles is large because of the unusually great viscoelastic elongation they exhibit in conjunction with characteristic strength-weight ratios over 3.5 times that of steel. This fact has tended to encourage the development of snatch force limiting methods aimed more at drag reduction rather than impact attenuation through augmentation of Δl in the rigging joining the canopy to the body. However, the introduction of high-strength Kevlar materials has renewed interest in impact attenuation methods compatible with the low relative elongation of risers and suspension lines made of Kevlar textiles. Drag reduction during deployment will reduce the snatch force in direct proportion to the differential velocity decrement achieved (Eq. 6-2) while the effectiveness of impact attenuation measures will tend to vary only as the square root of κ.

The deployment bag was developed as a means of limiting snatch forces and is now widely used for this purpose as well as a convenient means of packaging the decelerator. Reduction of Δv_{max} is augmented by the resistance of line and canopy restraints in the bag[569-571]. Another common method of drag reduction employs a hesitator band around the canopy mouth at the skirt in those systems deployed canopy first. The snatch force breaks the lashings of the skirt hesitator, thus freeing the canopy mouth for inflation. In personnel parachutes a similar function

is performed by the canopy sleeve.

Canopy-first deployment of parachutes with free skirt is still a common practice in personnel escape and light airdrop systems. When the canopy mouth opens partially during deployment, separation of canopy and body is accelerated, Δv_{max} is increased and the resultant snatch force is maximized. Typical recorded data from two parachute tests at the same dynamic pressure in Figure 6.7 illustrate the effect of the deployment bag.

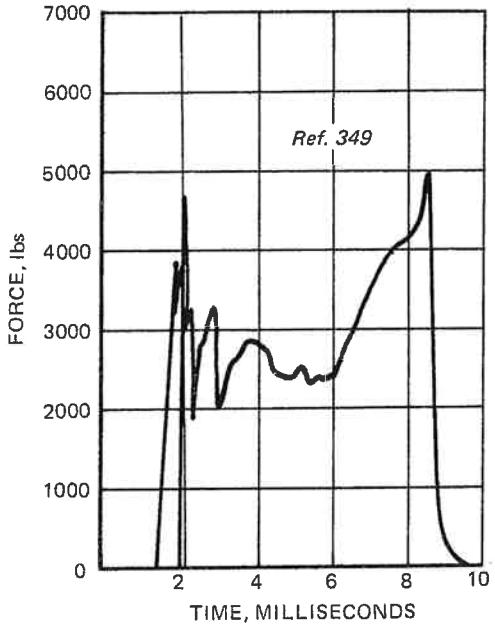


Figure 6.8 Force Record for Pilot Chute Bridle Test

High-Onset Impact Shock

Some decelerator configurations have been attended by local accelerations of components at very high rates during deployment such that the mass-inertia of the material creates stress concentrations and the elastic properties of the material limit the velocity at which strain can be propagated through the member. High-onset impact shocks of this type have been encountered in the bridle member joining a drogue riser to the deployment bag of the following stage when the length of the bridle was excessive. Similar conditions have existed in bridles attached to the projectile of a drogue gun or to an extraction rocket. However, the condition most difficult to cope with is found in the permanently attached pilot chute, because the drag of the fully inflated pilot chute not only augments but also, along with the momentum of the included air mass, adds directly to the impact load. Under such conditions when the total energy capacity of the bridle was exceeded, failures occurred in free lengths away from the joints or end fittings and frequently at two points near opposite ends at the same time. A classic example was found in the pilot chutes of the Apollo main parachute cluster. Double-break bridle failures were experienced in two different development tests and these events stimulated an intensive laboratory investigation[349] in which the failures were duplicated in a dynamic test rig, and force-time records obtained. Figure 6.8 gives a typical example. The recorded load onset is in the order of 7.8 million pounds per second in a two-ply bridle of 3100 lb 3/4 inch webbing. The resultant strain waves were propagated back and forth along the 23 foot bridle at a velocity of 5550 fps following a simulated pilot chute impact at Δv_{max} = 285 fps. Impact shock effects increase progressively with Δv_{max}, and the velocity at which the onset of strain waves becomes critical will vary from system to system as a function of the velocity of sound in the structural material.

INFLATION

Decelerator inflation is characterized as being either "infinite" or "finite" mass depending on the extent of system velocity decrease during this functional phase. A negligible velocity decrease results from an "infinite mass" inflation as exemplified by aircraft deceleration applications. A "finite mass" inflation produces measurable system velocity decrease as realized during personnel airdrop applications.

The inflation process is governed by the shape of the canopy gores in the skirt area and the mass and porosity parameters of the canopy. Early in the filling process other less tangible influences are at work which have introduced an element of randomness into the inflation characteristics of many parachute systems.

The Inflation Process

Stages in the inflation of a typical parachute in a finite mass system are illustrated schematically in Figure 6.9A. It has been observed that as the canopy mouth opens, (a) a substantial volume or "ball" of air (b) charges down the length of the limply streaming tube of fabric to the apex. At this instant, (c) the crown begins to fill continuously like a balloon being inflated through a conical duct (d) but canopy expansion is resisted by structural inertia and tension (e and f). By definition, full inflation is completed when the canopy first reaches its normal steady-state projected area, i.e., subsequent over-expansion (g) is a distortion due mainly to the momentum of the surrounding air mass.

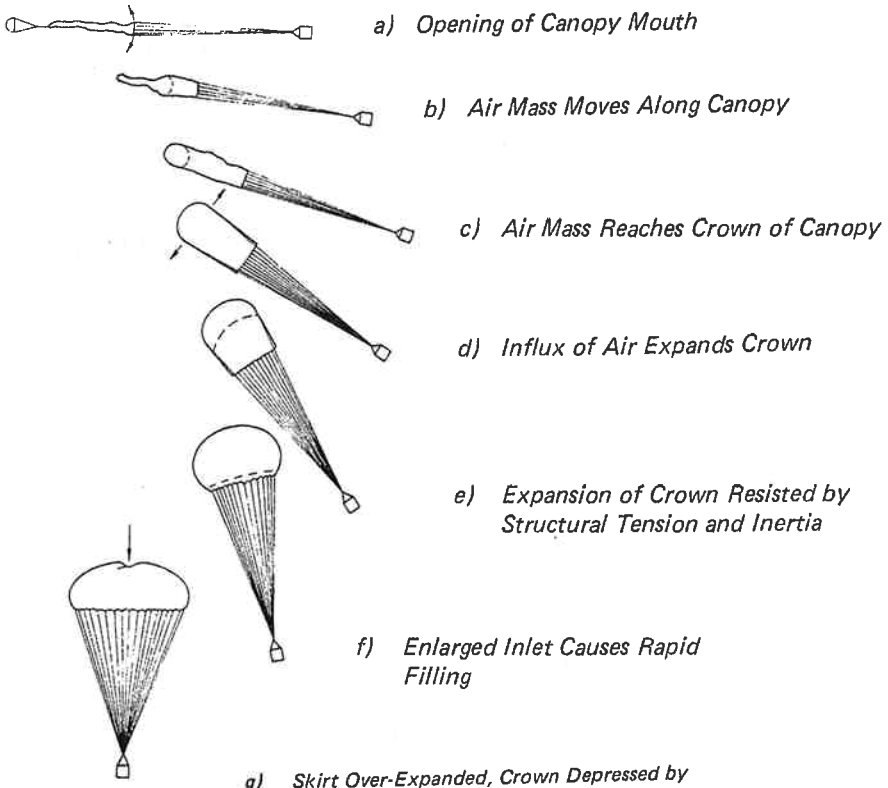


Figure 6.9A Stages in Parachute Inflation

Intermediate stages added to the inflation process by skirt reefing are illustrated in Figure 6.9B. The peak opening force usually occurs at the end of the rapid phase of reefed filling when the reefing line first comes taut (a'). A short time later (normally a small fraction of a second) the canopy is expanded by its radial momentum and the reefing line tension reaches its maximum (b'). During the reefed interval most canopy designs retain a constant inflated shape, but the Ringsail and low porosity gliding canopies continue to fill slowly. At disreefing, tension in the canopy skirt causes it to snap quickly to a larger diameter (c').

When compressibility effects are small, e.g., $v_s <$ 300 fps TAS, the characteristic inflation process of any given canopy entails the ingestion of an essentially constant volume of air through the mouth opening to completely develop the normal inflated shape. Of the total air ingested, a major fraction is retained in semi-stagnant form in the canopy while the rest passes through the porous walls. Inflation continues steadily as long as a favorable pressure distribution exists and no structural constraints such as skirt reefing are encountered, i.e., the integrated radial pressure forces remain greater than the integrated radial tension.

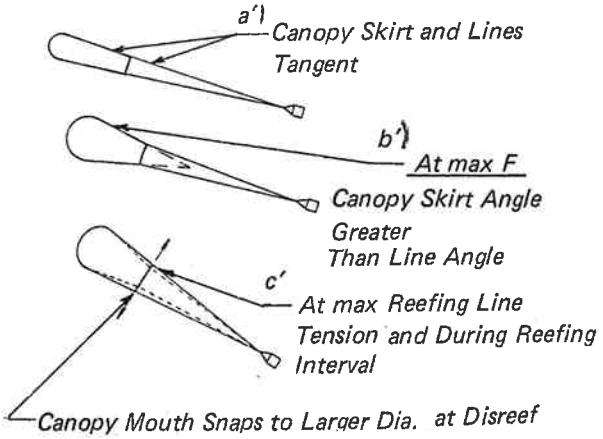


Figure 6.9B Intermediate Stages of Inflation Process Added by Skirt Reefing

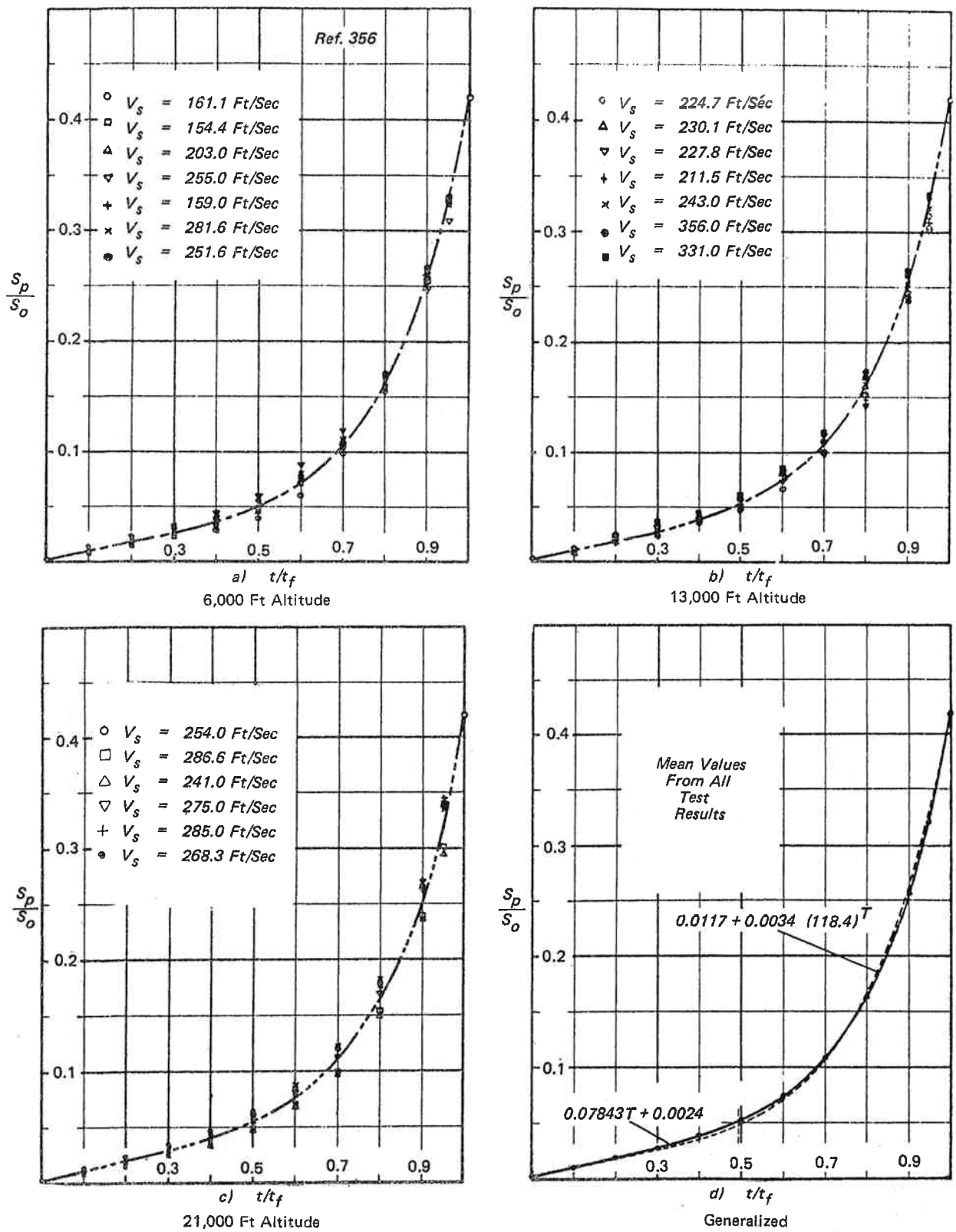


Figure 6.10A Normalized Canopy Area Growth During Inflation of 28 Ft (D_o) Solid Flat Circular Parachute

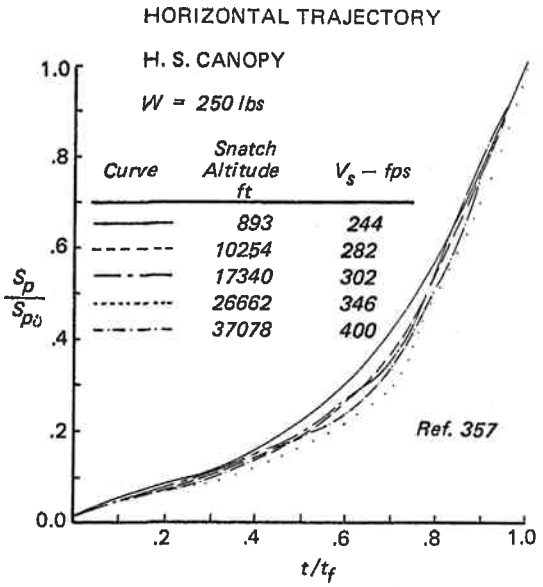


Figure 6.10B Normalized Canopy Area Growth During Inflation of 35 Ft (D_o) 10% Flat Extended Skirt Parachute

When the total porosity is excessive, equilibrium between radial pressure and structural tension will occur before the canopy is completely filled and the "squid" configuration results. The amount of porosity that can be tolerated in an inflating parachute varies with the constructed shape of the canopy as defined mainly by the effective angle of attack of the skirt. This is a function of the relative length of the suspension lines (l_e/D_o) and the shape of the gore pattern.

Slotted canopies of the ribbon and ringslot types, both flat and conical, retain a positive opening tendency at much higher total porosity levels as indicated by the curves of Figures 8.5 and 8.6. This is attributed to the difference in the character of the through-flow in slots relative to fabric pores, the former functioning like sharp-edged orifices with a marked jet contraction effect, thereby offering a relatively greater through-flow resistance[350]

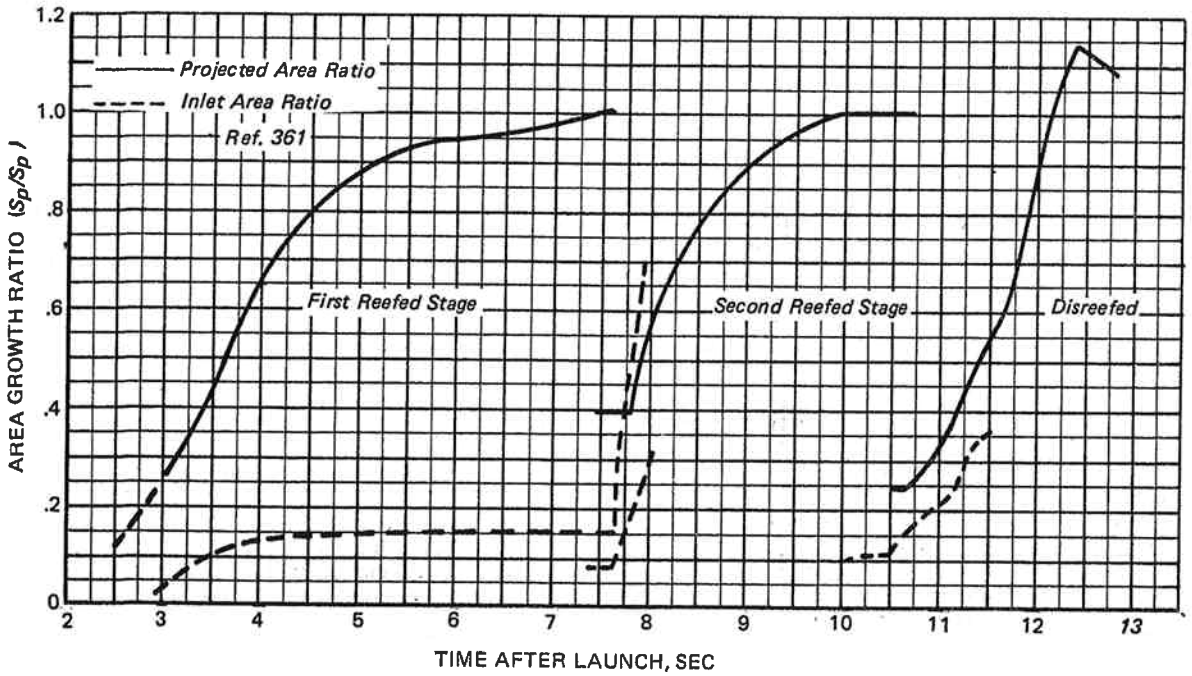
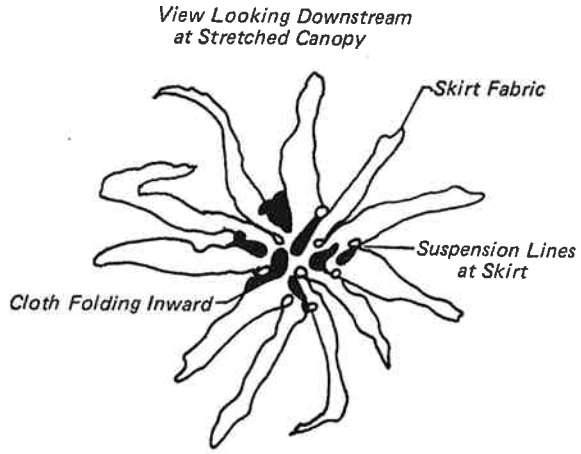
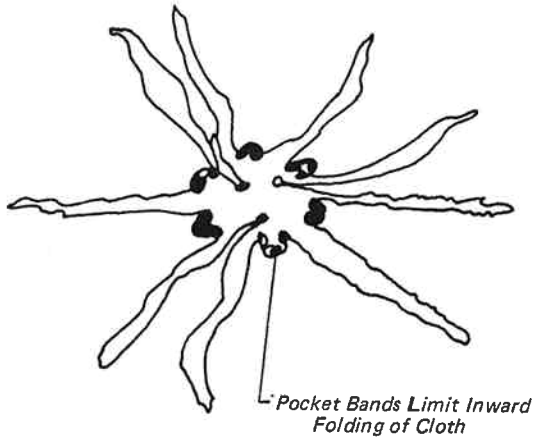


Figure 6.11 Measured Area Growth During Inflation of 85.6 Ft (D_o) Modified Ringsail Parachute With Two Reefed Stages (S_p' = Projected Area at End of Stage)



a) Conventional Skirt



b) With Pocket Bands

Figure 6.12 Schematic - Blanketing of Canopy Air Inlet by Inward Folding of Skirt Fabric Between Suspension Lines With and Without Pocket Bands

Canopy Area Growth During Inflation

The inflation of circular parachutes is attended by a characteristic increase in inflated diameter, or projected frontal area, with time as exemplified by the measurements obtained from various tests plotted in Figure 6.10 and 6.11. Additional projected area-time relationships acquired during wind tunnel and full scale drop test programs are found in Refs. 340, 341, and 351-355.

The changing shape and effective porosity during canopy inflation cause the drag coefficient to increase at the same time the projected area is increasing. The fineness ratio of the expanding canopy decreases to that of a bluff body, and the effective porosity, initially quite high in the pressurized crown area, decreases to a minimum value during steady descent.

If both C_{D_p} and S_p increase linearly with time, their product, C_DS, would increase as a function of t^2. Normally the projected diameter increase is non-linear with time so that C_DS becomes a function of t^n and the exponent usually falls between $n = 2$ and $n = 3$ depending on how C_{D_p} increases with time. These values of n are generally indicative of the filling behavior of non-reefed canopies or of a reefed canopy after disreefing.

Inflation of Clustered Canopies

Clustered canopies of all types have a strong tendency to inflate at different rates which leads to substantial inequity of load sharing. (See page 247 and Refs. 194, 358 and 359.) The least divergence between leading and lagging canopies occurs in systems having relatively long inflation times or low deceleration rates (e.g., the USD-5 two-canopy cluster[1]).

Synchronization of cluster canopy inflation is greatly improved with the permanently attached system described by Buhler and Wailes[360].

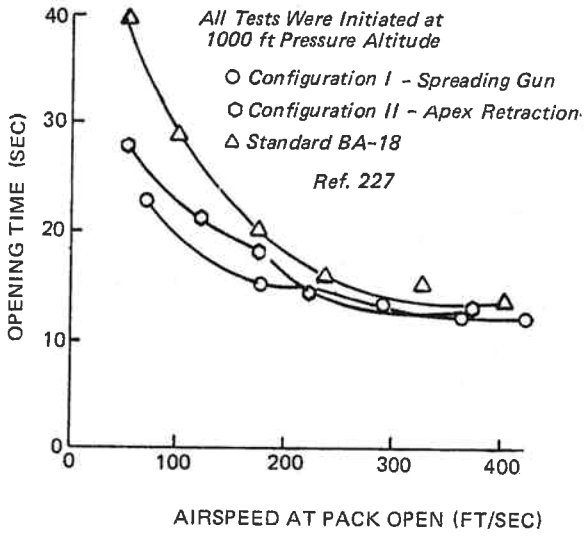


Figure 6.13 Effect of Skirt Spreading Gun and Canopy Apex Retraction on the Opening Time of Personnel Parachutes

The inflation of clustered canopies during the reefed interval is somewhat less divergent than after disreefing. Typically, pyrotechnic reefing line cutters have a timing variation in the order of ±10 percent at any given temperature. On the average, such timing variations result in non-synchronous disreefing of the canopies in a cluster. This in itself does not cause non-synchronous opening of the parachutes but aggravates the inequity of load sharing as shown by Moeller[362].

During the reefed interval any disparity in area growth between canopies tends to diminish as the level of system deceleration decreases. Non-synchronous disreefing may aggravate or alleviate the disparity between member canopies depending upon whether the lead-canopy or the lag-canopy disreefs first. The effect is most pronounced when the disreef time differential between canopies is a large fraction of the normal filling time[362]. Occasionally this has caused leading and lagging canopies to reverse their roles on disreefing. The theory that aerodynamic interference between canopies, so called "blanketing" was responsible, motivated a series of experiments with modified main parachute designs. No significant change in the disparity of opening loads was effected with two and three parachute clusters (Ref.217). Since each parachute in a cluster is being decelerated independently of its growth in drag area, no change in canopy or system design will alter that fact other than one which works to retard the growth of the leading canopy or accelerate the growth of lagging canopies[363].

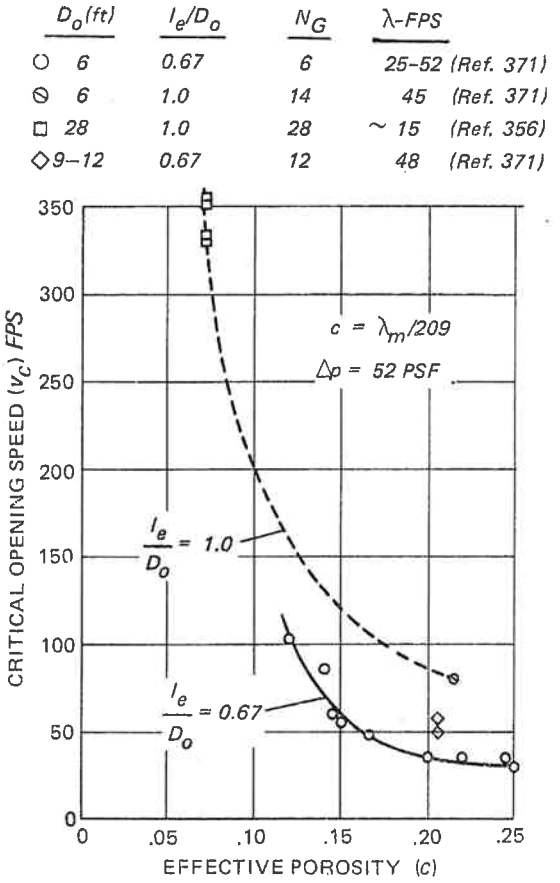


Figure 6.14 Parachute Critical Opening Speed Vs, Total Effective Porosity

Canopy Inflation Aids

As the canopy skirt mass reaches line-stretch and is re-accelerated by the snatch force, much of the slack material around the mouth where the air must enter begins to flutter. This has an intermittent blanketing effect (Figure 6.12a) which obstructs entry of the air and the beginning of effective in-flow in a random way that may inordinately lengthen the filling process and so delay the initial growth of canopy drag. This problem has been attacked in different ways with varying effectiveness and utility. ***Opening springs*** are used in small pilot chutes. ***Skirt stiffeners*** have been moderately successful in some canopies but are little used because an effective degree of stiffness is incompatible with typical packing requirements. ***Pocket bands*** can be employed in any canopy that has an adequate degree of skirt arching between radials when fully inflated. These limit the inward motion of the fluttering skirt fabric between radials as shown in Figure 6.12b and so reduce the mouth blanketing effect and greatly increase the statistical frequency of air inflow events at this critical moment in the inflation process. The result is, the total filling time of the canopy is made more repeatable about is minimum value for any given set of operational conditions[364].

Canopy ***apex retraction*** with a central line (Figures 6.13 and 6.68) also may be employed as an inflation aid at low dynamic pressures[45,227,358,365,366]. Reduction of canopy tension by this means enables the skirt to expand more readily, but at the same time it transfers the peak inflation pressure away from the central vent to an annular region of less structural strength.

Use of small ***internal canopy*** to quickly open the mouth of a large canopy has been tested in various forms[45,358,365,366] and is being developed to a serviceable level for specific applications.

The ***flared skirt*** or bell-mouth canopy shape increases the average angle of attack of the skirt panels between radials. The ***Exeter*** and ***Ringsail*** parachutes have this characteristic.

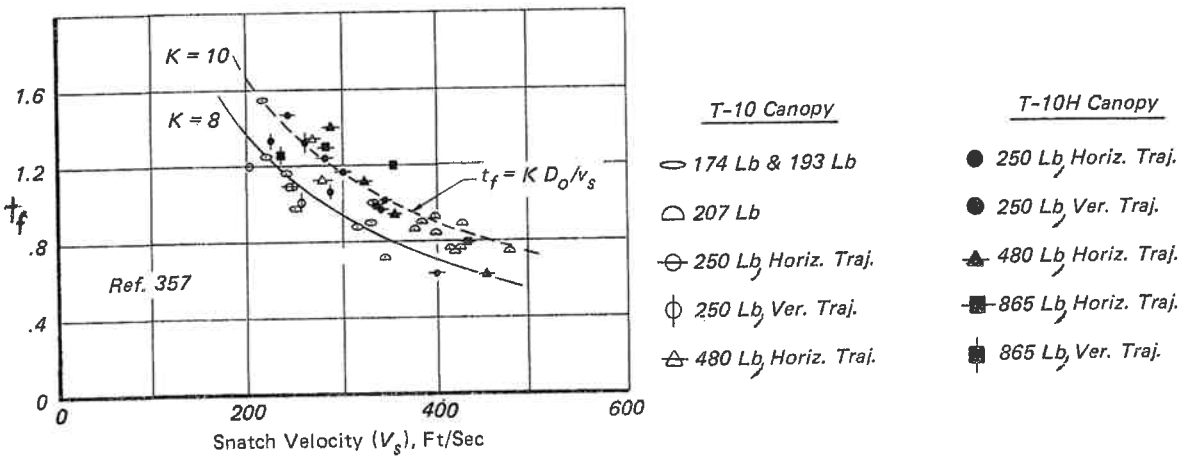


Figure 6.15 Measured Filling Time Vs Snatch Velocity of Solid Cloth Circular Parachute (Non-Reefed)

Canopy spreaders of the types described in Chapter 3, forcibly open the canopy mouth to a significant fraction of its final area. The effectiveness of the skirt spreading gun in terms of canopy opening time at different flight speeds is shown in Figure 6.13. The filling time is reduced significantly at low speeds, indicating a substantial reduction in the distance traveled, i.e., altitude lost during canopy inflation. Although the effect on filling time becomes small at intermediate to high speeds, the canopy mouth opening is greater than normal with a consequent shortening of the filling time and augmentation of the opening force, a feature important in air-crew escape systems which must operate safely over a broad spectrum of flight speeds [227, 367, 368]

Critical Opening Speed ("Squidding")

The critical (maximum) opening speed is defined as the lowest speed at which the canopy does not fully develop. For speeds above the critical opening speed a parachute opens only to a squid state; it will not open fully unless the speed is reduced.

O'Hara (Ref. 369) presents an analytical method for determining the critical opening speed. However, on the basis of experimental observation (Ref. 370), the critical opening velocity can be estimated by assuming that the drag of a squidding canopy is at least one-sixteenth the drag of the fully inflated canopy. This then means that if a canopy is selected with a critical opening speed not less than four times the equilibrium descent velocity, and the parachute is deployed at a velocity greater than its critical opening speed, the steady drag of the squidded canopy will be greater than the weight of the load (steady-state drag of fully inflated canopy), and the load will be continually retarded until the parachute canopy reaches the critical opening speed and it opens fully.

With respect to critical opening speed, the governing design parameters for a parachute canopy are:

(1) Total porosity or permeability of the canopy;
(2) Distribution of canopy porosity; and
(3) Shape of the canopy mouth opening.

The measured variation of the critical opening speed of solid cloth parachutes with effective porosity of the canopy is shown in Figure 6.14. The effective porosity in this case is for $\Delta p = 52$ *psf*, i.e., the British standard of 10 inches of water. Data points from Reference 356 are included, with $\lambda_m = 100$ *cfm/ft*^{2} for the 28 ft canopy corrected for the difference between Δp = 0.5 and 10 inches of water (see Figure 6.56). Note that at the period of Reference 371 the average air permeability of British parachute cloths ran two to three times that of U. S. parachute cloths. The unfavorable effect of this on the critical opening velocity of British parachutes was countered by development of the flared skirt of "Exeter" design.

Figure 6.14 shows that the critical opening speed is clearly an inverse function of the effective porosity, a logical consequence of two important factors:

(1) Inflation cannot proceed until the ratio of air inflow to air outflow becomes greater than unity.
(2) Inflation will continue until equilibrium is reached between internal air pressure and structural tension.

It is well known that parachute squidding can occur in any partially inflated condition. Other things being equal, the amount and distribution of porous

area across the canopy is the governing factor, and a relevant parameter would describe canopy porosity as a function of its radial position in the canopy [379].

Canopy Filling Time

The measured filling time of parachutes was found to vary inversely with true air speed at line stretch as shown in Figure 6.15. Also, it was noted that "the larger the parachute, the longer the filling time". From these observations came the familiar empirical formula for parachute filling time.

$$t_f = K D_o / v_s^n \qquad 6\text{-}7$$

which, with the substitution of v for v_s^n, may be written

$$K_s = t_f v / D_o \qquad 6\text{-}8$$

and K_s will be recognized as Scheubel's [380] constant filling distance expressed in canopy diameters. But since the average velocity, v, during the "finite mass" filling interval is not readily determined, the velocity at line stretch is used instead, and appropriate values for K and n are determined by curve fitting to measured data plots. For the flat circular ribbon parachute, Knacke [372] recommended the relationship

$$t_f = (8\, D_o / v_s^{.9})\, (\rho/\rho_o)^{.8} \qquad 6\text{-}9$$

where the altitude effect indicated by the density ratio was later deleted as inaccurate. No correlation of canopy filling time with either altitude or unit canopy loading is found in the data for the non-reefed solid cloth circular canopy presented in Figure 6.15. The 35 ft (D_o) extended skirt parachute in Figure 6.15 was deployed at altitudes ranging from near sea level to over 38 thousand feet [357]. The lightweight test specimens were of the standard T-10 troop parachute design with four 4-ft risers. The heavyweight test specimens were of the same basic geometry made of 2.25 oz nylon cloth (compared to 1.1 oz ripstop) and 1500 oz nylon cord (compared to 375 lb cord) but without the standard vent cap. Consequently, the average effective porosity of the T-10H canopy was approximately 34 percent greater than that of the standard T-10 canopy, the difference deriving mainly from the greater air permeability of the 2.25 oz cloth.

The difference in canopy effective porosities (estimated at $C \approx 0.032$ for the T-10 and $C \approx 0.043$ for the T-10H) causes a visible separation of the data points for the two versions in Figure 6.15, the more porous heavyweight canopies having the longer filling times. The simplified form of the filling time formula (Eq. 6-7 with $n = 1.0$) developed in Reference 357 is a convenient tool for appraising the significance of the discernable data trends in the figure. Below $v_s = 300$ fps no significant deviations from the constant filling distance theory are visible. The maximum filling time boundary of the T-10 canopy is delineated roughly by $K = 8$ while the mean filling time curve for the T-10H is marked by $K = 10$, both being reasonably valid to $v_s = 350$ fps. However, it was noted in Reference 357 that "a squidding velocity of approximately 325 fps appears to exist for the T-10 canopy, while the data for the high strength canopy design does not indicate a squid condition at speeds in excess of 400 fps".

Filling Intervals with "Infinite Mass". Most tests of drogue type decelerators approach the inifinite-mass case, and justify the assumption that $v = v_s$. This is reflected in the empirical formula derived by Fredette [374] for the filling time of slotted canopies. With $n = 1.0$

$$t_f = 0.65\, \lambda_g D_o / v_s \qquad 6\text{-}10$$

where $0.65\, \lambda_g = K_s$ is essentially equal to the canopy filling distance in nominal diameters. This relationship was derived from a number of subsonic and supersonic test measurements with a variety of experimental ribbon drogue parachutes compiled in References 209, 375 and 376. Despite the usual scatter, the data appeared to conform with this relationship well into the supersonic regime to about Mach 2.5. However, more recent work [19,377] has produced a general shift of the data toward longer supersonic filling times than are predicted by Equation 6-10.

Greene [378] shows good agreement between measured and predicted filling distances up to about Mach 2.5 in Figure 6.16, using the relationship

$$s_f / D_o = K_s\, (\rho_c / \rho_\infty) \qquad 6\text{-}11$$

where ρ_c is the air density in the canopy calculated with the assumption that at supersonic velocities the canopy fills behind a normal inlet shock. This assumption and given data supports the concept of a constant supersonic filling time for any given parachute, as exemplified by the straight line in the figure. Reasonable correlation with all data [19] is shown above Mach 1 up to Mach 3.2, the present maximum velocity attained in large parachute tests at altitudes in the range from 120 to 170 thousand feet. The results show a gradual transition from a roughly constant filling distance to a roughly constant filling time between Mach 0.3 and approximately Mach 1. This line of reasoning is strengthened by the empirical correction to Greene's theory presented in Reference 20.

A similar result is obtained by applying the density ratio to Equation 6-10 rearranged to a form

$$t_f / D_o = (.65 \lambda_g / v_s)\, (\rho_c / \rho_\infty) \qquad 6\text{-}12$$

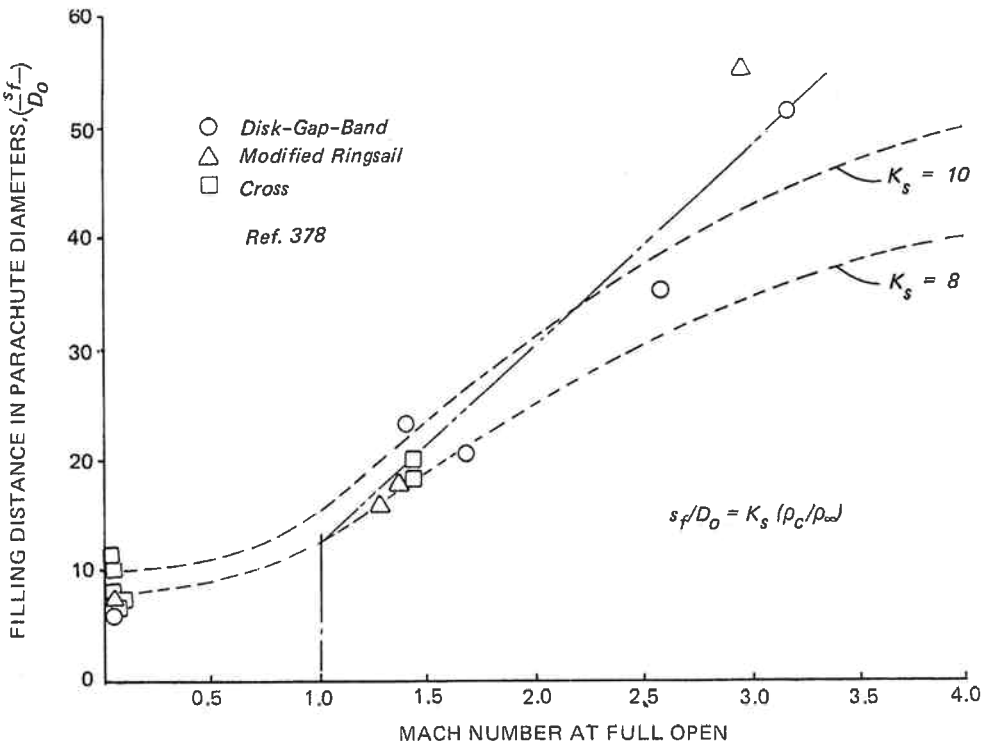


Figure 6.16 Effect of Compressibility on Filling Distance of Non-Reefed Parachutes

Comparison with empirical data in Figure 6.17 shows good correlation subsonically with Knacke's[372] ribbon parachute filling time (λ_g = *12.5* to *15* percent). The majority of the earlier measurements, also plotted, follow the general trend and it appears that Equation 6-10 would give increasingly unreliable results above v_s = *500 fps.*

Wolf[373], in the course of developing a simplified momentum theory of parachute inflation, defines another dimensionless filling time parameter in the relative filling distance form,

$$t_f^* = t_f v_o / r_p$$

and finds good correlation of this parameter with parachute mass ratio

$$R_m^* = 3m_p/\rho 4\pi r_p^3 \qquad 6\text{-}13$$

and Mach number as shown in Figure 6.18. The curves were computed for the disk-gap-band parachute for which available empirical data were of good quality. It can be demonstrated that a cross-plot of t_f^* at any mass ratio, R_m^*, on the theoretical curves between Mach 1.5 and 3 shows a linear relationship of filling distance with Mach number similar to that suggested in Figure 6.16. This further indication that the filling time of a given parachute may be constant in supersonic flow tends to support Greene's thesis that filling takes place behind a normal inlet shock. All canopies necessarily start filling as elongated tubular ducts, a form most likely to generate a normal shock at the inlet, and the data seem to attest that above Mach 1.5 to at least Mach 3 the airflow velocity into the canopy mouth stays nearly constant. Supersonic parachute dynamics after full inflation is another matter; the shock pattern has been observed to fluctuate rapidly between normal and oblique as the canopy pulsates. When test specimens of optimal supersonic drogue design are used and the variable opening element in their operation minimized, likely the inflation characteristic will fall somewhere between the limits represented by Equations 6-10 and 6-12. This can be anticipated on theoretical grounds when it is allowed that the inlet shock could change from normal to oblique during the inflation process. Then the average inflow velocity would be greater than sonic and the average air density less than is predicted for the normal shock case.

Reefed Canopy Filling Intervals. The reefed canopy fills like a non-reefed canopy for a short interval until the reefing line comes taut. Thereafter, the filling slows to a lower rate that may continue throughout the reefed interval. Canopy growth during the reefed interval is slight for most designs of normal porosity, and significant for both low porosity (high-

glide) and ringsail designs. The reefed Parawing, for example, develops bulbous lobes which are quite large in proportion to the reefed inlet area. The reefed Sailwing also exhibits a pronounced bulbous development. At disreefing, the canopy opens quickly and inflation is completed at a faster than normal rate because the reefing line is under tension when severed.

Dimensionless filling parameters for reefed canopies may be defined in various forms of which the following is a useful example:

$$K_s = \Delta t_{12} v_{12}/D_o \qquad 6\text{-}14$$

where Δt_{12} is the time required for the canopy to inflate from its initial condition at either line stretch or disreef to the full condition for the given stage, and v_{12} is the average velocity over the filling interval as in Equation 6-8.

Measured Filling Distance. In parachute tests approximating infinite mass conditions and well-instrumented finite mass tests, it is possible to determine the average velocity during the canopy filling intervals, because either the initial velocity does not decay significantly during filling or the velocity-time history is known. Values of the relative filling distance, K_s, calculated by substitution of test data of this type in Equations 6-8 and 6-14 are given in Table 6.1 for a number of different parachutes both reefed and non-reefed. For some of the non-reefed parachutes, finite mass conditions prevailed at low altitude while infinite-mass conditions prevailed at very high altitudes. Data for evaluation of the relative filling distance after disreefing under finite mass conditions are less available as indicated.

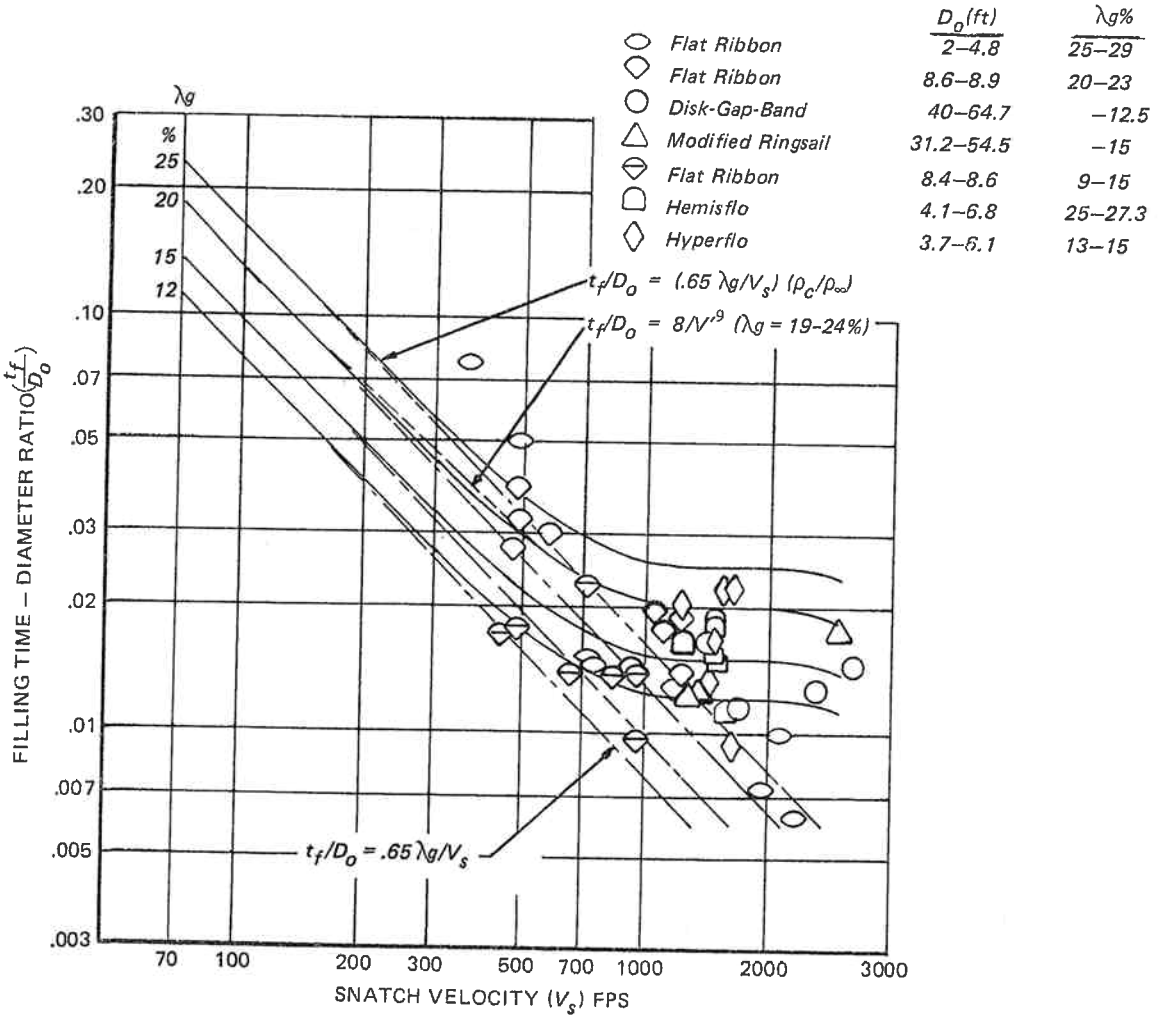


Figure 6.17 Apparent Variation of Filling Time With Velocity for Slotted Canopies (Infinite Mass Condition)

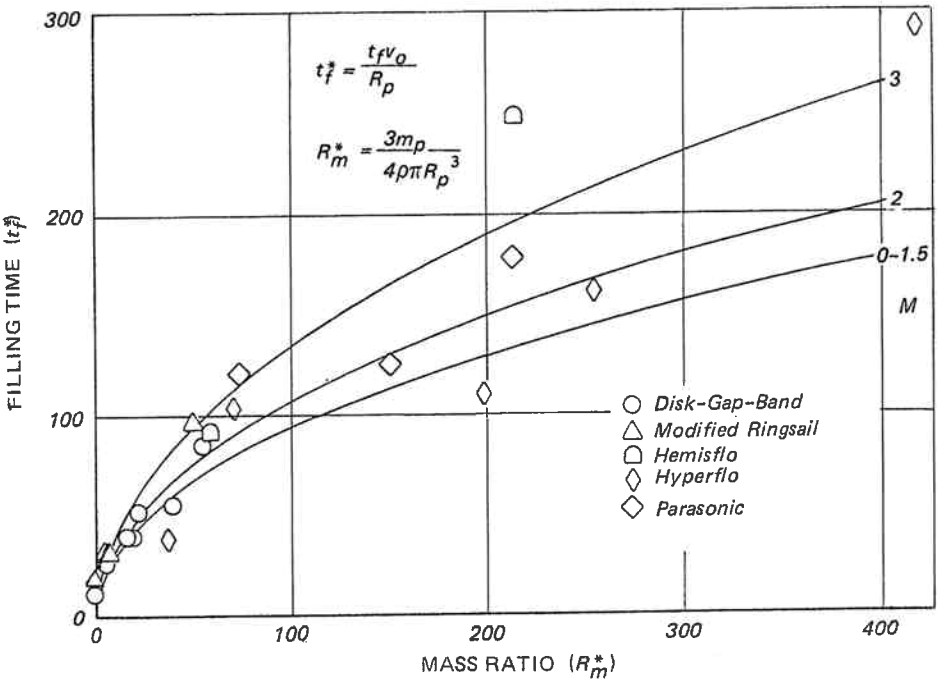


Figure 6.18 Upper Limit Effect of Compressibility on Parachute Filling Distance (Ref. 373)

Opening Forces

During the inflation of a parachute or similar towed ballistic type decelerator an aerodynamic force is developed tangential to the flight path that varies with time in the characteristic ways illustrated in Figures 6.19, 6.21, 6.22 and 6.23.

The opening force characteristics of solid cloth circular parachutes have been comprehensively evaluated in full scale aerial drop tests and analyzed in great detail by Berndt and DeWeese[381] using Air Force Type C-9 28 ft (D_o) personnel parachute as a test model. Similar work was carried out by Watson and DeWeese[357] with two structural versions (light and heavy) of the Type T-10 35 ft (D_o) 10% flat extended skirt parachute. Figure 6.24 utilizes data from the C-9 tests to provide a correlation between canopy shape during inflation and the corresponding instantaneous force. One point of interest is (6) which is near the initial force peak and represents the completion of that portion of the inflation process where the canopy is filling from "skirt-to-vent" (see inflation stage (c) in Fig. 6.9A). Additional force-time histories from the C-9 tests as shown in Figures 6.19 and 6.20 exhibit the pronounced double force pulse of this parachute, the second peak occurring close to full inflation.

The relative magnitude of the two peak forces, F_i/F_o, varies with snatch velocity, altitude, flight-path angle, and canopy loading as shown. The ratio of the initial to final peak loads, is shown to be strongly dependent on parameter A_K in Figure 6.20 a.

By definition

$$A_K = (F/\epsilon W_b)^{1/3} (\rho_o D_o^3/m_b)\, \sigma^{2/3} \qquad 6\text{-}15$$

where ϵ is the instantaneous elongation of the suspension lines in percent, based on an assumed linear spring constant for the suspension line bundle defined as

$$\kappa = P_u Z/\epsilon_u l_s$$

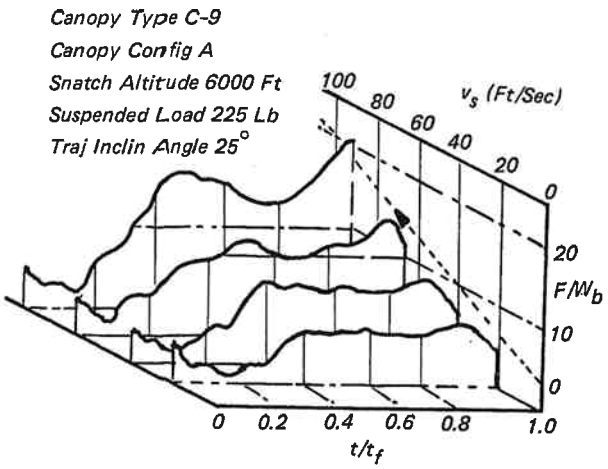
such that

$$\epsilon = FZ/\kappa_u l_s$$

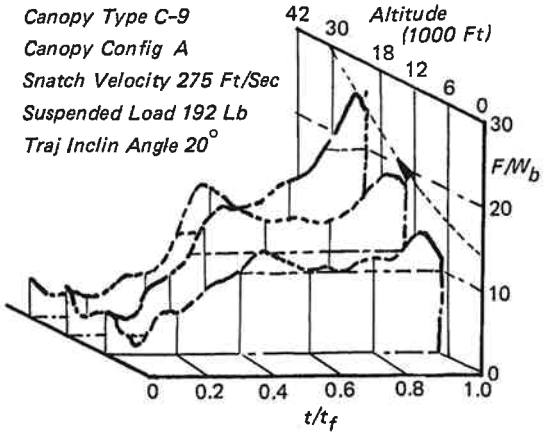
In short, the force ratio is a function of the elastic properties of the parachute structure as well as the system mass ratio and the density altitude (See also Reference 383).

The effect of Froude number on the maximum opening force parameter, $F_o/q_s S_o$, is shown to be small but significant in Figure 6.20 for different values of

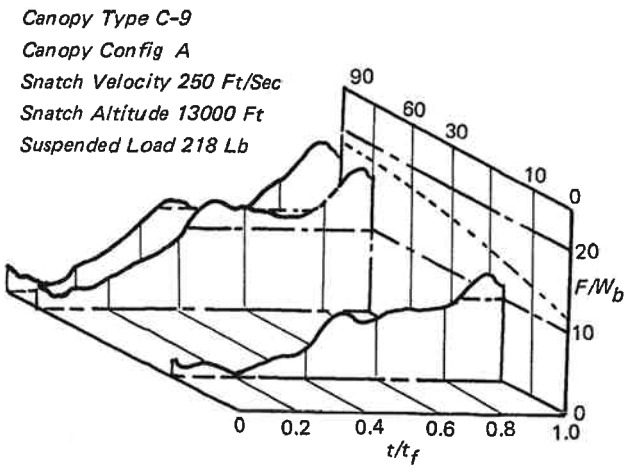
$$Fr^2 = v_s^2/D_o g \sin\theta$$



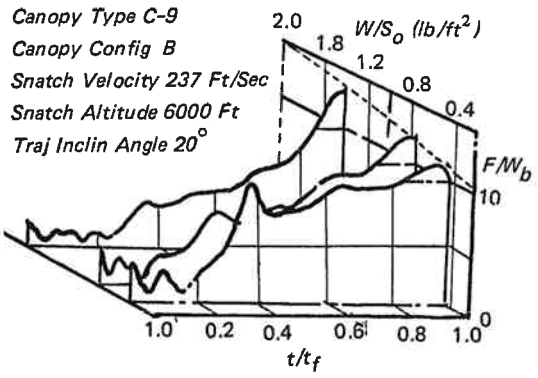
a) EFFECT OF VELOCITY AT SNATCH, v_s



b) EFFECT OF ALTITUDE AT SNATCH



c) EFFECT OF TRAJECTORY INCLINATION ANGLE



d) EFFECT OF CANOPY LOADING PARAMETER, W/S_o

Figure 6.19 Solid Cloth Circular Parachute Opening Force Characteristics Non-Reefed (Ref. 381)

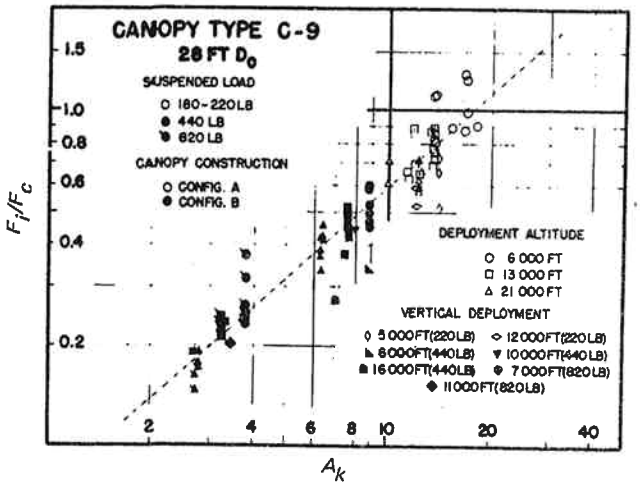
TABLE 6.1 PARACHUTE AVERAGE RELATIVE FILLING DISTANCES (MEASURED)

Parachute Type	Dia. D_o (ft)	Total Porosity λ_T (%S_o)	Reefing (% D_o) R_1	R_2	Mach No.	Rel. Fill Dist. (K_s) R_1	R_2	F.O.	Source Ref.
Modified Ringsail	85.6	12.5	10	26	.27	7.4	1.3	1.14	217
Ringsail	88.1	7.2	11	–	.27	7.6	–	I.D.	
Ribbon	8.6	14.6	–	–	.86	–	–	9.0	375
(Flat)	–	21.2	–	–	1.10	–	–	14.0	
	–	23.3	–	–	1.10	–	–	20.6	
Rotafoil	6.0	17.6	–	–	.46	–	–	18.3	
(G = 8)	7.0	23.1	–	–	.67	–	–	31.0	
Ribless	9.8	60*	–	–	.36	–	–	4.75	
Guide	–	–	–	–	.51	–	–	4.05	
Surface	–	–	–	–	.65	–	–	3.50	
	–	35*	–	–	1.10	–	–	6.0	
Ringsail	29.6	14.2	10.3	20	.57	8.0	I.D.	I.D.	217
	56.2	7.1	–	–	.20	–	–	7.0	
	63.1	7.1	12.0	–	.30	5.3	–	I.D.	
	84.2	7.7	10.5	–	.3-.4	5.4	–	2.56	
	128.8	9.8	12.5	–	.30	5.3	–	1.4	
Extended Skirt (10%)	34.5	100*	8.1	–	.45-.61	1.9	–	I.D.	1
Disk-Gap	40.0	12.5	–	–	<.2	–	–	6.0	19, 378
Band	–	–	–	–	3.2	–	–	51.0	
Cross	30.0	–	–	–	<.2	–	–	10.0	
	–	–	–	–	1.4	–	–	18.0	
Modified	31.2	15	–	–	<.2	–	–	7.0	
Ringsail	–	–	–	–	2.95	–	–	55.0	377
Full Ext. Skirt (14.3%)	67.2	100*	7.1	–	.35-.51	3.4	–	I.D.	200
Hyperflo	3.7-6.0	15	–	–	1.05	–	–	23.0	376
	–	–	–	–	1.4	–	–	36.0	
Hemsiflo	5.5-6.8	27	–	–	1.1	–	–	20.0	
	–	–	–	–	1.3	–	–	23.0	

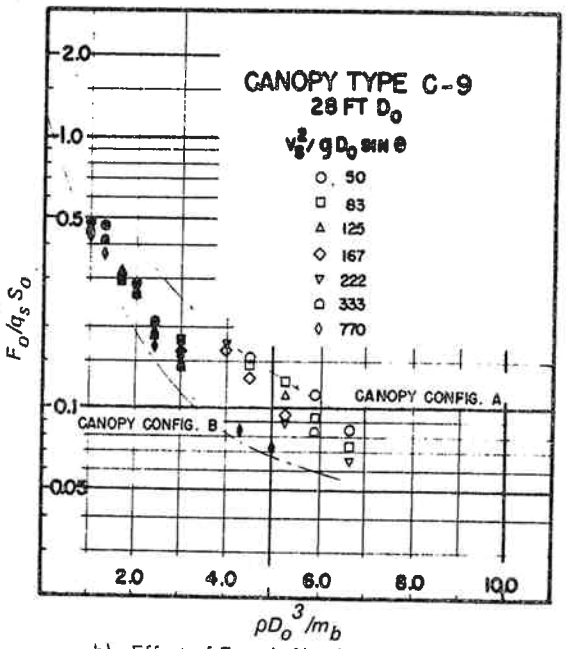
NOTE: I. D. = Insufficient Data; *Material Permeability in CFM/Ft^2

C-9 Configuration: A - Std lightweight construction

C-9 Configuration. B - Canopy. 90 lb/in 2.25 oz/yd^2 cloth
Lines: 1500 lb Braided cord



a) Variation of Peak Force Ratio With Parameter A_k



b) Effect of Froude Number on Opening Force Parameter vs Mass Ratio

Figure 6.20 Opening Force Characteristics, Type C-9 Parachute

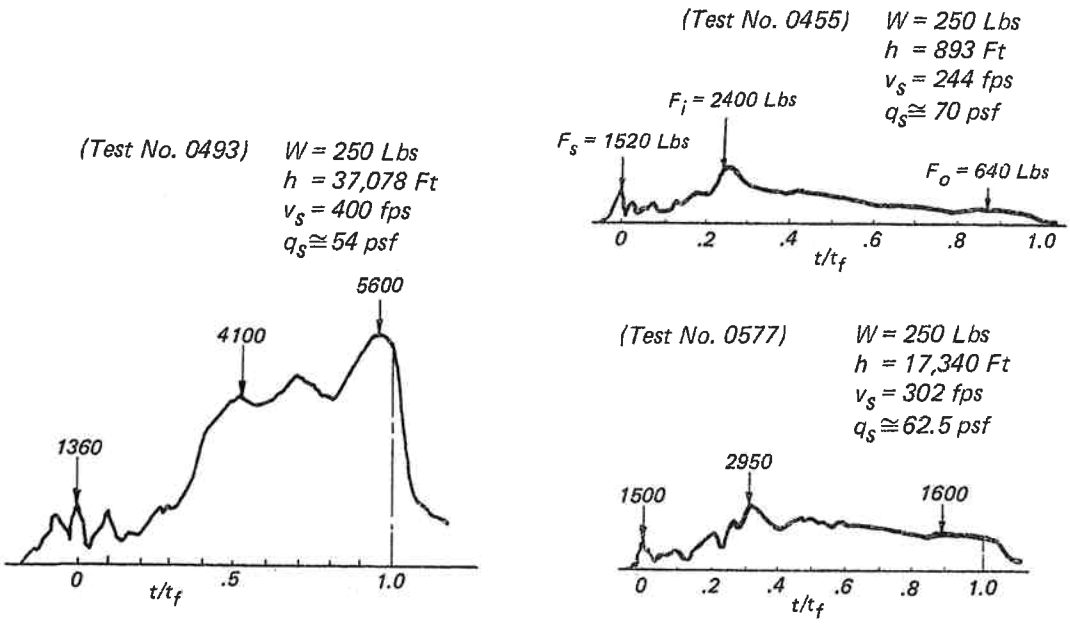


Figure 6.21 Measured Force vs Normalized Time During Inflation of T-10H (High Strength) 35 Ft (D_o) 10% Extended Skirt Parachute Deployed Lines - First Horizontally from Cylindrical Vehicle (Ref. 357)

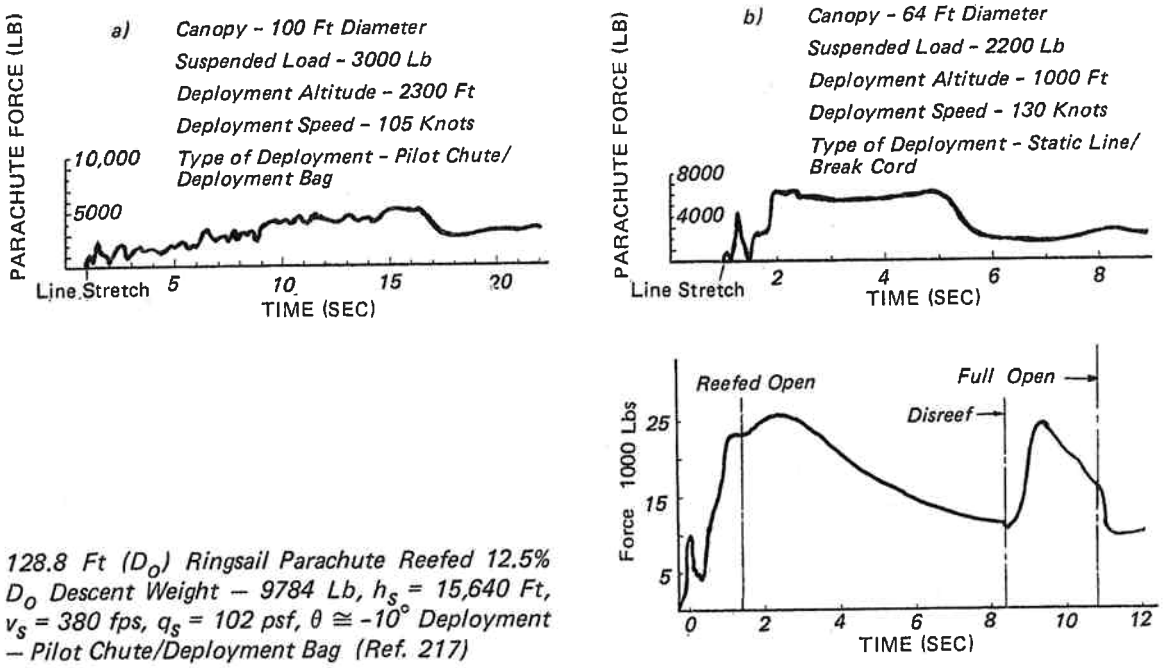


Figure 6.22 Airdrop and Recovery Parachutes - Typical Opening Force vs Time

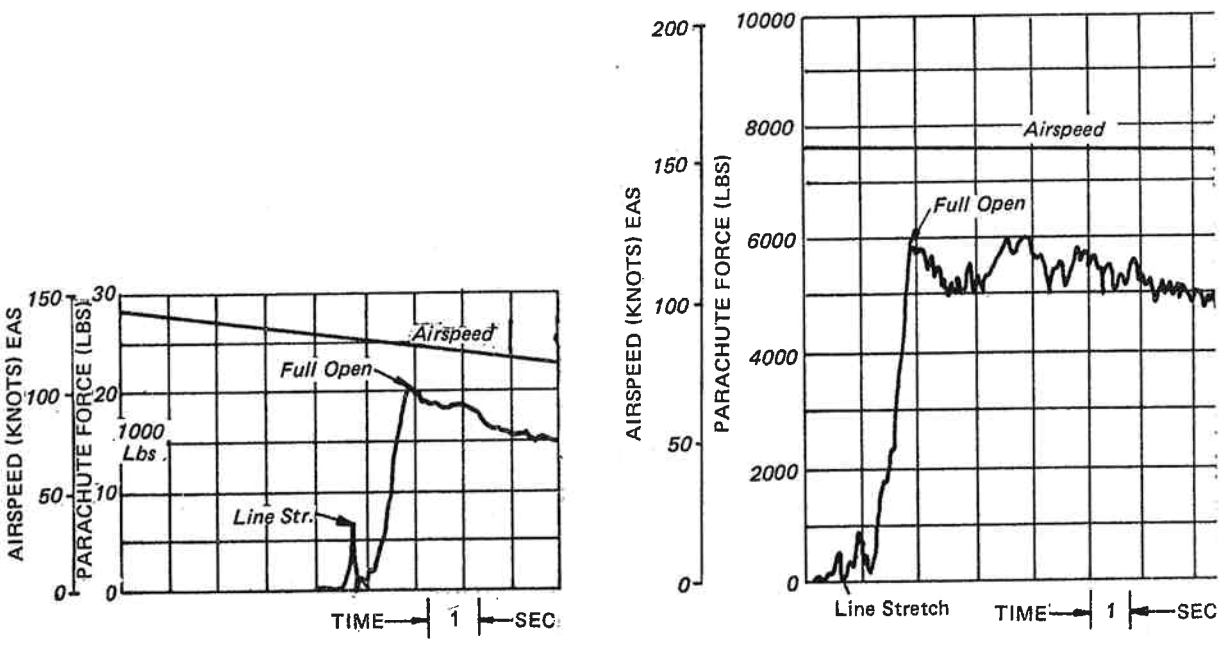


Figure 6.23 Typical Opening Forces of Aircraft Deceleration Parachutes (Ref. 382)

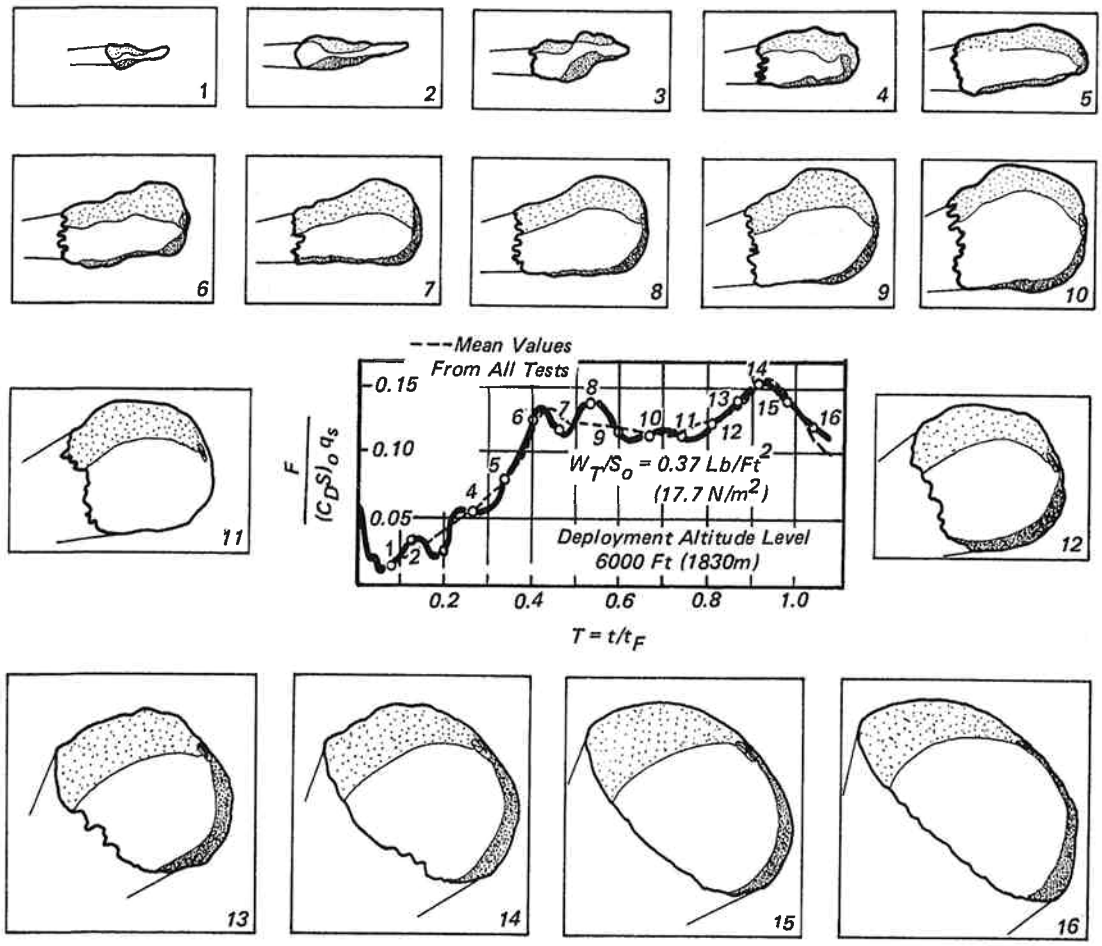
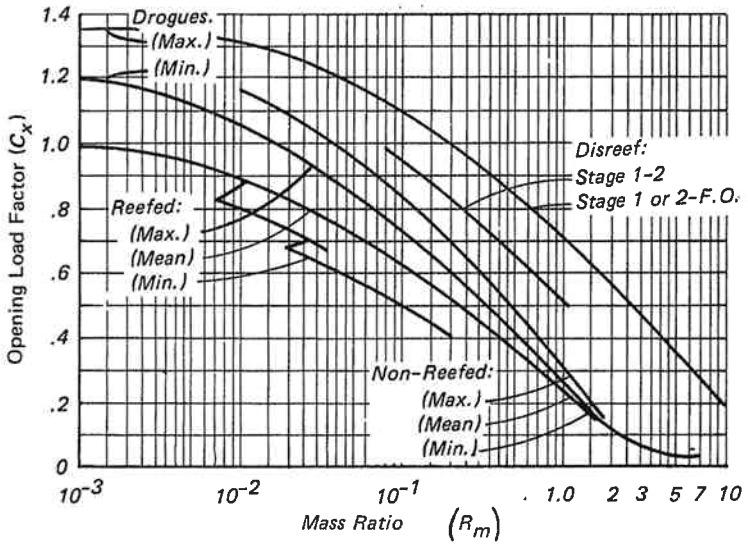
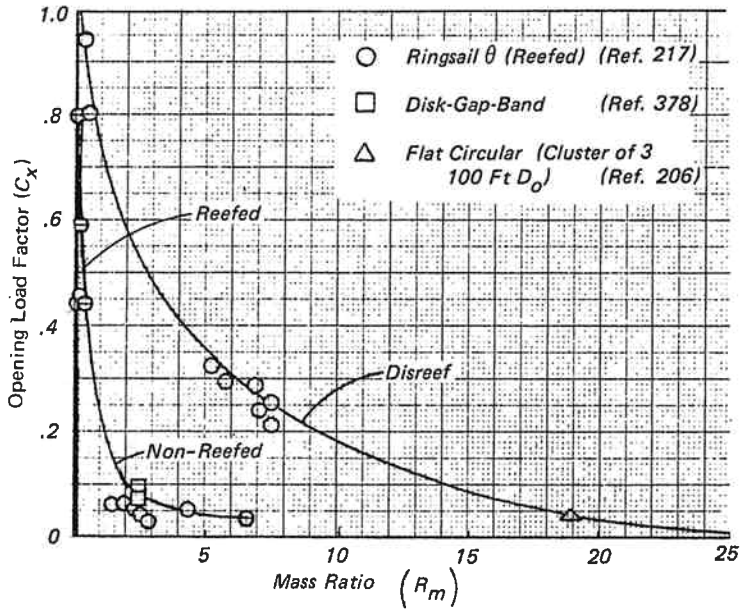


Figure 6.24 Comparison Between Inflating Canopy Shape and Generated Force.

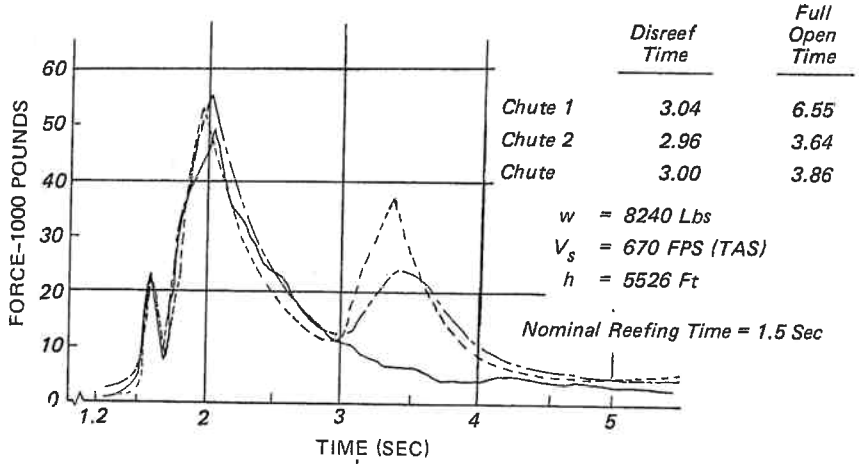


a) Averaged Composite Data From Many Sources

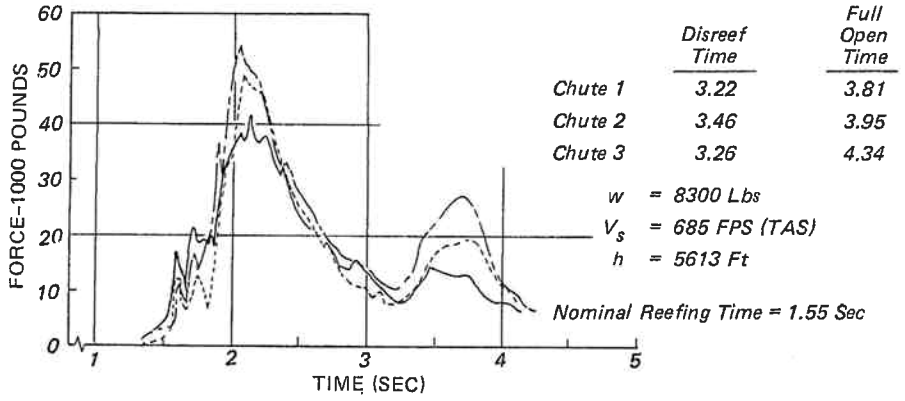


b) Selected Parachute C_x Avg. Disreef to Full and Non-Reefed

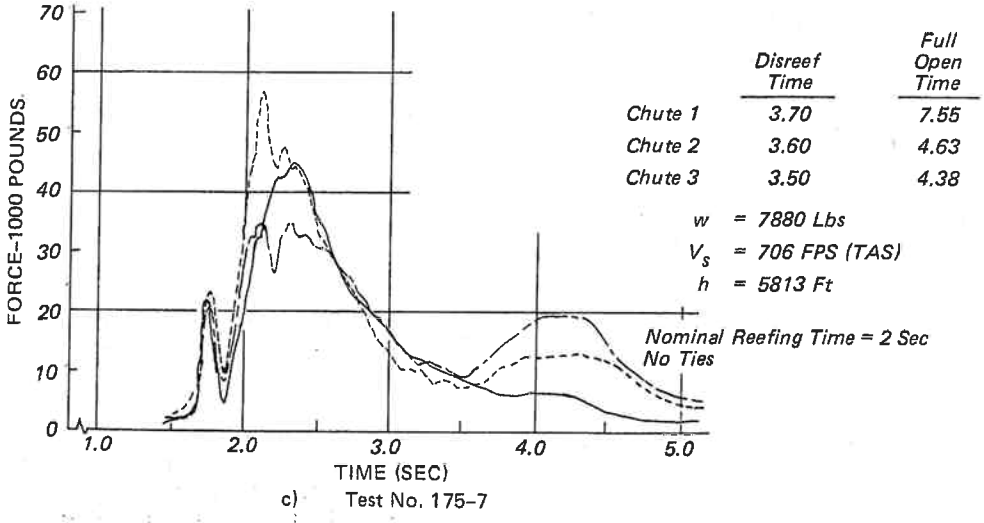
Figure 6.25 Parachute Opening Load Factor Vs Mass Ratio



a) Test No. 175-2



b) Test No. 175-3



c) Test No. 175-7

Figure 6.26 Opening Forces of 48 Ft (D_o) Ribbon Parachute in Clusters of Three with Canopies Tied Together at Skirt Tangency Points (Ref. 386)

in which the flight path angle, θ, is assumed to be essentially constant during the filling interval.

The Opening Load Factor. Typically the instantaneous force applied to the body during the canopy filling interval rises to a peak and then declines. The maximum opening force is represented by the dimensionless ratio, F_X/F_c, which was formerly called the "opening shock" factor (X). But in order to reserve the term "shock" for acceleration and onset effects, the ratio has been re-identified as the ***opening load factor***

$$C_X = F_X/F_c \qquad 6\text{-}16$$

where

$F_c \triangleq C_D S q_s$ (a fictitious steady drag force)

$C_D S$ = drag area at the end of the filling interval

q_s = dynamic pressure at the start of the filling interval = $\rho V_s^2/2$

Thus, for load estimating purposes the maximum opening force is calculated with the familiar empirical formula

$$F_X = C_D S\, q_s\, C_X \qquad 6\text{-}17$$

Empirical opening load factors are determined for reefed as well as non-reefed canopies. It is generally assumed that irrespective of the decelerator deployment method used the beginning of the filling interval is signaled by the snatch force for the first stage and by disreefing for subsequent stages.

It has been found that the peak opening load factor, C_X, of each stage under any given set of initial conditions is mainly a function of the system mass ratio as defined[384] as

$$\rho D_o^3/M$$

where

M = mass of body and decelerator

Other significant parameters influencing C_X in varying degrees are Froude number, Mach number, and a structural elasticity parameter that is called Kaplun number here for the investigator who first proposed it[385].

The relationship $C_X = f(\rho D_o^3/M)$ provides a useful tool for the correlation of empirical opening force data obtained from full-scale aerial drop tests when the mass ratio is defined in the form developed by French for non-reefed parachutes[384] and later modified for convenience in Reference 361.

$$R_m = \rho (C_D S)^{3/2}/M \qquad 6\text{-}18$$

where $(C_D S)^{3/2}$ represents the volume of air associated with the canopy in a form that can be determined readily for reefed as well as non-reefed decelerators of all types.

Empirically derived values of C_x and R_m, averaged graphically for a number of different parachutes to establish general trends, are plotted in Figure 6.25.

It will be shown in Chapter 7 how the slopes of the curves aid evaluation of the relative loads in clustered parachute during non-synchronous inflation. For this purpose the curves have been extended in Figure 6.25b to encompass the mass ratios of large lightly loaded parachute systems. Note that because R_m decreases with altitude, systems, such as the Viking Mars lander drogue chute tested at both low and very high altitudes, may have mass ratios in the order of $R_m \approx 2$ at low altitudes and $R_m \approx 10^{-2}$ at altitudes over 120 thousand feet.

Infinite Mass Load Factors. Model parachute inflation tests in the wind tunnel, full scale aircraft deceleration tests, and tests with very low system mass ratios are sources of the infinite-mass opening load factors given in Table 2-1 (Chapter 2). These may be considered minimum infinite-mass C_X values for parachutes of conventional nylon construction with canopy cloth and geometric porosity appropriate to each type. The given values of C_X are applicable to the estimation of parachute opening forces under near-infinite mass conditions at any altitude and over deployment velocity ranges appropriate to recorded test experience with each type.

Clustered Parachute Opening Forces

Representative force-time traces of parachutes in clusters are presented in Figures 6.26 and 6.27. Statistically, good synchronism of cluster parachute operation is a rare event, the norm being a marked lack of synchronism of inflation and large disparities in the opening loads experienced by the individual parachutes. This is true even when the parachutes are deployed simultaneously by a common pilot chute, begin to inflate at the same time, and disreef at the same time.

The disparity of cluster parachute operation may be evaluated as the ratio of individual peak opening forces to their mean value. The mean force is not necessarily the load each parachute would feel with synchronous inflation but in many cases is close to it. Summarized in Table 6.2 are representative examples of extremes encountered in various cluster test programs. Calculated mean values are in parenthesis; only maximum force ratios are noted. Performance of a statistically adequate number of tests would widen the extremes in some cases.

Although the possible mass fraction any one parachute may have to carry increases with the number of canopies in the cluster, the probability that a disproportionate number will lag through a large part of the

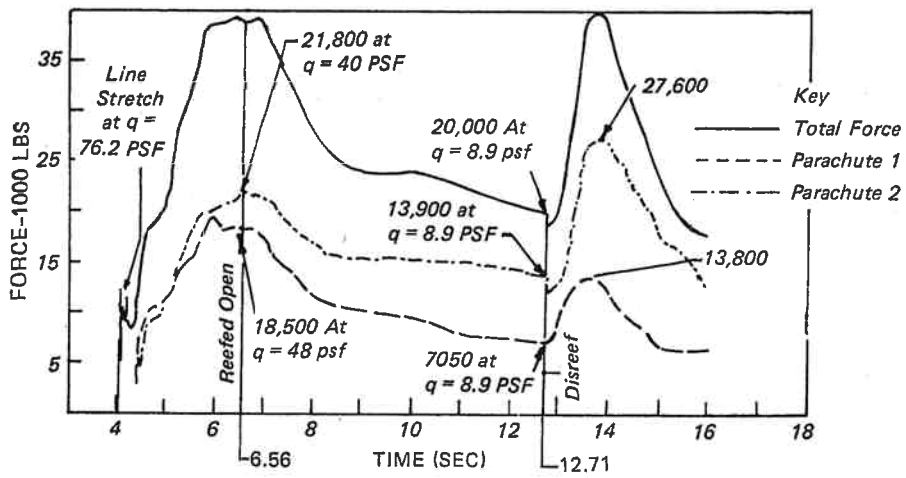


Figure 6.27 Opening Force-Time History for Cluster of Two 12.8 Ft D_o Ringsails Reefed 13% D_o for 8 Seconds Deployed at 299 FPS (TAS) at 10,246 Feet Altitude (Weight = 17,720 Pounds) (Ref. 217)

lead-canopy filling time diminishes. Systems having high peak deceleration may have a potential for a greater disparity of opening forces than was recorded.

What emerges from the test evidence is that the dominant operational characteristic of uncontrolled parachute clusters within the present state-of-the-art is one of highly erratic or non-uniform opening performance. On the other hand, the controlled B-1 capsule cluster described in Reference 360 exhibited a max/mean opening force ratio less than 1.3, which constitutes a strong endorsement of the permanently attached pilot chute technique developed in that program.

STEADY AERODYNAMIC FORCES

Typically, a deployable aerodynamic deceleration system begins to decelerate during the canopy inflation process. After the opening force transient and full inflation, canopy drag remains as the prime decelerating force.

Drag Coefficient

A body moving through air encounters a resistance commonly called drag, made up of pressure, inertial, and viscous forces generated or modulated by the following physical factors working together in varying degrees, as described by Howarth[387]

$$D = f(\rho v^2 l^2 R_e \sigma_M \epsilon_{Fn} \eta) \qquad 6\text{-}19$$

When the moving body is a parachute-like air-inflated decelerator made of flexible materials at least two additional parameters appear; structural elasticity and canopy porosity. With the introduction of an empirical aerodynamic drag coefficient, equation 6-19 is simplified to

$$D = C_D q S \qquad 6\text{-}20$$

and C_D depends upon body shape, Reynolds number, Mach number and Froude number for the rigid body of classical aerodynamics, and also upon Kaplun number, or relative elasticity, and the porosity of the flexible decelerator.

It is convenient to relate parachute drag coefficients to the canopy nominal area, S_o, derived from the design dimensions because accurate measurement of the inflated canopy for the determination of the projected area and C_{D_p} is seldom feasible. Therefore, the elastic expansion of the canopy under load is neglected. Also, C_{D_o}, calculated from an average measured value of $C_D S$, provides a fair criterion of the drag efficiency of the canopy which is not reflected by C_{D_p}. However, where purely aerodynamic considerations are the center of interest, it is desirable to evaluate C_{D_p} by the best method applicable to the available data.

Measured decelerator drag coefficients in general are influenced by a variety of factors including descent characteristics, airmotion, Mach number, and often the wake of the towing body. After these effects are accounted for the drag coefficient is found to vary with specific decelerator design parameters that affect the inflated shape and effective porosity of the canopy. Salient design parameters include: the shape of the gore pattern, effective length of suspension lines, air permeability of the fabric and geometric porosity. Scale or Reynolds number, relative elasticity, and the stiffness of the canopy also affect C_D but to a lesser degree. Among the various shape factors, fineness ratio is significant because it relates to the area ratio S_p/S_o. Clustering may be treated as a gross shape factor of the parachute system.

TABLE 6.2 MEASURED OPENING FORCES OF CLUSTERED PARACHUTES

No.	Parachutes D_o (ft)	Type	Test No.	W (lbs)	Launch v_o EAS (kts)	h (ft)	Peak Opening Forces Reefed lbs	Reefed Ratio*	Disreefed lbs	Disreefed Ratio*	Reef D_r/D_o (%)	Source Ref.
2	78	Extended Skirt	11	4946	150	2000	7400	1.20	5000	1.09	8.2	1
							4900	–	4200	–		
							(6150)	(1.0)	(4600)	(1.0)		
			12	4946	150	2000	5400	–	5400	–	8.2	
							6400	1.08	8300	1.22		
							(5900)	(1.0)				
3	48	Ribbon	6191	9370	427	5800	20200	–	19040	–	17.2	386
							55610	1.37	67810	1.42		
							46160	–	55910	–		
							(40657)	(1.0)	(47587)	(1.0)		
			175-7	8900	430	5900	44930	–	6530	–	17.2	
							56520	1.25	12790	–		
							34600	–	19430	1.50		
							(45350)	(1.0)	(12917)	(1.0)		
3	100	Solid Conical	58-828	11620	260	2450	13200	1.20	19450	2.08	6.4	206
							~8200	–	~550			
							11600	–	8000	–		
							(11000)	(1.0)	(9333)	(1.0)		
			58-921	10616	280	2500	12200	1.02	10800	–	6.4	
							11900	–	14000	1.17		
							11800	–	12000	–		
							(11970)	(1.0)	(12000)	(1.0)		
2	85.6	Ringsail	41-1	~9500	~150	15000	20300	1.12	22580	1.51	9.5 (mid-gore)	
							16090	–	7310	–		
							(18210)	(1.0)	(14945)	(1.0)		
2	128.8		8	17720	152	10250	21800	1.06	27600	1.33	13.0	
							19400	–	13800	–		
							(20600)	(1.0)	(20700)	(1.0)		
2	85.6	Modified Ringsail	48-4	10842	151	15190	14091	–	27320	1.49	8.4 (R-1)	
							16630	1.08	9321	–		
							(15360)	(1.0)	(18320)	(1.0)	24.8	
3	69.8		MQT-2	8510	240	15500	13250	1.11	3760	–	12.50	388
							12400	–	12500	–		
							10250	–	17900	1.57		
							(11967)	(1.0)	(11387)	(1.0)		
			MQT-14				11250	–	11000	–	8.85	388
							10400	–	9750	–		
							12500	1.10	14500	1.23		
							(11383)	(1.0)	(11750)	(1.0)		
			MQT-13				17750	–	8000	–	12.5	388
							24750	1.22				
							18450	–	9700	–		
							(20317)	(1.0)	(9400)	(1.0)		

Axial Force Coefficient

It is customary to use the term "tangential" with reference to vectors tangent to the flight path, the term "axial" is used instead when defining components of force and motion applied along the major longitudinal axis or axis of symmetry of the decelerator. The axial force equals the decelerator drag coefficient at angle of attack, $\alpha = 0$. The axial force coefficient, C_A, presented in Figure 6.28 are calculated from test data obtained on model wind tunnel tests (Ref. 389). The axial force coefficient is calculated as follows:

$$C_A = F_A/qS \qquad 6\text{-}21$$

The speed for these tests was $M = 0.1$. Axial force data for tests [391] with similar canopy designs at $M = 0.5$ and 0.8 are shown in Figure 6.29.

Parachute Cluster Drag Coefficient

The cluster drag coefficient C_{D_C} is less than C_{D_o} of the individual parachutes, the ratio C_{D_C}/C_{D_o} being inversely proportional to the number of parachutes as shown in Figure 6.30. While differences in rate of descent account for some differences in C_{D_C}, the data spread is too large to be the result of this factor alone. The divergent trends suggest the presence also of differences in both parachute and cluster rigging geometry not evident in the source information.

The effective rigging length used for reference purposes, and sometimes in cluster design, is based on the equivalent single parachute length ratio, $l_e/D_o = 1.0$. In terms of the nominal diameter of the individual canopies of the cluster this converts to

$$l_C/D_o = (n_C)^{1/2} \qquad 6\text{-}22$$

where l_C is the combined lengths of suspension lines and cluster risers to the riser confluence, and n_C is the number of canopies in the cluster. The following numerical values are obtained:

TABLE 6.3 EFFECTIVE RIGGING LENGTH FOR CLUSTERED PARACHUTES

n_C	2	3	4	5	6	7
l_C/D_o	1.41	1.73	2.0	2.24	2.45	2.65

For practical reasons, shorter rigging lengths are used in airdrop clusters of G-11A, 100 ft D_o and G-12D, 64 ft D_o parachutes: (See Table 6.4)

Empirical data from different sources on the normalized drag coefficients of clustered parachutes are plotted in Figure 6.30. The relative rigging lengths of the individual parachutes and of the clusters are indicated where known.

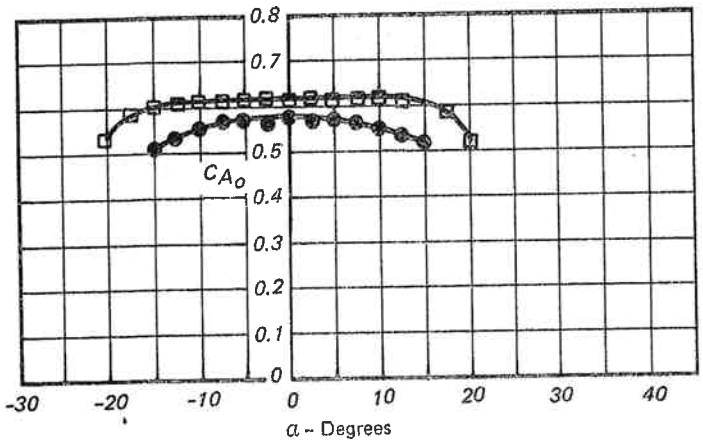
TABLE 6.4 EFFECTIVE RIGGING LENGTH FOR CLUSTERED G-11A AND G-12D PARACHUTES

	n_C	2	3	4	5	6	7
G-11A	$\frac{l_C}{D_o}$	1.2	1.4	1.6	1.8	1.8	2.2
G-12D	$\frac{l_C}{D_o}$	1.31	1.31	–	–	–	–

It will be seen that in steady descent the individual canopies stand apart, as in Figure 6.31. They also tend to wander about, constrained somewhat by the number in the cluster. Apparently the flowfield has a radial component away from the system axis in addition to the familiar pattern of flow about each canopy, which would tend to hold them apart, but this is not strong enough to prevent the canopies from occasionally contacting each other lightly. Thus, on the average it would appear that the mean relative flow at each canopy has an angle of attack of roughly $\alpha = 0$ degrees, provided the canopy is not gliding [390]. Since the cluster as a whole does not glide, the only way the member canopies might glide is to move away from the system axis and stand at an angle of attack to the relative flow. This behavior would result in some flattening of the outer or leading edges of the canopies and so would be visible in film records. That such evidence has not been observed tends to support the idea that on the average $\alpha \approx 0$ degrees, and random shifting of the aerodynamic force vectors driven by vortex shedding, causes the canopies to wander, possibly seeking a stable angle of attack. This reasoning justifies the proposition that the cluster drag coefficient may be represented as

$$C_D = C_{D_o} \cos \phi_C \qquad 6\text{-}23$$

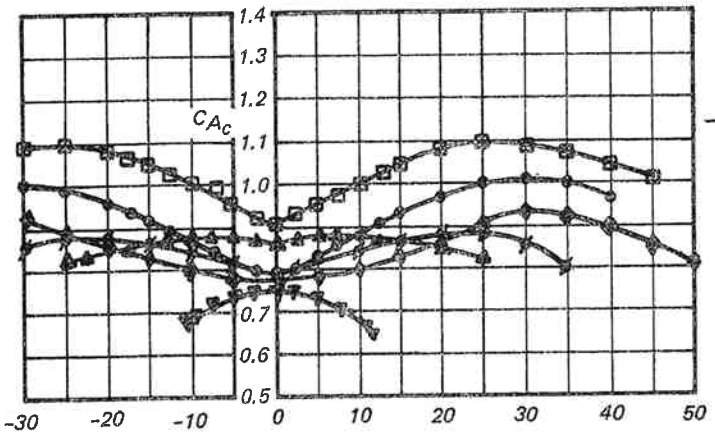
where ϕ_C is the integrated average angle of the cluster risers from the system axis. The implicit assumptions here are that there is not mutual interference and the dynamic pressure felt by each canopy is equal to q_e, i.e., the same as its equilibrium dynamic pressure descending alone at the system rate of descent. The angle ϕ_C is mainly a function of l_C/D_o and has its minimum value when all the canopies of the cluster are in contact with each other, as some have been rigged on occasion with tangent points on the skirt bound together. Then presumably, C_{D_C} would be a maximum and the assumption of non-interference may be tested by comparative evaluation.



☐ *Ringslot*

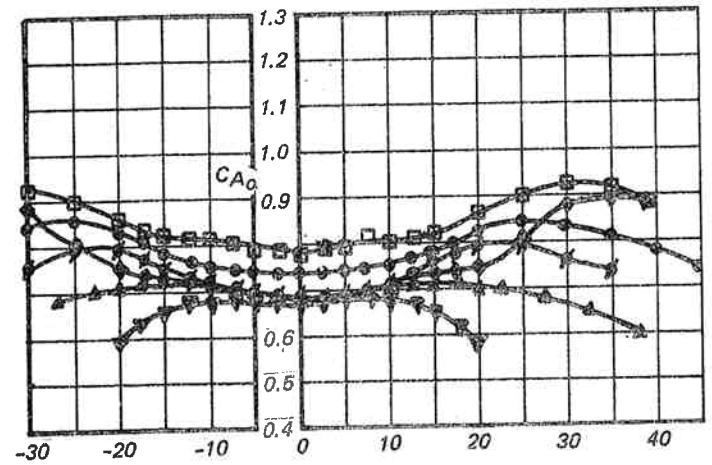
● *Ribbon*

A) Ringslot (50 Inch Prototype) and Ribbon (100 Inch Prototype), λ_g = 20%



SYMBOL	PERMEABILITY (Ft^3/Ft^2-Min)		EFFECTIVE POROSITY
▼	275		0.096
▲	120		0.042
●	30		0.010
◕	10		0.003
◆	(Rigid)	0	0.0
☐	(Flexible)	0	0.0

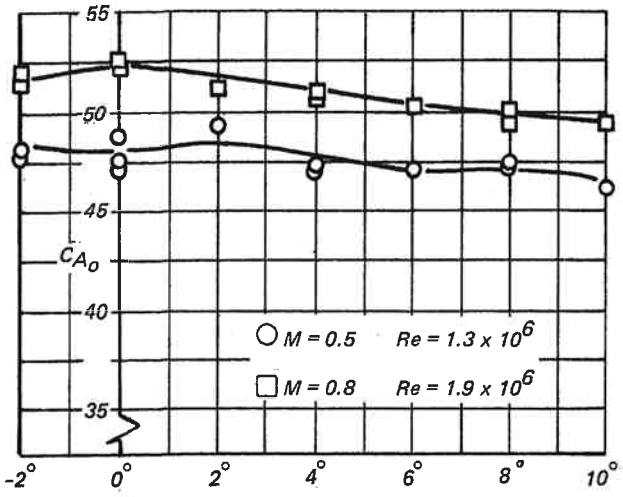
B) Ribless Guide Surface



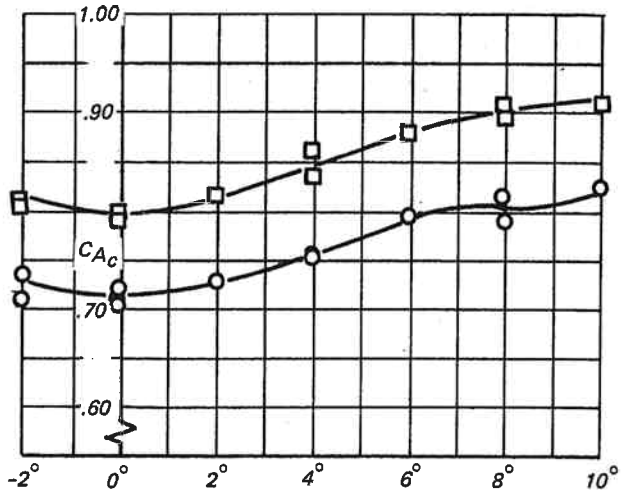
SYMBOL	PERMEABILITY (Ft^3/Ft^2-Min)		EFFECTIVE POROSITY
▼	275		0.096
▲	120		0.042
●	30		0.010
◕	10		0.003
◆	(Rigid)	0	0.0
☐	(Flexible)	0	0.0

C) Solid Flat Circular

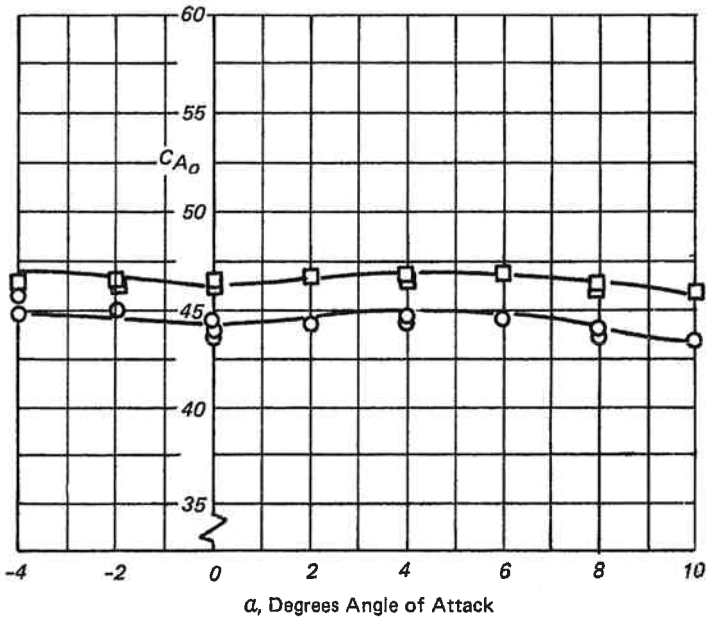
Figure 6.28 Axial Force Coefficient Versus Angle of Attack, M = 0.1



A) Ringslot (50 Inch Prototype, $\lambda g = 20\%$)



C) Ribless Guide Surface ($\lambda_m = 10\ Ft^3/Ft^2$ Min.)



B) Ribbon (100 Inch Prototype, $\lambda g = 20\%$)

Figure 6.29 Axial Force Coefficient Vs Angle of Attack, M = 0.5, 0.8

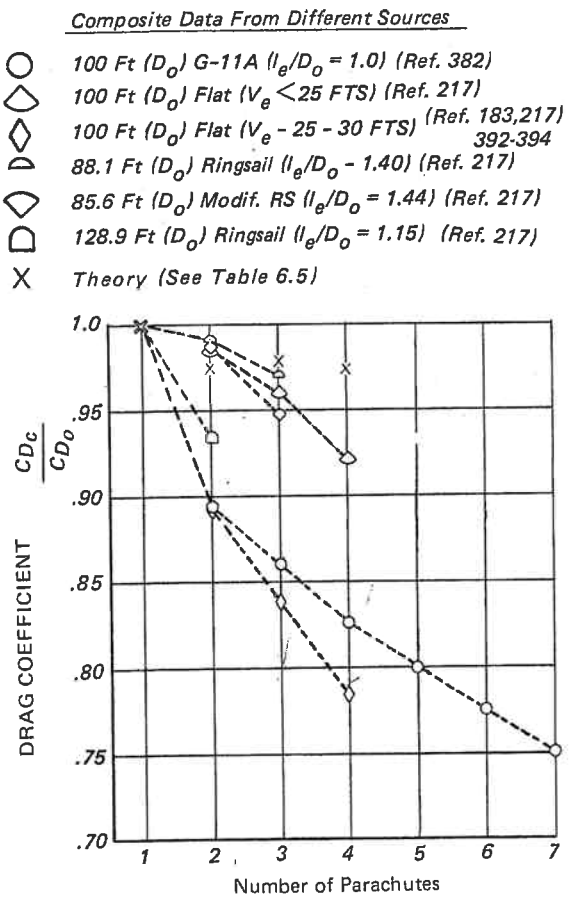


Figure 6.30 Effect of Clustering on Drag Coefficient

Graphical analysis of the contact geometry of different numbers of circular canopies in compact rotationally symmetrical clusters yields the following approximation relationship for the average riser angle.

$$\phi_C = K^*(l_C/D_o) \text{ radians} \qquad 6\text{-}24$$

where $K^* = r/D_o$ and r is the mean radius of the canopy centers from the cluster axis at the level of the skirts, as developed on a flat layout.

It is instructive to compare measured with calculated cluster drag coefficients on the basis of the assumptions made, and these purely geometrical considerations with

$$C_{D_C}/C_{D_o} = \cos(K^*/n_C^{1/2}) \qquad 6\text{-}25$$

for different number of canopies and corresponding values of K^* in Table 6.5. As shown in Figure 6.30 the agreement for $n_C = 2$ and $n_C = 3$ is good, but divergence increases rapidly for larger clusters. The implication is that if clustered canopies could be prevented from spreading far apart their drag performance would be greatly improved when $n_C = 4$ or more. Partial confirmation of this is found in Reference 386 for clusters of three 48 ft D_o conical ribbon parachutes tested both with and without canopy skirt connections at the tangency points. The average drag coefficient of the bound cluster was approximately 11 percent greater than of the free cluster.

Another implication of the comparison is that the best 3-canopy clusters are performing close to the theoretical maximum with whatever mutual interference may exist, while the best 2-canopy clusters even though free, clearly are benefitting from effects not accounted for by the theory. For example, two side-by-side canopies may experience two-dimensional flow augmentation of momentum drag analogous to the effect of aspect ratio.

A cluster of three 4.78 ft D_o ribbon drogues with $l_C/D_o = 2.8$ were tested on a supersonic rocket sled[376] with the results shown in Figure 6.32. Of the five tests performed, two were supersonic. Supersonic operation was characterized by partial squidding with canopy area ratios of $S_p/S_o = .25$ to $.35$, compared to $S_p/S_o = .435$ subsonic, and average angular excursions greater by a factor of 3.5 relative to the subsonic average. The trailing distance, l_T, was roughly $10d_b$.

Use of ribbon drogues in pairs is fairly common. The Apollo drogue system, consisting of a pair of 16.5 ft D_o, 25° conical ribbon parachutes, scarcely qualifies as a cluster because the risers were attached to separate points on the command module giving an effective rigging length considerably greater than $l_C = 5D_o$. The canopy trailing distance, l_T, was approximately $6d_b$. Consequently, there was no detectable interference between canopies and their drag performance was the same as two independent parachutes with a rigging length of $l_e = 2D_o$.

TABLE 6.5 PARAMETERS OF SYMMETRICAL PARACHUTE CLUSTERS

n_C	2	3	4	5	6	7
K^*	.318	.369	.461	.538	.637	.530
ϕ_C (radians)	.225	.213	.230	.241	.260	.203
C_{D_C}/C_{D_o}	.975	.977	.974	.971	.966	.979

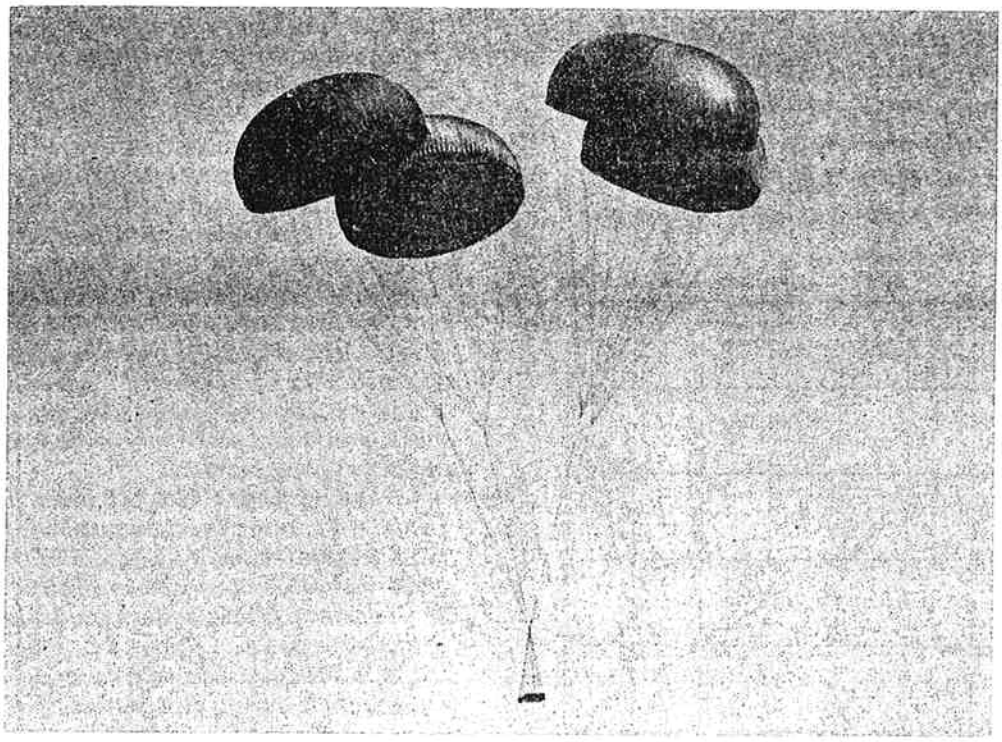


Figure 6.31 Cluster of Four 100 Ft. (D_o) G-11A Parachutes

Descent Characteristics

A vector diagram representing the two-dimensional characteristics of generalized decelerator systems in steady descent is shown in Figure 6.33. Note that the canopy angle of attack is defined for two different reference lines as follows. For high-glide canopies α is measured from the relative wind vector to a chord reference line as for airfoils (Fig. 6.33a). For the non-airfoil canopy designs, α is measured from the relative wind vector to the longitudinal axis of the parachute (Fig. 6.33b). In both cases α is measured from the relative wind vector to an axis in the canopy plane of symmetry. For convenience of measurement and aerodynamic analysis the force vector, F, may be resolved into various components of which lift, L, normal to the relative wind or flight path and drag, D, tangent to the flight path are the ones most frequently evaluated.

When the descending system oscillates, the motion appears ***pendular*** in character because the system center of mass is usually closer to the canopy than to the suspended body. The typical solid cloth parachute is unstable at $\alpha = 0$ degrees and has a stable trim attitude at angles in the order of $\alpha = 15$ to 30 degrees, but lacking any direction stabilizing mechanism, its random gliding tendency usually produces a variety of oscillations instead. However, in small models or at rates of descent less than approximately 25 fps, gliding periods of appreciable duration tend to predominate and the vertical velocity component is reduced to that of non-gliding descent.

Consequently, when the drag coefficient of a parachute is based on an average measured rate of descent, v_e, over a short period with a given unit surface load, W/S, and is calculated as

$$C_{D_o} = W/S_o \, q_e \qquad 6\text{-}26$$

the result obtained depends very much on the type of system motion prevailing at the time. Comparing C_{D_o} values for non-gliding ($\theta = 90^\circ$) and gliding descents as derived in Figure 6.33 the following relationship exists,

$$\frac{C_{D_o\,(glide)}}{C_{D_o\,(non\text{-}glide)}} = \frac{1}{\cos^2 \alpha} \qquad 6\text{-}27$$

As shown in Figure 6.34a, the drag coefficients obtained from a series of drop tests with W/S_o constant, vary more widely than do the mean values from tests with different unit loads.

Another factor contributing to the data scatter of full scale aerial drop tests, is the occasional presence of vertical air motion, a quantity of uncertain magnitude difficult to detect and seldom measured. The

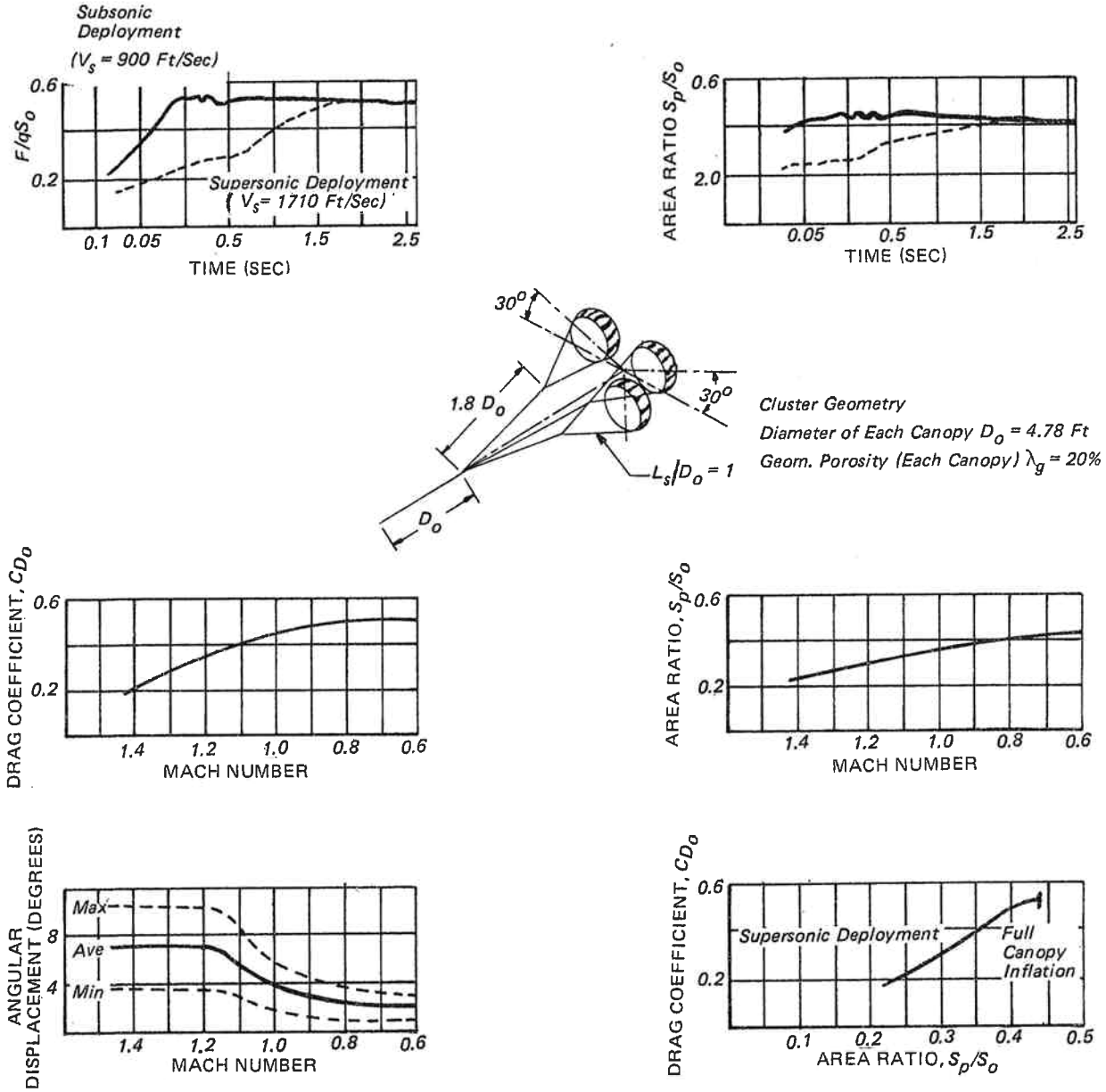


Figure 6.32 Performance Characteristics of Three Flat Circular Ribbon Drogues in Cluster Configuration (Ref. 376)

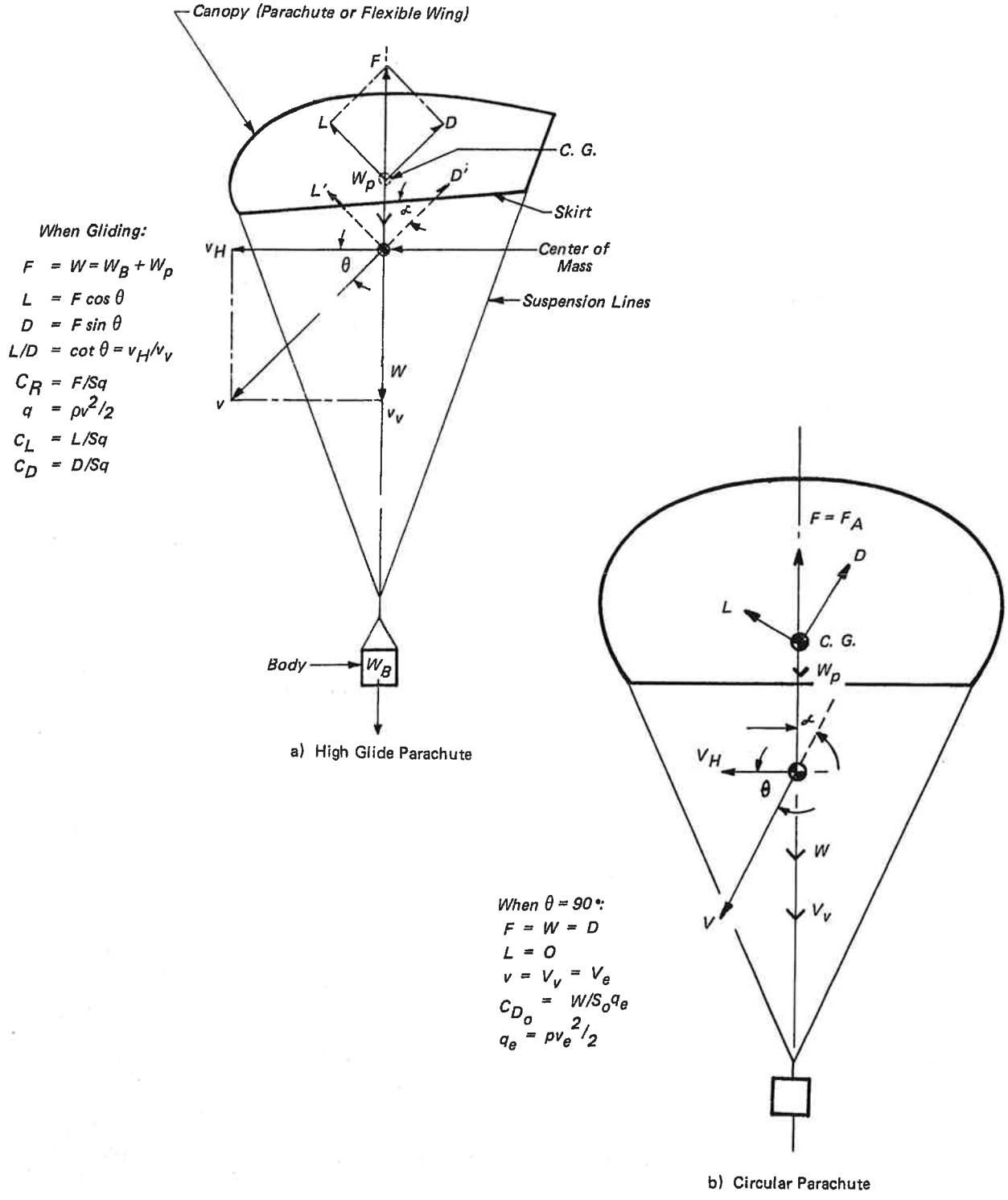
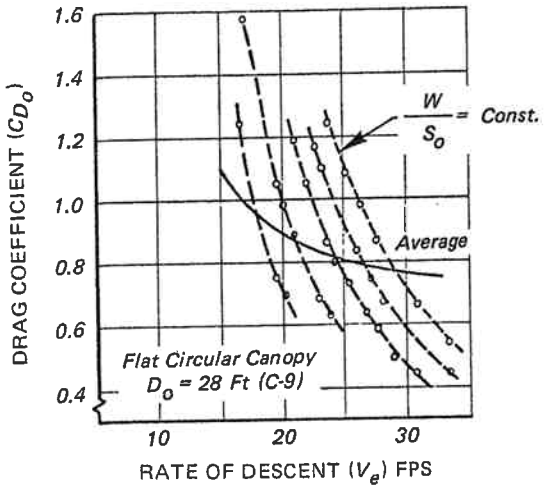
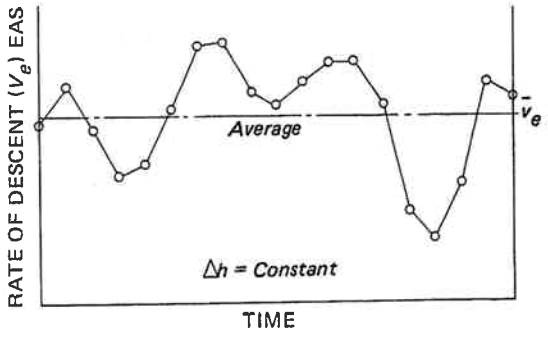


Figure 6.33 *Generalized Decelerator System in Stable Equilibrium Descent Through Homogeneous Air Mass (ρ = const.; $F_y = 0$, $M = 0$)*



a) Variation of Drag Coefficient Data for Different Constant Unit Loads vs Rate of Descent (From Ref 382)



b) Incremental V_e Measurements vs Time During Descent (From Ref. 217)

Figure 6.34 Averaging Drag Coefficient and Rate of Descent Data

accuracy of drag coefficient measurements is also affected by the actual air density-altitude profile at the time of the test. An instrumented aerology balloon may be sent aloft to obtain this data, but its timing is not always ideal.

Measurements of the Rate of Descent. Good range instrumental coverage of a protracted descent yields average values for v_e and q_e which show much less variation from test-to-test than is indicated by Figure 6.34a. An example of the graphical method of averaging v_e is illustrated in Figure 6.34b. Whatever caused the rate of descent to vary, the several effects were minimized by the averaging process.

A summary of rate of descent data obtained from a significant number of aerial drop tests of spacecraft landing parachutes measured by a similar method is presented in Table 6.6. Standard deviations ranging from σ = *2.4* to *3.3* percent show that a rate of descent variation of ±6 percent v_e, long used for design purposes with impact sensitive systems, is roughly a two-sigma value. The results of full scale aerial drop tests of a wide variety of parachutes are summarized in Figure 6.35. The majority of the data points are the averages of several tests; however, the results of single tests have been used to show general trends where their omission would imply gaps in present knowledge that do not exist.

Glide Ratio (L/D). The great majority of canopy designs of all types generate unsymmetrical aerodynamic forces, the force vector does not remain steadily tangent to the flight path and will create oscillation inducing moments if a stable glide is not possible. Usually a minor irregularity or dissymmetry in the canopy will stabilize the flow pattern sufficiently to induce a directional glide[46,142, 395, 396 & 562]

Interest in the performance of gliding parachutes centers around their steerability and the glide ratio characterized by *L/D(max).*

The glide ratio obtained depends upon familiar parameters of rigid wing aerodynamics — airfoil profile, thickness, aspect ratio, fineness ratio, spanwise profile, surface smoothness, and a number of others peculiar to flexible gliding parachute structures — air permeability, leading edge stiffness, trailing edge fullness, trailing edge tension, and relative suspension line length. It is useful to distinguish between three basic types of gliding parachute configurations.

Low glide parachute — $L/D(max) \approx 0.3$ *to* 0.8

Med-glide parachute — $L/D(max) \approx 1.0$ *to* 2.0

High-glide parachutes — $L/D(max) \approx 2.0$ *to* 4.0

The maximum glide ratios indicated are those obtained with complete operational systems. The performance of individual canopies in the wind tunnel is generally much better than can be realized in practice. When the wind tunnel models include scale suspension lines and suspended vehicles the correlation is improved. The variation of glide ratio with angle of attack is shown in Figure 6.36A for different kinds of canopies. Solid symbols indicate system data. Figure 6.36B illustrates the relationship between L/D, θ, and other components of the steady-state glide plus the characteristic performance of different gliding systems.

TABLE 6.6 SUMMARY, RATE OF DESCENT MEASUREMENTS

(Ref. 217)

Project Parachute	System Descent Weight (lbs)	No. of Chutes	No. of Tests	Average Rate of Descent, v_e Computation Method	(fps) 5000 ft	S.L.	Standard Deviation, σ ($\%v_e$) 5000 ft	S.L.	Average C_{D_o}
Apollo	4750	1	7	Average of Askania data each 1000 ft + 300 ft	29.9	27.8	2.8	–	.850
88.1 ft D_o Ringsail	9500	2	6	Same as above	30.0	27.9	2.7	–	.845
	9500	3	8	Askania data each second 5000 ft to 200 ft	24.8	23.0	2.4	–	.825
Gemini	4400	1	16	Average of Askania data from 5000 ft to 2000 ft	31.9	29.6	–	3.1	.760
84.2 ft D_o Ringsail									
Mercury	2160	1	34	Average of Askania data at 5000 ft + 300 ft and 500 + 200 ft	29.7	27.6	–	3.3	.760
63.1 ft D_o Ringsail									

As reported by Sleeman[397] good correlation of *L/D(max)* was found with the twin-keel parawing parameter $(S_{cp}/S_W) \cos \Lambda o$ (Figure 6.37) where S_{cp} is the area of the center panel and Λo is the leading edge sweep angle. It appears that the upper limit is reached at $(S_{cp}/S_W) \cos \Lambda o = 0.44$ and that *L/D (max)* is significantly influenced by the relative length of the suspension lines. A probable correction to the wind tunnel data for full scale free flight conditions is suggested by the broken line derived from the work reported in Reference 398 with a 4000 ft² twin-keel parawing having a flat planform span of 110 feet.

Other investigators have advanced the development of the Parafoil with a wide variety of models and testing methods, as reported in References 132 219 and 399. The effect of aspect ratio is seen to be significant as shown by the composite wind tunnel results for different Parafoil models in the following Table 6.7:

TABLE 6.7 PARAFOIL $(L/D)_{max}$ vs ASPECT RATIO

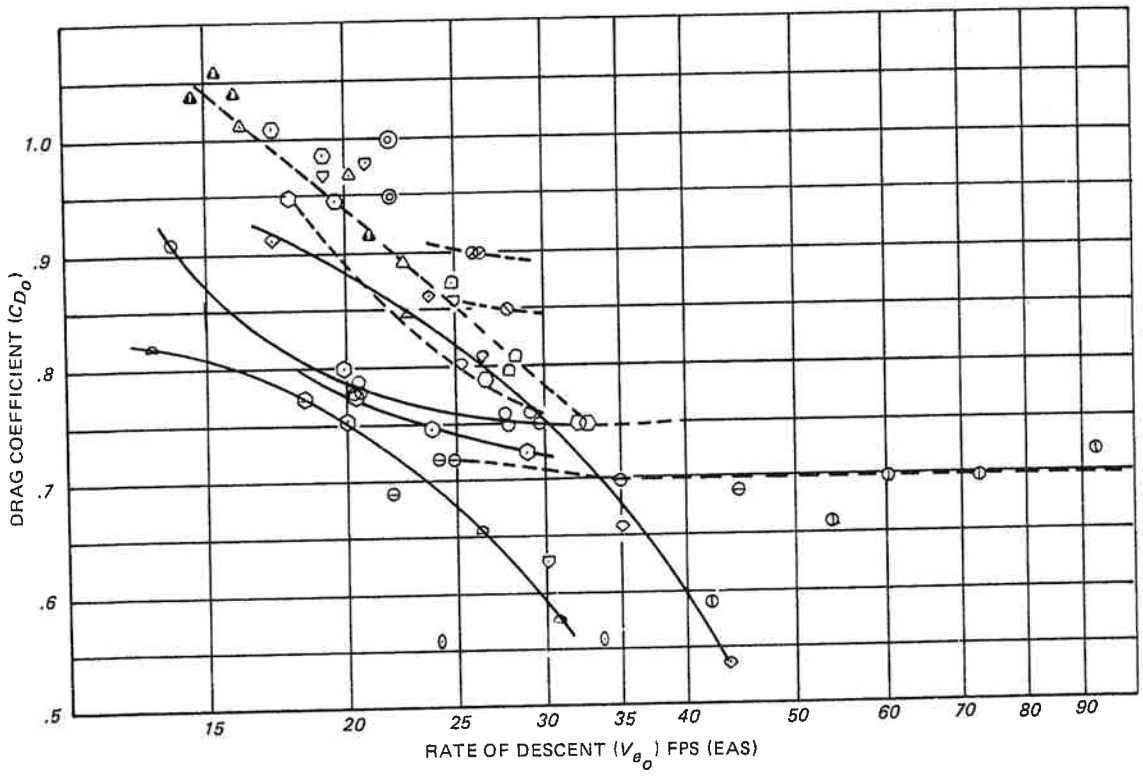
AR	1.0	1.5	2.0	2.5	3.0
(L/D) max	3.0	3.8	4.6	5.6	6.5
α (deg)	10	9	8	7	6

Performance data for *AR = 1.5* and *AR = 2.0* are plotted in Figures 6.36 and 6.37, the latter being uncorrected wind tunnel data. The probable magnitude of wind tunnel effects is indicated by free flight data in the following Table 6.8:

TABLE 6.8 PARAFOIL $(L/D)_{max}$ IN FREE FLIGHT

AR	S_W-ft²	W/S_W-psf	*(L/D)max*	Source Reference
1.5	300	0.52	3.1	132
		0.77	2.5	
		2.35	2.3–2.6	
2.0	360	0.55	3.7	219
	242	0.77	3.7	
	200	0.93	3.4	

Data from drop tests of the Volplane and Sailwing high-glide parachutes are found in References 402 and 403 respectively.



Parachute Type	D_o - Ft	l_e/D_o
Flat Solid Cloth	24-28	.75-1.0
Flat Solid Cloth	100	.95-1.0
Conical (10°-26°)	95-100	.95-1.0
Tri-Conical	79.6-100	
14.3% Extended Skirt	60-67.3	.92-1.0
10% Extended Skirt	56-67.2	1.0
10% Extended Skirt MC-1	35	.85
10% Extended Skirt	34.5-38	.87-.94
Hemispherical (G-13 Cargo)	24.5	1.0
Ringsail (λ_T = 7-8%)	56.2-84.2	.94-.97
Ringsail (λ_T = 7.2%)	88.1	1.4
Ringsail (λ_T = 10%)	128.8-189.5	1.15-1.18
Ringsail (λ_T = 7.8-14%)	29.6-41	1.0
Ringsail (λ_T = 11-14%)	17.5-34	.76-1.49
Annular (D_v/D_p = .63)	42-64	1.25
Ringslot (λ_T = 10%)	34.3-56	1.0

Figure 6.35 Parachute Drag Coefficient vs. Equilibrium Rate of Descent at Sea Level (Circular Canopies)

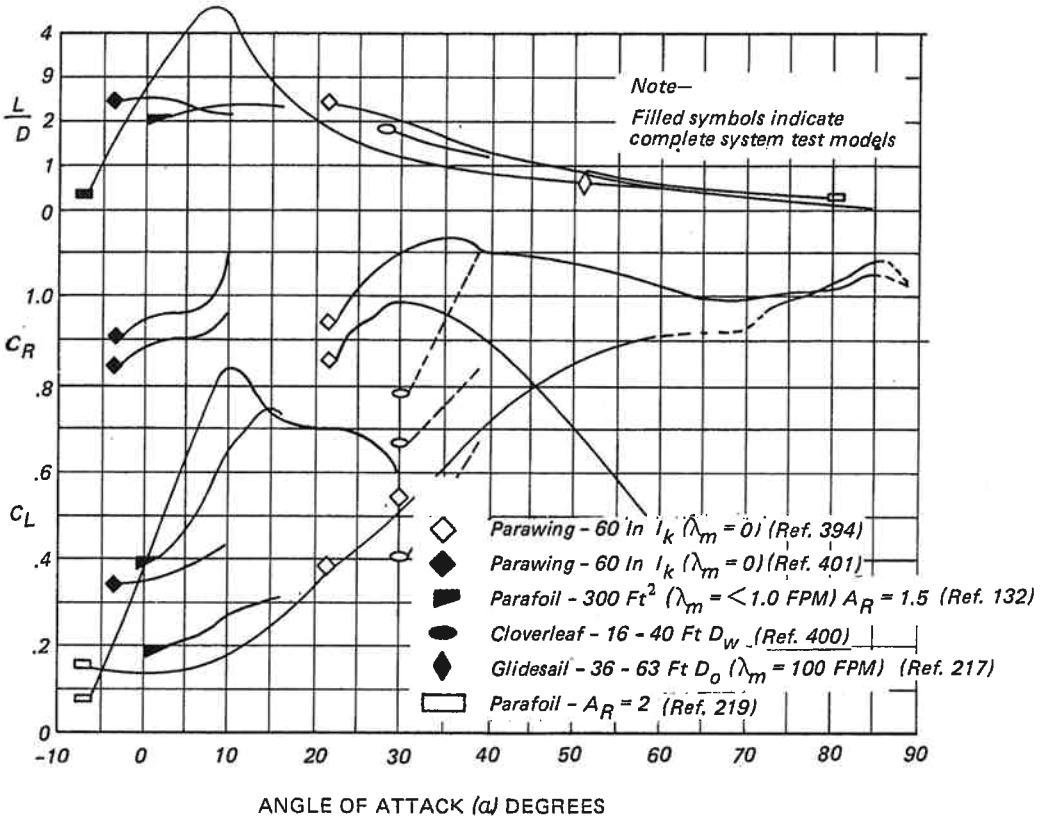


Figure 6.36A Variation of L/D and Aerodynamic Coefficients With Angle of Attack

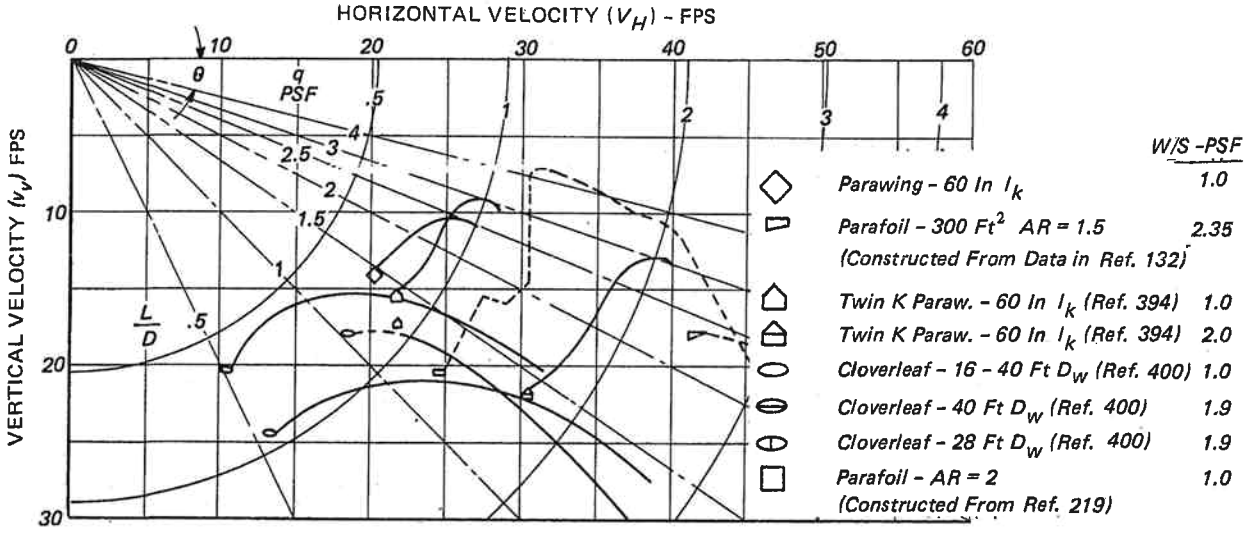
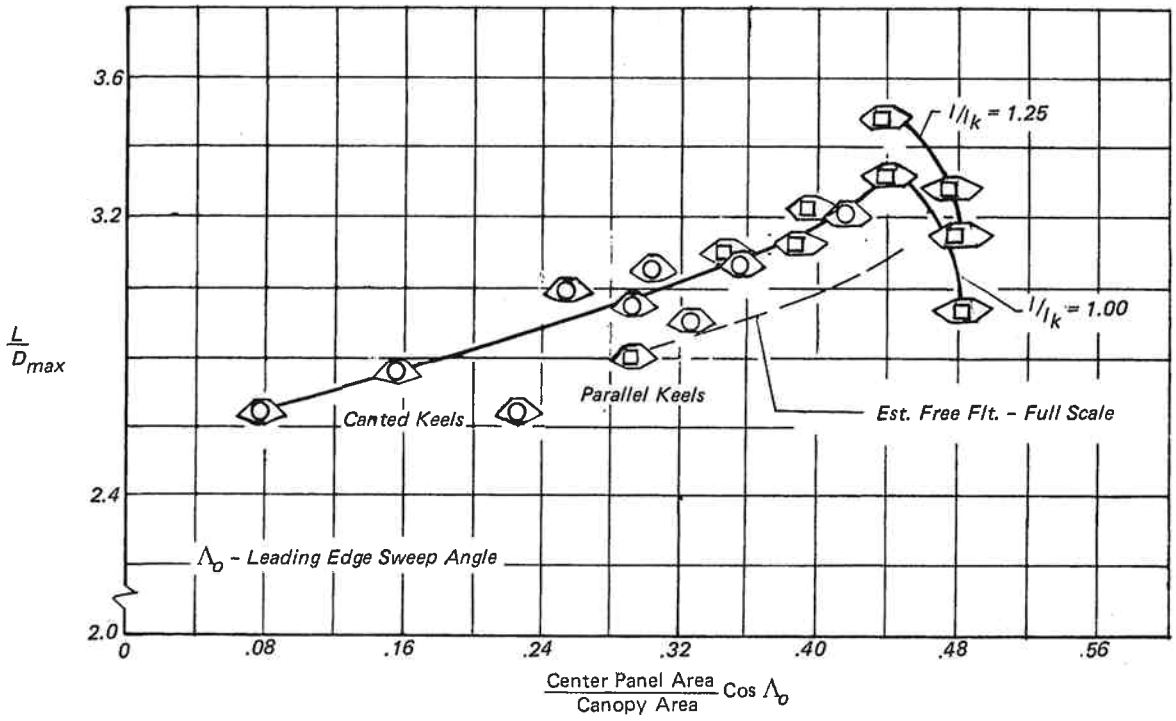
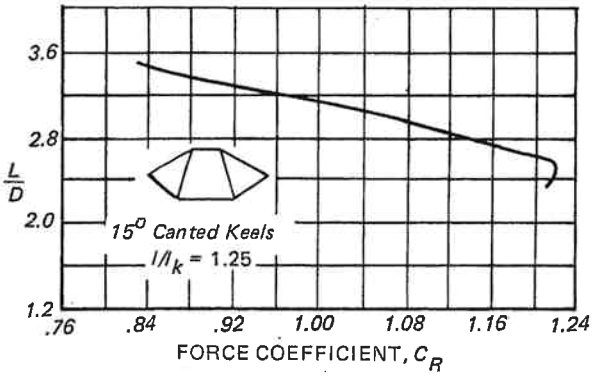


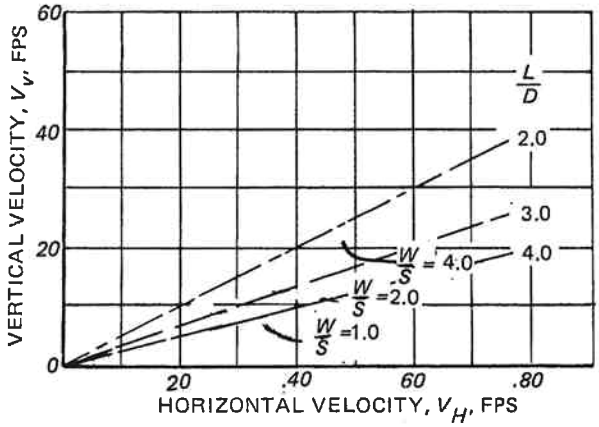
Figure 6.36B Effect of Wing Loading (W/S_W) on Components of Glide Over Controllable Range of L/D Modulation



a) Performance Summary of Twin-Keel Parawings Having a Formed Nose

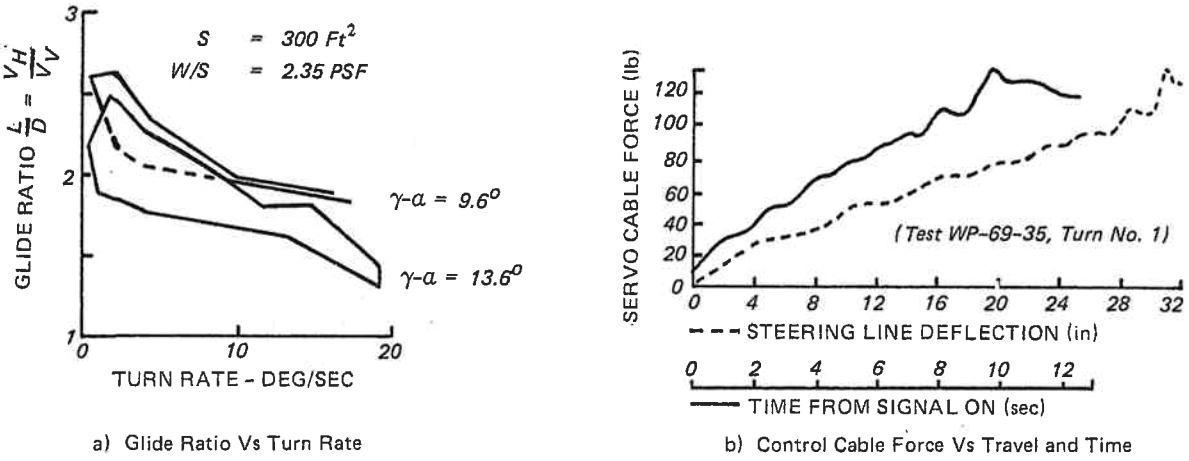


b) Performance Characteristics of an Advanced Twin-Keel Parawing



c) Glide Velocities for an Advanced Twin-Keel Parawing Having 15° Canted Keels

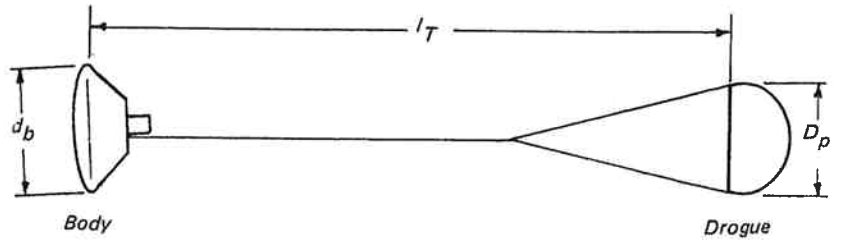
Figure 6.37 Twin-Keel Parawing Performance (Ref. 397)



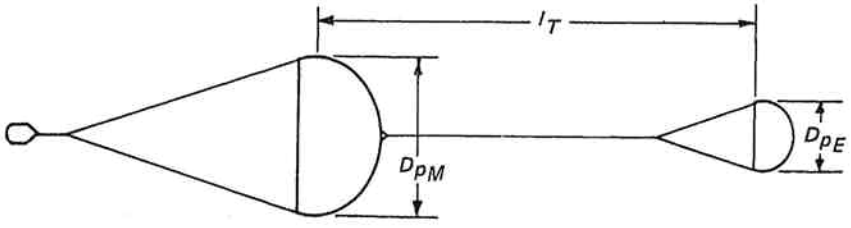
a) Glide Ratio Vs Turn Rate

b) Control Cable Force Vs Travel and Time

Figure 6.38 Parafoil Measured Turning Characteristics (Ref 132)



a) The Towed Decelerator System



b) The Tandem Canopy System

Figure 6.39 Decelerator Systems Subject to Strong Wake Effects

In-Flight Modulation of *L/D*. The in-flight modulation of steerable parachute glide ratio is effected by varying the length of one or more control lines which have been rigged to change the effective angle of attack of the surface. Since such systems usually deflect only the trailing edge, rather than the entire wing, a reduction in glide ratio by this means is analogous to the use of flaps to increase the drag component of the total force. The result is a rearward shift of the center of pressure, and a steeper glide path follows. Since the power required for *L/D* modulation by this means is considerably greater than for steering, separate flaps may be employed on the under surface to simply augment drag without changing the gliding trim of the wing suspension line rigging.

Turning Maneuvers. Turning a gliding parachute of any type is accomplished mainly by control line actions that shift the system center of gravity laterally to induce a bank. Wing-tip drag modulation also is employed for steering, a technique that has been applied to the Parafoil. Some steerable parachutes, such as the T & U Slot, which have a low *L/D* and steep glide angle also employ canopy rotation techniques. Since turning maneuvers generally are attended by changes in lift and drag that reduce glide ratio, the sinking speed is higher during turns than in straight flight. Thus, the average *L/D* for a given descent operation with numerous turning maneuvers will be less than *L/D(max)* or less than the designed-in trim *L/D* of the system. Figure 6.38 illustrates the effect of turn rates on the measured glide ratio of a small Parafoil in free flight for two different rigging configurations and how the control cable force varies with both deflection and time.

Towing Body Wake Effects

All towed decelerators are subject to wake effects in varying degrees. Predictably these effects are most pronounced when the ratios D_p/d_b and l_T/d_b are small, d_b being the "hydraulic" diameter of the towing body and l_T the trailing distance as shown in Figure 6.39a. The shape and drag coefficient of the towing body also is important. Other decelerator systems subject to strong wake effects are identified as tandem-canopy systems shown in Figure 6.39b. These include both aerial retrieval systems, in which the main canopy is trailed by a smaller parachute, and attached pilot chute systems where the pilot chute is permanently attached to the apex of the main canopy with a strong bridle-harness.

A substantial body of empirical data has been accumulated on the interaction between a decelerator and the wake of the towing body over a broad velocity spectrum (Refs. 313 and 404-417). On the other hand, useful detailed knowledge about the characteristics of tandem canopy systems is meager, although understanding of the specific data needed for successful design is fairly complete. In broad qualitative terms the towed decelerator is moving through highly turbulent air where the effective dynamic pressure is less than free stream and the direction of local flow components is variable. This influences both the inflation and operational characteristics of the decelerator and, consequently, the motion and stability of the system as a whole. Understanding the behavior of the system is aided by knowledge of the free body wake characteristics, as well as of the decelerator operational characteristics in undisturbed air.

Both subsonic and supersonic wake characteristics of bodies of widely varying shapes have been the subject of comprehensive analytical (Chap. 7) and experimental (References 407, 418-420, 421-428) studies Body shapes have mainly been bodies of revolution representative of both elongated vehicles and bluff spacecraft. The full-open parachute is also represented in the form of an impervious hemispherical cup. The turbulent subsonic wake is described in terms of both velocity and pressure distributions at different distances behind the body as shown in Figure 6.40. Good agreement between predicted and measured velocity distributions[418] for some of the simpler cases (bodies of revolution) is shown in Figures 6.41a and 6.41b. The passage of the vehicle through undisturbed air at a relative velocity, v, displaces the air radially from the flight path in a way that generates a series of energetic eddies in the wake (Von Karman's vortex street) having a mean velocity component, Δv, following the body. In consequence, a trailing decelerator attached to the body at some distance, l_T, experiences a relative flow velocity.

$$v_T = v - \Delta v \qquad 6\text{-}28$$

which varies with distance from the wake centerline according to the characteristic distribution shown in the figures. As indicated by Figure 6.42 this velocity distribution can be expressed in dimensionless form for bodies of revolution as

$$\Delta v/\Delta v' = f(Z_w) \qquad 6\text{-}29$$

where

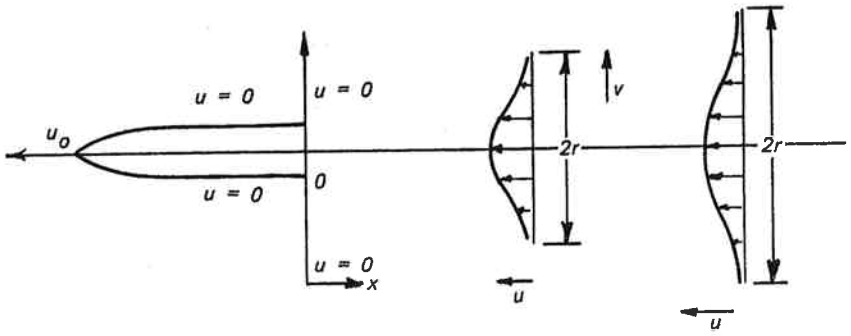
$\Delta v'$ = air velocity increment on wake centerline

$Z_w = r/r_m$

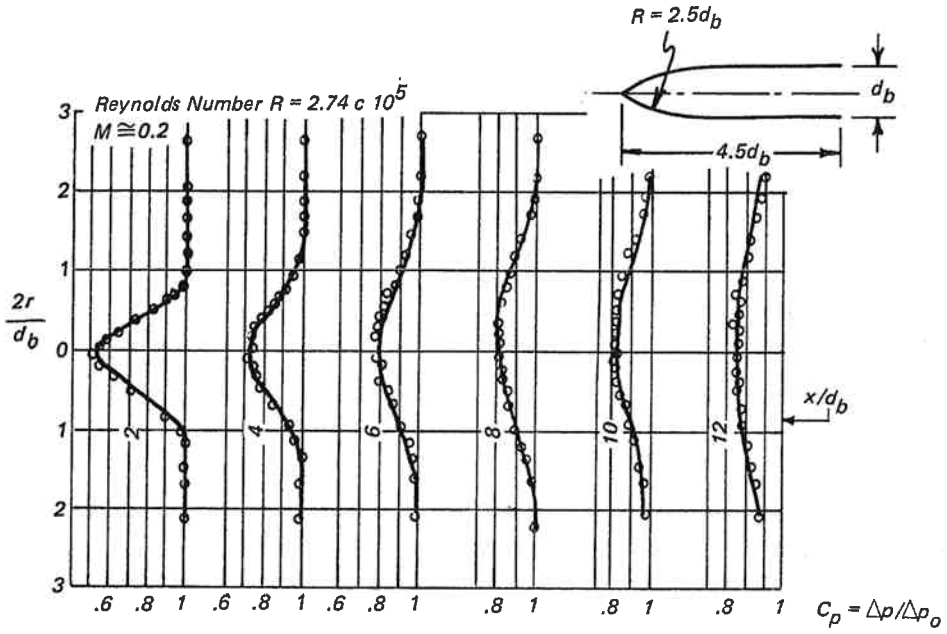
r = distance from wake centerline

and r_m = coordinate where $\Delta v = \Delta v'/2$

It is essentially invariant with body shape. Any inflated decelerator that is stable when centered on the wake feels a mean relative flow velocity of v_T which



a) Velocity Distribution for a Body Moving Through Fluid at Rest

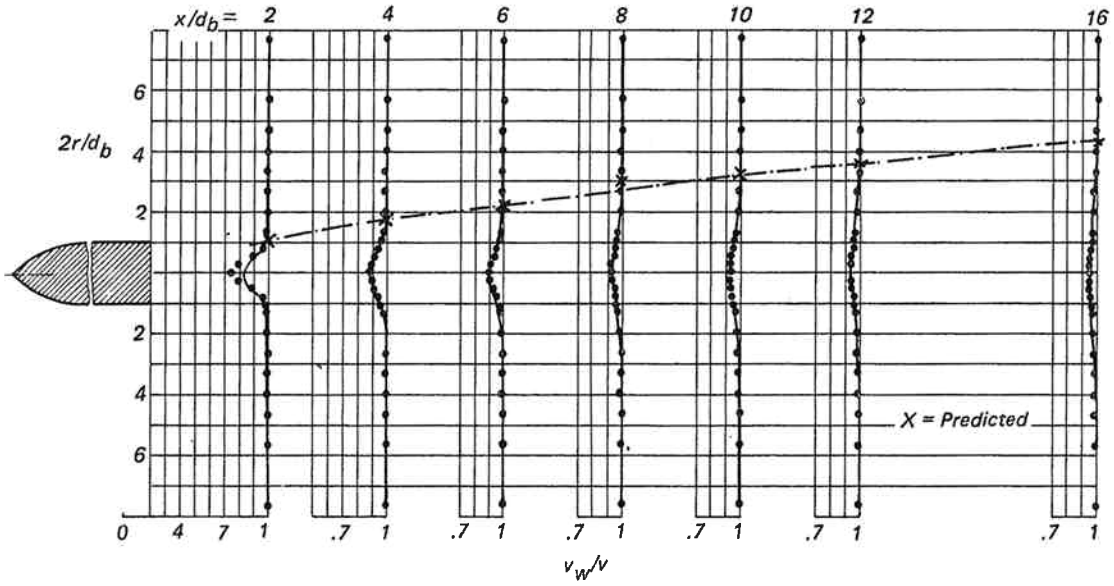


b) Pressure Distribution in the Wake of a Body of Revolution ($C_D = 0.35$) (Ref. 429)

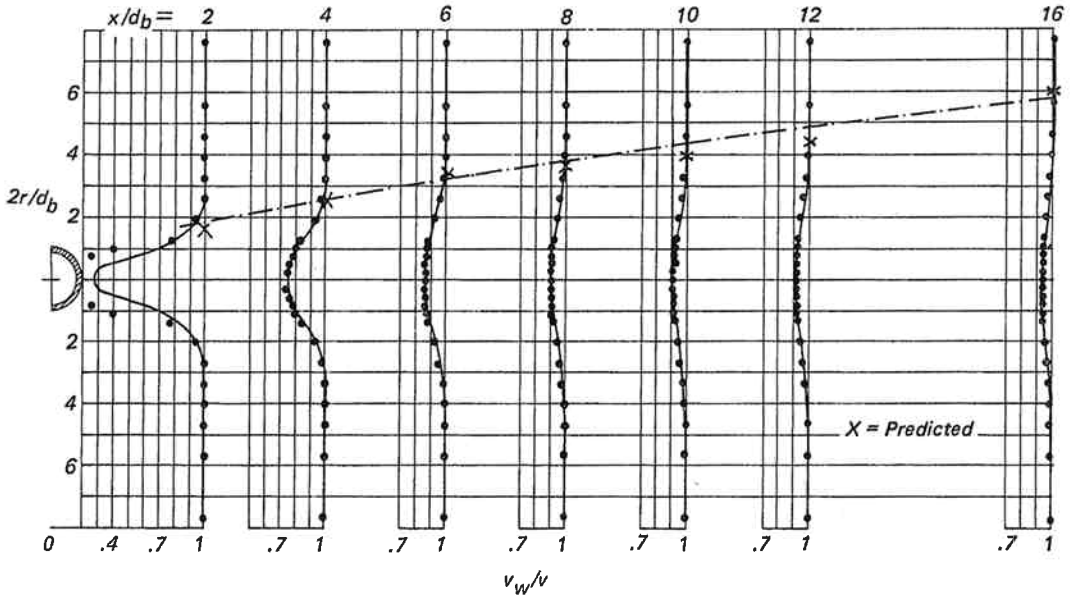
Figure 6.40 Subsonic Wake Flow Characteristics

is proportional to r_p, the radius of that portion of the wake flow that impinges on the canopy. Since the relative flow is highly turbulent, r_p likely will not differ greatly from $D_p/2$ so that a fair estimate of the ratio $(v_T/v)^2 = C_{D_p}/C_{D_\infty}$ could be made by the method described in Chapter 7 when the drag coefficient of the towing body is known[418]. The mechanics of this approach are equivalent to determining the mean dynamic pressure in the canopy flow field and applying the normal free stream drag coefficient. However, it is convenient to describe the experimental results in terms of the ratio of the apparent drag coefficient to the free stream drag coefficient, C_{D_p}/C_{D_∞}.

Subsonic Wake. When a decelerator is deployed and inflated in the wake region, the change in the turbulent flow is marked, and the primary effect is the reduction in drag that takes place relative to free stream conditions. This is reflected by the way in which C_{D_p}/C_{D_∞} varies with trailing distance, l_T/d_b, as shown in Figure 6.43 for small rigid models in the wind tunnel. Also shown is the ratio $(v'/v_\infty)^2$, v' being the relative air velocity on the wake centerline, which represents the minimum impact velocity behind this particular body that would be felt by a small decelerator at any given trailing distance. In other words, given $D_p/d_b < 1$, $C_{D_p}/C_{D_\infty}(min) \approx (v'/v_\infty)^2$. As the relative size of the decelerator in-



a) In Wake of Ogive Cylinder



b) In Wake of Hollow Hemisphere

Figure 6.41 Velocity Distribution in Wake of Bodies of Revolution (from Reference 418)

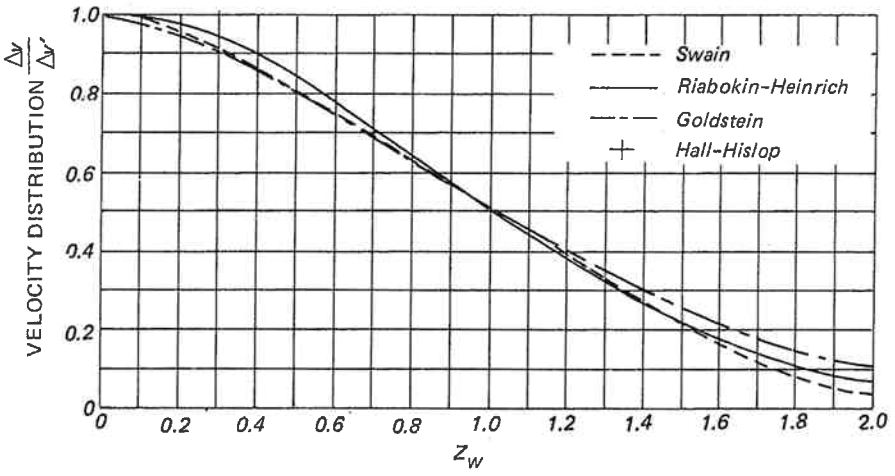


Figure 6.42 Velocity Distribution in Accordance With Analytical and Experimental Studies

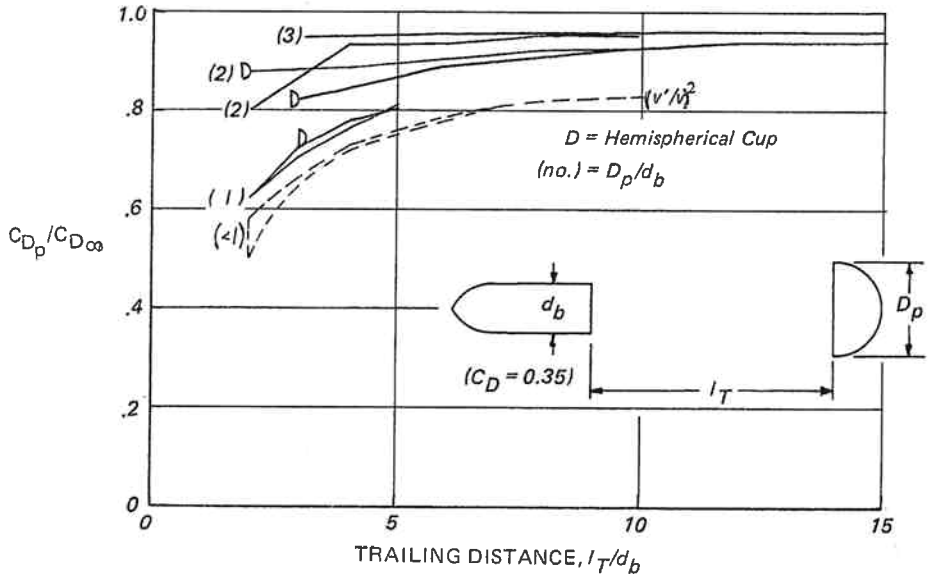


Figure 6.43 Wake Drag Coefficient for Small Circular Models (Disk & Hemispherical Cup) (Adapted from Ref. 382)

creases, the loss in drag effectiveness diminishes because the average velocity increment across D_p becomes progressively smaller, allowing C_{D_p} to approach its free stream value. The data cross-over at $D_p/d_b = 2$ to 3, suggests that the difference in wake effect on the two hemispherical cup models is less than the probable error of measurement.

The magnitude of the velocity increment and the width of the wake at any given distance from the body is proportional to the bluffness of the body indicated by its drag coefficient as shown in Figure 6.44 for two small bodies of revolution. The difference in velocity increments on the wake centerline becomes inconsequential at $x/d_b \approx 10$, but the difference in wake widths remains nearly constant at about 1.1 body diameters in this case.

Comparison of the impact pressure ratios on the wake centerline for the ogive-cylinder with and without the trailing decelerator models (Figure 6.45), on the assumption that errors of measurement were small, indicates that the presence of the decelerator may reduce the effective dynamic pressure somewhat. More significant is the marked increase in the wake velocity increment, $\Delta v'$, behind the hemispherical cup and the potential reduction in decelerator drag coefficient when towed by a bluff high drag body compar-

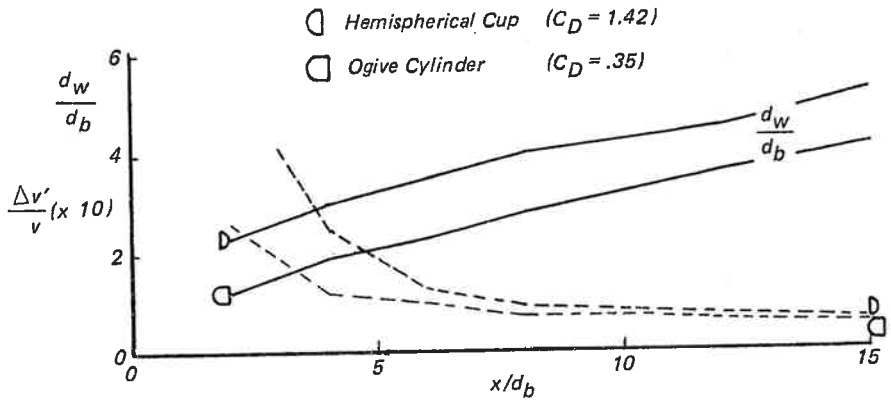


Figure 6.44 Wake Width & Center-Line Velocity Increment vs Distance From Body of Revolution (Adapted from Ref. 382)

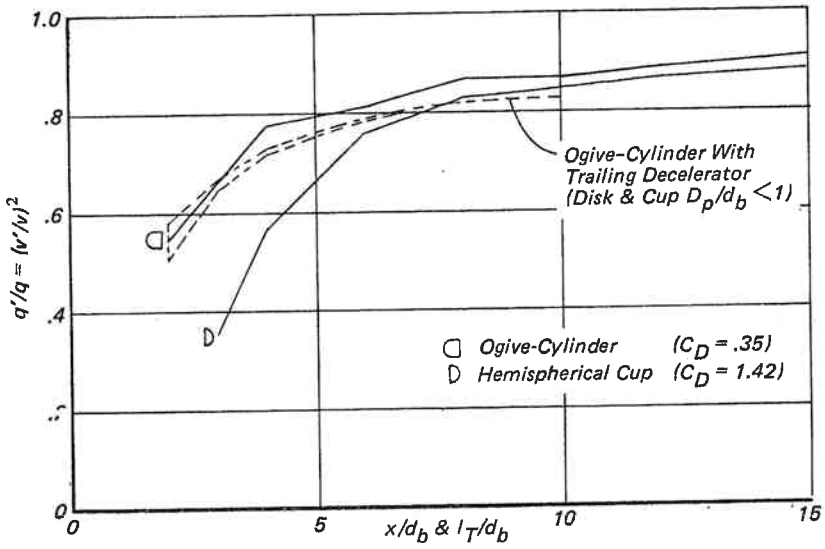


Figure 6.45 Impact Pressure Ratio on Wake Centerline Ogive-Cylinder & Hemispherical Cup (Adapted from Ref. 382)

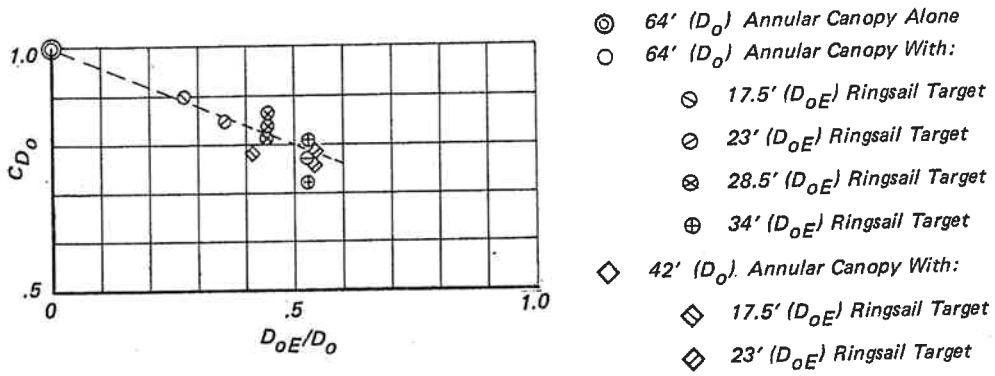


Figure 6.46 Drag Coefficient of Experimental Tandem Canopy Systems (Ref. 184)

TABLE 6.9 MID-AIR RETRIEVAL SYSTEM DRAG EFFICIENCIES & SPECIFIC DRAG AREAS

System		Tandem (MARS-L)	Conical Extension	Annular/Ringsail	
Main Canopy:		Tri-conical	Extended Skirt	Annular	
D_o	ft	79.6	67.2	42	64
$(C_DS)_{M\infty}$	ft^2	5385	2910	1315	3230
Target:		Ringslot	Conical Extension	Ringsail	
D_o	ft	18.75	27.6 (equiv.)	23	28.5
$(C_DS)_{E\infty}$	ft^2	124	133 (est.)	291	446
System $\Sigma (C_DS)$	ft^2	5385	2760	1420	3210
Drag Aerodynamic Efficiency	(η_T)	.977	.907	.884	.874
Specific Drag Area	ft^2/lb	53	33	25	34
Reference No.		180	183	183	

able to a full open parachute. Although the effects of scale, canopy porosity and structural elasticity on these characteristics are not well defined, it appears that the trailing member of the typical tandem canopy system at customary towing distances of 4 to 5 D_{pM} likely experiences a large loss in effective dynamic pressure relative to that of the typical body decelerator system with a trailing distance in the order of 7 d_b.

However, the wake of a free canopy, unlike the model constrained in the wind tunnel, is not axisymmetric, nor does the trailing pilot chute, or engagement chute, ride stably in the center of the wake. In a non-gliding type aerial retrieval system, for example, the engagement canopy is seen to wander about in a wide orbit and, if its ratio of drag to weight is marginal, it also occasionally sinks into the shifting main canopy wake, allowing the tow-line to become slack.

It has been possible to correct this behavior by converting the main parachute into a glide-chute through a minor modification which greatly improves the stability of descent[180]. The mechanism behind this improvement in stability is the elimination of the random pattern of vortex separation from the periphery of the canopy and its replacement by a more uniform pattern, analogous to the wake of a stalled wing of low aspect ratio, a pattern that is largely symmetrical about a vertical plane through the glide-chute axis. Then the engagement canopy, although itself not statically stable, is seen to ride relatively stable on the downstream side with the tow line at an angle of 40 to 50 degrees from the vertical.

The steady state drag characteristics of tandem canopy systems are evaluated for any given configuration in terms of the combined canopy areas.

$$\Sigma S_o = S_{oM} + S_{oE} \qquad 6\text{-}30$$

and the system drag coefficient

$$C_{D_o} = \Sigma(C_DS)/\Sigma S_o \qquad 6\text{-}31$$

where

$$\Sigma(C_DS) = W/q$$

A measure of the system aerodynamic drag efficiency is

$$\eta_T = \Sigma(C_DS)/[(C_DS)_{M\infty} + (C_DS)_{E\infty}] \qquad 6\text{-}32$$

$(C_DS)_{M\infty}$ and $(C_DS)_{E\infty}$ are the individual effective drag areas of the main and trailing canopies respectively when operating independently at the same rate of descent.

In Figure 6.46, as the size of the trailing canopy is reduced, C_{D_o} approaches the drag coefficient of the main canopy alone. However, in close-coupled systems the trailing canopy alters the flow about the main canopy such that generally for the main canopy in the system $(C_DS)_M < (C_DS)_{M\infty}$. Two examples of close-coupled systems are the parachute with conical extension and the annular parachute with ringsail "target" centered over the main "vent" opening. Both have been developed for mid-air retrieval operations. Measured drag efficiencies of different mid-air

retrieval systems are given in Table 6.9. This aerodynamic criterion of system performance is supplemented by specific drag area values, $\Sigma(C_D S)/W_p$, to provide a practical basis for discrimination. The specific drag area of a decelerator is a criterion of the weight efficiency of the flexible structures as a drag producing device. It affords a valid method of discriminating between different designs of equivalent performance for the same application (see Chapter 8 for further detail).

Transonic and Supersonic Wake. Drogues of high speed are frequently called upon to inflate and function effectively in a supersonic wake (Figure 6.47). The characteristics of the steady state wake of a body of revolution with free stream velocity greater than Mach 1.0 are illustrated schematically in Figure 6.48.

At some distance aft of the base of the body, the cross-sectional area of the wake "necks down" so that a shape is formed that is approximately conical. The height of this cone appears to vary with Mach number, but is of the order of magnitude of the body-base diameter. In general, the supersonic wake is determined by this critical region where the streamlines from the sides of the body coverage[430] The angle at which the streamlines converge is determined by a shock wave boundary layer type of interaction. In this interaction the streamlines assume the maximum expansion angle for which the boundary layer flow has sufficient energy to negotiate the pressure riser that results from the recompression at the convergence point.

Immediately behind the base of the body, and bounded by the converging streamlines, there is a region sometimes characterized as the still or "dead air" region. There are however, definite indications

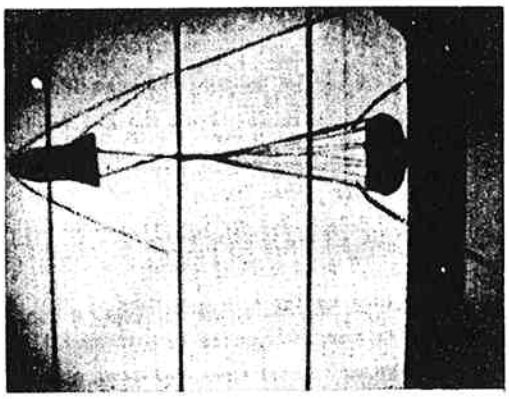


Figure 6.47 Schlieren Photograph of the Flow Fields About a Hyperflo Type Parachute at M 4.0 (Free flight test in Wind Tunnel)

(Photo Retouched to Emphasize Shock Waves)

of reverse flow conditions in this dead air region aft of the body base. For a two-dimensional case, it has been shown experimentally that the re-circulation velocity is very small. Behind a three dimensional body of revolution however, the recompression no longer takes place according to a simple function such as the Prandtl-Meyer expansion for two-dimensional flow. The boundaries of the dead-air region are thus no longer at constant pressure. A positive pressure-gradient exists in this region, allowing a subsonic reverse-flow jet for subsonic portions of the boundary-layer flow. Since only part of the boundary-layer flow is subsonic and the recompression pressure-coefficients appear to decrease with increasing Mach number[431] it is suspected that the effect of the reverse-flow will diminish with increasing Mach number. Indications of substantial reverse-flow in the wake of a

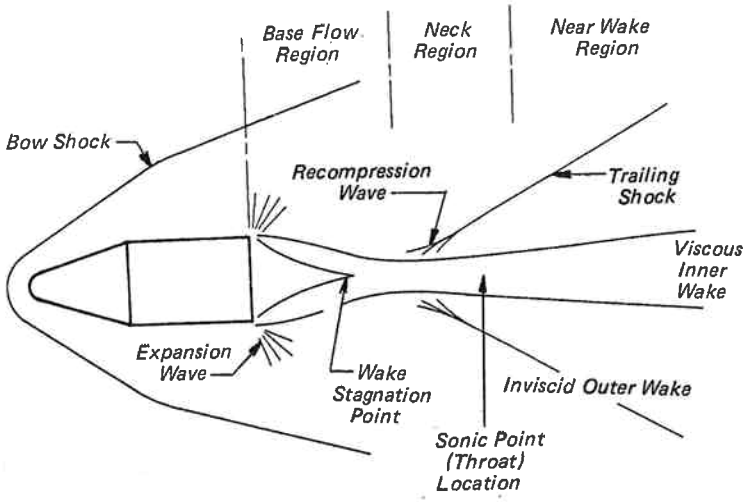
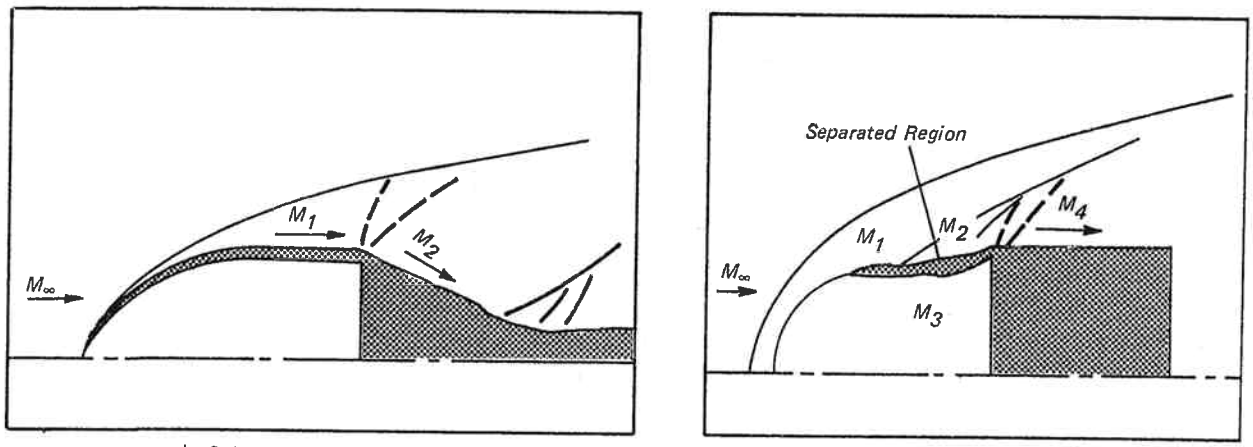


Figure 6.48 Schematic of Unmodified Supersonic Wake Details and Nomenclature for Body of Revolution

three dimensional body have been shown in wind tunnel tests[387]. The prime significance of these experimental data is that they verify the existence of a reverse flow at low supersonic free-stream velocities. For a free-stream Mach number of 1.2, this reverse-flow region extends for approximately two base diameters aft of the body base.

Behind the dead-air region, the supersonic wake spreads in a manner similar to an incompressible wake such that the width increases approximately with distance to the one-third power. Behind the neck or throat of the wake, the wake core appears to maintain an essentially constant width except for occasional irregularities due to vortices, and is generally similar to a subsonic wake. The primary source of air flow in the wake consists of boundary-layer air, which expands from an annulus at the base of the body to fill the throat area. The main stream turns through the angle ϕ at the vicinity of the wake throat, with resulting compression and formation of the trailing shock. This shock generally appears to form at an angle nearly equal to that of the bow shock. Supersonic flow patterns around two different bodies of revolution are illustrated in Figure 6.49.

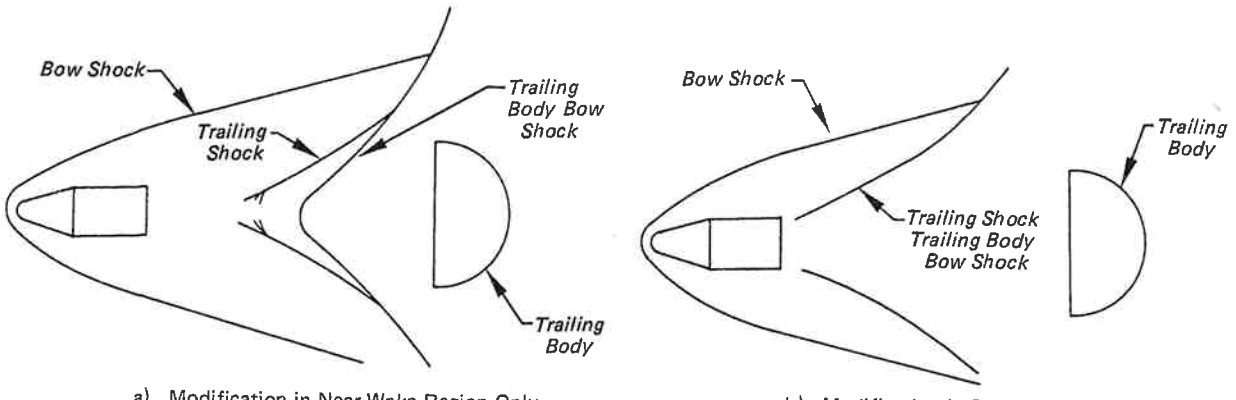
Body-Decelerator Flow Field Interactions. Any decelerator or other object placed in the near wake region will alter the wake to some extent. The decelerator and its bow shock wave can interact with the viscous inner-wake, the inviscid outer wake, the trailing shock wave, and even with the body bow shock wave, as shown in Figure 6.50a. Babish[313] considers



a) Ogive-Cylinder Primary Body

b) Skirted-Blunt Primary Body

Figure 6.49 Sketch of Flow Patterns Around Primary Bodies Alone at Supersonic Speeds



a) Modification in Near Wake Region Only

b) Modification in Base Flow Region

Figure 6.50 Types of Leading Body-Trailing Body Flow Field Interactions

alterations that take place only in the near wake region as not being body wake modifications. Alterations must take place in the base flow region, as shown in Figure 6.50b, to be considered a modified wake. Modification can take the form of non-convergence of the separated flow, increase in base pressure, or the location of the wake trailing shock wave in the base flow region.

The definition of wake modification is restricted for two reasons. First, as long as flow field alterations are limited to the near wake region or downstream, wake flow field and decelerator performance prediction techniques such as presented in References 563 and 432 are valid. Second, performance characteristics of the decelerator are significantly different when the base flow region is altered as compared to when only the near wake region is altered.

References 433 through 436 report the effects of wake flow type on the performance characteristics of trailing conical type decelerators. In close proximity to the forebody (wake modified) the decelerator may be stable but has a very low drag force; at slightly longer trailing distances (wake still modified) the decelerator is unstable and the drag force is subject to abrupt changes. At large trailing distances (wake closed) the drag force is high and stability is a function only of geometry limitations. The variation of decelerator drag coefficient with trailing distance of small rigid models at Mach 1.18 is shown in Figure 6.51.

Babish[313] defines a critical trailing distance as

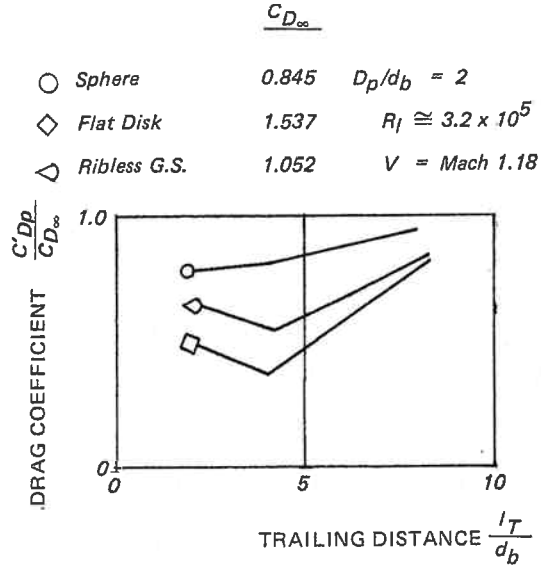


Figure 6.51 Drag Coefficient of Small Rigid Models in Wake of Simulated Ogive-Cylinder (Adapted from Ref. 433)

$(l_T/d_b)_{crit}$ beyond which there is no modification of the body base flow region by the decelerator. Use of critical trailing distance as a dependent parameter is suggested. The critical trailing distance was shown to increase with increasing size and bluntness and decreasing porosity of the decelerator and with decreasing bluntness of the towing body. No definite relationship between Mach number and $(l_T/d_b)_{crit}$ was established.

Reynolds number significantly affected the critical trailing distance as illustrated schematically in Figure 6.52. The weight of empirical evidence given in Reference 313 suggests that for any practical body-drogue combination the critical trailing distance is not likely to exceed $(l_T/d_b)_{crit} \approx 7$, which is a frequently used trailing distance in both subsonic and supersonic systems. In other words, the loss of decelerator drag in the near-wake makes it generally desirable to use a trailing distance greater than the probable critical trailing distance of the system.

Drogue Decelerator Performance in Wake. Numerous wind tunnel test programs have been accomplished where decelerator performance was measured in a body wake (Refs. 212,405-407,412,414,417,419,420, 433,437-439,440-466). Typical parameters which may be varied during these test programs include (1) free-stream Mach No., M_∞; (2) decelerator trailing distance, l_T/d_b; (3) body-decelerator diameter ratio D_p/d_b; and (4) decelerator porosity, λ_T.

As an example, Ref. 438 presents results from a wind tunnel test program conducted to determine the drag and performance characteristics of 5.3 ft nominal diameter disk-gap-band parachute configurations with various trailing distance and suspension line lengths. The parachutes, attached to 0.10 scale Viking entry forebodies and a faired body (Fig. 6.53) were investigated in the Mach number range from 0.2 to 2.6 at a nominal free-stream dynamic pressure of 80 psf.

The effects of the forebody shape on the parachute drag coefficient at $l_T/d_b = 9.14$ are presented in Fig. 6.54. At a given Mach number, the forebody wake effect produced by the entry vehicle and the lander resulted in essentially the same parachute drag coefficients. The parachute drag coefficient obtained in the wake of the forebodies in the vicinity of $M_\infty = 1.0$, was substantially less than the drag coefficient obtained behind the faired body. At $M_\infty = 1.0$, the parachute underinflation caused by the forebody wake resulted in parachute drag reductions of approximately 30 percent when compared to the drag coefficient obtained behind the faired body with minimum wake interference.

The variation of parachute drag coefficient with Mach number at various values of l_T/d_b are presented

in Fig. 6.55. For a given Mach number, the parachute drag coefficient increased with increasing l_T/d_b locations behind the Viking forebodies as shown in Figs. 6.55a and 6.55b respectively. These data also show a considerable decrease in drag coefficient with Mach number approaching 1.0, especially for the parachute configurations with the smaller l_T/d_b locations. Increasing the Mach number from 0.6 to 1.0 resulted in as much as 50 percent reduction in parachute drag coefficient as the parachute became underinflated in the wake of the forebody. The parachutes were tested behind a faired body to obtain relatively interference-free parachute drag characteristics. As shown in Fig. 6.55c. increasing the value of l_s/D_o also increased the parachute drag coefficient at a given Mach number behind the faired body.

Effect of Design Parameters on Decelerator Drag.

Knowledge of the effect of various decelerator design parameters on their performance contributes to a more reliable extrapolation or interpolation of available data in designing a recovery system for a particular application. As an example, investigations of the Viking drogue design performance through model wind tunnel tests (Refs. 467 , 468), during which design parameters such as geometric porosity, suspension line length, and reefing line length were varied,

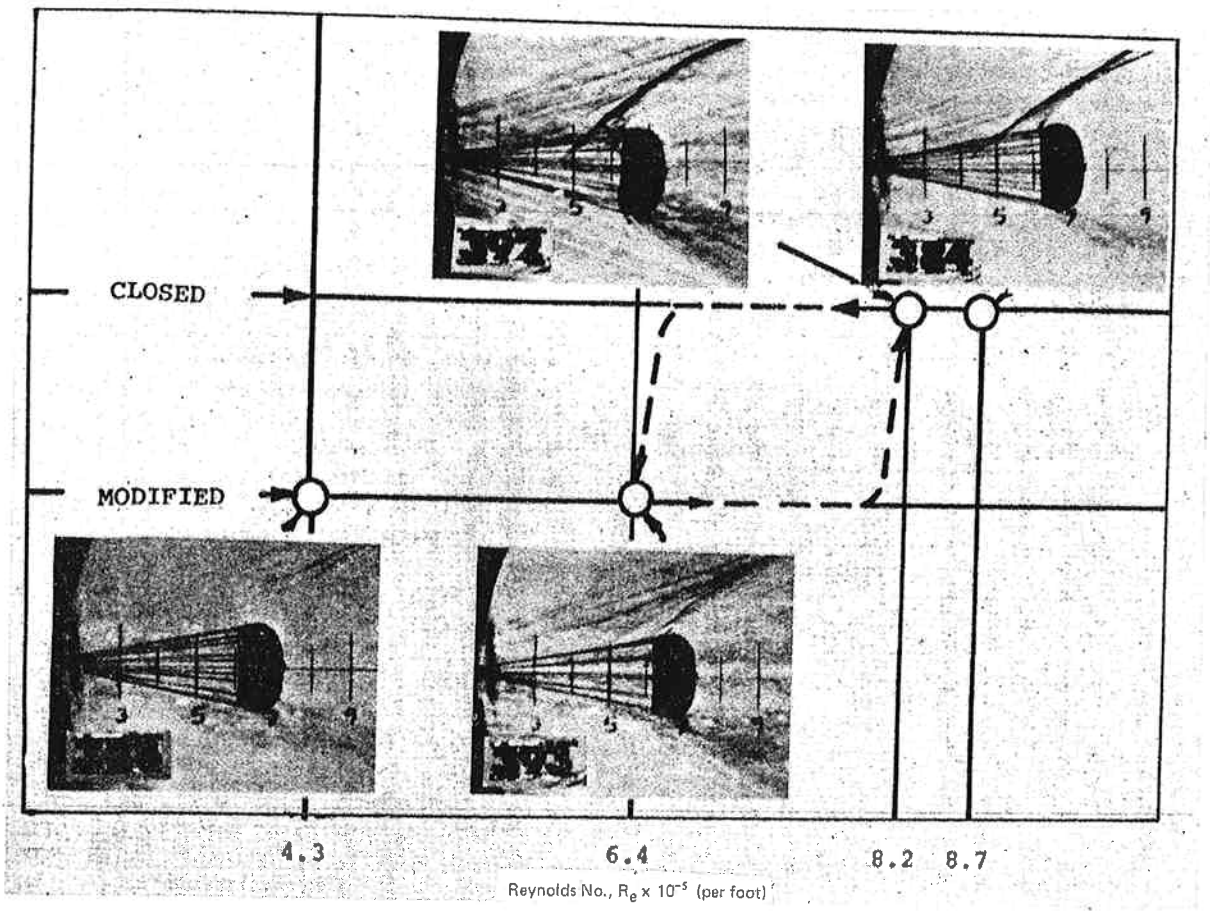
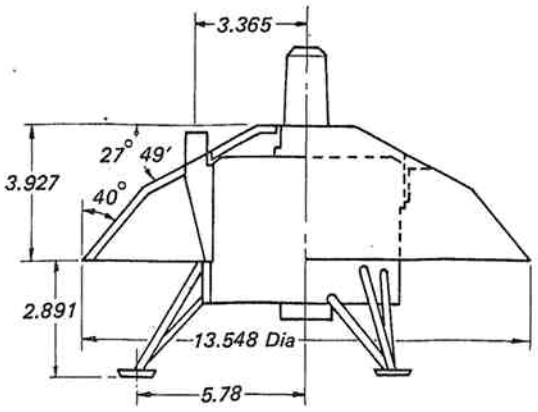
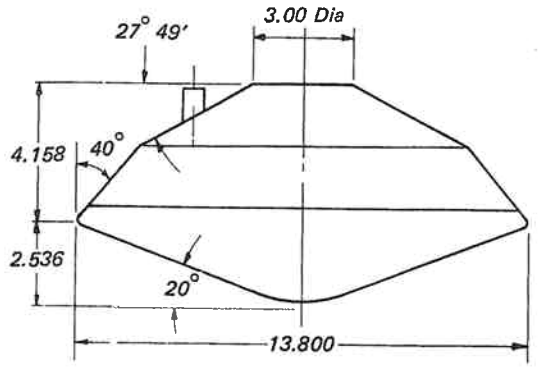


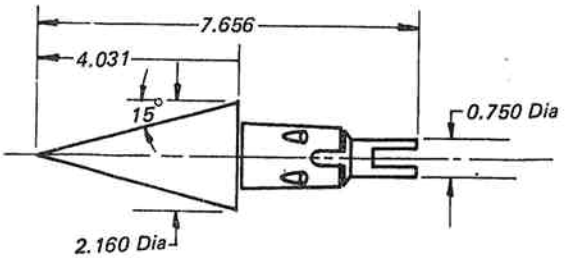
Figure 6.52 Wake Conditions Behind a Cone-Cylinder with a Trailing Hyperflo Type Parachute for Various Free-Stream Reynolds Numbers at $M = 3.0$ ($l_T/d_b = 6.2$)



a) Entry Vehicle



b) Lander



c) Faired Body

Figure 6.53 Scale Model Viking Entry Forebodies and a Faired Body

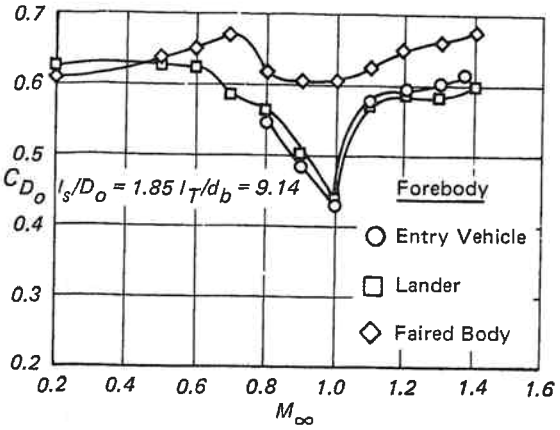
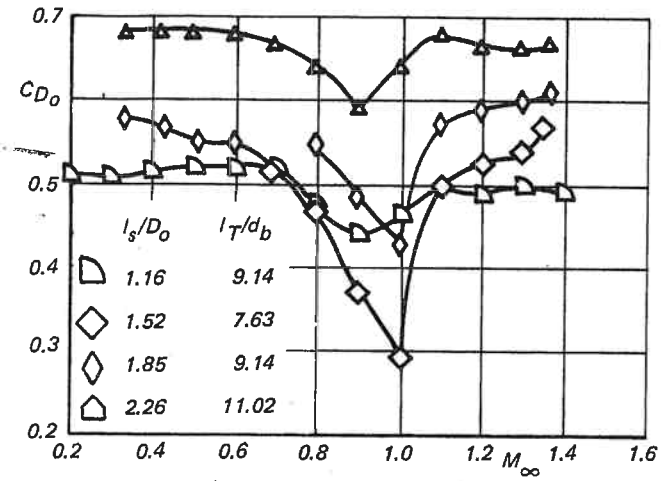
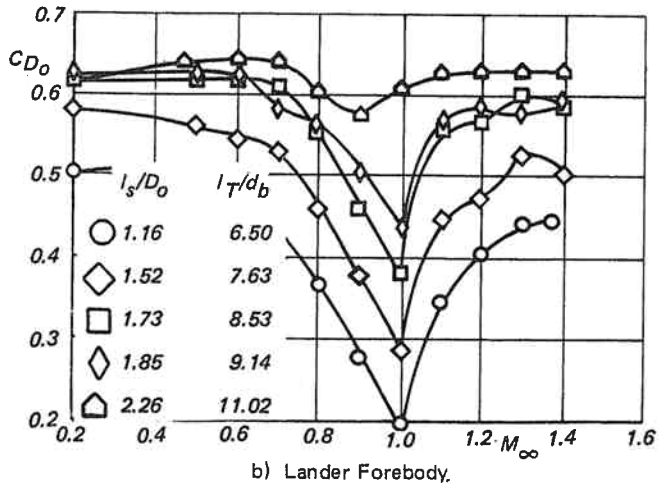


Figure 6.54 Effect of Forebody Shape on C_{D_o}

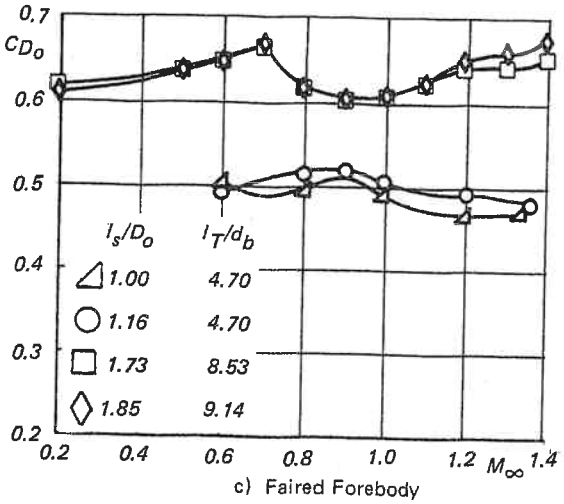


a) Entry Vehicle Forebody



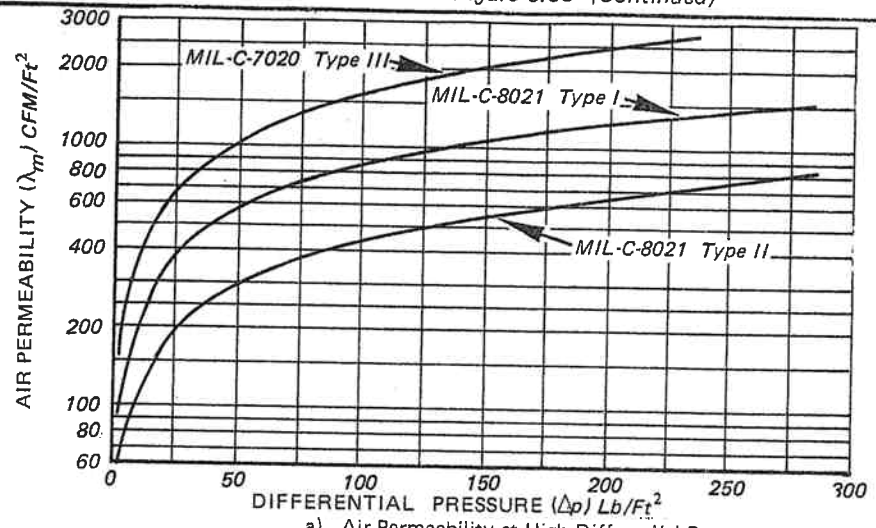
b) Lander Forebody

Figure 6.55 Variation of Disk-Gap-Band Parachute Coefficient with Free Stream Mach No.

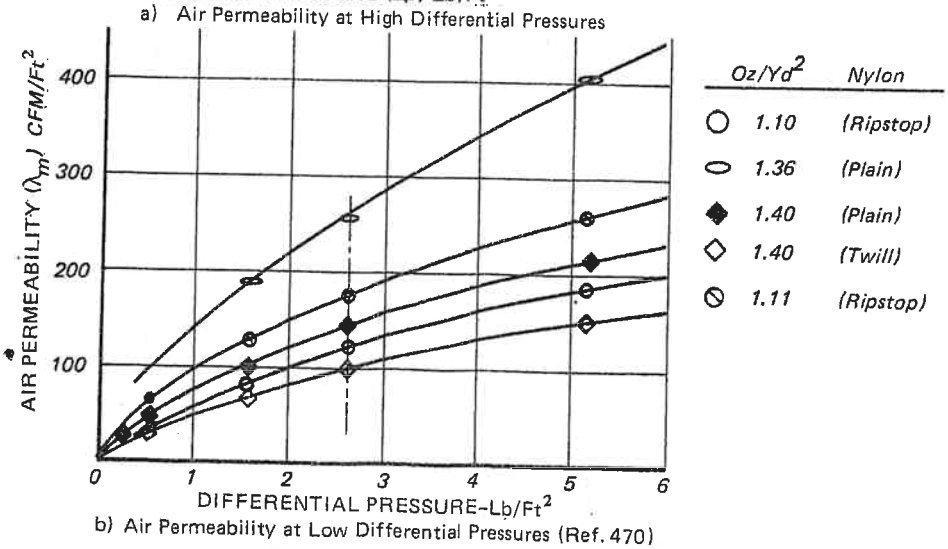


c) Faired Forebody

Figure 6.55 (Continued)

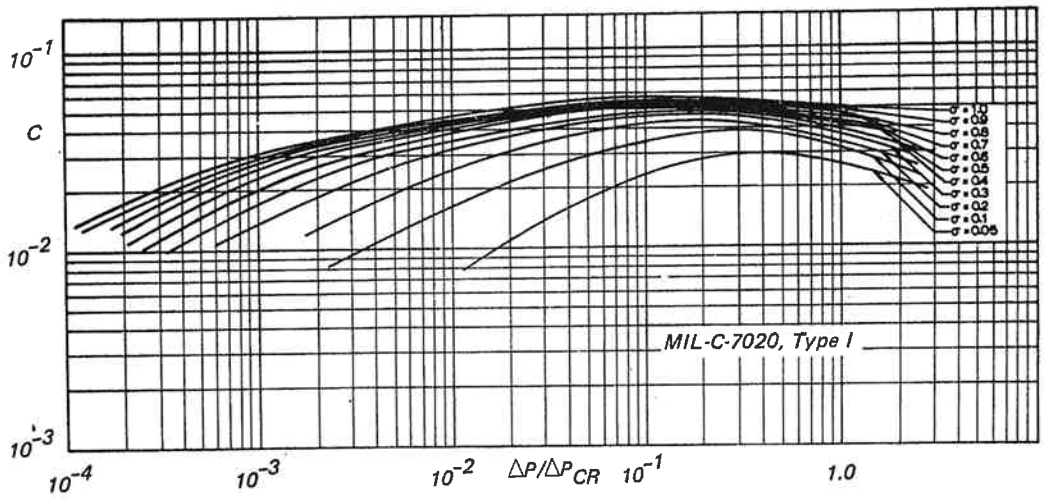


a) Air Permeability at High Differential Pressures

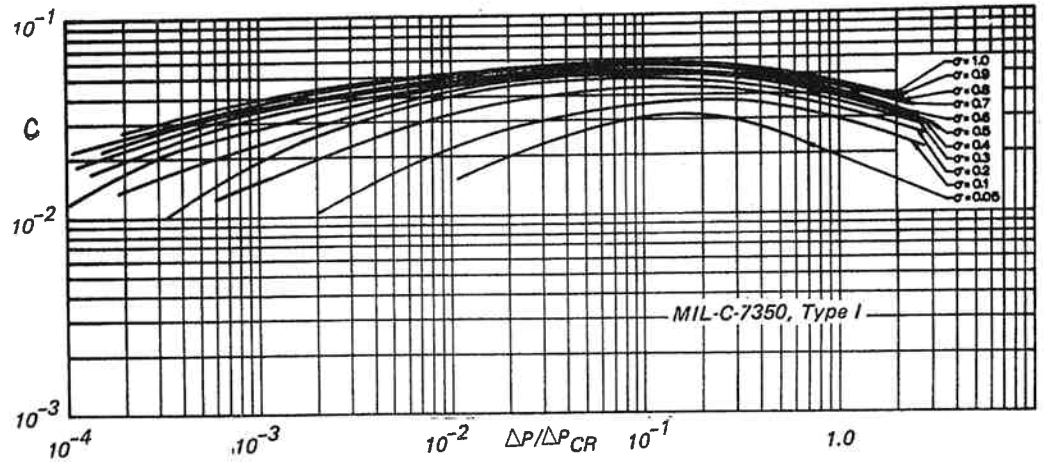


b) Air Permeability at Low Differential Pressures (Ref. 470)

Figure 6.56 Typical Variation of Mechanical and Effective Porosities of Nylon Parachute Cloth With Differential Pressure



a) 40 lb/in Nylon Cloth



b) 90 lb/in Nylon

Figure 6.57 Effective Porosity versus Pressure Ratio for Various Nylon Cloth Materials

provided results which compared favorably with full scale test data (Refs. 467, 469).

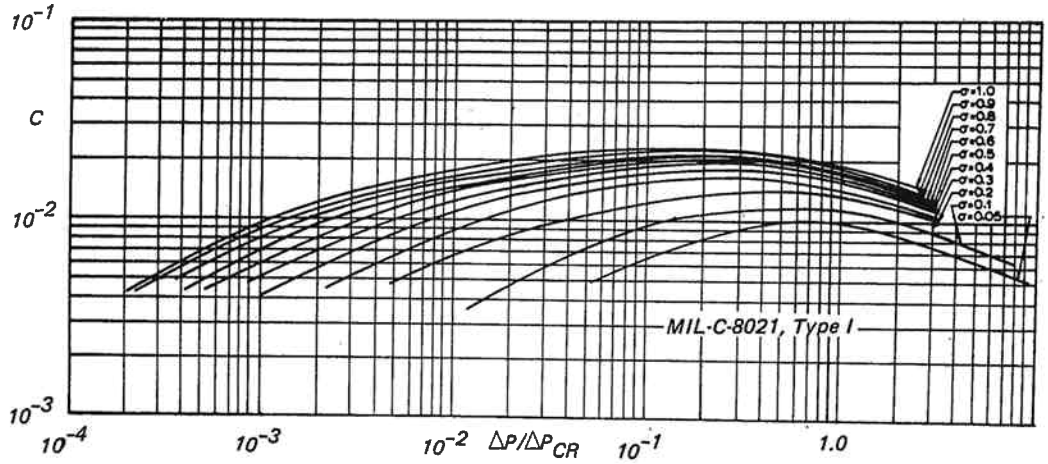
Canopy Porosity. Since most parachute operations are attended by well developed turbulence and large Reynolds numbers in the gross flow, viscosity effects on drag may be considered generally negligible. Therefore, it is reasonable to evaluate the average differential pressure across the canopy as

$$\Delta p = F/S_p = C_{D_p} q \qquad 6\text{-}33$$

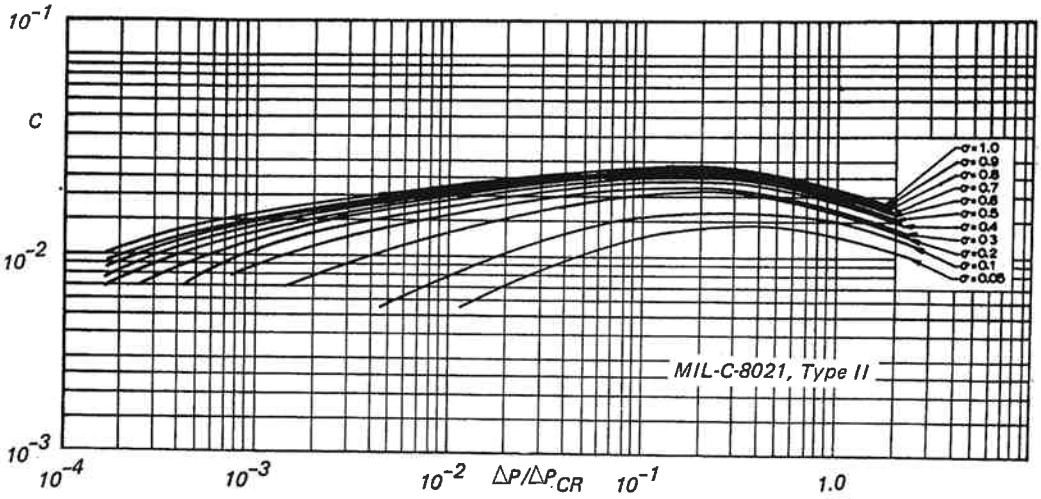
At moderate operating speeds, and during steady descent, it is this differential pressure that governs the permeability, λ_m, of the fabric surface. If precise knowledge of the effect of canopy porosity on parachute performance is desired, λ_m should be measured at several different points across the canopy before and after each test at differential pressures corresponding to those during both inflation and steady descent. The curves of Figure 6.56 are representative of the way in which λ_m varies with Δp for differential parachute fabrics. A useful characterization of canopy porosity is a dimensionless term called "effective porosity". Effective porosity is defined as

$$C = v_\lambda/(2\Delta p/\rho)^{1/2} = v_\lambda/v^* = \lambda_m/v^* \qquad 6\text{-}34$$

where v_λ is the average through-flow velocity of air and Δp is the pressure differential across the cloth[471]. When Δp reaches or exceeds the critical value (Δp_c) flow through the cloth pores becomes sonic. Added pressure will not cause the through-flow velocity to increase. Thus, for transonic and supersonic parachute operations the pressure ratio $\Delta p/\Delta p_{cr}$ should be taken into account along with the air density ratio σ which has a significant effect at high altitudes. The measured effective porosity of four different com-



c) 200 lb/in Nylon



d) 300 lb/in Nylon

Figure 6.57 (Continued)

monly used nylon parachute cloths is plotted as a function of $\Delta p/\Delta p_{cr}$ and σ in Figure 6.57.

It will be noted in Figs. 6.56 and 6.57 that in the region of $\Delta p = 2.6$ psf (0.5 inch water) and even up to $\Delta p = 20$ psf, both λ_m and c vary markedly with only small changes in Δp. Thus, it is not surprising that the cloth specifications allow a total variation of 40 to 46 percent in the rated air permeability. Consequently, λ_m also varies widely for any given fabric weave and is seldom known with any degree of accuracy. Part of the problem arises from deficiencies in the performance of different cloth permeability measuring instruments, some of which embody hidden losses due to viscosity and turbulence effects[472].

Figure 6.58 presents canopy drag coefficient data as a function of canopy total porosity, λ_T, for both small model and full scale parachutes of various types. Here it was assumed that the total porosity can be expressed as,

$$\lambda_T = \lambda_g + c_m \qquad 6\text{-}35$$

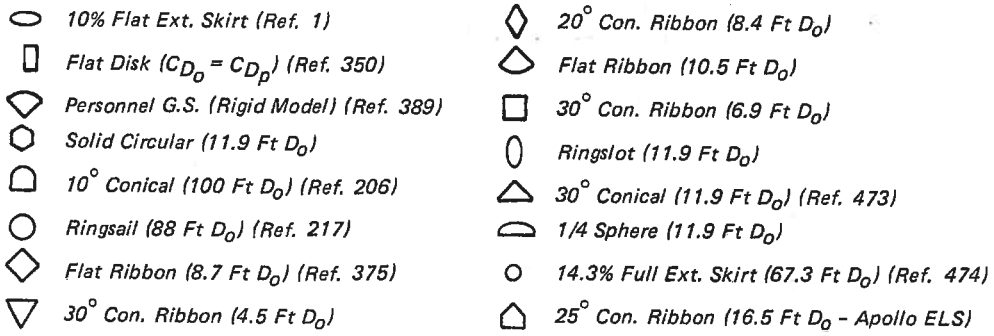
where, with λ_m given in cfm/ft^2 for solid cloth canopies, by Equation 6-34

$$c_m = (\lambda_m/2810)\,(S_\lambda/S_o) \times 100 \qquad 6\text{-}36$$

where S_λ = cloth area

2810 = value of v^* at $\Delta p = \frac{1}{2}''\,H_2O$

As shown in Fig. 6.58 the drag coefficient of a parachute is reduced in proportion to the total porosity of the canopy, i.e., the momentum transfer between canopy and air decreases as the average throughflow velocity increases. Included in the high porosity range are heavy ribbon drogues in which λ_T was augmented by the fixed reefing technique.



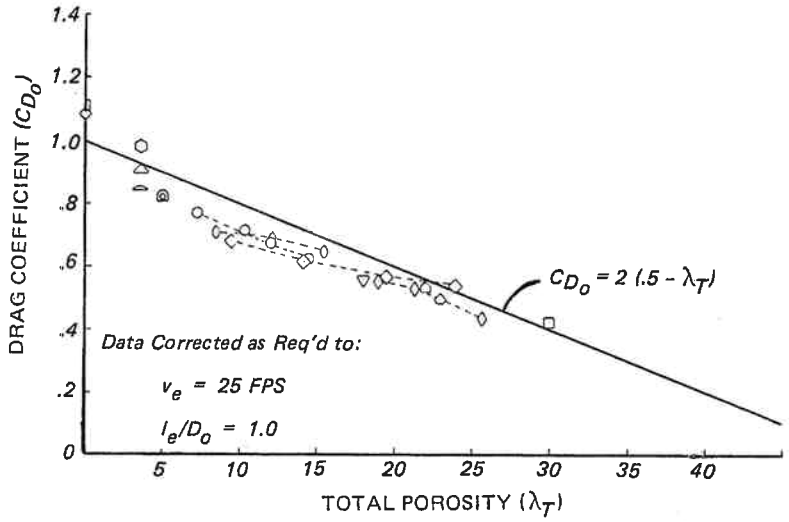


Figure 6.58 Effect of Canopy Porosity on Parachute Drag Coefficient

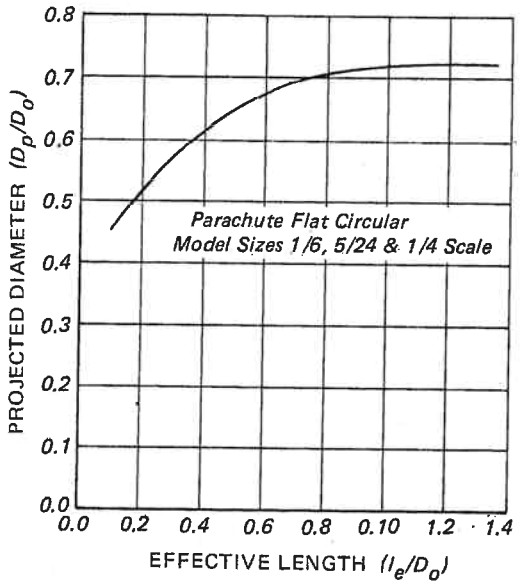


Figure 6.59 Variation of Canopy Projected Diameter With Effective Length of Suspension Lines in Small Models (Ref. 382)

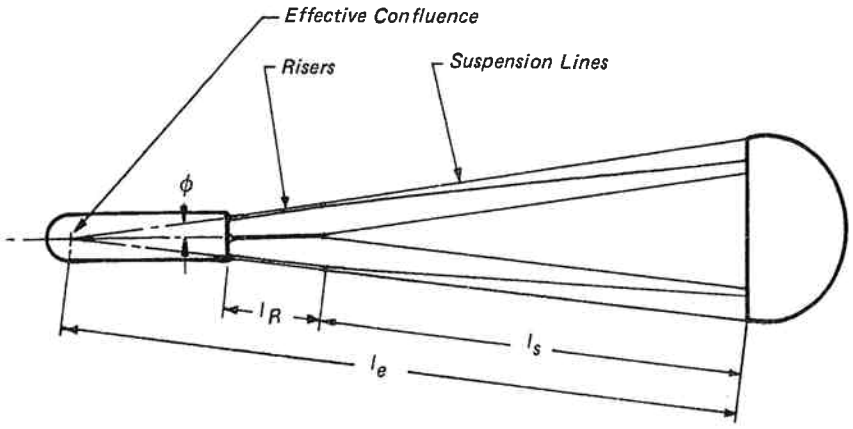


Figure 6.60 Effective Rigging Length With Multiple Riser Attachments

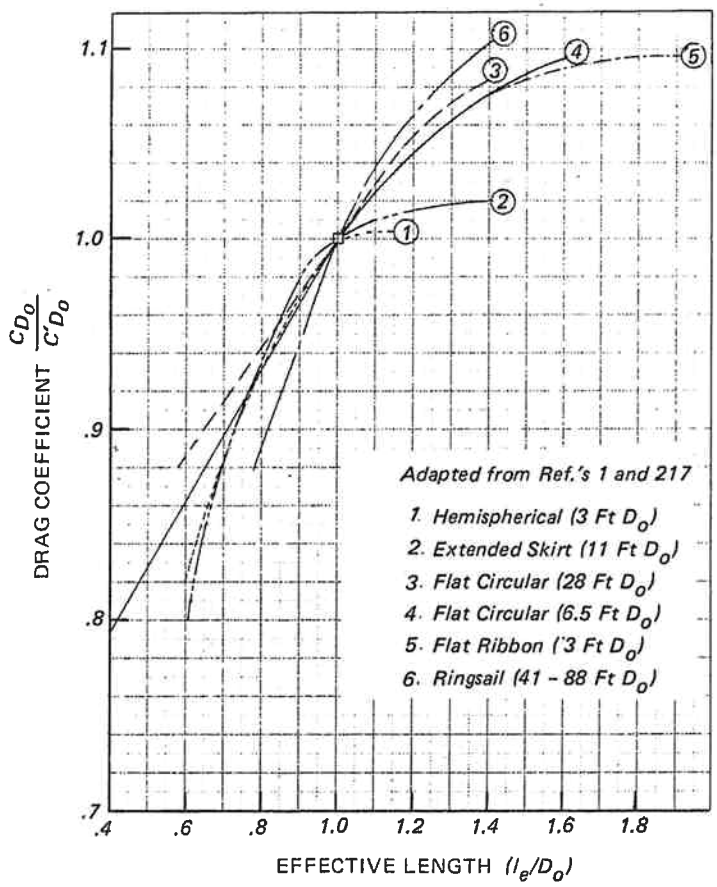


Figure 6.61 Effect of Suspension Line Effective Length on Parachute Drag Coefficient

Where necessary, drag coefficients were corrected to $l_e/D_o = 1.0$ and for larger parachutes, to $v_{e_o} = 25$ fps (see Figs. 6.35 and 6.61). Scale effects due to differences in Reynolds number apparently are insignificant.

The data in Fig. 6.58 are presented for their qualitative value as an aid to understanding parachute operation and are not intended for use in design calculations.

The variations apparent in drag characteristics of different parachute models probably result from one or more of the following factors:

Canopy shape
Random oscillation and gliding during descent
Structural elasticity
Relative stiffness
Wind tunnel constraint effects
Errors of measurement

Some are combined in what are called "scale effects".

Effective Length of Suspension Lines. The radial component of suspension line tension limits the inflated diameter of a canopy in a way that depends on the constraints placed on the freedom of the skirt by design, e.g., constructed profile. Since the radial force component is proportional to $\sin \phi$ and, hence, the distance from skirt to confluence, the projected diameter of the inflated canopy is a function of the effective suspension line or rigging length. The dependence of D_p/D_o on relative rigging length, l_e/D_o, is indicated by measurements made with small flat circular parachute models plotted in Figure 6.59. The projected diameter, in turn, determines the area ratio, S_p/S_o, and so has a strong influence on the drag coefficient of the parachute.

The distance between the canopy skirt and either the actual or effective confluence point of the rigging (lines plus riser and branches) is treated as the effective length in Figure 6.60. With four or more riser branches above the keeper, a common configuration,

$$l_e = l_s + l_R \qquad 6\text{-}37$$

It is evident that with only two risers, the parachute lacks rotational symmetry, having one confluence point in the longitudinal plane of symmetry at the line to riser attachments and an effective confluence much lower in the plane of the risers. This distorts the inflated canopy, making it slightly oval with major axis transverse, as in the familiar personnel parachute configuration.

Parachutes and drogues with multiple risers attached to separate hard points on the body have an effective confluence point upstream for which the effective length is greater than $l_s + l_R$ as shown in Figure 6.60. The variation of C_{D_o} with effective rigging length is shown in Figure 6.61 for a number of different circular parachutes.

It is evident that D_p must be strongly dependent on the effective length until with increasing length, the canopy skirt comes under sufficient tension to resist further radial expansion. Consequently, the increase of C_{D_o} with l_e varies significantly among the different canopy designs as shown, but divides mainly between the models with positive skirt angles and those with zero to negative skirt angles. This is the structural feature that determines the extent to which the canopy mouth can open before the skirt tension builds up enough to make D_p and C_{D_o} invarient with the effective length of the suspension lines.

Gore Shape. The influence of gore shape on the inflated profile of the canopy depends somewhat on whether the gore is assembled from bias-cut or block-cut sections of cloth. Gore shape is less influential with bias construction because of the radial and circumferential elongation of material that takes place at very light pressure levels. When bias-cut cloth is used, a marked change in gore coordinates is required to produce a desired change in the canopy profile, which in circular canopies tends to remain a smoothly rounded ellipsoid with its super-imposed characteristic radial pattern of bulging gores. Presumably, this effect is largely responsible for the improved C_{D_o} of "conical" canopies relative to the flat design; there is no significant difference in inflated profile, and less cloth is required to produce the same projected area.

When the gore is assembled from block-cut sections, the reduced circumferential elasticity of the cloth exercises a firmer control over the canopy profile and the small drag advantage of the conical canopy relative to the flat canopy largely disappears. Block construction is confined mainly to slotted canopy designs, and differences in gore coordinate schemes are more clearly reflected in their inflated profiles, particularly in the crown area.

In either case, bias or block, the gore shape that produces the largest ratio of S_p/S_o will generally yield the highest drag coefficient when other design parameters are equivalent. This area ratio is reflected in the fineness ratio of the inflated canopy, i.e., h_p/D_p, which varies noticeably from one design to another.

Another indicator appears when the average width to length ratio of the gore is excessive by as little as three percent in relation to the number of gores. This produces a surplus of cloth circumferentially around the canopy that cannot be completely filled out against the radial component of suspension line tension by the internal pressure force. In-folding of several gores results and S_p/S_o is sharply reduced. The same effect may be produced by rigging the cross-

vent lines shorter than the design vent diameter, a method sometimes employed to provide stress relief.

Skirt Angle of Attack. Another shape factor affecting C_D is a sharply negative conical skirt of substantial width which tends to streamline the canopy and delay flow separation, thereby weakening the turbulent wake, a factor which accounts for the relatively low drag coefficients of the Guide Surface drogues. In the Ballute this effect is amplified further.

Canopy Fineness Ratio. Some appendages added to the canopy, increase its fineness ratio and augment S_o at the same time. As noted, the ratio of the height of the inflated canopy to its projected diameter, h_p/D_p, varies from one design to another but apparently has little effect on the average drag coefficient until it is mechanically exaggerated by the addition of a super-structure such as the conical extension of this class of mid-air retrieval parachutes.

Another method of changing the fineness ratio of an inflated canopy, but with no actual change in S_o, is represented by skirt reefing. The usual problem arises with reefed parachutes, that of obtaining reasonably good measurement of inflated canopy dimensions. Some fineness ratio data have been obtained from wind tunnel work, References 217 and 350, and some from calculations based on photogrammetry and calculated geometrical relationships. The effect of canopy fineness ratio on C_{D_p} is shown in Figure 6.62 for various parachute configurations and related wind tunnel models.

Annular Shape. The large central "vent" of the annular canopy does not have the same effect on total drag that the vent of the other circular canopies have. Topologically the large vent is part of the outside or ambient environment and so is not included in the calculation of the canopy area, S_o. The configuration has two limits:

As D_v/D_p approaches zero the annular canopy reaches the configuration of the solid circular canopy with apex retracted by a central line.

As D_v/D_p approaches unity the aspect ratio of the annular surface approaches infinity and the airflow changes in character progressively from 3-dimensional toward 2-dimensional.

Scale or Nominal Diameter. [*In this context Reynolds number is nearly proportional to D_o only.*] The fact that large parachutes have less tolerance for porosity than small models of the same type may actually be the result of increased relative elasticity rather than greater sensitivity to the increased turbulence attending large ratios of inertial to viscous forces signified by high Reynolds numbers. The implication is that to maintain the same effective porosity in a more elastic canopy the design porosity must be reduced. The total porosity of large ribbon and ringslot canopies is made less than for small models to preserve reliability of opening. The gradual upward trend of C_D with canopy scale may result in

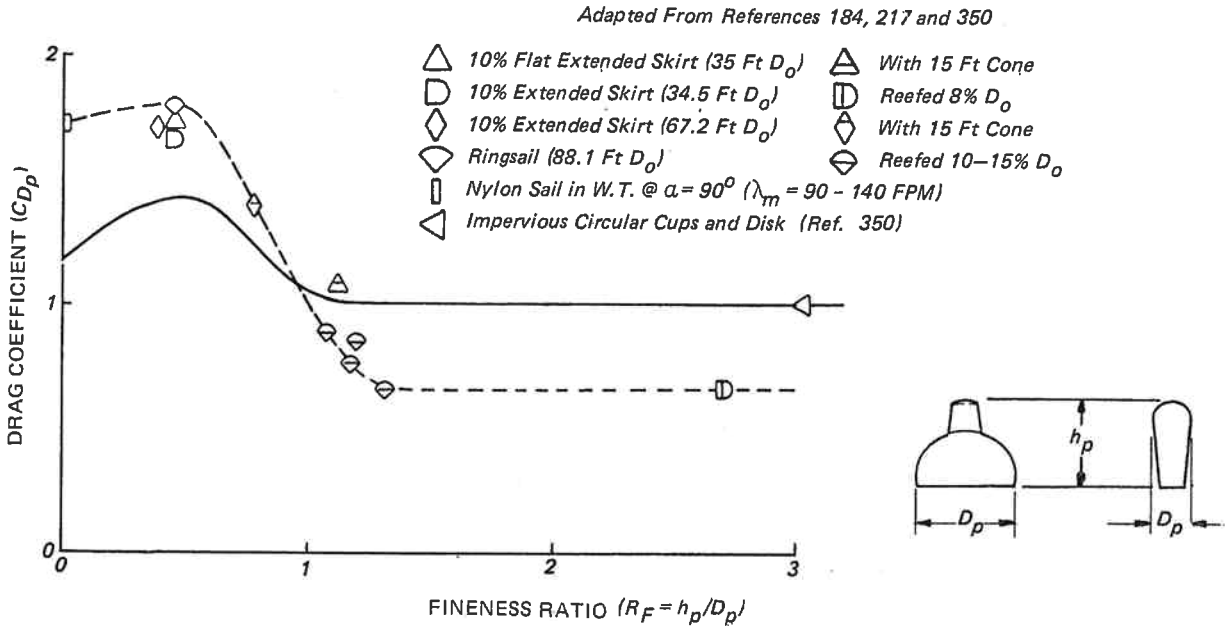


Figure 6.62 Effect of Canopy Fineness Ratio on Drag Coefficient

part from the reduced effective porosity prevailing during descent when Δp is much lower. This upward trend of C_D with increasing parachute scale or nominal diameter of the canopy is illustrated in Figure 6.63 for several different parachute types at the same unit canopy loading and effective line length ratio. It is evident that the configuration of a large parachute is not identical to that of the small parachute of the same design type after salient design parameters have been equalized:

The number of gores, being proportional to the diameter ratio, is greater.

The structure, when fabricated from the same materials, is proportionately thinner and more flexible.

The internal loads are generally higher because the canopy radius of curvature is larger and the total load increases as the square of the diameter, while the number of suspension lines increases as the number of gores, almost linearly with diameter.

With higher internal unit loads at the same unit canopy load the relative elongation of all components of the large canopy will be greater than for the small ones. This presumably is the elasticity factor leading to the use of a lower design porosity for the large slotted canopy, but in solid cloth canopies the design porosity is fixed by the fabric employed. Thus, another factor affecting C_{D_o} would be increased projected diameter ratio resulting from the higher relative elongation of the structure, the effect on λ_m being too small to be significant during steady descent. In view of this, it would appear that the increased relative projected area, S_p/S_o, is the dominant factor in parachute types which exhibit higher drag coefficients in large models than in small ones. The data trend for these parachutes is generally contrary to the evaluations made by earlier investigators.

DRAG AREA CONTROL

Some decelerator systems employ a canopy (or cluster of canopies) that is allowed to open and inflate fully without restraint. Examples are personnel parachutes, light cargo airdrop systems, and others in which the loading conditions are compatible with the structural strength of the decelerator and the vehicle and with the tolerance of the payload for impact shocks and deceleration.

Multi-stage systems are designed to limit peak loads and decelerations to acceptable levels through the use of drag area control. This is effected stepwise either with two or more decelerators of different sizes deployed sequentially, or with canopy reefing. Of the various reefing methods tested experimentally, skirt reefing with a short line loop in running rings around the air inlet or skirt of the canopy has been used most extensively.

Canopy Skirt Reefing

For practical skirt reefing systems of the types widely used, the reefing ratio is defined as the ratio of the diameter of the reefing line circle, D_r, to the canopy nominal diameter, D_o, frequently expressed

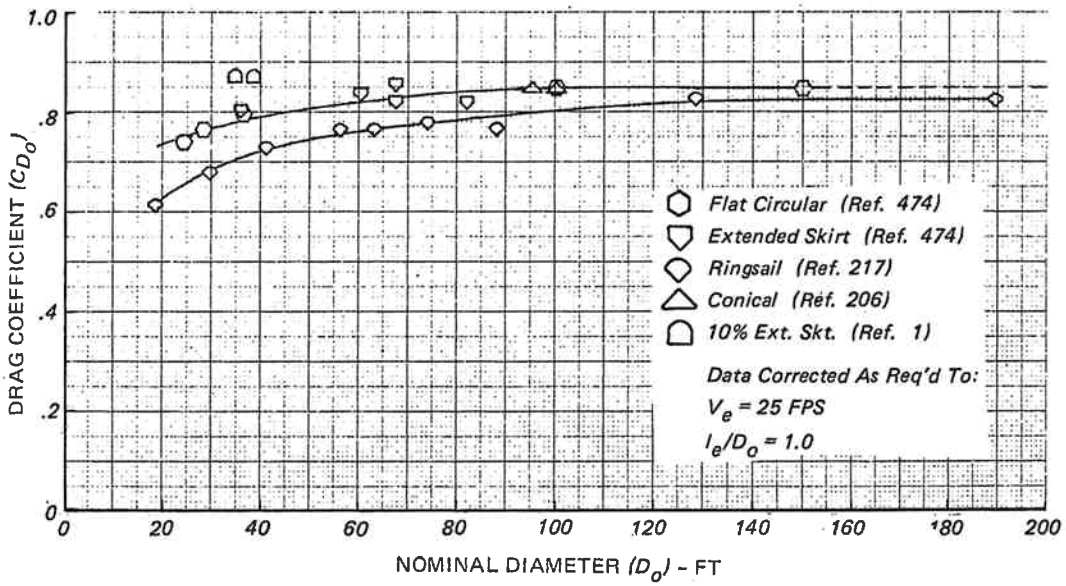


Figure 6.63 Variation of Parachute Drag Coefficient With Scale

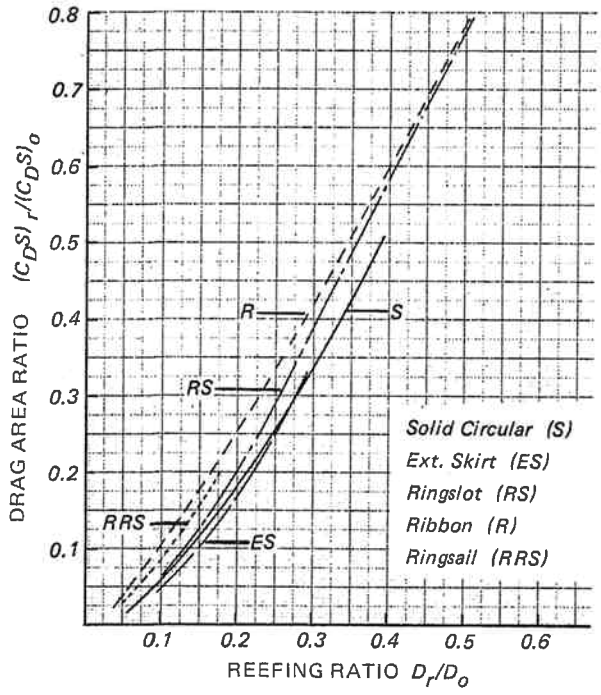


Figure 6.64 Drag Area Ratio vs. Reefing Ratio for Solid Circular, Extended Skirt, Ringslot, Ringsail and Ribbon Parachutes (from Ref. 393)

as a percentage. Because the reefed canopy continues to inflate for a while after the reefing line comes taut, it is desirable to distinguish between reefed drag area at the time the opening force reaches its maximum value, and reefed drag area at the instant of disreefing. Steady-state measurements of reefed drag area in the wind-tunnel are representative of the latter condition, because usually at disreef the system is approaching an equilibrium descent condition. Full-scale free-flight evaluation of reefed drag area is based on this assumption. Trajectory analysis of a system flight test yields F/q of the parachute as a function of time and whenever the rate of change becomes small, often the case at disreef, the instantaneous value of F/q is taken to represent the *reefed drag area,* $(C_DS)_r$. Average values for a number of tests are then evaluated in terms of $(C_DS)_r/(C_DS)_o$ as a function of D_r/D_o. The test data show considerable scatter so that the faired curves used for design purposes yield only approximate reefed drag areas in most cases and usually require verification by aerial drop tests of the new system.

Reefed Drag Area vs Reefing Ratio. For circular canopies the *reefing ratio* has been defined as D_r/D_o.[393] When the reefing line is under tension it does not form a circle, but a nearly regular polygon. Consequently, the canopy inlet area for a given reefing ratio varies to some extent with the number of gores in the canopy, becoming potentially a scale effect. However, within the present state-of-the-art this is a minor factor lost in normal data scatter.

The variation of $(C_DS)_r/(C_DS)_o$ with D_r/D_o is shown in Figure 6.64 for a number of different parachute types. The faired curves are derived from the average data of Reference 393 obtained from a large number of full scale drop tests and a few wind tunnel tests. At $(C_DS)_r/(C_DS)_o = 1.0$ the canopy is fully inflated and the curves tend to converge on $D_r/D_o = 0.637$ or $2/\pi$, which is the theoretical maximum reefing ratio of an idealized flat circular canopy (see Chapter 2). This point may be used as a guide in fairing through full scale tests data and helps determine the quality of the small model data.

Drag Coefficient vs Reefing Ratio. In a limited number of cases it has been possible to measure the projected diameter of the inflated canopy both reefed and full open and so provide a basis for evaluation of S_p and C_{D_p}. The results are plotted in normalized form in Figure 6.65. In view of Fig. 6.62 showing the effects of the fineness ratio of the inflated canopy on C_{D_p} it appears unlikely that the non-dimensional drag coefficient would be less than $C_{D_p}/C_{D_{PO}} = 0.35$ for any practical reefing ratio smaller than $D_r/D_o = 0.08$. At $D_r/D_o < 0.05$ twisting of the reefed parachute and twisted line malfunctions become potential hazards.

The data for 18 inch (D_o) models derived from measurements reported in Reference 475 are presented for comparison. While the slotted models follow the general trend established by the 35 inch (D_o) conical ribbon data, the solid cloth models show a radically different behavior. Photographs of these models in the wind tunnel reveal an over-expanded inflated profile characteristic of low porosity canopies, rather than the elongated profile seen in the typical full scale reefed canopy. Thus, both non-scale stiffness and porosity of the models may be responsible for the discontinuity in the drag coefficients of the solid cloth models for reefing ratios greater than $D_r/D_o \approx 0.18$, i.e., apparently the total drag does not increase in proportion to the increased projected area of these models.

Reefed High-Glide Parachutes

Reefing of high performance gliding parachutes was only partly successful over the normal range of deployment velocities until methods were developed for the temporary equalization of suspension line

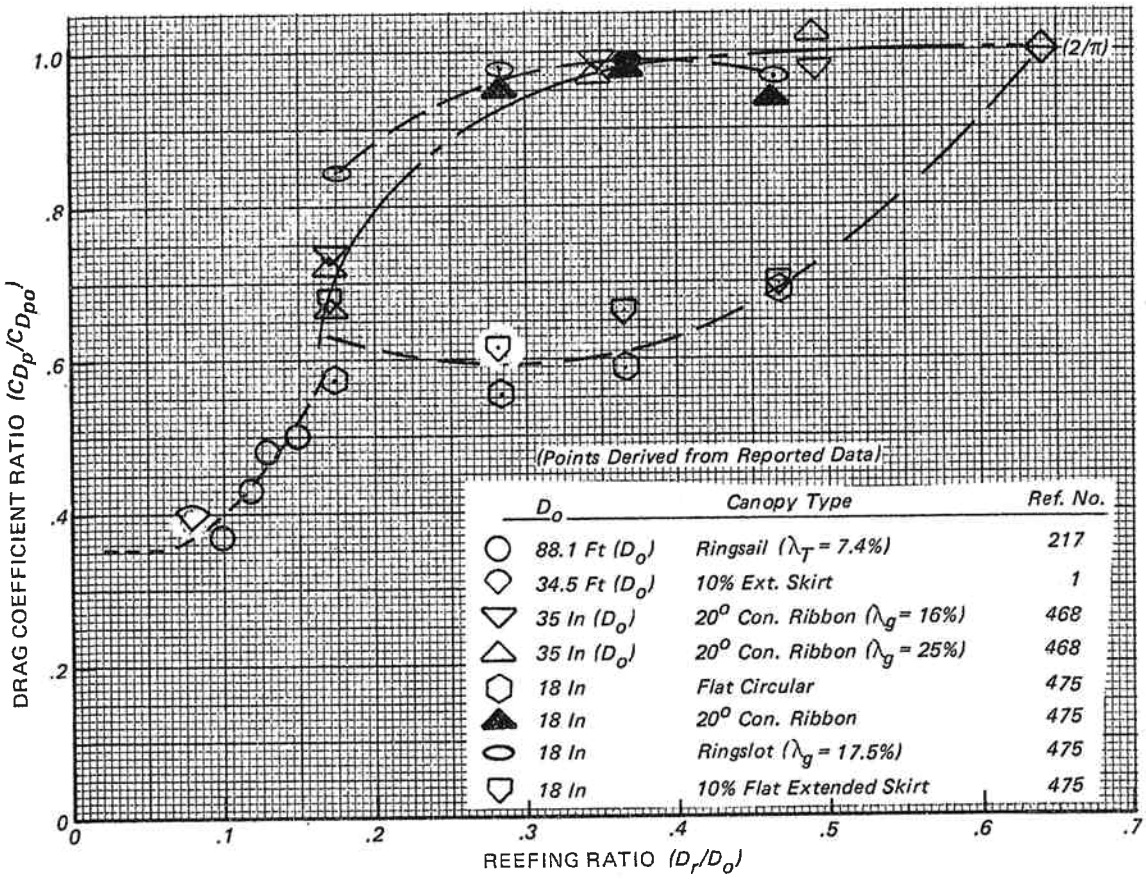


Figure 6.65 Variation of C_{D_p} With Reefing Ratio

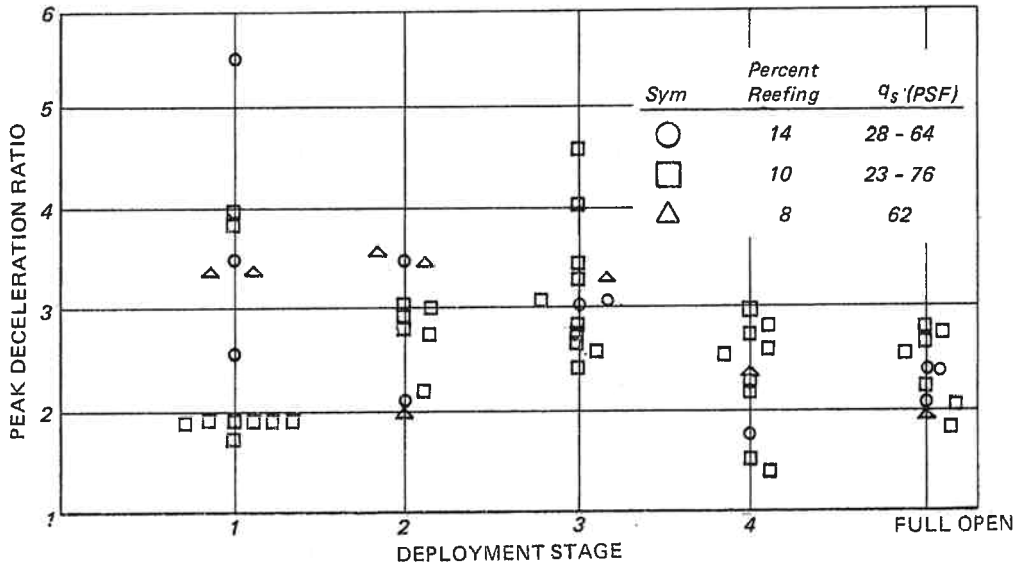


Figure 6.66 Measured Peak g's vs Opening Stage of 4000 Ft² (S_W) Twin Keel Parawing

lengths during deployment and opening. This approach was found necessary in order to bring the extremes of inequitable line load distributions within manageable limits. At the same time, it was essential that the reefing of the canopy neutralize the gliding tendency by forming balanced pockets or lobes in the pressurized areas, otherwise strong aerodynamic moments resulted.

The multi-stage reefing technique developed for a twin-keel Parawing of $S_W = 4000\ ft^2$ reported by Moeller and Linhart (Refs. 398 and 220), was an outgrowth of that developed earlier by Linhart and Riley[400] for a 40 ft (D_W) Cloverleaf steerable parachute, both involving three-lobed configurations. However, line equalization was needed only on the Parawing, the Cloverleaf having evolved from parachute practice with all lines of equal length. The development of flexible wing reefing systems was approached from two directions: conventional fixed wing aerodynamics and parachute aeroelastic dynamics. The first approach produced reefed systems suitable for low speed deployment, the second for the deployment speeds characteristic of spacecraft landing systems $(q = 30\ to\ 100\ psf)$. Performance of the four-stage reefing system developed for the 4000 ft^2 (S_W) twin-keel Parawing is illustrated in Figure 6.66.

Successful deployment and inflation of a (300) ft^2 Parafoil system at speeds of 125–130 kts EAS was demonstrated[132] employing a hybrid reefing system in which the line lengths were equalized for a wing angle of attack of 0°. It was necessary to reef the inlet area of the air cells across the full span to prevent fabric rupture by over-pressurization. Upon disreefing, the cell inlets opened fully. After two seconds time delay the Parafoil was allowed to pitch to the built-in glide trim angle. The effect of this reefing technique on measured Parafoil opening forces was evaluated in terms of a dimensionless coefficient defined as

$$C_{T_X} = F_X/qS_W \qquad 6\text{-}38$$

where q is the dynamic pressure at the start of filling (snatch and disreef) and S_W is the planform area of the canopy. Table 6.10 gives opening force coefficient values recorded in full scale drop tests of the 300 ft^2 Parafoil model with a suspended load of 650 lbs and a gross load of 705 lbs. Deployments were effected at dynamic pressures up to $q = 57\ psf$.

Performance characteristics of reefed Volplane, Sailwing, and Paraplane personnel parachutes obtained during drop tests are reported in Refs. 402, 403, and 476, respectively.



Figure 6.67 Parawing Descending in Reefed Mode



Figure 6.68 Clustered Canopies with Apexes Retracted

Multi-Stage Suspension Line Reefing

Temporary shortening of all suspension lines has the type of reefing effect on canopy drag area indicated by Figures 6.59 and 6.61. Moreover, temporary equalization of suspension line lengths on a high-glide parachute shortens them in varying amounts which automatically has the effect of constricting the projected area of the canopy (Figure 6.67). Use of this principle as a means of effecting multi-stage reefing was investigated experimentally on a 400 ft^2 (S_W) Parawing[136,477]. With a series of four reefed stages of increasing effective suspension line length, it proved feasible to limit disreef opening forces to approximately 3 g's. The suspension line reefed stages were preceded by one canopy reefed stage for which the opening forces were consistently low *(≈ 1.8 to 2.8 g's),* but measured snatch forces were consistently high *(≈ 6 to 12 g's).*

Canopy Apex Retraction

Originally conceived and tested as a reefing method, retraction of the canopy apex with an axial control line has more recently been used a means of both shortening the filling time and increasing the effective drag area of the fully inflated canopy. For this purpose the apex retraction line is made a fixed length which will pull the apex down a distance in the range of 0.25-0.40 D_O. The effects of this type of rigging on the inflated shape and steady state internal loads of flat circular parachutes are shown in Figures 6.68 and 6.69 respectively. The drag and stability characteristics from wind tunnel tests of small cloth parachute models with axial (apex retraction) lines are reported in Reference 478.

TABLE 6.10 PARAFOIL OPENING FORCE COEFFICIENT

Conditions	C_{T_X} Min.	Mean	Max.
Non-reefed	.37	.53	.69
Reefed:			
a) (Cell inlets reduced)	.12	.18	.23
b) (Cell inlets open)	.17	.35	.58
Disreef to full:			
a) Cells reefed	.19	.55	1.35
b) Cells open	.8	1.6	2.8

STABILITY

The stability of deployable aerodynamic deceleration systems is the joint product of the aerodynamic characteristics of the body and the decelerator and of the influence each has on the other. A stable winged craft may be destabilized by application of the drag of a stable decelerator at an unfavorable point on the body. A stable decelerator may be destabilized by the wake of the body. A body and a decelerator that are both unstable may be stabilized by joining them together with a harness of suitable design.

The motion of a system moving freely through air may exhibit two general classes of stability:

Static stability is the tendency of a system to develop steady-state restoring moments when disturbed from a position of equilibrium.

Dynamic stability is the tendency of a moving system to develop moments that act to damp unsteady motion (Figure 6.70a).

The system may have none, one, or more than one position of equilibrium. Its static stability at any given equilibrium position depends upon the way in which the aerodynamic moment changes when the system angle of attack is changed. The degree of static stability is proportional to $dC_M/d\alpha$, the slope of the moment curve when plotted against angle of attack (Fig. 6.70b). Static stability or a condition of stable equilibrium is necessary to obtain dynamic stability, but static stability does not ensure dynamic stability. Classical aerodynamics teaches that too much static stability may cause dynamic instability if damping is inadequate. A system is dynamically stable when the restoring moments work to decrease the amplitude of each succeeding oscillation toward zero or to a small steady state amplitude.

Static Stability - Circular Canopy

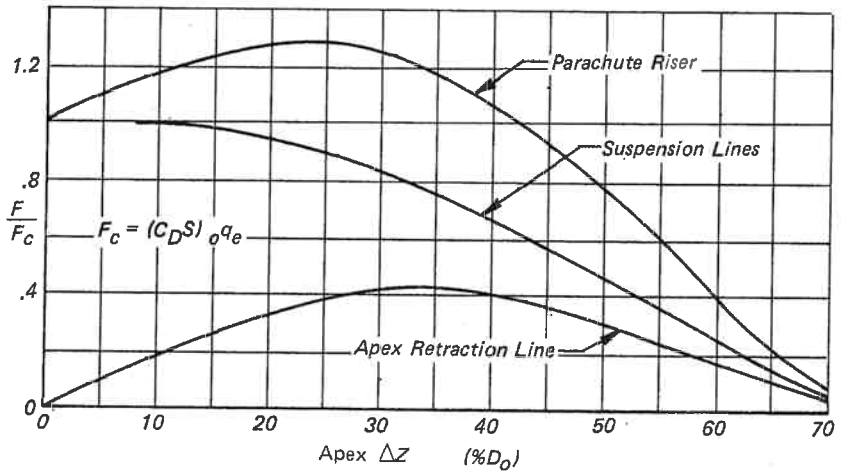
The system of axes used for static stability considerations is shown in Figure 6.71. By definition,

$$C_M = M/DqS \qquad 6\text{-}39$$

where D is the canopy diameter corresponding to the characteristic area S. The aerodynamic moment M, appears whenever the aerodynamic force vector departs from the system center of gravity; unsteady motion follows. This behavior is also described by evaluation of the axial and normal force components $F_A = C_A Sq$ and $F_N = C_N Sq$, when the canopy is constrained in the wind tunnel at a given angle of attack. Then the aerodynamic moment is $M = F_N l$ and

$$C_N = C_M (D/l) \qquad 6\text{-}40$$

where l is a significant length, such as the distance from the center of pressure of the canopy to the center of mass of the body shown in Figure 6.71. C_N



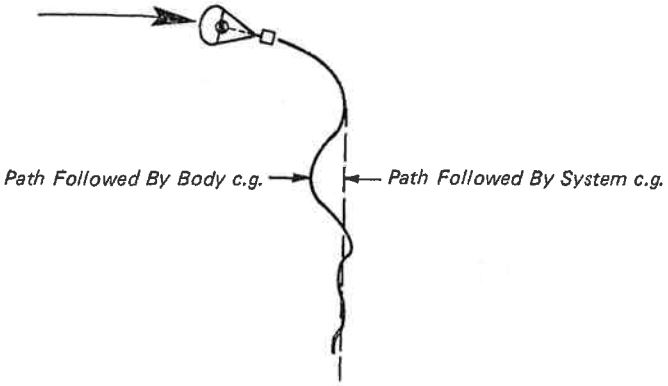
b) Forces in Parachute Suspension Members vs Apex Retraction Distance, ΔZ, During Equilibrium Descent

Figure 6.69 Retraction of Canopy Apex With Axial Line

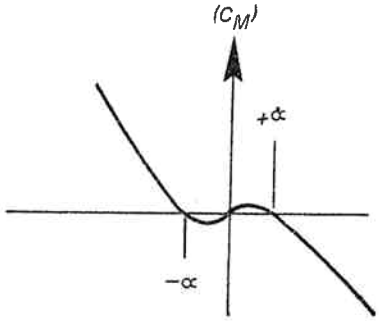
varies with α in the same way C_M varies, but the algebraic sign is opposite, i.e., a positive side-force causes a negative or destabilizing moment.

The static stability characteristics of small flexible canopy models, constrained in wind tunnel to maintain different angles of attack, are presented in Figure 6.72. The moment coefficient C_{M_p} in this case was calculated for D_p and S_p derived by photogrammetry. Unknown wind-tunnel and scale effects limit the usefulness of these data to a broad qualitative level. Static stability of the canopy is signified by negative values of $dC_M/d\alpha$. At $\alpha = 0$, varying degrees of static stability are indicated for the ringslot, ribbon, ribbed and ribless guide surface canopies, as constrained by the wind tunnel supports. Full scale ringslot and ribbon parachutes generally are not statically stable at $\alpha = 0$, but exhibit pendular oscillations of small to moderate amplitudes (±2 to 15 degrees) depending mainly on total porosity. The relative instability of the other models is generally indicative of full-scale parachute trends, the stable angle of attack corresponding roughly to the average amplitude of pendular oscillations experienced during equilibrium descent.

Of course, the parachute must swing beyond the stable α to feel an aerodynamic restoring moment, but planar oscillations seldom occur. The motion of the canopy through the air produces a series of vortices that form and shed periodically, but at different sectors in succession, causing the aerodynamic force vector to shift about in various ways. Usually the parachute attempts to glide but the rapid changes in direction generate oscillations instead. Rarely, a rotational sequence will be established and a steady coning motion of constant angular velocity will be sustained throughout the descent, possibly analogous to gliding in a tight spiral.



a) Damped Oscillation Transient Following Horizontal Deployment



b) Variation of Parachute Moment Coefficient with Canopy Angle of Attack

Figure 6.70 Typical Static and Dynamic Stability Characteristics of Parachute-Body System

The absolute size of the vortices formed is related to the diameter and inflated profile of the canopy and to its total porosity and the porosity distribution. The effect of using cloth of different permeabilities on the static stability of a small flat circular canopy in the wind tunnel is illustrated in Figure 6.73. In this set the moment coefficient, C_{M_o}, is based on D_o and S_o, and so is smaller than corresponding C_{M_p} values. However, the values of α_o when $C_M = 0$ are the same. Presumably high porosity produces improved static stability by reducing the vortex growth prior to shedding, thus weakening the aerodynamic side-force component or C_N. Although the opening load factor is also reduced, the opening tendency is weakened. Therefore, experience has taught that each different canopy type has a practical upper limit to the air permeability of the cloth used in its construction. It is evident that the static stability gained from increased porosity in any form is weak because the slope of the curves $(-dC_M/d\alpha)$ in the vicinity of $\alpha = 0$ is small relative to that provided by the inverted conical skirt and shallow inflated profile of the guide surface models, or by the axisymmetric interference flow channels of the cross parachute, for which the aspect ratio of the diametral arms is a pertinent parameter[479].

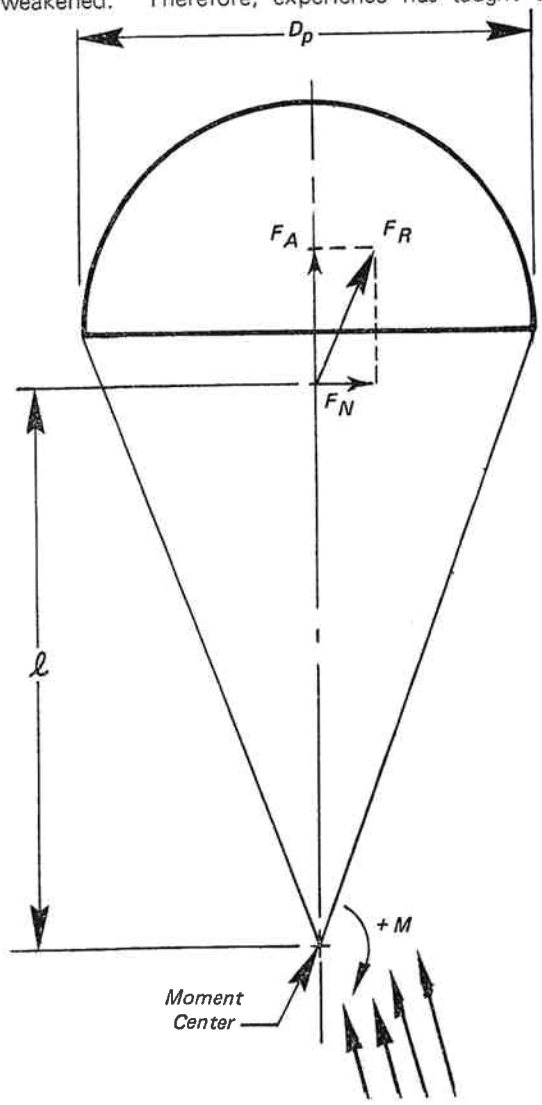


Figure 6.71 The System of Axes Used for Static Stability Considerations

Stabilization Parachutes. One class of drogue is designed specifically to stabilize body motion along a ballistic trajectory (bombs), and sometimes during a booster rocket thrust transient (ejection seats and escape capsules). The special stabilization type of riser harness structures used for this purpose are designed to minimize the angular deflection required to bring effective restoring moments into play. Three or more attachment points are provided on the body for harness legs or groups of suspension lines. Within limits, such parachute stabilization systems can be treated as rigid bodies because, with a reasonably clean body of adequate fineness ratio, the airstream is deflected by body lift and the parachute follows the "downwash", Figure 6.74. While the multi-line or geodesic coupling of the canopy to the base of the vehicle may help transmit pitch and yaw deflections to the canopy, this is not a necessary condition to the position-keeping of a stable canopy close to the wake centerline. On the other hand, if the initial deflection of the vehicle is large, the canopy remains clear of the downwash and a typical drag restoring moment is generated. Once the canopy is engulfed by the wake flow, subsequent restoring moments are generated by the dissymmetry of the flow impinging on the canopy, and its action may be viewed as roughly analogous to that of the flared base-cone on a rigid body.

The stabilizing effect of a Ballute operating in the wake of a model booster in the wind tunnel was reported in Reference 442. The test configuration and static stability characteristics of the system are shown in Figure 6.75. Pitching moment coefficients and rate of change are summarized as a function of angle of attack at different supersonic Mach numbers.

High Glide Canopy

Static longitudinal stability data acquired during tests of Parafoil type[480] and Parawing type[481] high glide canopies is presented in Figures 6.76 and 6.77, respectively. The system of axes used for the tests is shown in Figure 6.78. The Parafoil type designs tested (see Table 6.11 for physical characteristics) were

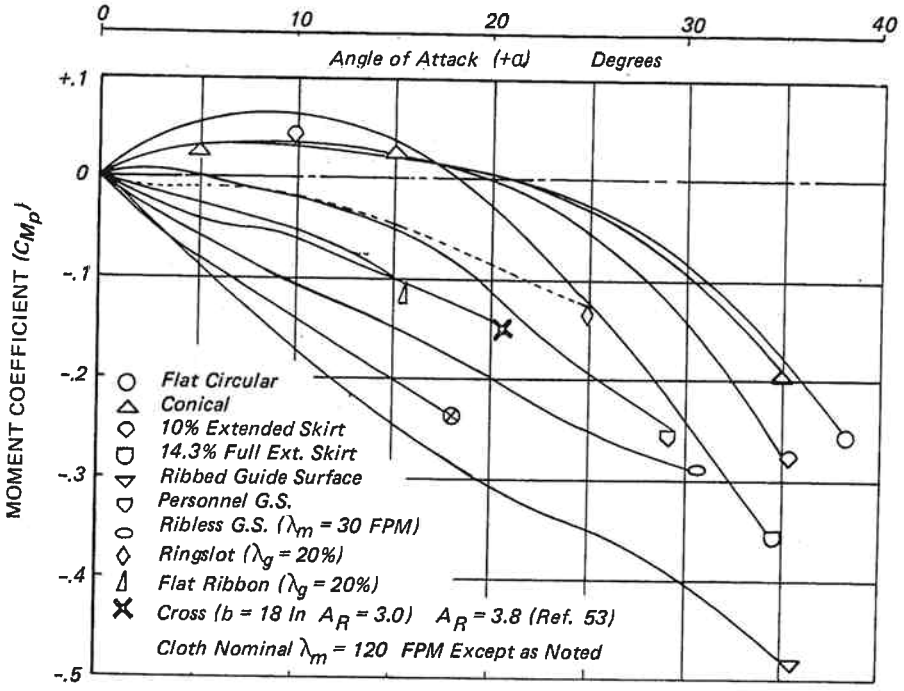


Figure 6.72 Measured Moment Coefficients vs Angle of Attack for Small Cloth Canopies in Wind Tunnel

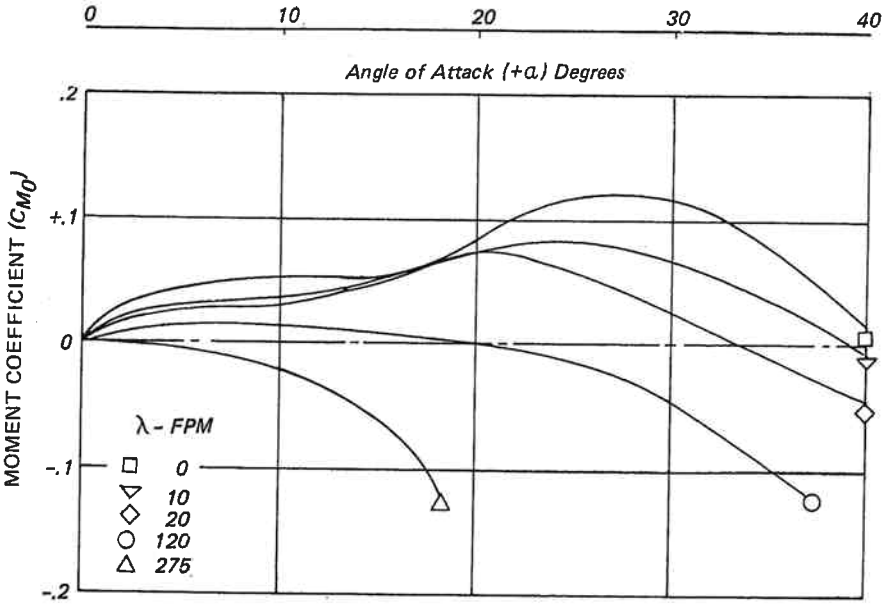


Figure 6.73 Effect of Air Permeability on C_{M_o} vs α of Small Solid Flat Circular Canopies in Wind Tunnel

statically longitudinally stable over the entire test angle of attack range of 0° to 70° except for a slight unstable break in the pitching moment curves at angles of attack just beyond that for stall. The static stability characteristics observed in these tests are representative of high glide canopies of this design.

The Parawing data shown is for a non-porous model design. The total test program investigated other models which incorporated porous material in the outer lobes. The angle of attack is changed by shortening of the aft keel lines. The range is normally limited at the low end (L/D_{max}) by the angle for partial nose collapse and at the high end by the onset of excessive oscillations.

As shown in Figure 6.77, an increase in dynamic pressure (which simulates an increase in wing loading) resulted in a negligible change in the longitudinal stability characteristics. A small decrease in performance was observed with the porous models with increasing dynamic pressure.

Tandem Parachutes

In mid-air retrieval systems the position-stability of the engagement canopy relative to the main canopy is of paramount importance. The engagement canopy constitutes a difficult target at best and when it wanders about erratically or orbits the main canopy at the end of its long tow-line the approach and closing maneuver of the pursuing aircraft becomes complicated.

The stability of the main parachute is of importance only as it influences the motion of the engagement chute, because the descent path is relatively steady most of the time. The principal problem encountered in a well-designed gliding system is lack of perfect longitudinal symmetry, due either to manufacturing tolerances or to non-uniform line elongation during the opening force transient, which causes the system to execute a slow turn as it descends. Insofar as position stability of the engagement canopy is concerned, the difference between MARS-H gliding and non-gliding configurations is illustrated by Figure 6.79 adapted from Reference 180. The significance of the coordinate system is illustrated in Figure 6.80 along with the dimensions pertinent to the stability analysis.

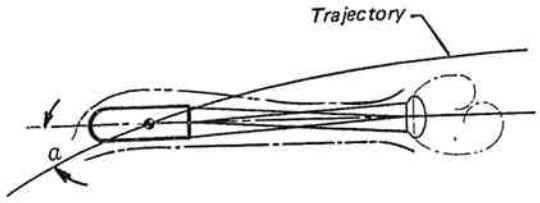


Figure 6.74 Schematic of Bomb Wake Downwash Due to Body-Lift (With Stabilization Para.)

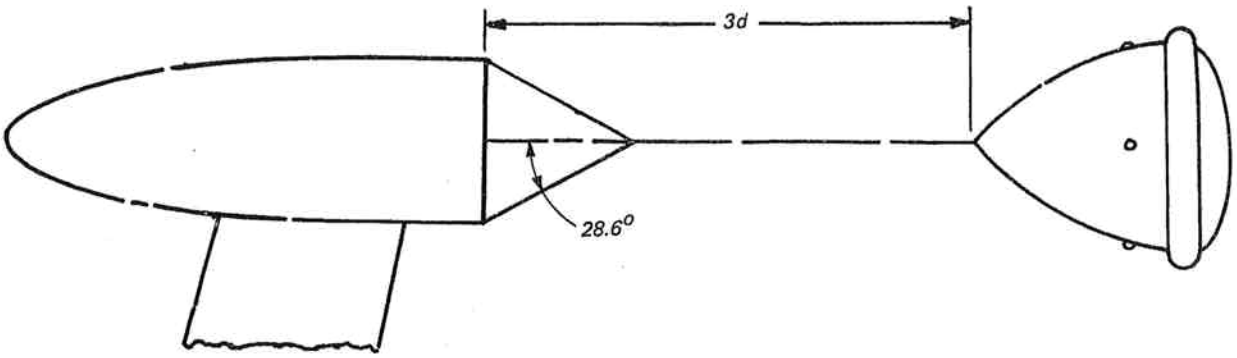
The glide configuration of the MARS-H main canopy is illustrated schematically in Figure 6.80c. The area of cloth replaced with the open mesh fabric (marquisette) was 7.1 percent S_o and, having an effective porosity in the order of $c = 0.60$ at $\Delta p = 2.6$ *psf*, the equivalent geometric porosity was approximately 4.26 percent. This proved to be excessive because in over half of the tests reported, the main parachute exhibited the bucking motion. As noted earlier the bucking motion is characteristic of any gliding canopy trimmed for a glide ratio greater than its inherent limit imposed by collapsing of the leading edge by the local stagnation pressure. The phenomenon, encountered in this case mainly when the equilibrium dynamic pressure was greater than $q_e = 0.8$ *psf*, was characterized by pitching oscillations of 15 to 20 degrees.

As a result of gliding parachute tests aimed at improved stability of tandem canopy systems, Epple[172] observed that three percent open area on the trailing side was sufficient, and little in the way of stability was gained when λ_g was increased from 3 to 3.7 percent. Accordingly, experimental glide configurations of the MARS-L 79.6 ft (D_o) tri-conical canopy were equipped with marquisette panels near the skirt for which $\lambda_g = 2.26$ and 3.1 percent respectively. A 75 ft (D_o) polyconical parachute similarly modified exhibited a steady glide of good stability with bucking tendency.

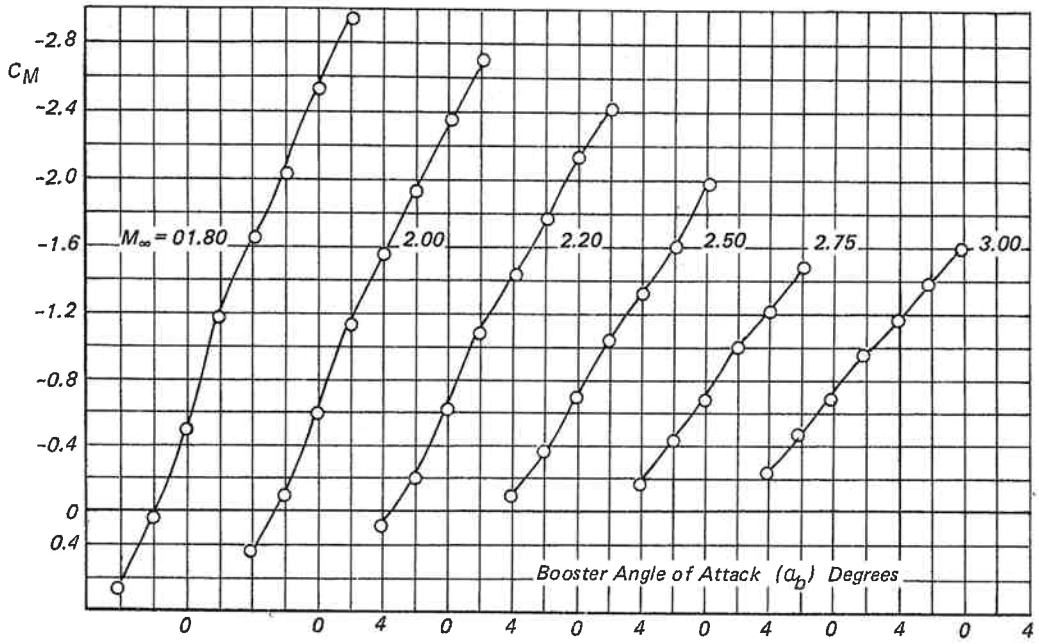
TABLE 6.11 DIMENSIONAL CHARACTERISTICS

Wing Dimensions	Wing II	Wing III
Span, ft (m)	4.50 (1.37)	6.13 (1.87)
Chord, ft (m)	5.79 (1.77)	6.56 (2.00)
Area, ft² (m²)	26.05 (2.42)	40.21 (3.74)
Aspect ratio	0.78	0.94
Thickness ratio	0.126	0.184
Inlet opening angle meas. from horizontal, deg	42	45

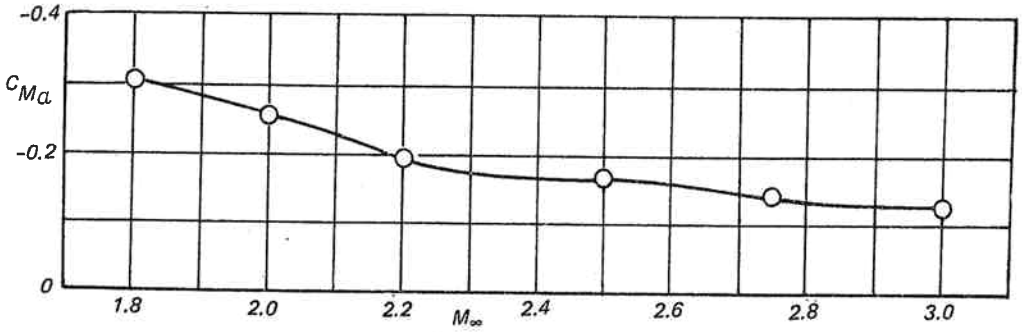
Note: Material – 1.1 oz. low porosity acrylic coated nylon



a) Model Booster With Ballute Drogue in Wind Tunnel



b) Variation of Pitching Moment Coefficient with α_b at Different Mach Numbers



c) Variation of the Rate of Change of Pitching Moment Coefficient with Mach Number at $\alpha = 0$

Figure 6.75 Static Stability of Booster Model with Ballute

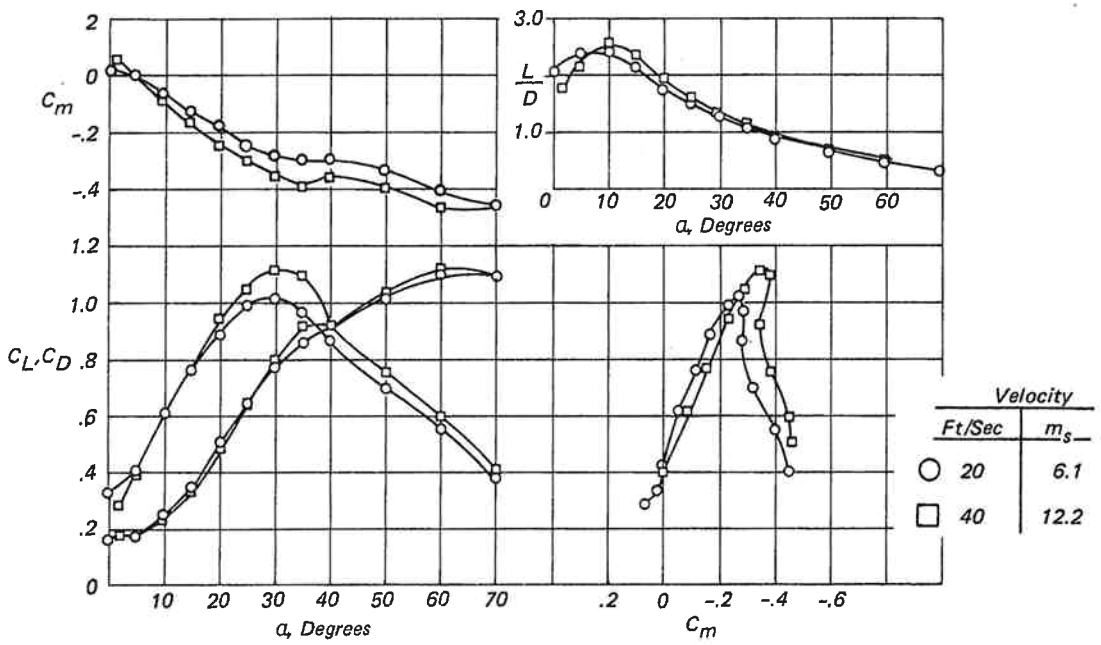


Figure 6.76 Longitudinal Aerodynamic Characteristics of Parafoil Designs II and III

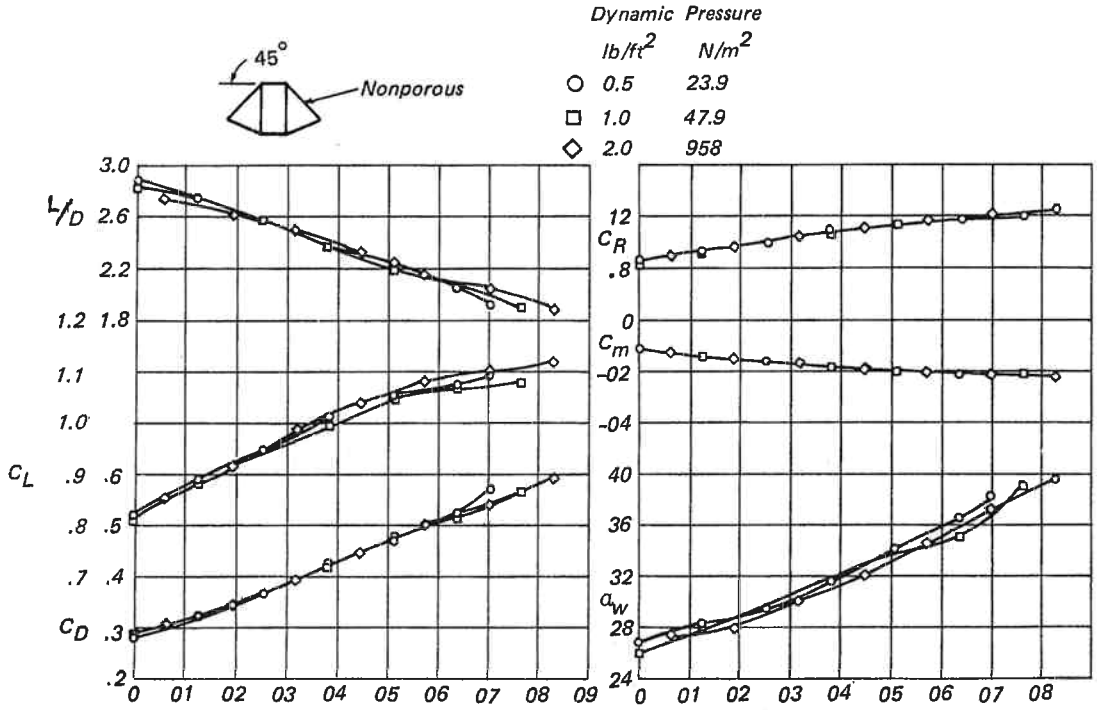
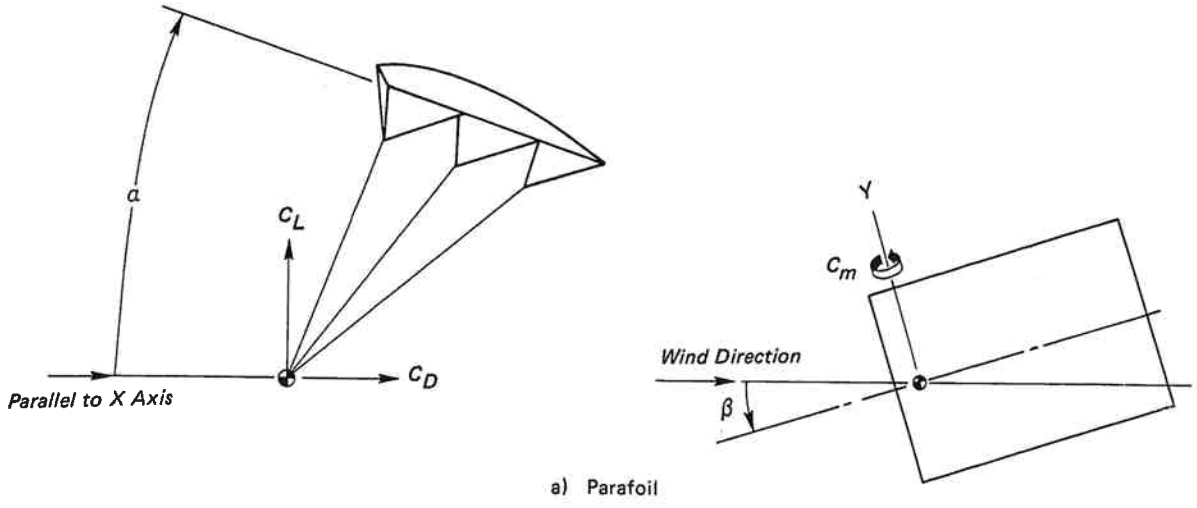
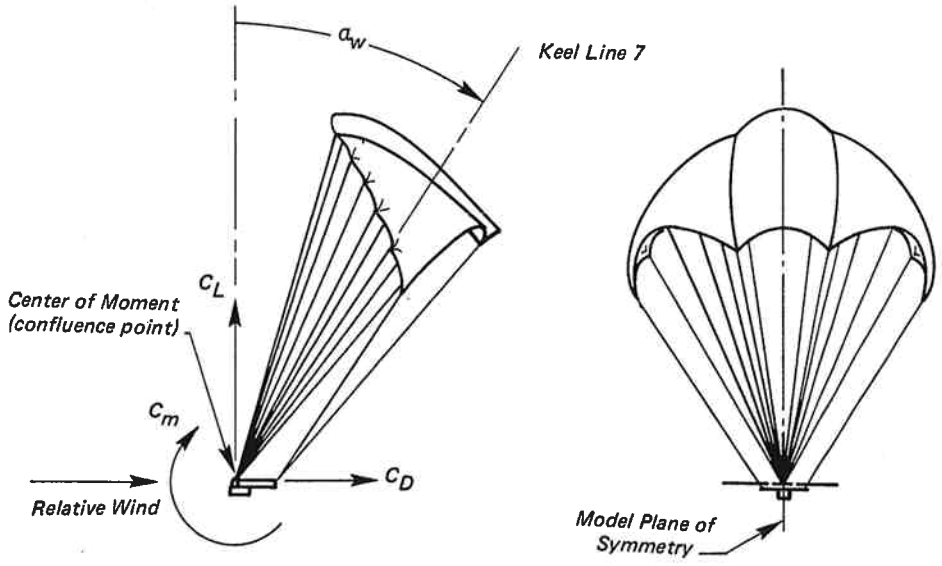


Figure 6.77 Effects of an Increase in Dynamic Pressure on Longitudinal Aerodynamic Characterisitcs of a Twin-Keel All Flexible Parawing



a) Parafoil



b) Parawing

Figure 6.78 System of Axis and the Positive Direction of the Forces, Moments and Angles Used in the Presentation of the Data

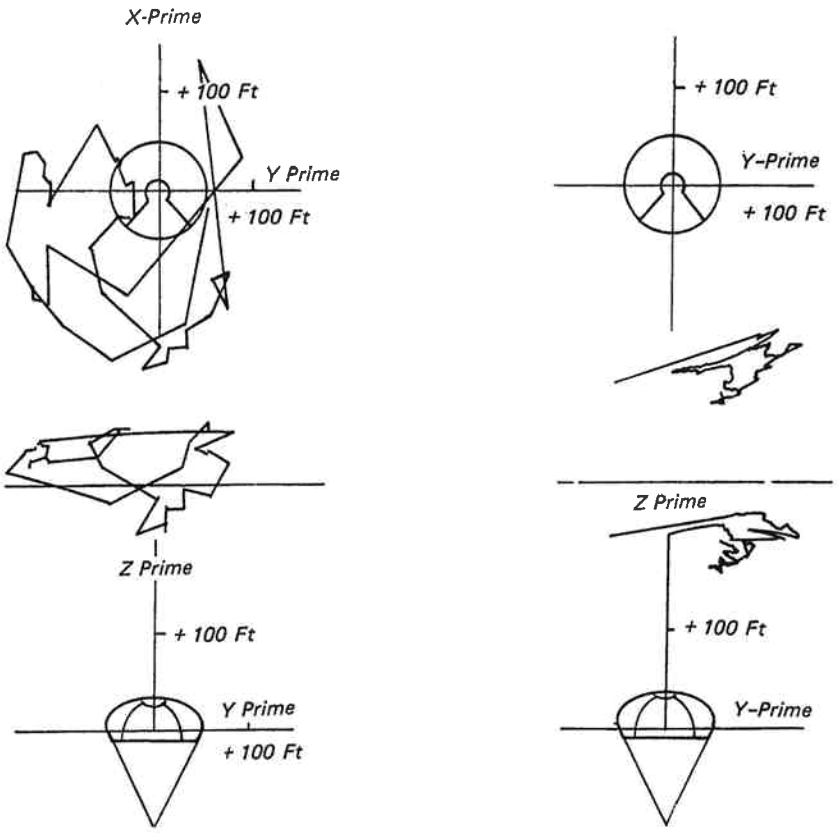


Figure 6.79 Effect of Gliding on Position Stability of MARS-H Engagement Canopy

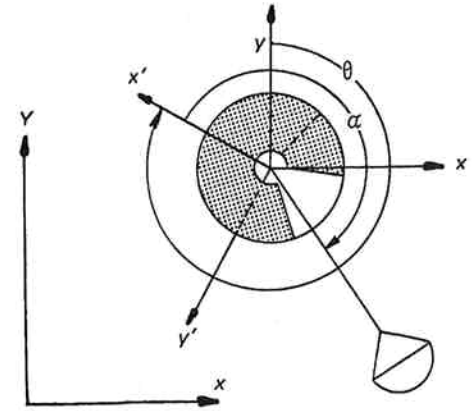
Effect of Clustering. Clustered parachutes are more stable than the individual member parachutes by a large margin, even though the member canopies tend to wander about at random during steady descent[390]. Since the gliding tendency of a cluster is generally negligible and the member canopies do not appear to be operating at an angle of attack much less than $\alpha = 0$ degrees relative to the local flow field about each, cluster stability may be attributed mainly to the fact that the motions of the member parachutes tend to be mutually opposed and self cancelling.

Cluster stability appears to vary somewhat with the number of parachutes and to some degree with the relative rigging length[566]. Those clusters in which the peripheral canopies have the least tendency to wander likely are the most stable and may be of optimum configuration for static stability if not for drag.

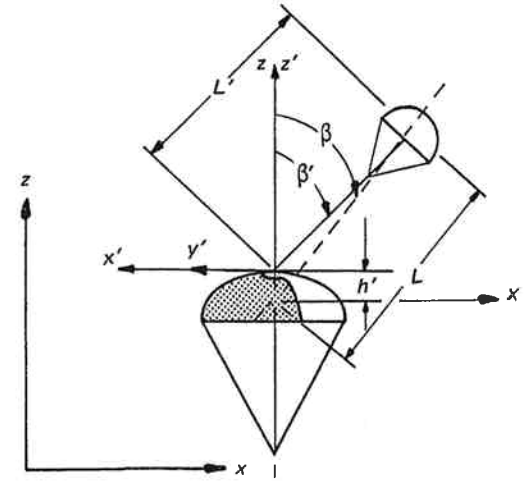
Two-parachute clusters, such as those subjected to intensive development for Apollo, are stable in the plane of the cluster but tend to oscillate in the normal plane. This could be likened to the transverse instability of gliding systems that have a high degree of static stability in the normal or pitch plane of the glide.

Dynamic Stability

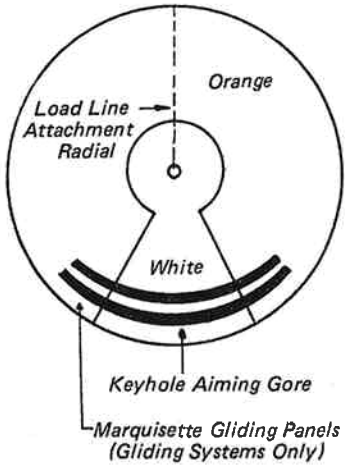
Empirical evaluation of the dynamic stability of aerodynamic decelerator systems entails measurement of the amplitude and frequency of angular deflections to determine the rate of amplitude decay or damping characteristics[564]. An analytical approach[482] is summarized in Chapter 7 which uses criteria for longitudinal dynamic stability to define the minimum value of $C_{N^{\alpha}}$ required if a parachute system is to be dynamically stable during gliding descent.



a) Top View of MARS Axis Systems and Parameters



b) Side View of MARS Axis Systems and Parameters



c) Top View of MARS Main Canopy

Figure 6.80 Schematic of Mid-Air Retrieval System and Coordinates

Typical dynamic stability of a ballute-type drogue in an entry body system is illustrated in Figure 6.81 as part of the results of supersonic wind tunnel tests with small free models reported in Reference 440.

In a parachute system the deployment and opening transient frequently generates a large amplitude oscillation as shown in Figure 6.70. This first oscillation is strongly damped by the combination of aerodynamic and gravity moments developed such that after roughly one and one half cycles an equilibrium descent condition is reached where continuing oscillation merely reflect the static stability characteristic of the parachute, as in Figure 6.71. Any subsequent disturbances caused by wind shear, gusts, etc., turbulence will be similarly damped [483]. Only exceptionally stable parachutes will damp to zero amplitude at $\alpha = 0$ degrees. Most gliding parachutes exhibit a fair degree of dynamic stability in pitch when trimmed to glide at a statically stable angle of attack less than 0 degrees.

INTERNAL LOAD DISTRIBUTION

The primary internal load path for decelerator opening loads is from fabric panels to radial or rib-like members, with some flow via concentrations in reinforcing bands, thence to suspension lines and risers and finally through the harness to hard points on the body. In a circular canopy the load in the radials increases progressively in a non-linear fashion from vent to skirt starting at roughly half its maximum value [221] The maximum radial load is generally reached at a point in the canopy corresponding to the maximum inflated diameter either reefed or non-reefed (see Figure 6.87).

The radial load in the cloth panels of the gore is zero at the skirt and increases along a gradient that varies with the canopy design. In solid cloth canopies the gradient is steep and reaches a maximum in the vicinity of 0.75 h_g then declines rapidly toward the crown, based on strain measurements with a fully inflated 3 ft (D_o) flat circular model in steady-state wind tunnel flow [565]. A similar gradient probably exists in slotted canopies with numerous vertical slot control tapes, otherwise the radial load is logically zero at all uncontrolled sail or ribbon edges.

Suspension Members

The distribution of suspension line loads varies widely from one type of system to another being of maximum uniformity during the opening transient in circular or axisymmetric drag devices. The greatest inequity of load distribution occurs in high glide canopies and clustered parachutes, despite measures taken to reduce such effects. A large Parawing instru-

mented to obtain individual suspension line loads showed the non-uniform load distribution plotted in Figure 6.82 through successive reefed stages. A line-length equalization method similar to that described in Reference 398 was used. Reported data on the measured distribution of suspension line and riser loads in the individual parachutes of a cluster of three circular parachutes are presented in the diagram of Figure 6.83. This cluster of three 48 ft (D_o) ribbon parachutes also shows pronounced inequity of opening loads between the member parachutes. Line and riser load distributions are roughly representative of the averages obtained from ten aerial drop tests. A typical four-branch cargo suspension sling is illustrated schematically in Figure 6.84. Load data from Reference 127, indicated that one leg of this type of harness may be subjected to as much as 36% of the total load.

Canopy

Maximum unit loads occur in an inflating canopy at those points where the product Δpr reaches a maximum, r being the local radius of curvature of the surface. The maximum stress is usually coincident with the maximum axial load, but not always. Correlation of canopy shape with instantaneous force during inflation provides important clues to internal load levels. The first peak opening load of a parachute frequently occurs during the inflation process before the canopy has completely filled as shown in Figures 6.24 and 6.85. Similar behavior is exhibited by reefed parachutes only after disreefing.

Measurement of Canopy Pressure Distribution

The difficulty of obtaining direct measurements of the pressure distribution in an inflating canopy is fairly evident. Since the dynamic process is not a series of steady states, the results of various static model tests in the wind tunnel proved useless. The dynamic testing problem was first solved by Melzig and Schmidt[340] for the infinite mass case. Two years later Melzig, with Saliaris[341], advanced the art further to the finite mass operating case. Finite mass drop tests were performed with different types of parachutes (solid flat, extended skirt, ringslot and flat ribbon) launched at various velocities corresponding to q_s = *34* to *46 psf.* The system mass ratios were such that at the time of the peak opening forces the projected areas of the canopies were uniformly small and in the range of S_p/S_o = *0.05* to *0.18.* Representative results of two tests are presented in Figure 6.85. Evidently the pressurized area of the canopy encompassed only transducers 3 and 4 in the crown and the two differential pressure coefficients indicated at any instant show a gradient downward from 4 to 3 which levels out toward a constant pressure distribution as filling progresses. Marked differences between the solid cloth and slotted canopies are indicated.

Sandia Laboratories acquired both steady state (Refs. 468 and 547 and dynamic (inflating canopy) pressure distribution measurements during wind tunnel test program with model conical ribbon canopies. Reference 355 presents results from the dynamic measurements which were acquired from time of canopy disreef (initial reefing ratios of 0.179,

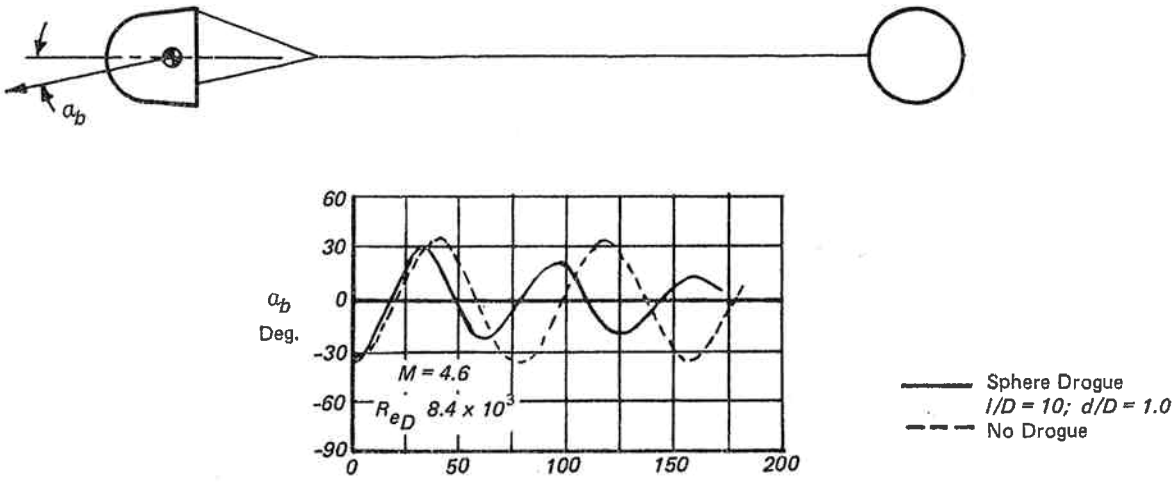


Figure 6.81 Effect of Sphere Drogue on Amplitude Decay of Entry-Body Angle of Attack (Ref. 440)

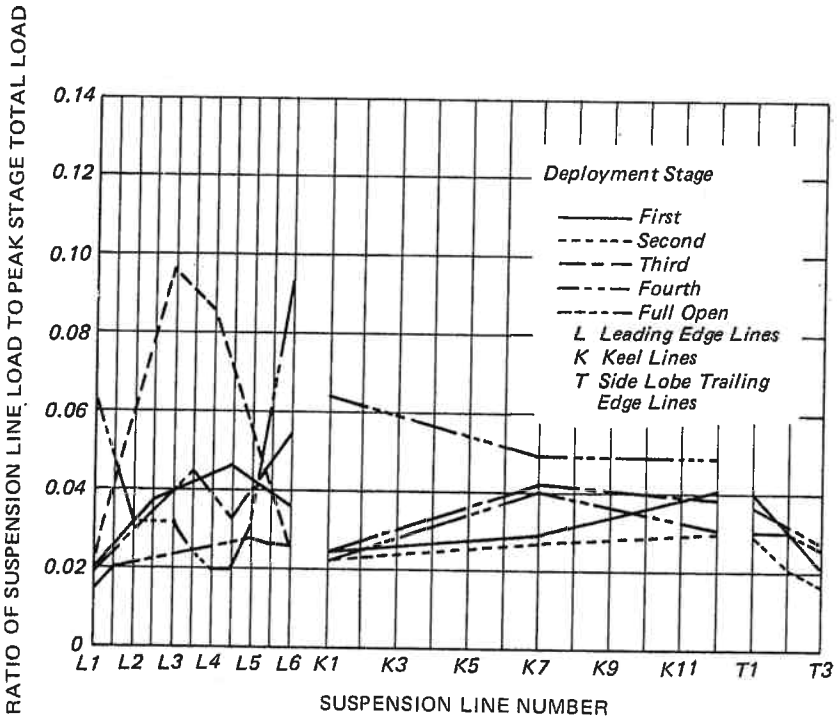


Figure 6.82 *Distribution of Suspension Line Loads for Each Opening Stage of Reefed 4000 Ft² (S_W) Twin Keel Parawing (Reference 398)*

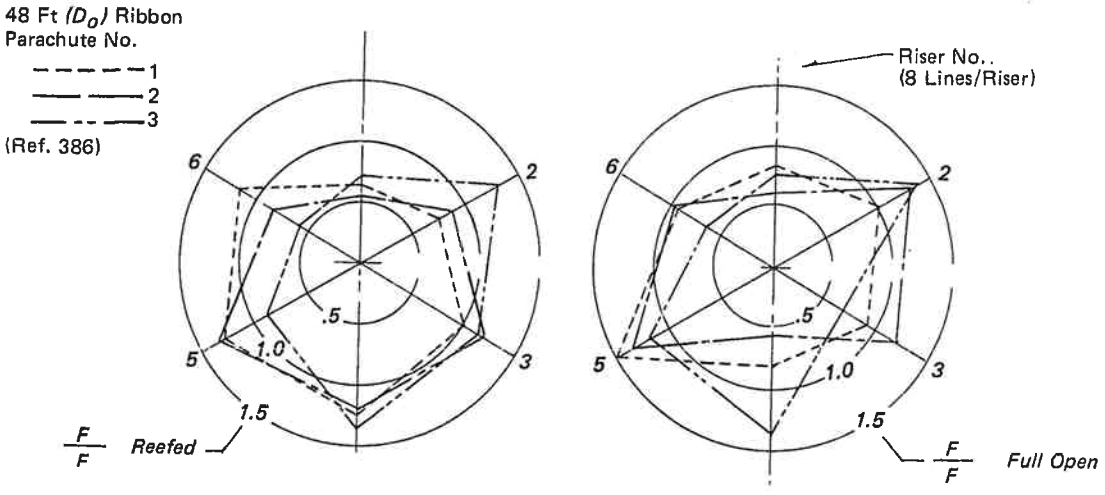


Figure 6.83 *Distribution of Suspension Line-Riser Loads in Each Parachute Cluster at ΣF (Max.)*

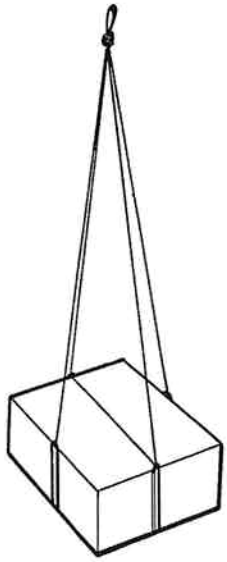


Figure 6.84 Cargo Suspension Sling With Four Legs

.358 and .458) through peak opening load.

The measured pressure distributions were correlated with inflated shapes to permit calculation of drag forces. These calculated forces (in the form of drag area since q_{test} = const) are compared with measured drag as shown in Figure 6.86 and served to validate the measured pressure distributions.

Measurement of Canopy Stress Distribution

Utilizing the Omega stress transducer described in Chapter 5, the circumferential stress developed in model Ringslot and solid flat [342, 484] canopies was measured under both static (full open) [342, 484] and dynamic (during inflation) [484, 485] conditions. In addition, Reference [484] reports results of limited measurements of the radial stress along the gore centerline of a fully inflated solid flat circular canopy. Comparison between radial and circumferential stress at various locations along the canopy profile are shown in Figure 6.88A. The radial stress measurements exceeded the circumferential stress at a location of 75% $D_o/2$. Figure 6.88 shows canopy circumferential stress measured during inflation of model solid flat circular canopies. Similar data obtained during tests of model ringslot canopies are shown in Figure 6.88B.

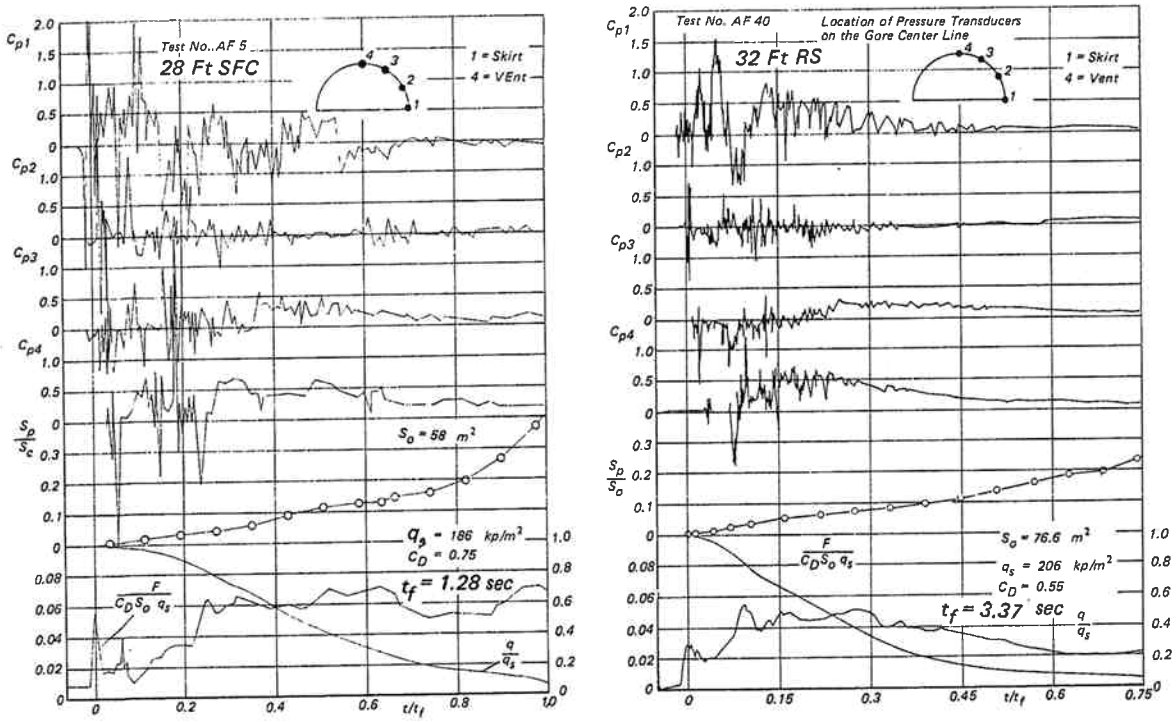


Figure 6.85 Differential Pressure Coefficient $C_p = \Delta p/q_s$ and Corresponding Projected Area Ratio S_p/S_o, Opening Shock Factor $F/C_D S_o q_s$ and Dynamic Pressure Coefficient q/q_s versus Time Ratio

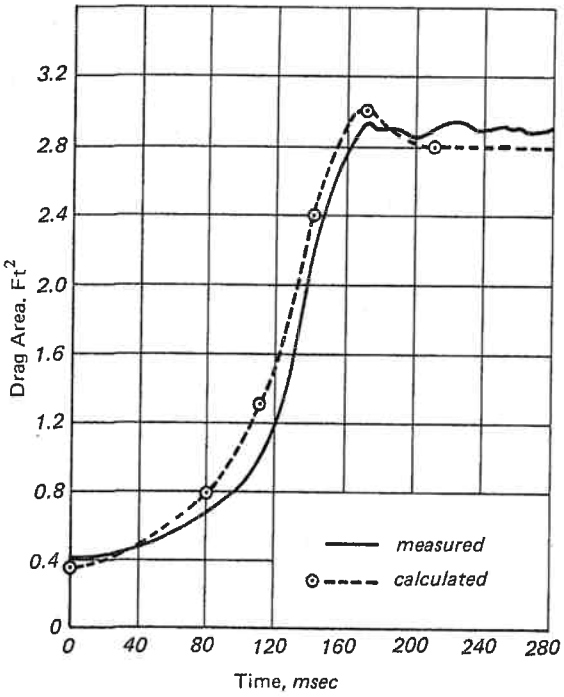


Figure 6.86 Calculated and Measured Drag Area

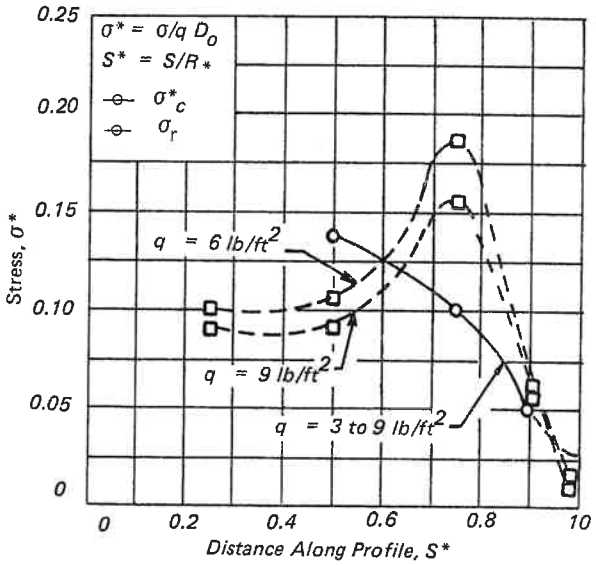
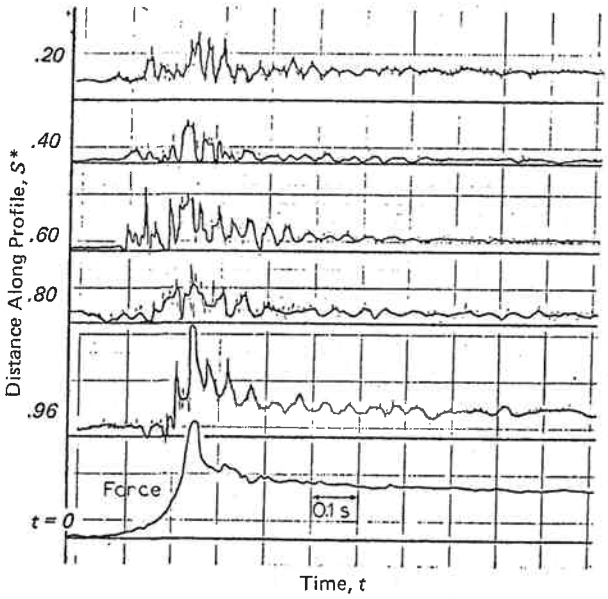
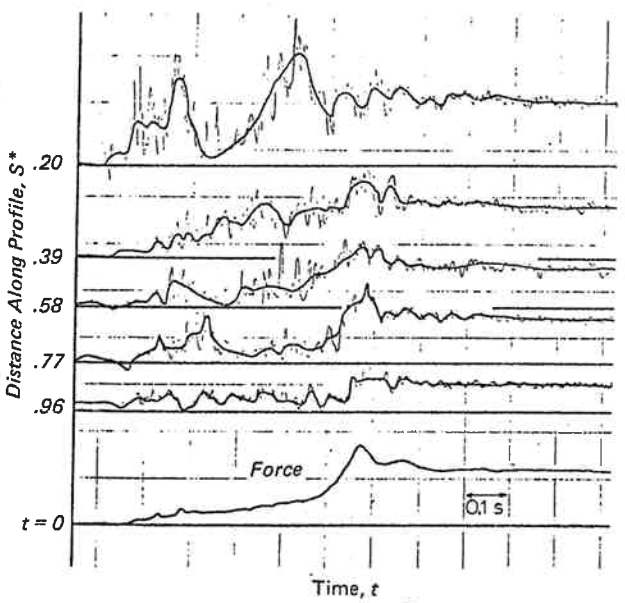


Figure 6.87 Measured Circumferential and Radial Stresses



D_o = 5 ft, q = 7.1 lb/ft^2

Figure 6.88A Canopy Stress and Total Force Measured on a 28 Gore Solid Flat Circular Model Parachute



q = 9.0 lb/ft^2

Figure 6.88B Canopy Stress and Total Force Measured on a 32 Gore Ringslot Model Parachute

AERODYNAMIC HEATING

Advances in aerospace technology since the 1950's have resulted in increasing environmental and operational temperatures for certain types of deployable decelerators, e.g., Ribbon, Hyperflo, Parasonic and Ballute drogues. This trend has been paralleled by the intensive development of new synthetic materials of improved physical and mechanical properties (Chapter 4). Consequently, it is possible today to construct flexible fabric structures amenable to storage and soaking at temperatures that would reduce a nylon or Dacron structure to a molten mass. Moreover, the strength retained by the new materials at elevated temperatures enables decelerators fabricated from them to tolerate a substantial degree of aerodynamic heating following deployment at high velocities

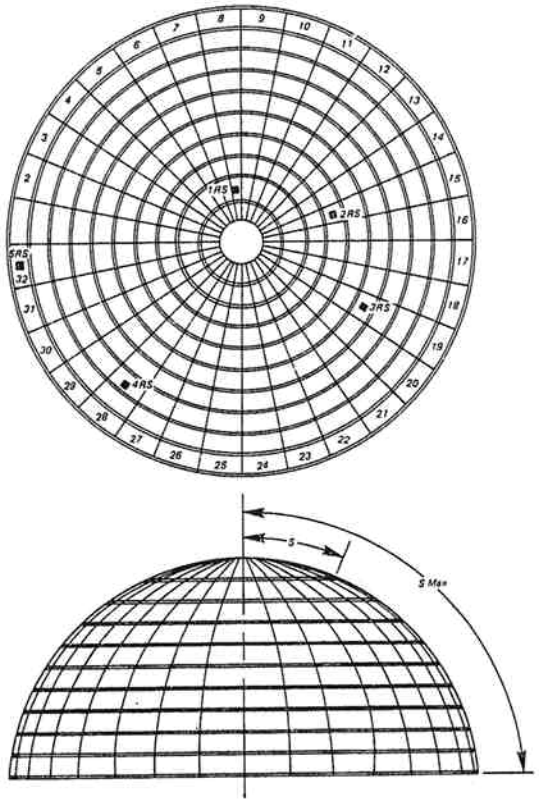
Heat Resistant Drogue Structures

The operational temperatures experienced by a drogue result primarily from compression of the air being penetrated, with some heating by viscous dissipation of kinetic energy, and usually reach their maxima at the stagnation point or in a region where near-stagnation conditions prevail. Being in the wake of the towing body, the air flow conditions are complex and the relative velocity may be somewhat less than free stream as suggested by the schematic diagram of Figure 6.90. Both viscous and inviscid wake flow impinge on the leading members of the decelerator structure. Critical heating areas are found on the skirt leading edge and in the roof panels of drogue chutes and on the forward surfaces of the Ballute cone and burble fence. The effects usually consist of superficial melting or charring under conditions where the surface temperature becomes relatively high and could cause catastrophic failure if sustained —superficial because the typical heat pulse is brief due to rapid deceleration and also because the heat capacity of the material, though small, provides a useful heat sink. The materials are characteristically of low thermal conductivity. In general experience, drogues constructed of nylon and polyester materials have sustained little more than superficial heat damage at deployment velocities up to Mach 3.3. The extent of the damage varies with the thickness of the canopy fabric. A 40 ft D_o disk-gap-band parachute made of 2 oz Dacron cloth suffered "extensive" damage when deployed at Mach 3.31 (Ref. 486).

Drogues designed for high speed operation under severe heating conditions have embodied several different types of structures and materials. A 4 ft D_o Parasonic drogue[487], SP-5, tested at Mach 5.5 was fabricated from Nomex aramid, HT-1, textiles. The side-walls and skirt consisted of bias cut cloth and the roof was a woven mesh of narrow, 0.25 inch-wide webbing. A protective coating of Dynatherm compound, D-65, with a thickness of 0.025 inches was added. The geometric porosity of the roof gave the canopy a total porosity of approximately 5 percent. Measured physical properties of the materials were as follows:

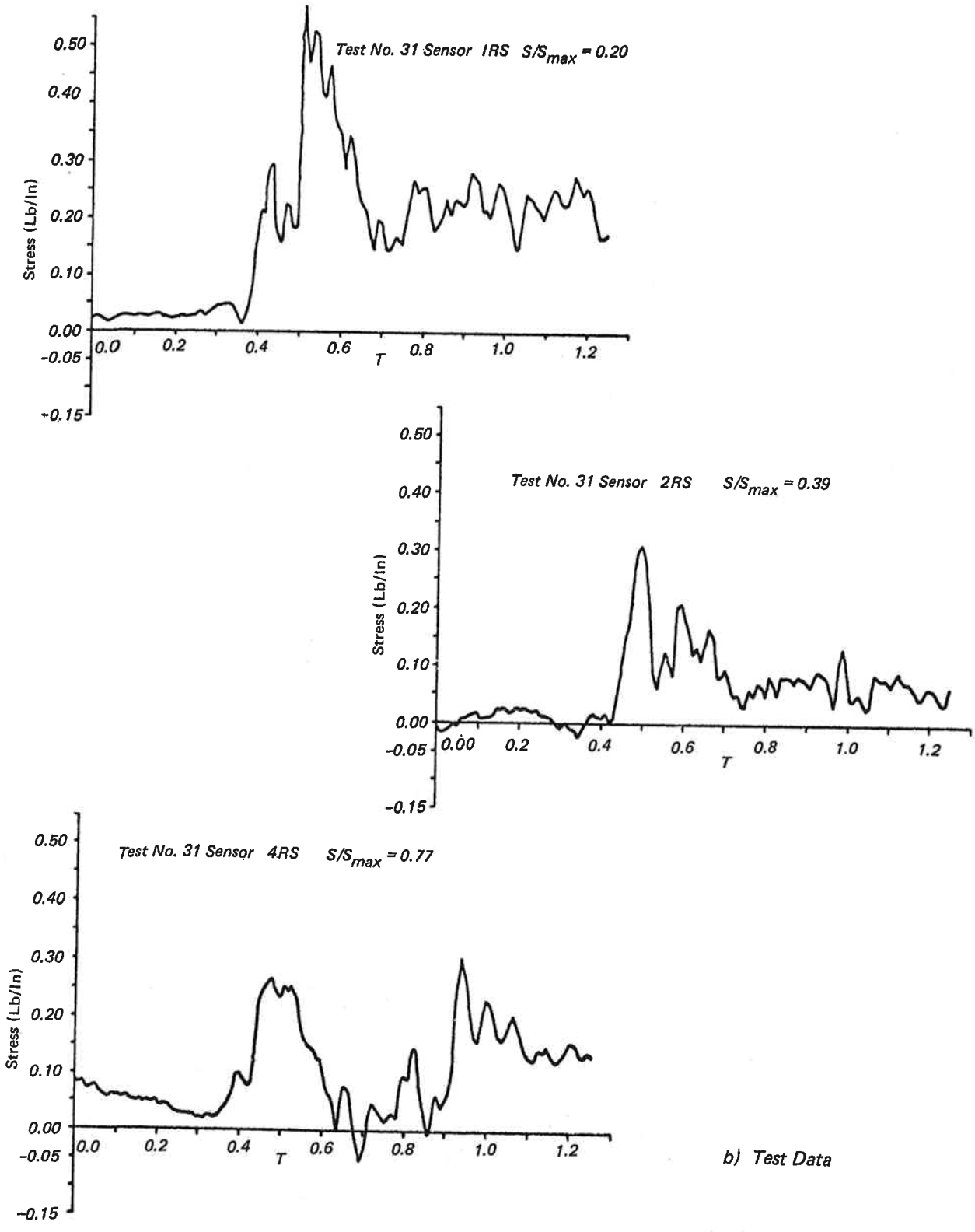
	Density (lb/ft^3)	Specific Heat (BTU/lb°F)	Thermal Conductivity (BTU/hr-ft-°F)
D-65 coating	68.6	0.25	0.053
HT-1 webbing	42.0	0.35	0.032

Laboratory test results[215] indicate the heat capacity of webbing specimens was increased by the coating from approximately 300 BTU/lb (bare) to 1000 BTU/lb at a heat flux rate of about 10 BTU/ft^2-sec.



a) Omega Sensors Orientation on Canopy

Figure 6.89 Measured Opening Forces and Canopy Stress of Model Ringslot Canopy.



b) Test Data

Figure 6.89 Measured Opening Forces and Canopy Stress of Model Ringslot Canopy (Continued)

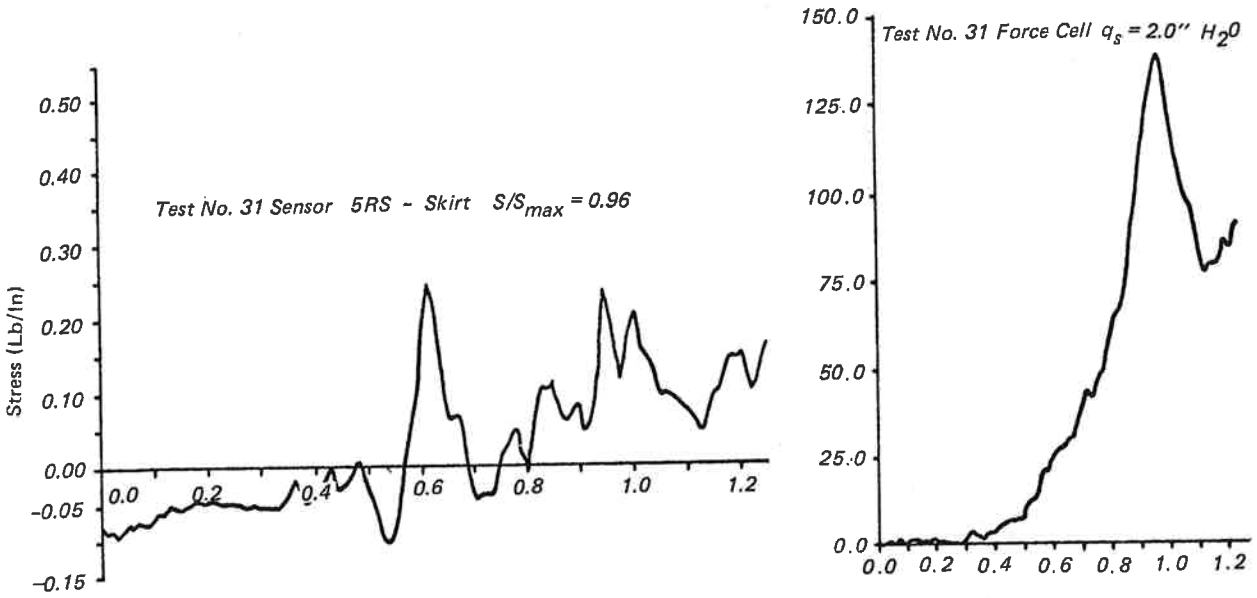


Figure 6.89b Continued

A 5 ft D_p Ballute, TB-4, tested at Mach 9.7 was fabricated from 11.84 oz/yd^2 Nomex, HT-122, coated inside and out with Dynatherm, D-65, compound. Material thicknesses were:

D-65 outer coating	.007 inch
HT-122	.023 inch
D-65 inner coating	.003 inch

This Ballute, being designed for purely supersonic operation, had no burble fence and was provided with a pre-inflation system consisting of two fluid filled latex bladders, one containing 0.75 lb methyl alcohol, the other 0.25 lb water, which would also act as a coolant. Under simulated Mach 8 conditions in a heat tunnel[215] the coating increased the time to failure of preloaded HT-72 specimens from 6 to 20 times at a flux-rate of 12.9 BTU/ft^2-sec.

A similar Ballute was fabricated from stainless steel cloth, SS-304, coated inside and out with a sealing compound, CS-105. These materials had the following properties:

	Thickness (inch)	Density (lb/ft^3)	Specific Heat (BTU/lb-°F)	Thermal Conductivity (BTU/hr-ft-°F)	Emissivity
CS-105 outer coat	.0038	172.5	0.30	0.0453	0.9
SS-304 fabric	.0100	142.0	0.13	0.0453	–
CS-105 inner coat	.0020	172.5	0.30	0.0453	–

The stainless steel textiles were assembled by spot welding. The base fabric was woven 100 x 100 yarns per inch, each yarn consisting of 7 strands of 0.0016 inch SS-304 filament. It retained 40 percent of its rated strength of 142-157 lb/in at a temperature of 1200°F. The coated fabric remained essentially impermeable for protracted periods, 20 to 60 minutes, under pressures of 2 to 4 psi at a temperature of 1500°F. Previous failures of stainless steel Ballutes in the wind tunnel at Mach 3 and $q = 119$ *psf* indicated a low probability of successful deployment in free flight at design conditions of Mach 5.7 and $q = 220$ *psf,* so this model was tested in the wind tunnel at Mach 2.8 and $q = 120$ *psf.* Operation of the Ballute was normal but temperatures due to aerodynamic heating were insignificant.

The difficulties experienced with the stainless steel cloth structures emphasize the importance of material energy absorption capacity under impact loading conditions. While textiles such as SS-304 and Beta-glass retain strength at temperatures above the melt-

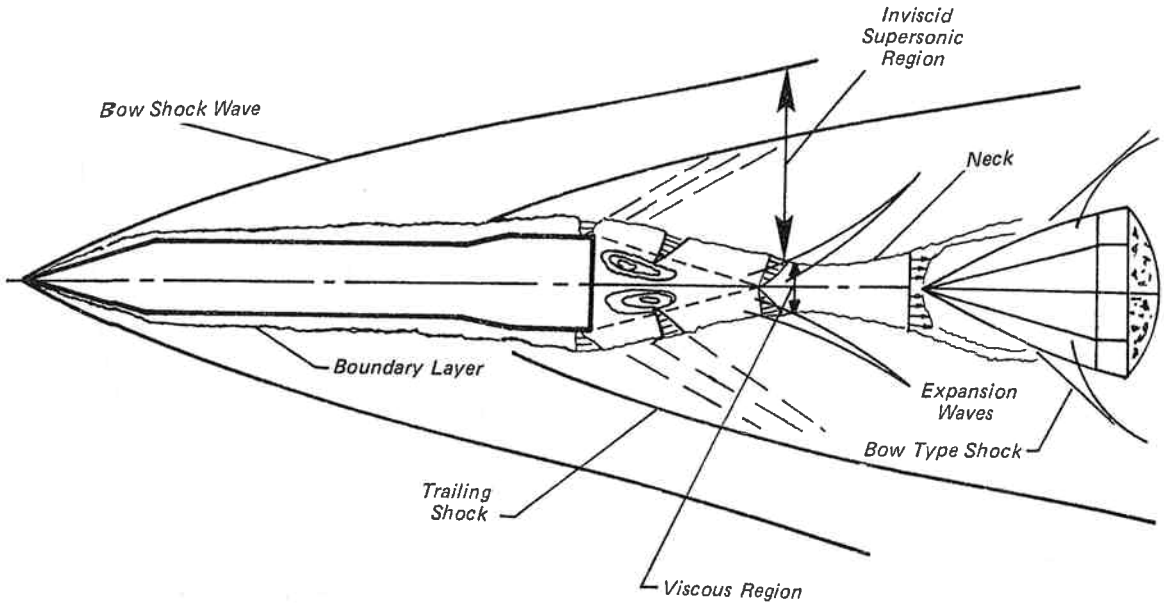


Figure 6.90 Typical Body - Drogue Supersonic Flow Field

ing points of polymers, their specific impact energy absorbing capacity remains below desired levels from the standpoint of structural efficiency. For decelerator applications involving only transient dynamic heating pulses, which embraces the majority of terrestrial operating requirements, the use of low melting point textiles is not ruled out, because their high specific impact energy absorbtion capacity permits thick fabrics to be used efficiently, depending upon superficial melting, evaporation, or charring to protect the main body of the material during the peak temperature transient. For example, the data from Reference 488 shows that a loading rate of 150 fps nylon tape has a specific energy absorbing capacity of 16,000 ft lb/lb at 70°F diminishing to 12,000 ft lb/lb at 400°F. Comparable figures for stainless steel textile tape are approximately 400 ft lb/lb at 70°F diminishing to 111 ft lb/lb at 1600°F, a ratio of 40 to 1 at 70°F, in favor of nylon, while at 400°F nylon has 108 times the energy absorbing capacity of stainless steel at 1600°F. Given a predicted surface temperature transient peaking briefly at 1600°F, these ratios make it economical and practical to use nylon instead of stainless steel and expend a fraction of the external nylon mass to keep the interior temperature below 400°F. The use of beaded edges on nylon ribbons, as reported in Reference 215 , is an example of how this approach may be efficiently implemented.

Predicted vs Observed Effects. Methods of calculating decelerator temperatures due to aerodynamic heating are given in Chapter 7. A comparison of predicted and observed effects is presented here.

Parasonic Drogue Flight Test. The Parasonic drogue, SP-5, described above was subjected to a flight test at Mach 5.5, 120,000 ft, using thermocouples to obtain temperature measurements through deployment and after re-entry. The following discussion of the test results in the light of a thermodynamic analysis was presented by Bloetscher and Arnold[487]

"The fact that the useful life of a decelerator occurs during a highly transient phase of flight suggests that the heat balance be solved on a similar basis. The assumed thermal environment inside the canopy is that due to free stream conditions subjected to a normal shock at the inlet face, body wake effects neglected. The initial peak heat flux rate on a roof element occurs immediately after deployment. It was calculated to be about 24 BTU/ft^2-sec. The heating rate decays rapidly as the vehicle gains altitude, becoming negligible after Δt = *15 seconds.* About 360 seconds after launch, aerodynamic heating decreases as the vehicle decelerates to terminal conditions."

Instrumental limitations may have caused the dif-

ference between the telemetered total temperature and the predicted adiabatic wall temperature. "Although the two temperatures, T_{t2} and T_{aw} in Figure 6.91 are not the same quantity, the difference is much greater than can be accounted for in applying a recovery factor to the total temperature to obtain the adiabatic wall temperature." The Nomex temperatures were measured with thermocouples in roof elements of the canopy near the periphery as shown in Figure 6.91a.

Significant operational factors emerge from this comparison:

1) The thermal environment inside the canopy is less than predicted by a turbulent flow nozzle analogy, the temperature rise being sensitive to the nature of the flow field.
2) Due to the rapid deceleration characteristic of such systems, the peak temperatures felt on the surface of the decelerator structure are considerably higher than those on the interior.

In consequence of (1) the need for heat resistant materials predicted by present methods of analysis may not be justified by subsequent tests. In consequence of (2) superficial heat damage may be experienced without serious weakening of critical members, hence, allowable surface temperatures may be high relative to the melting point of the materials used. Available heat resistant coatings further raise these limits.

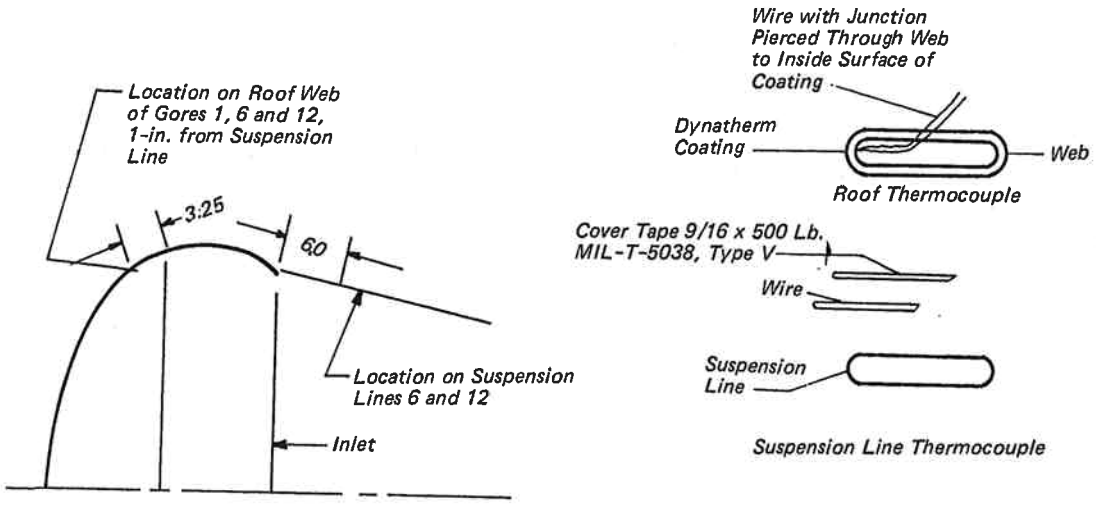
Textile Ballute Flight Test. The 5 ft Ballute, TB-4 described above, instrumented with thermocouples, was deployed at Mach 9.7, 226,700 ft. Thermal analysis methods for calculating Ballute fabric temperature values are presented in Chapter 7 for the actual TB-4 Ballute flight conditions. A comparison of calculated and measured temperatures made by Bloetscher[215] is paraphrased in the following paragraphs.

The deployment point of the Ballute decelerator determined from radar tracking data was 226,700 ft altitude and 9126 fps velocity. On the basis of the wake transition criteria presented, it was deterimned that, during the ascent flight phase of the trajectory, the decelerator likely was in a laminar wake. The cold wall heat flux rate for the most critical position of the decelerator surface was determined as a function of time of flight, based on the laminar flow heat transfer coefficient.

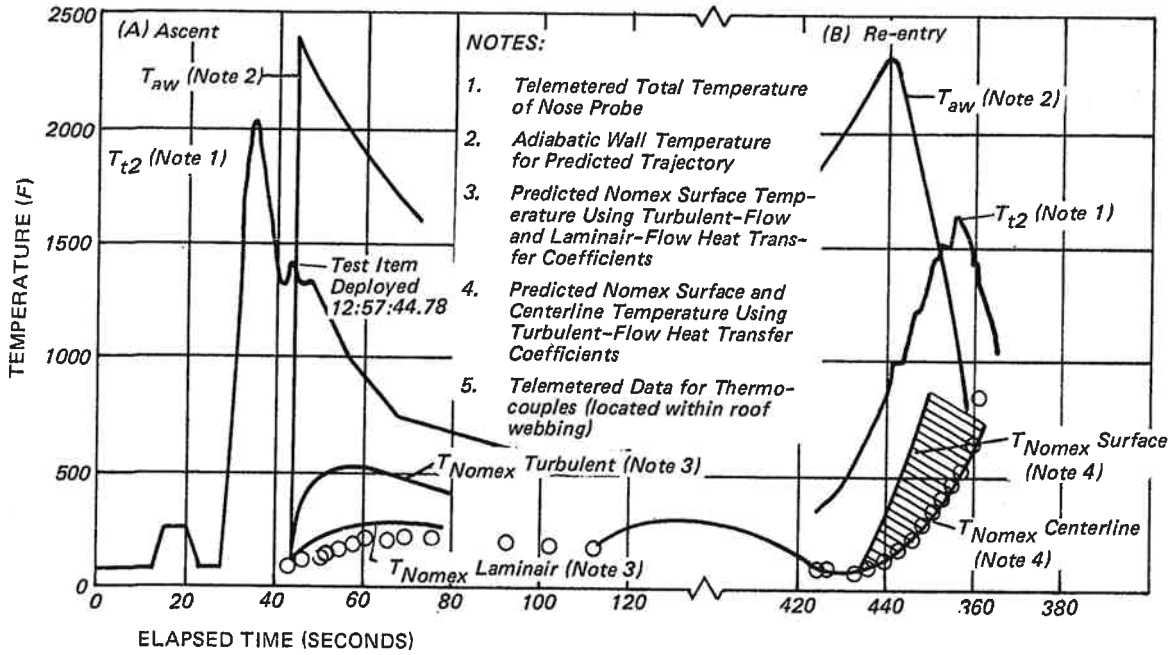
The re-entry phase of a calculated re-entry trajectory was examined next. Again, the wake transition criteria were applied. Transition criteria showed that the re-entry flight begins with the decelerator in a laminar wake. At about 695 seconds from launch and along the calculated re-entry trajectory, the wake transition point apparently begins to move forward toward the leading body. Until about 700 seconds (from launch) the decelerator is encompassed in a turbulent wake with transitions either on the leading body or immediately behind the body. Because of this criterion, the heat input into the decelerator material was calculated partially for the laminar wake case and then for the turbulent wake case. The laminar cold wall heat flux rates rise rather slowly as the bodies re-enter the atmosphere and gradually reach a heat flux rate of about 2 BTU/ft^2-sec at 695 seconds from launch. The heat flux rates increase on the critical position on the decelerator surface until a cold wall turbulent heat flux rate of about 19 BTU/ft^2-sec is reached at 700 seconds from launch. Thereafter, the heat flux rate decreases quite rapidly.

The temperature response of the decelerator material was calculated next on the basis of the cold wall heat flux rates and the transient heat conduction equations. The results are shown in Figure 6.92, as a function of time of flight, along with the telemetered temperature data. The leading vehicle total temperature probe data are presented for reference. Since the total temperature probe was not designed to read temperatures in excess of 2000°F, no correlation was attempted between the probe values and the Ballute thermocouple values. In the case of re-entry flight, the probe total temperature data were programmed to be terminated near apogee. Looking at the decelerator material temperature response during the ascent flight phase, the telemetered results show a quick rise to about 137°F and a subsequent cooling to about 80°F as the upper rarified atmosphere is reached. The predicted surface temperature, as well as outer Nomex surface temperature, is presented for this portion of the estimated trajectory path. The surface temperature in this case is predicted to reach about 280°F in about 10 seconds and then cool as the test items continue to gain altitude. Thus, the predicted temperature evidently overestimates the telemetered temperature by about 150°F during the ascent flight phase.

Turning to the re-entry flight phase, the same comparison is made. The telemetered results show that the material temperature had cooled to less than 0°F during the 10 minutes of flight in the rarified atmosphere. An estimate of this radiation cooling effect indicates that, for an absorption to emittance ratio of less than one, this is admissable. Although no test data are available on the absorption or emittance characteristics of the coating material, the material type shows a trend in the direction of a ratio less than one. As the test vehicle re-enters the denser atmosphere, the Ballute material temperature response indicates a slight rise initially and then rises to about 270°F at 696 seconds from launch whereupon tele-



a) Location of Thermocouples



b) Predicted vs Measured Temperatures

Figure 6.91 Aerodynamic Heating of Parasonic Drogue, SP-5, Deployed at Mach 5.5, 120,000 Ft. Altitude

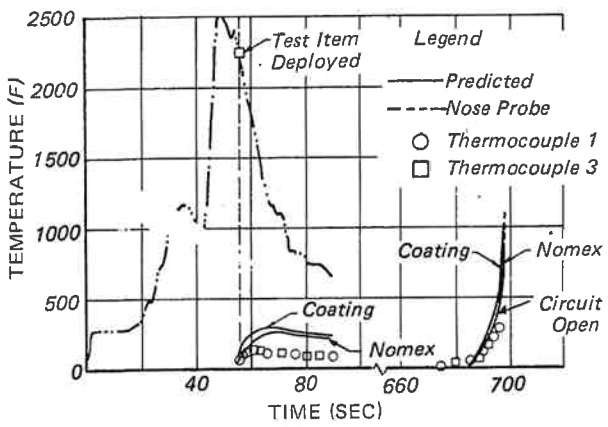


Figure 6.92 Aerodynamic Heating of a Nomex Ballute Flight Test TB-4

metry signals from these circuits cease. In the predicted case, the temperature is assumed to be 14°F at 684 seconds from launch along a calculated trajectory. The temperature response of the material is calculated from this temperature level.

The initial predicted temperature rise is based on a laminar wake and shows the temperature rising to about 400°F in 11 seconds. The comparable rise in the telemetered data is about 270°F. At the end of this period, the wake is predicted to undergo a transition to a turbulent flow. Thus, the heating rates at the Ballute surface rise quite significantly. The predicted temperature shows a rise to a value greater than 700°F in less than 5 seconds from the onset of transition to turbulent flow. This is in excess of its load carrying capability at an elevated temperature, and apparently it correlates with the cessation of telemetry readings for material temperatures.

TERMINAL PHASE

Aerial Engagement

Operation of the mid-air retrieval system may be terminated by engagement of either the main canopy or a small attached target canopy by the hook-and-line grappling rig tied to a power-winch aboard the recovery aircraft. Using fixed-wing recovery aircraft such as the JC-130A, the entire parachute system is collapsed apex first and reeled aboard along with the vehicle being recovered. Using helicopter recovery aircraft such as the CH-3E, similar engagement and retrieval have proved successful. An alternate technique has been developed with helicopters in which the main canopy is freed completely from the towline at both apex and riser attachments and only the target canopy is reeled aboard along with towline, the vehicle being towed back to base while suspended below the recovery aircraft[182]. This approach is illustrated in Figure 6.93.

With either system engagement and collapse of the target canopy by the grapple hook applies a transverse load to one side of the reinforced structure and the interwoven radial and circumferential members are stretched, sliding through the hook, until a firm engagement loop is formed and drawn taut. The target canopy is usually damaged in the process. The resultant impact load is transmitted downward to the vehicle through the attached towline and parachute structure and when the main parachute remains attached its canopy is collapsed by the apex-first motion. As the suspended vehicle is first decelerated and then reaccelerated up to the aircraft speed, the applied load peaks-out and then holds more or less constant as the braked reel of the power winch pays out the towline at a diminishing rate until arrested.

Measured peak engagement loads vary with system gross weight, engagement speed, type of recovery aircraft, and winch design. Collapse of the main canopy is well advanced at the time the engagement load reaches its maximum[184].

Landing Dynamics

A vehicle being recovered descends with parachute to touchdown at a moderate velocity having both vertical and horizontal components. Some angular motion may also be present as a result of pendular oscillation. The purely vertical approach is unusual but one approximated by ballistic systems landing in both still air and light winds. A horizontal velocity component of 5 to 10 fps can usually be tolerated along with angular deflections up to approximately 10 degrees, but acceptable limits vary widely for different types of vehicles and payloads.

Variations in the instantaneous descent velocity are caused by canopy pulsation and axial vibration, usually insignificant, and pendular oscillations (sometimes extreme). The horizontal velocity component may be the result of wind drift, gliding and also of a pendular oscillation or a coning motion. At the instant of contact the attitude and angular motion of the vehicle may be changing. In water landings, wave motion is a factor. Overland the topography (mainly slope), condition, texture, and composition of the landing surface is characterized by extremes familiar to all, but may be moderated to a tolerable level for all planned operations in which some measure of landing site selectivity can be excerised. Involuntary descent onto an inhospitable surface cannot always be avoided.

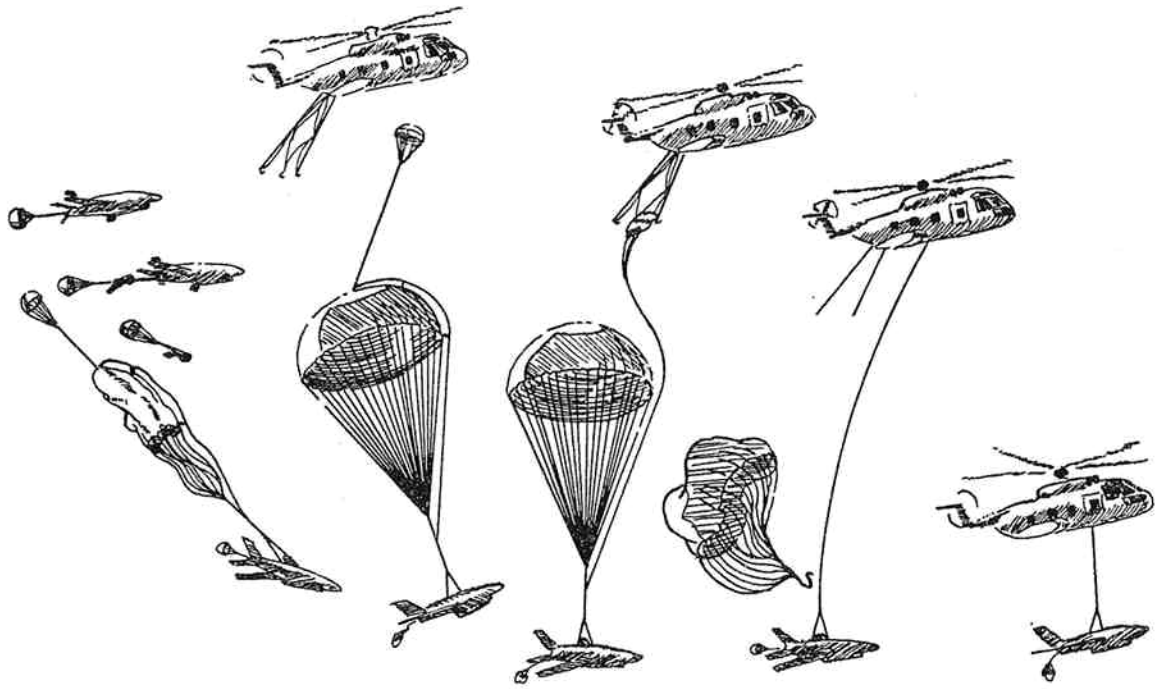


Figure 6.93 An Example of a Mid-Air Retrieval Sequence

Water Impact (Splashdown). In a water impact, as for soft ground, the penetration force, hence deceleration, is a function of the area, direction, depth and velocity of the penetrating body as well as fluid resistance characteristics of water. At normal landing velocities (20 to 35 fps) water provides effective impact attenuation for bodies of every type and degree of bluntness, e.g., the Apollo Command Module[489]. Most streamlined vehicles landing nosedown can easily tolerate water impact velocities of 100 fps or more.

Only relatively fragile structures, such as large empty fuel tanks or jettisoned booster rockets, have been subjected to critical water impact loading conditions when it has been impractical to lower them at sufficiently moderate velocities.

Airdrop. The water impact and penetration behavior of a flat-sided cargo package varies significantly with the density of the payload and the unit loading (weight/area) of the side that strikes the surface. When the unit loading is greater than approximately 100 psf the package readily penetrates the surface, and fluid resistance may provide satisfactory impact attenuation. At lower unit loads and normal splashdown velocities (*≈25 fps)* impact shock effects are augmented by the increased penetration resistance offered by the mass-inertia of the water.

With unit surface loads up to approximately 50 psf the water impact shock is very similar to that experienced landing on dry ground. Therefore, the customary impact attenuation measures are required. It has been observed that under these conditions the loaded pallet appears to slap the surface of the water without significant penetration and, being buoyant, stays relatively dry.

With unit surface loads in the range of 50 to 100 psf approximately, the flat surface impact is less severe, the water reacting more like a fluid, and the payload plunges slightly below the surface. When the average cargo density is less than 62 to 64 lb/ft^3 the package is observed to bob back and settle down to its normal flotation displacement as the displaced fluid moves away in a wave. While the water provides substantial impact attenuation under these conditions the usual energy absorbing media required for ground landing cannot be dispensed with because deceleration peaks remain high.

With unit surface loads greater than 100 psf the cargo plunges well below the surface, and while peak impact shocks may be adequately attenuated in most landings, some protective measures may still be required for unusual payloads as well as to prevent wetting of the payload due to leakage while submerged. Of course, the unit loading of rectangular packages

can be changed by rigging the suspension harness normal to the desired impact surface. Since angular impacts result from both cargo oscillation and surface wave motion, severe bending moments at splashdown may be mitigated in slender packages by selecting a suitable suspension attitude or each configuration. A choppy water surface tends to produce less severe impact shocks and increased onset times for packages with broad flat surfaces. The initial contact area is smaller and apparently a greater volume of air is trapped and compressed to provide added cushioning. The typical splashdown is attended by a horizontal drift component due mainly to surface wind, modified by parachute oscillation when present. Under these conditions, which are aggravated in rough water, cargo packages having poor buoyant stability are most likely to overturn on impact.

Manned Spacecraft. The Gemini and Apollo landing capsules with W/A typically greater than 100 psf exhibited the same type of behavior on spashdown described above, surface penetration (Refs. 489, 490-492) being sufficient for good water impact attenuation e.g., $a(max) < 5g$. However, with two diametrically opposed stable floating attitudes, it was necessary to provide Apollo with inflatable bladders for righting from the inverted attitude. Also roll stability was poor and often caused seasickness among the astronauts before stabilizing floats could be attached by the recovery crews.

Impact Attenuation

Attenuation of the landing impact occurs in some measure in every landing operation through deformation of vehicle and surface. Where acceptable levels of deceleration onset, peaks g's, and structural deformation are likely to be exceeded, some means of raising the level ot tolerance may be employed. The horizontal velocity component represents an increment of kinetic energy ($m_b v_H^2/2$) that is commonly dissipated by sliding friction between vehicle and landing surface. Operational planning is justified to ensure that the nature of the landing site will favor this type of action; otherwise tumbling or additional structural deformation may ensue.

A common practice is to disconnect the main descent canopy from the body immediately after contact to prevent aerodynamic forces from inducing destabilizing moments during the terminal deceleration cycle as well as dragging with the prevailing surface wind. Therefore, neglecting the momentary restraint provided by the main canopy, the total energy to be dissipated by the impact attenuation system may be represented by the vertical component,

$$E_V = m_b v_V^2/2 + W_b h_o \qquad 6\text{-}41$$

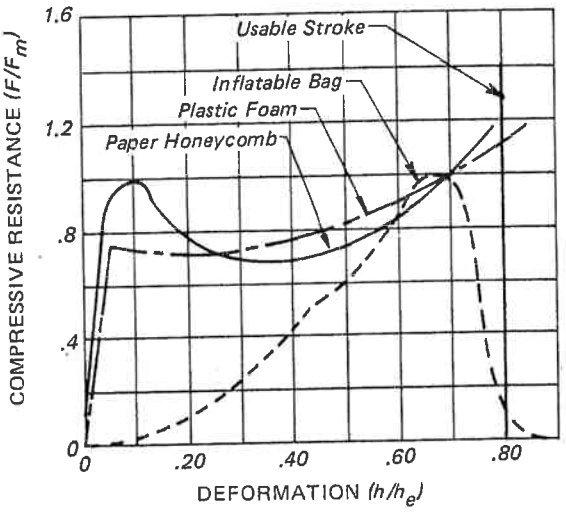


Figure 6.94 Variation of Compressive Resistance With Deformation of Energy Absorber (Ref. 382)

where h_o is the height above the landing surface when effective contact is first made and mechanical deformation of the resisting media (both onboard and on the surface) begins. The vertical energy component must be absorbed even when the onboard impact attenuator is subject to shearing stresses due to horizontal motion. This leads to redundancy of material because all of the energy absorbing medium cannot be brought into effective play along any one axis.

Passive energy absorbing media such as plastic foam and paper or aluminum "honey-comb" are characterized by their specific energy absorbing capacities (Table 4.41). While the total weight of material required is indicated by the ratio of the total to specific energy absorbing capacities, the distribution of the material under the vehicle is determined by other factors which include vehicle allowable maximum decelerations and decelerator or energy absorber performance characteristics. Under any combination of landing conditions the peak retarding force must not exceed

$$F_m = W_b (G_z + 1) \qquad 6\text{-}42$$

where W_b is the weight of the vehicle at its maximum landing weight condition and G_z is the maximum allowable vertical load factor. The way in which the retarding force varies during the working stroke for different energy absorbing media is illustrated in Figure 6.94. The unit stress or pressure, p, would vary in the same way if the cross section or "footprint" area, S_f, remained constant, but this is seldom the case.

The retarding force is related to the design dimensions of the impact attenuator by this expression

$$F = pS_f = f(h/h_e) \qquad 6\text{-}43$$

where h is the instantaneous height and h_e is the constructed height of the mechanism or energy absorbing medium. Useful performance parameters for each different mechanism are:

$K_h = \Delta h/h_e$	=	dimensionless effective working stroke
p/p_m	=	average to maximum stress or pressure ratio during Δt when S_f is constant
F/F_m	=	average to maximum force ratio during Δt
$K_e = a/a_m$	=	average to maximum deceleration ratio during Δt

where Δt is the time interval corresponding to Δh, and K_e is a measure of the dynamic efficiency of a given impact attenuation subsystem.

Crushable Materials. Principal crushable materials in use are urethane foam and honeycomb structures of different materials varying in cell size and density. These differences give the honeycombs different crushing strengths, as measured by the ultimate compressive stress per unit area, f_c, and cause the usable stroke to vary somewhat, but not greatly. Although the crushing stress varies during the working stroke, the average value, f_c, may be evaluated, along with the usable stroke, Δh, by suitable impact tests to determine specific energy

$$E = f_c\,(\Delta h/h_e)/w_e \qquad 6\text{-}44$$

where w_e is the weight density of the energy absorbing material. The end of the usable stroke is reached when the material has been crushed to a density which causes the compressive resistance to increase sharply (Fig. 6.94).

The characteristics of different honeycomb structures are summarized in Table 4.41. The anisotropic nature of the structure causes the crushing strength to decrease with the angle of impact as shown in Figure 4.7.

Airbags. A widely used landing impact attenuation method for sensitive payloads, the inflatable airbag system has improved steadily in effectiveness, if not in overall efficiency. One reason for this has been increasing stringency of requirements for protection of the vehicle and its contents from damage or injury. The resultant augmented redundancy of impact bags and/or static bags has tended to increase the total weight fraction invested in the subsystem, even though the working efficiency of the components has been increased.

Unlike block-type crushables the footprint area of an airbag may vary during the working stroke due to its shape and also as the result of drift. The center of pressure will shift for the same reasons. Characteristically, on contact the bottom of a given airbag will remain stationary on the ground until the inflated envelope has been deformed by lateral shear sufficient to overcome the static friction force and start sliding. Because the shear resistance of an inflated airbag is generally small, it tends to roll under the vehicle, and sliding is delayed until late in the working stroke. With a static coefficient of friction typically in the order of $C_f = 0.5$, both leading and trailing bag-girts and wall panels must come under considerable tension before sliding can begin.

The total horizontal drift during the impact bag working stroke is seldom greater than one-half the initial bag height, except for gliding systems. Thus, a typical impact bag will have completed its working stroke during a drift landing before it begins to slide, and the way in which its center of pressure shifts during the interval will be of paramount concern.

For a given vehicle, $p(max)$ may also be specified in terms of allowable unit skin pressure over specific areas of the body. When this becomes a critical design factor, measures such as the use of static airbags to expand the effective skin area may be taken, as found in some airbag impact attenuation systems.

A comparison of the measured and predicted performance characteristics of an experimental RPV impact bag system is presented in Figure 6.95. A similar RPV impact bag system exhibited the dynamic performance summarized in Table 6.12 when subjected to a series of vertical and swing drop tests. Figure 6.96 shows a vertical drop test for an airbag system. The inflated dimensions of the RPV impact bag are given in Figure 6.97.

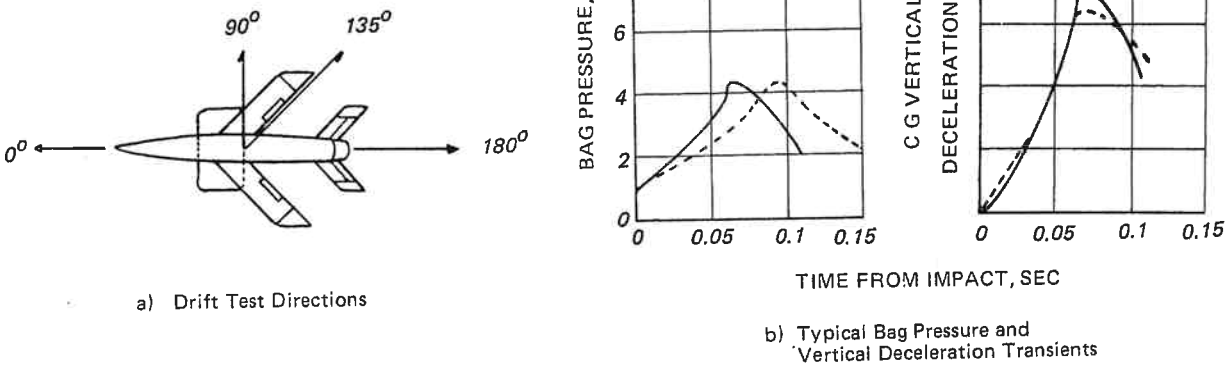
Retrorockets. Pre-contact velocity attenuation to reduce the landing impact has been accomplished successfully in a number of vehicle deceleration systems by means of retrorockets initiated with a surface proximity sensor. A variety of other retarding devices and self-powered mechanisms have been investigated experimentally. These have included: bootstrap mechanisms called ***contractable links,*** designed to impulsively shorten the distance between the supporting canopy and the suspended body. Retarders consisting of multiple explosive charges fired in rapid sequence under the canopy also have been tested[494].

Only the retrorocket has proven to be a practical pre-contact velocity attenuation device of sufficient reliability and efficiency to be employed in sensitive vehicle or manned spacecraft landing systems.

Reported test experience with retrorocket landing systems designed as the terminal active member of a

Drop No		Maximum Bag Pressure (psig) *		Maximum cg Deceleration (G_z)*	
Drop No.	Velocity, fps (19 fps Vertical)	Predicted	Actual	Predicted	Actual
1	Vertical	4.3	3.0	7.5	7.3
2	Vertical	4.3	4.4	7.5	7.5
3	Vertical	4.3	3.9	7.5	6.7
4	17 fps at 0^o	4.3	3.5	7.5	5.5
5	17 fps at 90^o	4.4	4.4	6.1	5.0
6	17 fps at 180^o	4.13	4.0	7.0	6.0
7	17 fps at 135^o	4.4	4.4	6.7	6.0
8	17 fps at 90^o	NA	NA	NA	>100

*Maximum bag pressures and G_z occur at approximately 0.07 seconds after ground contact.



a) Drift Test Directions

b) Typical Bag Pressure and Vertical Deceleration Transients

Figure 6.95 Experimental Impact Bag Performance (Ref. 493)

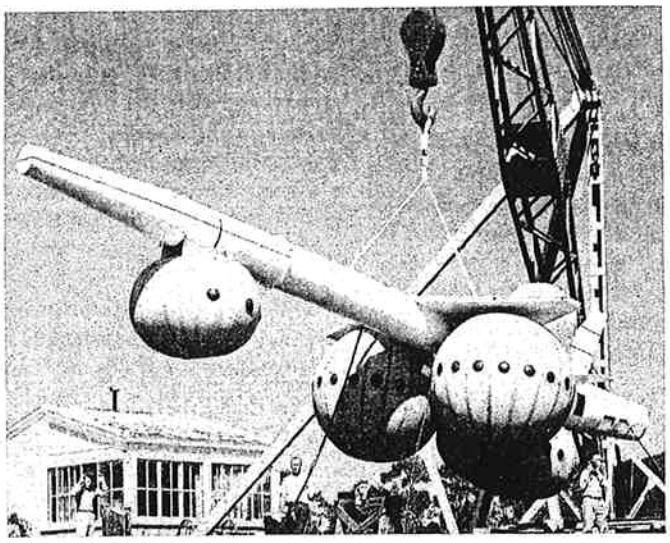
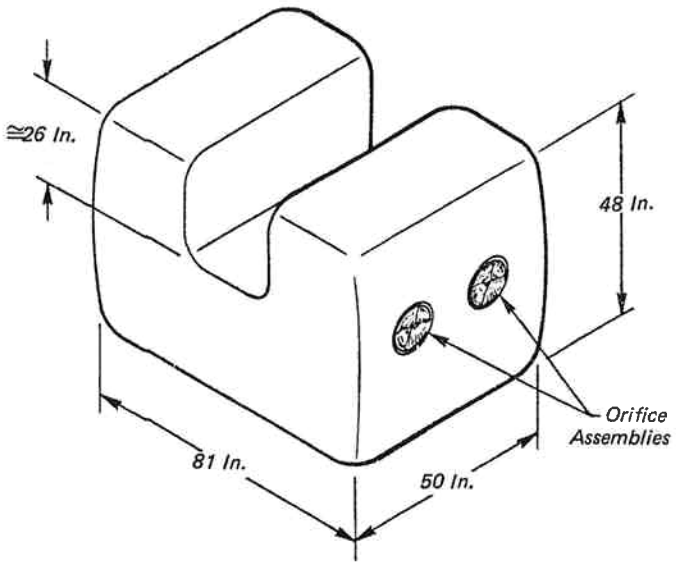


Figure 6.96 Airbag System Vertical Drop Test



Bag Material - Nylon Cloth/ Natsyn Elastomer
- 700 Lb/In Strength
- 26 Oz/Yd^2 Weight
Bag Weight - 25 Lbs
Bag Inflated Volume -71 Ft^3

- Modified a Qualifiable Bag to Demonstrate Impact Bag Principle
- Aft Surface of Bag Located Directly Below Drone c.g.
- Initial Bag Pressure = 1 PSIG
- Vent Relief Pressure = 4 PSIG
- Orifice Plate Vent Area = 154 In^2 (4 @ 38.5 In^2)
- Orifice Plate Release Pins = 3 Pins Each Plate, 0.081 In Dia, 1100 Soft Aluminum

Figure 6.97 Maximum Inflated Dimensions Impact Bag (Ref. 496)

deployable aerodynamic deceleration system is limited because few such subsystems have been commissioned for development. Although proven solid propellant rockets of short burn-time are available which provide a broad spectrum of performance chacteristics in terms of thrust, total impulse and specific impulse, none are ideally suited to the velocity attenuation requirements of the typical recovery system. Requirements and performance are brought closer together by employing a cluster of small rockets, rather than a single unit, as was done for the Redhead/Roadrunner landing system[495]. Here the rocket cluster was harness-mounted between parachute and vehicle with nozzles vectored in opposed pairs to prevent impingement of the exhaust jets on the payload.

Ground Proximity Airdrop System. Jackson and Peck[497] describe a projected Ground Proximity Airdrop System for delivering payloads of up to 35,000 lbs from altitudes less than 500 feet which employs a harness-mounted cluster of retrorockets. Typically, upon initiation by a pair of drop-cord type ground sensing probes, the rocket impulse would reduce the payload velocity from 60 fps to a nominal impact velocity of 22 fps.

Parachute Retrorocket Air Delivery System. Chakoian and Michal[125] describe the exploratory development of a Parachute-Retrorocket Air Delivery System designed for operations below 500 feet altitude. This system employs the same retrorocket cluster mentioned in Reference 497. Successful performance was demonstrated with loads of 4000 to 10,000 lbs dropped from heights of 300 to 500 feet (Figure 6.98). A photographic sequence of one of the drop tests is displayed. A typical operation is described as follows:

"When the cargo platform is about 25 feet above the ground, the horizontal velocity will have been diminished (by parachute drag) to near zero and the vertical velocity will have increased to approximately 60 to 70 fps. At this point, (1) the ground sensing probes, which have reeled out fully, impact the ground, (2) detonators in the probes are fired initiating the unconfined mild detonating fuses, (3) these in turn transmit the detonation to end primers in the probe reel-out brakes, (4) the signal is transferred to the confined detonating fuse, (5) primers are fired in the shuttle valves mounted on the rocket pack(s) and (6) upon firing, the shuttle valves allow high pressure gas to activate the dual primer ignition system of each rocket motor. The rockets fire and burn for 0.5 seconds. The cargo platform decelerates vertically at about 3g to approximately 25 fps before impact. Crushable paper honeycomb cushions the final impact."

Crew Escape Capsule System. Whitney[498] reports the following results of a demonstration test of a crew escape capsule retrorocket system with dummy vehicle (Figure 6.99) using a cluster of four rockets mounted on the main parachute harness above the

TABLE 6.12. SUMMARY OF IMPACT BAG DYNAMIC PERFORMANCE DATA

DYNAMIC MEASUREMENT	DROP NO. 1	2	3	4	5	6*	7	8*
C.G. Acceleration Fwd + (g's)	0.9	0.9	–	0.5	0.5	2.0	1.0	9.0
C.G. Acceleration Left + (g's)	1.0	1.3	–	–	1.5	1.0	0.5	9.0
C.G. Acceleration Up + (g's)	7.3	7.5	6.7	5.5	5.0	6.0	6.0	100.0@
L. Wing Tip Accel Up + (g's)	9.5	10.0	9.2	9.0	10.5	11.4	3.0	100.0
R. Wing Tip Accel Up + (g's)	7.5	7.0	7.0	7.5	7.5	12.9	NG	NG
Aft Fuselage Accel Up + (g's)	4.0	4.0	4.0	7.5	3.0	9.9	1.0	20.0
Aft Fuselage Accel Right (g's)	1.0	–	–	–	2.0	1.0	–	10.0@
Fwd Fuselage Accel Up + (g's)	8.0	11.0	9.5	8.0 2.2	7.5	20.0@	10.2	40.0
Right Bag Press Peak (PSIG)	3.0	3.2	2.8	2.3	(4.4)#	2.0	2.5	–
Left Bag Press Peak (PSIG)	–	4.4	3.9	3.5	4.4	4.0	4.4	–
Vertical Velocity @ Impact (FPS)	19.3	18.8	19.6	18.0	17.2	19.8	17.5	17.1
Horizontal Velocity @ Impact (FPS)	–	–	–	17.0$	17.0$	17.0$	17.0$	17.0$
Period of Stroke** (SEC)	0.15	0.20	0.18	0.15	0.18	0.18	0.23	–

* Accelerometer Values Approximate

\# Secondary Peak Pressure

** Period From Bag Pressure Build Up to Zero Bag Pressure

@ In Excess of Values Shown

$ These Values are Approximate

payload.

Ambient Temperature	84°F
Wind Velocity and Direction	6 knots/300°
Slope of Impact Area	0°
Descent Velocity (based on the average velocity during last five seconds before rocket ignition)	29.5 ft/sec
Release Altitude	2096 ft
Chutes Vehicle Oscillation Angle	2°
Release	Elapsed Time 0
Line Stretch	2.908 seconds
Full Open	15.508 seconds
Probes Impact	41.230 seconds
Rocket Ignition	41.308 seconds
Vehicle Impact	41.788 seconds
Probe Impact to Vehicle Impact	.588 second

Using the above data and the results of the rocket performance computer program in Reference 499, (see Figure 6.99), it was determined that the vehicle impacted at a velocity of 9.59 ft/sec. The test weight was 8083 lbs. The system launch weight including parachutes was 8627 lbs.

Soyuz Landing System. The only operational landing system employing retrorockets on manned spacecraft is that of the Russian three-man "Soyuz". No details are available but the soft-landing reliability record turned in to date bespeaks a well-developed retrorocket technology.

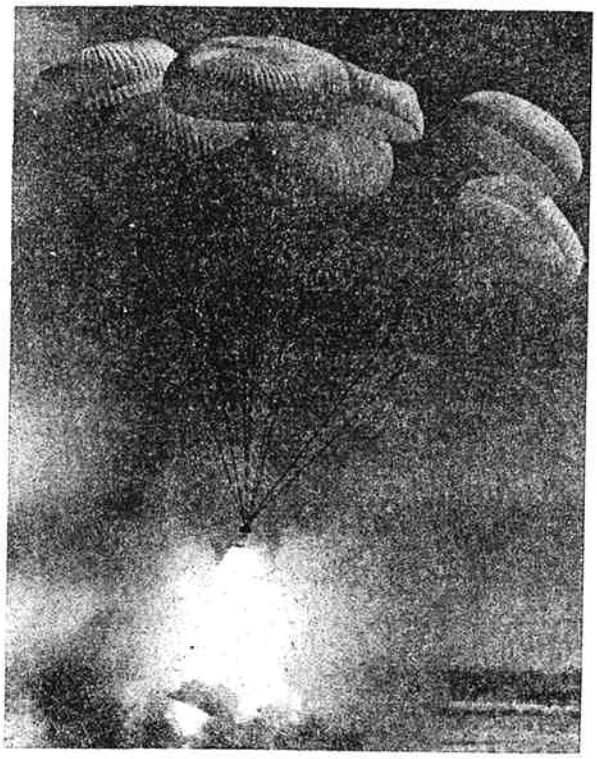


Figure 6.98 Low Level Air Drop with Pre-Contact Deceleration by Retrorockets

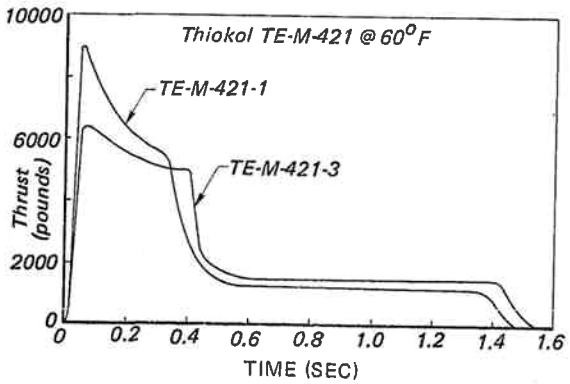


Figure 6.99 Thrust vs Time for TE-M-421-1 and TE-M-421-3 Rockets at 60° F (from Ref. 499)

RELIABILITY

The history of deceleration system operations, like that of any other human undertaking, is spotted with malfunctions and failures, some of them fatal. Of prime concern are the injury and survival rates of personnel who, by chance or choice, employed parachutes designed for

Emergency escape systems
Delivery of Paratroops
Spacecraft landing systems
Aircraft auxiliary control

Of secondary concern is the cost of losses in terms of material, time and dollars, except where the strategic advantage of a military operation may be jeoparized by decelerator failures in unmanned systems.

Typical Malfunctions

Although the following types of malfunctions are potential sources of failure of operational deceleration systems, they have been encountered mainly during development test programs through errors in establishing the test conditions or because of design deficiencies. All known design deficiencies are corrected prior to qualification acceptance so that subsequent failure rates are generally quite low.

Deployment malfunctions may be caused by obstructions in the deployment path, inadequate allowance for vehicle spin or tumbling, improper angle of ejection, insufficient ejection energy, inadequate reliability of initiators, improper packing, improper rigging, unforseen environmental factors, and impact shock waves in the towing riser.

Inflation and deceleration malfunctions may be caused by insufficient structural strength, premature deployment, deployment malfunction, riser abrasion, notching, or cutting, insufficient allowance for vehicle spin, insufficient allowance for vehicle-wake effects, insufficient allowance for nonuniform loading, excessive porosity, neglected operational variations, reefing line cutter failure, premature separation of reefing line, premature separation of a prior-stage decelerator, malfunction of a prior-stage decelerator, and undamped high-frequency oscillations.

Descent malfunctions may be caused by major damage to the primary drag or lifting surface, distortion of the primary drag or lifting surface by fouled rigging, interference between clustered canopies; impact of a previously jettisoned vehicle component, excessive undamped oscillations, excessive relative motion between primary lifting surface and suspended vehicle, fouled control lines, excessive porosity, and effects of dimensional instability on trim and control of lifting surface.

Aerial retrieval malfunctions may be caused by deployment malfunction, collapse or inadequate stability of engagement canopy, and insufficient structural reinforcement of parachute assembly for engagement impact.

Causes of Unreliability

Major causes of unreliability in decelerator operation may be identified as either inadequate design, materials failure due to accident, or human error in decelerator assembly, packing, and use. In designing for reliable performance, and in assessing the reliability of a given design, the possibility of failures from these three causes must be considered.

From the viewpoint of operational parachutes and other decelerator systems, inadequate design is generally not a major failure factor in actual field use. Since virtually every decelerator system goes through a design, a development, and a shake-down testing period, design errors are generally eliminated in development. The exceptions are those cases in which the design error can be said to be marginal, and in which the failure rate due to the design error is so low as to be undetectable even with an adequate test program, and indistinguishable from accidental causes.

Materials failures may be divided into two classes: failures of the fabric and static hardware portions of decelerators, and failures of the mechanical devices which are necessary to deceleration system operation. Failures in the fabric portions of canopies are probably the most difficult to assess on a theoretical basis. First, experience indicates that fabric failures must be considered from the viewpoint of critical or non-critical applications of the fabric in the parachute. Thus, for example, in many missions the blowing out of a panel in a canopy does not necessarily mean a failure of the mission. If the decelerator function is merely to land the load without damage in a general area, and the decelerator is designed with a normal margin of safety, the loss of a panel from the canopy may not affect the reliability of mission performance at all. On the other hand, in such a mission the failure of a riser or a suspension line could very well result in major damage or destruction of the load, and thus failure of the mission.

In cases in which both the deceleration of the load and the achievement of a reasonably precise touchdown point are vital, e.g., delivery of a special weapon, failure of a single panel might so change the trajectory of the decelerator system that the mission would be a failure even though the deceleration function had been accomplished successfully. Thus, mission analysis is a vital factor in determining which specific types of fabric failure cause decelerator system failure.

To pinpoint the exact reason for the failure of a canopy is a rather difficult engineering task. The tensile strength of a large number of samples of the fabric used for any given member of the canopy, tested under conditions simulating those of actual use, will be found to vary according to a normal distribution curve, with the actual strength values generally tending to group around a central average.

A similar study of stresses which are placed on the various canopy members during parachute deployment and descent will indicate that for each given phase of decelerator deployment and operation, a given range of stresses will act on each component. Again, a series of measurements will tend to show a range of such stresses at any given point, depending on the specific manner in which the canopy unfolds, etc. As in the strength case, these values usually will group around a central average with both extremes considerably less common than the mean.

To understand the reasons for many accidental failures of canopies, it is necessary to examine the relationship between distribution of strength of the material in each portion of the canopy and stress on each portion of the canopy in its operation. In every application of decelerators there is some probability of very low or very high stress, but the probability of the extremes is less than the probability of a stress closer to the average. Similarly, in every choice of a specific piece of fabric for the construction of a canopy there is a possiblity of getting a lower-strength piece or a higher-strength piece. Thus, it can be seen that the probability of accidental failure will depend largely on the probability of the specific portion of the canopy which fails being constructed of a low-strength piece of material that encounters an accidentally high stress during the operation. Many of the structural failures which do occur are caused by this factor, i.e., excessive overlap of the strength and stress distribution curves.

Failures of mechanical devices used in various decelerator systems present a more straight-forward problem than failures in fabric portions. With static hardware, items whose functions are primarily passive, the cause of failure may be attributed to the distribution of strength and stresses of the components, as in the case of fabrics. However, there is another class of mechanical devices which must perform active functions during the deployment or operation of the system. This class consists of reefing line cutters, interstage disconnects, deployment-initiation devices, etc. Here the reliability problem is one of mechanical functioning in an environment which may include low temperature, shock, vibration, acceleration, and possibly other interfering factors.

Human error is more difficult to deal with than the purely mechanical problems. Of course, human error in the process of parachute design is part of the design problem rather than the parachute-use reliability problem. However, human error in parachute construction and use is probably one of the primary causes of failure in the operation of many of the most common types of parachutes, including man-carrying parachutes and cargo parachutes. Major areas of possible error may be isolated as errors in manufacture not caught by inspection procedures, errors in rigging the parachute to the load, and errors in packing the parachute.

Human error in the manufacturing process is quite difficult to evaluate in reliability studies. Here, reliability is primarily a function of quality control by the manufacturer, and also depends on proper training of manufacturing personnel and on thorough and effective inspection. It would appear that such errors are relatively rare. In a recent study of parachute reliability[500] it was not possible to isolate human errors in the records of well over 5,000 parachute uses.

A distinction is made between human error in rigging and human error in packing, primarily because a functional failure due to an error in packing can be definitely detected in the parachute behavior, while a failure due to an error in rigging is probably more readily traced to the behavior of the body rather than of the decelerator itself. In the study cited above, it was found that parachute rigging errors which caused failure of the drop mission were most likely to occur in those airdrop applications in which irregularly shaped loads were employed. This appears to be particularly true in the case of heavy vehicles loaded on drop platforms, and other types of loads having protuberances, sharp corners, and unsymmetrical shapes. In these failures, the actual failure-mechanism can usually be traced to the snagging or tangling of some portion of the deploying canopy or lines on a portion of the load.

While it is true that this latter failure causes unreliability in the mission, the advisability of considering such failures as caused by unreliability of the parachute to the load in cargo drop, and to personnel in man-carrying applications, is not under control of the parachute design or engineering agency. Thus, unreliability due to rigging error can be corrected primarily by operational discipline rather than by processes which can truly be said to be under engineering control. Such problems probably should not be considered as part of the reliability of the parachute itself, although they undoubtedly affect reliability of the mission. Rigging problems in many other types of parachutes are not as serious from the human-error viewpoint. For such applications as missile and drone recovery, aircraft deceleration, and space vehicle recovery, where the load and parachute have been designed as a unit, the rigging error may be considered as a portion of the packing error.

Human error in packing has been found to be one of the major failure-producing factors in some types of parachute reliability studies[500]. Here, two distinct portions of the packing process are isolated for error control: (1) the canopy lay-out, folding, tying and stowing, and (2) the installation of hardware and auxiliary devices required for parachute operation. In the previously mentioned study of heavy-duty parachute reliability, survey of the records of parachute failures in normal use indicated that the majority of human-error-failures in packing were not in the canopy portion of the operation, but rather in the auxiliary-device installation.

Review of the packing process for large and complex parachute systems reveals what is probably the basic reason for a higher rate of error in the installation of the hardware items. Quality control measures applied to the parachute packing process require constant inspection as each step of packing proceeds. During lay-out, examination folding, and stowage of the canopy, the inspection process can follow each individual packing operation quite closely, since, the parts of the canopy involved are large and readily visible to the inspector. However, when hardware, auxiliary devices, reefing line cutters, and similar mechanical devices are installed, the parts involved are usually quite small. The operations required of the parachute packer are such that frequently his hands hide the part from the inspector. Further, after the completion of the operation, it is sometimes difficult for the inspector to see all portions of the part clearly. This is particularly true in the case of canopies which must be installed in compartments that are in integral portions of the load, and where electrical connections, etc., must often be made. Here, inspection becomes very difficult and it appears entirely possible that the inspector, no matter how diligent, might miss an error in the process which could eventually cause failure of the parachute in its mission.

Of course, examples of such errors are the exceptions rather than the rule. The observed rate from a study of failure records was about 14 in over 5500 packings of complex parachute systems, with an estimated 100 possible opportunities for error in each complete packing. Thus, over a half million chances for error were possible. However, in ultra-reliable systems an error rate of this magnitude may well be the major single cause of unreliability.

TABLE 6.13 8-YEAR MALFUNCTION STATISTICS PERSONNEL DROP RECORD

	Type of Parachute	Number of Drops	Number of Malfunctions	Percentage of Malfunctions
1968	T-10	324,170	951	0.29
	Maneuverable	29,024	6	0.02
	HALO	3,154	0	0.00
1969	T-10	267,000	570	.21
	Maneuverable	39,100	5	.01
	HALO	4,292	4	.09
1970	T-10	246,326	930	0.38
	Maneuverable	40,229	35	0.08
	HALO	5,261	5	0.09
	T-10 Res	894	136	15.29
1971	T-10	283,776	797	0.28
	Maneuverable	37,291	27	.07
	HALO	7,096	0	0.00
	T-10 Res	754	122	16.1
1972	T-10	229,917	599	.26
	Maneuverable/MC1-1	37,926	26	.068
	HALO	2,962	2	.06
	T-10 Res	644	99	15.30
1973	T-10	247,398	721	0.29
	Maneuverable/MC1-1	45,489	31	0.07
	HALO	1,984	1	0.05
	T-10 Res	641	79	12.32
1974	T-10	165,856	625	0.38
	Maneuverable/MC1-1	39,929	24	0.06
	HALO	3,692	0	0.00
	T-10 Res	602	82	13.62
1975	T-10	132,947	615	0.46
	Maneuverable/MC1-1	59,749	92	0.15
	HALO	5,180	0	0.00
	T-10 Res	654	112	17.13

TABLE 6.14 8-YEAR SUPPLY/EQUIPMENT DROP RECORD

	1968		1969		1970		1971		1972		1973		1974		1975	
Number of Drops	23,321		15,102		17,084		15,684		7,649		6,836		5,837		5,475	
Number of Malfunctions	183		126		163		86		68		90		53		70	
Percentage of Malfunctions	0.78		.83		0.95		0.54		0.88		1.31		0.91		1.28	
Malfunction Phases:	EF	IP	EF	IP	EF	IP	EF	IP	EF	IP	EF	IP	EF	IP	EF	IP
Extraction or Ejection	2	91	1	36	3	42	3	15	0	11	0	13	0	4	11	1
Deployment Recovery	5	76	22	58	7	54	6	47	4	43	29	41	13	32	32	18
Release	0	10	1	8	3	5	0	11	2	7	2	5	3	1	5	3

EF = Equipment Failure
IP = Incorrect Procedure

System Reliability

Representative statistics of U.S. Army on airdrop parachute system reliability in terms of numbers and types of malfunctions are summarized in Tables 6.13 and 6.14.

CHAPTER 7

ANALYTICAL METHODS

Although parachutes and similar devices are found to be complex both structurally and functionally, significant advantages have been made in the development of analytical tools for design analysis and the prediction of their performance. The parallel development of large capacity, digital computers has made it possible to work with mathematical models of sufficient completeness to produce results of acceptable accuracy in many instances. Accuracy of ±10 percent is considered good, representing current state-of-the-art, although ±5 percent is a near-term goal. Higher confidence in the predictability of limit loads, temperatures, and system motions through analytical means would reduce the extent of high cost full scale testing.

Because most mathematical models of decelerator systems embody empirical coefficients of different kinds, two of the major deterrents to the analytical approach are the shortage of data of the kind and quality needed, and the cost of obtaining such information. The most useful analytical methods are those capable of employing existing test data of the kinds easy to measure with accuracy and that are abundant in the literature. Where adequate empirical data are at hand, suitable computer programs have been developed and utilized, the results of which are generally more dependable than results of earlier less sophisticated methods. If quick solutions to new design or performance problems are to be found, short empirical methods useful for preliminary evaluation, as well as advanced computerized methods are needed. Unfortunately, the complex behavior of flexible aerodynamic structures during inflation and other dynamic loading conditions, cannot yet be analyzed with the same rigor with which aircraft or spacecraft structures are treated. There is virtually no dependable intermediate approach between the approximate empirical methods and the rigorous mathematical formulations dictated by theory. An engineering understanding of the short methods requires an appreciation of the theory and logic of the complex methods.

The nature and complexity of the physical phenomena surrounding decelerator operation is described distinctly by the authors of Reference 501. *Parachutes, drogues and similar decelerators function for periods of time that range from seconds to minutes. For example, the periods of operation of the Apollo drogue, pilot chute and main parachutes for a normal entry were one minute, two seconds, and five minutes respectively. The manner in which each of these components performs throughout its period of operation is of great interest, however, the brief moments during the deployment and inflation of each canopy are the most critical. It is during the inflation process that critical design loads usually occur along with other physical phenomena impinging on the ultimate reliability of the system.*

FUNDAMENTAL RELATIONSHIPS

The physical properties important to decelerator operation have been related in a number of dimensionless ratios drawn from classical aerodynamics, fluid mechanics and strength of materials studies, plus a few peculiar to this particular branch of aeromechanical engineering, e.g., air permeability, flexibility, and viscoelasticity with amplified hysteresis. A convenient way to present these fundamental relationships is in terms of scaling laws and similarity criteria.

Scaling Laws

Always a difficult subject because of its complexity, the derivation of suitable scaling laws for deployable aerodynamic deceleration components and systems has been a continuing objective.

Scaling Ratios for the Design of Model Tests. Several investigators have sought general scaling laws for maintaining dynamic similitude of the incompressible parachute inflation process. In general, to satisfy the laws of dynamic similarity in a scaled test all forces in the model equation of motion must be scaled to have the same relative effect as the forces in the full-scale equation of motion. This approach was advanced to a useful level by Barton[502] and further expanded by Mickey[361]. (Flexibility and elasticity ratios are added herewith to complete the following list.)

Quantity	Ratio
Length	$r_1/r_0 = r_1/r_0$
Time	$t_1/t_0 = (r_1/r_0)^{1/2}$
Force	$F_1/F_0 = (\rho_1/\rho_0)\,(r_1/r_0)^3$
Mass	$m_1/m_0 = (\rho_1/\rho_0)\,(r_1/r_0)^3$

Dimensionless Correlation Parameters

Factor	Parameter	Symbol	Name
Scale	$lv\rho/\mu$	Re	Reynolds No.
Compressibility	v/c_s	M	Mach No.
Fluid displacement	$v/(lg)^{1/2}$	Fr	Froude No.
Stretching resistance (1/elasticity)	$\kappa/\rho v^2 l$	Kp	Kaplun No.
Stiffness (1/flexibility)	$EI/\rho v^2 l^4$	Ω	Relative stiffness
Added air mass	$\rho l^3/m$	R_m	Mass Ratio
Air permeability	v_λ/v^*	c	Effective Porosity

Strain	$\epsilon_1/\epsilon_0 = (\rho_1/\rho_0)\,(r_1/r_0)$
Flexibility	$e_1/e_0 = (\rho_1/\rho_0)\,(r_1/r_0)^4$
Elasticity	$\Delta r_1/\Delta r_0 = (\rho_1/\rho_0)\,(r_1/r_0)^2$

An example of the application of some of these scaling ratios (Barton's) to Parawing testing will be found in Refs. 220 and 504 - 506.

Similarity Criteria

A second approach to the derivation of scaling laws is one of identifying dimensionless parameters which must have the same values in model tests as in full scale tests. This approach to the parachute inflation process was taken by Kapun [385], French [384], Rust [507] and Mickey [361]. The above table lists some of the dimensionless parameters identified by these investigators.

Because similarity criteria cannot be satisfied with all the parameters in one model test, those of greatest importance to the decelerator application of interest govern the design of the tests, e.g., Ref. 508. For reasons of economy, small model tests of all types (wind tunnel, indoor freedrops, aerial drops, towing) have been used extensively to generate empirical data. Because application of the model scaling laws has not been sufficiently refined, the results of such tests have been mainly of a broad qualitative value useful only for comparative purposes. Some steps to advance the state-of-the-art in this area have been taken, as exemplified by References 354 and 509 - 512.

Wind Tunnel Effects. The classic wind tunnel test is a constant velocity operation corresponding to the theoretical infinite mass decelerator system approximated by most drogue applications and the inflation of parachutes at high altitudes. Often the size of the test models is limited to less than full scale and usually has been only a few inches inflated diameter for both subsonic and supersonic investigations to minimize choking and wall effects. This has made it considerably more difficult to design and fabricate accurate scale models of flexible decelerators than of rigid bodies. Application of scaling laws is further complicated by the constraints placed on system geometry and freedom of motion by model supports, shock waves generated by supports, and the reflection of body shock waves from tunnel walls.

Evaluation of static stability coefficients as a function of canopy angle of attack is complicated by distortion of the inflated shape by the constraints used to control α. Parachute models of all sizes often are allowed to oscillate about the point of support. Since this point seldom coincides with the center of mass of a free-flying system the character of the oscillation is modified by the constraint. The fixity of the point of support also prevents gliding which is an integral component of the oscillatory motion in free descent.

Relative Stiffness and Elasticity. Of particular significance to small model test results is the relative stiffness parameter, the reciprocal of bending deflection or flexibility, in the form proposed by Kaplun [385]. This is a complex criterion virtually impossible to satisfy over a meaningful scale ratio with available materials. Although material stiffness is of negligible importance to most large decelerators over a wide range of sizes, the relative inflexibility of small models probably has much to do with the general lack of correlation of both steady and unsteady aerodynamic characteristics between small and full-scale test results 354,509.

Relative elasticity, (l/Kp), can be identified as a strong contributing factor to the growth of C_D with scale (see Fig. 6.53) and to variations in the dynamic characteristics of decelerators. With a material's resistance to stretching or its "effective spring constant"

expressed as $\kappa = P/\epsilon l$, it will be seen that $l/Kp = \epsilon\rho v^2 l^2/P$, i.e., the structural elasticity varies directly with the square of the model size for a given material when tested at the same dynamic pressure. In this case, the full scale decelerator could be one hundred times more elastic than a one-tenth scale model. But with relative elasticity, much small differences in scale can have significant effects on decelerator performance. For example, the response of a half-scale gliding parachute to control signals may be satisfactory, while that of the full scale prototype could be degraded below a safe level through the amplification of differential yawing oscillations and excessive lag between the azimuth heading of the parachute and of the suspended vehicle during turning maneuvers.

Scaling Laws for Other Planets

The significant physical factors relevant to decelerator operation on other planets are surface gravity (g_p/g_E) and atmospheric density (ρ_{op}/ρ_{oE}) along with the density altitude profile. These ratios enter the design of model tests to be performed on Earth through relationships such as:

Weight:	$W_P/W_E = g_P/g_E$
Froude number:	$Fr_P/Fr_E = \frac{1}{(g_P/g_E)^{1/2}}$
Mass Ratio:	$R_{mP}/R_{mE} = \rho_P/\rho_E$
Dynamic pressure:	$q_P/q_E = \rho_P/\rho_E$

Where the subscripts P and E represent "planet" and "Earth" respectively.

Heinrich[508], dealing specifically with the design of parachute model tests to be performed on Earth in which the dynamic stability during steady descent in the MARS environment would be correctly simulated derives scaling ratios using $g_m/g_E = 0.38$, e.g., it is shown that the model parachute diameter should be $D_E = D_m/.38$.

Barton[502] defined scaling laws for constructing models, for conducting tests with models, and for predicting full-scale system characteristics from the measured flight characteristics of models. For a specific planetary decelerator system these are identical to the scaling ratios listed above when the initial conditions $(r/r_o, v/v_o, \theta)$ are the same and the Froude number and mass ratio are calculated for the planetary conditions as shown.

PREDICTION OF SYSTEM MOTION

The elements of relative motion in an operating recovery system are at their maxima in the deployment and inflation process of aerodynamic decelerators. The expressions for estimating such motions with their related parameters are presented in the following paragraphs for typical methods of deployment and inflation.

System Motion During Decelerator Deployment

For a brief period during decelerator deployment, before the rigging joining the canopy to the body comes taut, the canopy and the body follow nearly independent flight paths. When wake effects are taken into account, the only remaining perturbing forces are the small ones involved in extracting the packed decelerator from its container. In this context the term "canopy" includes deployment bag and pilot-chute when present and the deploying assembly may be referred to as the "pack".

During this interval the effective drag area of the canopy depends on the method of deployment and may be evaluated in one of several ways:

The packed deployment bag alone can be treated as a bluff body, with or without pilot chute.

The pilot-chute or drogue-pilot drag area usually is the major source of drag whether the canopy is stretched out or stowed in a deployment bag.

Apex-first deployment of an uncontrolled canopy has unpredictable drag characteristics and should be avoided.

For a preliminary solution, a trajectory is needed. Point-mass two-degrees-of-freedom (DOF) digital computer programs are in common use for simple ballistic trajectory computations. Reference 513 affords a more rigorous method with a mathematical model of a six DOF body and five DOF decelerator elastically coupled incorporated in the digital computer program.

Minimum Ejection Velocity Required. When decelerator deployment is effected by ejection alone, unassisted by either pilot-chute or extraction rocket, a specific minimum ejection velocity is required under any given set of conditions to ensure complete canopy-stretch and clean separation of the deployment bag. Sometimes the mass of the deployment bag is augmented with mass of the sabot, or added ballast, to improve the separation process. The ejection velocity is critical for rearward ejection and deployment of a decelerator from a high-drag, low-mass vehicle which is decelerating rapidly. That is, the ejection takes place in an inertial field that may be several times stronger than gravitation.

A deployment bag designed for mortar ejection needs no canopy or suspension line restraints, only partitioning flaps. After the mouth closure flaps have

been unlocked, the bag offers very little internal resistance to extraction of the decelerator as it moves rearward under the impetus of its own decaying momentum, assisted by aerodynamic drag. For preliminary design purposes, with the assumption that the bag drag is at least equal to the internal resistance and m_c/m_b is small, the required ejection velocity can be estimated as

$$\Delta v = (2\, a\, l_d)^{1/2} \qquad 7\text{-}1$$

where the body deceleration,

$$a = g[q(C_D A)_b/W_b + \sin\theta\ ] \qquad 7\text{-}2$$

l_d is the stretched-out length of the decelerator (risers, lines and canopy) and $(C_D A)_b$ is the effective drag area of the body.

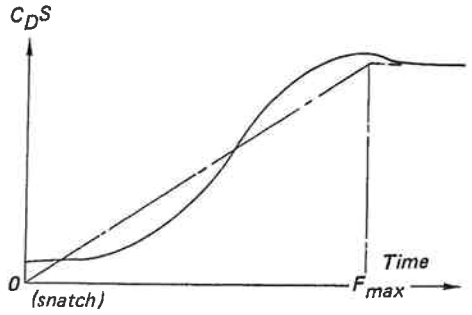
This method yields slightly conservative results, the deployment bag generally separating from the canopy with a small residual velocity. When a more precise estimate of the minimum ejection velocity is desired, the method presented in Reference 346 may be employed.

System Motion During Decelerator Inflation

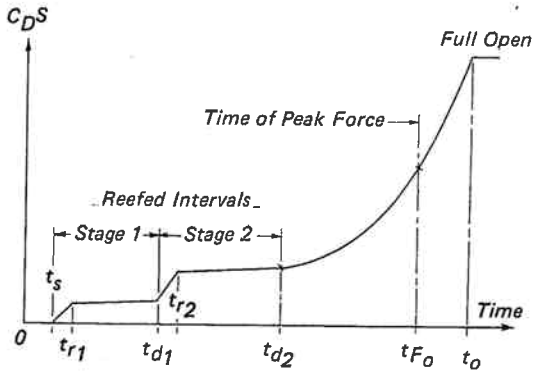
The motion of a deployable aerodynamic deceleration system with towing body during the critical operational inflation phase can be characterized generally as unsteady ballistic motion for which the trajectory lies in a vertical plane with an initial path angle θ. In gliding systems an attempt is made to neutralize the effects of lift during the deployment, inflation, and deceleration phases of the operation. Lift and out-of-plane motions become significant later, during more nearly steady-state conditions. The unsteady nature of the system motion along the ballistic trajectory is amplified by the impact loads and other force transients developed during deployment of the decelerator and during inflation. Therefore, it is best analyzed in conjunction with the decelerator inflation process and the prediction of opening loads.

However, where only preliminary trajectory calculations are desired for other purposes, approximation of the inflation process as a simplified drag transient yields satisfactory results. As a minimum, simple drag area step functions with zero filling time are assumed.

Drag Area Growth With Time. The drag-area input to the system equations of motion in its most general form includes that of vehicle and drogue as a function of Mach number, step-functions representing the drogue stages, and appropriate functions defining the growth of drag area with time for the inflation process of each decelerator. For the infinite mass condition approached during the opening of most drogues and reefed parachutes, canopy drag area growth, although non-linear, can usually be closely approximated as linear with time between snatch and peak opening forces (Fig. 7.1). For prediction of opening forces, rigorous methods require non-linear drag-area growth functions for both non-reefed canopies and for the inflation process of a reefed canopy following disreefing. For trajectory calculations alone, the details of the filling processes can be ignored or greatly simplified relative to the generalized drag-area growth history illustrated schematically in Fig. 7.1b.



a) Typical of Drogues and Reefed Parachutes



b) Generalized (Showing Reefed Stages)

Figure 7.1 Drag Area Growth History of Inflating Decelerators

Estimation of Filling Times. Empirical data and filling time formulae (pages 250 to 252) provide a convenient means of estimating decelerator filling times for system trajectory computations. Relative filling distance, K_s, as listed in Table 6.1 for a variety of parachutes are useful particularly for near-infinite mass systems. In this case $v = v_s$, and from equation 6.8

$$t_f = K_s D_o / v_s \qquad 7\text{-}3$$

Similarly, the filling time of a non-reefed parachute may be estimated using assumed or empirically estab-

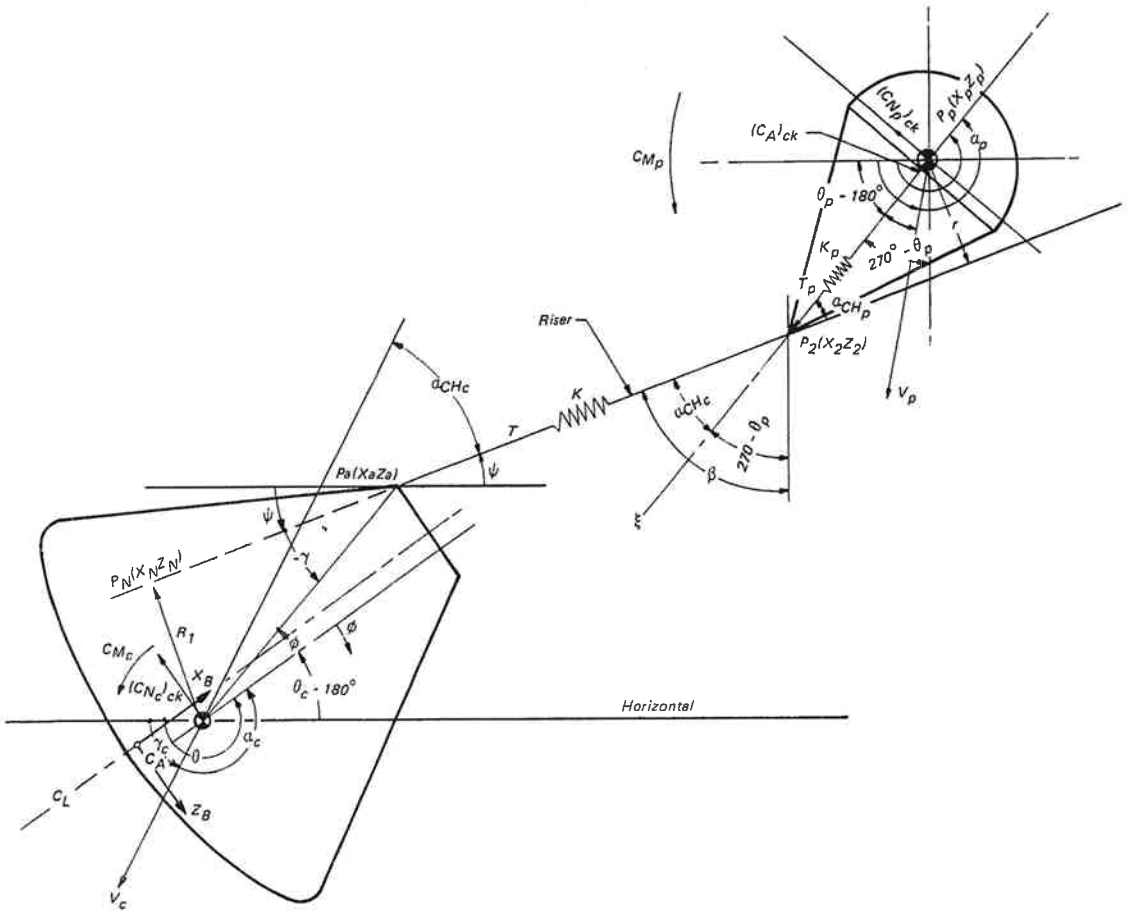


Figure 7.2 Schematic Geometry of Vehicle and Parachute

lished (see Figure 6.15) values for K_{s_o}.

For the types of parachutes listed in Fig. 6.17, and probably for any of similar design, the ratio t_f/D_o may be read directly from the curves at the appropriate values of v_s and λ_g.

Dynamic Interaction of Body and Decelerator

Some decelerator systems, such as that of Apollo, have eccentric riser attachments to a body of large moment of inertia and/or may be deployed while the body is in a deflected attitude (pitch or yaw) relative to the flight path. The typical result of deployment and inflation forces under such circumstances is the induction of pitching oscillations which in extreme cases are of such large amplitude that partial wrap-up of the riser on the body occurs. This type of body-decelerator interaction has been modeled mathematically and programmed for solution with digital computer[51.4] The program treats two point-masses, body and decelerator, with three degrees of freedom in the *x-z* plane (Fig. 7.2).

Applied to a body-decelerator system, the analysis enables determination of the magnitude of drogue riser forces and riser wrap-up on the body, if any; body, drogue, and main parachute dynamic history; and body stability with and without the decelerator. Input parameters are the following.

- Body mass, moment of inertia, and both static and dynamic aerodynamic characteristics.
- Elasticity of decelerator risers and lines.
- Canopy and added air masses.
- Decelerator static and dynamic characteristics.
- Variable location of harness attach points
- Number of harness attach points on body (2 or more)
- Offset of body c.g. from centerline.
- Decelerator opening aerodynamic behavior.
- Initial conditions: velocity, altitude, atti-

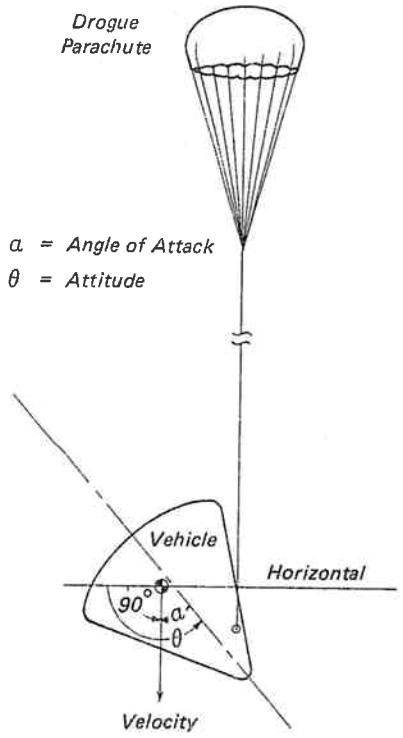


Figure 7.3 Vehicle Orientation at Drogue Parachute Line Stretch

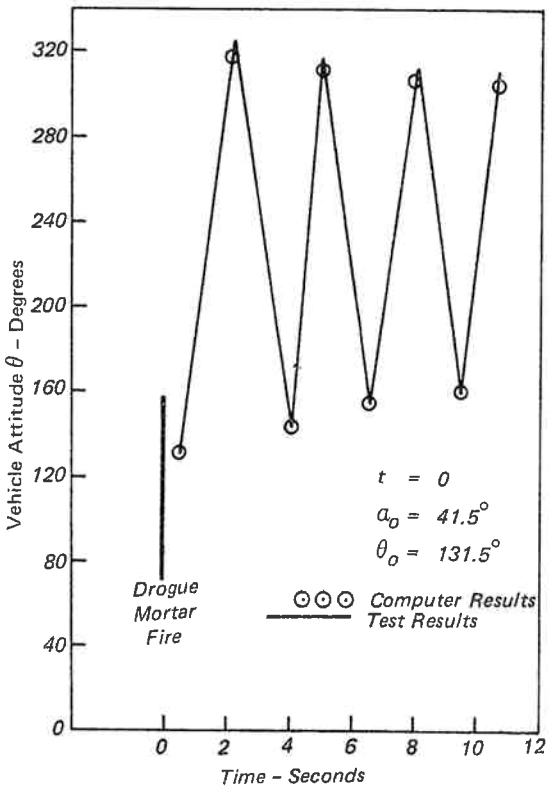
tude, and angular velocity.

Because the numbers of variables and coefficients are large and the equations of motion complex they are not reproduced here. The engineer with a specialized problem of this nature is referred to Ref. 514 or to Ref. 513. The results of a typical analysis of the system, shown schematically in Figures 7.2 and 7.3, are presented in Figure 7.4 to illustrate the type of problem that can be handled by the program and the nature of the solution.

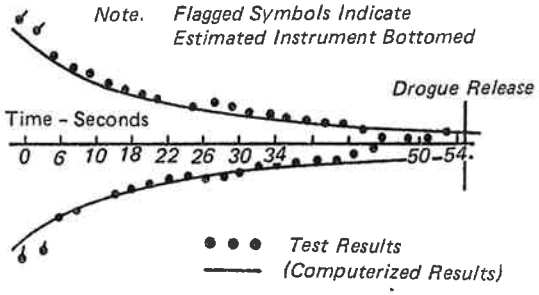
PREDICTION OF DEPLOYMENT IMPACT LOADS

The nature and causes of deployment impact loads are described starting on page 236. Simplified empirical formulae are presented to illustrate the relationship between pertinent system or decelerator parameters and the resultant snatch forces. The impact load is shown to be a function of the differential velocity at line stretch, the mass of the parachute, and the effective spring constant of the suspension lines.

Derivation of Simplified Snatch Force Equation. The simplified equation given on page 237 to illustrate the major factors related to the snatch force was derived with the assumption that the mass of the parachute was small relative to the mass of the body. This is not always the case, e.g., for decelerator extraction by pilot chute or drogue in which the decelerator pack plays the role of the body. In the more general case, the following considerations are pertinent to determination of the impact load (see Figure 7.5). With the assumption that the drag of the packed canopy is negligibly small, the velocity of the system after the snatch force has reaccelerated the canopy to the velocity of the body is

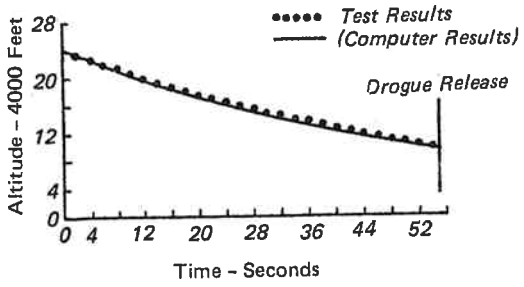


a) θ Vs Time, Computer and Drop Test Results (Single Drogue)

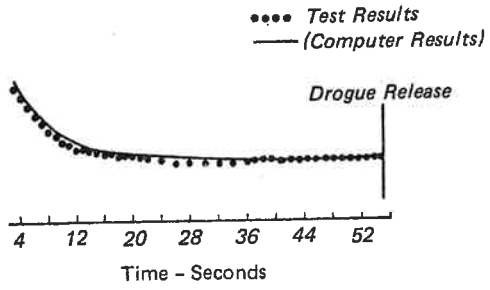


b) Vehicle Maximum θ Vs Time, Computer and Test Results (Twin Drogue)

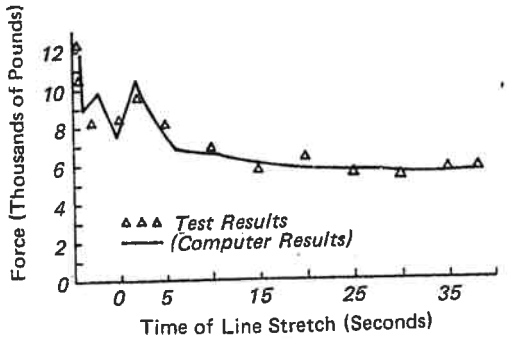
Figure 7.4 Results of Dynamic Interaction Analysis



c) Vehicle Altitude Vs Time. Computer and Test Results. (Twin Drogue)



d) Vehicle Dynamic Pressure Vs Time. Computer and Test Results (Twin Drogue)



e) Drogue Riser Vs Time, Computer and Test Results

Figure 7.4 Concluded

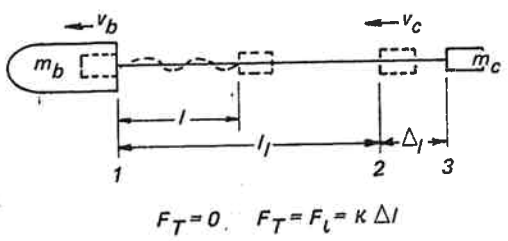


Figure 7.5 System Geometry During Deployment

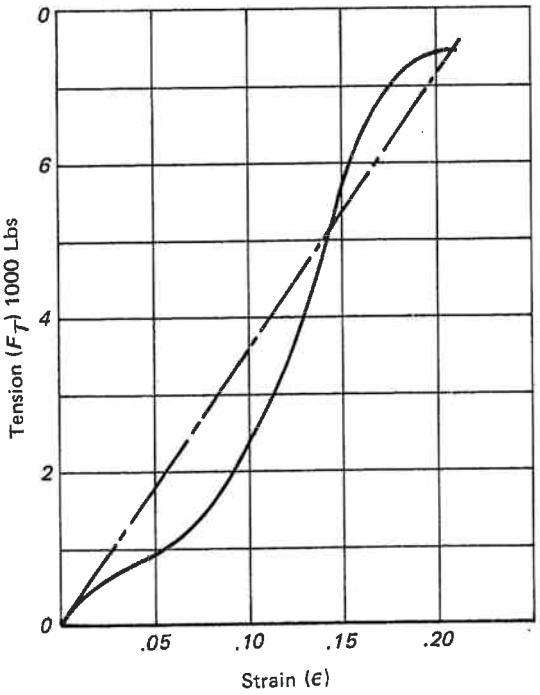


Figure 7.6 Average Static Load - Strain Characteristic of 1" Nylon Webbing

$$v'_b = \frac{m_b v_b + m_c v_c}{m_b + m_c} \qquad 7\text{-}4$$

and for conservation of energy *(KE + PE)*

$$\frac{m_b v_b^2}{2} + \frac{m_c v_c^2}{2} + o = \frac{(m_b + m_c)(v'_b)^2}{2} + \frac{\kappa \Delta l^2}{2} \qquad 7\text{-}5$$

If $v_c = v_b - \Delta v_{max}$, solution of equation 7-5, after making the appropriate substitutions, yields

$$m_b m_c \Delta v_{max}^2 = \kappa \Delta l^2 (m_b + m_c) \qquad 7\text{-}6$$

For a first approximation a linear relationship is assumed between the internal load and elongation of the connecting member. Thus, by Hooke's law $F_l = \kappa \Delta l$ with the substitution of $\Delta l = F_l / \kappa$ in equation 7-6

$$\Delta v_{max}^2 = \frac{F_l^2 (m_b + m_c)}{\kappa m_b m_c}$$

and solving for the impact load

$$F_l = \Delta v_{max} \left(\frac{\kappa m_b m_c}{m_b + m_c} \right)^{1/2} \qquad 7\text{-}7$$

When m_c/m_b is small, this equation reduces to Equation 6-2. Δv_{max} may be estimated with reasonable accuracy by the short method given on page 240

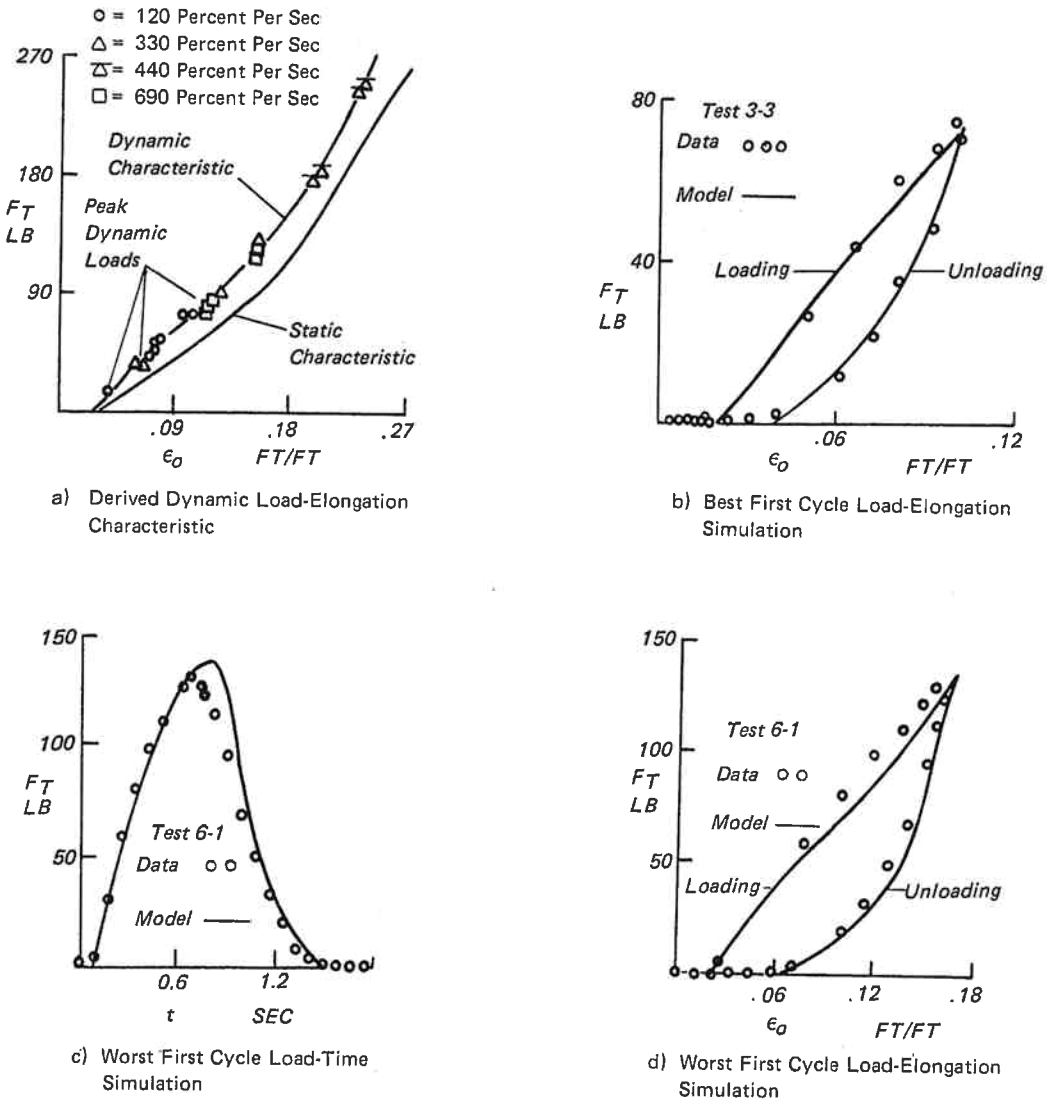


Figure 7.7 Measured Vs Simulated Dynamic Stress - Strain Characteristics of 400 lb Nylon Suspension Line Cord (Ref.329).

Effective Spring Constant

As noted on page 240, any evaluation of κ based on the static load-strain curve for the material is automatically unconservative, because the slope of the dynamic characteristic $dF_T/d\epsilon$ is steeper. Along with this, the common practice of defining an "ultimate" spring constant as

$$\kappa_{ult} = P_{ult}/\epsilon_{ult}l_l \qquad 7\text{-}8$$

yields a mean value greater than for the design-limit load range (Fig. 7.6) where $F_T/P_{ult} = 0.4$ to 0.6. Therefore, in order to use equations 6-1 and 6-2 for the prediction of deployment impact loads with reasonable assurance of success, laboratory tests should be performed to establish practical values of the average effective spring constant when dynamic loading and hysteresis data of the types illustrated in Figure 7.7 are not available. The dynamic stress-strain characteristics of nylon parachute textiles were investigated by Melzig[567], Groom[330] and McCarty[329].

McCarty[329] developed a computer sub-routine for the load-elongation characteristics of nylon parachute suspension lines. The results illustrated in Fig. 7.7 indicate the potential increase in analytical rigor that may be realized in decelerator opening load prediction and stress analysis methods through its adaptation to digital computer programs such as those cited

later in Spring-Mass-Momentum parachute inflation analytical method and the slotted parachute internal loads analysis method. Both static and dynamic characteristics of the 400 lb cord (MIL-C-5040E, Type II) used on the 35 ft (D_o) T-10 parachute were modeled.

Calculation of Δv_{max}.

At time zero, body and canopy moving together share the initial conditions v_o, h_o and θ_o. After an interval Δt_l they have separated by a distance l_l equal to the unstretched length of lines and risers, and in a rectangular coordinate system, with origin fixed relative to the Earth at t_o,

$$l = \left[(x_b - x_c)^2 + (z_b - z_c)^2\right]^{1/2} \qquad 7\text{-}9$$

where subscripts b and c refer to the centers of gravity of body and canopy respectively. In Figure 7.5 when $l = l_l$

$$\Delta v_{max} = \dot{l} = [(x_b - x_c)(\dot{x}_b - \dot{x}_c) + (z_b - z_c)(\dot{z}_b - \dot{z}_c)] \; // \qquad 7\text{-}10$$

where the horizontal and vertical velocity components of both body and canopy are derived from trajectory calculations for each

$$\dot{x} = v \cos\theta \qquad 7\text{-}11a$$

$$\dot{z} = v \sin\theta \qquad 7\text{-}11b$$

The following equations of motion may be employed

$$m\dot{v} = mg \sin\theta - \rho v^2/2 (C_D S) \qquad 7\text{-}12a$$

$$m\dot{\theta} = mg \cos\theta \qquad 7\text{-}12b$$

where m and $C_D S$ are appropriate values of the masses and effective drag areas respectively of body and canopy to make up two independent sets for solution over the interval Δt_l. As a minimum, a two-DOF computer program for the trajectories of two point-masses provides a satisfactory solution. The short method given in Chapter 6 also yields useful results.

Effect of Distributed Decelerator Mass

While the differential velocity at snatch can be determined from trajectory computations with satisfactory accuracy, the assumption of a concentrated mass results in excessively high predicted impact loads (even when the average effective spring constant is underestimated). Because the deployment sequence is completed in a short space-time interval, the change in air density is usually inconsequential and the trajectory of the deployment bag seldom deviates significantly from that of the towing body. These factors are sufficiently small in most cases to be negligible. However, the variation of the component masses during the stretching-out process as the deployment bag is being stripped off suspension lines and canopy has a significant effect on the predicted forces.

Good results were obtained by McVey and Wolf[348] using the following method of snatch force calculation for lines-first deployment of a parachute by pilot chute. When the sequence starts, the pilot chute is already fully inflated as shown in Figure 7.8.

For the case of a ***control volume,*** with one-dimensional motion losing or gaining mass, the momentum equation may be written

$$\Sigma F = d(Mv)/dt \pm \rho_l v_a v_r \qquad 7\text{-}13a$$

$$\Sigma F = M\, dv/dt + dM(v \pm v_a)/dt \qquad 7\text{-}13b$$

where (+) is for the system gaining mass, (–) is for the system losing mass, and

Mv = system momentum

v_a = absolute velocity of mass added or removed

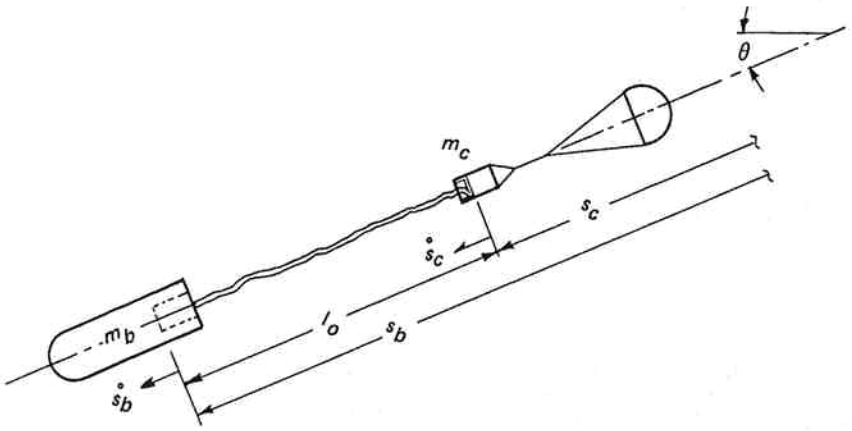


Figure 7.8 System Configuration During Deployment

v_r = velocity of mass added or removed relative to control volume

ρ_l = lineal mass density of line bundle

The incremental masses of lines and canopy leaving the deployment bag become part of the body mass. With reference to Fig. 7.8, the respective masses of body and bag are

$$M_b = m_b + \rho_l l_o \qquad \dot{M}_b = \rho_l \dot{l}_o$$
$$M_c = M_c - \rho_l l_o \qquad \dot{M}_c = \rho_l \dot{l}_o \qquad 7\text{-}14$$

Then equation 7-13a may be written

$$\Sigma F_b = M_b \ddot{s}_b \qquad 7\text{-}15$$

$$\Sigma F_c = M_c \ddot{s}_c + \rho_l \dot{l}_o (\dot{s}_b - \dot{s}_c) \qquad 7\text{-}16$$

Note that the elements of line mass are moving at a velocity $\dot{s}_b$ when they join the body mass.

From equations 7-15 and 7-16, with the substitution of external forces due to gravity, drag, line tension, and using the appropriate mass and mass flux equations, the following relationships are obtained.

$$(m_b + \rho_l l_o)\, \ddot{s}_b = (m_b + \rho_l l_o)\, g \sin\theta - (C_D A \rho \dot{s}_b^2/2) - F_T \qquad 7\text{-}17$$

$$(m_c - \rho_l l_o)\, \ddot{s}_c = (m_c - \rho_l l_o) g \sin\theta - (C_D S \rho \dot{s}_c^2/2) + F_T - \rho_l \dot{l}_o (\dot{s}_b - \dot{s}_c) \qquad 7\text{-}18$$

where $F_T = Z[P(\epsilon)]$

and $P(\epsilon)$ is obtained from the load-strain diagram for the suspension line material where the strain in the lines is

$$\epsilon = [(s_b - s_c)/l_o] - 1 \qquad 7\text{-}19$$

The velocity of the suspension line bundle issuing from the deployment bag is

$$\dot{l}_o = (F_T - F_l)/\rho_l (\dot{s}_b - \dot{s}_c) \qquad 7\text{-}20$$

where F_l is the average force required to extract the lines against the resistance of friction and the incremental retaining ties, i.e.,

$$F_l = \Sigma F \Delta t / t_x \qquad 7\text{-}21$$

where t_x is the time required to extract the complete line bundle from the deployment bag.

The foregoing equations, starting with a point-mass ballistic trajectory equation to include the flight path angle θ, may be solved with a digital computer. Along with the initial trajectory conditions, input data include:

a) The load-strain curve of suspension line material

b) The linear mass distribution of the stretched-out parachute

c) Pilot parachute mass and $C_D S$

d) Body and vehicle mass and $C_D A$

It is significant that trial calculations made with a constant canopy mass during the canopy stretchout interval, in place of input (b), yielded snatch forces 2 to 2.5 times greater than measured. Computed times to the peak snatch force also were several times greater than observed. Therefore, it may be concluded that the distributed mass assumption is appropriate, provided the details of the lineal mass distribution can be correctly depicted. As shown in Fig. 6.6, the way in which canopy mass is concentrated at the skirt has a significant effect on the predicted peak load. Likely the results obtained with the gross average mass distributions would be improved by using dynamic rather than static load-strain curves for the suspension line materials, because the former would cause the snatch acceleration to rise more rapidly and to a higher peak. Moreover, the effect of hysteresis would be to cause a rapid decline after the peak load event.

PREDICTION OF OPENING LOADS

Methods of predicting decelerator opening loads are progressively being developed to higher degrees of sophistication with large capacity digital computers. Most desirable are those methods for which the empirical coefficients required can be derived from the results of a few economical tests. Ideally, such tests would be performed with small models in a laboratory or wind tunnel, but these data have been subject to scaling inaccuracies. Next best data sources are the existing records of adequately instrumented full scale aerial drop tests from which dimensionless coefficients of useful generality may be derived by reanalysis. Desired basics such as pressure distributions and added air mass coefficients can be deduced by iteration of complex programs until predicted and measured results are in good agreement. This approach has produced several load prediction methods of good potential utility (References 361,348,373, 515 — 517). Each load prediction method embodies a different mathematical model of the canopy inflation process and requires empirical coefficients for their solution. The canopy mass-momentum method[373], for example, computes the force transient during inflation process directly with the input of measured average characteristics such as the initial air inlet radius, a radial drag coefficient and a radial added air mass coefficient, along with appropriate mass ratios. Because of its basic simplicity, the load factor method continues in use as a means of estimating approximate values of peak opening loads.

Load Factor Method

The load factor method of opening load prediction described in Chapter 6 frequently can be used in its simplest form to obtain quick preliminary estimates of decelerator design loads. A problem exists in determining which set of empirical data best fits the conditions surrounding the decelerator system being investigated in order to obtain an appropriate opening load factor (C_X).

General trends of C_X as a function of mass ratio, R_m, are indicated by the faired curves of Fig. 6.25 for a number of different types of parachutes both reefed and non-reefed. The trend for lightly loaded parachutes, i.e., with large mass ratios, indicates that the opening load factor can become very small for some systems. Data scatter makes the precise shape of the curves uncertain and obscures any correlation with parachute design differences that might exist. Only the pronounced change in opening behavior of reefed parachutes after disreefing is sharply delineated. On the other hand, at very small values of R_m the test conditions from which C_X data were derived approached the infinite mass case because deceleration during canopy inflation was slight.

Clustered Parachutes. In the calculation of the opening loads of clustered parachutes, synchronous inflation with peak loads the same for each member is a special case which provides a base reference for estimating probable maximum lead-parachute opening loads to be used as design limits. Two approaches are provided by available empirical data:

1. Apportionment of the total cluster load among the member parachutes in accordance with max/mean force ratios derived from Table 6.2.
2. Calculation of individual lead-parachute loads on the basis of mass ratios derived from probable mass fractions carried by lead-or-lag parachutes.

The first approach is described below; the second in Reference 217.

The Non-Synchronous Opening Load Factor. For the synchronous case, the total cluster force transmitted to the body through the main riser is

$$F_C = n_C F \cos \bar{\phi}_C \qquad 7\text{-}22$$

where $\bar{\phi}$ is the mean angle of the parachute risers from the cluster axis. F_C reaches a maximum value at the same time the force of each member parachute peaks at

$$F'_X = C_D S\, q\, C_X \qquad 7\text{-}23$$

For the non-synchronous case the opening force of the leading canopy can be written simply as

$$F_X = F'_X C_Y \qquad 7\text{-}24$$

where C_Y is an empirical load factor evaluated directly from the measured max/mean force ratios given in Table 6.2. Because the non-synchronous cluster deceleration impulse covers a longer time interval than the synchronous impulse the average force will be somewhat less for the same initial conditions. Thus, the evaluation of C_Y as follows for the average peak load, $\bar{F}_X$, of all the members of the cluster, is somewhat conservative

$$C_Y = F_X / \bar{F}_X \qquad 7\text{-}25$$

Experience recorded in Table 6.2 indicates that when the limit opening load is calculated with equation 7-24, appropriate values of C_Y for preliminary design of cluster parachutes are as follows:

n_C	C_Y
2	1.45
3	1.80
4 or more	2.0

Although somewhat higher non-synchronous opening forces may be possible they appear to be of sufficiently low probability to be covered by the design safety factor.

Mass-Time Method

A point-mass two-degrees-of-freedom digital computer program has been developed around equations of system motion in the following form[361]

$$\dot{x} = v \cos\theta \qquad (7\text{-}11a)$$

$$\dot{z} = v \sin\theta \qquad (7\text{-}11b)$$

$$\dot{v} = -(F_p + D_b + W_b \sin\theta)/m_b \qquad 7\text{-}26a$$

$$\dot{\theta} = -(g \cos\theta)/v \qquad 7\text{-}26b$$

where F_p is the tangential force of the decelerator with the effects of added air mass included:

$$F_p = C_D S\, q + v\dot{m}_a + (m_a + m_p)\,\dot{v} + W_p \sin\theta \qquad 7\text{-}27$$

and the effective drag area and added air mass of the inflating canopy are expressed as functions of time in the following way.

$$C_D S = (C_D S)_1 + [(C_D S)_2 - (C_D S)_1]\,[(t-t_1)/(t_2-t_1)]^n \qquad 7\text{-}28$$

$$m_a = K_a \rho\, (C_D S)^{3/2} \qquad 7\text{-}29$$

$$\dot{m}_a = (3/2)K_a\rho(C_DS)^{1/2}(C_D\dot{S}) \qquad 7\text{-}30$$

$$(C_D\dot{S}) = n[[(C_DS)_2-(C_DS)_1]/(t_2-t_1)] \qquad 7\text{-}31$$
$$[(t-t_1)/(t_2-t_1)]^{n-1}$$

where the variation of air density with altitude is included in the program and t_2-t_1 is the filling time while the canopy drag area grows from $(C_DS)_1$ to $(C_DS)_2$, computed as follows.

$$t_2-t_1 = K_s D_o/v_1 \qquad 7\text{-}32$$

The dimensionless filling time parameter, K_s, is obtained from empirical data such as that given in Figure 6.15 and Table 6.1. In preparing computer inputs it is convenient to diagram drag-area growth with time as in Figure 7.1. The inputs for each run comprise the following.

Initial conditions:

v_o, h_o, θ_o and t_s if different from t_o

System Characteristics:

Body - W_b, C_DA

Parachute - W_p, C_DS (each stage)

Filling time constants K_p (each stage) + exponents:

Reefed - $n = 1.0$

Disreef - $n = 2.5$ (recommended for first run)

Added mass coefficients:

Reefed - $K_a = 0$

Disreef - $K_a = 0.66$

Reefing line cutters - Δt_r (each stage)

A comparison of the computed force-time history using the Mass-time method with that obtained from one of the Apollo main parachute tests is presented in Figure 7.9). This was a "curve-fitting" run using measured filling and reefed intervals to verify the average reefed drag areas and the added mass coefficient derived from previous data-reduction runs for all of the tests with the same program. The following inputs were used in this example.

Initial Conditions: (Apollo Test 80-1R)[217]

v_o = 335 fps

h_o = 15,000 ft

θ_o = 5°

t_s = 2.28 sec

System Characteristics:

Body: W_b = 5160 lbs C_DA = 2.0 ft² (Cylindrical T.V.)

Parachute: W_p = 119 lbs (one 85.6 ft (D_o) Modified Ringsail)

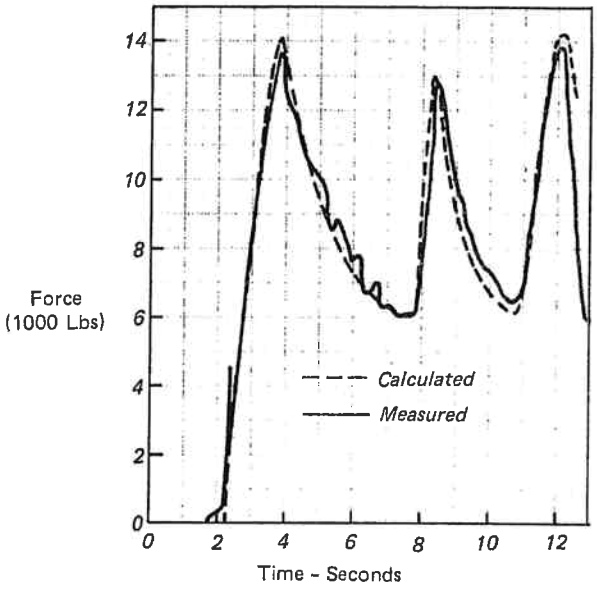


Figure 7.9 Mass Time Method; Calculated vs Measured Opening Loads

Area Stages	C_DS - ft² (at t_f)	(at disreef)	t_f-sec	Exp. n
Reef (1)	228	300	1.44	1.0
Reef (2)	860	900	0.57	1.0
Full Open	4300	—	1.79	3.11

Added air mass coefficients:

Reefed — $K_a = 0$

Disreef — $K_a = 0.66$

Reefed Intervals:

Stage	Δt-sec
Reef (1)	5.3
Reef (2)	2.8

Apparent Air Mass

The utilization of the apparent air mass terms for prediction of parachute opening loads with the various mathematical models of the inflation process presented in this section justifies consideration of the theoretical and experimental background established by classical aerodynamics.

Analysis of the resistance of bodies to accelerated motion in potential flow as found in classical hydrodynamic literature utilizes the concept of "Apparent

Mass". Simply stated, "the acceleration (motion) of a body mass, m, in an ideal fluid is equivalent to that of a body of mass, $m + m'$, in a vacuum, both being acted upon by the same force, F". The resistance to motion represented by the m' term accounts for the additional energy required in overcoming the inertia of the surrounding fluid. The resistance disappears under steady flow conditions. The mass, m', has been given the designation, "apparent mass" (also has at times been called virtual or added mass).

The values for the apparent mass term are well defined in literature for simple, solid bodies (spheres, disks) accelerating in an ideal fluid. The value for a sphere is 0.50, the fluid mass displaced by the sphere while that for a disk is 0.637 times the fluid mass displaced by a sphere of radius equal to the disk radius. In equation form

$$m'_{sphere} = K(\rho)\ (4/3\pi r^3) \doteq 0.50(\rho)\ (4/3\pi r^3)$$

$$m'_{disk} = K(\rho)\ (4/3\pi r^3) = .637(\rho)\ (4/3\pi r^3)$$

The preceding discussion has dealt with the classical development of the "apparent mass" concept as it applies to the analysis of non-steady motion in an ideal fluid.

In analyzing the test data acquired on spheres accelerating in a real fluid Bugliarello[518] investigated the following equation of motion

$$F = ma + R_u + R_a \qquad 7\text{-}33$$

where

- m = mass of body (sphere)
- a = acceleration of body
- F = force acting on body
- R_u = resistance to steady motion (skin fraction and profile drag)
- R_a = additional resistance to accelerated motion due to inertia of fluid

The resistance to steady motion, R_u, is usually expressed in the form

$$R_u = C_D\ 1/2\ \rho v^2 S \qquad 7\text{-}34$$

The additional resistance to accelerated motion, R_a, is often expressed as an "apparent mass" effect by writing

$$R_a = m'a \qquad 7\text{-}35$$

where $m' = K\rho V$

and K = apparent mass coefficient

ρ = fluid density

V = volume of fluid displaced by body;

Rewriting Eq. 7-33 to substitute Eqs. 7-34 and 7-35 provides

$$F = ma + C_D\ 1/2\ \rho v^2 S + K\ \rho\ V\ a \qquad 7\text{-}36$$

solving for K,

$$K = \frac{F - ma - C_D\ 1/2\ \rho v^2 S}{\rho\ V\ a} \qquad 7\text{-}37$$

As previously noted, ideal fluid values for K for a sphere and disk are 0.50 and 0.637 respectively. Bugliarello obtained experimental values for K in a real fluid of from less than zero to over 500. A similar scatter of K values for spheres and disks accelerating and decelerating in a real fluid have been obtained (Refs. **519** and **520**). From evaluation of his experimental data, Bugliarello concludes that "evaluation of the resistance to non-steady motion in a real fluid as consisting of the sum of two separate terms, one representing the resistance to steady motion and the other resistance to fluid inertia, is questionable". He goes on to postulate that, "the body experiences only one resistance in which the effects of friction, turbulence, and fluid inertia are commixed and interacting". He therefore incorporated the investigation of the following equation of motion into his analysis of test data,

$$F = ma + \text{Total Resistance} \qquad 7\text{-}38$$

Bugliarello as well as other investigators (e.g., Ref. **519**) expressed this total resistance as

$$\text{Total Resistance} = C\ 1/2\ \rho v^2 S \qquad 7\text{-}39$$

Equation 7-39 is the same form of the resistance (drag) in steady motion except the coefficient, C, differs from the steady state drag coefficient, C_D, due to its dependence on some characteristics of the non-steady state of motion. Substituting Eq. 7-39 in Eq 7-38 and solving for C,

$$C = \frac{F - ma}{1/2\ \rho v^2 S} \qquad 7\text{-}40$$

Dimensional analysis (Ref **519**) indicated the resistance coefficient, C, to be a function of a parameter, aD/v^2, where D is a characteristic length of the body. Bugliarello obtained the best correlation of his sphere experimental data by plotting C versus this parameter. These plots indicated that at high values of aD/v^2 the value for C (for a constant Reynold's number) approaches the theoretical value from potential flow analysis while at low values of aD/v^2 the value for C approaches the drag coefficient in uniform motion. Figure 7.10 depicts this trend.

The application of the apparent mass concept in the analysis of parachute opening dynamics originated with Scheubel[380] and Von Karman[521]. Since then numerous investigators have incorporated this parameter into parachute equations of motion both tangent and normal to the flight path. Inherent with flow fields surrounding parachutes are real fluid (viscous) effects such as boundary layers, flow separa-

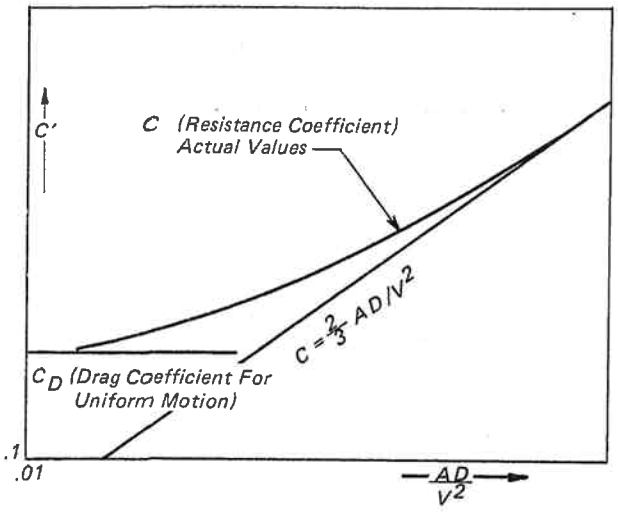


Figure 7.10 Resistance Coefficient vs Dimensionless Acceleration Parameter AD/V^2

tion and wakes. Application of the apparent mass concept where real fluid effects exist is not consistent with the constraints inherent in its development; i.e., restricted to ideal fluid flow, as noted by Mickey[501]. Mickey states that "it is only within the restriction of a simplified fluid model (incompressible, acyclic potential flow) that the concept of added (apparent) mass has a precise meaning". Ibrahim[522 523] explicitly stated that his investigation of apparent mass and apparent moment inertia of cup-shaped bodies did not include any consideration of viscous effects.

The Added Air Mass of a Parachute

Ibrahim's work[522] justified the conclusion that the included and apparent air masses could be lumped and treated as a single added mass.

$$m_a = m' + m_i \qquad 7\text{-}41$$

However, it is well not to lose sight of the difference in functional character of the two components. The included air mass is present during steady state operations. The inertial effect of the apparent mass enters the picture only during unsteady conditions. During canopy inflation the apparent mass component increases to a maximum value proportional to the total kinetic energy imparted to the air and then disappears as soon as the system has reached a steady state. The included mass, on the other hand, grows with the canopy volume to a maximum and then, after a transient rebound, levels off at a constant equilibrium volume to vary only with subsequent changes in air density, e.g., due to descent.

Ibrahim[522] defining a non-dimensional added mass coefficient, $B = 4/3\pi K$, determined values of this coefficient for impervious spherical cups resembling inflated parachute canopies, as well as for solid and hollow spheres.

TABLE 7.1 ADDED AIR MASS COEFFICIENT OF HOLLOW SHELLS

Shape	$B = 4/3\pi K$
Solid Sphere	2.094
Hemispherical Cup	4.475
Deep Spherical Cup (210")	5.591
Hollow Sphere with pinhole	2π

The included air mass of the hollow shape is accounted for here along with the apparent mass so that

$$B = m_a/\rho r^3 \qquad 7\text{-}42$$

Since B is a shape factor essentially invarient with density, by substitution of $D_p/2$ for r and V_a for m_a/ρ, Equation 7-42 may be adapted for the description of parachute added mass independent of altitude as,

$$B = 8\,V_a/D_p^3 \qquad 7\text{-}43$$

where V_a is the volume of the added air mass. It is pertinent to note that the fraction associated with m' was provided by Darwin in 1953 to equal the "drift" volume of the fluid particles disturbed by the accelerating body (as reported in Reference 522.

The added mass defined by Equation 7-41 was employed in an analysis of parachute opening characteristics by Mickey, McEwan and Ewing[361]. Taking the easily computed effective drag area of an inflating canopy, C_DS, rather than D_p, Ewing defined and evaluated an empirical added mass coefficient $K_a = m_a/\rho(C_DS)^{3/2}$ which when reduced to the same form as Equation 7.42 becomes

$$K_a = V_a/(C_DS)^{3/2} \qquad 7\text{-}44$$

where C_DS is the effective drag area at any given stage in the filling process. With C_{Dp} variable, the assumption that K_a is constant shape factor for the canopy throughout the inflation process was justified as follows:

a. The quasi-dimension, $(C_DS)^{1/2}$ is more directly related to the aerodynamic events engendering m_a than is D_p, because it embodies the many other physical parameters represented by the drag coefficient including canopy porosity.

b. The several features of the airflow into and around the inflating canopy of a decelerating system maintain a constant relationship.

The conical portion of the canopy functions as an air duct[361,524,525] with small momentum losses feeding the pressurized crown area containing a partially stagnant mass of air. Although the canopy itself grows shorter and fatter, both r and C_{Dp} increasing, the total flow field simply expands in volume without a significant change in shape.

The thrust of these observations appears to be substantiated by experiment. A computer study of the opening characteristics of the Apollo main parachutes showed that the force-time histories during the opening transient could be predicted with good accuracy for all six of the different single parachute tests evaluated with $K_a = 0.66$ constant (see Figure 7.9). For the fully inflated parachute (with a nominal total porosity of $\lambda_T = 12.7$ *percent*), $(C_D S)_o = 4300\ ft^2$, indicating a maximum volume for the added air mass by Equation 7-44,

$$V_a = K_a (C_D S)_o^{3/2} = 186{,}500\ ft^3$$

This is the volume of a sphere 70.9 feet in diameter. The nominal inflated diameter of the canopy was $D_p \approx 59$ *feet*. Substitution of these values in Equation 7-43 yields $B = 7.26$ which is larger than $B = 2\pi$ given for a hollow sphere with the enclosed air mass included, an apparently unrealistic result. But it is evident, as Ibrahim pointed out, that the effects of canopy porosity, flexibility, and turbulent boundary layer are not accounted for by potential flow theory. Moreover, the dynamic growth of the canopy, attended by elastic expansion under load, also clearly is not represented by the hollow shell model. Elsewhere it is shown that the increased projected area resulting from elastic expansion is a dominant factor even in steady descent.

The projected diameter of the expanded canopy can be estimated from the ratio of the opening load to the ultimate load. The opening loads in some tests were about 40 percent of the ultimate for which the corresponding structural elongation was in the order of 10 percent. The indicated projected diameter is $D_{p_o} = 59(1.1) \approx 65$ *feet*. Under somewhat heavier loading conditions, as reported in Ref. 221, $D_{p_o} \approx 68$ *feet* was measured. Substitution of these values in Equation 7-31 yields

$$B = 4.75 \text{ to } 5.43$$

which values are representative of shapes comparable to a spherical cup somewhat deeper than a hemisphere (Table 7.1), justifying the oblate spheroid used in some parachute inflation analysis.

Apparent Moment of Inertia

In decelerators of all types both turning rates and stabilizing moments are affected to a degree by the inertial resistance of the system mass to angular acceleration part of which consists of the *apparent* moment of inertia of the added air mass associated with the inflated canopy. The concept of the apparent moment of inertia is clarified by Ibrahim[526] (referring back to the apparent air mass reasoning) with the following argument.

> "Similarly, in rotational motions the Apparent moment of inertia can be determined from energy considerations using the velocity potential of the rotational motion. The kinetic energy of rotation is given by
>
> $$E_\omega = I'\Omega^2/2$$
>
> Hence, the apparent moment of inertia per unit length of a rotating elliptic cylinder, for example, will be
>
> $$I' = 2E_\omega/\Omega^2 = \pi\rho(a^2-b^2)^2/8$$
>
> [where a and b are semi-axes of the ellipse and Ω is the angular velocity of rotation of the cylinder about its axis.] "

A dimensionless representation of the apparent moment of inertia for purposes of comparison is defined by

$$A' = I'/I_R$$

where I_R is the moment of inertia of a sphere of fluid equal in diameter to the canopy D_p, or

$$I_R = (8/15)\,\rho\pi\,(D_p/2)^5 \qquad 7\text{-}47$$

I' was evaluated experimentally by measuring the period of oscillation of small rigid models in two fluids of different densities, air and water. The results are plotted in Figure 7.11 as a function of geometric porosity.

Six-Degrees of Freedom Kinematic Model

The limitations of the mass-time method and of the dynamic interaction model are largely overcome by the six-degrees of freedom kinematic model for the study of parachute deployment and inflation dynamics developed by Talay[515,527] on the foundation laid by Gamble [528].

Because flight conditions on another planet such as Mars cannot be precisely duplicated on Earth, it is

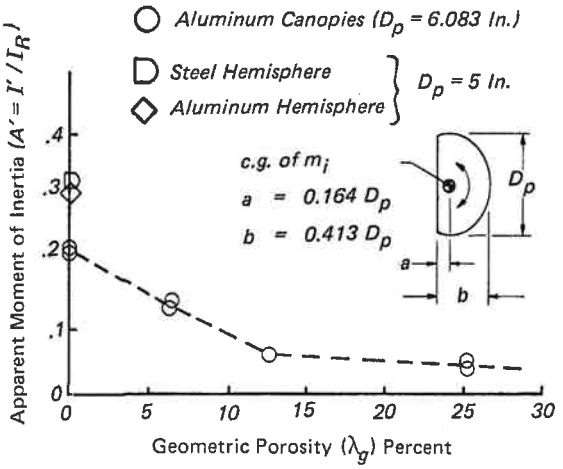


Figure 7.11 Measured Apparent Moment of Inertia ofRigid Canopy Models vs (λ_g)

desirable to be able to supplement Earth environment test results with an accurate analysis of decelerator system dynamics. The analysis can give assurance that allowable vehicle attitude and attitude rates defined by the capability of the guidance and control system will not be exceeded during the parachute deceleration phase. To accomplish this, the types and magnitudes of the input parameters required must be well defined. The following parameters were identified[515] by iterative computation to force an optimum agreement between simulation and flight test results of such quantities as vehicle velocity, dynamic pressure, Mach number, harness and line tensions, attitude and attitude rate histories.

Vehicle aerodynamic roll damping coefficient
Parachute aerodynamic pitch and yaw damping coefficients
Parachute axial force coefficient
Suspension line elasticity
Suspension line damping
Parachute angular rates at bagstrip
Suspension line permanent deformation

These inputs and the values obtained from one Viking balloon-launched test were considered valid for use as a starting base for work involving dynamic analysis of the supersonic deployment of a disk-gap-band parachute.

Talay[515] concluded, "Significant voids in the knowledge of decelerator technology, particularly with regard to parachute aerodynamic characteristics and suspension system physical properties, appear to be a major obstacle to obtaining accurate simulations and to the use of the model in a predictive mode".

Canopy Mass-Momentum Method

Inelastic Non-Reefed Model. Employing a set of momentum equations along lines suggested in Reference 501, this model of the canopy inflation process, presented by Wolf[373], starts with Thomson's fundamental equation for a system of variable mass (a form of equation 7-13)

$$m\ddot{\bar{s}} = \bar{F} + \dot{m}\,(\dot{\bar{s}}_e - \dot{\bar{s}}) \qquad 7\text{-}48$$

where $\dot{s}_e$ is the absolute velocity of mass entering the system tangent to the flight path.

Two phases of the inflation process are identified as proposed by Berndt[356]. During the initial phase, the canopy fills from the skirt until a small region near the vent is filled out.

The second phase encompasses expansion of the inflated portion to the fully inflated shape of the canopy. This analysis is concerned only with the second or final inflation phase.

However, it is necessary to take the initial phase of inflation into account through appropriate data reduction for evaluation of the empirical coefficients, e.g., r_o and s_o as defined in context to initiate the second phase.

From equation 7-48 the equations of motion of body and parachute tangent to the flight path become

$$(m_b + m_p - m_{ci})\ddot{s}_b = (m_b + m_p - m_{ci})\, g \sin\theta - F \qquad 7\text{-}49$$

$$(m_{ci} + m_s)\ddot{s}_c = m_{ci} g \sin\theta + F - C_D S q_c + \dot{m}_{ci}(\dot{s}_b - \dot{s}_c) - \dot{m}_s \dot{s}_c \qquad 7\text{-}50$$

where m_{ci} is the mass of the inflated portion of the canopy. Conservation of momentum normal to the flight path yields this expression for the rate of change of trajectory angle

$$(m_b + m_p + m_s)\dot{s}_b\dot{\theta} = (m_b + m_p)\, g \cos\theta \qquad 7\text{-}51$$

To make both body and parachute follow the same ballistic path it is assumed in equation 7-51 that the parachute tangential velocity is the same as that of the body, i.e., the parachute is flexible but not elastic.

The radial motion of the inflating canopy is described by

$$(m_{ci} + m_r)\ddot{r} = 2 C_r q_c S_c \sin\phi - F\tan\phi - (\dot{m}_{ci} + \dot{m}_r)\dot{r} \qquad 7\text{-}52$$

To provide the constant length constraint imposed by the assumption of inelasticity, this additional equation is required for the distance along a line and radial seam from the confluence point to the major periphery of the inflated portion of the canopy shown by Figure 7.12

$$(s_b - s_c)^2 + r^2 = (l_s + h_s - \pi r/2)^2 \qquad 7\text{-}53$$

Filling Time Vs Parachute Mass Ratio. All equations are reduced to a dimensionless form convenient for solution with a digital computer using v_o as the reference velocity and the canopy projected radius at full inflation, r_p, as the reference length. The dimensionless parameters of interest here are

filling time

$$t_f^* = t_f v_o / r_p \qquad 7\text{-}54$$

and parachute mass ratio

$$K_p^* = 3m_p / 4\rho\pi r_p^3 \qquad 7\text{-}55$$

A solution for dimensionless filling time as a function of parachute mass ratio is plotted in Fig. 6.18 for comparison with experimental data. This set of computations was based on the given and measured characteristics of the disk-gap-band parachute experimental prototypes for the Viking Mars Lander drogue. The effect of varying v_o in terms of Mach number is also shown.

The relative filling distance in terms of projected radius, r_p, is roughly three times greater than that based on the nominal diameter, D_o. In addition, when comparing Wolf's solution with others, such as Greenes (Fig. 6.16), differences in the definition of filling time must be taken into account. The filling distance based on only the second phase or final filling interval as defined, will generally be little more than half that for the total filling interval including initial and final phases. With allowance for these differences, the results of the two approaches are in fair agreement, particularly in regard to the trend toward constant filling time in supersonic flow.

Opening Force vs System Mass Ratio. Continuing with the remaining equation required for the complete solution of the parachute inflation process, dimensionless equations convenient for digital computer programming are presented which embody the following dimensionless parameters.

Parachute force	$\underline{f}$	$= F/q_o S_p$
System total mass ratio	K_m	$= K_b + K_p^*$
Body mass ratio	K_b	$= 3m_b/4\pi\rho r_p^3$
Parachute total mass ratio	K_p^*	$= 3m_p/4\pi\rho r_p^3$
Canopy mass ratio	K_c	$= K_p^* m_c/m_p$
Froude number	Fr	$= v_o/(gr_p)^{1/2}$
Velocity	$\underline{\dot{s}}$	$= v/v_o$
Distance	$\underline{s}$	$= s/r_p$
Canopy radius	$\underline{r}$	$= r/r_p$
Time	$\underline{t}$	$= tv_o/r_p$

Terms $(\dot{x})$ and $(\ddot{x})$ signify respectively the first and second derivatives of the variable with respect to dimensionless time $\underline{t}$. Added air mass coefficients for

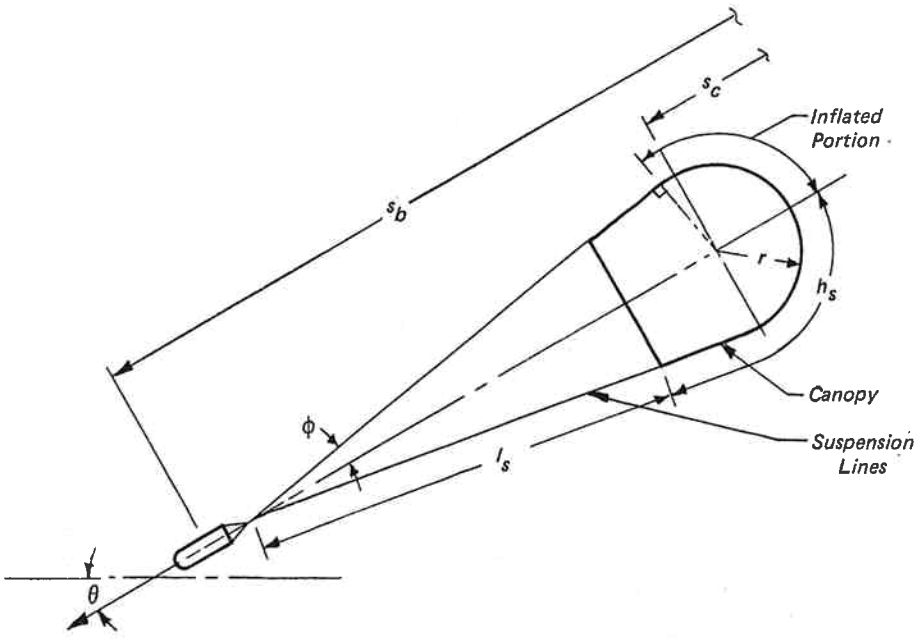


Figure 7.12 Canopy Geometry and Trajectory Coordinates

axial and radial acceleration of the canopy:

Axial $B_s = 3m_s/4\pi r_p^3$

Radial $B_r = 3m_r/4\rho\pi r_p^3$

Parachute quasi-steady drag and radial force coefficients

Drag $C_D = F_D/q_c S_c$

Radial force $C_r = F_r/2\, q_c S_c \sin\phi$

With the assumption that the canopy mass per unit area is constant, the mass of the inflated portion of the canopy is

$$m_{ci} = m_c (r/r_p)^2$$

The acceleration of the body tangent to the flight path is (equation 7-49 + equation 7-50)

$$(K_m - K_c \underline{r}^2)\ddot{\underline{s}}_b = K_m \sin\theta/Fr^2 - 3C_D \underline{r}^2 \dot{\underline{s}}_c^2/8 - (K_c \underline{r}^2 + B_s \underline{r}^3)\ddot{\underline{s}}_c - 3B_s \underline{r}^2 \dot{\underline{r}} \dot{\underline{s}}_c + 2K_c \underline{r} \dot{\underline{r}} (\dot{\underline{s}}_b - \dot{\underline{s}}_c) \quad 7\text{-}56$$

Canopy acceleration along the flight path is the second derivative of equation 7-53

$$\ddot{\underline{s}}_c = \ddot{\underline{s}}_b + \underline{f}_1 \ddot{r}/2\underline{f}_2 + \frac{\dot{r}^2}{4}\left[\underline{f}_1^2/\underline{f}_2^3 - (\pi^2 - 4)/\underline{f}_2\right] \quad 7\text{-}57$$

where

$$\underline{f}_1 = \pi(s_o - \pi r/2) + 2r$$

$$\underline{f}_2 = \left[(\underline{s}_o - \pi \underline{r}/2)^2 - \underline{r}^2\right]^{1/2}$$

$$\underline{s}_o = (l_s + r_o)/r_p$$

Radial acceleration of the canopy is obtained from equation 7-52

$$(K_c \underline{r}^2 + B_r \underline{r}^3)\ddot{\underline{r}} = 3C_R \underline{r}^2 \dot{\underline{s}}_c^2 (\sin\phi)/4 - (2K_c \underline{r} + 3B_R \underline{r}^2)\dot{\underline{r}}^2 - 3\underline{f}(\tan\phi)/8 \quad 7\text{-}58$$

where from equation 7-35

$$\underline{f} = \frac{8}{3}(K_m - K_c \underline{r}^2)(\sin\theta/Fr^2 - \ddot{\underline{s}}_b)$$

and from equation 7-51, the rate of change of the trajectory angle is obtained in this form

$$Fr^2 (K_m + B_s \underline{r}^3)\dot{\underline{s}}_b \dot{\theta} = K_m \cos\theta \quad 7\text{-}59$$

Equations 7-56 through 7-59 provide a set of ordinary differential equations that can be solved for the variables s_b, s_c, r and θ as a function of t. In addition to the initial conditions and the masses of body, parachute and canopy, solution of the equations requires sufficient test data for each different parachute design to establish average values of the empirical coefficients B_s, B_r, C_D, C_R, $\underline{r}_o$ and r_p/D_o. Also, the variation of C_D and C_R with the Mach number must be known when pertinent to the problem.

It is evident that when the peak opening force occurs, the dimensionless parameter for parachute force becomes

$$\underline{f}_x = F_x/q_o S_p \quad 7\text{-}60$$

This is related to the customary opening load factor

$$C_X = F_x/q_s C_D S = \underline{f}_x/C_{D_p} \quad 7\text{-}61$$

when $q_o = q_s$, which is reasonable for near-infinite mass systems. For the infinite mass case $q_o < q_s$, due to system deceleration between line-stretch at t_s and the start of the second phase of filling at t_o. However, the difference is slight in most instances, because the system total drag area is usually small during the first phase of filling. The only practical difference between the two opening load factors is that $C_D S$ can be obtained from test data more readily than either C_{D_p} or S_p, and with greater accuracy, whether or not good film records are available.

Application of the method was demonstrated[373] for the disk-gap-band parachutes for which adequate test data were available[19]. The following empirical coefficients were evaluated and used in the computation of dimensionless opening loads.

$B_s = 0.5$ $\qquad C_R = 0.77\, C_{D_p}$

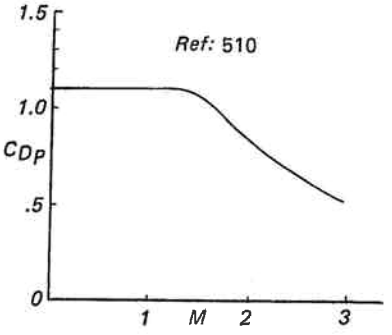
$B_r = 1.0$ $\qquad 2r_p/D_o = 0.707$

$K_p = 0.1 K_m$ $\qquad \underline{r}_o = 0.25$

$K_c = 0.5 K_p$ $\qquad \underline{s}_o = 4.5$

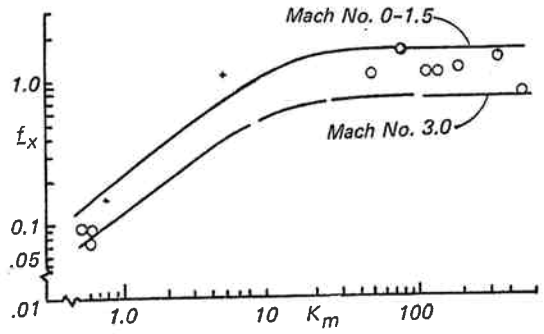
$C_{D_p} = f(M)$

The computed variation of f_x with K_m at Mach = 0 to 1.5 and Mach 3 is compared with measured data points in Figure 7.13b Experimental results appear to correlate well with theoretical.



a) Variation of C_{D_P} With Mach No.

Figure 7.13 Measured and Predicted Characteristics of Disk-Gap-Band Parachute



b) Variation of Opening Force With System Mach Ratio

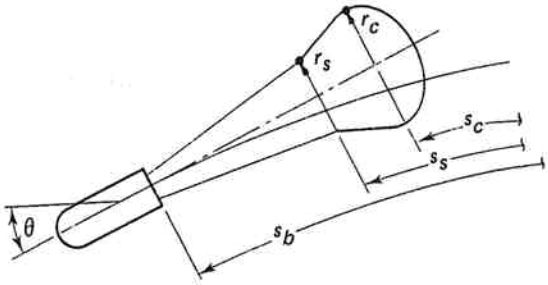
Figure 7.13 Continued

Spring-Mass-Momentum Model

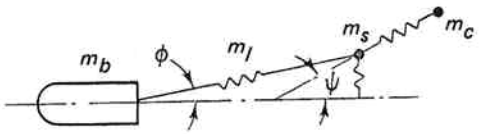
This parachute inflation analytical method is described in Reference 348 and represents an extension of the simpler model presented. Major assumptions are:

- The canopy is treated as two lumped masses, each with two-degrees of freedom.
- Aerodynamic forces are approximated by the sum of quasi-steady and fluid inertia forces.
- Quasi-steady forces include a drag force proportional to parachute cross-sectional area and a radial force proportional to the inflated canopy area forward of the maximum radius point.
- Fluid inertia forces proportional to axial and radial acceleration are included.
- The portion of the canopy from the skirt to the maximum radius point is approximated by a conical frustum while the canopy aft of the maximum radius is approximated by an oblate spheroid with constant velocity.
- Elastic forces are obtained from static load-strain data for materials used in the parachute structure.
- Towing body and parachute follow the same ballistic path.
- The volume segments associated with the canopy skirt and inflated crown exchange mass only with the surrounding air and not with each other.

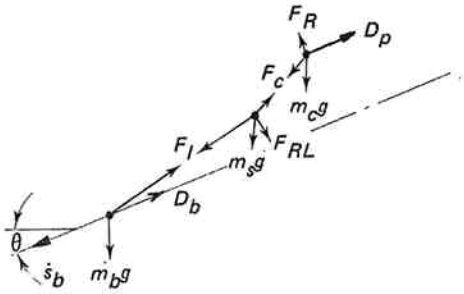
The form of the momentum equation is defined by equation 7-13a. Trajectory coordinates used in the phase-2 inflation model are defined in Figure 7.14a. Six-degrees of freedom are required: three flight path coordinates – (body, canopy skirt, maximum radius point), two radial coordinates (canopy skirt and maximum radius) and the flight path angle. The elastically connected mass components and system forces during inflation are illustrated schematical-



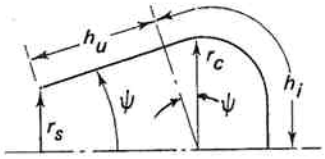
a) Body-Parachute Trajectory Coordinates



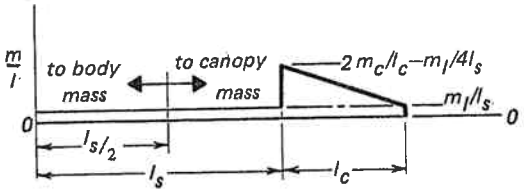
b) Elastic Components



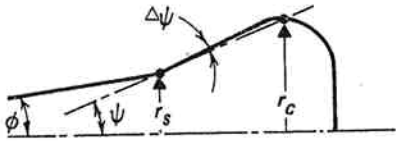
c) System Forces During Inflation



d) Inflating Canopy Geometry



e) Assumed Parachute Mass Distribution



f) Definition of Overinflation Angle of Reefed Canopy

Figure 7.14 Details of Spring Mass-Momentum Model of Inflating Polysymmetric Parachute

ly in Figs. 7.14b and c. Inflating canopy geometry is defined in Figure 7.14d. Motion of the body along the flight path is described by this relationship.

$$m_b \ddot{s}_b = m_b g \sin\theta - F_I \cos\phi - C_D A \rho \dot{s}_b^2/2 \qquad 7\text{-}62$$

Rate of change of flight path angle

$$(m_b + m_p + ma_{sc})\dot{\theta}\dot{s}_b = (m_b + m_p) g \cos\theta \qquad 7\text{-}63$$

Conservation of momentum for the mass concentrated at the parachute skirt (by equation 7-14b)

$$m_s \ddot{s}_s = F_c \cos\psi + F_I \cos\phi + m_s g \sin\theta + \dot{m}_s (\dot{s}_c - \dot{s}_s) \qquad 7\text{-}64$$

and

$$(m_s + ma_{R_s})\ddot{r}_s = F_c \sin\psi - F_I \sin\phi - F_{RL} + \dot{m}_s (\dot{r}_c - \dot{r}_s) - \dot{m} a_{Rs} \dot{r}_s \qquad 7\text{-}65$$

Similarly, for the inflated canopy mass point

$$(m_c + ma_{sc})\ddot{s}_c = F_c \cos\psi - C_D S_c p \dot{s}_c^2/2 + m_c g \sin\theta - \dot{m} a_{sc} \dot{s}_c \qquad 7\text{-}66$$

$$(m_c + ma_{Rc})\ddot{r}_c = -F_c \sin\psi - \dot{m} a_{Rc} \dot{r}_c + C_R (2S_c \sin\psi)(\cos\psi) \rho \dot{s}_c^2/2 \qquad 7\text{-}67$$

For the added air mass terms

$$ma_{sc} = B_{sc} \rho 4\pi r_c^3/3$$

$$ma_{Rs} = B_{Rs} \rho \pi r_s^2 h_u \cos\psi$$

$$ma_{Rc} = B_{Rc} \rho \pi r_c^3 [4 e_c/3 + \sin\psi \cos\psi]$$

The parachute mass is distributed as shown in Figure 7.14e. It is assumed that half the suspension line mass is concentrated in the skirt and the other half attached to the body. For reefed parachutes an over-inflation angle ($\Delta\psi$) was defined as shown in Figure 7.14f).

Finite-Element Elastic Models

Keck [516] and Sundberg [529] have developed finite-element models of the inflating parachute consisting of a series of point masses connected by massless elastic members representing body, suspension lines and canopy. In Sundberg's axi-symmetrical parachute model, the elastic members have non-linear load-elongation characteristics, mass points in the canopy lie on the radials, and the towing body is treated as a finite point mass with drag. Also, the change in canopy porosity with material stretch is accounted for. The motion of an individual suspension line is confined to a plane containing the common centerline of canopy and body. Aerodynamic forces are applied to both suspension lines and canopy, enabling investigation of canopy interactions with transverse waves and tension waves in the suspension lines.

Basically, the dynamics of the system is analyzed by solving Newton's second law (expressed in the vector form as $F = ma$) for every mass point. Typically, 50–100 mass points are used to model the suspension lines, and 25–50 the canopy. The acceleration vector of an individual mass point is written

$$a_i = [m_i g_x + (F_{i+\frac{1}{2}} - F_{i-\frac{1}{2}})/2 + T_{i+\frac{1}{2}} - T_{i-\frac{1}{2}} + T_{ri}]/m_i \qquad 7\text{-}68$$

where F is an aerodynamic force component tangent to the structure (surface) and T is a tension force, T_{ri} being the radial component of the hoop tension.

A sample of the data required for modeling parachute deployment and inflation is given in Reference 529. The process begins with canopy and suspension lines accordion folded in the deployment bag. The modeling includes line deployment and canopy stretchout, inflation and disreefing. Solutions obtained with the model, show the tension wave motion which occurs during deployment and early inflation.

Keck's model [516] includes point masses along the gore center-line as well as radials. Like Sundberg's model, it consists of a network of point mass nodes connected by massless elastic members. Assumption of polysymmetry of parachute structure and the forces acting on it permits the inflation analysis to deal with the motion of only one gore. The four differential equation of motion of each node are programmed for solution by digital computer. Inputs to

Number of nodes

Mass of each node

Unstretched lengths of interconnecting members

Breaking strengths of interconnecting members

Initial positions and velocities of nodes

The original model had eleven radial nodes and nine centerline nodes, requiring the computer to solve eighty differential equations simultaneously. Because the computer run-time proved prohibitive, the number of nodes was reduced to seven and five respectively.

Initial results using the simplified model consisted of a detailed description of canopy shape during inflation, showing the proper growth pattern, including bulging of the gore between radials, and the terminal over-inflation process. A comparison of experimental and predicted force-time data yielded shorter filling times and higher peak loads than measured, indicating the need for some further refinement of the mathematical model.

Theoretical Approach

Payne [517] takes a fresh look at parachute opening dynamics with the objective of developing a simplified model of parachute inflation from first principles without any appeal to experimental measurements. Confining his simplifying assumptions to parameters

of secondary importance, Payne identifies and accounts for the salient physical processes that may be considered fundamental to decelerator inflation. Shortcomings of previous theoretical work in this respect include:

Neglect of the included air mass in the momentum change (transient) force calculation

Use of "ram" pressure rather than Δp across the canopy in the evaluation of relative porosity

Assumption that the canopy inflow velocity is the same as the free stream velocity

Neglect of effect of suspension line tension on canopy growth rate

Neglect of suspension line elasticity

By taking all of these factors into account, Payne's analysis of the time-histories of canopy radius and force coefficient during the inflation process display the oscillatory growth character found in the typical test record obtained in free flight. A summary of the equations used is given for both the finite and infinite mass cases. Each is a set of differential equations for force, canopy pressure component due to velocity head, and canopy size.

Probable Accuracy of Opening Load Prediction Methods

Applied under the most favorable conditions such as frequently prevail during full-scale development test programs, an accuracy of ±10 percent may be realized with the load-factor method. Under similar circumstances the accuracy of the mass-time method for the prediction of single parachute opening loads is approximately ±5 percent. The accuracy of decelerator opening load predictions made for preliminary design purposes and prior to any testing is uncertain for the best of methods, but on the basis of general experience, ±15 percent is a reasonable expectation.

STRESS ANALYSIS

The stress analysis of deployable aerodynamic decelerator structures is better described as an internal unit loads analysis because it is sufficient to determine loads per single member or per unit width, rather than per unit area, in order to calculate either the strength of materials required, or existing margins of safety. The term "stress" is used to designate unit loads.

Margin of Safety

The margin of safety is defined

$$M_S = (P_R A_P / f'_c S_F) - 1 \qquad 7\text{-}69$$

where

P_R = rated ultimate strength of material, either a measured minimum or a minimum given in the material specification.

A_P = allowable strength factor embodying allowances for various conditions which either reduce strength or increase the unit load.

f'_c = critical unit tensile load in the structural member (usually derived from the design limit load in the decelerator main riser).

S_F = safety factor to cover the uncertainties inherent in load and strength predictions.

The allowable strength factor is the product

$$A_P = u\, e\, o\, \kappa\, \tau\, \iota\, s \cos\phi \qquad 7\text{-}70$$

where the sub-factors are individual allowable strength fractions for specific strength reducing or unit load increasing conditions as follows:

u = joint or seam efficiency

e = abrasion and wear

o = moisture absorption due to humidity, etc.

κ = fatigue due to repeated loading or use

τ = temperature

ι = vacuum

s = asymmetrical or unequal loading

ϕ = line or riser convergence angle from load axis

It is convenient to combine the safety factor and the allowable strength factor in one overall design factor:

$$D_F = S_F / A_P \qquad 7\text{-}71$$

Recommended values of these factors as they pertain to a given decelerator system operation are given in Table 8.6. For design purposes the minimum acceptable strength of material is

$$P'_R = D_F f'_c \qquad 7\text{-}72$$

Ideally, the material selected will have a rated strength of $P_R = P'_R$ or slightly greater for a structure of minimum weight, i.e., all margins of safety will be the smallest attainable positive numbers. In these terms the margin of safety is simply

$$M_S = (P_R / P'_R) - 1 \qquad 7\text{-}73$$

and the allowable strength of a given structural member is

$$P_A = \sum P_R A_P \qquad 7\text{-}74$$

of all components or plies.

Prediction of Internal Loads

During decelerator inflation a point is reached where the canopy surface, reacting to differential pressure generated by the momentum change of the

inflowing air, is subjected to internal fabric tension. Owing to the geometry of the canopy structure, with fabric panels bulging between bounding seams and reinforcements, the fabric tension is transferred to the nearest boundary members along the warp and fill yarns of the cloth. With a bulge of double curvature this bi-axial tension is shared between warp and fill in direct proportion to the local radius of curvature of each component only when all boundary members are part of the primary load-bearing structure. Free edges at vents, slots and skirt cannot carry loads across the gaps. The ability of boundary seams and reinforcements to transfer loads depends in part on their orientation relative to the primary load axis of the canopy and in part on their location on the surface.

The shape and construction of the canopy as a whole defines the load transfer paths across the surface and generally the fabric will be subject to critical stresses in those areas for which the local radius of curvature is a maximum when the differential pressure reaches its maximum value. Ultimately the surface loads converge on the suspension line attachments at the skirt and are transferred downward through lines and risers either to a body harness or to one or more hard points on the body structure. This integrated axial load is the one commonly measured in various decelerator tests.

Canopy of General Shape

For the canopy of general profile and planform the unit load in either the warp or fill directions is related to the differential pressure and the local radius of curvature by classical membrane theory for a material of negligible thickness and zero bending strength or stiffness in this way:

$$f'_1 = pr_1 - f'_2 (r_1/r_2) \qquad 7\text{-}75$$

where p is the differential pressure, r_1 and r_2 are radii of the surface bulge in mutually perpendicular planes and f'_2 is the unit load in the r_2 plane. Running loads in the surface are f'_1 and f'_2 in units of force per unit width.

when $r_1 = r_2$ then $f'_1 = f'_2$ and $f' = pr/2$

when $r_2 = \infty$ then $r_1/r_2 \approx 0$ and $f' = pr$

Then for a fabric surface of general curvature the critical unit load may be characterized as

$$f'_c = C_s (pr)_{max} \qquad 7\text{-}76$$

Where C_s is a shape factor with some value between 0.5 and 1.0 at a point in the canopy where the product pr is a maximum either in the warp or fill direction. Equation 7.76 with $C_s = 0.5$ is applicable to a spherical surface and with $C_s = 1.0$ it is applicable to surfaces of simple curvature such as a cylinder or cone. For other shapes it is possible to estimate C_s from test data, if calculation of the shape factor from thin shell membrane theory is not practical.

The assumption of a uniform pressure distribution over the inflated portion of a canopy is a reasonable one in many instances so that representation of the mean unit pressure as

$$p = F/S_p \qquad 7\text{-}77$$

yields a value close to the maximum at critical points in the canopy. Also, the pressurized surface of a canopy at any stage of inflation is roughly spherical so that letting

$$r = D_p/2 \qquad 7\text{-}78$$

represent a generally conservative assumption in view of the bulging of the fabric panels between bounding seams and reinforcements.

The combination of equations 7-77 and 7-78 in equation 7-76 with $C_s = 0.5$ yields the familiar expression for the unit load in any canopy when the inflated portion of its shape is nearly spherical

$$f'_c = F_X/\pi D_p \qquad 7\text{-}79$$

Where F_X is the peak opening load and D_p the projected inflated diameter of the canopy at that instant.

This simplified expression is useful for the quick estimation of canopy unit loads in preliminary calculations for either design or test analysis. Similarly, at the point of transition from a cylindrical shape to a cylindrical (or conic) inlet region, $C_s = 1.0$ yielding

$$f'_c = 2F_x/\pi D_p$$

Suspension Lines. For a decelerator of any shape the mean unit suspension line load is

$$f_l = F/Z \cos \phi \qquad 7\text{-}80$$

Since deviations from the mean, even in polysymmetric parachutes, can be large and high-glide parachutes in particular are subject to extremely nonuniform load distributions, the geometry of each case at the time $F(max)$ occurs tends to be special and should be analyzed in detail. The location of the line on the canopy and material elasticity, as well as the angular deflection, must be accounted for in unsymmetrical parachutes.

Circular Parachutes

The axi-symmetric circular parachute being polysymmetric in every salient detail, constitutes the most simple decelerator structure for internal loads analysis. However, in comparison with other engineering structures, it still presents a problem of formidable complexity when a mathematical model of adequate rigor is required.

The first consideration is the lay of the cloth in

the gore sub-assemblies. In the typical solid cloth canopy, warp and fill yarns cross the gore centerline at an angle of 45 degrees, as shown in Figure 7.15, and, with warp and fill of equal strength, by symmetry the unit load (from equation 7-76 with $C_s = 0.5$) is

$$f' = 0.5\,(pr_b) \qquad 7\text{-}81$$

where r_b, the local radius of curvature in the bias plane, has an intermediate value between the transverse bulge radius and the canopy meridional radius.

Block-cut cloth construction with warp at 90 degrees to the gore centerline is found mainly in the canopies of slotted design. Although vertical tapes, when used, carry small loads across the horizontal slots, the ribbons and sails of such canopies tend to arch with simple curvature and the unit load of interest occurs transversely in the warp, represented simply (equation 7-76 with $C_s = 1.0$)

$$f' = pr \qquad 7\text{-}82$$

where r is the radius of the sail arch in a plane normal to the gore centerline. This load is carried laterally to the radials where the unbalanced (normal) components are transformed as running loads into increments of tension in the radial members forming the sides of the gore. In contrast, the warp and fill yarns of the bias cut cloth transfer their tension along diagonals which add vectorially to produce both normal running loads along, and radial components in the radial members (Fig. 7.15).

The bias-constructed canopy can be treated in the same terms as the block-constructed or slotted canopies simply by applying the amplification factor to the measured stress-strain characteristics of the cloth warp and fill. This consideration was first pointed out by Topping[530] who suggested a value of 1.41, i.e., the transverse strain is simply

$$\epsilon \approx 1.41\,\epsilon_b \qquad 7\text{-}83$$

where ϵ_b is the material strain along the warp or fill axis.

Solid Cloth Canopies

Two different methods have been developed applicable to the computation of the internal loads of solid cloth canopies:

1. The inflation energy transfer approach[525] in which the strain energy of the canopy cloth, plus that of the suspension system is equated to the work applied by the air influx during canopy inflation.
2. The pressure-strain equilibrium approach (Ref. 531) in which a distributed pressure load is applied to the elastic canopy-suspension line structure such that the resultant tensile strain duplicates the inflated shape of the canopy.

The Inflation Energy Transfer Method

Houmard[525] uses a method of computing the internal loads of a parachute structure in which the total strain energy of canopy cloth and suspension system is equated to the work applied by the inflowing air during the inflation process. This work is treated as the sum of two parts:

- $\Delta(pV)$ the product of the differential pressure and the change in volume
- $F(E\Delta l)$ the longitudinal pressure force acting through a distance equal to the stretch in suspension lines combined with the change in the canopy height during inflation

Two basic variables are used in the derivation of the equations for the computer program:

1. Meridian station from apex to skirt edge
2. Non-dimensional time from deployment bag strip to full inflation (t/t_f)

The variables are evaluated by measurement of motion picture records of the inflating parachute. These define the size and shape of the canopy as a function of time as shown in Figure 7.16. The method was applied to the Viking 53 ft (D_o) disk-gap-band parachute, with 48 suspension lines and $l_s/D_o = 1.7$, for which a large quantity of pertinent test data had been obtained. The growth of the maximum projected area and the area defined by the skirt edge during the filling interval (Fig. 7.16b) was verified by a series of subsonic drop tests of full-scale Viking parachute systems from altitudes in the order of 50,000 feet.

The meridian length at any inflation stage is equated to the stretched length of a meridian tape under the predicted instantaneous dynamic loads, a uniform distribution among the 48 radials being assumed. The relative elongation of the radials at each load level is taken from averaged load strain data for the polyester materials used after the load is multiplied by a factor of 1.25 to account for increased stiffness due to dynamic loading.

The inflated shape of the canopy at any stage was treated as a combination of an oblate hemispheroid, a segment of an oblate hemispheroid, and a conical frustum, with maximum volume at full inflation. Pertinent dimensions of the parachute during inflation between two consecutive points in time are given in Fig. 7.16.

Inflation air pressure distributions are determined on the basis of the following simplifying assumptions about the flow field inside the canopy:

The conical frustum portions of the canopy are un-inflated, i.e., $\Delta p = o$.

The work done in displacing the external air mass is negligible.

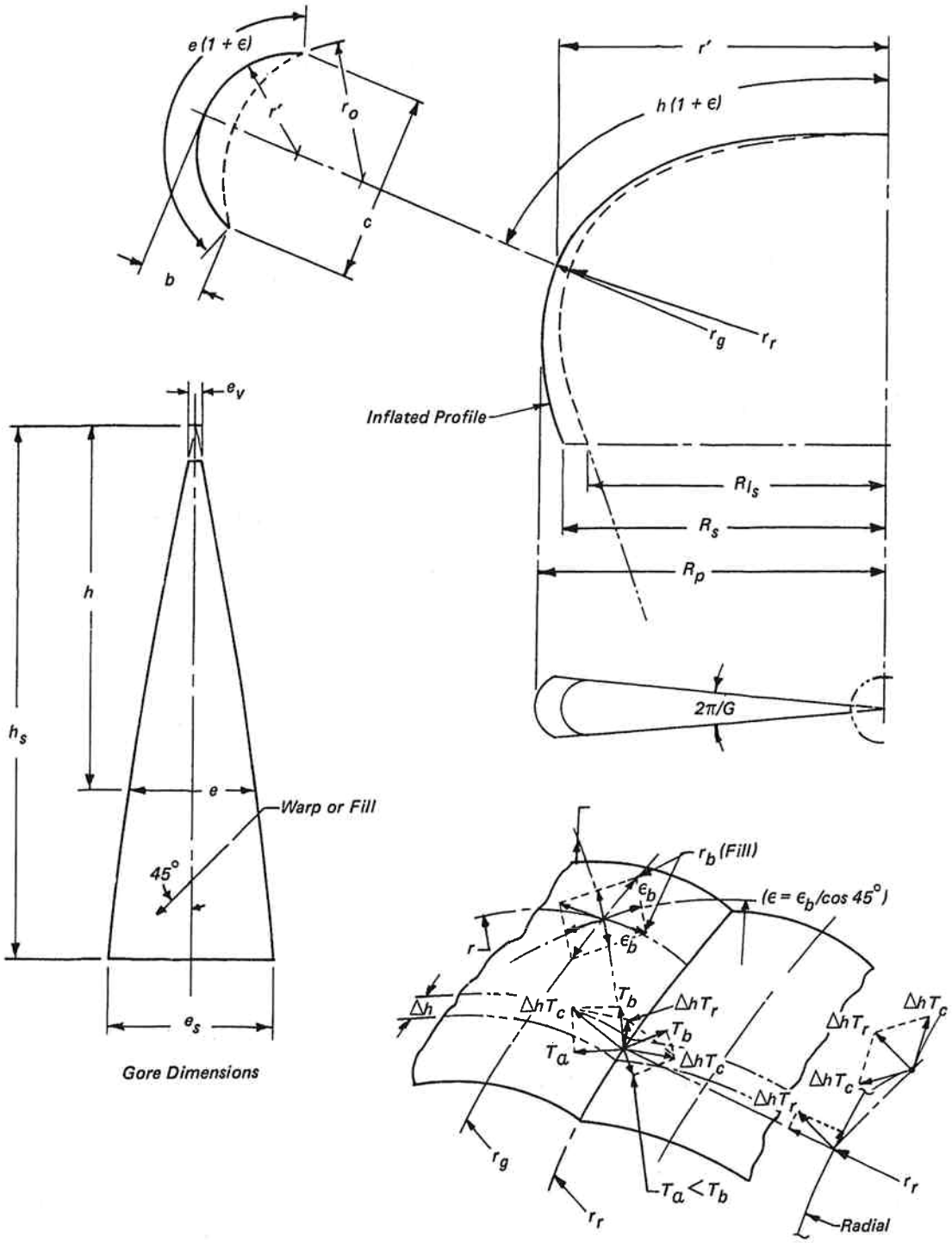
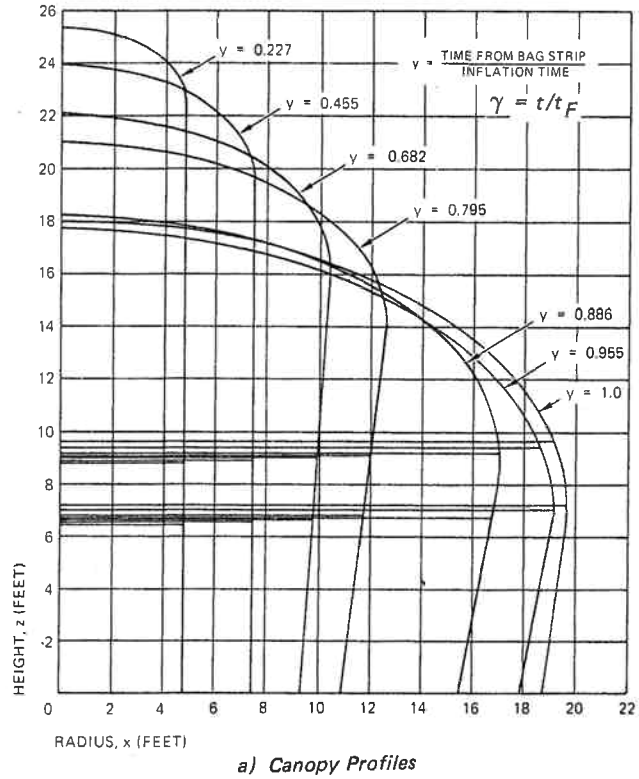
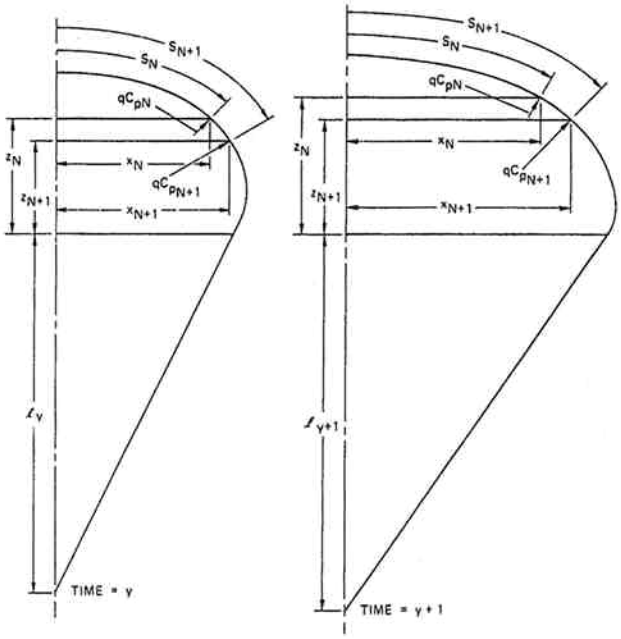


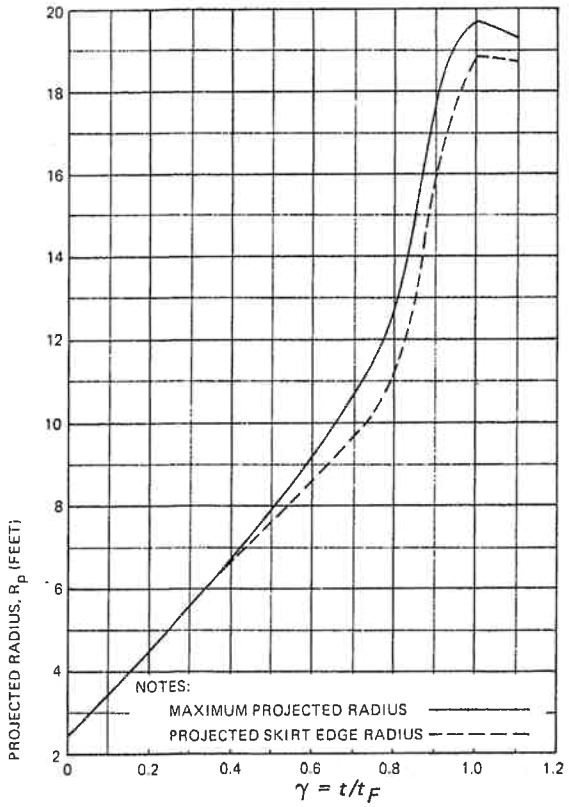
Figure 7.15 Stress-Strain Relationships in Circular Canopy of General Profile and Bias Construction



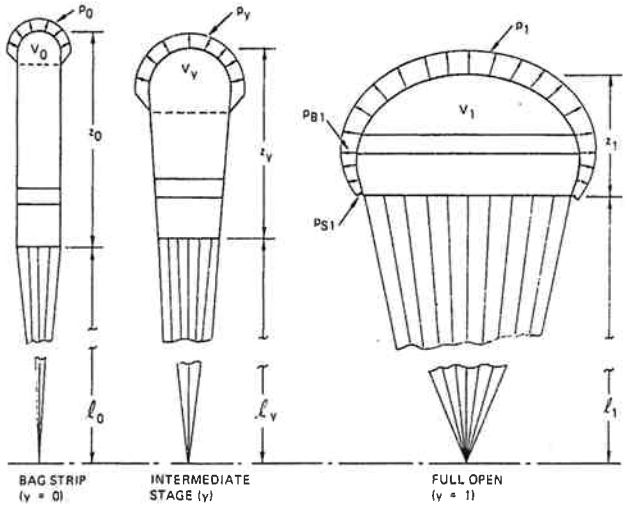
a) Canopy Profiles



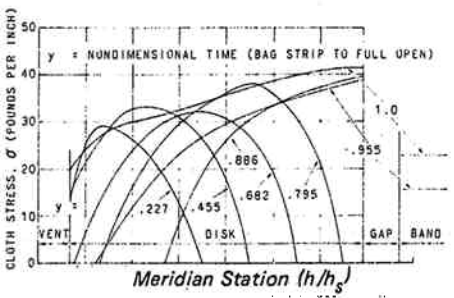
c) Shape at Two Consecutive Time Points



b) Canopy Growth



d) Inflation Stage Sequence



e) Design Limit Cloth Stress Distribution at Various Stages of Inflation

Figure 7.16 Variation of Canopy Shape and Stress During Inflation (Ref. 525)

The positive internal differential pressure is constant over the surface of the oblate hemispheroid and tapers linearly to zero for intermediate stages as shown in Fig. 7.16.

The peripheral band is first subjected to internal pressure when $D_{p(max)}$ falls in the gap area.

The energy capacity of the canopy cloth is conservatively evaluated at 175% of the area under the load-strain curves of the material to take advantage of the increased efficiency of the 45° bias construction.

Although a fabric structure of bias construction theoretically can absorb twice the energy of one of block construction, about 25% of this gain may be lost due to pinching and shearing action of the crimped warp and fill yarns in the weave.

The theory and associated initial parameters of geometry, loads and material properties provide the basis of a digital computer program. The program was used to predict the cloth stresses in the Viking parachute as a guide for the selection of materials. The distribution of predicted stresses is presented in Fig. 7.16 for various stages of inflation.

The Pressure-Strain Equilibrium Method

The CANO 1 digital computer program[532] may be adapted for the prediction of the internal loads of solid cloth parachutes on the basis of the following assumptions:

Meridional curvature is constant over each Δh segment of the canopy, and curvatures are tangent at the junction of adjacent segments.

The horizontal cloth segments of width Δh have simple curvature ($r_g = \infty$ in Fig. 7.15).

The vertical members between segments are the fill yarns.

The edges of the horizontal segments lie in planes at an angle to normal plane ζ (Fig. 7.15).

The projection of a horizontal segment on normal plane ζ is a circular arc.

These assumptions are equally applicable to the solid cloth canopy of 45 degree bias construction when the warp and fill stress-strain properties of the cloth are translated to the horizontal-vertical gore coordinate system, e.g., by Equation 7-75. A suitable segment width, $\Delta h/h_s$, may be determined for any given canopy structure by inspection supported by a few trial runs of the program.

Slotted Parachutes. The following method of computing the internal loads of ribbon, ringslot and ringsail parachute structures, i.e., those having canopies made of concentric rings, was developed by Mullins and Reynolds for stress analysis of the Apollo Earth Landing System[221]. Reference 531 describes application of this method to the parametric analysis of ribbon parachute structures. The structural model of the canopy required is illustrated schematically in generalized form in Figure 7.17. A polysymmetric structure of this type can be completely described by defining one gore and one suspension line with attached riser branch.

The gore height is divided into a convenient number of segments by designating sail edges, intermediate points and/or ribbon centerlines by station numbers. A tabulation is prepared of gore width and height, Δh, dimensions, and all sail or ribbon and tape materials and unit strengths are identified, member-by-member at all stations. Radial tapes, vertical tapes, vent lines and suspension lines are similarly identified. The size and shape of the canopy reefed and after disreefing is determined by photogrammetry. The inflated profile is specified in terms of diameter at the principal station numbers from skirt to vent. The vent diameter provides an absolute scale of reference because the heavily reinforced hem stretches very little under load.

Pressure Distribution and Equilibrium Equations. Preliminary estimates of canopy pressure distribution are made in the form shown in Fig. 7.18. The differential pressure loads and structural tension loads are related as shown in the diagrams of Fig. 7.17 and in the following equilibrium equations.

Full Open After Disreefing (below the skirt).

$$f'_1 = F/Z \cos\phi \qquad 7\text{-}84$$

$$\phi = \sin^{-1}\left[R_{ls}/l'_e\,(1+\epsilon_l)\right] \qquad 7\text{-}85$$

where l'_e is the initial (unstretched) length of lines and risers combined.

Reefed Opening (below the effective skirt).

$$f'_l = F/Z \cos\phi \qquad 7\text{-}86$$

$$f'_r = F/Z \cos\psi \qquad 7\text{-}87$$

$$f'_s = F\,(\tan\psi - \tan\phi)/2Z \sin(\pi/Z) \qquad 7\text{-}88$$

$$\phi = \sin^{-1}\left[R_r/l'_e\,(1+\epsilon_l)\right] \qquad 7\text{-}89$$

$$R_r = l'_r\,(1+\epsilon_r)/2Z \sin(\pi/Z) \qquad 7\text{-}90$$

$$R_c = R_r + C'\,(1+\epsilon_c)\sin\psi \qquad 7\text{-}91$$

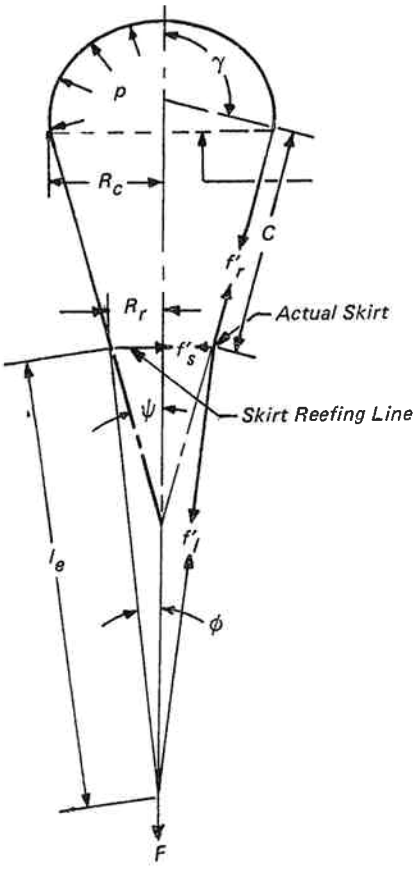
where l'_r is the initial length of the reefing line and C' is the unstretched length of the straight portion of the canopy radial below the inflated crown.

In Plane A-A:

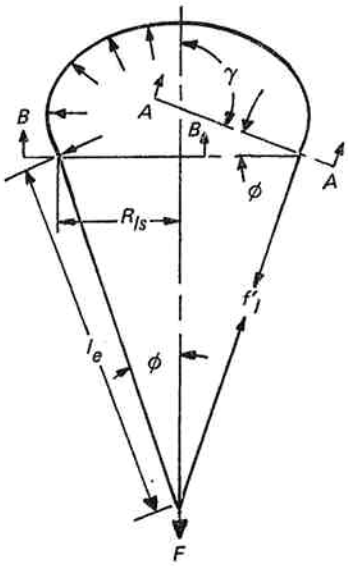
$$r_s = e_s/2\beta \qquad 7\text{-}92$$

area

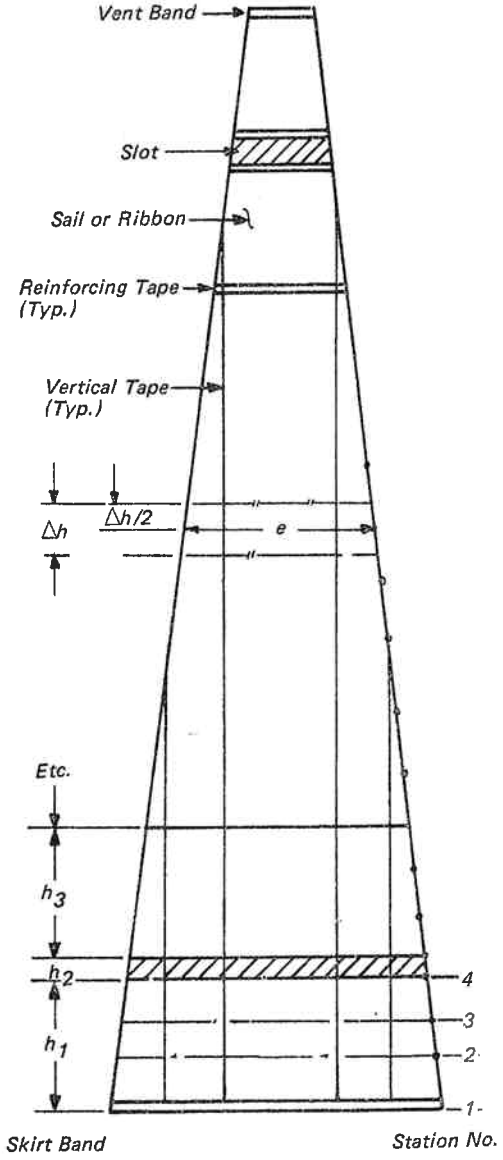
$$A_1 = (R_A{}^2/2)\left[\sin(2\alpha/Z)\right] \qquad 7\text{-}93$$



c) Inflated Profile – Reefed

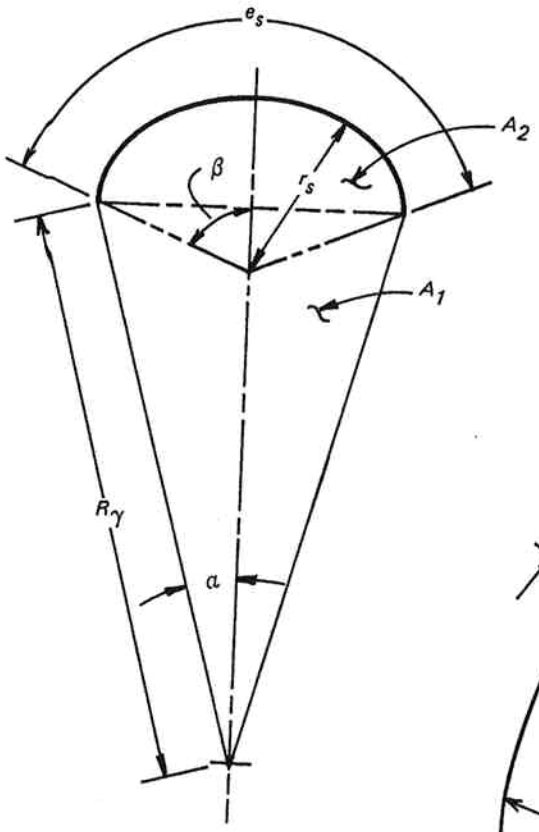


b) Inflated Profile Full Open After Disreefing

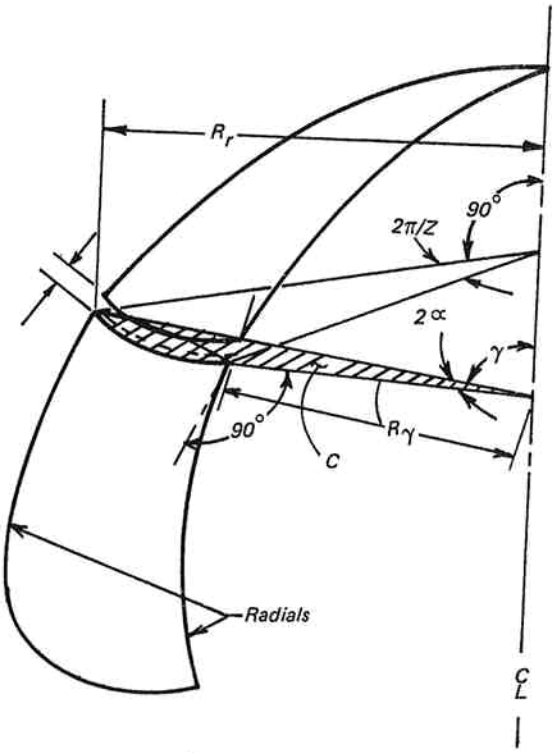


a) Gore Structure

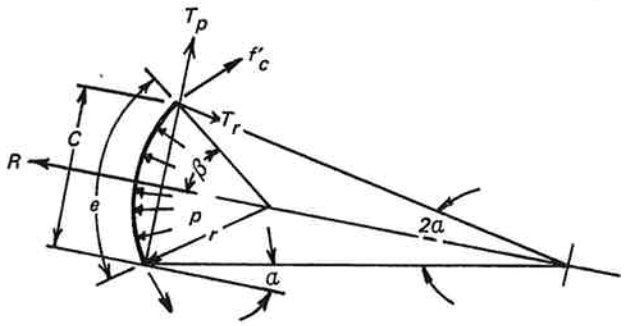
Figure 7.17 Structural Model of Slotted Parachute



d) View of Plane A–A

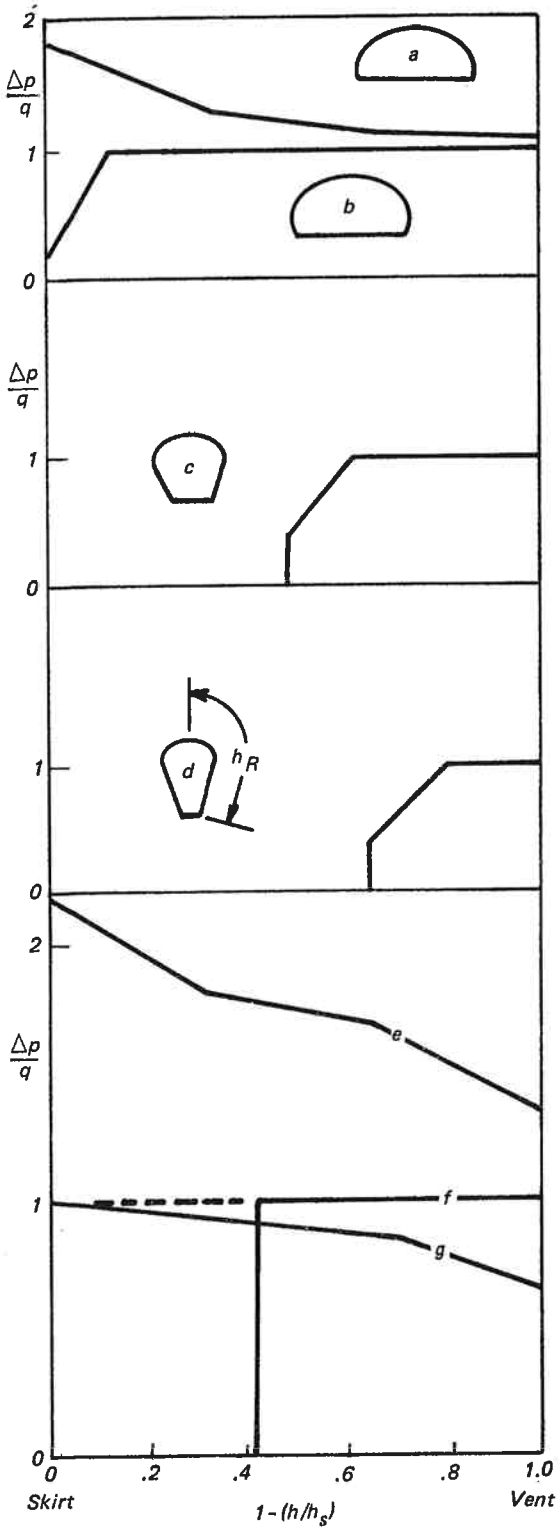


f) Inflated Gore



e) View of Plane C

Figure 7.17 Continued



a) 85.6 Ft D_o Mod. Ringsail
Over Expanded
($F < F_o$)

b) Full Open
($F = F_o$)
W/C_DS = 1.5-2 PSF

c) Reefed Stage 2
($F = F_{R2}$)
W/C_DS = 6-8 PSF

d) Reefed Stage 1
($F = F_{R1}$)
D_r/D_o = .082
W/C_DS = 24-34 PSF

e) 16.5 Ft D_o Conical Ribbon
Drogue Full (Over Expanded)
($F = F_o$)
(D_r/D_o = 0.637 by Fixed Reefing)
W/C_DS = 57-78 PSF

f) Drogue (Reefed)
D_r/D_o = .43
$F = F_r$
W/C_DS = 100-140 PSF

g) 7.2 Ft D_o Ringslot Pilot Chute
$F = F_o$
W/C_DS = 5.7 PSF
(W/C_DS = 266-373 PSF @ Main Canopy Stretch)

Figure 7.18 Pressure Distribution in Inflating Parachutes (Ref. 221)

area

$$A_2 = (R_\gamma^2/2)(2\beta - \sin 2\beta) \qquad 7\text{-}94$$

The projected area in Plane B-B is

$$A = Z(A_1 + A_2)\sin\gamma \qquad 7\text{-}95$$

The local differential pressure is

$$p = p'F/AK' \qquad 7\text{-}96$$

where p' is the pressure coefficient from an estimated pressure distribution curve, e.g., $\Delta p/q$, Fig. 7.18 and K' is the integration factor, a function of the shape of the pressure distribution curve and the geometric porosity.

Equilibrium of a Typical Horizontal Element. From a summation of forces in direction R, the unit tension in a horizontal member is

$$f'_c = pR_r \sin(\pi/Z)/\sin\beta \qquad 7\text{-}97$$

The arc length is

$$e = 2\beta R_r \sin(\pi/Z)/\sin\beta \qquad 7\text{-}98$$

The length of the horizontal member is

$$e_H = e'_H(1 + \epsilon_H) \qquad 7\text{-}99$$

where e'_H is the unstretched length. A value for β is found by iteration to give

$$e_H = e \qquad 7\text{-}100$$

The unit tension in each horizontal member is resolved into three mutually perpendicular components:

1. Tangent to the meridional member

$$\Delta f'_R = f'_c \sin(\pi/Z)\cos\gamma\,(\cos\beta + \sin\beta \sin\alpha/\cos\alpha) \qquad 7\text{-}101$$

2. Normal to the meridional member in a plane which includes the central axis

$$f'_N = f'_c [\sin\beta/\cos\alpha - \sin\alpha\,(\cos\beta + \sin\beta \sin\alpha/\cos\alpha)] \qquad 7\text{-}102$$

3. A circumferential force

$$f'_\pi = f'_c \cos(\pi/Z)\,(\cos\beta + \sin\beta \sin\alpha/\cos\alpha) \qquad 7\text{-}103$$

Equilibrium of a Segment of a Meridional Member (Δh).

$$R_\gamma = f'_R/2f'_N$$

where the load in one meridional member starting at the skirt is

$$f'_R = F/Z\sin\gamma \qquad 7\text{-}104$$

and the number of gores $N = Z$, the number of suspension lines. At subsequent stations f'_R is computed by subtracting the accumulated $\Delta f'_R$ from the initial value. Since the ends of two horizontal members are acting on each meridional member, the load at station j is

$$f'_{Rj} = f'_{R(j-1)} - (2\Delta f'_R \Delta h/2)_{(j-1)} - (2\Delta f'_R \Delta h/2)_j \qquad 7\text{-}105$$

and the length of segment j is

$$\Delta h_j = \Delta h'_j(1 + \epsilon_R) \qquad 7\text{-}106$$

where $\Delta h'_j$ is the unstretched or manufactured length. For complete details, see Reference 221.

Solution Algorithm. A flow diagram for the digital computer program is presented in Figure 7.19A. A user's manual which includes a listing of the program will be found in Reference 532.

Equations 7-84 and 7-85 are solved simultaneously by the method given in Figure 7.19B for the unreefed parachute. Equations 7-86 and 7-87 through 7-91 are resolved simultaneously by the method given in Figure 7.19C for the reefed parachute. The remaining equations 7-92 through 7-106 are resolved simultaneously by the method given in Figs. 7.19B or 7.19C.

Input data include:

- Parachute geometry (reefed and unreefed)
- Material load-strain curves
- Pressure distribution curves (reefed and unreefed)
- Main riser load, F, (reefed and unreefed)

One of the basic assumptions of the slotted canopy analysis is that the horizontal sails or ribbons arch outward with the warp yarns lying in planes normal to the radial or meridional members. But it was observed that the vertical members of the ribbon and ringslot canopies introduced a pronounced distortion near the skirt that prevented the horizontals from bulging normally by pulling them upward. As a result, the vertical members pick up a component of the grid pressure load and transfer it to the radial members. This is generally analogous to the stress-strain relationships of the solid cloth canopy illustrated in Fig. 7.15 except for the 45 degree displacement of warp and fill axis.

The effect of the vertical members on the internal load distribution of the canopy was accounted for in an analysis based on the following assumptions.

- Meridional curvature is constant over each Δh segment of the canopy, and curvatures are tangent at the junction between adjacent segments. The horizontal ribbons have simple curvature ($r_g = \infty$).
- The vertical members act as equivalent fill yarns uniformly distributed across the gore.
- The edges of a horizontal ribbon lie in planes at an angle to normal plane C (Fig. 7.17).
- The projection of a horizontal ribbon on normal plane C is a circular arc.
- The additional equations required are not develop-

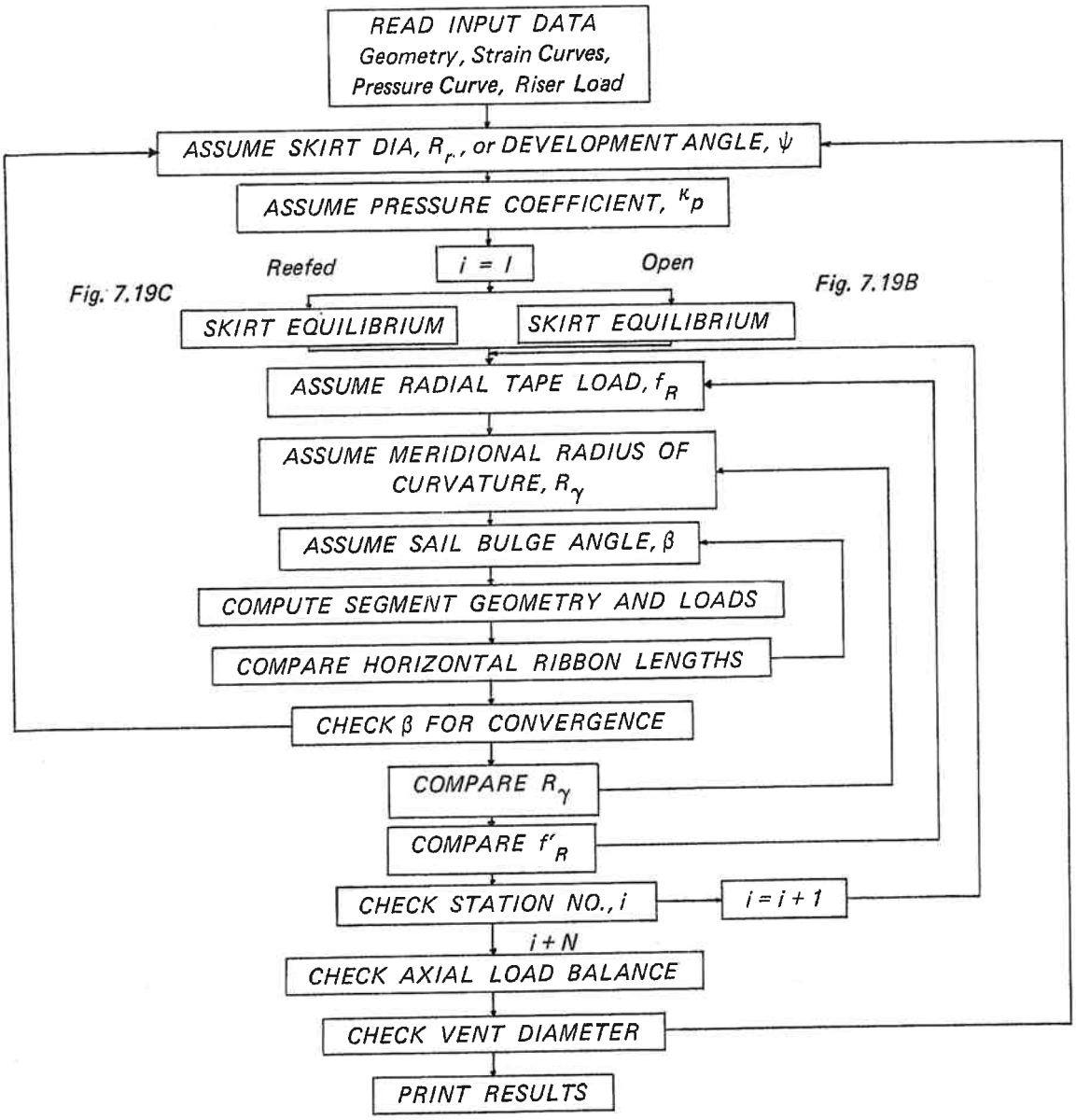


Figure 7.19A Flow Diagram for Program CANO

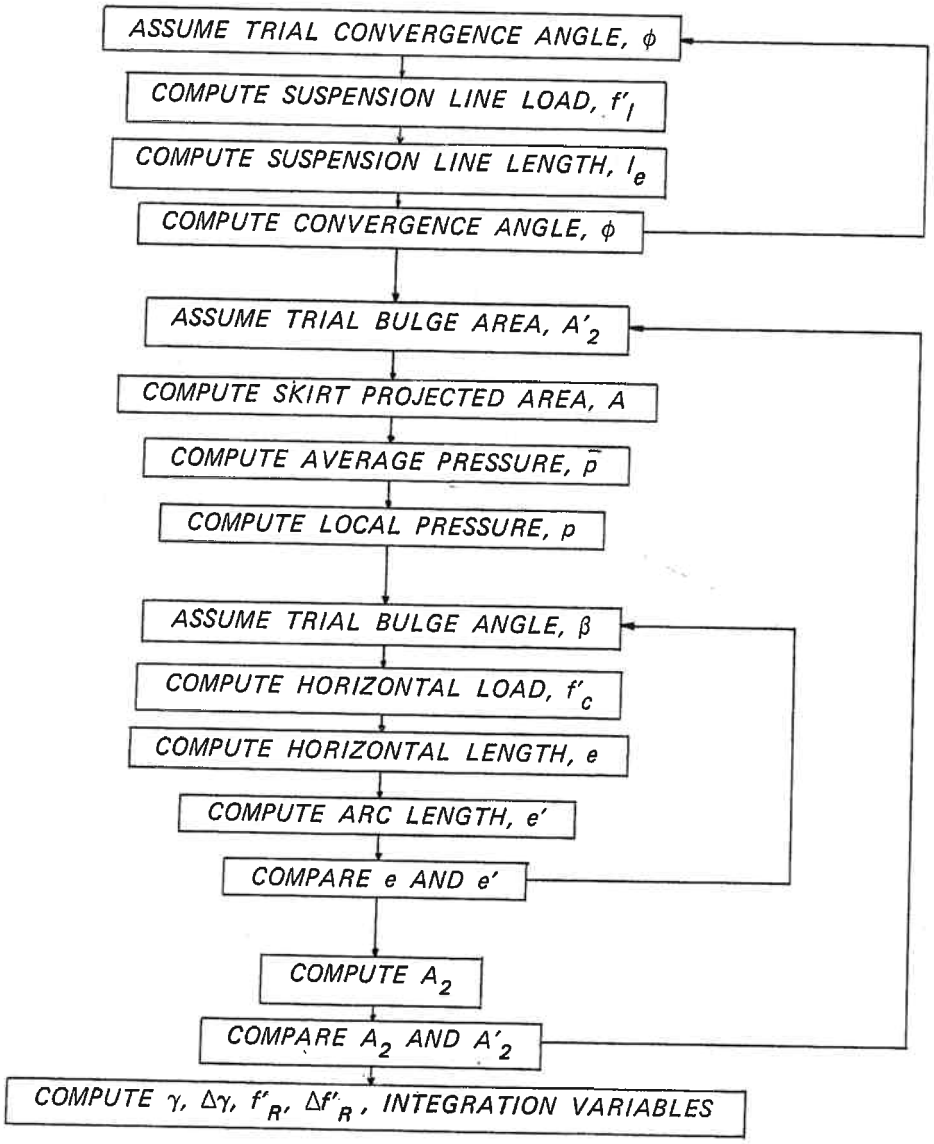


Figure 7.19B Flow Diagram Detail Showing Skirt Equilibrium for an Unreefed Parachute

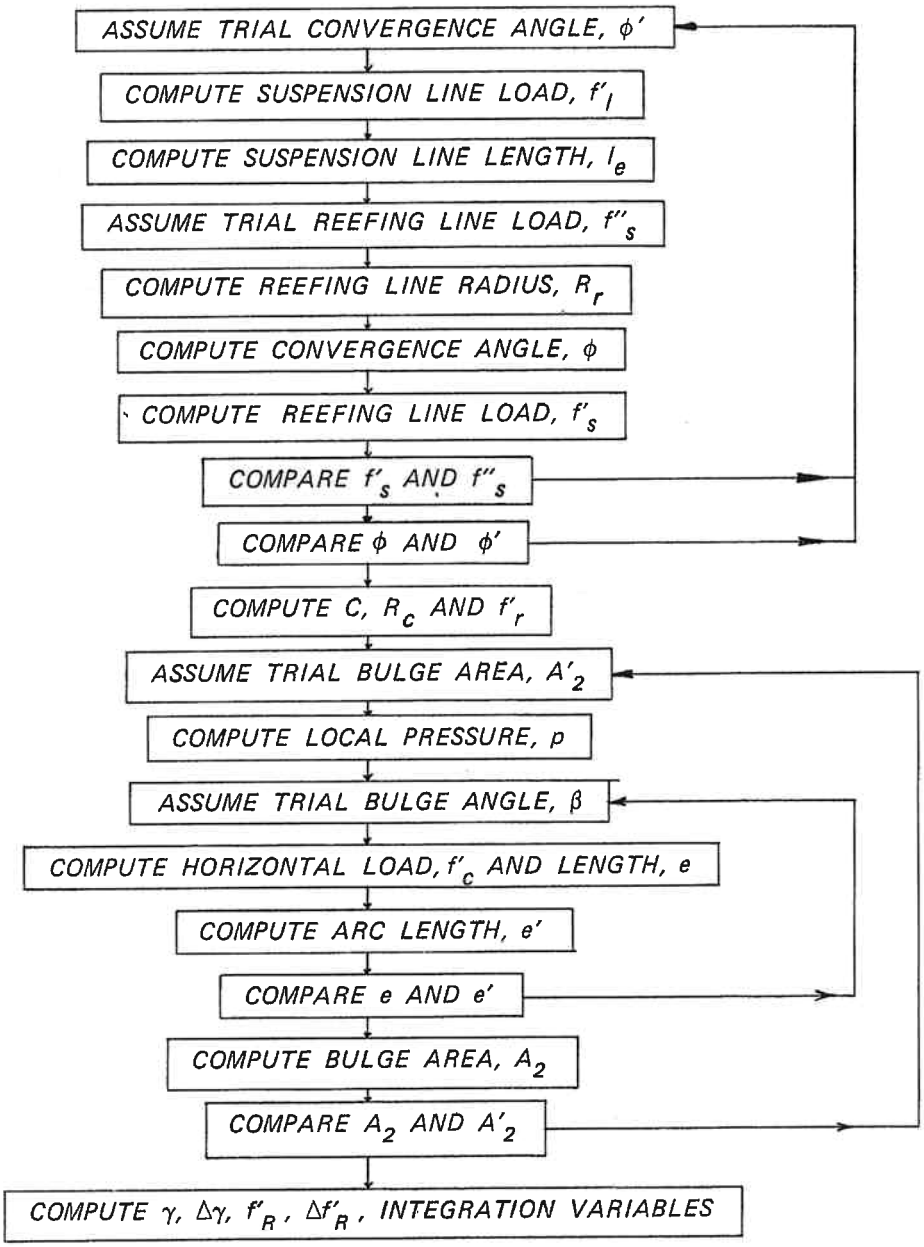


Figure 7.19C Flow Diagram Detail Showing Skirt Equilibrium for a Reefed Parachute

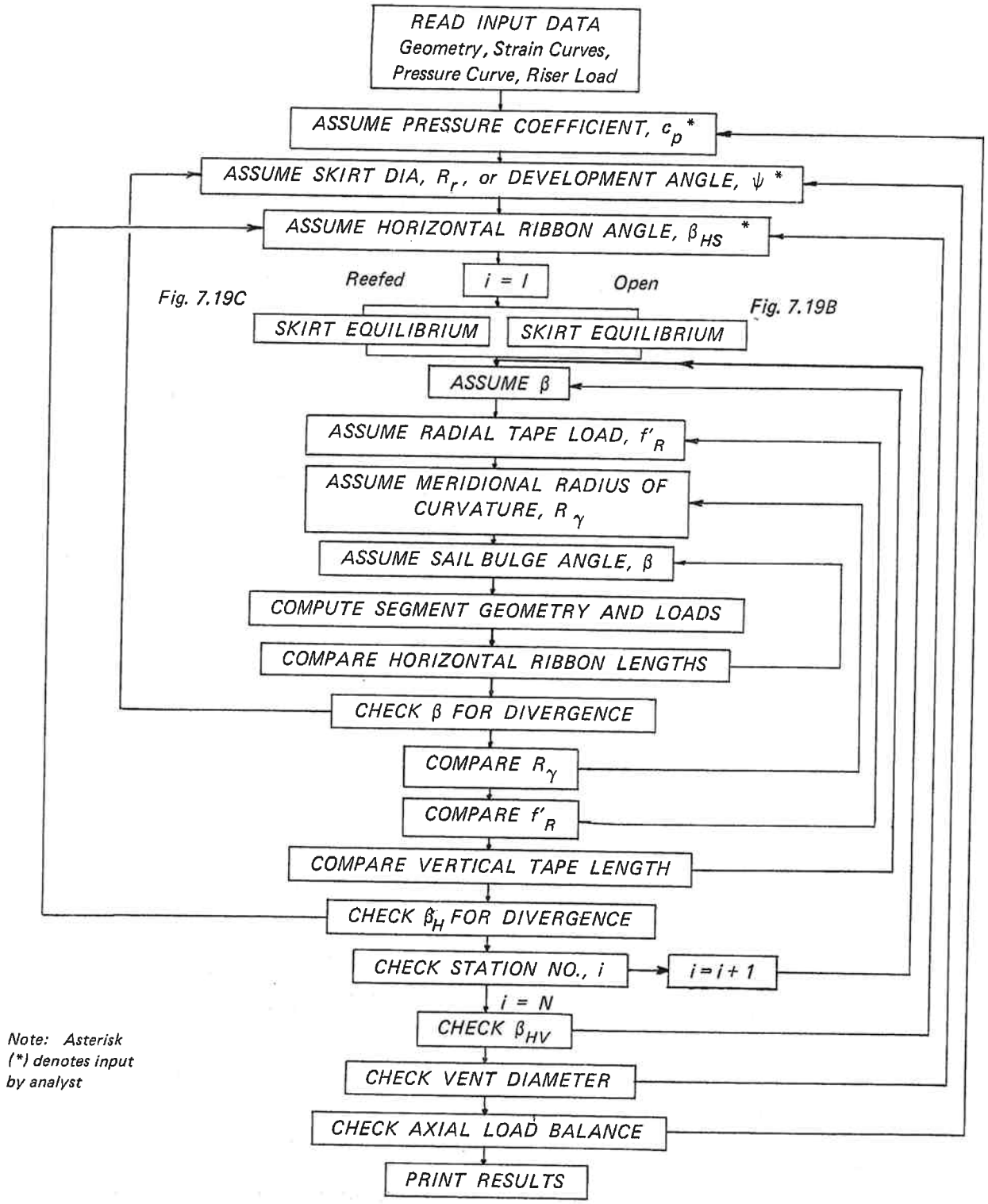


Figure 7.20 Flow Diagram for Program CANO 1

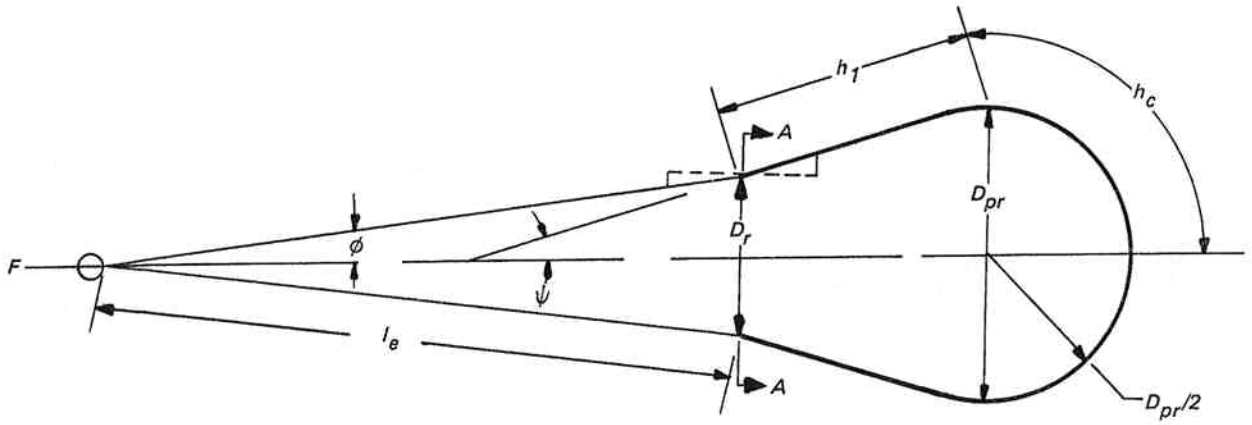
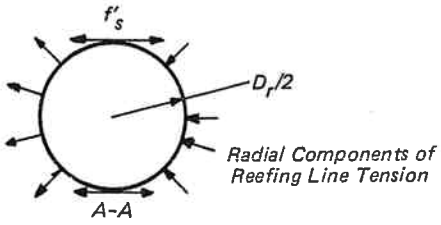


Figure 7.21 Relative Reefing Line Load



ed here. They may be resolved simultaneously by the method given in Figure 7.20, the program for which is also listed in Reference 532. Application of CANO 1 to the parametric analysis of ribbon parachute structures in Reference 531led Reynolds and Mullins to a number of significant conclusions:

1. The CANO 1 structural analysis method predicts canopy inflated shape with reasonable accuracy.
2. Vertical members can have a significant effect on the inflated profile of the canopy or on the horizontal ribbon loads.
3. Vertical members can have a significant effect on the load carried by the radial members, mainly in the skirt and side-wall area.
4. The number of gores in the canopy has a significant effect on the circumferential and meridional loads in the canopy. In particular, the load carried by the vertical members is strongly affected by and is inversely proportional to the number of gores.
5. The effect of canopy cone angle of circumferential and meridional loads can be significant. The steeper cone angles are characterized by higher circumferential loads while the flatter canopy has higher meridional loads.

Reefing Line Loads

Tension begins to build up in the reefing line at that point in the inflation process when the angle of the canopy radial members, ψ, becomes greater than the convergence angle of the suspension lines, ϕ. From this point on, the ratio of the instantaneous loads in reefing line and parachute riser can be approximated from the geometry given in Figure 7.21.

$$f'_s/F = (\tan\psi - \tan\phi)/2\pi \qquad 7\text{-}107$$

where
$$\phi \approx \sin^{-1}(D_r/2l_e)$$
$$\psi \approx \sin^{-1}[(D_{pr}-D_r)/2h_1]$$
$$h_1 \approx (D_o/2)-h_c$$
$$h_c \approx \pi D_{pr}/4$$

Equation 7-107 derives from the simple relationship for hoop tension in a flexible band

$$f'_s = pr$$

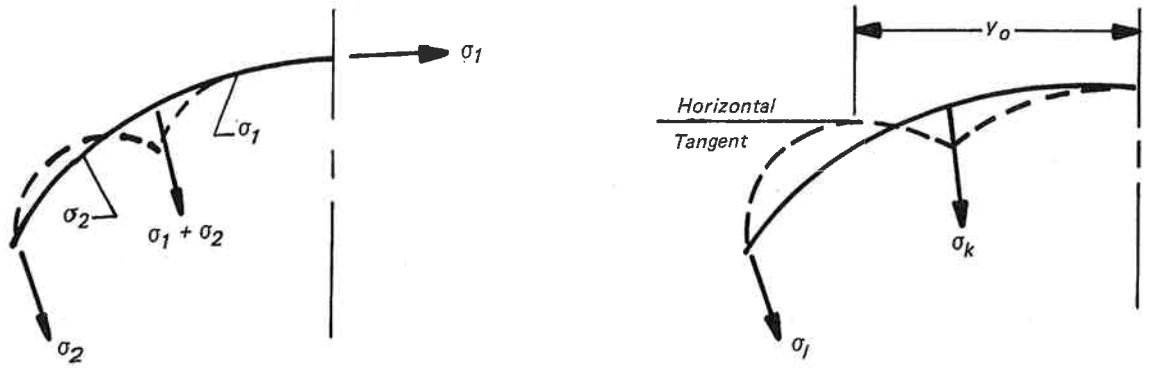
where $p = F(\tan\psi-\tan\phi)/\pi D_r$ = distributed radial component of F

$$r = D_r/2$$

Although $f'_s(max)$ occurs a short while after $F(max)$, a conservative result will be obtained by assuming the two loads are coincident[217].

High-Glide Parachute Structures

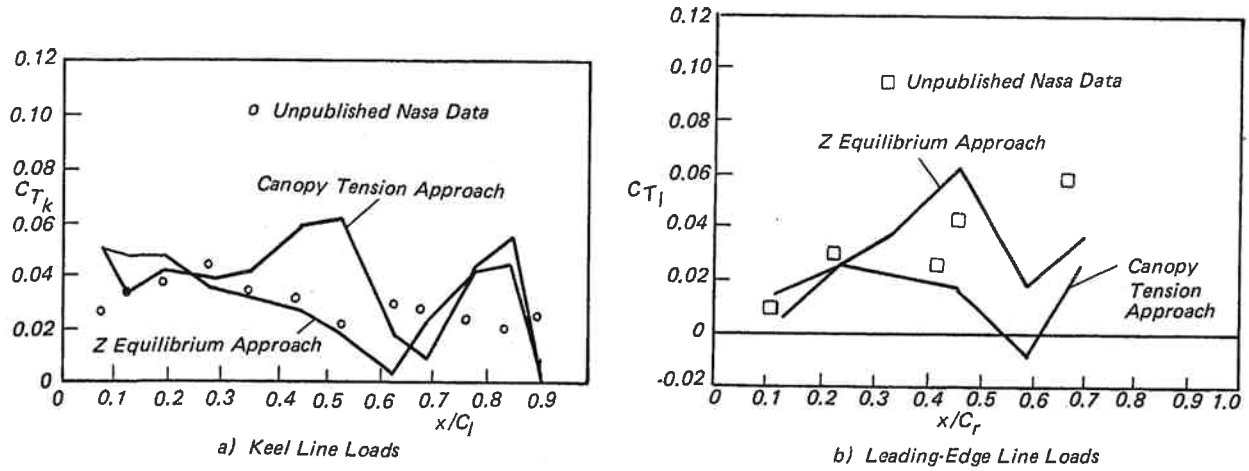
Defining the shape of a gliding parachute surface at the instant the canopy is subjected to a critical differential pressure is a major problem of internal loads analysis. The complexities are greater than with axi-



a) Canopy Tension Approach

b) Z-Equilibrium Approach

Figure 7.22A Circular Approximation of Spanwise Profile of the Twin Keel Parawing



a) Keel Line Loads

b) Leading-Edge Line Loads

Figure 7.22B Comparison of Predicted and Measured Line Loads for Twin-Keel Parawing

symmetric structures, despite use of reefing techniques to reduce disymmetry during the early stages of the inflation process. The nature of the problem is illustrated by Kenner[380] in his analysis of a twin-keel parawing that failed during the second reefed stage. His approach was to sub-divide the surface into a number of small triangular elements, with reinforcing tapes defining some boundaries. The load-strain and stiffness properties of each surface and tape element were specified, and the state of initial stress in each element was determined by an iteration process to ensure a correct start on the solution. Then the element and system stiffness matrices corresponding to the initial stresses and initial configuration were formed. The boundary conditions were selected to represent the flight conditions as closely as possible. The critical parawing lobe was free except for the restraints at the center-lobe reef point and the suspension line attach point to the test vehicle. The result was a 234-DOF representation of the finite element model. Failure to obtain convergence of the model on the measured applied loads by the linear incremental method made it necessary to use a piecewise linear iteration technique to obtain a solution. Among his conclusions, Kenner stated, "although the iterative solution converged only approximately, the results predicted stress levels sufficient to cause failure in the region where a failure was experienced in the drop test". Lack of suspension lines at all reinforcement tapes was indicated as the probable cause of failure.

Another approach to the internal loads analysis of single and twin keel parawings is illustrated in Reference **533** where Spangler and Nielsen describe a method of predicting the aerodynamic performance of all flexible parawings. The spanwise profile of the

fully inflated canopy was approximated with a circular arc in a conical surface as shown in Figure 7.22A. Two approaches to the transfer of the surface load to the suspension lines were tested analytically with the results indicated by the comparison of predicted and measured line loads shown in Figure 7.22B.

While the Z-equilibrium approach appears to be adequately conservative over most of the structure, the applicability of this steady-state model to dynamic inflation conditions is uncertain and such application was not proposed by the authors. The analytical method (Ref. 380), represents one potential starting point toward development of a more complete mathematical model designed for the prediction of internal fabric stresses in the canopy as well as suspension line loads.

AERODYNAMIC HEATING TEMPERATURES

Discussed in Chapter 6 were several different types of decelerator structures and materials subject to aerodynamic heating, including::

Woven cloth and mesh surfaces, effective porosities ranging from C = 0 to 0.3 approximately.

Flat ribbon grids with ribbon widths ranging from 0.25 to 2.0 inches and geometric porosities of λ_g = 5 to 35 percent.

Circular canopies with both concave (parachute) and convex (Ballute) surfaces of varying thickness subject to high heat flux rates.

Nylon, Dacron, Nomex, stainless steel, etc., textiles either bare or with protective coatings of various compounds.

The nature of available empirical data constrains definition of component models that are both realistic and amenable to practical analytical treatment. A porous cloth or mesh surface has been treated as one composed of two-dimensional cylindrical elements bounded by slots, or as a cluster of nozzles consisting of circular orifices with rounded entries. Since bare yarns are not smooth cylinders but porous bundles of fibers or filaments, this characterization would be best for coated yarns in a porous mesh. Flat ribbon grids of any type act more like clusters of sharp edged orifices than nozzles, even with beaded edges on the ribbons. However, treating narrow coated ribbons as cylinders of equivalent cross section and a rectangular orifice as equivalent to a round one of the same hydraulic diameter has given good results[487] The skirt leading edge of a parachute or the side-walls of a Ballute have been treated as slabs of poor thermal conductivity.

Total Energy Balance

Expressed in the form given in Reference 534, the total energy balance is

$$\underset{(a)}{HS_1(T_{AW}-T_W)} + \underset{(b)}{I\alpha S_2} - \underset{(c)}{\sigma S_3 \epsilon (T_W^4 - T_t^4)} - \underset{(d)}{\sigma F_4 S_4 \epsilon (T_W^4 - T_E^4)} = \rho_m V_m C_{pm} (dT/dt) \qquad 7\text{-}108$$

Term *(a)* is the energy input caused by the canopy motion through the air in the wake of the towing body; term *(b)* is the energy input by solar radiation; term *(c)* is the energy loss by radiation to space, and term *(d)* is the energy loss by radiation to the Earth. This total is equal to the rate at which energy is stored in the decelerator, where T is the average instantaneous temperature of the decelerator mass, and T_W is the temperature of the decelerator surface, $\rho_m V_m$, and C_{pm} is the average specific heat of the materials in the structure. Terms *(b)* and *(d)* are generally negligible relative to *(c)*. Also, compared to equilibrium temperatures of practical interest the temperature of space, $T_t = 7^\circ R$, is negligible. As applied in Reference 534 analysis the numerical subscripts identify the parameters at the stations shown in Fig. 7.23. For calculation of maximum temperatures the heat storage term may be omitted and equation 7-108 becomes simply a balance between the convective and radiative heat fluxes.

$$HS_1(T_{AW}-T_e) = \sigma S_3 \epsilon T_e^4 \qquad 7\text{-}109$$

T_e = the equilibrium surface temperature

H = convective heat transfer coefficient

S_1 = surface area exposed to aerodynamic heating

T_{AW} = adiabatic wall temperature

σ = modified Stefan-Boltzman constant ($= 0.173 \times 10^{-8}$ Btu/ft^2 - hr - $^\circ$R^4)

S_3 = projected surface area radiating to space

ϵ = emmissivity of material for long wavelength radiation

For calculation of the instantaneous material temperature, the following must be known at each point of the trajectory.

The local heat transfer coefficient

The surface emittance

The thermal diffusivity of the material

Temperature-time histories may be computed using the assumption of infinite object thermal conductivity coupled to the total capacity of the canopy as a heat sink[534]. For this purpose the simplified heat

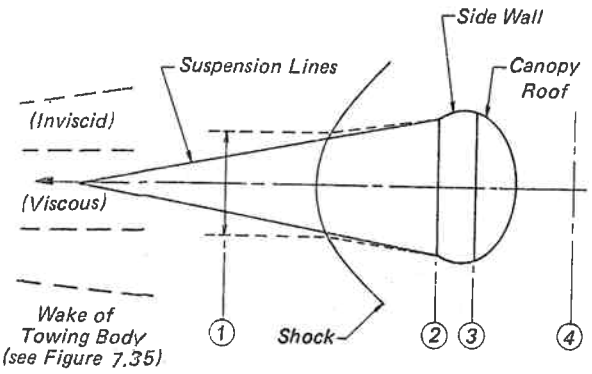


Figure 7.23 Flow Field of Supersonic Drogue for Dynamic Heating Analysis

balance equation is rewritten

(heat in) - (heat out) = (heat stored)

$$HS_1 (T_{AW} - T_e) - \sigma S_3 \epsilon T_e^4 = \rho_m V_m C_{pm} (d\bar{T}/dt) \quad 7\text{-}110$$

The recovery or adiabatic wall temperature is close to the free-stream total temperature through the relationship

$$T_{AW}/T_\infty = [1 + bM_\infty^2 (\gamma - 1)/2]/ \quad 7\text{-}111$$
$$[1 + M_\infty^2 (\gamma - 1)/2]$$

because values of the recovery factor fall between

$$0.85 \approx P_r^{1/2} = b \text{ (laminair)} \leqslant b \leqslant \quad 7\text{-}112$$
$$b \text{ (turbulent)} = P_r^{1/3} \approx 0.90$$

except that $P_r^{1/3}$ applies only to locations on flat plates beyond the transition region and not to other geometries[535]

Equation 7-109 written as

$$T_e^4/(T_{AW} - T_e) = (H/\sigma\epsilon)(S_1/S_3)$$

is a convenient form for solution by trial and error. However, the following method may be used to obtain an explicite solution for T_e[534]

$$T_e = \tfrac{1}{2}[-L^{1/2} + (L - 2(L - m/L^{1/2}))^{1/2}] \quad 7\text{-}113$$

where

$$L = \left[\frac{m^2}{2} + \left[\frac{m^4}{4} + \frac{64n^3}{27}\right]^{1/2}\right]^{1/3} +$$
$$\left[\frac{m^2}{2} - \left[\frac{m^4}{4} + \frac{64n^3}{27}\right]^{1/2}\right]^{1/3}$$

$$m = (H/\sigma\epsilon)(S_1/S_3)$$

$$n = (H/\sigma\epsilon)(S_1/S_3) T_{AW}$$

A source of uncertainty in equations 7-109 and 7-110 lies in the evaluation of the convective heat transfer coefficient, H. In dimensionless form the convective heat flux is characterized by the Nusselt number which is a function of the following parameters

$$Nu = HI/K = f(R_e, M, P_r, K_n, T_w/T_o', \text{geometry}) \quad 7\text{-}114$$

where I is a characteristic length of the surface element, as in R_e, parallel to the flow, and K is the thermal conductivity of the fluid.

From the standpoint of boundary layer growth the canopy skirt is best simulated by the turbulent-flow flat-plate model. In a woven mesh the characteristic length is provided by the size of the element treated as the diameter of a cylinder. Such dimensions range from $I = 0.004$ to 0.050 inches, while heavily coated yarns, netting cords, or their equivalents may extend this range to $I \approx 0.25$ inches diameter. The conical surface of the Ballute represents a much larger scale, the characteristic length being commensurate with D_p. The flat ribbon grid normal to the flow does not fit the direct boundary layer convective heating concept and so merits a different approach. Thus, for geometrical reasons alone, H must vary widely.

Because the flow conditions causing aerodynamic heating usually produce super-cricital pressure ratios, sonic flow velocities probably exist in the "nozzle-throats" of the porous surface. With this assumption, a unit "sonic" Reynolds number may be defined for such nozzles as

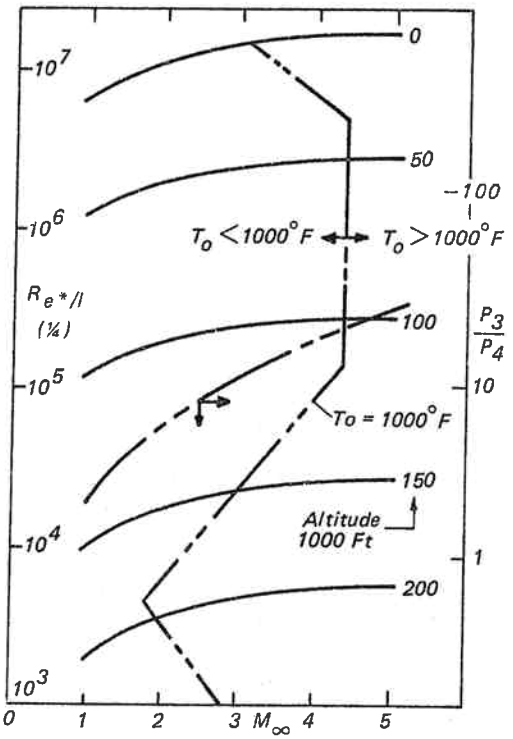


Figure 7.24 Sonic Reynolds No. and P_3/P_4 vs. Mach No. (Ref. 534)

$$R_e^*/l = \rho^* c_s^*/\mu^* \qquad 7\text{-}115$$

which, calculated for a normal shock compression and isentropic expansion starting with standard atmospheric properties, provides a criterion of how H may vary with speed and altitude, as shown in Figure 7.24. The broken line for a theoretical stagnation temperature of $T_o = 1000°F$ illustrates the heat transfer problem in relation to flight speed or Mach number at Station (1) in Figure 7.24. Since the analysis in Reference 534 did not consider the presence of a forebody wake and corresponding modifications of the canopy shock wave, the heat flow parameters at Station (1) are free stream (trajectory) values. For calculation of wake flow conditions for canopies operating in body wake a flow field analysis (see page 373) should be accomplished to define flow parameters at this location. Because measured stagnation temperatures are substantially less than calculated and material temperatures are only small fractions of T_o, the regime to the left of this boundary represents the approximate operational envelope for all types of drogues fabricated from nylon and polyester textiles which are subject to a heat pulse. The regime to the right of the boundary is the one for which thermodynamic analysis would be advisable for determination of probable material temperatures.

It will be recognized that the velocity of sound in the quasi-nozzle throats is a function of both the composition and temperature of the airflow there and that the effect of temperature variations from the idealized conditions would change the slopes of the altitude profiles of R_e^*/l vs M in Figure 7.24. Similar charts may be constructed for other planetary atmospheres as the data from space-probes and other sources accumulate.

The upstream flow Mach number M, in the body wake has only an indirect influence of the heat transfer to the fabric surface elements in the determination of temperature and pressure both inside and behind the canopy. For the flow and heat transfer around the surface elements, the local static pressure ratio across the canopy surface elements, P_3/P_4 is a more suitable parameter.

Values for this pressure ratio may be established experimentally[536] or analytically using the theory discussed on page 375 .

The Prandtl number, under normal atmospheric conditions, has a value

$$P_r = C_p \mu/K \approx 0.7 \qquad 7\text{-}116$$

and may vary no more than ±10 percent at temperatures up to 6,000°R. Thus, for practical purposes, P_r may be considered nearly constant for air at all flight speeds up to Mach 10.

The Knudsen number becomes significant when the molecular mean free path is large relative to the scale of the process. For the boundary layer type of flow, the transition from the continuum to slip-flow regimes occurs when the molecular mean free path, λ, reaches some fraction of the boundary layer thickness σ. This relationship is expressed by the ratio

$$K_n = \lambda/\delta = M^2/R_e \qquad 7\text{-}117$$

The observed limit of continuum boundary layer flow[535] is $K_n < 0.01$ and the slip-flow transition to free molecule flow is considered to extend from $K_n = 10^{-4}$ to 10^{-2}. The conditions under which the continuum model of flow first fails is called ***slip-flow*** because it may be analyzed by assigning temperature and velocity "slip" at fluid-solid interfaces.

In Reference 534 the critical Knudsen number is taken as the mean value

$$M^2/R_e = 10^{-3}$$

by which the corresponding "critical" Reynolds number is simply

$$R_{e_c} = 1000\, M^2 \qquad 7\text{-}118$$

Then, as a minimum, the value for continuum flow conditions, through porous meshes at $M = 1.0$ would be $R_{e_c} = 1000$, or in Fig. 7.23 for $l = 0.25$ to 0.004 inches

$$R_e^*/l = 4.8 \times 10^4 \text{ to } 3.0 \times 10^6$$

The corresponding transition altitude limits are roughly 140 thousand feet for the coarse heavy mesh and 40 thousand feet for the fine mesh.

Applied to a 5 ft D_p Ballute deployed at velocities such that the local Mach number $M' = 5$ to 10, the critical Reynolds number is

$$R_{e_c} = 2.5 \times 10^4 \text{ to } 10^5$$

Since it is reasonable to write

$$R_e^*/l = R_e/lM' \qquad 7\text{-}119$$

the equivalent values in Fig. 7.25 are approximately

$$R_e^*/l = R_{e_c}/5M' = 10^3 \text{ to } 2 \times 10^3$$

and the transition altitudes are well over 200,000 ft.

Thus, the assumption of continuum flow conditions for most Ballute applications appears reasonable but slip-flow conditions may apply to some applications of supersonic drogues with mesh roofs. Drogues with flat ribbon grids in the roof area and $l \geq 0.25$ inches presumably would experience the transition from continuum flow to slip-flow conditions at altitudes greater than 140,000 feet, but it is doubtful that boundary layer growth in orifices of small length to diameter ratio would be significant.

The low velocity high pressure flow over the upstream face of a ribbon grid appears analogous to that in a viscous boundary layer and it would therefore be

reasonable to use Reynolds and Nusselt numbers based on the ribbon width. From this quasi-stagnant reservoir in the canopy the hot compressed air expands and accelerates through the sharp-edged orifices comprising the inter-ribbon slots, presumably separating from the lip and contracting somewhat until sonic velocity is reached a short distance behind the surface. At the separation point on the lip, the radius of which would be relatively small, viscous dissipation could be a significant factor in the heat transfer equation, and consequently maximum temperatures may occur on the edges of the ribbons.

Scott and Eckert[536] describe this process in greater detail. Experiments were performed to determine the inter-relationships between R^*_e, Nu and P_3/P_4, with Nu based on the stagnation conditions of the approaching flow behind a normal shock

$$Nu = Hl/K_o = [\dot{q}/(T_{AW}-T_W)](l/K_o) \qquad 7\text{-}120$$

where K_o is the thermal conductivity of the air at the stagnation temperature.

The measured pressure distribution across the upstream face of a ribbon was quite uniform, being within one percent of the stagnation pressure for all Reynolds numbers up to $R^*_e = 8.4 \times 10^6$. Average values of the Nusselt numbers across the upstream and downstream faces of the ribbons were evaluated as a function of R^*_e and combined with similar data from other sources in Figures 7.25 and 7.26. The measured distribution of heat transfer coefficients is shown in Figure 7.27. It will be noted that the ratio H/H_{ST} increases rapidly toward the edges of the ribbon in a way that varies sharply with R^*_e. The variation of R^*_e is shown in Figure 7.28. These correlations make it possible to estimate a value of H for the calculation of the probable maximum material temperature in a ribbon grid subject to a transient heat pulse characteristic of the typical supersonic drogue operation. The more complex considerations relating to conditions where aerodynamic heating may be sustained long enough for thermal equilibrium to be approached are given full treatment in Reference 536 Under equilibrium conditions the maximum temperature is expected to be in the center of the ribbons rather than at the edges.

The Disk-Gap-Band Canopy in Low Density Environment.

Gillis[486] reports that a 40 ft D_o disk-gap-band canopy sustained extensive damage from aerodynamic heating after deployment at Mach 3.31 and an altitude over 100,000 feet. A post-flight examination of the parachute revealed that the heating damage had originated in the stagnation region of the crown rather than on the skirt hem, as a previous heating analysis had predicted. This finding motivated development by Bobbit[537] of an analytical method for predicting the aerodynamic heating at the flow stagnation line. Equilibrium surface temperatures calculated by this method are plotted in Figure 7.29 for two different flight tests of the parachute at high altitudes where the dynamic pressure was in the order of 9 to 12 psf. The results suggest that the observed failure of the polyester canopy could have been predicted.

The Ballute in the Wake of an Axi-Symmetric Body

Calculation of Ballute material temperatures generated by a transient dynamic heat pulse is complicated by towing body wake effects that cannot be neglected, as was done in the analysis of drogue parachutes. Because, as indicated in Reference[215] a viscous turbulent cylindrical wake between the two bodies would be approximately twice the diameter of a laminar type wake, it was necessary to establish a criterion to indicate whether the wake would be laminar or turbulent. One approach is to test the boundary layer on the towing body. If this boundary layer is turbulent, the cylindrical wake will be turbulent. The boundary layer transition from laminar to turbulent was assumed to occur in the customary Reynolds number range of $R_{e\delta} = 400$ to 600, when the following equation is used

$$R_{e\delta} = \rho_1 v_\infty \delta/\mu_1 = 0.695\,(\rho_w \mu_w/\rho_1 \mu_1)^{0.114} (\rho_1 v_\infty x/\mu_1)^{0.5} \qquad 7\text{-}121$$

where δ is the momentum thickness.

When the above criterion indicates laminar flow, a transition analysis may be performed to determine its state. In the absence of wake transition data for the flow between two bodies, free wake data may be used. This entails evaluation of the following wake transition parameter

$$R^*_{e\,x_\infty} (M_\infty/M_e)^2 = (\rho_\infty v_\infty x^*/\mu_\infty)(M_\infty/M_c)^2 \qquad 7\text{-}122$$

where * denotes a transition value. The wake transition parameter as evaluated for Ballute flight test TB-4 is shown in Figure 7.30.

For a laminary boundary layer, the heat transfer coefficient on the Ballute surface was

$$H/H_c = (p'/p_\infty)(r'/D_p)\,(x'/D_p)^{0.5} / \sqrt{3}(p_c/p_\infty)^{0.5} \left[\int_0^{x'/D_p} (p'/p_\infty)\,(r'/D_p)^2\, d(x'/D_p)\right] \qquad 7\text{-}123$$

where c denotes "cone", and the prime indicates properties evaluated fro conditions existing at the edge of the boundary layer and at the particular station under consideration. Given the flow properties of the wake and dimensions of the Ballute, the pressure distribution over the surface may be calculated by the tangent-cone method since the flow prop-

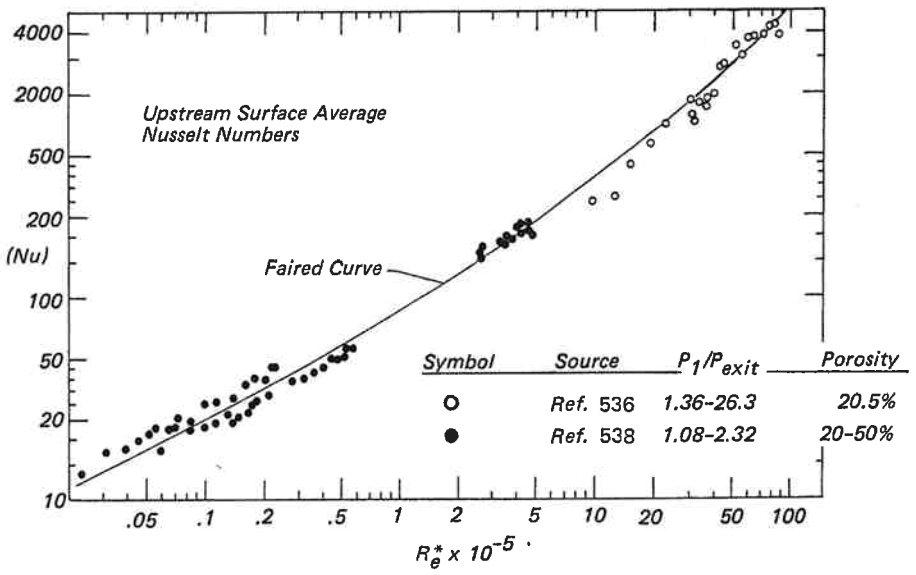


Figure 7.25 Experimental Heat Transfer Results (Upstream) for Parachute Ribbon Grids

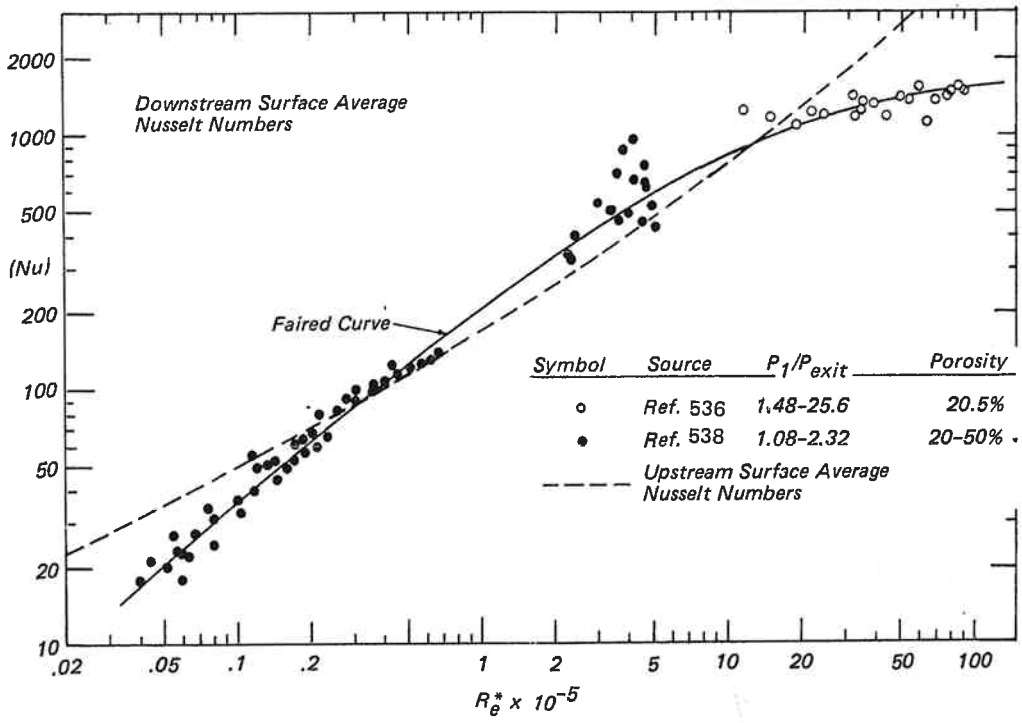


Figure 7.26 Comparison of Upstream and Downstream Experimental Heat Transfer Results

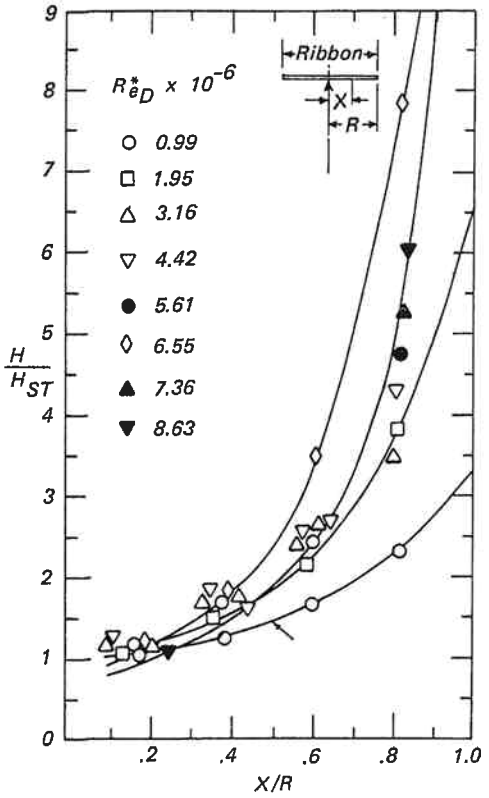


Figure 7.27 Distribution of Heat Transfer Coeffi - cients on Upstream Side of Ribbon Grid (Ref. 536)

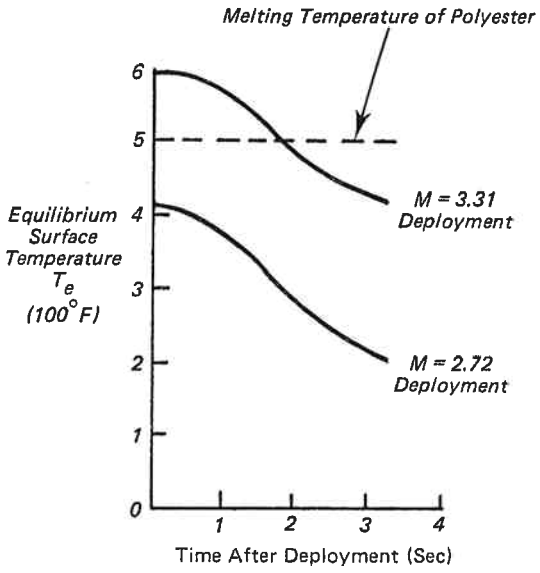


Figure 7.29 Calculated Temperatures in Crown of 40 Ft D_o Disk-Gap-Band Parachute (Ref. 486)

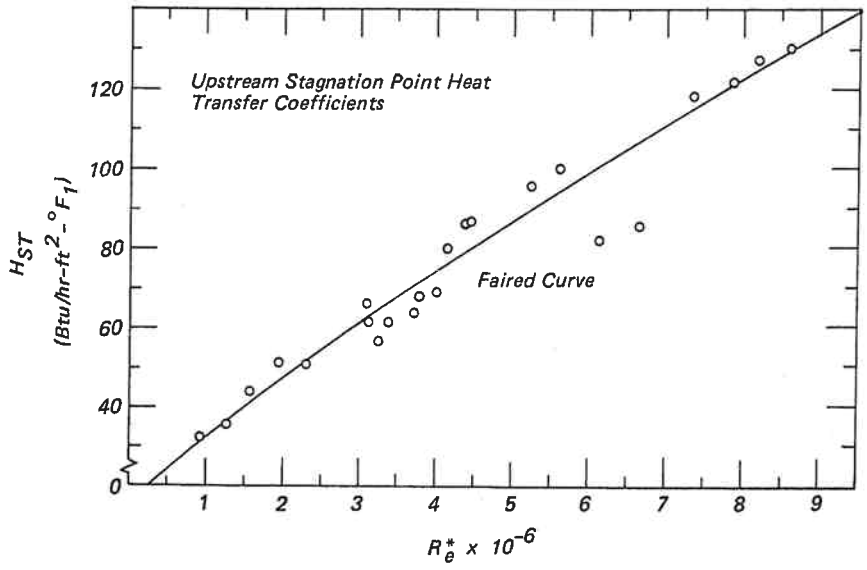


Figure 7.28 Stagnation Point Heat Transfer to Ribbon Grid

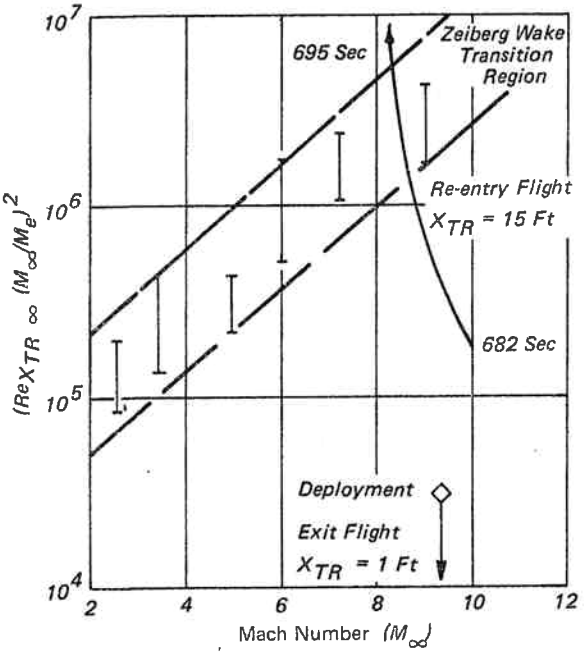


Figure 7.30 Unified Wake Transition Criterion for Ballute Flight Test TB-4 (Ref. 215)

erties of the wake and the geometry of the decelerator are known (see Fig. 7.31).

For a turbulent boundary layer, the heat transfer distribution over the Ballute surface was calculated

$$\dot{q}_w = 0.0296\,\rho' u' (Q_1 - Q_w)/ \qquad 7\text{-}124$$
$$(\rho^* u' x/\mu^*)^{0.2} P_r^{2/3}$$

Where the starred quantities must be evaluated using the local pressure and the reference enthalpy

$$Q^* = Q' + 0.45(Q_w - Q') + 0.20(Q'_{AW} - Q') \qquad 7\text{-}125$$

As in the laminar flow case, evaluation of the turbulent flow heat flux rates depends upon the properties of the wake flow found ahead of the Ballute. Some simplification of method is realized by confining the investigation to determination of the maximum temperature rise in the decelerator material during flight along a prescribed trajectory. Equations 7-124 and 7-125 were used.

The local surface Mach number, M', was assumed to result from flow crossing an oblique shock at Mach number M_e, as was suggested in Fig. 7.31. Empirical data on Ballute pressure distributions support a method of estimating the location and value of the peak pressure coefficient. Application of the method to the conditions of Ballute Test TB-4 is illustrated in Figure 7.32. The Ballute was treated as a slab of low thermal conductivity. For these and other details of the analysis, see Reference 215 and supporting References 222 and 539 - 541.

The cold wall heat flux rates calculated for Ballute Test TB-4 are plotted in Figure 7.33. A comparison of calculated and measured material temperatures is presented in Figure 6.92.

WAKE FLOW CHARACTERISTICS

The drag and stability of drogue-type decelerators are strongly influenced by the character of the wake-flow from the towing body impinging on the inflated canopy. Supersonically, aerodynamic heating of the structure also depends on the way in which the body wake modifies the flow about the decelerator. Because of the marked differences between subsonic and supersonic wake-flow phenomena, the two subjects are treated separately.

Subsonic Wake

As shown by empirical data in Chapter 6, the body towing the decelerator imparts momentum to the air and the resultant disturbance has a characteristic velocity distribution across a plane normal to the flight path (Fig. 6.41), Δv_w being a maximum on the wake centerline. The wake, a turbulent core of a diameter proportional to the size and shape of the body, is symmetrical about the axis of bodies of revolution at $\alpha = 0$, and becomes assymetric when the body shape attitude, or angle of attack induces a side or lift-force component. Downstream the disturbed air progressively mixes with the ambient air mass, the wake becomes broader and slower (Fig. 6.44) and gradually returns to normal, as shed vortices dissipate their acquired energy in frictional heat.

Consequently, a towed decelerator experiences a reduction in the average impact pressure across the canopy, along with a change in the distribution of Δp, which for a given body is inversely proportional to the relative sizes, D_p/d_b, and trailing distance, l_T/d_b. The relative change in differential pressure is determined by the square of the velocity ratio $(v_w/v)^2$ and also may be represented by a fictitious relative drag coefficient as in Fig. 6.43 for different diameter ratios and trailing distances. Thus, in order to determine the proper size of the decelerator and the length of its riser, it is desirable to be able to predict the Δp that will be felt by each element of the canopy at any given trailing distance. The subsonic wake flow problem takes its simplest form for a body of revolution at zero angle of attack with no trailing decelerator. Empirical data, such as the small model wind-tunnel test measurements plotted in Fig. 6.35, indicate that introduction of the decelerator into the body wake likely has a negligible effect on the upstream velocity, so that solution of the bare body problem may yield

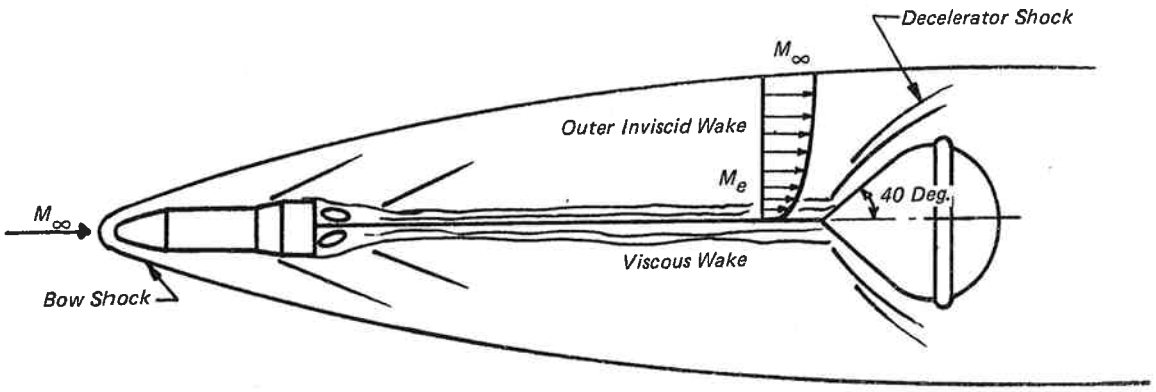


Figure 7.31 Vehicle-Ballute Flow Field Schematic

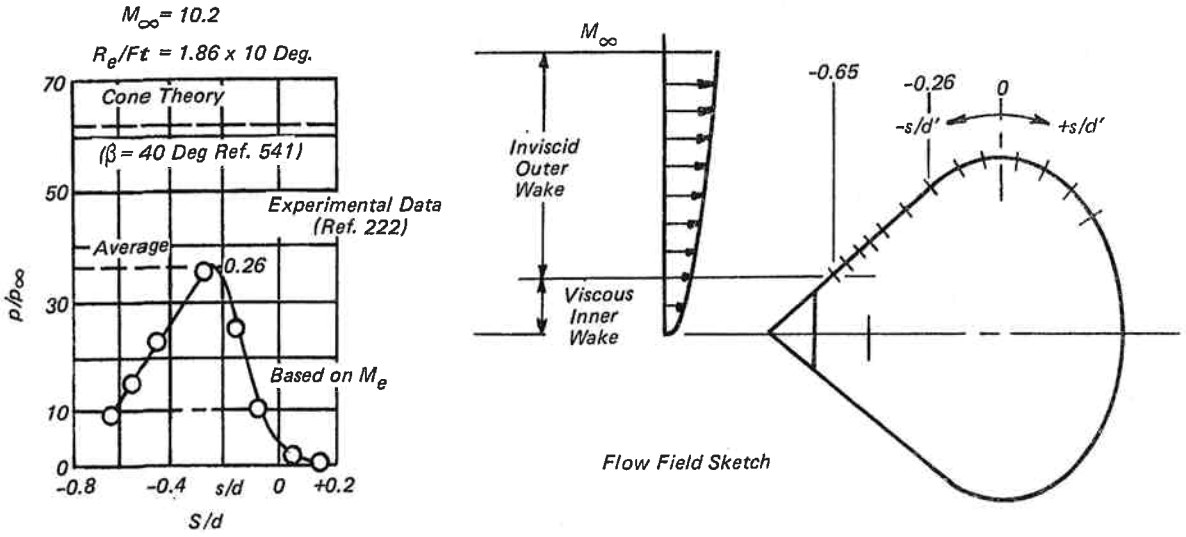


Figure 7.32 Pressure Distribution Over Ballute (Test TB - 4)

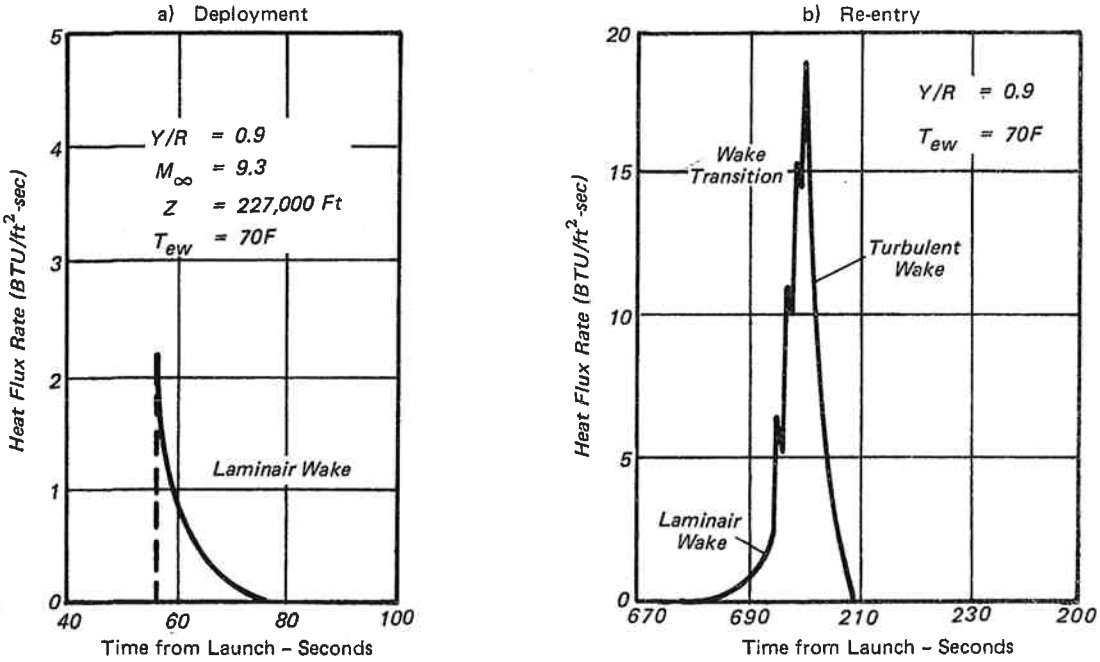


Figure 7.33 Ballute Cold Wall Heat Flux Rate (Test TB - 4)

useful results of more than academic interest.

The following solution for the velocity distribution in the wake of bodies of revolution was developed by Heinrich and Eckstrom[418]

$$\frac{\Delta v_W}{v} = \frac{a_W}{(x/d_b)^m e^{\frac{-(2r/d_b)^2}{0.435 K_W^2 (x/d_b)^{2n}}}} \qquad 7\text{-}126$$

where $\Delta v_W = v - v_W$

v_W = mean wake velocity in x direction at r

a_W = centerline velocity increment coefficient

r = radial distance from wake centerline

K_W = wake width coefficient for $r = r_W$ where $\Delta v_W/\Delta v_W\ (max) = 0.10$

m = center line velocity increment exponent

n = wake width exponent

It was shown that the constant coefficients and exponents were functions of the body drag coefficient, and the test data presented justified use of the following relationships in the region between $x/d_b = 2$ to 20 when $C_D < 1.1$.

$$a_W = 0.42\, e^{0.99 C_D}$$

$$K_W = 0.54\, e^{0.84 C_D}$$

$$m = 0.85$$

$$n = 0.47$$

The dimensionless wake width is $2r_W/d_b = K_W (x/d_b)^n$.

A comparison of typical experimental and theoretical results is shown in Fig. 6.44, the hemispherical cup representing the main canopy of a tandem parachute system.

In order to use these empirical relationships to determine the drag of a canopy of radius r_p/d_b at a position x/d_b in the body wake, it is necessary to determine the average dynamic pressure across the canopy. At any radial distance, r, the dynamic pressure ratio is

$$q_W/q = (v_W/v)^2 \qquad 7\text{-}127$$

Since $v_W/v = 1 - (\Delta v_W/v)$

$$q_W/q = [1 - (\Delta v_W/v)]^2$$

and the average dynamic pressure acting on the canopy may be obtained by integrating equation 7-127 across the canopy radius

$$(q_W/q)_p = \frac{1}{r_p}\left[1 - \int_0^{r_p} (\Delta v_W/v)^2\, dr\right]$$

where $\Delta v_W/v$ is the function of r given by equation 7-126 and x/d_b is determined by the length of the drogue suspension lines plus riser (Fig. 6.60). It may be assumed that the wake originates at the point of major flow separation on the body.

A similar integration was performed[542] for the velocity distribution equation in this form

$$\frac{V_W}{V} = 1 - K_1\, e^{K_2 (2r/d_b)^2} \qquad 7\text{-}128$$

where

$$K_1 = \frac{0.107}{(x/d_b)^m}\left[\frac{(C_D \pi)}{4 K_b^2}\right]^n$$

$$m = 2/3$$

$$n = 1/3$$

$$K_2 = \frac{-0.415}{(x/d_b)^m (C_D \pi K_b)^m}$$

The diameter of the wake, D_W, was defined by the value of r at any x where $q_W/q = 0.99$. Integration of the velocity distribution over the inflated canopy mouth resulted in this expression for the dynamic pressure ratio.

7-129

$$\frac{q_W}{q} = 1 - \frac{K_1}{K_3}\left[\frac{K_1}{2} - 2 + e^{K_3}\left(2 - \frac{K_1}{2} e^{K_3}\right)\right]$$

where

$$K_3 = (D_p/D_W)^2\, ln\left[K_1/(1 - \sqrt{0.99})\right] \qquad 7\text{-}129$$

A method of solving equation 7-129 is given in Figures 7.34, 35 and 36.

The near-wake of bodies lacking rotational symmetry is unsymmetrical, but if the body lift force component is small, it may be presumed that symmetry of wake-flow downstream will improve. Thus, except in extreme cases, reasonable solutions of equations 7-126 and 7-129 may be obtained by substitution of the hydraulic diameter of the body frontal area for d_b.

Supersonic Wake

The problem of determining the pressure distribution over a decelerator immersed in a supersonic body wake was illustrated in the preceding section related to the prediction of aerodynamic heating effects. The presence of the decelerator alters the character of the upstream flow significantly, so no generalized wake-flow solution can be presented based solely on the body drag coefficient as in the subsonic case described. However, Henke[543] developed a method of predicting the boundary layer and wake characteristics of axi-symmetric bodies moving at supersonic

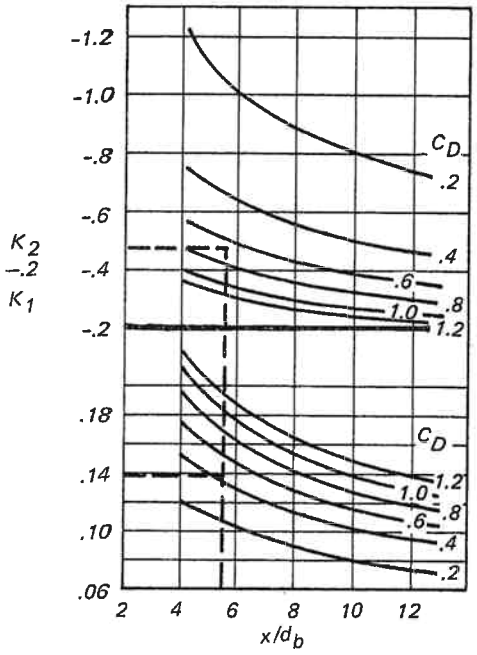


Figure 7.34 Wake Coefficients vs (x/d_b)

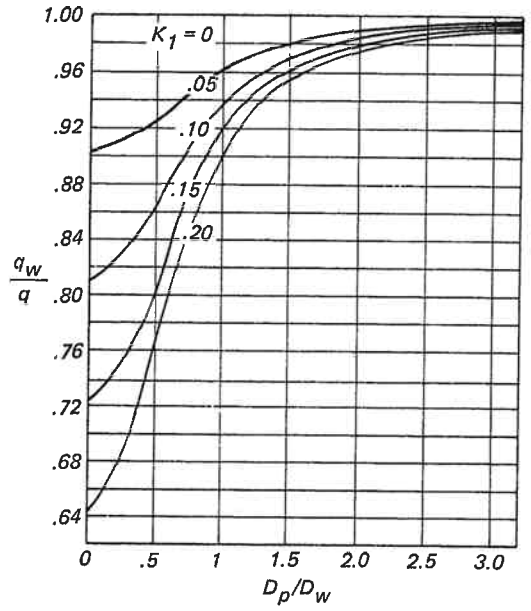


Figure 7.36 Average Dynamic Pressure on Decelerator in Body Wake

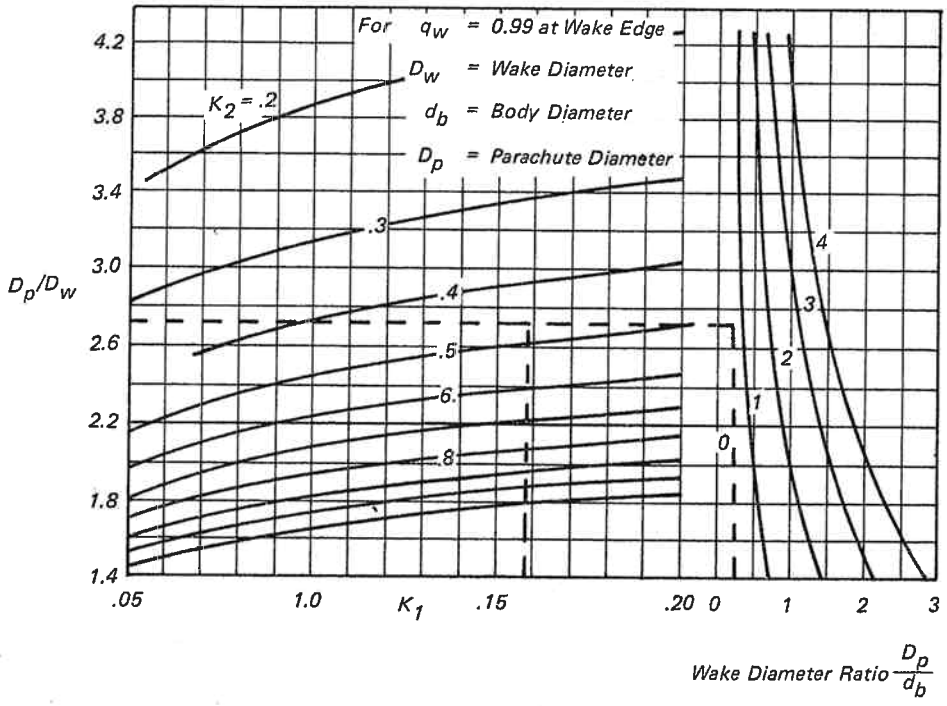


Figure 7.35 Diameter of Wake

speed: based on the body geometry and free stream conditions. The method is applicable to axi-symmetric or two-dimensional bodies and may be used for approximating the flow over quasi-symmetric bodies. Also presented is a method for computing the drag of Parasonic drogues using the wake flow field immediately ahead of the canopy as the free-stream conditions.

Noreen, Rust and Rao[432] developed a method for calculating the flow field characteristics of a body-decelerator system in supersonic flow. Two separate flow field analyses are involved: (1) the body and its wake and (2) the decelerator.

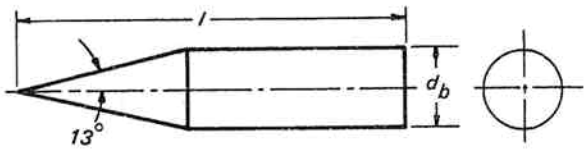
The body and wake analysis (drawing heavily on the work presented in Reference 543) examines the flow about the body extending axially from the bow shock downstream to the secondary body bow shock and normally from the surface of the forebody outward to its bow shock. The analysis assumes that the flow conditions upstream of the body are uniform. The body and wake analysis requires the following:

a. freestream conditions
b. body geometry
c. bow shock and standoff distance.

In addition to body geometry and freestream conditions, the body sub-routine produces the calculated local static pressure, total pressure and Mach number on the body surface at various axial locations and on various planes containing, and rotated about, the axis. Since the flow characteristics at the base of the body are likely to be affected by a possible transition into turbulence on the body surface, the transition point location on the body surface and on various ϕ planes is also printed out. Reynold's number, based on momentum thickness, inviscid density, local inviscid velocity, local momentum defect, and momentum thickness at the base for different ϕ planes, is provided. Integration of the local momentum defect around the surface at the body base provides the total momentum defect, which will be used in wake computations.

Wake computations begin with body boundary layer and base condition inputs. The program selects either laminar or turbulent wake conditions, based on the transition Reynold's number, and prints out the input values of the viscosity model. At every l_T/d_b location behind the base of the body and at every iteration of wake computation, various wake geometry and flow field parameters are provided for either the viscous or inviscid wake.

Using the above methods, sample calculations were completed for a cone-cylinder body in a supersonic flow with $M = 2.98$ and a Re/ft of 8.86×10^5. The results of these calculations were checked[432] with wind tunnel experiments conducted at the Rosemount Aeronautical Laboratories, University of Minnesota, at the Supersonic Gas Dynamics Facility of the Flight Dynamics Laboratory at Wright-Patterson Air Force Base, and at the Arnold Engineering Development Center's Von Karman Gas Dynamics Facility. Figure 7.37 shows the geometry of the body and the two sizes that were tested; calculations were made for the $d_b = 2$ inch body.



$l/d_b = 6.195$

Test Facilities

$L = 7.428$ In. $d_b = 1.200$ In.	U of M
$L = 12.390$ In. $d_b = 2.00$ In.	AFFDL - SGF AEDC - VKF

Figure 7.37 Geometry of Bodies Used for Experiments

The analysis used for the decelerator extends axially from the upstream tip of the decelerator downstream to its base. The wake of the decelerator is not included in the analysis. Normal to the axis of symmetry, the analysis extends from the decelerator surface to its bow shock wave; flow field characteristics outside of the bow shock can be obtained from the wake analysis of the body.

The information required for the decelerator analysis includes the upstream flow properties, the pressure and temperature distributions, and the geometry of the decelerator. The upstream flow conditions can either be calculated using the primary body analysis or input to the program. In order to obtain a pressure drag coefficient, the base pressure of the body must be obtained. The method calculates all the flow properties from the decelerator surface to the shock wave. Thus, the shock shape, surface pressures, and pressure drag are obtained.

In order to predict the flow field surrounding an aerodynamic decelerator in the wake of a body, several assumptions and restrictions have been made:

1. the flow is inviscid and steady
2. the gas is thermally and calorically perfect
3. the flow is supersonic everywhere in the region of interest
4. the wake flow field is known, either from theory or experiment

The first three assumptions permit one to develop a method of characteristics for rotational, non-homoenergic flow. The fourth assumption establishes an effective "upstream" boundary condition for the problem.

A primary and obvious limitation of this decelerator flow field analysis is that, since a characteristic method is used, it is limited to supersonic velocities. The most important implications of this fact are that the decelerator must have an attached bow shock and the analysis will only extend to the sonic line. Although this limitation is, in a certain sense, severe, there is yet a large number of bodies to which the method will apply.

A second limitation of the method is that the wake of the secondary body is not analyzed. The result of this is that base pressure must be obtained from another source to obtain a complete pressure distribution for a drag coefficient calculation.

Two main assumptions are made in using the method: first, it is assumed that a boundary. layer analysis is not needed to obtain the desired results, and second, that a reasonable sized decelerator tow line will not invalidate the calculation with an attached shock.

A detailed discussion of the computation in the shock layer flow field, such as the location of the shock points, net points, body points, and the properties along an initial right-running characteristic, is presented in Reference 432.

In order to check the results of a sample calculation using the analysis, experiments were conducted to measure decelerator (30° half-angle cone) bow shock shape and surface pressure distribution. These tests were conducted at the University of Minnesota's Rosemount Aeronautical Laboratories in a 12 in. x 12 in. blow-down wind tunnel at $M = 3.0$. The results presented in Reference 432 produced differences between calculated and measured values on the order of 10 percent.

STABILITY

The analytical treatment of decelerator system stability, beginning with parachute stability, depends upon empirical coefficients which traditionally have been obtained from wind tunnel tests. In free flight the instability of the body-decelerator system is evidenced by various types of angular deflections, relative to reference axes, which vary in amplitude and, when periodic, in frequency. Dynamic stability of a system is evidenced by the amplitude history of the oscillations, in particular, following a disturbance or perturbation of system motion. This makes the motion of a decelerator system during steady descent, where external disturbances can be strong, highly variable in character when static stability is poor, as it is with the typical parachute.

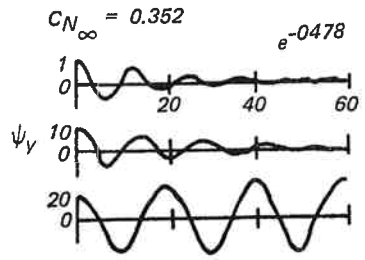
On the other hand, the flight stability of drogue decelerator systems is quite repeatable and fairly predictable on the basis of wind-tunnel test results when the effect of the constraints imposed on the wind tunnel models can be identified. Viscoelasticity and flexibility of decelerator structures, coupled with the variable porosity of the canopies, makes their treatment in terms of classical rigid-body aerodynamic analysis, an inexact process at best. However, the economics of decelerator testing in general makes it desirable to learn as much as possible from wind tunnel tests, or from model towing tests when the latter are less costly than free flight tests by an adequate margin.

Typical examples of parachute oscillatory motions predicted for different disturbances by the methods presented in References 482 and 544 are shown in Figures 7.38 and 7.39.

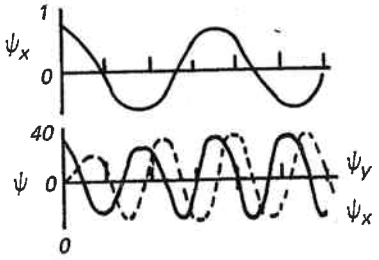
Drogue-Body Systems

As suggested by Fig. 6.74, the motion of the unstable drogue system may be significantly different from that of the unstable descent system, particularly when the body wake largely envelopes the canopy. The effect of downwash due to body lift, as noted in Chapter 6, is to reduce the average angle of attack, α', of the canopy to the relative air flow. Since the drogue system center of gravity is virtually coincident with the body center of gravity, a wind-tunnel mounting trunnion placed at that point affords good dynamic similitude. This approach has been widely used for the evaluation of both the static stability and dynamic stability of drogue-body and bomb stabilization systems in the wind tunnel.

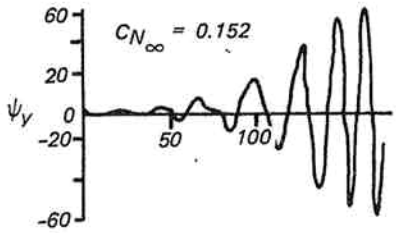
Statically, the system restoring moment is measured as a function of α_b, the body angle of attack. To the extent that the drogue follows the body motion as α_b varies and remains on the longitudinal axis of the body without axial pulsing, the system may be treated as a rigid body roughly analogous to the flared cone-cylinder configuration. This may hold for angles as large as $\alpha_b = 10$ degrees. However, this analogy is likely to break down for bluff bodies that develop little lift, such as an ejection seat, and for systems in which the drogue is large relative to the frontal area of the body. Then the drogue tends to trail directly downstream and body deflections are resisted by the drag moment of the canopy. For the latter configuration the limiting case is represented by a tethered parachute with negligible wake flow from the upstream mount, corresponding to a free system in which the body is very slender yet massive. The aircraft deceleration parachute may fall in this latter category, for which the empirical data on C_M *vs* α given in Fig. 6.72 would be pertinent to any deflection of the parachute axis from the relative wind axis. The motion during free flight and steady descent is usually less critical except for the special case of the reefed canopy, which generally functions as an effec-



a) *Computer Solutions for 1°, 10° and 20° Pitch Displacements of the Stable System*



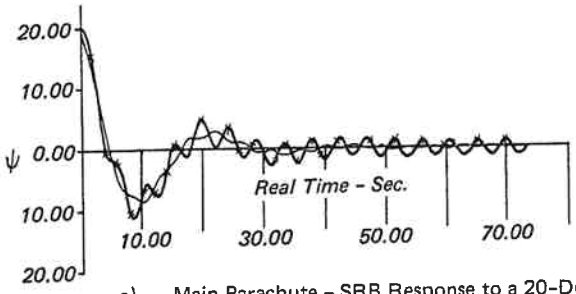
c) *Stable System Response to 1° and 40° Lateral Displacements*



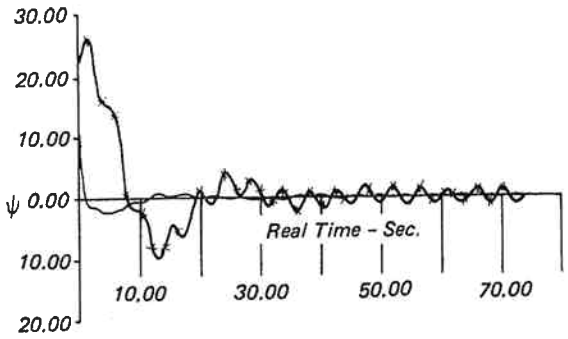
b) Divergent

b) *Response of the Unstable System to a 1° Pitch Displacement*

Figure 7.38 Dynamic Stability of Descending Parachute (Ref. 482)



a) Main Parachute – SRB Response to a 20-Deg Pendulum Disturbance (X-SRB, 2-Sec Intervals)



b) Main Parachute – SRB Angle of Attack Response to a 20-Deg Pendulum Distrubance (X-SRB, 2-Sec Intervals)

Figure 7.39 Typical Parachute Dynamic Stability Predictions (Shuttle Booster Recovery System (Ref. 515)

tive drag stabilizer because of its long relative towing distance and negligible added air mass.

Systems in Steady Descent

The generalized canopy of Fig. 6.33 develops an aerodynamic force, represented by the vector F, the direction of which changes as the relative airflow over the canopy changes. In three dimensions the airflow separates at the canopy lip erratically at various points around the periphery and eddies into a number of attached vortices which grow to some characteristic size and energy before being shed into the turbulent wake. Most circular canopies have no surface feature that would stabilize this flow pattern and either prevent unsymmetrical growth and separation of the vortices or cause them to remain attached in contrarotating pairs. Consequently, with parachute axis constrained by the suspended weight moment to a small angle of attack, the aerodynamic force vector of such canopies is constantly shifting in direction with varying degrees of randomness, and being unable to enter a stable glide, the system oscillates instead. However, it has been observed that a large enough angular deflection can throw the system into a steady coning motion, which may be viewed as a stable glide in a tight spiral.

The differences found between different types of circular parachutes is reflected by the way in which the moment generated by the shifting aerodynamic force varies with the angle of attack of the canopy (see Figures 6.72 and 6.73) The angle of attack at which $dC_M/d\alpha$ changes sign and produces a restoring moment with further angular displacement is identified[482] as the stable glide angle α_o. At this angle of attack the canopy is statically stable, and when a suitable structural dissymmetry is introduced, the parachute is able to take on a stable glide. A stable flow pattern over the canopy is then established which may be likened to that over a thick wing of low aspect ratio with attached tip vortices. Since the angle of attack ranges from $\alpha = 35$ to 15 degrees, such a wing must be gliding in a stalled condition, and transverse oscillations remain potential in the operation.

Dynamic Stability of Gliding Systems. The dynamic stability of a descending system gliding steadily with the canopy at α_o was the subject of a three-dimensional analysis by White and Wolf[482]

System geometry and coordinate systems used are shown in Figure 7.40. The following simplifying assumptions were made:

The system consists of an axi-symmetric parachute rigidly connected to a neutral body.

The aerodynamic force and hydraulic inertia of the body are negligible.

There are five degrees-of-freedom, with the roll of the parachute about its axis of symmetry being ignored.

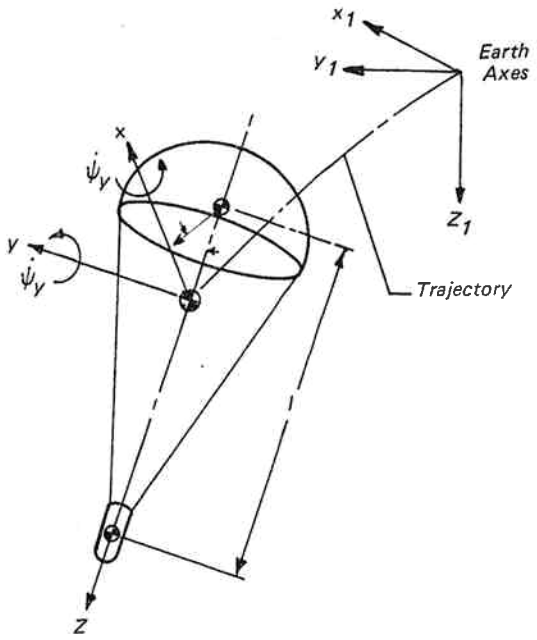


Figure 7.40 Parachute System Geometry and Coordinate System

The added air mass and apparent moment of inertia tensors of the canopy may be approximated by single scalar values (m_a, I_a).

The aerodynamic forces may be treated as quasi-static based on the instantaneous angle of attack of the canopy.

The canopy center of pressure lies on the canopy centroid.

Flat Earth and no wind conditions prevail.

A stability criterion for small disturbances was derived in the form of a set of linearized equations of motion about α_o. They show the longitudinal and lateral motions to be uncoupled, as in the study of aircraft linearized stability. In the analysis, a side force coefficient C_N is used which varies with α in the same way that C_M varies, the quantitative difference being merely

$$C_N = C_M\,(D/l) \qquad 7\text{-}130$$

when the distance between the canopy center of pressure and the system reference point, l, is different from the characteristic diameter, D, as is usually the case. For small disturbances, linear variation of force coefficients in the vicinity of α_o is assumed as shown in Figure 7.41.

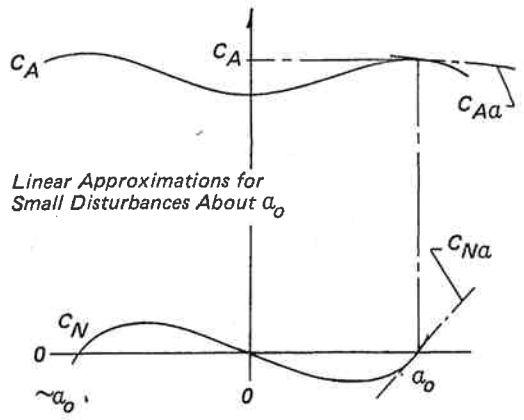


Figure 7.41 Typical Variation of Parachute Force Coefficients with α

$$C_N = C_{N\alpha}\alpha' \qquad 7\text{-}131$$

$$C_A = C_{A_o} + C_{A\alpha}\alpha' \qquad 7\text{-}132$$

where $\alpha' = \alpha_o - \alpha$

A conservative and greatly simplified relationship results which is independent of α_o when $C_{A\alpha} = 0$. Given small disturbances, this is quite accurate for a number of different canopies, because the axial force coefficient C_A commonly reaches a flat peak at α_o. While the parachute may be statically stable at α_o, it can also be dynamically unstable. In this event a given parachute, when subjected to a disturbance, may be unable to continue gliding and instead may oscillate or fall into a coning motion.

Dynamic Stability - *Longitudinal Motion.* Criteria for dynamic stability are used to define a minimum value of $C_{N\alpha}$ which is fairly restrictive and difficult for most parachute shapes to meet

$$C_{N\alpha}(min) = C_{A_o}[i(1 + r_c)^2 - Kr_a]/[i(1 + r_c)^2 + K] \qquad 7\text{-}133$$

where $C_{A_o} = C_A$ at α_o

$$i = Kr_c/(1 + r_c)^2 + B_i(D_o/l)^3/15$$

$$r_c = (m_c/m_b)(1 + r_a) + r_a$$

$$r_a = m_a/(m_c + m_b) = 2B_m(D_o/l)/[3K - 2B_m(D_o/l)]$$

$$K = C_{T_o} Fr^2/2 + (2B_m/3)(D_o/l)$$

$$B_i = 60\, I_a/\pi\rho D_o^5$$

$$B_m = 6\, m_a/\pi\rho D_o^3$$

$$Fr^2 = v_o^2/gl$$ ("Descent" and Froude No.)

v_o = velocity along glide path

m_a = added air mass

m_c = mass of parachute

m_b = mass of body

I_a = apparent moment of inertia of parachute

D_o/l = parachute slenderness ratio

With $C_{A_o} = 0.7$ and $C_{A\alpha} = 0$, which is roughly representative of a canopy with $\lambda_T \approx 15\%$, evaluation of $C_{N\alpha}$ *(min)* as a function of the parachute mass ratio, m_c/m_b with equation 7-133 plotted in Figure 7.42 shows the general effects of Froude number and slenderness ratio on the longitudinal stability of the gliding system. The curves indicate that the minimum $C_{N\alpha}$ required for dynamic stability is improved i.e., becomes smaller and so less difficult to satisfy with small parachute mass ratios ($m_c/m_b = 0.03$ to 0.05 is representative of a broad range of systems). Higher mass ratios attended by a higher stability criterion would represent uncommon systems with very heavy canopies relative to the body weight. Increasing the descent Froude number improves stability directly in proportion to v_o^2 which is not a practical design approach. and inversely in proportion to the system length, l, which is countered by the inverse effect of the increased slenderness ratio. Consequently, the minimum value of the dynamic stability criterion tends to be fixed by the system performance requirements in terms of the deployment and descent velocities which work together to determine m_c/m_b and Fr, in conjunction with a given slenderness ratio.

A practical range of slenderness ratios, $D_o/l = 0.5$ to 1.3 (approximately), may have a significant effect on $C_{N\alpha}$ *(min)* because, as noted, common values of m_c/m_b are small. A typical descent Froude number is $Fr^2 \approx 0.5$ and, with descent velocity constant, may be varied between 1.0 and .385 respectively for the changes in l indicated by the slenderness ratio range. In Fig. 7.42 it will be seen that for $m_c/m_b = 0.03$ to 0.05 the effect on $C_{N\alpha}$ *(min)* of such variations is proportionately greater for the slenderness ratio than for Fr^2 and so would not cancel each other. In order to maintain good stability in the presence of small disturbances the slope of the curve $dC_N/d\alpha$ for the canopy selected must be substantially greater than $C_{N\alpha}$ *(min).*

Lateral Motion. The criteria developed by the foregoing analysis show that small transverse disturbances will lead to neutrally stable oscillations, provided the longitudinal pitching disturbances also are

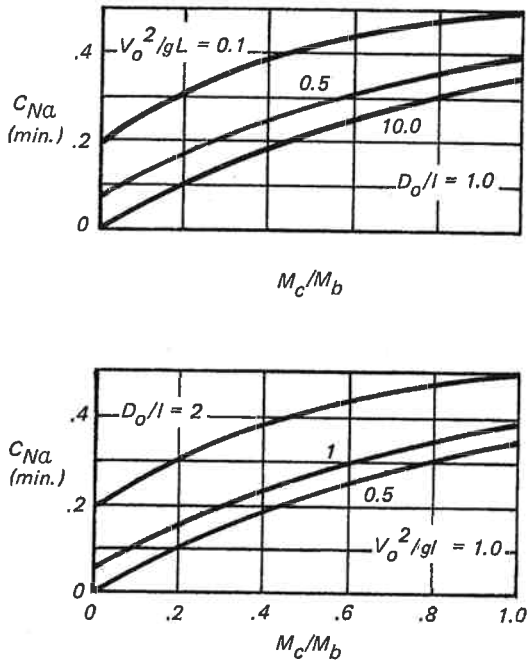


Figure 7.42 Effect of Froude Number and Slenderness Ratio on Stability $C_{A_o} = 0.7$ Zero Porosity

small. Therefore, it may be concluded that a coning motion of an otherwise stable system cannot be induced by a small lateral disturbance, being rather a large disturbance phenomenon.

Large Disturbance Analysis. The limitations of the linearized analysis were circumvented by performing computer solutions of the equations of motion using the following expressions for the variation of the force coefficients with angle of attack.

The parachute characteristics were defined by representative values of C_A, $C_{A\alpha}$, a_o, K, i, r_c and r_a, as defined above for equation 7-133 and $C_{N\alpha}$ *(min)* was determined. Values of $C_{N\alpha}$ *(min)* ± *57%* were then used in computations to show the effects of disturbances of various amplitudes on the dynamic stability of the system both longitudinally and laterally.

Longitudinal Disturbances. Longitudinal disturbances of $\psi_Y' = 1°$, *10°*, and *20°* were investigated using $C_{N\alpha} = C_{N\alpha}$ *(min) + 57%*. The effects on the subsequent pitch oscillations, ψ_Y, of a typical parachute are shown in Figure 7.38a. The complete linear theory predicts an exponential damping rate of $e^{-.0478t^*}$ with a dominant short period of $t_p^* =$ *13.03*, where $t^* = tv_o/l$. The 10° disturbance damps out at a lesser rate than the 1° disturbance, but the 20° disturbance triggers a new oscillation mode of large amplitude (±*32°*) which persists. In other words after the small disturbances, the system was able to maintain a stable glide at a_o, but the large disturbance was sufficient to throw the canopy to the negative angle of attack attitude causing $C_{N\alpha}$ to change sign. This would normally overcome glide and produce the familiar oscillating descent of a statically unstable parachute.

With $C_{N\alpha} = C_{N\alpha}$ *(min) - 57%* a disturbance of $\psi_Y' = 1°$ was sufficient to cause the system motion to diverge to a large oscillation amplitude (±*65°*) as shown in Figure 7.38b.

Lateral Disturbances. Lateral disturbances of $\psi_X' =$ *1°* and *40°* were investigated in the statically stable system as shown in Figure 7.38c. The response to the 1° disturbances was a neutral sinusoidal motion with a period of $t^* = 35.2$ in agreement with the linear theory. The induced longitudinal oscillation was negligibly small. In contrast, the large disturbance immediately induced a longitudinal motion of comparable magnitude (≈*40°*). Both ψ_Y and ψ_X approach stable oscillations of ±*38.7°*, with ψ_Y lagging ψ_X. The canopy has stopped gliding and is descending vertically with the body following a helical path of constant radius, a typical coning motion.

In Reference 479, Wolf extends the work done in Reference 482, summarized above, to embrace a non-rigid two-body system consisting of a rigid parachute flexibly connected to a rigid body with a riser of fixed length.

Elastic Systems with Unsteady Conditions

The non-linear equations of motion for a general body-elastic parachute system are developed by Ibrahim and Engdahl[544]. The mathematical model is characterized by a minimum number of simplifying

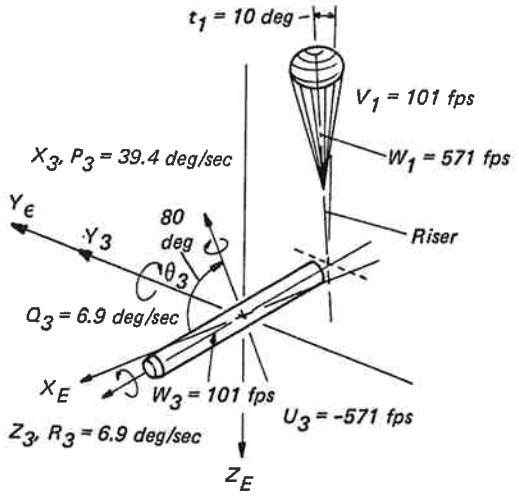
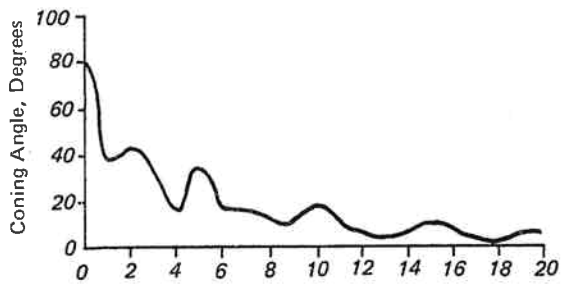
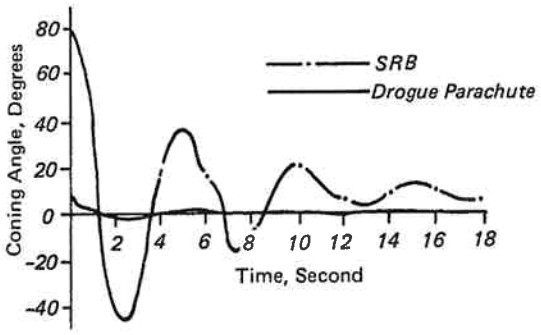


Figure 7.43 Drogue Effect Initial Conditions



a) Initial Deployment Conditions for SRB/Drogue Combination



b) SRB Coning Angle as Reduced by the Action of the Drogue Parachute

Figure 7.44 Predicted Drogue Effects on SRB Motion

assumptions as follows:

The parachute is axisymmetric with canopy of fixed shape and elastic suspension lines.

The riser is elastic and transmits only axial forces to the body

The body is rigid and axisymmetric

The aerodynamic centers of pressure remain on the axes of symmetry of body and parachute and are independent of c.g. locations

The energy modification of the air mass caused by parachute motion is represented by tensors of apparent mass and apparent moment of inertia and is negligible for the body motion

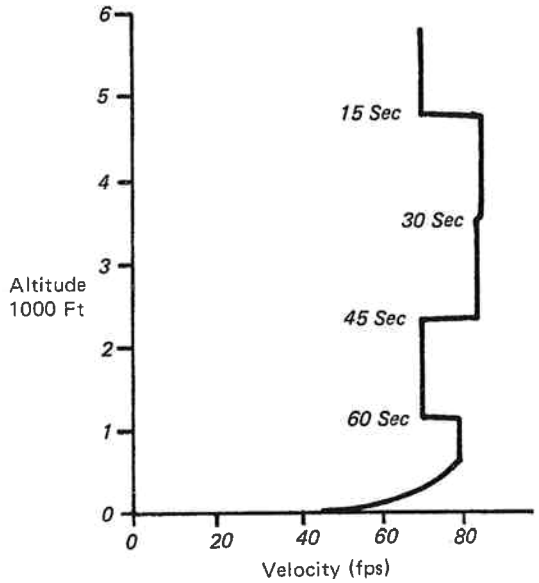
Body wake effects on the main parachute are negligible

A wind velocity field and a gust velocity field perturbation represent the unsteady air mass

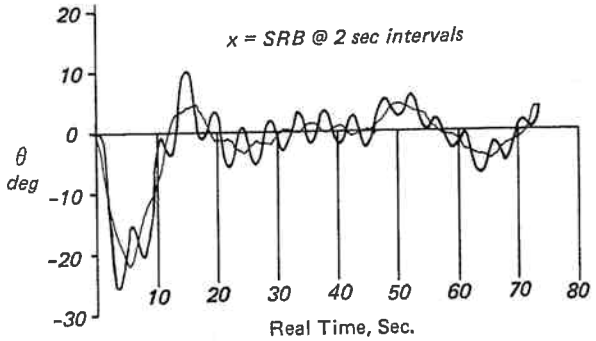
A flat Earth suffices for trajectory computation

The parachute-riser body system is treated as a three-body system with six degrees of freedom. Since the riser connects the parachute to the body, the unconstrained system reduces to one having 15 degrees of freedom.

Application of the method is illustrated with an analysis of the descent dynamics and stability characteristics of both the drogue-stabilization phase and the main descent phase of the space shuttle solid rocket booster recovery system. The predicted effects of the drogue on booster motion following deployment at the initial conditions given in Figure 7-43 are plotted as a function of time in Figures 7.44 (a, b). Typical response of the descending main parachute body system to disturbances in both steady and unsteady air are illustrated in Figure 7.45.



a) Air Mass Velocity Profile

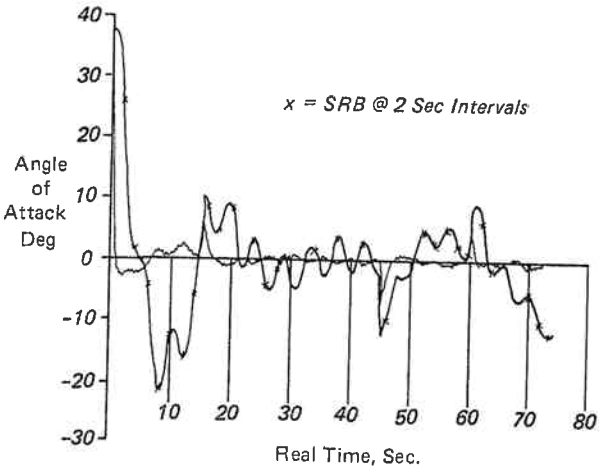


b) Main Parachute – SRB Response to Non-Steady Air Mass

Figure 7.45 Shuttle Booster (SRB) Main Parachute Stability

High-Glide Systems

The development of analytical methods of predicting the static and dynamic stability characteristics of high-glide parachute systems was first undertaken



c) System Angle of Attack Response to Non-Steady Air Mass

Figure 7.45 Continued

using three-degree of freedom, rigid body equations of motion. Stability derivatives used in the calculations were obtained from static and dynamic force tests of semi-rigid models tethered in the wind tunnel.

Chambers[545], investigating the dynamic lateral stability and control of a single keel parawing with rigid spars utilized lateral and longitudinal static stability derivatives of the types shown in Figure 7.46. Walker[564], investigating the static and dynamic longitudinal stability of a semi-rigid parafoil, induced pitching oscillations in a one-degree-of-freedom wind tunnel model to obtain the pitching and damping moment stability coefficients as a function of time shown in Figure 7.47.

The revision of theory required in the transition from rigid to all-flexible high-glide parachutes was investigated by the authors of Reference 546. A comparison of measured and predicted aerodynamic characteristics of both rigid and flexible single Keel parawings was illustrated, e.g., Figure 7.48. This figure shows the rigid body theory correctly predicting the reversal of the slope of C_m *vs* C_L going from rigid to flexible models but not the magnitude of C_m. It was concluded that any analytical approach to the all-flexible parawing will probably have to take rigging constraints into account.

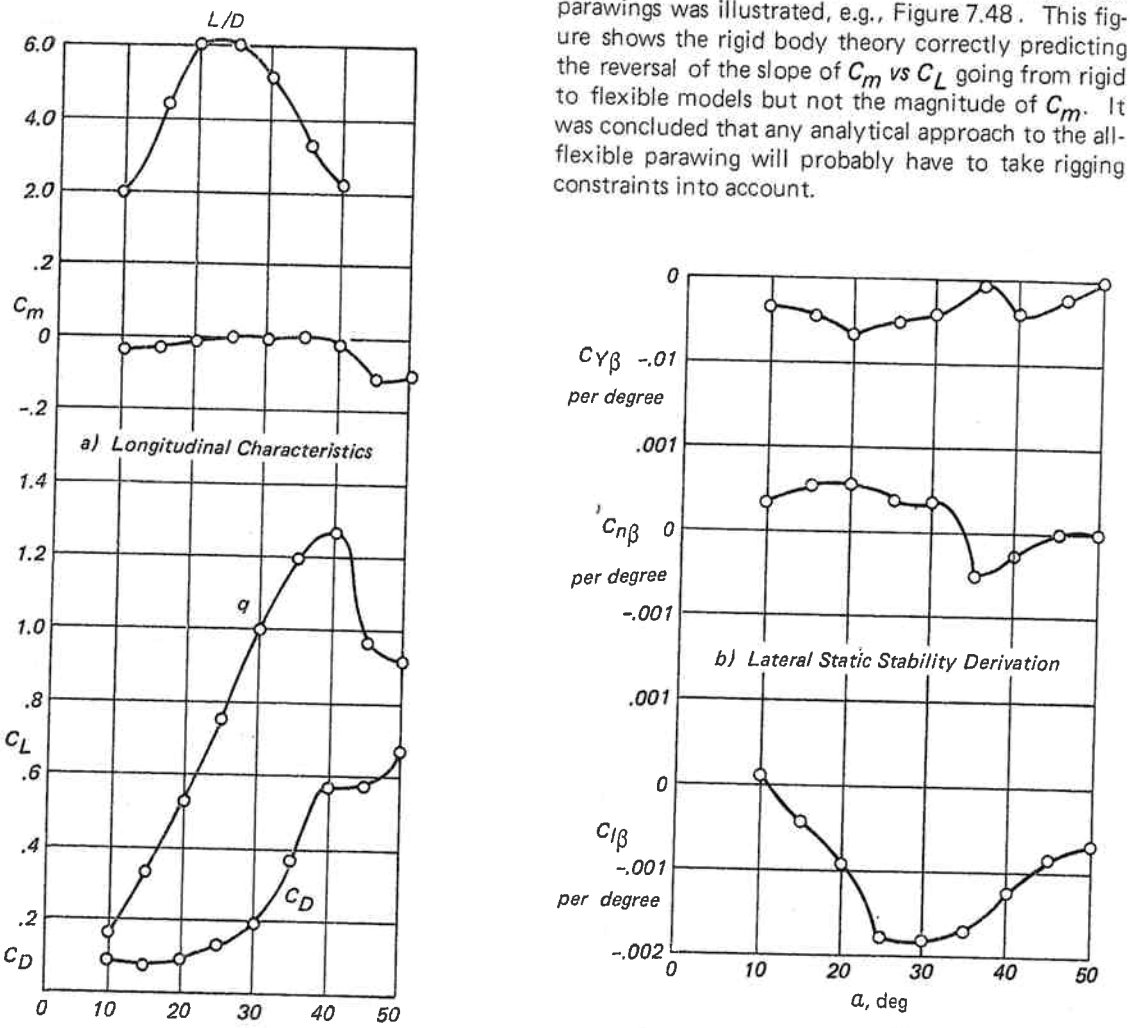
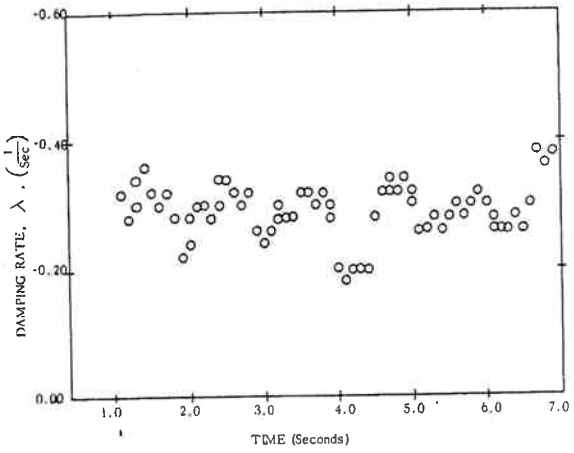
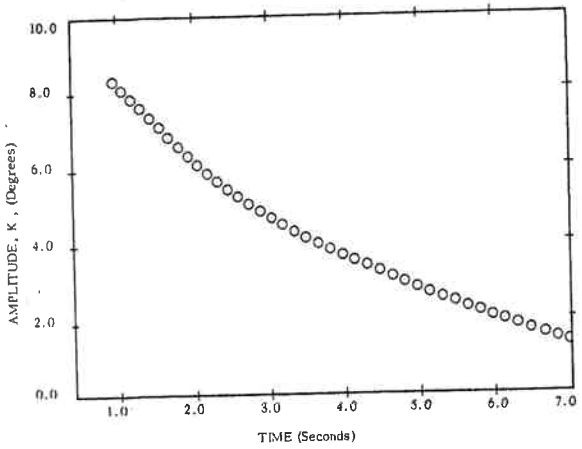


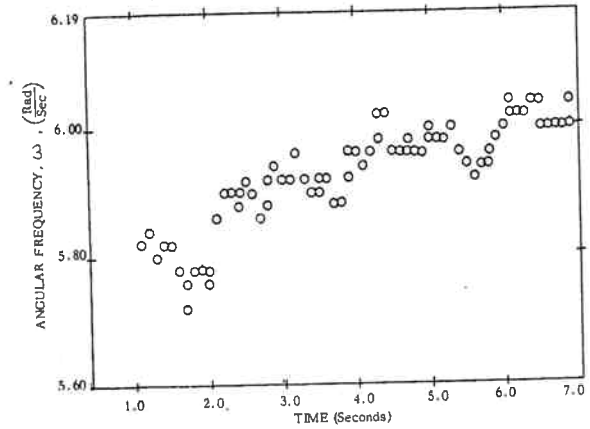
Figure 7.46 Summary of Aerodynamics of Sonic Rigid Model Single Keel Parawing (Ref. 545)



a) Variation of Damping Rate with Time (Test No. 7)

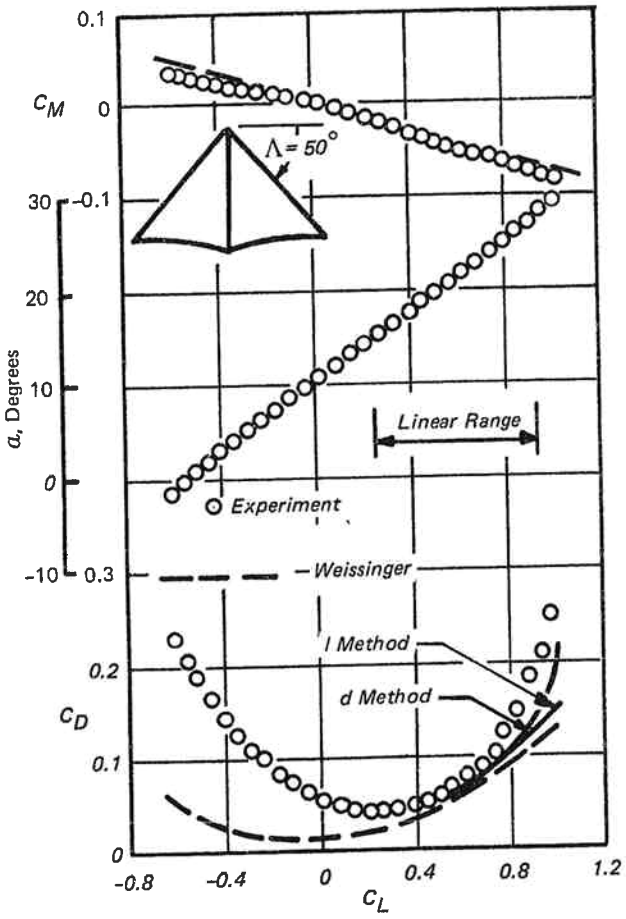


b) Variation of Amplitude with Time (Test No. 7)



c) Variation of Angular Frequency with Time (Test No. 7)

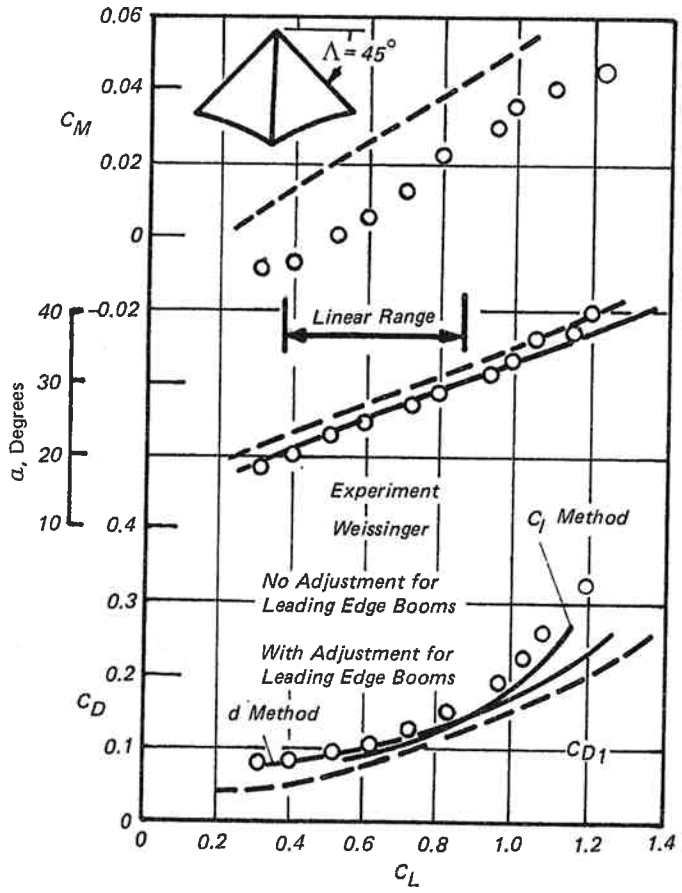
Figure 7.47 Typical Dynamic Pitching Characteristics of Tethered Semi-Rigid Parafoil Model (Ref. 564)



a) Characteristics of a Rigid Wing with $A = 3$ and $2\beta = 102.9°$.

Figure 7.48 Comparison of Predicted and Measured Aerodynamic Characteristics of Rigid and Flexible Parawing Models (Ref. 546)

A theoretical method for predicting the aerodynamic performance of all-flexible parawings is described in Reference 533.



b) Characteristics of a Flexible NASA Planform Parawing with $A = 2.83$ and $2\beta = 130.5°$.

Figure 7.48 Comparison of Predicted and Measured Aerodynamic Characteristics of Rigid and Flexible Parawing Models (Continued)

PREDICTION OF LANDING DYNAMICS

As summarized by Jones[548], analytical predictions of the performance of the landing impact attenuation system can be obtained by one of two methods: the statistical method or the absolute performance method. In the statistical method, a probability density function is defined for each touchdown condition and attenuator characteristic; then Monte Carlo techniques are used to establish a probability of successful landing. In the absolute performance method it is required that no landing failure occur for any touchdown condition within a specified range. The two methods can be combined to establish conditional probabilities of successful landing.

The problem is sufficiently complex to require the use of a high-speed digital computer, but simplified computer analysis using closed form equations of motion are inadequate to provide accurate performance predictions[548]. Therefore, only numerical integration methods can be expected to yield adequately dependable results.

Mathematical Models

The vehicle may be treated as a rigid body except where its elastic response to the impact is a critical factor to the success of the landing. Both rigid and elastic models can be treated in either two-dimensional or three-dimensional terms. The two-dimensional mode allows three-degrees of freedom, and the vehicle is constrained to move in a vertical plane containing the vehicle plane of symmetry and the line of maximum relative surface slope. The three-dimensional mode allows the vehicle six-degrees of freedom (3 translations and 3 rotations).

Solid landing surfaces may be modeled as either rigid and unyielding or soft. For rigid surfaces, forces tangential to the surface are generated by a coeffi-

cient or friction or by an assumed rigid abutment. For soft surfaces, including water, the penetration forces must be determined as functions of the area, direction, depth and velocity of vehicle penetration as well as of the penetration characteristics of the surface material[548].

Application of the Monte Carlo technique to an analysis of the landing dynamics of a manned vehicle without an impact attenuation subsystem is illustrated in Reference 549. The simulation technique was developed and used for a post-design evaluation of the Apollo Command Module (*CM*) landing capability. The analysis was carried forward in three successive stages:

1. Contact conditions on arbitrary terrain were established for the wind-driven CM and parachute system in terms of landing velocity and attitude.
2. Impact loading was characterized in terms of the resultant contact angle and velocity.
3. Failure criteria were developed for:
   The allowable structural loading statistics of CM inner structure.
   The probability of the command module tumbling and of structural failure resulting from the tumbling dynamics.

For the Apollo Command Module water landing, statistics indicating the probability of occurrence of various impact conditions, successful impact, and axial loads are presented in Reference 550.

Impact Attenuation

A convenient analytical approach for preliminary design purposes is to determine the approximate dimensions of the energy absorbing device required for the simple vertical impact case and then examine its probable behavior during drift landings along different axes, both without and with initial angular motion. This avoids unnecessary redundancy when partial effectiveness of the vertical system is adequate for the limit oscillation and drift conditions specified. For more stringent requirements the vertical energy absorbing capacity will be augmented.

The impulse-momentum equation is useful for appraisal of vertical impact design requirements:

$$\bar{F}(\Delta t) = m_b\,[(\Delta v) + g(\Delta t)] \qquad 7\text{-}134$$

where $\Delta v = (2\Delta h \bar{a})^{1/2}$

$$\bar{a} = K_e g(G_z - 1)$$

and $\bar{F}$ is the average retarding force that must be exerted by the energy absorbing mechanism during the space-time working interval defined by Δh and Δt. G_z is the maximum allowable vertical load factor of the vehicle. The definition of Δv reflects the assumption that the vertical velocity will be reduced to zero at the same time all the impact energy has been absorbed. In this context, the following assumptions also may be made about the system.

$\Delta v = v_m$ the maximum probable rate of descent with main canopy.

$K_e = a/a_m$ is a constant proportional to the dynamic efficiency of the energy absorber, where a_m is the maximum deceleration.

$K_h = \Delta h/h_e$ is a constant characteristic of the energy absorber for vertical deformation, where h_e is the initial undeformed vertical dimension.

The working intervals are expressed in this form.

(time) $\Delta t = v_m/K_e g(G_z - 1)$ 7-135

(stroke) $\Delta h = v_m^2/2K_e g(G_z - 1)$ 7-136

Numerous drop tests of different types of energy absorbing systems have served to indicate the practical range of values of parameters such as K_e and K_h. For the present purpose it is sufficient to know only broadly conservative values.

The descent characteristics and performance limitations of many systems can be taken into account conservatively by letting

$$K_e = 0.5$$

$$K_h = 0.7$$

and $$v_m/\bar{v}_e = 1.06$$

where $\bar{v}_e$ is the average rate of descent at contact for

$$v_m \approx \bar{v}_e + 2\sigma$$

With these substitutions in equations 7-135 and 7-136

$$\Delta t = 1.06\, v_e/0.5g(G_z - 1) \qquad 7\text{-}137$$

$$h_e = 1.60\, v_e^2/g(G_z - 1) \qquad 7\text{-}138$$

equations 7-137 and 7-138 are plotted in Figure 7.49 to indicate the general characteristics of the energy absorbing subsystem required to soft-land a specific vehicle decelerator system, as characterized by v_e and G_z.

The energy-abosrbing subsystem defined by Δt and h_e will have excess capacity for the simple vertical landing case and so will provide a reasonable basis for a preliminary dynamic analysis of critical attitude-angle and drift conditions. The ratio of h_e to the base dimensions of the vehicle is indicative of the type of energy absorbing medium required, whether crushable solids, surface penetrating members, deformable structures, compressible strut-skid landing gear, air bags, etc. The nature of the stability problem to be resolved will be indicated by this dimensional ratio and also by the horizontal distance traveled during the working interval, e.g., $\Delta s = v_H(\Delta t)$, where v_H is a specified maximum drift velocity along a given axis. If one (or both) base dimensions of the vehicle is small relative to h_e, ways of increasing the

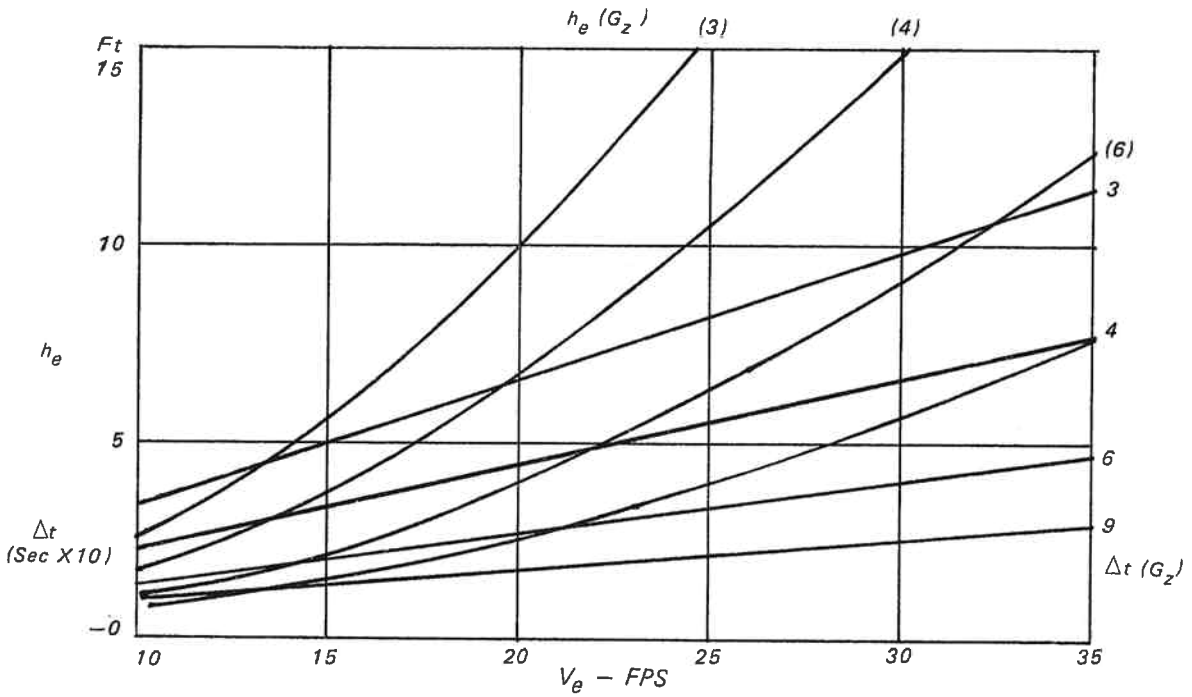


Figure 7.49 General Characteristics of Impact Attenuation System Vs Vehicle Vertical V_e and Load Factor

effective width with extensible outriggers or inflatable sponsons may be considered.

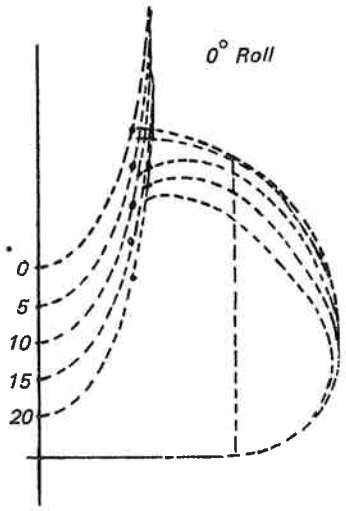
In preparation for the landing dynamic stability analysis, further detail design development is necessary to establish how the retarding force of the energy absorber varies during the working stroke for different angles between the base of the vehicle and the surface, and on different angles between the base of the vehicle and the surface, and on different horizontal axes, where this makes a difference. Shifting of the force vector relative to the vehicle center of gravity during the working stroke must be defined for the calculation of pitch and roll moments. Also, the coefficient of friction between the energy absorber and the landing surface must be known or estimated.

The results of the dynamic analysis will reveal the adequacy of the energy absorbing capacity of the preliminary design sub-system and suggest wherein stroke, tread or span, footpring, etc., may be revised to obtain an efficient solution of adequate stability for the range of touchdown variables specified.

Stimler[493] using a flexible six-degrees of freedom digital computer program, shows good correlation between predicted and measured performance characteristics of an impact bag mounted on the underside of an RPV. The program could handle up to five airbags located at different positions on the base of the vehicle. The mathematical model was developed to deal with fixed airbags and bags that could shift in position under lateral friction forces. Inputs to the computer program included: initial and final (relief) bag air pressures; discharge orifice area, and bag volume, footprint area, and center of pressure as functions of stroke, (see Fig. 7.50) along with the vehicle mass and inertial properties and the initial velocity vector. Trade-off studies were made to obtain the time histories of vehicle, e.g., velocity, airbag internal pressure, vehicle deceleration, angular motion in pitch and roll, and the velocities of tail and wing-tip upon contact with the ground. A comparison of typical predicted and measured results is given in Figure 6.95.

Impact Bags. The air-inflated envelope equipped with pressure relief orifices has proven to be amenable to performance prediction with minimal dependence on empirical coefficients (e.g., Ref.493). Several such bags are used in one system to obtain a satisfactory distribution of support under the vehicle, often in combination with static pressurized compartments or bags designed to augment the base span of the vehicle and to prevent terminal contact with the ground. The volume and footprint area of each bag as a function of compressed height may be determined for various angles of contact and along both longitudinal and transverse axes. Significant shifting of the center of pressure of each bag can be similarly identified, all as inputs to the equations of motion in a computer program designed to handle any number of bags at different locations relative to the vehicle center of gravity.

The working stroke of each bag is described by compression of the air to a peak pressure, at which



$A_0 = 1347\ In^2$ or 100%

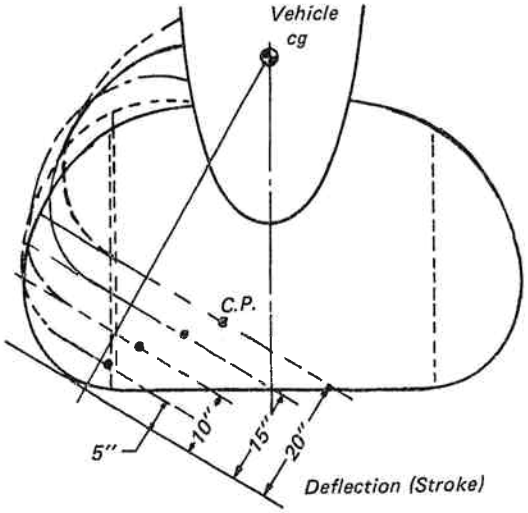
$A_5 = 1271\ In^2$ or 94.4%

$A_{10} = 1158\ In^2$ or 86.0%

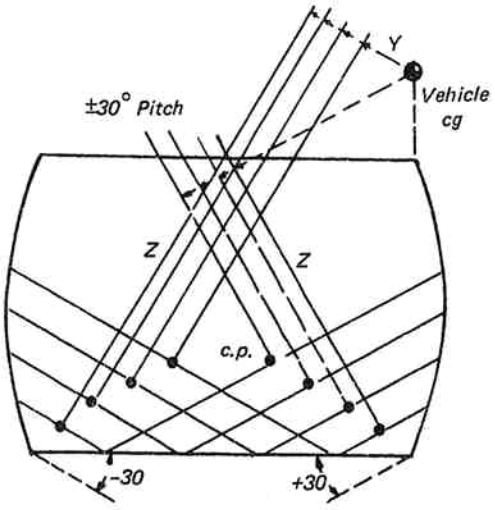
$A_{15} = 1022\ In^2$ or 76.0%

$A_{20} = 892\ In^2$ or 66.2%

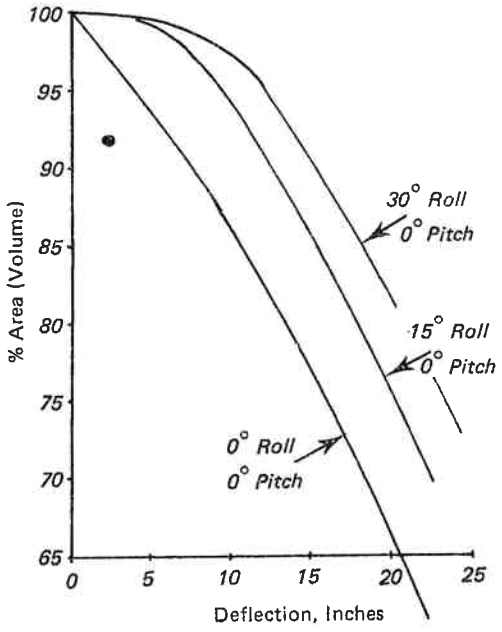
a) Footprint Analysis of Impact Bag For 0° Roll. 0° Pitch Condition. MQM-34D



b) Footprint Analysis of Impact Bag For 30° Roll. 0° Pitch Condition. MQM-34D



c) Footprint Analysis of Impact Bag For ±30° Pitch. 0° Roll Condition. MQM-34D



d) Impact Bag Cross-Sectional (Volume) Variation For Different Roll Angles and Deflection (Stroke) Conditions.

Figure 7.50 Characteristic Impact Bag Input Data for Analysis of Landing Dynamics

point the discharge orifices open, followed by an air exhaust cycle continuing to terminal contact. The instantaneous retarding force exerted by each bag is simply

$$F = S_f (P_2 - P_o) \qquad 7\text{-}139$$

Where S_f is the instantaneous footprint area and P_o and P_2 are the ambient and internal absolute air pressures respectively.

Air Compression Cycle. Adiabatic compression is a reasonable assumption for which the following relationships are useful.

$$V_2/V_1 = (P_1/P_2)^{1/\gamma} = (P_1/P_2)^{0.717} \qquad 7\text{-}140$$

$$T_2/T_1 = (P_2/P_1)^{\gamma-1/\gamma} = (P_2/P_1)^{0.283} \qquad 7\text{-}141$$

Where $\gamma = 1.3947$ for air at ordinary temperatures. The initial volume, temperature, and pressure are known. Then with $P_2 = f(V_2)$; $V_2 = f(h_b)$ and $S_f = f(h_B)$, the force exerted by each bag can be expressed in terms of its compressed height, h_B, which through the equation of motion, becomes a function of time starting with an initial value $h_{B1} = h_e$, when the vertical velocity component is h_{B1} at contact.

For a solution the compression process is advanced in time until $P_2 = P_o + \Delta P_m$, the pressure at which the air discharge orifices open. At this point the instantaneous values of the variables P_2, V_2, T_2, S_{f2}, h_{B2} and h_{B2} define the initial conditions for the air exhaust cycle.

Air Exhaust Cycle. The total area of the discharge orifices must be sufficient for an initial volumetric discharge rate at the peak pressure Δp_m of

$$\dot{V} = \dot{h}_{B2} S_{f2} \qquad 7\text{-}142$$

This is the rate at which the bag volume is being reduced by deformation between the descending vehicle and the ground. For an effective air discharge velocity, v_j, the total orifice area required is

$$\Sigma A_j = (P_2/P_3)^{.717} \dot{V}/v_j \qquad 7\text{-}143$$

and for adiabatic expansion with a discharge coefficient, C_j, the following form of the discharge velocity equation is useful

$$v_j = (C_j) 2.05 P_3 \bar{V}_3 [(1/T_2) (P_2/P_3)^{.283} (P_2/P_3)^{.283} - 1)]^{1/2} \qquad 7\text{-}144$$

where P_3 is the ambient absolute atmospheric pressure and $\bar{V}_3$ is the specific volume of air at the ambient conditions.

With A_j determined and held constant for the balance of the stroke, and velocity h_B decreasing, it will be seen that the internal air pressure tends to decrease rapidly when the footprint area of the bag stops increasing at a substantial rate (e.g., Ref. 493). The result is a low dynamic efficiency in terms of a/a_m, which may be improved either by causing the discharge area to decrease continuously during the cycle or by using an air bag shape that increases rapidly in footprint area as it is compressed between vehicle and ground. Both approaches have been tested with good results.

When the solution is advanced in time for a given landing condition, a satisfactory impact bag design will be indicated when the velocity h_B approaches a small residual value as h_B approaches zero with the ratio $a/a_m \gtrsim 0.65$ approximately, e.g., reasonably good dynamic efficiency is necessary to minimize the bulk and weight of the impact bags.

Pre-Contact Retardation

It is clear from Fig. 7.49 that, except for high allowable load factors, the vertical dimension h_e of the impact attenuation system must be relatively large for the small vehicles even at moderate descent velocities. The customary approach toward reduction of the size and weight of the energy absorbing package is to allow a residual impact velocity of 5 to 10 fps and establish acceptable levels of damage. The other approach occasionally taken is to employ a self-powered precontact retardation device, the operation of which is initiated at an appropriate height above the landing surface. For complete velocity attenuation, that height would be $\lesssim 0.7 h_e$ in Fig. 7.49, provided the dynamic efficiency yielded $K_e = 0.5$ or better; it is generally feasible to employ a mechanical probe of that length. The most successful pre-contact retardation systems employ retrorockets.

Retrorocket Landing Analysis. Although retrorockets are usually viewed as devices for attenuating only the vertical velocity component, systems have been devised which are capable of sensing and reducing drift at the same time. For example, during the first few milliseconds after contact a universally pivoted rigid probe with telescoping tip will indicate the instantaneous magnitude and direction of the vehicle velocity vector relative to the landing surface[497]. During the next few milliseconds these signals can activate that portion of a cluster of retrorockets required to attenuate both the vertical and horizontal velocity components to acceptable magnitudes. Since practical solid propellant rockets for landing purposes commonly have burn times of less than 500 milliseconds, a cluster of many small rockets may afford a more efficient solution than a few large ones, while providing at the same time a convenient method of varying the retarding impulse in step-wise increments to fit the instantaneous requirement. Where vehicle landing weight variations are large a suitable meter

program (possibly only a function of total flight time) may be used to bias the retrorocket firing signal to the number needed for that specific operation. For this type of system, the total retarding impulse required consists of the basic design minimum augmented as required by two factors as follows:

$$I = K_V m_b (\Delta v) + K_t g m_b (\Delta t) \qquad 7\text{-}145$$

Where K_V is the reserve factor required to cover drift and variations in weight, and K_t is a sustainer factor extending the rocket burn at a final vertical thrust level slightly less than the vehicle weight (gm_b) to minimize the residual impact velocity.

When m_b corresponds to the maximum landing weight condition the magnitude of K_V depends solely on the manner in which the thrust of the rocket cluster is vectored to counter drift during the primary deceleration interval. $K_V = 1.0$ only if the entire output of the rocket cluster can be directed along the resultant velocity vector $v = (v_V^2 + v_H^2)^{1/2}$. This is mechanically difficult to accomplish in a few milliseconds, but the cost of gaining additional time is only length added to the initiating probe.

The alternative approach (with $v_H \approx v_V$) using five individual clusters, one vertical and four horizontal, requires $K_V \approx 3.5$ when the direction of drift is a matter of chance, as in all uncontrolled landings.

Decelerator System Weight Optimization

It is occasionally helpful in decelerator system design to know the optimum rate of descent at touchdown for which the combined weight of the main decelerator and impact attenuation subsystem would be a minimum. While other practical considerations may dictate the design rate of descent in the final analysis, it is instructive to have some feel for the probable cost in added weight when the specified design figure is less than optimum, as is often the case.

A familiar relationship used in this analysis is the sum of the weight components

$$(W_p + W_R)/W = K_1/v_e^n + K_2 \Delta v + K_3 \qquad 7\text{-}146$$

where W_p = weight of main decelerator subsystem $(= K_1/v_e^n)$

W_R = weight of landing "retro-subsystem"

W = gross descent weight

K_1 = main decelerator weight factor

K_2 = retro-subsystem weight factor

Δv = reduction in descent velocity effected by retro subsystem

K_3 = gravitational factor

Letting

$$R_w = (W_p + W_R)/W \qquad 7\text{-}147$$

and

$$\Delta v = v_e$$

the expression is simplified to

$$R_w = K_1 v_e^{-n} + K_2 v_e + K_3 \qquad 7\text{-}148$$

The minimum occurs when $(dR_w/dv_e) = 0$ or, by differentiation, when

$$-n K_1 v_e^{(-n-1)} + K_2 = 0$$

Then the optimum rate of descent is

$$v_e^* = (K_2/nK_1)^{1/(-n-1)} = (nK_1/K_2)^{1/(n+1)} \qquad 7\text{-}149$$

Irrespective of whether the retro-subsystem is a passive impact energy absorber, such as an airbag, or an active decelerator like a retrorocket, the total impulse absorbed or delivered by the retro-subsystem may be represented by this relationship for complete deceleration from v_e to zero.

$$I = W_R i_R = (W_b/g) v_e + W_b (\Delta t) \qquad 7\text{-}150$$

or rearranged with $W_b = W$, i.e., neglecting W_p as small

$$W_R/W_b = v_e/i_R g + \Delta t/i_R \qquad 7\text{-}151$$

where i_R is the effective specific impulse of the retro-subsystem based on the installed weight of the subsystem and Δt is the effective working interval. Then it is clear that

$$K_2 = 1/i_R g$$

and

$$K_3 = \Delta t/i_R$$

For redundant retro-subsystems the total impulse capacity, I_R is greater than I as defined for the basic vertical impulse required, and the effective specific impulse $(i_R = I/W_R)$ is correspondingly small because W_R is larger than the theoretical minimum attainable. It will be seen that this works to reduce the optimum rate of descent and increase the size of the main decelerator.

Variation of the optimum design rate of descent with the effective specific impulse or efficiency of the retro-subsystem is illustrated in Figure 7.51 for different values of K_1 and with $n = 1.726$ (from Ringsail parachute weight data). For example, a very simple basic solid propellant landing rocket installation might afford $i_R = 150$ sec. for which, with $K_1 = 10.5$, $v_e^* = 65$ fps, but with provisions added for neutralizing drift and a consequent redundancy factor of say 3.0, the effective specific impulse would be reduced to $i_R = 50$ sec. and $v_e^* = 43.6$ fps. It can be shown that the end result would be more than double the total weight fraction of the combined decelerator subsystem from approximately 2.5% W_b to 5.3% W_b.

Partial Deceleration With Retrorockets. Simplified retrorocket landing systems for air dropping cargo,

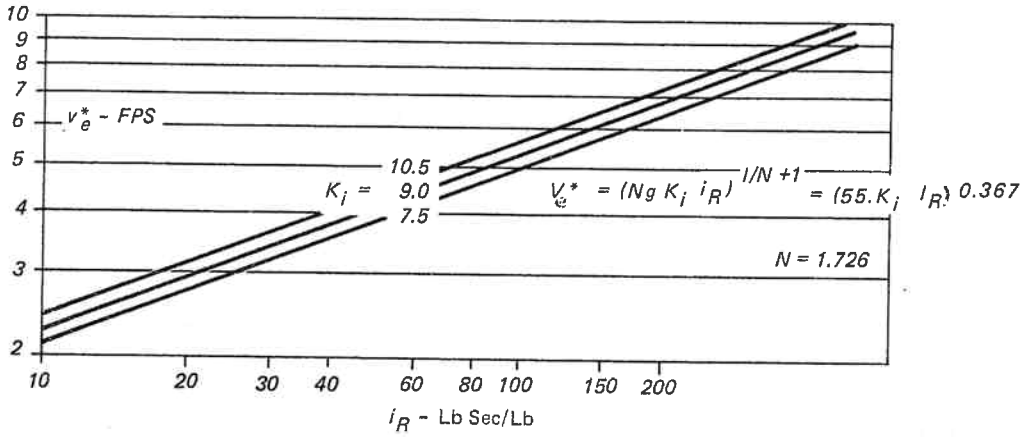


Figure 7.51 Variation of Optimum Design Rate of Descent with Effective Specific Impulse of Landing Retrorocket

such as that described in Reference 497, may be designed for $\Delta v < v_e$, with no provisions for attenuation of drift or for disconnecting the main parachute. Within the constraints imposed by the parameters of the low-level drop trajectory, decelerator system weight optimization may not be feasible, but the penalty for this could be relatively small, as suggested by the following analysis.

For this purpose, equation 7-151 may be re-written

$$W_R/W = (1/i_R g)\beta_1 v_e + \beta_2 t_b/i_R \qquad 7\text{-}152$$

where

$$i_R = I/W_R$$

$$I = (W/g)\, v_e + Wt_b$$

i.e., for the special case in which $\Delta v = v_e$, and $\beta_1 = \Delta v/v_e$ is the factor accounting for Δv *(design)* $< v_e$.

In this context the effective specific impulse for partial deceleration is defined by the expression

$$i'_R = [(w/g)\Delta v + Wt_b]/W_R \qquad 7\text{-}153$$

so that $i_R/i'_R = \dfrac{v_e/g + t_b}{\Delta v/g + t_b}$

Factor β_2 represents the reduction in the gravitational component that may result from support during the working interval derived from retention of the parachute. However, β_2 is likely to be close to unity for most systems because the parachute is usually disconnected when retro-thrust is initiated.

Since the rocket weight for this system will be less than for the one required for $\Delta v = v_e$, i_R will be larger and, as shown in Figure 7.51, the optimum design rate of descent will be increased accordingly. This trend is generally compatible with the requirements for the precision air-dropping of material as described in Reference 497. However, if v_e^* proves to be less than v_e *(design)* due to the effects of vectored nozzles and the weight of auxiliary retrorocket equipment on i_R, the combined decelerator system weight will be somewhat greater than the optimum. Once the weight of the retrorocket subsystem has been determined, a simple parametric analysis can be performed with equation 7-148 to appraise the weight penalty for operating at a design rate of descent other than v_e^*.

RELIABILITY ASSESSMENT

The assessment of parachute reliability, either from the design prior to the start of the actual experimental development program, or from test data gathered during a developmental and test program, is a problem which must be approached in a logical step-by-step manner if meaningful results are to be obtained. Space is not adequate in this section to present detailed instructions on the complete procedure for parachute reliability assessment. Reference 500 *presents a complete methodology for parachute-reliability assessment and many of the necessary auxiliary data, including values for human-error rates observed in parachute packings, the reliability of certain mechanical devices commonly used in parachute systems, and mathematical tables which facilitate computations. The discussion presented below is a brief outline of the major points which must be considered in the assessment of parachute reliability.*

Definition of Reliability

Reliablity is inversely related to the expected rate of failure; it can be measured by subtracting the expected probability of failure from unity. The important concept to note here is the use of the term "expected rate of failure". The calculated reliability of a system cannot be used to forecast, on an absolute basis, the performance of a single example of

that system in a single use. It gives the "odds", but does not foretell the result of any single event. It refers to the rate of successful uses to be expected when a large number of identical systems are used, or when a given system is used a large number of times. Thus, reliability may be defined as the probability of successful operation of the parachute system under given conditions in the long run.

An examination of the definition of reliability indicates that in itself it is not adequate for the basis of assessment of any given parachute system. It is necessary, before starting the analysis, to choose the boundaries defining the system. A decision must be reached by the evaluating agency as to the exact point in the parachute use at which the consideration of reliability will start, and the exact point at which it will end. For example, if a simple static-line-deployed system is considered, the reliability evaluation may include the fastening which holds the end of the static line to the aircraft, or may not, depending on whether the system designer or evaluator chooses to consider this a portion of the parachute system. Similarly, if a cargo parachute-system has an automatic canopy-release which separates the canopy from the load at touchdown, this may or may not be considered as part of the system from a reliability viewpoint, depending upon the objectives of the analysis.

Another factor which is important in the overall definition of the reliability to be assessed is the matter of the use-conditions under which this reliability will be considered. Therefore, it is also necessary to specify the limits of applicability of the system with respect to the deployment speed and altitude, the load, the permissible aircraft maneuvers during release, etc. Finally, as discussed previously, a definition of success or failure of the parachute mission is necessary as a yardstick upon which to base the computations of system reliability.

Reliability Distributions

In any given parachute mission, the reliability of each portion of the parachute system is determined, in effect, at a virtually instantaneous time, rather than over a period of time. For example, the maximum load on the suspension lines, and thus the maximum probability of a line breaking, comes either in the opening-shock or in the snatch force. Similarly, the reefing-line cutter is called upon to perform at a particular instant, and its success or failure in this performance is measured at that instant rather than over a time period. The other devices and components of the parachute system are also called upon to perform or to resist their maximum loads at a virtually instantaneous time.

Consequently, from a reliability viewpoint, a parachute is a "one-shot" system. When called on to perform in its mission, its reliability is not dependent on the length of time the mission will last, but rather upon success or failure in a single operation at a single time. The distribution of the probability of parachute failure can only take on a finite number of values, and is called a discrete distribution. The probability distribution best describing such a system is the Binomial Distribution, which expresses mathematically the probability ($f(x)$) that failure will occur exactly a times in N independent trials of the system, where p is the expected probability of failure :

$$f(x) = N!\, p^x\, (1-p)^{N-x}/x!\,(N-x)! \qquad 7\text{-}154$$

It should be noted that $x = 1, 2, 3 \ldots . N$, and that if p is the probability of failure, then $(1-p)$ represents the probability of success.

Examination of the expression for the Binomial Distribution given in equation 7-154 indicates that both the numerator and denominator of the fraction involved contain factorials, and that when the numbers become large, the expression is rather difficult to evaluate. For cases in which N (the number of trials) is quite large and (p) (the probability of failure) is quite small, the Poisson probability distribution is a good approximation to the binomial:

$$f(x) = n^x e^{-n}/x! \qquad 7\text{-}155$$

In this distribution, n is the average number of times the event (failure) occurs, or the "expectation" of x; numerically, $n = Np$. Since only one factorial is involved, that of x, and since x must be small to apply the Poisson distribution as an approximation to the Binomial, it can be seen that numerical manipulations are considerably simplified by the approximation.

Single-Use Versus Multiple-Use

One important factor governing the application of reliability methods to parachute missions must be considered before the the discussion of the details of reliability assessment; the condition of the parachute at the start of the mission. Some types of parachutes (for example, those which are used to decelerate weapons and are destroyed in the process of use) must be new at the start of each mission. Others, such as the usual man-carrying parachutes, aircraft-deceleration parachutes, and cargo or "airdrop" parachutes, may be used for a number of missions. In the single-use cases, since all the parachutes are new at start of the mission, it may be assumed that all have equal reliability. Of course, if the parachute has been subjected to severe environments in storage (high temperature, acid fumes, etc.), this assumption will not be valid. However, such situations are not legitimately a portion of a reliability investigation, since

they are analogous to the inadequate-design situation and are not actually related to the parachute; and they are isolated instances which cannot be controlled. Thus, to make the parachute-reliability assessment feasible at all, it must be assumed that accidental damage or deterioration during storage after packing has not occured.

In the case of the multiple-use parachute, it is necessary to establish the effect of prior use on reliability. Such factors as wear, age, damage on landing, weakening of fabric members by previous loading, and effects of exposure to sunlight during previous uses must be evaluated with respect to their effects on overall reliability. The problem here is one of determining whether the inspection and repair process which follows the parachute-use prior to packing for the next mission returns the parachute to the equivalent of new condition. This is a matter which will be determined by the facts of the individual case. If it is found that the re-used parachute is equivalent from a reliability viewpoint to a new parachute, then the analysis proceeds as if the parachute were a single-use item. If it is found that inspection and repair does not return the parachute to its "as-new" condition, then some allowance must be made for the deteriorating effect of prior use in assessing the parachute reliability.

Overall System Reliability

The simplest case in the evaluation of the reliability of a parachute system is that of a single-canopy system which has been tested a number of times under reasonably close conditions of operation of load, altitude, velocity of release, and aircraft attitude at release. Under these conditions, the simplest estimate of parachute failure rate is the actual failure rate observed: the number of failures observed divided by the total number of drops. The reliability is this value subtracted from unity. This gives a "point estimate"; that is, a reliability value given as a single number based on the available number of trials. For some purposes, especially if only a crude estimate of reliability is required, this "best estimate" is satisfactory. It must be realized, of course, that the accuracy of such a point estimate or best estimate depends upon the number of trials which were made.

Such an estimate of reliability has several advantages; it is relatively simple to compute and can utilize any consistent data that are available. However, it must be realized that the single-number value representing the reliability gives no information about the degree of confidence that may be placed in this number as a true measure of the potential performance of the system. It is quite possible that the true reliability is either lower or higher than the given maximum-likelihood estimate, since, in theory, reliability expresses the probability of a given number of successes in all possible uses of the parachute system, while, for most practical cases, the test data available represent only a small fraction of all possible uses. But the point estimate does have legitimate use in reliability assessment of parachute systems, because when only limited test-data are available it is often the only assessment which can be made; even with ample data, it provides a rapid method for determining whether or not reliability requirements are being met.

To take into account the possibility that the true reliability may be either lower or higher than the maximum-likelihood (point) estimate computed from a single series of trials by the simple method, a more refined measure of reliability is needed. The basis for this type of reliability value, the confidence-interval estimate, may be understood by realizing that, roughly speaking, if an estimate of the reliability of a system is made, there is associated with that estimate a probability of it's being incorrect. The lower such an estimate of reliability (expressed as a probability of "at least" a given fraction of successes), the higher is the probability of the estimate being correct. The estimate of the reliability can be denoted in the present case by R_p; the probability of the estimate being correct will be called the confidence coefficient (denoted by the subscript g); the interval between the reliability value given and unity is called the confidence interval. A probabilistic interpretation of these concepts is that if in many empirical trials with F failures out of a total of N trials, the reliability is estimated to be at least R_g, then the estimate will be correct on the average of at least g (percent) of the time.

In order to compute R_g, it must be recalled that if the true reliability is R, then in a single use of the system the probability of failure is $(1-R)$ and the probability of success is R. Using the Binomial Distribution described above, the probability of F or less failures in N trials is given by:

$$\sum_{i=o}^{F} (1-R)^i R^{N-i} N!/i!(N-1) \qquad 7\text{-}156$$

As R decreases, the values obtained from equation 7-156 also decrease; the estimate R_g will be that value of R which causes equation 7-156 to be equal to $1-g$, for then the probability of obtaining more than F failures in N tests will be g. If F is small while N is large (that is, if there are not many failures in a large number of parachute uses) the Poisson approximation to the Binomial may be used

$$1-g \approx \sum_{i=o}^{F} N^i (1-R)^i e^{N(1-R)}/i! \qquad 7\text{-}157$$

When R_g is computed from equation 7-157 , it is possible to state that the reliability lies between R_g and 1, with the assurance of being correct given by

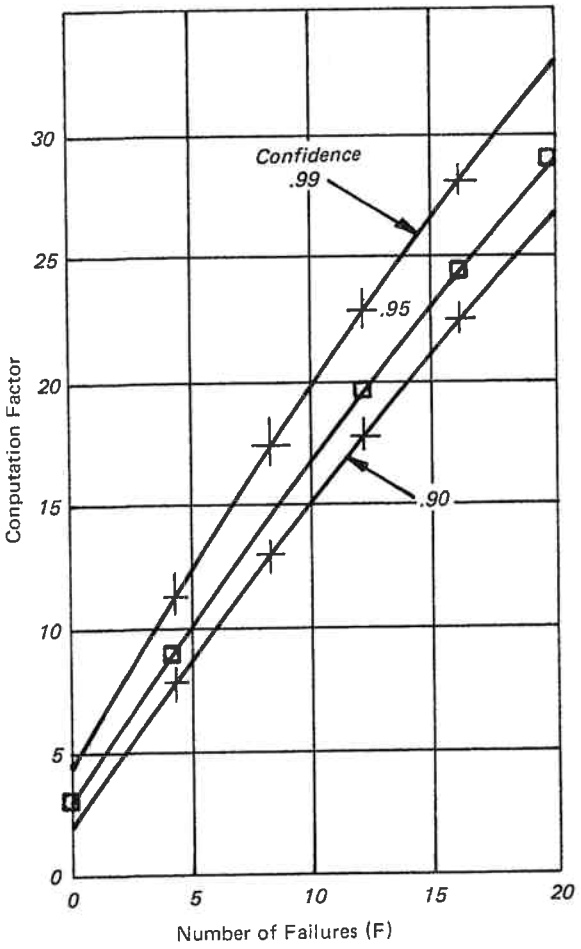


Figure 7.52 Reliability From a Series of Trials

the confidence coefficient, g.

To facilitate computations of R to a given confidence coefficient, tables have been developed and are presented in Reference 500. Values taken from these tables for 90, 95 and 99 percent confidence coefficients are plotted in Fig. 7.52. To calculate the reliability at the selected confidence-coefficient from N trials with F failures, the plot is entered at F, and the value for the computation factor read from the appropriate curve. Then, reliability with the chosen confidence coefficient, R_g, is computed from

$$R_g = 1 - \frac{\text{computation factor}}{N} \qquad 7\text{-}158$$

The choice of the confidence coefficient for use in interval reliability-analysis depends, to some extent, upon the objectives of the evaluation. Of course, any desired confidence-coefficient may be used in the calculations, although in practice the choice of a 100 percent confidence-level will obviously result in a reliability of zero, unless the parachute under analysis is absolutely perfect and can never fail. In the choice of a confidence coefficient for calculation, it must be realized that the higher the confidence coefficient used, the lower the reliability computed for the same set of data (and the higher the failure rate), and vice versa.

The choice of confidence in practical cases tends to be dictated by the amount of test data available for the evaluation. As can be seen from Figure 7.53 the data required to demonstrate high reliability with very high confidence is quite extensive, even if no failures at all are encountered in the testing. Thus, unless the test data can be obtained from other trials of the system, made for purposes other than reliability testing, the cost of doing the testing is probably the controlling factor in the choice of confidence coefficient. Studies of the amount of testing required versus the optimum confidence-coefficient for calculation (Ref. 500) indicate that 90 percent confidence is probably the best choice for most computations of reliability. By working at this level, the evaluating agency gets the greatest return for a given amount of test effort.

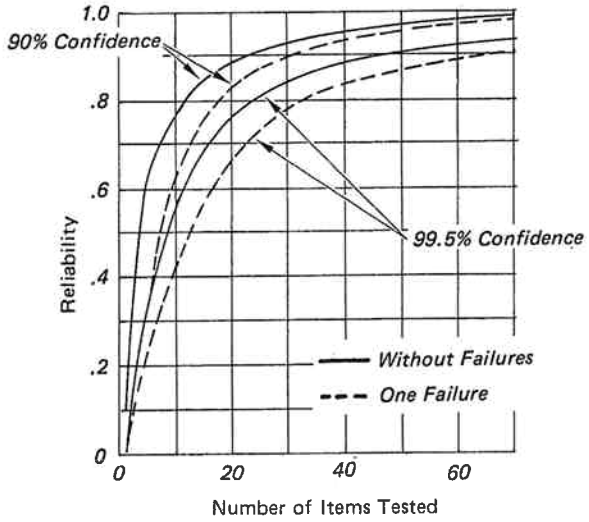


Figure 7.53 Reliability of Levels for a Series of Tests with and without Failures

The major advantage of the confidence-interval estimate of reliability over the point estimate is the fact that the confidence coefficient expresses the degree of reliance which the evaluating agency may place in its results. Obviously, if the reliability-evaluation of a given parachute system is based only on a limited number of trials, there is the possibility that in the next series of trials the results will be somewhat different. The point-estimate tends to ignore this fact; the confidence-interval estimate expresses numerically the probability that the failure rate on the next series of trials may be different from that

used in the computations. The disadvantages of the latter estimate, of course, are the requirement for larger amounts of data and a somewhat more complex method of computation.

In the discussion of both point estimates and confidence-interval estimates above, the viewpoint taken was that of the single-canopy system. In many parachute applications, instead of a single-canopy, multiple canopies are used, either in clusters or in sequence. Reliability data obtained on a single canopy may be applied to either type of multiple-canopy used, if due allowance is made for the effects of simultaneous or sequential use of the canopies on the reliability of the complete system.

In the case of canopies in clusters, it is necessary to determine the number of canopies which must operate successfully to decelerate the load to the velocity required for a successful drop. If it is found that all canopies which are used must operate, then the overall reliability of a system with clustered canopy system, R_m, is equivalent to the reliability of an individual canopy, R, raised to the power of the number of canopies used, N:

$$R_m = R^N \qquad 7\text{-}159$$

If a successful drop requires fewer than the total number of canopies used (n = number actually required), the overall reliability, R'_m, of the system may be calculated from:

$$P_d = \sum_{r=m+1}^{N} P_r \qquad 7\text{-}160$$

where P_d = probability of failure of the entire cluster

P_r = probability of failure of r identical canopies

N = number of canopies in the cluster; and

m = maximum number of canopies that can fail without affecting the mission

Then the overall reliability of the system, R'_m (when N exceeds n), can be expressed

$$R'_m = 1 - P_d \qquad 7\text{-}161$$

In the case of multi-stage systems, in which each canopy must open sequentially to decelerate the load, the reliability of each canopy is considered as a series term in a simple product model.

Component Reliability Analysis

The case in which there are sufficient test data on the complete parachute system to allow assessment of reliability on either a point or a confidence-interval basis is the exception rather than the rule. Of course, in the analysis of parachute designs before the system is actually built and tested, there can be no test data. In the case of systems under development, the tests are generally conducted at varying altitudes and speeds, and under varying load-conditions to establish engineering parameters, so that the data are rarely collected under conditions homogeneous enough to allow good reliability estimation. Thus, it is necessary to have some other method of assessing the reliability of parachutes.

Product Rule. Since any parachute system may be resolved into a series of individual components, and since it can be demonstrated that the reliability of the overall system is equivalent to the product of the reliability of each of its individual components (Ref. 551) an analysis of the reliability of the components of the system allows the synthesis of a reliability value for the complete system. The basic mathematical model used in this case is simple; the system reliability (R) is equal to the product of the component reliabilities (R_c):

$$R = \pi R_c \qquad 7\text{-}162$$

This model allows the reliability evaluation to take into account all of the mechanical factors involved in the parachute operation from the start of deployment until touchdown, or during any portion of the operation desired, as the basis for the reliability evaluation. However, a major factor in parachute reliability is human error in the parachute-packing process. Thus, it is necessary to introduce another term in the model to take into the failure due to this human error. This term, called the operational reliability term, R_p, is used as an additional portion of the product expression:

$$R = R_p \, \pi R_c \qquad 7\text{-}163$$

If desired, an additional term may be included in this model, as another factor in the product, to represent the probability of an error in rigging causing system failure. As discussed previously, this is a matter of choice on the part of the evaluation agency. Generally, rigging errors, which seem to occur most often in parachutes which are used for heavy-cargo drops, are not considered part of the parachute-reliability study.

Evaluation of Component Terms. The evaluation of the terms in the model in the process of reliability analysis of a specific parachute-system may be divided into two major types of tasks: the evaluation of component terms; and the evaluation of the operational term. In such an evaluation, it is possible to work toward a point-estimate or a confidence-interval estimate of the system reliability, although, of course, the data requirements for an interval-estimate are considerably more stringent than for a point-estimate. In general, when parachute designs are being evaluated for potential reliability prior to the actual construction of hardware, it will be quite difficult to

obtain enough data of the type required to permit confidence-interval estimates, unless the parachute system uses at least some components that have been previously used in other systems, and for which performance data are available. In the case of parachute systems which are in the development or test phases, and upon which some performance data are available, confidence-interval estimates of reliability can be made in a great many cases.

For the analysis of the reliability of a parachute system using the product-rule reliability model (for either point or confidence-interval evaluations) data will be required on the performance of all critical components of the parachute system; generally, this includes the suspension lines and risers, the hardware devices which are critical to system operation, and any mechanical actuators, control components, etc., which must operate properly for the system to perform its mission successfully. It is not necessary to have performance data on every component of the parachute system to evaluate reliability; only those components most likely to experience failures are actually studied in detail in the analysis.

The best data for use in the reliability analysis is actual-performance data obtained on the components in previous use under conditions similar to the use of the system under analysis, or in tests which closely simulate the conditions of use. In some cases, it is possible to obtain such data on virtually every component of the parachute system; this is true for those systems which are made up of components which have been used in other systems. Generally however, for systems which are relatively new in design, such data will be available only for the standardized hardware items such as reefing-line cutters, interstage disconnects, or standard components from which such disconnects are built up, and similar components. Despite the small size of these components in relation to the major canopy, if their function is essential to the operation of the system their importance from a reliability viewpoint is as great as that of the canopy.

Where test data are available, the reliability of the part is computed in precisely the same manner as for the reliability of the overall system as discussed under overall system reliability starting on page 392 . For a point-estimate, the failure rate of the observed sample is taken as the desired component failure rate. For a confidence-interval estimation the data in Fig. 7.52 are applicable, or Reference **500** .

In many actual cases of reliability analysis of new parachutes, either in the design stage or in actual development-testing, it will be found that while reliability data can be developed for most mechanical and hardware components, the canopy and its suspension lines (and generally the risers, if any) are unique, and have not had enough use or testing to allow reliability analysis from actual performance data. In such cases, if even limited test-data are available, it is possible to use a method of analysis which compares the distribution of the strength of the components under study determined from tests of the materials from which they are constructed and from other considerations to be discussed below. Studies of suspension-line riser load-distributions and of the strength distributions of parachute fabrics (Ref. **500**) indicate that both these distributions are essentially normal; that is, the spread of values obtained from a large series of tests may be described by the normal probability density functions (Ref. **575**):

$$f(x) = \frac{1}{\sigma\sqrt{2\pi}} (exp)^{-\frac{(x-\bar{x})^2}{2\sigma^2}} \qquad 7\text{-}164$$

where σ = standard deviation of x

and $\bar{x}$ = mean of x

The characteristics of this probability function are such that for any given series of test results, the probability of occurrence of a specific value is equivalent to the integral from zero to the desired value, or equivalent to the area under the normal curve up to the ordinate of interest (see Figure 7.54). Thus, if the distribution of stresses on the suspension-line or riser and the distribution of strength of the materials from which it is made are both normal and are plotted on the same set of axes, the probability of the stress exceeding the strength is equivalent to the area of intersection of the two distributions (Fig. 7.55). The probability of failure may be analyzed by studying the characteristics of the strength distribution and stress distribution for a specific canopy. Methods for performing this analysis, and tables and graphs which facilitate computation, are presented in Reference **500**. The data requirements are essentially a series of test results on samples of the parachutes, obtained under reasonably consistent conditions, and information on the strength distribution of the fabric materials. Test results, of course, must be obtained from a specific test-program; one is generally conducted during the parachute-development process. Data on strength of materials, including both means and standard deviations as required, are presented in Reference **500** for most of the commonly used parachute webbings, tapes, and cords.

It must be realized that the construction of the parachute does, to some extent, change the strength characteristics of the fabrics from which they are made. The primary problems here are the effects of sewing on fabric strength and the effects of the use of multiple layers of fabric on both strength and standard deviation of strength. Means for allowing for such factors are discussed in detail in Reference **500** based on the results of studies of stress on materials

described in References 285 and 552.

Where test data from which load-distribution information can be derived are not available, it is possible to utilize engineering estimates of component reliability for those portions of the system for which no data can be obtained. This will usually be the case in reliability analysis of parachute designs prior to the start of development, and possibly in the case of items in development for which test programs have not yet been run. These estimates should be based on performance records of similar components, engineering analysis of the design, and experience with reli-

$$f(x) = \frac{1}{\sigma\sqrt{2\pi}}(\exp) - \frac{(x - \bar{x})^2}{2\sigma^2}$$

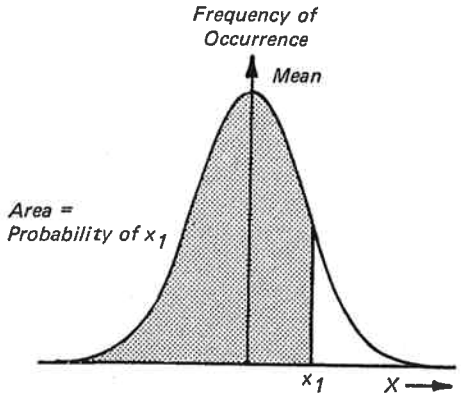


Figure 7.54 The Normal Distribution

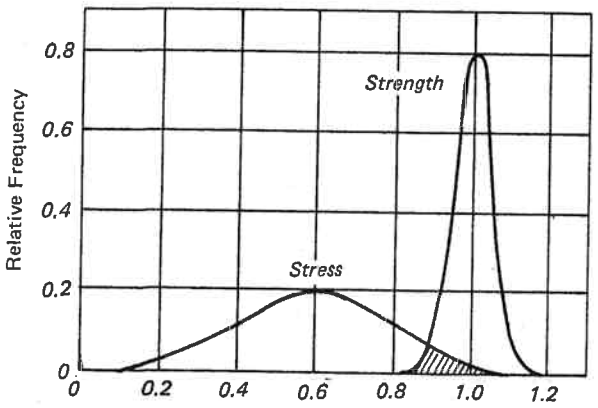


Figure 7.55 Exaggerated Stress-Strength Distribution

ability prediction. Of course, it will not be possible to utilize such data in interval-type estimates, but they are adaptable to point-estimates if no other means of reliability analysis of the specific component are possible. Such estimates should be used with caution, since it must be realized that the reliability of every component of the parachute system is important to overall reliable performance in the mission.

Evaluation of Operational Terms

The operational term in the product-reliability model, R_p, represents the probability of correct, error-free packing of the parachute into its deployment bag or other container. According to the desires of the evaluating agency, and if data are available, it may also include the probability of correct stowage of the deployment bag into a compartment on the load, such as the recovery-parachute compartment in the drone or missile, the deceleration-chute compartment in an aircraft, or the parachute compartment of a special weapon.

Implicit in this term is the assumption that if the parachute is properly stowed in its container, the deployment process will proceed successfully. This means that the reliability evaluation is assuming that the design of the deployment bag or other container is adequate for successful operation of the system. Such an assumption must be based on a program of good deployment-bag design and adequate testing to insure that the design is successful. With parachute systems in the development process this is no problem, since if the canopy does not deploy from the bag, it is obvious that further reliability testing is useless. From the viewpoint of the parachute system in the design stage, prior to construction, this means that the reliability being evaluated is "inherent" reliability; that is, the reliability which can be achieved with proper deployment-bag and stowage design.

The evaluation of the operational terms should be based on a statistical study of previous packings of similar canopies in similar systems. Data for the packing of relatively large canopies, such as might be used in cargo drops, missile and drone deceleration, aircraft deceleration, and weapons delivery have been collected and analyzed and are presented in Reference 500. These data are in a form that can be directly applied to most types of parachute analysis. In considering personnel parachutes, it is strongly recommended that a similar type of study be done on packing errors in personnel canopies, since here the characteristics of the canopy, and possibly of a portion of the packing process, are somewhat different.

In the analysis of multiple-canopy systems, it is necessary to include one packing-term in the reliability model for each canopy used. This creates no additional complexity, since if the canopies are of similar type, the same reliability value for the packing process can be used for each.

Computation of Reliability

The computation of system reliability, once data on all component reliabilities and on operational reliability have been obtained, is a relatively simple process. As can be seen from equation 7-163 , the overall reliability is the product of all the component reliabilities and the operational reliability. However, for a system with a large number of components, this computation, while not complex, can be extremely laborious if one term is included for each component. The computing process can be shortened considerably by including only those terms in the model which are of numerical significance in calculating the results. Obviously, those components of the system with very high reliability will not affect the overall system reliability to any significant degree if components of lower reliability are also present. (The numerical values of reliability range from zero to unity; it is obvious that the lowest component-reliability will have the greatest effect on over-all system reliability. For example, if a system is composed of three components with reliabilities of, say 0.999, 0.999 and 0.900 respectively, the overall reliability, the product of the three numbers, will be 0.898, which differs by only 2/10 of one percent from the value for that of the lowest component, 0.900.)

Thus, a preliminary analysis of the parachute system in which all components are divided into two major groups, those of extremely high reliability, and those which have a possibility of having lower reliability, will eliminate a considerable portion of the computations. It is not possible to write hard-and-fast rules for the classification of components in this process. The experience and judgment of the engineer evaluating this system is the key factor in making such decisions. However, it may be pointed out that, in general, failures which will affect mission success of hardware items, deployment bags, reefing lines, break cords, radial canopy-reinforcements, and other similar components appear to be so rare as to be generally negligible unless the parachute system is of unusual design. On the other hand, consideration of the failure rates of such components as risers, bridles, suspension lines, reefing-line cutters, and mechanical disconnects, will probably be required for most systems.

A preliminary qualitative analysis of a parachute system to select those components known to be very highly reliable can thus eliminate terms for these components from the model, and considerably simplify the computational process.

Once the list of components to be considered in the final reliability-computations has been compiled, it is necessary to conduct an analysis to determine whether these components are series-components or parallel-components in the reliability sense. The seri component is defined as one which must operate su cessfully if the parachute system is to operate succe fully in its mission, and is represented by a sin term in the model. One example of such a com nent is a riser; another, generally, is a suspension li since experience has shown that the breaking of suspension line throws so great a load on the ne boring lines that they usually break also. Par components (those which are designed as redun sub-systems) have more than one component forming the same function, where the operatio any one will insure system success. An example reefing-line cutters, where two or even four ma used on the same canopy, and the functioning o one will cut the reefing line. Another example o arrangement is inter-stage disconnects, where tw connect-mechanisms are often installed and the tioning of either will serve to separate the stages entire redundant system is represented by one t the model. In such a case, the component-reli term for the model is calculated from the redu reliability formula: for any number, n, of p components, the reliability of the parallel (redu system will be:

$$R_b = 1 - (1-R_{b1})(1-R_{b2}) \ldots . (1-R_{bn})$$

If a point-estimate of reliability is made, sults of the use of equation 7.165 are the value for substitution for the redundant-cor term in the reliability model. If a confidence analysis is made, and all the reliability value parallel components have been calculated to confidence coefficient, then this confidenc cient is the one applicable to the term us model. If the redundant systems have had calculated to differing confidence coeffic overall confidence coefficient will be that c est term.

Once the final component-list for the a been made up, and the redundancy proble settled, the calculation of a point-estimate reliability is a straight forward task of product of the operational reliability an sary component-reliabilities. The compu confidence-interval reliability estimate r only the application of the product rule ponent and operational-reliability terms, computation of an overall confidence Mathematically exact computations of ar fidence coefficient for a system from interval reliability values for its compon tremely complex task. However, an a method has been developed (see Ref.500 tates this computation with a minimum ical complexity. Essentialiy the meth

pre-selecting the final confidence-coefficient desired, and then computing operational and all component reliability-terms to such confidence coefficients is equal to the final desired confidence-coefficient. Details of the method, and tables which facilitate selection of the proper values of confidence coefficient, are presented in Reference 500.

The only addition complexity which may arise in the reliability evaluation is that of a re-use factor, for those parachute systems which are recoverable and re-usable after the mission. As was explained in the introductory portions of this section, it is necessary to determine whether the inspection and repair process after parachute use returns the parachute to an "as new" condition. If so, the reuse factor may be ignored. If not, it is necessary to make some sort of engineering judgment as to the effect of reuse on the strength of the parachute materials, and to adjust the stress-strength computations accordingly.

Interpretation

The result of the computation of the reliability of a parachute system by the methods described above can be used to evaluate the long-run performance which can be expected of large numbers of such systems. It must be emphasized again that this reliability value does not reflect the absolute performance of any individual system. It merely gives the "odds" that an individual trial of the parachute will be successful. However, the process of reliability evaluation has broader and possible more valuable applications than the single-number overall evaluation of potential system performance.

In the process of the evaluation of the component reliability model, the individual components of the parachute system most likely to fail are evaluated, as is the effect of the possible human error rate in manufacturing, rigging, and packing. These sub-results are really the key to the study of the potential causes of failure in a parachute system, as well as a guide to the efficient expenditure of effort in the improvement of system reliability (see below).

To produce the most efficient parachute system for a given cost, efforts should be concentrated on achieving approximately the same degree of reliability for all components and for the packing process. Effort expended in this matter has the greatest payoff in increasing the reliability of the system.

As was shown previously, the level of system-reliability is influenced primarily by those components with the highest expected failure-rates. Since the process of reliability analysis detailed herein detects these components explicitly, it can be of major value in locating those portions of the parachute system upon which the expenditure of further development effort will most improve system reliability.

The accuracy of the results of the reliability assessments described herein will depend to a considerable extent upon the types and sources of data available for the analysis. The interpretation of the values obtained must be made in light of the quality of the data used in the reliability assessment. This is particularly important in the case of point-estimates, since the final value of the reliability is a single number which does not reflect the amount of data nor the quality of the data which were used in its generation. In the case of a confidence-interval analysis, the confidence coefficient which accompanies the reliability value does give more information, at least from the viewpoint of data quantity, than in the point-estimate case. Here however, the quality of the data must also be assessed. It is necessary to examine carefully all test and use records utilized to ascertain whether or not the conditions of use closely match those of the analysis. This is particularly important from the viewpoint of loads, deployment speed, and, to a lesser extent, deployment altitude.

CHAPTER 8

DESIGN

The design of recovery systems and decelerators makes varied demands on the state-of-the-art over a broad range of operational conditions and complexity of performance requirements characteristic of modern aerospace vehicles and research instruments. Most new applications have novel features calling for resourcefulness, innovation, or inventiveness on the part of the designer. One purpose of this chapter is to set forth various design methods and practices, evolved over the years, affording a maximum probability of creating a successful product with minimum expenditure of time and funds.

Decelerator technology has benefitted from rapid improvement in the rigor of analytical methods made possible and practical by development of complex and flexible computer programs and by increasing accessibility of large digital computers to the industry at large. While empirical data and full-scale testing are still of major importance to the design process, the facility with which system and component designs can be executed and analyzed, their performance predicted, and test data reduced and evaluated has both speeded the design process and improved depth and quality of results. A number of different parachute design programs are now developed in great detail. With the input of a few basic system parameters, a comprehensive series of similar designs can be compared with respect to performance, weight, and drag efficiency for a single application.

Thus, a parametric analysis, difficult and time-consuming to perform only approximately by hand, can be carried out quickly and precisely by the computer. Similarly, test data processing programs exist which yield numerical tabulations and graphical plots of variables as functions of time and design parameters. The ease with which complex mathematical models can be repeatedly exercised in the computer also makes it possible to derive empirical coefficients through sensitivity studies in which predicted performance is brought into agreement with measured performance in successive iterations.

It appears the time is rapidly approaching, or has arrived, when a decelerator having a specific combination of performance characteristics can be designed in toto by analytical integration of various physical features (e.g., shape and porosity factors) appropriate to the dynamic and steady-state environments of a given application. This trend is well developed in the design of supersonic drogues, but less so for large subsonic canopies in which traditional approaches of selecting an established type having the approximate characteristics desired still predominates. Of course, there has always been a propensity among innovative designers to adopt an established canopy type which most closely satisfied requirements and then attempt fine tuning modification of existing shape and porosity factors. The success level of this approach has varied from none to fair, suggesting the need for a clearly defined engineering method.

It will be recognized that one of the first purposes served by preliminary design and parametric analysis of different recovery systems is to support a cost effectiveness study to establish the economic feasibility of recovering a given vehicle or payload. On occasion, this approach, by showing expendability to be the least costly mode of operation, has eliminated the recovery subsystem from further consideration in the development of a vehicle system. This handbook reflects the fact that decisions arising from such feasibility analyses in most instances are positive.

The preceding discussion of decelerator performance characteristics (Chapter 6) and analytical methods (Chapter 7) has already touched on a wide variety of design considerations of varying scope and importance. The purpose here is to set forth in orderly sequence the major steps in decelerator subsystem and component design processes and to identify specific practices found through long experience to yield generally satisfactory results. The procedure neccessarily begins with basic precepts largely self-evident as fundamental to good engineering practice in any field.

As the decelerator must be integrated with the recovery subsystem design, so the recovery subsystem must be integrated with vehicle design (even if superimposed as a kind of after-thought on an existing vehicle). While the basic application may be simple and performance requirements straightforward, a substantial quantity of background information must be obtained and accounted for to ensure complete adequacy of the new recovery system in terms of flightworthiness, serviceability, durability and reliability. One method of obtaining this information is to perform an operational analysis of the vehicle system or other application with which the recovery

system is to be identified. This approach should begin with consideration of materials procurement, acceptance testing, component fabrication subsystem assembly, packaging, and storage, then follow through the installation, pre-flight checkout, vehicle operation environments, subsystem operational environments, retrieval methods, and requirements for refurbishment and reuse. Critical factors and important interfaces with other vehicle subsystems will expose unnecessary requirements which have been introduced into the system design specification by intuitive judgements.

Clearly, the recovery subsystem requirements should not specify use of any particular method or device without prior comprehensive comparison analysis of all those potentially useful. Development risk factors merit special emphasis. In the past, errors of judgement in this area have led vehicle system design programs into costly development work centered on what proved to be an essentially unworkable recovery system or major component thereof.

This chapter follows the general order of a decelerator subsystem design procedure starting with essential design criteria and performance requirements and proceeding through component selection criteria, sizing, staging, performance, opening loads analysis, strength of materials and weight, packaging installation, and choice of deployment methods.

DESIGN CRITERIA

The recovery system must be designed to perform its functions of deployment, deceleration, stabilization, descent control, and termination or landing without imposing detrimental loads, deformation, vibrations or impact shocks on the towing body (person, vehicle, payload, etc.) or on components of the recovery system itself.

Towing Body and Mission Constraints

Primary recovery system design criteria are embedded in the physical characteristics of the towing body, payload or vehicle, its performance envelope, tolerances for deceleration, shock and vibration, and its mission. These define requirements and constraints for design of the recovery subsystem, including:

- Velocity/altitude profile for initiation of the decelerator subsystem.
- Required or allowable descent velocity components (v_V & v_H) at a given altitude.
- Allowable load factors on all axes ($G_{x, y, z}$)
- Environmental factors:
  - On-board storage temperature.
  - Nature of landing surface.
  - Surface wind velocity.
- Location and volume of stowage space.
- Allowable weight of decelerator subsystem.
- Location and strength of suitable hard-points for harness attachment.

Decelerator Subsystem Characteristics

Usually it is evident from operational requirements that the basic decelerator system should be of a specific type, e.g.:

- Ballistic
- Gliding, non-steerable
- Gliding, steerable

When the choice of subsystem type is not clear, comparative analysis becomes necessary, employing some form of value matrix to establish figures of relative merit for the variety of subsystems available. Discrimination cannot be based solely on weight and efficiency factors because of significant differences in:

- Aerodynamic characteristics (C_A, C_{D_o}, L/D).
- Development status and available performance data
- Complexity and economy of fabrication
- Dynamic response and stability
- Reefing characteristics and opening load factors
- Serviceability and reliability
- Control system requirements
- General compatibility with vehicle mission

When quantitative evaluation of a given factor is not feasible, a qualitative value judgement must be made, guided by such relevant experience as can be brought to bear. One method is to make all quantitative evaluations possible and then distribute copies of the matrix to qualified personnel with a request to estimate relative merit of the system for each factor within the individual's competence to judge. Then one or more candidate systems can be selected for preliminary design studies.

The Ballistic Decelerator. The ballistic decelerator in its most general form, consists of one or more main parachutes and one or more drogue-chutes with suitable staging controls, actuators and deployment aids. Upon deployment of the first stage drogue, the lift of the vehicle is largely neutralized, and the system follows a simple ballistic trajectory until it has decelerated to a velocity such that wind-shear begins to

have a significant effect. Thereafter, continued deceleration is attended by increasing wind shear deflections and the system arrives at the landing surface drifting with the prevailing wind.

The criteria governing selection of the type of main parachute for a given application include the following.

a) Opening reliability is well established and can be demonstrated over the full range of required deployment conditions.

b) Opening shock characteristics both reefed and non-reefed at the appropriate system mass ratios are acceptable.

c) Static and dynamic stability characteristics are within acceptable limits.

d) Drag coefficient (C_{D_o}) is a maximum compatible with other required performance characteristics.

e) Construction is compatible with requirements for a high specific drag area $(C_D S/W_P)$ in the final design.

One of the final design requirements is the terminal rate of descent, v_e. If the rate of descent is specified as an allowable maximum, v_{e_m}, then a reasonable design value is $v_e = v_{e_m}/1.06$, which allows a roughly two-sigma deviation for most parachute systems.[217] The specified landing altitude and a standard atmosphere table yields both the air density, ρ, and $\sigma^{-1/2}$, from which the design equilibrium dynamic pressure, q_e, may be calculated by one of two simple methods from the design rate of descent v_e (TAS):

$$q_e = \rho v_e^2/2 = \rho_o v_{e_o}^2/2 \qquad 8\text{-}1$$

It is helpful to know v_{e_o} for use later in determining the main parachute drag coefficient, and also in determining the true rate of descent at other altitudes as follows:

At ordinary altitudes: $v_e = v_{e_o}\sigma^{-1/2}$ 8-2a

At very high altitudes: $v_e = v_{e_o}\sigma^{-1/2}\epsilon_g^{1/2}$ 8-2b

Where the appropriate density and gravitation factors may be read from the curves of Figure 8.1.

For rates of descent of 25 fps (EAS) or less, the canopies of highest drag efficiency are of the solid-cloth, bias-cut construction and differences in overall performance between the best flat circular, conical, polyconical and 10% extended skirt types, are essentially negligible, all having nearly the same basic inflated shape and total porosity. Thus, the design reference drag coefficient C_{D_o} can be determined on the basis of $v_e = 25$ fps EAS without selecting the specific canopy type to be used. The constructed shape can be defined later on the basis of other considerations.

For rates of descent greater than 25 fps (EAS), the canopies of highest drag efficiency are the flat circular (solid cloth), 10% extended skirt and the Ringsail with $l_e/D_o = 1.15$-1.2. Of these, the flat circular and extended skirt designs are of bias construction and the Ringsail is of block construction. At $v_e = 25$ fps the design reference drag coefficient can fall in the range of $C_{D_o} = 0.85$-0.90 for all three canopy types. As v_e increases with increased unit loading, C_{D_o} declines rapidly for the first two canopy types but levels off at a constant value for the Ringsail. Thus, for design rates of descent approaching $v_e = 30$ fps, the

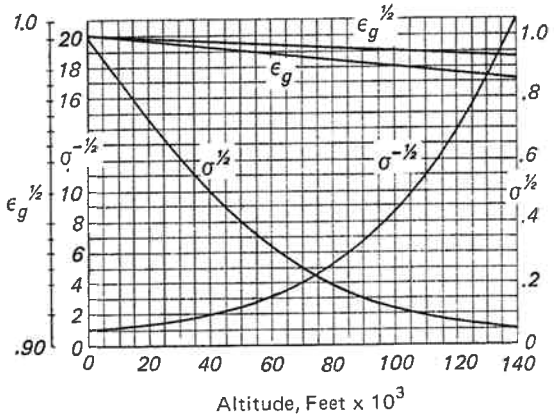


Figure 8.1 Density and Gravity Ratios as a Function of Altitude

type of canopy selected can make a significant difference in both drag efficiency and systems growth potential in terms of later increases in the recoverable weight.

If the system rate of descent at sea level is not likely to exceed 25 fps, selection of canopy type can be based on other factors such as non-reefed opening characteristics, C_X and K_s, stability, and specific drag area. However, as noted, differences in these performance characteristics can be leveled by reefing (in the case of C_X differences non-reefed), or they may be related in other cases to specific details of shape and construction. Hence, the alternative approach to type selection would be to specify particular characteristics desired and integrate the governing design parameters into a total parachute design.

Sizing the Main Parachute. Since more than one main parachute may be needed, i.e., a cluster, given the system recoverable weight, W, the total effective drag area required is indicated by $\Sigma C_D S = W/q_e$. Criteria for determining the need for a cluster of identical parachutes, rather than a single main canopy include:

a) A single main parachute would be too large,

too heavy, too bulky or too long as a single package for convenient handling stowage, etc.

b) The single parachute would be too slow to open or not sufficiently stable.

c) The non-synchronous inflation characteristic of cluster parachutes is either acceptable or will be regulated by a special synchronizing mechanism.

d) The system reliability goal can be attained more efficiently with a cluster (e.g., Apollo ELS).

When the number of main parachutes, n_C, has been established, the required drag area of the individual canopies may be calculated, e.g., $C_D S = \Sigma C_D S/n_C$. In addition, the drag coefficient ratio C_{D_C}/C_{D_o} can be determined with the aid of such data as in Figure 6.30 for clustered canopies.

The actual surface area of the main canopy is simply $S_o = C_D S/C_{D_C}$, and since $C_{D_C} = C_{D_o}$ for the single parachute system, the appropriate drag coefficient can be obtained from empirical data such as that plotted in Figure 6.35 as a function of v_e (EAS). Note that v_e (EAS) is used in lieu of the unit canopy loading $W/C_D S$, so it would be incorrect to employ v_e (TAS) at altitude for this determination.

Numerical Examples

Sample calculations for sizing the main parachute are summarized in Table 8.1 for three different ballistic systems designated A, B and C, in which the system design weight, W, includes the recovery subsystem weight.

System A calculations in Table 8.1 are straight-forward through $\Sigma C_D S$ required. Then we enter Figure 6.35 with $v_{e_o} = 18.3$ *fps* to estimate the probable best C_{D_o}. Note however, that $C_D S = 754$ *ft*^{2} calls for a relatively small canopy, and Figure 6.63 indicates that the 10% flat extended skirt models are best performers in this size range, but only when made as de-

TABLE 8.1 SAMPLE CALCULATIONS FOR SIZING MAIN PARACHUTE

System		A	B	C
Given: W	lbs	300	4000	50,000
Maximum R/D (v_{e_m})	fps (TAS)	20	25	30
Altitude @ v_{e_m} (h)	ft	2000	5000	(S.L.)
Design: $v_e = v_{e_m}/1.06$	fps (TAS)	18.9	23.6	28.3
At altitude $\sigma^{-1/2}$		1.030	1.077	1.0
$v_{e_o} = v_e/\sigma^{-1/2}$	fps	18.3	21.9	28.3
q_e	psf	0.398	.570	0.952
Required: $\Sigma C_D S$	ft^2	754	7017	52,520
Best C_{D_o} (Fig. 6.35)		0.98	0.90	0.89
Corresponding ratio l_e/D_o		1.0	1.0	1.18
Number of canopies (n_c)		1	1	3
Est. Ratio C_{D_C}/C_{D_o} (Fig. 6.30)		1.0	1.0	0.97
Tentative Ratio l_e/D_o		1.0	1.1	1.70
Est. Ratio C_{D_o}/C'_{D_o} (Fig. 6.61)		1.0	1.03	1.13
Design: C_{D_o}		0.98	0.93	0.92
Canopy area S_o	ft^2	769	7545	19,029
Nominal diameter D_o	ft	31.3	98	156

scribed in Reference 1. With the support of other 10% extended skirt data at low rates of descent, it is reasonable to read just above the top broken line $C_{D_0} = 0.98$, while the corresponding rigging ratio is seen to be $l_e/D_0 = 1.0$.

The shape curve (2) in Figure 6.61 discourages evaluation of optimum line length for extended skirt parachutes of minimum weight, i.e., no apparent advantage is to be gained with a relative line length other than unity. Thus, no correction of the estimated C_{D_0} is justified and it appears that a 31.3 ft (D_0) 10% extended skirt parachute of optimized detail design per Reference 1 will provide a sound basis for preliminary design of System A.

System B calculations in Table 8.1 are straight-forward through $\Sigma C_D S$ required. This calls for a large parachute, i.e., $D_0 > 50$ ft as an order of magnitude, but not so large that any great benefit would be derived from a cluster, except for special considerations which might require a shorter filling time, better stability, or enhanced reliability. Both filling time and reliability of a cluster could be compromised somewhat by the non-synchronous filling characteristic if corrective measures are not taken.

Entering Figure 6.35 with $v_{e_0} = 21.9$ fps (EAS), we find a probable best $C_{D_0} = 0.90$ for large flat circular, conical and polyconical canopies with $l_e/D_0 = 0.95 - 1.0$. The scale effect is already accounted for in this size range, as shown in Figure 6.63. General experience with other large parachutes suggests the possibility that the optimum rigging length for a parachute of minimum weight is close to $l_e/D_0 = 1.1$. This can be verified later when the required strength of materials has been determined. Entering Figure 6.61 with $l_e/D_0 = 1.1$, the average curves (3), (4) and (5) for flat circular canopies is approximately $C_{D_0}/C'_{D_0} = 1.03$, yielding a design $C_{D_0} \approx 0.93$.

The data scatter justifies the assumption that either a flat circular, conical or polyconical parachute with $D_0 = 98$ ft and $l_e/D_0 = 1.1$ would provide a sound basis for preliminary design of System B. The term *polyconical* could be interpreted to embrace the bi-and tri-conical versions, and it is generally easier to obtain a high level of drag efficiency with these than with the more conventional flat circular parachute design.

System C calculations in Table 8.1 are straight-forward through $\Sigma C_D S$ required. A single canopy of this drag performance would have a nominal diameter on the order of 270 ft. Rather than risk extending the state-of-the-art in this direction (the largest known parachute had a flat canopy of 200 feet in diameter [382]), the better part of valor is to employ a cluster of identical parachutes. As shown in Figure 6.30, the loss in drag efficiency will be least for the smallest number of member canopies and a simple trial calculation shows $n_c = 3$ to be a reasonable number, with $C_{D_c}/C_{D_0} = 0.97$ attainable by good design. Then for each parachute of the cluster:

$$C_D S = \Sigma C_D S/3 = 17{,}507 \text{ ft}^2$$

The recommended cluster rigging length of $l_c/D_0 = n_c^{1/2} = 1.73$ permits each parachute to have an effective line length of at least $l_e/D_0 = 1.7$. Entering Figure 6.35 with $v_{e_0} = 28.3$ fps, find a possible best $C_{D_0} = 0.89$ for single large Ringsail parachutes with $l_e/D_0 = 1.15 - 1.18$. In Figure 6.61 curve (6) yields $C_{D_0}/C'_{D_0} = 1.06$ at $l_e/D_0 = 1.18$ and $C_{D_0}/C'_{D_0} = 1.13$ extrapolated to $l_e/D_0 = 1.7$. Thus, the corrected drag coefficient for cluster canopy design is $C_{D_C} = (.89)(.97)(1.13/1.06) = 0.92$ and a cluster of three 156 ft (D_0) Ringsail parachutes with $l_e/D_0 = 1.7$ and $l_C/D_0 = 1.73$ provides one of several possible bases for the preliminary design of System C.

Determination of Number of Suspension Lines. In all circular parachutes (and many others) the number of suspension lines, Z, is customarily made equal to the number of gores, N, to maintain structural continuity. An old rule of thumb is that this number should be approximately equal to the nominal diameter of the canopy (D_0) in feet which yields a gore width at the skirt in the order of π feet. In general, $Z = D_0$ for lightweight structures but $Z > D_0$ is sometimes justified by scale and strength requirements. To preserve rotational symmetry, the number of riser branches Z_R above the confluence point is made an even number, preferably four or more. Therefore, it is good practice to use $Z \approx D_0$ (in feet) an even number divisible by four or six.

Determination of Suspension Line Length. As shown in Figure 6.61 the effective rigging length (l_e) of the parachute, has a strong influence on C_{D_0} through its effect on the projected area of the inflated canopy. The length of suspension lines (including riser branches) to be specified depends upon the following considerations.

Single parachute configuration of minimum weight i.e., maximum specific drag area.

Single parachute system stability (pendular oscillation amplitude) if critical.

Number of parachutes in a cluster.

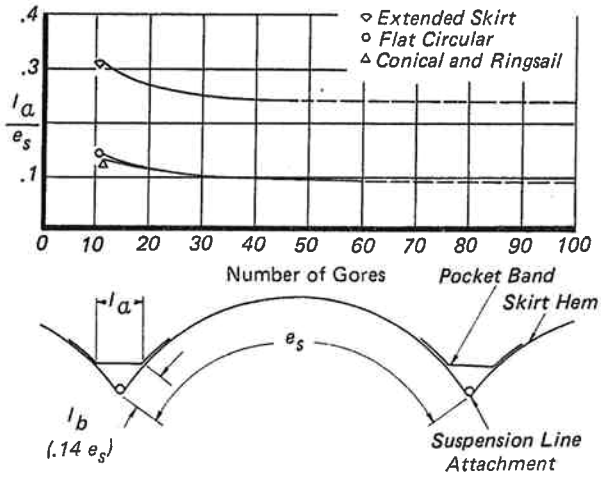


Figure 8.2 Pocket Band Dimensions for Circular Canopies

With $C_D S$ constant, a simple trade-off study between canopy and suspension lines for $W_p = K_1 S_o + K_2 l_e$ wherein $C_{D_o} = f(l_e)$ as in Figure 6.61 will show that the parachute weight is a minimum for a particular value of l_e/D_o. In a single parachute system it is difficult to justify use of other than the optimum rigging length, but in some cases practical considerations make a deviation beneficial.

In parachute clusters as shown in Table 6.3, a generally desirable rigging length is $l_C/D_o = n_C^{1/2}$ most of which can be provided by suspension lines of the member parachutes. A considerable gain in both $C_D C$ and in structural efficiency may be realized. The latter benefit derives from differences in strength/weight ratios of materials and a cluster riser design factor which is usually larger than the parachute suspension line design factor.

Scale Effect on C_{D_o}. If the type of parachute selected shows a marked variation of drag coefficient with scale, as shown in Figure 6.63, this should be taken into account in the final evaluation of $S_o = C_D S/C_{D_o}$.

Pocket Bands. Pocket bands are indispensable in some circular canopy types to make the filling time more repeatable about its minimum value through elimination of random delays in the start of inflation. Their use may benefit the opening of other canopy types with which they are not commonly associated and should always be given consideration early in the design. Pocket band dimensions are standardized, as indicated by the curves of Figure 8.2. It is important to use $l_b = 0.14\, e_s$ constant, because the ratio l_a/e_s corresponding to the shape of the gore bulges in the fully inflated canopy varies in ways that are not easily predicted. In the extended skirt, canopies pocket bands, when used, are placed on the skirt at alternate line junctions only, to minimize restriction of the perimeter when fully inflated.

Slot Control Tapes. All canopies having open slots in the crown area, e.g., ringslot and Ringsail, require slot control tapes to help regularize the inflation process, (i.e., by minimizing the time required for inflow rate to build to and exceed outflow rate). As a minimum, the single center-line tape illustrated in Figure 8.3 has proven effective for this purpose. The vertical length of the tape from the vent need be no

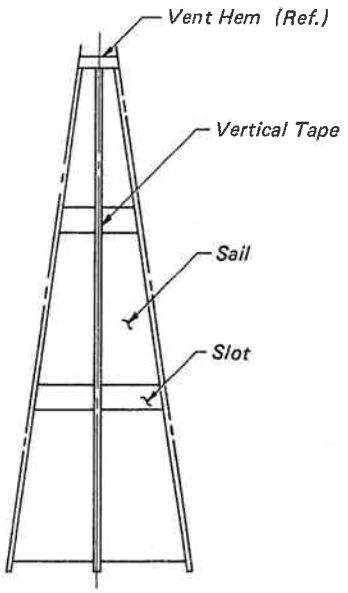


Figure 8.3 Typical Crown Slot Control Tape on Circular Canopies

TABLE 8.2 EFFECT OF SHORTENED VENT LINES $(D_V/D_O = 0.10)$

Vent line shortening %	5	10	15	20
$\Delta l_V/l_V$	0.05	0.10	0.15	0.20
Canopy $(D_V/D_O)(\Delta l_V/l_V)$	.005	.010	.015	.020
Added circumferential fullness %	0.5	1.0	1.5	2.0

more than $0.50h_s$, (Ref. 217) but it usually is made equal to the gore height in ringslot canopies, when only one vertical tape is used in each gore.

Canopy Fullness and Vent Line Shortening. The inflated shape of the basic circular canopy design is frequently modified in minor ways for specific purposes, mainly stress relief. When such measures are carried too far, a major deformation of the canopy may be induced, commonly described as *infolding,* and several gores can be affected. This deficiency can be avoided by following good design practice.

Stress relief of critical internal loads occurring near the vent is accomplished with an increase of gore pattern width across the crown area, reducing the local radius of fabric-bulge curvature between radials. A similar effect is obtained by the simple expedient of making the vent lines somewhat shorter than the nominal vent diameter. However, this change is felt across the entire canopy and reduces the constructed radius proportionally, while total cloth area and length of the perimeter remain unchanged. When the resultant slack in the cloth exceeds an amount which can be absorbed circumferentially in the normally inflated canopy, an infolded radial crease appears in one side and the tension in the suspension lines attached to the affected gores is sharply reduced. Degraded aerodynamic performance and structural strength result.

A quantitative appraisal of the approximate limit of vent-line shortening which may be used is indicated by the comparison of Table 8.2 in which the nominal vent diameter is 10% D_O, i.e., $S_V = 1\%\ S_O$. When the circumferential fullness added to the normal canopy exceeds ~0.6%, infolding is possible and one or more gores will have a tendency to tuck in during the majority of tests performed. Therefore, unless the vent diameter is less than 10% D_O, vent line shortening in excess of 5% should not be used. More specifically, the product $(\Delta l_V/l_V)\ (D_V/D_O)$ should not exceed 0.005. Best practice remains as described, and in quantitative terms, very adequate stress relief can be obtained from added circumferential fullness in the crown area which tapers linearly from 10% at the vent band to zero at $h_f/h_s = 0.3\text{-}0.4$. No shortening of vent lines is recommended; ordinarily they will be measured under sufficient tension to fall a few percent short of the nominal D_V.

The development of gore coordinates for a circular canopy of general profile is illustrated in Figure 8.4. The functional relationship between the profile dimensions r' and h' may be defined by the designer to satisfy his requirements for the gross inflated profile, guided by experience with experimental models of many different sizes and shapes. Within limits, the deviation of the inflated canopy from the constructed profile can be anticipated, and this understanding utilized to minimize the high hoop stresses characteristic of a perfect surface of revolution. In short, the tendency for the gores to bulge outward between the radials is employed for stress relief so that additional circumferential fullness needs to be added toward this end only, across the crown area, defined by dimension h_f. Through this device the fabric pressure loads are transformed into radial loads and the radial seams become the primary load-bearing members of the canopy structure.

Traditionally, circular canopies of all sizes have been treated as polyhedral forms made up of N flat gores with the coordinates

$$e = 2r' \sin(180^\circ/N) \qquad 8\text{-}3$$

but when $N > 24$ the difference between e and e' for a surface of revolution is entirely negligible and it is convenient to use the less cumbersome formula

$$e' = 2\pi r'/N \qquad 8\text{-}4$$

Similarly, the functional relationship between gore height dimension h and the profile dimensions r' and h' may be simplified, as in the case of the flat canopy for example.

$$h = r' \cos(180^\circ/N)$$

and when $N > 24$ the difference between h and r' is less than 1.0%, or for practical purposes, $h = r'$ may be used in the gore layout of large flat canopies.

Modification of the gore coordinates for stress relief in the crown area is generally adequate with $\Delta e_V = 0.10 e_V$ tapering to zero at $h_f/h_s = 0.3\text{-}0.4$, but there is room for considerable flexibility here. This method of introducing circumferential fullness for

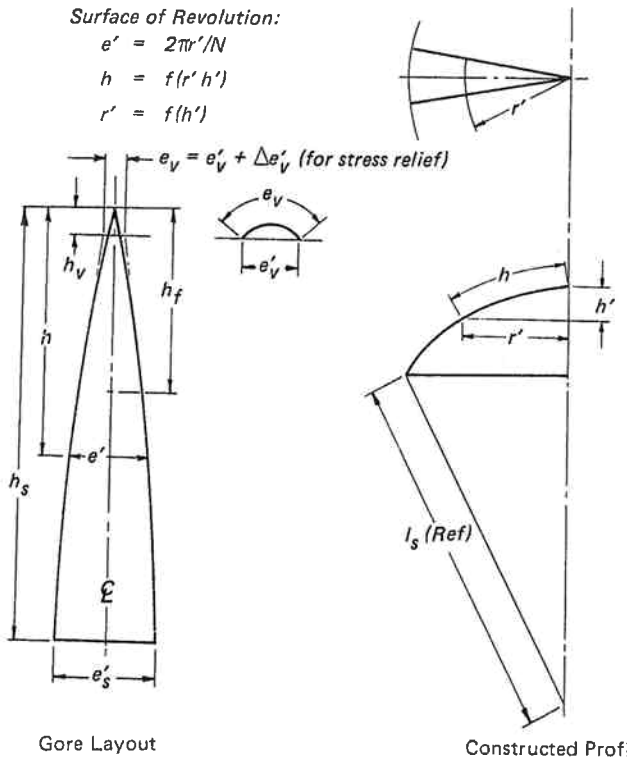


Figure 8.4 The Development of Gore Coordinates for Circular Canopy of General Profile

stress relief is preferable to the use of shortened vent lines because it is both more selective and more efficient.

Note that the nominal gore height h_s extends to the apex or vent center, and for layout of shaped canopy gores may be divided into a number of equal segments, Δh, usually ten. In most designs the curvature of the gore sides is so slight that an excellent approximation is obtained by making the layout with straight-line elements between measured points of *e/2* vs *h* along either side of the gore centerline. The flared-skirt detail also may be added with straight-line elements in the same manner used for the extended skirt gore layout.

Non-Uniform Porosity Distribution. Non-uniformly distributed canopy porosity is exemplified by parachutes having varying slot widths between horizontal ribbons or cloth rings or a wide annular slot at some radial location between the central vent and the periphery of the inflated canopy. A very wide single slot may establish a limiting diameter for expansion of the inflating canopy. A canopy can inflate to a size larger than the wide slot diameter if the ratio of air inflow to outflow remains greater than unity; so that a favorable pressure distribution is maintained. This is strongly influenced by the mouth inlet area. Inflation and canopy growth will stop at the wide slot if the outward radial pressure on the skirt is insufficient to overcome the inward component of structural tension resisting expansion of the canopy mouth. A skirt reefing line will have this effect with a wide slot of relatively small diameter, e.g., reefed first stage of the modified Ringsail of the Apollo ELS. A wide annular slot near the periphery of the canopy may limit the full inflated diameter to that defined by the slot, as in the D-G-B parachute of the Viking Mars Lander.

In this form, ventilation concentrated in one part of the canopy functions as a shape-controlling mechanism so that its magnitude in terms of geometric porosity may be less important than its location. The cylindrical skirt (band) of the D-G-B outside the "gap" appears to function as a flow spoiler promoting rapid vortex shedding, thereby limiting the growth of the lift-inducing flow pattern which drives pendular oscillations. Minor changes in the fullness and angle of attack of this band can be visualized which would significantly augment both drag and stability of the parachute as a whole while a moderate amount of crown ventilation would mitigate the high opening load.

Experience with the much-used slotted canopy designs (ribbon, ringslot, and Ringsail) has established

recommended nominal total porosity levels for each which decrease with increasing scale in order to maintain the critical opening velocity of the parachute at a safely high value. Figures 8.5 and 8.6 provide guidelines for the design of ribbon and ringslot canopies (flat or conical). Similar data for proportioning the crown slots of the Ringsail canopy are given in Ref. 217. This scale effect is attributed to decreasing Kaplun number or increasing relative elasticity of the parachute structure with increasing size, which also causes the total porosity to increase.

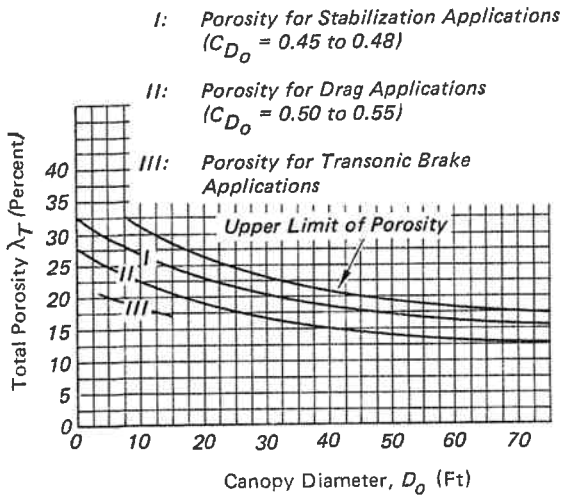


Figure 8.5 Total Porosity vs. Canopy Diameter for Flat Circular Ribbon Canopies

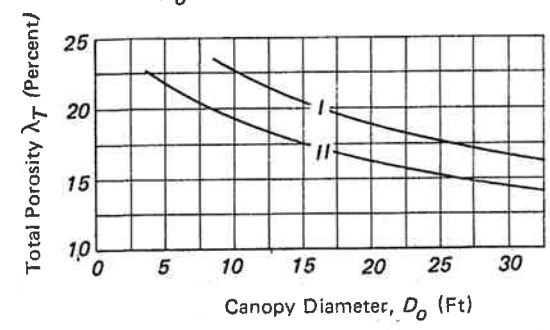


Figure 8.6 Recommended Total Porosity of Ringslot Canopy Designs

Reefing the Main Parachute. Drag area staging by reefing is the recommended first step to take (before inclusion of a drogue chute) after determining that the opening force of the non-reefed main parachute would be excessive when deployed at any of the design conditions on the given velocity/altitude profile of the body or vehicle to be recovered.

Criteria defining an acceptable peak opening force are found in the allowable load factors for the vehicle or payload and also in the allowable weight of the decelerator subsystem.

The main parachute, being the largest component, gains weight rapidly with increases in the design limit opening load. Consequently, it is good practice to minimize the main parachute opening forces to the extent permitted by the decelerator subsystem operational requirements. A load factor of $F/W = 3$ is a reasonable goal for many applications.

When allowable recovery load factors are relatively high, the design limit load of the main parachute can be governed either by the allowable weight criterion or by the strength of a lightweight parachute structure which will satisfy all requirements for handling (repacking, reuse, etc.), durability and serviceability. As a minimum example, within certain scale limitations, a parachute made of 1.1 oz/yd^2 nylon ripstop with suspension lines of 350 lb nylon cord is sufficiently durable to satisfy many recovery system requirements. The allowable maximum opening load of such a parachute can be quickly estimated, e.g., $F_X = C_D S q_s (C_X)$ with $C_X = f(R_m)$ in Figure 6.25 and $R_m = (C_D S)^{3/2}/M$. The utility of this approach is illustrated with a numerical example for System A (introduced in Table 8.1) typical of a class of small RPV's for which the maximum speed at recovery command would be represented by v_d = 150-250 kts (EAS) at low altitudes (say $\rho = .0022$ sl/ft^3).

The parachute with $D_o = 31.3$ ft and $C_D S = 754$ ft^2 would normally have about twenty-eight gores and twenty-eight lines. The system mass ratio is $R_m = 4.9$ calculated from the given data ($M = 300/g = 9.33$ sl). With the aid of Fig. 6.25, we can estimate $C_X \sim 0.04$ and predict probable opening forces for different deployment velocities in level flight as shown in Table 8.3 using $F_X = (.04)\ 754\ q_s$ and letting $v_s = v_d$.

Comparing these forces with $F_X = ZP_R/D_F = 5158$ lbs., where $P_R = 350$ lbs and $D_F = 1.9$, we see the possibility of employing a lightweight parachute, non-reefed, at recovery speeds up to 200 + kts (EAS) in level flight, provided the allowable load factor of the vehicle is greater than $G_X \sim 17$. Given a lesser load factor, canopy reefing will be required for any vehicle system not flexible enough for acceptable reduction of recovery speed or dynamic pressure at deployment.

TABLE 8.3 SYSTEM A OPENING FORCES (NON-REEFED)

Deployment	v_d	kts	150	200	250
(EAS)	v_s	fps	253	338	422
q_s		psf	76	136	212
Opening:	F_X	lbs	2292	4102	6394
Ratio	F/W		7.64	13.7	21.3

The *opening load factor* method of load prediction provides a convenient tool for estimation of the reefed drag area required. With vehicle load factor given, the maximum allowable opening force is close to

$$F_X = W_b (G_x - \sin\theta) - C_D A q_s \qquad 8\text{-}5$$

Body drag $(C_D A\ q)$ may be neglected when it is small compared to F_X. Given the dynamic pressure, q_s, the reefed drag area should not be greater than

$$(C_D S)_r = F_X / q_s C_{X_r} \qquad 8\text{-}6$$

Further, after disreefing, the peak opening force will not exceed F_X if the dynamic pressure at disreef is limited to

$$q_{dr} = F_X / (C_D S)_o C_{X_{dr}} \qquad 8\text{-}7$$

Equalization of Opening Load Peaks. When the vehicle load factor governs, equality of peak opening loads reefed and after disreefing is the usual design objective for the prime design condition of the parachute subsystem. Secondary design conditions tested after the reefing ratio has been established may cause the reefed opening force to vary, but the peak opening force on disreefing will remain essentially constant because the disreef dynamic pressure shows only a small variation.

When peak opening loads exceed allowable maxima with one stage of reefing, a second reefed stage may be introduced. The length of the reefed intervals should be made as short as is consistent with adequate deceleration prior to disreefing. While a near-equilibrium descent condition may be attained in a few seconds, the travel distance during canopy inflation is critical for some systems (or some design conditions), so that disreefing may be timed short, causing the dynamic pressure at disreef to be greater than the equilibrium value by a factor in the order of 1.2 — less when the flight path angle at disreef is small. This may be estimated for preliminary calculations.

On the average, a fair estimate of the reefed drag area required can be made quickly by letting $q_{dr} = 1.1\ q_e$

where $q_e = W/[(C_D S)_r + C_D A]$ 8-8

When the canopy growth during the reefed interval is significant, this change should be allowed for in calculations. One method of estimating the reefed drag area required is illustrated with a numerical example for System B, introduced in Table 8.1:

Given:

Recoverable weight	$W = 4{,}000$ lbs $(M = 124.3$ sl$)$
Main canopy	$C_D S = 7{,}017\ ft^2$
Altitude	$h = 10{,}000$ ft $(\rho = .00176\ sl/ft^3)$
Trajectory angle	$\theta = -90^\circ\ (\sin\theta = 1.0)$
Allowable load factor	$G_X = 6$
Vehicle drag area	$C_D A = 4\ ft^2$

Calculations:

Mass ratio $R_m = 0.00176\ (7{,}017)^{3/2}/124.3 = 8.32$

Disreef opening load factor $C_{X_{dr}} = 0.20$ (Fig. 6.25)

Note that the presently unknown weight of the parachute is part of the recoverable weight, but like the vehicle drag, is generally small enough to be neglected in this type of calculation where G_X is applicable to the vehicle weight only. Thus, the allowable opening load on disreefing (by Equation 8-5) is close to

$$F_X = 4000\ (6-1) = 20{,}000\ \text{lbs}$$

Then the dynamic pressure at disreef (Equation 8-7) should not exceed

$$q_{dr} = 20{,}000/7017\ (.20) = 14.25\ psf$$

and the reefed drag area required (from Equation 8.8) is approximately

$$(C_D S)_r = 1.1\ W/q_{dr} - C_D A = 309 - 4 = 305\ ft^2$$

TABLE 8.4 PERMANENT REEFING SHAPE AS A FUNCTION OF NO. OF GORES

Number of Gores (N)	6	8	10	12	16	20	>24
$\pi_o = N \left(\sin \frac{180}{N}\right)\left(\cos \frac{180}{N}\right)$	2.598	2.828	2.939	3.00	3.062	3.090	$\sim\pi$
Reefing Ratio $(D_R/D_o = 2/\pi_o)$	.770	.707	.681	.667	.653	.647	.637

Note that vehicle drag is negligible in the disreef opening load calculation, but may be significant in the reefed drag area estimate.

This method of making a preliminary estimate of the reefed drag area is not concerned with either length of reefed interval or the reefing ratio needed to determine reefing line length. It simply provides a starting point on which to base trajectory computations leading to a refinement of the reefing requirements. The resultant variation of dynamic pressure with time evaluated along with opening force calculations indicates the reefed time delay to be specified for experimental verification later.

Determination of Reefing Line Length. The reefed drag area required is often determined by methods based on near-equilibrium conditions corresponding to the testing methods used to obtain the empirical data represented by the curves of ζ vs D_r/D_o plotted in Figure 6.64. This provides a convenient means of estimating the approximate length of reefing line for a circular parachute, i.e., $l_r = \pi D_r$. The result should be verified experimentally by full scale aerial drop tests at the limit design conditions when, as is usually the case, opening loads are critical and equal peak loads are desired for each stage of opening.

Numerical Example

It was determined that for the given conditions of System B (Table 8.1), the 98 ft D_o parachute with $(C_DS)_o = 7017\ ft^2$ should have a reefed drag area of $(C_DS)_r = 351\ ft^2$.

The length of the reefing line may be estimated as follows:

$\zeta = 351/7017 = .0421$

In Figure 6.64 the curve for solid flat, etc., parachutes yields

$D_r/D_o = 0.087$ (8.7% nominal)

$D_r = (.087)\ 98 \sim 8.52$ ft

$l_r = \pi D_r = 26.8$ ft (reefing line length)

In addition, the inflated diameter, D_{p_r}, of the reefed canopy may be estimated with the aid of Figure 6.65 for use later in calculating the reefing line load.

For $D_r/D_o = 0.087$, $C_{D_p}/C_{D_{p_o}} \sim 0.40$

Given:

$C_{D_o} = 0.93$ and $D_p/D_o = 2/3$

$C_{D_{po}} = (9/4)\, C_{D_o} = 2.09$

$C_{D_{p_r}} = 0.40\ (2.09) = .84$

$S_{p_r} = 351/.84 = 418\ ft^2$

and

$D_{p_r} = 23.1$ ft

Permanent Skirt Reefing. The permanent skirt reefing of parachutes is accomplished in different ways, depending somewhat upon the purpose. If the purpose is prevention of over-expansion of the canopy to limit opening load peaks, a heavy reefing line is stitched inside the skirt at the radial seam intersections. Since no reduction in the normal full open area of the canopy is desired, in this case the reefing ratio used is close to, but not less than $D_r/D_o = 2/\pi_o$ where π_o is the shape factor of a regular polygon given in Table 8.4. If the purpose of fixed reefing is the attainment of a desired equilibrium descent velocity or test dynamic pressure with improved stability (as in a system test,) the conventional skirt reefing line and running rings are used without a line cutter.

Cluster Opening Forces. The synchronous opening forces of a cluster as a whole and of its individual member parachutes may be predicted by the same m methods used for single parachutes. For the non-synchronous case, the approach described in Chapter 7, is illustrated here with numerical examples based on a cluster of three 156 ft (D_o) parachutes of System C, first introduced in Table 8.1.

Numerical Examples

Given:

$M = 50{,}000/g = 1554$ sl.

$C_DA = 100\ ft^2$ (assumed body drag area)

D_o = 156 ft

n_c = 3

D_r/D_o = 0.10 (reefing ratio to be verified)

h = 2000 ft MSL (ρ = 0.002241 sl/ft^3)

q_s = 60 psf (133 kts EAS)

$\Sigma C_D S$ = 52,520 ft^2

ζ = 0.07 (Figure 6.64 for Ringsail)

Calculations (synchronous opening):

At the end of the reefed interval (disreef)

$\Sigma(C_D S)_r = 0.07\ (\Sigma C_D S) = 3676\ ft^2$

Canopy growth during the reefed interval should be taken into account when known. Test data given in Reference 217 show a growth ratio for the Ringsail parachute in the order of

$(C_D S)_r$ (disreef) / $(C_D S)_r$ at F_r (max) = 1.56 (at D_r/D_o = 0.10

Then, at F_r (max)

$\Sigma(C_D S)_r = 3676/1.56 = 2356\ ft^2$

The reefed mass ratio by Equation 6-18 is

$R'_{m_r} = 0.002241(2356)^{3/2}/1554 = 0.164$

The opening load factor may be estimated with the aid of Fig. 6.25; reading the *reefed* curve

$C_{X_r} = 0.55$

The combined reefed opening force would be in the order of

$\Sigma F_r = 2356\ (60)\ 0.55 = 77{,}750$ lbs

or $F'_r = 25{,}900$ lbs for each of three

In the normal course of events, at the end of the reefed interval, the system will be approaching an equilibrium descent condition with

$q_{dr} \sim 1.1\, q_e$

and by Equation 8-7

$q_{dr} = 1.1\ (50{,}000)/(3676 + 100) = 14.57$ psf

The full open mass ratio is

$R'_m = 0.002241\ (52{,}520)^{3/2}/1554 = 17.4$

Reading the disreef curve of Fig. 6.25

$C'_X \sim 0.06$

and $\Sigma F_o = 52{,}520\ (14.57)\ 0.06 = 45{,}900$ lbs

or $F'_o = 15{,}300$ lbs for each of three

Averaging the reefed and full opening forces indicates that by adjustment of the reefing ratio equal load peaks in the order of

$F'_r = F'_o = 21{,}000$ lbs

may be obtained in each parachute for the synchronous opening case. The revised reefed drag area may be estimated by working backward from $\Sigma F_o = 3F'_o = 63{,}000$ lbs above, with R_m and C_X unchanged. The desired dynamic pressure at disreef is approximately

$q_{d_r} \sim 63000/\Sigma C_D S\, C_X = 20$ psf

Then at disreef $\Sigma(C_D S)_r = (1.1\, W/20) - 100 = 2650\ ft^2$

For the same growth ratio, the reefed drag area at $F_{(max)}$ is

$\Sigma(C_D S)_r = 2650/1.56 \sim 1700\ ft^2$

The revised mass ratio for the reefed parachute is

$R'_{m_r} = \rho\,(1700)^{3/2}/M = 0.10$

and per Fig. 6.25

$C'_{X_r} = 0.62$

then $\Sigma F_r = 1700\ (60)\ 0.62 = 63{,}240$ lbs or $F'_r = 21{,}080$ lbs for each of three.

The revised reefing ratios are

$\zeta = 2650/\Sigma C_D S = 0.05$

using $D_r/D_o \sim 0.08$ from Figure 6.64.

Calculations (non-synchronous opening):

Cluster empirical load factor for an uncontrolled cluster from page 341.

$C_Y = 1.80$

and the design limit load for each parachute (per Equation 7.24) would be in the order of

$F_X = 1.8\ (21{,}000) = 37{,}800$ lbs

With a cluster controlled by the method described on page 262

$C_Y \sim 1.3$

and at design limit $F_X = 27{,}300$ lbs both reefed and after disreefing. For a cluster, the mass ratio of the lead canopy may be defined by

$R_m = R'_m/K_c$

In the theoretical worst case $K_c = n_c$ and the mass ratios, opening load factors, and predicted maximum opening forces change as shown in Table 8.5 where:

$R_{m_L} = R'_m/3$; $C_Y = C_{X_L}/C'_X$

and $F' = 21{,}000$ lbs.

Comparison of these results with the test data in Table 6.2 indicates two characteristics of free clusters:

1) Reefed max/mean force ratios of lead canopies tend to approach the worst case C_Y in

TABLE 8.5 LEAD CANOPY WORST CASE OPENING LOADS

Configuration	R'_m	R_{m_L}	C'_X	C_{X_L}	C_Y	$F(max) = C_Y F'$ lbs
Reefed	0.10	0.033	0.62	0.77	1.24	26,000
Full Open	17.4	5.80	0.06	0.32	5.33	112,000

equivalent systems such as that identified with Reference 431.

2) Full open max/mean force ratios after lead canopy disreefing are never likely to approach the worst case indicated by $C_Y(max)$ because of the low probability of having all but one of the canopies carry no load throughout lead canopy inflation.

Equalization of Cluster Opening Load Peaks. The test data of Table 6.2 justify use of different cluster opening load factors reefed and on disreef in the present numerical example as follows:

Reefed $C_Y = 1.3$

Full open $C_Y = 2.0$

The two opening load peaks may be equalized for the design limit case by revising the reefing ratio derived from the synchronous opening calculations ($D_r/D_o = 0.08$). Without repeating the calculations, it will be seen that the original reefing ratio of $D_r/D_o = 0.1$ comes close to satisfying the requirement and the following design limit loads are indicated.

Reefed $F'_r = 25{,}900\,(1.3) = 33{,}670$ lbs

Full open $F'_o = 15{,}300\,(2.0) = 30{,}600$ lbs

These may be rounded off for each stage to

$F_X = 32{,}000$ lbs

In other words, a reefing line diameter of 10 percent D_o is close to optimum for the free cluster, while as indicated above, 8 percent D_o would be used with the controlled cluster, and the design limit load would be reduced to $F_X \sim 27{,}000$ lbs.

Strength of Materials. The strength of materials required in the decelerator structure is determined, first, by approximate preliminary internal loads analysis based on predicted design limit opening loads. Later, the structure may be refined, as desired, through application of one of the more rigorous computerized methods of structural analysis (see Chapter 7). From the design limit loads predicted for each opening stage when the canopy is reefed, the critical unit load in each structural member, f'_c, is calculated and multiplied by a design factor to determine the minimum acceptable strength of material. Equation 7-72 states

$$P'_R = D_F f'_c$$

where the design factor, $D_F = S_F/A_P$; S_F is the *safety factor* and A_P is the allowable strength factor. For parachutes, recommended components of the allowable strength factor are given in Table 8.6, with recommended safety factors and corresponding design factors. When actual minimum joints and seam efficiencies are known, e.g., the results of laboratory tests, these values of u should be used. For asymmetry of loading, $s = 1.0$ is used when no quantitative evaluation can be made from system or decelerator geometry and test experience. Factors i (vacuum) and t (temperature) should be evaluated for the conditions expected to prevail at the time of the deceleration operation, because the recovery of losses caused by the on-board mission environment is rapid and can usually be quantified.

The main parachute of System B, introduced in Table 8.1, provides the basis for a numerical example which illustrates the short method of calculating the approximate strength of materials required in a polysymmetric parachute structure.

Given: Unmanned vehicle $W = 4000$ lbs

Design limit load (reefed and after disreefing)

$F_X = 20{,}000$ lbs

Main parachute $D_o = 98$ ft

$S_o = 7545$ ft^2

$C_D S = 7017$ ft^2

Reefed $(C_D S)_r = 351$ ft^2

$D_r/D_o = 0.087$ or $D_r = 8.53$ ft

Approximate projected diameters

Full (2/3 D_o) $D_p \sim 65.3$ ft

Reefed $D_{p_r} \sim 23.1$ ft

Effective suspension line length

$l_e = 108$ ft ($\sim 1.1\,D_o$)

TABLE 8.6 RECOMMENDED PARACHUTE DESIGN FACTORS

(Use 1.0 for any sub-factor not otherwise quantifiable)

Application	S_F	Joint u	Abrasion e	H_2O o	Fatigue k	Temp. τ	Vac. ι	Unequal Loads s	Convergence $\cos\phi$	A_P	D_F
Vehicle Recovery											
RPV, Etc.	1.5	.85	.99	.99	1.0				.95	.79	1.9
Manned	1.35	.80	.92	.92	.92				.95	.59	2.3
Emergency Escape											
Bailout	2.0	.80	.95	.95	.95				.95	.65	3.1
Other	1.35	.80	.92	.92	.92				.95	.59	2.3
Airdrop											
Paratroop	2.0	.80	.95	.95	.95				.95	.65	3.1
Cargo	1.5	.80	1.0	.95	.95				.95	.69	2.2
Aircraft Decelerator	1.5	.80	.95	.95	.95				.95	.65	2.3
Special											
Spec. Weapons	1.5	.80	1.0	1.0	1.0				.94	.75	2.0
Other	1.5	.85	.99	.99	1.0				.95	.79	1.9

NOTE:
- u Use measured joint efficiencies when known
- e Abrasion
- o Moisture absorption
- k Fatigue
- τ Evaluate for temperature of decelerator structure during peak load operating conditions
- ι Evaluate effect of exposure to vacuum at time of deployment or peak loading
- s Evaluate assymmetrical unequal loading when significant
- ϕ Convergence angle of lines or risers at time of peak load when known
- A_P Modify allowable load factor as required by *measured* sub-factors
- D_F Modify design factor as required by refined A_P

Calculations:

Structural safety factors:

Parachute (Table 8.6) $S_F = 1.5$

Risers (good practice) $S_F = 2.0$

Design factors:

Parachute $D_F = 1.90$

Risers $D_F = 2.5$

Allowable strength factor (all nylon materials)

$A_P = u\,e\,o\,k\cos\phi = 0.79$

where	Lines & Risers	Canopy
u =	0.85	0.85
e =	0.99	0.99
o =	.99	.99
k =	1.00	0.95
$\cos\phi$ =	0.95	1.00

Suspension lines. Allowable strength:

$P_A = 0.79\,P_R$

Unit load $f'_t = 20{,}000/Z$

Required minimum strength

$$P'_R = 1.9\,f'$$

Number of lines	Z	88	96	104
	f' lbs	227	208	192
	P'_R lbs	431	395	365

Use $Z = 96$ and $P_R = 400$ lbs (braided nylon cord). This result justifies the use of 96 suspension lines and 96 gores in the canopy (with 8 riser branches and 96/8-12 lines per branch).

The margin of safety by Equation 7-78 is

$$M_s = (400/395) - 1 = 0.013$$

Canopy Radial Tapes. Let the canopy be of 45 degree bias construction with one inch, 4-needle, French fell seams reinforced with flat nylon tapes. The tapes must be pre-marked at each diagonal cross-seam intersection, as located in the gore pattern lay-out, to ensure uniform distribution of cloth fullness along the seam. (Two marking patterns, one for each side of the gore, are required.) The strength of the radial tape should be at least

$$P'_R = 0.90\,P'_R \text{ (suspension lines)} = 356 \text{ lbs}$$

Availability of materials limits the choice to a 400 lb, 3/4 inch tape or a 525 lb, one-inch tape, the latter being fifty-percent heavier. Use of the 400 lb tape in the interest of structural efficiency entails a modification of the radial seam, and several acceptable alternatives may be considered. Design of a 3/4 inch, 3-needle fell seam would also improve structural efficiency and could be recommended.

$$M_s = (400/356) - 1 = 0.124$$

Risers. Unit load, $f' = 20{,}000/8 = 2500$ lbs. Required minimum strength, $P'_R = 2.5, f' = 6250$ lbs per branch. Available nylon webbing materials include:

Strength lbs	Width in	Thickness in	Unit Weight lb/ft
6500	1.75	.110	.0604
8700	1.75	.10	.0500
9000	1.0	.195	.0500

Of these, the 8,700 lb webbing would be a good choice, being lighter than 6500 lb material and thinner than the 9000 lb material.

$$M_s = (8700/6250) - 1 = 0.39$$

Reefing Line. Test measurements, such as those reported in Reference[217] indicate that tension in the reefing line builds up slowly during inflation and peaks out shortly after the reefed opening force passes its maximum. With reference to Figure 7.21, this may be caused by the canopy development angle $(\psi - \phi)$, being relatively small at $F_r\,(max)$, because D_{p_r} has not reached its maximum value at that time and the rate of canopy inflation has been reduced to low level by restraint of the inlet area. Thus, by the given relationship, f'_s/F passes its maximum while F is decreasing and $(\psi - \phi)$ is increasing, a process far enough removed from impact dynamics to be treated as a static load problem. By substitution of the given values in Equation 7-107.

$$h_c = \pi D_{p_r}/4 = 18.14 \text{ ft}$$

$$h_1 = (D_o/2) - h_c = 30.85 \text{ ft}$$

$$\sin\phi = D_r/2l_e = 0.03949$$

$$\sin\psi = (D_{p_r} - D_r)/2h_1 = 0.2361$$

$$f'_s/F = (\tan\psi - \tan\phi)/2\pi = 0.03238$$

where

$$\tan\psi = .2430$$

$$\tan\phi = .03952$$

Since $F < F_r\,(max)$ and D_{p_r} is representative of canopy size at the end of the reefed interval, a very conservative evaluation of the reefing line tension is

$$f'_s = .03238\,(20{,}000) = 648 \text{ lbs}$$

and $P'_R = 1.9\,f'_s = 1231$ lbs

Use of a braided nylon cord with $P_R = 1250$ lbs would provide an adequate safety factor for the verification test program with

$$M_s = (1250/1231) - 1 = 0.15$$

Canopy Cloth. The crown of the reefed canopy is subjected to the highest unit load, which (from Equation 7-79) is approximately

$$f'_c = F_X/\pi D_{p_r}$$

$$= 20{,}000/\pi(23.1) = 276 \text{ lb/ft or } \sim 23 \text{ lb/in}$$

This load may be increased to allow for the possibility that the projected diameter may have been significantly smaller at F_X than 23.1 ft. A lateral reinforcement located at the point of maximum stress may be applied, however, to react to the pressure load. The cloth strength required should be

$$P'_R = 1.9\,(23)\,1.1 = 48 \text{ lb/in}$$

Then, as a minimum, 1.6 oz/yd^2 ripstop nylon with $P_R = 50$ lb/in could be used in the crown of the canopy and

$$M_s = (50/48) - 1 = 0.42$$

The pressurized area of the crown is assumed to be that of a spherical segment of diameter D_{p_r}. The

radial distance along the surface from pole to equator would then be $h_c = 18.14$ ft as calculated above.

With a lighter material in the balance of the canopy the transition may be made at the nearest cross seam, i.e., one located at $h_c + \Delta h$, where Δh is a small increment.

The strength of material required over the major area of the canopy is a function of the final opening load peak. With $R_m = 8.32$ this peak will occur in mid-inflation before the canopy is full open. Assuming that the final opening load peak will occur at an inflation stage similar to that reported in Ref. 573 results in $D_p/D_o = 0.27$. Then with the substitution of $D_p = 26.5$ ft in Equation 7-79, the approximate unit load is

$$f'_c = 20{,}000/\pi(26.5)$$
$$= 240 \text{ lb/ft or } 20 \text{ lb/in}$$

and $P'_R = 1.9(20) = 38$ lb/in

This result justifies the use of 1.1 oz/yd^2 ripstop nylon with $P_R = 42$ lb/in in the balance of the canopy and

$$M_s = (42/38) - 1 = 0.0526$$

Reinforcing Bands. Since the primary pressure loads are transferred directly from the fabric to the canopy radials, added reinforcing bands are redundant and the determination of their strengths is somewhat arbitrary. Critical loads in skirt and vent bands have been encountered during non-uniform opening conditions, such as inflation to a false apex and sail-like deployments with canted skirt, and sometimes in tests at stringent off-design overload conditions.

Skirt Band. The radial to suspension line joint is designed to transfer any side loads into the skirt band. Therefore, as a minimum, the strength of the skirt band should be equal to that of the line. Because failure of the skirt band could be followed by more extensive canopy damage, and also because the weight of the band is not a critical factor, a substantially stronger tape or web is used. Use of a narrow stiff skirt band, rather than a broad soft one, is recommended because, as noted earlier, this is one of the aids in getting canopy filling started at line stretch. Thus, for the parachute of this example a minimal skirt band reinforcement would be represented by either a 500-lb 9/16-inch webbing or a one-inch tape of the same strength, both being quite flexible. But for a significant increase in stiffness (after stitching to the skirt hem), as well as large margin of safety, a 1,000-lb half-inch tubular web could be used at small cost in increased weight.

Vent Bands and Intermediate Bands. It has been observed in many severe off-design tests that complete break-up and collapse of the canopy could have been prevented if the vent band had not failed. For this reason, it has long been good practice to use a grossly over-strength tape or webbing reinforcement on the vent hem, relative to any load that might be predicted by pressurized membrane stress theory. One approach is to assume that the canopy fabric carries no load over the area of interest, as would be the case with a split gore.

A logical place for an intermediate reinforcing band is near the transition between the 1.6 oz and 1.1 oz cloth at $h_c = 18$ ft from the canopy apex. Neglecting the vent radius, the total load to be carried across the split gore by the two bands is approximately

$$\Sigma f' = f'_c h_c = 276(18.1) = 4996 \text{ lbs}$$

With the load divided equally between the bands

$$P'_R = 1.9(4996/2) = 4746 \text{ lbs each}$$

where it is assumed that only the fabric between the bands is not loaded. In actual practice a vent band of 4,000-lb one-inch webbing could be used with confidence.

Cross-Vent Lines. Although the vent-line load is substantially less than the suspension line load, it is good practice to use the same material for the cross-vent lines with stitched joints to the radials of equivalent strength, 400-lb braided nylon cord in this example.

Verification of Preliminary Strength of Materials Estimate. Traditionally, full scale aerial drop tests of prototype parachute models have been performed at design and over-design conditions to verify strength of materials calculated by the foregoing (or similar) approximate methods. Now, such methods merely provide initial inputs for suitable computer programs, e.g., CANO, and the like (Chapter 7), which permit complete refinement and optimization of the structural design for uniformly small margins of safety in all members where redundant load paths do not exist and the available selection of materials strengths is broad. Of course, the problem becomes more complex in annulate parachutes (ribbon, ringslot, Ringsail) with a multiplicity of horizontal or circumferential members; also, primary reinforcing bands still require special treatment.

Confidence in the final design, prior to any full scale tests, depends upon the rigor with which the inflated shapes and pressure distributions are deemed to have been derived. Shortcomings in this respect can be appraised by a few simple tests for verification of both the reefing parameters and the inflated shapes, reefed and after disreefing, at each peak load; the need for more comprehensive tests will then be established. There is good justification for the proposition that the use of advanced computer programs for both the prediction of design limit opening loads and for parachute structural design can greatly reduce the number and complexity of the development tests which customarily have been performed for such purposes.

The Gliding Parachute. Criteria governing selection of a gliding parachute system differ greatly, depending upon whether operational requirements can be satisfied with a nonsteerable gliding parachute of minimal L/D or whether the performance of a *steerable* parachute of high L/D is mandatory. The complexities and operational problems associated with control of the gliding system should not be accepted lightly.

The non-steerable gliding system may be the same in all details as the ballistic parachute system, except that the main canopy is modified to descend in a stable directional glide with a ratio approximately $L/D = 0.3\text{–}0.7$. The prime justification for this approach is the substantial improvement in system stability realized[172] While there may be an attendant reduction in rate of descent for a given canopy size, with a consequent gain in effective drag efficiency, this is usually a secondary consideration. If the glide-chute modification consists of augmented ventilation on one side of the canopy, the increased total porosity usually cancels the gain in efficiency due to gliding.

One of the most effective ways to make a circular canopy glide with a reduced rate of descent is to raise the trailing edge a short distance. But preservation of structural symmetry through the opening transient would require use of a temporary one-step control device, such as in early Glidesail experiments (Ref. 217). To avoid this, a similar canopy configuration is approximated by augmenting canopy porosity near the skirt on the trailing side, as in mid-air retrieval parachutes[181] Losses may be minimized by distributing the added ventilation across the trailing edge as close to the skirt as possible and by using only the minimum required for stable gliding (see Ref.172).

Because perfect symmetry about a longitudinal plane can only be approached as a limit in the construction of a gliding canopy, the typical flight path is characterized by a slow turn in one direction. Thus, operational considerations affecting the choice of the non-steerable gliding system include:

The horizontal velocity component adds vectorially to wind drift in a random way.

After the opening sequences the system will descend with a small rate of turn in one direction which may be different in magnitude and direction for each operation.

Rigging and installation of the gliding canopy may entail special provisions to ensure proper orientation of the canopy relative to the vehicle.

The most efficient gliding canopy may require use of a step-control to be actuated after disreefing for transition to the gliding configuration.

For good stability of descent the glide ratio can be relatively small, such that the horizontal velocity component and turn rate, when combined with the effects of wind drift, may be found essentially negligible for many applications benefitting from the gain in stability realized. This appears to be the case for mid-air retrieval systems and may also be true for surface landers employing an impact-attenuation or retrorocket subsystem. In the latter case, the orientation of the canopy with respect to the vehicle may also be of no consequence.

Selection and sizing of the non-steerable gliding canopy is guided by the same considerations set forth for the ballistic system. Modification of a solid cloth canopy to effect gliding is currently done by replacement of cloth panels on one side near the skirt with a high porosity material of open mesh or net weave. A similar modification of the Ringsail design consists simply of omitting a suitable number of sails of the trailing side. Determination of geometric porosity required is described in Chapter 6.

The steerable gliding systems fall into two broad categories distinguished in terms of attainable glide ratios:

Class	$(L/D)_{max}$	Type Designation
Middle	1.0–2.0	Medium-Glide Parachutes
Upper	2.0–4.0	High-Glide Parachutes

It will be recognized that $(L/D)_{max}$ of the system as a whole is significantly less than that of the individual canopy tested under ideal conditions. Moreover, the average L/D attained in straight-away flight is a maximum and is reduced by turning maneuvers. The operational analysis of the vehicle recovery or landing system will indicate a performance level practical in terms of glide-range, maneuverability and wind penetration capability balanced against those cost factors represented by complexity, serviceability, and development risk.

The design L/D required is governed by operation-

TABLE 8.7 STEERABLE PARACHUTE COMPARISON FOR SYSTEM D

Type	Parawing (single-keel)	Parafoil ($AR = 1.5$)
C_R at $(L/D)_{max}$	0.91	0.74
Planform area (S_W) ft^2	9.82	1207
Wing loading (W/S_W) psf	1.53	1.24
Aspect ratio (AR)	2.88	1.5
(Projected)	(2.17)	(1.5)
Wing span (b) ft $(b^2 = ARS_W)$	53.2	42.6
Chord (c) ft	–	28.3
Keel length (l_k) ft $(l_k = S_W/.692^{½})$	37.2	–
Total fabric (S_O) ft^2	982	4492
Area ratio (S_W/S_O)	1.0	0.27
Relative weight factor $(S_O/C_R S_W)$	0.91 1.1	0.20 5.0

al criteria such as:

Maximum wind conditions.

Maximum allowable sinking speed.

Desired gliding range from altitude.

Unit wing loading.

The minimum acceptable turning rate is based on operational requirements for:

Target seeking (spot landing).

Obstacle avoidance (safety).

General maneuverability, e.g., number of turns to be executed during the descent.

Requirements for L/D modulation in flight must be tempered by consideration of the stable angle of attack range for each type between leading edge collapse, α for $(L/D)_{max}$, and the stalled condition. It will be recognized that ram-air cell canopies lacking a rounded leading edge, exhibit only the sharp drop in L/D that attends leading edge collapse in other types at low angles of attack. Because canopy porosity is virtually zero, some steerable parachutes are subject to severe oscillations of large amplitude after stalling, like a low porosity parachute. However, this behavior varies with the shape of the canopy. In either case, as shown in Fig. 6.36, the sinking speed increases rapidly as L/D is reduced by increasing α.

Design requirements expressed in terms of allowable values for v_V (landing) and v_H (wind penetration) automatically define the operational L/D required for the design wing loading W/S_W, as shown in Fig. 6.36A for the equilibrium gliding condition.

$$L/D = v_H/v_V = \cot\theta \qquad 8\text{-}9a$$

$$v = v_V/\sin\theta \qquad 8\text{-}9b$$

$$q = \rho v^2/2$$

and

$$C_R S_W = W/q \text{ or } (W/S_W = C_R q) \qquad 8\text{-}10$$

Where S_W is the planform area of the canopy, C_R the total aerodynamic force coefficient, and θ the glide-path angle below the horizontal.

Given lift and drag coefficients as a function of angle of attack

$$C_R = (C_L^2 + C_D^2)^{½} \qquad 8\text{-}11a$$

or given

$$L/D = \cot\theta$$

$$C_R = C_D/\sin\theta \qquad \text{8-11b}$$

Because $(L/D)_{max}$ occurs close to the angle of attack where a rapid drop in L/D is imminent, it is sometimes desirable to design for L/D at α for v_V minimum.

Sizing the Gliding Parachute. Given the recoverable weight W, and having established the operational L/D required, selection of the type of canopy to be used is guided by the following criteria:

$(L/D)_{max} > L/D$ (required).

C_R at L/D (required) is close to the best attainable.

The ratio of the canopy planform area to the total fabric area (S_W/S_O) is large.

Complexity of reefing requirements is acceptable.

Turning rate satisfies minimum maneuverability.

Since it is usually desirable to have a canopy of minimum bulk and weight, C_R and S_W/S_O must be considered together. Other things being equal, the canopy design of least weight will be obtained when S_O/C_RS_W is a minimum, i.e., the least area of fabric is needed to produce the effective lifting surface. Area S_O necessarily includes all ribs, gussets, and flares, as well as the upper and lower surfaces, because these control the airfoil profile of the canopy and are essential to its aerodynamic performance. In this respect, single surface canopies have an advantage. Significant differences in suspension line rigging and reefing requirements will influence the final selection.

The required planform area (by Equation 8-10) is

$$S_W = W/C_Rq$$

Numerical Examples

Methods of selecting and sizing a steerable gliding canopy for a given application are illustrated by the following numerical examples:

System D is for an RPV to be recovered at the conclusion of its mission by being flown under full control to a designated landing area where a spot landing is made after initiation of recovery at or above 5,000 ft MSL (2,500 ft above ground level). At the design altitude of 2,500 ft MSL the nominal rate of descent is to be $v_V = 15$ *fps* with a landing weight $W = 1500$ *lbs.* The gliding system shall be able to penetrate winds up to $v_H = 20$ *kts (TAS) (33.8 fps).*

As a minimum the glide ratio in straight-away flight should be $v_H/v_V = 2.25$. Selection of the simplest steerable parachute design capable of meeting the requirements is generally the most economical approach. Examination of Figs. 6.36A and 6.36B suggests that either a Parafoil of $AR = 1.5$ or a single-keel Parawing could be expected to satisfy this requirement, with a margin for error, by designing to $(L/D)_{max} = 2.4$. On this basis:

$$v_V = 15 \text{ fps}$$

$$v_H = 15(2.4) = 36 \text{ fps}$$

$$\cot\theta = 2.4 \quad \theta = 22.62^\circ \quad \sin\theta = 0.385$$

$$v = 15/.385 = 39 \text{ fps (TAS)}$$

At 2500 ft MSL, $\rho = 0.002208$ sl/ft^3 and the design dynamic pressure is $q = .001104(39)^2 = 1.68$ psf. Then the canopy effective area required is

$$C_RS_W = 1500/1.68 = 892.9 \text{ ft}^2$$

Determination of C_R at $(L/D)_{max}$ requires performance data obtained, ideally, from large scale free flight tests, otherwise from wind tunnel testing of carefully constructed models. The comparative calculations summarized in Table 8.7 for Parawing and Parafoil are based on data derived from the most recent source references containing large model test measurements in a form suitable for this evaluation, e.g., Fig. 6.36A.

When decelerator system weight and bulk are the dominant criteria, usually the case, then the flexible wing having the smallest aerodynamic area ratio represented by S_O/C_RS_W would be selected, provided there is not a large difference in the strength of materials required. Otherwise differences in reefing requirements, maneuverability and the useful range of L/D modulation may govern. Pertinent characteristic data of the kind and quality needed are not equally available for the different flexible wing designs. This fact, as well as the relative weight factor, would justify selection of the single-keel Parawing for further study as the primary component of System D.

System E is for a payload of 1415 lbs to be spot-dropped with a target-seeking steerable parachute system for which the allowable weights are 150 lbs and 55 lbs for the control package and the parachute pack respectively. The system shall be capable of gliding at $\theta = 45^\circ$ against a 25 kt (42.2 fps) headwind while descending at 30 fps at sea level.

The forward glide velocity must be at least

$$v_H = 30 + 42.2 = 72.2 \text{ fps}$$

At any altitude above sea level the TAS will be greater than this figure.

The minimum glide ratio in straight-away flight must be

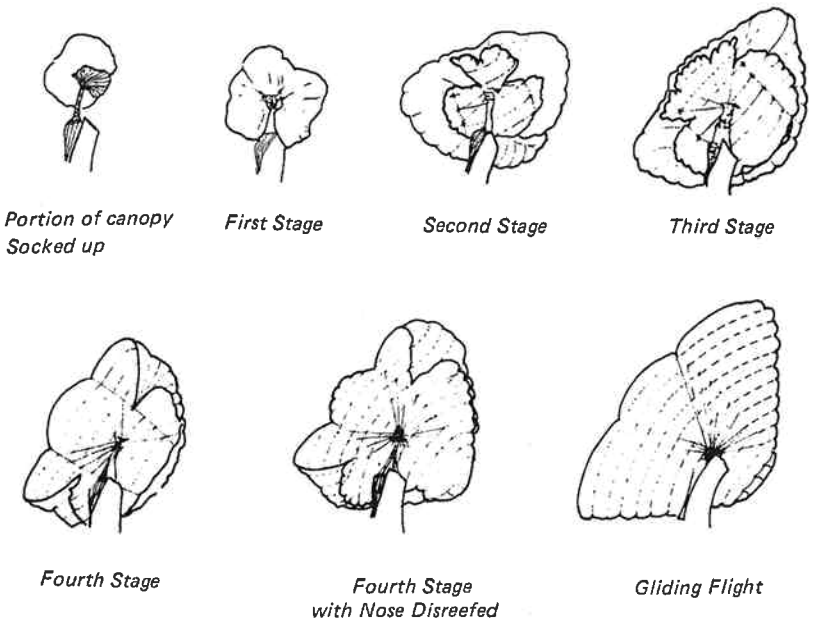


Figure 8 7 Twin - keel Parawing Inflation with Suspension Line Reefing in Four Steps;

$v_H/v_V = 72.2/30 = 2.41 (= \cot\theta)$

In still air $\theta = 22.6^\circ$ $(\sin\theta = 0.384)$

The glide velocity is

$v = 30/.384 = 78.2$ fps

and $q = \rho_o (78.2)^2/2 = 7.27$ psf

$W = 1415 + 150 + 55 = 1620$ lbs

With the minimum required effective aerodynamic area is

$C_R S_W = W/7.27 = 223\ ft^2$

Of the various steerable parachute types, the one having experience at moderately high wing loadings is the Parafoil of $AR = 1.5$ with $C_R = 0.74$ at $(L/D)_{max} = 2.3$ to 2.5 demonstrated (References 132 and 474). Then

Wing area, $S_W = 223/.74 = 301\ ft^2$

Span, $b = [(1.5)\,301]^{1/2} = 21.3$ ft

Chord, $c = 21.3/1.5 = 14.2$ ft

Aspect Ratio. Some steerable parachute designs tend to have a characteristic aspect ratio not subject to much variation in design analysis. On the other hand, those of highest glide ratio may be designed with different aspect ratios, varying somewhat in resultant aerodynamic performance. The flat planform aspect ratio is defined as

$AR = b/c = b^2/S_W$ 8-12

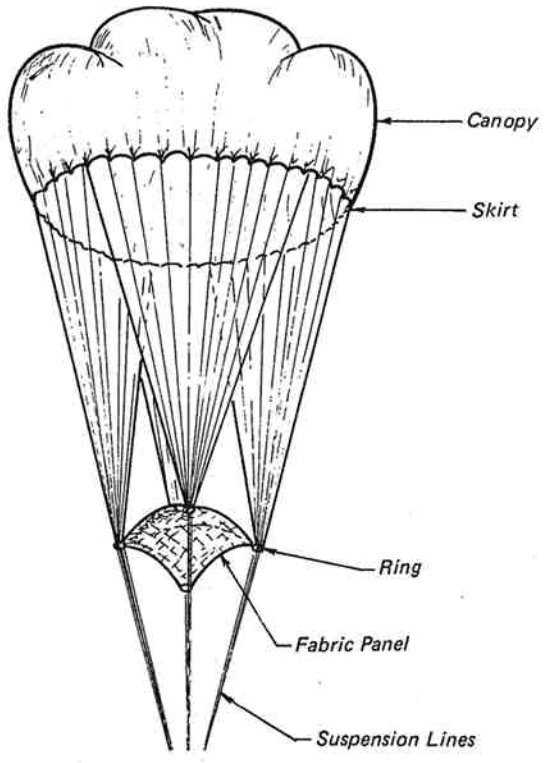


Figure 8.8 Continuous Suspension Line Reefing by Sliding Rings with Drag-Panel

While flat aspect ratios are reduced geometrically by deflection on the wing tips, as in Parawing and Sailwing, the deflected tips tend to act like end-plates and so would augment the effective aspect ratio. Those rectangular canopy designs having negligible wing tip deflection usually have chord-wise suspension flares which act as end plates to augment the effective value of the geometric aspect ratio.

The influence of aspect ratio on steerable parachute $(L/D)_{max}$ often cannot be separated from the effects of other design parameters. Although a single-keel Parawing of $AR = 2.89$ affords $(L/D)_{max} = 2.3$ and twin-keel Parawing of $AR = 3.0$ affords $(L/D)_{max} = 2.8$ in free flight with $W/S_W = 0.95\text{-}1.25$ psf[398] Sleeman[397] notes that numerous configurations identified in Fig. 6.37 exhibit no meaningful correlation between $(L/D)_{max}$ and either aspect ratio or the center panel area ratio, (S_{cp}/S_W) but, as shown in the figure, the parameter $(S_{cp}/S_W) \cos \Lambda_o$ is relevant.

The data point identified as 5a in Fig. 6.37 is for the 4000 ft^2 Parawing of Reference[398]. Its position relative to the wind tunnel data, may be interpreted as an indication of the required correction between wind tunnel model and full-scale free-flight Parawing performance, suggested by the broken line in the figure.

The effect of aspect ratio on Parafoil $(L/D)_{max}$ is broadly indicated by the wind tunnel data of Table 6.7 and a wind tunnel correction factor may be deduced from free flight data in Table 6.8. Variation of wing loading over the range tested, apparently has little effect on $(L/D)_{max}$. Use of Parafoil aspect ratios of two or greater has obvious advantages, but it will be noted in Fig. 6.36A that the unusually rapid variation of L/D with α near $(L/D)_{max}$ would make glide trimming difficult in an automatic system, while, as indicated in Fig. 6.36B errors in trim could cause a sharp increase in rate of descent. Presumably these characteristics are mitigated in free flight systems because jumpers have been able to glide Parafoils of $AR = 2$ at $L/D \sim 3.7$ under good control, and skilled human pilots have been able to, on occasion, execute a flared landing to touch-down at a very low velocity[219]. This level of performance has not yet been demonstrated with either an automatically or a remotely piloted Parafoil system.

Steerable Parachute Profile Control. In contrast to ballistic parachutes in which all suspension lines are of equal length, advanced steerable parachutes have suspension line arrays varying in length as required to minimize the concavity of the inflated canopy. Span-wise, concavity is controlled by the spacing of line-groups; chord-wise fabric pendants or flares minimize the number of lines required and channel airflow as do strakes and wing-tip end plates on an airplane. It is particularly important to maintain a straight chord-wise profile at the trailing edge, as any concavity there greatly augments drag (e.g., battens used in lieu of ribs in boat sails).

Providing a rounded leading edge which remains inflated at low angles of attack has been dealt with in different ways and with varying success:

1) Parafoil and Volplane at the cost of added drag avoid the problem by omitting that feature.
2) Parawing (twin-keel only) and Sailwing have a curved under-lip of the canopy supported by short ribs and air pressure. These collapse when the stagnation point moves forward at low angles of attack.

Reefing High-Glide Parachutes. There are currently two basic approaches to the reefing of gliding canopies. To the extent that both employ air-inlet control lines in running rings attached to the canopy, they are similar to the skirt reefing of parachutes. The essential difference between the two approaches is that the canopy is rigged to deploy in a low-drag zero-lift configuration *normal* to the air-stream in one, and *parallel* to the air-stream in the other. The latter has proven successful with Parafoil and Volplane, while the former has developed to a useful level in single-keel and twin-keel Parawings. Both are complex, requiring several stages and a multiplicity of reefing lines, rings, and line cutters.

The *parallel* zero-lift attitude of the wing is obtained by suitable rigging of the fore and aft suspension line and riser lengths with a cluster of step-release links. In the parallel deployment technique, the first reefed stage entails reduction of the inlet area of the ram-air cells to slow their inflation, as in parachute skirt reefing. The method is illustrated in Reference 132. The second stage consists of the now fully-inflated cells still constrained parallel to the air-stream by the intermediate suspension-line to riser attachments. The third and final stage is initiated by release of the temporary riser attachments using pyrotechnic line cutters, allowing the wing to pitch up to its trim angle of attack for the desired glide ratio. The general effect of this on opening force coefficients is indicated by the model test data given in Table 6.10. A comprehensive full scale design verification test program would be necessary for any new application and, as noted earlier, the use of the chained-loop method of cell reefing is not recommended.

The normal zero-lift attitude of the wing is obtained by equalizing the lengths of all suspension lines to that of the shortest lines through secondary attachment loops with a suitable intermediate or "step" release unit. Then, parachute skirt-reefing practice is

followed to create a sequence of canopy inflated area areas commensurate with the initial dynamic pressure for each stage [398]. In this case, the experimental model was equippped with four suspension line reefing steps to effect the opening sequence illustrated in Figure 8.7

Another continuous suspension line reefing system is illustrated schematically in Figure 8.8. This method was developed to mitigate the high opening shock effects experienced by sport jumpers using low porosity gliding canopies. The porous fabric panel with attached running rings on groups of suspension lines is stowed against the skirt of the packed canopy. Upon deployment, the initial influx of air is throttled by the drag-panel and the first stage of inflation is retarded. After the canopy mouth has partially opened, continued opening is resisted by tension in the drag panel applied through the running rings as they slide down the length of the suspension lines. The drag panel is driven by the axial component of the suspension line spreading force against its diminishing drag force. This reefing method is applicable to any type of canopy, but its quantitative effects on the inflation characteristics of either gliding or ballistic parachutes have not been evaluated.

Equalization of Opening Load Peaks. The opening load factors of low porosity , medium and high glide parachutes, are predictably high, approaching $C_X \sim 3$ for the non-reefed infinite mass case (References 132 220 and 400). However, available opening force data for different types have not been reduced to a useful general form, e.g., C_X vs R_m as for ballistic parachutes. Consequently, the designer will have to search out and analyze current source references to develop data curves for the canopy type selected.

Given the opening load factor data in a generalized or dimensionless form, the procedure for balancing opening load peaks is similar to that for parachutes. The common need for more than one reefed stage and as many as four or five opening stages with corresponding load-peaks complicates the calculations, but reasonable solutions are attainable, as illustrated by practical results in References 220 and 398.

Decelerator Staging. The need for a drogue-chute in the decelerator system will be established by basic operational requirements, by the limitations of a reefed main decelerator of maximum allowable weight or bulk, and sometimes by other criteria such as:

The decelerating vehicle may become unstable at a velocity (dynamic pressure) beyond the performance capability of the main decelerator.

The range of flight conditions defined by the operational recovery envelope may be too broad for reliable deployment of the main decelerator at an acceptable confidence level.

A fairly decisive indication of need for a prior stage drogue-chute can be obtained from a calculation for the opening force for main parachute. The reefed opening force must not exceed the allowable load at a maximum dynamic pressure condition on the recovery initiation envelope. This dynamic pressure has not been specified for System B of the example, but the allowable load has $(F_X = 20{,}000\ lbs)$, which enables the following appraisal to be made as a matter of interest to the drogue discussion farther on. Given the parachute of System B, its mass ratio for reefed opening is

$$R_m = 0.00176(305^{3/2}/124.3 = 7.5(10^{-2})$$

and from Fig. 6.25 (reefed max) $C_X = 0.66$. Since the growth in $(C_D S)_r$, if any, which may take place during the reefed interval is unknown in this case, $(C_D S)_r$ is assumed to be the same for reefed opening. Then the dynamic pressure at line stretch should not exceed

$$q_s = F_X/305(.66) = 99.3\ psf$$

for which the corresponding velocity at 10,000 feet altitude is $v_s = 336$ fps (TAS) or 171 kts (EAS). While this flight speed may be reasonable for airdrop operations and certain types of vehicles capable of controlled pre-recovery set-up maneuvers, it is more representative of conditions at the end of a drogue deceleration interval for a broad class of recoverable vehicles, including entry capsules and manned spacecraft. Ordinarily without a drogue, the dynamic pressure would be excessive for the design opening load limit to be satisfied with the reefed main parachute alone, except as the allowable q_s at deployment may be raised sufficiently by additional stages of reefing.

When the design conditions are such that the number of different drag area stages required is large and the flight path angle is $\theta = -90°$, the method of estimating the number of parachutes and the reefed stages of each presented in Reference 554 may be found useful. As noted earlier, the results of these approximate methods provide initial inputs suitable for computerized trajectory computation programs of any desired degree of sophistication.

Small first and second stage drogues are subject to forebody wake effects as described in Chapter 6. During the staging transition between decelerators, before the following stage $C_D S$ has grown to an effective level, a descending system experiences a brief period of reacceleration by gravitation. Because of this, the dynamic pressure at line-stretch of the following stage may be significantly greater than it was when the preceding stage decelerator was releas-

ed. (Of course the reverse is true in the case of an ascending system, a condition seldom encountered in practice.) Being a function of θ as well as the inter-stage ballistic coefficient of the system and the staging interval, Δq tends to be a maximum for steep descents when the flight path angle is approaching 90 degrees. Prior to the staging operation, the system usually has decelerated to a near-equilibrium velocity.

Drogue Sizing and Type Selection. The drag area $(C_D A)$ of the (body) or payload, and the maximum dynamic pressure at which the reefed main decelerator can be safely deployed, provide a basis for estimating the required drogue drag area. The maximum allowable dynamic pressure at the end of the drogue working interval can be defined with reasonable precision for most recovery systems because one of the advantages afforded by the drogue chute is the important one of enabling the main decelerator to be deployed at essentially the same speed and altitude in every operation initiated above a predetermined minimum altitude. Typically, drogue disconnect is initiated by a baroswitch, and the system is approaching its equilibrium descent velocity at the time. When the critical maximum dynamic pressure (q_{s_m}) occurs under non-equilibrium conditions, suitable trajectory computations must be performed, and the following simplified method of making a preliminary estimate of $(C_D S)$ is not applicable.

The equilibrium dynamic pressure with full open drogue is

$$q_e = W/[(C_D S) + C_D A] \qquad 8\text{-}13$$

This is somewhat less than the dynamic pressure felt at main canopy line-stretch because of the re-acceleration following drogue disconnect. A reasonable allowance is made by letting $q_{s_m} = 1.15\, q_e$ for which the drogue drag area required, using Equation 8-13, is approximately

$$(C_D S) = (1.15W/q_{s_m}) - C_D A \qquad 8\text{-}14$$

The body C_D or $C_D A$ is usually given as a function of Mach number. Drogue drag coefficients vary widely with both body C_D and free stream Mach number as shown in Fig. 6.55. However, the drogue disconnect condition is usually subsonic and Fig. 6.43 provides data for estimation of C_D/C_{D_∞} for a given drogue trailing distance. Relative trailing distances frequently used are $l_T/d_b = 6\text{-}7$ so that conservative drag coefficients will be obtained as follows:

D_p/d_b	C_D/C_{D_∞}
<1	0.8
2-3	0.9

Since C_D/C_{D_∞} is the same as the wake dynamic pressure ratio (q_w/q_∞), the alternative method given in Chapter 7 may be used instead, to predict the average dynamic pressure across the drogue canopy in the body wake. This method is based on the drag coefficient of the towing body, and d_b may be calculated as the hydraulic diameter of the projected frontal area for other than circular shapes.

The drogue drag coefficients given in Table 2.2 were measured under conditions designed to minimize wake effects so that a reasonable value for $S_o = C_D S/C_{D_o}$ may be obtained with the assumption that $C_{D_\infty} = C_{D_o}$.

Selection criteria for the type of drogue chute best suited for the application include:

Maximum flight Mach number at deployment.

Supersonic inflation stability and C_X.

Subsonic drag efficiency or $C_D S/W$.

Installation characteristics and serviceability.

Reefing characteristics.

Of course, the development status of each drogue type must be sufficiently well-advanced to support evaluation of the criteria with firm data.

Numerical Example

Prior calculations for System B (Table 8.1) indicate that a reasonable maximum allowable dynamic pressure for deployment of the main parachute with one reefed stage is $q_{s_m} = 77$ psf.

Given:

Recoverable weight	$W = 4000$ lbs
Trajectory angle	$\theta = -90°$
Body subsonic drag area	$C_D A = 4.0$ ft^2 $(C_D = 0.2)$
Body diameter	$d_b = 5.0$ ft
Allowable load factor	$G_X = 6.0$

Drogue requirements:

Trailing distance	$l_T = 7.0\, d_b$
Deployment at:	
Velocity	Mach 1.5
Altitude	$h = 20{,}000$ ft
Flight path	$\theta = 0°$

Calculations:

Drogue drag area required (subsonic) from Equation 8-14:

$$(C_D S) = [1.15\,(4000)/77] - 4 = 55.7 \text{ ft}^2$$

Size estimate for trial $C_{D_o} = 0.5$ to identify order of magnitude:

$$S_o = 55.7/.5 = 111.4 \text{ ft}^2 \quad D_o = 11.9 \text{ ft}$$

Then

$D_p/d_b = 8.3/5 = 1.7$ $(D_p \sim 0.7\ D_o = 8.3\ ft)$

and

$C_D/C_{D_\infty} \sim 0.9$

Appraisal of selection of criteria for deployment at Mach 1.5 indicates that the Hemisflo drogue affords best inflation stability and supersonic, non-reefed drag coefficient. However, when reefed, its supersonic performance is indistinguishable from that of the flat or conical ribbon types (References 215 and 555) which afford a higher subsonic drag coefficient. All three are ribbon parachutes and satisfy other selection criteria equally. The conical ribbon canopy with a constructed angle of 15 to 25 degrees is a good candidate, and variable porosity may be considered optional.

Calculation of Wake Dynamic Pressure. The estimated wake effect factor of the foregoing example may be verified by the method given in Chapter 7 using Equation 7-126 with the empirical coefficients and exponents given. For a particular drogue system with body C_D and drogue trailing distance known, the equation expresses the wake relative velocity (v_w/v) as a function of the relative distance of a point from the centerline of the wake (r/d_b). Recognizing the approximate nature of the solution, rather than integrate the resultant dynamic pressure distribution across the canopy, as suggested by Equation 7-129 a satisfactory solution can be obtained by a simpler procedure in which only v_w/w on the wake centerline $(r = 0)$ and at $r/d_b - D_p/2d_b$ are calculated.

From the example:

Body $C_D = 0.2$

Drogue $x/d_b = 7$

$D_p/d_b = 1.70 \quad (= 2r_p/d_b)$

The coefficients for Equation 7-126 are:

$$a_w = 0.42e^{0.99(.2)} = 0.512$$

$$K_w = 0.54e^{0.84(.2)} = 0.639$$

The exponents:

$$m = 0.85;\ n = 0.47$$

By substitution, Equation 7-126 reduces to:

$$\Delta v_w/v = 0.0979e^{-0.903(2r/d_b)^2}$$

and the wake boundary is at

$$2r_w/d_b = 0.639(7)^{0.47} = 1.60$$

Thus, the drogue canopy is essentially equal in diameter to the wake, and the corresponding ratios are:

$2r/d_b$	$\Delta v_w/v$
0	0.0979
1.70	0.0072

The shape of the non-dimensional velocity distribution curve shown in Figure 6.42 justifies use of a simple linear average, so that:

$$\Delta v_w/v\,(avg) = 0.0562$$

$$v_w/v\,(avg) = 0.944$$

and $(q_w/q_\infty) = 0.9447^2 = 9,891$

which corresponds to the estimated drag coefficient ratio used $(C_D/C_{D_\infty} = 0.9)$.

For other values of D_p/d_b it would not be difficult with the aid of Fig. 6.42, to strike a graphical average for $\Delta v_w/v$ commensurate in accuracy with the accuracy of the empirical coefficient given. For this purpose, enter Fig. 6.42 with $Z_w = D_p/r_w$ calculated for $x/d_b = l_T/d_b$ of the body drogue system to locate the canopy radius on the velocity distribution curve.

Drogue Reefing. Since the drogue drag area is frequently determined by the maximum allowable dynamic pressure for deployment of the main canopy, the predicted drogue opening force at the maximum dynamic pressure condition on the recovery system initiation envelope may exceed the system design load factor (Equation 8-5). In this case the drag of the vehicle is usually a significant fraction of the total and should be included in the calculation. The maximum allowable reefed drag area may be estimated with Equation 8-6.

Continuing the numerical example for System B, the maximum dynamic pressure at Mach 1.5, 20,000 feet is

$$q_m = 0.7\,PM^2 = 1532\ psf$$

Where

$$P = 972.5\ psf$$

Given a vehicle drag area at Mach 1.5 of $C_DA = 6.0\ ft^2$, the allowable drogue opening load from Equation 8-5 is

$$F_X = 4000(6-0) - 6(1532) \sim 14,800\ lbs$$

A trial calculation is made with $C_X = 1.0$ to establish the order of magnitude of (from Equation 8-6)

$$(C_DS)_r = 14,800/1532 = 9.7\ ft^2$$

Then $\psi^{3/2} = 30.2$, and the mass ratio at 20,000 feet altitude is *approximately*

$$R_m \sim 0.00127(30.2)/124 = 3.1(10^{-4})$$

Reading Fig. 6.25, it appears that the opening load factor could have a maximum value in the order of $C_X = 1.2\text{-}1.3$, but the limited amount of data available on reefed supersonic ribbon parachutes, e.g.,

Reference 555, shows opening load factors at Mach 1.5 falling on or below the mean curves, which support the preliminary estimate of $C_X = 1.0$, and $(C_D S)_r \sim 10\ ft^2$ will provide a reasonable starting point for trajectory computations.

For comparison, the probable maximum non-reefed drag area of this drogue at Mach 1.5 is in the order of

$$(C_D S) = \frac{0.3}{0.4}(111.4) = 33.4 - 44.6\ ft^2$$

while supersonic wake effects not considered at this point could reduce drag area and C_X significantly.

Use of Body Drag. The foregoing example raises the question, "Why deploy the drogue when the vehicle is still decelerating rapidly by virtue of its own drag?" This decision is not made arbitrarily. Best practice is to establish the upper boundaries of the speed/altitude envelope for initiation of recovery at the lowest level compatible with the vehicle mission, performance characteristics, and reliability goal as derived from operational analysis.

Ordinarily, supersonic deployment of the drogue will not be required unless:

A higher rate of deceleration is desired than can be obtained by body drag alone.

Mechanical methods of reducing the body ballistic coefficient, such as flaps and spoilers, are inadequate or impractical.

Subsonic and/or transonic stability of the vehicle is marginal or deficient.

Drogue stabilization is a basic requirement of the vehicle upon loss of power at supersonic speeds, or other operational considerations.

The rate of descent is such that the vehicle does not go subsonic at an adequate altitude for recovery.

Loss of vehicle control constitutes a command signal for automatic initiation of recovery.

Preliminary Strength of Materials Determination. For parachutes deployed under near-infinite mass conditions, an empirically derived starting point for structural design is provided by the strength of nylon suspension line and canopy materials given in Tables 8-8A and 8-8B for different classes of construction. For other than ribbon parachutes, strength requirements are also indicated for finite mass conditions. The appropriate structural class may be determined by estimating the approximate strength of suspension lines required from the relationship

$$P_R = D_F F_X / Z \qquad 8\text{-}15$$

A more complete preliminary strength of materials determination may be made using the convenient short methods presented in Chapter 7.

Identification of structural weight class is presented for the System B conical ribbon drogue:

Numerical Example

Given: Conical Ribbon Drogue

$D_o = 11.9\ ft$

$D_F = 1.9$

To be deployed reefed at Mach 1.5 and $q = 1532\ psf$.

Solution:

The deployment conditions and opening load justify the use of 18 to 20 gores in the canopy to minimize the gore-width between the joints at the skirt.

By Equation 8-15 the strength of suspension

TABLE 8.8 A

MATERIAL-STRENGTH REQUIREMENTS FOR RIBBON PARACHUTES

Class	Suspension Line Material (T.S., Lb, Nylon)	Ribbon Material (T.S., Lb, Nylon)
I	375	100
II	550	200
III	1500	300
IV	2300	500
V	4000	1000
VI	6000	1500
VII	9000	2000
VIII	12000	3000

TABLE 8.8 B

MATERIAL-STRENGTH REQUIREMENTS FOR OTHER THAN RIBBON PARACHUTES

Class	Suspension Line Material (T.S., Lb, Nylon)		Surface Material (oz, Nylon)
I	375		1.1
II	550	Finite-Mass	1.6
III	1500	Condition	2.25
IV	2300		3.5
V	4000		4.75
VI	6000	Infinite-Mass	7.0
VII	9000	Condition	14.0
VIII	12000		14.0

line material required is

$$P_R = 1.9(15{,}000)/[\begin{matrix}18\\20\end{matrix} = [\begin{matrix}1583\\1425\end{matrix} \text{ lbs}$$

The corresponding structural class in Table 8-8A is Class III for Ribbon parachutes with 1500 lb lines and 300 lb ribbons in the canopy. This result provides a reasonable basis for preliminary weight estimates and a more detailed structural analysis.

It should be noted that while the method of determining the structural weight class may be unconservative for reefed parachutes, the need for somewhat stronger material in the crown of the canopy generally entails a weight increment smaller than the probable error of the weight calculation and this error tends to be positive most of the time.

Protection of Decelerator Structures from High Temperatures. High temperature environments anticipated in storage, operations, or sterilization, will indicate the probable need for materials other than nylon, after reasonable measures have been taken to insulate the decelerator pack from heating transients. Provision of insulation and other thermal protection measures fall in the province of vehicle design proper and need not be considered here.

The basic drogue structure should be fabricated from one of the high strength to weight textiles having viscoelastic properties at both normal and elevated temperatures, which will afford a maximum impact energy absorbing capacity. In those areas and members where predicted surface temperatures may cause melting or excessive loss of strength, one or more of the following protection measures may be found adequate.

1. Modify the design factor for the affected members only by incorporating a temperature loss factor (2) estimated with the aid of Figure 8.9 for a probable average temperature applicable to the material cross section.
2. When the material thickness determined by approach (1) is judged to be excessive from the standpoint of reduced structural flexibility, consider application of one of the protective coatings listed in Chapter 4 which will increase (τ) and the allowable strength of the base textile to the level required for acceptable structural flexibility.
3. Subject structural test specimens to a combination of loading and heating transients representative of the predicted conditions during deployment and inflation. Measure the material temperatures at different depths within the cross-section of critical areas. Evaluate an average temperature suitable for determination of τ and the allowable strength factor for design of the affected parts of the structure.

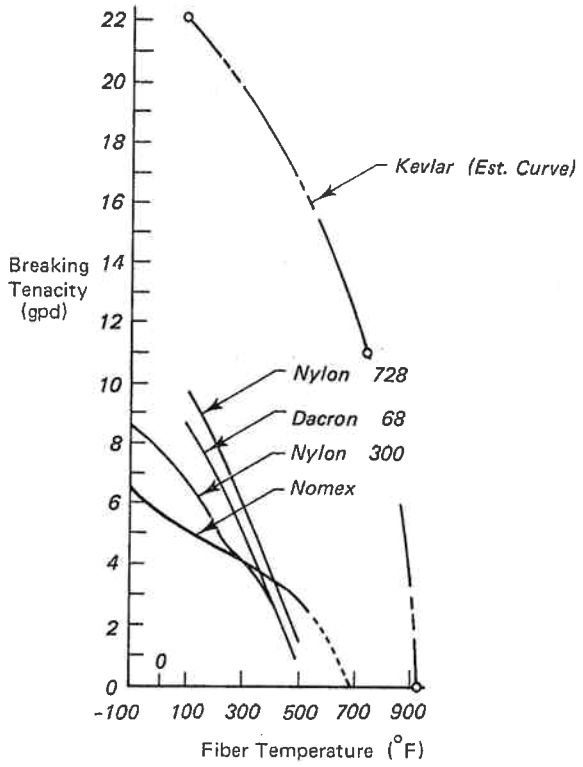


Figure 8.9 Temperature Strength Loss of High Tenacity Synthetic Textile Fibers

In those systems where the aerodynamic heating effects are found to be too protracted for solution by the above measures, the present state-of-the-art affords a choice of flexible materials such as glass, stainless steel, etc.; fabrics which retain some strength at very high temperatures, but have a relatively small energy absorbing capacity. However, no deployable drogue applications are presently known in which protracted aerodynamic heating to near-equilibrium temperatures are likely, or which, if experienced, would be attended by a tolerable low-shock deployment and inflation. Fortunately, stable deceleration by body drag alone usually can be counted on for the first stage.

On the other hand, pre-entry inflation of an attached inflatable decelerator made of such materials is presently feasible, (e.g., References **20, 223** and **224**), and while there is no immediate prospect of an aerospace vehicle program having this type of operational requirement, the entry decelerator presumably would not be subject to excessive impact loading of those high temperature materials cited above, now available for its construction.

Selection of Deployment Method. Salient criteria for the selection of the deployment method include:

Reliability
Duration of deployment interval
Structural loads generated
Location and weight of decelerator pack
Type and size of obstruction (if any) to be cleared
Flight velocity and dynamic pressure
Weight and bulk

The deployment methods and equipment described in Chapter 3 fall into four general categories:

1. Extraction and stretching of the decelerator by a drag device, e.g., pilot chute or prior stage drogue.
2. Forcible ejection of the decelerator pack by a mortar, "blast bag", thruster, or the like.
3. Extraction and stretching of the decelerator by static line or inter-stage bridle.
4. Extraction and stretching of the decelerator by a projectile (deployment-gun slug, etc.) or by a small rocket.

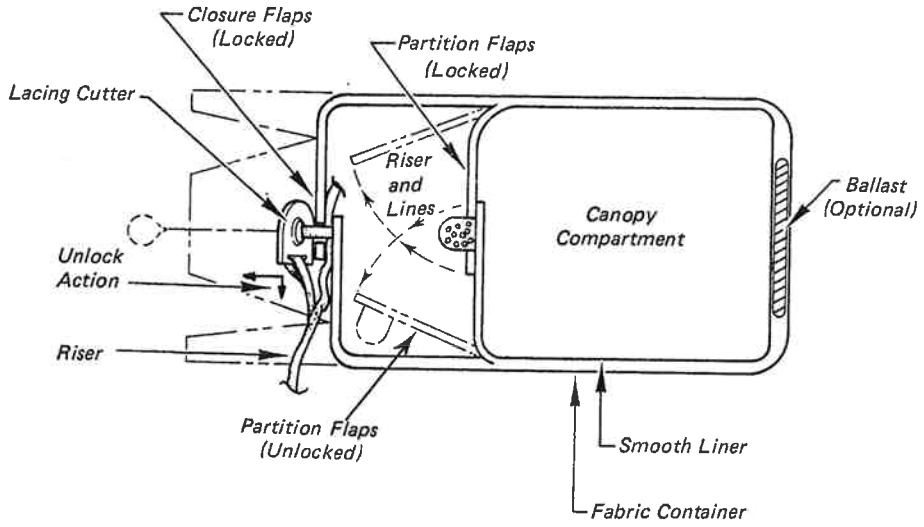
The limitations imposed by the recovery system application tend to narrow the scope of the deployment method categories that need to be considered at one time. Pilot drag devices and low ejection velocities are generally adequate for vehicles having high ballistic coefficients or operating under conditions where the dynamic pressure is appropriate for the deployment time required. Forcible ejection at relatively low velocities also may be satisfactory under such conditions. Huckins[347] discusses the particular class of problems associated with parachute deployment from an entry vehicle having a low ballistic coefficient. Because such vehicles decelerate rapidly, the forcible ejection system requires a relatively high ejection velocity, while use of a prior stage drogue for deployment of the main parachute is subject to severe wake effects that make it less attractive. The extraction rocket may be judged best adopted to such conditions and affords the deployment system of least weight, except when a pilot chute or prior stage drogue can be so employed.

Mortar Ejected Deployment Bags. The deployment bag required for mortar deployment of decelerator (Figure 8.10A) has the simplest design requirements, because its resistance to line and canopy *unfurling* should be minimum. No locks are required on the internal canopy partitioning flaps, nor constraints on the suspension lines. Disorganization of the suspension line bundle is prevented by stowing the lines in short bights secured by free elastic bands, i.e., the bands are not attached to the inner walls of the deployment bag. Unlike the bag-bridle extraction process, mortar ejection imparts momentum to the entire mass of the pack at once through compression, so that no temporary internal tension members are needed to maintain order among the decelerator components as they deploy. At stretch-out, the bag's own momentum carries it away. For this reason, it has been good practice to augment the deployment bag mass by stitching a dense metal disk into the end-lining. The mortar pressure-sabot also may be used for this purpose, when securely attached to the end of the bag.

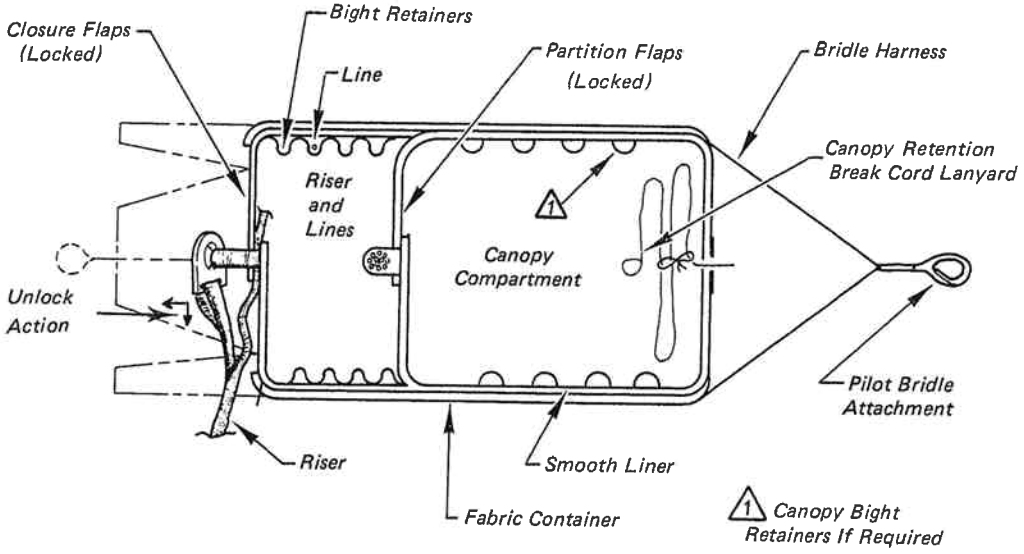
Inasmuch as the decelerator may be pressure-packed directly in the mortar, the dimensions of the deployment bag are less critical than for free packs which must be inserted after packing. In the former configuration, the open end of the bag is necessarily at the muzzle, and the decelerator riser is secured to the bag closure lock at that end, emerging directly through an opening between the muzzle and the muzzle cover. When the integral mortar pack is ejected, it turns end-for-end immediately as the riser tension builds up to unlock the bag mouth. In the latter configuration, the free pack may be inserted with the locked end-closure against the sabot. Then the riser is led out to the muzzle along one side of the pack and the ejected pack does not have to turn over. However, this arrangement usually has no significant operational advantage; the integral mortar pack is widely used because of its greater simplicity and bulk efficiency.

Bridle Extracted Deployment Bags. The deployment bag design required for extraction by pilot chute, prior stage drogue, or other means (Figure 8.10B) must incorporate a strong bridle harness and longitudinal members capable of transferring the extraction tension along the length of the pack to the end closure. The end closure and reversible locking system must be strong enough to withstand the inertial (set-back) force of the decelerator mass in the pack. Disorganization of suspension lines is prevented by securing bights of the line bundle at frequent intervals with elastic or breakaway ties attached to the bag side walls. A similar set of breakaway cords may be used to restrain bights of the canopy bundle in its compartment, both prior to and during extraction, but under most deployment conditions, the internal partitioning flaps and wall friction are sufficient to control the canopy mass.

The stabilizing effect of internal friction is most effective in a firm dense pack; soft packs are easily disorganized. All the internal constraints, working together with the bag mouth closure, prevent the decelerator from being dumped precipitously from



A) Integral Mortar Bag Pack



B) Bridle-Extraction Bag Pack

Figure 8.10 Schematic Arrangement of Two Different Deployment Bag Designs

the container until it has been released by increasing bridle tension which actuates the unlocking device, e.g., lacing cutters or equivalent. Subsequently, they function to ensure orderly unfurling of lines and canopy during the stretch-out process, and the deployment bag prevents premature initiation of canopy inflation. Complete stretch-out is promoted by a bridle on the apex of the canopy attached either permanently or with a breakaway cord strong enough to give the decelerator an effective tensioning impulse. The permanently attached bridle must be long enough to permit complete stripping of the bag from the canopy and strong enough to retain the pilot chute against its augmented impact load. The breakaway bridle attachment is used most often when deployment is effected by a prior stage drogue, but also may be used when retention of deployment bag and pilot chute may have an adverse effect on the inflation or operation of the main canopy.

Pilot Chutes. Many different types of pilot chutes have been developed and some are available as off-the-shelf items, primarily for personnel parachutes and small target drone recovery systems. The central design requirements for a pilot chute are:

Fast, reliable opening

Good stability

Effective drag area sufficient to extract and decelerate the main canopy (or deployment bag) at an acceptable rate when the dynamic pressure is the operational minimum for the system.

The first requirements can be satisfied by canopies of many different types, particularly the smaller ones equipped with opening springs. Opening springs are not practical in large pilot chutes, and other aids such as pocket bands or the flared skirt may be used. The Ringslot canopy is frequently used for large pilot chutes, while ribbon canopies may be employed at high dynamic pressures where greater strength is needed. In the small to intermediate size range, a low porosity Ribless Guide Surface pilot chute has satisfactory opening characteristics and is used over a broad speed range through the transonic regime.

Stability requirements are satisfied by the different canopy designs cited above, including the vane type with an internal opening spring. Maximum oscillations on the order of ±5 degrees are usually tolerable in the wake of the vehicle, deployment bag, and stretched-out main canopy, as deployment progresses.

The C_DS requirement depends on the definition of the minimum stretch-out rate acceptable. The pilot chute drag area may be expressed by the ratio

$$R_p = (C_DS)_p/(C_DS)_o$$

where $(C_DS)_o$ is the drag area of the fully inflated main canopy. The drag area ratios given in Table 8.9 have been found to be generally adequate over the speed ranges indicated, but when the main canopy deployment time is critical, the probable Δv_{max} should be evaluated by one of the methods given in Chapter 7.

TABLE 8.9 PILOT PARACHUTE RELATIVE DRAG AREA

Deployment Speed kts EAS	Pilot Chute R_p
50 - 200	.03
200 - 300	.02
>300	.01

In addition, for preliminary design purposes the pilot chute drag coefficients and infinite mass opening load factors given in Table 8.10 may be used. In order to obtain adequate pilot chute extraction effort in the wake of the body or vehicle, the length of the bridle should be sufficient to provide a canopy trailing distance of $l_T \sim 6d_b$. For operation in the wake of a reefed main canopy, $l_T \sim 4D_{p_r}$ is generally adequate. In those instances where adequacy of the pilot chute is in doubt, the wake effect should be appraised by one of the methods given in Chapter 7.

TABLE 8.10 PILOT PARACHUTE PERFORMANCE

Type	C_X	C_{D_o}
Vane	2.5	0.55
Ringslot	1.5	0.60
Ribbon	1.4	0.53
Ribless Guide Surface	2.0	0.44

Snatch Force. One of the instances in which the snatch force constitutes a critical design load is when a permanently attached pilot chute is used for deployment of the main decelerator. As noted in Chapter 7, when the shock onset is excessive, traveling strain waves are induced, the effects of which are complex and not yet amenable to analytical treatment with any assurance of success. Therefore, the following numerical example is calculated by the short method afforded by Equations 6-1 and 6-2.

Numerical Example

A permanently attached pilot chute has the following characteristics pertinent to the problem:

Given:

$C_DS = 24.4\ ft^2$

Component	Weight lbs	Mass lbs	Length ft
Canopy	1.27	.0395	–
Suspension lines	0.57	.0177	10.87
Bridle	1.53	.0476	28.84

Load/strain characteristics of lines and bridle per Fig. 7.6 with $P_u = 7046$ lbs, $q_s = 70$ psf at 18,000 ft MSL ($\rho \sim .00135\ sl/ft^3$). The pilot chute is fully inflated throughout the operation.

Calculations:

The drag at main canopy stretch is simply

$$D = 24.4\,(70) = 1708\ lbs$$

Since the pilot chute is fully inflated, the canopy mass includes the added air mass or

$$m_c' = M_c + m_a = .0395 + .107 = 0.146\ slugs$$

where (see Page 344)

$$m_a = \rho(C_D S)^{3/2} K_a$$
$$= .00135\,(24.4)^{3/2} K_a$$

and K_a is the added air mass coefficient, for which a reasonable empirical value is $K_a = 0.66$ (see Chapter 6). The effective pilot chute mass for Equation is

$$m = 0.146 + (.0177 + .0476)/2 = 0.179 \text{ sl}$$

The average effective spring constant may be estimated for the design limit load condition represented by $P_u/2 = 3523$ lbs where $\epsilon = 0.121$ (Fig. 7-6). Extending a tangent from this point on the curve to $T = 0$ yields $\epsilon = .062$, which may be treated as the creep in the static test which will not be present under dynamic loading conditions. Also, lines and bridle are under some preload due to the inertia of the main parachute, which reaches full line and canopy stretch at this time. Then by Equation 6-5

$$K_t = 3523/(10.87 + 28.84)\,(.121 - .062)$$
$$= 1504 \text{ lb/ft}$$

Substitution of these values in Equation 6-2 gives

$$F_i = \Delta v_m\,[.179(1504)]^{1/2} = 16.4\,\Delta v_m$$

and by Equation 6-1, the snatch force is approximately

$$F_s = 16.4\,\Delta v_m + 1708$$

then the snatch force would be equal to the limit load for a separation velocity in the order of

$$\Delta v_m = (3523 - 1708)/16.4 = 111 \text{ fps}$$

The probable separation velocity may be estimated with the aid of Fig. 8.16, for which the characteristics of the main parachute also are required as follows:

Component	Weight lbs	Mass sl	Length ft
Canopy in deployment bag	96.9	3.01	–
Suspension lines	29.2	0.91	120.3
Risers	11.7	0.36	11.4
Pilot chute	3.37	0.10	–

Here the effective parachute mass is

$$m_p = 3.01 + .10 + (.91 + .36)/2 = 3.75 \text{ sl}$$

and length

$$l_o = 120.3 + 11.4 = 131.7 \text{ ft}$$

The ballistic parameter of the parachute pack with pilot chute is

$$\rho(C_D S)_p l_o/2m_p = .00135(24.4)\,131.7/2(3.75)$$
$$= .0578$$

Then from Fig. 8.16 for $K_b = 0$, $\Delta v_m/v_o = 0.593$

The deployment conditions for the main parachute are given as $q = 90$ psf at 18,000 ft MSL for which the corresponding true air speed is

$$v_d = [2(90)/.00135]^{1/2} = 365 \text{ fps}$$

then

$$\Delta v_m \sim (.593)\,365 = 216.4 \text{ fps}$$

This will be reduced somewhat by resistance to extraction by the suspension line constraints in the deployment bag. The average force over the interval Δt is estimated to be $F = 20$ lbs, and for an assumed uniform separation acceleration

$$\Delta t = 2 l_o/\Delta v_m = 2(132)/216 = 1.22 \text{ sec}$$

The velocity reduction due to this impulse is approximately

$$\Delta v_x = F\Delta t/m_p = 20(1.22)/3.75 = 6.5 \text{ fps}$$

So that at main canopy line stretch

$$\Delta v_m = 216.4 - 6.5 \sim 210 \text{ fps}$$

but the pilot chute continues to decelerate for an additional interval as it strips the deployment bag from, and stretches the main canopy. The additional distance traveled derived from the canopy dimensions is roughly 54 feet, including an estimated 5% elongation of the structure. Assuming that the relative acceleration continues constant at $a = 216/1.22 = 177$ ft/sec^2 over this distance with $v_1 = 210$ fps

$$v_2 = (v_1^2 + 2a\Delta s)^{1/2} =$$
$$= [210^2 + 2(177)54]^{1/2} = 251 \text{ fps}$$

and the pilot chute impact load will be considerably greater than the assumed limit load. This result justifies increasing the effective spring constant to that represented by the maximum slope of the static load curve in Fig. 7.6 . Whereupon:

$$T = 5000 \text{ lbs}$$
$$\epsilon = 0.142$$
$$\epsilon_o = 0.082$$

and

$$K_t = 5000/39.7(.060) = 2099 \text{ lb/ft}$$

Then by Equation 6-2 with $\Delta v_m = v_2 = 251$ fps

$$F_i = 251\,[.179(2099)]^{1/2} = 4864 \text{ lbs}$$

and

$$F_s = 4864 + 1708 = 6572 \text{ lbs}$$

which is close enough to the ultimate to risk failure.

Ejection Mortars. Of the various devices described in Chapter 3, designed to forcibly eject a decelerator pack into the airstream and initiate deployment, the mortar is most frequently used when extraction (deployment) by pilot chute or other drag device is not feasible. The size and weight of the pack to be ejected is not so much a limiting factor as is the ability of the vehicle to withstand the reaction impact. Usually the ejected mass is a relatively small fraction of vehicle mass and the ejection velocity is in the range from 100 to 150 fps so that a mortar of small length-to diameter ratio *(l/d)* may be used without generating excessive reaction loads. When it is necessary to minimize the reaction moment applied to the vehicle, the mortar axis may be directed close to the vehicle mass center.

To obtain good mortar performance, the decelerator should be pressure packed to a high density *(~35-34 lb/ft^3)* and the mortar cartridge and breech developed to maintain the internal pressure ratio, p/p_m as close as possible to unity during the working stroke; $p/p_m = 0.7$ is readily attainable and values greater than 0.8 have been realized in refined designs (Ref. 556). A high pressure breech with eroding gas injection orifice may be used for this purpose. Without this feature the pressure ratios up to $p/p_m \sim 0.6$ using boron potassium nitrate as a propellant, one of the few that burn efficiently at low pressures. When the peak mortar reaction load is not critical to vehicle design, substantial savings in hardware and development costs may be realized by eliminating the high-pressure breech. Because the weight of the propellant charge is relatively small, it has been practical to burn common propellants at low pressure in many mortar applications.

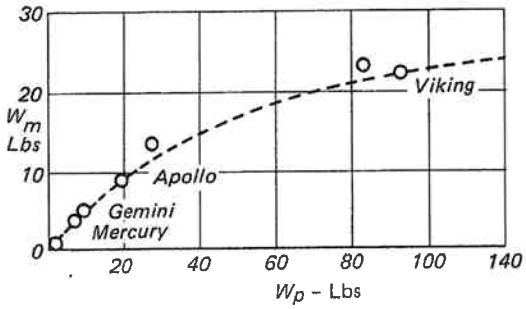
Since the piston (sabot) area is constant, the reaction force ratio $F/F_m = p/p_m$.

The mortar muzzle cover is usually retained by shear pins of a predetermined failure point but capable of resisting any probable pre-deployment inertial or pressure load with a large margin of safety. Consequently, an overly soft pack would be severely compressed, absorbing considerable energy, before the cover is pushed off.

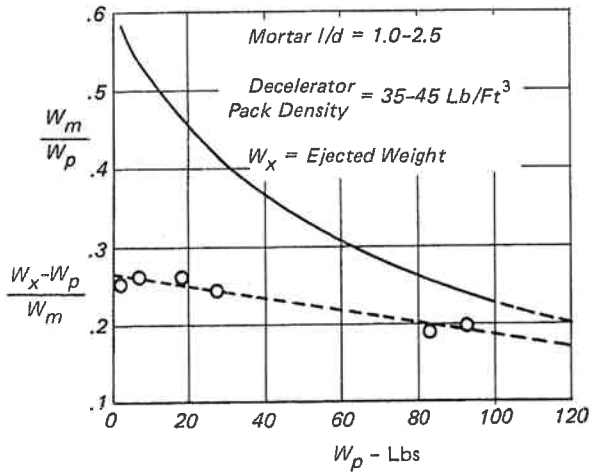
The ejected mass consists of the decelerator pack plus the sabot and muzzle cover, but the weight of these latter items is chargeable to the mortar. Thus, for convenience of weight estimation the ratio of the mortar weight to the decelerator pack weight is defined as

$$W_m/W_p = W_m/[W_x - (W_s + W_c)]$$

where W_x is the weight ejected, W_s is the sabot and W_c the cover weight. The ratio $(W_x + W_c)/W_m$ decreases somewhat with increasing mortar size along with W_m/W_p as shown in Fig. 8.11. Actual weight data for mortars of good efficiency having muzzle velocities in the range from $v_x = 100\text{-}140$ fps are also plotted in Fig. 8.11. The broken curves indicate practical minima for good mortar designs and pack densities of 35 to 45 lb/ft^3. As noted, the mortars for spacecraft landing systems generally have the highest specific performance.



a) Mortar Weight vs Decelerator Pack Weight



b) Variation of Mortar Weight Ratios with W_p

Figure 8.11 Ejection Mortar Weight Data

Numerical Example

According to Figure 8.11, an efficient mortar design such as that described in Reference 556 would yield:

Given: Decelerator pack weight = 60 lbs

$$W_m/W_p = 0.305$$

Mortar weight,

$$W_m = 18.3 \text{ lbs}$$

$$(W_x - W_p)/W_m = 0.218$$

Sabot plus cover weight,

$$W_s + W_c = W_x - W_p = 0.218\, W_m = 4.0 \text{ lb}$$

Ejected weight,

$$W_x = W_p + W_s + W_c = 64.0 \text{ lbs}$$

Extraction Rockets. As a deployment device, the extraction rocket has advantageous characteristics that merit exploitation:

The system is flexible and well suited for difficult deployment conditions.

There is no deployment reaction as with a mortar.

The extraction impulse is applied continuously and independently of flight altitude or dynamic pressure.

The system is highly reliable and of minimum weight.

Numerical Example

It is desired to extract and stretch the decelerator with a small rocket in an interval of 1.0 second.

Given: Decelerator: pack weight = 60 lbs
stretched length = 100 ft

Vehicle: deceleration, a = 3g
path angle ϕ = - 45 deg

Assumptions:

1) The decelerator mass is uniformly distributed along its length.
2) Rocket burn time = 1.0 sec.
3) Propellant specific impulse = 220 sec.
4) Propellant mass fraction = 0.65 (Fig. 8.12).

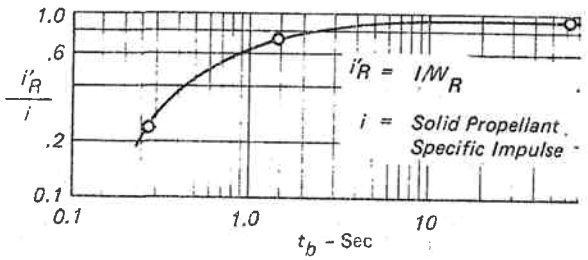


Figure 8.12 Rocket Specific Impulse Ratio vs Burn Time (Ref. 574)

Calculations:

Required $\Delta v \sim = 2(100/1.0) = 200$ fps

Total impulse $= F t_b = m\Delta v + \frac{a}{g} W + W \sin\theta\, t_b$

$= 387.8$ lb-sec

Where:

$m = W/2g = 0.933$ sl (neglecting rocket)

$\frac{a}{g} = 3$

$W = w/2 = 30$ lb

$\sin\theta = .707$

Rocket: Total Impulse = 388 lb-sec
propellant wt = 388/220 = 1.76 lb
weight = 1.76/.65 = 2.71 lb

Additional components chargeable to the extraction rocket installed weight include its container/launcher and a suitable steel cable bridle.

Since the initial acceleration of the rocket before the bridle comes taut will be very high, the bridle impact load on the decelerator pack must be attenuated by suitable means such as a series of breakaway lashings and/or a length of nylon webbing in series with the steel cable bridle. If a short bridle coupling is desired between rocket and deployment bag, a pair of vectored nozzles may be used to protect the pack from jet damage. A 45 degree thrust vector on each side of the rocket axis in the above example would increase the weight of the rocket by roughly 40 percent.

Weight and Volume. Decelerator weight appraisal and accounting is an important adjunct to recovery system design. A detailed weight statement consists of a table listing all the members of the decelerator assembly, their lengths (or areas) and their unit weights. Total lengths (or areas) are summed and multiplied by the corresponding unit weights to obtain the weight of each set of components. This is a long procedure that can only be carried out accurately after the structural design is well defined. Since actual material unit weights are seldom known with precision in advance of procurement, a generally conservative solution is obtained using the maximum unit weights given in MIL and similar specifications.

For preliminary design purposes, various short methods of estimating decelerator weights have been developed. These depend upon available weight statistics for decelerators of different structural classes, types, sizes and design-limit opening loads. Single parachutes weighing as much as 900 lbs have been fabricated.

The decelerator pack volume is a function of the packing method used and, to some extent, of the

density of the textile material (nylon, dacron, nomex, etc.). Packing methods differ primarily in the unit compressive pressure that can be applied to the folded decelerator fabric in the container. This varies somewhat with the shape of the container and whether the pressure is applied to the container as a whole after it has been filled or progressively on segments of the decelerator as successive folds of fabric are inserted. Progressive compression during packing is the method most commonly used and yields the highest average pack densities. On occasion, parachute packs of over two-thirds the density of solid nylon have been made with the aid of a hydraulic press.

Parachute Weight. The weight of new parachute designs may be estimated with the aid of available

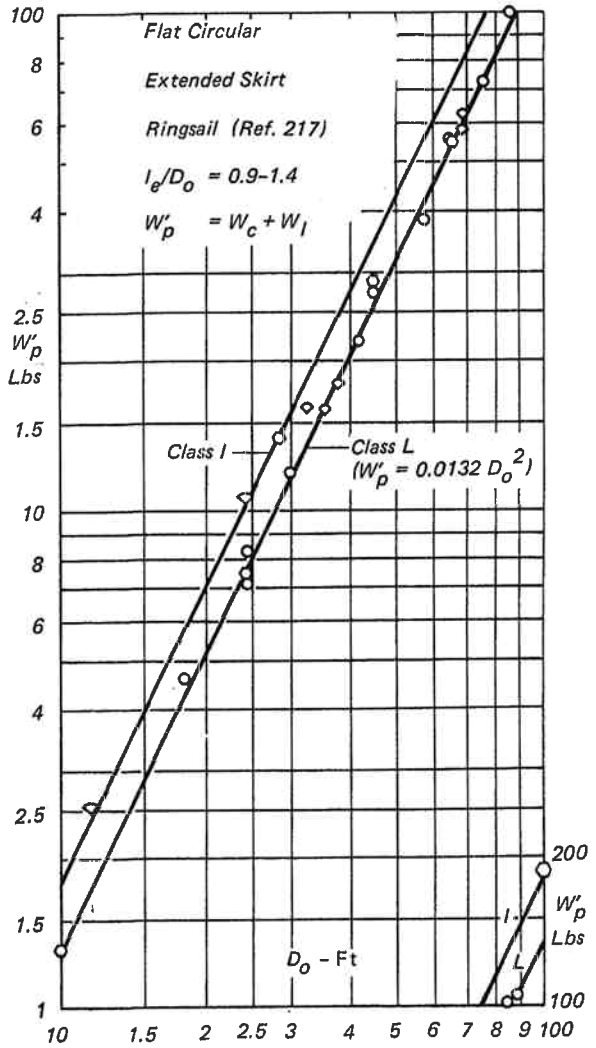


Figure 8.13 Parachute Weight vs D_o Typical for Classes L and I

weight statistics for existing models of similar design and/or class of construction. Such data usually plot as straight lines on log-log graphs of weight versus D_o as shown in Fig. 8.13 for parachutes in the lightweight classes L and I. All members of one construction class tend to fall on the same line and the different class lines are generally parallel as appears in Fig. 8.14. Deviations from the mean represent the effects of differences in line length ratios (l_e/D_o), canopy reinforcements and relative number of gores (N/D_o). Also, the actual unit weights of the textiles used are usually less than the maxima given in MIL specifications.

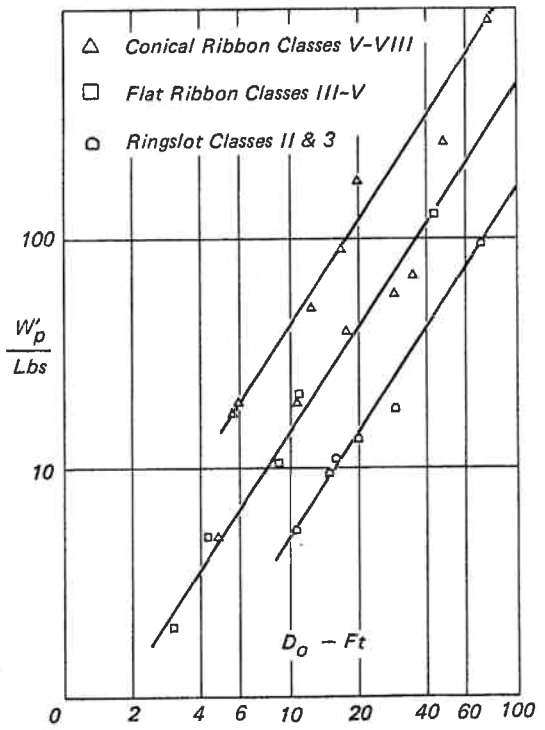


Figure 8.14 Parachute Weight vs D_o and Construction Class

When the number of existing parachute models is insufficient for curve plotting, the combined weight of canopy and suspension lines may be estimated with fair accuracy utilizing this relationship given in Reference 217.

$$W'_p = S_o w_c + Z l_e w_l \qquad 8\text{-}16a$$

Where w_c is the unit weight of an existing canopy of similar construction calculated from the measured weight with Equation 8-16a rewritten in this form:

$$W_c = (W'_p - Z l_e W_l)/_o \qquad 8\text{-}16b$$

and w_l is the unit weight of the suspension line cord appropriate to each design (obtained from pertinent specifications). The use of l_e in place of l_s is justified

because the length of riser branches above the keeper (when present) is relatively short and may not be known or conveniently determined.

Statistical weight data for several different types of polysymmetric circular parachutes have been reduced to the form given in Table 8.11 from which coefficients a and b may be obtained for calculation of parachute weight with this expression.

$$W'_p = a D_o^2 + b D_o \qquad 8\text{-}17$$

The solution provides a reasonable weight estimate for a parachute falling in one of the construction classes given in Tables 8.8A and 8.8B and having a relative line length of $l_e/D_o = 1.0$.

A good approximation of the weight of a conventional riser assembly may be made with this expression

$$W_R = 1.1\, Z_R\, W_w\, (l_B + l_R) \qquad 8\text{-}18$$

Where l_R is the length of the riser below the keeper, l_B the length of the branches above the keeper and W_w is the unit weight of the webbing plies in one of Z_R branches.

Complete Decelerator Pack Weight. In addition to canopy, suspension lines and risers, the completely packed decelerator assembly includes a variety of hardware items (links, reefing rings, cutters, etc.), the deployment bag, and miscellaneous rigging components. For preliminary design purposes the pack weight and volume may be estimated with reasonable accuracy from the calculated decelerator and riser weights as follows.

$$W_p = 1.1\,(W'_p + W_R) \qquad 8\text{-}19$$

$$V_p = W_p/\delta_p \qquad 8\text{-}20$$

Where the average pack density, δ_p, may be obtained from Table 8.12 for the packing method found to be compatible with the overall mission constraints.

Complete Recovery System Weight. Recovery system weight statistics for a large number of different vehicles have been compiled. A summary breakdown of the weight fractions in percent of vehicle gross weight of the recovery system structure, parachute subsystem, and control/actuation subsystem is presented in Fig. 8.15.

TABLE 8.11 CONSTANTS *a* AND *b* FOR VARIOUS CANOPY TYPES AND CANOPY MATERIALS

Canopy Type		1.1 oz	1.6 oz	2.25 oz	3.5 oz	4.75 oz	14 oz	1.1, 1.6, 2.25 oz	300 lb	1000 lb
Flat Circular	a	0.018345	0.02526	0.03885	0.0612					
	b	-0.0113	-0.0104	-0.03185	-0.0221					
Extended Skirt	a	0.01435	0.02043					0.02951		
	b	-0.00993	-0.01017					-0.02420		
Personnel Guide	a	0.011963	0.01734							
	b	-0.008290	-0.01038							
Ribbed & Ribless Guide	a					0.09	0.36			
	b					0.60	1.02			
Ribbon	a								0.0585	0.3849
	b								-0.1445	-0.4521
Ringslot	a			0.05424	0.1496					
	b			-0.16050	-0.4090					

TABLE 8.12 DECELERATOR PACK DENSITIES

Packing Method	Density Range	
	lb/ft^3	lb/in^3
Manual (normal)	21-23	.012-.013
Manual (firm)	24-27	.014-.016
Vacuum	30-33	.017-.019
Lacing	30-40	.017-.023
Air-press	31-41	.018-.024
Hydropress (normal)	40-44	.023-.025
Hydropress (heavy)	45-47	.026-.027
Reference densities:		
Folded parachute (uncompressed)		0.011
Nylon textile (webbing)		0.023
Solid nylon (monofilament)		0.0386

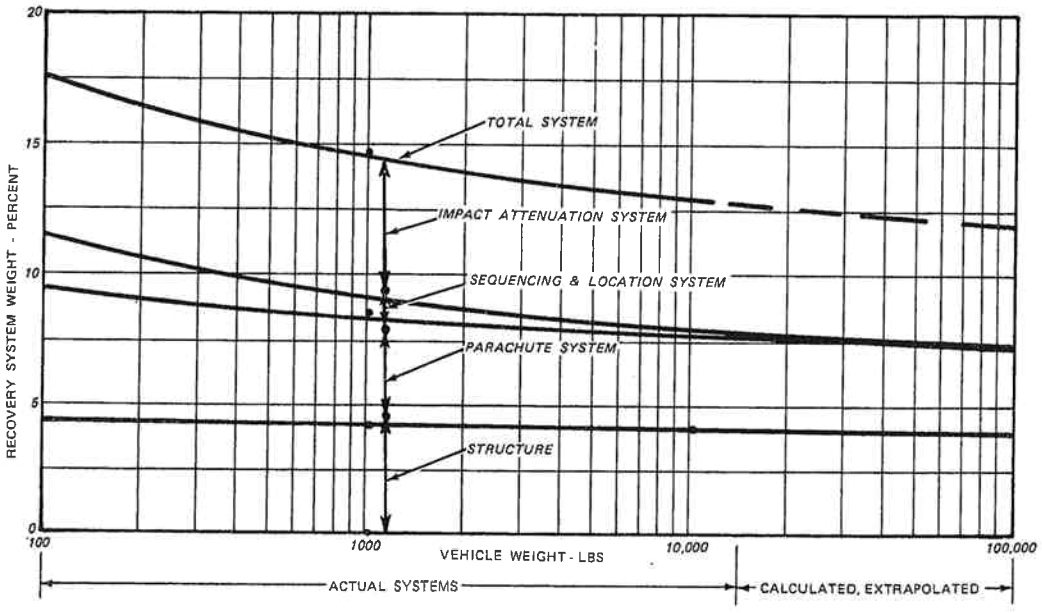


Figure 8.15 Recovery System Weight Breakdown

LIST OF REFERENCES

1. Knacke, T. W., Dimmick, L. L., Design Analysis of Final Recovery Parachutes - B-70 Encapsulated Seat and the USD-5 Drone, ASD-TDR-62-75, (AD 277 424), April 1962
2. McIntyre, P. A., Development of a Recovery System for the AN/USD-501 Surveillance Drone, AIAA Paper 68-935, presented at AIAA, Aerodynamic Deceleration System Conference, El Centro, CA, (A68-42008), September 1968
3. Engelland, J. A., Byrne, W. M. Jr., High Altitude Supersonic Target (HAST) - Phase I, AFATL-TR-71-25, (AD 889 909L), February 1971
4. Henke, D. W., Jeppesen, N. L., Drone Recovery - Present And Future, AIAA Paper 73-465, presented at AIAA, Aerodynamic Deceleration Systems Conference, Palm Springs, CA (A73-31451), May 1973
5. Engelland, J. A., Peterson, G.L., Design Study in Techniques of Recovery of Target Avionics Packages from Rocket Powered Targets, AFATL-TR-69-75, (AD 860 128), June 1969
6. Burke, S. T., Bixby, H. W., Recovery System for Terrier, R-844, (AD 98294), June 1954
7. Rosenlof, K. D., Test of the Final Stage Parachute Recovery System for QYTM-61B, Matador, AFFTC-TN-56-22, (AD 112 436), February 1957
8. Rosenlof, K. D., Parachute Component Tests for QTM-61B Final Stage Parachute Recovery System AFFTC-TN-58-12, (AD 131 457), May 1958
9. Anon., Aerobee 350 Recovery System, NASA CR-118628, (N71-25883), December 1970
10. Johnson, D. W., Evolution of the Recovery System for High Altitude Sounding Rockets, AIAA Paper 68-959, presented at AIAA, Aerodynamic Deceleration Systems Conference, El Centro, CA (A68-4333), September 1968
11. McFall, J. C., Flat-Spin Recovery System, NASA TM X-54520, (N65-35207), April 1964
12. Olsen, R., Sloan, G. J., An Improved Decelerator System for Upper Atmosphere Soundings, AIAA Paper 68-960, presented at AIAA, Aerodynamic Deceleration Systems Conference, El Centro, CA, (A68-42031), September 1968
13. Blanco, T. T., Berman, R. J., Steck, H. J., Recovery of High Performance Re-Entry Vehicles, paper presented at AIAA, Aerodynamic Deceleration Systems Conference, Houston, TX (A66-40597) September 1966
14. Ryan, J. E., Aerodynamic Deceleration From as High as Mach 4.0 for the ALARR (Air Launched, Air Recoverable Rocket), paper presented at AIAA, Aerodynamic Deceleration Systems Conference, Houston, TX, September 1966
15. Graham, J. J., Ballute Development for Loki-Dart and Arcas Rocketsondes, AFCRL-68-0622, (AD 681 455), November 1968
16. Pepper, W. B., Development of a Parachute Recovery System for a Reentry Nose Cone (NRV), SAND75-0564, September 1977
17. Cassanto, J. M., Smrz, J. P., Eichel, D. A., Proof Tests of the Terminal Parachute Recovery System for the Biosatellite Journal of Spacecraft and Rockets, Volume 5, p. 348-351, (A68-21404), March 1968
18. The Viking Mission to Mars, NASA SP-304, NASA Scientific and Technical Information Office, Washington, D.C., 1974
19. Whitlock, C. H., Bendura, R. J., Inflation and Performance of Three Parachute Configurations from Supersonic Flight Tests in a Low Density Environment, NASA-TN-D-5296, (N69-30063), July 1969
20. Murrow, H.N., et al, Development Flight Tests of the Viking Decelerator System, AIAA Paper 73-455, presented at AIAA, Aerodynamic Deceleration Systems Conference, Palm Springs, CA, (A73-31441) May 1973
21. Moog, R.D., et al, Qualification Flight Tests of the Viking Decelerator System AIAA Paper 73-457, presented at AIAA, Aerodynamic Deceleration Systems Conference, Palm Springs, CA, (A73-31443) May 1973
22. Nolte, L. T., Probing a Planetary Atmosphere: Pioneer Venus Spacecraft Description, AIAA Paper 75-1160, September 1975
23. Kiker, J. W., Lee, J. B., Hinson, J. K., Earth Landing Systems for Manned Spacecraft, Paper presented at AGARD meeting, Turin, Italy (X63-12690), April 1963
24. Project Gemini, A Chronology, NASA SP-4002, NASA Scientific and Technical Information Office, Washington, D.C.
25. Norman, L.C., et al, Gemini Land Landing System Development Program, Volume I: Full Scale Investigations, NASA TN-D-3869, (N67-19278(), March 1967
26. Norman, L. C., McCullough, J. E., Coffey, J. C., Gemini Land Landing System Development Program, Volume II: Supporting Investigations, NASA TN-D-3870, (N67-19279), March 1967
27. Knacke, T. W., The Apollo Parachute Landing System, AIAA paper presented at AIAA, Aerodynamic Deceleration Systems Conference, El Centro, CA, (AD 854 169), September 1968
28. West, R. B., Apollo Experience Report - Earth Landing System, NASA TN-D-7437, (N74-11699), November 1973
29. Minnick, J. I., Studies on the Recovery and Resuability of the Saturn S-1C Booster, Volume I, Boeing Company Report D2-23233-1, (X65-11337), September 1964
30. Godfrey, R. E., Space Shuttle Booster Recovery Planning, AIAA Paper 73-441, presented at AIAA Aerodynamic Deceleration Systems Conference, Palm Springs, CA, (A73-31427), May 1973
31. Blackeen, R. F., Space Shuttle Solid Rocket Booster Recovery System Definition, NASA CR-120106 (N74-13579), October 1973
32. Anon., AFSC Design Handbook DH 2-8, Life Support, Second Edition, September 1978
33. MIL-S-9470B (USAF), (2), Seat System, Upward Ejection, Aircraft, General Specification for, March 1971

34 MIL-S-18471D, System, Aircrew Automated Escape, Ejection Seat Type, General Specification for, February 1970

35 MIL-S-25969B (USAF), Capsule Emergency Escape Systems, General Requirements for, March 1970

36 Unused

37 Unused

38 Unused

39 The Foundations of Space Biology and Medicine, NASA Publication, U.S. Government Printing Office Stock No. 033-000-00606-3, Volume II, Book I

40 Parker, J. F., West, V. R., Bioastronautics Data Book, 2nd Edition, NASA SP-3006, 1973

41 Nichols, C. W., Evaluation of Automatic Personnel Emergency Back Parachute, FTC-TR-66-42, (AD 804 578), December 1966

42 Woolman, R. D., Performance Data for Four Free-Type, Back Style, Automatic Personnel Parachute Assemblies, AFFTC-TR-74-35, (AD B001 863), January 1975

43 Brown, H. R., Capt., USAF, Development and Evaluation of a Deployment System for Personnel Parachutes Equipped with Vent Pull-down Lines, AFFTC-TR-74-18, (AD 920 186), May 1974

44 Matsuo, J. T., Design, Development and Qualification Testing of the U. S. Navy T-33B Aircraft Ejection Seat with Drogue Parachute System and NES-21A Personnel Parachute Assembly, TR 6-74, (AD B003 894), December 1974

45 Matsuo, J. T., Design Development and Qualification Testing of the U.S. Navy NES-21A Parachute Assembly, TR 1-74, (AD A001 754), July 1974

46 Menard, G. L. C., Personnel Parachute Four-Line Release System, Performance Investigation of Application to 28-Foot Diameter Flat Circular Personnel Recovery Parachute Assemblies, TR 9-74, (AD B005 618), December 1974

47 Finney, R. G., Parachute Canopy Deflation Pockets, TR 6-67, (AD 818 498), July 1967

48 Richards, E. H., Eberhardt, R. G., Matsuo, J. T., Comparison of Deflation Times for Parachute Canopies with and without Center Tabs on the Water Deflation Pockets, NPTR TN 1001-77, May 1977

49 Moy, H. R., Investigation of Low Bulk Personnel Parachute Canopy, 21 Ft. Conical, April 1953

50 Neipling, L. E., Qualification and Evaluation of Models XD and D Skysail Parachutes, Technical Report No. 5-63, November 1963

51 Woolman, R. D., Performance Evaluation of a Disc-Gap-Band Personnel Parachute Assembly, AFFTC-TR-74-36, (AD B002 975), February 1975

52 Drew, G. R., Development of the STAR Parachute Canopy, Technical Report No. 2-74 (AD 920 031L), May 1974

53 Niccum, R. J. et al, Drag and Stability of Cross Type Parachutes, FDL-TDR-64-155, (AD 460 890), February 1965

54 Brosnahan, T. J., Performance Evaluation of Parachute Canopies with Stretch Fabric Sections, AFFTC-TR-76-29, August 1976

55 U.S. Air Force Technical Order 14D1-1-1

56 Anon., U.S. Navy Aircraft Crew System Manual (Parachute), Navair Manual 13-1-612

57 Drake, V.N., Comparative Ejection Trials 1972 Using Aeroconical and I-24 Parachutes, A&AEE Note No. 3137 (AD 920 182), December 1973

58 Moy, H. R., Advanced Concept Ejection Seat (ACES) Development and Qualification, ASD-TR-73-2, (AD 909 656L), January 2973

59 Moy, H. R., Recovery System for Advanced Performance Ejection Seat, paper presented at 11th Symposium of Survivability and Safe Equipment Association, 1973

60 Peck, W. R., Manzuk, R. J., Design Philosophy of the S111S-3 Ejection Seat Escape System, AIAA paper presented at AIAA, Aerodynamic Deceleration Systems Conference, Dayton, OH, (A70-41808), September 1970

61 Shannon, R. H., Till, A. N., SR-71 Ejection Experience

62 Rivedal, J., The 600 Knot Yankee Escape System, SAFE Engineering, Volume 2, 2nd Qtr, p. 12-18 (A73-16200) March 1972

63 Drew, G. R., Qualification Testing of the U.S. Navy NS-5 Parachute Recovery System, TR-2-68, (AD 857 485L), July 1969

64 Bull, J. O., Serocki, E. L., Compilation of Data on Crew Emergency Escape System, AFFDL-TR-66-150, (AD 801 787) September 1966

65 Sierra, C. R., The F-111 Crew Module, AIAA paper presented at AIAA, Aerodynamic Deceleration Systems Conference, Houston, TX, September 1966

66 Charleville, J. L., The F-111 Crew Module Development, AIAA paper presented at AIAA, Aerodynamic Deceleration Systems Conference, Dayton, OH, (A70-41807), September 1970

67 McMullen, T. H., Evolution of the B-1 Crew Escape System, AIAA paper presented at AIAA, Aerodynamic Deceleration Systems Conference, Palm Springs, CA, (A73-31426), May 1973

68 Whalley, I. A., Development of the B-1 Crew Module Parachute Recovery System, AIAA Paper No. 73-467, presented at AIAA, Aerodynamic Deceleration Systems Conference, Palm Springs, CA, May 1973

69 Rutan, E. L., Stroup, F. B., Evaluation of the C-130E Stability and Control Characteristics During Tandem, Sequential and Single-Platform LAPES Deliveries and Airdrop Deliveries, AFFTC-TR-67-18, (AD 823 602), November 1967

70 Stroup, F. B., Rutan, E. L., Stability and Control Tests During Heavyweight Low Level Cargo Deliveries from a C-130E, Society of Experimental Test Pilots, Technical Review, Volume 8, No. 4, p. 1-22, (A68-21136), 1967

71 Tingdahl, M. A., Cargo Handling System, A/A32H-4, FTC-TDR-63-46, (AD 430 643), February 1964

72 Ducote, R. J., Evaluation of the A/A32H-4 Dual Rail Cargo Handling System for Airdrop and Low Level Cargo Deliveries, FTC-TR-67-35, (AD 830 011), December 1967

73 Hunter, H. J., C-141A Aircraft Aerial Delivery System Category I Evaluation Tests, FTC-TR-66-32, (AD 804 577), December 1966

74 Hunter, H. J., Performance Evaluation of a 25,000 to 35,000 Pound Capacity Extraction System for the C-141A Aircraft, TM 67-111, (AD 824 145), August 1967

75 Hunter, H. J., Boyer, G. E., Evaluation Tests of C-5A Airplane Aerial Delivery System, Phase II - Airdrop and Jettison Capability, FTC-TR-71-47, (AD 890 101L), November 1971

76 Tingdahl, M. A., Hunter, H. J., Evaluation Tests of C-5A Airplane Aerial Delivery System, Phase III - Modified Aerial Delivery System Components, FTC-TR-72-52, (AD 907 283L), December 1972

77 Ferrier, B. D., Adverse Weather Aerial Delivery System, TAC Test 70A-037A, (AD 889 197L), November 1971

78 Dehmer, P. A., Pendulum Release Extraction Parachute System (PREPS), TAC Test 68-224, (AD 853 569L), June 1969

79 Anon., Engineering Design Handbook - Design for Air Transport and Airdrop Material, AMC-PAM-706-130, (AD 830 262), December 1967

80 Hastings, R. P., Airdrop Test of the XM-551 Army Full-Tracked Vehicle from a C-130 Aircraft, FTC-TDR-64-30, (AD 451 656), October 1964

81 Olson, T. A., C-130 Dual Rail Aerial Delivery System for Heavy Equipment Drop, FTC-TDR-62-17, (AD 276 443), May 1962

82 Olson, T. A., 463L Universal Cargo Handling System, FTC-TDR-62-27, August 1962

83 Tingdahl, M. A., G-12D Low Altitude Aerial Delivery System LAADS), FTC-TR-67-8, (AD 816 783), June 1967

84 Ford, J. P., et al, Joint Initial Operational Test and Evaluation/Developmental Check Test of C-141 Container Delivery System, TECOM Project No. 4-ES-065-000-001, (AD B004 760), April 1975

85 Laine, C. O., Development and Evaluation of a C-130 Aircraft Low Altitude Parachute Extraction System (LAPES) for Aerial Delivery of Single and Tandem Cargo Platforms at Ground Proximity, AFFTC-TR-68-3, (AD 828 563), March 1968

86 Fried, G., Feasibility Investigations of a Modified Low Altitude Parachute Extraction System (LAPES) and an Evaluation of the Type V Platform, AFFTC-TR-75-1, July 1965

87 Hinck, R. W., Joint Test of 1528 LAPES - Phase I, TAC Project 72B-203T, (AD 911 933L), June 1973

88 Foss, W., Joint Test of 1528 LAPES - Phase II, TAC Project 73TB-1002X, September 1973

89 Weintraub, P. L., Low Altitude Aerial Delivery (Fighter Aircraft), Results of Qualification Testing of the M4A (Modified) Container Aerial Delivery System, FTC-TR-66-36, (AD 803 796), November 1966

90 Morris, F. B., Development of a High Speed, Low Altitude Aerial Delivery Parachute System for Use with a Modified C-130 Aircraft, FTC-TR-70-33, (AD 893 670L), November 1970

91 Franklin, I. L., High-Speed, Low-Level Aerial Delivery System (HSLLADS), TAC Project 73A-079T, (AD 917 743L), March 1974

92 Mihlbachler, C. B., Parachute Altitude Recognition System Employing the AN/APQ-155 Parachute Deployment Set, ASD-TR-74-35, (AD B000 930), October 1974

93 Wuest, Evaluation of a Radar and a Barometric Altimeter Activated Two-Stage Airdrop System, AFFTC-TR-75-25, August 1975

94 Barnicle, E. J., Military Potential Test of Interim High Level Container Airdrop System (HLCADS), TR-74-23-AD, (AD 776 898), November 1973

95 Krizavskas, J., Feasibility Investigation of a Two-Stage Platform-Mounted Airdrop System, AFFTC-TR-75-22, July 1975

96 Farinacci, A. L., Bruner, D. B., High-Level Airdrop System, TR 73-55-AD, (AD 766 306), March 1973

97 Massey, W. N., et al, Development and Evaluation of a Two-Stage, High Altitude, Container Airdrop System, AFFTC-TR-74-32, (AD B001 145), November 1974

98 Barnard, G. A., Development of a High-Level Container Airdrop System, AIAA Paper 75-1386, presented at AIAA, Aerodynamic Deceleration Systems Conference, Albuquerque, NM, (A76-13182), November 1975

99 Rice, R. H., Acceptance Tests of G-13 Parachutes, FTL-53-7, January 1954

100 Graham, C. R., G-13, 500 Lb. Cargo Parachute, FTC-LR-54-20, September 1954

101 Graham, C. R., 64 Ft. Nominal Diameter Parachute with 10% Extended Skirt, FTC-54-8, (AD 289 124), May 1954

102 Marshall, C. W., G-12B 64 Ft. Cargo Parachute Cluster Tests, AFFTC-LR-58-102, March 1958

103 Graham, C. R., G-11A Parachute Ultimate Drop Test Conditions, FTL-54-23, September 1954

104 Cooksley, K. T., Development Test II (Service Phase) of G-11A Vent Control System for Division Ready Force (DRF) Vehicle Loads, TECOM Project No. 4-ES-060-011-005, (AD B003 848), April 1975

105 Giebutowski, E. J., A Discussion of the Applicability of Parachutes with Pulled-Down Vents for Airdrop of Supplies and equipment from a 500 Ft. Altitude, 72-23AD, (AD 750 585), October 1971

106 Tingdahl, M. A., Internal Parachute Study Phase II (Clusters), FTC-TM-67-109, May 1967

107 Laine, C. O., 50,000 Lb. Capacity Recovery System, AFTTC-TR-69-35

108 Toni, R. A., Mueller, W. R., Prototype Cluster-Parachute Recovery System for a 50,000 Lb. Unit Load, Volume I, NLABS-TR-69-82-AD, (AD 701 004), January 1969

109 Toni, R. A., Knor, M. M., Prototype Cluster-Parachute Recovery System for a 50,000 Lb. Unit Load, Volume II, NLABS-TR-69-83-AD, (AD 701 005), January 1969

110 Graham, C. R., 200 Ft. Diameter Solid Flat Parachute; Engineering Test of, FTL-54-1, (AD 289 123), February 1954

111 Graham, C. R., 150 Ft. Diameter Straight Gore Solid Flat Parachute, FTL-54-18, August 1954

112 Anon., A Study of Design and Materials for Development of Low Cost Aerial Delivery Parachutes, WADS-TR-59-385, (AD 237 460), September 1959

113 Ruprecht, F. A., A Study of Design and Materials for Development of Low Cost Aerial Delivery Parachutes, ASD-TDR-62-309, (AD 284 442), June 1962

114 Anon., Letter of Report of Engineering Design Test (Air Drop) of the 500-Pound Capacity Plastic Film Low Cost Parachute, USATECOM Project No. 4-5-7498-02, November 1966

115 Hunter, H. J., An Airdrop System for Testing Large Parachutes for Recovery of Loads in Excess of 50,000 Lb., AIAA Paper No. 72-471, presented at AIAA, Aerodynamic Deceleration Systems Conference, Palm Springs, CA, (A73-31455), May 1973

116 Petry, G. A., Hester, R. L., One-Hundred Ton Airdrop from a C-5 Aircraft, AIAA Paper No. 70-1203, presented at AIAA, Aerodynamic Deceleration Systems Conference, Dayton, OH, (A70-41814), September 1970

117 Marshall, C. W., Extraction Systems, AFFTC-TR-58-6, (AD 152 288), July 1958

118 Marshall, C. W., Extraction Parachute Clustering Techniques, FTC-TN-58-18, (AD 152 294), October 1958

119 Hunter, H. J., Hastings, R. P., 35 Ft. Ringslot Parachute Extraction System Development, FTC-TDR-64-17, (AD 445 072), July 1964

120 Brown, W. L., Performance Evaluation of a Cluster of Two 28 Ft. D_o Ringslot Extraction Parachutes Towed From a C-130 Aircraft, FTC-TR-65-25, (AD 468 768), August 1965

121 Morris, F. B., Performance Evaluation of Heavy Duty 28 Ft. D_o Ringslot Extraction Parachutes, AFFTC-TR-69-43, (AD 863 642), December 1969

122 Anon., Cargo Aircraft Compartment Dimensional Data, MIL-HDBK-318, April 1977

123 Black, J. M., Development, Test and Evaluation of an Extraction Parachute Subsystem for Airdrop from the C-5A Aircraft, AFFTC-TR-69-29, (AD 860 702), October 1969

124 Anon., The Criteria for Non-Standard Air Drop Loads, AFD-TM-ENE-77-1, December 1977

125 Chakoian, G., Michal, J. L., A Parachute Retrorocket System for Low Altitude Airdrop of Cargo and Other Special Applications, AIAA Paper No. 68-956, presented at AIAA, Aerodynamic Deceleration Systems Conference, El Centro, CA, (A68-42029), September 1968

126 Chakoian, G., A Parachute Retrorocket Recovery System for Airdrop of Heavy Loads, NLABS-TR-70-34-AD, (AD 699 342), November 1969

127 Michal, J. L., et al, Final Engineering Report - Parachute Retrorocket Airdrop System, TR 72-16, (AD 736 361), December 1970

128 Chakoian, G., Plan for Advanced Development of a Parachute Retrorocket Airdrop System, TR-73-59-AD, (AD 765 422), October 1972

129 Ulrich, R. R., D'Onofrio, A. J., An Active Optical Ground Sensor for a Parachute Retrorocket Airdrop System (PRADS), HDL-TM-73-2, (AD 911 216L), February 1973

130 Croom, D. R., Deployment Loads Data from a Free-Flight Investigation of All-Flexible Parawings Having 371.612 Meters^2 (4000 Ft^2) of Wing Area, NASA TM-X-2326, (N72-11956), November 1971

131 Pepper, W. B., A Study of Gliding Parachutes for Accurate Cargo Delivery, SC-TM-72-0298, (AD 891 842L), July 1971

132 Speelman, R. J., et al, Parafoil Steerable Parachute, Exploratory Development for Airdrop System Application, AFFDL-TR-71-37, (AD 742 294), April 1972

133 Moeller, J. H., Linhart, E. M., Parawing Technology for Spacecraft Land Landing, AIAA Paper No. 70-1187, (AD 906 155L), September 1970

134 Knacke, T. W., Steerable Parachutes, paper presented at Symposium for Aerodynamic Deceleration, Braunschwerg, West Germany, (AD 905 223L), September 1969

135 Slayman, R. G., Bair, H. Q., Rathbun, T. W., 500-Pound Controlled Airdrop Cargo System, USAAVLABS Tech Report No. 70-31, (AD 877 587), September 1970

136 Morgan, H. L. Jr., McHatton, A. D., Aerodynamic and Deployment Characteristics of Multistage Canopy and Suspension Line Reefing Systems for a Twin-Keel All-Flexible Parawing, NASA TN-D-6306, (N71-30748), July 1971

137 Vickery, E. D., Evaluation of Recovery Parachute; Low Altitude Airdrop Exploratory Development, TR-69-12-AD, (AD 672 087), August 1966

138 Oates, R. W., Lifting of Aerodynamic Decelerators, NLABS-TR-68-66-AD, (AD 669 665), November 1966

139 Boyer, G. E., Fisher, C. W., Performance Evaluation of T-10 Canopies with Anti-Inversion Devices, AFFTC-TR-70-17, October 1970

140 Foster, K. R., Product Improvement Test (Service Phase) of T-10 Personnel Parachute (Modified) with 3 ¾ Inch Mesh Net, TECOM Project No. 8-EG-060-010-003, (AD B004 284L), March 1975

141 Foss, W., Modified High-Altitude, Low-Opening Parachute, TAC Project 73A-125T, (AD 915 755), December 1973

142 Menard, G. L. C., Performance Evaluation 35 Ft. Diameter Extended Skirt Maneuverable Personnel Parachute Canopy Assembly with "TU" Orifice, TR-8-66, (AD 815 808L), April 1967

143 Franklin, B. R., Service Test of Maneuverable Troop Back Personnel Parachute, Modified, TECOM Project No. 8-EG-065-000-001, (AD 868 721L), March 1970

144 Schwarz, R. G., Product Improvement Test (Service Phase) of MC-1-1 Personnel Parachute (Modified) with 3 ¾ Inch Mesh Net and Apex Centering Loops, TECOM Project No. 8-EG-065-000-018, (AD B004 210L), May 1975

145 Nichols, C. W., Performance Evaluation of Para-Commander Mark I Personnel Parachute, FTC-TR-66-16, (AD 484 799), June 1966

146 Kanowski, M. B., Quick Opening Reserve Parachutes, AFFTC-TN-59-10, (AD 215 481), July 1959

147 Laine, C. O., Army Troop Reserve Parachute, Ballistically Deployed Pilot Chute, FTC-TDR-63-4, (AD 299 149), March 1963

148 Calkins, R. B., Performance Evaluation of a Gas-Deployed Reserve Parachute, FTC-TR-71-10, (AD 882 766), April 1971

149 Wolstenholme, D. E., Dolighan, T., Check Test of Parachute, Reserve, Personnel, Troop Chest, Ballistically Deployed, AB 1470-2, (AD 892 431L), November 1971

150 Hibbert, W. A., The Automatic Operation of Reserve Parachutes for Paratroops, A&AEE Memo No. 3001, (AD 825 400), September 1967

151 Deering, J. O., Low Level Multiple Personnel Delivery Capsule, SEG-TR-66-10, (AD 880 624), October 1966

152 Falcone, J. F., Concept for a Multiple Personnel Airdrop System, TR-74-15-AD, (AD 771 945), November 1973

153 Ewing, E. G., Deployable Aerodynamic Deceleration Systems, NASA-SP-8066, NASA Space Vehicle Design Criteria - (Structures), (N71-31303), June 1971

154 Burk, S. M., Summary of Design Considerations for Airplane Spin Recovery Parachute Systems, NASA TN-D-6866, (N72-27033), August 1972

155 Pepper, W. B., Biesterveld, J. R., An Omnidirectional Gliding Ribbon Parachute and Control System, AIAA Paper No. 73-486, presented at AIAA, Aerodynamic Deceleration Systems Conference, Palm Springs, CA, (A73-31468), May 1973

156 Rychnovsky, R. E., Comparison of a Hybrid Parachute System to Conventional Parachute Systems for Laydown Delivery of a Bomb, SLL-74-0217, (SLL-74-0217), September 1974

157 McGirr, P. G., Aebischer, A. C., Weinberg, S. A., Development and Testing of Ballute Stabilizer/Decelerators for Aircraft Delivery of a 500 Lb. Munition, AIAA Paper 73-485, presented at AIAA, Aerodynamic Deceleration Systems Conference, Palm Springs, CA, (A73-31467), May 1973

158 Graham, J. J., Ballute Stabilization for Various Munition Configurations, AFATL-TR-72-75, BK-2, (AD 908 927L), April 1972

159 Aebischer, A. C., MK 82 Ballute Retarder System, AFATL-TR-72-179, (AD 907 851), September 1972

160 Carpenter, G. R., Development Test of the Low Drag BSU-49/B Air Inflatable Retarder (AIR), ADTC-TR-76-69, (AD B014 093), September 1976

161 Evors, R. A., Evaluation of a Ballute Retarder System for the MK 82 Bomb, ADTC-TR-73-31, (AD 911 336L), May 1973

162 Miller, M. C., Preliminary Investigation for Applying a Ram Air Inflatable Decelerator (RAID) as the Retardation System for the 800 Lb. Modular Bomb - Summary Report, EC-TR-73052, (AD 917 734L), February 1974

163 St. Germain, R. S., Feasibility Test of Ballute Stabilization System for M118 Bomb, ADTC-TR-69-18, (AD 849 122), February 1969

164 Miller, M. C., Utilization of a RAID as the Aerodynamic Decelerator System for a 2000 Lb. FAE Bomb, EC-TR-74029, (AD 919 923), June 1974

165 Litz, C. J. Jr., Advanced Concept Studies for Aircraft Flares and Dispensing Systems, (AD 864 086L), July 1969

166 Matura, J. R., Product Improvement of Illuminating Ammunition, Tech Report No. 3920, (AD 858 282L), April 1969

167 Bloetscher, F., Slow Descent Recovery System Technology Study and Data Program, AFFDL-TR-74-7, (AD 783 268), April 1974

168 Reed, E. A. III., AN/SSQ-41 Two Stage Parachute System, NADC-72174-VT, (AD 904 276L), October 1972

169 Gombos, E. R., Reed, E. A. III., AN/SSQ-41A/53 Sonodrop Q41 System Qualification Test Q53 Developmental Test, NADC-72209-VT, (AD 905 899L), December 1972

170 Bombos, E. R., AN/SSQ-53 Two Stage Flocelerator System Qualification Tests October - November 1972, NADC-73012-30, (AD 907 217L), January 1973

171 Stauffer, R. L., Evaluation of Methods for Adapting the Fulton Skyhook Air Rescue System for Air-to-Air Rescue by Fighter Aircraft, NADC-AM-7036, (AD 878 565L), June 1970

172 Epple, H. K., Results of Tests with a Tandem Recovery System using a Gliding Main Parachute, Aerospace Corporation, Report TOR-0200 (4110-01)-27, (AD 854 743), May 1969

173 Colgate, R. T., Gliding 77.6 Ft. Mid-Air Retrieval System Parachute Tests, AFFTC-TR-75-28, June 1975

174 Brattland, H. A., HH-53C/80H Mid-Air Retrieval Systems, AFFTC-TR-74-19, (AD 920 999L), June 1974

175 Brattland, H. A., Limited Tests of the CH-3E/80H Mid-Air Retrieval System (MARS), AFFTC-TR-74-25, (AD B004 630), October 1974

176 Lindgren, M. S., Jenkins, B. C., Development and Qualification Test Report MK5-B Parachute Recovery System, Program 162, Lockheed Missile and Space Company Report LMSC/A381549

177 Houston, J. B., Test of the Recovery System for the High Altitude Supersonic Target, ADTC-TR-73-58, (AD 912 731L), August 1973

178 Epple, H. K., Performance and Characteristics of 67.2 Ft. Extended Skirt Canopy Parachute with Single Conical Extension, SSD-TDR-65-42, (AD 616 885), April 1965

179 McClow, J. H., Preliminary Development Testing of 53 Ft. Parachute with Conical Extension for Aerial Retrieval, SSD-TR-66-204, (AD 803 032), November 1966

180 Higgins, M. W., Speelman, R. J. III., A Stability Analysis of Tandem Parachute Mid-Air Recovery Systems, AFFDL-TR-74-149, (AD A015 746), May 1975

181 Everett, W. J., Development of an Improved Mid-Air Retrieval Parachute System for Drone/RPV Aircraft, AIAA Paper No. 73-469, presented at AIAA, Aerodynamic Deceleration Systems Conference, Palm Springs, CA, (A73-31453), May 1973

182 Anon., AQM-34 Drone Mid-Air Retrieval Parachute System, Volumes I - XI, Pioneer Parachute Document No 335-1044, (AD A006 373) - (AD A006 383), February 1974

183 Ewing, E. G., Vickers, J. R., Feasibility Study of a Universal Aerial Recovery System, Volume I, SSD-TR-66-47, (AD 488 839), April 1966

184 Ewing, E. G., Design Development of a Universal Aerial Recovery System, Phase III (Product Improvement), SAMSO 68-244, (AD 835 917L), June 1968

185 Stauffer, R. L., The Feasibility Evaluation of an Air-to-Air Rescue Concept Designated Packaged Offset Retrieval Technique (PORT-I), NADC-72037-VT, (AD 902 316L), July 1972

186 Wieseman, W., Feasibility Test Evaluation of Engagement Techniques for the PORT-II, Wing Fending Line Air-to-Air Rescue Concept, NADC 72038-VT, (AD 904 686L), September 1972

187 Miller, J. G., Shillinger, G. L., Development of Surface Retrieval Capability by In-Flight Fixed-Wing Aircraft in Support of Project Biosatellite, NASA-AMES Research Center Report

188 Schmarje, D. P., Unmanned Water-to-Air Recovery System, paper presented at Symposium on Parachute Technology and Evaluation, AFFTC-TDR-64-12, Volume II, (AD 452 431), September 1964

189 Behling, E. A., Pilmer, R. B., Jumper, E. J., Long-Line Loiter Personnel Retrieval System: Triaxial Acceleration Tests, AMRL-TR-70-104, (AD 749 418), May 1972

190 Sears, C. W., Dixon, B. C., Long-Line Loiter Support Equipment, AMRL-TR-70-142, (AD 884 090L), March 1971

191 Simons, J. C., Dixon, B. C., Long-Line Loiter: Improvement of Some Free-Fall and Circling-Line Techniques, ASD-TR-69-95, Volume I, (AD 695 800), September 1969

192 DeWeese, J. H., McCarty, R. E., Parachute Design and Performance Data Bank, AFFDL-TR-74-45, (AD A019 491), January 1975

193 Unused

194 Laine, C. O., Development of a 50,000 Lb. Capacity Recovery System, Phase I. Performance Evaluation of a 135 Ft. D_o Flat Circular Parachute, AFFTC-TR-69-35, (AD 859 357), September 1969

195 Unused

196 Poynter, D. F., The Parachute Manual, First Edition, 1972

197 Anon., History of Smoke Jumping, Forest Service, U.S. Department of Agriculture, Missoula, Montana, April 1976

198 Morrison, R. S., Development and Evaluation of an Oil Containment Barrier Aerial Delivery System, AFFTC-TR-75-1,

199 Warren, J. B., Performance Evaluation of an Oil Containment Barrier Sequential Aerial Delivery System, FTC-TR-73-53, (AD 916 944L), January 1974

200 Marshall, C. W., Development of a Parachute System for Minuteman I Missile Launch from C-5A Aircraft, AFFTC-TR-75-2, April 1975

201 Carten, A. S., The Flight Test Aspects of the Air-Launched Balloon System (ALBS) Development Program, AFGL-TR-76-0196, August 1976

202 Massey, W. N., Air Launched Balloon System, AFFTC-TR-77-42, February 1978

203 Carten, A. S., Flight Tests of the Air-Launched Balloon System Prototype Model, AFGL-TR-78-0074, March 1978

204 Heick, R. J., Performance Characteristics of Standard G-12D and G-11A Cargo Type Parachutes at Overload Conditions, Technical Report T-5, ATA 61035, March 1962

205 Schmarje, D. P., Evaluation of the 67 Ft. D_o Recovery Parachute, FTC-TDR-62-39, (AD 296 088), January 1963

206 Gimalouski, E. A., Development of a Final Stage Recovery System for a 10,000 Pound Weight, WADC-TR-59-109, (AD 215 534), December 1958

207 Unused

208 Mason, J. S., Parachute Recovery System Tests USAF Q-2C Drone Missile, AFFTC-TN-59-11, (AD 215 533), May 1959

209 Engstrom, B. A., Performance of Trailing Aerodynamic Decelerators at High Dynamic Pressures, WADC-TR-58-284, Part II, (AD 247 186), January 1960

210 Naval Surface Weapons Center, White Oak Laboratory, Silver Spring, MD, 20910, Department CU-11

211 Ludtke, W. P., Effects of Canopy Geometry on the Drag Coefficient of a Cross Parachute in the Fully Open and Reefed Conditions for a W/L Ratio of 0.264, (NOLTR-71-111, (AD 731 023), August 1971

212 Homan, M. L., Aerodynamic Characteristics of Several Flexible Decelerators at Mach Numbers from 1.8 to 2.5, AEDC-TR-71-6, (AD 879 024), January 1971

213 Toni, R. A., A 14.2 Ft. D_o Variable Porosity Conical Ribbon Chute for Supersonic Application, AIAA Paper No. 73-472, presented at AIAA, Aerodynamic Deceleration Systems Conference, Palm Springs, CA, (A73-31456), May 1973

214 Unused

215 Bloetscher, F., Aerodynamic Deployable Decelerator Performance Evaluation Program, Phase II, AFFDL-TR-67-25, (AD 819 915), June 1967

216 Unused

217 Ewing, E. G., Ringsail Parachute Design, AFFDL-TR-72-3, (AD 745 335), January 1972

218 Ewing, E. G., Rotafoil Performance Evaluation, Radioplane Report No. 705, January 1953

219 Nicolaides, J. D., Tragarz, M. A., Parafoil Flight Performance, AFFDL-TR-71-38, (AD 731 143), June 1971

220 Moeller, J. H., et al, Free-Flight Investigation of Large All-Flexible Parawings and Performance Comparison with Small Parawings, NASA CR-66918, (N70-25071), March 1970

221 Mullins, W. M., et al, Investigation of Prediction Methods for Loads and Stresses of Apollo Type Spacecraft Parachutes, Volume II - Stresses, NVR-6432, (N74-19674), June 1970

222 Alexander, W. C., Investigation to Determine the Feasibility of Using Inflatable Balloon Type Drag Devices for Recovery Applications in the Transonic, Supersonic and Hypersonic Flight Regimes, Part II, Mach 4 to Mach 10 Feasibility Investigation, ASD-TDR-62-702, (AD 295 489), December 1962

223 Bohon, H. L., et al, Deployment and Performance Characteristics of 1.5 Meter Supersonic Attached Inflatable Decelerators, NASA TND-7550, (N74-28408), July 1974

224 Engstrom, B. A., et al, Feasibility Study of Hypersonic Parachute Free Flight Test Capability - Phase I, ASD-TR-61-600, (AD 275 578), March 1962

225 Barzda, J. J., Goodale, B. A., et al, Investigation of Stored Energy Rotors for Recovery, ASD-TDR-63-745, (AD 428 998), December 1963

226 Bleikamp, R. H., et al, Investigation of Propellant Actuated Devices for Use in Emergency Crew Escape Systems for Advanced Aerospace Vehicles - Phase III - Design Study, AFFDL-TR-65-26, (AD 464 738), April 1965

227 Brown, H. R., Evaluation of Personnel Parachute Deployment and Inflation Aids, FTC-TR-70-34, (AD 879 422), December 1970

228 Anon., Cargo Parachute Releases of 20,000 and 35,000 Pound Capacity, TIR 18.4.4.2(1), (AD 801 224L), September 1966

229 Unused

230 Anon., Aviation-Crew Systems Manual, Parachutes, December 1974

231 TM 10-500/T.O. 13C7-1-5, Airdrop of Supplies and Equipment, General, November 1968

232 Federal Trade Commission, Rules and Regulations Under the Textile Fiber Products Identification Act, November 1974

233 V-T-276G (3), Federal Specification, Thread Cotton, August 1972

234 V-T-295C, Federal Specification, Thread, Nylon, February 1977

235 V-T-285D, Federal Specification, Thread, Polyester, October 1975

236 MIL-T-43636, Military Specification, Thread, Nylon, Non-Melting, April 1969

237 Coskren, R. J., Abbott, N. J., Ross, H. J., Kevlar 29 and 49 in Parachute Fabrics, AIAA Paper No. 75-1360, presented at AIAA' Aerodynamic Deceleration Systems Conference, Albuquerque, NM, (A76-13158), November 1975

238 MIL-C-5040E (2), Military Specification, Cord, Nylon, April 1972

239 MIL-C-7515E (1), Military Specification, Cord, Nylon, Coreless, March 1977

240 MIL-C-83242 (USAF), Military Specification, Cord, Aromatic Polyamide, Non-Melting, October 1969

241 MIL-W-5665H (1), Military Specification, Webbing, Textile, Cotton Warp, August 1976

242 MIL-W-4088H (2), Military Specification, Webbing, Textile, Woven Nylon, May 1974

243 MIL-W-27265C (1), Military Specification, Webbing, Textile, Woven Nylon, Impregnated, September 1971

244 MIL-W-83729 (2) (USAF), Military Specification, Webbing, Textile, Woven Nylon, June 1970

245 MIL-W-5625H (1), Military Specification, Webbing, Textile, Nylon, Tubular, May 1970

246 MIL-W-27657B (USAF), Military Specification, Webbing, Textile, Woven Nylon, for Decelerators, August 1977
247 MIL-W-9049C (ASG), Military Specification, Webbing, Textile, Nylon, Locking Loop, August 1968
248 MIL-W-25339A (ASG), Military Specification, Webbing, Textile, Polyester, February 1961
249 MIL-W-25361C (1), Military Specification, Webbing, Textile, Polyester, Low Elongation, October 1974
250 MIL-W-19078C (AS), Military Specification, Webbing, Textile, Polyester, Latex Impregnated, April 1972
251 MIL-W-38283A (USAF), Military Specification, Webbing, Textile, Aromatic Polyamide, Non-Melting, May 1973
252 MIL-W-38282 (1) (USAF), Military Specification, Webbing, Textile, Aromatic Polyamide, Non-Melting, Tubular, September 1964
253 MIL-W-81528 (AS), Military Specification, Webbing, Textile, Aromatic Polyamide, High Temperature Resistant, Nylon, Tubular, April 1967
254 MIL-T-5661D, Military Specification, Tape and Webbing, Textile, Woven, Reinforcing Cotton, September 1970
255 MIL-T-5237D, Military Specification, Tape Textile; Webbing Textile; Rayon, March 1970
256 MIL-T-5038F, Military Specification, Tape and Webbing, Textile, Reinforcing, Nylon, May 1974
257 MIL-T-8363B, Military Specification, Tape and Webbing, Textile, Woven, Nylon, January 1974
258 MIL-T-5666C, Military Specification, Tape, Textile, Nylon, Multiple Tubular, August 1969
259 MIL-T-6134C, Military Specification, Tape, Textile, Nylon, Parachute Construction, February 1971
260 MIL-T-5698G (1), Military Specification, Tape Textile: Webbing, Textile, October 1971
261 MIL-T-27736A, Military Specification, Tape, Textile, Nylon, for Ring Slot Parachutes, February 1968
262 MIL-C-4279D (1), Military Specification, Cloth, Muslin, Cotton, (Parachute Canopy), June 1975
263 MIL-C-19262 (WP)(2), Military Specification, Cloth, Parachute, Rayon (Fortisan)(for Ring Slot Types), December 1964
264 MIL-C-7020F, Military Specification, Cloth, Parachute, Nylon, March 1969
265 MIL-C-7350D (1), Military Specification, Cloth, Parachute, Nylon, March 1969
266 MIL-C-8021D (1), Military Specification, Cloth, Parachute, Nylon, Cargo and Deceleration, August 1971
267 MIL-C-7219D (1), Military Specification, Cloth, Nylon Duck, November 1971
268 MIL-C-498C, Military Specification, Cloth, Parachute, Synthetic-Fiber, April 1972
269 MIL-C-38351A (USAF), Military Specification, Cloth, Parachute, Aromatic Polyamide, Non-Melting, August 1972
270 Hartnett, J. P., et al, Values of the Emissivity and Absorptivity of Parachute Fabrics, WADC TN-57-433, (AD 151 072), December 1957
271 MIL-T-87128 (USAF), Military Specification, Thread, Para-Aramid, Intermediate Modulus, May 1978
272 MIL-C-87129 (USAF), Military Specification, Cord, Coreless, Para-Aramid, Intermediate Modulus, August 1978
273 MIL-T-87130 (USAF), Military Specification, Tape and Webbing, Textile, Para-Aramid, Intermediate Modulus, May 1978
274 MIL-W-87127 (USAF), Military Specification, Webbing, Textile, Tubular, Para-Aramid, Intermediate Modulus, May 1978
275 Anon., Emerging Aerospace Materials and Fabrication Techniques, AFML-TR-69-11, (AD 849 740), December 1968
276 Freeston, W. D. Jr., et al, Mechanical Properties of High-Temperature Fibrous Structural Materials, Part I - Metal Textiles AFML-TR-67-267, (AD 826 243L), October 1967
277 Jones, R. S., et al, Thermally Stable Polymeric Fibers - Part III, AFML-TR-67-172, (AD 826 243), October 1969
278 Corce, J. D., Aerodynamic and Thermal Performance Characteristics of Supersonic X Type Decelerators at Mach 8, AEDC-TR-77-7, February 1977
279 Abbott, N. J., Lannefeld, T. E., Schulman, S., Fabrics for Gliding Decelerators, AIAA Paper No. 70-1180, presented at AIAA, Aerodynamic Deceleration Systems Conference, Dayton, OH, (A70-41833), September 1970
280 MIL-H-9884D, Military Specification, Honeycomb Material, Cushioning, Paper, November 1973
281 Ripperger, E. A., Briggs, W. R., The Crushing Strength of Paper Honeycomb, TR-73-31-AD, (AD 763 913), March 1973
282 Smith, R. H., The Design and Development of Radio Frequency Transparent, Omnidirectional, Energy Absorbing Element System, Northrop Corporation, Ventura Division, NVR 5014, January 1967
283 Mehaffie, S. R., State of the Art of Impact Attenuation Concepts for RPV Applications, AFFDL-TM-76-51-FER, May 1976
284 Federal Standard No. 751a, Stitches, Seams and Stitchings, January 1965
285 Coplan, M. J., Bloch, M. G., A Study of Parachute Seam Design Criteria, Part I - Investigation of the Strength of Nylon and Rayon Cloth Seams, WADC-TR-56-313, (AD 110 407), June 1956
286 MIL-C-6635C (1), Military Specification, Canopy, Parachute, Ribbon, General Specification for Construction of, February 1965
287 MIL-C-9401B, Military Specification, Canopy, Parachute Ringslot, General Specification for Construction of, January 1968
288 00-S-256E (3), Federal Specification, Sewing Machines, Industrial (General Specification), January 1970
289 Mehaffie, S. R., Wade, D. K., X-ray Opaque Coating for Non-Destructive Evaluation of Nylon Parachute Components, AIAA Paper No. 75-1359, presented at AIAA, Aerodynamic Deceleration Systems Conference, Albuquerque, NM, (A76-13157), November 1975

290 Pepper, W. B., Maydew, R. C., Aerodynamic Decelerators - An Engineering Review, Journal of Aircraft, Volume 8, p 3-17, (A71-17692), January 1971

291 Lundstrom, R. R., et al, Flight Tests of Viking Parachute System in Three Mach Number Regimes, NASA-TND-7692, (N75-10147), October 1974

292 Lundstrom, R. R., et al, A Method for Making Large-Scale Decelerator Tests in a Simulated Mars Environment, (A68-23664)

293 McFall, J. C. Jr., Murrow, H. N., Parachute Testing at Altitudes Between 30 and 90 Kilometers, Journal of Spacecraft and Rockets, Volume 4, (A67-29433), June 1967

294 Raper, J. L., et al, The Viking Parachute Qualification Test Technique, AIAA Paper No. 73-456, presented at AIAA, Aerodynamic Deceleration Systems Conference, Palm Springs, CA (A73-31442), May 1973

295 Preisser, J. S., A Method for Controlling Parachute Deployment Conditions in Simulated Planetary Environments, NASA-TM-X-61215, (N68-34772), May 1968

296 Mayer, P. C., Wind Tunnel and Air Gun Testing of an Antimateriel Munition Orientation/Stabilization Device, AFATL-TR-74-146, (AD 923 344), September 1974

297 Braun, G., Compressed-Air Accelerator Installation for Model Parachutes, (SLA-73-739), February 1973

298 Ward, L. K., Myers, A. W., Free-Flight Testing of Aerodynamic Decelerators in a Supersonic Wind Tunnel, AEDC-TR-67-93, (AD 815 090), June 1967

299 Ward, L. K., Hodapp, A. E., Choate, R. H., Description of a Model Launcher and Techniques used for Obtaining Model Free Flight Measurements in the VKF Continuous Flow Wind Tunnels at Mach Numbers from 1.5 through 10, AEDC-TR-66-112, (AD 487 477), August 1966

300 Platou, A. S., The Wind Tunnel Free Flight Testing Technique, AIAA Paper No. 68-388, presented at AIAA, Aerodynamic Testing Conference, San Francisco, CA, (A68-25361), April 1968

301 Haigh, W. W., Burt, G. E., Free Flight Wind Tunnel Test of a Sphere and Cable Deployed from a Conical Model with Intact Recovery of all Components, AIAA Paper No. 68-387, presented at AIAA, Aerodynamic Testing Conference, San Francisco, CA, (A68-25360), April 1968

302 Burt, G. E., Wind Tunnel Investigation of the Deployment of Conical Wake Decelerators from the Base of a 7 Deg. Half-Angle Cone in Free Flight at Mach 6, AEDC-TR-70-2, (AD 864 682), February 1970

303 Burns, W. J., Decelerator Performance Study Free-Flight Wind Tunnel Test, SAMSO TR-70-8, February 1970

304 Hall, D., Service Test of C-5A Aircraft (Airdrop - Materiel), USAACEBD-AB-4668-3, (AD 890 766L), December 1971

305 Hunter, H. J., Evaluation Tests of C-5A Airplane Aerial Delivery System, Pahse I, AFFTC-TR-70-15, (AD 871 803), June 1970

306 Pyle, J. S., Phelps, J. R., Baron, R. S., Performance of a Ballute Decelerator Towed Behind a Jet Airplane, NASA TM-X-56019, (N74-14760), December 1973

307 Fike, R. L., Kinney. R. B., Perkins, H. C., The Design of a Research Water Table, NASA CR-121255, (N74-12083), August 1973

308 Ibrahim, S. K., Design and Instrumentation of a Water-Flow Channel and Application to Some Aerodynamic Problems, RTD TDR-63-4024, (AD 435 738), March 64

309 Vachon, W. A., Scale Model Testing of Drogues for Free Drifting Buoys, R-769, (N74-21922), September 1973

310 Heinrich, H. G., Ibrahim, S. K., Application of the Water Surface Wave Analogy in Visualizing the Wave Pattern of a Number of Primary and Secondary Body Combinations in Supersonic Flow, WADC-TR-59-457, (AD 231 291), September 1959

311 Preisiverk, E., Application of the Methods of Gas Dynamics to Water Flow with Free Surface, Parts I and II, NACA TM 934 and 935

312 Harleman, D., Studies on the Validity of the Hydraulic Analogy to Supersonic Flow, AF TR-59-85, Pt 4

313 Babish, C. A. III, The Influence of Aerodynamic Decelerators on Supersonic Wakes: With an Application of the Gas Hydraulic Analogy, AFFDL-TR-72-54, (AD 751 982), August 1972

314 Niehus, G., The Applicability of the Gas/Shallow-Water Analogy in Quantitative Form to Flows About Blunt Bodies, DFLR Research Report FB-68-21, (AD 892 662), 1968

315 Tory, A. C., Haywood, K. H., The Hydrogen Bubble Technique of Flow Visualization Factors Affecting Bubble Size and Buoyancy, ASME Fluids Engineering Conference, Pittsburgh, PA, (A71-29471), May 1971

316 Dereng, V. G., Parachute Gore Shape and Flow Visualization During Transient and Steady State Conditions, AIAA Paper No. 73-474, presented at AIAA, Aerodynamic Deceleration Systems Conference, Palm Springs, CA (A73-31458)

317 Klimas, P. C., Rogers, D. F., Helium Bubble Survey of a Parachute Opening Flowfield Using Computer Graphics Techniques, AIAA Paper No. 75-1368, presented at AIAA, Aerodynamic Deceleration Systems Conference, Albuquerque, NM, (A76-13165), November 1975

318 Hale, R. W., Stowell, R. C., Development of An Integrated System for Flow Visualization in Air Using Neutrally-Buoyant Bubbles, SAI-RR 7107, (AD 756 691), December 1971

319 Fejer, A. A., Flow Visualization Techniques for the Study of the Aerodynamics of Bluff Bodies and of Unsteady Flows, AFOSR-TR-72-0907, (AD 759 266), February 1972

320 Pope, D. L., Low Speed Flow Visualization Using Holography and the Development of a Rapid Data Reduction System for Holographic Interferometry, NPS-57C074062, (AD 783 791), June 1974

321 Klimas, P. C., Helium Bubble Survey of a Parachute Opening Flowfield, TR-73-48-AD, (AD 761 098), December 1972

322 De Santis, G. C., The Internal and External Flow Field Associated with Parachutes During Inflation, (AD 713 520) 1970

323 Unused

324 Speelman, R. J., Parachute Deployment Process Testing Technique, Journal of Aircraft, Volume 14, No. 4, p 401-402, April 1977

325 Federal Test Method Standard 191, Textile Test Methods, July 1970

326 Coskren, R. J., et al, Investigation of the High Speed Impact Behavior of Fibrous Materials, Part I: Design and Apparatus, WADD-TR-60-511, (AD 247 493), September 1960

327 Lindh, K. G., Tension Impact Tests on Nylon Webbing Structures, AIAA Paper No. 70-1182, (AD 906 156L), September 1970

328 Madden, R., et al, The Shock Tube as a Tool for Dynamic Testing of Fabrics, NASA CR-132284, (N73-32157), 1973

329 McCarty, R. E., A Computer Subroutine for the Load-Elongation Characteristics of Parachute Suspension Lines, AIAA Paper No. 75-1362, presented at AIAA, Aerodynamic Deceleration Systems Conference, Albuquerque, NM, (A76-13160), November 1975

330 Groom, J. J., A Characterization of Nylon Parachute Webbing With Hysteresis Effects in a Simple Dynamic System, AIAA Paper No. 75-1361, presented at AIAA, Aerodynamic Deceleration Systems Conference, Albuquerque, NM, (A76-13159), November 1975

331 Poole, L. R., Force Strain Characteristics of Dacron Parachute Suspension Line Cord Under Dynamic Loading Conditions, AIAA Paper No. 73-446, presented at AIAA, Aerodynamic Deceleration Systems Conference, Palm Springs, CA, (A73-31432), May 1973

332 Heinrich, H. G., Greig, R. C., Effective Porosity of Ribbon Grids, AFFDL-TR-65-110, (AD 478 684), December 1965

333 MIL-STD 810C, Military Standard, Environmental Test Methods, March 1975

334 Pirrello, C. J., Hardin, M. V., Heckart, M. V., An Inventory of Aeronautical Ground Research Facilities, Volume III - Structural and Environmental Facilities, NASA CR-1876, (N72-12183), November 1971

335 Stubbs, S. M., Investigation of Technique for Conducting Landing Impact Tests at Simulated Planetary Gravity, NASA TN D-6459, (N71-36247), September 1971

336 Datz, K. J., The Tonopah Test Range, Sandia Laboratories, SLA-74-0231, August 1974

337 Canning, T. N., Seiff, A., Modern Ballistic Ranges and Their Uses, NASA TM-X-66530, (N71-13577), August 1970

338 McVey, D. F., Strain Measurement in Parachute Webbing with Elastomeric Strain Gages, Sandia Laboratories, SLA-73-5764, September 1973

339 Klewe, H., Development and Use of Special Transducers for Testing Rescue- and Recovery-Systems in Aeronautics and Astronautics, IAI Symposium, Cranfield, Bedford, England, (A75-28768), March 1975

340 Melzig, H. D., Schmidt, P. K., Pressure Distribution During Parachute Opening - Phase I, Infinite Mass Operating Case, AFFDL-TR-66-10, (AD 482 534), March 1966

341 Melzig, H. D., Saliaris, C., Pressure Distribution During Parachute Opening - Phase II, Finite Mass Operating Case, AFFDL-TR-68-135, (AD 850 942), February 1969

342 Heinrich, H. G., Noreen, R. A., Stress Measurements on Inflated Model Parachutes, AFFDL-TR-72-43, (AD 907 447L), December 1972

343 Heinrich, H. G., et al, Functioning of the Omega Sensor on Textile Samples Under High Loading Rates, AFFDL-TR-74-78, (AD 786 029), September 1974

344

345 Unused

346 Huckins, E. K. III, Poole, L. R., Method for Estimating Minimum Required Ejector Velocity for Parachute Deployment, NASA TN-D-6300, (N71-23164), April 1971

347 Huckins, E. K., III, Techniques for Selection and Analysis of Parachute Deployment Systems, NASA TN-D-5619, (N70-15202), January 1970

348 McVey, D. F., Wolf, D. F., Analysis of Deployment and Inflation of Large Ribbon Parachutes, Journal of Aircraft, Volume II, No. 2, (A73-31437), February 1974

349 Lindh, K. G., McEwan, A. J., Analysis of Tension Impact Tests on the Nylon Webbing Structure of an Apollo Pilot Chute Riser, NASA CR-101772, (X69-16565), May 1969

350 Hoerner, S. F., Fluid Dynamic Drag, Published by the Author, Midland Park NJ, 1965

351 Eckstrom, C. V., Murrow, H. N., Flight Tests of Cross, Modified Ringsail, and Disk-Gap-Band Parachutes from a Deployment Altitude of 3.05 km (10,000 Ft.), NASA TM-X-2221, (N71-28021), June 1971

352 Dickinson, D., Schlemmer, J., Hicks, F., Balloon Launched Decelerator Test Program Post-Test Test Report (45 Day) BLDT Vehicle AV-3, NASA CR-112178, (N73-20012), January 1973

353 Berndt, R. J., DeWeese, J. H., Filling Time Prediction Approach for Solid Cloth Type Parachute Canopies, paper presented at AIAA Aerodynamic Deceleration Systems Conference, Houston, TX, (A66-40592), September 1966

354 Heinrich, H. G., Hektner, T. R., Opening Dynamic Characteristics of a 32 Ft. Ringslot Parachute Stiffness Index 0.24 and a 45.2 Inch Model, Stiffness Index 0.40, AFFDL-TR-72-18, (AD 743 099), May 1972

355 Henrich, H. G., Pressure and Canopy Profile Data on 20 Degree Conical Ribbon Parachute Canopy During Inflation, SAND 77-7012, July 1977

356 Berndt, R. J., Experimental Determination of Parameters for the Calculation of Parachute Filling Times, Jarbuch 1964 der WGLR, Vieweg & Sohn, Braunschweig, West Germany, (p. 299-316) 1965

357 Watson, L. L., DeWeese, J. H., Opening Force and Filling Time of 35 Foot Diameter 10% Flat Extended Skirt Canopies, AFFDL-TM-74-207-FER, November 1974

358 Heinrich, H. G., Noreen, R. A., Monahan, R. H., Model Studies of Inflation Uniformity of Clustered Parachutes, AFFDL-TR-71-15, (AD 888 282L), August 1971

359 Norman, L. C., Suit, K. L., An Investigation of the Initial Century Series Ringsail Parachute, NASA TN-D-5968, (N70-35910), August 1970

360 Buhler, W. C., Wailes, W. K., Development of a High Performance Ringsail Cluster, AIAA Paper No. 73-468, presented at AIAA, Aerodynamic Deceleration Systems Conference, Palm Springs, CA, (A73-31452), May 1973

361 Mickey, F. E., et al, Investigation of Prediction Methods for Loads and Stresses of Apollo Type Spacecraft Parachutes, Volume I - Loads, Northrop Corporation, Ventura Division, NVR-6431, (N74-19673), June 1970

362 Moeller, J. H., A Method of Load Prediction for Parachutes in Cluster, Journal of Aircraft, Volume 4, p. 339-342, (A67 32578) July - August 1967

363 Ewing, E. G., Another Look at the Filling Problem of Clustered Parachutes, Northrop Corporation, Ventura Division, NVR 3502, April 1964

364 Calkins, R. B., Development and Evaluation of an Inflation Aid for Type C-9 Canopies with Deflation Pockets, AFFTC-TR-68-18, (AD 837 640), June 1968

365 Altgelt, R. E., Ward, J. A., Developing the Fast-Opening Parachute, AIAA Paper No. 68-932, presented at AIAA, Aerodynamic Deceleration Systems Conference, El Centro, CA, (A68-42023), September 1968

366 Heinrich, H. G., Hektner, T. R., Opening Dynamics of a T-10 Parachute with Inflation Aids, AFFDL-TR-69-112, (AD 869 329), March 1970

367 Neipling, L. E., Qualification Testing of the U.S. Navy NB-11 Parachute Recovery System, TR-6-69, (AD 881 227L), January 1971

368 Calkins, R. B., Evaluation of Parachute Opening Characteristics of Type C-9 Canopies Fail Safe Spreading Gun Installed, AFFTC-TR-69-18, (AD 855 132), April 1969

369 O'Hara, F., Some Notes on the Critical Opening Speed and the Opening Forces of Parachutes, AFEE Report No. Res 25, (ATI 201 918), May 1947

370 Johns, T. F., Parachute Design, Technical Note ARM 365, (ATI 25415), December 1946

371 Brown, W. D., Parachutes, Pitman & Sons, London, 1951

372 Knacke, T. W., Design, Use and Construction of FIST Type Parachute, MCREXE-672-19LL, (ATI 56533), June 1948

373 Wolf, D., A Simplified Dynamic Model of Parachute Inflation, Journal of Aircraft, Volume II, No. 1 (Also see Sandia Laboratories, SC-DC-721743), January 1974

374 Fredette, R. O., Parachute Research Above Critical Aerodynamic Velocities, Cook Research Laboratories, May 1961

375 Downing, J. R., et al, Recovery Systems for Missiles and Target Aircraft, AF TR 5853
Part I - Subsonic Sled Test Phase (AD 112 981), March 1954
Part II - Subsonic Free-Flight Validation Phase, (AD 114 101), March 1955
Part III - High Subsonic and Transonic Track Borne Parachute Tests, (AD 112 635), December 1956
Phase IA - (AD 76877), March 1954

376 Pedersen, P. E., Study of Parachute Performance at Low Supersonic Deployment Speeds; Effects of Changing Scale Clustering, ASD-TR-61-186, (AD 267 502), July 1961

377 Eckstrom, C. V., High Altitude Flight Test of a 40 Ft. Diameter (12.2 Meter) Ringsail Parachute at a Deployment Mach Number of 2.95, NASA TN-D-5796, (N70-31624), June 1970

378 Greene, G. C., Opening Distance of a Parachute, Journal of Spacecraft and Rockets, Volume 7, No. 1, p. 90-100, (A70-19725), January 1970

379 Heinrich, H. G., Noreen, R. A., Wind Tunnel Feasibility Study of Aerodynamic Reefing of Subsonic Parachutes, AFFDL-TR-72-126, (AD 749 209), May 1973

380 Scheubel, F. N., Notes on Opening Shock of a Parachute, Progress Report No. IRE-65, Foreign Exploitation Section, WPAFB, (ATI 34073), April 1946

381 Berndt, R. J., DeWeese, J. H., The Opening Force of Solid Cloth, Personnel Type Parachutes, AIAA Paper No. 70-1167, presented at AIAA, Aerodynamic Deceleration Systems Conference, Dayton, OH, (A70-43992), September 1970

382 Anon., Performance of and Design Criteria for Deployable Aerodynamic Decelerators, ASD-TR-61-579, (AD 429 971), December 1963

383 Preisser, J. S., Greene, G. C., Effect of Suspension Line Elasticity on Parachute Loads, Journal of Spacecraft and Rockets, Volume 7. p. 1278-1280 (A70-44531), October 1970

384 French, K. E., Model Law for Parachute Opening Shock, AIAA Journal, Volume 2, No. 23, p. 2226-2228, (A65-12612), December 1964

385 Kaplun, S., Dimensional Analysis of the Inflation Process of Parachute Canopies, Aeronautical Engineering Thesis, California Institute of Technology, (AD 90633), 1951

386 Stone, J. W., et al, Investigation of the Clustered Opening of Single and Clustered Large Parachutes, Volume II - Analysis of the Free-Flight Test of Clustered Large Parachutes, unpublished AFFDL Report, June 1968

387 Howarth, L. (ed), Modern Developments in Fluid Dynamics, High Speed Flow, Volume II, Oxford at the Clarendon Press, 1953

388 Buhler, W. C., B-1 Crew Module Parachute Recovery System: Qualification Tests of Recovery Parachute Systems, Pioneer Parachute Document No. 115, April 1974

389 Heinrich, H. G., Haak, E. L., Stability and Drag of Parachutes with Varying Effective Porosity, AFFDL-TR-71-58, (AD 729 858), February 1971

390 Niccum, R. J., Investigation of Flow Field During the Inflation of Clustered Parachutes, AFFDL-TR-66-106, Volume I, (AD 810 495), November 1966

391 Haak, E. L., Hubert, R. J., Drag and Stability of Guide Surface, Ribbon, and Ringslot Parachutes at High Subsonic Speeds, AFFDL-TR-65-108, (AD 475 190), September 1965

392 Ewing, E. G., Development Program for a Ringsail Parachute (Century Series) Final Report, Northrop Corporation, Ventura Division, NVR 5028, December 1966

393 Knacke, T. W., Reefing of Parachutes - Drag Area Ratio vs Reefing Ratio, ASD-TR-76-2, (AD A036 497), July 1976

394 Naeseth, R. L., Fournier, P. G., Low-Speed Wind-Tunnel Investigation of Tension-Structure Parawings, NASA TN-D-3940, (N67-32747), June 1967

395 Menard, G. L. C., Performance Investigation of Various Configurations of Personnel Maneuverable Parachute Canopy Assemblies, TR-5-71, (AD 893 225L), February 1972

396 Steele, J. L.(Maj), Evaluation of Steerable Parachutes; Final Report, Project No. 20-69-10, (AD 907 186L), January 1973

397 Sleeman, W. C. Jr., Glide Performance of Advanced Parawings, AIAA Paper No. 70-1186, presented at AIAA, Aerodynamic Deceleration Systems Conference, Dayton, OH, (A70-41829), September 1970

398 Moeller, J. H., Linhart, E. M., Parawing Technology for Spacecraft Land Landing - A Progress Report, AIAA Paper No. 70-1187, presented at AIAA, Aerodynamic Deceleration Systems Conference, Dayton, OH, (A70-41828), September 1970

399 Menard, G. L. C., Performance Evaluation Tests Parafoil Maneuverable Gliding Parachute Assembly; Aspect Ratio - 2; Area: 360 Square Ft., TR-2-69, (AD 864 272L), September 1969

400 Linhart, E. M., et al, Investigation of Various Textile Parachutes and Control Systems to Achieve Steerability, Phases III and IV, FDL-TDR-64-81, (AD 482 081), February 1966

401 Libbey, C. E., Reefing Tests of a 5 Foot (1.524 Meter) All-Flexible Parawing, LWP-417, NASA Langley Research Center, June 1967

402 Menard, G. L. C., Performance Evaluation Tests of Volplane Maneuverable Personnel Gliding Parachute Assembly - Aspect Ratio: 2.2 Area: 312 Square Feet, TN 1006-70, June 1970

403 Menard, G. L. C., Performance Evaluation Tests of Sailwing, Maneuverable, Personnel, Gliding Parachute Assembly, Aspect Ratio: 4; Area: 400 Square Feet, TN 1005-70, June 1970

404 Reichenau, D. E. A., Wake Properties Behind a Ejection Seat Escape System and Aerodynamic Characteristics with Stabilization Parachutes at Mach Numbers from 0.6 to 1.5, AEDC-TR-71-30, (AD 880 650), February 1971

405 Myers, A. W., Hahn, J. S., Drag and Performance Characteristics of Flexible Aerodynamic Decelerators in the Wake of Basic and Modified Arapaho "C" Test Vehicle Configurations at Mach Numbers from 2 to 5, AEDC-TR-67-75, (AD 813 808), May 1967

406 Campbell, J. F., Flow Field Survey and Decelerator Drag Characteristics in the Wake of a Model of the X-15 Airplane at Mach 2.30 and 4.65, NASA TN-D-3285, (N66-16563), February 1966

407 Homan, M. L., Wake Properties Behind a Flared Cylindrical Forebody and Aerodynamic Characteristics of Several Flexible Aerodynamic Decelerators at Mach Numbers From 1.75 to 4.75, AEDC-TR-70-161, (AD 870 914), June 1970

408 Babish, C. A. III, Drag Level Staging Through Modification of Supersonic Wake Fields by Trailing Aerodynamic Decelerators, Paper presented at AIAA, Aerodynamic Deceleration Systems Conference, Houston, TX, (A66-40595), September 1966

409 Heinrich, H. G., Drag and Dynamics of Single and Clustered Parachutes in Freestream, and with Wake and Ground Effects, AFFDL-TR-66-104, (AD 809 541), November 1966

410 Jaremenko, I. M., Wakes, Their Structure and Influence Upon Aerodynamic Decelerators, NASA CR-748, (N67-22777), April 1967

411 Nerem, R. M., Henke, D. W., Theoretical and Experimental Studies of Supersonic Turbulent Wakes and Parachute Performance, AIAA Paper No. 68-947, presented at AIAA, Aerodynamic Deceleration Systems Conference, El Centro, CA, (A68-42005), September 1968

412 Jaremenko, I. M., Aerodynamic Characteristics of the Ballute in the 0.1 to 10 Mach Number Speed Regime, AIAA Paper No. 67-228, presented at AIAA, Aerospace Sciences Meeting, New York, NY, (A67-18518), January 1967

413 Heinrich, H. G., Hulcher, G. D., Behavior of Extraction Parachutes in the Wake of a Powered Airplane Model, AFFDL-TR-68-15, (AD 842 569), August 1968

414 Lutz, R. G., Rhudy, R. W., Drag and Performance of Several Aerodynamic Decelerators at Mach Number 8, AEDC-TR-70-143, (AD 873 000), August 1970

415 Heinrich, H. G., Rose, R. E., Flow Characteristics of Rigid Ribbon Parachute Canopies in Supersonic Flow, AFFDL-TR-65-103, (AD 478 442), December 1965

416 Sims, L. W., The Effects of Design Parameters and Local Flow Fields on the Performance of Hyperflow Supersonic Parachutes and High Dynamic Pressure Parachute Concepts, AFFDL-TR-65-150, Volume II, (AD 476 824), October 1965

417 Sims, L. W., The Effects of Design Parameters and Local Flow Fields on the Performance of Hyperflow Supersonic Parachutes and High Dynamic Pressure Parachute Concepts, AFFDL-TR-65-150, Volume I, (AD 476 520), October 1965

418 Heinrich, H. G., Eckstrom, D. J., Velocity Distribution in the Wake of Bodies of Revolution Based on Drag Coefficient, ASD-TDR-62-1103, (AD 427 736), December 1963

419 Baker, D. C., Static Stability Characteristics of the B-1 Escape Capsule with Drogue Parachutes at Mach Numbers From 0.3 to 2.2, AEDC-TR-71-204, (AD 887 905L), September 1971

420 Heinrich, H. G., Hess, R. S., Drag Characteristics of Plates, Cones, Spheres and Hemispheres in the Wake of a Forebody at Transonic and Supersonic Speeds, RTD-TDR-63-4242, (AD 457-056), December 1964

421 Brown, C. A., Campbell, J. F., Experimental Wake Survey Behind Viking '75 Entry Vehicle at Angles of Attack of 0°, 5° and 10°, Mach Numbers from 0.20 to 1.20, and Longitudinal Stations from 1.50 to 11.00 Body Diameters, NASA TM-X-2830, (N74-13979), November 1973

422 Henke, D. W., Establishment of an Unsymmetrical Wake Test Capability for Aerodynamic Decelerators, Volume III. Experimental Wake Survey and Body Surface Pressure Data, AFFDL-TR-67-192, Volume III, (AD 675 182), August 1968

423 Heinrich, H. G., Riabokin, T., Analytical and Experimental Considerations of the Velocity Distribution in the Wake of a Body of Revolution, WADD TR-60-257, (AD 245 246), December 1959

424 Heinrich, H. G., Hess, R. S., Pressure Distribution in the Wake of Two Bodies of Revolution at Transonic and Supersonic Speeds, ASD-TDR-62-1104, (AD 427 748), December 1963

425 Brown, C. A. Jr., Campbell, J. F., Tudor, D. H., Experimental Wake Survey Behind a 120° Included - Angle Cone at Angles of Attack of 0° and 5°, Mach Numbers from 1.60 to 3.95, and Longitudinal Stations Varying from 1.0 to 8.39 Body Diameters, NASA TM-X-2139, (N71-18480), January 1971

426 Brown, C. A. Jr., Campbell, J. F., Experimental Wake Survey Behind Viking '75 Entry Vehicle at Angles of Attack of 0° and 5° Mach Numbers from 1.60 to 3.95, and Longitudinal Stations from 1.0 to 8.39 Body Diameters, NASA TM-X-2313, (N72-10261), October 1971

427 Brown, C. A. Jr., Campbell, J. F., Experimental Wake Survey Behind a 140° Included - Angle Cone at Angles of Attack of 0° and 5°, Mach Numbers from 1.60 to 3.95, and Longitudinal Stations Varying from 1.0 to 8.39 Body Diameters, NASA TM-X-2409, (N72-12209), November 1971

428 Campbell, J. F., Brown, C. A., Evaluation of Experimental Flow Properties in the Wake of a Viking '75 Entry Vehicle, IAAA Paper 73-475, presented at AIAA, Aerodynamic Deceleration Systems Conference, Palm Springs, CA, (A73-31459), May 1973

429 Hall, A. A., Hislop, G. S., Velocity and Temperature Distribution in the Turbulent Wake Behind a Heated Body of Revolution, Proceedings of Cambridge Philosophical Society, Volume 34, 1938

430 Broderick, M. A., Turner, R. D., Design Criteria and Techniques for Deployment of Aerodynamic Drag Devices, ASD-TR-61-188, (AD 269 368), May 1961

431 Love, E. S., Base Pressure at Supersonic Speeds of Two-Dimensional Airfoils and on Bodies of Revolution, With and Without Fins, Having Turbulent Boundary Layers, NACA TN-3819, January 1957

432 Noreen, R. A., Rust, L. W. Jr., Rao, P. P., Analysis of the Supersonic Flow Field About a Forebody-Decelerator Combination, AFFDL-TR-71-35
Volume I - Theoretical Methods and Result Comparisons, (AD 893 254L), March 1972
Volume II - Calculation Procedures and Computer Program, (AD 901 908L), March 1972

433 Heinrich, H. G., Hess, R. S., Stumbris, G., Drag Characteristics of Plates, Cones and Spheres in the Wake of a Cylindrical Body at Transonic Speeds, TRD-TDR-63-4023, (AD 457 055), January 1965

434 Coats, J. D., Static and Dynamic Testing of Conical Trailing Decelerators for the Pershing Re-Entry Vehicle, AEDC-TN-60-188, (AD 245 015), October 1960

494 MacCarthy, R. W., et al, Handbook for the Design of Guided Missile Recovery Systems, Radioplane Company Report No. R-65, March 1951

495 Anon., Redhead/Roadrunner Target Missile System - Final Report, North American Report No. 64H-460, (AD 482 818), February 1966

496 Hamrick, B. R., Childers, G. C., Final Test Report for the MQM-34D Air Bag Ground Drop Impact Test, Teledyne Ryan Aeronautical Report No. 29242-1, October 1973

497 Simmons, R. L., Data on the Reliability of Parachutes Used in Emergency Bailouts and Ejections and Reliability of Aircraft Deceleration Chutes, Paper presented at Symposium on Parachute Technology and Evaluation, El Centro, Ca, FTC-TDR-64-12, Volume I, (AD 452 430), April 1964

498 Whitney, M. C., Crew Escape Capsule Retrorocket Concept, Volume I - Demonstration Program, AFFDL-TR-76-107, May 1977

499 Peters, J. M., Crew Escape Capsule Retrorocket Concept, Volume II - Selection of Retrorocket System, AFFDL-TR-76-107, May 1977

500 Jailer, R. W., et al, Analysis of Heavy-Duty Parachute Reliability, WADD TR 60-200, (AD 246 490), June 1960

501 Mickey, F. E., Wolf, D. F., Khajeh-Nouri, B., Investigation of Analytical Techniques for Solving the Parachute Inflation Process, NASA CR-101771, (X69-16550), June 1969

502 Barton, R. L., Scale Factors for Parachute Opening, NASA TN-D-4123, (X67-35778), September 1967

503 Unused

504 Eichblatt, D. L., et al, Experimental Verification of Scale Factors for Parawing Opening Characteristics, NASA TN-D-4665, (N68-31956), August 1968

505 Moore, R. H., Eichblatt, D. L., Hughes, T. F., Experimental Verification of Scale Factors for Parawing Opening Characteristics with Developmental Ratio From 1.13 to 1.3, NASA TN-D-5071, (N69-19950), March 1969

506 Linhart, E. M., Buhler, W. C., Wind Tunnel and Free Flight Investigation of All-Flexible Parawings at Small Scale, NASA CR-66879, (N70-19796), June 1969

507 Rust, L. W. Jr., Theoretical Investigation of the Parachute Inflation Process, Northrop Ventura Report NVR-3887, July 1965

508 Heinrich, H. G., Model Laws Governing Parachute Performance in Martian Environment, Paper presented at the WGLR-DGRR-Tagung, Bag Godesbeeg, Germany, (N67-27805), October 1966

509 Heinrich, H. G., Hektner, T. R., Flexibility as Parameter of Model Parachute Performance Characteristics, AFFDL-TR-70-53, (AD 875 993), August 1970

510 Bobbitt, P. J., Mayhue, R. J., Galigher, L. L., Supersonic and Subsonic Wind-Tunnel Tests of Reefed and Unreefed Disk-Gap-Band Parachutes, AIAA Paper No. 70-1172, presented at AIAA, Aerodynamic Deceleration Systems Conferencee, Dayton, OH, (A70-41841), September 1970

511 Brown, H. R., An Experimental Investigation of Model Parachutes Under Finite Mass Conditions, AFIT Thesis, December 1975

512 Heinrich, H. G., Noreen, R. A., Hedtke, J. C., Analysis of the Opening Dynamics of Solid Flat and Ringslot Parachutes with Supporting Wind Tunnel Experiments, AFFDL-TR-71-95, (AD 739 554), February 1972

513 Doyle, G. R. Jr., Burbick, J. W., Users Manual - Dynamics of Two Bodies Connected by an Elastic Tether - Six Degrees of Freedom Forebody and Five Degrees of Freedom Decelerator, NASA CR-120261, (N74-29304), April 1974

514 Neustadt, M., et al, A Parachute Recovery System Dynamic Analysis, Journal of Spacecraft and Rocket, Volume 4, p. 321-326, (A67-21513), March 1967

515 Talay, T. A., Parachute Deployment Parameter Identification Based on an Analytical Simulation of Viking BLDT AV-4, NASA TN-D-7678, (N74-31344), August 1974

516 Keck, E. L., A Computer Simulation of Parachute Opening Dynamics, AIAA Paper No. 75-1379, presented at AIAA, Aerodynamic Deceleration Systems Conference, Albuquerque, NM, (A76-13175), November 1975

517 Payne, P. R., A New Look at Parachute Opening Dynamics, Reprint from the Aeronautical Journal of the Royal Aeronautical Society, London, England, p. 85-93, (AD A001 447), February 1973

518 Bugliarello, G., The Resistance to Accelerated Motion of Spheres in Water, University of Minnesota Thesis, July 1954

519 Iversen, H. W., Balent, R., A Correlating Modulus for Fluid Resistance in Accelerated Motion, Journal of Applied Physics, Volume 22, Number 3, March 1951

520 Luneau, J. L., On the Influence of Acceleration Upon Resistance to Motion in Fluids, FTD Translation FTD-TT-63-334, September 1963

521 Von Karman, T., Note on Analysis of the Opening Shock of Parachutes at Various Altitudes, AFF Scientific Advisory Group, (ATI 200 814), August 1945

522 Ibrahim, S. K., Apparent Added Mass and Moment of Inertia of Cup-Shaped Bodies in Unsteady Incompressible Flow, Doctor of Philosophy Thesis, University of Minnesota, May 1965

523 Ibrahim, S. K., The Potential Flow Field and the Added Mass of the Idealized Hemispherical Parachute, AIAA Paper presented at AIAA, Aerodynamic Deceleration Systems Conference, Houston, TX, (A66-40591), September 1966

524 Heinrich, H. G., Noreen, R. A., Saari, D. B., A Parachute Opening Shock Theory Based on Non-Linear Time Histories of Inflow Velocity and Projected Area, AMEL 75-10, (AD A005 271), June 1974

525 Houmard, J. E., Stress Analysis of the Viking Parachute, AIAA Paper No. 73-444, presented at AIAA, Aerodynamic Deceleration Systems Conference, Palm Springs, Ca, (A73-31430), May 1973

526 Ibrahim, S. K., Experimental Determination of the Apparent Moment of Inertia of Parachutes, FDL-TDR-64-153, (AD 465 722), April 1965

527 Talay, T. A., Morris, W. D., Whitlock, C. H., An Advanced Technique for the Prediction of Decelerator System Dynamics, AIAA Paper No. 73-460, presented at AIAA, Aerodynamic Deceleration Systems Conference, Palm Springs, CA, (A73-31446), May 1973

528 Gamble, J. D., A Mathematical Model for Calculating the Flight Dynamics of a General Parachute-Payload System, NASA TN-D-4859, (N69-14504), December 1968

529 Sundberg, W. D., Finite-Element Modeling of Parachute Deployment and Inflation, AIAA Paper No. 75-1380, presented at AIAA, Aerodynamic Deceleration Systems Conference, Albuquerque, NM, (A76-13176), November 1975

530 Topping, A. D., et al, A Study of Canopy Shapes and Stresses for Parachutes in Steady Descent, WADC-TR-55-294, (AD 103 963), October 1955

531 Reynolds, D. T., Mullins, W. M., Stress Analysis of Ribbon Parachutes, AIAA Paper No. 75-1372, presented at AIAA, Aerodynamic Deceleration Systems Conference, Albuquerque, NM, (A76-13168), November 1975

532 McEwan, A. J., et al, Descriptions of Computer Programs for the Analysis of Apollo Parachutes, Northrop Ventura Report NVR-6428, June 1969

533 Spangler, S. B., Nielsen, J. N., Theoretical Investigation of the Aerodynamic Characteristics of All-Flexible Parawings, AIAA Paper No. 70-1188, presented at AIAA, Aerodynamic Deceleration Systems Conference, Dayton, OH, (A70-41827), September 1970

534 Scott, C. J., The Prediction of Material Temperatures on Woven Retardation Devices, AFFDL-TR-67-170, (AD 831 048), March 1968

535 Gebhart, B., Heat Transfer, McGraw-Hill Inc., Second Edition, 1971

536 Scott, C. J., Eckert, E. R. G., Experiments on the Thermal Performance of Ribbon Parachutes, AFFDL-TR-64-192, (AD 468 307), May 1965

537 Eckstrom, C. V., et al, High Altitude Flight Test of a Disk-Gap-Band Parachute Deployed Behind Bluff Body at a Mach Number of 2.69, NASA TM-X-2671, (N73-15042), December 1972

538 Schoeck, P. A., et al, Experimental Studies for Determining Heat Transfer on Ribbons of FIST -Type Parachutes, WADC-TN-59-345, February 1960

539 Nerem, R. M., Supersonic Wake Phenomena with Application to Ballute-Type Decelerators, Goodyear Aerospace Corp Report No. GER-11820, November 1964

540 Nerem, R. M., Pressure and Heat Transfer on High-Speed Aerodynamic Decelerators of the Ballute Type, AIAA Paper presented at AIAA, Aerodynamic Deceleration Systems Conference, Houston, TX, (A66-40605), September 1966

541 Ames Research Staff, Equations, Tables and Charts for Compressible Flow, NACA R-1135, 1953

542 Unused

543 Henke, C. W., Establishment of an Unsymmetrical Wake Test Capability for Aerodynamic Decelerators, Volume II, Analysis of High Speed Axisymmetric Wakes and Parasonic Parachute Performance, AFFDL-TR-67-192, (AD 840 269), August 1968

544 Ibrahim, S. K., Engdahl, R. A., Parachute Dynamics and Stability Analysis, NASA CR-120326, (N74-30433), February 1974

545 Chambers, J. R., An Investigation of the Dynamic Lateral Stability and Control of a Parawing Vehicle, NASA TM-X-57693, (N66-29713), May 1966

546 Mendenhall, M. R., Spangler, S. B., Nielsen, J. N., Review of Methods for Predicting the Aerodynamic Characteristics of Parawings, AIAA Paper No. 68-10, presented at AIAA, Aerospace Sciences Meeting, New York, NY, (A68-17438), January 1968

547 Heinrich, H.G., Pressure and Profile Data of 20° Conical Ribbon Parachutes, Volumes I & II, SAND77-7005, May 1977

548 Jones, R. H., Landing Impact Attenuation for Non-Surface Planing Landers, NASA SP-8046, (N70-38294), April 1970

549 Chenoweth, H. B., Monte Carlo Simulation of the Apollo Command Module Land Landing, Journal of Spacecraft, Volume *, p. 1074-1078, (A71-42776), October 1971

550 Whitnah, A. M., Howes, D. B., Statistics Concerning the Apollo Command Module Water Landing, NASA TM-X-2430, (N72-11790), November 1971

551 Chorafas, D. M., Statistical Processes and Reliability Engineering, Van Nostrand, Princton, 1960

552 Miller, C. R., A Study of Parachute Seam Design Criteria, Part II - Investigations of the Strength of Nylon Webbing Joints, WADC-TR-56-313, (AD 110 406), June 1956

553 Summa, J. M., Theoretical Dynamic Stability of a Tethered Parafoil, AIAA Student Journal, Volume 6, p. 137-144, (A69-10415), October 1968

554 Higgins, M. W., Preliminary Recovery System Design, A Simplified Approach to Determining Staging, Timing and Altitude Requirements, unpublished AFFDL report

555 Maydew, R. C., Johnson, D. W., Supersonic and Transonic Deployment of Ribbon Parachutes at Low Altitudes, Journal of Aircraft, Volume 9, No. 7, (A72-10312), July 1972

556 Pleasants, J. E., Parachute Mortar Design, Journal of Spacecraft and Rockets, Volume 11, No. 4, (A73-31445), April 1974

557 Malik, P. W., Souris, G. A., Project Gemini, A Technical Summary, NASA CR-1106, June 1968

558 Bailey, R. A., Aerial Delivery of Cargo by CH-46 and CH-53 Helicopters, CMC-54-67-05, (AD 839 225L), August 1968

559 Anon., Naval Weapons Center Supersonic Research Tracks, NWC TP 5120, (AD 923 306L), May 1972

560 Pirrello, C. J., et al, An Inventory of Aeronautical Ground Research Facilities, Volume I - Wind Tunnels, NASA CR-1874, (N72-12182), November 1971

561 Anon., Test Facilities Handbook (Tenth Edition), AEDC, May 1974

562 Pepper, W. B., Holt, I. T., Development of a Gliding Guided Ribbon Parachute for Transonic Speed Deployment, SC-TM-71-0088, (AD 891 134L), June 1971

563 Brunner, T. W., Nerem, R. M., Initial Results on Theoretical Prediction of Drag for a Trailing Decelerator at Supersonic Speeds, AIAA Paper No. 70-1177, presented at AIAA, Aerodynamic Deceleration Systems Conference, Dayton, OH, (A70-41836), September 1970

564 Walker, H. R. Jr., Static and Dynamic Logitudinal Stability of a Semi-Rigid Parafoil, AIAA Paper No. 70-1191, presented at AIAA, Aerodynamic Deceleration Systems Conference, Dayton, OH, (A70-41825), September 1970

565 Heinrich, H. G., Exploratory Studies Concerning Radial Stress Distribution of Solid Flat Circular Model Parachutes, University of Minnesota, September 1974

566 Braun, J. F., Walcott, W. B., Wind Tunnel Study of Parachute Clustering, ASD-TDR-63-159, (AD 402 777), April 1963

567 Melzig, H. D., The Dynamic Stress-Strain Behavior of Parachute Cloth, NASA CR-92353, (N68-37936), December 1967

568 U.S. Standard Atmosphere, 1976, October 1976

569 Heinrich, H. G., A Parachute Snatch Force Theory Incorporating Line Disengagement Impulses, AIAA Paper No. 73-464, presented at AIAA, Aerodynamic Deceleration Systems Conference, Palm Springs, CA (A73-31450), May 1973

570 Babish, C. A., Performance Characteristics of 5 Ft. Diameter Nylon and Kevlar Hemisflo Ribbon Parachutes at Pressures up to 6000 PSF, AFFDL-TR-78-75, May 1978

571 Pepper, W. B., Cronin, D. C., Experimental Research on Parachute Deployment Load Control by Use of Line Ties, Journal of Aircraft, Volume 6, p. 79-80, (A69-25386), January-February 1969

572 Steinberg, S., Siemers, P. M., Slayman, R. G., Development of the Viking Parachute Configuration by Wind Tunnel Investigations, AIAA Paper No. 73-454, presented at AIAA, Aerodynamic Deceleration Systems Conference, Palm Springs, CA, (A73-31440), May 1973

573 Berndt, R. J., The Opening Force and Filling Time of Flat Circular Solid Cloth Type Canopies, AFFDL-TM-74-88-FER, unpublished

574 Ewing, E. G., A Minimum Weight Landing System for Interplanetary Spacecraft, Proceedings of I.A.S. Recovery of Space Vehicles Symposium, September 1960

575 Dixon, W. J., Massey, F. J., Introduction to Statistical Analysis, McGraw-Hill, 1951

576 Lewis, W. R., Minimum Airdrop Altitudes Using Standard Parachute Equipment, ADED Report 62-2, (AD 600 741), April 1964

577 Williamson, B. J., Murdock, D., Engineering and Service Test of Standard Air Delivery Equipment (Personnel and Cargo) at High Drop Zone Evelations, Yuma Proving Ground Report 0071, (AD 885 239L), April 1971

578 Everett, W. J., Jolly, W. G., Knor, M. M., Air Drop of U.S. Coast Guard's Air-Delivered Anti-Pollution Transfer System (ADAPTS), AIAA Paper No. 70-1205, presented at AIAA, Aerodynamic Deceleration Systems Conference, Dayton, OH, (A70-41813), September 1970

579 Abbott, N. J., Donovan, J. G., Schoppee, M. M., The Effect of Temperature and Strain Rate on the Tensile Properties of Kevlar and PBI Yarns, AFML-TR-74-65, Part II, (AD B002 047), May 1974

580 Esland, W. R., Hercules C MK I Airdrop of Heavy Stressed Platforms by Reefed Main Extraction, A&AEE Note No. 3007, (AD 825 349), October 1967

581 Horner, A. J., Hercules C MK I Aircraft, Air-Drop of Supplies Stressed Platforms Using the 42 Ft. Parachute in a Reefed Main Extraction Technique, A&AEE Note No. 3122, (AD 911 935), January 1973

Acceleration Measurement, 232
Actuation Subsystems, 111, 117
Adapters, 136
Aerial Engagement, 319
Aerial Pickup, 60
Aerodynamic Forces, Steady, 232
Aerodynamic Heating, 313
Air Force Flight Test Center, 216
Air Permeability, Testing, 210, 211
Airbags, 322
Aircraft
  Crew Modules, 30
  Deceleration Systems, 49
  Landing Approach Parachutes, 53
  Landing Deceleration Parachutes, 5
  Spin Recovery Parachutes, 53
  Tow Testing, 206
Airdrop
  Material, 37
  Parachute Systems, 41
  Special Systems, 44
  Personnel, 46
  Test Vehicles, 224, 226
Air-to-air Retrieval, 60
Altitude Switches, 115
Analysis, Fundamental Relationships, 332
Apex, Retraction, Canopy, 299
Applications, *see Specific use*
Apollo Earth Landing System, 15
Atmosphere Properties, 111
Attached Inflatable Decelerator (AID), 57
Automatic Ripcord Releases, 120
Axial Force Coefficient, 264

Background, xxxiii
Ballistic Ranges, 217
Balloon, Carrier, 202
Ballutes, 77
Bomb Deceleration, 56
Bomb Lifting Decelerator, 57
Bomblet, Decelerator, 58
Boosted Test Vehicles, 227
Boosted Vechile Testing, 202
Booster Recovery, 18
Break Cords, 131
Bridles, 131

Canopy
  Apex Retraction, 299
  (circular), Static Stability, 299
  Filling Time, 250
  Geometry, 78
  High Glide, 303
  Inflation Aids, 248
  Porosity, 289
  Pressure Distribution Measurement, 309
  Sizing, 403
  Skirt Reefing, 295
  Spreader Gun, 121
  Stress Distribution Measurement, 311
  Types, 80
"CDS" Parachute Delivery System, 38
China Lake, 217
Clevises, 137
Cluster Parachute Drag Coefficient, 264
Cluster Parachute Stability, 307
Clustered Canopies, 247
Clustered Parachute Parachute Opening Forces, 261, 341, 411
Coefficient, *see Specific use*
Conical Extension Parachute, 63
Connector Links, 134
Construction Details, 185
Control Devices, 111
Control/Actuation Sub-systems, 111
Critical Opening Speed ("Squidding"), 249
Crushable Materials, 322
Cut Knives, 136

Data Bank, Parachute, xxxv
Decelerator Characteristics, 73
Decelerators, Non-Parachute
  Balloon Types, 109
  Paravulcoon, 110
  Rotating Blades, 110
Deployment,
  Bags, 131, 132, 427
  Components, 130
  Forces (Snatch), 236
  General, 235
  Method Secection, 427
  Sequences, 235
Descent Characteristics, 268
Design Criteria, 402
Design Factors, 413, 414
Diameter, Nominal, 73, 79, 294
Differential Velocity, 240
Disconnects, 127
Drag Area Control, 295
Drag Coefficients, 73, 262
Drogue Body; Systems, Stability, 378
Drogue Reefing, 424
Drogue Structure, Heat Resistant, 313
Drop Testing, 200
Dugway Proving Ground, 215
Dynamic Pressure Measurement, 232

Dynamic Stability, 307

ECM Jammer Deceleration, 59
Edwards Air Force Base, 213
Effective Length of Suspension Lines, 293
Effective Porosity, 289
Ejection Devices, 119, 427
Ejection Seats, 27
Emergency Recovery, 21
Encapsulated Seats, 30
Environmental Simulation, 212
Environments, Earth & Planetary, xxxv
Equipment, Manufacturing, 191
Equipment, Test, 213
Experimental Materials, 177
Extraction Parachutes, 44

Fabrication Methods, 181
Fabrics, 173
Fabrics, Coated, 178
Facilities, Test, 213, 216
Filling Distance, 252
Filling Time, 250
Flare Parachutes, 58
Flight Test Vehicles, 224
Flotation Devices, 140
Force Measurement, 232
Forces, *see definite types*
Fort Bliss, 213
Friction (Material) Testing, 210
Function and Performance Checks, 208

Gemini Parachute Landing System, 11
Gliding Parachutes, 77
Gore Shape, 79, 293

"HAARS" Parachute System, 40
Hardware, *also see specific items,* 134
Harnesses, 134
Hems, 185
Heating, Aerodynamic, 313, 366
Heat Resistant Drogue Structures, 313
High Glide Canopy, 301
High Glide Systems, 383
High Temperature Resistant Materials, 177
Hill Air Force Base, 215
History (Background), xxxiii
Holloman Air Force Base, 213
Holloman High Speed Test Track, 217
Hurricane Mesa, 218

Impact Attenuation, 321
Impact Attenuation Subsystems, 138, 387
Impact Strength, 209
Infinite Mass Condition, 74
Infinite Mass Load Factors, 261
inflation
  Decelerator, 243
  Aids, 248
  Decelerator, System Motion, 334
Internal Load Distribution, 308
Internal Load Prediction, 351
Instrumentation
  Range, 232
  Test Vehicle, 231

Joint Testing, 208

Kevlar, *also see Textile Fibers & Yarns,* xxxv
Kirtland Air Force Base, 218

Laguna Army Air Field, 215
Landing Approach Parachute, 53
Landing Bags, 139, 388
Landing Condition Simulation, 212
Landing Deceleration (Drag) Parachutes, 50
Landing Dynamics, 319, 386
"LAPES" Airdrop System, 39
L/D In-Flight Modulation, 277
Lighweight Materials, 177
Load Couplers, 137
Load Distribution
  Canopy, 308
  Internal, 308
  Suspension Members, 308
Load Prediction, *see specific types of load*
Location Devices, 139

Malfunctions, 326
Manned Spacecraft Parachute Landing Systems, 9
Manufacture, 143
Manufacturing Equipment, 191
Materials, *also see Textiles, Forms,* 143
Material
  Crushables, 179
  Film, 179
  Honeycomb, 179
  Low Cost, 184
  Strength, 413, 425
  Testing, 208
Measure Units, xxxv
Measurement of
  Acceleration, 232
  Dynamic Pressure, 232
  Force, 232
  Pressure, 232

Pressure Distribution, 227
Strain, 227
Stress, 231
Temperature, 230
Mercury Parachute Landing System, 10
Mid-Air Retrieval, 66, 319
Mine Deceleration, 58
Miscellaneous Special Use Parachutes, 69
Missile Recovery, 5
Moment of Inertia, 345
Mortars, 431

National Parachute Test Range, 214
Naval Weapons Center, China Lake, 217
Nominal Area, 79
Nominal Diameter, 73, 79, 299

Opening Forces, 253, 341
Opening Load
Factors, 261, 341
Predictions, 341, 351
Operations, 197
Ordnance Applications, *also see specifics,* 56
Oscillation, *see Stability*

Parachute Data Bank, xxxv
Parachutes, design features
annular, 92
bi-conical, 84
conical, solid, 83
cross, 93
disk-gap-band, 100
extended skirt, flat, 86
extended skirt, full, 87
flat-circular, solid, 82
glide (high) types, 104
glide (low) types, 103
glide (medium) types, 103
guide surface, ribbed, 90
guide surface, ribless, 91, 92
hemisflo, 97
hemispherical, 98
parafoils, 107
parawing, single keel, 105
parawing, twin keel, 106
personnel, 23, 24, 47, 49
ribbon, conical, 96
ribbon, flat-cirbular, 95
ringsail, 99
ringslot, 98
rotafoil, 101
sailwing, 108
volplane, 108
vortex-ring, 102
Pilot Chutes, 130, 428
Pocket Bands, 406
Porosity, canopy, 289
Prediction of parameters, *see specific types*
Pressure distribution measurement, 227
Pressure measurement, 232
Pressure packing, 195

Quality Assurnce, 190

Range Instrumentation, 232
Rate of Descent Measurement, 271
Release, canopy, 125
Recovery System Requirements, *also see Specific System heading,* 1
Reefing
canopy skirt, 295, 409
drogue, 424
high glide parachutes, 421
line cutters, 121
milti-stage suspension line, 298
rings, 136
Re-entry Vehicle Recovery, 5
Reliability, 326, 392
Requirements, Aerodynamic Decelerator, *also see Specific System heading,* 1, 2
Retrorockets, 322
Reynolds Number, 294
Risers, 187
RPV Recovery Systems, 2

Sandia Laboratories, 56, 215
Sandia Track, 218
Scaling Laws, 331, 332, 406
Seams, 186
Similarity Criteria, 332
Simulated Deployment Testing, 207
Simulation, Environmental, 212
Simulation, Landing Condition, 212
Skirt Hesitators, 132
Sled Launch Testing, 204
Sled Tow Testing, 205
Sled Tracks, High Speed, 217
Sleeve, 132
SMART (Track), 218
Smoke Jumping Parachute, 68
Snatch Force Derivation, 336, 337
Snatch Forces, 236, 242, 336
Snaps, 136
SNORT (Supersonic Naval Ordnance Research Track), 217
Sonar Buoy Deceleration, 59
Sounding Rocket Recovery, 5
Spacecraft Recovery, 6, 7

Special Use Parachutes, 66
Spin Recovery Systems, 49
Sport Parachute, 67
"Squidding", 249
Stability, 299, 378
Stability, Dynamic, 307
Stabilization Parachutes, 301
Staging, Decelerator System, 422
Static Line, 131
Static Stability, Circular Canopy, 299
Steady Aerodynamic Forces, 262
Stitching, Attachments, 186, 188
Stitching, Patterns, 186
Stitching, Types, 182
Stowage Components, 128
Strain Measurement, 227
Strength, Joints and Seams, 182
Strength, Material, 425
Stress Measurements, 231
Support Testing, 207
Surface-to-Air Pick-up, 66
Surface Vehicle (Cars, etc) Deceleration, 66
Suspension Lines, Effective Length, 293, 405
System Reliability, 328
System Motion, 333

Tandem Parachutes, 64, 303
Target Drone Recovery Systems, 2
Target Parachutes, 58
Tearing Strength, 209
Temperature Measurement, 230
Temperature Protection, 426
Terminal Phase, 319
Testing
  Aircraft-Tow, 204
  Air Permeability, 210
  Coefficient of Friction, 210
  (Drop) From Aircraft, 200
  Environmental Simulation, 212
  From Whirltower, 202
  Material, 208
  Simulated Deployment, 207
  Sled Launch, 204
  Sled Tow, 205
  Support, 207
  Water Tow, 205
  Wind Tunnel, 218
Test Facilities and Equipment, 213
Test Methods and Capabilities, 198
Test Tracks, 217
Test Vehicle Instrumentation, 231
Test Vehicles, 224, 227
Testile
  Fibers and yarns, 143
  Manufactured, 145
  Natural, 144
  Properties, 144
  Tensile Strength, 145
Textile Forms
  Abrasion Resistance, 154
  Air Permeability, 153
  Cords, Braided, 159
  Fabrics, 173
  Sewability, 154
  Strength to Weight Ratio, 153
  Tear Resistance, 156
  Threads, 155
  Webbings and Tapes, 162
Tonopah Test Range, 215
Torpedo Deceleration, 58
Towing (Aircraft) Testing, 204
Towing Body Wake Effects, 277
Track Test Vehicles, 227
Turning Maneuvers, 277

Vehicle Recovery, General, 2
Volume, 432

Wake Effects, 277
Wake Flow Characteristics, 373
Wake, Performance of Drogue Decelerator, 285
Wake, Supersonic, 278, 373
Wake, Transonic and Supersonic, 283, 375
Water Impact (Splashdown), 320
Water Tow Testing, 205
Weight
  Complete Decelerator Pack Weight, 434
  Complete Recovery System Weight, 434
  Decelerator System Optimization, 391
  Parachute, 433
Whirltower, 202
White Sands Missile Range, 213
Wind Tunnel Effects, 332
Wind Tunnel Testing, 204, 206, 218
Wright-Patterson Air Force Base, 56

Yuma Proving Ground (U.S. Army), 215

☆ U. S. GOVERNMENT PRINTING OFFICE: 1979 — 657-064/2301